



T. Pradeep
Publications 2016

Contents

1. Publications
2. Book Chapter
3. Lectures Delivered
4. Patents/Technology/New Grants
5. Media Reports

Journal Papers Published in 2016

1. Unusual reactivity of dithiol protected clusters in comparison to monothiol protected clusters: Studies using $\text{Ag}_{51}(\text{BDT})_{19}(\text{TPP})_3$ and $\text{Ag}_{29}(\text{BDT})_{12}(\text{TPP})_4$, Atanu Ghosh, Debasmita Ghosh, Esma Khatun, Papri Chakraborty and T. Pradeep, *Nanoscale*, (2016) (DOI: 10.1039/C6NR07692K).
2. Confined metastable 2-line ferrihydrite for affordable point-of-use arsenic free drinking water, Anil Kumar Avula, Anirban Som, Paolo Longo, Chennu Sudhakar, Radha Gobinda Bhui, Soujit Sen Gupta, Anshup, Mohan Udhaya Sankar, Amrita Chaudhary, Ramesh Kumar and T. Pradeep, *Adv. Mat.*, (2016) (DOI: 10.1002/adma.201604260).
3. Diffusion controlled simultaneous sensing and scavenging of heavy metal ions in water using atomically precise cluster – cellulose nanocrystal composites, Nishil Mohammed, Avijit Baidya, Vasanthanarayan Murugesan, Anil Kumar Avula, Mohd Azhardin Ganayee, Jyoti Mohanty, Tam, Kam (Michael) and T. Pradeep, *ACS Sustainable Chem. Eng.*, 4(11) (2016) 6167-6176 (DOI:10.1021/acssuschemeng.6b01674).
4. Structure-conserving spontaneous transformations between nanoparticles, K. R. Krishnadas, Ananya Baksi, Atanu Ghosh, Ganapati Natarajan and T. Pradeep, *Nat. Commun.*, 7 (2016) 13447 (DOI: 10.1038/ncomms13447).
5. Cooking induced corrosion of metals, Soujit Sen Gupta, Ananya Baksi, Vidhya Subramanian and T. Pradeep, *ACS Sustain. Chem. Eng.*, 4 (2016) 4781-4787 (DOI: 10.1021/acssuschemeng.6b00980).
6. Nucleolin-aptamer therapy in retinoblastoma: molecular changes and mass spectrometry–based imaging, Nithya Subramanian, Amitava Srimany, Jagat R Kanwar, Rupinder K Kanwar, Balachandran Akilandeswari, Pukhraj Rishi, Vikas Khetan, Madavan Vasudevan, T. Pradeep and Subramanian Krishnakumar, *Mol. Ther. Nucleic Acids*, 5 (2016) e358 (DOI: 10.1038/mtna.2016.70).
7. Towards a Janus cluster: Regiospecific decarboxylation of $\text{Ag}_{44}(4\text{-MBA})_{30}@\text{Ag}$ nanoparticles, Indranath Chakraborty, Anirban Som, Tuhina Adit Maark, Biswajit Mondal, Depanjan Sarkar and T. Pradeep, *J. Phys. Chem. C*, 120 (28) (2016) 15471-15479 (DOI: 10.1021/acs.jpcc.6b04769).
8. Desorption electrospray ionization (DESI) mass spectrometric imaging of the distribution of rohitukine in the seedling of *Dysoxylum binectariferum* Hook. f., Mohana Kumara P, Amitava Srimany, Suganya Arunan, Ravikanth G, Uma Shaanker R and T. Pradeep, *PLoS. ONE*, 11(6) (2016) 1-14 (DOI:10.1371/journal.pone.0158099).
9. $[\text{Au}_{25}(\text{SR})_{18}]_2^{2-}$: A noble metal cluster dimer in the gas phase, Ananya Baksi, Papri Chakraborty, Shridevi Bhat, Ganapati Natarajan and T. Pradeep, *Chem. Commun.*, 52 (2016) 8397-8400 (DOI: 10.1039/c6cc03202h).

10. Sparingly soluble constant carbonate releasing inert monolith for enhancement of antimicrobial silver action and sustainable utilization, Swathy Jakka Ravindran, Nalenthiran Pugazhenthiran, Sudhakar Chennu, Anil Kumar Avula and T. Pradeep, *ACS Sustain. Chem. Eng.*, 4 (2016) 4043-4049 (DOI: 10.1021/acssuschemeng.6b00979).
11. Diffusion and crystallization of dichloromethane within the pores of amorphous solid water, Radha Gobinda Bhui, Rabin Rajan J. Methikkalam, Soumabha Bag and T. Pradeep, *J. Phys. Chem. C*, 120 (2016) 13474-13484 (DOI: 10.1021/acs.jpcc.6b00436).
12. Monitoring of changes in lipid profiles during PLK1 knockdown in cancer cells using DESI MS, Balasubramanyam Jayashree, Amitava Srimany, Srinidhi Jayaraman, Anjali Bhutra, Narayanan Janakiraman, Srujana Chitipothu, Subramanian Krishnakumar, Lakshmi Subhadra Baddireddi, Sailaja Elchuri and T. Pradeep, *Anal. Bioanal. Chem.*, 408 (2016) 5623-5632 (DOI: 10.1007/s00216-016-9665-y).
13. Electrospun nanofiber mats as “smart surfaces” for desorption electrospray ionization mass spectrometry (DESI MS)-based analysis and imprint imaging, R. G. Hemalatha, Mohd Azhardin Ganayee and T. Pradeep, *Anal. Chem.*, 88 (2016) 5710-5717 (DOI: 10.1021/acs.analchem.5b04520).
14. Highly luminescent monolayer protected Ag₅₆Se₁₃S₁₅ clusters, C. K. Manju, Indranath Chakraborty and T. Pradeep, *J. Mater. Chem. C*, 4 (2016) 5572-5577 (DOI: 10.1039/c6tc01388k).
15. Thio residue from thermal processing of cometary ices containing carbon disulfide and ammonia, Rabin Rajan J. Methikkalam, S. Pavithraa, S. P. Murali Babu, H. Hill, Raja Sekhar, T. Pradeep and B. Sivaraman, *Adv. Space. Res.*, 58 (2016) 438-443 (DOI:10.1016/j.asr.2016.04.028).
16. Unusual reactivity of MoS₂ nanosheets, Biswajit Mondal, Anirban Som, Indranath Chakraborty, Ananya Baksi, Depanjan Sarkar and T. Pradeep, *Nanoscale*, 8 (2016) 10282-10290 (DOI: 10.1039/c6nr00878j).
17. Extraction of silver by glucose, Ananya Baksi, Mounika Gandhi, Swathi Chaudhari, Soumabha Bag, Soujit Sen Gupta and T. Pradeep, *Angew. Chem. Int. Ed.*, 55 (2016) 7777-7781 (DOI: 10.1002/anie.201510122).
18. Atomically precise and monolayer protected iridium clusters in solution, Shridevi Bhat, Indranath Chakraborty, Tuhina Adit Maark, Anuradha Mitra, Goutham De and T. Pradeep, *RSC Adv.*, 6 (2016) 26679-26688 (DOI: 10.1039/c5ra27972k).
19. Developmental patterning and segregation of alkaloids in areca nut (seed of Areca catechu) revealed by magnetic resonance and mass spectrometry imaging, Amitava Srimany, Christy George, Hemanta R. Naik, Danica Glenda Pinto, N. Chandrakumar and T. Pradeep, *Phytochemistry*, 125 (2016) 35-42 (DOI: 10.1016/j.phytochem.2016.02.002).

20. Possible isomers in ligand protected Ag₁₁ cluster ions identified by ion mobility mass spectrometry and fragmented by surface induced dissociation, Ananya Baksi, Sophie H. Harvey, Ganapati Natarajan, Vicki H. Wysocki and T. Pradeep, *Chem. Commun.*, 52 (2016) 3805-3808 (DOI: 10.1039/C5CC09119E).
21. Cluster mediated crossed bilayer precision assemblies of 1D nanowires, Anirban Som, Indranath Chakraborty, Tuhina Adit Maark, Shridevi Bhat and T. Pradeep, *Adv. Mater.*, 28 (2016) 2827-2833 (DOI: 10.1002/adma.201505775).
22. Rapid dehalogenation of pesticides and organics at the interface of reduced graphene oxide-silver nanocomposite, Dibyashree Koushik, Soujit Sen Gupta, Shihabudheen M. Maliyekkal and T. Pradeep, *J. Haz. Mater.*, 308 (2016) 192-198 (DOI:10.1016/j.jhazmat.2016.01.004).

* Some of these may appear in 2017

** "Papers with T. Pradeep as the/a corresponding author are reproduced in the following pages."

OTHER PUBLICATIONS

23. **Editorial:** Joyful Years with the Journal: Balancing the Editor–Professor Life, Thalappil Pradeep, *ACS Sustainable Chem. Eng.*, 4 (12) (2016) 6252 (DOI: 10.1021/acssuschemeng.6b02786).
24. Direct observation of the formation pathway of [Mo132] keplerates, Subharanjan Biswas, Dolores Melgar, Amitava Srimany, Antonio Rodríguez-Forteza, T. Pradeep, Carles Bo, Josep M. Poblet and Soumyajit Roy, *Inorg. Chem.*, 55 (2016) 8285-8291 (DOI: 10.1021/acs.inorgchem.5b02570).
25. **Meeting report:** Bridging innovations in academic institutions to society, T. Pradeep, Baldev Raj, V. Ramgopal Rao, Anil Kumar, Bodh Raj Mehta, G. U. Kulkarni, Tata Narasinga Rao, A. K. Ghosh, Satish Vasu Kailas, Kishore M. Paknikar, Mohan Kumar, S. G. Sreekanteswara Swamy, Anshup, Nitin Kale, Praveen Poddar, Radhica Sastry, Saket Kumar, Abhijeet Gaan, Krishnan Swaminathan, Prashanth Vijayanth, Vijaya Lakshmi, Rajeev Kumar, D. R. Prasada Raju, Debapriya Dutta, Sanjay Bajpai, Soujit Sen Gupta, Devaraju, *Curr. Sci.*, 110 (2016) 482-486.

BOOK CHAPTER

26. Evolution of atomically precise clusters through the eye of mass spectrometry, Shridevi Bhat, Indranath Chakraborty, Ananya Baksi, Raghu Pradeep Narayanan and T. Pradeep, *Nanoscience : Volume 3* Paul O'Brien (Ed.) and P John Thomas (Ed.), Royal Society of Chemistry, London, 3 (2016) 343-385 (DOI:10.1039/9781782623717-00343).



Cite this: DOI: 10.1039/c6nr07692k

Unusual reactivity of dithiol protected clusters in comparison to monothiol protected clusters: studies using $\text{Ag}_{51}(\text{BDT})_{19}(\text{TPP})_3$ and $\text{Ag}_{29}(\text{BDT})_{12}(\text{TPP})_4$ †

Atanu Ghosh, Debasmita Ghosh, Esmā Khatun, Papri Chakraborty and Thalappil Pradeep*

We report the synthesis and unique reactivity of a new green dithiol protected cluster (DTPC), $\text{Ag}_{51}(\text{BDT})_{19}(\text{TPP})_3$ (BDT and TPP are 1,3-benzenedithiol and triphenylphosphine, respectively). The cluster composition was confirmed by electrospray ionization (ESI) and matrix-assisted laser desorption ionization (MALDI) mass spectrometric studies as well as by other supporting data. Surprisingly, the chemical reactivity between this DTPC and $\text{Au}_{25}(\text{SR})_{18}$ involves only metal ion exchange in $\text{Au}_{25}(\text{SR})_{18}$ without any ligand exchange, while reactions between monothiol protected clusters (MTPCs) show both metal and ligand exchange, an example being the reaction between $\text{Ag}_{25}\text{DMBT}_{18}$ and $\text{Au}_{25}\text{PET}_{18}$ (where DMBT and PET are 2,4-dimethylbenzenethiol and phenylethanethiol, respectively). The conclusions have been confirmed by the reaction of another DTPC, $\text{Ag}_{29}(\text{BDT})_{12}(\text{TPP})_4$ with $\text{Au}_{25}\text{BT}_{18}$ (where BT corresponds to butanethiol) in which only metal exchange happens in $\text{Au}_{25}\text{BT}_{18}$. We also show the conversion of $\text{Ag}_{51}(\text{BDT})_{19}(\text{TPP})_3$ to $\text{Ag}_{29}(\text{BDT})_{12}(\text{TPP})_4$ in the presence of a second monothiol, DMBT which does not get integrated into the product cluster. This is completely different from the previous understanding wherein the reaction between MTPCs and a second thiol leads to either mixed thiol protected clusters with the same core composition or a completely new cluster core protected with the second thiol. The present study exposes a new avenue of research for monolayer protected clusters, which in turn will give additional impetus to explore the chemistry of DTPCs.

Received 29th September 2016,
Accepted 22nd November 2016

DOI: 10.1039/c6nr07692k

www.rsc.org/nanoscale

Introduction

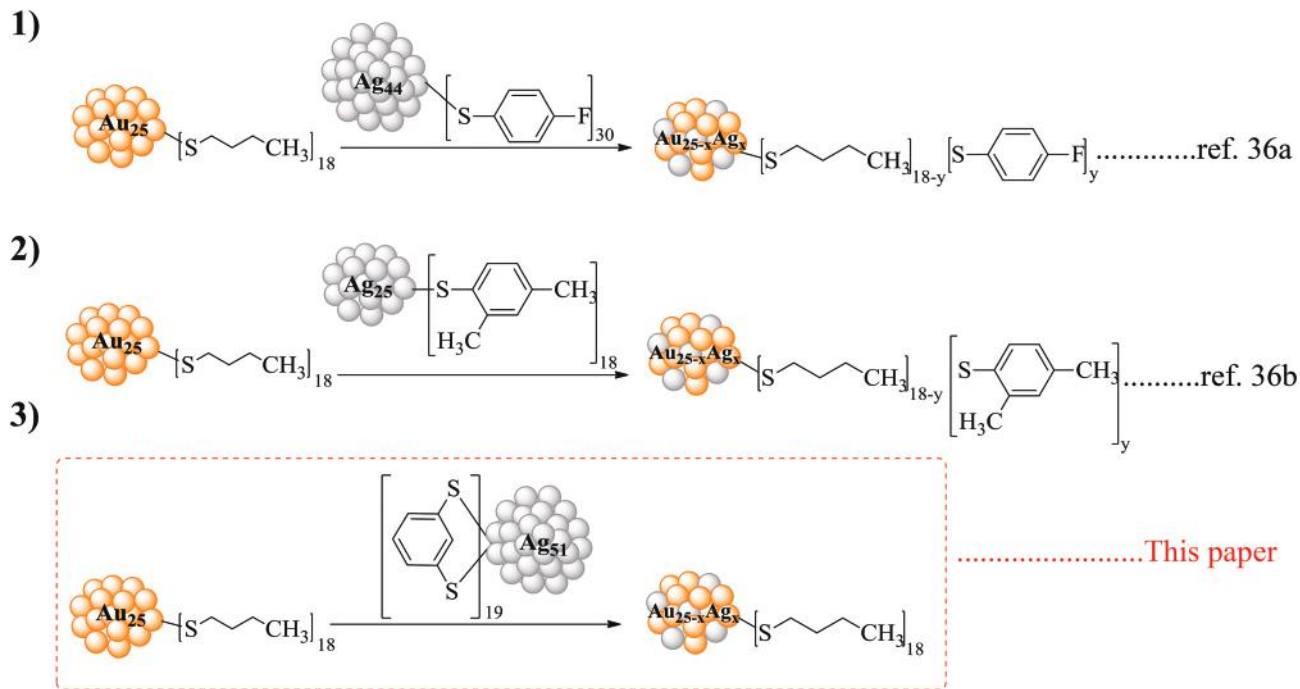
The discipline of soluble atomically precise noble metal clusters protected with thiols is expanding rapidly.^{1–4} These materials are potential candidates for drug delivery, cancer therapy, catalysis, sensing, *etc.*^{4–14} Recently, they have been used for electrochemical and photocatalytic water splitting to produce hydrogen gas which is a promising fuel for the future.^{15–17} Synthesis, characterization and crystal structures of these materials have generated increasing interest in the last decade.^{4,18–31} Introduction of new thiols which in turn results in a new cluster system is considered as a promising synthetic

strategy for this new class of materials.^{7,29,32,33} The use of new thiols has resulted in several silver clusters, especially $\text{Ag}_{25}\text{DMBT}_{18}$,³⁴ $\text{Ag}_{44}\text{FTP}_{30}$,²³ $\text{Ag}_{44}\text{MBA}_{30}$,²² *etc.* (DMBT, FTP and MBA refer to 2,4-dimethylbenzenethiol, 4-fluorothiophenol and 4-mercaptobenzoic acid, respectively). The introduction of dithiols has led to completely new cluster systems such as $\text{Ag}_{29}(\text{BDT})_{12}(\text{TPP})_4$ (BDT and TPP are 1,3-benzenedithiol and triphenylphosphine respectively);³⁵ the chemistry of such systems is yet to be explored in detail. The metal thiol interface in such dithiol protected clusters (DTPCs) is distinctly different from the monothiol system and this difference must have profound influence on their chemistry and associated properties. In this paper, we have presented an unprecedented chemical reaction of a dithiol protected silver cluster in one of the most studied class of chemical reactions, namely metal atom substitution, using our newly reported DTPC, $[\text{Ag}_{51}(\text{BDT})_{19}(\text{TPP})_3]^{3-}$. This spontaneous reaction in solution at room temperature transforms only the metal core leaving the thiolate shell intact, in contrast to monothiol protected clusters (MTPCs), where simultaneous changes of both the core and the shell occur during such an event.³⁶ This difference in the chemistry of monothiol and dithiol is compared in Scheme 1. Besides, we

DST Unit of Nanoscience (DST UNS) and Thematic Unit of Excellence, Department of Chemistry, Indian Institute of Technology Madras, Chennai 600036, India.

E-mail: pradeep@iitm.ac.in; Fax: +91-44 2257-0545

† Electronic supplementary information (ESI) available: UV-vis and ESI MS spectra of BT and OT ligated Au_{25} cluster; UV-vis and ESI MS spectra of cluster II; MALDI MS spectra for cluster I and cluster II; time dependent ESI MS spectra for inter-cluster reactions and ligand exchange reactions; concentration dependent ESI MS spectra for the inter-cluster reaction; ESI MS and UV-vis spectra comparison for ligand catalyzed inter-cluster conversion process. See DOI: 10.1039/c6nr07692k



Scheme 1 Reactions (1) and (2) are reproduced from the recent literature which show that the well known $\text{Au}_{25}\text{BT}_{18}$ cluster undergoes both metal and ligand exchange reactions upon exposure to monothiol protected $\text{Ag}_{44}(\text{FTP})_{30}$ or $\text{Ag}_{25}(\text{DMBT})_{18}$ clusters. Reaction (3) shows that unlike (1) and (2), the $\text{Au}_{25}\text{BT}_{18}$ cluster undergoes only metal exchange reaction upon exposure to the newly reported dithiol protected $\text{Ag}_{51}(\text{BDT})_{19}(\text{TPP})_3$ cluster.

show the conversion of one cluster to another, catalyzed by a different thiol which by itself does not get integrated into the reactant or the product. This observation is also completely different from the behavior of MTPCs, which has been known for a few years.^{1,18,19,37,38-43} The difference in chemistry involving the conversion of DTPCs is shown in Scheme 2.

Experimental

Chemicals and materials

Butanethiol (BT, 99%), octanethiol (OT, 99%), 1,3-benzenedithiol (BDT, $\geq 99\%$), 2,4-dimethylbenzenethiol (DMBT, 99%), sodium borohydride (95%), tetraoctylammonium bromide (TOABr, 98%), and *trans*-2-[3-(4-*tert*butylphenyl)-2-methyl-2-propenylidene] malononitrile (DCTB, $>98\%$) were purchased from Sigma-Aldrich. Gold(III) chloride trihydrate was synthesized in our laboratory. Silver nitrate (AgNO_3) was purchased from Rankem chemicals and PPh_3 was from Spectrochem. All the chemicals were used as received without further purification. All solvents (dichloromethane (DCM), *n*-hexane, tetrahydrofuran (THF), dimethylformamide (DMF), chloroform (CHCl_3) and methanol) were purchased from Rankem and were of analytical grade. The water used for the syntheses was of Milli-Q grade with a resistivity of 18.2 M Ω cm.

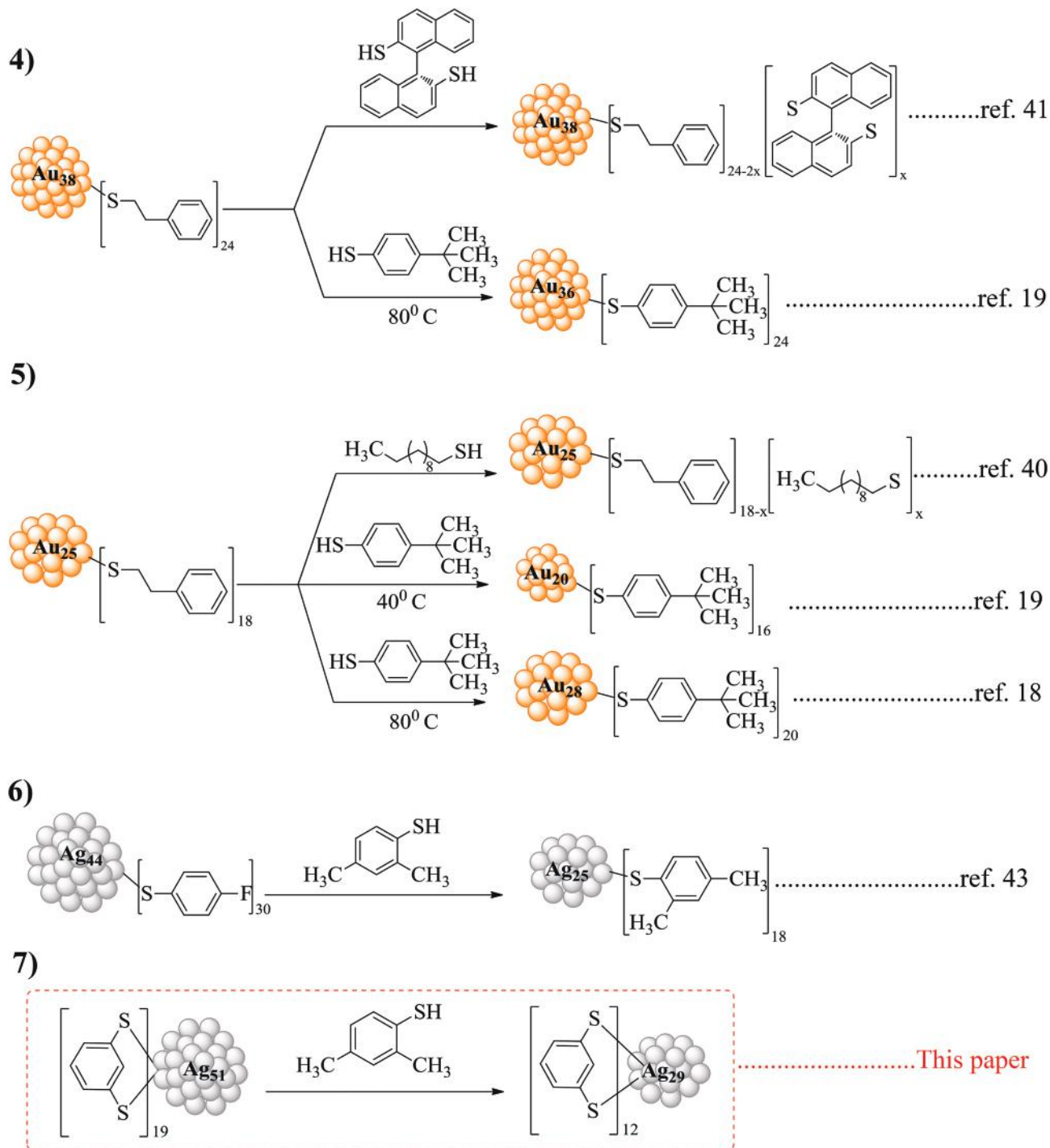
Synthesis of $\text{Ag}_{51}(\text{BDT})_{19}(\text{TPP})_3$

The material was synthesized by modifying the procedure used for $\text{Ag}_{29}(\text{BDT})_{12}(\text{TPP})_4$.³⁵ Initially 20 mg of AgNO_3 was dissolved

in 5 mL of methanol. To that, 9 mL of chloroform was added. After 1 min of stirring, 0.5 mL of chloroform solution containing 13.5 μL of BDT was added to the above mixture and it was covered with a black cloth. After 5 min, 0.5 mL of the chloroform solution containing 200 mg of PPh_3 was added to the above mixture under stirring conditions. Ice cold aqueous solution (0.5 mL) of NaBH_4 (11 mg) was added to the above mixture after 5 minutes. Immediately the color of the solution changed from colorless to dark brown upon addition of NaBH_4 . The reaction was continued for 3 h under dark conditions. After 3 h of stirring, the green colored supernatant was collected through centrifugation. Centrifugation was carried out for 10 min at a speed of 14 000 rpm. The volume of the supernatant was reduced to 5 mL by rotary evaporation. Then the supernatant was cleaned with millipore water 3–4 times to remove the water-soluble ingredients. During this process, the volume of the supernatant was reduced to 1.5 mL. Then the cluster was precipitated from the above solution by the addition of an equal volume of hexane. The precipitate was collected through centrifugation (3000 rpm, 3 min) and dissolved in DMF for further characterization. Hereafter we call it cluster I.

Synthesis of $\text{Au}_{25}\text{BT}_{18}$ and $\text{Au}_{25}\text{OT}_{18}$

An $\text{Au}_{25}\text{BT}_{18}$ cluster was synthesized by using a reported method.⁴⁴ Briefly, $\text{HAuCl}_4 \cdot 3\text{H}_2\text{O}$ (40 mg) was dissolved in 7.5 mL of THF and 65 mg of TOABr was added to this under stirring conditions. Stirring was continued for 15 min. During



Scheme 2 Reactions (4)–(6) are reproduced from previous reports which show that monothiol protected Au₂₅, Au₃₈ and Ag₄₄ clusters react with a second thiol leading to either mixed thiol protected clusters with the same core composition or a new cluster core protected with the second thiol. Unlike the above reactions, in a DTCP (shown as reaction (7)), the second thiol does not get integrated into the product. The second thiol acts as a catalyst for the conversion of Ag₅₁BTD₁₉ to Ag₂₉BTD₁₂.

this period, the color of the solution changed from yellow to orange-red. To this solution, 55 μL of butanethiol (BT) was rapidly added under vigorous stirring (1200 rpm). The mixture was stirred for 2 h during which it turned colorless. After that, 39 mg of NaBH₄ dissolved in 2.5 mL of ice-cold water was

added rapidly to the reaction mixture, again under vigorous stirring. Stirring was continued for 6 h. The solvent was removed from the reaction mixture by rotary vacuum evaporation. Methanol was added for the removal of thiol and other impurities. The insoluble cluster was collected as a precipitate

through centrifugation. The process was repeated 4 times and subsequently 4 mL acetone was added to dissolve the cluster. Other impurities such as insoluble thiolate and the Au₁₄₄ cluster were removed by centrifugation. The supernatant was collected and dried by rotary evaporation. Au₂₅OT₁₈ was synthesized following the same procedure and 89 μ L thiol was used for the synthesis.

Reaction of Ag₅₁(BDT)₁₉(TPP)₃ (cluster I) with Au₂₅BT₁₈ or Au₂₅OT₁₈

A required amount of the Ag₅₁BDT₁₉TPP₃ cluster (cluster I) was dissolved in 3 mL of DMF in such a way that the absorbance at 420 nm was 1. To this solution, different quantities of the Au₂₅BT₁₈ cluster were added and UV-vis spectra of the mixture were taken at different time intervals. Each time 200 μ L of the sample mixture was taken from the mixture and diluted three times for ESI MS measurements. The same was repeated with the Au₂₅OT₁₈ cluster.

Reaction of Ag₅₁(BDT)₁₉(TPP)₃ (cluster I) with DMBT thiol

Ag₅₁BDT₁₉TPP₃ cluster (cluster I) was dissolved in 3 mL of DMF in such a way that the final absorbance at 420 nm was 0.8. To that, different volumes of DMBT were added. The UV-vis spectra of the mixture were taken at different time intervals. It was observed that during this process, the color of the mixture changed from green to red. Each time, a 200 μ L sample mixture was taken from the mixture and was diluted twice for ESI MS measurements and diluted four times for fluorescence measurements.

Characterization

UV-vis measurements

Absorption spectra of the cluster solution were measured with a Perkin Elmer Lambda 25 UV-vis absorption spectrophotometer. Spectra were typically measured in the range of 190–1100 nm. The clusters were dissolved in the respective solvents and spectra were recorded in quartz cells with a 10 mm path length.

Luminescence measurements

Luminescence measurements were carried out using the HORIBA JOBIN VYON Nano Log instrument. The band pass for excitation and emission was set at 3 nm. Diluted cluster solutions were used for these measurements.

MALDI MS measurements

Matrix-assisted laser desorption ionization (MALDI) mass spectra of the clusters were measured using a Voyager DE PRO Bio spectrometry Workstation (Applied Biosystems) MALDI TOF MS instrument. A pulsed nitrogen laser of 337 nm was used for desorption ionization and TOF was operated in the delayed extraction mode. Typical delay times employed were of the order of 75–150 ns. DCTB in DMF (12.5 mg mL⁻¹) was used as the matrix. The measurements were performed in

negative ion mode. For each measurement, typically 500 scans were acquired.

ESI MS measurement

A Waters Synapt G2-Si High Definition mass spectrometer equipped with Electrospray ionization, Matrix-assisted laser desorption ionization and ion mobility separation was used. All the samples were analyzed in the negative mode of electrospray ionization. The instrumental parameters were first optimized for Ag₅₁(BDT)₁₉ and other samples were analyzed using similar settings with slight modifications depending on the sample. The instrument was calibrated using CsI as the calibrant.

XPS

X-ray photoelectron spectroscopy (XPS) measurements were performed using an Omicron ESCA Probe spectrometer with polychromatic Mg Ka X-rays ($h\nu = 1253.6$ eV). The powder sample was taken on a Mo plate using double sided adhesive conductive carbon tape. Experiments were carried out at an X-ray power of 300 W and pass energies of 50 eV for survey scans and 20 eV for specific regions. The base pressure of the instrument was in the 10⁻¹⁰ mbar range during spectrum collection. Binding energies of the core levels were calibrated with C 1s B.E, set at 284.9 eV.

SEM and EDAX analyses

Scanning electron microscopy (SEM) and energy dispersive X-ray (EDAX) analyses were performed in a FEI QUANTA-200 SEM. For measurements, the powder sample was used.

Characterization of Au₂₅BT₁₈ and Au₂₅OT₁₈

Characterization of Au₂₅ was reported earlier in great detail by various studies. In view of this, we have presented only essential details of characterization here (Fig. S1†). The UV-vis and ESI MS spectra of the as synthesized Au₂₅BT₁₈ cluster are comparable with the published data (S1A†). Similarly, UV-vis and ESI MS spectra presented in Fig. S1B† confirm the formation of the Au₂₅OT₁₈ cluster.

Results and discussion

Most of the results of chemical reactivity are presented with our newly synthesized cluster I. The synthesis of cluster I involves the known synthetic protocol of Ag₂₉(BDT)₁₂(TPP)₄ (hereafter we call it as cluster II) with slight modification.³⁵ We note that the formation of cluster I is strongly affected by the concentration of NaBH₄ used in the synthesis. We varied this for a fixed concentration of Ag⁺ and thiol. At a lower concentration of NaBH₄, only cluster II was formed, whereas at a higher concentration, we observed a completely new cluster with associated properties. This drastic change in the product composition is depicted in Fig. 1 where the synthesis was performed at three concentrations of NaBH₄ (Fig. 1A₁, B₁ and C₁) keeping the concentration of other reactants and conditions the same. While cluster II formed at every concentration of

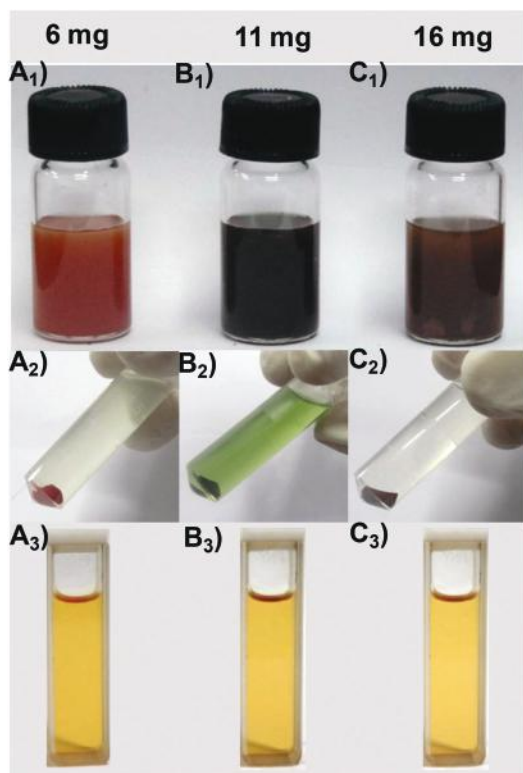


Fig. 1 Photographs of synthesis. A_1 , B_1 and C_1 show the synthesis performed using 6, 11 and 16 mg of NaBH_4 , respectively. This corresponds to 10, 19 and 28 mM of NaBH_4 in the reaction mixture. A_2 , B_2 and C_2 are the results of centrifugation of A_1 , B_1 and C_1 , respectively. Image B_2 shows that the green supernatant is formed only from 11 mg of NaBH_4 . The precipitates in A_2 , B_2 and C_2 were dissolved in DMF and the photographs of the corresponding DMF solutions are presented in A_3 , B_3 and C_3 , respectively.

NaBH_4 (precipitate shown in Fig. 1A₂, B₂ and C₂), cluster I formed only for 11 mg of NaBH_4 (green supernatant, Fig. 1B₂). Using the polarity difference of solvents, two clusters were separated. In all the cases, the precipitate was dissolved in DMF. Photographs of the DMF solutions of the clusters are shown in Fig. 1A₃, B₃ and C₃. Measured optical and mass spectral data of all the above cluster solutions matched with those reported for $\text{Ag}_{29}\text{BDT}_{12}$ (Fig. S2†).³⁵ While this is identified as $\text{Ag}_{29}\text{BDT}_{12}$, the other cluster (cluster I, green supernatant, Fig. 1B₂) shows a completely different optical spectrum presented in Fig. 2A. The spectrum shows 5 features at 775, 698, 665, 605 and 415 nm. Under the synthesis conditions, only cluster formation is possible and no complex or silver sulfide colloids are likely. Comparison of the spectrum with all the silver clusters known so far has also suggested the same. A photograph of cluster I in visible light, presented in the inset of Fig. 2A, shows that the material is green in color which is also different from the color of cluster II.

The optical features of purified cluster I are completely different from the well known reported silver clusters, $\text{Ag}_{25}\text{DMBT}_{18}$,³⁴ $\text{Ag}_{29}\text{BDT}_{12}$,³⁵ $\text{Ag}_{44}(\text{SR})_{30}$,^{22,23} $\text{Ag}_{152}(\text{PET})_{60}$,⁴⁵ $\text{Ag}_{68}(\text{SBB})_{34}$,⁴⁶ $\text{Ag}_7(\text{DMSA})_4$ ⁴⁷ and $\text{Ag}_9(\text{H}_2\text{MSA})_7$.⁴⁸ This prompted us to measure the mass spectrum of cluster I to

determine the exact molecular mass and formula of the $\text{Ag}_m(\text{BDT})_n$ cluster. The ESI MS was measured in $-ve$ mode. Details of the sample preparation and instrumental conditions are given in the Experimental section. The mass spectrum is presented in Fig. 2B with a mass range of m/z 1000–10 000. There is a peak at m/z 2721.56. The expanded spectrum presented in Fig. S3† shows that the peaks are separated by m/z 0.33 which implies that the cluster core contains 3- charge. The corresponding composition is $[\text{Ag}_{51}(\text{BDT})_{19}]^{3-}$. The presence of a small quantity of $[\text{Ag}_{29}(\text{BDT})_{12}]^{3-}$ as a side product is marked with a blue asterisk. ESI MS data (Fig. 2B) shows that the cluster is highly pure as no peaks other than those of interest were found in the mass range of m/z 1000–10 000. The isotopic structures of silver are important to assign accurate composition. In view of the difference in the abundances of ^{107}Ag and ^{109}Ag isotopes, the isotopic pattern is likely to reflect characteristic features for this cluster. In Fig. 2C we presented a comparison of the experimental isotopic pattern (black trace) with simulation (red trace) which matches perfectly. Minor variations in the intensities of adjacent peaks are matched perfectly besides a complete match of the mass spectral peak positions. The composition $[\text{Ag}_{51}(\text{BDT})_{19}]^{3-}$ may be confirmed from this spectra. We note here that such an accurate match of isotopic patterns is rarely seen in cluster mass spectrometry of clusters. Confirmation of the assignment was also made with the help of a MALDI MS study. MALDI MS of the sample was taken using the matrix, *trans*-2-[3-(4-*tert*butylphenyl)-2-methyl-2-propenylidene] malononitrile, popularly known as DCTB. At threshold fluence, the mass spectrum (black trace, Fig. S4†) shows a monoanionic peak at m/z 8162 which is assigned to $[\text{Ag}_{51}\text{BDT}_{19}]^-$ and a dianionic peak at m/z 4081. The MALDI MS spectrum shows silver attached peaks along with the molecular ion peak which was also seen for cluster II (red trace, Fig. S4†). Both the dithiol protected clusters show the same behavior which is quite different from the MALDI MS of monothiol protected clusters reported so far. This is the first report on MALDI MS of dithiol protected atomically precise silver clusters. At present, we do not have any definite explanation for the above observation. It could be that in dithiol protected clusters, there may be hanging ligands with one thiol attached to the cluster core, the other end being free may bind with the silver ion. Or the sulphur bound to the cluster core readily accepts free silver. MALDI MS analyses also show that the cluster is highly pure as no peaks other than those of interest were found in the mass range of m/z 3000–50 000 (Fig. S5†). With increasing laser fluence, additional peaks were observed in the mass spectrum. The peaks appeared at regular intervals of $\sim m/z$ 8100. These peaks are due to the dimer ($\sim m/z$ 16 200), trimer ($\sim m/z$ 24 300), tetramer ($\sim m/z$ 32 400) and pentamer ($\sim m/z$ 40 500) of the $\text{Ag}_{51}\text{BDT}_{19}$ cluster. Such association reactions are expected in the gas phase upon desorption.⁴⁹ The corresponding peaks are marked in Fig. S5.† This is the first report where monolayer protected silver clusters are seen to form aggregates upon exposure to higher laser fluence. The appearance of dimers, trimers and oligomers of cluster I suggests the feasibility of the interaction between the clusters.

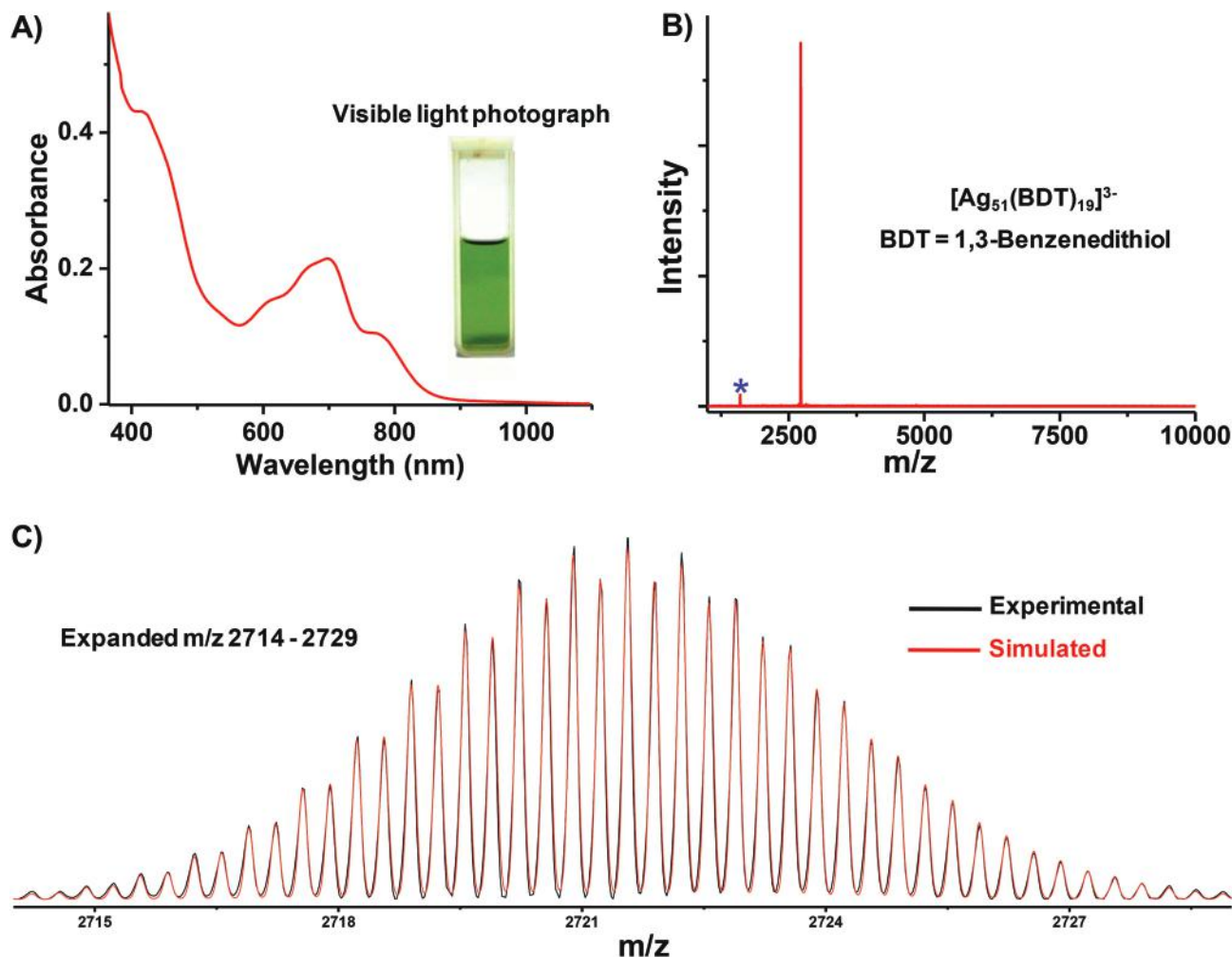


Fig. 2 (A) UV-vis spectrum of the purified cluster in DMF. The spectrum has distinct features which are characteristic of small clusters. Inset: Visible light photograph of the cluster solution. (B) ESI MS spectrum of the purified cluster in negative mode, in the region of m/z 1000–10 000. The main peak at m/z 2721.56 corresponds to $[\text{Ag}_{51}(\text{BDT})_{19}]^{3-}$. The peak at m/z 1603 is marked with a blue asterisk which is due to the presence of a small quantity of the $[\text{Ag}_{29}(\text{BDT})_{12}]^{3-}$ cluster as a side product. (C) Comparison of the experimental (black trace) and simulated (red trace) isotopic patterns which match perfectly. Minor variations in intensity between successive peaks match perfectly besides a complete match of the mass spectral positions. It confirms the assigned composition, $[\text{Ag}_{51}(\text{BDT})_{19}]^{3-}$.

The composition was further proven by elemental analysis. An Ag:S ratio of 1:0.76 was seen in energy dispersive spectroscopic (EDS) analysis, in agreement with the formula (Fig. S6[†]). X-ray photoelectron spectroscopy (XPS) shows an Ag $3d_{5/2}$ peak at 368.0 eV and S $2p_{3/2}$ at 163.0 eV (Fig. S7[†]). Although it is likely that both Ag(I) and Ag(0) are present in the cluster, no clear separation between them was seen in XPS (Fig. S7A[†]). These observations are in agreement with the expected values of such clusters. The Ag:S ratio value was 1:0.74, in agreement with the expected composition. The number of phosphines in cluster **I** was confirmed by detailed ESI MS studies (Fig. S8[†]). The spectrum shows sequential loss of three phosphines, from the parent peak. The peak at m/z 2721.56 corresponds to $[\text{Ag}_{51}(\text{BDT})_{19}]^{3-}$. So the actual formula of the parent material is $[\text{Ag}_{51}(\text{BDT})_{19}(\text{TPP})_3]^{3-}$. The yield of cluster **I** is only 30–35% as both the clusters (**I** (supernatant) and **II** (precipitate)) are formed together in a single synthesis

(Fig. 1B₂). The purified material is stable for 3–4 days in the solution phase at 30 °C and for a month at 4 °C. Cluster **I** is weakly luminescent. A comparison of the luminescence properties of cluster **I** and cluster **II** is shown in Fig. S9[†].

An aspect of cluster science studied intensely today is chemical reactivity.^{36,50–52} We investigated the reaction between cluster **I** and the well known $\text{Au}_{25}\text{BT}_{18}$ cluster. In general, reactions between clusters exchange both the metal and the ligand between the reacting clusters.³⁶ It was surprising to see that cluster **I** underwent reactions with $\text{Au}_{25}\text{BT}_{18}$ by metal atom exchange alone without affecting the ligand shell. The results of the investigation are presented in Fig. 3 where, as a function of time of reaction, more and more silver of the cluster **I** get substituted by gold of $\text{Au}_{25}\text{BT}_{18}$ leading to $[\text{Ag}_{51-x}\text{Au}_x\text{BDT}_{19}]^{3-}$ alloy clusters. In 45 minutes, the reaction mixture loses all of cluster **I** indicating high chemical reactivity of the system. Corresponding transfer is also seen in $\text{Au}_{25}\text{BT}_{18}$

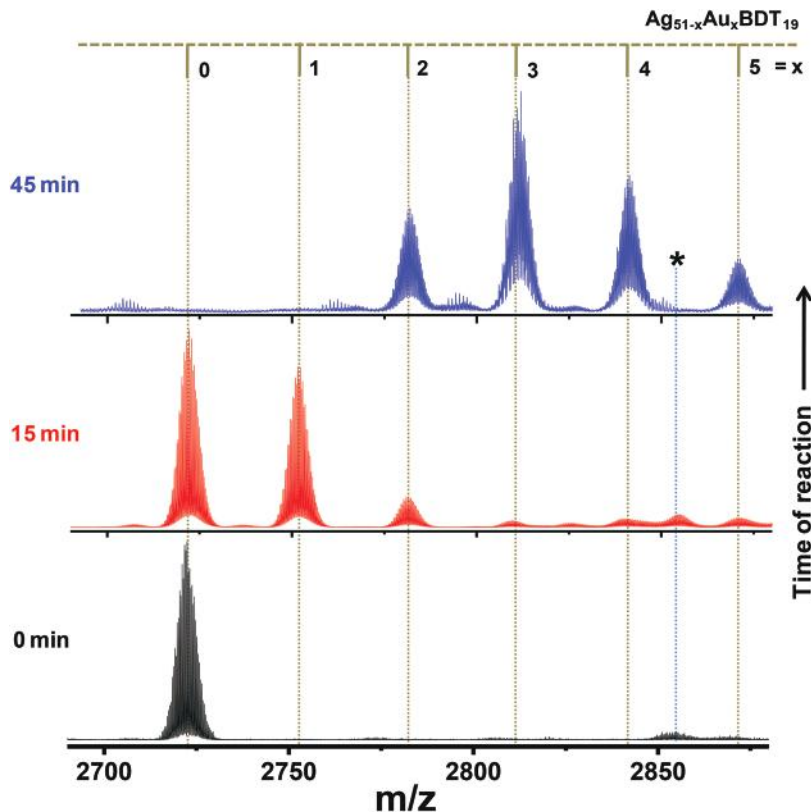


Fig. 3 Time dependent ESI MS spectra of the cluster I region during the reaction with the $\text{Au}_{25}\text{BT}_{18}$ cluster. As the time of reaction increases, more and more silver gets substituted by gold derived from $\text{Au}_{25}\text{BT}_{18}$, leading to the formation of $[\text{Ag}_{51-x}\text{Au}_x\text{BDT}_{19}]^{3-}$ alloy clusters. Within 45 min of reaction, the parent peak vanishes completely. Although metals exchange between the two reacting clusters, there is no change in the ligand shell of the cluster. All clusters could be defined.

as well where systematic silver addition occurs. Fig. 4 shows the formation of the $[\text{Au}_{25-y}\text{Ag}_y\text{BT}_{18}]^-$ alloy cluster. The absence of change in the ligand structure is uncommon in the reaction of Au_{25} .³⁶ We noted that no free BT or BDT enters into the solution. This chemical reactivity was also probed by optical absorption spectroscopy presented in Fig. S10.† The reaction was studied at various concentrations of clusters. The results are presented in Fig. S11.† In order to confirm the absence of a ligand exchanged product, we repeated the reaction of cluster I with the $\text{Au}_{25}\text{OT}_{18}$ cluster. The results of this reaction are presented in Fig. S12.† As the masses of the protecting ligands, BT (m/z 90) and OT (m/z 146) are quite different (Fig. S12A†), it is expected that new peaks will appear in the mass spectrum if ligands are changed in the reaction. In the $\text{Au}_{25}\text{OT}_{18}$ region we did not see any new peaks other than the metal exchanged product $[\text{Au}_{25-y}\text{Ag}_y\text{OT}_{18}]^-$ (Fig. S12B†). Fig. S12C and D† show the comparison of the $[\text{Ag}_{51-x}\text{Au}_x\text{BDT}_{19}]^{3-}$ region upon reaction of cluster I and $\text{Au}_{25}\text{BT}_{18}$ (and $\text{Au}_{25}\text{OT}_{18}$). All the peaks are the same for these two cases ($\text{Au}_{25}\text{BT}_{18}$ and $\text{Au}_{25}\text{OT}_{18}$). The absence of new peaks with differently ligated Au_{25} clusters confirms that the ligand shell is not involved in this type of reactions. We hope that the above observation will be helpful for the synthesis of new alloy clusters keeping the ligand shell unaffected.

We were also curious to study the difference between the reactivity of clusters I and II in the metal atom exchange reaction. For this, an equimolar mixture of clusters I and II was reacted with $\text{Au}_{25}\text{BT}_{18}$. While a rapid disappearance of cluster I was observed, cluster II underwent a much slower reaction. Mass spectral data at two different times are presented in Fig. S13.† Cluster II also underwent only the metal exchange reaction when it was reacted with $\text{Au}_{25}\text{BT}_{18}$ separately (Fig. S14†). These experiments show that while dithiol on the cluster surfaces cannot be exchanged with monothiol, metal atom exchange is feasible. Independent studies have also shown that dithiols in solution can exchange monothiol on Au_{25} surfaces (Fig. S15†). These observations together would imply that metal atom alone exchanges are more likely than metal thiolate exchanges in these clusters. In contrast, metal thiolate ligand and metal thiolate exchanges are manifested in $\text{Au}_{25}\text{SR}_{18}$.³⁶ However, both cluster I and cluster II undergo only metal exchanges. It is likely that thermodynamics of these processes are critical in such events. Further insight into the process requires understanding of the initial metal atom transfer without disrupting the dithiol binding. The nature of the intermediate as well as inter-cluster approach facilitating atom transfer are important aspects to study further. We have very little understanding of the events involved in the inter-cluster

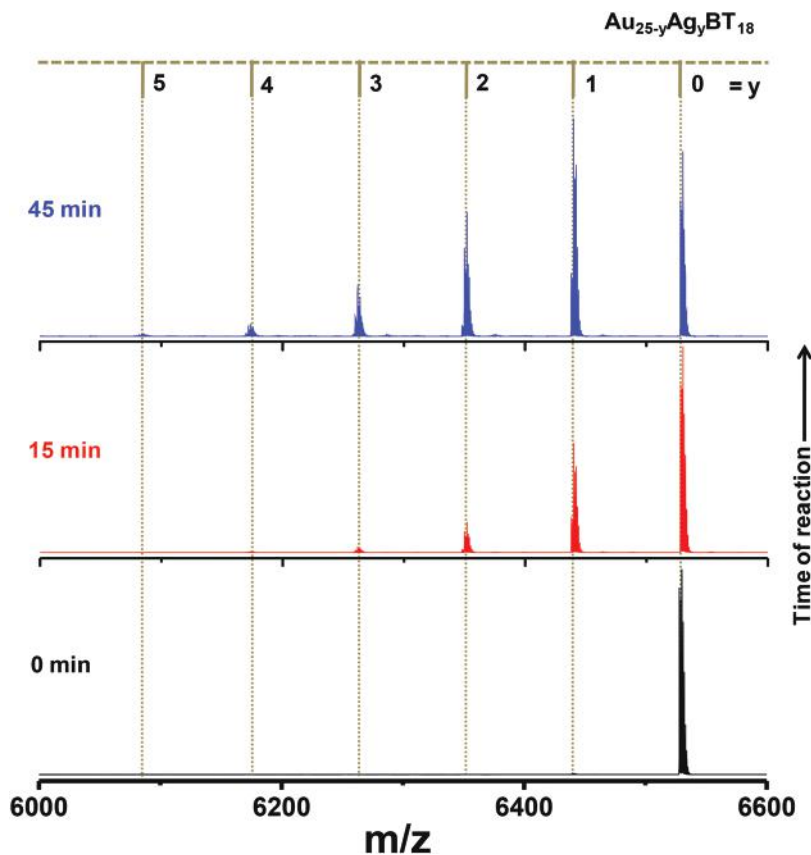


Fig. 4 Time dependent ESI MS spectra of the $\text{Au}_{25-y}\text{Ag}_y\text{BT}_{18}$ cluster region during the reaction with cluster I. New peaks appear at the lower mass region with a separation of m/z 89. This is due to the substitution of gold (m/z 197) of the $\text{Au}_{25}\text{BT}_{18}$ cluster with Ag (m/z 108) of cluster I. The peaks are marked as $[\text{Au}_{25-y}\text{Ag}_y\text{BT}_{18}]^-$. No peaks other than those due to metal exchange were found.

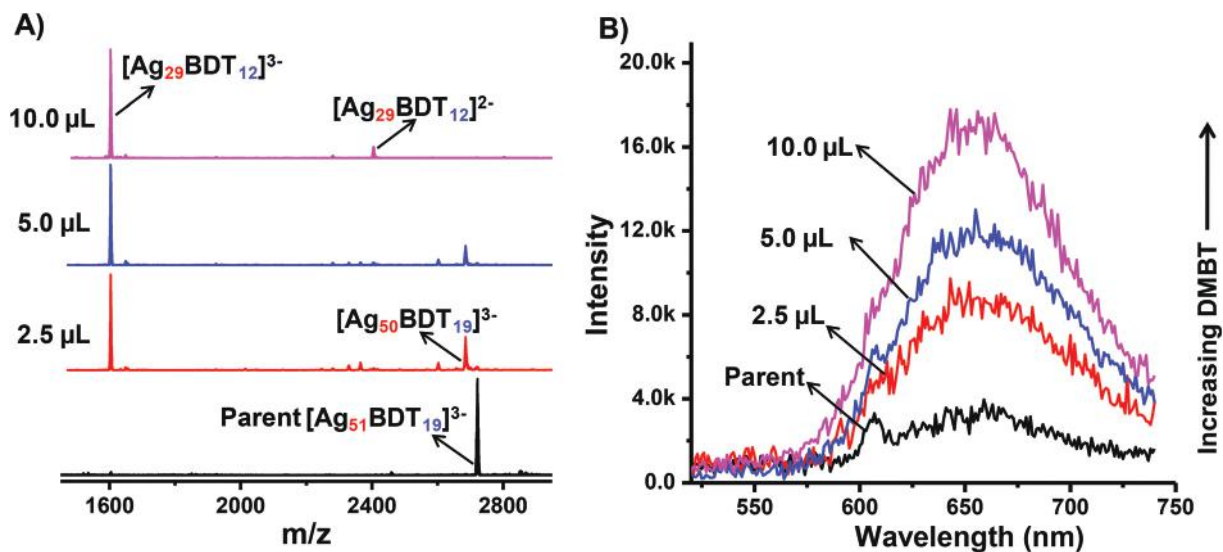


Fig. 5 Thiol (DMBT) catalyzed inter-conversion of cluster I to cluster II. (A) Comparison of ESI MS spectra of parent cluster I with reaction mixtures containing different volumes of DMBT with a fixed amount of cluster I after 24 h of reaction. The ESI MS spectrum of the parent cluster I is presented with a black trace. Red, blue and pink traces are the ESI MS spectra of 2.5, 5 and 10 μL DMBT added solutions of cluster I. Complete conversion of cluster I to cluster II occurred for 10 μL of DMBT whereas for 2.5 and 5 μL of DMBT, more cluster I remained without conversion. (B) Emission spectra of the corresponding solutions. Intensity of emission enhances with increasing the volume of DMBT in solution. As cluster II is more luminescent than cluster I, enhancement of emission intensity confirms the formation of more and more cluster II in solution upon increasing the volume of DMBT. The sample was excited at 450 nm.

reaction. In our recent paper we have discussed the possible mechanism of the inter-cluster reaction between two mono thiol protected clusters.^{36b} Here the situation is more complicated due to the presence of dithiol.

The co-existence of clusters **I** and **II** and the preferential formation of either of them as a function of NaBH_4 prompted us to study their inter-conversion. To our surprise, we noted that upon addition of DMBT (2,4-dimethylbenzenethiol) to cluster **I**, mass spectra showed the appearance of cluster **II** with an increase of time. This is shown in Fig. S16.† The peak at m/z 1603 due to cluster **II** increases gradually while the peak at m/z 2721 due to cluster **I** disappears. We noted that this transformation occurs with rapid loss of one silver atom leading to the formation of $[\text{Ag}_{50}\text{BDT}_{19}]^{3-}$ marked in Fig. S16† and 5A. The cluster $[\text{Ag}_{50}\text{BDT}_{19}]^{3-}$ may be viewed as the dimer of $\text{Ag}_{25}(\text{BDT})_9$ linked with BDT as BDT is a dithiol. $\text{Ag}_{25}(\text{BDT})_9$ is equivalent to $\text{Au}_{25}(\text{SR})_{18}$ and the dimer of the same has been detected recently.⁵³ At the end of the reaction, the solution consists of only cluster **II** as seen in the optical absorption spectra, and the spectra of clusters **I** and **II** are compared with the reaction product in Fig. S17.† The mass spectra shown in Fig. S16† show that there is no incorporation of DMBT in the cluster formed, which implies that it acts as a catalyst in the reaction. Experimental and simulated isotope distributions of the final product are shown in Fig. S16B and C† which confirm the formation of cluster **II**. We have also seen that the inter-cluster conversion is highly dependent on the concentration of DMBT. Fig. 5A shows that after 24 h of reaction, while complete conversion occurs for 10 μL of DMBT (pink trace), for 2.5 and 5 μL of DMBT more clusters remain without conversion (red and blue traces). Emission spectra of the corresponding samples are shown in Fig. 5B. As cluster **II** is more luminescent than cluster **I**, the intensity of the emission spectra increases with an increase in the amount of cluster **II** in solution. This reflects in the emission spectra of different volumes of DMBT-added cluster **I** solutions. In the case of the 10 μL DMBT-added cluster solution, the intensity is maximum as the amount of cluster **II** is maximum (Fig. 5B). Such catalytic inter-cluster transformation by thiols has not been reported earlier. The transformation is not a reversible process. It is not specific to DMBT also. The transformation can be carried out in the presence of other thiols (Fig. S18†).

Conclusions

In conclusion, we show the extreme dependency of the reducing agent concentration in cluster synthesis which resulted in the formation of a new cluster, $\text{Ag}_{51}(\text{BDT})_{19}(\text{TPP})_3$. The cluster undergoes metal atom exchange without ligand exchange, upon reaction with $\text{Au}_{25}(\text{SR})_{18}$. The complete absence of ligand exchange products has been proven by carrying out reactions with two differently ligated Au_{25} clusters. The experiment showed an increased reactivity of $\text{Ag}_{51}(\text{BDT})_{19}(\text{TPP})_3$. An unusual inter-cluster transformation catalyzed by thiol is demonstrated. We hope that these unusual properties will

generate increasing interest in dithiol protected clusters and exploration of their properties. While the inter-cluster reaction and exchange of metal atoms without ligand exchange poses new questions about the intermediate and mode of atom transfer, these questions require computational inputs with high sophistication. Cluster dimers mediated through thiols⁵³ and the possibility of metal transfer upon interaction of clusters³⁶ would suggest that the current observations are indeed feasible.

Conflicts of interest

The authors declare no competing financial interests.

Acknowledgements

We thank the Department of Science and Technology, Government of India for constantly supporting our research program on nanomaterials. A. G. thanks the University Grants Commission and P. C. thanks the Council of Scientific and Industrial Research (CSIR) for their research fellowships. D. G. and E. K. thank IIT Madras for Institute Doctoral Fellowships. A. G. and D. G. also thank Dr Ananya Baksi and Mr Depanjan Sarkar for their help during ESI MS measurement. A. G. also thanks Dr Aniruddha Molla and Jyotirmoy Ghosh for their help and suggestions.

References

- 1 W. Kurashige, Y. Niihori, S. Sharma and Y. Negishi, *Coord. Chem. Rev.*, 2016, **320–321**, 238–250.
- 2 R. Jin, *Nanoscale*, 2015, **7**, 1549–1565.
- 3 I. Diez, M. I. Kanyuk, A. P. Demchenko, A. Walther, H. Jiang, O. Ikkala and R. H. A. Ras, *Nanoscale*, 2012, **4**, 4434–4437.
- 4 A. Mathew and T. Pradeep, *Part. Part. Syst. Charact.*, 2014, **31**, 1017–1053.
- 5 L. R. Arcot, K. M. A. Uddin, X. Chen, X. Wenchao, K. Xianming, L. S. Johansson, R. H. A. Ras and O. J. Rojas, *Cellulose*, 2015, **22**, 4027–4034.
- 6 P. Kunwar, J. Hassinen, G. Bautista, R. H. A. Ras and J. Toivonen, *ACS Nano*, 2014, **8**, 11165–11171.
- 7 Y. Wang, X.-K. Wan, L. Ren, H. Su, G. Li, S. Malola, S. Lin, Z. Tang, H. Häkkinen, B. K. Teo, Q.-M. Wang and N. Zheng, *J. Am. Chem. Soc.*, 2016, **138**, 3278–3281.
- 8 G. Li, H. Abroshan, Y. Chen, R. Jin and H. J. Kim, *J. Am. Chem. Soc.*, 2015, **137**, 14295–14304.
- 9 A. Ghosh, V. Jeseentharani, M. A. Ganayee, R. G. Hemalatha, K. Chaudhari, C. Vijayan and T. Pradeep, *Anal. Chem.*, 2014, **86**, 10996–11001.
- 10 A. Mathew, P. R. Sajanlal and T. Pradeep, *Angew. Chem., Int. Ed.*, 2012, **51**, 9596–9600.
- 11 M. Arenz, U. Landman and U. Heiz, *ChemPhysChem*, 2006, **7**, 1871–1879.

- 12 Y. Liu, H. Tsunoyama, T. Akita and T. Tsukuda, *Chem. Commun.*, 2010, **46**, 550–552.
- 13 Y. Zhu, H. Qian, B. A. Drake and R. Jin, *Angew. Chem., Int. Ed.*, 2010, **49**, 1295–1298.
- 14 N. de Silva, J.-M. Ha, A. Solovyov, M. M. Nigra, I. Ogino, S. W. Yeh, K. A. Durkin and A. Katz, *Nat. Chem.*, 2010, **2**, 1062–1068.
- 15 K. G. Stamplecoskie and P. V. Kamat, *J. Am. Chem. Soc.*, 2014, **136**, 11093–11099.
- 16 Y.-S. Chen, H. Choi and P. V. Kamat, *J. Am. Chem. Soc.*, 2013, **135**, 8822–8825.
- 17 M. A. Abbas, T.-Y. Kim, S. U. Lee, Y. S. Kang and J. H. Bang, *J. Am. Chem. Soc.*, 2016, **138**, 390–401.
- 18 Y. Chen, C. Liu, Q. Tang, C. Zeng, T. Higaki, A. Das, D.-E. Jiang, N. L. Rosi and R. Jin, *J. Am. Chem. Soc.*, 2016, **138**, 1482–1485.
- 19 C. Zeng, Y. Chen, K. Iida, K. Nobusada, K. Kirschbaum, K. J. Lambright and R. Jin, *J. Am. Chem. Soc.*, 2016, **138**, 3950–3953.
- 20 S. Tian, Y.-Z. Li, M.-B. Li, J. Yuan, J. Yang, Z. Wu and R. Jin, *Nat. Commun.*, 2015, **6**, 10012.
- 21 Y. Chen, C. Zeng, C. Liu, K. Kirschbaum, C. Gayathri, R. R. Gil, N. L. Rosi and R. Jin, *J. Am. Chem. Soc.*, 2015, **137**, 10076–10079.
- 22 A. Desireddy, B. E. Conn, J. Guo, B. Yoon, R. N. Barnett, B. M. Monahan, K. Kirschbaum, W. P. Griffith, R. L. Whetten, U. Landman and T. P. Bigioni, *Nature*, 2013, **501**, 399–402.
- 23 H. Yang, Y. Wang, H. Huang, L. Gell, L. Lehtovaara, S. Malola, H. Häkkinen and N. Zheng, *Nat. Commun.*, 2013, **4**, 2422.
- 24 Y. Wang, H. Su, C. Xu, G. Li, L. Gell, S. Lin, Z. Tang, H. Häkkinen and N. Zheng, *J. Am. Chem. Soc.*, 2015, **137**, 4324–4327.
- 25 J. Yan, H. Su, H. Yang, S. Malola, S. Lin, H. Häkkinen and N. Zheng, *J. Am. Chem. Soc.*, 2015, **137**, 11880–11883.
- 26 H. Hakkinen, *Nat. Chem.*, 2012, **4**, 443–455.
- 27 H. Qian, M. Zhu, Z. Wu and R. Jin, *Acc. Chem. Res.*, 2012, **45**, 1470–1479.
- 28 A. Dass, S. Theivendran, P. R. Nimmala, C. Kumara, V. R. Jupally, A. Fortunelli, L. Sementa, G. Barcaro, X. Zuo and B. C. Noll, *J. Am. Chem. Soc.*, 2015, **137**, 4610–4613.
- 29 D. Crasto, G. Barcaro, M. Stener, L. Sementa, A. Fortunelli and A. Dass, *J. Am. Chem. Soc.*, 2014, **136**, 14933–14940.
- 30 X.-Y. Li, H.-F. Su, K. Yu, Y.-Z. Tan, X.-P. Wang, Y.-Q. Zhao, D. Sun and L.-S. Zheng, *Nanoscale*, 2015, **7**, 8284–8288.
- 31 D. Sun, G.-G. Luo, N. Zhang, R.-B. Huang and L.-S. Zheng, *Chem. Commun.*, 2011, **47**, 1461–1463.
- 32 T. Higaki, C. Liu, C. Zeng, R. Jin, Y. Chen, N. L. Rosi and R. Jin, *Angew. Chem., Int. Ed.*, 2016, **55**, 6694–6697.
- 33 Y. Chen, C. Zeng, D. R. Kauffman and R. Jin, *Nano Lett.*, 2015, **15**, 3603–3609.
- 34 C. P. Joshi, M. S. Bootharaju, M. J. Alhilaly and O. M. Bakr, *J. Am. Chem. Soc.*, 2015, **137**, 11578–11581.
- 35 L. G. AbdulHalim, M. S. Bootharaju, Q. Tang, S. Del Gobbo, R. G. AbdulHalim, M. Eddaoudi, D.-E. Jiang and O. M. Bakr, *J. Am. Chem. Soc.*, 2015, **137**, 11970–11975.
- 36 (a) K. R. Krishnadas, A. Ghosh, A. Baksi, I. Chakraborty, G. Natarajan and T. Pradeep, *J. Am. Chem. Soc.*, 2016, **138**, 140–148; (b) K. R. Krishnadas, A. Baksi, A. Ghosh, G. Natarajan and T. Pradeep, *Nat. Commun.*, 2016, **7**, 13447.
- 37 M. S. Bootharaju, V. M. Burlakov, T. M. D. Besong, C. P. Joshi, L. G. AbdulHalim, D. M. Black, R. L. Whetten, A. Goriely and O. M. Bakr, *Chem. Mater.*, 2015, **27**, 4289–4297.
- 38 Y. Shichibu, Y. Negishi, T. Tsukuda and T. Teranishi, *J. Am. Chem. Soc.*, 2005, **127**, 13464–13465.
- 39 Y. Niihori, W. Kurashige, M. Matsuzaki and Y. Negishi, *Nanoscale*, 2013, **5**, 508–512.
- 40 Y. Niihori, M. Matsuzaki, T. Pradeep and Y. Negishi, *J. Am. Chem. Soc.*, 2013, **135**, 4946–4949.
- 41 B. Molina, A. Sanchez-Castillo, S. Knoppe, I. L. Garzon, T. Burgi and A. Tlahuice-Flores, *Nanoscale*, 2013, **5**, 10956–10962.
- 42 E. S. Shibu, M. A. H. Muhammed, T. Tsukuda and T. Pradeep, *J. Phys. Chem. C*, 2008, **112**, 12168–12176.
- 43 M. S. Bootharaju, C. P. Joshi, M. J. Alhilaly and O. M. Bakr, *Chem. Mater.*, 2016, **28**, 3292–3297.
- 44 A. Ghosh, J. Hassinen, P. Pulkkinen, H. Tenhu, R. H. A. Ras and T. Pradeep, *Anal. Chem.*, 2014, **86**, 12185–12190.
- 45 I. Chakraborty, A. Govindarajan, J. Erusappan, A. Ghosh, T. Pradeep, B. Yoon, R. L. Whetten and U. Landman, *Nano Lett.*, 2012, **12**, 5861–5866.
- 46 A. Ghosh and T. Pradeep, *Eur. J. Inorg. Chem.*, 2014, **2014**, 5271–5275.
- 47 Z. Wu, E. Lanni, W. Chen, M. E. Bier, D. Ly and R. Jin, *J. Am. Chem. Soc.*, 2009, **131**, 16672–16674.
- 48 T. U. B. Rao, B. Nataraju and T. Pradeep, *J. Am. Chem. Soc.*, 2010, **132**, 16304–16307.
- 49 J. Cyriac, V. R. Rajeev Kumar and T. Pradeep, *Chem. Phys. Lett.*, 2004, **390**, 181–185.
- 50 A. Ghosh, T. Pradeep and J. Chakrabarti, *J. Phys. Chem. C*, 2014, **118**, 13959–13964.
- 51 C. Yao, J. Chen, M.-B. Li, L. Liu, J. Yang and Z. Wu, *Nano Lett.*, 2015, **15**, 1281–1287.
- 52 C. Yao, Y.-J. Lin, J. Yuan, L. Liao, M. Zhu, L.-H. Weng, J. Yang and Z. Wu, *J. Am. Chem. Soc.*, 2015, **137**, 15350–15353.
- 53 A. Baksi, P. Chakraborty, S. Bhat, G. Natarajan and T. Pradeep, *Chem. Commun.*, 2016, **52**, 8397–8400.

Electronic Supplementary Information (ESI) for the paper:

**Unusual reactivity of dithiol protected clusters in comparison to monothiol
protected clusters: Studies using Ag₅₁BDT₁₉ and Ag₂₉BDT₁₂**

Atanu Ghosh, Debasmita Ghosh, Esma Khatun, Papri Chakraborty and Thalappil Pradeep*

*Department of Chemistry, DST Unit of Nanoscience (DST UNS) and Thematic Unit of
Excellence (TUE)*

*Indian Institute of Technology Madras
Chennai, 600 036, India*

E-mail: pradeep@iitm.ac.in

Table of content:

Name	Description	Page no.
S1	Characterization of Au ₂₅ BT ₁₈ and Au ₂₅ OT ₁₈ clusters	2
S2	UV-vis and ESI MS spectrum of cluster II	3
S3	Expanded ESI MS region of cluster I	4
S4	MALDI MS data of clusters I and II	5
S5	Laser fluence dependent MALDI MS data of cluster I	6
S6	SEM/EDAX	7
S7	XPS	8
S8	ESI MS spectrum of cluster I	9
S9	Comparison of luminescence property of cluster I and cluster II	10
S10	Time dependent UV-vis spectra of the reaction between cluster I and Au ₂₅ BT ₁₈	11
S11	Concentration dependent ESI MS spectra of the reaction between cluster I and Au ₂₅ BT ₁₈	12
S12	Reactions of cluster I with BT and OT ligated Au ₂₅ clusters	13
S13	Comparison of reactivity of cluster I and cluster II with Au ₂₅ BT ₁₈	14
S14	Reaction of cluster II with Au ₂₅ BT ₁₈	15
S15	Reaction of Au ₂₅ BT ₁₈ cluster with BDT thiol	16
S16	Time dependent ESI MS spectra for inter-cluster conversion process	17
S17	A UV-vis study of the inter-cluster conversion process	18
S18	Transformation of Cluster I to cluster II	19

Supplementary Information 1

Characterization of Au₂₅BT₁₈ and Au₂₅OT₁₈ clusters

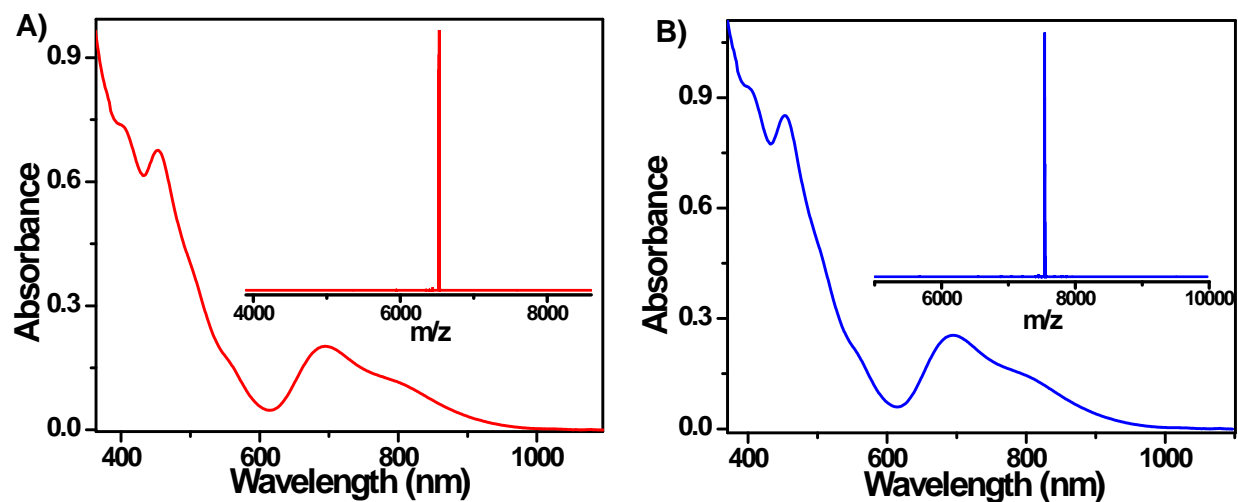


Fig. S1 **A)** UV-vis spectrum of as synthesized Au₂₅BT₁₈ cluster which matches with the published report.¹ Inset: ESI MS spectrum of the cluster solution. Presence of single peak at m/z 6530 confirms the composition and purity of the sample. **B)** UV-vis spectrum of Au₂₅OT₁₈ cluster. Inset: ESI MS spectrum of the cluster solution. Composition and purity of the cluster is confirmed from the presence of single peak at m/z 7540.¹

Supplementary Information 2

UV-vis and ESI MS spectrum of cluster II

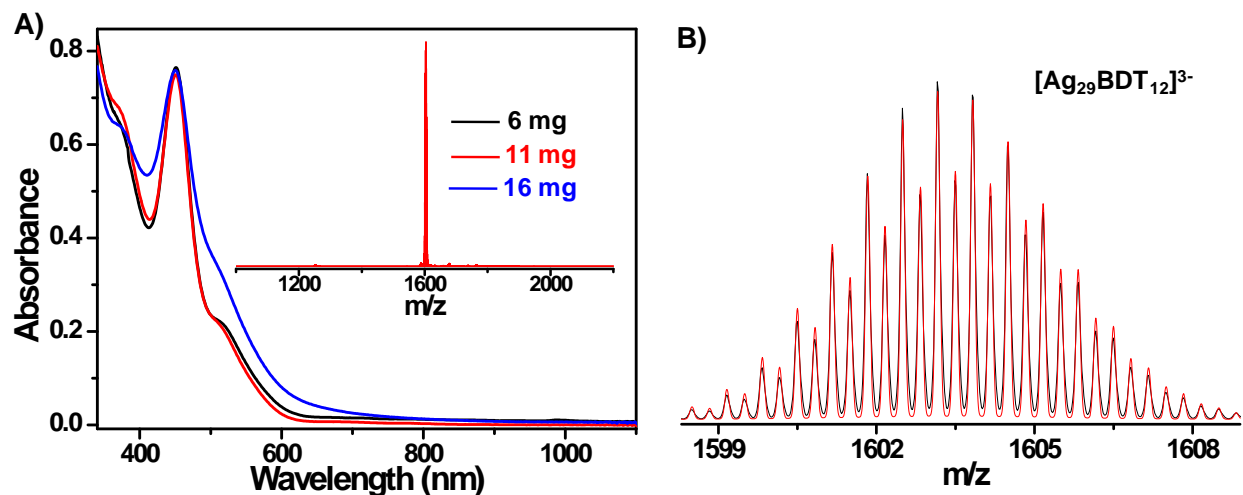


Fig. S2 A) UV-vis spectra of DMF solutions of the clusters. Black, red and blue traces are for the solutions of 1A₃, B₃ and C₃ of main manuscript, respectively. All the spectra match with those of $[Ag_{29}BDT_{12}]^{3-}$ (cluster II).² Inset: ESI MS of the cluster solution. As all the solutions gave the same spectra, we have presented only one of them. Presence of a single peak at m/z 1603 confirms the formation of cluster II.² B) Comparison of experimental (black trace) and simulated isotopic pattern (red trace) which matches perfectly.

Supplementary Information 3

Expanded ESI MS region of cluster I

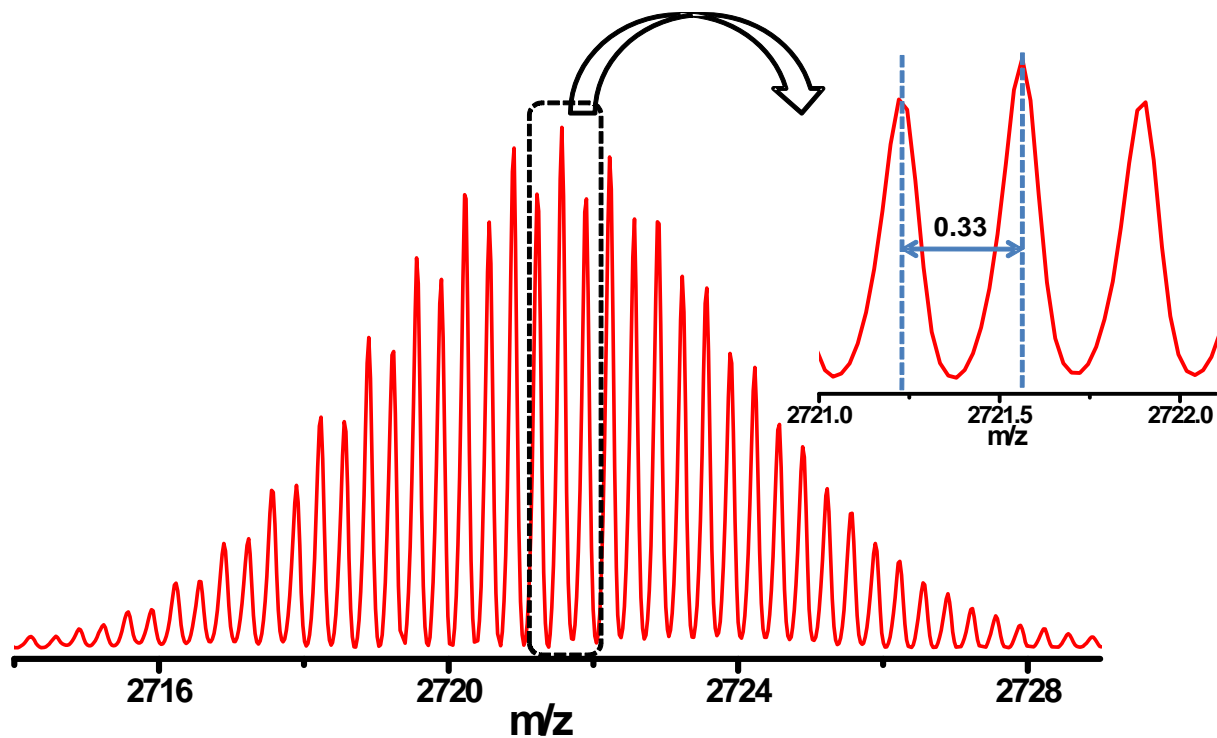


Fig. S3 Peak at m/z 2721.56 is expanded here. Separation between the two peaks is m/z 0.33 which confirms that the cluster has 3- charge.

Supplementary Information 4

MALDI MS data of cluster I and cluster II

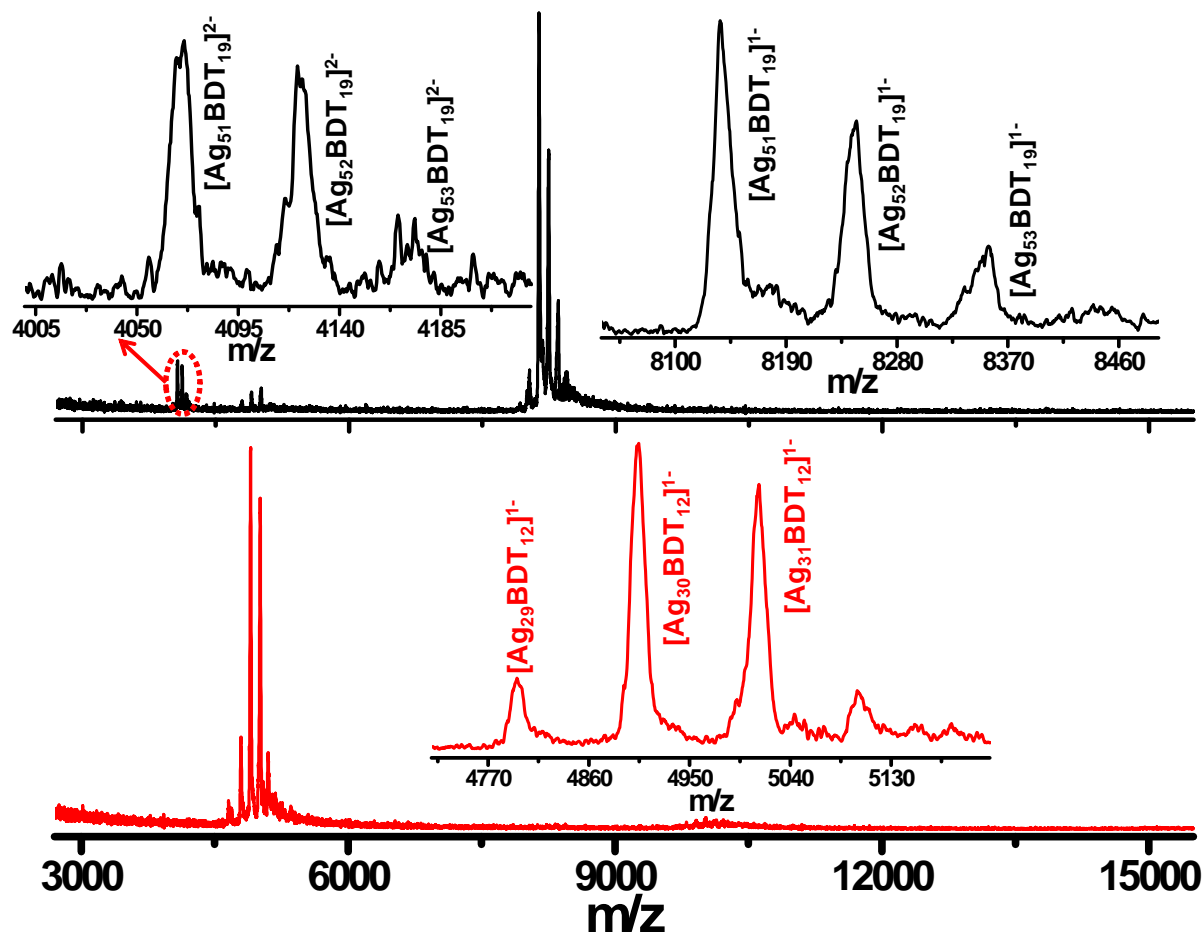


Fig. S4 MALDI MS spectra of cluster **I** (black trace) and cluster **II** (red trace). The spectra were measured in the -ve mode at threshold laser fluence. Monoanionic and dianionic peaks of the cluster **I** are expanded which shows the presence of silver attached peaks along with the molecular ion ($[Ag_{51}BDT_{19}]^{-}$) peak. MALDI MS spectrum of the purified cluster **II** (red trace) also shows the presence of silver attached peaks along with the molecular ion ($[Ag_{29}BDT_{12}]^{-}$) peak. This silver attached peaks with the molecular ion peak may be a characteristic feature of dithiol protected clusters.

Supplementary Information 5

Laser fluence dependent MALDI MS data of cluster I

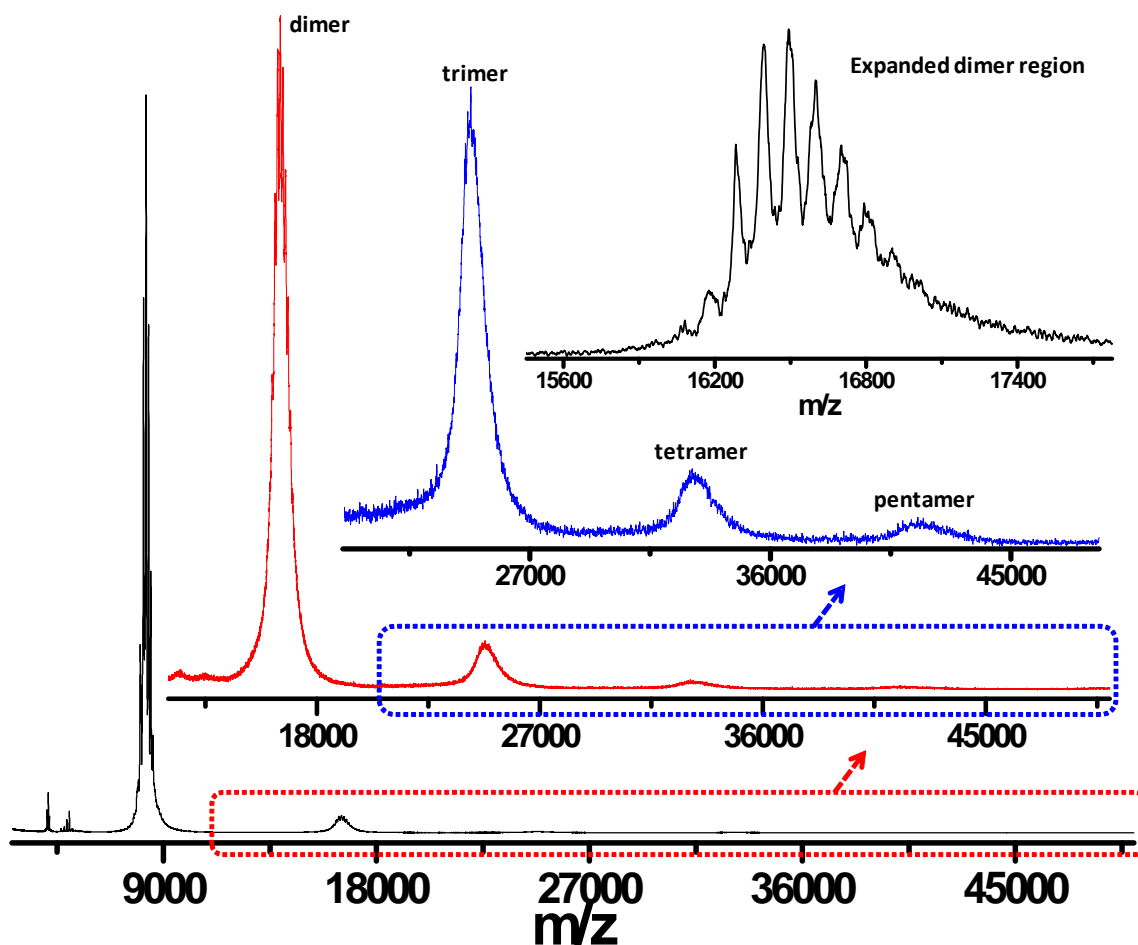


Fig. S5 MALDI MS data of cluster I measured at higher laser fluence. Expansion of higher mass region shows the presence of peaks at regular intervals of $\sim m/z$ 8100 along with the molecular ion peak. These higher mass peaks are due to the formation of dimer ($\sim m/z$ 16200), trimer ($\sim m/z$ 24300), tetramer ($\sim m/z$ 32400) and pentamer ($\sim m/z$ 40,500) of $Ag_{51}BDT_{19}$ cluster which are marked. Inset: The peak corresponding to the dimer is expanded which also shows the silver attached peaks.

Supplementary Information 6

SEM/EDAX

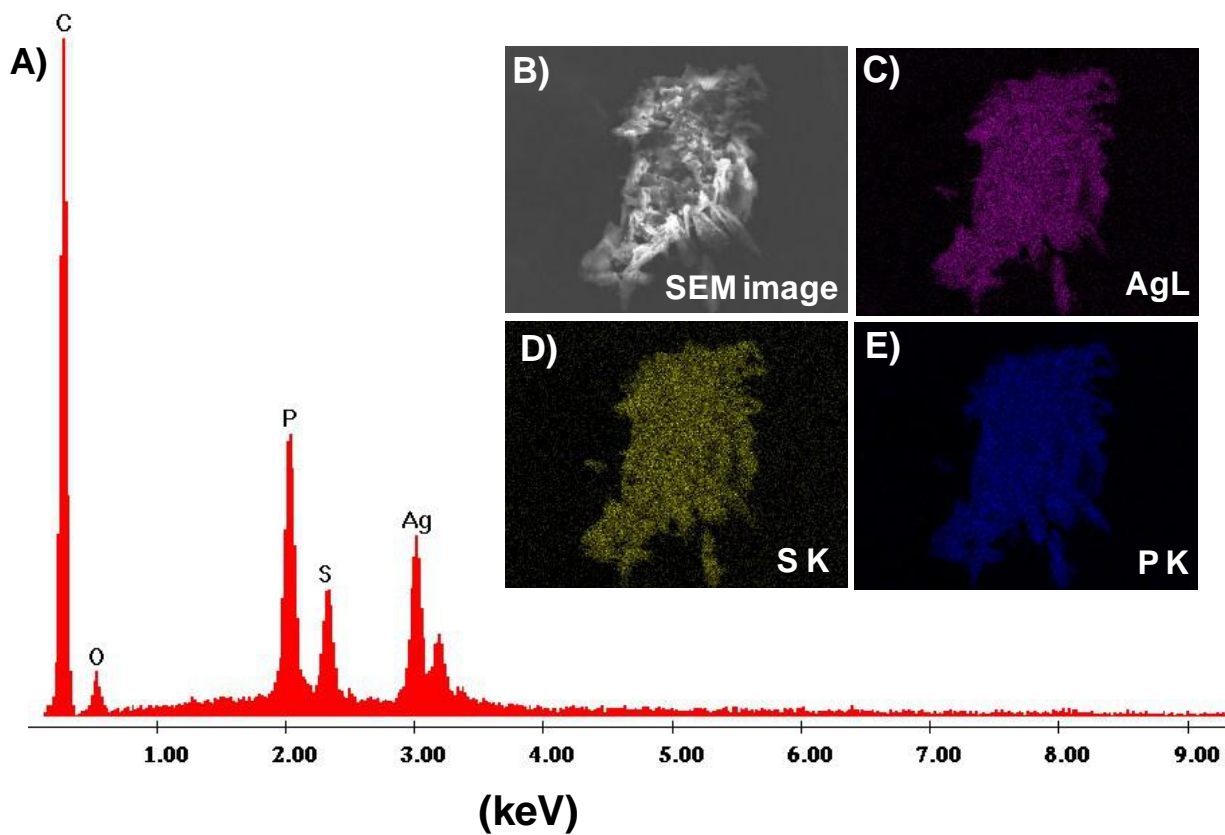


Fig. S6 (A) EDAX spectrum of $\text{Ag}_{51}\text{BDT}_{19}$ and (B) SEM image of $\text{Ag}_{51}\text{BDT}_{19}$ aggregate from which the EDAX spectrum was taken. Ag:S atomic ratio measured is 1:0.76, as expected (actual is 1:0.74).

Supplementary Information 7

XPS

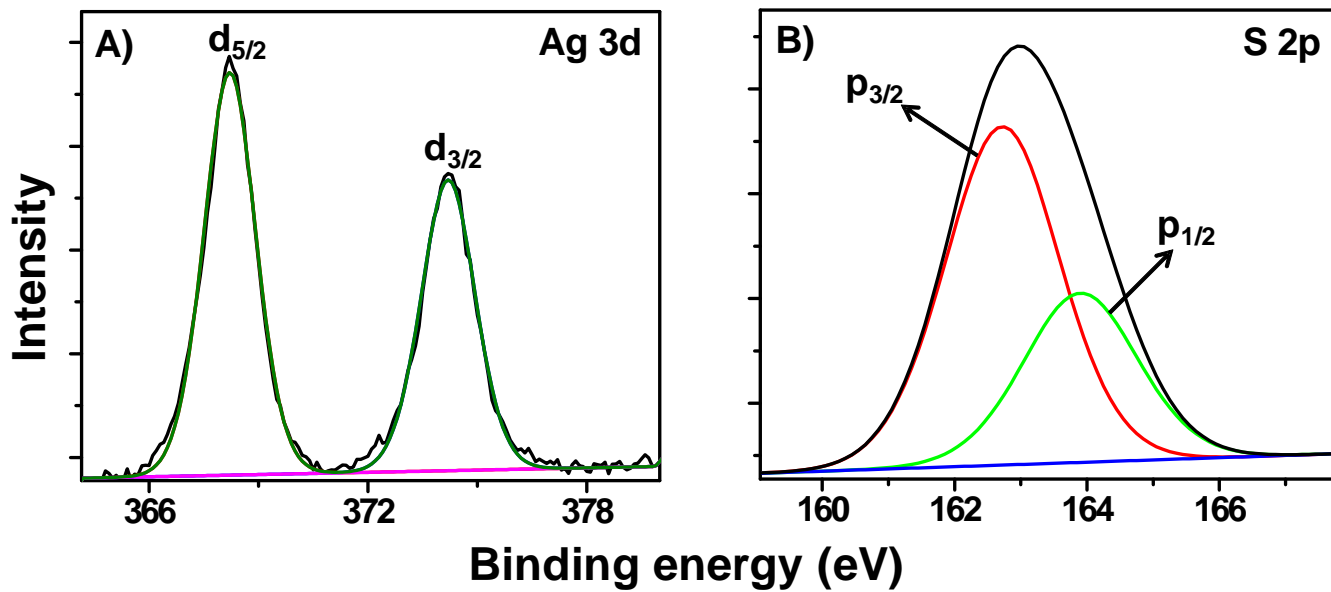


Fig. S7 (A) and (B) represent the XPS spectra for Ag 3d and S 2p, respectively with multiple component fitting. It shows that Ag is almost in the zero oxidation state.

Supplementary Information 8

ESI MS spectrum of cluster I

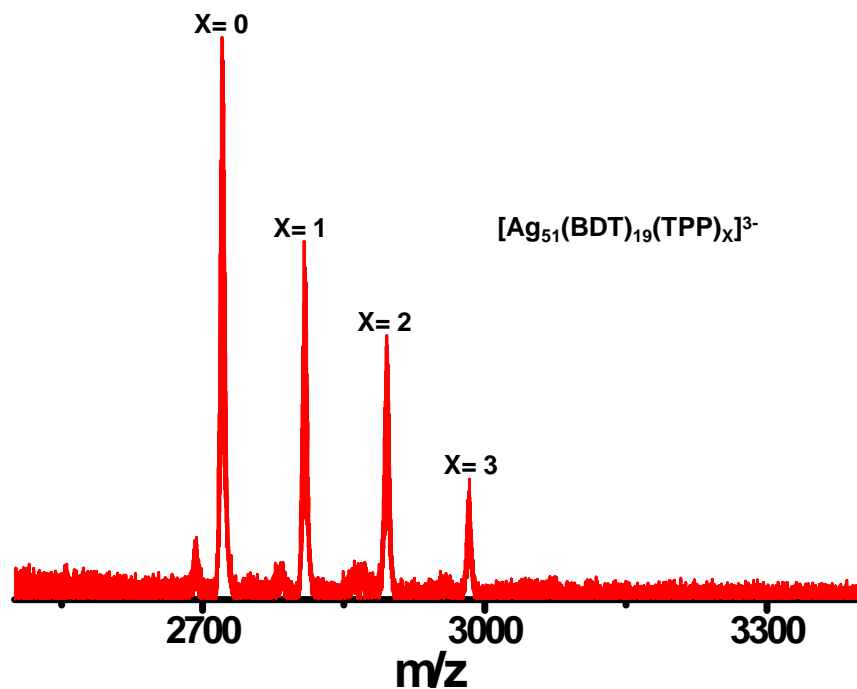


Fig S8 ESI MS spectrum of the purified cluster in the negative mode. The peaks are separated by $m/z = 87.5$. As the cluster has 3- charge, the peak separation of 87.5 is assigned to the loss of one phosphine (molecular mass 262.3) from the parent ion. It shows the sequential dissociation of three phosphines from the parent peak. The peak at m/z 2721.56 (where $X=0$) corresponds to $[Ag_{51}(BDT)_{19}]^{3-}$. Therefore the assigned composition of the parent material is $[Ag_{51}(BDT)_{19}(TPP)_3]^{3-}$.

Supplementary Information 9

Comparison of luminescence property of cluster I and cluster II

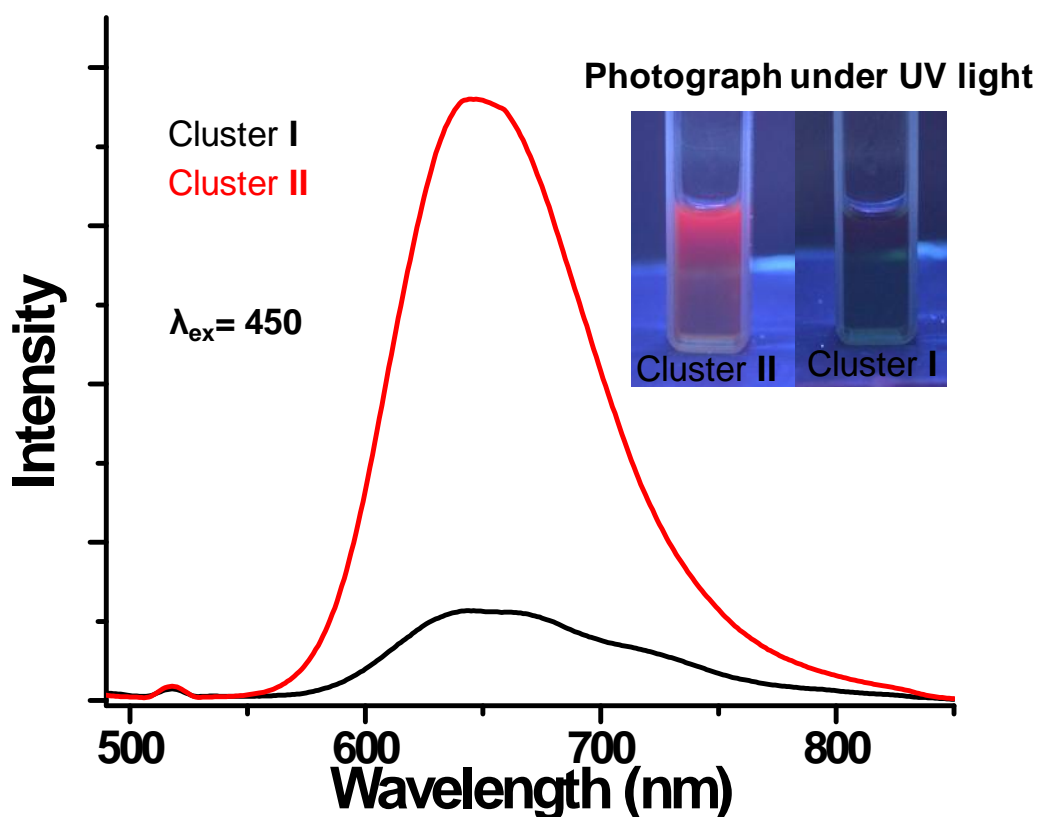


Fig S9 Comparison of luminescence property of Ag_{51} (cluster I) and Ag_{29} (cluster II) clusters. Both, the luminescent spectra and the photograph under UV light (inset) show that the cluster I is weakly luminescent in comparison to cluster II.

Supplementary Information 10

Time dependent UV-vis spectra of the reaction between cluster I and Au₂₅BT₁₈

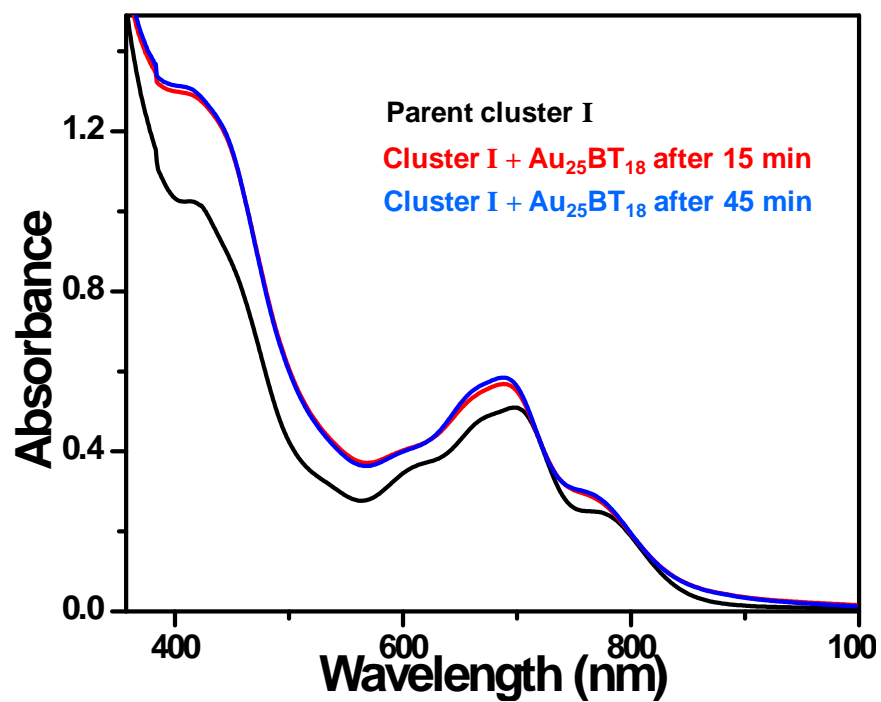


Fig. S10 Time dependent UV-vis spectra of inter-cluster reaction.

Supplementary Information 11

Concentration dependent ESI MS spectra of the reaction between cluster I and Au₂₅BT₁₈

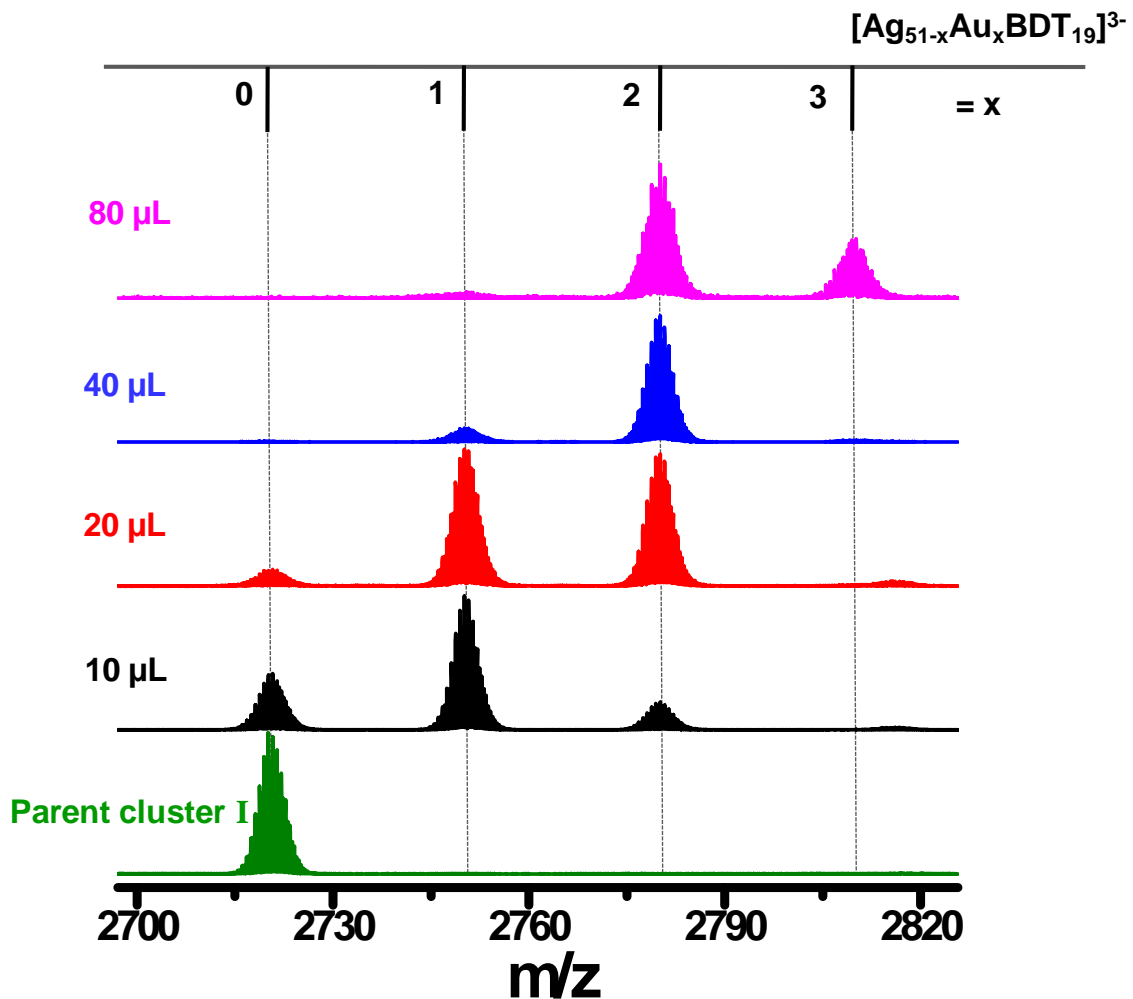


Fig. S11 Reaction of cluster I (fixed concentration) with increasing concentrations of Au₂₅BT₁₈ clusters. As the amount of Au₂₅BT₁₈ cluster increases in the reaction medium, more and more silver of cluster I get substituted by gold of Au₂₅BT₁₈ cluster leading to the formation of $[\text{Ag}_{51-x}\text{Au}_x\text{BDT}_{19}]^{3-}$ alloy.

Supplementary Information 12

Reactions of cluster I with BT and OT ligated Au₂₅ clusters

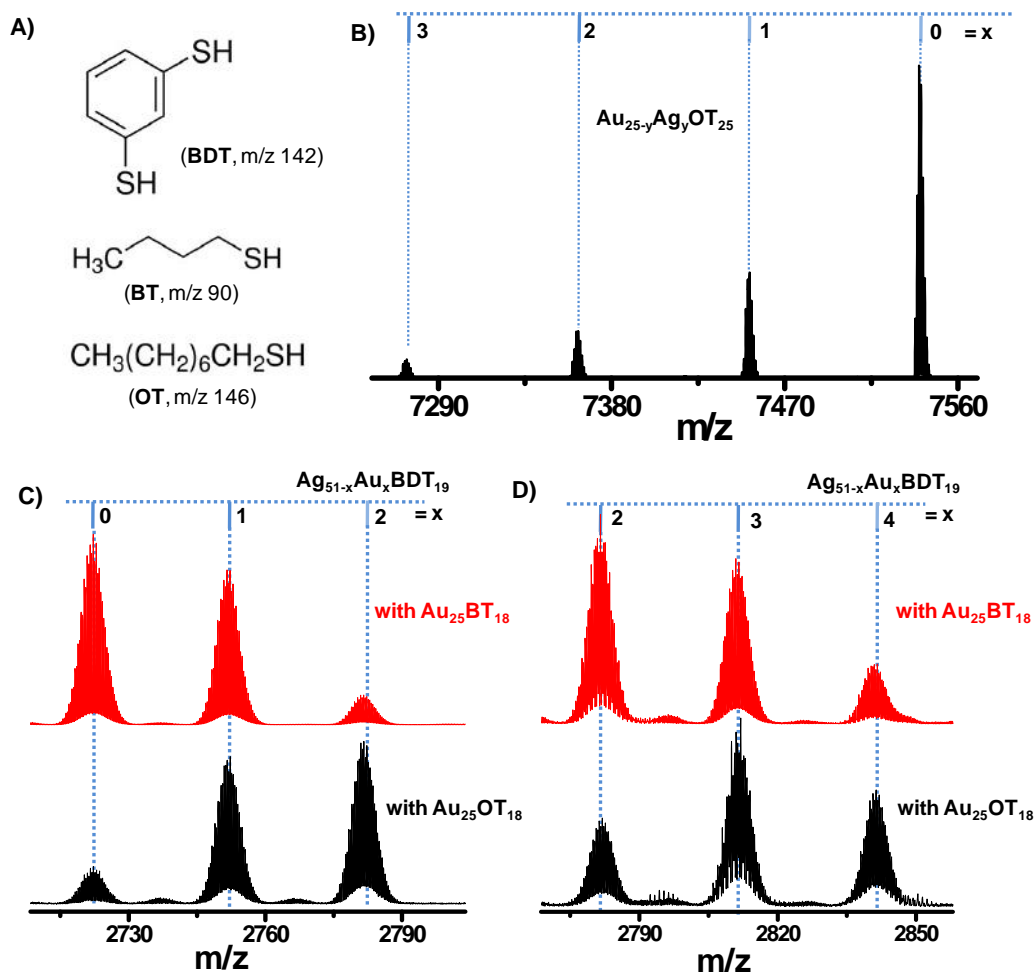


Fig. S12 **A)** Compositions and masses of protecting ligands, BDT, OT and BT thiols. **B)** The Au₂₅OT₁₈ region during reaction with cluster I. The peaks are due to the formation of [Au_{25-y}Ag_yBT₁₈]⁻ alloy cluster. No peaks other than those of metal exchange were found. **C)** and **D)** compares the [Ag_{51-x}Au_xBDT₁₉]³⁻ region while cluster I reacting with BT and OT ligated Au₂₅ clusters. No new peaks were observed here. Absence of new peaks upon using the differently ligated Au₂₅ clusters confirms that the ligand shell is not involving for this type of reaction.

Supplementary Information 13

Comparison of reactivity of cluster I and cluster II with $\text{Au}_{25}\text{BT}_{18}$

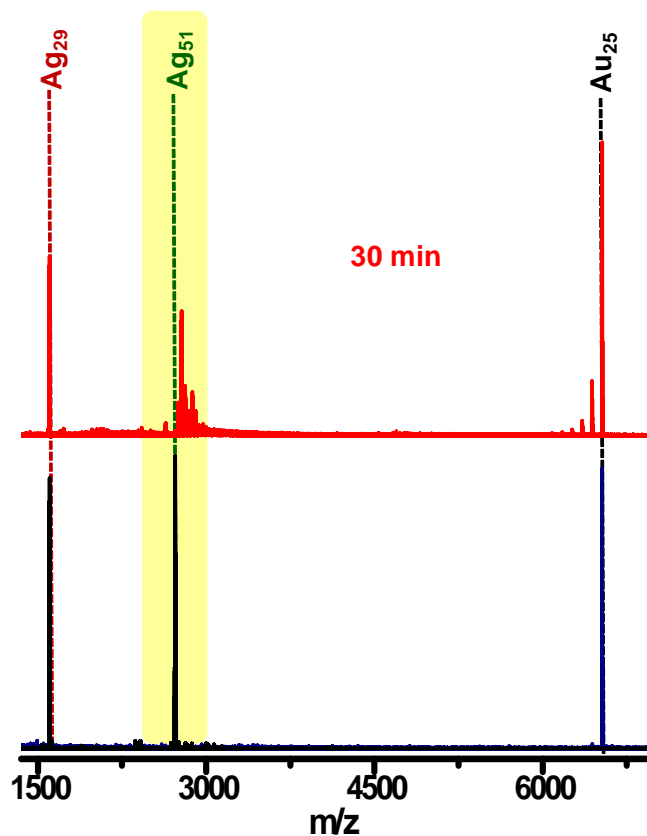


Fig. S13 Reactions of equimolar mixture of cluster **I** and **II** with $\text{Au}_{25}\text{BT}_{18}$ cluster. After 30 min of reaction cluster **I** disappeared (highlighted portion) whereas cluster **II** underwent slow reaction.

Supplementary Information 14

Reaction of cluster II with Au₂₅BT₁₈

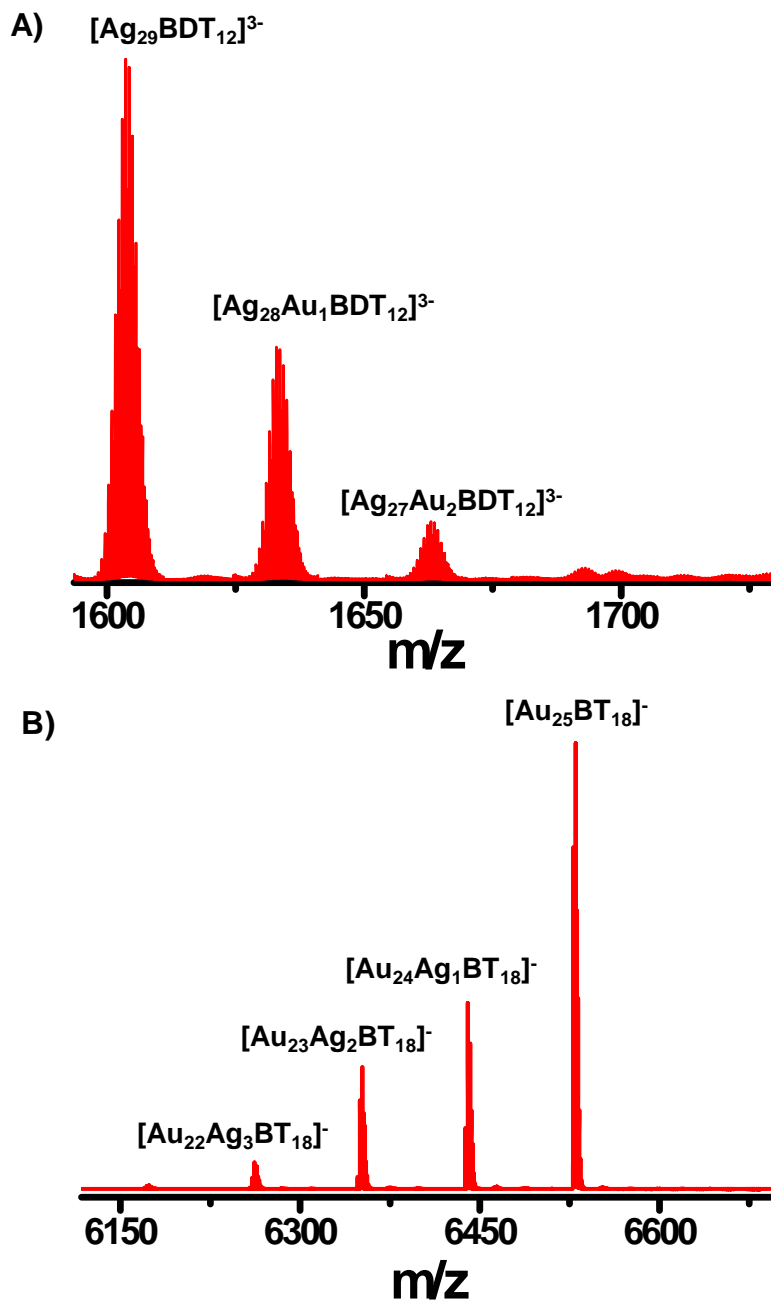


Fig. S14 ESI MS spectra of reaction of cluster II with Au₂₅BT₁₈ cluster. **A)** Cluster II undergoes only metal exchange reaction leading to the formation of [Ag_{29-x}Au_xBDT₁₂]³⁻ alloy cluster. **B)** On the other side, Au₂₅BT₁₈ also under goes metal exchange reaction leading to the formation of [Au_{25-x}Ag_xBT₁₈]⁻ alloy cluster.

Supplementary Information 15

Reaction of $\text{Au}_{25}\text{BT}_{18}$ cluster with BDT thiol

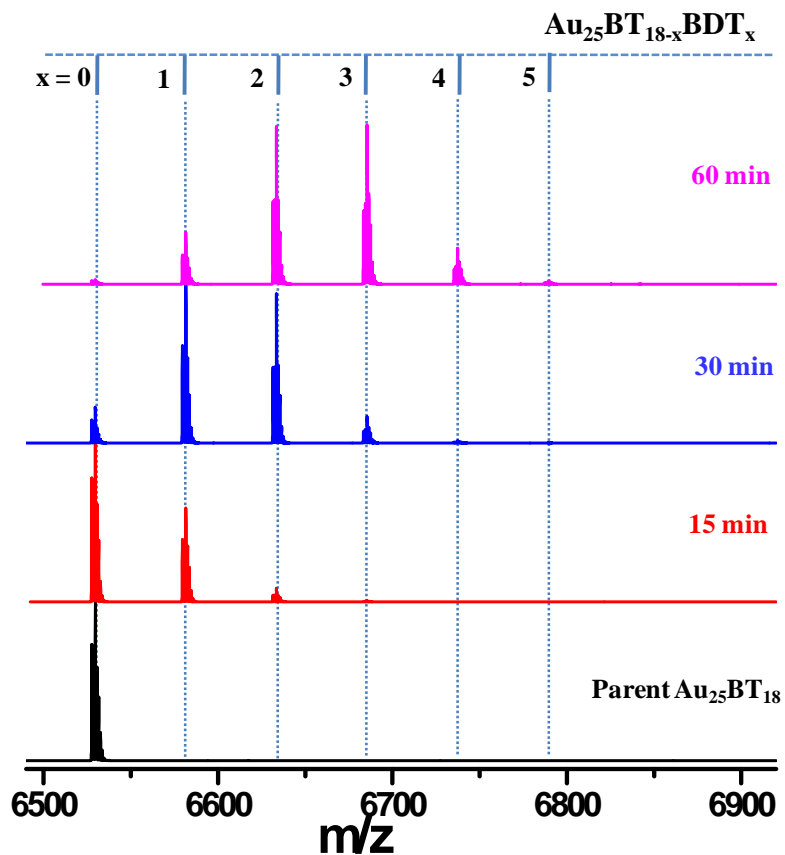


Fig. S15 Time dependent ESI MS spectra for the reaction of $\text{Au}_{25}\text{BT}_{18}$ with BDT thiol. As time increases more and more BT ligands of $\text{Au}_{25}\text{BT}_{18}$ get exchanged by BDT thiol.

Supplementary Information 16

Time dependent ESI MS spectra for inter-cluster conversion process

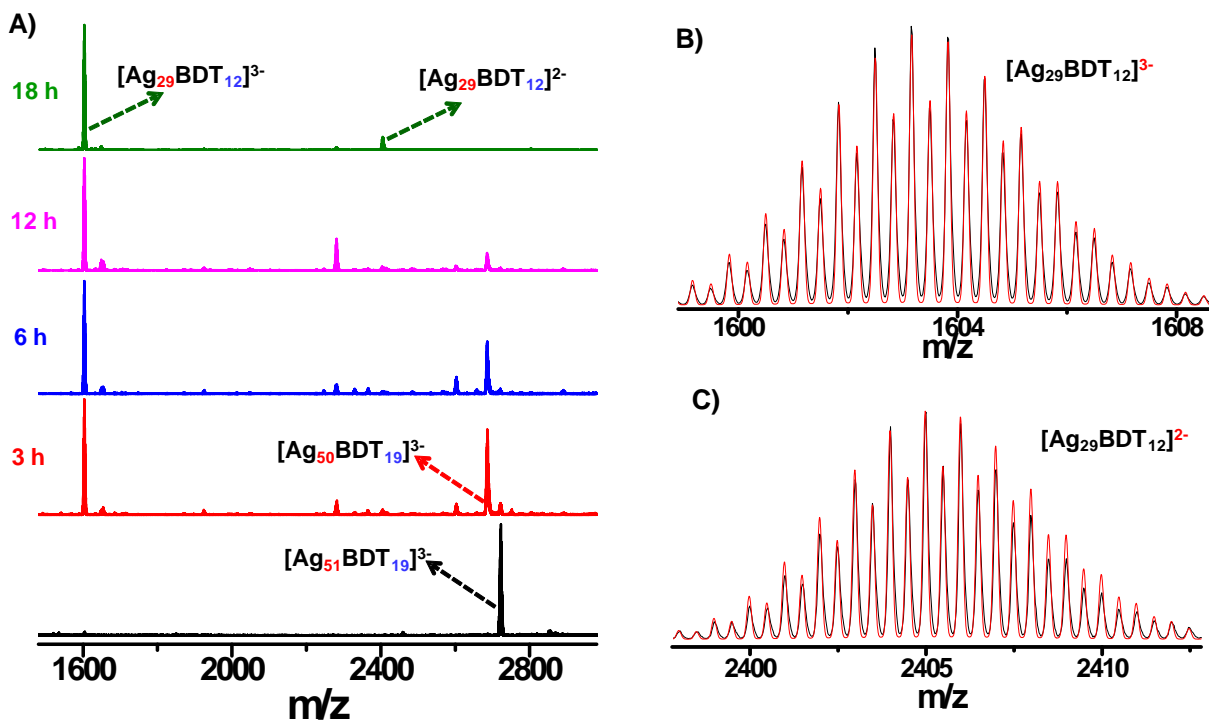


Fig. S16 A) Time dependent ESI MS spectra for the reaction of cluster **I** with DMBT (15 μ L). As time progresses, peak at m/z 2721 = due to the parent cluster **I** disappears slowly. At the same time, peak at m/z 1603 which is due to the cluster **II** increases gradually. After 18 h of reaction, cluster **I** was completely converted to cluster **II**. Upon addition of DMBT, cluster **I** immediately loses one Ag ion and forms $[Ag_{50}BDT_{19}]^{3-}$ which is marked in the figure. **B)** and **C)** Compare the experimental (black trace) and simulated (res trace) isotopic distribution for 2- and 3- charge states of cluster **II**.

Supplementary Information 17

A UV-vis study of the inter-cluster conversion process

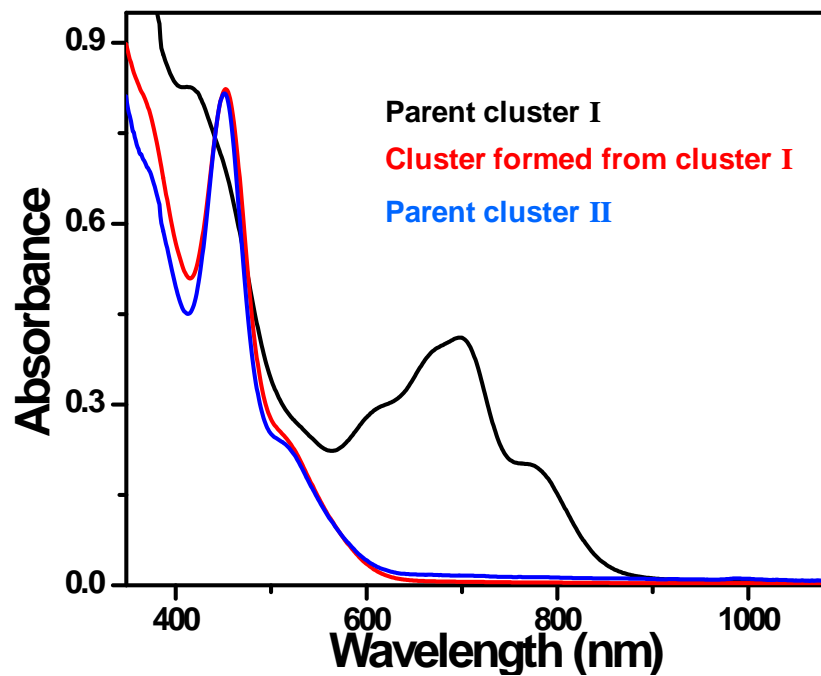


Fig. S17 Optical absorbance spectra where spectra of cluster **I** (black trace) and **II** (blue trace) are compared with the reaction product (red trace). It confirms the formation of cluster **I**.

Supplementary Information 18

Transformation of Cluster I to cluster II

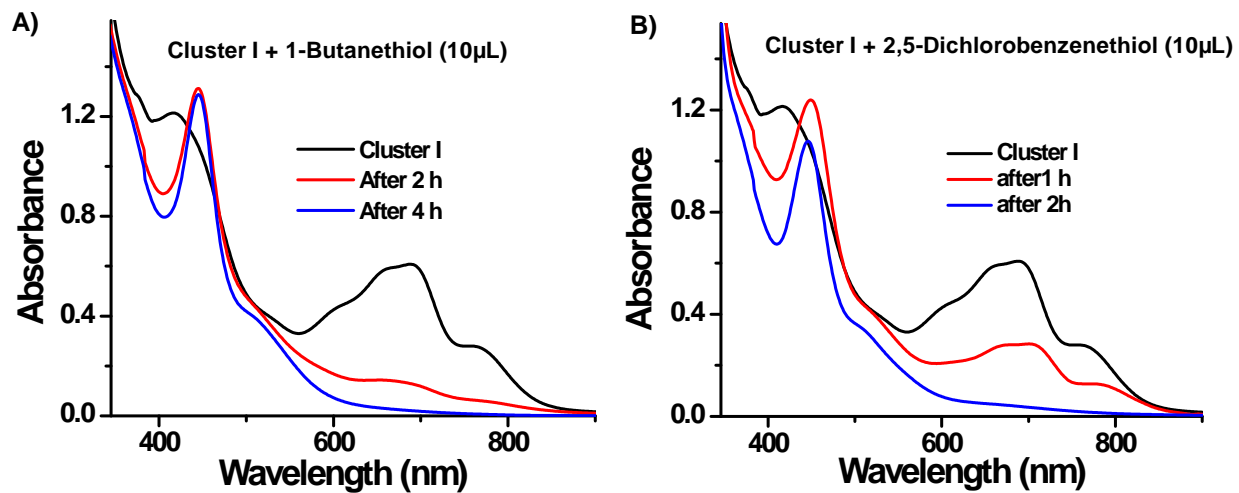


Fig. S18 A) Time dependent UV-vis spectra for the transformation of Ag₅₁ to Ag₂₉ in presence of 1-butanethiol. B) Time dependent UV-vis spectra for the transformation of Ag₅₁ to Ag₂₉ in presence of 2,5-dichlorobenzenethiol.

- 1 A. Ghosh, J. Hassinen, P. Pulkkinen, H. Tenhu, R. H. A. Ras and T. Pradeep, *Anal. Chem.*, 2014, **86**, 12185-12190.
- 2 L. G. AbdulHalim, M. S. Bootharaju, Q. Tang, S. Del Gobbo, R. G. AbdulHalim, M. Eddaoudi, D.-e. Jiang and O. M. Bakr, *J. Am. Chem. Soc.*, 2015, **137**, 11970-11975.

Confined Metastable 2-Line Ferrihydrite for Affordable Point-of-Use Arsenic-Free Drinking Water

Avula Anil Kumar, Anirban Som, Paolo Longo, Chennu Sudhakar, Radha Gobinda Bhui, Soujit Sen Gupta, Anshup, Mohan Udhaya Sankar, Amrita Chaudhary, Ramesh Kumar, and Thalappil Pradeep*

Nanomaterials with intrinsically high surface energy, prepared using naturally abundant ingredients can be helpful in creating green products.^[1] Several nanoscale materials have been prepared recently for applications of water purification, which exhibit improved performance vis-à-vis existing compositions, thereby enhancing the effectiveness of point-of-use water purifiers. However, such materials cannot be used in the native form for water purification because of difficulties in particle separation, potential danger in view of their leaching into the purified water,^[2] and poor hydraulic conductivity of the filtration device. Examples such as activated alumina,^[3] activated carbon,^[4,5] iron oxide,^[5,6] silicon dioxide,^[7] granular ferric hydroxide (GFH),^[8] reduced graphene oxide (RGO)-metal/metal oxide composites,^[9–11] and magnetite-reduced graphene oxide composite (M-RGO)^[12] are well known in the literature. Important requirement in the context of arsenic (As) removal media is the simultaneous removal of both As(III) and As(V) species present in natural water with enhanced kinetics, enabling fast delivery of clean water.

Hydrous nanoscale metal oxides are available abundantly in nature,^[13] they are formed in geological time scale by slow crystallization, often assisted by mild temperature and pressure variations. However, this leads to the destruction of adsorption sites. Researchers have looked at new methods to synthesize iron oxide/hydroxide/oxyhydroxide compositions in the laboratory and used them for water purification.^[13] They exist in rich variety of structures and hydration states. They are commonly fine-grained (nanophase) and poorly crystalline. The competition between surface energies and energetics of phase transformation suggests that metastable micrometer-sized or larger polymorphs can often be stabilized at the nanoscale. Such size-driven crossovers in stability help to explain patterns of occurrence of different iron oxides in nature.^[14] Many of

them have been shown to be effective for the removal of As(III) and As(V) and such chemistry for arsenic remediation has been investigated.^[15–17] Here, we present a simple method to maintain the metastable 2-line ferrihydrite phase at room temperature by confining it in biopolymeric cages. This material is termed as confined metastable 2-line ferrihydrite (CM2LF) having unprecedented adsorption capacity for both As(III) and As(V) in field conditions. We describe an affordable water purification device using such a composite, developed over several years, undergoing large scale field trials in India, as a potential solution for the eradication of arsenic from drinking water.^[18] The material is green and causes no additional environmental impact for its production and in the course of use.

CM2LF appears to be largely amorphous in transmission electron microscopy (TEM) (Figure 1A). We believe that this is due to the small size of the crystalline domains of the material which might not be located under high resolution transmission electron microscopy (HRTEM). Nanoscale features are evident in the image, which are uniform throughout. Fast Fourier transform (FFT) diffraction pattern is shown in inset a₁. The phase continues to remain the same at ambient conditions, but gradually gets converted to more stable forms of hematite (α -Fe₂O₃, rhombohedral, JCPDS 89-8103) and goethite (α -FeOOH, orthorhombic, JCPDS 81-0464)^[19] upon electron beam irradiation. FFT diffraction pattern (Figure 1Bb₁) of the irradiated material along with lattice resolved images of these phases (inset b₂, b₃, and b₄) are shown in Figure 1B. The phases were confirmed by the lattice planes of hematite (b₂, b₄) and goethite (b₃), which matches with the Cambridge crystallographic data (CCD). Electron beam induced time dependent HRTEM images of initial CM2LF, As(III) adsorbed and As(V) adsorbed samples show the conversion of amorphous to crystalline state. Lattice resolved images of these samples are shown in Figure S1 of the Supporting Information. Scanning electron microscope (SEM) image of the initial granular material is shown in Figure S2A (Supporting Information). The material was kept in water and was found to be stable even after six months without any leaching of Fe. Stability of the composition is attributed to abundant –O and –OH functional groups of chitosan, which help in the formation of metastable amorphous metal oxyhydroxide and also ensure strong covalent binding of the nanoparticle surface to the matrix. Iron oxyhydroxide nanoparticles bind to chitosan network, possibly through covalent sharing of oxygen, leading to metastable 2-line ferrihydrite phase similar to the formation of ALOOH nanoparticles in chitosan network, comparable to the mechanism reported by Sankar et al.^[20] Figure 1C₁ shows the annular dark-field

A. A. Kumar, A. Som, C. Sudhakar, Dr. R. G. Bhui, S. Sen Gupta, Anshup, M. U. Sankar, A. Chaudhary, R. Kumar, Prof. T. Pradeep
DST Unit of Nanoscience (DST UNS) and Thematic Unit of Excellence (TUE)
Department of Chemistry
Indian Institute of Technology Madras
Chennai 600036, India
E-mail: pradeep@iitm.ac.in

Dr. P. Longo
Gatan Inc.
5794 W Las Positas Blvd, Pleasanton, CA 94588, USA



DOI: 10.1002/adma.201604260

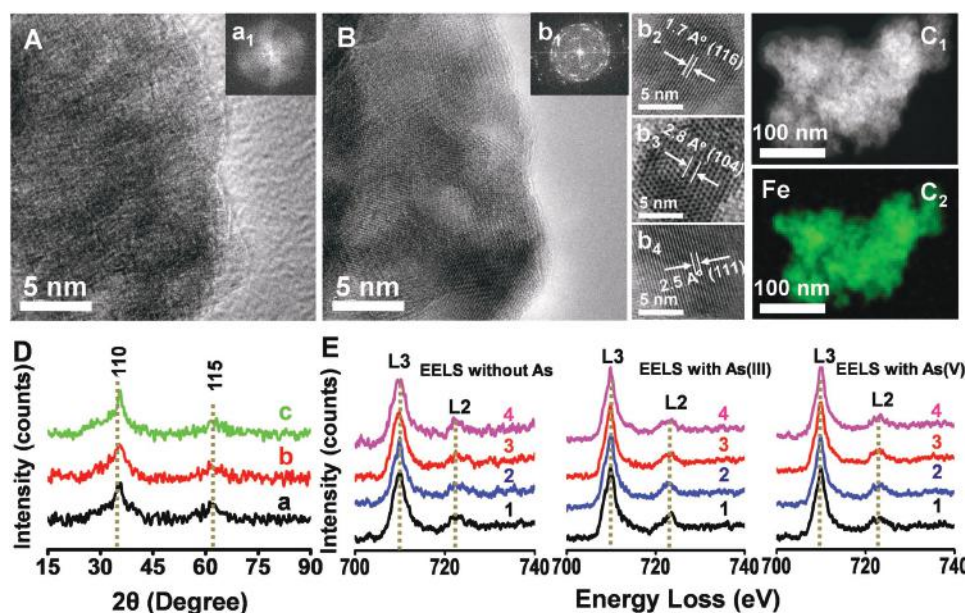


Figure 1. A) HRTEM amorphous feature of CM2LF along with dark field image (inset a₁). B) Beam induced crystallization of CM2LF along with dark field image and lattice resolved images (inset b₁, b₂, b₃, and b₄). C₁ and C₂) ADF-STEM image and Fe elemental mapping images of the initial material. D) XRD of CM2LF (a) before As adsorption (initial material), (b) after As(III), and (c) after As(V) adsorption. E) Dual EELS spectrum of iron L3, L2 region (Fe L3, L2) of CM2LF in four different locations (1, 2, 3, and 4) of the same sample.

scanning transmission electron microscopy (ADF-STEM) image of the initial composite (i.e., before arsenic adsorption) and elemental map (Figure 1C₂) of the image shows that Fe is uniformly distributed in the material. The ADF-STEM images along with the elemental maps of O, Fe, and As after the adsorption of As(III) and As(V) onto the composite are shown in Figure S2B and S2C (Supporting Information), respectively. Uniform distribution of As is seen in the material. Powder X-ray diffractogram (PXRD) pattern of the adsorbent shows the 2-line ferrihydrite phase (Figure 1D), which matches with the CCD (JCPDS, 46-1315). As(III) and As(V) adsorption does not change the PXRD profiles. No new phase was observed in PXRD of the used materials (Figure 1Db,c) which clearly shows the long-term stability of CM2LF nanocomposite in water.

Infrared spectroscopic investigation of CM2LF shows that the distinct chitosan features at 1662 cm⁻¹ due to C=O of amide I, 1329 cm⁻¹ due to N-H deformation and C-N stretching vibration and 1157 cm⁻¹ corresponding to asymmetric C-O-C stretching^[21,22] are shifted to 1636, 1375, and 1069 cm⁻¹, respectively indicating strong interaction with the ferrihydrite particles (Figure S3, Supporting Information). NaHAsO₂ shows As-O stretching peaks at 843 and 1210 cm⁻¹ which are blueshifted to 808 and 1070 cm⁻¹ after adsorption. Similarly, Na₂HAsO₄ shows peaks at 851 and 1175 cm⁻¹ due to As-O stretching, which are blueshifted to 808 and 1070 cm⁻¹ after interaction with CM2LF. These are shown in Figure S3 (Supporting Information).

Dual electron energy loss spectroscopy (Dual EELS) studies were performed to understand local effects in view of nanoscale nature of the materials (Figure 1E). However, no drastic changes were observed in the L2, L3 regions of Fe 2p edges upon As(III)/As(V) interaction, which may be correlated with the X-ray photoelectron spectroscopy (XPS). Fe 2p does not

undergo a significant chemical shift upon As(III)/As(V) interaction (to be discussed later in the text). We believe that this is due to adsorption, which leads to no significant chemical changes.

CM2LF is stable in dry and wet conditions. Figure S4 (Supporting Information) shows the Young's moduli of the materials evaluated to be 2.42 and 2.64 MPa in dry and wet conditions, respectively and the values are comparable to standard Ennore sand used as reference.^[23] The corresponding data of Mohr-Coulomb failure pattern are shown in Figure S5 (Supporting Information). The data show that CM2LF has higher shear strength in comparison to sand (friction angle, $\phi = 34.68^\circ$). This stability, in loose and wet conditions, is important in device fabrication. Indirectly, this also suggests that the material does not leach out anything which is desirable for a material used for drinking water purification.

CM2LF due to its inherently porous structure and high surface area (172 m² g⁻¹) can be used to make a point-of-use arsenic water purifier. Its structure, while allowing ion penetration within, protects the composite as a whole from scale forming species, so as to maintain uptake kinetics. The synthesized material exhibits inherent green strength and has an uptake capacity of 100 mg g⁻¹ in the field conditions, the highest arsenic adsorption capacity known so far, allowing the creation of affordable water purifiers. While FeOOH in its various forms are known to uptake arsenic in both As(III) and As(V) forms, a point of use gravity fed purifier requires highest uptake capacity to be viable. Uptake capacity of CM2LF for As(III) and As(V) follows Langmuir adsorption isotherm; the data are presented in Figure S6 (Supporting Information).

After evaluating the performance of the material in batch experiments, a prototype filter was developed. About 60 g of the composite (particle size $\approx 72 \mu\text{m}$) was packed in a water

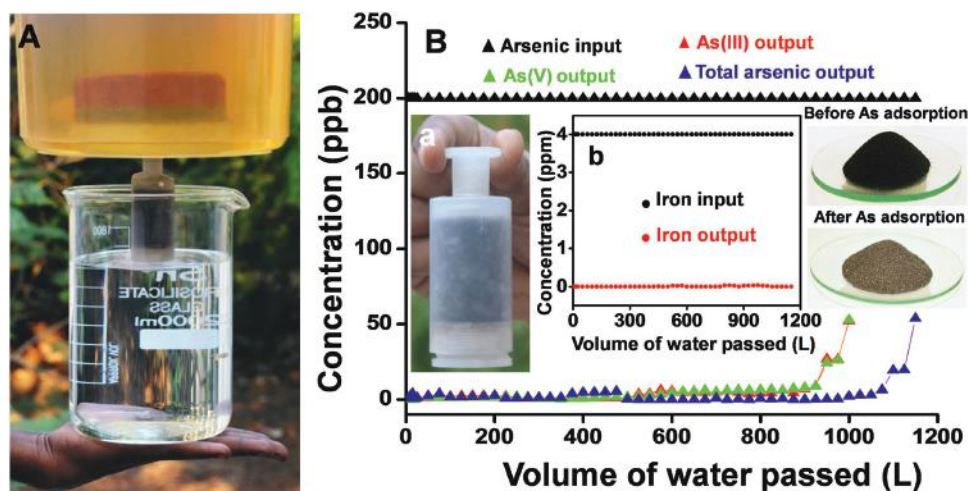


Figure 2. Set-up used for filtration containing arsenic (As(III + V)) and iron (Fe(II + III)) contaminated water using a cartridge with the reported material, along with a porous clay prefilter. B) Arsenic concentration in the water using a 60 g cartridge with the input as shown in A), inset (a) is the cartridge having 20 g adsorbent, inset (b) is iron output for the same input. The photographs of granular CM2LF before (black) and after (brown) As adsorption are in the inset.

purification cartridge (diameter, 10 mm; height, 35 mm) and a filter was assembled in an antigravity fashion. Output water was analyzed after acidification (5% HNO_3) and digestion, to ensure that all particulate matter that leached out, if at all, was also evaluated. In **Figure 2A**, we show a prototype used to conduct the experiments with over 1000 L of water at a flow rate of 12 to 15 mL min^{-1} , under gravity. Slight variation in the flow rate in the course of the long experiment was due to difference in the pressure head of the input water container. A particulate filter made from porous clay was sandwiched with a nano-composite filter, shown in **Figure 2Ba**. The input water contains 4 mg L^{-1} (4 ppm) of Fe along with 200 $\mu\text{g L}^{-1}$ (200 ppb) of a mixture of As(III) and As(V) in 1:1 ratio. This 1:1 composition is as seen in nature^[24] and referred to as As(mix). Various combinations of ions Fe(II), Fe(III), As(III), As(V), and As(mix) have been tried to understand the performance of the material.

The flow rates were optimized for best performance. Data in **Figure 2B** show that As(III), As(V), and As(mix) were removed below the World Health Organization (WHO) limit of 10 $\mu\text{g L}^{-1}$ for 1100 L synthetic and natural tap water samples using 60 g of the composite. The breakthrough was achieved at 1150 L, suggesting a capacity of 100 mg g^{-1} for the material. This capacity is 1.4 to 7.6 times larger than the best values reported in the literature.^[25] The composite after arsenic adsorption shows a mild change in color (**Figure 2B** inset). The TEM-energy dispersive spectroscopy (EDS) and SEM-EDS elemental mappings of As(III) and As(V) saturated composites are presented in **Figures S7** and **S8** (Supporting Information), respectively, which confirm the presence of adsorbed arsenic homogeneously. As arsenic is generally found with Fe in the natural environment, tests were conducted with an input load of 4 mg L^{-1} Fe(II), which was removed to below the WHO limit of 300 $\mu\text{g L}^{-1}$ over the entire range of volume investigated (**Figure 2b**). Fe(II) was chosen as the input as natural ground water from a depth of 50–120 ft from where it was extracted typically in affected areas through tube wells, where Fe is present in the +2 form, due to anaerobic conditions. Fe(II) becomes

Fe(III) by aerial oxidation, intensifying the color of the water. Similar experiments were also conducted for Fe(III), As(III), As(V), and As(mix) separately and in various combinations of these and all the output values were below permissible limits. Experiments were conducted in the arsenic affected regions of West Bengal, Uttar Pradesh, Bihar, Assam, Jharkhand, Chhattisgarh, and Karnataka states of India in larger scale field trials as well, with similar results. Highest As contamination was seen in water sources of West Bengal, in the range of 200 $\mu\text{g L}^{-1}$, although even higher concentrations are seen occasionally. Therefore, this was chosen as the input concentration in test conditions.

Experiments were conducted to remove arsenic using the porous clay composite alone in presence and absence of iron (Fe(II/III)). A decrease of 40 $\mu\text{g L}^{-1}$ was seen out of 200 $\mu\text{g L}^{-1}$ As (mix) input using the porous filter alone without Fe(II/III). It was never possible to meet the water quality norm of 10 $\mu\text{g L}^{-1}$ through this device in the absence of Fe(II)/Fe(III)/both. Studies revealed that As(III)/As(V)/As(mix) removal was due to particulates of Fe(II)/Fe(III) hydroxides which could not be passed through the porous clay. Dynamic light scattering (DLS) studies showed the existence of three major particle size distributions in this water samples (**Figure S9**, Supporting Information). All the arsenic and iron containing water samples used for testing in this study were maintained at $\text{pH} \approx 7.83$.

Superior arsenic uptake capacity of the composite is due to its inherent structure. Arsenic uptake is uniform across the material and this does not change the inherent structure of the composite. This largely amorphous nature of the composite was also shown in the X-ray diffraction patterns (XRD), which reveals a metastable 2-line ferrihydrite structure in its most disordered form and it does not change upon As(III)/As(V) uptake. Uptake of arsenic appears to be surface adsorption as revealed by XPS studies (survey spectrum is shown in **Figure S10A** (Supporting Information), before and after As(III) and As(V) adsorption). Two broad peaks of Fe 2p were observed at 708.9 eV binding energy (BE) for Fe 2p_{3/2} and 722.3 eV for

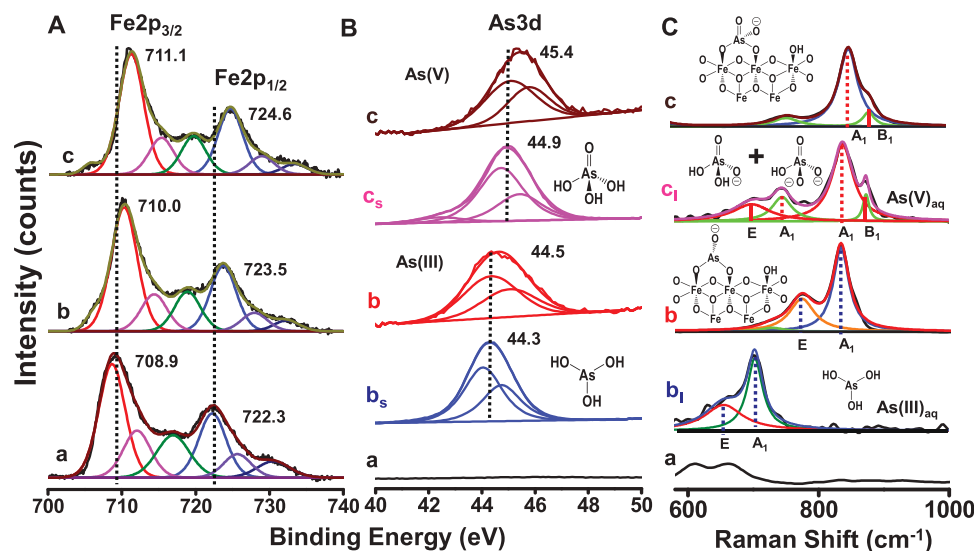


Figure 3. XPS of CM2LF showing A) Fe 2p and B) As 3d regions (a) before As adsorption, (b) after As(III) adsorption, and (c) after As(V) adsorption, independently compared with (b_s) standard As(III) of solid NaAsO₂ and (c_s) standard As(V) of solid Na₂HAsO₄ · 7H₂O respectively. The lines in A and B indicate relative peak shifts. C) Raman spectrum of (a) CM2LF solid, (b) and (c) standard aqueous 100 × 10⁻³ M solutions of As(III) and As(V) and (b and c) after adsorption of As(III) and As(V) on CM2LF. The structures in inset b₁ and c₁ show the speciation of As in solution at pH 7 and the structures in b and c show the probable structure of As(III/V) on CM2LF, respectively.

Fe 2p_{1/2}, respectively for the initial material. The presence of satellite peak at 716.8 eV confirms +3 oxidation state of Fe (Figure 3Aa). The interaction of As(III)/As(V) does not change the oxidation state of Fe in CM2LF significantly. Similar Fe 2p doublet was observed at 710.0/723.5 and 711.1/724.6 eV, respectively for these samples, as shown in Figure 3Ab,c. Small change in the binding energy is due to the strong surface interaction of As with Fe(III). This explanation is supported by literature.^[26,27] The C 1s core-level does not show any significant change while the other core levels, namely, As 3d (Figure 3B and Figure S10B, Supporting Information) and O 1s (Figure S10C, Supporting Information) show small changes upon arsenic interaction with CM2LF. There is a small shift of 0.2 and 0.5 eV, respectively for As(III) and As(V) to higher BE upon interaction with CM2LF, in comparison to the respective arsenic standards (Figure 3Bb_s,c_s). Data support physical interaction of As–O bonds with Fe in CM2LF. There is also a small shift in O 1s to higher BE upon As(III) and As(V) interaction with CM2LF (529.2 and 529.3 eV, respectively), in comparison to initial material (529.0 eV before arsenic adsorption), supporting strong interaction of O²⁻ with Fe(III) and As(III)/As(V) upon adsorption (Figure S10C, Supporting Information).

Raman spectrum of CM2LF is shown in Figure S11a (Supporting Information). The peaks around 230 and 300 cm⁻¹ correspond to Fe–O and Fe–OH symmetric stretching. The standard arsenic materials, NaAsO₂ and Na₂HAsO₄ · 7H₂O in solid state have characteristic peaks in the 700–900 cm⁻¹ window due to symmetric stretching (A₁) of As–O bonds (see Figure S11, Supporting Information). As(III) in solution phase shows two peaks at pH 7 corresponding to the symmetric stretching mode A₁ at 702 cm⁻¹ and the antisymmetric stretching mode E at 650 cm⁻¹ due to the species, H₂AsO₃ (C_{3v} symmetry, Figure 3Cb₁). A redshift in the peak position was observed for As(III) after interaction with CM2LF, the

peaks at 863 cm⁻¹ (A₁) and 796 cm⁻¹ (E) are due to the strong bidentate binding interaction of As–O with Fe–O as shown in Figure 3Cb. Similarly, in solution phase at pH 7, As(V) has two species H₂AsO₄⁻ and HAsO₄²⁻ in 1:1 ratio (ABCD₂ and AB₂CD type molecules both having C_s symmetry) exhibiting symmetric stretching (A₁) at 836 and 743 cm⁻¹, and symmetric bending (B₁ and E) at 875 and 696 cm⁻¹; assigned respectively to these two species (Figure 3Cc₁). Shifted peaks were observed at 852 cm⁻¹ (A₁) and 884 cm⁻¹ (B₁) after the interaction of As(V) with CM2LF. The near complete disappearance of the peaks at 680–750 cm⁻¹ confirms that H₂AsO₄⁻ converts to HAsO₄²⁻ upon adsorption (Figure 3Cc). The interaction of HAsO₄²⁻ with CM2LF is preferably bidentate in nature as shown in the inset of Figure 3Cc.

Figure 4 shows the mechanism of formation of CM2LF, where the ferric ions deposited on chitosan are converted to FeOOH nanoparticles (FeOOH NPs) upon incubation in alkaline medium at room temperature. It gradually makes nanocrystallites, confined in the chitosan network. The mechanical strength originates due to the formation of 3D cage-like structure of chitosan with embedded FeOOH NPs. These FeOOH NPs are accessible for water and dissolved ions. The interaction mechanism of As(III) and As(V) individually with CM2LF is shown Figures S12 and S13 (Supporting Information).

The effects of pH and common ion effect for the adsorption of As(III) and As(V) on CM2LF were studied. It was seen that pH in the range of 4–10 does not alter the adsorption capacity of CM2LF for As(III) and As(V), as shown in Figure S14 (Supporting Information). The effect of common ions on the As uptake is summarized in Table S1 (Supporting Information). CM2LF removes As(III) and As(V) efficiently even in the presence of other ions of relevance to drinking water. Total organic carbon (ToC) release from the components used in making

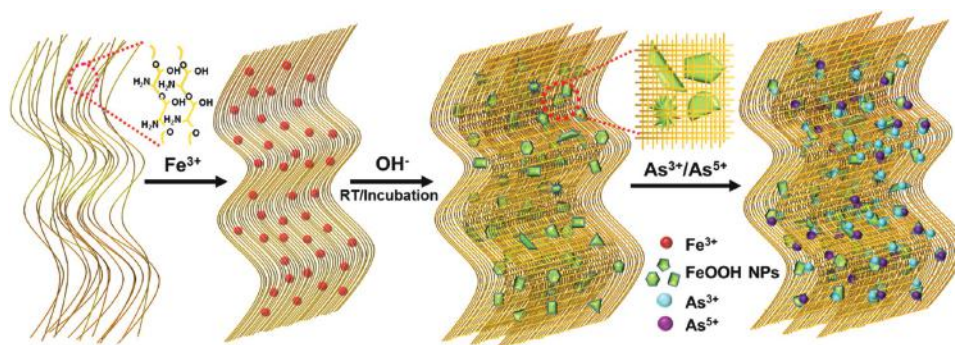


Figure 4. Schematic representation for the preparation of CM2LF and removal of As(III) and As(V) species from water.

CM2LF and the composite before and after As uptake was tested and these values were less than 1 mg L^{-1} , except for chitosan, as shown in Table S2 (Supporting Information). For chitosan, the ToC was 3.39 mg L^{-1} which may be due to the varying degree of polymerization; the smaller particles contribute to higher ToC. However, the acceptable United States Environmental Protection Agency (USEPA) limit for ToC in drinking water is 4 mg L^{-1} . Milli-Q water was used for experiments with CM2LF as the tap water routinely shows a ToC of 8.60 mg L^{-1} .

We have developed a reactivation protocol to regenerate the As saturated CM2LF. The composite was first soaked with Na_2SO_4 solution and incubated for 1 h at room temperature. The pH of the solution was subsequently adjusted to 4 using 1 M HCl solution. The solution was further incubated for about 3–4 h. The material was then washed with DI water to remove excess $\text{SO}_4^{2-}/\text{Cl}^-$ ions. This reactivated material was used for arsenic adsorption for the next cycle. Using the above mentioned protocol we have reactivated and reused the same material for next seven cycles without any loss of arsenic adsorption capacity. The data are shown in Figure S14C and S14D (Supporting Information) for As(III) and As(V), respectively. The toxicity characteristic leaching protocol (TCLP, <https://www.epa.gov/sites/production/files/2015-12/documents/1311.pdf>) studies were conducted using the saturated composites to know the leaching of adsorbed arsenic and iron. The tests showed a leaching of $1 \mu\text{g L}^{-1}$ (total As), $2 \mu\text{g L}^{-1}$ (total As) and $24 \mu\text{g L}^{-1}$ (total Fe) for As(III), As(V) and iron, respectively.

The adsorption capacity of CM2LF was compared with pure ferrihydrite and chitosan separately with respect to the adsorbent dosage as shown in Figure S15 (Supporting Information). The maximum adsorption capacity of As was found to be 36.9 mg g^{-1} for ferrihydrite and 8.0 mg g^{-1} for chitosan in comparison to 100.0 mg g^{-1} for the composite. Performance data of CM2LF in batch experiments were also compared to other commercially available materials, viz., activated alumina, activated carbon, iron oxide (Fe_2O_3), silicon dioxide (SiO_2), GFH, and organic templated boehmite nanostructure (OTBN) are shown in Figures S16, S17, and S18 (Supporting Information). The arsenic adsorption capacities of commercial/noncommercial materials are reported as 15.9, 17.9, 20.2, 16.1, 70.0, and 13.1 mg g^{-1} for activated alumina,^[3] activated carbon,^[4,5] iron oxide,^[5,6] silicon dioxide,^[7] GFH,^[8] and magnetite-reduced graphene oxide composite (M-RGO),^[12] respectively. Data confirm that the arsenic removal capacity of CM2LF is 1.4 to 7.6 times better than

all the compared materials. XPS data of all these commercial/noncommercial materials upon As(III) and As(V) adsorption and comparison of the data with As(III) and As(V) standards are presented in Figures S19, S20, and S21 (Supporting Information). The As 3d peaks of some of the materials shift slightly to lower BE, while some others shift slightly to higher BE but none of them show a drastic shift in these peaks, similar to CM2LF.

A domestic water filtration unit was prepared as shown in the photograph in the inset of Figure S22a (Supporting Information). A filter used three stage water filtration – first, a $0.5 \mu\text{m}$ polypropylene yarn wound cartridge filter for removal of particulates; second, iron removal media; and third, 900 g arsenic adsorbent, CM2LF. The water input and output are marked in the photograph. Performance data for the removal of arsenic and iron using three stage filtration, with a 1:1 ratio of As(III) and As(V), together at $200 \mu\text{g L}^{-1}$ and either of Fe(II) and Fe(III) at 4 mg L^{-1} , as contaminants are shown in Figure S22A (Supporting Information), for a total volume of 6000 L water passed ($>15 \text{ L per day}$ for a year). The output was below the WHO limit of 10 and $300 \mu\text{g L}^{-1}$ for As and Fe, respectively, throughout the experiment. The inset, Figure S22b (Supporting Information) shows water flow rate from the unit at an applied pressure of 7 psi. Reduced quantity of adsorbent and higher flow rates are possible in the optimized design, at different levels of operation, especially in the community scale.

To summarize, As(III) and As(V) as well as mixed forms of the same could be effectively scavenged by a composite with fast kinetics allowing the creation of an affordable arsenic-free drinking water solution for point-of-use applications. The unprecedented large capacity in field conditions is attributed to the inherent structure of the composite with confined metastable 2-line ferrihydrite in biopolymer cages, which allows the creation of effective adsorption sites. The arsenic adsorption capacity of the composite is 1.4 to 7.6 times better than the available compositions. Synthesis of the composition involves simple raw materials and the process requires no electrical power and no organic solvents. With this material, arsenic-free drinking water can be delivered for a family of five at an estimated cost of US \$2 per year in resource limited settings.

Experimental Section

Materials: Ferric chloride ($\text{FeCl}_3 \cdot 6\text{H}_2\text{O}$), sodium hydroxide (NaOH), sodium sulphate (Na_2SO_4), ferrous sulphate ($\text{FeSO}_4 \cdot 7\text{H}_2\text{O}$), and ferric

sulphate ($\text{Fe}_2(\text{SO}_4)_3 \cdot x\text{H}_2\text{O}$) were purchased from Rankem Glasswares and Chemicals, Pvt. Ltd. India. Biopolymer (Chitosan) was purchased from Pelican Biotech & Chemicals Labs Pvt. Ltd. India. Sodium arsenite (NaAsO_2) and sodium arsenate ($\text{Na}_2\text{HAsO}_4 \cdot 7\text{H}_2\text{O}$) were purchased from SD Fine Chemicals Limited. All chemicals were of analytical grade and were used without further purification. The porous filters developed by CSIR-Institute of Minerals and Materials Technology (IMMT) were purchased from Watsan Envirotech Private Limited. Deionized water was used throughout the experiments unless otherwise mentioned.

Synthesis of CM2LF: The granular composites, composed of iron oxyhydroxide–chitosan nanostructures, were synthesized by a green synthetic route, which in general involves the hydrolysis of a metal precursor–chitosan complex using an alkaline medium followed by washing and drying at ambient conditions. Metal ion precursor used for the preparation of the composite was Fe^{3+} . All syntheses were carried out in deionized water, while natural ground water or tap water was used for testing.

An iron oxyhydroxide–chitosan nanostructure was synthesized as follows: About 0.13 g chitosan was dissolved in 10 mL, 1% HCl by continuous stirring for 12 h. This was precipitated at pH 9 using 0.2 M NaOH. About 0.5 g Na_2SO_4 was added in one step. After 5 min of incubation, 10 mL, 1 M ferric hexachloride was added. The mixture was brought to pH 8, using 2 M sodium hydroxide by slow addition. The final composition was further incubated for about 12 h, at ambient temperature to embed the synthesized FeOOH nanoparticles in biopolymer cages. The resulting gel was washed with copious amount of water to remove soluble salts and was dried at room temperature (28–30 °C). The resulting composite, namely, CM2LF, was insoluble in water and appeared as black-red to brownish granules. The dried composite was crushed to specific sizes (optimized $52 \times 72 \mu\text{m}$) and used for arsenic adsorption. The yield was 1.0 g. The method of preparation of the composite is water positive by two to three orders of magnitude; i.e., it produces 500 L of clean water for every 1 L of water consumed for its production. The as-prepared granular composite was stable and did not disintegrate in water for over two years.

The CM2LF prepared within the chitosan matrix, which induces structural integrity, is biodegradable and inexpensive. Other polymers such as banana silk can also be used for this purpose. The organic polymer acts as a template, controls the size of the particles, and gives mechanical strength to the composite after drying at room temperature. When the ferrihydrite nanoparticles were prepared within the matrix, they bind strongly with it, due to which no nanoparticles get into the purified water. It is well-known that hydrous iron oxide, as found in nature, exhibits reasonable mechanical strength (as they occur in crystalline form). In the case of CM2LF composite, it is largely amorphous. Here, the role of chitosan is crucial in improving the mechanical strength of CM2LF composite by binding with ferric oxyhydroxide nanocrystals. As 2-line ferrihydrite has been examined extensively in terms of its structure,^[28,29] we focused only on its arsenic uptake properties.

Testing Protocol for Arsenic Efficacy in Batch: 25 mg of CM2LF was shaken with 100 mL of natural tap water (see Table S1 in the Supporting Information for water quality parameters). Arsenic removal efficiency of CM2LF was measured by spiking the natural tap water with As(III) and As(V) separately at a concentration of 1.1 mg L^{-1} . Thereafter, the water was left standing for 1.5 h and subsequently the leftover arsenic concentration in treated water was analyzed using inductively coupled plasma mass spectrometry (ICP-MS) after acidification with 5% HNO_3 . Experiments with water filtration cartridges are described in the main text.

Instrumentation: HRTEM images of the sample were obtained with JEM 3010 (JEOL, Japan) operating at 200 kV with an ultrahigh resolution polepiece. Elemental mapping using TEM was done on an Oxford Semistem EDS system. The samples for HRTEM were prepared by dropping the dispersion on amorphous carbon films supported on a copper grid and subsequent drying. ADF-STEM measurements were carried out using a Gatan GIF Quantum ER fully loaded Tecnai F20. This analysis was carried out at 200 kV and the data were acquired in digital micrograph and the chemical analysis was carried out with 1 eV

energy resolution. This entire ADF-STEM analysis was carried out in Dual EELS mode to measure the accurate chemical shift. Identification of the phase(s) of all the samples was carried out by XRD (Bruker AXS, D8 Discover, USA) using $\text{Cu K}\alpha$ radiation at $\lambda = 1.5418 \text{ \AA}$. XPS measurements were done using ESCA Probe TPD spectrometer of Omicron Nanotechnology. Polychromatic $\text{Mg K}\alpha$ was used as the X-ray source ($h\nu = 1253.6 \text{ eV}$). Samples were spotted as dropcast films on a sample stub. Constant analyzer energy of 20 eV was used for the measurements. Binding energy was calibrated with respect to C 1s at 284.5 eV. Surface enhanced Raman spectroscopy was performed using a CRM 200 micro Raman spectrometer of WiTec GmbH (Germany). The substrate was mounted on a sample stage of a confocal Raman spectrometer. The spectra were collected at 532 nm laser excitation. For Raman measurements, the corresponding nanomaterial/standard material (as in dried powder form)-coated glass substrates were analyzed keeping the laser and other parameters same. A super-notch filter placed in the path of the signal effectively cuts off the excitation radiation. The signal was then dispersed using a 600/1800 grooves per mm grating and the dispersed light was collected by a Peltier-cooled charge coupled device. Surface morphology, elemental analysis, and elemental mapping studies were carried out using a SEM equipped with EDS (FEI Quanta 200). For the SEM and EDS measurements, samples were spotted on an aluminum sample stub. Total arsenic and iron concentrations in water were detected using ICP-MS (Agilent Technologies, 7700x ICP-MS and PerkinElmer NexION 300X ICP-MS) with appropriate standards. Brunauer-Emmett-Teller (BET) surface area was measured using Micromeritics ASAP 2020. Samples were degassed at 200 °C for 4 h under vacuum and analysed at 77 K with ultra high pure nitrogen gas.

Supporting Information

Supporting Information is available from the Wiley Online Library or from the author.

Acknowledgements

The authors thank Avijit Baidya, Mohd. Azhardin Ganayee, Rahul Narayanan, and P. Srikrishnarka for taking photographs of the set-up used for arsenic testing, for their technical support in conducting Raman analysis, IR measurements, and help in making the Schematic and TOC figures, respectively. The authors thank Edamana Prasad and Madhu Babu for their help in measuring DLS measurements. The authors thank Ligy Philip and Ramprasad for help in ToC measurements. The authors also thank R. G. Robinson, Lini K. Nair, and Manu Santhanam (Department of Civil Engineering) for their help in conducting direct shear stress and compressive strength analyses. Radha Gobinda Bhuiin is currently working at University Erlangen-Nürnberg, Egerlandstr, Germany. National Centre for Catalysis Research at IIT Madras thanked for the BET analyses. Authors thank the Department of Science and Technology (Government of India) for constantly supporting our research program on nanomaterials.

Received: August 9, 2016

Revised: October 16, 2016

Published online:

- [1] T. Pradeep, Anshup, *Thin Solid Films* **2009**, *517*, 6441.
- [2] R. Damoiseaux, S. George, M. Li, S. Pokhrel, Z. Ji, B. France, T. Xia, E. Suarez, R. Rallo, L. Madler, Y. Cohen, E. M. V. Hoek, A. Nel, *Nanoscale* **2011**, *3*, 1345.
- [3] T. F. Lin, J. K. Wu, *Water Res.* **2001**, *35*, 2049.

- [4] B. Deng, M. Caviness, Z. Gu, *ACS Symp. Ser.* **2005**, 915, 284.
- [5] S. Yao, Z. Liu, Z. Shi, *J. Environ. Health. Sci. Eng.* **2014**, 12, 58.
- [6] Y. Jia, T. Luo, X.-Y. Yu, Z. Jin, B. Sun, J.-H. Liu, X.-J. Huang, *New J. Chem.* **2013**, 37, 2551.
- [7] H.-T. Fan, X. Fan, J. Li, M. Guo, D. Zhang, F. Yan, T. Sun, *Ind. Eng. Chem. Res.* **2012**, 51, 5216.
- [8] W. Driehaus, M. Jekel, U. Hildebrandt, *Aqua (Oxford)* **1998**, 47, 30.
- [9] T. S. Sreepasad, S. M. Maliyekkal, K. P. Lisha, T. Pradeep, *J. Hazard. Mater.* **2011**, 186, 921.
- [10] W. Gao, M. Majumder, L. B. Alemany, T. N. Narayanan, M. A. Ibarra, B. K. Pradhan, P. M. Ajayan, *ACS Appl. Mater. Interfaces* **2011**, 3, 1821.
- [11] D. Koushik, S. Sen Gupta, S. M. Maliyekkal, T. Pradeep, *J. Hazard. Mater.* **2016**, 308, 192.
- [12] V. Chandra, J. Park, Y. Chun, J. W. Lee, I. C. Hwang, K. S. Kim, *ACS Nano* **2010**, 4, 3979.
- [13] U. Schwertmann, R. M. Cornell, *Iron Oxides in the Laboratory*, 2nd Ed., Wiley-VCH, Weinheim, Germany **2000**.
- [14] A. Navrotsky, L. Mazeina, J. Majzlan, *Science* **2008**, 319, 1635.
- [15] S. Dixit, J. G. Hering, *Environ. Sci. Technol.* **2003**, 37, 4182.
- [16] J. Gimenez, M. Martinez, J. de Pablo, M. Rovira, L. Duro, *J. Hazard. Mater.* **2007**, 141, 575.
- [17] Y. Jia, L. Xu, Z. Fang, G. P. Demopoulos, *Environ. Sci. Technol.* **2006**, 40, 3248.
- [18] A. Ghosh, Y. Krishnan, *Nat. Nanotechnol.* **2014**, 9, 491.
- [19] S. Das, M. J. Hendry, J. Essilfie-Dughan, *Environ. Sci. Technol.* **2011**, 45, 268.
- [20] M. U. Sankar, S. Aigal, S. M. Maliyekkal, A. Chaudhary, A. A. Anshup Kumar, K. Chaudhari, T. Pradeep, *Proc. Natl. Acad. Sci. USA* **2013**, 110, 8459.
- [21] V. K. Mourya, N. N. Inamdar, A. Tiwari, *Adv. Mater. Lett.* **2010**, 1, 11.
- [22] K. Rout, M. Mohapatra, S. Anand, *Dalton Trans.* **2012**, 41, 3302.
- [23] V. Gade, T. Dave, V. Chauhan, S. Dasaka, In *Proc. Indian Geotechnical Conf., Roorkee, Roorkee, India* **2013**.
- [24] D. Das, G. Samanta, B. K. Mandal, T. R. Chowdhury, C. R. Chanda, P. P. Chowdhury, G. K. Basu, D. Chakraborti, *Environ. Geochem. Health* **1996**, 18, 5.
- [25] S. Kumar, R. R. Nair, P. B. Pillai, S. N. Gupta, M. A. R. Iyengar, A. K. Sood, *ACS Appl. Mater. Interfaces* **2014**, 6, 17426.
- [26] A. P. Grosvenor, B. A. Kobe, M. C. Biesinger, N. S. McIntyre, *Surf. Interface Anal.* **2004**, 36, 1564.
- [27] R. P. Gupta, S. K. Sen, *Phys. Rev. B* **1974**, 10, 71.
- [28] K. M. Towe, W. J. Bradley, *J. Coll. Inter. Sci.* **1967**, 24, 384.
- [29] F. M. Michel, L. Ehm, S. M. Antao, P. L. Lee, P. J. Chupas, G. Liu, D. R. Strongin, M. A. Schoonen, B. L. Phillips, J. B. Parise, *Science* **2007**, 316, 1726.

ADVANCED MATERIALS

Supporting Information

for *Adv. Mater.*, DOI: 10.1002/adma.201604260

Confined Metastable 2-Line Ferrihydrite for Affordable Point-of-Use Arsenic-Free Drinking Water

*Avula Anil Kumar, Anirban Som, Paolo Longo, Chennu Sudhakar, Radha Gobinda Bhui, Soujit Sen Gupta, Anshup, Mohan Udhaya Sankar, Amrita Chaudhary, Ramesh Kumar, and Thalappil Pradeep**

Supporting Information

for *Adv. Mater.*, DOI: 10.1002/adma.201604260

Confined metastable 2-line ferrihydrite for affordable point-of-use arsenic free drinking water

Avula Anil Kumar¹, Anirban Som¹, Paolo Longo², Chennu Sudhakar¹, Radha Gobinda Bhuin¹, Soujit Sen Gupta¹, Anshup¹, Mohan Udhaya Sankar¹, Amrita Chaudhary¹, Ramesh Kumar¹ and Thalappil Pradeep^{1}*

Figure S1. Time dependent microscopic analyses (HRTEM) of CM2LF, amorphous vs. crystallization features of CM2LF

Figure S2. SEM and ADF-STEM analyses of CM2LF

Figure S3. Infrared spectrum (IR) of CM2LF

Figure S4. Direct shear test of CM2LF

Figure S5. Mohr-Coulomb failure pattern of CM2LF

Figure S6. Arsenic uptake kinetics of CM2LF for As(III) and As(V)

Figure S7. TEM-EDX analysis of CM2LF

Figure S8. SEM-EDX analysis of CM2LF

Figure S9. Dynamic light scattering (DLS) analysis of arsenic in presence of iron (Fe-As interaction) in solution

Figure S10. X-ray photoelectron spectrum (XPS) analysis of CM2LF

Figure S11. Raman spectrum of CM2LF

Figure S12. Proposed mechanism of As(III) adsorption on CM2LF

Figure S13. Proposed mechanism of As(V) adsorption on CM2LF

Figure S14. Adsorption efficiency of CM2LF on varying pH and reactivation and reuse of the composite

Figure S15. Comparison of pure ferrihydrite and chitosan with CM2LF

Figure S16. Performance data (batch study) of CM2LF in comparison to activated alumina and activated carbon with respect to arsenic removal

Figure S17. Performance data (batch study) of CM2LF in comparison to iron oxide and silicon dioxide with respect to arsenic removal

Figure S18. Performance data (batch study) of CM2LF in comparison to granular ferric hydroxide (GFH) and organic templated boehmite nanostructure (OTBN) with respect to arsenic removal

Figure S19. XPS data of activated alumina and activated carbon upon arsenic adsorption

Figure S20. XPS data of iron oxide and silicon dioxide upon arsenic adsorption

Figure S21. XPS data of GFH and OTBN upon arsenic adsorption

Figure S22. Performance data (cartridge study) for the proof of concept prototype of Inline domestic unit for arsenic and iron removal

Table S1. Effect of other ions on the As adsorption capacity of CM2LF

Table S2. ToC due to CM2LF before and after As adsorption

Table S3. Physicochemical characteristics of influent natural water

Supporting Information Text

Materials and Methods

High Resolution Transmission Electron Microscopy (HRTEM) images of the sample were obtained with JEM 3010 (JEOL, Japan) operating at 200 kV with an ultra-high resolution (UHR) pole piece. Elemental mapping on TEM was done on an Oxford semi STEM EDS system. The samples for HRTEM were prepared by dropping the dispersion on amorphous carbon films supported on a copper grid and dried. Surface morphology, elemental analysis and elemental mapping studies were carried out using a Scanning Electron Microscope (SEM) equipped with Energy Dispersive Analysis of X-rays (EDAX) (FEI Quanta 200). For the SEM and EDAX measurements, samples were spotted on the aluminium sample stub. Annular Dark-Field Scanning Tunneling Electron Microscopy (ADF STEM) measurements were carried out using a Gatan GIF Quantum ER fully loaded Tecnai F20. This analysis was carried out at 200 kV and data acquired in digital micrograph and chemical analysis was

carried out with 1 eV energy resolution. This entire ADF STEM analysis was carried out in DualEELS (Dual Electron Energy Loss Spectroscopy) mode to measure the accurate chemical shift. X-ray Photoelectron Spectroscopy (XPS) measurements were done using ESCA Probe TPD spectrometer of Omicron Nanotechnology. Polychromatic Mg K α was used as the X-ray source ($h\nu = 1253.6$ eV). The samples were spotted as drop-cast films on a sample stub. Constant analyzer energy of 20 eV was used for the measurements. Binding energy was calibrated with respect to C 1s at 284.5 eV. Total arsenic and iron concentrations in water were detected using inductively coupled plasma mass spectrometry (ICP-MS) (Agilent Technologies, 7700x ICP-MS and PerkinElmer NexION 300D ICP-MS) with appropriate standards.

Mechanical testing of CM2LF: The shear strength of the composite was measured at dry and wet conditions, separately. Around ~ 90 g of granular media was packed in a 6 cm x 6 cm x 6 cm (L x B x H) sample holder and horizontal shear stress was measured under normal stress of 50, 100 and 200 kPa, respectively.

Supporting Information Figures

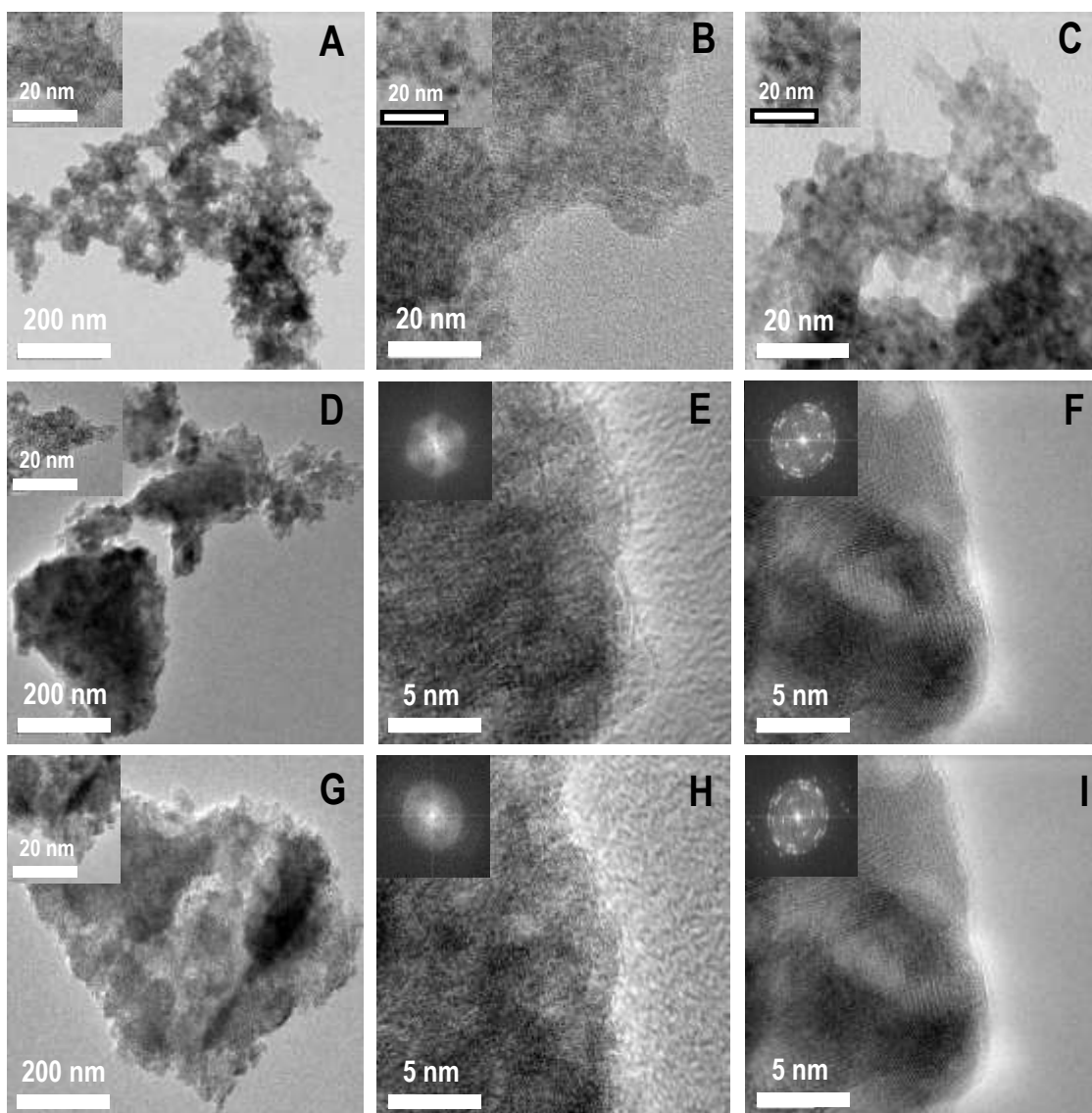


Figure S1. Time dependent TEM images of CM2LF, (A, D and G) initial material, As(III) adsorbed and As(V) adsorbed CM2LF before electron beam irradiation showing amorphous nature of the material (the insets shows the high resolution images). (B, E and H) Short time electron beam induced crystallization of the initial, As(III) adsorbed and As(V) adsorbed CM2LF showing a little crystalline behavior of the material (inset images). (C, F and I) Long time electron beam induced crystallization of the initial, As(III) adsorbed and As(V) adsorbed CM2LF showing the more crystalline nature of the material (inset images).

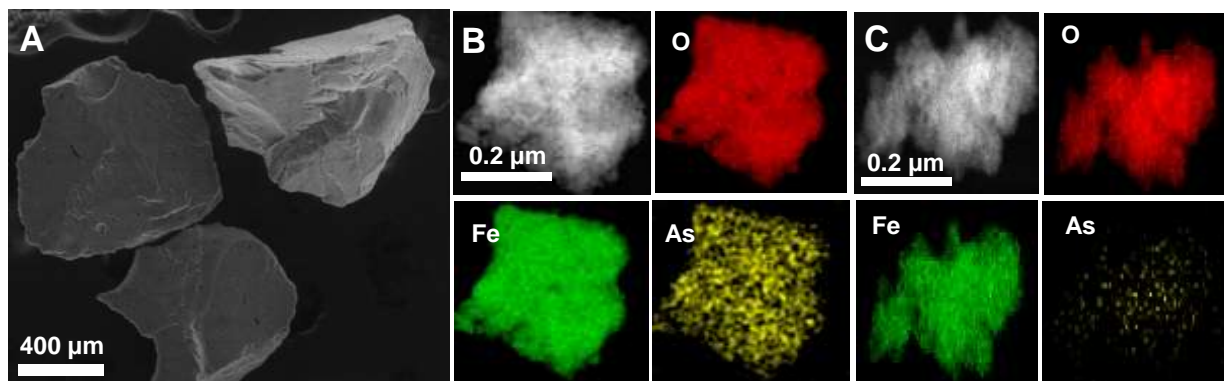


Figure S2. (A) SEM image of the initial granular material (52 X 72 μm), which was stored in water for about 6 months. (B and C) ADF-STEM images of As(III) and As(V) adsorbed material, respectively and the corresponding elemental maps of O, Fe and As(III).

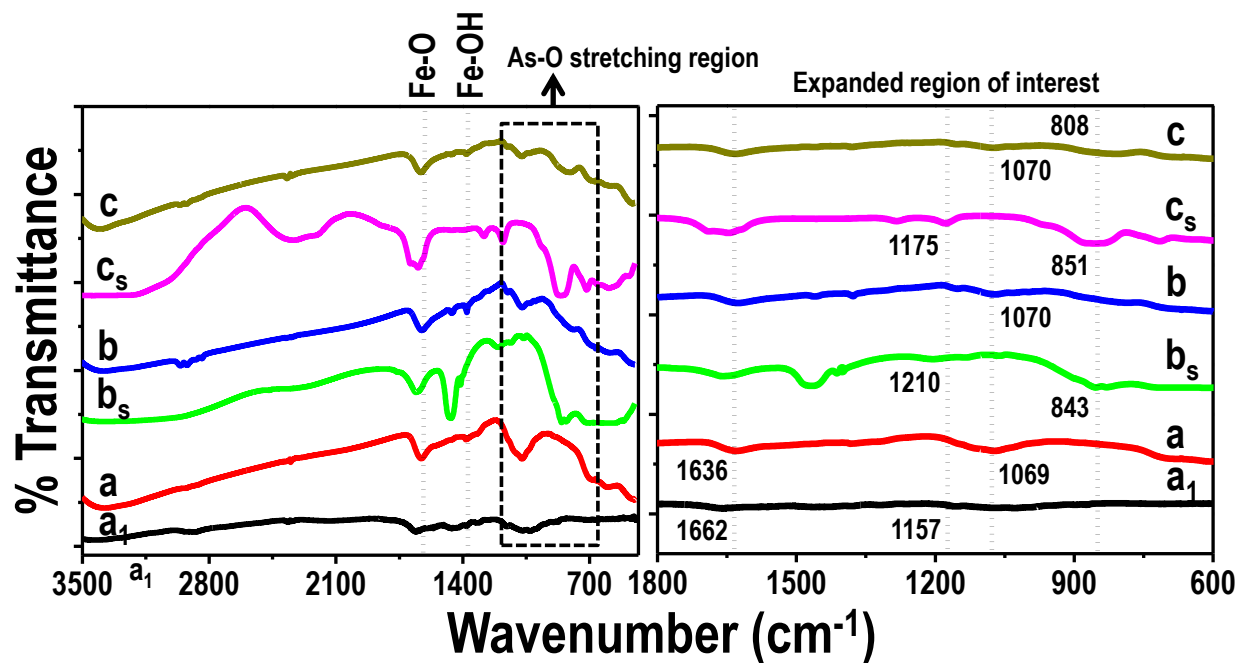


Figure S3. Infrared spectrum (IR) of (a₁) bio-polymer (chitosan), (a) the initial material (i.e., CM2LF), (b) after As(III) adsorption and (c) after As(V) adsorption on CM2LF, independently compared with respective arsenic standards (b_s) As(III) standard and (c_s) As(V) standard, respectively and the corresponding stretching and bending region of Fe-O, Fe-OH and As-O are shown in the expanded region. The corresponding peak shifting are also shown in the expanded region.

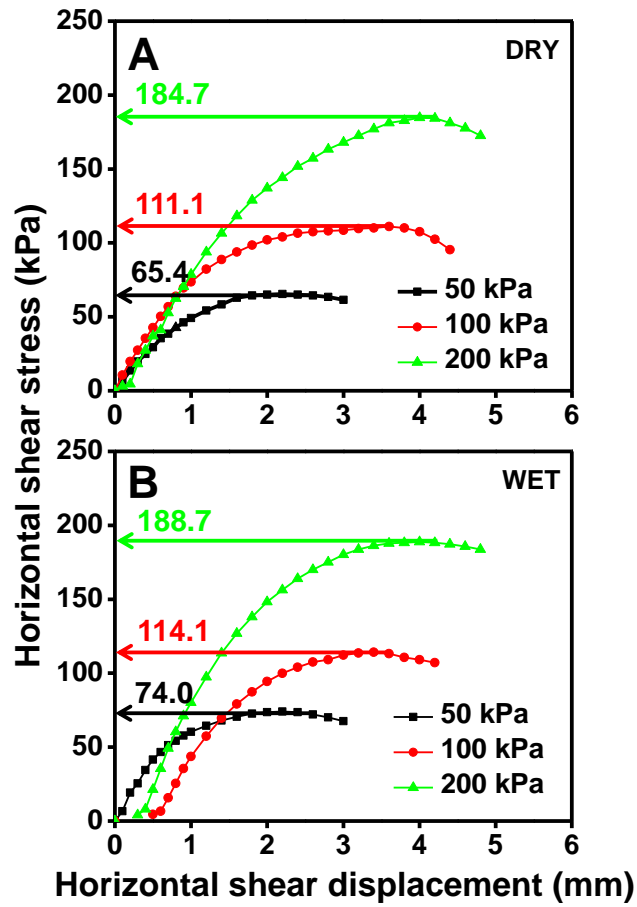


Figure S4. Direct shear test of CM2LF. (A and B) Plot of horizontal shear stress vs. horizontal shear displacement of loosely packed CM2LF measured at dry condition (A) and wet condition (B), respectively.

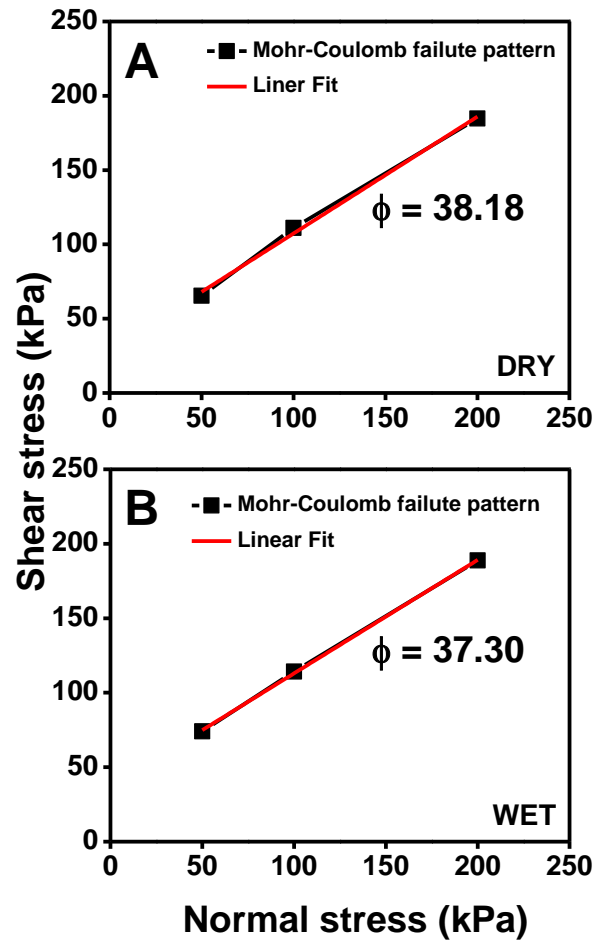


Figure S5. Mohr-Coulomb failure pattern of CM2LF. (A and B) Plot of shear stress vs. normal stress of loosely packed CM2LF showing the straight-line approximation of the Mohr-Coulomb failure pattern measured at dry condition (A) and wet condition (B), respectively.

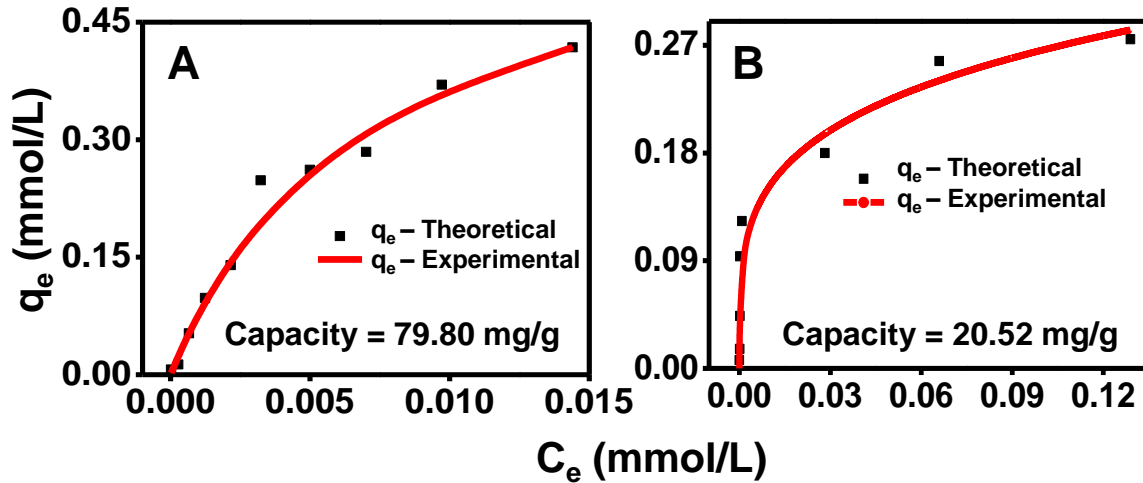


Figure S6. Arsenic uptake kinetics of CM2LF for As(III) and As(V). (A and B) Langmuir isotherm for As(III) adsorbed (mmol/g) as a function of As(III) concentration (mmol/L) (A) and Langmuir isotherm for As(V) adsorbed (mmol/g) as a function of As(V) concentration (mmol/L) (B) conducted with 30 mg initial adsorbent dose in 30 mL deionized water with 90 min as contact time, respectively. Fitted curve is based on Langmuir isotherm.

Arsenic adsorption isotherm of as-synthesized CM2LF composite was measured in the lab in 0.04 M NaCl at pH 7.0, to mimic field conditions. As-synthesized composite adsorbs approximately 1.064 mmol/g and 0.27 mmol/g each at an equilibrium concentration of 0.15 mM of As(III) and As(V), respectively. Langmuir isotherm was evaluated using Equation (1).

$$\frac{C_e}{q_e} = \frac{C_e}{q_{max}} + \frac{1}{q_{max}b} \quad \text{Equation (1)}$$

where, C_e (mmol/L) is the equilibrium concentration of arsenic in the solution, q_e (mmol/L) is the quantity of arsenic adsorbed at equilibrium and q_{max} (mmol/L) is the monolayer adsorption capacity, and b (L/mmol) is the Langmuir adsorption constant, related to the free energy of adsorption.

The Langmuir isotherm was used to estimate the maximum adsorption capacity of CM2LF under the conditions 298 K, pH 7.0 with 90 min of contact time and 1.0 g/L adsorbent dose while varying initial arsenic concentration from 0.5 to 30 mg/L. The values of the isotherm

constants $1/q_{\max}$ and $1/q_{\max}b$, for As(III) adsorption are 1.60 and 0.0114, respectively while that for As(V) adsorption are 3.63 and 0.008, respectively.

The linear plot of C_e/q_e versus C_e (mmol/L) along with a high value correlation coefficient indicates that Langmuir isotherm provides a better fit of the equilibrium data. The Langmuir monolayer capacity (mg/g) of CM2LF for As(III) adsorption is calculated to be 79.80 mg/g while for As(V) adsorption is 20.52 mg/g. This difference is because the adsorbent works better at higher concentrations of As(III) and at lower concentrations of As(V). This is because basic pH is more suitable to remove As(III) while acidic pH is more suitable to remove As(V). The Langmuir model is based on the assumption of homogeneous monolayer coverage with all adsorption sites being identical and energetically equivalent.

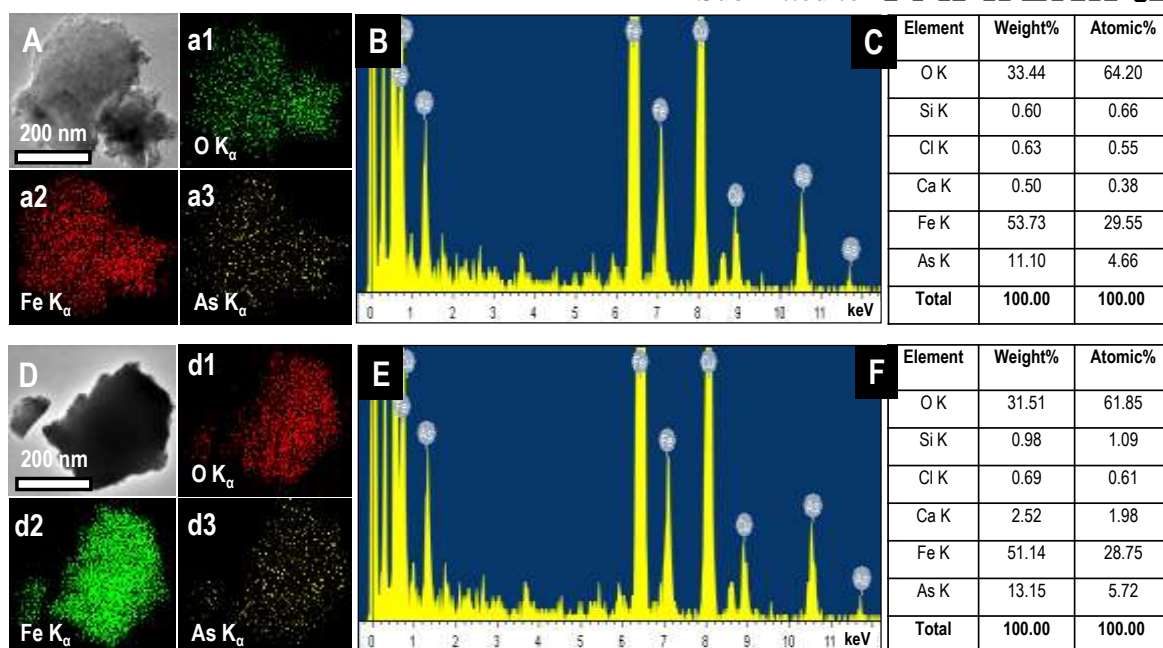


Figure S7. TEM-EDX analysis of CM2LF. (A) X-ray elemental mapping of different elements, (B) Elemental EDX spectrum and (C) Elemental EDX analysis of As(III) adsorbed CM2LF. Same data for As(V) adsorbed CM2LF.

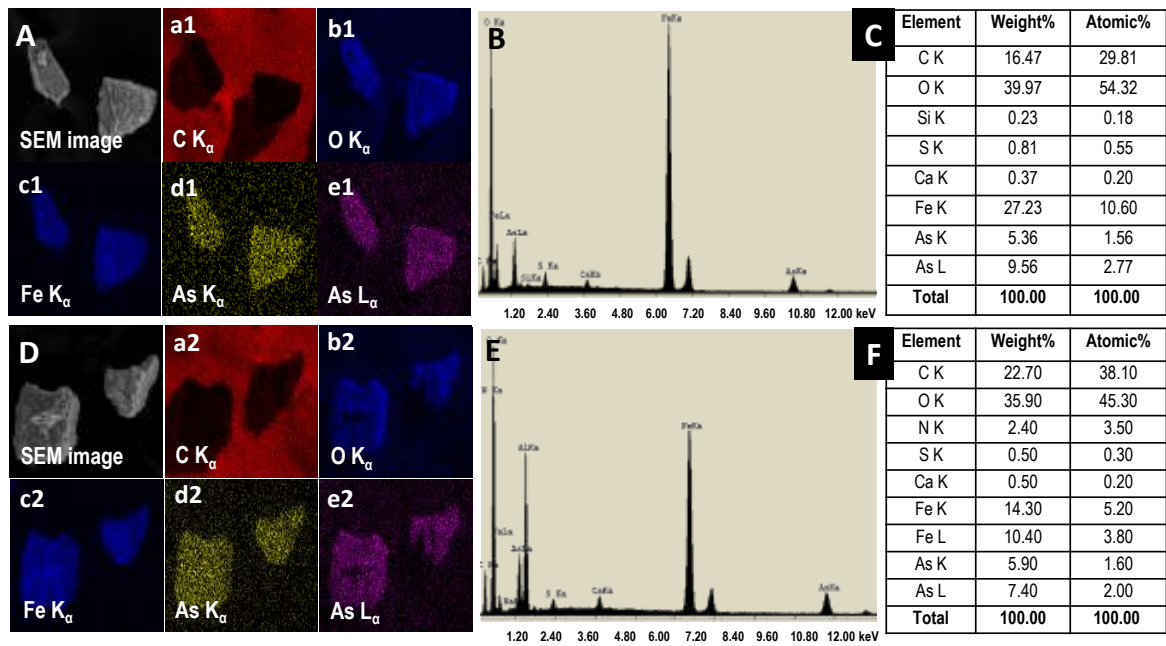


Figure S8. SEM-EDX analyses of CM2LF: (A) X-ray elemental mapping of different elements, (B) Elemental EDX spectrum and (C) Elemental EDX analysis of As(III) adsorbed CM2LF, respectively. Same data for As(V) adsorbed CM2LF.

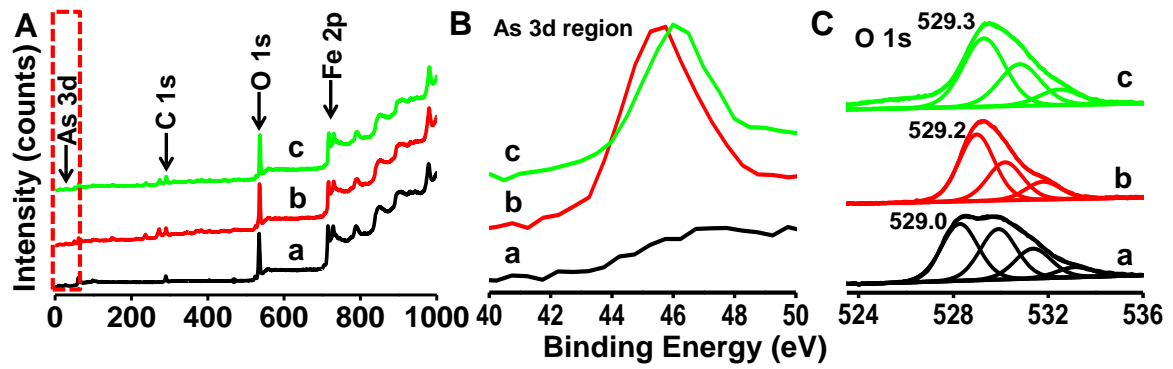


Figure S10. (A) X-ray photoelectron spectrum (XPS) analysis of CM2LF and (B) is the As 3d expanded region of the same plot (a) before As adsorption (b) after As(III) adsorption and (c) after As(V) adsorption. (C) Deconvoluted XPS spectrum of O 1s of CM2LF (a) before As adsorption (b) after As(III) adsorption and (c) after As(V) adsorption.

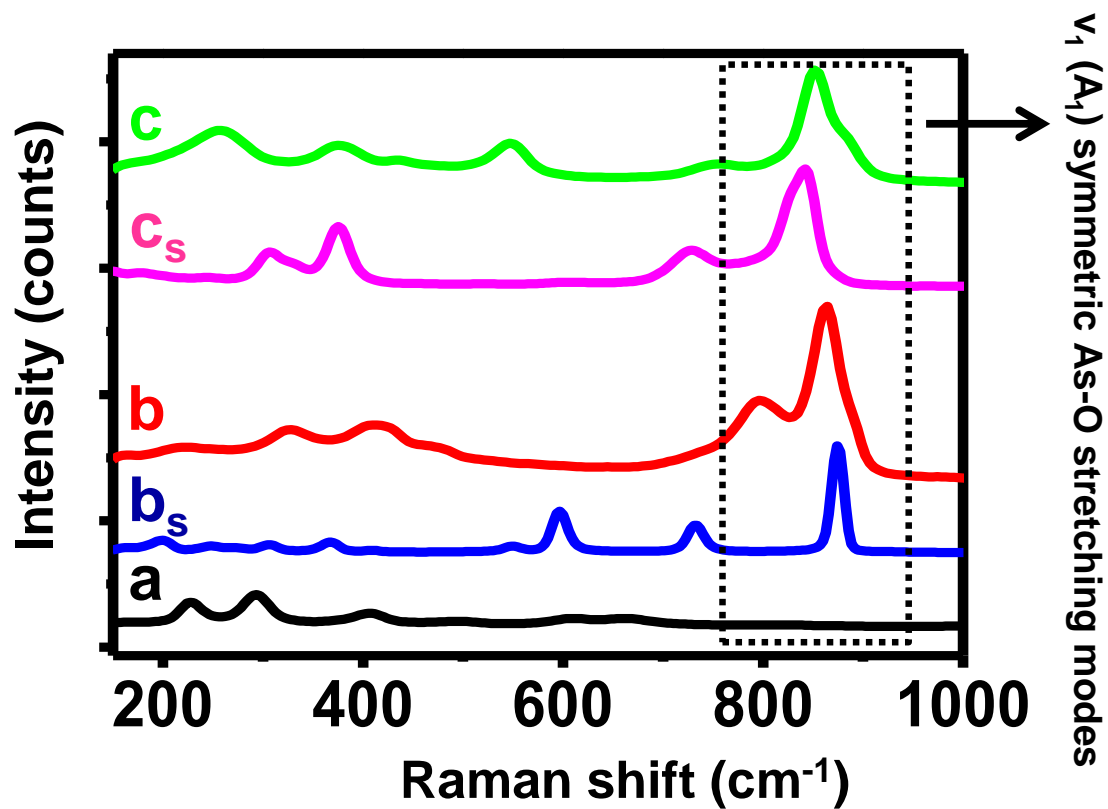


Figure S11. Raman spectrum of (A) CM2LF, (b_s) standard As(III) in solid state, (b) As(III) after treated with CM2LF, (c_s) standard As(V) in solid state and (c) A(V) after treated with CM2LF.

Proposed mechanism for As(III) adsorption

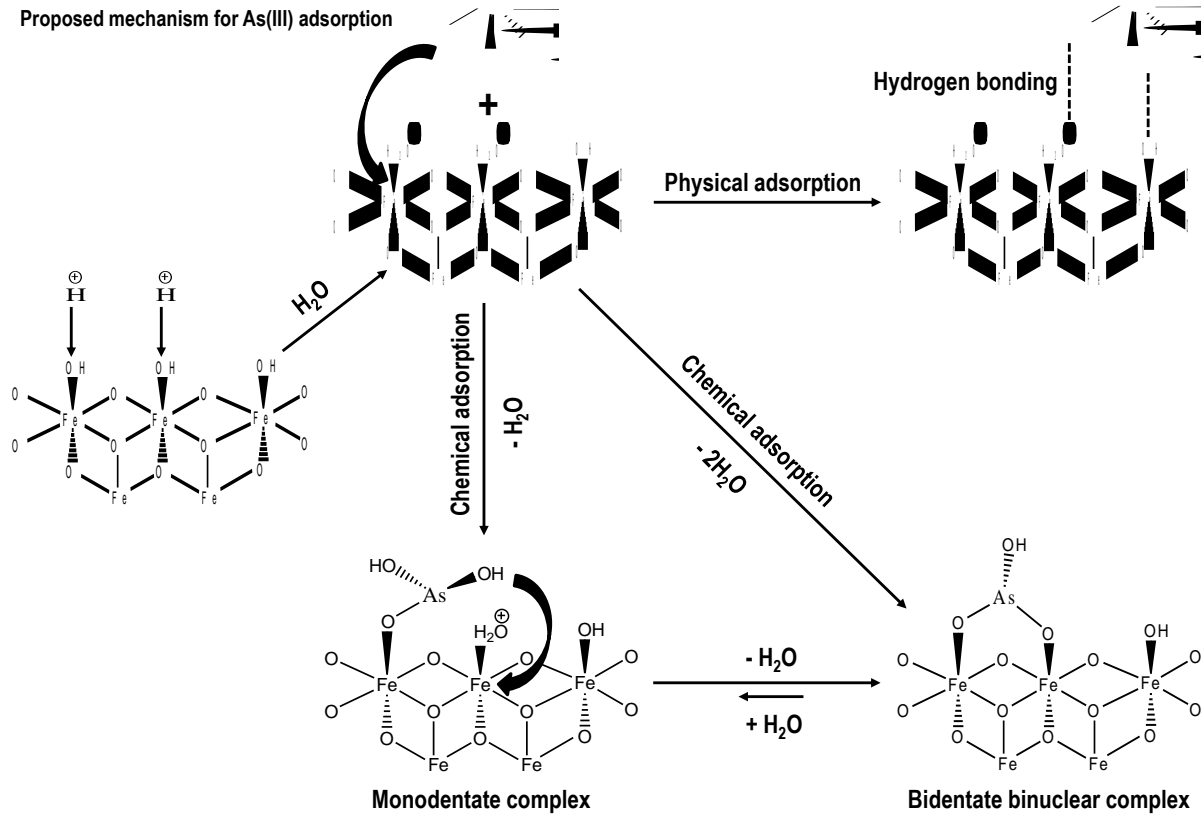


Figure S12. Adsorption mechanism of As(III) on CM2LF.

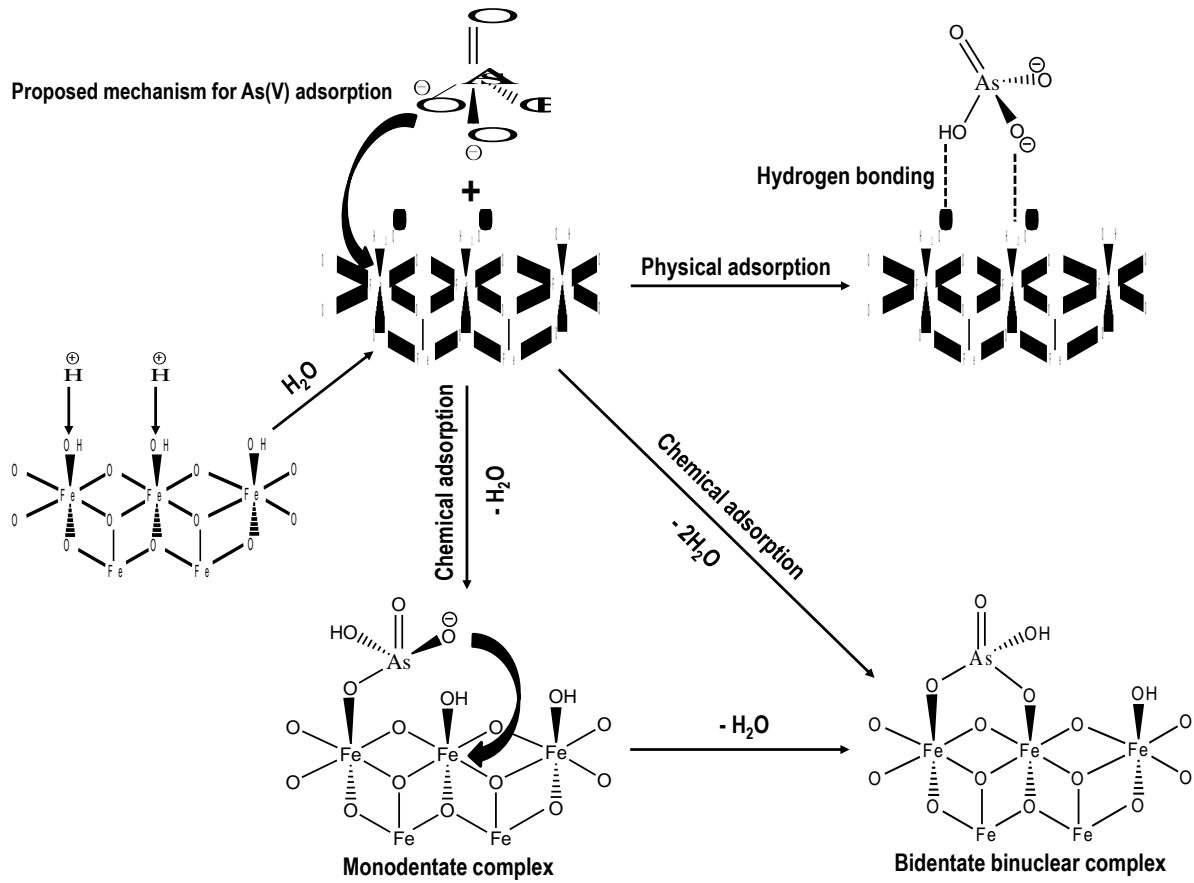


Figure S13. Adsorption mechanism of As(V) on CM2LF.

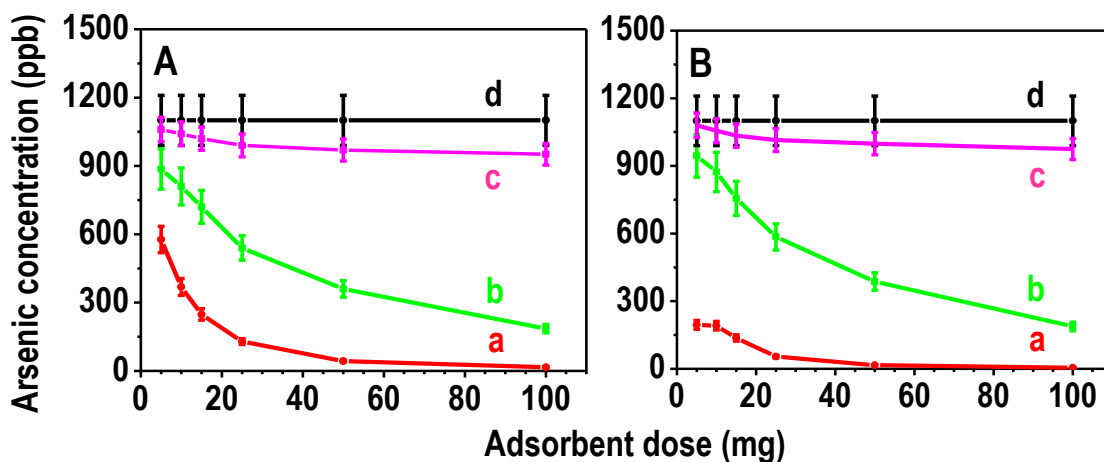


Figure S15. Performance data (batch study) of arsenic removal capacity of CM2LF compared with pure ferrihydrite and chitosan. Residual (A) arsenite and (B) arsenate concentrations as a function of (a) CM2LF dosage, in comparison to (b) pure ferrihydrite and (c) chitosan, with an input arsenic concentration of 1.1 mg L^{-1} , which is shown as (d). Volume taken was 100 mL of ground water, for different doses, varying from 5-100 mg of the materials and the incubation time was 90 min.

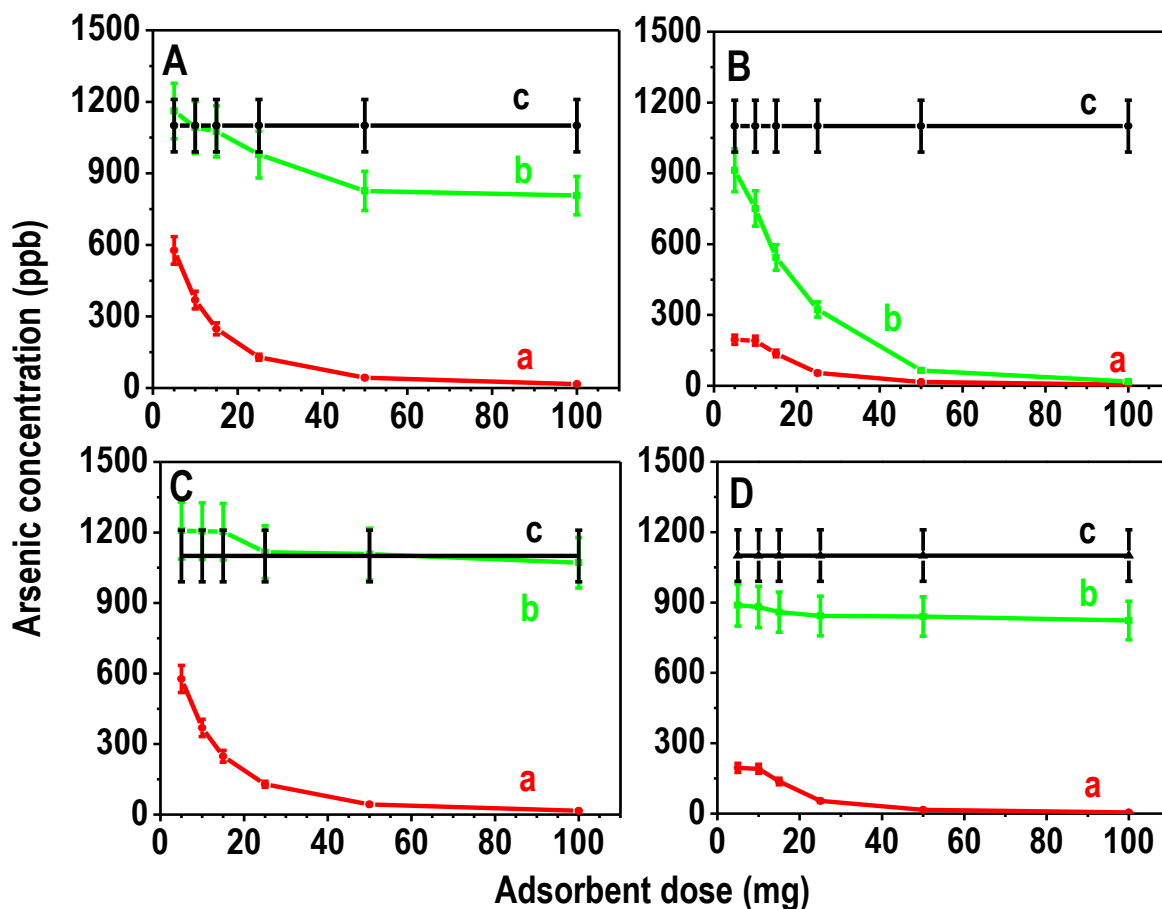


Figure S16. Performance data (batch study) of arsenic removal capacity of CM2LF compared with activated alumina and activated carbon. (A and B) Residual arsenite (A) and arsenate (B) concentrations as a function of (a) CM2LF dosage in comparison to (b) activated alumina with an (c) input arsenic concentration of 1.1 mg L^{-1} . (C and D) Residual arsenite (C) and arsenate (D) concentrations as a function of (a) CM2LF dosage in comparison to (b) activated carbon with an (c) input arsenic concentration of 1.1 mg L^{-1} . Volume taken was 100 mL ground water and the incubation time was 90 min .

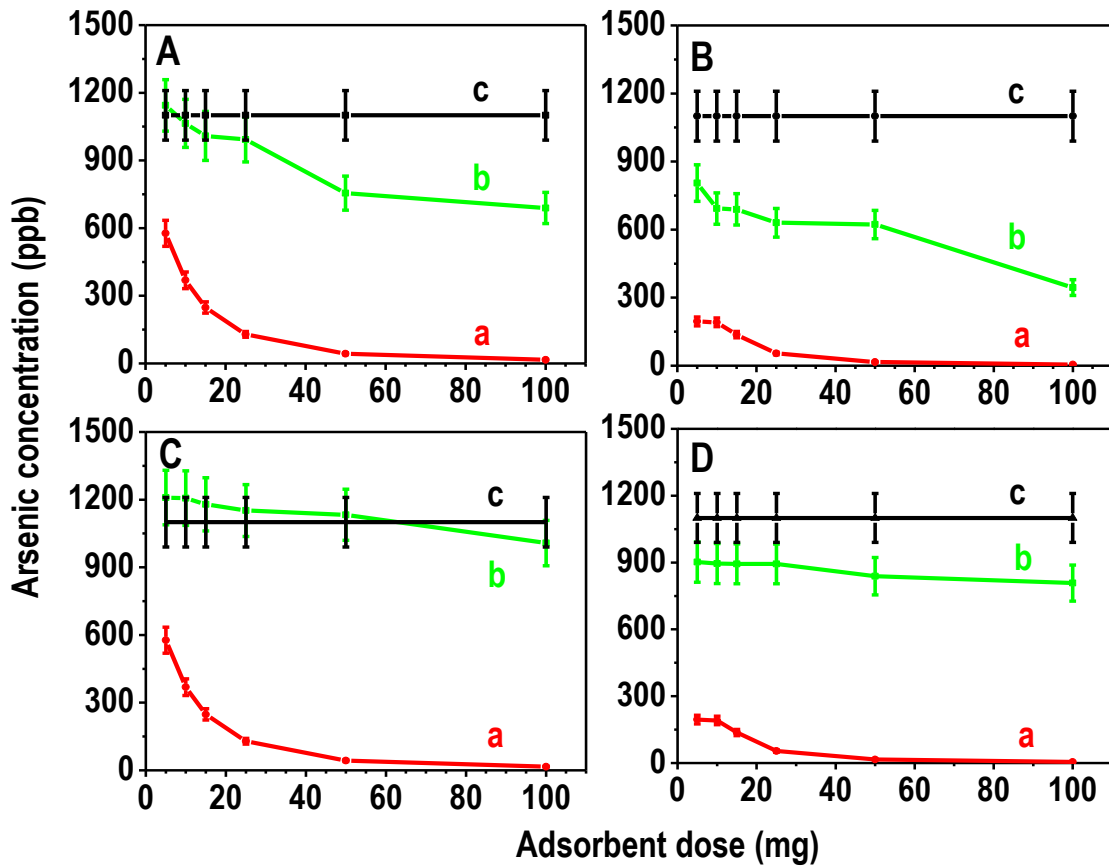


Figure S17. Performance data (batch study) of CM2LF in comparison to iron oxide (Fe_2O_3) and silicon dioxide (SiO_2) with respect to arsenic removal. (A and B) Residual arsenite (A) and arsenate (B) concentrations as a function of (a) CM2LF dosage in comparison to (b) iron oxide dosage with an (c) input arsenic concentration of 1.1 mg L^{-1} . (C and D) Residual arsenite (C) and arsenate (D) concentrations as a function of (a) CM2LF dosage in comparison to (b) silicon dioxide dosage with an (c) input arsenic concentration of 1.1 mg L^{-1} . Volume taken was 100 mL ground water and incubation time was 90 min.

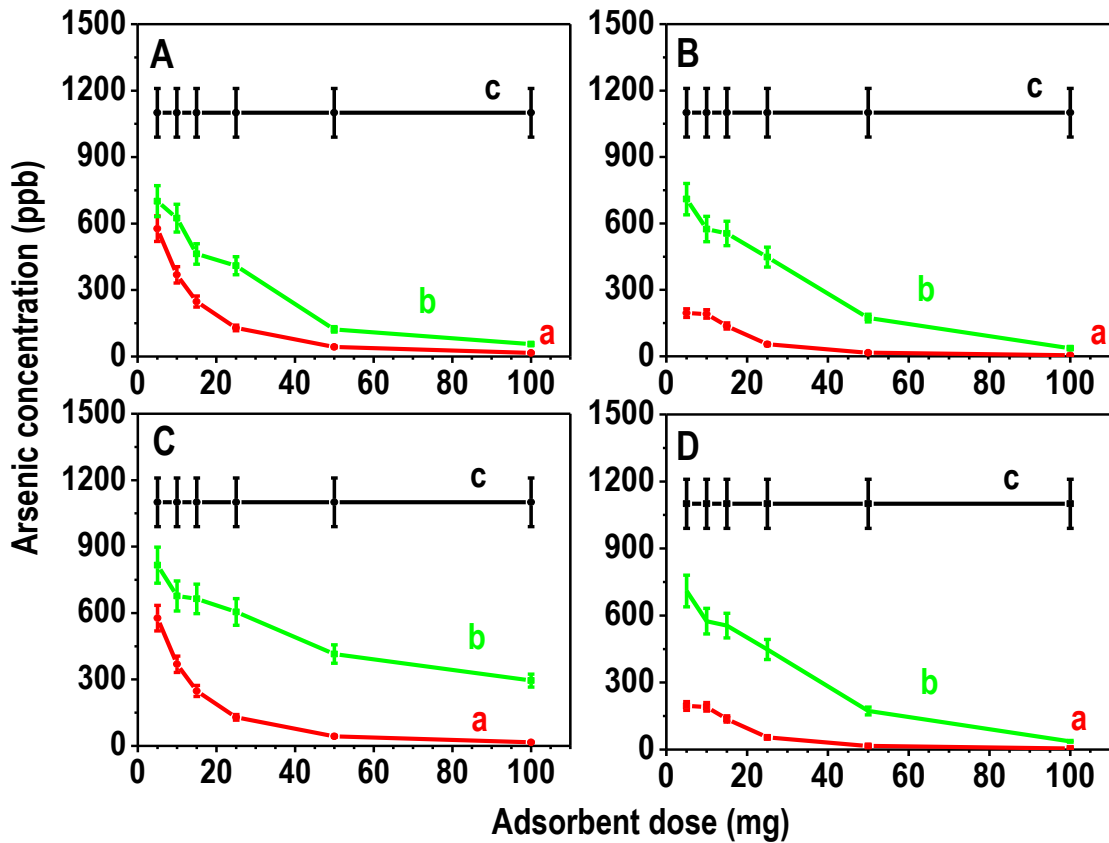


Figure S18. Performance data (batch study) of CM2LF in comparison to granular ferric hydroxide (GFH) and organic templated boehmite nanostructure (OTBN) with respect to arsenic removal. (A and B) Residual arsenite (A) and arsenate (B) concentrations as a function of (a) CM2LF dosage in comparison to (b) GFH dosage with an (c) input arsenic concentration of 1.1 mg L⁻¹. (C and D) Residual arsenite (C) and arsenate (D) concentrations as a function of (a) CM2LF dosage in comparison to (b) OTBN dosage, respectively with an (c) input arsenic concentration of 1.1 mg L⁻¹. Volume taken was 100 mL ground water and incubation time was 90 min.

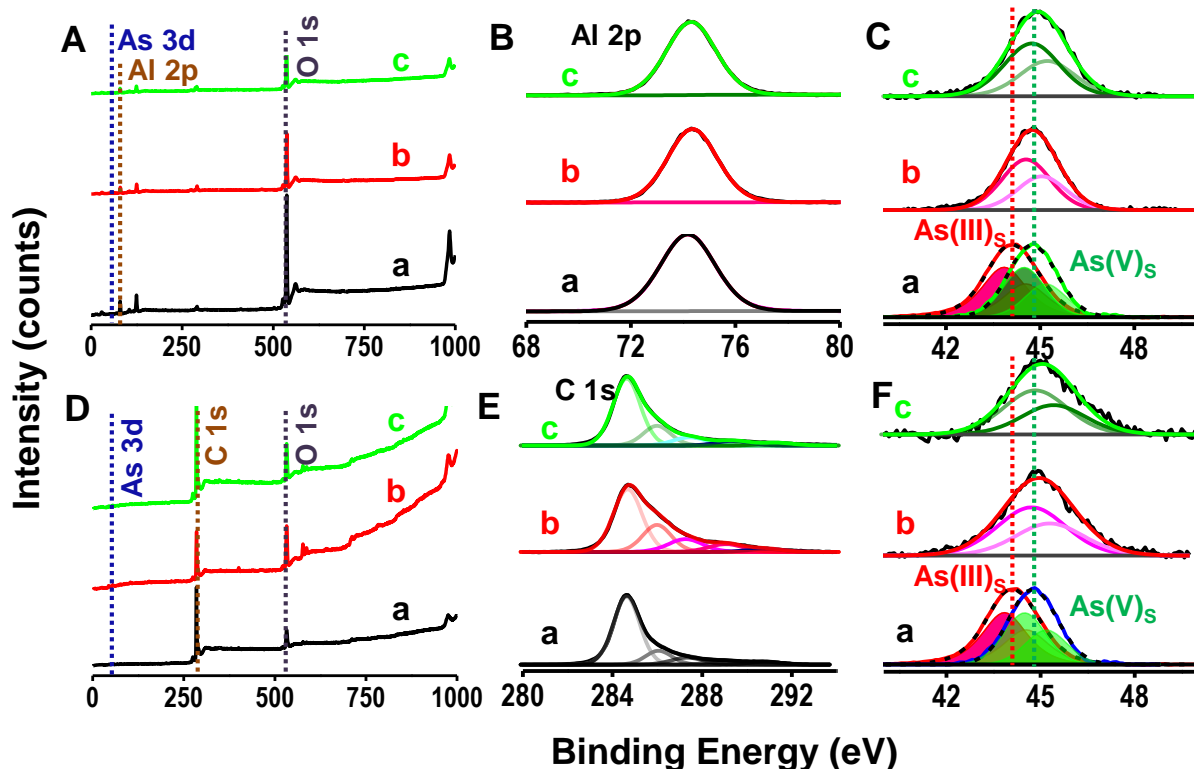


Figure S19. XPS data of activated alumina and activated carbon upon arsenic adsorption. (A) Survey spectrum, (B) Aluminium 2p (Al 2p) region and (C) Arsenic 3d (As 3d) region of activated alumina (a) before As adsorption, (b) after As(III) adsorption and (c) after As(V) adsorption, independently compared with (b_s) standard As(III) and (c_s) standard As(V), respectively. (D) Survey spectrum, (E) Carbon 1s (C 1s) region and (F) Arsenic 3d (As 3d) region of activated carbon (a) before As adsorption, (b) after As(III) adsorption and (c) after As(V) adsorption, independently compared with (b_s) standard As(III) and (c_s) standard As(V), respectively.

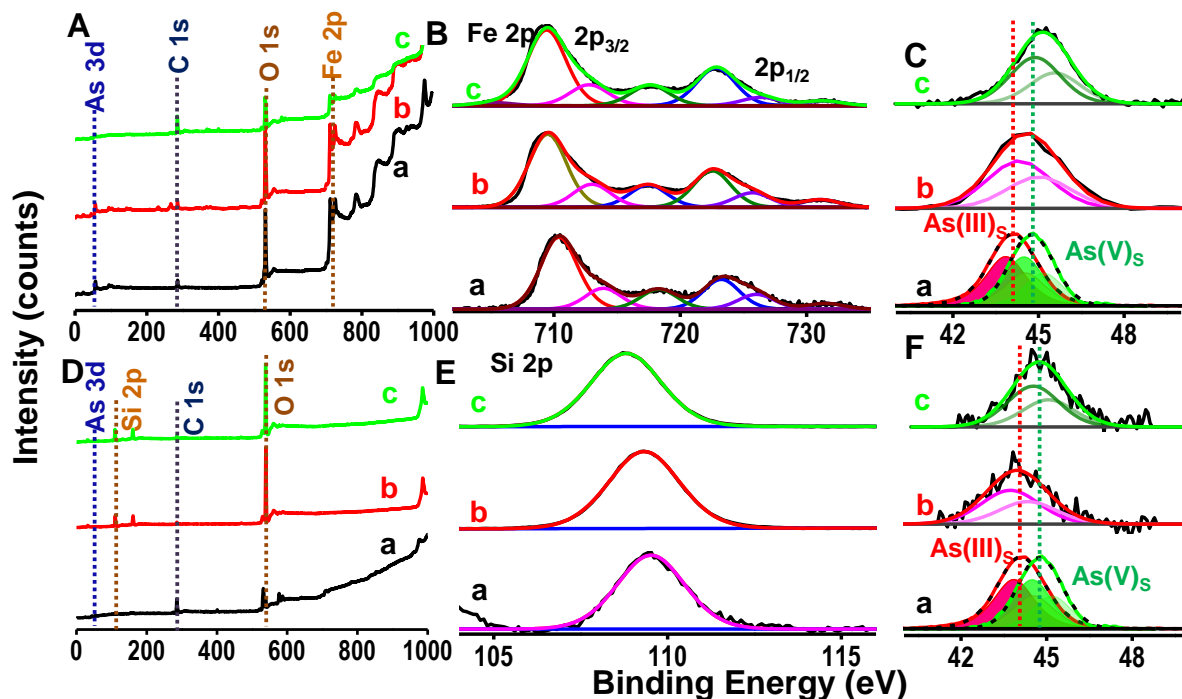


Figure S20. XPS data of iron oxide and silicon dioxide upon arsenic adsorption. (A) Survey spectrum, (B) Iron 2p (Fe 2p) region and (C) Arsenic 3d (As 3d) region of iron oxide (a) before As adsorption, (b) after As(III) adsorption and (c) after As(V) adsorption, independently compared with (b_s) standard As(III) and (c_s) standard As(V), respectively. (D) Survey spectrum, (E) Silicon 2p (Si 2p) region and (F) Arsenic 3d (As 3d) region of silicon dioxide (a) before As adsorption, (b) after As(III) adsorption and (c) after As(V) adsorption, independently compared with (b_s) standard As(III) and (c_s) standard As(V), respectively.

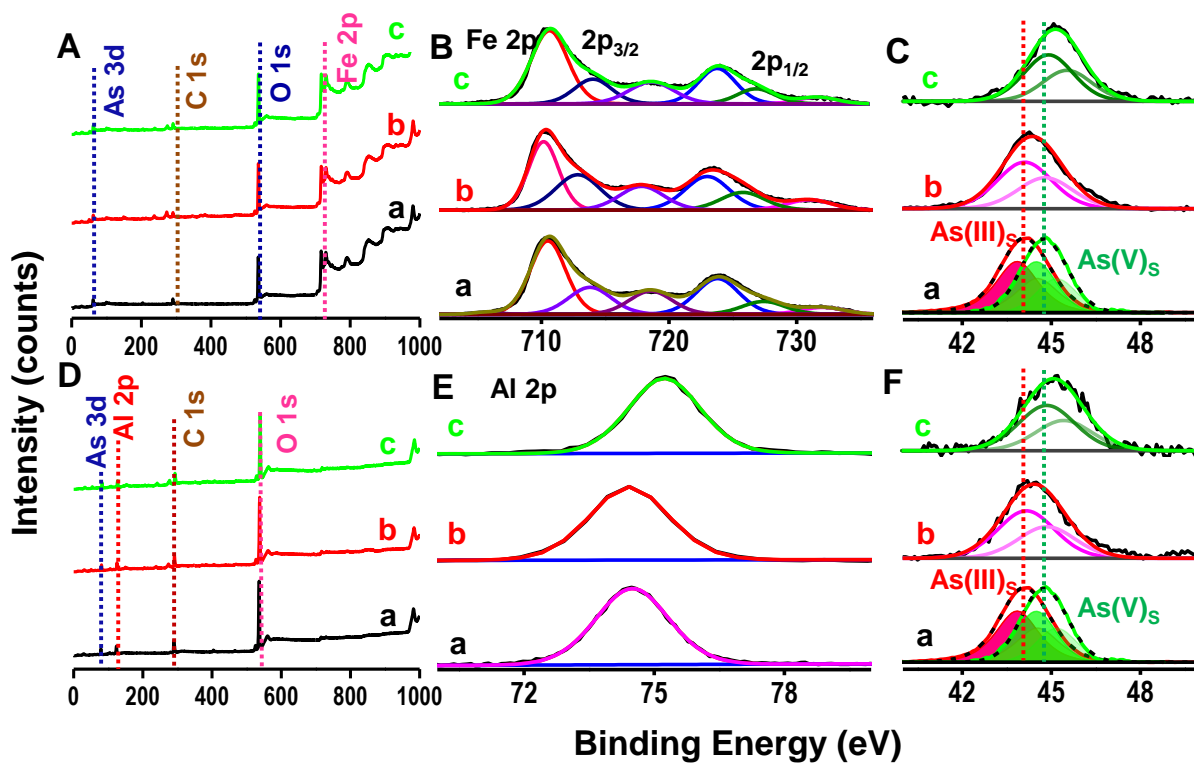


Figure S21. XPS data of GFH and OTBN upon arsenic adsorption. (A) Survey spectrum, (B) Iron 2p (Fe 2p) region and (C) Arsenic 3d (As 3d) region of GFH (a) before As adsorption, (b) after As(III) adsorption and (c) after As(V) adsorption, independently compared with (b_s) standard As(III) and (c_s) standard As(V), respectively. (D) Survey spectrum, (E) Aluminium 2p (Al 2p) region and (F) Arsenic 3d (As 3d) region of OTBN (a) before As adsorption, (b) after As(III) adsorption and (c) after As(V) adsorption, independently compared with (b_s) standard As(III) and (c_s) standard As(V), respectively.

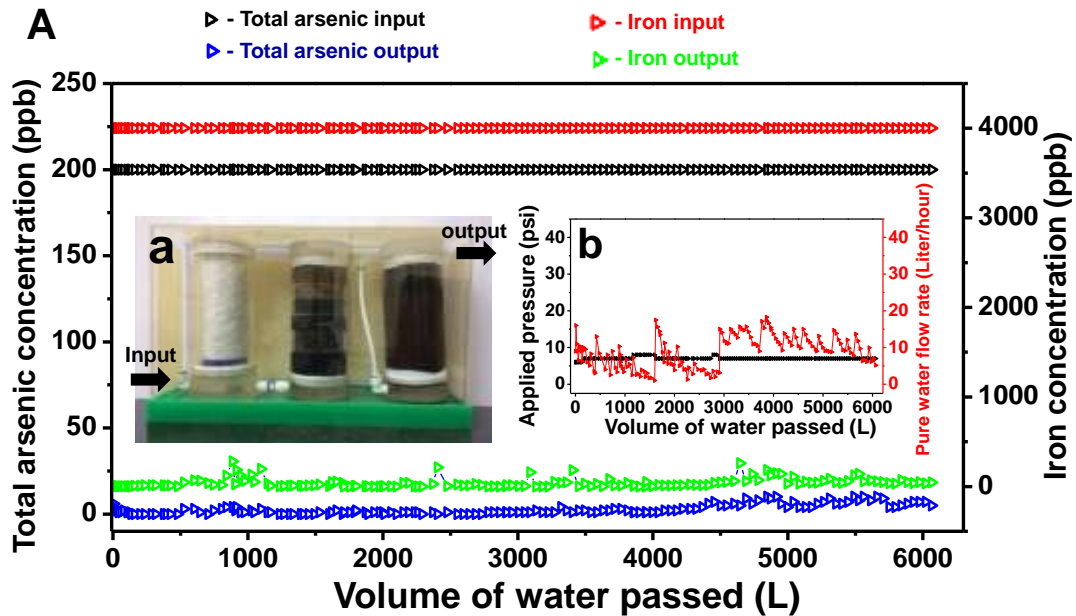


Figure S22. (A) Performance data for the removal of arsenic and iron. Inset (a) shows the proof of concept prototype of Inline domestic unit for removal of arsenic (As(III) + As(V)) and iron (Fe(II) + Fe (III)) contamination from water using three stage filtration, having first cartridge with 0.5 μm polypropylene yarn-wound candle filter for removal of micro-particulates, second cartridge with iron removal media and third cartridge with 900 g arsenic adsorbent. Inset (b) shows pure water flow rate from the unit at corresponding applied pressure. Slight variation in flow rate is due to the change in head pressure in week long experiments.

Table S1.

Arsenic uptake capacity of CM2LF under various ionic strengths with an input arsenic concentration of 1.1 mg L^{-1} , respectively for both As(III) and As(V). 100 mL arsenic contaminated ground water was taken for 25 mg of the composite and the incubation time was 90 min.

Type of ion	Concentration of ion used	Input As(III)	Uptake As(III)	Input As(V)	Uptake As(V)
Fluoride	0.6 ppm	1.1 ppm	1.09 ppm	1.1 ppm	1.09 ppm
Chloride	87 ppm	1.1 ppm	1.09 ppm	1.1 ppm	1.08 ppm
Nitrate	1.9 ppm	1.1 ppm	1.09 ppm	1.1 ppm	1.10 ppm
Sulphate	33 ppm	1.1 ppm	1.09 ppm	1.1 ppm	1.09 ppm
Silicate	16 ppm	1.1 ppm	1.09 ppm	1.1 ppm	1.09 ppm
Sodium	54 ppm	1.1 ppm	1.08 ppm	1.1 ppm	1.10 ppm
Potassium	2.5 ppm	1.1 ppm	1.09 ppm	1.1 ppm	1.10 ppm
Magnesium	15 ppm	1.1 ppm	1.09 ppm	1.1 ppm	1.09 ppm
Calcium	29 ppm	1.1 ppm	1.09 ppm	1.1 ppm	1.09 ppm
Carbonate	100 ppm	1.1 ppm	1.09 ppm	1.1 ppm	1.09 ppm
Bicarbonate	100 ppm	1.1 ppm	1.09 ppm	1.1 ppm	1.09 ppm

Table S2.

ToC leaching from various components used in making the CM2LF composite in comparison to the CM2LF before and after arsenic saturation. Volume taken was 100 mL Milli-Q water for 100 mg of the composite and the incubation time was 90 min. Milli-Q water was taken for the experiments for the composite, as the tap water routinely shows a ToC of 8.60 ppm.

Sample analysed	ToC
Blank water	0.17 ppm
Blank Chitosan	3.39 ppm
Chitosan @ pH 9	0.57 ppm
CM2LF without Arsenic	0.65 ppm
Saturated CM2LF with As(III)	0.69 ppm
Saturated CM2LF with As(V)	0.76 ppm

Table S3.

Physicochemical characteristics of influent natural water.

(Note: All parameters are expressed in mg L⁻¹, except for pH and conductivity)

Parameters	Value
Total coliforms (CFU/mL)	1-2 x 10 ³
pH @ 25°C	7.8
Conductivity (µS/cm)	640.0
Fluoride	0.57
Chloride	86.34
Nitrate	1.84
Sulphate	32.41
Silicate	15.87
Lithium	ND
Sodium	53.74
Ammonium	ND
Potassium	2.33
Magnesium	14.34
Calcium	28.72

ND - not detected

Natural drinking water (without treatment so that there is a residual bacterial count in it) was used for testing to ensure that the material functions in the field.

Diffusion-Controlled Simultaneous Sensing and Scavenging of Heavy Metal Ions in Water Using Atomically Precise Cluster–Cellulose Nanocrystal Composites

Nishil Mohammed,[†] Avijit Baidya,[‡] Vasanthanarayan Murugesan,[‡] Avula Anil Kumar,[‡] Mohd Azhardin Ganayee,[‡] Jyoti Sarita Mohanty,[‡] Kam Chiu Tam,^{*,†} and T. Pradeep^{*,‡}

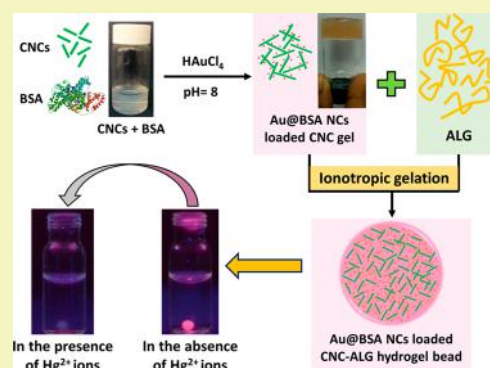
[†]Department of Chemical Engineering, Waterloo Institute for Nanotechnology, University of Waterloo, 200 University Avenue West, Waterloo, ON N2L 3G1, Canada

[‡]DST Unit of Nanoscience and Thematic Unit of Excellence, Department of Chemistry, Indian Institute of Technology Madras, Chennai 600 036, India

S Supporting Information

ABSTRACT: Development of a system that can simultaneously sense and scavenge toxic heavy metal ions at low concentrations is an ideal solution for *in situ* monitoring and purification of contaminated water. In this paper, we report on the synthesis and application of a novel system, luminescent atomically precise cluster–cellulose nanocrystal composite, namely, bovine serum albumin-protected gold nanoclusters (Au@BSA NCs)-loaded cellulose nanocrystal–alginate hydrogel beads, that can simultaneously sense and scavenge heavy metal ions, specifically mercury ions in water. Characterization of the system performed using scanning electron microscopy coupled with energy dispersive spectroscopy and X-ray photoelectron spectroscopy elucidated the physical and chemical characteristics of the system. Additionally, we proposed a new method to visualize the diffusion phenomenon and calculate the effective diffusion coefficient of heavy metal ions in hydrogel beads by monitoring the fluorescence-quenching dynamics of Au@BSA NCs upon binding with mercury ions. Finally, practical applications of this nanocomposite were demonstrated using batch adsorption experiments as well as using a dip pen device loaded with the hydrogel beads for *in situ* monitoring of heavy metal ions in water.

KEYWORDS: Cellulose nanocrystals, Nanoclusters, Nanocomposites, Adsorption, Sensing, Hydrogels, Diffusion, Water Purification



INTRODUCTION

Water is being increasingly contaminated by a wide variety of pollutants from industrial, municipal, and agricultural sources like heavy metal ions, dyes, food additives, pharmaceuticals, detergents, agrochemicals, etc. Thus, access to clean water is becoming more challenging, and efficient technologies that can purify this contaminated water have become essential.^{1,2} Among all these pollutants, toxic heavy metal ions, which accumulate in the food chain continue to be a major concern. Various physical, chemical, and biological treatment methods can be employed to remove heavy metal ions from water. Of all these treatment methods, adsorption implemented using a well-designed system offers the best solution for producing high quality treated water at affordable cost. This technique offers many advantages, such as simplicity in design and operation, low initial investment, effectiveness, and insensitivity to other substances present in the water stream. Researchers around the globe are searching for various low cost nonconventional adsorbent materials.^{3–7}

In this context, the use of sustainable nanomaterials such as cellulose nanocrystals (CNCs) for the adsorption of heavy metal ions from water is gaining momentum, and several

researchers have examined its feasibility.^{8–13} CNCs are rod-like nanoparticles obtained from cellulosic biomass, having diameters in the range of 5–20 nm and lengths of a few hundred nanometers. They can be produced at the industrial scale by acid hydrolysis of pulp fibers. Because of their high specific surface area, good mechanical strength, biodegradability, and high functionality,¹⁴ adsorbents based on these nanomaterials have the capacity to remove a wide variety of pollutants from wastewater.^{15,16} Even though these nanomaterials were found to outperform several conventional adsorbents used in developing countries, their practical application for large-scale water treatment systems is limited as they are difficult to separate from the water bodies after adsorption. This can be solved by incorporating them into

Special Issue: Building on 25 Years of Green Chemistry and Engineering for a Sustainable Future

Received: July 19, 2016

Revised: October 14, 2016

Published: October 16, 2016

matrices, like hydrogel beads, that can be easily used in batch as well as column adsorption processes.^{17–19}

Mercury, in both organic and inorganic forms, is one of the most hazardous environmental contaminants among all heavy metal ions.²⁰ Different approaches have been used for the determination of trace levels of mercury. Fluorescence-based techniques are important in the determination of ionic mercury. However, for trace levels of heavy metals, ultrasensitive methods that are readily implementable in the field have to be developed, working at the limit of single ions.²¹

Aspicules,²² atomically precise quantum clusters of noble metals, have been gaining attention in the field of sensor owing to their enhanced photostability, high quantum yield and ease of functionalization. Their discrete energy states, resulting from a size range corresponding to Fermi wavelength of electrons, endow them with luminescent properties in the visible range. Though a wide range of ligands have been utilized for synthesizing aspicules, biomolecules like proteins and peptides are emerging owing to their simplicity in synthesis, biocompatibility, and wide range of applications. Noble metal clusters protected with BSA, lysozyme, and lactoferrin are some notable examples.^{23–28} Xie et al.²⁹ first reported the use of BSA-protected gold nanoclusters (Au@BSA NCs) for sensing Hg²⁺ ions. Several other groups have used the protein-protected quantum cluster systems for sensing heavy metal ions like Hg²⁺, Cu²⁺, and Pb²⁺. Though highly sensitive, the colloidal stability of these clusters limit their application in the field, and thus, a suitable substrate to anchor them is required. We have previously demonstrated the ability of Au@BSA to bind with nanofibers and have used it for detecting Hg²⁺ ions. Such confinement on a substrate also leads to an increase in the luminescence intensity.³⁰

Until now there have been no reports on CNCs-based nanocomposites that can be used for the simultaneous sensing and scavenging of heavy metal ions in water. In this paper, we report on the synthesis and application of novel nanocomposite hydrogel beads, viz., Au@BSA NCs-loaded cellulose nanocrystal–alginate hydrogel beads that can simultaneously sense and scavenge heavy metals ions, specifically Hg²⁺ ions in water. Several researchers have attempted to probe diffusion and calculate the effective diffusion coefficient using various techniques that are rather complex. Herein, we report a novel approach based on the fluorescence-quenching dynamics of Au@BSA NCs upon Hg²⁺ mercury ion binding, which can be used to probe diffusion and determine the diffusion coefficient of Hg²⁺ ions in the hydrogel beads. The sensing occurs as a result of the adsorption of Hg²⁺ ions on Au@BSA NCs, which is controlled by several parameters like analyte concentration, porous and anionic nature of the hydrogel bead, etc. We performed batch adsorption experiments to elucidate the adsorption characteristics that are pertinent to the sensing application. At this stage of development, the practical application of this system for the removal of Hg²⁺ ions in contaminated water is limited to small-scale operations. Finally, the practical application of these hydrogel beads is demonstrated using a dip pen device containing these hydrogel beads for *in situ* monitoring of heavy metal ions in water.

EXPERIMENTAL SECTION

Materials. CNCs supplied by the University of Maine Process Development Centre were used in this study. Sodium alginate (ALG) was purchased from FMC Biopolymer. Sodium chloride (NaCl), calcium chloride (CaCl₂), and tetrachloroauric acid trihydrate

(HAuCl₄·3H₂O) were purchased from Sigma-Aldrich. Bovine serum albumin (BSA) was purchased from Sisco Research Laboratories Pvt. Ltd. Divalent acetates of mercury, copper, zinc, nickel, lead, cadmium, manganese, cobalt, iron, and magnesium were purchased from Merck. Chromium(III) nitrate nonahydrate (Cr(NO₃)₃·9H₂O) was purchased from Lobachemie, and sodium arsenite (NaAsO₂) was purchased from SD Fine Chemicals Limited. Purified water from a Milli-Q Millipore system (>18 MΩcm) was used for all the experiments. All chemicals were used directly without additional purification.

Methods. Preparation of Nanocomposite. Preparation of the nanocomposite was performed in two steps. In the first step, synthesis of Au@BSA NCs-loaded CNC gel was carried out. During this step, 1 mL of 6 mM HAuCl₄·3H₂O aqueous solution was added dropwise to a 4 mL reaction mixture containing 25 mg BSA and 150 mg CNCs and stirred overnight. After 30 min, the pH of this solution was adjusted to ~12 by adding 200 μL of 1 M NaOH, and then, the whole reaction mixture was stirred overnight. The reaction mixture turned into a gel-like structure, and the formation of Au@BSA NCs was indicated by the characteristic color change from pale yellow to deep brown, with intense red fluorescence under UV light. In the second step, the final nanocomposite, viz. Au@BSA NCs-loaded CNC-ALG hydrogel beads, was prepared by further cross-linking the earlier synthesized Au@BSA NCs-loaded CNC gel using ALG by an ionotropic gelation method in the presence of Ca²⁺ ions. During this step, the desired ratio of Au@BSA NCs-loaded CNC gel and ALG solution were thoroughly homogenized and loaded into syringes. This homogenized solution was then extruded through syringes mounted with a 24-gauge-sized needle using a syringe pump at a flow rate of 0.8 μL/min into 20 mL of 2 wt % CaCl₂ solution that was gently stirred to prevent the beads from adhering to each other. The hydrogel beads that were formed were then allowed to cross-link in a CaCl₂ solution for 15 min, after which they were washed with water several times to remove residual CaCl₂ and BSA and used for further experimentations.

Batch Adsorption Studies. In a typical batch adsorption experiment, 500 mg of water-swollen hydrogel beads were stirred overnight in a vial containing 5 mL of heavy metal ion solution of either Hg²⁺ or Cu²⁺ at neutral pH and 25 °C. The initial and final concentrations of the heavy metal ion solutions were measured using ICP-MS after acidification (5% HCl for Hg²⁺ and 5% HNO₃ for Cu²⁺). Removal % and uptake of heavy metal ions (q_e) by hydrogel beads were calculated using eqs 1 and 2.^{31,32}

$$\text{Removal \%} = \frac{(C_0 - C_e)}{C_0} \times 100 \quad (1)$$

$$\text{Uptake } (q_e) = \frac{(C_0 - C_e)V}{m} \quad (2)$$

where q_e is the amount of heavy metal ions adsorbed per g of adsorbent (mg/g) in equilibrium, C_e is the equilibrium concentration of free heavy metal ions in the bulk solution (mg/L), C_0 is the initial heavy metal ion solution concentration (mg/L), V is the volume of solution (L), and m is the mass of adsorbent (g).

Adsorption capacity of this nanocomposite for Hg²⁺ and Cu²⁺ uptake was also evaluated using the Langmuir adsorption isotherm. This was performed by plotting the equilibrium heavy metal ion uptake (q_e) against the equilibrium concentration of heavy metal ion (C_e) for batch adsorption experiments performed with different initial heavy metal ion concentrations, ranging from 20 to 100 ppm. This equilibrium data was fitted using the linearized form of the Langmuir adsorption isotherm model mentioned in eq 3.

$$\frac{1}{q_e} = \frac{1}{K_L q_m C_e} + \frac{1}{q_m} \quad (3)$$

where q_m is the maximum amount of heavy metal ions which can be adsorbed per gram of adsorbent (mg/g) in equilibrium, and K_L is a constant related to the energy of adsorption (L/mg) which depicts the affinity between the heavy metal ion and adsorbent. Parameters q_m and K_L were determined from the intercept and slope of the plot of $1/q_e$ versus $1/C_e$, respectively.

Development of an Ideal Sensor–Scavenger System. Three hydrogel bead systems containing the CNC:ALG ratios of 1:2, 1:1, and 2:1 were prepared by mixing different ratios of Au@BSA NCs-loaded CNC gel and ALG solutions. Leaching of Au@BSA NCs from the hydrogel beads placed in water for 2 days were analyzed by inspecting the supernatant, both visually under UV light and measuring the absorbance at 280 nm using a UV–vis spectrophotometer. Also, the mercury removal percentages of the three systems were compared using batch adsorption studies.

Sensing Experiments. Further, the sensitivity of this nanocomposite to various heavy metal ions was also analyzed. For the single hydrogel bead-sensing experiment, one bead was placed in each HPLC vial containing 1 mL of 1 ppm concentration of various heavy metal ion solutions like Hg^{2+} , Cu^{2+} , Zn^{2+} , Ni^{2+} , Pb^{2+} , Cd^{2+} , Cr^{3+} , As^{3+} , Mn^{2+} , Co^{2+} , and Fe^{2+} . The fluorescence of Au@BSA NCs inside the hydrogel beads when immersed in these heavy metal ion solutions was monitored to evaluate the sensitivity and selectivity of the system. A hydrogel bead was also placed in the solution of Mg^{2+} and Ca^{2+} ions, which are the common ions contributing to the hardness of water, in order to study the effect of counterions.

Characterization of Nanocomposite. Photographs of the hydrogel beads were recorded, and the size distribution and mean diameter of hydrogel beads were measured using a vernier caliper. Morphology, elemental analysis, and elemental mapping studies of the hydrogel beads were performed using a scanning electron microscope (SEM) equipped with energy dispersive analysis of X-rays (EDAX) (FEI Quanta 200). For the SEM and EDS measurements, freeze-dried hydrogel bead samples were spotted on an aluminum sample stub. X-ray photoelectron spectroscopy (XPS) measurements were conducted using an Omicron ESCA Probe spectrometer with unmonochromatized Al K α X-rays (energy = 1486.6 eV). High resolution transmission electron microscopy (HRTEM) of Au@BSA NCs was performed with JEOL 3010, a 300 kV instrument. The samples for HRTEM were prepared by dropping the dispersion on a carbon-coated copper grids and drying under ambient conditions. UV–visible absorption spectra and photoluminescence spectra of Au@BSA NCs were acquired using PerkinElmer Lambda 25 UV–vis spectrophotometer and Jobin Yvon NanoLog spectrofluorometer, respectively.

Quenching Dynamics to Study Diffusion. Dark field fluorescence microscopy was employed to monitor the quenching dynamics of Au@BSA NCs upon the diffusion of Hg^{2+} ions into the hydrogel beads. Fluorescence imaging and spectra of hydrogel beads were performed using the Cytoviva HSI system containing an Olympus BX-41 microscope equipped with a Dage high resolution camera. Dark field fluorescence microscopy was used in an excitation window corresponding to DAPI/FITC/TEXAS RED (DAPI, 452–472 nm; FITC, 515–545 nm; TEXAS RED, 600–652 nm), and emissions were collected using a triple pass emission filter DAPI/FITC/TEXAS RED (DAPI, 452–472 nm; FITC, 515–545 nm; TEXAS RED, 600–652 nm). We have chosen similar excitation and emission filters for simultaneous visualization of the fluorescent area along with the quenched area. The distinct red fluorescence of the cluster allows us to easily distinguish between the quenched and fluorescent part of the hydrogel bead.

Hydrogel beads of a size greater than 1 mm was imaged under a dark field fluorescence microscope. The intense red color of the bead indicates the uniform distribution of the clusters. Hydrogel beads were initially kept in Millipore water, and the fluorescence intensity was observed for some time to confirm that it did not change in the control condition. Then, a single bead was immersed in 100 ppm of Hg^{2+} ion solution, and time-dependent quenching of the red emission from Au@BSA NCs was observed. Images were captured at regular time intervals. By monitoring the fluorescence area from these images, the diffusion kinetics of the Hg^{2+} ions were studied. The rate of diffusion of ions corresponds to the rate of fluorescence quenching. As the time scale of reaction between the metal ion and the cluster which quenches the luminescence is much faster than ionic diffusion, the error due to the former event is insignificant. The diffusion of Hg^{2+} ions into the hydrogel bead was monitored by studying the reduction in the fluorescence diameter of the bead.

The diffusion coefficient (D) is an essential parameter to model diffusion by solving Fick's second law.

$$\frac{\partial^2 C}{\partial x^2} = -D \frac{\partial C}{\partial t} \quad (4)$$

where C is the concentration, x is the position, and t is the time. Solving this equation requires knowledge of flux and concentration varying over time. The rate of change of mercury concentration (dC_0) can be equated to the rate of change in fluorescence intensity (dF_1) using the following equation:

$$dC_0 = dF_1 \quad (5)$$

By substituting the above equation in Fick's law, we obtain the coefficient for fluorescence quenching which is similar to D for Hg^{2+} ions. This was calculated by analyzing the variation of red intensity along the bead diameter at various time points. The variation in red intensity along the diameter of the bead was extracted using an image analysis code run using the open software called R. The code is included in the section S10 of the Supporting Information (SI). For ease of calculation, the equation representing the concentration was assumed to be a multiple of two independent functions, distance and time. The variation in red intensity for various time points was fitted to a sine curve representing the variation along the diameter. Then, the maximum intensity (taken from the center of the sine curve) was plotted against time to obtain the function describing the change of intensity with time. This was fitted to an exponential curve.

The solution for Fick's equation under homogenization seems to fit the equation of fluorescence as a function of distance and time as given by

$$F = 0.66 \sin\left(\frac{x\pi}{1260}\right) e^{(-t/1594)} - 0.11 \quad (6)$$

Also, the minimum measurable distance, i.e., length of one pixel, and the error from fitting the exponential decay for time constant were used to calculate error. The detailed calculations are included in section S11 of the SI.

Dip Pen Experiments. A concept dip pen device was fabricated to demonstrate the application of these hydrogel beads for *in situ* monitoring of heavy metal ions in water. A capillary column of inner diameter 2 mm and length 5 cm was filled with hydrogel beads of diameter 1.9 mm along the length of the column. This capillary column was dipped into a glass vial containing 5 mL of 50 ppm mercury ion solution. Photographs of the dip pen device placed in the mercury ion solution were taken at regular intervals to monitor fluorescence quenching of Au@BSA NCs, as a result of the capillary rise of mercury ion solution through the hydrogel beads.

RESULTS AND DISCUSSION

Preparation of Nanocomposite. Highly fluorescent Au@BSA NCs with a characteristic red emission are formed as a result of *in situ* reduction of Au ions encapsulated in BSA protein upon adjusting the reaction pH to ~ 12 by the addition of NaOH.²⁹ When the synthesis of these nanoclusters takes place in the reaction mixture containing CNCs, it leads to the formation of a gel-like structure due to the ion-mediated gelation of CNCs by the cationic Au ions. Chau et al.³³ and Shafiei-Sabet et al.³⁴ have reported that CNCs at a particular concentration tend to form gel-like structures upon the addition of cations due to stronger propensity of CNCs for side-by-side association. Gelation of CNCs can be induced by the increasing ionic strength of CNC suspension with the addition of salts. Salt addition reduces the Debye length of CNCs, and as a result, the electrostatic repulsion between them is suppressed and dominant attractive forces like van der Waals forces and hydrogen bonding come into play.^{33,34}

When the nanocomposite solution containing Au@BSA NCs, CNCs, and ALG was introduced to a CaCl₂ solution, hydrogel beads were instantaneously formed, as a result of ionotropic gelation of ALG by Ca²⁺ ions. ALG is an anionic polysaccharide composed of (1–4)-linked β-D-mannuronate (M) and α-L-gulonate (G) units which in the presence of divalent cations, such as Ca²⁺, form hydrogels via ionic cross-linking of calcium bridges between the M and G units of the adjacent chains.³⁵ Figure 1 shows the Au@BSA NCs-loaded CNC gel and Au@BSA loaded CNC-ALG hydrogel beads under white light and UV light.

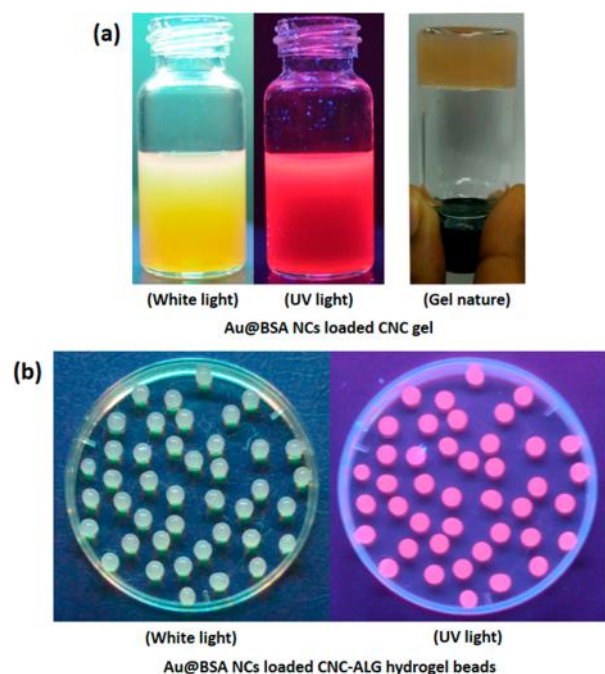


Figure 1. Photographs of (a) Au@BSA NCs-loaded CNC gel and (b) Au@BSA NCs-loaded CNC-ALG hydrogel beads under white light and UV light. The luminescence intensity in the sample bottle ((a), middle) is nonuniform as the excitation is from the top, and it becomes attenuated at the bottom.

Au@BSA clusters were studied independently in the group, and previous studies including ours^{36,37} have established that the clusters showing emission at 660 nm are composed of 30 atoms of Au. They also exhibit well-defined mass spectra, measured using matrix-assisted laser desorption ionization (MALDI). However, as the focus here is on sensing and scavenging, we are not discussing these aspects in greater detail.

Development of an Ideal Sensor–Scavenger System. Among the three nanocomposite hydrogel bead systems, the 1:2 CNC:ALG system was found to be an ideal sensor–scavenger system. This system showed lesser leaching of Au@BSA NCs as compared to 1:1 and 2:1 systems when placed in water for 2 days. Figure 2(a) shows the photographs of the vials containing the three systems, taken at the start and end of the leaching experiment. More intense red luminescence was observed for the supernatant for the 1:1 and 2:1 system compared to the 1:2 system, due to the higher leaching of Au@BSA NCs from these systems. This is further confirmed by the higher UV absorbance of the supernatants from the 1:1 and 2:1 systems compared to the 1:2 system measured at 280 nm, as shown in Figure 2(b). Mechanical integrity tests performed by

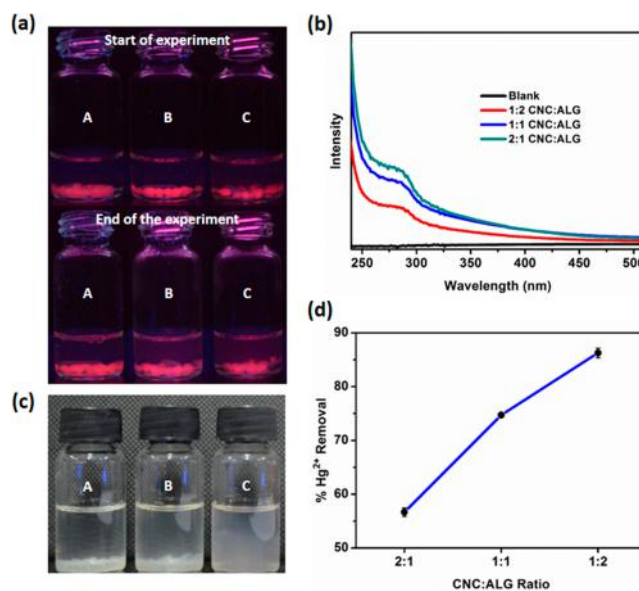


Figure 2. (a) Photographs of the vials containing (A) 1:2, (B) 1:1, and (C) 2:1 CNC:ALG nanocomposite hydrogel systems taken at the start and end of the leaching experiment. (b) UV absorbance spectra of the supernatant from the three systems taken at the end of the leaching experiment. (c) Photographs of the vials containing (A) 1:2, (B) 1:1, and (C) 2:1 CNC:ALG nanocomposite hydrogel systems taken at the end of mechanical integrity experiment. (d) Plot of Hg²⁺ removal % with varying CNC:ALG ratios.

stirring the beads vigorously overnight showed that the 1:2 system was more robust compared to other systems as shown in Figure 2(c). Figure 2(d) shows that the 1:2 system also displayed higher Hg²⁺ removal compared to the 1:1 and 2:1 systems. Because of their high surface area and negative charge of CNCs, they are also capable of absorbing heavy metal ions. A control batch adsorption experiment performed by stirring 10 mg/mL CNCs and 50 ppm of Hg²⁺ overnight showed that CNCs themselves were capable of removing 50% Hg²⁺ (Figure S1). The carboxylate groups present along the polymeric chains of ALG coupled with the porous nature of the hydrogel beads also contribute to the adsorption of heavy metal ions.^{38,39} Thus, the synergistic adsorption by the CNCs and ALG in the nanocomposite contributed to an increased adsorption performance of the 1:2 system compared to the other two systems.

Sensing Experiments. Au@BSA NCs fluoresce with a deep red emission, which when entrapped inside these hydrogel beads also impart the characteristic red fluorescence to the beads under UV light. A single hydrogel bead sensitivity experiment, performed using 1 ppm concentration of all the major heavy metal ions such as Hg²⁺, Cu²⁺, Zn²⁺, Ni²⁺, Pb²⁺, Cd²⁺, Cr³⁺, As³⁺, Mn²⁺, Co²⁺, and Fe²⁺ employing the 1:2 CNC:ALG system showed that the nanocomposite is highly selective to Hg²⁺ ions. The nanocomposite itself was prepared using CaCl₂ that dissociates into Ca²⁺ and Cl⁻ ions, where Ca²⁺ ions will aid in the cross-linking of alginate chains and Cl⁻ ions remain free in the solution or diffuse into hydrogel beads. No fluorescence quenching of Au@BSA NCs was observed when the nanocomposites were stored in this solution for several hours, and hence, it is clear that Au@BSA NCs are not sensitive to Cl⁻ ions. No sensitivity to Ag⁺ was seen for this cluster system.²⁸ In addition, Xie et al.²⁸ and Hu et al.²⁵ have reported on the selectivity of Au@BSA NCs using various chemical

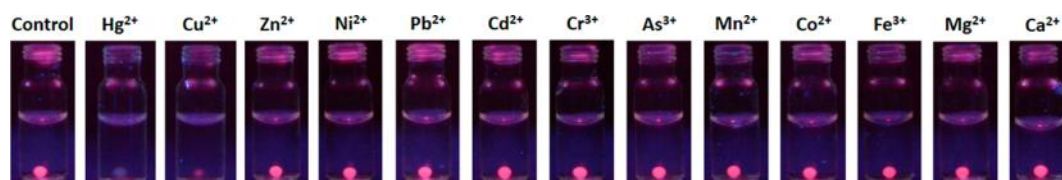


Figure 3. Photographs of vials containing hydrogel beads placed in 1 ppm concentrations of various heavy metal ions.

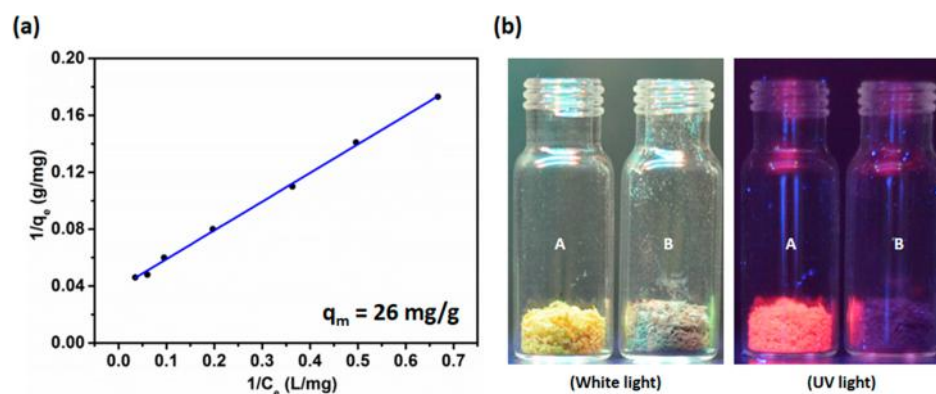


Figure 4. (a) Equilibrium Hg^{2+} batch adsorption data, fitted using the linearized form of Langmuir adsorption isotherm. (b) Photographs of the vials containing nanocomposite (A) before and (B) after adsorption of Hg^{2+} ions under white light and UV light.

species and have demonstrated that they are highly selective to Hg^{2+} ions.

Figure 3 shows that the fluorescence of hydrogel beads were completely quenched in the presence of Hg^{2+} ions, and slight fluorescence quenching also occurred in the presence of Cu^{2+} ions. There are several proposed mechanisms for the fluorescence quenching of Au@BSA NCs by Hg^{2+} ions,²⁶ such as (a) high affinity metallophilic bonding between the d^{10} centers of Hg^{2+} and Au^+ that disrupts the fluorescence from Au–BSA interactions²⁸ and (b) photoinduced electron transfer process wherein the Hg–S bonds are formed with BSA which causes the reduction of Hg^{2+} to Hg^+ and the latter species creates interference during excitation, thereby quenching the fluorescence.²⁵ Apart from this, at a similar heavy metal ion concentration, the binding affinities of Hg^{2+} with Au^+ are much stronger compared to other toxic metal ions, which also makes Au@BSA NCs more sensitive to Hg^{2+} ions.²⁸ The selectivity of the nanocomposite to heavy metal ions is based on the type of gold nanoclusters incorporated in them. For example, Pb and As selectivity can be imparted to the nanocomposite by incorporating gold nanoclusters reported earlier by Zhu et al.⁴⁰ and Subhasish et al.,⁴¹ respectively. Earlier reports have also shown that Cu^{2+} ions can also quench the fluorescence of Au@BSA NCs via ion-induced aggregation as they possess a strong affinity toward BSA and histidine.^{42,43} Hence, the slight fluorescent quenching of hydrogel beads observed in the case of Cu^{2+} ions can be attributed to this fact.

The fluorescence of the hydrogel beads after exposure to varying concentrations of Hg^{2+} was examined. The experiment showed that hydrogel beads are sensitive to as low as 1 ppm. Even though the sensitivity of this nanocomposite has been studied using a much lower concentration of Hg^{2+} ions, the minimum sensitivity reported in this study is 1 ppm. The quenching of Au@BSA NCs fluorescence upon binding to Hg^{2+} ions is limited by the diffusion of Hg^{2+} ions into the hydrogel beads, which in turn is controlled by several other factors, such as size, charge, concentration gradient of diffusing ions,⁴⁴ cross-

linking density of hydrogels,⁴⁴ interfacial properties of hydrogel matrix materials with the solute,⁴⁵ etc. At a lower concentration of Hg^{2+} ions, the rate of diffusion will be drastically reduced, and visual detection of the fluorescence quenching of Au@BSA NCs upon Hg^{2+} ions diffusion may require a sufficiently longer time for the current nanocomposite. For the dynamic quenching experiments, we have conducted studies using 100, 10 and 1 ppm of Hg^{2+} and noticed that the fluorescence of Au@BSA NCs was completely quenched in 45 min, 3 h and 24 h, respectively. Further studies are underway to develop systems that can detect lower concentrations of Hg^{2+} within a shorter time span. Our preliminary experiments using photoluminescence spectroscopy have shown that the fluorescence of nanocomposite is sensitive down to 1 ppb Hg^{2+} .

Adsorption of Heavy Metal Ions. Among all the heavy metal ions tested for the sensing experiments, the adsorption capability of the nanocomposite for the most sensitive ion, namely, Hg^{2+} , was estimated using the Langmuir adsorption isotherm. Figure 4(a) shows the fitting of equilibrium data using the linearized form of Langmuir adsorption isotherm, and the maximum adsorption capacity (q_m) was calculated to be 26 mg/g. Figure 4(b) displays the photographs of the crushed and freeze-dried nanocomposite material before and after adsorption, under white light and UV light. After binding to Hg^{2+} , the color of the nanocomposite changed from yellowish brown to deep brown. Also, the fluorescence of the nanocomposite was completely quenched confirming the higher binding of Hg^{2+} to the nanocomposite. Adsorption studies were also carried out using Cu^{2+} , which also showed some fluorescent quenching during the single hydrogel bead-sensing experiment (Figure S2).

Characterization of Nanocomposite. Average diameter of the hydrogel beads measured using a vernier caliper was 2.70 mm, which was illustrated in Figure S3. The average size distribution of the 10 samples were used for this measurement. The SEM image of the freeze-dried hydrogel bead (Figure 5a) shows undulations and folds on the bead surface. The inset of

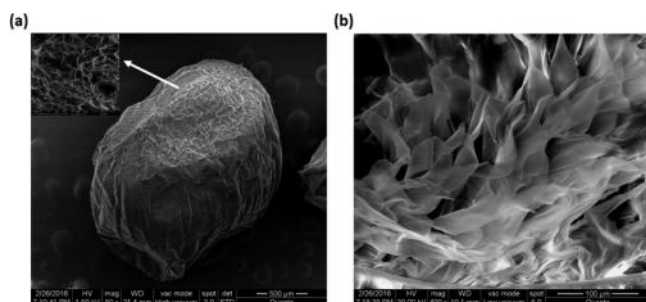


Figure 5. SEM image showing the (a) surface morphology and (b) porous nature of the hydrogel bead, after drying.

Figure 5a also shows these investigations at a higher magnification. The cross-sectional image of the hydrogel bead (Figure 5b) shows the porous nature of the nanocomposite which can also contribute to the increased surface area of the binding as well as diffusion of heavy metal ions. SEM-EDS elemental analysis and elemental mapping of the control, Hg^{2+} -saturated nanocomposite, and Cu^{2+} -saturated nanocomposite are presented in Figures S4, S5, and S6, respectively. A comparison of the results from Figures S4 and S5 confirms the homogeneous adsorption of Hg^{2+} throughout the nanocomposite. Similarly, comparison of Figures S4 and S6 reveal the homogeneous adsorption of Cu^{2+} throughout the nanocomposite. Au@BSA NCs, which gives the characteristic red fluorescence as well the sensing property to the nanocomposite, have also been characterized. The TEM image (Figure S7a) shows that these nanoclusters are around 2 nm in size. The UV-vis spectrum (Figure S7b) shows a peak at ~ 280 nm, and the photoluminescence spectrum shows an emission maximum at 660 nm, when excited at 365 nm. These are the characteristic features for BSA-protected Au nanoclusters.^{30,36} Although we have studied such clusters through mass spectrometry previously,²⁷ this was not possible in view of the nanocomposite nature of the present material that prevents ionization and desorption of the cluster. XPS analysis of the nanocomposite was performed to elucidate the fluorescence quenching as well as to confirm the adsorption of Hg^{2+} by the nanocomposite. XPS spectra in the Au 4f region of the nanocomposite before and after adsorption of Hg^{2+} are shown Figure S8a. Comparing the XPS spectra, it is observed that the adsorption of Hg^{2+} on the nanocomposite has led to an

increase in the binding energy of Au from 84.5 to 84.9 eV. This is reportedly due to oxidation of the Au core by the Hg^{2+} ion, which causes quenching of red fluorescence.³⁰ Also, the peak of Hg 4f_{7/2} seen at 101.8 (Figure S8b) implies that there is a reduction of Hg^{2+} to Hg^0 , which occurs when Hg^{2+} ions are adsorbed on the nanocomposite.³⁰

Quenching Dynamics to Study Diffusion. Practical knowledge of the mass transfer characteristics of the sorption process, especially diffusion occurring through porous media during this sorption process, is essential for various applications, especially from an industrial standpoint. It is necessary to determine the optimal flow rate and residence time in columns and reactors. Numerous methods and experiments have been devised to estimate the value of D , which is an essential parameter for modeling diffusion. However, all the methods are elaborate, involving diffusion cell set up, Couette flow setup, radio tracers, rotation disc measurement, and scanning electrochemical micrograph. The coefficient can also be estimated by monitoring the bulk solution concentration, but it often contains many uncertainties.⁴⁶ In this study, a novel and relatively simpler method was used, wherein the quenching dynamics of the Au@BSA NCs was observed under dark field fluorescence microscopy upon diffusion of Hg^{2+} into the hydrogel bead.

Figure 6 shows the quenching of nanocomposite fluorescence with respect to the diffusion of Hg^{2+} ions at various time intervals. It is shown that the intensity of red emission was slowly quenched from the surface of the bead and progressed inward. The blue and green intensities, also shown in the images, were found to be constant over time. The plot showing the variation in red intensity along the bead diameter at time $t = 100$ s for 100 ppm concentration of Hg^{2+} is given in Figure S9a. It was observed that the fluorescence of the hydrogel bead was completely quenched after time $t = 2500$ s. The red intensity from a completely quenched bead ($t = 2500$ s) was subtracted from the other images, thus ensuring that the intensity used for calculation was only from the fluorescent cluster. Our previous reports indicate that the reaction of Au@BSA NCs with the Hg^{2+} ion is generally fast and uniform,³⁰ and hence, we also assume that the reaction rate far exceeds the diffusion rate. Figure S9b shows the sine curve fitting of the variation in red intensity for various time intervals. The maximum intensity (taken from the center of sine curve) plotted against time as shown in Figure S9c follows a typical exponential decay. The

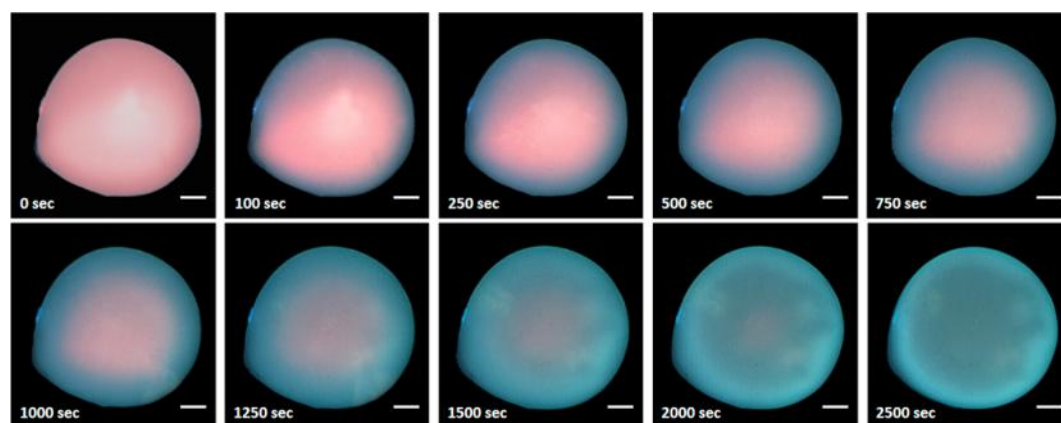


Figure 6. Quenching of nanocomposite fluorescence with respect to the diffusion of Hg^{2+} ions at various time points (scale bar shown in the pictures is 200 μm). Initial concentration of Hg^{2+} in the solution 100 ppm.

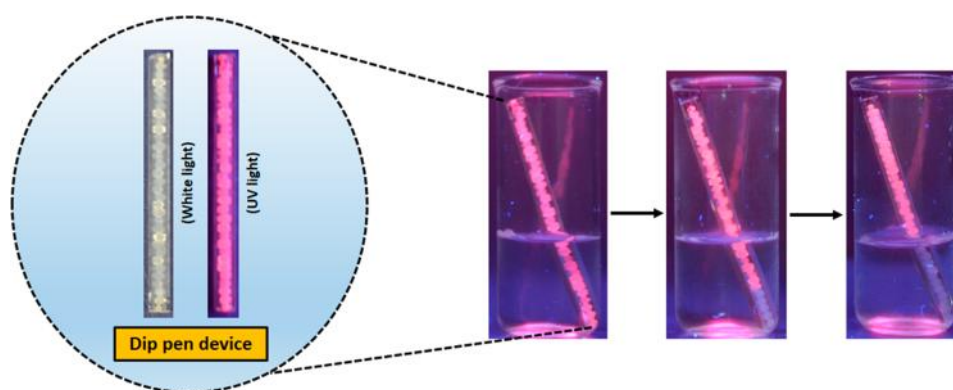


Figure 7. Photograph of the dip pen device and the gradual change in the fluorescence of the hydrogel beads within them when the device was dipped in the mercury solution.

variation of the concentration as a function of distance and time (eq 6) was obtained by multiplying the individual equations of distance and time, respectively. We solved for D by inserting this function into Fick's equation (eq 4).

The diffusion coefficient of the bead calculated using this technique was found to be $1.01 (\pm 0.3) \times 10^{-6} \text{ cm}^2/\text{s}$. There were no data in the literature on the diffusion of mercury through these beads, and hence, we were unable to make any comparison. However, the diffusion coefficient for Cu^{2+} in water was measured by Marcinkowsky and Phillips⁴⁷ using radioactive tracers and by Quickenden and Jiang⁴⁸ using a rotating disk electrode. Both these investigators measured the diffusion coefficient in the range from 6.2×10^{-6} to $7.5 \times 10^{-6} \text{ cm}^2/\text{s}$. Jang et al. measured the diffusion coefficient of Cu^{2+} for 3.2% calcium alginate beads to be in the range from 1.0×10^{-5} to $1.4 \times 10^{-5} \text{ cm}^2/\text{s}$.⁴⁹ However, for small analytes, the diffusion rate through a bead is similar to that of the diffusion in water.⁴⁹ Hg^{2+} ions being heavier than Cu^{2+} ions seemingly diffuse slower through the hydrogel bead. The lower diffusion rate could also be due to the binding of Hg^{2+} ions with the clusters and high affinity of this reaction.

To ensure that the diffusion coefficient can be equated to the fluorescent intensity of the bead, we have placed a single hydrogel bead in control solution (Millipore water) for nearly 24 h and monitored any reduction in nanocomposite fluorescence as a result of leaching of Au@BSA NCs. No visible change in color of the control solution was observed, indicating no leaching of the Au@BSA NCs. However, in the sample, the complete quenching of the Au@BSA fluorescence was observed within 2500 s when we used 100 ppm of Hg^{2+} . In general, we have placed the hydrogel bead in water for at least 15 min before the start of experiment to ensure that there is no visible leaching of Au@BSA NCs. Within the time span of 1 h of the experiment, we do not believe that there would be any leaching of clusters to impact our calculation of diffusion coefficient.

The analysis and calculations reported here can be improved through better mathematical models. The use of confocal fluorescence microscopy can yield detailed real time three-dimensional visualization of the diffusion process. Here, we have presented a simpler procedure that allows for the direct visualization of the diffusion in porous beads. The scope can be extended to study diffusion of other molecules, especially proteins and DNA, which can be tagged to a fluorescent moiety.

Dip Pen Experiments. The hydrogel beads that were placed along the length of a dip pen device quenched its red fluorescence gradually when it was dipped in the mercury solution. The capillary rise of the mercury solution through the capillary column promoted the diffusion of Hg^{2+} ions through the hydrogel beads that contained Au@BSA NCs. Figure 7 shows the photographs of the dip pen device and gradual change in the fluorescence of the hydrogel beads upon exposure to the mercury solution.

Even though the use of Au@BSA NCs in our nanocomposite raises questions regarding its appropriateness for commercial applications, there are several reasons that make this nanocomposite promising for use in water treatment applications, namely, the following:

- The Au@BSA NCs provide excellent fluorescence signals even at reduced concentration; hence, only less than 19.7 μg of Au is needed to produce one hydrogel bead. Thus, in most cases, cost may not be an issue. This quantity could be reduced further, depending on the fluorescence intensity required for detection.
- Au@BSA NCs have very good selectivity and sensitivity toward Hg^{2+} ions as demonstrated in several earlier reports,^{25,28,30} and their incorporation into the current nanocomposite makes it also selective toward Hg^{2+} ions.
- Au@BSA NCs when incorporated into this nanocomposite were found to be stable at high temperature without much loss in their characteristic red fluorescence. This was evident when we oven-dried the nanocomposite at a temperature of 100 °C. The freeze-dried nanocomposite containing Au@BSA NCs was stable, and they fluoresce with bright red emission even after six months when stored at room temperature. This improved stability is due to the protective environment provided by the alginate polymer chains wrapping around the fluorescent Au@BSA NCs. Figure S12 also shows the photograph of the freeze-dried nanocomposite hydrogel beads which have been stored for more than six months under UV light. Thus, the practical applicability of the nanocomposites containing Au@BSA NCs with respect to storage and usability in high temperature conditions, such as in mining effluents, is possible.
- The sensing and adsorption of Hg^{2+} are controlled by diffusion; hence, this nanocomposite can be used as a probe to visualize the diffusion phenomena, allowing us to determine the diffusion coefficient. This is the first time such a method was proposed, and this was possible

because of several properties of the nanocomposite hydrogel bead, such as three-dimensional spherical structure, high porosity, hydrophilic and anionic matrix that drives the diffusion of cationic Hg^{2+} ions via electrostatic interaction, and homogeneous nanocluster distribution giving uniform fluorescence intensity throughout the nanocomposite.

- (e) The protein-templated nanocluster such as Au@BSA NCs can be synthesized *in situ* via a one-pot synthesis procedure. In contrast, most metallic clusters are synthesized separately and then incorporated in the substrate. Here, leaching of nanoclusters can become a challenging problem when used in a continuous process. On the other hand, the synthesis of Au@BSA NCs takes place in a reaction mixture containing CNCs. Due to the ion-mediated gelation of CNCs by the cationic Au ions, a gel-like structure is formed, and hence, the leaching of nanoclusters is drastically reduced. Apart from gold, only biomolecule (BSA), biodegradable polymers (CNCs, alginate), and eco-friendly chemicals (NaOH, CaCl_2) were used in the synthesis when compared to systems prepared from electrospun nanofibers based on petroleum-based polymers, etc.³⁰
- (f) Also, the binding affinity of mercury did not vary after incorporating the cluster into the matrix. This was examined by comparing the sensitivity of the clusters alone and cluster-incorporated nanocomposites to different concentrations of Hg^{2+} ions using photoluminescence spectroscopy. Figure S13 shows the variation of normalized fluorescence intensities of Au@BSA NCs and Au@BSA NCs CNC-ALG nanocomposite after binding with Hg^{2+} ions at regular time intervals. A similar trend observed for Au@BSA NCs and Au@BSA NCs CNC-ALG nanocomposites reveals that the affinity of mercury did not vary after incorporating the cluster into the matrix.
- (g) In terms of response and sensitivity, there are greater possibilities of improvement of this system compared to other reported systems. Because this nanocomposite can be manipulated into smaller-sized hydrogel beads and also into various shapes such as film, stick, or candle, depending on the end use, diffusion of Hg^{2+} ions can be enhanced using forced diffusion processes such as vacuum suction. In terms of selectivity, there is also an ability to incorporate different types of gold nanoclusters into the nanocomposite to make them selective to other heavy metal ions species of interest. Selectivity can be brought in also though molecular functionalization of the clusters.

In summary, a novel nanocomposite that can simultaneously sense and scavenge toxic heavy metal ions like Hg^{2+} in contaminated water was developed and demonstrated. Nanostructures of the components, namely, cellulose nanocrystals and protein protected clusters, allowed the creation of this fast-responsive system. The sensing and scavenging property of this system is controlled by the diffusion of ions. At this stage of development, the system was not reusable due to the poor recovery of fluorescence of Au@BSA NCs upon Hg^{2+} binding. Better analysis and calculations may be performed to improve the modeling of quenching dynamics to study the diffusion of Hg^{2+} ions in hydrogels.

CONCLUSIONS

In conclusion, we have developed a novel nanocomposite that can simultaneously sense and scavenge toxic heavy metal ions in contaminated water. Au@BSA NCs leaching experiments and batch adsorption experiments using Hg^{2+} ions suggested that a nanocomposite with a 1:2 CNC:ALG ratio is an ideal sensor–scavenger system. The sensitivity of this nanocomposite was found to be highly selective to Hg^{2+} ions among all other heavy metal ions tested. The fluorescence of the nanocomposite was found to be completely quenched in the presence of Hg^{2+} due to high affinity metallophilic $\text{Hg}^{2+}/\text{Au}^{2+}$ interaction on the Au@BSA NCs surface. Adsorption of Hg^{2+} ions by the nanocomposite showed a visible change in their color, and the maximum adsorption capacity measured using Langmuir adsorption isotherm was 26 mg/g. We also reported a novel method to probe diffusion and calculated the diffusion coefficient by visualizing the dynamic fluorescence quenching of Au@BSA NCs as the Hg^{2+} ions diffuse into the hydrogel beads. The diffusion coefficient calculated using this novel method was $1.01 (\pm 0.3) \times 10^{-6} \text{ cm}^2/\text{s}$, which is considered to be in the same range as reported for other ions in polymeric matrices using various other techniques. Further, the practical application of this nanocomposite was demonstrated using a dip pen experiment, wherein the fluorescence of the capillary column containing these hydrogel beads was quenched as the Hg^{2+} ions got adsorbed and diffused through them. Similar types of novel nanocomposites selective to other heavy metal ions can be designed. Systems incorporating these nanocomposites can be used as a simultaneous sensor–scavenger system and also as a tool to probe diffusion. The possibility to create various sustainable formulations with simultaneous sensing and scavenging offers new possibilities of applications for such materials.

ASSOCIATED CONTENT

Supporting Information

Supporting Information is available free of charge on the ACS Publications Web site. The Supporting Information is available free of charge on the ACS Publications website at DOI: 10.1021/acssuschemeng.6b01674.

Adsorption of Hg^{2+} by CNCs; Langmuir adsorption isotherm and photograph showing the change in the nanocomposite color before and after Cu^{2+} adsorption; photograph showing the vernier caliper used for measurement of hydrogel bead diameter and average size distribution of 10 hydrogel beads used to measure the bead diameter; SEM-EDS elemental analysis and elemental mapping of control, Hg^{2+} -saturated and Cu^{2+} -saturated nanocomposite; TEM image, UV–vis absorption spectrum, and photoluminescence spectrum of Au@BSA NCs; XPS spectra of the Au 4f region for the nanocomposite before and after Hg^{2+} adsorption; XPS spectra of the Hg 4f region of the nanocomposite after Hg^{2+} adsorption; plot showing the variation in red intensity along the bead diameter at $t = 100 \text{ s}$ for 100 ppm concentration of Hg^{2+} ; plot showing the fitting of the variation in red intensity for various time points to a sine curve; plot of the maximum intensity (taken from the center of sine curve) plotted against time; R-code to obtain the variation of red intensity along the bead diameter; error calculation for diffusion coefficient estimation; photograph of freeze-dried nanocomposite

hydrogel beads which have been stored for more than six months under UV light; plot showing the variation of normalized fluorescence intensities of Au@BSA NCs and Au@BSA NCs CNC-ALG nanocomposite after binding with Hg²⁺ ions at regular time intervals. (PDF)

AUTHOR INFORMATION

Corresponding Authors

*Tel: +1-519-888-4567, ext. 38339. Fax: 519-888-4347. E-mail: mkctam@uwaterloo.ca. (K. C. Tam).

*Tel: +91-44-2257-4208. Fax: +91-44-2257-0545/0509/4202. E-mail: pradeep@iitm.ac.in. (T. Pradeep).

Notes

The authors declare no competing financial interest.

ACKNOWLEDGMENTS

Nishil Mohammed wishes to acknowledge the support from the MITACS Globalink Research Award for carrying out this research project at Indian Institute of Technology Madras, Chennai, India. Kam Chiu Tam wishes to acknowledge the funding from Canada Foundation for Innovation (CFI), National Sciences and Engineering Research Council of Canada (NSERC), and Grand Challenges Canada for their support for his research programs on the use of sustainable nanomaterials for water treatment. T. Pradeep wishes to acknowledge the Nanomission of the Department of Science and Technology (DST), Government of India, for their constant support for his research programs on nanomaterials. The authors also wish to thank Chennu Sudhakar, E. Sundar Raj, and A. A. Arokia Gnani Loyola for their assistance in performing XPS and SEM-EDS experiments.

REFERENCES

- (1) Viessman, W.; Hammer, M.; Perez, E.; Chadik, P. *Water Supply and Pollution Control*; Pearson, Prentice Hall: Hoboken, NJ, 2009.
- (2) Ahuja, S. *Handbook of Water Purity and Quality*; Ahuja, S., Ed.; Academic Press, 2009.
- (3) Ali, I.; Gupta, V. K. Advances in water treatment by adsorption technology. *Nat. Protoc.* **2007**, *1* (6), 2661–2667.
- (4) Crini, G. Non-conventional low-cost adsorbents for dye removal: A review. *Bioresour. Technol.* **2006**, *97* (9), 1061–1085.
- (5) Bhatnagar, A.; Sillanpää, M. Utilization of agro-industrial and municipal waste materials as potential adsorbents for water treatment—A review. *Chem. Eng. J.* **2010**, *157* (2–3), 277–296.
- (6) Sharma, P.; Kaur, H.; Sharma, M.; Sahore, V. A review on applicability of naturally available adsorbents for the removal of hazardous dyes from aqueous waste. *Environ. Monit. Assess.* **2011**, *183* (1–4), 151–195.
- (7) Fu, F.; Wang, Q. Removal of heavy metal ions from wastewaters: A review. *J. Environ. Manage.* **2011**, *92* (3), 407–418.
- (8) Yu, X.; Tong, S.; Ge, M.; Wu, L.; Zuo, J.; Cao, C.; Song, W. Adsorption of heavy metal ions from aqueous solution by carboxylated cellulose nanocrystals. *J. Environ. Sci.* **2013**, *25* (5), 933–943.
- (9) Liu, P.; Sehaqui, H.; Tingaut, P.; Wichser, A.; Oksman, K.; Mathew, A. P. Cellulose and chitin nanomaterials for capturing silver ions (Ag⁺) from water via surface adsorption. *Cellulose* **2014**, *21* (1), 449–461.
- (10) Sheikhi, A.; Safari, S.; Yang, H.; van de Ven, T. G. M. Copper Removal Using Electrosterically Stabilized Nanocrystalline Cellulose. *ACS Appl. Mater. Interfaces* **2015**, *7* (21), 11301–11308.
- (11) Singh, K.; Arora, J. K.; Sinha, T. J. M.; Srivastava, S. Functionalization of nanocrystalline cellulose for decontamination of Cr(III) and Cr(VI) from aqueous system: computational modeling approach. *Clean Technol. Environ. Policy* **2014**, *16* (6), 1179–1191.
- (12) Nata, I. F.; Sureshkumar, M.; Lee, C.-K. One-pot preparation of amine-rich magnetite/bacterial cellulose nanocomposite and its application for arsenate removal. *RSC Adv.* **2011**, *1* (4), 625–631.
- (13) Yang, R.; Aubrecht, K. B.; Ma, H.; Wang, R.; Grubbs, R. B.; Hsiao, B. S.; Chu, B. Thiol-modified cellulose nanofibrous composite membranes for chromium (VI) and lead (II) adsorption. *Polymer* **2014**, *55* (5), 1167–1176.
- (14) Peng, B. L.; Dhar, N.; Liu, H. L.; Tam, K. C. Chemistry and applications of nanocrystalline cellulose and its derivatives: A nanotechnology perspective. *Can. J. Chem. Eng.* **2011**, *89* (5), 1191–1206.
- (15) Carpenter, A. W.; De Lannoy, C. F.; Wiesner, M. R. Cellulose nanomaterials in water treatment technologies. *Environ. Sci. Technol.* **2015**, *49* (9), 5277–5287.
- (16) Mahfoudhi, N.; Boufi, S. Nanocellulose as a Millennium Material with Enhancing Adsorption Capacities. In *Biodegradable and Biobased Polymers for Environmental and Biomedical Applications*; John Wiley & Sons, Inc.: Hoboken, NJ, 2016; pp 349–383.
- (17) Mohammed, N.; Grishkewich, N.; Berry, R. M.; Tam, K. C. Cellulose nanocrystal–alginate hydrogel beads as novel adsorbents for organic dyes in aqueous solutions. *Cellulose* **2015**, *22* (6), 3725–3738.
- (18) Mohammed, N.; Grishkewich, N.; Waeijen, H. A.; Berry, R. M.; Tam, K. C. Continuous flow adsorption of methylene blue by cellulose nanocrystal–alginate hydrogel beads in fixed bed columns. *Carbohydr. Polym.* **2016**, *136*, 1194–1202.
- (19) Mohammed, N.; Grishkewich, N.; Tam, K. C.; Berry, R. Pristine and surface functionalized cellulose nanocrystals (CNCs) incorporated hydrogel beads and uses thereof. U.S. Patent US 2016/0175812 A1, 2016.
- (20) Trasande, L.; Landrigan, P. J.; Schechter, C. Public health and economic consequences of methyl mercury toxicity to the developing brain. *Environ. Health Perspect.* **2005**, *113* (5), 590–596.
- (21) Nolan, E. M.; Lippard, S. J. Tools and Tactics for the Optical Detection of Mercuric Ion. *Chem. Rev.* **2008**, *108* (9), 3443–3480.
- (22) Natarajan, G.; Mathew, A.; Negishi, Y.; Whetten, R. L.; Pradeep, T. A Unified Framework for Understanding the Structure and Modifications of Atomically Precise Monolayer Protected Gold Clusters. *J. Phys. Chem. C* **2015**, *119* (49), 27768–27785.
- (23) Chen, L. Y.; Wang, C. W.; Yuan, Z.; Chang, H. T. Fluorescent gold nanoclusters: Recent advances in sensing and imaging. *Anal. Chem.* **2015**, *87* (1), 216–229.
- (24) Zheng, J.; Nicovich, P. R.; Dickson, R. M. Highly fluorescent noble-metal quantum dots. *Annu. Rev. Phys. Chem.* **2007**, *58*, 409–431.
- (25) Hu, D.; Sheng, Z.; Gong, P.; Cai, L.; Zhang, P. Highly selective fluorescent sensors for Hg(2+) based on bovine serum albumin-capped gold nanoclusters. *Analyst* **2010**, *135*, 1411–1416.
- (26) Chevrier, D. M.; Chatt, A.; Zhang, P. Properties and applications of protein-stabilized fluorescent gold nanoclusters: short review. *J. Nanophotonics* **2012**, *6* (1), 064504.
- (27) Chaudhari, K.; Baksi, A.; Pradeep, T. Protein-protected luminescent noble metal quantum clusters: an emerging trend in atomic cluster nanoscience. *Nano Rev.* **2012**, *3* (0), 1–16.
- (28) Xie, J.; Zheng, Y.; Ying, J. Y. Highly selective and ultrasensitive detection of Hg(2+) based on fluorescence quenching of Au nanoclusters by Hg(2+)-Au(+) interactions. *Chem. Commun. (Cambridge, U. K.)* **2010**, *46* (6), 961–963.
- (29) Xie, J.; Zheng, Y.; Ying, J. Y. Protein-directed synthesis of highly fluorescent gold nanoclusters. *J. Am. Chem. Soc.* **2009**, *131* (3), 888–889.
- (30) Ghosh, A.; Jeseentharani, V.; Ganayee, M. A.; Hemalatha, R. G.; Chaudhari, K.; Vijayan, C.; Pradeep, T.; Atanu, G.; Jeseentharani, V.; Ganayee, M. A.; et al. Approaching sensitivity of tens of ions using atomically precise cluster-nanofiber composites. *Anal. Chem.* **2014**, *86* (22), 10996–11001.
- (31) Aravindhan, R.; Fathima, N. N.; Rao, J. R.; Nair, B. U. Equilibrium and thermodynamic studies on the removal of basic black dye using calcium alginate beads. *Colloids Surf., A* **2007**, *299* (1–3), 232–238.

- (32) Hameed, B. H.; Din, A. T. M.; Ahmad, A. L. Adsorption of methylene blue onto bamboo-based activated carbon: Kinetics and equilibrium studies. *J. Hazard. Mater.* **2007**, *141* (3), 819–825.
- (33) Chau, M.; Sriskandha, S. E.; Pichugin, D.; Thérien-Aubin, H.; Nykypanchuk, D.; Chauve, G.; Méthot, M.; Bouchard, J.; Gang, O.; Kumacheva, E. Ion-Mediated Gelation of Aqueous Suspensions of Cellulose Nanocrystals. *Biomacromolecules* **2015**, *16* (8), 2455–2462.
- (34) Shafiei-Sabet, S.; Hamad, W. Y.; Hatzikiriakos, S. G. Ionic strength effects on the microstructure and shear rheology of cellulose nanocrystal suspensions. *Cellulose* **2014**, *21* (5), 3347–3359.
- (35) Lee, K. Y.; Mooney, D. J. Alginate: properties and biomedical applications. *Prog. Polym. Sci.* **2012**, *37* (1), 106–126.
- (36) Mohanty, J. S.; Baksi, A.; Lee, H.; Pradeep, T. Noble metal clusters protected with mixed proteins exhibit intense photoluminescence. *RSC Adv.* **2015**, *5* (59), 48039–48045.
- (37) Mohanty, J. S.; Xavier, P. L.; Chaudhari, K.; Bootharaju, M. S.; Goswami, N.; Pal, S. K.; Pradeep, T. Luminescent, bimetallic AuAg alloy quantum clusters in protein templates. *Nanoscale* **2012**, *4* (14), 4255–4262.
- (38) Fan, J.; Shi, Z.; Min, L.; Li, H.; Yin, J. Mechanically strong graphene oxide/sodium alginate/ polyacrylamide nanocomposite hydrogel with improved dye adsorption capacity. *J. Mater. Chem. A* **2013**, *1* (25), 7433–7443.
- (39) Rocher, V.; Bee, A.; Siaugue, J.-M.; Cabuil, V. Dye removal from aqueous solution by magnetic alginate beads crosslinked with epichlorohydrin. *J. Hazard. Mater.* **2010**, *178* (1–3), 434–439.
- (40) Zhu, H.; Yu, T.; Xu, H.; Zhang, K.; Jiang, H.; Zhang, Z.; Wang, Z.; Wang, S. Fluorescent Nanohybrid of Gold Nanoclusters and Quantum Dots for Visual Determination of Lead Ions. *ACS Appl. Mater. Interfaces* **2014**, *6* (23), 21461–21467.
- (41) Roy, S.; Palui, G.; Banerjee, A. The as-prepared gold cluster-based fluorescent sensor for the selective detection of AsIII ions in aqueous solution. *Nanoscale* **2012**, *4* (8), 2734–2740.
- (42) Yu, P.; Wen, X.; Toh, Y. R.; Huang, J.; Tang, J. Metallophilic bond-induced quenching of delayed fluorescence in Au 25@BSA Nanoclusters. *Part. Part. Syst. Character.* **2013**, *30* (5), 467–472.
- (43) Durgadas, C. V.; Sharma, C. P.; Sreenivasan, K. Fluorescent gold clusters as nanosensors for copper ions in live cells. *Analyst* **2011**, *136*, 933–940.
- (44) Golmohamadi, M.; Wilkinson, K. J. Diffusion of ions in a calcium alginate hydrogel-structure is the primary factor controlling diffusion. *Carbohydr. Polym.* **2013**, *94* (1), 82–87.
- (45) Gehrke, S. H.; Fisher, J. P.; Palasis, M.; Lund, M. E. Factors Determining Hydrogel Permeability. *Ann. N. Y. Acad. Sci.* **1997**, *831* (1), 179–184.
- (46) Legrand, J.; Dumont, E.; Comiti, J.; Fayolle, F. Diffusion coefficients of ferricyanide ions in polymeric solutions - comparison of different experimental methods. *Electrochim. Acta* **2000**, *45* (11), 1791–1803.
- (47) Arthur, E. M.; Phillips, H. O. Diffusion Studies. Part II. Tracer Diffusion coefficient of Copper(II) in HCl and HClO₄ at 25 C. *J. Chem. Soc. A* **1971**, *0*, 101–103.
- (48) Quickenden, T. I.; Jiang, X. The diffusion coefficient of copper sulphate in aqueous solution. *Electrochim. Acta* **1984**, *29* (6), 693–700.
- (49) Chen, D.; Lewandowski, Z.; Roe, F.; Surapaneni, P. Diffusivity of Cu²⁺ in calcium alginate gel beads. *Biotechnol. Bioeng.* **1993**, *41*, 755–760.

Supporting Information

Diffusion controlled simultaneous sensing and scavenging of heavy metal ions in water using atomically precise cluster – cellulose nanocrystal composites

Nishil Mohammed,[†] Avijit Baidya,[‡] Vasanthanarayan Murugesan,[‡] Avula Anil Kumar,[‡] Mohd Azhardin Ganayee,[‡] Jyoti Sarita Mohanty,[‡] Kam Chiu Tam^{,†} and T. Pradeep^{*,‡}*

[†] Department of Chemical Engineering, Waterloo Institute for Nanotechnology, University of Waterloo, 200 University Avenue West, Waterloo, ON, N2L 3G1, Canada

[‡] DST Unit of Nanoscience and Thematic Unit of Excellence, Department of Chemistry, Indian Institute of Technology Madras, Chennai, 600 036, India

* mkctam@uwaterloo.ca, pradeep@iitm.ac.in

Table of contents

S.No.	Description	Page No.
1.	Hg ²⁺ adsorption by CNCs	S2
2.	Cu ²⁺ adsorption by nanocomposite	S3
3.	Size determination of hydrogel beads using vernier caliper	S4
4.	SEM–EDS characterization of the control nanocomposite	S5
5.	SEM–EDS characterization of the Hg ²⁺ saturated nanocomposite	S6
6.	SEM–EDS characterization of the Cu ²⁺ saturated nanocomposite	S7
7.	Characterization of Au@BSA NCs	S8
8.	XPS characterization to study cluster quenching and Hg ²⁺ binding mechanism	S9
9.	Red intensity profile for quenching experiment	S10
10.	R-code to obtain the variation of red intensity along the bead diameter	S11
11.	Error calculation for diffusion coefficient estimation	S12
12.	Stability of the freeze dried nanocomposite hydrogel beads	S13
13.	Affinity of Hg ²⁺ ions with Au@BSA NCs and Au@BSA NCs CNC-ALG nanocomposite	S14

Supporting information 1: Hg^{2+} adsorption by CNCs

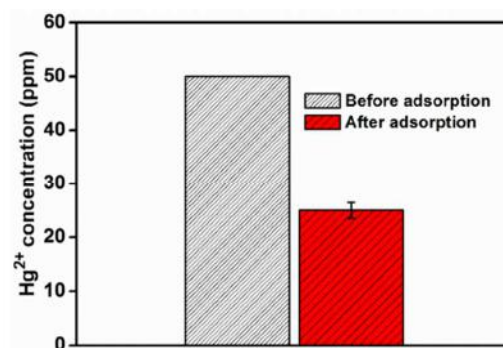


Figure S1. Concentration of Hg^{2+} before and after adsorption with CNCs (Adsorbent dosage = 10 mg/mL, Adsorbate concentration = 50 ppm, pH = 7, Temperature = 25 °C).

Supporting information 2: Cu^{2+} adsorption by nanocomposite

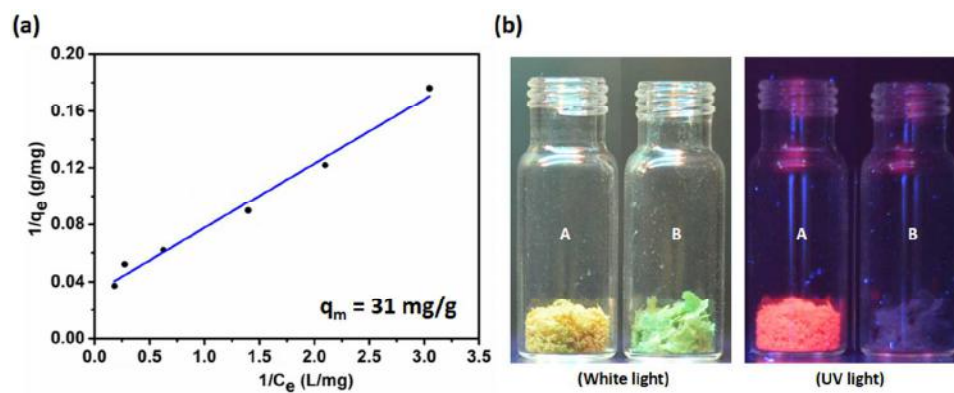


Figure S2. (a) Equilibrium Cu^{2+} batch adsorption data fitted using linearized form of Langmuir adsorption isotherm. (b) Digital photographs of the vials containing nanocomposite (A) before and (B) after adsorption of Cu^{2+} ions under white light and UV light, respectively.

Supporting information 3: Size determination of hydrogel beads using vernier caliper

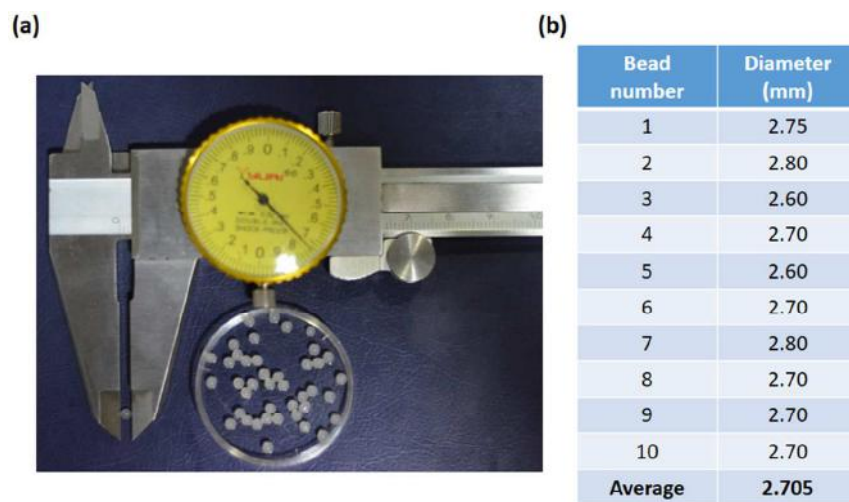


Figure S3. (a) Photograph of the vernier caliper used for the measurement of hydrogel bead diameter. (b) Average size distribution of the hydrogel beads used to measure the bead diameter.

Supporting information 4: SEM–EDS characterization of the control nanocomposite

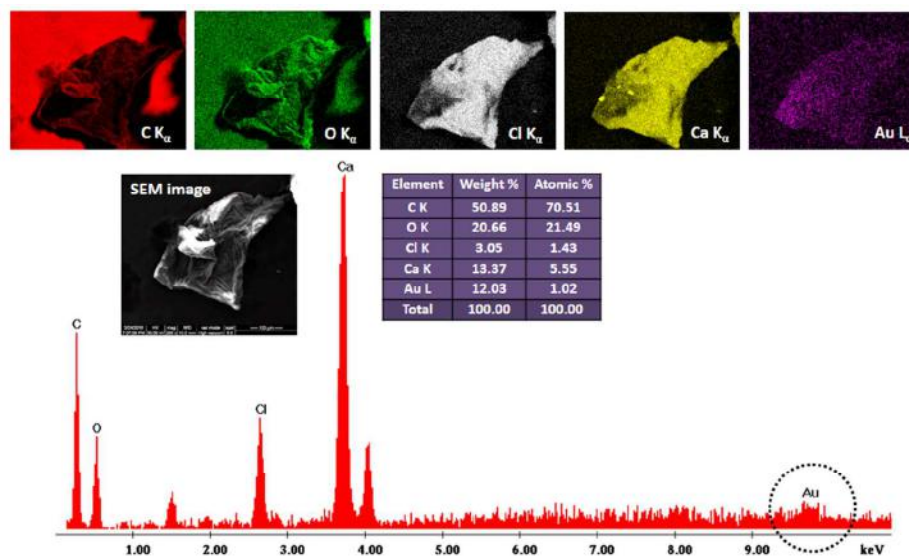


Figure S4. SEM-EDS elemental analysis and elemental mapping of control nanocomposite.

Supporting information 5: SEM-EDS characterization of the Hg²⁺ saturated nanocomposite

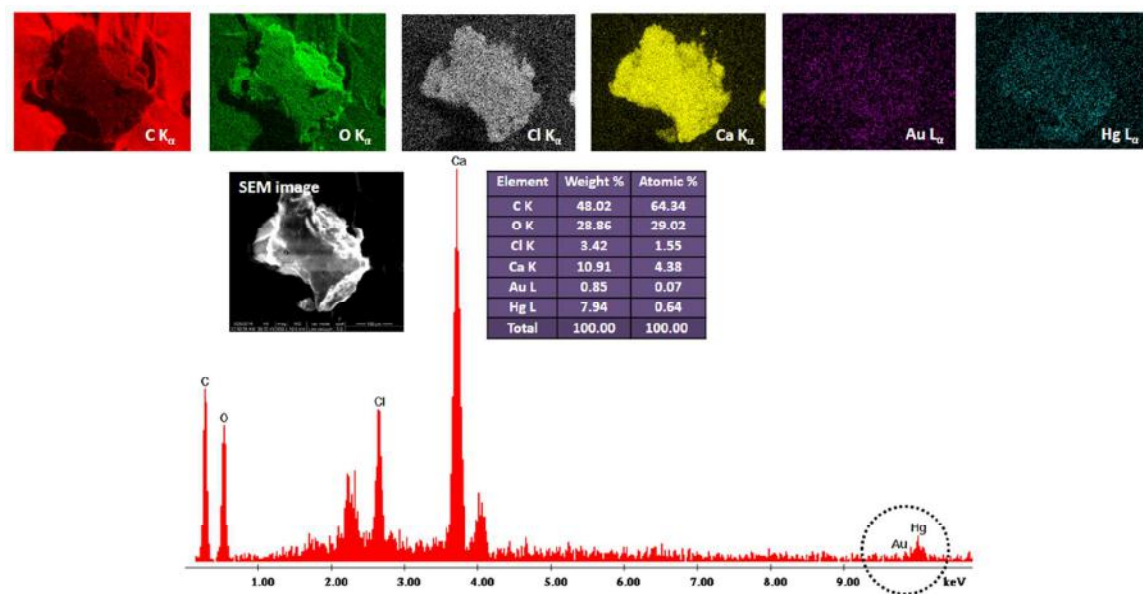


Figure S5. SEM-EDS elemental analysis and elemental mapping of Hg²⁺ saturated nanocomposite.

Supporting information 6: SEM-EDS characterization of the Cu^{2+} saturated nanocomposite

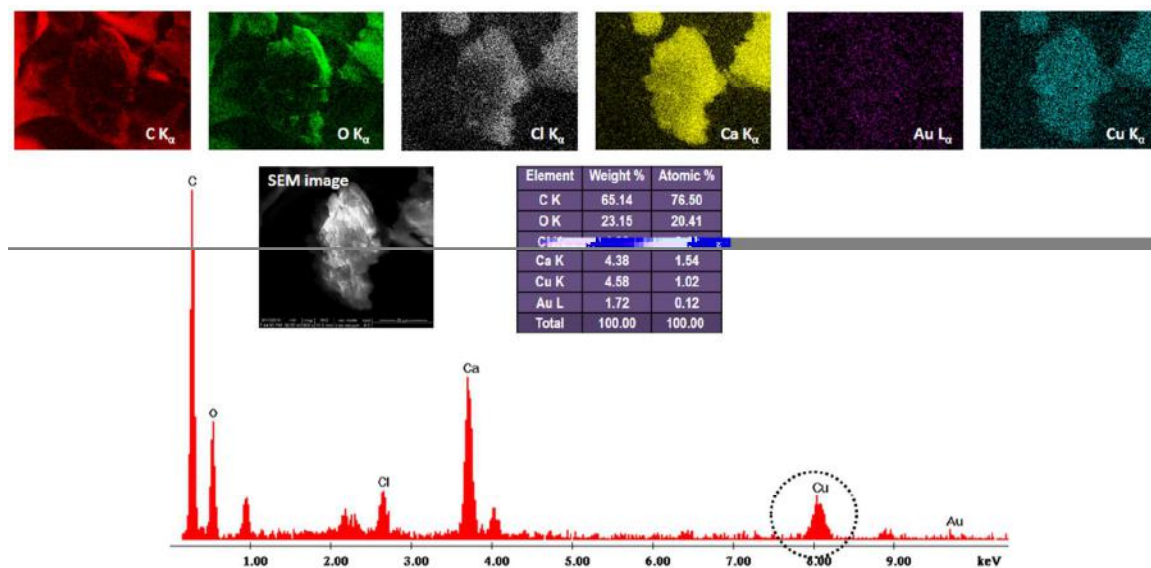


Figure S6. SEM-EDS elemental analysis and elemental mapping of Cu^{2+} saturated nanocomposite.

Supporting information 7: Characterization of Au@BSA NCs

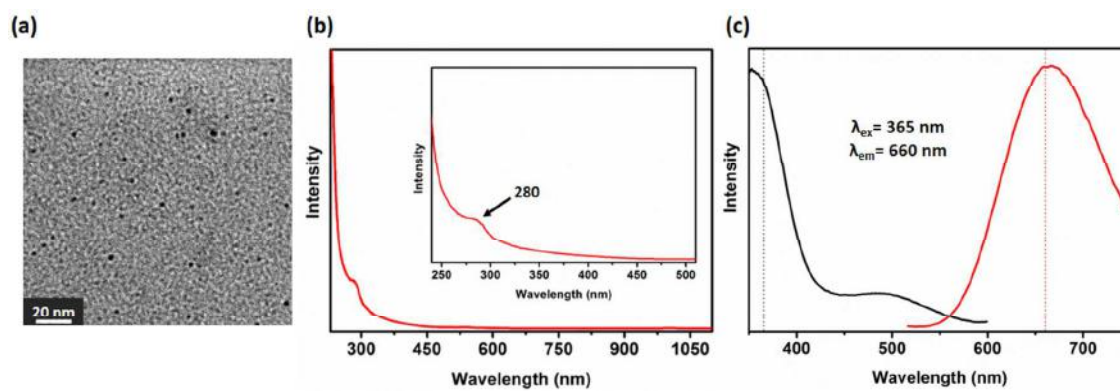


Figure S7. (a) TEM image (b) UV-Vis absorbance spectrum and (c) Photoluminescence spectra showing the excitation (black line) and emission (red line) peaks of Au@BSA NCs.

Supporting information 8: XPS characterization to study cluster quenching and Hg^{2+} binding mechanism

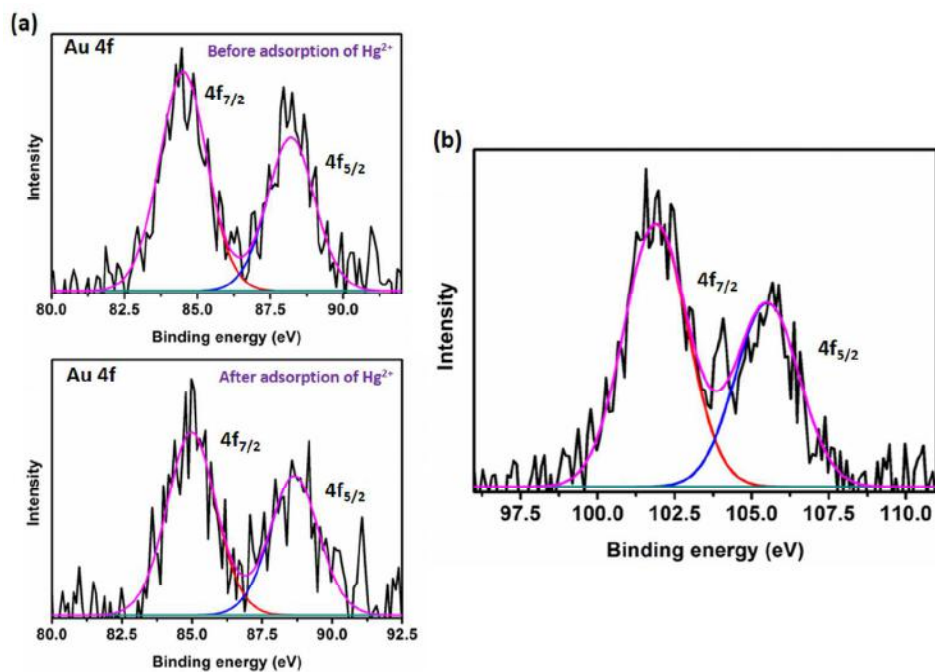


Figure S8. (a) XPS spectra of Au 4f region for the nanocomposite before (up) and after (down) Hg^{2+} adsorption. (b) XPS spectra of Hg 4f region of the nanocomposite after Hg^{2+} adsorption (Hg 4f data are given only after Hg^{2+} adsorption as the control nanocomposite does not have Hg^{2+}).

Supporting information 9: Red intensity profile for quenching experiment

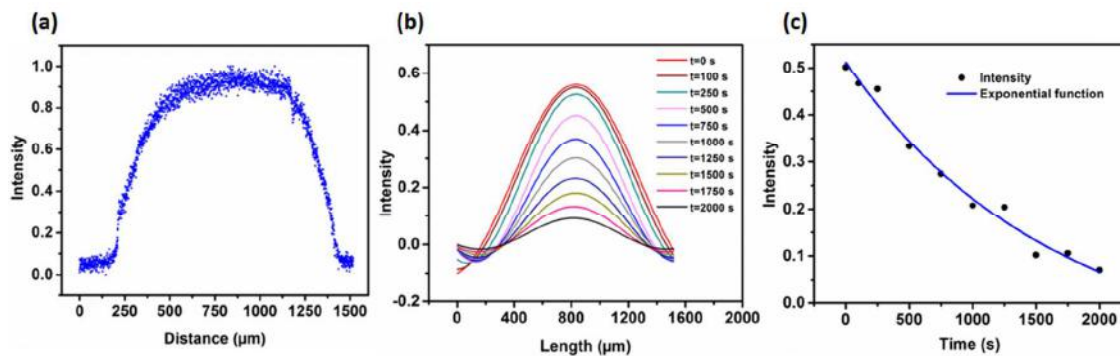


Figure S9. (a) Plot showing the variation in red intensity along the bead diameter at $t = 100$ s for 100 ppm concentration of Hg^{2+} . (b) Plot showing the fitting of the variation in red intensity for various time points to a sine curve. (c) Plot of the maximum intensity (taken from the centre of sine curve) plotted against time.

Supporting information 10: R-code to obtain the variation of red intensity along the bead diameter

```
library(jpeg)
readJPEG("/Users/Romy/Downloads/Quenching30.jpg")
r <- readJPEG("/Users/Romy/Downloads/Quenching30.jpg")
Red <- as.data.frame(r[, ,1])
Green <- as.data.frame(r[, ,2])
Blue <- as.data.frame(r[, ,3])
center_red <- as.data.frame(Red[1024,])
center_green <- as.data.frame(Green[1024,])
center_blue <- as.data.frame(Blue[1024,])
center_red <- as.data.frame(t(center_red))
center_green <- as.data.frame(t(center_green))
center_blue <- as.data.frame(t(center_blue))
for (i in 1:nrow(center_red))
{
  center_red[i,2] <- i
  center_green[i,2] <- i
  center_blue[i,2] <- i
}
colnames(center_red) <- c("intensity", "pixel.no")
colnames(center_green) <- c("intensity", "pixel.no")
colnames(center_blue) <- c("intensity", "pixel.no")
center_red[,3] <- "RED"
center_blue[,3] <- "BLUE"
center_green[,3] <- "GREEN"
center_pixels <- rbind(center_red, center_blue, center_green )
library(plotly)
plot_ly(center_pixels, y = intensity, color = V3, type = "Scatter", mode =
"markers")
```

Supporting information 11: Error calculation for diffusion coefficient estimation

$$D = \frac{l^2}{\pi^2 \tau}$$

To calculate error,

$$\Delta D = \frac{l(2\tau\Delta l + \Delta\tau l)}{\pi^2 \tau^2}$$

Here:

$$\tau = 1594 \text{ s,}$$

$$l = 0.126 \text{ cm,}$$

$$\Delta l = 0.75 \times 10^{-4} \text{ cm (size of one pixel) and}$$

$$\Delta\tau = 478.7 \text{ sec (error from fitting the decay equation)}$$

Substituting this in the equation, we get:

$$\Delta D = 0.3 \times 10^{-6} \text{ cm}^2/\text{sec}$$

Supporting information 12: Stability of the freeze dried nanocomposite hydrogel beads

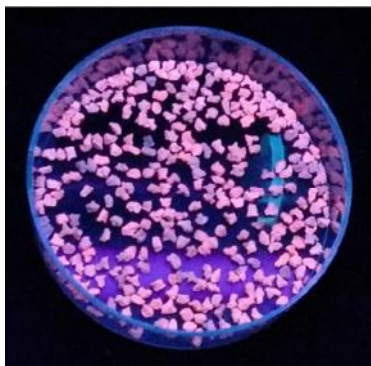


Figure S12. Photograph of the freeze dried nanocomposite hydrogel beads which have been stored for more than 6 months, under UV light.

Supporting information 13: Binding affinity of Hg^{2+} ions with Au@BSA NCs and Au@BSA NCs CNC-ALG nanocomposite

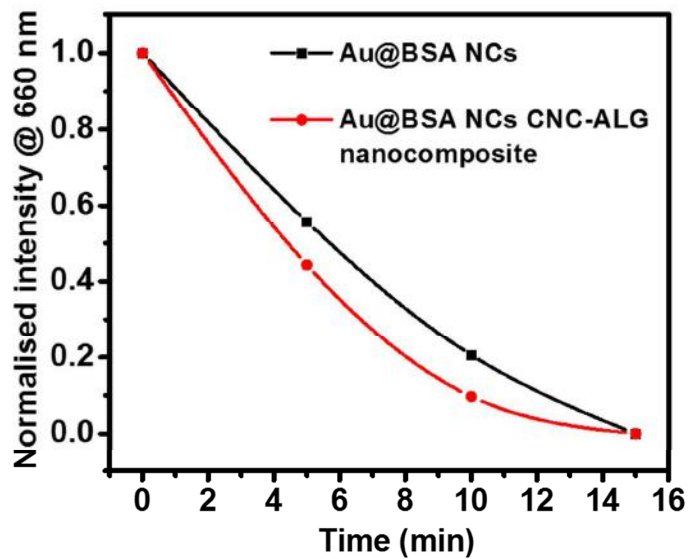


Figure S13. Normalized fluorescence intensities of Au@BSA NCs and Au@BSA NCs CNC-ALG nanocomposite after binding with Hg^{2+} ions at regular time intervals.

ARTICLE

Received 21 Apr 2016 | Accepted 5 Oct 2016 | Published 10 Nov 2016

DOI: 10.1038/ncomms13447

OPEN

Structure-conserving spontaneous transformations between nanoparticles

K.R. Krishnadas^{1,*}, Ananya Baksi^{1,*}, Atanu Ghosh^{1,*}, Ganapati Natarajan¹ & Thalappil Pradeep¹

Ambient, structure- and topology-preserving chemical reactions between two archetypal nanoparticles, $\text{Ag}_{25}(\text{SR})_{18}$ and $\text{Au}_{25}(\text{SR})_{18}$, are presented. Despite their geometric robustness and electronic stability, reactions between them in solution produce alloys, $\text{Ag}_m\text{Au}_n(\text{SR})_{18}$ ($m+n=25$), keeping their $\text{M}_{25}(\text{SR})_{18}$ composition, structure and topology intact. We demonstrate that a mixture of $\text{Ag}_{25}(\text{SR})_{18}$ and $\text{Au}_{25}(\text{SR})_{18}$ can be transformed to any arbitrary alloy composition, $\text{Ag}_m\text{Au}_n(\text{SR})_{18}$ ($n=1-24$), merely by controlling the reactant compositions. We capture one of the earliest events of the process, namely the formation of the dianionic adduct, $(\text{Ag}_{25}\text{Au}_{25}(\text{SR})_{36})^{2-}$, by electrospray ionization mass spectrometry. Molecular docking simulations and density functional theory (DFT) calculations also suggest that metal atom exchanges occur through the formation of an adduct between the two clusters. DFT calculations further confirm that metal atom exchanges are thermodynamically feasible. Such isomorphous transformations between nanoparticles imply that microscopic pieces of matter can be transformed completely to chemically different entities, preserving their structures, at least in the nanometric regime.

¹Department of Chemistry, DST Unit of Nanoscience (DST UNS) and Thematic Unit of Excellence (TUE), Indian Institute of Technology Madras, Chennai 600036, India. * These authors contributed equally to this work. Correspondence and requests for materials should be addressed to T.P. (email: pradeep@iitm.ac.in).

Ambient chemical transformations between nanoparticles leading to hybrid systems that preserve structure and topology are a challenging and poorly explored area in materials science. Atomically precise nanoparticles of noble metals^{1–10}, often called nanoclusters, which constitute an exploding discipline in nanomaterials, are promising candidates to explore such transformations because of their well-defined structures and drastic changes in their properties, in comparison to their bulk form, arising due to electronic confinement. Most intensely explored of these properties are optical absorption and emission^{11–15}; near infrared emission of some of the clusters and their large quantum yields have resulted in new applications^{16–20}. Nanoparticles are generally considered stable and are expected to preserve their structural integrity in solution. Chemical reactions between nanoparticles are rarely investigated²¹.

Here we show that two archetypal examples of noble metal nanoclusters, $\text{Au}_{25}(\text{SR})_{18}$ (refs 22–27) and $\text{Ag}_{25}(\text{SR})_{18}$ (ref. 28), manifest dramatic chemical reactivity. We use mass spectrometry to study these reactions in detail. The reaction proceeds in solution through a series of metal atom exchanges leading to alloy clusters, $\text{Ag}_m\text{Au}_n(\text{SR})_{18}$ ($m+n=25$; $n=1–24$), preserving the $\text{M}_{25}(\text{SR})_{18}$ stoichiometry; the values of m and n are determined by the starting concentrations of the reactant clusters. These alloy clusters possess an identical structural framework and topology as that of the reactant clusters, therefore presenting a unique example of nanoparticle reactivity. Such reactions proceed through inter-cluster adducts which form spontaneously on mixing. Molecular docking simulations show that van der Waals (vdW) forces between these clusters play an important role in the initial stages of the reaction, and density functional theory (DFT) calculations suggest that bond formation occurs between the staples of the clusters during the reaction. Structure-conserving reactions between nanomaterials of this kind suggest new possibilities of such transformations of materials in general.

Results

Formation of the entire range of $\text{Ag}_m\text{Au}_n(\text{SR})_{18}$ alloys. The clusters, $\text{Ag}_{25}(\text{DMBT})_{18}$ (**I**) and $\text{Au}_{25}(\text{PET})_{18}$ (**II**) were prepared

and characterized by well-established methods described in Methods section. The ligands PET (2-phenylethanethiol) and DMBT (2,4-dimethylbenzenethiol) (Supplementary Fig. 1a for structures) were chosen for two reasons. Firstly, PET is one of the most commonly used protecting ligands for the Au_{25} core and DMBT is the only ligand known so far to protect the Ag_{25} core. Furthermore, molecular masses of these ligands are equal, allowing easy identification of Ag–Au exchanges between **I** and **II**. If the ligands were of unequal masses, exchanges of the ligands themselves (DMBT–PET exchange) and that of metal–ligand fragments ((Ag–DMBT)–(Au–PET) exchange), which also occur²¹, would complicate the mass spectrometric measurements (see later). Electrospray ionization mass spectra (ESI MS) of **I** and **II** show their characteristic features (Fig. 1a,b). Isotopic patterns of these features are identical to their respective theoretical patterns, as shown in Supplementary Fig. 1b,c. The characteristic ultraviolet/visible (UV/vis) absorption features of **I** and **II** confirm their identity (Supplementary Fig. 2). Matrix-assisted laser desorption ionization mass spectra (MALDI MS) were also measured for confirmation (Supplementary Figs 3 and 4). All of these data collectively prove the identity and purity of the samples.

To study the reaction between **I** and **II**, various volumes of the solution of **II** were added to a solution of **I** and the reaction was monitored by time-dependent UV/vis absorption and mass spectrometric measurements (see Methods section for details) of these solutions. The sample was injected to the mass spectrometer within less than 1 min of mixing the solutions and the data collection was completed within 2 min. The mass spectrum collected within 2 min after the addition of solution of **II** to solution of **I** at a molar (**I:II**) ratio of 0.3:1.0 is presented in Fig. 1c. Features of **I** and **II** are prominent in this mass spectrum, but reaction product peaks are seen next to the parent peaks. Inset of Fig. 1c is an expansion of the same spectrum in the region between m/z 5,300 to 7,150 showing the emergence of a series of peaks separated by m/z 89. Each of these peaks in this window show features separated by m/z 1, indicating that these clusters are singly charged species. Mass separation of 89 Da indicates the occurrence of Ag–Au exchange ($M_{\text{Au}} - M_{\text{Ag}} = 89$ Da) between **I** and **II**. The molecular masses of DMBT and PET ligands are

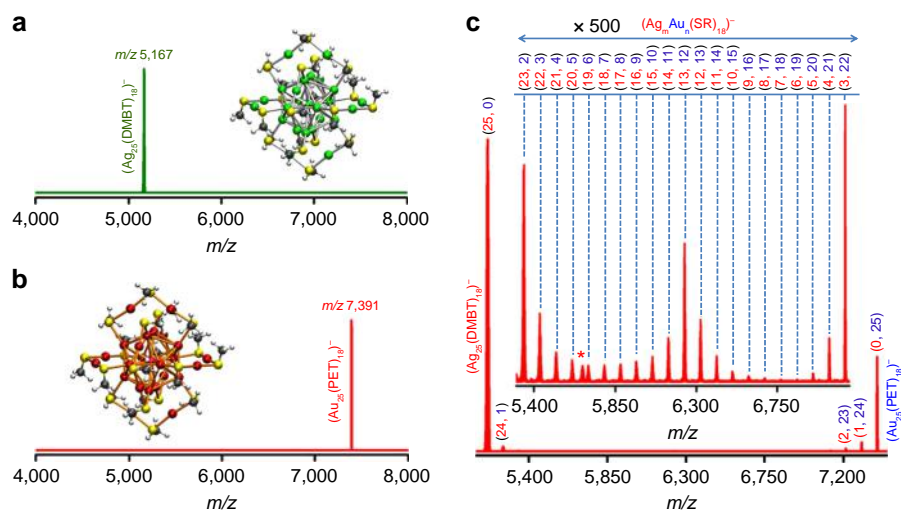


Figure 1 | Mass spectra of reactant clusters and their entire range of alloys. Electrospray ionization mass spectra (ESI MS) of $\text{Ag}_{25}(\text{DMBT})_{18}$ (**a**), $\text{Au}_{25}(\text{PET})_{18}$ (**b**) and a mixture of the two at a $\text{Ag}_{25}:\text{Au}_{25}$ molar ratio of 0.3:1.0 measured within 2 min after mixing (**c**). The peak labels in (**c**) shown as numbers in red (m) and blue (n) in parentheses give the numbers of Ag and Au atoms, respectively, in the alloy clusters of formula $\text{Ag}_m\text{Au}_n(\text{SR})_{18}$. Schematic structures of **I** and **II** (with the R group as $-\text{CH}_3$, not the real ligands) are also shown. Colour codes for the atoms in the inset pictures: red (Au), green (Ag), yellow (sulfur), black (carbon) and white (hydrogen). The inset in (**c**) is the expanded region of the same mass spectrum between m/z 5,300 to 7,150. **c** and its inset shows that entire range ($n=1–24$) of alloy clusters, $\text{Ag}_m\text{Au}_n(\text{SR})_{18}$ ($m+n=25$), are formed. The peak labelled with “*” in (**c**) is due to an unassigned dianionic species. DMBT is 2,4-dimethylbenzenethiol and PET is 2-phenylethanethiol.

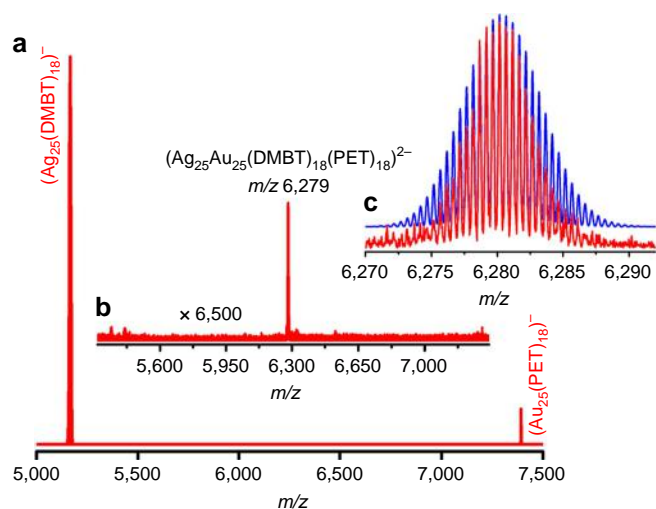


Figure 2 | Mass spectrometric detection of the intermediate. Full range electrospray ionization mass spectrum (ESI MS) of the mixture of $\text{Ag}_{25}(\text{DMBT})_{18}$ (**I**) and $\text{Au}_{25}(\text{PET})_{18}$ (**II**) at molar ratio (**I:II**) of 0.3:1.0 measured within 2 min after mixing (**a**), zoomed in region of panel a in the range between m/z 5,270 and 7,340 showing a feature due to the dianionic adduct, $(\text{Ag}_{25}\text{Au}_{25}(\text{DMBT})_{18}(\text{PET})_{18})^{2-}$ formed between **I** and **II** (**b**) and theoretical (blue) and experimental (red) isotope patterns of the adduct features (**c**). DMBT is 2,4-dimethylbenzenethiol and PET is 2-phenylethanethiol.

equal (138 Da) and hence the exchanges of ligands (DMBT-PET exchange) and that of metal-ligand fragments ((Ag-DMBT)-(Au-PET) exchange) are not evident from this set of experiments. However, such exchanges were observed in reactions between **I** and $\text{Au}_{25}(\text{SBU})_{18}$ (SBU = *n*-butanethiol) (Supplementary Fig. 5). On the basis of the observation of Ag-Au exchanges, a general formula, $\text{Ag}_m\text{Au}_n(\text{SR})_{18}$, is given for the alloy clusters formed from **I** and **II**. The numbers in red (*m*) and those in blue (*n*) in the parentheses of Fig. 1c represent the numbers of Ag and Au atoms, respectively, in the formula, $\text{Ag}_m\text{Au}_n(\text{SR})_{18}$. Since the ligand exchange is not detected for these alloys, we do not know the exact numbers of DMBT and PET ligands present in the alloy clusters and hence we use -SR instead of both DMBT and PET separately in the general formula. The total number of metal atoms (25) and that of ligands (18) is preserved in the alloy clusters. Figure 1c also indicates that the entire range of alloy clusters, $(\text{Ag}_m\text{Au}_n(\text{SR}))_{18}$ ($n = 1-24$; $m + n = 25$) that is, $\text{Ag}_{24}\text{Au}_1(\text{SR})_{18}$ to $\text{Ag}_1\text{Au}_{24}(\text{SR})_{18}$, are formed in the solution as soon as **I** and **II** are mixed. Another notable observation from Fig. 1c is the higher abundance of $\text{Ag}_{13}\text{Au}_{12}(\text{SR})_{18}$ (see the peak labelled (13, 12) in Fig. 1c inset) compared with the other alloy clusters. A possible reason for this is discussed in Supplementary Note 1.

Detection of the intermediate. We detected the dianionic adduct, $(\text{Ag}_{25}\text{Au}_{25}(\text{DMBT})_{18}(\text{PET})_{18})^{2-}$, formed between **I** and **II** at a molar ratio (**I:II**) of 0.3:1.0. Instrumental parameters optimized for this set of experiments are listed in Supplementary Notes 2 and 3. Features due to undoped **I** and **II** were observed in the mass spectrum shown in Fig. 2a. The region between m/z 5,270 and 7,340 in this mass spectrum are shown in Fig. 2b. A peak at m/z 6,279 was observed in Fig. 2b which was assigned to $(\text{Ag}_{25}\text{Au}_{25}(\text{DMBT})_{18}(\text{PET})_{18})^{2-}$. Comparison of the theoretical and experimental isotope patterns shown in Fig. 2c confirms this assignment. A separation of 0.5 mass units between the peaks in

the experimental isotope pattern confirms the dianionic charge state of the adduct. Time-dependent mass spectrometric measurements presented in Supplementary Fig. 6 show that this adduct vanishes almost completely within 5 min and monoanionic alloy cluster products are formed. The prominent features observed at this time are those due to undoped reactant clusters (**I** and **II**). No features due to alloy clusters were detected (except that of $\text{Ag}_{24}\text{Au}_1(\text{SR})_{18}$, which appears at m/z 5,255; not shown in Fig. 2b).

From Fig. 2a (and from Fig. 1c), we also note that the intensity of **II** is much smaller compared with that of **I** even though higher amounts of **II** are present in the 0.3:1.0 reaction mixture. This could be an indication that some of the **II** might be transformed into mass spectrometrically undetectable or poorly detectable intermediate species during the reaction. For example, anionic Au_{25} can act as an electron donor, which will generate neutral Au_{25} , which may not have the same efficiency for mass spectrometric detection (note that we have not used any charge inducing agents such as Cs^+ in our measurements to impart charge to neutral species). Furthermore, **II** forms the dianionic adducts with **I** (Fig. 2b and panel a in Supplementary Fig. 6) and also with the alloy clusters formed (panel b in Supplementary Fig. 6). There could be other intermediate species also during the course of the reaction, and probing the details of these events and the intermediates are beyond the scope of the present study. However, these measurements indicate that we have captured one of the earliest events in this reaction, namely the formation of a dianionic adduct of reactant clusters, before the formation of alloys.

Formation of the adduct, $(\text{Ag}_{25}\text{Au}_{25}(\text{DMBT})_{18}(\text{PET})_{18})^{2-}$, may seem unlikely, considering the overall negative charges of the individual clusters, which may contribute to repulsive interactions between them, preventing their closer approach. However, the charge on these clusters, $\text{Au}_{25}(\text{SR})_{18}$ and $\text{Ag}_{25}(\text{SR})_{18}$, is not localized but dispersed over atoms in their core, staples and ligands^{23,29}. Hence, the two clusters may not experience considerable repulsive interactions between them when they approach each other. Metallophilic interactions³⁰⁻³⁴ between the closed-shell Ag(I) and Au(I) centres that are present in the $\text{M}_2(\text{SR})_3$ staples of **I** and **II**, and π - π interactions between the aryl groups of the ligands, may also contribute to attractive forces between the two clusters. The sulfur atoms of monothiol ligands (DMBT and PET) involved in these reactions are bound to the metal atoms in the clusters, and these ligands do not have any other functional groups which are free to act as linker molecules between the clusters, unlike in the cases of a few previous reports^{35,36}. Moreover, we did not detect the presence of any extra DMBT or PET ligands in the adduct in mass spectrometric measurements, as in the case of clusters having different ligands³⁷. These observations suggest that van der Waals (vdW) interactions between the clusters can be one of the factors responsible for adduct formation.

Nature of the intermediate. A complete search over the relevant rotational and translational degrees of freedom of one of the clusters w.r.t. the other, and ligand orientational degrees of freedom of each of the two clusters in the adduct with DFT is unfeasible due to the computational cost. Hence, we used a combined approach utilizing the highly efficient force-field-based method of molecular docking to first identify a global minimum energy geometry of the two clusters in close proximity, subject to some constraints (see Methods and Supplementary Note 4 for details of the method) and then optimized this geometry using DFT to yield a more realistic adduct structure. In our initial molecular docking simulations, $\text{Au}_{25}(\text{PET})_{18}$ was taken as the

'ligand', that is, the movable molecule whose degrees of freedom would be varied, and $\text{Ag}_{25}(\text{DMBT})_{18}$ as the 'receptor' (macromolecule) which was the fixed and completely rigid central molecule. The reason for choosing $\text{Au}_{25}(\text{PET})_{18}$ as the movable and flexible molecule was that PET ligands have a greater torsional flexibility than the DMBT ligands due to the longer chain length which would result in lower energy minima during the optimization over the greater number of torsional degrees of freedom. We have used the reported crystal structure coordinates^{22,28} of $\text{Ag}_{25}(\text{SR})_{18}$ and $\text{Au}_{25}(\text{SR})_{18}$, without any structural relaxation, as the input for the molecular docking study. Different types of atoms in the ligands DMBT and PET and the charges on them are given in Supplementary Fig. 7 and Supplementary Tables 1 and 2, respectively.

From the docking simulations, we identified a force-field global minimum geometry (FFGMG) (Supplementary Data 1 for coordinates) of the adduct $(\text{Ag}_{25}\text{Au}_{25}(\text{DMBT})_{18}(\text{PET})_{18})^{2-}$, as shown in Supplementary Fig. 9. The approach of the two clusters resulted in significant changes in the orientation of the PET ligands (Supplementary Fig. 8 and Fig. 11) at the interface between the clusters so as to permit interdigitation (Supplementary Fig. 10) between the ligands of these clusters.

We then optimized this FFGMG of the adduct using DFT to see if any structural changes might occur due to the additional structural relaxation permitted in DFT (See Methods and Supplementary Note 4; Supplementary Data 2 for coordinates). The exchange-correlation functional employed was the generalized gradient approximation of Perdew, Burke and Ernzerhof (GGA-PBE)³⁸. The van der Waals corrections have not been included in this optimization for the reasons explained in Supplementary Note 5. Interestingly, the geometry obtained from the DFT-optimization of the FFGMG of adduct, shown in Fig. 3, reveals that the staples of **I** and **II** have joined through a bond (A–F; 2.90 Å) between a bridging sulfur atom (labelled A) of **II** and an Ag atom (labelled F) of **I**. We note that Ag atom can bind with more than two thiolate ligands as in the case of $\text{Ag}_{44}(\text{SR})_{30}$ clusters¹⁰. Note that the distance between these atoms

in the FFGMG of adduct was longer (3.90 Å) (Supplementary Fig. 9) compared with the A–F bond distance in its DFT-optimized geometry (DFT-OG). A comparison of the FFGMG of the adduct and its DFT-OG shows that the distances between the closest metal and sulfur atoms (Supplementary Fig. 12; Supplementary Note 6) and the ligand orientations (Fig. 3, Supplementary Fig. 9) in these adducts have changed.

A comparison of the average bond distances (Supplementary Table 3) reveals that almost all the bond lengths in both of the clusters in the DFT-OG of adduct have increased significantly compared with the corresponding values in the DFT-OGs of the isolated clusters. For example, average M–sulfur (M = Ag/Au) bond distance in **I** and **II**, in their DFT-OG of adduct, is about 0.1 Å (for **II**) and 0.08 Å (for **I**) longer than the respective values for the DFT-OGs of isolated **I** and **II**. Similarly, average distances of the shorter and longer metal–metal bonds in the icosahedra of **I** (Supplementary Fig. 13 and ref. 39 for description) have also increased in its DFT-OG. Further, the average distance between the central metal atom and the icosahedral surface metal atoms also showed an increase of about 0.04 Å (for **II**) and 0.07 Å (for **I**) in the DFT-OG of adduct. In addition to these changes, the $\text{M}_2(\text{SR})_3$ (M = Ag/Au) staples of the two clusters underwent significant changes in terms of their bond angles (Supplementary Fig. 13) as some of the S–M–S (M = Ag/Au) fragments of the staples became more linear compared with their original V-shape in isolated state. In summary, our combined molecular docking simulations and DFT calculations show that formation of the $(\text{Ag}_{25}\text{Au}_{25}(\text{DMBT})_{18}(\text{PET})_{18})^{2-}$ adduct is feasible during the reaction between **I** and **II**. The predicted adduct structure which features an intercluster Ag–S bond might be one of the initial configurations before further structural and chemical transformations take place in the interfacial region involving the ligands and staple metal atoms.

Tuning the composition of alloy clusters. Our experiments showed that the equilibrium distribution of alloy clusters formed is

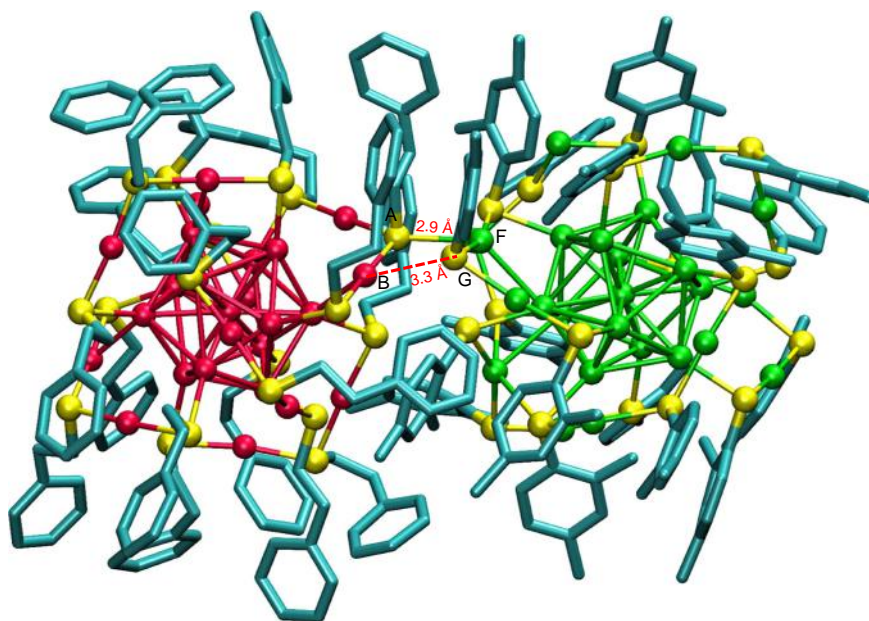


Figure 3 | DFT-optimized structure of $(\text{Ag}_{25}\text{Au}_{25}(\text{DMBT})_{18}(\text{PET})_{18})^{2-}$. The geometry of $(\text{Ag}_{25}\text{Au}_{25}(\text{DMBT})_{18}(\text{PET})_{18})^{2-}$ adduct (with **II** on the left and **I** on the right) obtained from DFT-optimization of the structure obtained from a force-field-based molecular docking simulation (shown in Supplementary Fig. 9). The hydrogen atoms are omitted from the ligands for clarity. Colour code for the atoms: Au (red), Ag (green), S (yellow) and C (blue). DMBT is 2,4-dimethylbenzenethiol and PET is 2-phenylethanethiol.

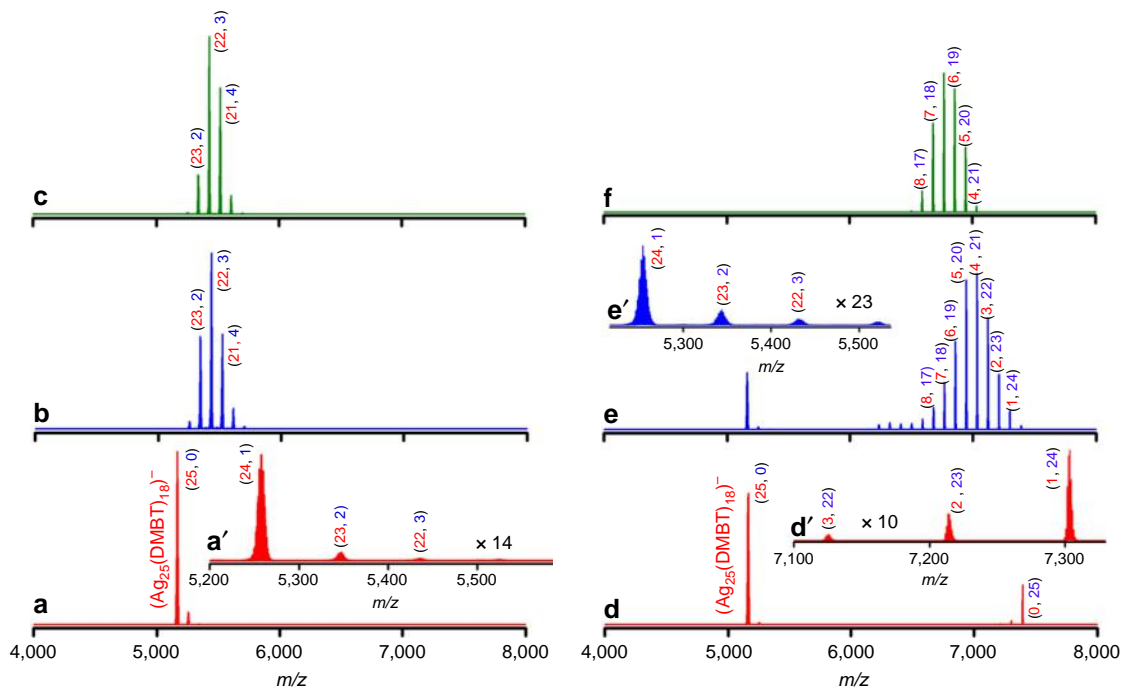


Figure 4 | Formation of Ag-rich or Au-rich $\text{Ag}_m\text{Au}_n(\text{SR})_{18}$ ($m+n=25$) clusters. Electrospray ionization mass spectra (ESI MS) spectra of a mixture of $\text{Ag}_{25}(\text{DMBT})_{18}$ (**I**) and $\text{Au}_{25}(\text{PET})_{18}$ (**II**) at molar ratios (**I:II**) of 6.6:1.0 (**a–c**) and 0.3:1.0 (**d–f**). DMBT is 2,4-dimethylbenzenethiol and PET is 2-phenylethanethiol. **a–c** and **d–f** correspond to the mass spectra measured within 2 min after mixing, after 10 min and after 1 h, respectively. The peak labels shown as numbers in red (m) and blue (n) in parentheses give the numbers of Ag and Au atoms, respectively, in the alloy clusters, $\text{Ag}_m\text{Au}_n(\text{SR})_{18}$. Insets **a'** and **e'** shows the Ag-rich clusters with $n=1–3$. Inset **d'** shows the Au-rich clusters with $n=22–24$.

determined by the relative initial concentrations of the reactant clusters. Figure 4 shows the mass spectra measured at various time intervals during the reaction between **I** and **II** at molar ratios (**I:II**) of 6.6:1.0 (panels **a–c**) and 0.3:1.0 (panels **d–f**), respectively. Temporal changes in the UV/vis absorption features for these reaction mixtures are presented in Supplementary Figs 14 and 15, respectively. Since the concentration of **II** in the reaction mixture was less in the 6.6:1.0 mixture, its feature was not observed in the mass spectrum shown in panel **a** of Fig. 4; however, the doping of Au atoms into **I** (which is in excess) was observed in the spectra measured within 2 min after the addition of **II**, as shown in inset **a'** in Fig. 4. The feature due to undoped **I** disappeared within 10 min and alloy clusters derived from **I** (containing 1–5 Au atoms) appeared, as shown in Fig. 4b. The mass spectrum after 1 h (Fig. 4c) is almost similar to the spectrum after 10 min (Fig. 4b), which shows that no further doping occurred at this composition, even at longer time intervals of the reaction.

To further confirm these observations, we carried out time-dependent MALDI MS measurements (see Supplementary Note 7 for details) for this (6.6:1.0) composition. As shown in Supplementary Fig. 16a, the peak due to undoped **I** and its Au-doped alloys along with their fragments appeared within 2 min after mixing. No features due to **II** and its Ag-doped alloys and their fragments were observed in these measurements. The MALDI MS spectra measured 10 min and 1 h after mixing (Supplementary Fig. 16b,c, respectively) were almost the same and show the formation of Au-doped (containing 1–5 Au atoms) alloys of **I**. Hence, these observations indicate that added **II**, which was lesser in concentration, was consumed completely by **I** present in higher concentration.

When the reaction was carried out at **I:II** molar ratio of 0.3:1.0, features due to the undoped **I** and **II** were observed in the spectra measured within 2 min after mixing, as shown in Fig. 4d. Further,

Ag-doping in **II** was also observed in this spectra (see inset **d'**). Note that the spectra shown in Fig. 4d and in Fig. 1c are the same and these features are described earlier. Mass spectra measured 10 min after mixing (Fig. 4e) show the decrease in intensities of **I** and **II** along with the increase in intensities of Ag-doped **II**. Au-doped alloys of **I** were also observed in this mass spectra (see inset **e'**) but they are significantly lesser in intensity compared with Ag-doped alloys of **II**. After about 1 h, the features due to undoped and Au-doped **I** disappeared completely and only the Ag-doped alloys of **II** (containing 17–21 Au atoms) were observed in the mass spectrum, as shown in Fig. 4f. There were no significant changes in the mass spectra measured at longer time intervals. MALDI MS measurements, presented in Supplementary Fig. 17, further confirm this observation. Alloy clusters with intermediate level of doping (10–14 metal atoms) were observed in a reaction mixture with **I:II** ratio of 1.0:1.0, as shown in Supplementary Figs 18 and 19. The results described above suggest that the reaction between **I** and **II** at this composition (0.3:1.0), Ag-doping into **II** and Au-doping into **I** were initiated as soon as the two clusters were mixed. However, as the reaction proceeded, the undoped **I** and its Au-doped alloys were consumed by **II** (and its Ag-doped alloys) leading to a mixture of Ag-doped **II**.

The results described above suggest that the cluster which is lesser in concentration in the reaction mixture acts as the source of the dopant metal atom, ligand or metal-ligand fragment, to the cluster higher in concentration. The equilibrium distribution of alloy products for reaction mixtures at various $\text{Ag}_{25}:\text{Au}_{25}$ molar ratios are presented in Supplementary Fig. 20 which implies that the numbers of Ag and Au atoms in the $\text{Ag}_m\text{Au}_n(\text{SR})_{18}$ alloy clusters can be continually varied across the entire range ($n=1–24$), simply by varying the initial concentrations of **I** and **II**. We note that attempts to synthesize

Au-doped $\text{Ag}_{25}(\text{SR})_{18}$ clusters by galvanic exchange by reaction of Au^{3+} with $\text{Ag}_{25}(\text{SR})_{18}$ gave only $\text{Ag}_{24}\text{Au}_1(\text{SR})_{18}$ (ref. 40), similar to the monosubstituted Pd, Pt and Cd alloys of **I** and **II** (refs 41–45). Hence, the reaction between **I** and **II** provides a simple method to synthesize alloy clusters $\text{M}_{25}(\text{SR})_{18}$ ($\text{M} = \text{Ag}/\text{Au}$) with the desired number of Ag and Au atoms.

Energetics of the exchange reactions. We carried out DFT calculations (see Methods) to understand the energetics of single Au/Ag atom substitution into the various symmetry unique sites in $\text{M}_{25}(\text{SR})_{18}$ and the overall single metal atom substitution reaction, $\text{Ag}_{25}(\text{DMBT})_{18} + \text{Au}_{25}(\text{PET})_{18} \rightarrow \text{Ag}_{24}\text{Au}_1(\text{DMBT})_{18} + \text{Au}_{24}\text{Ag}_1(\text{PET})_{18}$, between **I** and **II**. The calculated energies for (1) single Au substitution into $\text{Ag}_{25}(\text{DMBT})_{18}$, (2) single Ag substitution into $\text{Au}_{25}(\text{PET})_{18}$ and (3) the overall single metal atom substitution reaction are listed in Fig. 5(a–c), respectively. Additional results of the calculations are presented in Supplementary Tables 4–8. Note that the reactions mentioned above do not correspond to any experimental stoichiometry and the reaction energies reported do not give quantitative reaction enthalpies. The energies reported herein do not contain zero-point corrections. However, this method is known to correctly reproduce the experimentally observed site preferences in metal atom substitutions in $\text{M}_{25}(\text{SR})_{18}$ systems^{46,47}. As shown in Fig. 5d, three distinct sites are available in $\text{Ag}_{25}(\text{DMBT})_{18}$ for the first dopant Au atom: these are, (1) the centre of the icosahedron (C), (2) the twelve icosahedral vertex atoms (I) and (3) the twelve staple atoms (S). A similar situation exists for single Ag atom doping into $\text{Au}_{25}(\text{PET})_{18}$ since the structure of the two clusters are identical.

Our calculations show that the substitution of Au into all three positions of $\text{Ag}_{25}(\text{DMBT})_{18}$ is exothermic. Substitution of Au atom into the centre (C) of $\text{Ag}_{25}(\text{DMBT})_{18}$ is the most exothermic (-904 meV) compared with the substitution into I (-540 meV) and S (-578 meV) positions, as shown in Fig. 5(a). This is in contrast to the endothermic substitution of an Ag atom into $\text{Au}_{25}(\text{PET})_{18}$ where the C position is the least preferred^{46,47}, as shown in Fig. 5b. Figure 5c indicates that overall reaction is exothermic for all the combinations of dopant atom locations. Hence, calculations show that exothermicity of the overall

exchange reaction between $\text{Ag}_{25}(\text{DMBT})_{18}$ and $\text{Au}_{25}(\text{PET})_{18}$ is due to the exothermicities of the metal atom substitution reactions into favourable locations in $\text{Ag}_{25}(\text{DMBT})_{18}$ and $\text{Au}_{25}(\text{PET})_{18}$.

We think that relative changes in the strengths of various metal–metal bonds in the parent and doped clusters could be one of the factors determining the preference of Ag/Au atoms for the C positions of these clusters. Standard bond dissociation energies (in kJ mol^{-1}) for the various bond types present in $\text{Ag}_{25}(\text{SR})_{18}$ and $\text{Au}_{25}(\text{SR})_{18}$ are: Ag–Ag (162.9 ± 2.9), Au–Au (226.2 ± 0.3), Ag–Au (202.5 ± 9.6) (ref. 48). These values indicate that the order of the bond strengths is: Au–Au > Ag–Au > Ag–Ag. In $\text{M}_{25}(\text{SR})_{18}$ ($\text{M} = \text{Ag}/\text{Au}$) clusters, there are twelve interactions between a metal atom at the central atom (C) position and those in the icosahedral (I) positions. Hence, bonding interactions in $\text{Ag}_{24}\text{Au}_1(\text{SR})_{18}$ between the central atom (Au) and icosahedral atoms (Ag) are more preferred due to the significantly increased bonding enthalpy ($162.9 - 202.5 = -39.6$ kJ mol^{-1}) compared with the Ag–Ag interactions in undoped $\text{Ag}_{25}(\text{SR})_{18}$. Therefore, the substitution of an Au atom into the C position of $\text{Ag}_{25}(\text{SR})_{18}$ would be most exothermic compared with substitution of an Au atom into I and S positions, as shown in Fig. 5(a). Similarly, the substitution of an Ag atom into the C position of $\text{Au}_{25}(\text{SR})_{18}$ results in twelve weaker Ag–Au interactions at the cost of the twelve stronger Au–Au interactions, originally present in $\text{Au}_{25}(\text{SR})_{18}$. This results in a decrease in bonding enthalpy ($226.2 - 202.5 = +23.7$ kJ mol^{-1}) in $\text{Au}_{24}\text{Ag}_1(\text{SR})_{18}$ compared with $\text{Au}_{25}(\text{SR})_{18}$. Hence, substitution of an Ag atom into the C position of **II** is the least preferred compared with those into I and S positions, as shown in Fig. 5b.

Discussion

The formation of an adduct indicates that bimolecular events involving the intact clusters occur in solution and such events could be one of the pathways of intercluster reactions. In the light of our results, we suggest that initial binding between **I** and **II** during the reaction might occur through (i) the attractive vdW forces between the metal atoms and sulfur atoms, and between the alkyl/aryl groups of ligands and (ii) metallophilic interactions between the metal atoms and sulfur atoms in the staples of the two clusters. These interactions would lead to the weakening of

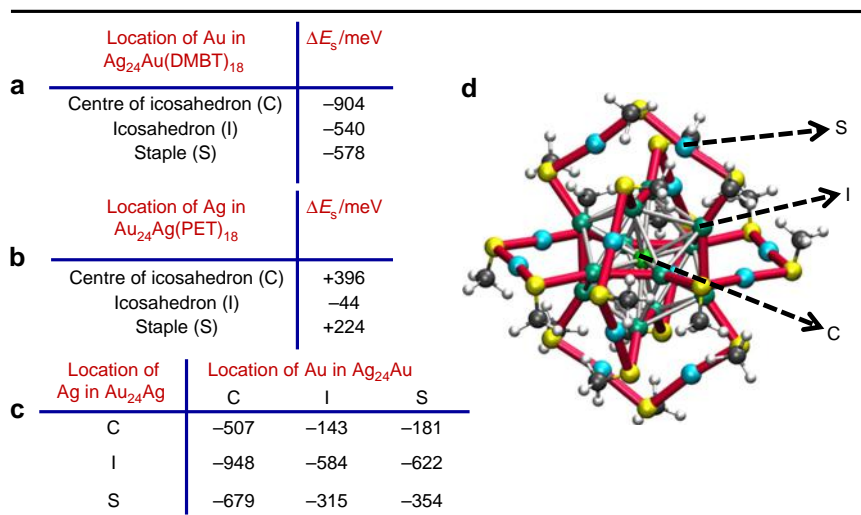


Figure 5 | Calculated energies of reactions. Calculated energies for the substitution reaction (ΔE_s) of Au in $\text{Ag}_{25}(\text{DMBT})_{18}$ (**a**), Ag in $\text{Au}_{25}(\text{PET})_{18}$ (**b**) and the overall reaction energies (**c**), in meV, as a function of their positions in the product clusters, $\text{Ag}_{24}\text{Au}_1(\text{DMBT})_{18}$ and $\text{Au}_{24}\text{Ag}_1(\text{PET})_{18}$. DMBT is 2,4-dimethylbenzenethiol and PET is 2-phenylethanethiol. The overall structure of $\text{M}_{25}(\text{SR})_{18}$ ($\text{M} = \text{Ag}/\text{Au}$) and their distinct metal atom positions (C, I and S) are shown in (**d**). For the labels on the picture, refer to text.

some of the M–S ($M = \text{Ag}/\text{Au}$) staple bonds at the interface between the two clusters before the exchange of M, and M–L and L ($M = \text{metal}$, $L = \text{ligand}$) units within the adduct. The DFT-optimized adduct structure shows interesting changes in the structural features of **I** and **II**. One of the most significant pieces of information from our study is the observation of weak bonding between the staples of the two clusters. Such events have been proposed in our earlier study²¹. Further, the interstaple bonding was facilitated by a large number of strained bonds in both the clusters in both core and staple regions, as described earlier. The bonds A–B and G–F (Fig. 3) also might break, leading to staple opening in the subsequent steps of the reaction before exchange of gold and silver atoms. Structural rearrangements in the vicinity of such intercluster bonds could lead to metal and/or ligand exchange.

We note that since the distance between the clusters in the force-field minimum geometry is on the order of 5 Å, electron transfer might occur between these clusters, as such processes have been observed at similar separations for proteins⁴⁹. These processes may generate anionic metal–ligand fragments from one of the clusters, such as $M(\text{SR})_2^-$ ($M = \text{Ag}/\text{Au}$), which could attack the $M_2(\text{SR})_3$ staples or the rings⁵⁰ of the other cluster, as suggested in our earlier report²¹.

The preservation of the structure and topology in the alloy products can be understood from the structural models and the crystal structure data available for $M_{25}(\text{SR})_{18}$ clusters. Based on the divide and protect view⁵¹ of the structure or inherent structure rule⁵² proposed for thiolate protected noble metal clusters, these clusters can be viewed as a combination of a symmetrical core of metal atoms surrounded by metal–thiolate units, often referred to as staple motifs. According to these schemes, the $M_{25}(\text{SR})_{18}$ ($M = \text{Ag}/\text{Au}$) clusters can be represented as $M@M_{12}(\text{M}_2(\text{SR})_3)_6$ where a central atom, M, is surrounded by the M_{12} icosahedron. The resulting M_{13} core can be considered to be protected by six $M_2(\text{SR})_3$ semirings or staple motifs (Fig. 5d). Here, we use the term inherent structure for the basic framework including the geometry of the core (icosahedron, dodecahedron and so on) and that of the staple motifs (M–SR, $M_2(\text{SR})_3$, $M_3(\text{SR})_4$, and so on). The actual shapes of the clusters and slight changes in bond angles and bond lengths, which are essentially dependent on the nature of the element M (Ag/Au) and R groups are not addressed here. Crystal structures of $\text{Ag}_{25}(\text{DMBT})_{18}$ and $\text{Au}_{25}(\text{PET})_{18}$ show that the inherent structural framework of the icosahedral core and staples, described above, are identical and the presence of different ligand R groups do not affect this structure^{22,23,28}. In addition, crystal structure data of alloys have also shown that the substitution of Ag atoms into all the three available positions (C, I and S) in $\text{Au}_{25}(\text{SR})_{18}$ does not alter this framework^{53,54}. The recently reported structure⁴⁰ of $\text{Ag}_{24}\text{Au}_1(\text{SR})_{18}$ shows that the Au atom occupies the C position, preserving the inherent structure. These results are in agreement with DFT calculations⁵⁵ which show that incorporation of twelve Au atoms into the core (or into the staples) of $M_{25}(\text{SR})_{18}$ ($M = \text{Au}/\text{Ag}$) does not alter the inherent structure. A schematic of the structures of $\text{Au}_{13}\text{Ag}_{12}(\text{SR})_{18}$ and $\text{Ag}_{13}\text{Au}_{12}(\text{SR})_{18}$ is presented in Supplementary Fig. 21.

A simplified representation of the inherent structure of $M_{25}(\text{SR})_{18}$ is obtained by the consideration of the ring structures in its bonding network⁵⁰. In this model, these clusters can be represented as $M@(\text{M}_8(\text{SR})_6)_3$ where the central atom M is considered to be surrounded by three, interlocked $M_8(\text{SR})_6$ Borromean rings^{50,56} (see the path traced by the thick, red bonds in Fig. 5d). This ring representation and the $M@M_{12}(\text{M}_2(\text{SR})_3)_6$ model are valid for both $\text{Au}_{25}(\text{SR})_{18}$ and $\text{Ag}_{25}(\text{SR})_{18}$, and in general for their arbitrary mixed-metal compositions, $\text{Ag}_m\text{Au}_n(\text{SR})_{18}$, as is evident from their crystallographic data^{22,28,53}. In this structural viewpoint, the stability of the inherent structure may be attributed

to the interlocked rings^{50,56} and its stiff framework³⁹. Hence, such a stable structural configuration would remain intact while atomic units are substituted, involving geometrical distortions and opening and reclosing of parts of the ring structure. Hence, it is the inherent $M@(\text{M}_{12})(\text{M}_2(\text{SR})_3)_6$ or $M@(\text{M}_8(\text{SR})_6)_3$ structure and topology of the bonding network which is preserved during the metal (M), ligand (L) and metal–ligand (M–L) fragment substitution reactions occurring between these clusters.

In conclusion, we report the spontaneous alloying between geometrically robust and electronically stable noble metal clusters $\text{Ag}_{25}(\text{SR})_{18}$ and $\text{Au}_{25}(\text{SR})_{18}$ in solution, producing $\text{Ag}_m\text{Au}_n(\text{SR})_{18}$ ($n = 1\text{--}24$; $m + n = 25$), preserving the inherent structure throughout the entire series. This suggests transformation of a mixture of $\text{Ag}_{25}(\text{SR})_{18}$ and $\text{Au}_{25}(\text{SR})_{18}$ to $\text{Ag}_m\text{Au}_n(\text{SR})_{18}$ by successive substitution reactions, which converts one kind of nanoparticle to another, preserving the structure. We detected a dianionic adduct, formed between the two clusters, which could be one of the earliest intermediates in this reaction. Molecular docking simulations combined with DFT calculations show that van der Waals forces as well as bonding between the staple motifs are crucial in forming these adducts. Detection of the dianionic adduct formed between $\text{Ag}_{25}(\text{SR})_{18}$ and $\text{Au}_{25}(\text{SR})_{18}$ suggests that these clusters themselves, not only their fragments, might be involved in these reactions. This reaction can be used to synthesize bimetallic AgAu clusters, $M_{25}(\text{SR})_{18}$ ($M = \text{Ag}/\text{Au}$) clusters with desired composition, simply by adjusting the concentrations of the reactant clusters. DFT calculations reveal that substitutions of Au atoms into all the three symmetry unique sites available in $\text{Ag}_{25}(\text{SR})_{18}$ are energetically favourable and exothermic, and this contributes to making the overall reaction exothermic. We hope that our results suggest the prospect of complete transformation of one piece of matter to another, chemically dissimilar one, one atom at a time, preserving structure in the process. Although this has been demonstrated only for two prototypical systems now, the availability of such structures with chemical and structural diversity would enrich this area.

Methods

Materials. The following chemicals were purchased from Sigma Aldrich: Chloroauric acid trihydrate ($\text{HAuCl}_4 \cdot 3\text{H}_2\text{O}$), 2-phenylethanethiol (PET), *n*-butanethiol (*n*-BuS), 2,4-dimethylbenzenethiol (DMBT), tetraoctylammonium bromide (TOAB), tetraphenylphosphonium bromide (PPh_4Br) and sodium borohydride (NaBH_4). All the solvents used (methanol and dichloromethane (DCM)) were of analytical grade. Silver nitrate (AgNO_3) was purchased from RANKEM India.

Synthesis of clusters. $\text{Au}_{25}(\text{PET})_{18}$ and $\text{Au}_{25}(\text{SBU})_{18}$: these clusters were synthesized according to reported methods²¹. $\text{Ag}_{25}(\text{SR})_{18}$ was prepared using the procedure of Bakr *et al.*²⁸ with slight modifications in the ratio of reagents. Purity of the samples was ensured by ultraviolet/visible (UV/vis) absorption spectroscopy and electrospray ionization mass spectrometry (ESI MS).

Alloying reaction between $\text{Ag}_{25}(\text{SR})_{18}$ and $\text{Au}_{25}(\text{SR})_{18}$. Alloying reaction between these clusters was carried out at room temperature ($\sim 30^\circ\text{C}$) by mixing the stock solutions (in DCM) of the two clusters. A fixed volume of the stock solution of $\text{Ag}_{25}(\text{DMBT})_{18}$ (**I**) was added into about 1 ml of DCM, and then different volumes of stock solutions of $\text{Au}_{25}(\text{PET})_{18}$ (**II**) were added into it, in order to vary the composition of the reaction mixtures. The reaction mixture was not stirred magnetically but mixed using a pipette. Immediate colour changes, time-dependent ultraviolet/vis absorption and ESI MS measurements revealed that the reaction occurred as soon as the two clusters were mixed.

Instrumentation. Electrospray ionization mass spectrometric (ESI MS) measurements were carried out using a Waters Synapt G2-Si instrument. ESI MS had a maximum resolution ($m/\Delta m$) of 50,000 in the mass range of interest. We used Applied Biosystems Voyager DEPro mass spectrometer for matrix-assisted laser desorption ionization mass spectrometric (MALDI MS) measurements. More details about the measurements are given in Supplementary Notes 2, 3 and 7. UV/Vis spectra were recorded using a Perkin-Elmer Lambda 25 UV/vis spectrometer. Absorption spectra were typically measured in the range of 200–1100 nm.

Computational details. We carried out molecular docking simulations of $\text{Au}_{25}(\text{PET})_{18}$ and $\text{Ag}_{25}(\text{DMBT})_{18}$ clusters in order to find out how closely they could approach each other and which atoms and their interactions would be involved in the adduct formation. We used the Autodock 4.2 molecular docking software⁵⁷ that uses a force-field which includes van der Waals (Lennard-Jones 12-6 potential), hydrogen bonding, desolvation and electrostatics terms and treats the intramolecular bonds and bond angles of both the molecules as rigid, apart from selected bond torsions of the ligands. We used the crystal structure coordinates^{22,28} of $\text{Au}_{25}(\text{PET})_{18}$ and $\text{Ag}_{25}(\text{DMBT})_{18}$, without any structural relaxation, as the input for the docking simulations. Additional details of our methods are given in Supplementary Note 4.

For the DFT-optimization of the force-field global minimum geometry of $(\text{Ag}_{25}\text{Au}_{25}(\text{DMBT})_{18}(\text{PET})_{18})^{2-}$ obtained from the Autodock program (as described above), we used the real-space grid-based projector augmented wave (GPAW) package⁵⁸. The $\text{Ag}(4d^{10}5s^1)$, $\text{Au}(5d^{10}6s^1)$, and $\text{S}(3s^23p^4)$ electrons were treated as valence and the inner electrons were included in a frozen core. The GPAW setups for gold and silver included scalar-relativistic corrections. The exchange-correlation functional employed was the generalized gradient approximation of Perdew, Burke and Ernzerhof (GGA-PBE)³⁸. The van der Waals corrections have not been included in this optimization for the reasons explained in the Supplementary Note 5. We used the LCAO basis set method of GPAW with a 0.2 Å grid spacing for electron density and a convergence criterion of $0.05 \text{ eV } \text{Å}^{-1}$ for the residual forces on atoms for the structure optimization, without any symmetry constraints. The size of the simulation box was taken to be $40 \times 40 \times 40 \text{ Å}^3$.

For the DFT calculations on the energetics of metal exchange reactions, we adopted the same methods and parameters as described earlier for $(\text{Ag}_{25}\text{Au}_{25}(\text{DMBT})_{18}(\text{PET})_{18})^{2-}$, except that the more accurate finite-difference method of GPAW was used to compute the total energies of the geometries obtained from an initial optimization using the LCAO basis set method. The crystal structures of $\text{Au}_{25}(\text{SR})_{18}$ (ref. 22) and $\text{Ag}_{25}(\text{SR})_{18}$ (ref. 28) were used for the initial calculations. The structures of $(\text{Au}_{25}(\text{PET})_{18})^{-}$ and $(\text{Ag}_{25}(\text{DMBT})_{18})^{-}$ were first geometry optimized, and then a single metal (Ag or Au) atom was replaced in a symmetry non-equivalent position and the geometries of the resulting $(\text{Au}_{24}\text{Ag}(\text{PET})_{18})^{-}$ and $(\text{Ag}_{24}\text{Au}(\text{DMBT})_{18})^{-}$ configurations were then optimized and the energy of the cluster was taken at this energy minimum. We calculated the total energies of Au and Ag atoms using spin-polarization applying Hund's rule to the ground-state electronic configuration of the isolated atoms. The reaction energies of Au/Ag exchange into different positions in both of the clusters were calculated as $E(\text{Reaction}) = E(\text{Products}) - E(\text{Reactants})$.

The structures of **I** and **II**, (with $-\text{CH}_3$ instead of PET and DMBT) in Fig. 1a,b were built up with the help of Avogadro software package⁵⁹. We used the coordinates from the crystal structure of $\text{Au}_{25}(\text{SR})_{18}$, without any structural relaxation, for building these two structures since the overall structures of these two clusters are the same. The actual structures of $\text{Ag}_{25}(\text{DMBT})_{18}$ and $\text{Au}_{25}(\text{PET})_{18}$ are not exactly the same due to the arrangement of the ligand -R groups and the bond angles in the ligand shell. All visualizations were created with visual molecular dynamics (VMD) software⁶⁰.

Data availability. The authors declare that the data supporting the findings of this study are available within the paper and its Supplementary Information Files.

References

1. Templeton, A. C., Wuelfing, W. P. & Murray, R. W. Monolayer-protected cluster molecules. *Acc. Chem. Res.* **33**, 27–36 (2000).
2. Jin, R. Quantum sized, thiolate-protected gold nanoclusters. *Nanoscale* **2**, 343–362 (2010).
3. Lu, Y. & Chen, W. Sub-nanometre sized metal clusters: from synthetic challenges to the unique property discoveries. *Chem. Soc. Rev.* **41**, 3594–3623 (2012).
4. Pichugina, D. A., Kuz'menko, N. E. & Shestakov, A. F. Ligand-protected gold clusters: the structure, synthesis and applications. *Russ. Chem. Rev.* **84**, 1114–1144 (2015).
5. Walter, M. *et al.* A unified view of ligand-protected gold clusters as superatom complexes. *Proc. Natl Acad. Sci. USA* **105**, 9157–9162 (2008).
6. Häkkinen, H. The gold-sulfur interface at the nanoscale. *Nat. Chem.* **4**, 443–455 (2012).
7. Kurashige, W., Niihori, Y., Sharma, S. & Negishi, Y. Precise synthesis, functionalization and application of thiolate-protected gold clusters. *Coord. Chem. Rev.* **320–321**, 238–250 (2013).
8. Jiang, D. The expanding universe of thiolated gold nanoclusters and beyond. *Nanoscale* **5**, 7149–7160 (2013).
9. Jadzinsky, P. D., Calero, G., Ackerson, C. J., Bushnell, D. A. & Kornberg, R. D. Structure of a thiol monolayer-protected gold nanoparticle at 1.1 Å resolution. *Science* **318**, 430–433 (2007).
10. Desireddy, A. *et al.* Ultrastable silver nanoparticles. *Nature* **501**, 399–402 (2013).
11. Zhu, M., Aikens, C. M., Hollander, F. J., Schatz, G. C. & Jin, R. Correlating the crystal structure of a thiol-protected Au_{25} cluster and optical properties. *J. Am. Chem. Soc.* **130**, 5883–5885 (2008).

12. Knoppe, S., Häkkinen, H. & Verbiest, T. Nonlinear optical properties of thiolate-protected gold Clusters: a theoretical survey of the first hyperpolarizabilities. *J. Phys. Chem. C* **119**, 27676–27682 (2015).
13. Barcaro, G., Sementa, L., Fortunelli, A. & Stener, M. Optical properties of nanoalloys. *Phys. Chem. Chem. Phys.* **17**, 27952–27967 (2015).
14. Wu, Z. & Jin, R. On the ligand's role in the fluorescence of gold nanoclusters. *Nano Lett.* **10**, 2568–2573 (2010).
15. Muniz-Miranda, F., Menziani, M. C. & Pedone, A. Influence of silver doping on the photoluminescence of protected $\text{Ag}_n\text{Au}_{25-n}$ nanoclusters: a time-dependent density functional theory investigation. *J. Phys. Chem. C* **119**, 10766–10775 (2015).
16. Chang, H.-C., Chang, Y.-F., Fan, N.-C. & Ho, J. A. Facile preparation of high-quantum-yield gold nanoclusters: application to probing mercuric ions and biothiols. *ACS Appl. Mater. Interfaces* **6**, 18824–18831 (2014).
17. Mathew, A., Varghese, E., Choudhury, S., Pal, S. K. & Pradeep, T. Efficient red luminescence from organic-soluble Au_{25} clusters by ligand structure modification. *Nanoscale* **7**, 14305–14315 (2015).
18. Mathew, A., Sajanlal, P. R. & Pradeep, T. Selective visual detection of TNT at the sub-zeptomole level. *Angew. Chem. Int. Ed.* **51**, 9596–9600 (2012).
19. Chakraborty, I., Udayabhaskararao, T. & Pradeep, T. Luminescent sub-nanometer clusters for metal ion sensing: a new direction in nanosensors. *J. Hazard. Mater.* **211–212**, 396–403 (2012).
20. Chen, Y. S., Choi, H. & Kamat, P. V. Metal-cluster-sensitized solar cells. A new class of thiolated gold sensitizers delivering efficiency greater than 2%. *J. Am. Chem. Soc.* **135**, 8822–8825 (2013).
21. Krishnadas, K. R. *et al.* Intercluster reactions between $\text{Au}_{25}(\text{SR})_{18}$ and $\text{Ag}_{44}(\text{SR})_{30}$. *J. Am. Chem. Soc.* **138**, 140–148 (2016).
22. Heaven, M. W., Dass, A., White, P. S., Holt, K. M. & Murray, R. W. Crystal structure of the gold nanoparticle $[\text{N}(\text{C}_6\text{H}_{17})_4][\text{Au}_{25}(\text{SCH}_2\text{CH}_2\text{Ph})_{18}]$. *J. Am. Chem. Soc.* **130**, 3754–3755 (2008).
23. Akola, J., Walter, M., Whetten, R. L., Häkkinen, H. & Grönbeck, H. On the structure of thiolate-protected Au_{25} . *J. Am. Chem. Soc.* **130**, 3756–3757 (2008).
24. Parker, J. F., Fields-Zinna, C. A. & Murray, R. W. The story of a monodisperse gold nanoparticle: $\text{Au}_{25}\text{L}_{18}$. *Acc. Chem. Res.* **43**, 1289–1296 (2010).
25. Shichibu, Y. *et al.* Extremely high stability of glutathione-protected Au_{25} clusters against core etching. *Small* **3**, 835–839 (2007).
26. Negishi, Y., Chaki, N. K., Shichibu, Y., Whetten, R. L. & Tsukuda, T. Origin of magic stability of thiolated gold clusters: acase study on $\text{Au}_{25}(\text{SC}_6\text{H}_{13})_{18}$. *J. Am. Chem. Soc.* **129**, 11322–11323 (2007).
27. Tofaneli, M. A. & Ackerson, C. J. Superatom electron configuration predicts thermal stability of $\text{Au}_{25}(\text{SR})_{18}$ nanoclusters. *J. Am. Chem. Soc.* **134**, 16937–16940 (2012).
28. Joshi, C. P., Bootharaju, M. S., Alhilaly, M. J. & Bakr, O. M. $[\text{Ag}_{25}(\text{SR})_{18}]^{-}$: the 'golden' silver nanoparticle. *J. Am. Chem. Soc.* **137**, 11578–11581 (2015).
29. Lugo, G., Schwanen, V., Fresch, B. & Remacle, F. Chargere distribution effects on the UV-vis spectra of small ligated gold clusters: a computational study. *J. Phys. Chem. C* **119**, 10969–10980 (2015).
30. Pyykkö, P. Relativistic effects in chemistry: more common than you thought. *Annu. Rev. Phys. Chem.* **63**, 45–64 (2012).
31. Sculfort, S. & Braunstein, P. Intramolecular d^{10} - d^{10} interactions in heterometallic clusters of the transition metals. *Chem. Soc. Rev.* **40**, 2741–2760 (2011).
32. Ni, W.-X. *et al.* Metallophilicity-driven dynamic aggregation of a phosphorescent gold(I)-silver(I) cluster prepared by solution-based and mechanochemical approaches. *J. Am. Chem. Soc.* **136**, 9532–9535 (2014).
33. Schmidbaur, H. The aurophilicity phenomenon: decade of experimental findings, theoretical concepts and emerging applications. *Gold Bull.* **33/1**, 3 (2000).
34. Schmidbaur, H. & Schier, A. A briefing on aurophilicity. *Chem. Soc. Rev.* **37**, 1931–1951 (2008).
35. Compel, W. S. *et al.* Dynamic diglyme-mediated self-assembly of gold nanoclusters. *ACS Nano* **9**, 11690–11698 (2015).
36. Akola, J. *et al.* Thiolate-protected Au_{25} superatoms as building blocks: dimers and crystals. *J. Phys. Chem. C* **114**, 15986–15994 (2010).
37. Kurashige, W. *et al.* Au_{25} Clusters containing unoxidized tellurolates in the ligand shell. *J. Phys. Chem. Lett.* **5**, 2072–2076 (2014).
38. Perdew, J. P., Burke, K. & Ernzerhof, M. Generalized gradient approximation made simple. *Phys. Rev. Lett.* **77**, 3865–3868 (1996).
39. Yamazoe, S. *et al.* Hierarchy of bond stiffnesses within icosahedral-based gold clusters protected by thiolates. *Nat. Commun.* **7**, 10414 (2016).
40. Bootharaju, M. S., Joshi, C. P., Parida, M. R., Mohammed, O. F. & Bakr, O. M. Templated atom-precise galvanic synthesis and structure elucidation of a $[\text{Ag}_{24}\text{Au}(\text{SR})_{18}]^{-}$ nanocluster. *Angew. Chem. Int. Ed.* **55**, 922–926 (2016).
41. Yan, J. *et al.* Total structure and electronic structure analysis of doped thiolated silver $[\text{M}\text{Ag}_{24}(\text{SR})_{18}]^{2-}$ ($\text{M} = \text{Pd}, \text{Pt}$) clusters. *J. Am. Chem. Soc.* **137**, 11880–11883 (2015).
42. Qian, H. *et al.* Monoplatinum doping of gold nanoclusters and catalytic application. *J. Am. Chem. Soc.* **134**, 16159–16162 (2012).

43. Negishi, Y., Kurashige, W., Niihori, Y., Iwasa, T. & Nobusada, K. Isolation, structure, and stability of a dodecanethiolate-protected Pd₁Au₂₄ cluster. *Phys. Chem. Chem. Phys.* **12**, 6219–6225 (2010).
44. Wang, S. *et al.* Metal exchange method using Au₂₅ nanoclusters as templates for alloy nanoclusters with atomic precision. *J. Am. Chem. Soc.* **137**, 4018–4021 (2015).
45. Tofanelli, M. A., Ni, T. W., Phillips, B. D. & Ackerson, C. J. Crystal structure of the PdAu₂₄(SR)₁₈⁰ superatom. *Inorg. Chem.* **55**, 999–1001 (2016).
46. Walter, M. & Moseler, M. Ligand-protected gold alloy clusters: doping the superatom. *J. Phys. Chem. C* **113**, 15834–15837 (2009).
47. Guidez, E. B., Mäkinen, V., Häkkinen, H. & Aikens, C. M. Effects of silver doping on the geometric and electronic structure and optical absorption spectra of the Au_{25–n}Ag_n(SH)₁₈[–] (*n* = 1, 2, 4, 6, 8, 10, 12) bimetallic nanoclusters. *J. Phys. Chem. C* **116**, 20617–20624 (2012).
48. Haynes, W. M. in *CRC Handbook of Chemistry and Physics* 96th Edition (Eds Lide, D. R. & Bruno, T. J.) (CRC Press, 2015–2016).
49. Miyashita, O., Okamura, M. Y. & Onuchic, J. N. Interprotein electron transfer from cytochrome *c*₂ to photosynthetic reaction center: tunneling across an aqueous interface. *Proc. Natl Acad. Sci. USA* **102**, 3558–3563 (2005).
50. Natarajan, G., Mathew, A., Negishi, Y., Whetten, R. L. & Pradeep, T. A unified framework for understanding the structure and modifications of atomically precise monolayer protected gold clusters. *J. Phys. Chem. C* **119**, 27768–27785 (2015).
51. Häkkinen, H., Walter, M. & Grönbeck, H. Divide and protect: capping gold nanoclusters with molecular gold-thiolate rings. *J. Phys. Chem.* **B110**, 9927–9931 (2006).
52. Pei, Y. & Zeng, X. C. Investigating the structural evolution of thiolate protected gold clusters from first-principles. *Nanoscale* **4**, 4054–4072 (2012).
53. Kumara, C., Aikens, C. M. & Dass, A. X-ray crystal structure and theoretical analysis of Au_{25–x}Ag_x(SCH₂CH₂Ph)₁₈[–] alloy. *J. Phys. Chem. Lett.* **5**, 461–466 (2014).
54. Li, Q. *et al.* Heavily doped Au_{25–x}Ag_x(SC₆H₁₁)₁₈[–] nanoclusters: silver goes from the core to the surface. *Chem. Commun.* **52**, 5194–5197 (2016).
55. Aikens, C. M. Origin of discrete optical absorption spectra of M₂₅(SH)₁₈[–] nanoparticles (M = Au, Ag). *J. Phys. Chem. C* **112**, 19797–19800 (2008).
56. Tlahuice-Flores, A., Black, D. M., Bach, S. B. H., Jose-Yacamán, M. & Whetten, R. L. Structure and bonding of the gold subhalide cluster I-Au₁₄₄Cl₆₀^{2–}. *Phys. Chem. Chem. Phys.* **15**, 19191–19195 (2013).
57. Morris, G. M. *et al.* Autodock4 and AutoDockTools4: automated docking with selective receptor flexibility. *J. Comput. Chem.* **16**, 2785–2791 (2009).
58. Enkovaara, J. *et al.* Electronic structure calculations with GPAW: a real-space implementation of the projector augmented-wave method. *J. Phys. Condens. Matter.* **22**, 253202 (2010).
59. Hanwell, M. D. *et al.* Avogadro: an advanced semantic chemical editor, visualization, and analysis platform. *J. Cheminform* **4**, 17 (2012).
60. Humphrey, W., Dalke, A. & Schulten, K. VMD—Visual molecular dynamics. *J. Mol. Graphics* **14**, 33–38 (1996).

Acknowledgements

K.R.K. and A.G. thank the University Grants Commission for their senior research fellowships. A.B. thanks IIT Madras for an Institute Post Doctoral Fellowship. We thank Department of Science and Technology, Government of India for consistently supporting our research program.

Author contributions

K.R.K. designed and conducted experiments. A.B. carried out ESI MS measurements. A.G. synthesized the clusters. G.N. carried out DFT calculations and molecular docking simulations. T.P. supervised the whole project. The paper was written by all of the authors.

Additional information

Supplementary Information accompanies this paper at <http://www.nature.com/naturecommunications>

Competing financial interests: The authors declare no competing financial interests.

Reprints and permission information is available online at <http://npg.nature.com/reprintsandpermissions/>

How to cite this article: Krishnadas, K. R. *et al.* Structure-conserving spontaneous transformations between nanoparticles. *Nat. Commun.* **7**, 13447 doi: 10.1038/ncomms13447 (2016).

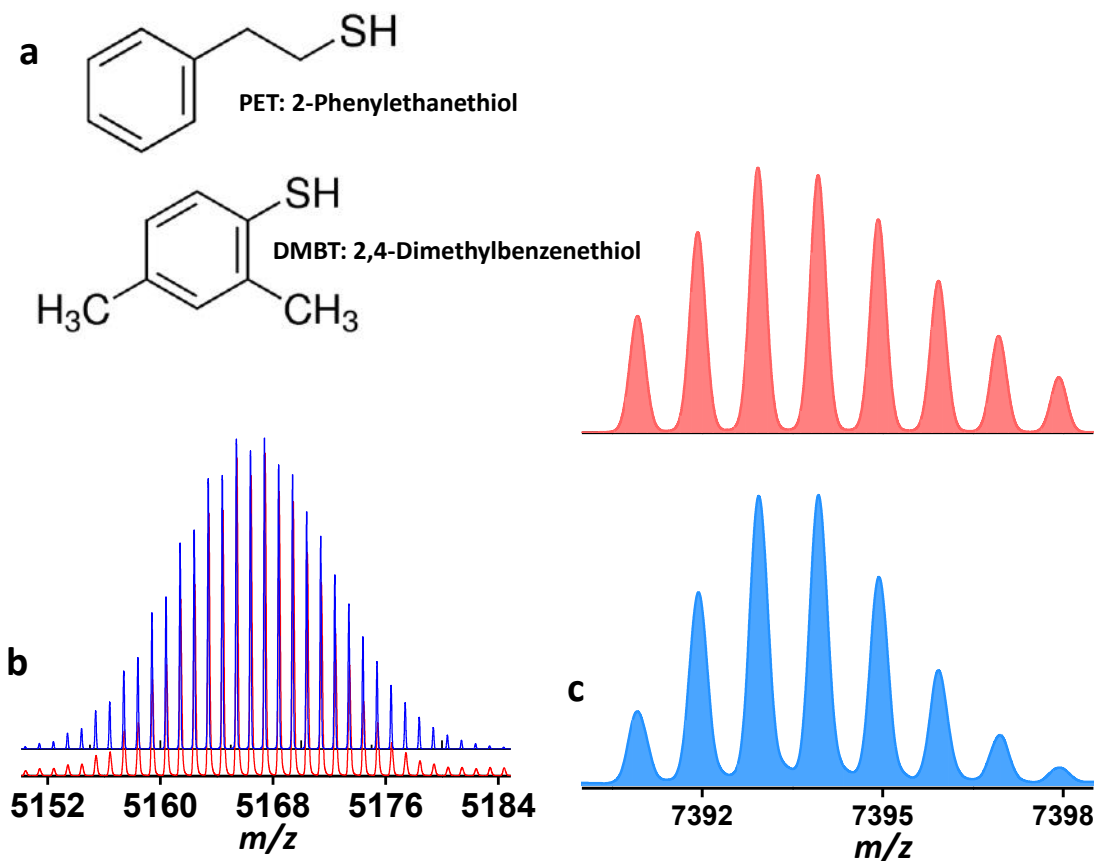
Publisher's note: Springer Nature remains neutral with regard to jurisdictional claims in published maps and institutional affiliations.



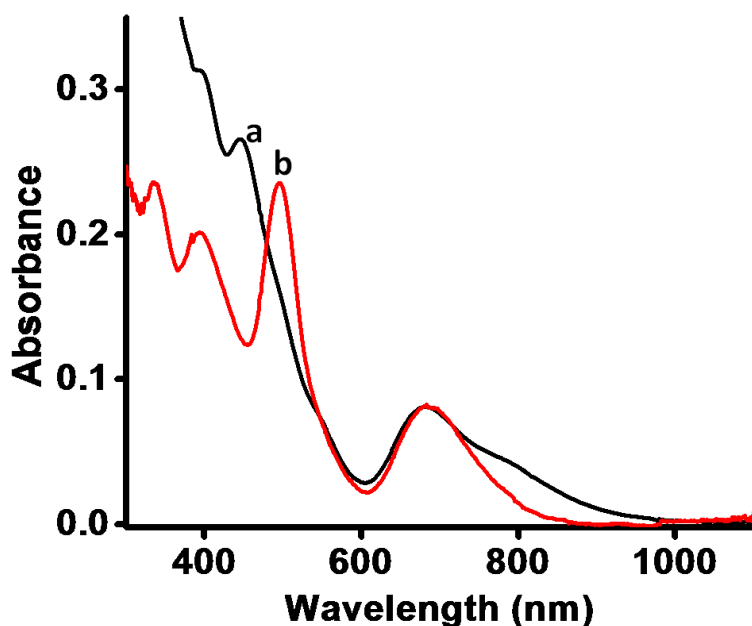
This work is licensed under a Creative Commons Attribution 4.0 International License. The images or other third party material in this article are included in the article's Creative Commons license, unless indicated otherwise in the credit line; if the material is not included under the Creative Commons license, users will need to obtain permission from the license holder to reproduce the material. To view a copy of this license, visit <http://creativecommons.org/licenses/by/4.0/>

© The Author(s) 2016

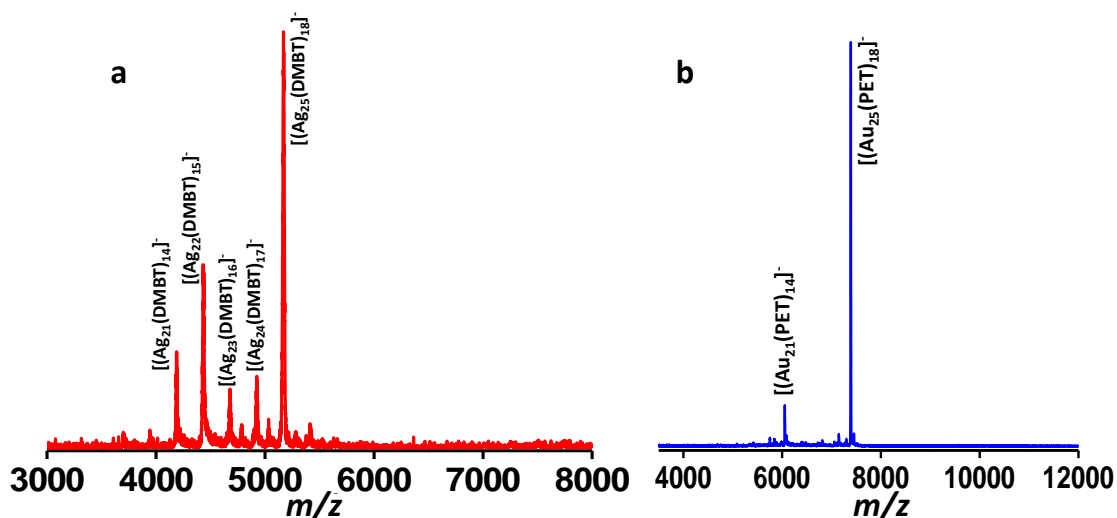
Supplementary Figures



Supplementary Figure 1. Molecular structures of the ligands and the isotope patterns of the clusters Molecular structures of ligands 2-phenylethanethiol (PET) and 2,4-dimethylbenzenethiol (DMBT) (a), theoretical (red) and experimental (blue) isotope patterns for Ag₂₅(DMBT)₁₈ (b) and Au₂₅(PET)₁₈ (c). These data illustrate the resolution and the spectral quality available for these systems.

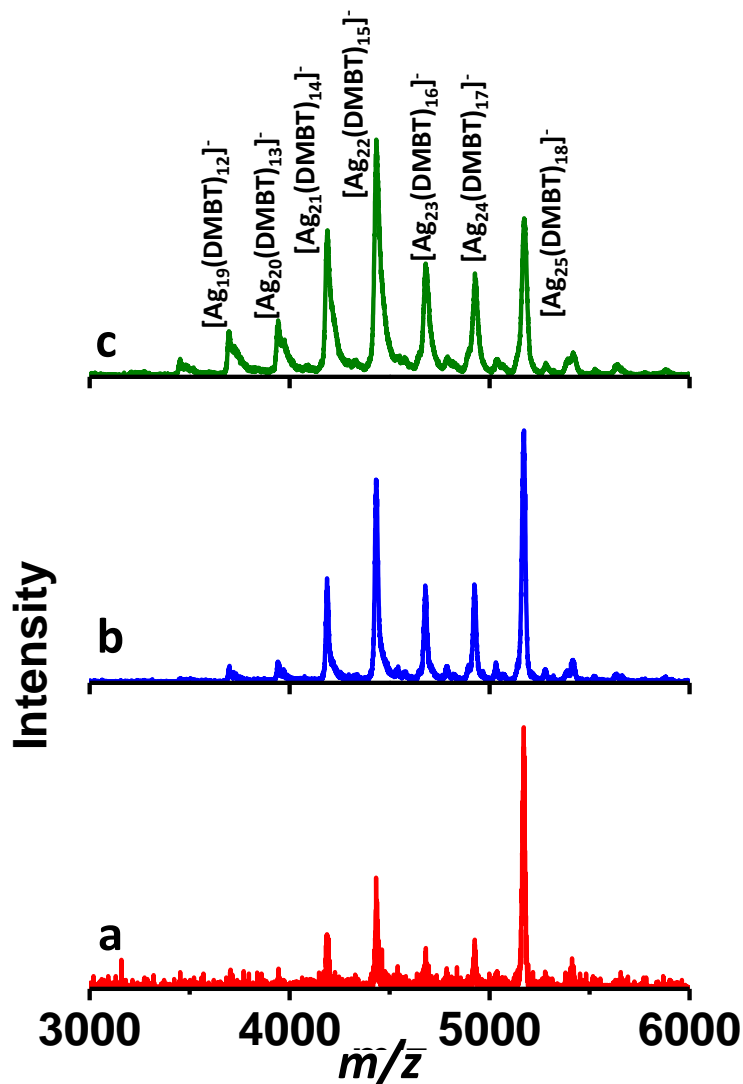


Supplementary Figure 2. UV/Vis absorption features of clusters Characteristic UV/Vis absorption features of Ag₂₅(DMBT)₁₈ (a, black) and Au₂₅(PET)₁₈ (b, red). PET is 2-phenylethanethiol and DMBT is 2,4-dimethylbenzenethiol.

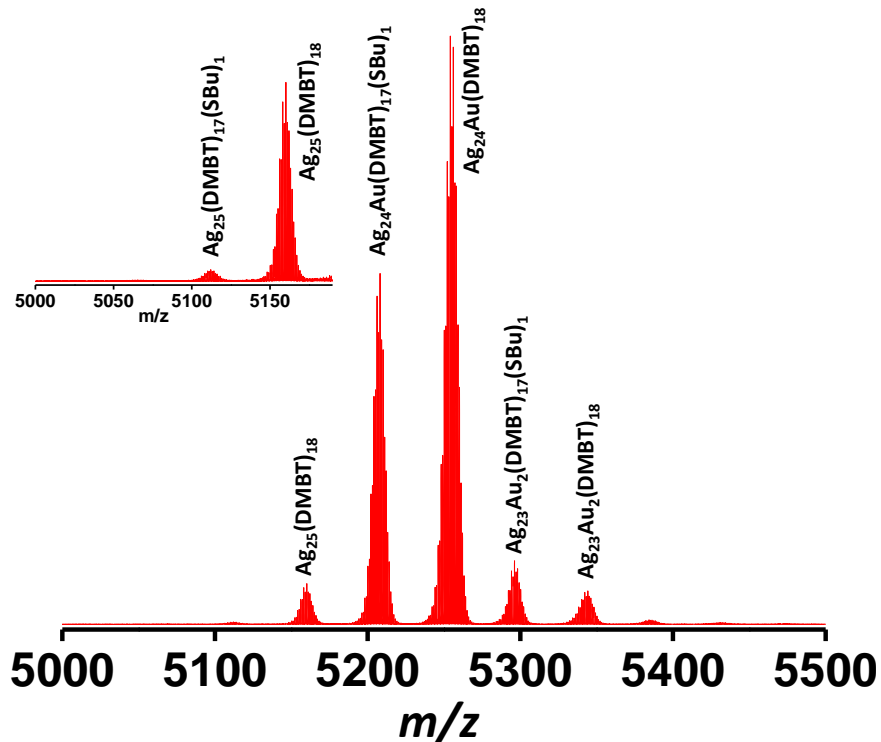


Supplementary Figure 3. Matrix assisted laser desorption ionization mass spectra of the clusters Negative ion mode Matrix assisted laser desorption ionization mass spectra (MALDI MS) of Ag₂₅(DMBT)₁₈ (a) and Au₂₅(PET)₁₈ (b). Characteristic fragment peaks are shown in each

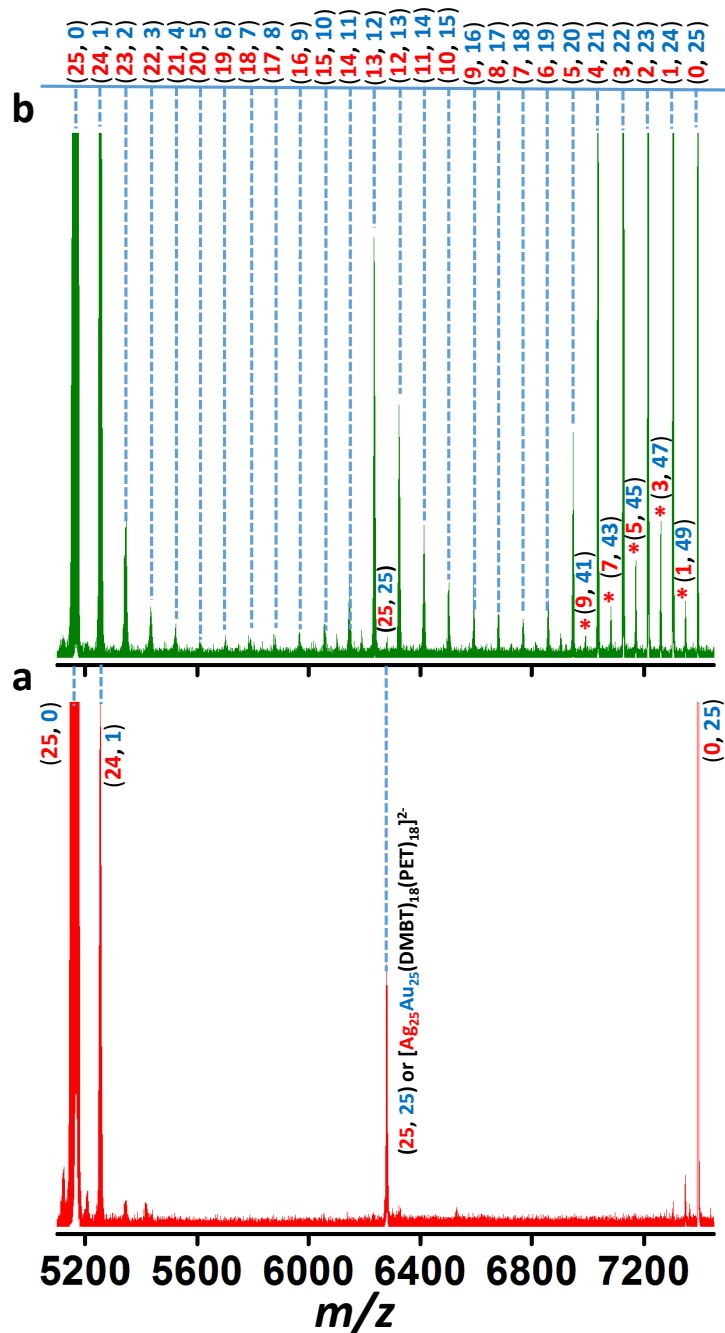
spectrum. PET is 2-phenylethanethiol and DMBT is 2,4-dimethylbenzenethiol. The loss of Ag-DMBT (in $\text{Ag}_{25}(\text{DMBT})_{18}$) and that of $\text{Au}_4(\text{PET})_4$ (in $\text{Au}_{25}(\text{PET})_{18}$) are the expected fragmentation patterns of these clusters.



Supplementary Figure 4. Matrix assisted laser desorption ionization mass spectra (MALDI MS) of $\text{Ag}_{25}(\text{DMBT})_{18}$ at various laser fluences MALDI MS spectra of $\text{Ag}_{25}(\text{DMBT})_{18}$ at laser fluences of 1150 (a), 1350 (b) and 1450 (c). With increasing fluence, more fragmentation is observed. Laser fluence is shown as given by the instrument.

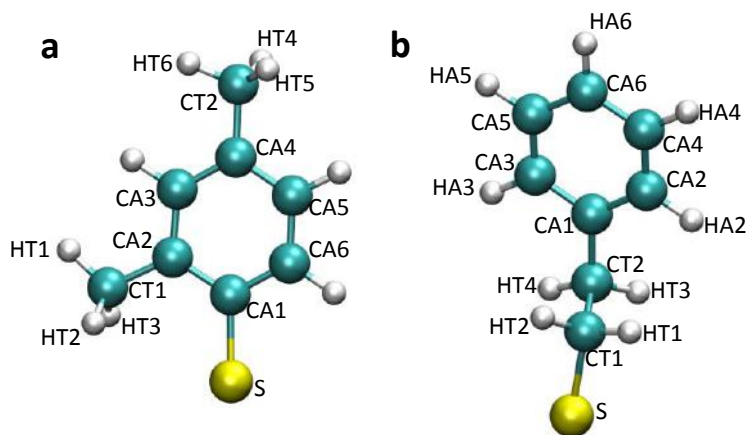


Supplementary Figure 5. Electrospray ionization mass spectra (ESI MS) showing ligand and metal-ligand fragment exchanges ESI MS spectra showing the exchange products resulting from Ag-Au, (DMBT)-(SBu) and (Ag-DMBT)-(Au-SBu) exchanges between $\text{Ag}_{25}(\text{DMBT})_{18}$ and $\text{Au}_{25}(\text{SBu})_{18}$. The inset shows that parent $\text{Ag}_{25}(\text{SR})_{18}$ undergoes DMBT-SBu exchange also. PET is 2-phenylethanethiol and DMBT is 2,4-dimethylbenzenethiol.

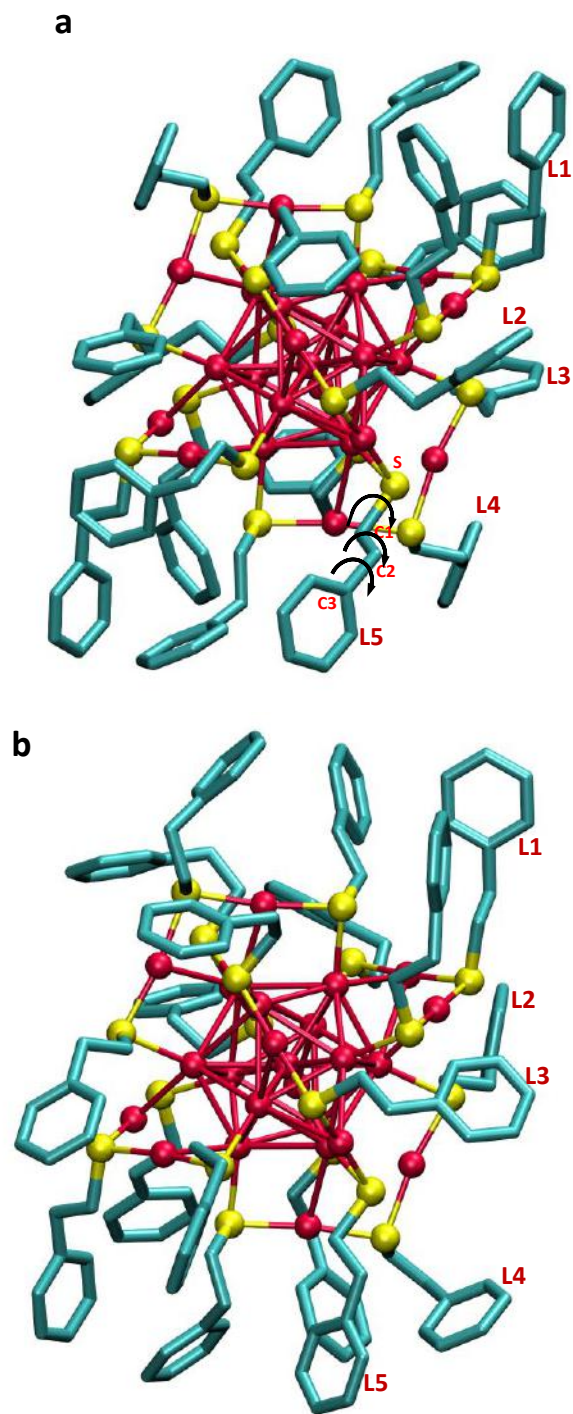


Supplementary Figure 6. Evolution of alloy clusters from the dianionic adduct Electrospray ionization mass spectra (ESI MS) of a reaction mixture at the $\text{Ag}_{25}(\text{DMBT})_{18}:\text{Au}_{25}(\text{PET})_{18}$ molar ratio of 0.3:1.0 measured (a) within 2 min after mixing and (b) 5 minutes after mixing. Panel a shows the peak due to $[\text{Ag}_{25}\text{Au}_{25}(\text{DMBT})_{18}(\text{PET})_{18}]^{2-}$, the adduct formed between $[\text{Ag}_{25}(\text{DMBT})_{18}]^{-}$ and $[\text{Au}_{25}(\text{PET})_{18}]^{-}$. PET is 2-phenylethanethiol and DMBT is 2,4-dimethylbenzenethiol. Panel (b) shows that this peak disappeared almost completely within 5

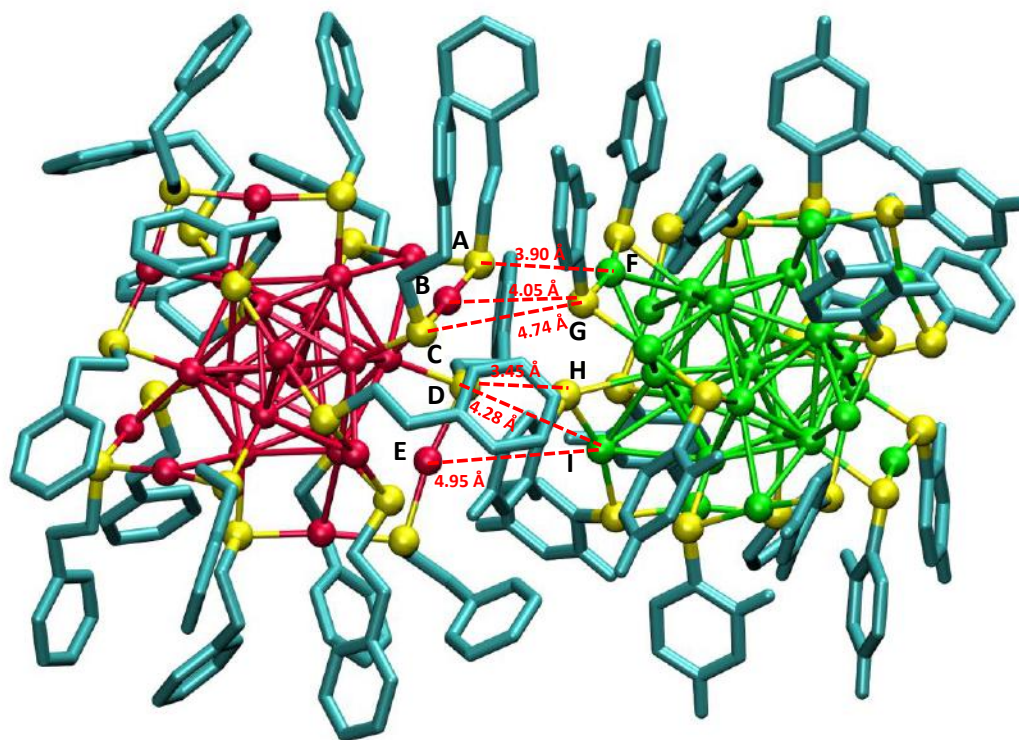
min after mixing of the clusters and monoanionic alloy clusters are formed. Numbers in the parentheses of the labels of main peaks in (a) and (b) correspond to the general formula, $[Ag_mAu_n(SR)_{18}]^-$ ($m+n=25$) (for monoanionic alloys). Numbers in the parentheses of the labels of the peaks marked with * in panel (b) correspond to the general formula, $[Ag_mAu_n(SR)_{36}]^{2-}$ ($m+n=50$) (for the dianionic adducts). Some of these ions exist in (a) also.



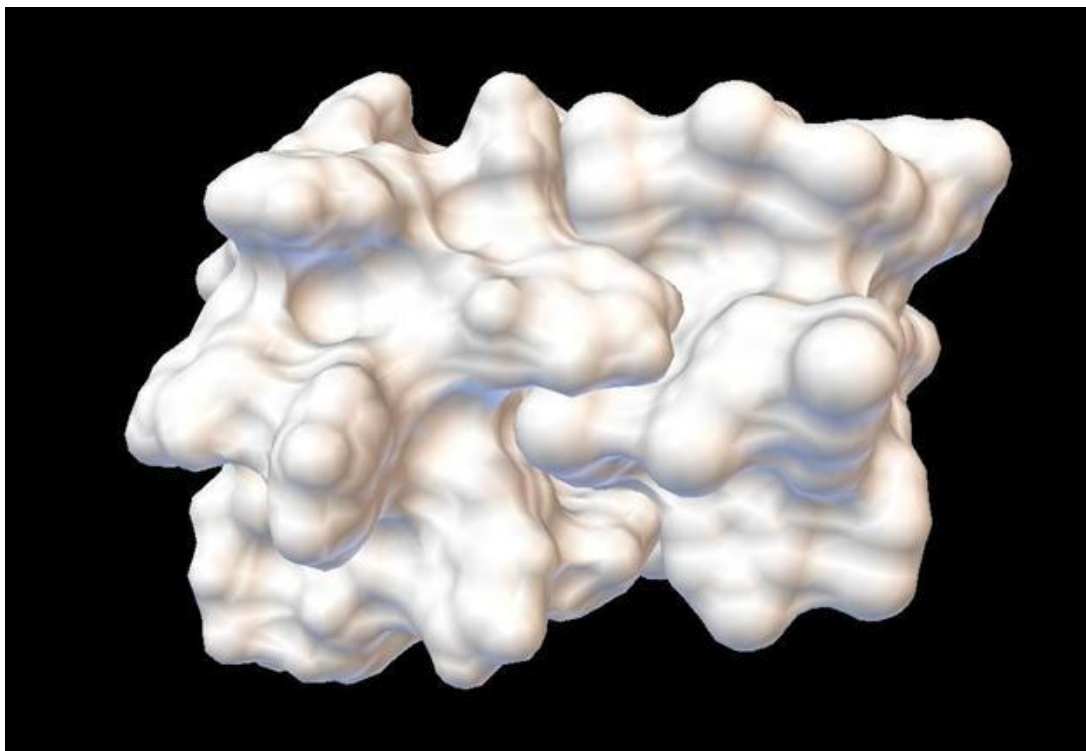
Supplementary Figure 7. Molecular structures and the labeling of the different types of atoms in (a) 2,4-dimethylbenzenethiol (DMBT) and (b) 2-phenylethanethiol (PET) ligands.



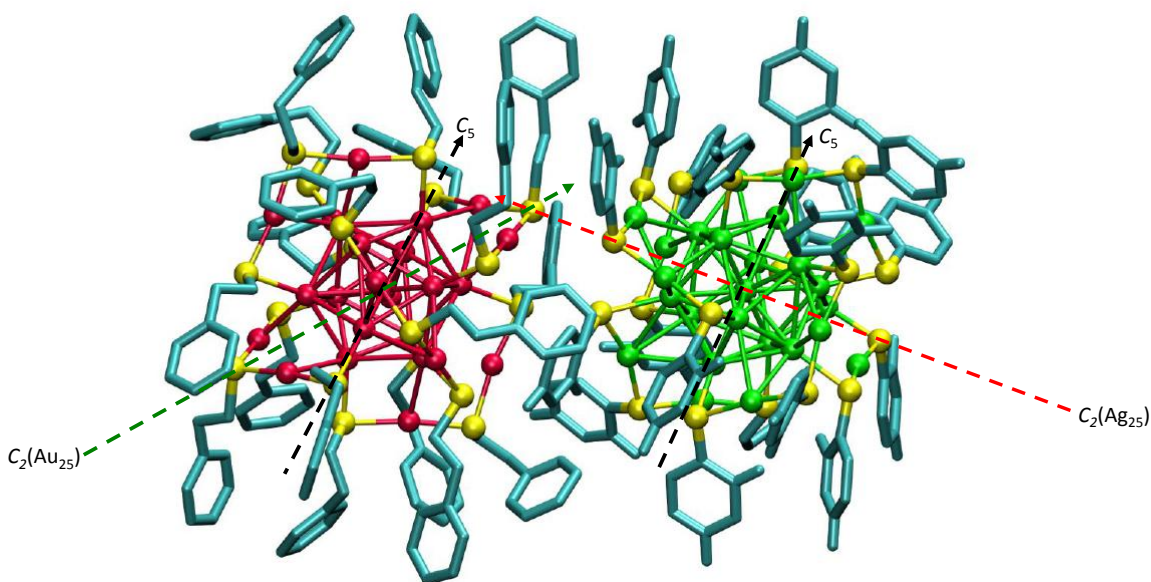
Supplementary Figure 8. Initial and final configurations of $\text{Au}_{25}(\text{PET})_{18}$ in the force-field global minimum of adduct Initial (a) and after (b) configuration of $\text{Au}_{25}(\text{PET})_{18}$. PET (2-phenylethanethiol) ligands which have undergone rotations are marked in each picture with corresponding directions of rotations marked in them.



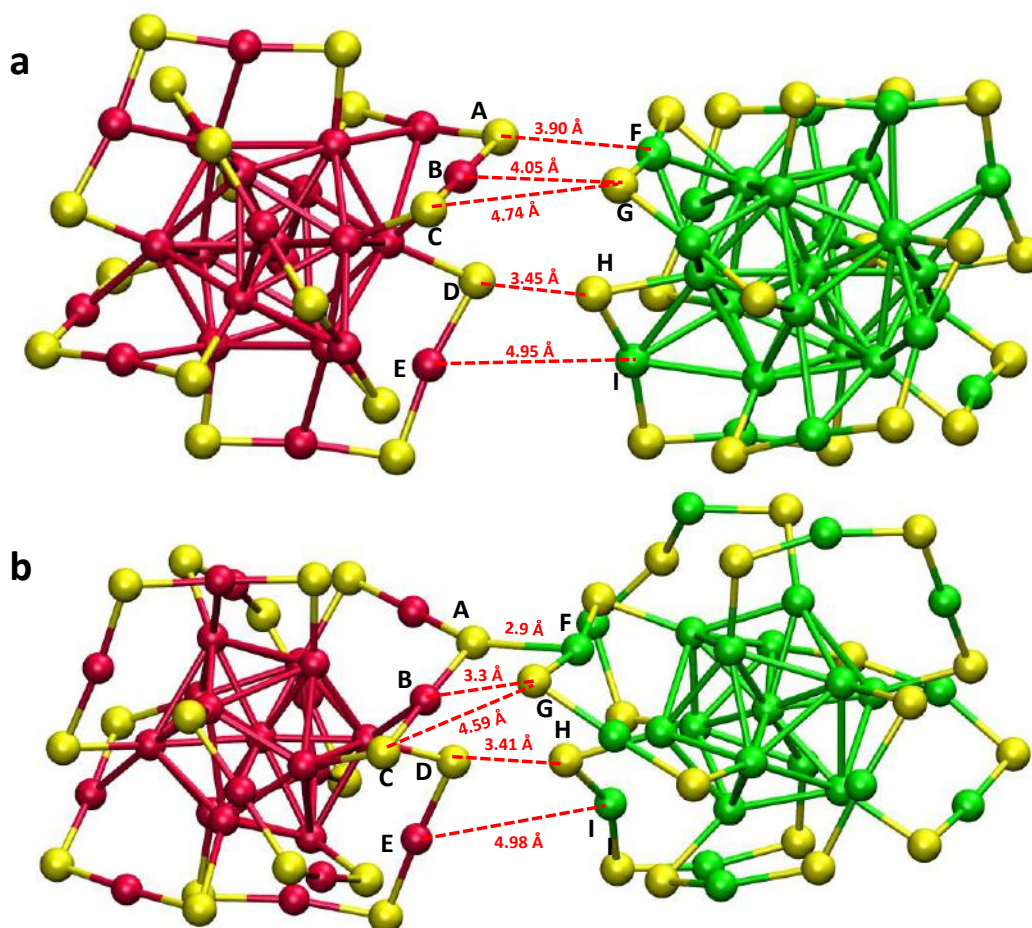
Supplementary Figure 9. Minimum energy configuration of the clusters in the force-field global minimum of adduct. The $\text{Au}_{25}(\text{PET})_{18}\text{-Ag}_{25}(\text{DMBT})_{18}$ (**II-I**) force-field global minimum of adduct from a molecular docking simulation with **II** on the left and **I** on the right. Dashed lines show the shortest distances found between atoms in the staples of the two clusters which are marked with letters A to E on **II** and F to I on **I**. Distances between the pairs of metal and sulfur atoms labelled are AF ($\text{S}_b(\text{Au}_{25})\text{-Ag}$)=3.90 Å, BG ($\text{Au-S}_b(\text{Ag}_{25})$)=4.05 Å, CG ($\text{S}_{nb}(\text{Au}_{25})\text{-S}_b(\text{Ag}_{25})$)=4.74 Å, DH ($\text{S}_{nb}(\text{Au}_{25})\text{-S}_{nb}(\text{Ag}_{25})$)=3.45 Å, DI ($\text{S}_{nb}(\text{Au}_{25})\text{-Ag}$)=4.28 Å and EI (Au-Ag)=4.95 Å. The brackets after the pair of letters gives details of the element types and the bridging and non-bridging sulfur positions on staples that are denoted by the subscripts b and nb, respectively. The hydrogen atoms are omitted from the ligands for clarity. Color code for the atoms: Au (red), Ag (green), S (yellow), C (blue). PET is 2-phenylethanethiol and DMBT is 2,4-dimethylbenzenethiol.



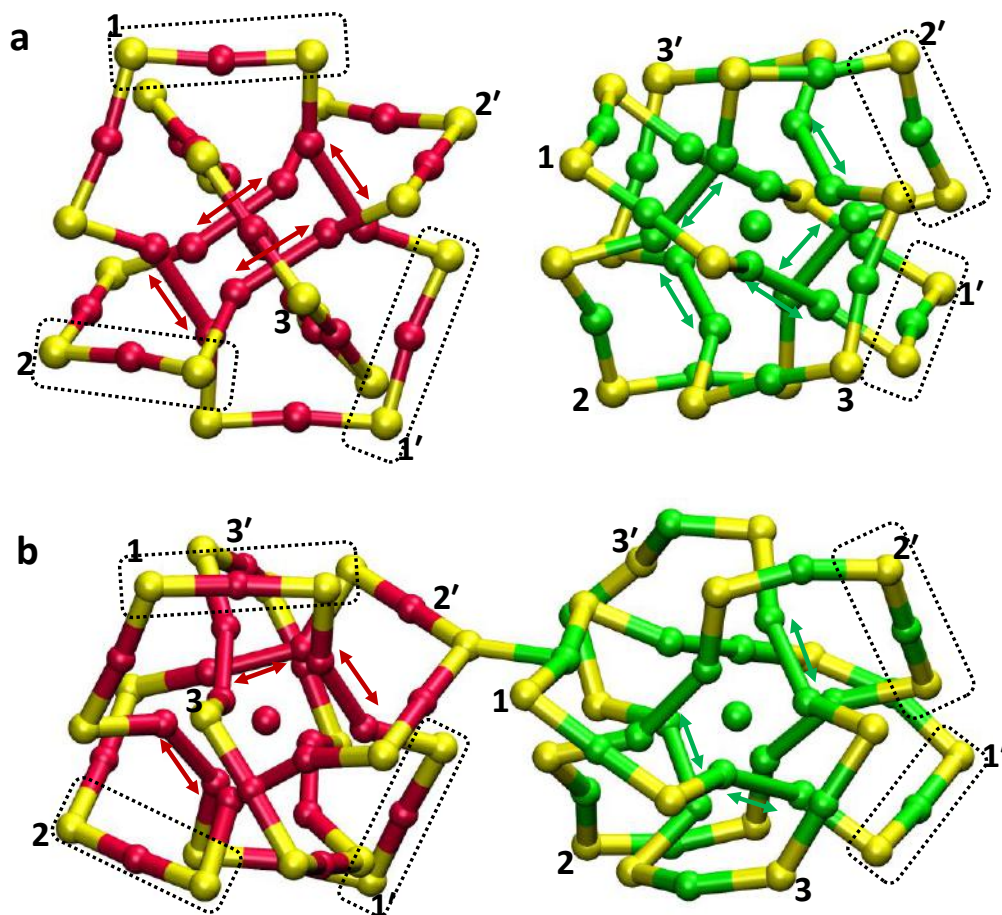
Supplementary Figure 10. Molecular surfaces of the clusters in the force-field global minimum of adduct The relative orientation of the $\text{Ag}_{25}(\text{DMBT})_{18}$ (right) and $\text{Au}_{25}(\text{PET})_{18}$ (left) in the minimum energy configuration (shown in Figure 3 and Supplementary Fig. 9) depicting that the overlap between the molecular surface or envelope of the ligands of the two clusters has maximal area of contact. PET is 2-phenylethanethiol and DMBT is 2,4-dimethylbenzenethiol.



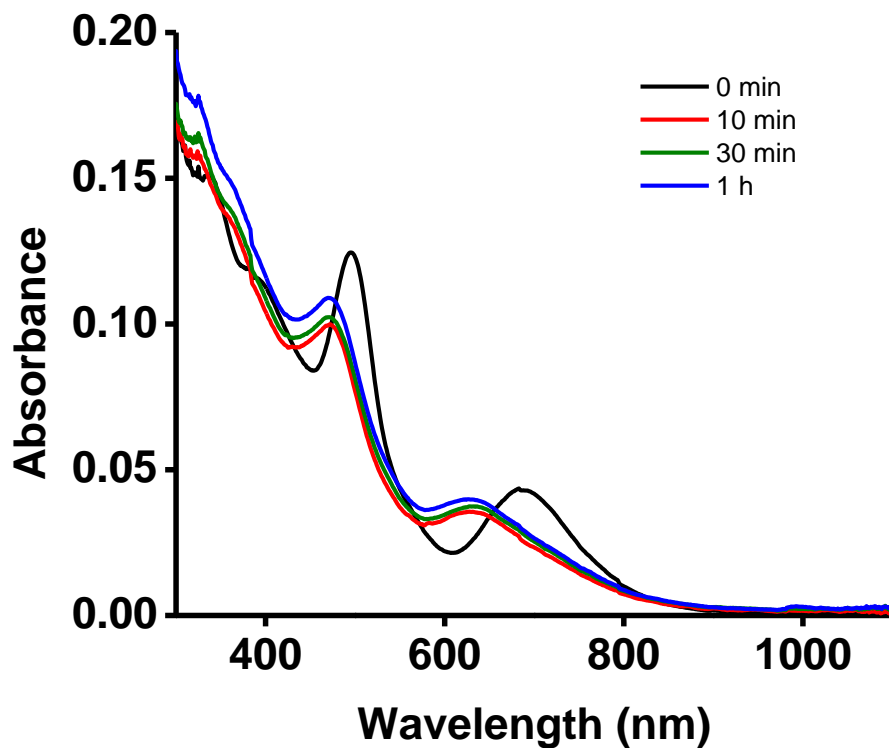
Supplementary Figure 11. Orientation of the clusters in their force-field global minimum of adduct The orientation of the $\text{Au}_{25}(\text{PET})_{18}$ and $\text{Ag}_{25}(\text{DMBT})_{18}$ in their docked configuration is shown with respect to their relevant symmetry axes. One of the C_2 axes of $\text{Au}_{25}(\text{PET})_{18}$ is shown by the green dashed arrow and one of the C_2 axes of $\text{Ag}_{25}(\text{DMBT})_{18}$ is shown by the red dashed arrow. The two C_5 axes shown by the vertical black dashed arrows are nearly parallel to each other. PET is 2-phenylethanethiol and DMBT is 2,4-dimethylbenzenethiol.



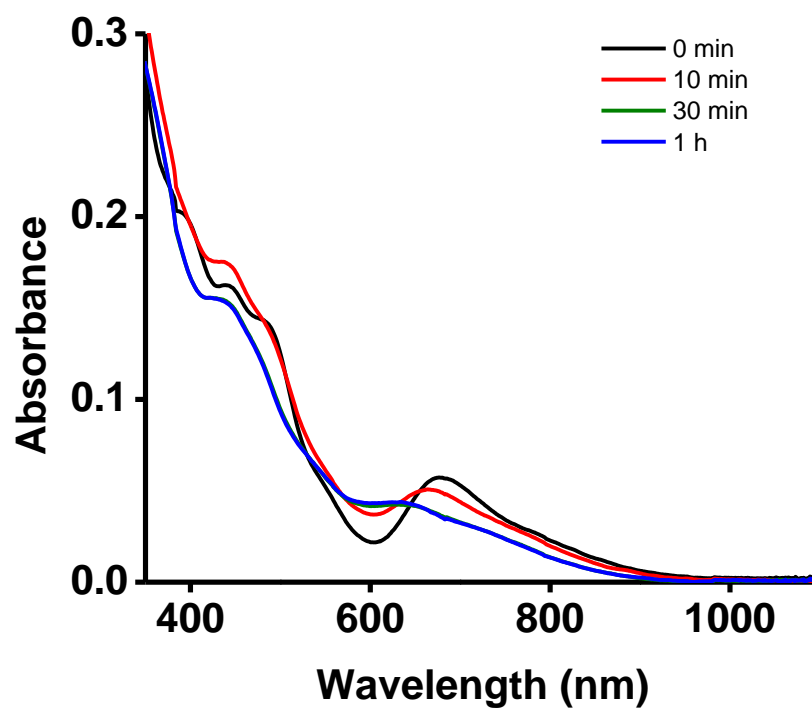
Supplementary Figure 12. Comparison of the distances between the closest metal atoms and the sulfur atoms at the interface of $\text{Au}_{25}(\text{PET})_{18}$ (left) and $\text{Ag}_{25}(\text{DMBT})_{18}$ (right) in the force-field global minimum of adduct (a) and its DFT-optimized geometry (b). Ligands are omitted for clarity. Color code: red (Au), green (Ag) and yellow (sulfur). PET is 2-phenylethanethiol and DMBT is 2,4-dimethylbenzenethiol.



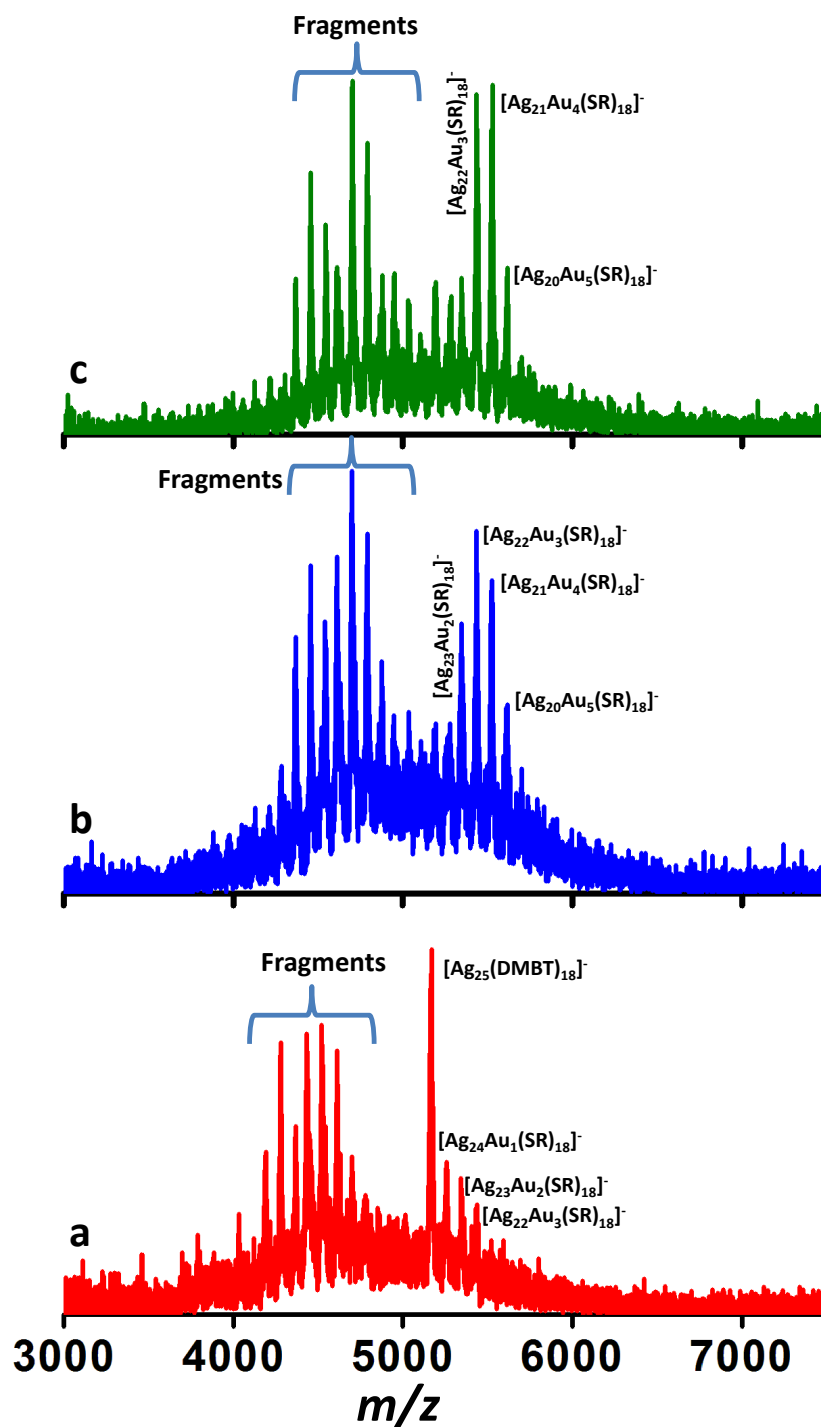
Supplementary Figure 13. Comparison of the changes in the $M_2(SR)_3$ staples (labeled 1-1', 2-2' and 3-3') of $Au_{25}(PET)_{18}$ (left) and $Ag_{25}(DMBT)_{18}$ (right) (ligands omitted for clarity) in their force-field global minimum of adduct (a) and its DFT-optimized geometry (b). Color codes: red (Au), green (Ag) and yellow (S). In (a) and (b), the opposite pairs of $M_2(SR)_3$ staples labeled 1-1', 2-2' and 3-3' are joined by the shorter M-M bonds (labeled by red and green arrows) of the icosahedron to form $M_8(SR)_6$ rings. The other metal atoms in the icosahedron and the longer M-M bonds are omitted for clarity. Please refer to Supplementary Ref. 1 below for the description of the shorter and the longer bonds. Comparison of 1-1', 2-2' and 3-3' in each of these adducts show that the some of the S-M-S fragments (marked in dotted rectangles) of the staples became more linear in b compared to the V-shape in (a). PET is 2-phenylethanethiol and DMBT is 2,4-dimethylbenzenethiol.



Supplementary Figure 14. Time-dependent change in the UV/Vis absorption spectra during the reaction between Ag₂₅(DMBT)₁₈ and Au₂₅(PET)₁₈ at a molar ratio (Ag₂₅:Au₂₅) of 6.6:1.0. PET is 2-phenylethanethiol and DMBT is 2,4-dimethylbenzenethiol.

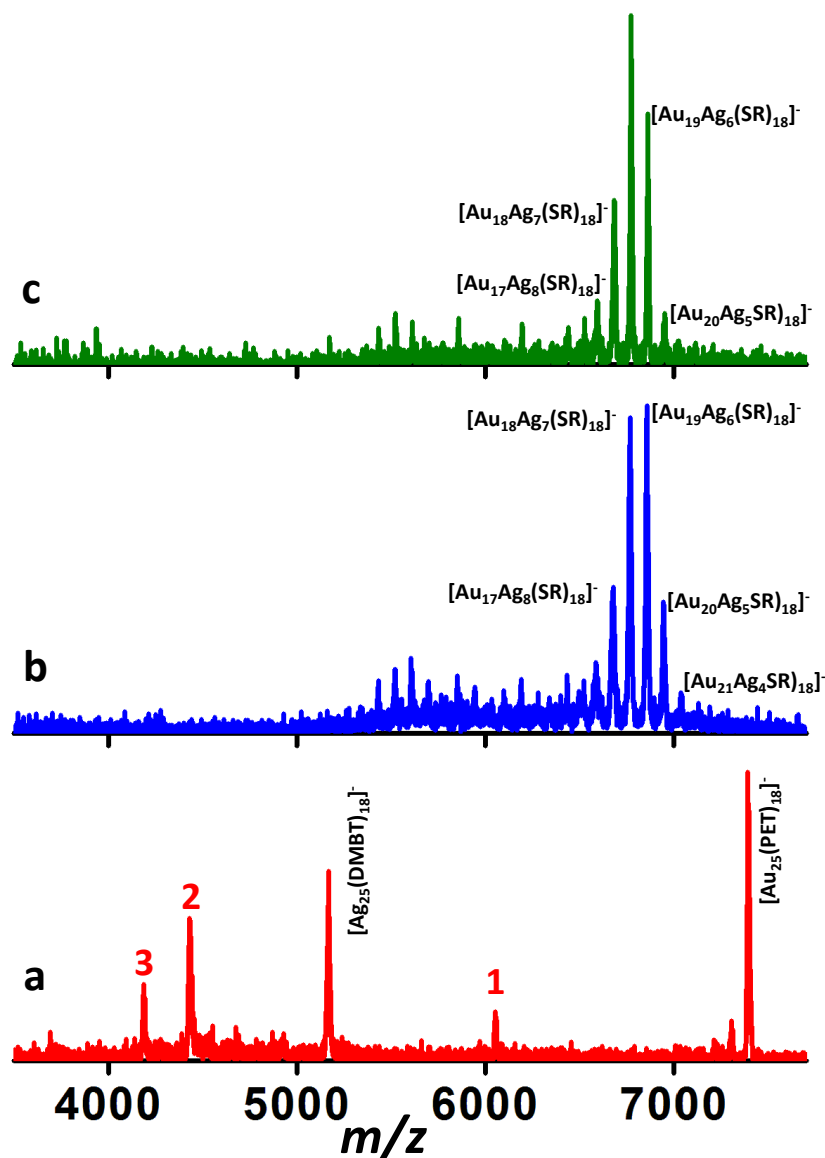


Supplementary Figure 15. Time-dependent change in the UV/Vis absorption spectra of a mixture of Ag₂₅(DMBT)₁₈ and Au₂₅(PET)₁₈ at a molar ratio (Ag₂₅:Au₂₅) of 0.3:1.0. PET is 2-phenylethanethiol and DMBT is 2,4-dimethylbenzenethiol.



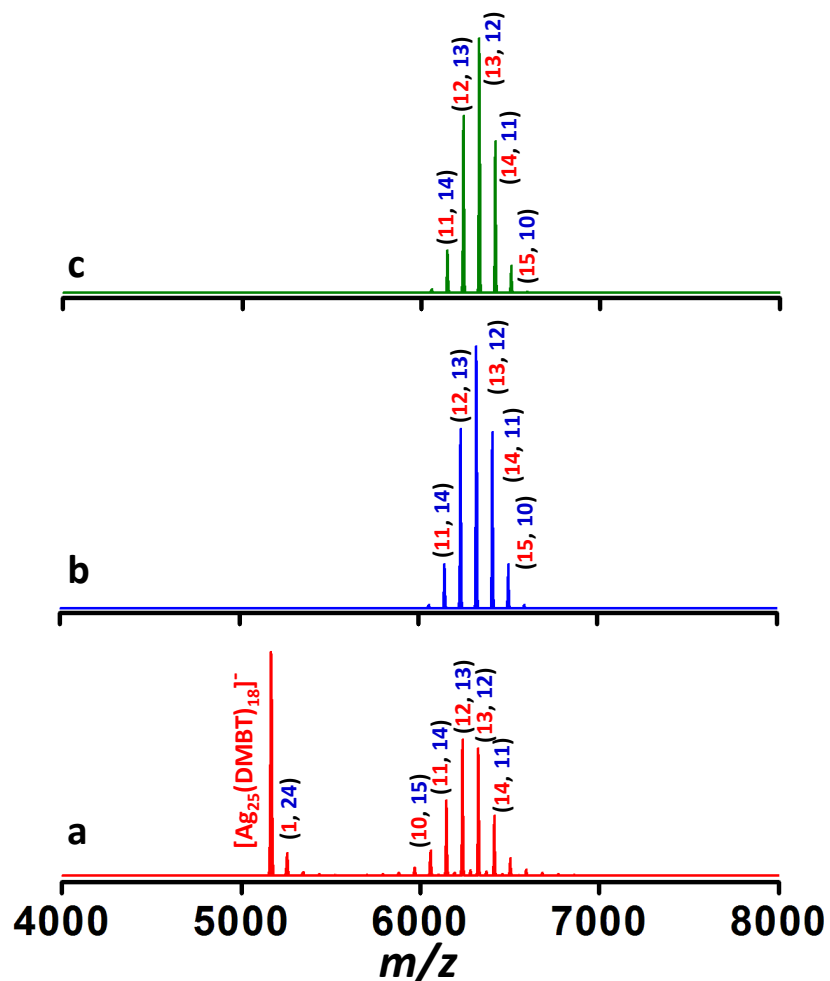
Supplementary Figure 16. Matrix assisted laser desorption ionization mass spectrometric (MALDI MS) analyses of 6.6:1.0 ($\text{Ag}_{25}:\text{Au}_{25}$) reaction mixture MALDI MS spectra of the reaction mixture of $\text{Ag}_{25}(\text{DMBT})_{18}$ and $\text{Au}_{25}(\text{PET})_{18}$ at molar ratio ($\text{Ag}_{25}:\text{Au}_{25}$) of 6.6:1.0

measured within 2 min after mixing (a) and after 10 min (b) and after 1 h (c). Since the mass of DMBT (2,4-dimethylbenzenethiol) and PET (2-phenylethanethiol) ligands are the same, exchange of these ligands between the clusters is not evident in the mass spectrum and hence the exact numbers of each of these ligands are unknown and hence SR is used instead of DMBT and PET in the peak labels. Spectra were measured at threshold laser intensity, however, fragmentation was observed.

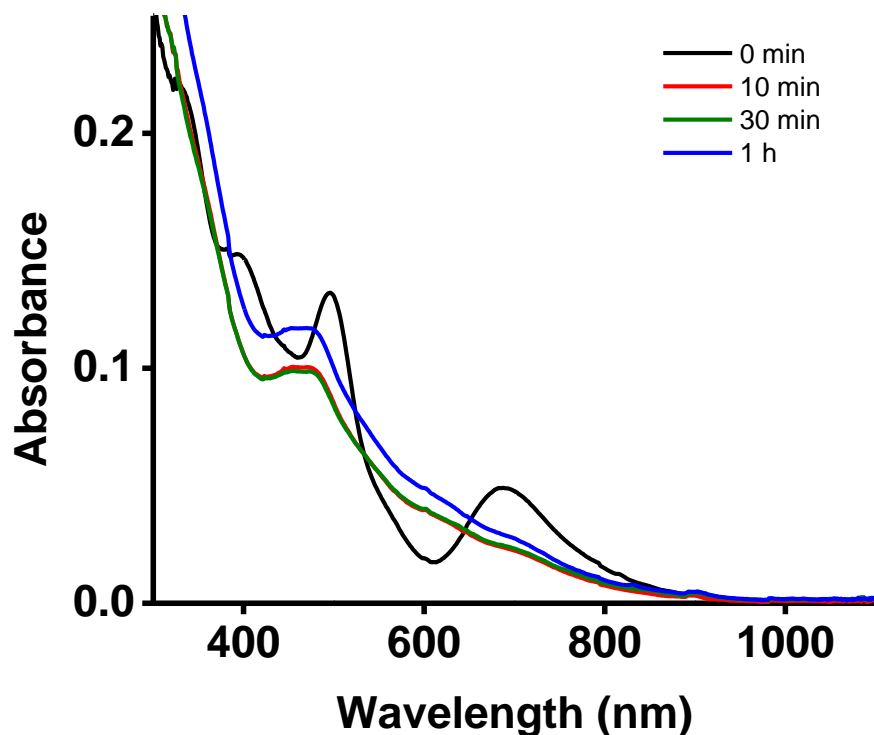


Supplementary Figure 17. Matrix assisted laser desorption ionization mass spectrometric (MALDI MS) analysis of 0.3:1.0 ($\text{Ag}_{25}:\text{Au}_{25}$) reaction mixture MALDI MS spectra of the

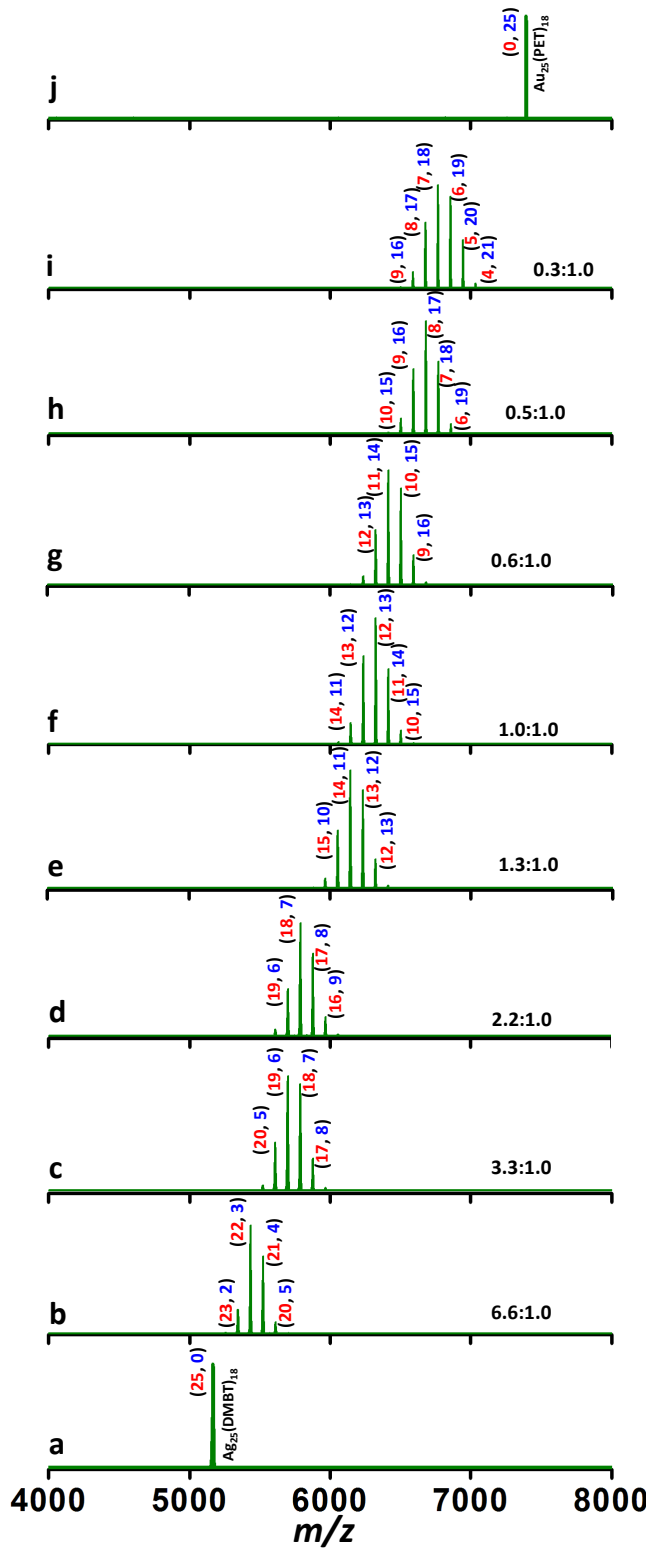
reaction mixture of $\text{Ag}_{25}(\text{DMBT})_{18}$ and $\text{Au}_{25}(\text{PET})_{18}$ at molar ratio ($\text{Ag}_{25}:\text{Au}_{25}$) of 0.3:1.0 measured within 2 min after mixing (a), after 10 min (b) and after 1 h (c). Since the mass of DMBT (2,4-dimethylbenzenethiol) and PET (2-phenylethanethiol) ligands are the same, exchange of these ligands between the clusters is not evident in the mass spectrum and hence the exact numbers of each of these ligands are unknown. Therefore, SR is used instead of DMBT and PET in the peak labels. The peak labeled as 1 in panel a is due to the fragment, $\text{Au}_{21}(\text{PET})_{14}$, from $\text{Au}_{25}(\text{PET})_{18}$, as shown previously in Supplementary Figure 3b. The peaks labeled as 2 and 3 are due to the fragments, $\text{Ag}_{22}(\text{DMBT})_{15}$ and $\text{Ag}_{21}(\text{DMBT})_{14}$, respectively, from $\text{Ag}_{25}(\text{DMBT})_{18}$, as shown in Supplementary Figure 3a. As can be seen, reactions can be observed within 2 min making alloy clusters. Panels b and c show the same product features which indicate that the reaction was completed within about 10 min.



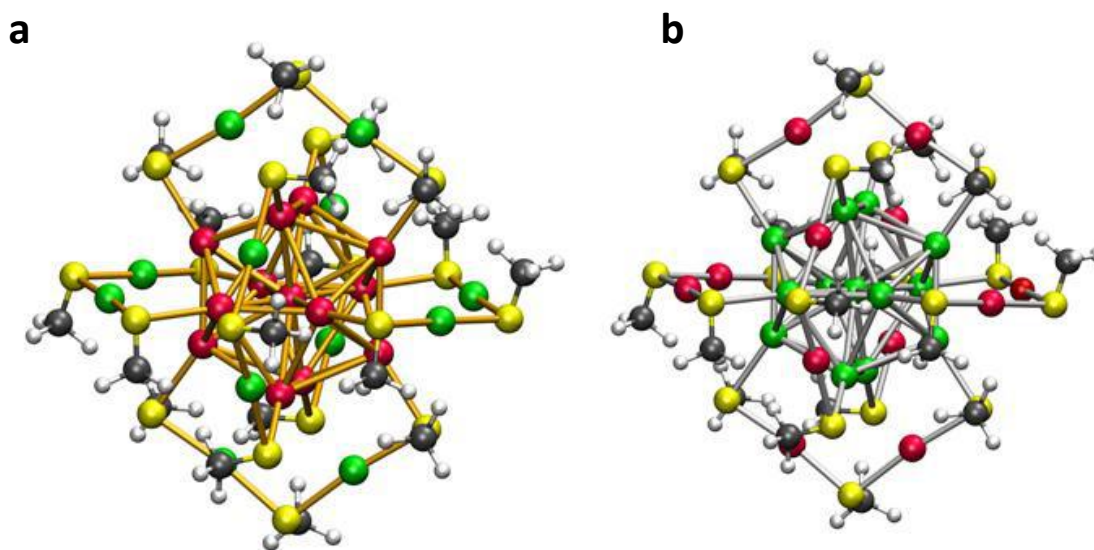
Supplementary Figure 18. Evolution of alloy clusters with intermediate level of doping. Time-dependent change in the electrospray ionization mass spectra (ESI MS) during the reaction between $\text{Ag}_{25}(\text{DMBT})_{18}$ and $\text{Au}_{25}(\text{PET})_{18}$ at a molar ratio ($\text{Ag}_{25}:\text{Au}_{25}$) of 1.0:1.0 within 2 min after mixing (a), after 10 min (b) and after 1 h (c). The peak labels given as numbers in red (m) and blue (n) in parentheses give the number of Ag and Au atoms, respectively in the alloy clusters, $\text{Ag}_m\text{Au}_n(\text{SR})_{18}$. PET is 2-phenylethanethiol and DMBT is 2,4-dimethylbenzenethiol.



Supplementary Figure 19. Time-dependent change in the UV/Vis absorption spectra during the reaction between $\text{Ag}_{25}(\text{DMBT})_{18}$ and $\text{Au}_{25}(\text{PET})_{18}$ at a molar ratio ($\text{Ag}_{25}:\text{Au}_{25}$) of 1.0:1.0. PET is 2-phenylethanethiol and DMBT is 2,4-dimethylbenzenethiol.



Supplementary Figure 20. Tuning the composition of $\text{Ag}_m\text{Au}_n(\text{SR})_{18}$ clusters Electrospray ionization mass spectra (ESI MS) showing the equilibrium distribution of alloy clusters, $\text{Ag}_m\text{Au}_n(\text{SR})_{18}$ formed at various $\text{Ag}_{25}:\text{Au}_{25}$ molar ratios, as indicated in panels b-i. Panels a and j correspond to pure reactant clusters, $\text{Ag}_{25}(\text{DMBT})_{18}$ and $\text{Au}_{25}(\text{PET})_{18}$, respectively. PET is 2-phenylethanethiol and DMBT is 2,4-dimethylbenzenethiol. The spectra shown in panels b-i were measured about 1 h after (because product distribution does not change thereafter indicating the completion or equilibration of the reaction) mixing of the two reactant solutions. The peak labels given as numbers in red (m) and blue (n) in parentheses give the number of Ag and Au atoms, respectively, in the alloy clusters, $\text{Ag}_m\text{Au}_n(\text{SR})_{18}$. The data show that $\text{Ag}_{25}(\text{SR})_{18}$ can be transformed to $\text{Ag}_m\text{Au}_n(\text{SR})_{18}$ clusters in the entire range, $n=1-24$.



Supplementary Figure 21. Structures of $\text{Au}_{13}\text{Ag}_{12}(\text{SR})_{18}$ and $\text{Ag}_{13}\text{Au}_{12}(\text{SR})_{18}$ Schematic of the structures of $\text{Au}_{13}\text{Ag}_{12}(\text{SR})_{18}$ (a) and $\text{Ag}_{13}\text{Au}_{12}(\text{SR})_{18}$ (b). Note that the overall structures of these two clusters are the same, irrespective of the positions of the atoms. This also indicates that overall structures of the $\text{Ag}_m\text{Au}_n(\text{SR})_{18}$ ($m+n=25$) clusters will be the same and irrespective of the values of m and n . Color codes of atoms: Red (Gold), Green (Silver), Yellow, (Sulfur), Black (Carbon) and White (Hydrogen). The $-\text{R}$ group is taken as CH_3 .

Supplementary Tables

Supplementary Table 1: Charges on the atoms of $[\text{Ag}_{25}(\text{DMBT})_{18}]^-$. For the labels of atoms, please refer to Supplementary Figure 7. DMBT is 2,4-dimethylbenzenethiol.

Atom	Corrected partial charges
Ag (center)	+0.038000
Ag (icosahedron)	0.106465
Ag (staples)	0.325465
CA1	0.004031
CA6	-0.167510
CA2	0.024025
CA5	-0.169990
CA3	-0.256960
CT1	-0.082780
CA4	0.010246
CT2	-0.097200
HA3	0.147461
HA1	0.155527
HT3	0.035745
HT1	0.036475
HT2	0.034854
HA2	0.131897
HT6	0.052728
HT5	0.049215
HT4	0.035223

S	-0.288600
---	-----------

Supplementary Table 2: Charges on the atoms of [Au₂₅(PET)₁₈]. For the labels of atoms, please refer to Supplementary Figure 7. PET is 2-phenylethanethiol.

Atom	Corrected partial charge
Au (center)	-0.08
Au (icosahedron)	0.038729
Au (staples)	0.124729
CT1	-0.027855
HT1	0.039546
HT2	0.136658
CT2	0.0150473
HT3	0.037078
HT4	0.026858
CA1	-0.004147
CA2	-0.133917
HA2	0.146177
CA4	-0.173749
HA4	0.143557
CA6	-0.101539
HA6	0.131833
CA5	-0.149795
HA5	0.141473
CA3	-0.186006
HA3	0.160190
S	-0.361495

Supplementary Table 3: Comparison of average bond distances between isolated clusters and the adduct PET is 2-phenylethanethiol and DMBT is 2,4-dimethylbenzenethiol. See Supplementary Fig. 13 and Supplementary Ref. 1 below in main manuscript for the description of longer and shorter M-M bond in icosahedral surface of Au₂₅(SR)₁₈ and Ag₂₅(SR)₁₈. The bond distances for the crystal structures of Au₂₅(PET)₁₈ and Ag₂₅(DMBT)₁₈ were taken from the Supplementary Ref. 2 and 3, respectively.

	All M-S bonds (M=Ag/Au) (Å)	M-S bonds in staples only (Å)	M _{icosahedral} -S bonds (Å)	Shorter M-M bonds on the I positions (M=Ag/Au) (Å)	Longer M-M bonds on the I positions (M=Ag/Au) (Å)	Central M-icosahedral M distances (Å)
Au₂₅(PET)₁₈ From crystal structure		2.32±0.01	2.38±0.01			2.79±0.01
Au₂₅(PET)₁₈ DFT-optimized	2.39	2.36	2.44	2.82	3.05	2.85
Au₂₅(PET)₁₈ in DFT-optimized adduct	2.49	2.46	2.56	2.82	3.09	2.89
Ag₂₅(DMBT)₁₈ Crystal structure		2.445–2.94 6	2.453–2.5 10			2.7486–2.7 847
Ag₂₅(DMBT)₁₈ DFT-optimized	2.48	2.45	2.56	2.90	3.00	2.83
Ag₂₅(DMBT)₁₈ in DFT- optimized adduct	2.56	2.53	2.62	3.03	3.05	2.90

Supplementary Table 4: DFT energies of undoped clusters and isolated metal atoms. Values for Ag and Au are taken from Supplementary Ref. 4 below. E_0 is the DFT-optimized energies of the individual clusters and isolated Ag/Au atoms. PET is 2-phenylethanethiol and DMBT is 2,4-dimethylbenzenethiol.

Structure	E_0/eV
Ag ₂₅ (DMBT) ₁₈	-2033.613
Au ₂₅ (PET) ₁₈	-2045.064
Ag	-0.186
Au	-0.203

Supplementary Table 5: Isomers of Ag₂₄Au(DMBT)₁₈ and their DFT energies. E is the DFT-optimized energies of individual isomers (C, I and S) of Ag₂₄Au(DMBT)₁₈. ΔE is the difference between the energy of Ag₂₄Au(DMBT)₁₈ and that of Ag₂₅(DMBT)₁₈. DMBT is 2,4-dimethylbenzenethiol.

Isomer	Location of Au in Ag₂₄Au(DMBT)₁₈	Energy E/eV	$\Delta E/meV$
C	Centre of icosahedron	-2034.535	-921.4
I	Icosahedron	-2034.171	-557.3
S	Staple	-2034.209	-595.5

Supplementary Table 6: Isomers of Au₂₄Ag(PET)₁₈ and their DFT energies. *E* is the DFT-optimized energies of individual isomers (C, I and S) of alloy clusters. ΔE is the difference between the energy of Au₂₄Ag(PET)₁₈ and that of Au₂₅(PET)₁₈. PET is 2-phenylethanethiol.

Isomer	Location of Ag in Au ₂₄ Ag(PET) ₁₈	Energy <i>E</i> /eV	ΔE /meV
C	Centre of icosahedron	-2044.651	+413.7
I	Icosahedron	-2045.091	-27.1
S	Staple	-2044.822	+241.5

Supplementary Table 7: DFT energies of the substitution reaction, Au + Ag₂₅(DMBT)₁₈ → Ag₂₄Au(DMBT)₁₈ + Ag. ΔE_s is the energy of the corresponding substitution reaction mentioned above. PET is 2-phenylethanethiol and DMBT is 2,4-dimethylbenzenethiol.

Isomer	Position of Au in Ag ₂₄ Au(DMBT) ₁₈	ΔE_s /meV
C	Centre of icosahedron	-904.4
I	Icosahedron	-540.3
S	Staples	-578.5

Supplementary Table 8: DFT energies of the substitution reaction, Ag + Au₂₅(PET)₁₈ → Au₂₄Ag(PET)₁₈ + Au. ΔE_s is the energy of the corresponding substitution reaction mentioned above. PET is 2-phenylethanethiol and DMBT is 2,4-dimethylbenzenethiol.

Isomer	Position of Ag in Au ₂₄ Ag(PET) ₁₈	ΔE_s /meV
C	Centre of icosahedron	+396.7
I	Icosahedron	-44.1
S	Staples	+224.5

Supplementary Notes

Supplementary Note 1: Possible reason for the abundance of $\text{Ag}_{13}\text{Au}_{12}(\text{SR})_{18}$

Our DFT calculations show that substitution energy for an Au atom to occupy the I and the S positions of $\text{Ag}_{25}(\text{SR})_{18}$ are almost the same which indicates that Au_{12} can be located in positions I or the S of $\text{Ag}_{25}(\text{SR})_{18}$ with equal probability. Thus substitution of the twelve staple (S)/icosahedral (I) Ag atoms in $\text{Ag}_{25}(\text{SR})_{18}$ by twelve Au atoms produce $\text{Ag}_{13}\text{Au}_{12}(\text{SR})_{18}$. Hence, more of $\text{Ag}_{13}\text{Au}_{12}(\text{SR})_{18}$ could be formed as a result of Au substitution into $\text{Ag}_{25}(\text{SR})_{18}$ on either at the I or at the S positions. Therefore, the probability of formation of $\text{Ag}_{13}\text{Au}_{12}(\text{SR})_{18}$ is higher due to the availability of two types of (I and S) twelve-atom sites for Au atoms.

Further, $\text{Ag}_{13}\text{Au}_{12}(\text{SR})_{18}$ can also be derived from $\text{Au}_{25}(\text{SR})_{18}$ as a result of Ag substitution. Our DFT calculations shows that an Ag atom prefers to occupy the I position rather than the S positions. The complete substitution of all the I positions in $\text{Au}_{25}(\text{SR})_{18}$ by Ag atoms would result in the formation of $\text{Ag}_{12}\text{Au}_{13}(\text{SR})_{18}$. The thirteenth Ag atom can occupy any one of the twelve S positions in the staples (note that C site (center of icosahedron) is least preferred for Ag atom substitution), resulting in the formation of $\text{Ag}_{13}\text{Au}_{12}(\text{SR})_{18}$. Thus the probability of the formation of $\text{Ag}_{13}\text{Au}_{12}(\text{SR})_{18}$ is higher due to the availability of the twelve staple (S) sites for the thirteenth Ag atom.

We do not think that the abundance of $\text{Ag}_{13}\text{Au}_{12}(\text{SR})_{18}$ is due to any shell closing effects as this abundance is observed only when the concentrations of the reacting clusters are comparable. Though this species was observed with higher abundance immediately after mixing (Figure 1c), and it existed for about 5 min (Supplementary Figure 6), no such species was observed after 1h (panel i of Supplementary Figure 20). Further, Supplementary Figure 20 shows that $\text{Ag}_{13}\text{Au}_{12}$ was not observed with any significantly higher abundance (even at higher concentrations of Au_{25}), in contrast to what is seen in Figure 1c and Supplementary Figure 6. These observations show that significantly higher abundance of $\text{Ag}_{13}\text{Au}_{12}$ is observed only for a few minutes after mixing the clusters. As the reaction proceeds, this species also undergoes further doping. If the observed abundance of $\text{Ag}_{13}\text{Au}_{12}(\text{SR})_{18}$ is due to its higher stability due to any shell closing effects, this species is expected to remain at higher abundance for longer time intervals of the reaction.

In summary, the $\text{Ag}_{13}\text{Au}_{12}(\text{SR})_{18}$ detected can be due to a number of isomers depending on (i) the cluster from which it is derived and (ii) the exact locations of the $\text{Ag}_{12}/\text{Au}_{12}$ and the thirteenth Ag/Au atom. However, standard mass spectrometry cannot distinguish all the isomers of the formula, $\text{Ag}_{13}\text{Au}_{12}(\text{SR})_{18}$. We think that the abundance of $\text{Ag}_{13}\text{Au}_{12}(\text{SR})_{18}$ could be due to the larger number of ways by which $\text{Ag}_{13}\text{Au}_{12}(\text{SR})_{18}$ can be formed.

Supplementary Note 2: General instrumental parameters used for ESI measurements

All samples were analyzed by Waters Synapt G2Si High Definition Mass Spectrometer equipped with electrospray ionization (ESI) and ion mobility (IM) separation. All the samples were analyzed in negative ESI mode. The instrumental parameters were first optimized for Au₂₅(PET)₁₈ and other samples were analyzed using the similar setting with slight modification depending on the sample. About 0.1 mg of as prepared samples were diluted with dichloromethane (DCM) to get about 10 µg/mL sample concentration and directly infused to the system without any further purification. The instrument was calibrated using NaI as calibrant for the high mass. The optimized conditions were as follows:

Sample concentration: 10 µg /mL

Diluents: DCM

Sample flow rate: 10-20 µL/min

Source Voltage: 1.5-2.5 kV

Cone Voltage: 120-140 V

Source Offset: 80-120 V

Trap Collision Energy: 0 V

Transfer Collision Energy: 0 V

Source Temperature: 80-100°C

Desolvation Temperature: 150-200°C

Desolvation Gas Flow: 400 L/h

Trap Gas Flow: 2mL/min

Supplementary Note 3: Instrumental parameters used for the detection of the Ag₂₅Au₂₅(DMBT)₁₈(PET)₁₈ adduct.

By slightly modifying the instrumental setting, we were able to identify [Ag₂₅Au₂₅(DMBT)₁₈(PET)₁₈]²⁻. The conditions are as follows:

Sample concentration: 10 µg /mL

Diluents: DCM

Sample flow rate: 10-20 $\mu\text{L}/\text{min}$
Source Voltage: 0.1-0.5 kV
Cone Voltage: 0-50 V
Source Offset: 0-20 V
Trap Collision Energy: 0 V
Transfer Collision Energy: 0 V
Source Temperature: 60-80°C
Desolvation Temperature: 100-150°C
Trap Gas Flow: 5 mL/min

Supplementary Note 4: Methods of molecular docking study of $\text{Au}_{25}(\text{PET})_{18}$ and $\text{Ag}_{25}(\text{DMBT})_{18}$

We used the Autodock 4.2 and AutoDock Tools programs⁵. The initial structures of the molecules were the crystal structures of both $\text{Ag}_{25}(\text{DMBT})_{18}$ and $\text{Au}_{25}(\text{PET})_{18}$ ^{6, 2}. $\text{Au}_{25}(\text{PET})_{18}$ was taken as the “ligand” i.e. the movable molecule whose degrees of freedom would be varied and $\text{Ag}_{25}(\text{DMBT})_{18}$ as the “receptor” which was the fixed and completely rigid central molecule. We assigned charges by following the procedure to Guberman-Pfeffer *et al.*⁷, with slight modifications. The charges of the C, H and S atoms of the ligands were derived from a two-stage RESP fitting procedure based on partial charges and geometry optimization of the protonated PET and DMBT ligands at B3LYP/6-31G(d,p) level of theory. We used the Bader partial charges of Au and Ag atoms from optimized structures of $\text{Au}_{25}(\text{SCH}_3)_{18}$ and $\text{Ag}_{25}(\text{SCH}_3)_{18}$. The optimization was carried out using GPAW with the PBE functional⁸ and DZP (double zeta plus polarization) LCAO basis set. The $\text{Ag}(4d^{10}5s^1)$, $\text{Au}(5d^{10}6s^1)$, and $\text{S}(3s^23p^4)$ electrons were treated as valence and the inner electrons were included in a frozen core. The GPAW setups for gold and silver included scalar-relativistic corrections. The grid spacing for the finite difference method was 0.2 Å. The convergence criterion of 0.05 eV/Å for the residual forces on atoms was used for the structure optimization, without any symmetry constraints. After optimization using an LCAO basis set, the finite difference grid method of GPAW was used to obtain more accurate values of electronic density for Bader charge calculations. The same method was applied to $\text{Ag}_{25}(\text{DMBT})_{18}$ also. We made a correction to the calculated charges following Guberman-Pfeffer *et al.*⁷, except that we applied the charge correction factor for all the atoms except the central atom and hydrogen atoms. The equation used for obtaining the correction factor (δq) was:

$$Q_{\text{total}} = 25Q_{(\text{Au/Ag})} + 144Q_{\text{C}} + 18Q_{\text{S}} + 162Q_{\text{H}} + 186\delta q \dots \dots (1)$$

where, Q_{total} = total charge on the cluster (-1) and $Q_{(\text{Au/Ag})}$, Q_{C} , Q_{S} , Q_{H} are the charge on metal atoms, carbon, sulfur and hydrogen atoms obtained by Bader method.

Hence, $\delta q = \{Q_{\text{total}} - [25Q_{\text{Au/Ag}} + 144Q_{\text{C}} + 18Q_{\text{S}} + 162Q_{\text{H}}]\}/186$. The division by 186 is because we have not applied the correction factor to the Bader charges on the metal atom in the center of icosahedra and the hydrogen atoms on the ligands. The correction factors obtained were $0.000373e$ for $\text{Au}_{25}(\text{PET})_{18}$ and $0.020535e$ for $\text{Ag}_{25}(\text{DMBT})_{18}$.

The van der Waals radius σ (Å) and well depth ϵ (kcal/mol) for Ag and Au of 2.63 Å and 2.96 Å and 4.560 kcal/mol and 5.295 kcal/mol, respectively, were taken from well-tested sources in literature^{9,10} and these atom types were added to the Autodock parameter file which does not contain them by default.

Since the computation of many torsional configurations of the ligands using a force-field increases the configuration space and therefore the number of computations required greatly, the use of molecular docking software is highly advantageous as it is specifically designed for speeding up the process of calculating torsions by the use of pre-calculated grid maps of the force-field of the receptor and ligand. The reason for choosing $\text{Au}_{25}(\text{PET})_{18}$ as the movable and flexible molecule was that PET ligands have a larger torsional flexibility than the DMBT ligands, which would result in lower energy minima during the optimization over the torsional degrees of freedom.

The size of the search space in which $\text{Au}_{25}(\text{PET})_{18}$ was to be moved was a cube with a side of length 126 points with point spacing 0.375 Å. The cube was centered on the central silver atom of $\text{Ag}_{25}(\text{DMBT})_{18}$. The initial configuration of the clusters was chosen in a random orientation and positioned a sufficient distance away from the parent cluster so that binding interactions would be minimal. The Lamarckian genetic algorithm method was used within Autodock to find the global minimum with respect to the positional, orientation and torsional degrees of freedom of $\text{Au}_{25}(\text{PET})_{18}$ keeping $\text{Ag}_{25}(\text{DMBT})_{18}$ fixed at the center of the box. We have treated all the M-M, M-S, C-C, and C-H bonds as rigid, while allowing torsional flexibility upto 54 torsions on the S-C1, C1-C2 and C2-C3 bonds on all 18 of the ligands of the $\text{Au}_{25}(\text{PET})_{18}$ cluster, where the carbons are numbered along the chain starting from the S end (See Supplementary Fig. 8).

The 10 lowest minima structures that were obtained with binding free energies ranging from -4.62 to -17.53 kcal/mol with $\text{Au}_{25}(\text{PET})_{18}$ in various orientations and at varying distances on various different sides the $\text{Ag}_{25}(\text{DMBT})_{18}$. The free energies of binding were calculated by summing the intermolecular and internal and torsional terms and subtracting the unbound energy which is a calculation that is performed within the Autodock program. The relative orientation of the clusters in the minimum energy configuration is shown in Supplementary Fig. 11 and is such that the overlap between the molecular surfaces, or van der Waals envelope, of the ligands of the two clusters has maximal area of contact and their protrusions and pocket fit closely together in a lock and key fashion, as can be seen in Supplementary Fig 10. Two of the C_5 axes are nearly aligned with each other as seen in Supplementary Fig 11. Strength of interactions between atoms in the staples of the two clusters in the minimum energy configuration can be partially gauged by comparing their interatomic distances to the sum of their van der Waals radii, since the attractive van der Waals interaction ($-A/r^{-6}$) is stronger than the repulsive term (B/r^{-12}) at distances close to and greater their van der Waals radii.

Supplementary Note 5: Justification for not including the van der Waals corrections in the DFT-optimization of the force-field global minimum geometry of $[\text{Ag}_{25}\text{Au}_{25}(\text{DMBT})_{18}(\text{PET})_{18}]^{2-}$

Since the orientations of the ligands in the Autodock force-field minimum of $[\text{Ag}_{25}\text{Au}_{25}(\text{DMBT})_{18}(\text{PET})_{18}]^{2-}$ (see Supplementary Fig. 9), in which the vdW potential is explicitly included, are very similar to the orientation of the ligands in the DFT-optimized (with no vdW corrections) structure (see Fig. 3 in main manuscript), we concluded that the addition of vdW corrections to DFT optimization will not make a significant difference to the structure of the ligands of the dimer, or in other parts of the structure. Besides, our focus is not the dimer intermediate but the reaction leading to metal exchange and that finding does not get affected by improving the accuracy of the dimer structure by including the van der Waals corrections in the DFT optimization.

Supplementary Note 6: Nature of the bonding in the adduct $[\text{Ag}_{25}\text{Au}_{25}(\text{DMBT})_{18}(\text{PET})_{18}]^{2-}$

The shortest distances between the pairs of different types of metal and sulfur atoms (S-Au, S-Ag, Au-Ag) in the staples, shown in Supplementary Fig. 9, of the two clusters in the adduct

show that all these interatomic distances are greater than those needed for covalent bonding. Thus in our force-field minimum geometry, only weak non-covalent interactions between (i) metal atoms of one cluster and sulfur atoms in the staples of the neighbouring cluster and (ii) the alkyl/aryl groups of the ligands of the clusters are only expected in this force-field global minimum geometry of adduct at this separation between **I** and **II**, unlike in the case of one-dimensional chains of clusters¹¹.

However, DFT optimization of the force-field global minimum of adduct (Supplementary Fig. 12 and 13) revealed that the clusters **I** and **II** undergo significant structural distortions in the adduct geometry in terms of the bond lengths and bond angles. Moreover, the DFT-optimized geometry shows the formation of a weak bonding between Ag atom and the sulfur atoms in the staples of **I** and **II**. However, the local minimum in DFT-PES, shown in these figures, cannot be confirmed as the actual global minimum of the DFT PES of the dimer, without a complete search of PES but it is reasonable to assume that this would at least resemble in essential aspects such as the overall separation and orientation of the two clusters to one of the lower lying minima in the DFT PES.

The energy difference (binding energy) between the DFT-optimized adduct geometry and the sum of the DFT-optimized energies of isolated clusters was -90 eV. A quite significant lowering of the total energy of the cluster is observed. However, the per atom binding energy is $90/698 \text{ eV} = 0.12 \text{ eV}$ (698 is the total number of atoms in the adduct, $[\text{Ag}_{25}\text{Au}_{25}(\text{DMBT})_{18}(\text{PET})_{18}]^{2-}$). The large magnitude of the binding energy can be attributed to a number of factors such as the presence of large number of atoms and large common interfacial area, which facilitates attractive binding interactions, such Ag-S(Au_{25}) chemical bonding in the adduct, pi-pi interactions, ligand orbital overlaps, dipole-dipole interactions. Secondly, there is additional structural relaxation taking place through the structures resulting in distortions such as bond strain, angular and dihedral distortions in the core and staples, which lower the total energy below that of the sum of the DFT-optimized geometry of the two isolated clusters. However, we are unable to decompose the total energy into these different contributions. Such a substantial energy reduction for an intermediate indicates that the overall reaction is also thermodynamically favorable.

Supplementary Note 7: MALDI MS measurements

The matrix used was trans-2-[3-(4-tertbutylphenyl)-2-methyl-2-propenylidene]malononitrile (DCTB, > 98%). A solution of 6.2 mg of DCTB in 0.5 mL of dichloromethane was used for the measurements. Appropriate volumes of the sample solutions and DCTB solutions in DCM were mixed thoroughly and spotted on the sample plate and allowed to dry at ambient conditions. All the MALDI MS measurements were carried out at the threshold laser fluence in order to minimize fragmentation. All the spectra reported are of negative ions.

Supplementary References:

1. Yamazoe, S. *et al.* Hierarchy of bond stiffnesses within icosahedral-based gold clusters protected by thiolates. *Nat. Commun.* **7**, 10414 (2016).
2. Heaven, M. W., Dass, A., White, P. S., Holt, K. M. & Murray, R. W. Crystal structure of the gold nanoparticle $[\text{N}(\text{C}_8\text{H}_{17})_4][\text{Au}_{25}(\text{SCH}_2\text{CH}_2\text{Ph})_{18}]$. *J. Am. Chem. Soc.* **130**, 3754-3755 (2008).
3. Bootharaju, M. S., Joshi, C. P., Parida, M. R., Mohammed, O. F. & Bakr, O. M. Templated atom-precise galvanic synthesis and structure elucidation of a $[\text{Ag}_{24}\text{Au}(\text{SR})_{18}]^-$ nanocluster. *Angew. Chem. Int. Ed.* **55**, 922-926 (2016).
4. Krishnadas, K. R., Ghosh, A., Baksi, A., Chakraborty, I., Natarajan, G. & Pradeep, T. Intercluster reactions between $\text{Au}_{25}(\text{SR})_{18}$ and $\text{Ag}_{44}(\text{SR})_{30}$. *J. Am. Chem. Soc.* **138**, 140-148 (2016).
5. Morris, G. M., Huey, R., Lindstrom, W., Sanner, M. F., Belew, R. K.,Goodsell, D. S. & Olson, A. J. Autodock4 and AutoDockTools4: automated docking with selective receptor flexibility. *J. Comput. Chem.* **16**, 2785-2791 (2009).
6. Joshi, C. P., Bootharaju, M. S., Alhilaly, M. J. & Bakr, O. M. $[\text{Ag}_{25}(\text{SR})_{18}]^-$: The "Golden" silver nanoparticle. *J. Am. Chem. Soc.* **137**, 11578-11581 (2015).
7. Guberman-Pfeffer, M. J., Ulcickas, J. & Gascón, J. A. Connectivity-based biocompatible force field for thiolated gold nanoclusters *J. Phys. Chem. C* **119**, 27804-27812 (2015).
8. Perdew, J. P., Burke, K. & Ernzerhof, M. Generalized gradient approximation made simple. *Phys. Rev. Lett.* **77**, 3865-3868 (1996).
9. Pohjolainen, E., Chen, X., Malola, S., Groenhof, G. & Häkkinen, H. A unified AMBER-compatible molecular mechanics force field for thiolate-protected gold nanoclusters *J. Chem. Theory Comput.* **12**, 1342-1350 (2016).

10. Heinz, H., Vaia, R. A., Farmer, B. L. & R. R. Naik Accurate simulation of surfaces and interfaces of face-centered cubic metals using 12–6 and 9–6 Lennard-Jones potentials. *J. Phys. Chem. C* **112**, 17281–17290 (2008).
11. Nardi, M. D. *et al.* Gold nanowired: a linear $(\text{Au}_{25})_n$ polymer from Au_{25} molecular clusters. *ACS Nano* **8**, 8505-8512 (2014).

Cooking-Induced Corrosion of Metals

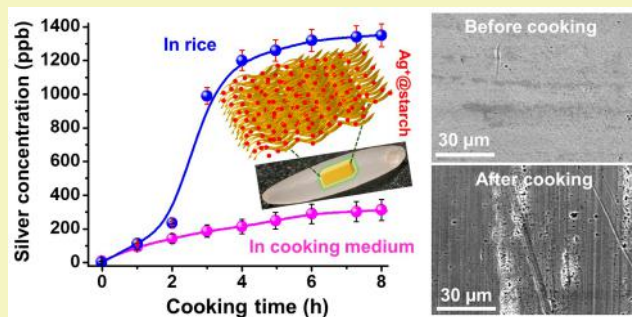
Soujit Sen Gupta,[†] Ananya Bakshi,[†] Vidhya Subramanian,^{†,‡} and T. Pradeep^{*,†}[†]DST Unit of Nanoscience (DST UNS), Thematic Unit of Excellence (TUE), Department of Chemistry, Indian Institute of Technology Madras, Chennai 600036, India[‡]Department of Biotechnology, Indian Institute of Technology Madras, Chennai 600036, India

S Supporting Information

ABSTRACT: Uptake of metal ions into rice occurs while it is being cooked in metal vessels, leading to corrosion of the utensils. This study deals with silver, copper, and aluminum uptake during cooking in respective vessels, with a special emphasis on silver. The metal uptake is routed through solution, enhanced in the presence of specific anions like carbonate, and attenuated when the rice is polished. The concentration of silver in rice increases with the time of cooking with a concomitant decrease in the concentrations of Fe and Zn, suggesting a substitution mechanism for metal ion uptake. The results for some common rice varieties of use across the Indian subcontinent are presented. Similar behavior

was observed for cooking in copper and aluminum vessels. Among the three metals studied, aluminum showed reduced uptake. Studies have been done to probe the interaction of metal ions with glucose and sucrose, and efficient complex formation was detected with all these ions, implying that starch can also form complexes with them. The cooking practices used in this study are reminiscent of local customs and practices that were chosen deliberately to relate to the true implications of these results.

KEYWORDS: Cooking, Rice, Corrosion, Silver, Aluminum



INTRODUCTION

While the study of heavy metal uptake by plants has a long history, the presence of the same metals in the human food chain and its dietary implications are relatively recent aspects of study.¹ In this context, it is important to notice that metal ion uptake can happen not only during cultivation but also during processing.^{2–4} Research has revealed the presence of arsenic in rice and other cereals.^{5–7} Spatial mapping of arsenic using secondary ion mass spectrometry (SIMS) has shown that rice bran is the target location for the deposition of arsenic.⁸ Differential uptake of arsenic is observed in various rice cultivars grown in arsenic-rich soil.^{9,10} As even extremely small doses of heavy metals such as cadmium, chromium, lead, and mercury in the diet pose considerable risks to human health,¹¹ their absorption in rice grains is a major public health concern in the entirety of South and Southeast Asia, where rice is a staple.^{12,13}

While rice plants of different cultivars take up heavy metals from the soil, heavy metals may also accumulate in rice during the process of cooking. During cooking of rice, uptake of metals by the rice grains may occur in two ways: from the cooking medium (water) used and from the cooking vessel.^{14,15} The major determinant of uptake during cooking is the chemical property of the metal, especially its affinity for the carbohydrates in rice grains. The aqueous dissolution of various metal species in the cooking medium determines the metal ion concentration in food and its health impacts upon con-

sumption. The chemistry of the carbohydrate on the surface of the vessel, especially at elevated temperatures, can also be a deciding factor for metal uptake. All of these are greatly influenced by the corrosive cooking medium, characteristic of south Asian cooking, composed of acids, typically present in ingredients such as tamarind. In this context, we decided to explore the metal ion uptake during cooking of select food items.

Our study shows that cooking of rice in copper, aluminum, and silver vessels causes corrosion of the surface of the vessels and uptake of the respective metals by rice in the process. While vessels made of copper and aluminum and their alloys are commonly used in a large number of Indian households,^{16,17} the use of silver in cooking utensils was common in wealthy traditional households. Vessels made of silver and copper and its alloys with zinc (brass) and tin (bronze) were traditionally used for storage of water and preservation of food in much of preindependent India.¹⁸ Silver foils are still in use in many parts of India to decorate milk sweets to be consumed along with the sweet.^{19,20} Our selection of these metals is in conformity with the tradition and common practice of cooking in South Asia.

Received: May 6, 2016

Revised: August 4, 2016

Published: August 11, 2016

Table 1. Concentrations (in parts per billion) of Different Metals in Rice Samples, As Purchased from the Market

sample no.	name of the rice	Cr	Mn	Fe	Cu	As	Pb	Sb	Zn	Ag	Al
1	Tamil Nadu Ponni (unpolished, boiled)	432.1	1454.8	3892.4	8380.8	2.3	0.0	3.2	4485.6	11.6	25.2
2	Tamil Nadu Ponni (polished, boiled)	324.6	1442.8	3245.8	7117.2	1.8	0.0	2.4	2681.2	18.4	15.1
3	Karnataka Ponni (unpolished, half-boiled)	298.7	1976.3	3206.0	7546.9	0.0	0.0	2.2	3548.0	13.2	21.5
4	Karnataka Ponni (polished, half-boiled)	245.3	2101.6	2906.2	7280	0.0	0.0	2.8	3419.6	13.5	9.7
5	IR20 (unpolished, raw)	312.4	854.0	1934.5	7052.4	1.5	0.0	2.4	1962	12	7.7
6	IR20 (polished, raw)	243.0	675.4	1743.7	6320.4	1.2	0.0	2.1	1669.9	9.5	3.8
7	Basmati (unpolished, boiled)	332.9	1327.2	2034.1	7844.0	0.0	0.0	4.0	3664	15.2	18.6
8	Basmati (polished, boiled)	309.5	1225.6	1993.4	8549.6	0.0	0.0	5.6	3532.4	18.3	12.9
9	Kerala brown (unpolished, raw)	322.1	958.0	3987.7	4454.8	1.8	0.0	2.0	2109.6	6.8	22.7
10	Idly (unpolished, boiled)	289.8	1184.4	1482.0	8813.6	0.0	0.0	10.4	2297.6	15.2	4.1

METHODS AND EXPERIMENTS

Materials. Metal vessels (purities of >95% silver, >97% copper, and >97% aluminum) were purchased from the local market, to mimic the local cooking practices. The scanning electron microscopy (SEM) images of silver, copper, and aluminum vessels, before use as purchased from the market, are given in Figure S1 along with respective SEM/EDS images (energy dispersive spectroscopy), to determine their chemical compositions. For each metal being tested, three cooking vessels of identical size were used as replicates. Quantitative analysis showed the metal content to be >95% Ag, >97% Cu, and >97% Al (weight percent) in all three vessels of each type, with some oxygen and a small amount of Cu for Ag, Zn for Cu, and Fe for Al vessels (quantitative data are provided in Figure S1). Nitric acid (assay, 69–71%) and hydrogen peroxide [assay, 100%; 30% (w/v)] were purchased from Fisher Scientific. Sodium chloride, sodium carbonate, sodium phosphate, and sodium hydroxide were purchased from Sigma-Aldrich. All 10 rice samples, namely, (1) Tamil Nadu Ponni (unpolished, boiled), (2) Tamil Nadu Ponni (polished, boiled), (3) Karnataka Ponni (unpolished, half-boiled), (4) Karnataka Ponni (polished, half-boiled), (5) IR20 (unpolished, raw), (6) IR20 (polished, raw), (7) Basmati (unpolished, boiled), (8) Basmati (polished, boiled), (9) Kerala brown (unpolished, raw), and (10) Idly (unpolished, boiled), were purchased from the local market and were used without any further treatment. The initial concentrations of various metals in rice are listed in Table 1.

Throughout our paper, “unpolished rice” refers to the decorticated rice grain with an intact bran cover (consisting of pericarp, tegmen, and aleurone layers), whereas “polished rice” denotes decorticated rice from which the bran layer has been removed during milling.

Experimental Procedure. In a typical experiment, 2 g rice samples were placed in Ag, Cu, and Al vessels and cooked in 20 mL of deionized (DI) water at a constant temperature of 80 °C, over hot plates. A glass lid was used in each case to prevent excessive evaporation of water, and for this reason, boiling was not used. A lid and a reduced temperature were used to avoid connecting a reflux condenser on the metal vessel and also because of the former's resemblance to standard cooking conditions in the region, where the cooking vessel with a lid is heated over a flame. A finite amount of the supernatant was collected at equal time intervals from the same vessel. Initially, 20 mL of water was added in each case for cooking. After every hour, 1 mL of the supernatant was withdrawn for analysis, which was compensated by 1 mL of fresh DI water. Under this optimized condition (arrived at using various control experiments), rice can be cooked in 2 h. The temperature was maintained for longer periods to evaluate the maximal limit of silver uptake by rice. For each metal vessel, experiments were conducted simultaneously in three separate vessels. The vessels were cleaned, and the experiments were repeated thrice for each metal and each rice variety. The nine resulting data points for each metal vessel and each rice variety were averaged.

Antibacterial Test. These tests were conducted with DI water incubated in silver vessels at 80 °C. The bacterial strain used was *Escherichia coli* MTCC 739 (Gram-negative bacteria). *E. coli* was inoculated in sterile nutrient broth and incubated overnight at 37 °C. A 1.5 mL bacterial suspension containing 10^8 colony-forming units

(CFU)/mL of cells was centrifuged (12000 rpm for 1 min), and the pellet was resuspended in 0.8% saline to create a final volume of 1 mL of suspension (final concentration of 1.5×10^8 cells/mL). This mixture was then added to a flask containing 14 mL of DI water containing 70 mg of NaCl, which was used as the control. The concentration of free silver in the samples was kept below the solubility product of silver chloride. The mixture was dispersed in saline for 3 h, centrifuged (12000 rpm for 1 min), and resuspended in 50 μ L of saline. A 5 μ L aliquot of the bacterial suspension was combined with 20 μ L of a fluorescent probe containing 3.34 mM green fluorescent nucleic acid stain, SYTO 9, and 20 mM red fluorescent nucleic acid stain, propidium iodide (PI) [live/dead backlight bacterial viability kit, L7012 from Invitrogen (see below)]. The mixture was incubated in the dark for 15 min, and an ~ 10 μ L aliquot was placed on a 1 mm thick ultrasonically cleaned glass slide (SCHOTT), which was then covered with a coverslip, sealed, and examined under a fluorescence microscope.

Live/Dead Staining Experiment. Live/dead staining experiments are used extensively to discriminate live and dead cells by intracellular staining. The stain utilized is a combination of two dyes, namely, SYTO 9 and PI. SYTO 9 is a green fluorescent nucleic acid stain capable of entering both live and dead cells. The green emission of SYTO 9 is enhanced when it is bound to a nucleic acid and shows a lower-intensity fluorescence signal if unbound. Contrary to this, PI, which is often used as a counterstain, exhibits red fluorescence in multicolor fluorescence techniques and is capable of penetrating only cells with disrupted cell membranes. This red fluorescent nucleic acid stain binds to DNA with no preferential sequence and exhibits 20–30-fold fluorescence enhancement when bound. In cases in which both dyes are used in the same sample, PI exhibits an affinity for nucleic acids stronger than that of SYTO 9, thus displacing SYTO 9 in dead cells where it is capable of penetration.²¹ This in turn leads to depiction of live cells as green and dead cells as red during fluorescence microscopy.

Effects of Silver, Copper, and Aluminum Ions on Humans.

Silver at concentrations in the range of 0.01–0.50 mg/day shows very low toxicity to humans.²² It is widely used as an antibiotic and antibacterial agent for ages.²³ According to the World Health Organization, the maximal permissible limit of silver in drinking water is 0.1 mg/L and the lethal dose of silver salts was found to be ~ 10 g for humans. Excessive exposure leads to deposition of silver on skin, a condition called argyria. Copper is essential for life and is the third most abundant trace element in human body after iron and zinc.²⁴ Many enzymes and proteins contain copper in living organisms. The availability of copper is significant in meats, cereals, and pulses. The safe estimated dietary intake of copper is 0.9–1.5 mg/day.²⁵ The human body has no known requirement for aluminum. Most of the aluminum introduced intravascularly into the body is from drinking water and from conjugates with albumin and is subsequently removed renally. If the aluminum content exceeds the renal removal capacity, it is deposited in various tissues, which might lead to mortal harm.²⁶ The safe limit of aluminum uptake is in the range of 0.10–0.20 mg/day. Excess exposure of aluminum to humans through food causes acute kidney injury²⁷ and neurodegeneration causing Alzheimer's disease.²⁸ From the reports cited above, it is evident that large scale uptake of

these metals can cause serious health effects. However, uptake of these metals into humans through cooked rice has not been examined in our study.

Instrumentation. We employed an inductively coupled plasma mass spectrometry (ICP MS) PerkinElmer NexION 300X instrument equipped with an argon plasma source for quantification of metals in rice. Silver was calibrated with a silver atomic absorption spectroscopy (AAS) standard solution (1000 mg/L) purchased from Fisher Scientific (product AAAGH). Other elements like Al, Cu, Fe, Zn, and Mn were calibrated by PerkinElmer Instrument Calibration Standard 2 (product N9301721). In all cases, five calibration points were used: 0 (called the blank) 10, 100, 1000, and 10000 ppb. In all the cases, five concentrations of the calibrant were analyzed first until a calibration curve was achieved with an R^2 of 0.9999. After that, the two samples of known concentration (>100 and <1000 ppb) were checked at least three times to obtain reproducible data with a deviation of <0.5 ppb (for samples with concentrations of >1000 ppb). The detection limit for ICP MS is 0.1 ppb for these ions. Blank concentrations of different metal ions in Milli-Q, deionized, and tap water used in the experiment are shown in Table S2.

For analysis, 1 mL of the supernatant (starch) solution was withdrawn at regular time intervals (1 h) and 50 μ L of concentrated nitric acid was added (to yield a 5% acid concentration, which is comparable with the standards of the instrument). For the analysis of metal ion concentration in the supernatant solution during the course of cooking, 1 mL of the solution was pipetted out and the same quantity of DI water was added to the vessel at a time interval of 1 h. After 6 h, the cooked rice was digested for metal ion uptake.

For digestion, 2 g of a rice sample (dry weight) was taken in a Teflon tube and to it were added 5 mL of HNO_3 and 3 mL of H_2O_2 . This mixture was digested using an Anton Parr microwave digester with a power of 800 W, programmed at a ramping time of 10 min, and then it was held for 15 min at 800 W. After cooling, the sample was diluted 10 times with DI water and analyzed using ICP MS. A similar procedure in which the entire amount of cooked rice was digested was followed after the rice had been completely cooked. This is termed “digested rice” in the text. All the experiments were repeated thrice, and an average value is reported. Scanning electron microscopy (SEM) equipped with energy dispersive analysis (EDS) (FEI Quanta 200) was used to record the surface morphology, elemental composition, and elemental mapping of the samples. EDAX Genesis was used to evaluate EDS data. For this analysis, a small amount of the cooked rice was oven-dried and ground into a fine powder prior to analysis. Whole grain was also used for the study without grinding. The ground rice sample was used for laser desorption ionization (LDI) analysis, on an Applied Biosystems Voyager DE Pro matrix-assisted LDI MS instrument. A pulsed 337 nm nitrogen laser was used for desorption ionization. An average of 10 spectra (each spectrum consists of 200 laser shots) were recorded in each case. Electrospray ionization mass spectrometry (ESI MS) analysis was performed using an Applied Biosystems 3200 QTRAP LC MS system in the mass range of m/z 100–1700. The following optimized conditions were used: declustering potential (DP) of 30 V, entrance potential (EP) of 10 V, ion spray voltage (IS) of 2 kV, and collision energy (CE) of 10–100 (instrument units). A 1:1 (v/v) $\text{H}_2\text{O}/\text{MeOH}$ mixture was used as the solvent. XPS measurements were taken with an Omicron ESCA Probe spectrometer with monochromatic Mg $K\alpha$ X-rays ($h\nu = 1253.6$ eV). Most of the spectra were deconvoluted to their component peaks using CasaXPS. The energy resolution of the spectrometer was set at 0.1 eV at a pass energy of 20 eV. The binding energy was corrected with respect to C 1s at 284.5 eV. UV–vis spectra were recorded using a PerkinElmer Lambda 25 spectrophotometer. A Cytoviva HSI system was used for the live and dead staining experiment. Excitation was at 550 nm, and emission was collected using a band-pass filter at 500–550 nm for SYTO 9 and a long-pass filter 590–800 nm for PI. In all cases, measurements were taken using a 100 \times oil (Cargille) immersion objective.

RESULTS AND DISCUSSION

Ten different varieties of rice, including polished and unpolished types, that are commonly used across the Indian subcontinent were selected for our study. While the studies were performed on several varieties, for the purpose of illustration, the uptake in Tamil Nadu Ponni rice, a commonly used native variety, is discussed here. Figure 1 shows a gradual

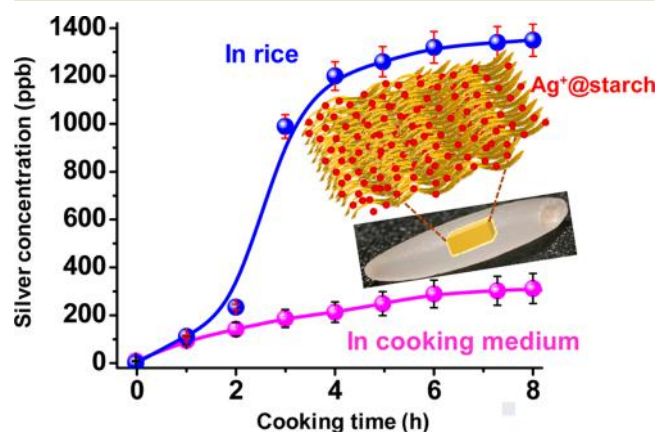


Figure 1. Concentration of silver in digested rice and in the supernatant solution (cooking medium), as a function of cooking time. The presence of silver in the polymeric starch matrix is schematically represented in the expanded inset. The error bar shows the variation of nine data points.

increase in the amount of silver in rice during cooking. Experiments were performed under various conditions to determine the most desirable consistency and softness of the cooked rice (Figures S3–S6 and experimental details given in the Supporting Information). Experiments were performed repeatedly as discussed in Methods and Experiments. Variation between the measurements was within 1%. The uptake of silver in rice and in starch solution (cooking medium) during the course of cooking shows two distinct patterns. Uptake in rice shows a rapid enhancement after an initial lag eventually reaching an equilibrium level, suggesting an equilibrium level of concentration. The extent of uptake and its kinetics depend on the rice variety. Nevertheless, rapid silver uptake while cooking after an initial lag is common in all varieties (the time-dependent uptake curves in the other rice varieties are shown in Figure S7, and the highest silver uptake by various rice varieties is compared in Figure S8) followed by a gradual saturation. As cooking progresses, the medium is gradually enriched with starch because of its dissolution in the cooking medium. As shown in Figure 1, rice shows a constant increase in silver concentration when cooked in a silver vessel with time while the concentration of silver in the supernatant reached equilibrium within a couple of hours. An \sim 5-fold increase in silver concentration in cooked rice was observed just with an increase in cooking time from 2 to 3 h. Control experiments were performed (without rice, with other parameters remaining constant), and it was seen that the concentration of silver ions released in water was lower initially (>20 ppb after 30 min) but gradually increased and reached around 170 ppb after samples had been heated for 3 h. The same finding is reflected in the uptake of silver by rice. It is proposed that silver is being released as silver ions in the solution that is taken up by rice by forming stable complexes (discussed later in the text).

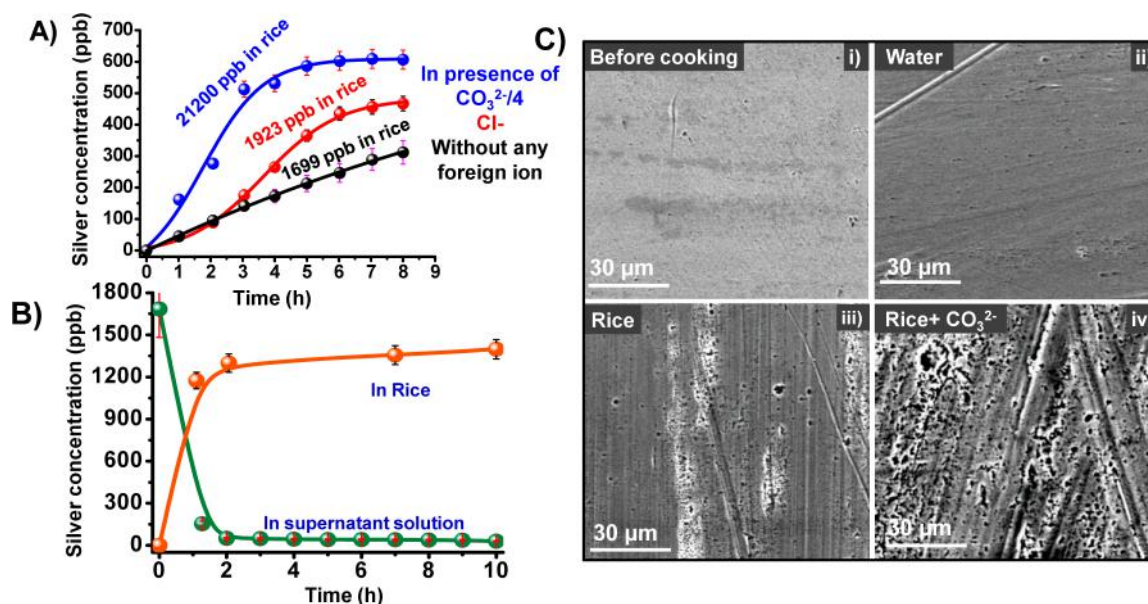


Figure 2. (A) Effect of silver ion uptake in the presence of equal concentrations of anions. CO_3^{2-} and Cl^- are compared (the cation was the same; Na_2CO_3 and NaCl were used). Corresponding concentrations of silver in cooked rice are indicated on the top of each plot. (B) Uptake of silver ions from solution when the cooking medium was 1800 ppb Ag^+ in a glass vessel. Complementary behavior was observed for the supernatant. (C) Variation in the surface morphology of silver foils due to cooking, viewed via SEM: (i) foil before the experiment and those after the experiments in (ii) DI water, (iii) rice (without any external anion), and (iv) rice in the presence of CO_3^{2-} . The error bar shows the variation of nine data points.

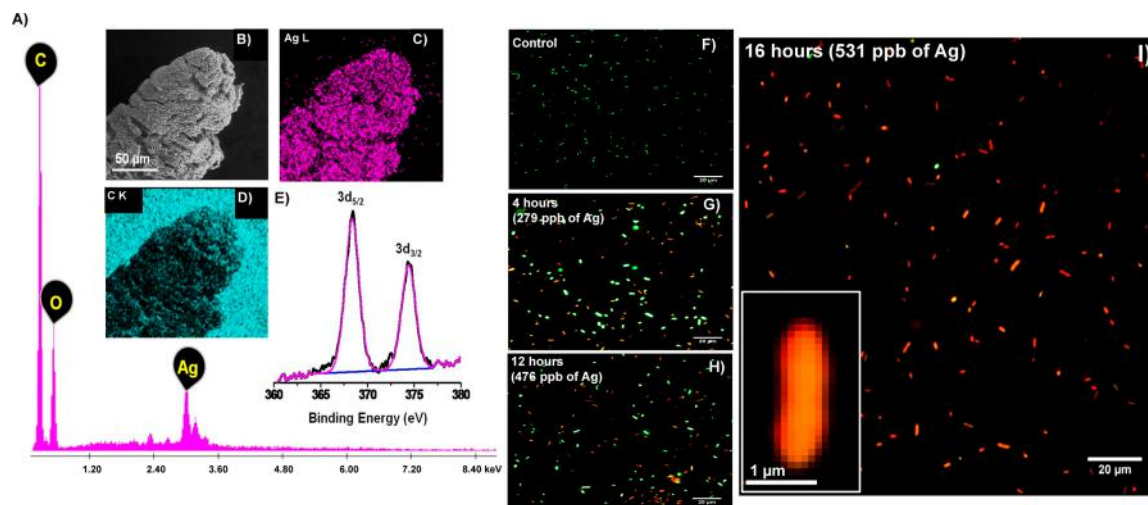


Figure 3. (A) SEM/EDS of a rice grain when it is cooked in a silver vessel showing the presence of silver. (B) SEM image of the cooked (after drying) rice. (C and D) Elemental mapping of silver and carbon. (E) Monovalent form of Ag in the rice confirmed from Ag 3d XPS. (F–I) Fluorescence images of *E. coli* MTCC 739 showing the antibacterial activity of water kept in a silver vessel. One bacterium is magnified in the inset of panel I.

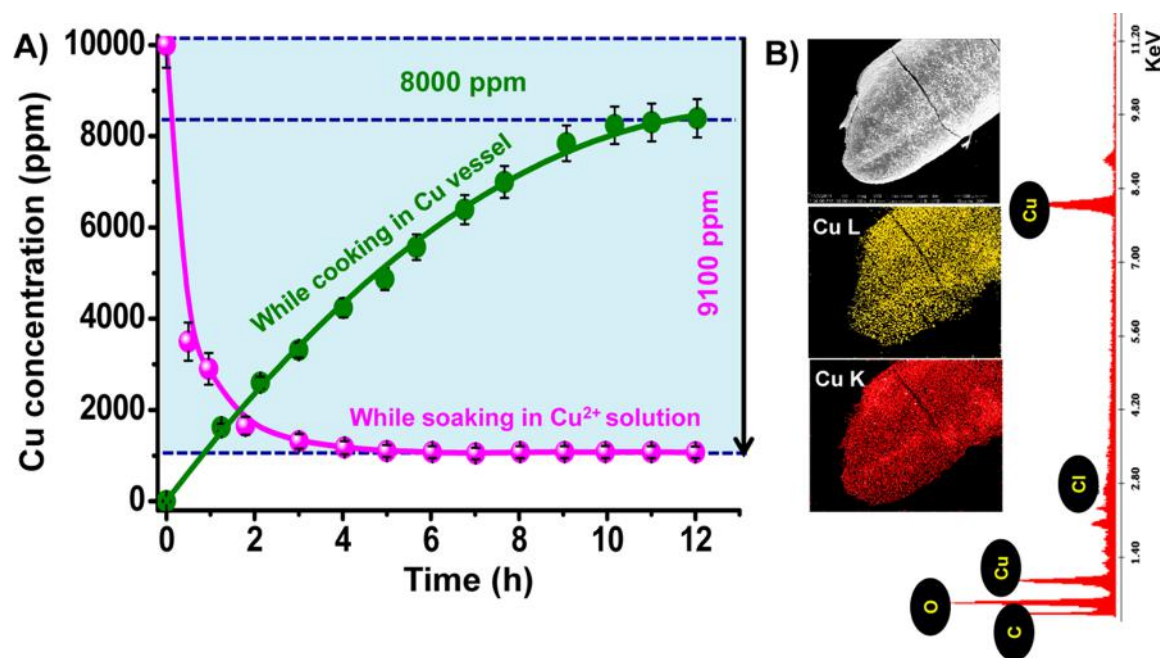
It seems plausible that silver is transported from the cooking medium (water) to rice. This conjecture was tested using various ions that can modify the silver ion concentration in solution. The ions chosen were carbonate (CO_3^{2-}), phosphate (PO_4^{3-}), and chloride (Cl^-), which are expected to form the corresponding silver species in solution, keeping the cationic (Na^+) identity unaltered (i.e., using sodium salt in each case). The solubilities of the corresponding silver salts are 0.032, 0.0065, and 0.0019 g/L for carbonate, phosphate, and chloride, respectively. Silver ion uptake in these solutions follows the general trend of solubility as stated above (Figure 2A), where data for Cl^- and CO_3^{2-} -containing solutions are compared along with the control. Phosphate follows an in-between trend.

This conclusion was further verified by cooking rice in a silver nitrate solution in a glass vessel (Figure 2B).

The uptake kinetics follow the same trend as shown in Figure 1, namely, a rapid uptake in rice and a concomitant change in solution. When silver ions are present in solution, uptake in rice is rapid. Saturated uptake can be as large as 1000 ppm when a silver salt is supplied, which makes the rice look yellow in color. The metal ion concentration in solution after cooking does not increase while the cooked rice is being cooled, implying that silver is strongly bound to the carbohydrate. The data presented show that metal ion uptake is mediated through solution. Release of silver from the vessel is manifested on the surface of the vessel in terms of corrosion. Scanning electron microscopic investigations of a polished metal surface show

Table 2. Concentrations (in parts per billion) of Metal Ions in Rice [Tamil Nadu Ponni (boiled, unpolished)] during Cooking, at Various Times When the Rice Is Cooked in a Silver Vessel

time	Cr	Mn	Fe	Co	Cu	As	Zn	Al	Ag
0 min	432.1	1454.8	3892.4	6.8	8380.8	2.3	4485.6	25.2	11.6
5 min	421.2	1423.4	3712.9	6.8	8217.8	2.3	4281.4	22.1	40.3
10 min	423.5	1435.4	3706.2	6.8	8243.7	2.1	4012.8	20.8	60.7
30 min	418.7	1385.3	3605.8	6.7	8312.5	1.9	3987.5	19.1	100.4
1 h	428.2	1312.5	2623.3	6.9	8106.9	2.1	3824.7	19.4	145.6
2 h	426.3	1276.2	2317.6	6.8	8267.0	1.9	3432.5	19.3	265.2
3 h	426.4	1206.9	2008.1	6.8	8334.4	2.3	3213.3	19.0	812.5
6 h	428.3	1109.8	1231.6	6.7	8298.4	2.2	2870.1	19.1	1384.4

**Figure 4.** (A) Concentration of Cu in rice (olive line) upon cooking in a copper vessel showing a gradual increase up to 8 h, reaching a saturation at 8000 ppm. The magenta line shows the decrease in the concentration of Cu in the solution when rice is cooked in a 10000 ppm Cu^{2+} solution in a glass vessel. (B) SEM/EDS of dried rice soaked in a 10000 ppm copper solution. Elemental maps show a uniform distribution of copper throughout the whole rice. The EDS spectrum is shown at the extreme right. The error bars show the variation of nine data points.

gradual roughening with time of cooking, which is also enhanced by the presence of other ions (Figure 2C). The rice was also cooked in a Teflon beaker in the presence of a silver foil with a 0.5 mm thickness and a 6 cm \times 6 cm area immersed in the medium. After cooking, the silver foils were washed thoroughly with DI water and dried at room temperature, and a small portion was analyzed via SEM. Highly polished silver foils were used in this study.

The presence of silver in rice was proven by several analyses as shown in Figure 3. The SEM/EDS spectrum (Figure 3A) and elemental mapping (Figure 3B–D) show a uniform distribution of silver throughout the cooked rice grain. SEM/EDS mapping of a horizontally cut rice grain is shown in Figure S9, indicating the presence of silver. This experiment confirms the uptake of silver uniformly throughout the grain. The XPS spectrum of the cooked grain in the Ag 3d region confirms the existence of monovalent silver in the grain. Ag 3d_{5/2} was observed at 367.5 eV, as expected for Ag(I).²⁹ A high silver ion concentration in the presence of carbonate and the corresponding yellowish color of rice made us consider the possibility of formation of silver nanoparticles within rice. Metallic silver nanoparticles have strong absorption at 400 nm

known as a plasmon band.³⁰ The peak position varies slightly depending on the protecting ligand. However, there was no plasmonic feature in the UV–vis absorption spectrum of the same sample (Figure S10). This confirms that silver nanoparticles were not formed in rice while it was being cooked. This aspect was studied as carbohydrates can reduce silver to form silver nanoparticles, which is more facile in the presence of ions like carbonate. LDI MS of silver-saturated rice was performed, and small silver clusters were detected (Figure S11). However, a similar kind of mass spectrum can be obtained by LDI of Ag salts, too, as Ag⁺ ions can form aggregates in the gas phase during laser ablation.^{31,32}

Release of Ag ions into the solution from the metal can occur in water under experimental conditions (i.e., at 80 °C). In DI water with a conductivity of 0.7 μS , silver release is up to 531 ppb at 80 °C, for a 16 h incubation. This follows a constant increase up to 16 h, which was monitored up to 24 h (Figure S11). Such a silver ion concentration is enough to cause biological activity as seen by live and dead staining of *E. coli* as shown in Figure 3I (all the antibacterial experiments were conducted at room temperature after the water had been cooled). Live and dead staining was used to see this effect (see

Antibacterial Test for details). The fraction of live bacteria (green) decreases with an increasing contact time of the sample (Figure 3G,H), and there were no live bacteria (all are red) after a 3 h exposure to silver-containing water. The concentration of silver was 531 ppb at this time (heating for 16 h). One of the dead bacterium is magnified in the inset of Figure 3I.

The data suggest that silver ions are complexed strongly with starch, although it was not possible to identify the chemical identity of the complex thus formed. In view of this, we examined the interaction of glucose (the composing unit of starch molecule) with silver in aqueous solution, using ESI MS. Ag–glucose complexes are known to form in solution and can be seen via ESI MS analysis. Boutreau et al. have shown that the α -anomer of glucose can effectively form complexes with silver through the -OH groups at positions 3 and 4.³³ Peaks at m/z 287, 367, etc., corresponding to G–Ag⁺, 2G–Ag⁺, etc., complexes, respectively were observed via ESI MS in positive ion mode. The species was confirmed by isotope distribution as well as ESI MS/MS studies. Glucose aggregates also show similar kinds of complexes in the gas phase (see Figure S12A). Sucrose (disaccharide composed of glucose and fructose) also forms complexes with silver (see Figure S12B). Therefore, we can conclude that polysaccharides like starch can also form complexes with silver.

Experiments were also performed with polished and unpolished varieties of the same rice and showed that the latter take up more silver than the former (for the same rice variety). Thus, the bran layer appears to be the principal site of silver uptake from the cooking medium (Figures S7 and S8).

To understand whether silver is exchanging with other metal ions, careful examination of the concentration of other essential metal ions was performed. ICP MS data of different metal ions in cooked rice prepared in silver vessels are listed in Table 2. The data suggest a considerable decrease in the concentration of Fe and Zn in rice when it is cooked in a silver vessel. This observation suggests the substitution of these binding sites by silver. In this case, rice was cooked in three different vessels (as discussed in Methods and Experiments), and it was analyzed after specific time intervals. Seven different sets of experiments were performed using 2 g of dry rice and 20 mL of DI water.

The uptake of copper and aluminum during cooking in respective vessels was also studied. The optimized cooking procedure described above was followed. In the case of a copper vessel, uptake of up to 8000 ppm was observed. As seen with silver, a gradual increase in copper concentration in the cooked rice was observed. When the rice was cooked with DI water containing 10000 ppm of Cu²⁺ in a glass vessel, a gradual decrease in Cu²⁺ concentration was seen in the supernatant. Approximately 900 ppm of Cu was observed in the supernatant, and rice contained 9100 ppm (magenta line in Figure 4A). The presence of Cu was further proven via SEM/EDS analysis of the dried rice sample. A uniform distribution of Cu was observed in the rice (see Figure 4B).

The uptake of metal was the lowest upon cooking in an aluminum vessel, compared to those in silver and copper vessels. The extent of uptake reached a maximum of 580 ppb for Al after 2 h of cooking, which declined to 100 ppb after 6 h, but the uptake was far higher when the rice was soaked in Al³⁺-containing water, where ~5000 ppb of Al was found in the cooked rice after 6 h of cooking. The lower solubility of Al salts in water is likely the cause of the lower uptake during cooking in aluminum vessels. Furthermore, the binding of starch to Al is

likely to be weaker than that to Cu and Ag, accounting for lower uptake. In addition, the protective layer of oxide on the aluminum vessel surface may retard corrosion and consequently slow the release of Al into the solution. Here a dried rice sample also showed a uniform distribution of Al in SEM/EDS (Figure S13).

CONCLUSION

Our study probed the biomolecule-induced corrosion of metal surfaces during cooking, leading to unprecedented uptake of metal ions in foodstuffs, leading to a potential impact on human health. Metals such as silver, copper, and aluminum are taken up by rice from the cooking vessels made of the respective metals, and this leads to microscopic corrosion of the vessels. Uptake occurs via solution by the formation of soluble ionic species of the metals. The presence of anions in solution, whose metal salt is water-soluble, enhances the metal ion uptake. Uptake is enhanced by the presence of bran. Ag uptake happens with a corresponding decrease in the Fe and Zn concentration in rice, suggesting a substitution mechanism for metal ion uptake. The uptake of metals by rice from utensils occurs principally through the ionic route. Cooking methods enhance the release of ions into the medium, such as the use of acids, salts, and complexation agents that can have much stronger effects.

ASSOCIATED CONTENT

Supporting Information

The Supporting Information is available free of charge on the ACS Publications website at DOI: 10.1021/acssuschemeng.6b00980.

Additional details describing the experimental details, SEM images of different vessels before use, initial concentrations of different metal ions in water, release of silver in deionized water, temperature-dependent release of silver, time-dependent release of silver at 80 °C in DI water, pH-dependent release of silver, time-dependent silver uptake by different rice varieties, maximal silver uptake by different rice varieties, SEM/EDS of cooked rice horizontally cut with adsorbed silver, UV–vis spectra of the supernatant solution, LDI MS of silver-saturated rice, ESI MS of Ag–glucose and Ag–sucrose complexes, and SEM/EDS of cooked rice soaked in an aluminum salt solution (PDF)

AUTHOR INFORMATION

Corresponding Author

*E-mail: pradeep@iitm.ac.in.

Notes

The authors declare no competing financial interest.

ACKNOWLEDGMENTS

The work was supported by the Department of Science and Technology, India. A.B. thanks CSIR for a fellowship. S.S.G. thanks the SERB, CII, and Thermax India Pvt. Ltd. for a research fellowship.

REFERENCES

- (1) Peralta-Videa, J. R.; Lopez, M. L.; Narayan, M.; Saupé, G.; Gardea-Torresdey, J. The biochemistry of environmental heavy metal uptake by plants: Implications for the food chain. *Int. J. Biochem. Cell Biol.* 2009, 41, 1665–1677.

- (2) Tom, M.; Fletcher, T. D.; McCarthy, D. T. Heavy metal contamination of vegetables irrigated by urban stormwater: a matter of time? *PLoS One* **2014**, *9*, e112441.
- (3) Huang, Z.; Pan, X.-D.; Wu, P.-G.; Han, J.-L.; Chen, Q. Health risk assessment of heavy metals in rice to the population in Zhejiang, China. *PLoS One* **2013**, *8*, e75007.
- (4) Baxter, I. R.; Ziegler, G.; Lahner, B.; Mickelbart, M. V.; Foley, R.; Danku, J.; Armstrong, P.; Salt, D. E.; Hoekenga, O. A. Single-kernel ionic profiles are highly heritable indicators of genetic and environmental influences on elemental accumulation in maize grain (*Zea mays*). *PLoS One* **2014**, *9*, e87628.
- (5) Meharg, A. A.; Zhao, F.-J. *Arsenic & rice*; Springer Science +Business Media: Berlin, 2012.
- (6) Abedin, M. J.; Cotter-Howells, J.; Meharg, A. Arsenic uptake and accumulation in rice (*Oryza sativa* L.) irrigated with contaminated water. *Plant Soil* **2002**, *240*, 311–319.
- (7) Zavala, Y. J.; Duxbury, J. M. Arsenic in rice: I. Estimating normal levels of total arsenic in rice grain. *Environ. Sci. Technol.* **2008**, *42*, 3856–3860.
- (8) Sun, G.-X.; Williams, P. N.; Carey, A.-M.; Zhu, Y.-G.; Deacon, C.; Raab, A.; Feldmann, J.; Islam, R. M.; Meharg, A. A. Inorganic arsenic in rice bran and its products are an order of magnitude higher than in bulk grain. *Environ. Sci. Technol.* **2008**, *42*, 7542–7546.
- (9) Zhao, F. J.; Ma, J. F.; Meharg, A. A.; McGrath, S. P. Arsenic uptake and metabolism in plants. *New Phytol.* **2009**, *181*, 777–794.
- (10) Meharg, A. A.; Hartley-Whitaker, J. Arsenic uptake and metabolism in arsenic resistant and nonresistant plant species. *New Phytol.* **2002**, *154*, 29–43.
- (11) Zavala, Y. J.; Gerads, R.; Gürleyük, H.; Duxbury, J. M. Arsenic in rice: II. Arsenic speciation in USA grain and implications for human health. *Environ. Sci. Technol.* **2008**, *42*, 3861–3866.
- (12) Azizur Rahman, M.; Hasegawa, H.; Mahfuzur Rahman, M.; Mazid Miah, M. A.; Tasmin, A. Arsenic accumulation in rice (*Oryza sativa* L.): Human exposure through food chain. *Ecotoxicol. Environ. Saf.* **2008**, *69*, 317–324.
- (13) Rahman, M. A.; Hasegawa, H.; Rahman, M. A.; Rahman, M. M.; Miah, M. A. M. Influence of cooking method on arsenic retention in cooked rice related to dietary exposure. *Sci. Total Environ.* **2006**, *370*, 51–60.
- (14) Sengupta, M. K.; Hossain, M. A.; Mukherjee, A.; Ahamed, S.; Das, B.; Nayak, B.; Pal, A.; Chakraborti, D. Arsenic burden of cooked rice: Traditional and modern methods. *Food Chem. Toxicol.* **2006**, *44*, 1823–1829.
- (15) Rani, M. R. S.; Bhattacharya, K. R. Rheology of rice-flour pastes: Effect of variety, concentration, and temperature and time of cooking. *J. Texture Stud.* **1989**, *20*, 127–137.
- (16) Waldron, H. A. Lead poisoning in the ancient world. *Med. Hist.* **1973**, *17*, 391–399.
- (17) Prakash, B. Use of metals in kyurvedic medicike. *Indian J. Hist. Sci.* **1997**, *32*, 1.
- (18) Kosambi, D. D. *An introduction to the study of Indian history*; Popular Prakashan: Mumbai, 1975.
- (19) Das, M.; Dixit, S.; Khanna, S. K. Justifying the need to prescribe limits for toxic metal contaminants in food-grade silver foils. *Food Addit. Contam.* **2005**, *22*, 1219–1223.
- (20) Khedekar, S.; Patgiri, B.; Ravishankar, B.; Prajapati, P. Standard manufacturing process of Makaradhwaja prepared by Swarna Patra-Varkha and Bhasma. *AYU (An international quarterly journal of research in Ayurveda)* **2011**, *32*, 109–115.
- (21) Stiefel, P.; Schmidt-Emrich, S.; Maniura-Weber, K.; Ren, Q. Critical aspects of using bacterial cell viability assays with the fluorophores SYTO9 and propidium iodide. *BMC Microbiol.* **2015**, *15*, 36.
- (22) Marambio-Jones, C.; Hoek, E. M. V. A review of the antibacterial effects of silver nanomaterials and potential implications for human health and the environment. *J. Nanopart. Res.* **2010**, *12*, 1531–1551.
- (23) Lansdown, A. Silver in health care: antimicrobial effects and safety in use. In *Biofunctional textiles and the skin*; Karger Publishers: Basel, Switzerland, 2006; Vol. 33, pp 17–34.
- (24) Uauy, R.; Olivares, M.; Gonzalez, M. Essentiality of copper in humans. *Am. J. Clin. Nutr.* **1998**, *67*, 952S–959S.
- (25) *Guidelines for drinking-water quality: recommendations*; World Health Organization: Geneva, 2004; p 1.
- (26) Proudfoot, A. T. Aluminium and zinc phosphide poisoning. *Clin. Toxicol.* **2009**, *47*, 89–100.
- (27) Brown, R. O.; Morgan, L. M.; Bhattacharya, S. K.; Johnson, P. L.; Minard, G.; Dickerson, R. N. Potential aluminum exposure from parenteral nutrition in patients with acute kidney injury. *Ann. Pharmacother.* **2008**, *42*, 1410–1415.
- (28) Vasudevaraju, P.; Govindaraju, M.; Palanisamy, A.; Sambamurti, K.; Rao, K. Molecular toxicity of aluminium in relation to neurodegeneration. *Indian J. Med. Res.* **2008**, *128*, 545–556.
- (29) Kaushik, V. K. XPS core level spectra and Auger parameters for some silver compounds. *J. Electron Spectrosc. Relat. Phenom.* **1991**, *56*, 273–277.
- (30) Jain, P.; Huang, X.; El-Sayed, I.; El-Sayed, M. Review of some interesting surface plasmon resonance-enhanced properties of noble metal nanoparticles and their applications to biosystems. *Plasmonics* **2007**, *2*, 107–118.
- (31) Franski, R.; Gierczyk, B.; Kozik, T. Loss of Ag₃ moiety from clusters Ag_n + (n = 4, 6, 8, 10, 12) upon collision induced dissociation. *Int. J. Mass Spectrom.* **2011**, *306*, 91–94.
- (32) Rashidzadeh, H.; Guo, B. Generation of large gas-phase silver cluster ions by laser desorption/ionization of silver-containing salts. *Chem. Phys. Lett.* **1999**, *310*, 466–470.
- (33) Boutreau, L.; Leon, E.; Salpin, J.-Y.; Amekraz, B.; Moulin, C.; Tortajada, J. Moulin, C.; Tortajada, J., Gas-phase reactivity of silver and copper coordinated monosaccharide cations studied by electrospray ionization and tandem mass spectrometry. *Eur. Mass Spectrom.* **2003**, *9*, 377–390.

Cooking Induced Corrosion of Metals

Soujit Sen Gupta,¹ Ananya Bakshi,¹ Vidhya Subramanian^{1,2} and T. Pradeep^{1*}

¹DST Unit of Nanoscience (DST UNS), and Thematic Unit of Excellence (TUE), Department of Chemistry, Indian Institute of Technology Madras, Chennai - 600 036, India

²Department of Biotechnology, Indian Institute of Technology Madras, Chennai-600036, India

*Email: pradeep@iitm.ac.in

Index

<i>Experimental Details</i>	<i>Page S2</i>
<i>Figure S1 (SEM image of different vessels before use)</i>	<i>Page S3</i>
<i>Table S2 (Initial concentration of different metal ions in water)</i>	<i>Page S4</i>
<i>Figure S3 (Release of silver in deionized water)</i>	<i>Page S5</i>
<i>Figure S4 (Temperature dependent release of silver)</i>	<i>Page S6</i>
<i>Figure S5 (Time dependent release of silver at 80°C in DI water)</i>	<i>Page S7</i>
<i>Figure S6 (pH dependent release of silver)</i>	<i>Page S8</i>
<i>Figure S7 (Time dependent silver uptake by different rice varieties)</i>	<i>Page S9</i>
<i>Figure S8 (Maximum silver uptake by different rice varieties)</i>	<i>Page S10</i>
<i>Figure S9 (SEM/EDS of cooked rice horizontally cut adsorbed silver)</i>	<i>Page S11</i>
<i>Figure S10 (UV-Vis spectra of supernatant solution)</i>	<i>Page S12</i>
<i>Figure S11 (LDI MS of silver saturated rice)</i>	<i>Page S13</i>
<i>Figure S12 (ESI MS of Ag-Glucose and Ag-Sucrose complexes)</i>	<i>Page S14</i>
<i>Figure S13 (SEM/EDS of cooked rice soaked in aluminium salt solution)</i>	<i>Page S15</i>

Experimental Details:

Three metal vessels were used for this study. For each metal vessel, experiments were done simultaneously in three separate vessels (of equal size and weight) to check reproducibility and calculate standard deviation. The vessels were cleaned and the experiments were repeated thrice for each metal and each variety of rice. The resulting 9 data points for each metal vessel and each rice variety were averaged. All the experiments were performed in deionized water. In a typical reaction, 2 g of rice was taken in silver vessels and cooked in presence of 20 mL of DI water at 80 °C on hot plate. This specific temperature was chosen as reasonable silver release was observed in DI water at this temperature and there was no reason to use a condenser to keep the volume nearly constant. We have performed the experiments with tap water also but seemingly DI water worked better with good reproducibility and greater control on the data. A glass lid was used in each case to avoid evaporation of water. Equal amount of the supernatant was collected in equal time interval. In this optimized condition (from various control experiments) rice can be cooked in 2 hours of time. We performed cooking for a longer time to see maximum limit of silver uptake by the rice at experimental conditions. For real time application, the same experiment was performed at higher temperature to check the uptake of silver, where the rice was cooked within 20 min.

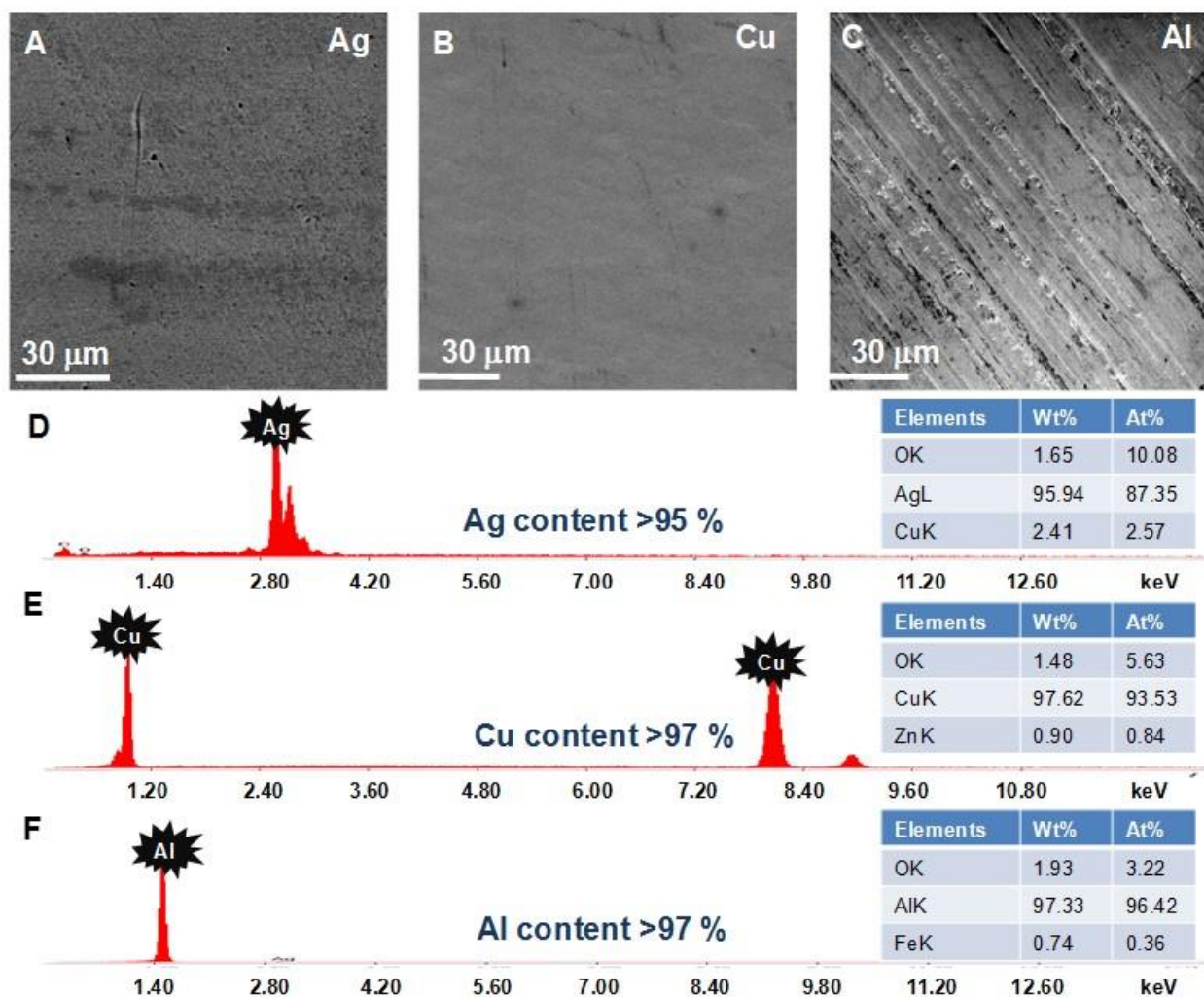


Figure S1: SEM image of A) silver, B) copper and C) aluminium vessels before use. D, E, F) SEM/EDS data of the above. The values are in wt% with some oxygen present in it. As for silver vessel (>95%), the impurities were copper (< 3 %) and oxygen (<2%). For copper vessel (>97%) the impurities were zinc (<1%) and oxygen (<2%) and for aluminum (>97%) it was iron (<1%) and oxygen (<2%).

	Ag	Al	Cu	Mn	Zn	Ni
MQ water	0.0	0.0	1.8	0.0	8.8	0.0
DI water	0.1	0.0	1.8	0.0	3.8	0.0
Tap water	0.1	0.0	1.3	15.9	446.9	0.0

Table S2: Blank concentration of metal ions in MilliQ, de-ionized and tap water. All the results are in ppb.

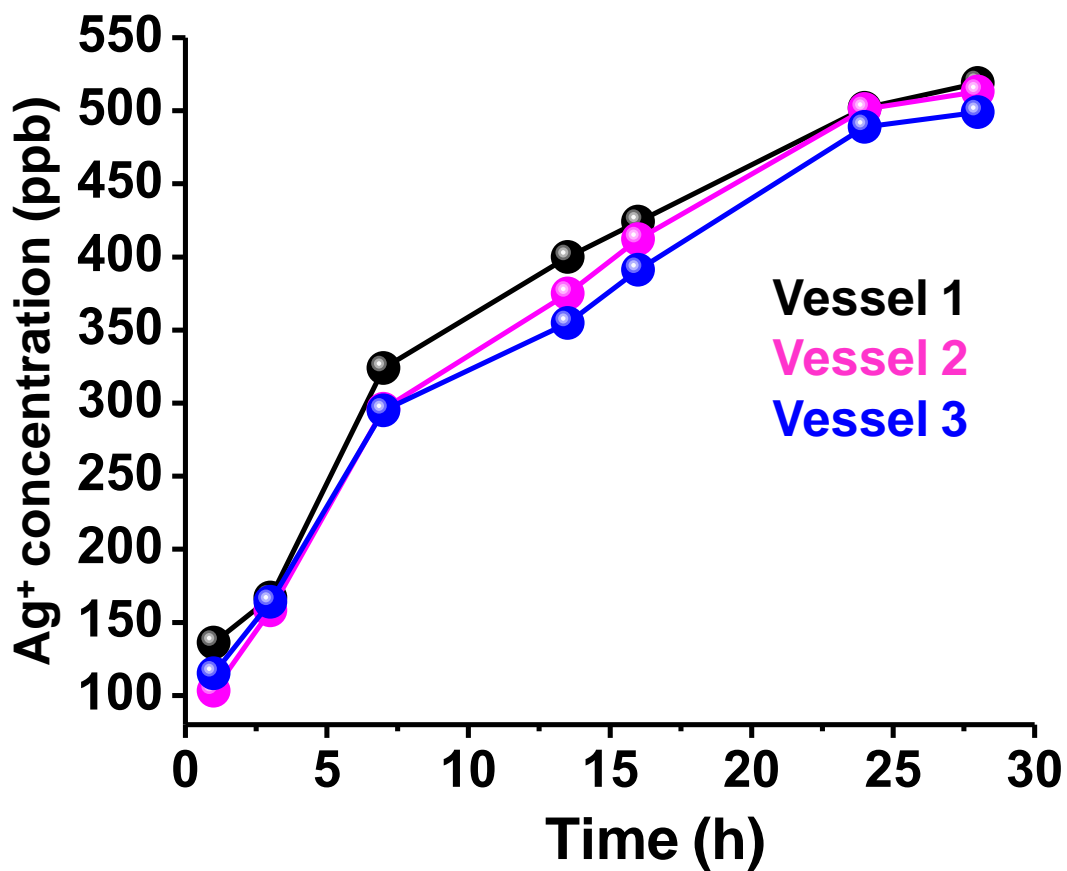


Figure S3: Comparison among time dependent silver release in deionized water at 80°C showing almost similar type of behavior for all three vessels used in this study.

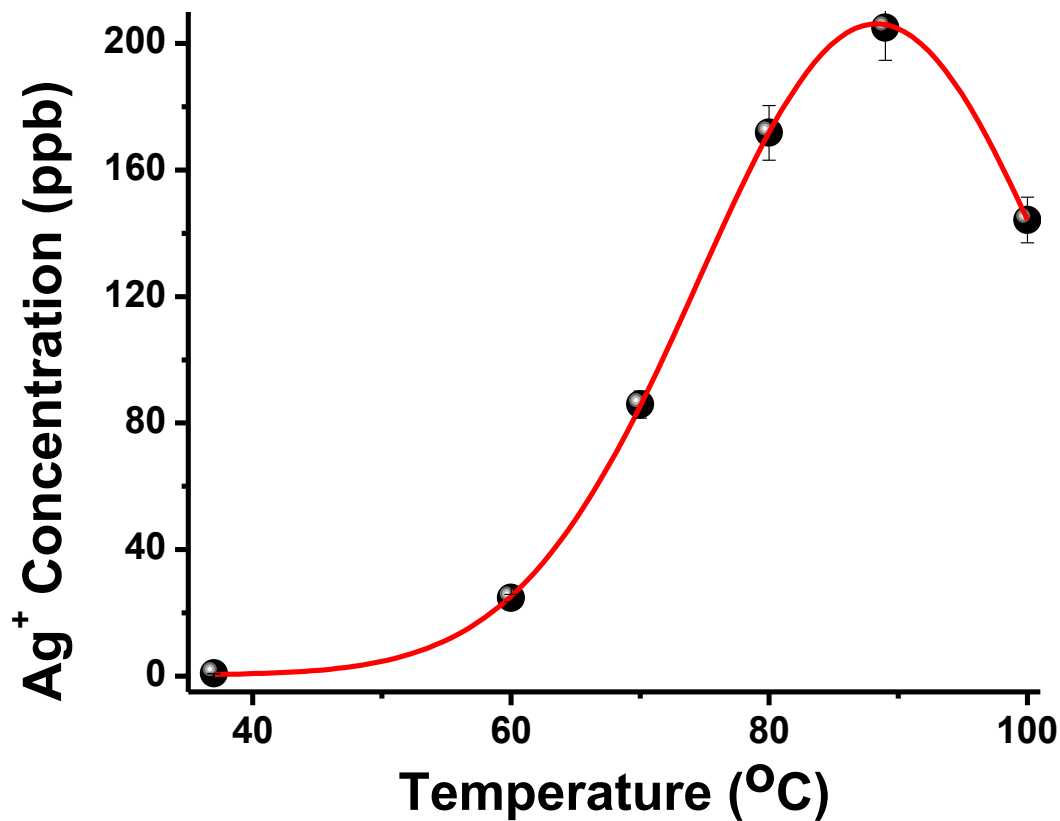


Figure S4: Temperature dependent silver release after 3 h in deionized water showing highest silver release at 90°C. Release at 80°C is comparable with 90°C data. To avoid excessive evaporation of water, we have conducted our all experiments at 80°C. At 100°C water starts boiling and at this temperature liquid and gaseous state exist together. Bubbles formed during heating reduces the available surface area of the silver vessel due to cavitation, which might be the reason for the reduction in silver release. Error bar shows the variation of 9 data points.

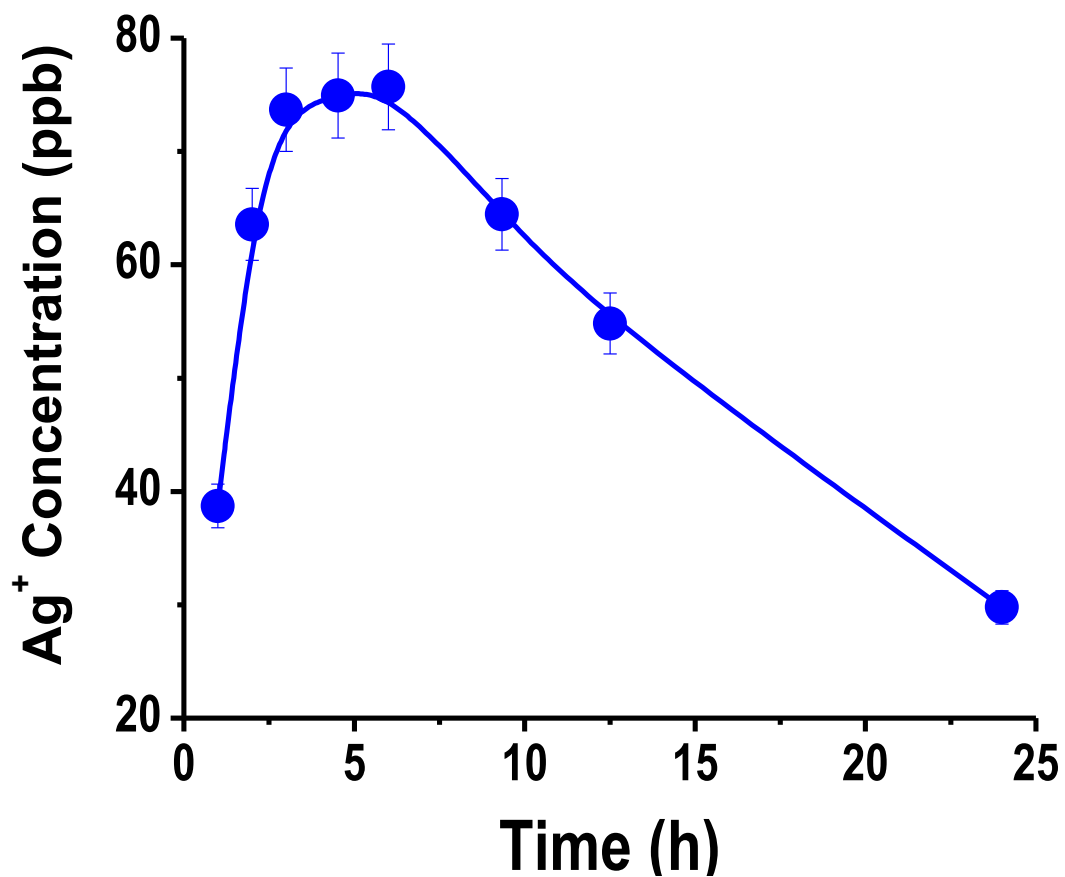


Figure S5: Time dependent silver release in tap water showing gradual increase in silver concentration in water up to 7 hours. After that silver concentration showed constant decrease with time. Error bar shows the variation of 9 data points.

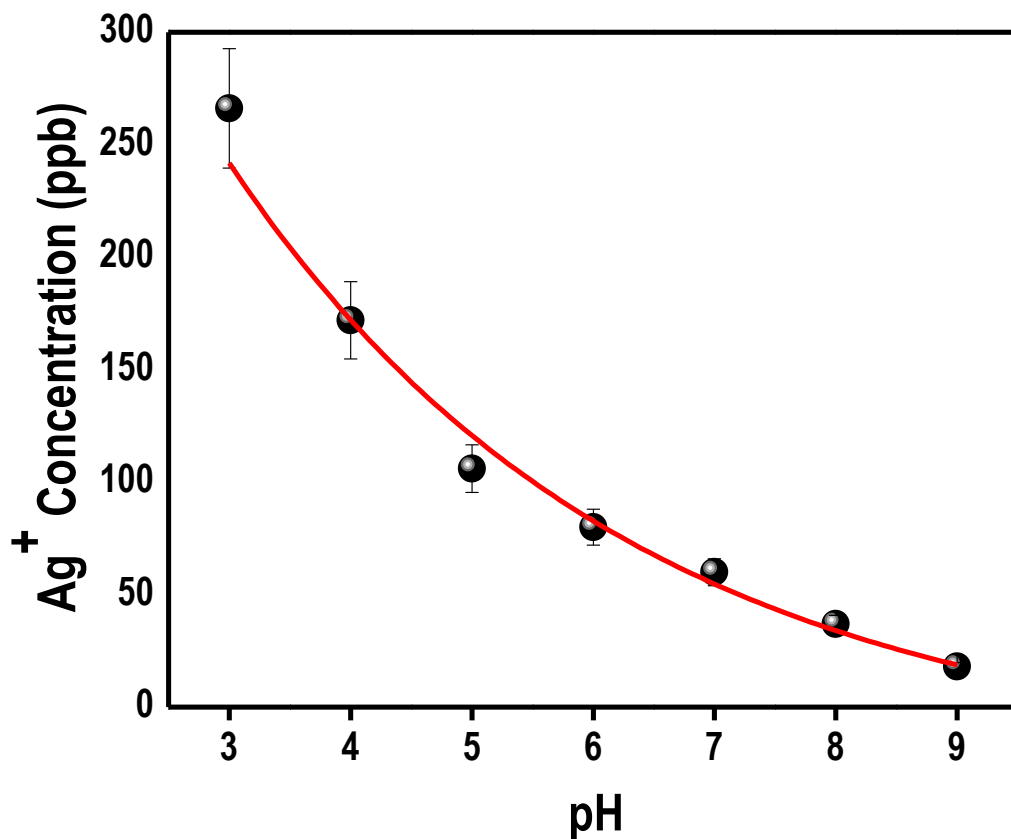


Figure S6: pH dependent study showing enhanced silver concentration of silver in acidic condition in DI water when heated for 1 h at 70°C. Acidic pH was maintained using acetic acid and basic pH was maintained using sodium bicarbonate. To correlate our data to real cooking, we have done rest of our experiments at neutral pH. The error bar represents the variation of nine data points.

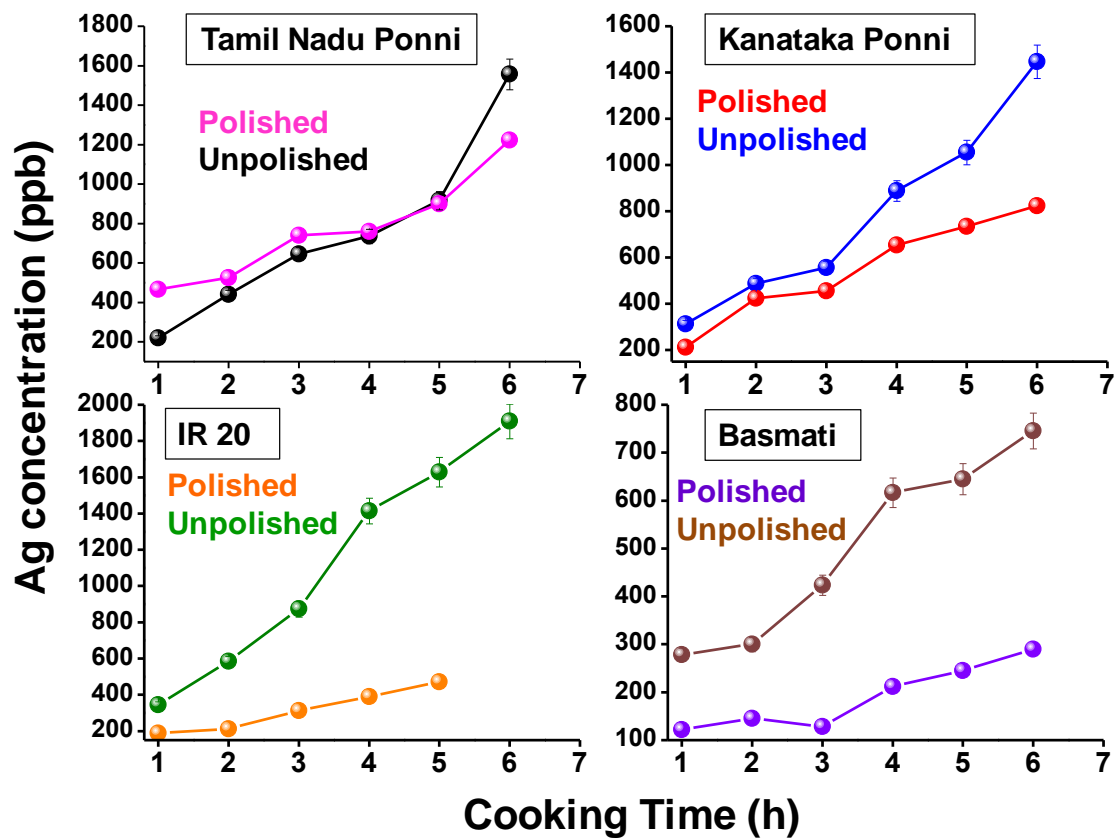
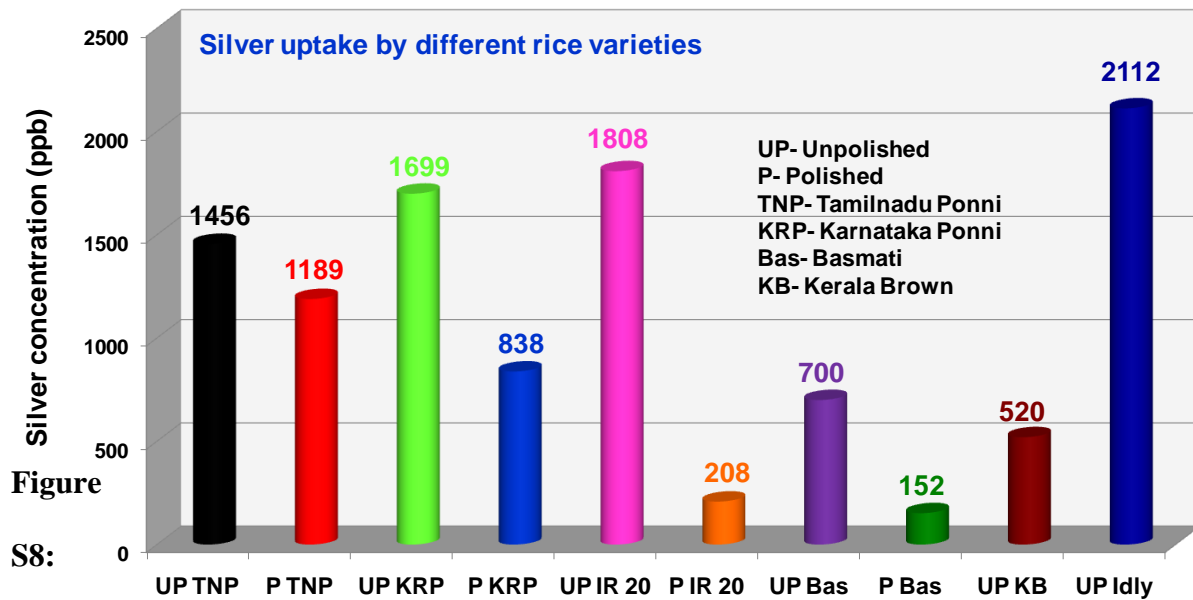


Figure S7: Comparison among several polished and unpolished rice varieties showing that the latter have better silver uptake capacity. Conditions of cooking were the same. Error bar shows the variation of 9 data points.



S8:

Comparison of silver uptake capacity of different rice varieties. All the other experimental conditions were kept the same. In all cases 2g of rice was cooked in 20 mL of DI water at 80°C for 6 h and then digested and silver concentration was analyzed by ICP MS.

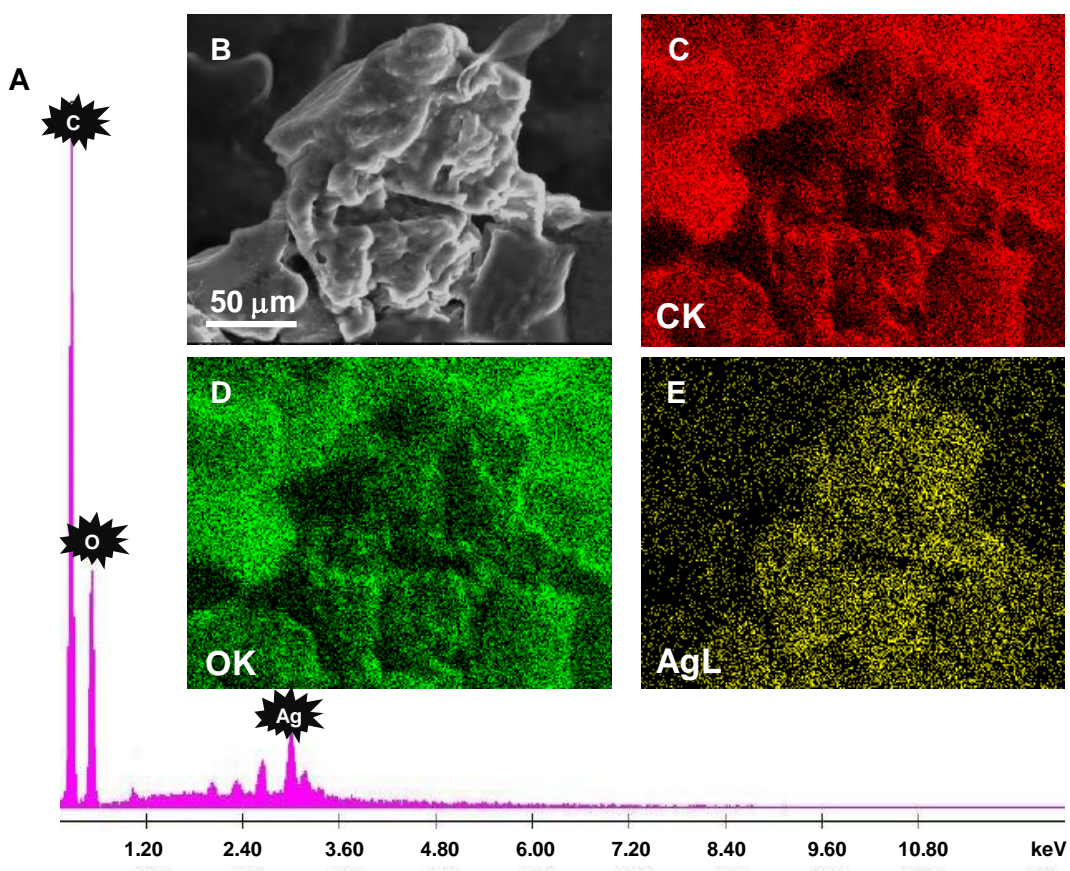


Figure S9: A) SEM/EDS of the silver adsorbed rice showing the uptake of silver. B) The SEM image shows the horizontal cut of the rice section for which elemental mapping was taken. C-E) elemental maps of carbon, oxygen and silver.

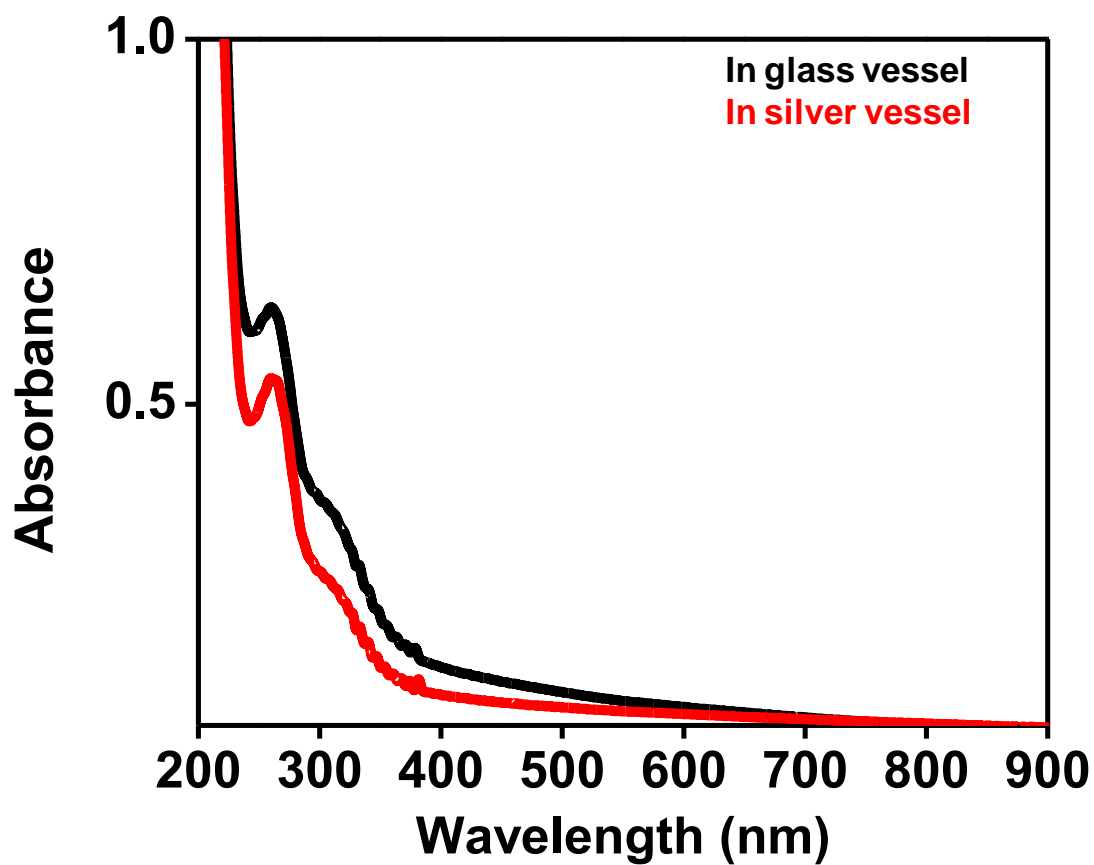


Figure S10: UV-Vis absorption spectra of supernatant solution from rice cooked in glass and silver vessel is showing similar kind of absorption feature. Absence of plasmonic feature confirms that silver nanoparticles are not formed upon interaction of starch and silver.

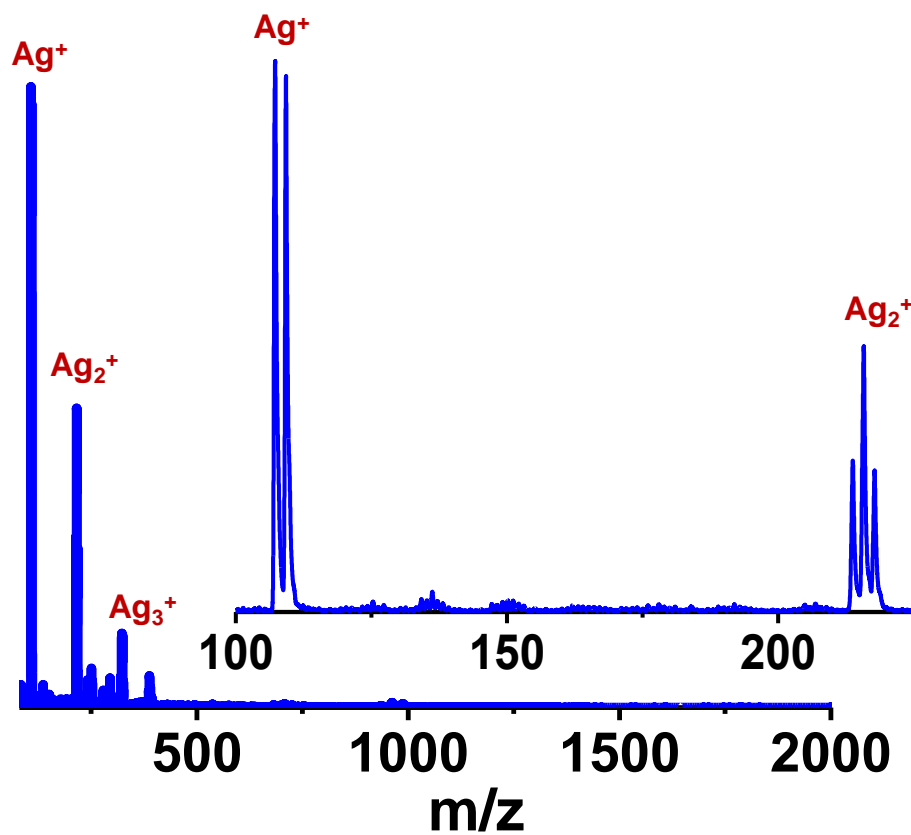


Figure S11: LDI MS of silver saturated rice (dry) in linear positive mode showing the formation of small silver clusters due to laser ablation on silver containing rice. This type of cluster formation is common with silver ion containing samples.

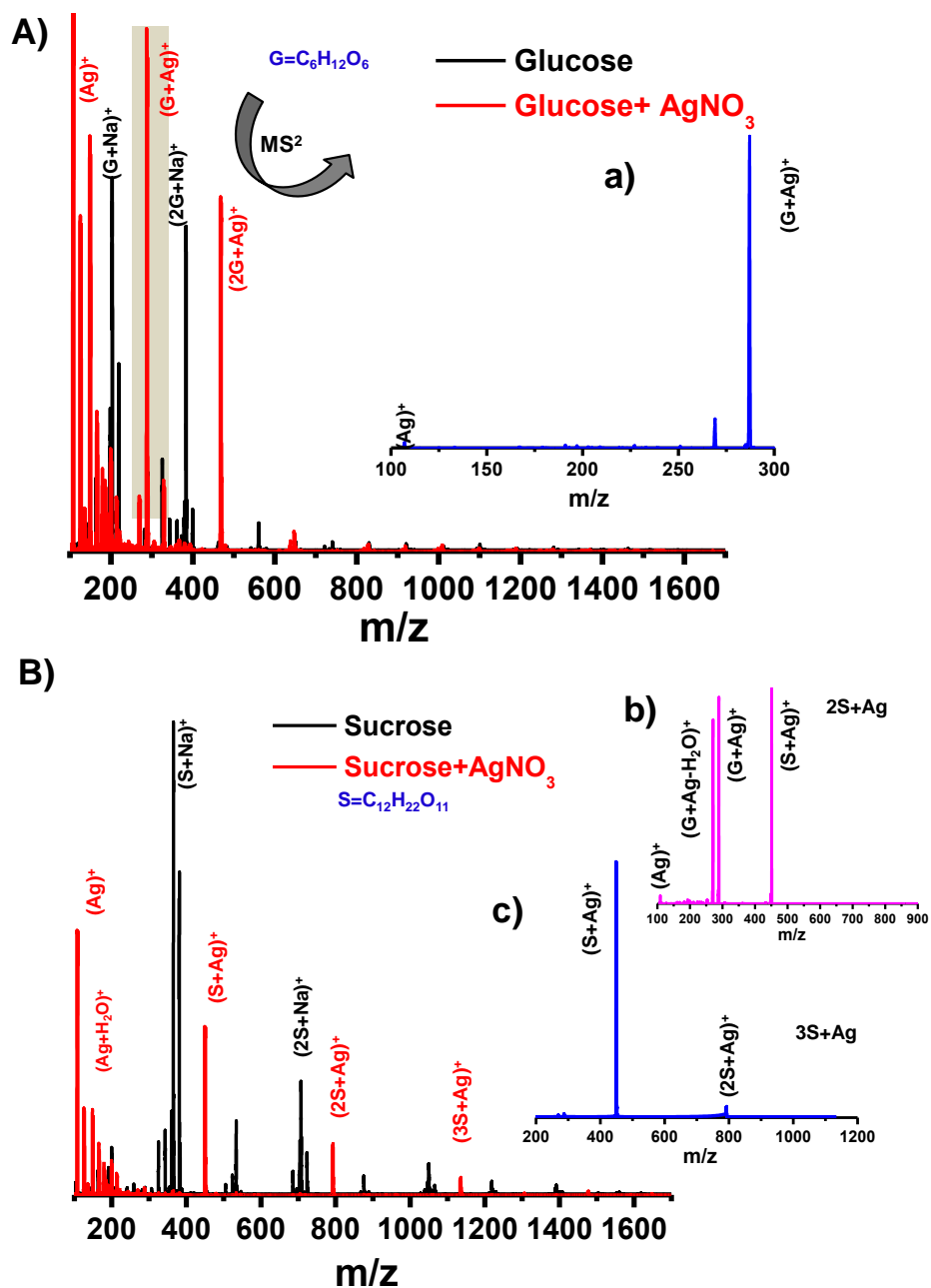


Figure S12: A) Comparative ESI MS of glucose and Ag-glucose complex in positive ion mode showing complexation of silver with glucose. ESI MS/MS of Ag-Glucose complex is shown in the inset a), where one glucose loss was observed to give free Ag^+ ion. B) Similar complexation behavior was observed for sucrose also. ESI MS/MS of dimer and trimer (shown in inset b) and c) are showing similar fragmentation patterns.

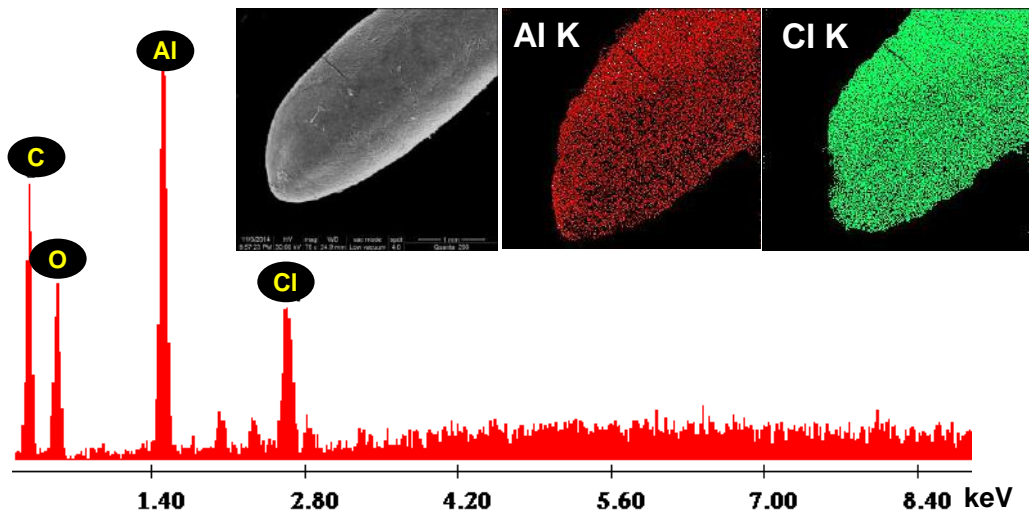


Figure S13: SEM/EDS of dried rice soaked in 1000 ppm aluminium containing solution and the corresponding elemental mapping showing uniform distribution of aluminium throughout the rice.

Nucleolin-aptamer therapy in retinoblastoma: molecular changes and mass spectrometry-based imaging

Nithya Subramanian^{1,2}, Amitava Srimany³, Jagat R Kanwar², Rupinder K Kanwar², Balachandran Akilandeswari¹, Pukhraj Rishi⁴, Vikas Khetan⁴, Madavan Vasudevan⁵, Thalappil Pradeep³ and Subramanian Krishnakumar^{1,6}

Retinoblastoma (RB) is an intraocular childhood tumor which, if left untreated, leads to blindness and mortality. Nucleolin (NCL) protein which is differentially expressed on the tumor cell surface, binds ligands and regulates carcinogenesis and angiogenesis. We found that NCL is over expressed in RB tumor tissues and cell lines compared to normal retina. We studied the effect of nucleolin-aptamer (NCL-APT) to reduce proliferation in RB tumor cells. Aptamer treatment on the RB cell lines (Y79 and WERI-Rb1) led to significant inhibition of cell proliferation. Locked nucleic acid (LNA) modified NCL-APT administered subcutaneously (s.c.) near tumor or intraperitoneally (i.p.) in Y79 xenografted nude mice resulted in 26 and 65% of tumor growth inhibition, respectively. Downregulation of inhibitor of apoptosis proteins, tumor miRNA-18a, altered serum cytokines, and serum miRNA-18a levels were observed upon NCL-APT treatment. Desorption electrospray ionization mass spectrometry (DESI MS)-based imaging of cell lines and tumor tissues revealed changes in phosphatidylcholines levels upon treatment. Thus, our study provides proof of concept illustrating NCL-APT-based targeted therapeutic strategy and use of DESI MS-based lipid imaging in monitoring therapeutic responses in RB.

Molecular Therapy—Nucleic Acids (2016) 5, e358; doi:10.1038/mtna.2016.70; published online 30 August 2016

Subject Category: nucleic acids chemistry aptamers, dnazymes

Introduction

Retinoblastoma (RB) is a childhood eye cancer that constitutes around 3% of all childhood malignancies globally. RB leads to complete vision loss if untreated and causes mortality at advanced stages if not enucleated.¹ Therefore, better treatment modalities are needed for eye salvage and good life by developing targeted therapies specific for RB cells. The retina majorly consists of glycerophospholipids which are further classified into phosphatidylethanolamines (PEs) and phosphatidylcholines (PCs).^{2,3} Recently, lipid imaging using desorption electrospray ionization mass spectrometry (DESI MS) has emerged as a powerful methodology to precisely measure metabolites in tissues and to study lipid changes between normal versus cancerous tissue.⁴ DESI MS-based lipid imaging would potentially assist to study the biology of retinal diseases.

Nucleolin (NCL) is a multifunctional protein that actively participates in the rDNA transcription, translocation of rRNA,^{5,6} growth, and proliferation of cells. It interacts with G-quadruplex structures in the promoter regions of c-Myc, untranslated regions (5' UTRs) of various mRNAs,^{7–9} and microprocessor machinery for the microRNA biogenesis^{10,11} NCL protein expression on the cell surface has been identified in many epithelial cancers.^{8,12,13} The presence of surface NCL in cancer

cells in contrast to the non-neoplastic cells makes it a promising target for the cancer therapy.^{8,14,15} Aptamers are oligonucleotides developed using Systemic Evolution of Ligands by EXponential enrichment (SELEX) method. These molecules possess high affinity towards the target molecules owing to its specific three dimensional structures. Aptamers¹⁶ are utilized as diagnostic and therapeutic tools in oncology. An aptamer against NCL, NCL-APT also known as AS1411 (Antisoma, UK), is a US Food and Drug Administration (FDA)-approved NCL targeting agent. It binds to NCL on the cell surface, preferentially gets internalized, and inhibits cancer cell growth sparing normal cells^{17–19} and hence we utilized this aptamer to study its effect against RB.

DESI MS can potentially grade the stages in cancer, detect the surgical tumor margins, and study lipogenesis in tumor.^{4,20–22} DESI MS-based lipid imaging of cultured RB cells was recently optimized by spotting cells onto Whatman filter paper²³ and this method was utilized for studying the aptamer siRNA chimera-mediated changes in cell lines.²⁴ There is no information on the expression status of NCL in RB and on the use of lipid imaging to study the effect of NCL-APT *in situ*. In this report, we studied the role of NCL in RB and targeted it using a NCL-APT and LNA modified NCL-APT (LNA-NCL-APT). We also studied the NCL-APT influence on

¹Department of Nanobiotechnology, Vision Research Foundation, Kamalnayan Bajaj Institute for Research in Vision and Ophthalmology, Chennai, India; ²Nanomedicine Laboratory of Immunology and Molecular Biomedical Research (NLMIBR), School of Medicine (SoM), Centre for Molecular and Medical Research (C-MMR), Faculty of Health, Deakin University, Geelong, Australia; ³DST Unit of Nanoscience and Thematic Unit of Excellence, Department of Chemistry, Indian Institute of Technology Madras, Chennai, India; ⁴Department of Ocular Oncology and Vitreo Retina, Medical Research Foundation, Sankara Nethralaya, Chennai, India; ⁵Bionivid Technologies, Bangalore, India; ⁶L&T Ocular Pathology Department, Vision Research Foundation, Kamalnayan Bajaj Institute for Research in Vision and Ophthalmology, Chennai, India. Correspondence: Subramanian Krishnakumar, Department of Nanobiotechnology, Vision Research Foundation, Kamalnayan Bajaj Institute for Research in Vision and Ophthalmology, Chennai 600006, India. E-mail: drkrishnakumar_2000@yahoo.com or Jagat R Kanwar, Nanomedicine Laboratory of Immunology and Molecular Biomedical Research (NLMIBR), School of Medicine (SoM), Centre for Molecular and Medical Research (C-MMR), Faculty of Health, Deakin University, Geelong, Victoria 3216, Australia. E-mail: jagat.kanwar@deakin.edu.au Or Thalappil Pradeep, DST Unit of Nanoscience and Thematic Unit of Excellence, Department of Chemistry, Indian Institute of Technology Madras, Chennai 600036, India. E-mail: pradeep@iitm.ac.in

Keywords: cancer therapy; DESI MS imaging; nucleolin aptamer; retinoblastoma xenograft

Received 14 December 2015; accepted 21 July 2016; published online 30 August 2016. doi:10.1038/mtna.2016.70

relevant genes, microRNAs, and lipids expressed on the RB cells using *in vitro* and *in vivo* models. We showed that DESI MS based lipid imaging can help in understanding NCL-APT treatment induced changes in RB.

Results

NCL expression in RB and uptake of NCL-APT

The lack of information on the status of NCL in RB intrigued us to investigate the expression of NCL on RB tumor samples and it was analyzed by qPCR, immunohistochemistry (IHC), flow cytometry, and immunoblotting. The change in NCL mRNA expression across the RB tumors normalized to normal retina varied between 0.45-and 6.56-fold with mean expression levels of 3.94 ± 1.87 -fold. The samples with NCL mRNA upregulated more than twofold (marked by the threshold line) were considered as significant. The RB cell lines showed NCL mRNA upregulation of 4.8-fold in Y79 and 3.0-fold in WERI-Rb1 cells upon normalizing with MIO-M1, a nonmalignant control cell line (Figure 1a). IHC studies of NCL protein expression in 25 cases of RB primary tumor sections showed membrane/cytoplasmic positivity in the RB cells. The healthy cadaveric retinal tissues ($n = 2$) showed faint nuclear staining and no cytoplasmic staining (Figure 1b, i, ii). The staining pattern within the tumor was heterogeneous and on an average, 50% of cells showed positive, and in a few cases, more than 70% of cells were positive for NCL protein (Figure 1b, iii, iv).

Cytoplasmic NCL protein expression levels studied by immunoblotting in both the non-neoplastic retina and RB samples showed overexpression of NCL in the RB tissues.

Densitometry analysis of the blots showed significant upregulation of NCL in cytoplasm of the RB tumor cells (Figure 1c). Ten RB tumors were analyzed by flow cytometry which were found to be highly positive (>60% of cells) for NCL and the respective scatter plot is shown in Figure 1d. The overlay plot shows the expression of NCL in Y79 and WERI-Rb1 cells as analyzed by flow cytometry (Supplementary Figure S1A). AS1411 or NCL-APT has been shown to preferentially internalize into the cancer cells by utilizing the cell surface NCL. Elevated levels of NCL in the cytoplasm and cell surface of the RB tumor cells could thus aid in NCL-APT uptake and functional activity in RB tumor cells respectively. Preferential uptake of FITC labelled NCL-APT was observed in Y79 and WERI-Rb1 cells than MIO-M1 cell line (Supplementary Figure S1B). Also, the cell cycle changes analyzed post-NCL-APT treatment in cell lines showed increase in G0-G1 phase in WERI-Rb1 and arrest in S phase in Y79. MIO-M1 cells did not exert considerable changes in different cell phases (Supplementary Figure S1C). Thus, we were able to observe the differential expression of NCL in the RB cells and cell lines and NCL-APT internalization mediated cell cycle changes.

NCL-APT regulates oncogenic miRNAs in RB

NCL is shown to involve in microprocessor machinery and regulates the DICER expression.¹⁰ As the dicer participation in microprocessor is essential for miRNA expression, we investigated the influence of the NCL-APT on miRNA expression in RB. miR-15a, miR-16, and miR-221 family were earlier reported for their altered expression upon NCL-APT treatment

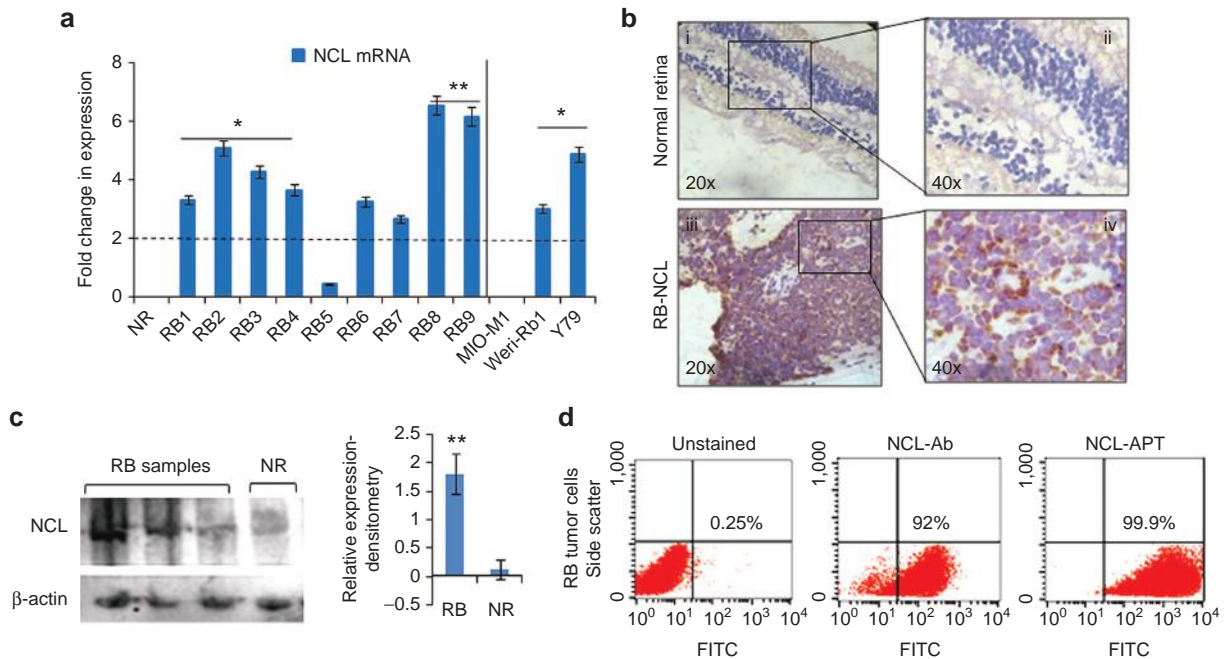


Figure 1 Expression of nucleolin in RB tumor samples and cell lines. (a) Fold changes in gene expression of NCL in various primary cells and cell lines. (b) Immunohistochemistry of the normal retina section (i, ii), RB tissue sections (iii, iv). (c) Expression of NCL in the cytoplasmic fraction of RB tumor tissues by immunoblotting for NCL and β -actin, graph on the right shows the densitometry analysis of tumor samples normalized to normal retina (NR). (d) Scatter plots show the expression of NCL and the NCL-APT binding to RB tumor (RB cells from the enucleated eyes). The error bar represents the SD and the * indicates significance of $P < 0.05$ and ** indicates significance of $P < 0.001$ when compared to the normal retina.

in breast cancer. Thus, we studied the miRNA profiles in RB cell line after 48 hours of treatment with NCL-APT.^{14,15} NCL-APT-treated WERI-Rb1 cells were subjected to miRNA microarray and the global miRNA expression profiling was performed. Hierarchical clustering of the miRNA showed significant ($P < 0.05$) downregulation of 46 miRNAs (Figure 2a).

From the differentially regulated 46 miRNAs, four miRNAs (miR-196b, miR-152, miR-1, and miR-330) and mature miRNAs of oncomir-1 cluster (miR-17–92 cluster) previously reported in RB²⁵ were studied using qPCR for their native expression in RB cell lines by normalizing to MIO-M1 cells. The fold change in expression of the mature miRNAs of miR-17–92 cluster was similar except for miR-17 and miR-18a in both the RB cell lines, while other three miRNAs except miR-330 were highly expressed in Y79 than WERI-Rb1 (Supplementary Figure S2A). These miRNAs upon NCL-APT treatment in both the RB cell lines were found downregulated, with marked effect in WERI-Rb1 cells confirmed by qPCR (Figure 2b). Thus, the miRNA-17–92 cluster and the other miRNAs downregulated in the miRNA profiling were validated for their changes in expression in both the RB cell lines.

NCL-APT perturbs RB *in vitro* and *in vivo*: effect on miRNAs, apoptotic proteins

We next investigated the functional activity of the NCL-APT on the RB cell growth and proliferation. The phenotypic changes monitored post NCL-APT treatment confirmed the cell cycle blockage at S phase (Supplementary Figure S2B). The antiproliferative property of the NCL-APT was tested using dimethyl thiazolyldiphenyl tetrazolium bromide (MTT) assay in RB cell lines and MIO-M1 cell line. Various concentrations of NCL-APT (1, 5, 10, and 20 $\mu\text{mol/l}$) were studied in Y79, WERI-Rb1 and MIO-M1 cell lines and cell viabilities of 40 ± 5.0 , 42 ± 1.2 , and $90 \pm 1.9\%$, respectively were obtained at 20 $\mu\text{mol/l}$ by MTT assay after 48 hours of treatment. A concentration of 10 $\mu\text{mol/l}$ was used to study the molecular effects of NCL-APT as the viability was 74 and 63% in Y79 and WERI-Rb1 cell lines, respectively with uncompromised viability in MIO-M1 cell line (Figure 3a). Thus the inhibition of cell division lead to cytotoxicity leading to decrease in viability of RB cell lines sparing the control retinal MIO-M1 cell line.

As LNA modification of nucleic acids imparts increased serum half life, we studied the stability of LNA modified NCL-APT and found to be more stable than NCL-APT up to 120

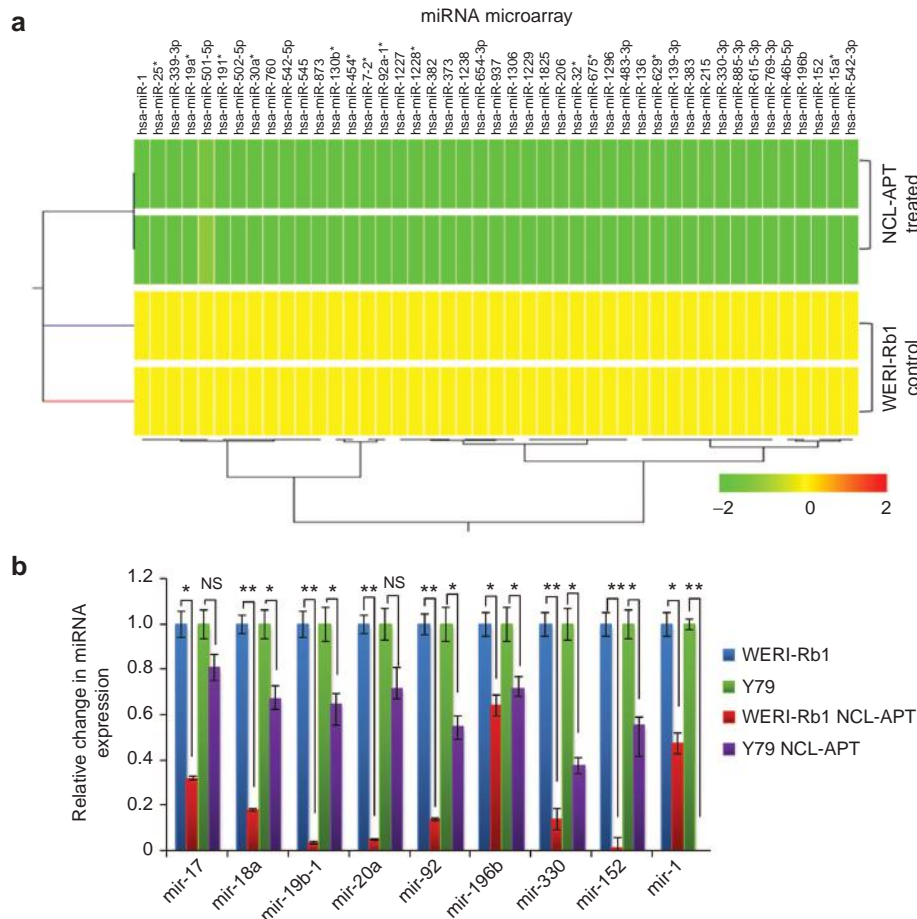


Figure 2 Effect of NCL-APT on miRNA expression. (a) Hierarchical clustering of the miRNAs from the WERI-Rb1 cell line and cells treated with NCL-APT. The colour range indicates the status of expression (yellow being midrange and green being downregulation). (b) Fold changes in the miRNA levels - miR-196b, miR-330, miR-152, miR-1, miR-17, miR-18a, miR-19-1, and miR-20a in Y79 and WERI-Rb1 cell lines treated with NCL-APT normalized with untreated cells.

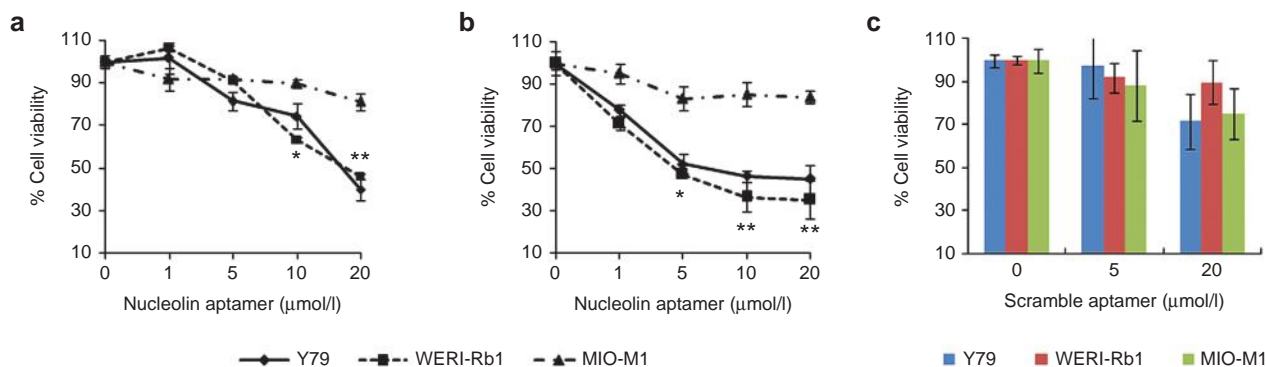


Figure 3 Effect of NCL-APT on cell proliferation. NCL-APT and LNA-NCL-APT were assessed at the concentration of 1, 5, 10, and 20 μmol/l on the cell lines after 48 hours of treatment. Graph showing the percentage cell viability exhibited by the NCL-APT (a) and LNA-NCL-APT (b) on Y79, WERI-Rb1 and MIO-M1 cells at 48 hours using MTT assay. The Scrambled aptamer is treated at the concentration of 5 and 20 μmol/l. (c). Graph showing the cell viabilities upon scrambled aptamer treatment assessed by MTT assay. The mean of triplicate data ± SD are plotted and the * indicates significance of $P < 0.05$, ** indicates significance of $P < 0.001$ and NS indicates not significant.

hours under physiological pH and in serum (**Supplementary Figure S3**). This LNA-NCL-APT having LNA bases at three positions exhibited higher *in vivo* stability with unaltered cytostatic effect and was therefore included in the study.²⁶ The antiproliferative effect of LNA-NCL-APT was assessed in Y79, WERI-Rb1, and MIO-M1 cell lines and found to have 45 ± 6.8 , 35 ± 9.0 , and $84 \pm 5.8\%$ of cell viability after 48 hours of treatment at the dose of 10 μmol/l. The activities were very similar not significantly different from the NCL-APT (**Figure 3b**). The scrambled aptamer carrying C's instead of G's in NCL-APT was tested against the RB and MIO-M1 cell lines. The scrambled aptamer did not affect significantly the cell viability of RB and MIO-M1 cell lines even at 20 μmol/l, thus confirming specificity of NCL-APT activity (**Figure 3c**).

The effect of NCL-APT and LNA-NCL-APT was studied *in vivo* in the RB tumor using Y79 xenograft in nude mice. The Y79 xenograft model has been shown for the aggressive tumor growth characteristics and hence we used Y79 xenograft model than the WERI-Rb1-based xenograft model.²⁷ The Y79 xenografted mice treated with NCL-APT and LNA-NCL-APT subcutaneously (s.c.) near the tumor sites showed tumor growth reduction with the difference in mean tumor volume of 380 and 440 mm³ respectively from the vehicle control group which was 1,289 mm³ (**Figure 4a**). The percentage tumor growth reduction/inhibition calculated were 22.2 and 26% in NCL-APT and LNA-NCL-APT treated s.c. at day 21 (**Figure 4b**). Notably, the effect of LNA-NCL-APT by intraperitoneal (i.p.) injection showed better tumor growth reduction of about 65% with difference in mean tumor volume of 450 mm³ at day 15. The excised tumors from respective treatments showed clear size differences between the tumors (**Figure 4c**).

The NCL-APT and LNA-NCL-APT showed significant anti-tumor activity in Y79 xenograft model at day 18 and day 21. The molecular mechanism behind the tumor growth reduction was addressed by analyzing the tumor mRNA, miRNA and apoptotic protein expression in representative samples of untreated, NCL-APT and LNA-NCL-APT (s.c.) and LNA-NCL-APT (i.p.) treated xenograft tissues. Additionally, serum onco-miRNAs and cytokine levels were studied for correlating the tumor growth changes. Tumor miRNA expression was studied for the miR-17–92 cluster^{25,28,29} and miR-330,

miR-206, miR-196b, and miR-152 that were differentially regulated by NCL-APT treatment in RB cell lines. The miR-196b was downregulated in all the treated samples followed by the miR-330, miR-206, miR-196b, and miR-18a in most of the treated samples (**Figure 5a**). As observed in the miRNA microarray of cells treated with NCL-APT, the above miRNAs were downregulated in the xenografted tumor tissues. This signifies the influence of NCL-APT on the miRNA changes resulting in the changes of tumor growth.

Serum miRNA acts as bio-marker for diagnosis and prognosis of diseases.^{30,31} Data from the RB patients showed that miR-17–92 cluster was overexpressed in serum, and hence changes in this serum miR-17–92 levels were of our interest.³² The relative changes in serum miRNA between normal nude mice and Y79 xenografted mice serum showed elevated levels of miR-18a and miR-19b-1 expression, followed by miR-17. The miR-17 and miR-19b-1 were downregulated in NCL-APT s.c. and LNA-NCL-APT i.p. groups, while miR-18a expression was affected at similar levels in all the treatment groups (**Figure 5b**). The immunoblot analysis of the apoptotic proteins, Bcl2 and survivin showed that their expressions were downregulated in all treated tissues with varying FOXM1 expression in different modes of treatments as observed by densitometry (**Figure 5c**). Thus the NCL-APT treatment *in vitro* and *in vivo* lead to RB growth inhibition mediated by the integrated regulation of mRNAs, oncogenic miRNAs and apoptotic markers.

LNA-NCL-APT-mediated changes in apoptotic marker and cytokine levels: an integrative analysis

The integrated changes in proteome, miRNA and gene expression upon aptamer treatment and its analysis would be able to elucidate the molecular mechanism in RB. Hence we studied the changes in the tumor-apoptotic proteins and cytokines in the xenograft treated with LNA-NCL-APT. The apoptosis markers studied by protein array from the tumor tissues treated with PBS and LNA-NCL-APT showed a significant difference in the extrinsic and intrinsic pathway mediators. There was significant decrease in XIAP, survivin, livin, cytochrome c, HSP27, clusterin and p21 with increase in the levels of Bad, Bcl-xl, Fas, TNFαR, and p53 (**Figure 5d**). Additionally, the cytokines expression was studied for the involvement of

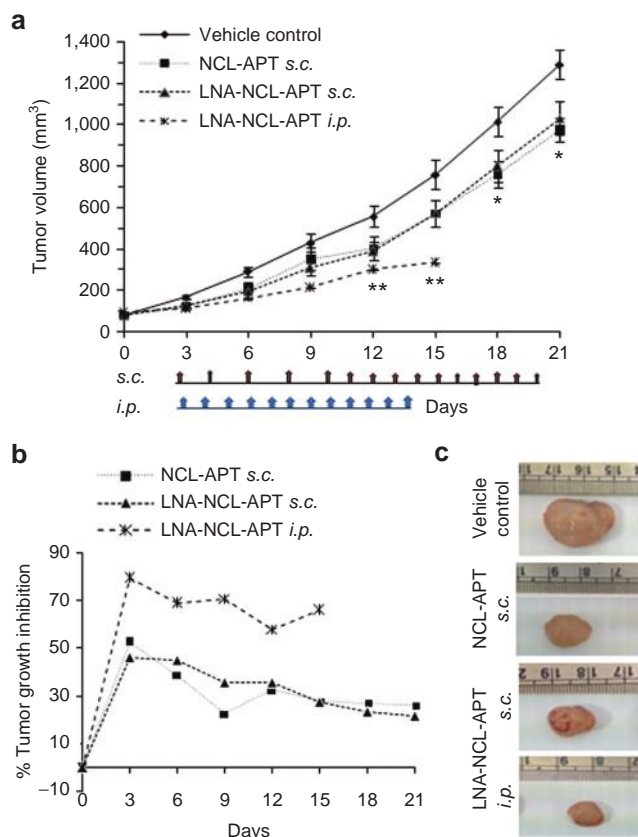


Figure 4 Antitumor effect of NCL-APT and LNA-NCL-APT on Y79 xenograft model. (a) Graph showing the change in percentage tumor growth inhibition of the groups injected with NCL-APT and LNA-NCL-APT subcutaneously near the tumor site and LNA-NCL-APT by intraperitoneal route. Photographs showing the representative animals (b) and excised tumors (c) showing the changes in tumor growth upon treatment by s.c. and i.p. routes. The error bar in panel A represents the SEM and the * indicates significance of $P < 0.05$ and ** indicates significance of $P < 0.001$.

immune mechanisms in tumor regression. Compared to the vehicle control, the LNA-NCL-APT treated groups showed significant ($*P < 0.05$) increase in the expression of CXCL1, CXCL12, TIMP1, MCSF, and i-309 with decreased levels of IL2, ITAC, and CCL2. Also, there was no significant difference in expression of TNF- α and IFN- γ . Thus, there were mixed expression of the chemotactic cytokines and the mitogenic cytokines upon the LNA-NCL-APT treatment (Figure 5e). IHC studies of LNA-NCL-APT i.p. treated tissues also exhibited decreased levels of the nuclear PCNA expression (Figure 5f).

Integrated network modelling and analysis of statistically significant enriched miRNA, genes and pathways revealed key pathways were altered during NCL-APT treatment. The affected pathways were apoptosis, cancer, cell cycle, immune response, and homeostasis, harboring genes like TP53, HSPD1, Bcl2, CXCL12, AKT1, MDM2, p21, CCL2, BIRC5, and IL2. Further, the integrome network of the above affected miRNAs, mRNAs and proteins showed miR-1, miR-17, and miR-206 to be key regulators of transcriptional response and by affecting apoptotic response by NCL-APT treatment (Supplementary Figure S4).

Lipid profiling of xenograft tissues

The lipid content of the cell is important in the cellular metabolism and to maintain the normal behaviour of cells. Phosphatidylcholines are the major lipid present in the cell membrane and altered PCs and choline metabolites levels leads to changes in gene expression and cell proliferation as in the case of malignancy.³³ In the current work, we studied the indirect effect of NCL in PCs levels using aptamer and siRNA strategy. The mass spectra were obtained for the Y79, WERI-Rb1, and MIO-M1 cell lines (Figure 6a) and the peaks observed in DESI MS were identified as PCs by MS/MS and database search. The lipids corresponding to the different PCs are listed in Supplementary Table S1. The high intensity peaks observed in different RB cell lines were m/z 754.6 [PC(32:1)+Na]⁺, 782.6 [PC(34:1)+Na]⁺, 810.6 [PC(36:1)+Na]⁺, and 832.7 [PC(38:4)+Na]⁺ (Figure 6a). The changes in expression of lipids [PC(32:1)+Na]⁺ and [PC(36:1)+Na]⁺ differ significantly from the untreated to NCL-APT and LNA-NCL-APT treated cells of Y79 and WERI-Rb1 (m/z 782.6 and 810.6) (Figure 6b,c). Two other significant lipid peaks, m/z 754.6 [PC(34:1)+Na]⁺ and 832.7 [PC(38:4)+Na]⁺ were also studied in NCL-APT-treated RB cell lines (Supplementary Figure S5B). The effect of NCL on lipid levels was counter verified using silencing strategy. The siRNA against NCL was transfected, studied for NCL downregulation and its effect in lipid levels. Upon NCL downregulation in RB cell lines, the intensities of lipid peaks above studied were reduced (Supplementary Figure S5C). Thus, the use of NCL-APT or silencing NCL has similar effect on the predominantly identified lipids in RB cell lines studied by DESI MS.

To access if there is global alteration of lipid by NCL-APT, we further evaluated the effect of both the NCL-APTs in prostate cancer cell line (PC3). The mass spectrum obtained from PC3 was presented with Y79 tumor xenograft and Y79 cells (Supplementary Figure S6A). The high intensity peaks (m/z 754.6 and 782.6) observed in PC3 cell line were affected upon APT treatment, while MIO-M1 (m/z 782.6 and 832.7) showed less intense changes by LNA-NCL-APT and not by the NCL-APT treatment (Supplementary Figure S6B, C).

The Y79 xenografts treated with NCL-APT and LNA-NCL-APT by s.c. route and i.p. route were subjected to lipid profiling. Analysis of tumor sections showed a decrease in intensities of lipids of m/z 782.6 and 810.6 in the NCL-APT s.c. and LNA-NCL-APT i.p. treated tissues followed by LNA-NCL-APT s.c. treated tissue with insignificant changes in few areas of the tissues (Figure 7). In addition to the peaks studied above, two other lipid peaks m/z 754.6 and 832.7 studied in APT-treated xenograft tissues were found to have similar changes (Supplementary Figure S6D). Overall majority of treated tissues were identified with lesser intensities of lipids with the i.p. mode of treatment showing lowest levels of lipids. The drastic changes in lipid levels proportionately correlates with the aptamer treatment, as the inhibition of lipid synthesis or decrease in lipids levels directly affects cell proliferation. Thus, we found that blocking of NCL function using NCL-APT has affected the lipid levels in the cells, thereby regulating the cell growth.

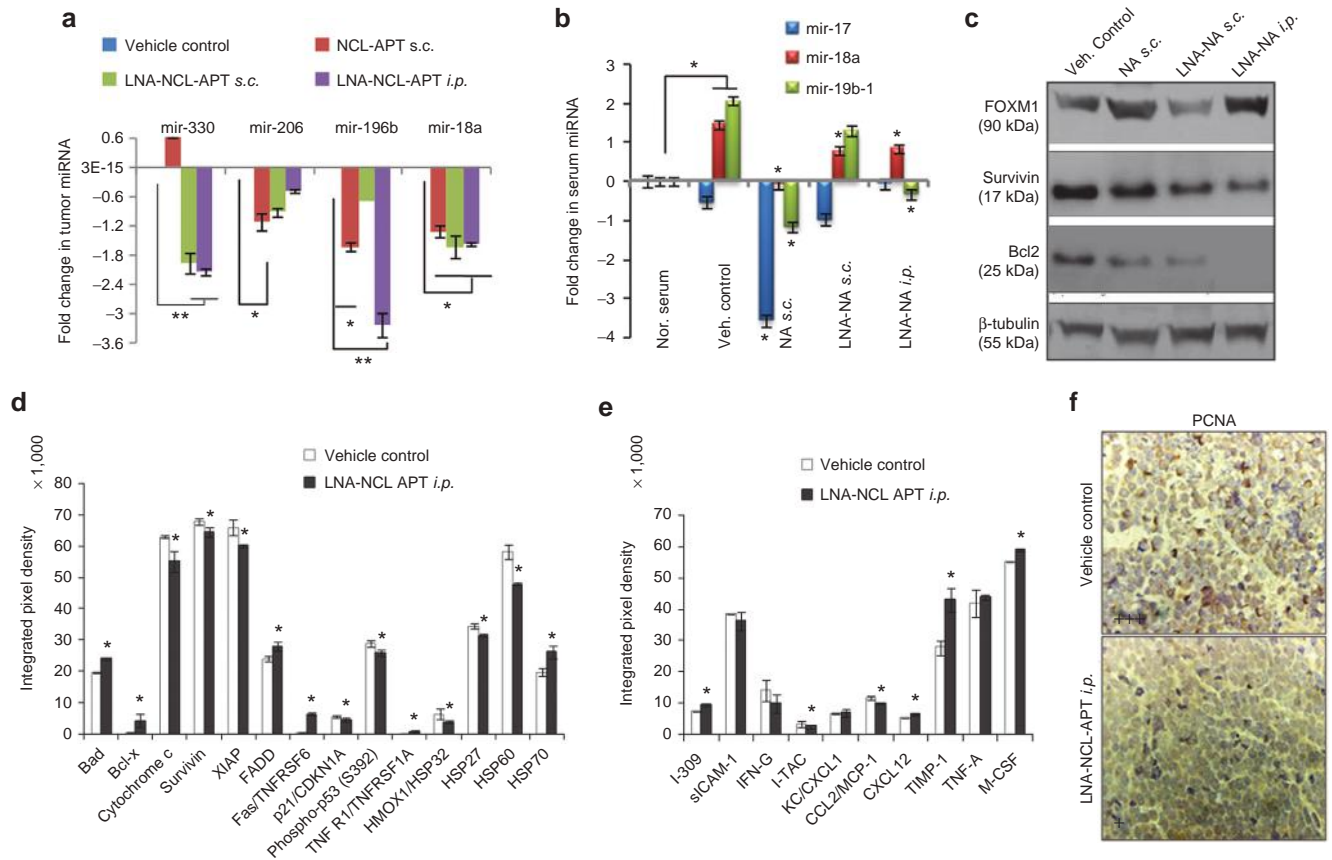


Figure 5 Molecular changes accompanying NCL-APT and LNA-NCL-APT treatment on Y79 xenograft. (a) Graph showing the levels of Y79 xenograft tumor tissue miRNA (miR-330, miR-206, miR-196b and miR-18a) normalized to vehicle control using U6 as internal control. (b) Graph showing the levels of serum miRNA post treatment with nucleolin aptamer. Normal serum (mice without tumor) was used for normalizing the expression levels. (c) Western blotting for Bcl2, Survivin, FOXM1 proteins from xenograft tissues of the control group and treated group tissues. The levels of apoptotic markers (d) in tumor tissue and serum cytokines (e) using protein array. The integrated pixel densities of the spots were quantified using ImageJ software and plotted as graph. The error bar represents the SD and the * indicates significance of $P < 0.05$ and ** indicates significance of $P < 0.001$, for panel A, treated groups were normalized to vehicle control group, for panel B - normal serum was compared to vehicle control, then the vehicle control group was used to analyze the significance in treated groups. (f) IHC for PCNA expression. The images are taken under 40X objective. The intensity of expression is indicated in the bottom left.

Discussion

Our study showed the differential expression of NCL protein on the surface and cytoplasm of RB tumor cells. Targeting NCL using NCL-APT in the RB cell lines lead to downregulation of oncogenic miRNAs and lead to inhibition cell proliferation. NCL-APT and LNA modified NCL-APT-mediated inhibition of NCL, reduced phosphatidylcholine levels as confirmed by DESI MS of aptamer treated RB cells. Functional blocking of NCL from transcription and translation processes concomitantly resulted in the altered gene expression and lipid (PCs) levels. Similarly, the internalized NCL-APT leads to the cell cycle blockage due to the S phase arrest followed by increase in the G0-G1 population. These changes in cell cycle and cell proliferation inhibition are in agreement with the observations reported regarding the G-rich oligonucleotides.^{34,35}

The maintenance of stability of oncogenic mRNAs and miRNAs is one of the essential steps in tumorigenesis. NCL plays a pivotal role in mRNA stabilization and enhanced translation in cancer.^{7,8} Global miRNA profiling of NCL-APT-treated RB

cell line in the current study showed majorly downregulation of miRNAs with a few upregulated miRNAs confirming the importance of the NCL in the miRNA biogenesis.¹¹ We further studied the expression of oncogenic miRNA pertaining to RB, miR-17-92 cluster and found downregulation upon treatment. The differentially expressed miRNA studied includes miR-196b, miR-373, miR-330, miR-152 and miR-1. The observation of miRNA downregulation upon NCL-APT treatment may be related to the regulation at transcription level leading to halt in the miRNA synthesis and processing. The NCL binding to the promoter G-quadruplex structure controls the transcription of c-myc gene.³⁶ The promoter regions of these miRNA were predicted for the presence of G-quadruplex and i-tetraplex structures that could have mediated the effect.³⁷

The tumor suppressor property of miR-152 and miR-1 in ovarian cancers³⁸ and bladder cancer³⁹ were reported earlier and in the current study these miRNAs were downregulated upon NCL-APT treatment, which could be attributed due to the promoter structure. NCL involvement in miRNA promoters, however, needs further investigation. The miR-330 is

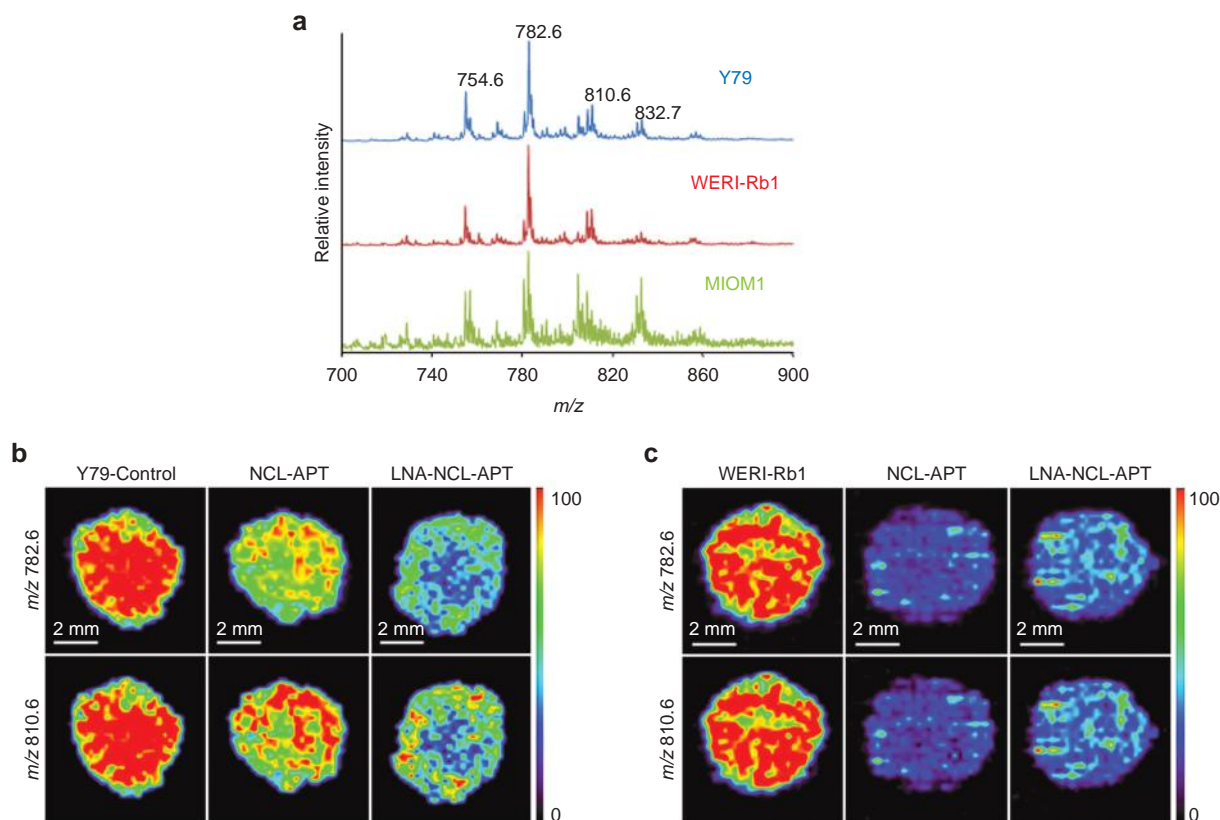


Figure 6 DESI MS imaging of aptamer treated RB cell lines. (a) DESI-MS spectra of Y79, WERI-Rb1 and MIO-M1 cells grown in cell. Cells were washed with 1XPBS twice and spotted on Whatmann membrane and imaged using methanol as solvent using positive mode and data acquired from 50 to 2,000 Daltons. Changes in the lipid expression accompanying the treatment with nucleolin aptamer in RB cell line, Y79 (b) WERI-Rb1 (c).

reported as tumor suppressor miRNA in prostate cancer, but a recent report suggested inverse role in glioblastoma.⁴⁰ The oncogenic role of miR-196b has been studied in glioblastoma and its expression correlated to poor disease prognosis⁴¹ and this miRNA was upregulated in RB tumors too. Thus, the mature miRNAs of established onco-miRNA-1 cluster, miR-17, miR-18a and miR-19b and miR-196b, miR-330, miR-152, miR-206, and miR-1 were found to be downregulated in the RB cell lines upon aptamer treatment.

The *in vivo* studies for evaluating the anti-tumor activity of NCL-APT and LNA-NCL-APT in Y79 xenograft revealed better effect in the i.p. mode of delivery than the s.c. mode of delivery. The NCL-APT and LNA-NCL-APT both showed tumor growth inhibition with later aptamer having 4% better efficacy in tumor inhibition under s.c. mode, while the i.p. mode of LNA-NCL-APT delivery showed 65% of tumor growth inhibition. The absence of the i.p. mode of delivery for NCL-APT in the current study alleviates our ability to appreciate LNA-NCL-APT over NCL-APT. This difference in the tumor reduction suggests that the delivery mode is important to attain better therapeutic efficacy. Intraperitoneal mode has been recognized for the better absorption and availability of substance injected.⁴² Also NCL-APT was delivered earlier studies by both i.p. or s.c. modes in mouse and in patients by continuous infusion method.^{11,43} Thus, the bioavailability of

the LNA-NCL-APT to the tumor could have attributed to the results observed which desires further investigation.

The mechanism behind the antitumor activity of the LNA-NCL-APT was studied by analyzing the tumor miRNAs and serum biomarkers in the i.p. mode of treatment as the efficacy is better than the s.c. mode. The miRNA expression in the treated tumor revealed that there is consistent downregulation of miR-18a and miR-196b in the treated tumors. The decreased expression of the miR-18a and miR-196b could have enhanced the antitumor activity of aptamer in RB.²⁵ The aptamer treatment had downregulated the levels of Bcl2, survivin, and FOXM1 differentially. FOXM1 is overexpressed in cancers, controlled through miRNA expression and cell cycle changes.⁴⁴ Perturbation in cell division by stathmin silencing in RB cell lines showed FOXM1 upregulation.⁴⁵ FOXM1 upregulation has shown to induce genomic instability, leading to induction of p21, p53, and apoptosis of cells.⁴⁶ Thus, our observation of differential regulation of FOXM1 needs further analysis. The protein array supports the apoptotic onset by the decrease of IAPs, increase in Bad and p53. The cytokine levels were also varying with some of the chemotactic attractants getting downregulated with minor or no changes in the levels of the TNF- α and IFN- γ . Thus, the multifunctional NCL protein expressed under cancerous condition modulates various activities.

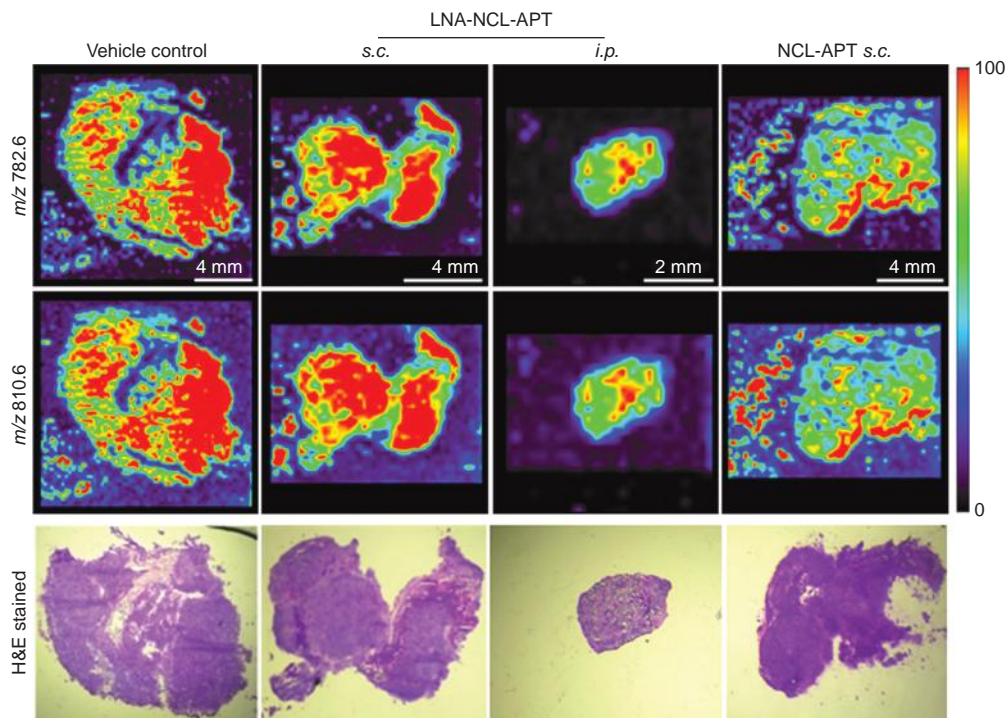


Figure 7 Changes in PC levels upon *in vivo* assessment of NCL-APT and LNA-NCL-APT. (a) DESI MS images of cryosection from the vehicle control and treatment groups. Images represent the distribution of phosphatidylcholines across the tissue sections. (b) H&E stained images of the tissue sections. Images were presented without alteration, acquired at 10X magnification.

DESI MS is extensively used for lipidome analysis thereby discriminating stages of cancer, surgical margins of cancerous to noncancerous regions and tumor heterogeneity.^{47,48} We utilized DESI MS for observing the changes in the intensity of PCs levels upon NCL-APT treatment in RB cell lines and tumor tissues. To check if NCL modulates the PCs levels in other cancers, the effect of NCL-APT was tested using prostate cancer model, PC3 cell line. We confirmed that inhibiting NCL using NCL-APT effectively brought down the PC levels in PC3 cell lines too. Thus, we intended to check this mechanism in the *in vivo* model and the observed results in *in vivo* confirm the role of the NCL in the lipid metabolism using DESI MS. This approach of using DESI MS-based lipid imaging could also monitor the therapeutic progress.

Thus, we hypothesize that perturbing NCL function using NCL-APT impaired lipid synthesis and thereby altered PC levels on the cell membrane. This could indirectly explain the mechanism behind the tumor growth inhibition in the *in vivo* conditions. Similar observations using conditional knock on and knock off mice for the MYCN-oncogene were obtained in the lipid profiling of hepatocellular carcinoma.⁴⁹ Similarly, the importance of changes in lipids for the discrimination of the grades of astrocytoma²¹ evidently showed that DESI MS can be applied in cancer diagnosis. The tear fluids studied earlier had cholesterol, triglycerides, sphingomyelins, PCs, and PEs.⁵⁰ Probably in future, the lipid level changes in the tear fluids could also be analyzed for studying the disease state or therapeutic progression.

To conclude, our data reports for the first time NCL overexpression in RB. The NCL-APT binds preferentially to RB cells

and inhibits cell proliferation. NCL-APT treatment leads to changes in mRNA, miRNA and lipid levels resulting in effective tumor growth inhibition *in vivo*. The NCL-APT treatment reduced the serum onco-miRNAs. Our data also substantiates the use of intraperitoneal mode of delivery and LNA modification for the therapeutic efficacy of NCL-APT. The data confirm the effectiveness of DESI MS based lipid profiling for the monitoring of lipid level changes during treatment. Thus, further studies using orthotopic or intraocular models of RB warrant the use of aptamer in RB therapy. Future research on tear lipidome of RB using DESI MS could regard as a non-invasive method for studying the treatment mediated effects.

Materials and methods

Cell lines and RB sample collection. Y79 and WERI-Rb1 (Riken cell bank, Japan) were cultured in RPMI 1640 medium and MIO-M1 (kind gift from Dr. G. A. Limb) in Dulbecco's modification of Eagle's medium (DMEM), respectively at 37 °C in a 5% CO₂ humidified incubator. RB tumor samples were collected from the freshly enucleated eyeballs, surgically removed as a part of the treatment regimen with written consent from parents/guardian. Normal retina samples were collected from the healthy cadaveric eyes, post corneal transplantation supplied by C U Shah Eye Bank, Medical Research Foundation, Sankara Nethralaya. This study was conducted at Vision Research Foundation, Sankara Nethralaya, India, and was approved by the Vision Research Foundation Institutional Ethics Board (Ethical clearance no: 249B-2011-P).

RB cells were collected in Rosewell Park Memorial Institute (RPMI) media containing 10% FBS, placed on 6-well plate, minced well, passed through 23 gauge needle and the suspended cells were washed and used for assays.

Expression of NCL in cell lines, tumors and NCL-APT uptake. The NCL expression was studied by quantitative polymerase chain reaction (qPCR), flow cytometry, IHC and western blotting on the RB tissues and normal retina. qPCR analysis was performed using SYBR green-based method. We performed flow cytometry to study the expression of surface NCL, on unfixed RB cell lines as well on RB tumor cells obtained from enucleated eyes. IHC was performed on deparaffinized tissue sections, post-antigen retrieval. Western blotting was performed on cytoplasmic lysate for NCL and β -actin. The aptamer binding and uptake was performed on live, fresh, unfixed or nonpermeabilized cells and analysed by flow cytometry.

NCL-APT treatment—miRNA microarray and miRNA regulations. The effect of NCL-APT on Y79, WERI-Rb1 and MIO-M1 cell lines were studied by treating cells with various concentrations of NCL-APT and LNA-NCL-APT (0.5 to 20 μ mol/l) and scrambled aptamer (5 and 20 μ mol/l) using MTT assay. The effective dose or a concentration with lesser cytotoxicity was chosen for further studies. miRNA microarrays were performed in duplicates for WERI-Rb1 untreated and NCL-APT-treated cells. Validation of the miRNAs was performed using RNU6B as normalizing control for small RNA. The aptamer-treated cells were compared to untreated cells and normalized to it. Similarly, the vehicle control samples were used for normalizing the changes observed in the aptamer treated tissue samples.

In vivo experiments: protein array and integrome analysis. Animal study was performed commercially utilizing the facility of Syngene International (Bangalore, India) and experimentations were approved by the Institutional Animal Ethics Committee (IAEC Protocol Approval No: SYNGENE/IAEC/430/10–2013). Following aseptic procedure, Y79 cells, 1×10^7 in 200 μ l of serum free media containing 50% of Matrigel was injected subcutaneously in the back of 5-week-old female nude mice (Hsd: Athymic *Nude-Foxn1nu/Foxn1nu*). Once the tumor was palpable, the animals were randomized into four groups ($n = 6$) and treated with aptamers either s.c. or i.p. with 12.5 nmol/dosing for 21 days. Tumor volume and body weight were measured every 3 days. The excised treated tumor tissues were subjected for mRNA, miRNA, protein arrays. For the integrome analysis, commonly enriched biological categories were taken along with their statistical significance and differentially expressed genes and miRNA involved for downstream integrome network analysis using Bridgelsland Software (Bionivid Technology Pvt Ltd, Bangalore, India) and CytoScape V 2.8 to understand treatment specific differential regulome.

DESI MS of cell lines and xenograft tumor tissues treated with NCL-APT and LNA-NCL-APT. The effect of NCL silencing/

knockdown (siNCL) and NCL-APT on the alteration in lipid profile was studied using DESI MS. A 2D DESI ion source from Prosolia (Indianapolis, IN) was coupled with Thermo Scientific LTQ XL ion trap mass spectrometer (Thermo Scientific, San Jose, CA). The treated cells (5×10^5 cells) were washed with PBS and resuspended uniformly to 15 μ l $1 \times$ PBS, spotted on Whatman 42 filter paper and left for drying in laboratory condition for 5 minutes. The samples were analyzed from the filter paper by DESI MS in positive ion mode using HPLC grade methanol from Sigma-Aldrich (Bangalore, India) as solvent and conditions published earlier.²³ The snap frozen tumor tissues were sectioned using a Leica cryostat and thaw mounted on glass slides and analyzed by DESI MS using the same conditions used for the cell lines. In brief, the following parameters were maintained throughout the DESI MS experiments; spray voltage: 5kV, solvent flow rate: 5 μ l/minute, nebulizer gas pressure: 150 psi, spray angle: 60° to the surface, surface to spray tip distance: 2 mm, atmospheric inlet of the mass spectrometer to spray tip distance: 3 mm. During imaging by DESI MS, a pixel size of 250 \times 250 μ m was chosen for both the cell lines and tissues. For MS/MS experiments, collision induced dissociation (CID) was used.

Statistical analysis. The *in vitro* results are represented as mean \pm SD ($n \geq 3$), while the *in vivo* results are represented as mean \pm standard error of the mean ($n = 6$). Significance was calculated using student's *t*-test (paired, two-tailed) and the *P* values were indicated with * for $P < 0.05$ and ** for $P < 0.001$.

For detailed methods, kindly refer to **Supplementary Section**.

Supplementary material

Table S1. List of masses of the phosphatidylcholines predicted by MS/MS and database search.

Figure S1. NCL expression, NCL-APT uptake and cellular effects on RB cell lines.

Figure S2. miRNA expression and effect of NCL-APT on the morphology of RB cell lines.

Figure S3. Stability and effect of NCL-APT and LNA-NCL-APT in cell lines.

Figure S4. Schematic showing gene regulatory network upon NCL-APT treatment in RB.

Figure S5. Effect of NCL-APT treatment and siRNA against NCL on lipids by DESI MS.

Figure S6. Effect of NCL-APT treatment on lipids by DESI MS. **Supplementary Section.**

Acknowledgments Thanks to Sowmya Parameswaran for critical comments, proof reading of manuscript and Sukanya Mohan for technical help. Core lab facility and Department of Biochemistry of Vision Research Foundation are acknowledged for the use of flow cytometry, fluorescent microscopy and Flurochem Chemiluminescent imaging facilities. Thanks are due to the Nano Mission, Government of India for equipment support. The graduate fellowship from Deakin University (to N.S.), fellowships from CSIR and IIT Madras (to A.S.)

are acknowledged. This work was supported by Department of Biotechnology, India (Grant BT/01/CE1B/11/V/16-(to S.K.)) and Australia-India Strategic Research Fund (BT/Indo-Aus/06/08/2011 (to S.K., J.R.K. and R.K.K.)). The authors declare no conflict of interest.

Author contributions N.S., J.R.K., R.K.K., T.P., and S.K. designed research; P.R. and V.K. performed enucleation; N.S., B.A., and A.S. performed research; N.S., R.K.K., A.S., M.V., T.P., and S.K. analyzed data; and N.S., J.R.K., P.R., V.K., A.S., T.P., and S.K. wrote the paper.

- Dimaras, H, Kimani, K, Dimba, EA, Gronsdahl, P, White, A, Chan, HS *et al.* (2012). Retinoblastoma. *Lancet* **379**: 1436–1446.
- Gülcan, HG, Alvarez, RA, Maude, MB and Anderson, RE (1993). Lipids of human retina, retinal pigment epithelium, and Bruch's membrane/choroid: comparison of macular and peripheral regions. *Invest Ophthalmol Vis Sci* **34**: 3187–3193.
- Martinez, M, Ballabriga, A and Gil-Gibernal, JJ (1988). Lipids of the developing human retina: I. Total fatty acids, plasmalogens, and fatty acid composition of ethanolamine and choline phosphoglycerides. *J Neurosci Res* **20**: 484–490.
- Eberlin, LS (2014). DESI-MS imaging of lipids and metabolites from biological samples. *Methods Mol Biol* **1198**: 299–311.
- Cong, R, Das, S, Ugrinova, I, Kumar, S, Mongelard, F, Wong, J *et al.* (2012). Interaction of nucleolin with ribosomal RNA genes and its role in RNA polymerase I transcription. *Nucleic Acids Res* **40**: 9441–9454.
- Daniely, Y and Borowiec, JA (2000). Formation of a complex between nucleolin and replication protein A after cell stress prevents initiation of DNA replication. *J Cell Biol* **149**: 799–810.
- Abdelmohsen, K, Tominaga, K, Lee, EK, Srikantan, S, Kang, MJ, Kim, MM *et al.* (2011). Enhanced translation by Nucleolin via G-rich elements in coding and non-coding regions of target mRNAs. *Nucleic Acids Res* **39**: 8513–8530.
- Abdelmohsen, K and Gorospe, M (2012). RNA-binding protein nucleolin in disease. *RNA Biol* **9**: 799–808.
- González, V and Hurley, LH (2010). The C-terminus of nucleolin promotes the formation of the c-MYC G-quadruplex and inhibits c-MYC promoter activity. *Biochemistry* **49**: 9706–9714.
- Pickering, BF, Yu, D and Van Dyke, MW (2011). Nucleolin protein interacts with microprocessor complex to affect biogenesis of microRNAs 15a and 16. *J Biol Chem* **286**: 44095–44103.
- Pichiorri, F, Palmieri, D, De Luca, L, Consiglio, J, You, J, Rocci, A *et al.* (2013). *In vivo* NCL targeting affects breast cancer aggressiveness through miRNA regulation. *J Exp Med* **210**: 951–968.
- Koutsoumpa, M and Papadimitriou, E (2014). Cell surface nucleolin as a target for anti-cancer therapies. *Recent Pat Anticancer Drug Discov* **9**: 137–152.
- Krust, B, El Khoury, D, Nondier, I, Soundaramoury, C and Hovanessian, AG (2011). Targeting surface nucleolin with multivalent HB-19 and related Nucant pseudopeptides results in distinct inhibitory mechanisms depending on the malignant tumor cell type. *BMC Cancer* **11**: 333.
- Fujiki, H, Watanabe, T and Suganuma, M (2014). Cell-surface nucleolin acts as a central mediator for carcinogenic, anti-carcinogenic, and disease-related ligands. *J Cancer Res Clin Oncol* **140**: 689–699.
- Hovanessian, AG, Soundaramoury, C, El Khoury, D, Nondier, I, Svab, J and Krust, B (2010). Surface expressed nucleolin is constantly induced in tumor cells to mediate calcium-dependent ligand internalization. *PLoS One* **5**: e15787.
- Megapatche, AP, Erb, U, Büchler, MW and Zöllner, M (2014). CD44v10, osteopontin and lymphoma growth retardation by a CD44v10-specific antibody. *Immunol Cell Biol* **92**: 709–720.
- Bates, PJ, Laber, DA, Miller, DM, Thomas, SD and Trent, JO (2009). Discovery and development of the G-rich oligonucleotide AS1411 as a novel treatment for cancer. *Exp Mol Pathol* **86**: 151–164.
- Destouches, D, El Khoury, D, Hama-Kourbali, Y, Krust, B, Albanese, P, Katsoris, P *et al.* (2008). Suppression of tumor growth and angiogenesis by a specific antagonist of the cell-surface expressed nucleolin. *PLoS One* **3**: e2518.
- Reyes-Reyes, EM, Teng, Y and Bates, PJ (2010). A new paradigm for aptamer therapeutic AS1411 action: uptake by macropinocytosis and its stimulation by a nucleolin-dependent mechanism. *Cancer Res* **70**: 8617–8629.
- Calligaris, D, Caragacianu, D, Liu, X, Norton, I, Thompson, CJ, Richardson, AL *et al.* (2014). Application of desorption electrospray ionization mass spectrometry imaging in breast cancer margin analysis. *Proc Natl Acad Sci USA* **111**: 15184–15189.
- Eberlin, LS, Dill, AL, Golby, AJ, Ligon, KL, Wiseman, JM, Cooks, RG *et al.* (2010). Discrimination of human astrocytoma subtypes by lipid analysis using desorption electrospray ionization imaging mass spectrometry. *Angew Chem Int Ed Engl* **49**: 5953–5956.
- Eberlin, LS, Tibshirani, RJ, Zhang, J, Longacre, TA, Berry, GJ, Bingham, DB *et al.* (2014). Molecular assessment of surgical-resection margins of gastric cancer by mass-spectrometric imaging. *Proc Natl Acad Sci USA* **111**: 2436–2441.
- Srimany, A, Jayashree, B, Krishnakumar, S, Elchuri, S and Pradeep, T (2015). Identification of effective substrates for the direct analysis of lipids from cell lines using desorption electrospray ionization mass spectrometry. *Rapid Commun Mass Spectrom* **29**: 349–356.
- Jayashree, B, Srimany, A, Jayaraman, S, Bhutra, A, Janakiraman, N, Chitipothu, S *et al.* (2016). Monitoring of changes in lipid profiles during PLK1 knockdown in cancer cells using DESI MS. *Anal Bioanal Chem* **408**: 5623–5632.
- Kandalam, MM, Beta, M, Maheswari, UK, Swaminathan, S and Krishnakumar, S (2012). Oncogenic microRNA 17-92 cluster is regulated by epithelial cell adhesion molecule and could be a potential therapeutic target in retinoblastoma. *Mol Vis* **18**: 2279–2287.
- Roy, K, Kanwar, RK, Cheung, CHA, Fleming, CL, Veedu, RN, Krishnakumar, S, *et al.* (2015). Locked nucleic acid modified bi-specific aptamer-targeted nanoparticles carrying survivin antagonist towards effective colon cancer therapy. *RSC Adv* **5**: 29008–29016.
- Chávez-Barrios, P, Hurwitz, MY, Louie, K, Marcus, KT, Holcombe, VN, Schafer, P *et al.* (2000). Metastatic and nonmetastatic models of retinoblastoma. *Am J Pathol* **157**: 1405–1412.
- Conkrite, K, Sundby, M, Mukai, S, Thomson, JM, Mu, D, Hammond, SM *et al.* (2011). miR-17-92 cooperates with RB pathway mutations to promote retinoblastoma. *Genes Dev* **25**: 1734–1745.
- Nittner, D, Lambert, I, Clermont, F, Mestdagh, P, Köhler, C, Nielsen, SJ *et al.* (2012). Synthetic lethality between Rb, p53 and Dicer or miR-17-92 in retinal progenitors suppresses retinoblastoma formation. *Nat Cell Biol* **14**: 958–965.
- Bianchi, F, Nicassio, F, Marzi, M, Belloni, E, Dall'olio, V, Bernard, L *et al.* (2011). A serum circulating miRNA diagnostic test to identify asymptomatic high-risk individuals with early stage lung cancer. *EMBO Mol Med* **3**: 495–503.
- Shwetha, S, Gouthamchandra, K, Chandra, M, Ravishankar, B, Khaja, MN and Das, S (2013). Circulating miRNA profile in HCV infected serum: novel insight into pathogenesis. *Sci Rep* **3**: 1555.
- Beta, M, Venkatesan, N, Vasudevan, M, Vetrivel, U, Khetan, V and Krishnakumar, S (2013). Identification and insilico analysis of retinoblastoma serum microRNA profile and gene targets towards prediction of novel serum biomarkers. *Bioinform Biol Insights* **7**: 21–34.
- Ridgway, ND (2013). The role of phosphatidylcholine and choline metabolites to cell proliferation and survival. *Crit Rev Biochem Mol Biol* **48**: 20–38.
- Edwards, SL, Poongavanam, V, Kanwar, JR, Roy, K, Hillman, KM, Prasad, N *et al.* (2015). Targeting VEGF with LNA-stabilized G-rich oligonucleotide for efficient breast cancer inhibition. *Chem Commun (Camb)* **51**: 9499–9502.
- Xu, X, Hamhuyia, F, Thomas, SD, Burke, TJ, Girvan, AC, McGregor, WG *et al.* (2001). Inhibition of DNA replication and induction of S phase cell cycle arrest by G-rich oligonucleotides. *J Biol Chem* **276**: 43221–43230.
- González, V, Guo, K, Hurley, L and Sun, D (2009). Identification and characterization of nucleolin as a c-myc G-quadruplex-binding protein. *J Biol Chem* **284**: 23622–23635.
- Zhang, R, Lin, Y and Zhang, CT (2008). Greglist: a database listing potential G-quadruplex regulated genes. *Nucleic Acids Res* **36**(Database issue): D372–D376.
- Xiang, Y, Ma, N, Wang, D, Zhang, Y, Zhou, J, Wu, G *et al.* (2014). miR-152 and miR-185 co-contribute to ovarian cancer cells cisplatin sensitivity by targeting DNMT1 directly: a novel epigenetic therapy independent of decitabine. *Oncogene* **33**: 378–386.
- Yoshino, H, Chiyomaru, T, Enokida, H, Kawakami, K, Tatarano, S, Nishiyama, K *et al.* (2011). The tumour-suppressive function of miR-1 and miR-133a targeting TAGLN2 in bladder cancer. *Br J Cancer* **104**: 808–818.
- Yao, Y, Xue, Y, Ma, J, Shang, C, Wang, P, Liu, L *et al.* (2014). miR-330-mediated regulation of SH3GL2 expression enhances malignant behaviors of glioblastoma stem cells by activating ERK and PI3K/AKT signaling pathways. *PLoS One* **9**: e95060.
- Ma, R, Yan, W, Zhang, G, Lv, H, Liu, Z, Fang, F *et al.* (2012). Upregulation of miR-196b confers a poor prognosis in glioblastoma patients via inducing a proliferative phenotype. *PLoS One* **7**: e38096.
- Kelley, DE, Henry, RR and Edelman, SV (1996). Acute effects of intraperitoneal versus subcutaneous insulin delivery on glucose homeostasis in patients with NIDDM. Veterans Affairs Implantable Insulin Pump Study Group. *Diabetes Care* **19**: 1237–1242.
- Rosenberg, JE, Bambury, RM, Van Allen, EM, Drabkin, HA, Lara, PN Jr, Harzstark, AL *et al.* (2014). A phase II trial of AS1411 (a novel nucleolin-targeted DNA aptamer) in metastatic renal cell carcinoma. *Invest New Drugs* **32**: 178–187.
- Wierstra, I (2013). FOXM1 (Forkhead box M1) in tumorigenesis: overexpression in human cancer, implication in tumorigenesis, oncogenic functions, tumor-suppressive properties, and target of anticancer therapy. *Adv Cancer Res* **119**: 191–419.

45. Mitra, M, Kandalam, M, Sundaram, CS, Verma, RS, Maheswari, UK, Swaminathan, S *et al.* (2011). Reversal of stathmin-mediated microtubule destabilization sensitizes retinoblastoma cells to a low dose of antimicrotubule agents: a novel synergistic therapeutic intervention. *Invest Ophthalmol Vis Sci* **52**: 5441–5448.
46. Teh, MT, Gemenetidis, E, Chaplin, T, Young, BD and Philpott, MP (2010). Upregulation of FOXM1 induces genomic instability in human epidermal keratinocytes. *Mol Cancer* **9**: 45.
47. Ifa, DR and Eberlin, LS (2016). Ambient ionization mass spectrometry for cancer diagnosis and surgical margin evaluation. *Clin Chem* **62**: 111–123.
48. Tata, A, Zheng, J, Ginsberg, HJ, Jaffray, DA, Ifa, DR and Zarrine-Afsar, A (2015). Contrast agent mass spectrometry imaging reveals tumor heterogeneity. *Anal Chem* **87**: 7683–7689.
49. Perry, RH, Bellovin, DI, Shroff, EH, Ismail, AI, Zabuawala, T, Felsher, DW *et al.* (2013). Characterization of MYC-induced tumorigenesis by in situ lipid profiling. *Anal Chem* **85**: 4259–4262.
50. Rantamäki, AH, Seppänen-Laakso, T, Oresic, M, Jauhiainen, M and Holopainen, JM (2011). Human tear fluid lipidome: from composition to function. *PLoS One* **6**: e19553.



This work is licensed under a Creative Commons Attribution-NonCommercial-NoDerivs 4.0 International License. The images or other third party material in this article are included in the article's Creative Commons license, unless indicated otherwise in the credit line; if the material is not included under the Creative Commons license, users will need to obtain permission from the license holder to reproduce the material. To view a copy of this license, visit <http://creativecommons.org/licenses/by-nc-nd/4.0/>

© The Author(s) (2016)

Supplementary Information accompanies this paper on the Molecular Therapy–Nucleic Acids website (<http://www.nature.com/mtna>)

Nucleolin-aptamer therapy in retinoblastoma: Molecular changes and mass spectrometry based imaging

1. Supporting information

1.1. SI MATERIALS AND METHODS

RB tumor cells, cell lines –RNA extraction and qPCR

Real time PCR was performed to check the expression levels of NCL in RB tumors vs. normal retina and between the cell lines used in the study. RNA extraction from the tumor cells, normal retina, Y79, WERI-Rb1 and MIO-M1 cell lines was performed using Trizol based method followed by cDNA synthesis using Verso cDNA synthesis kit (ABgene, Epsom, Surrey, United Kingdom) with oligo dT primers and 1 µg of the total RNA, qPCRs were performed using SYBR green based method using ~ 50 ng of cDNA for NCL and β2M, β2-microglobulin. The thermal profiles are initial denaturation at 95 °C for 10 min, cycle denaturation for 95 °C for 10 s, annealing and extension at 60 °C for 1 min. Data collections were set at extension step as well in the melt curve step. The quantitative PCR was performed in Applied Biosystem 7500 by using Sybr-green Dynamo HS master mix (Thermo Scientific, Mumbai, India). The primer sequences for NCL and β2M were as follows; FP: 5'-GACTTCAACAGTGAGGAGGATGCCA-3' and RP: 5'-CAAAGCCGCCTCTGCCTCCAC-3' for NCL and FP: 5'-TATCCAGCGTACTCCAAGA-3' and RP: 5'-GACAAGTCTGAATGCTCCAC-3' for β2M. Other primers used in the study were listed in Table S2. Comparative quantification (normal retina vs. primary RB tumors or cell lines) was determined using the formula $2^{-\Delta\Delta C_t}$ and relative expression values normalized to the β2M endogenous control were used for plotting. Experiments were performed in triplicate for each sample.

Expression of nucleolin on tumors and cell lines

The expression level of NCL was studied by immunohistochemistry (IHC) of the RB tissue sections and normal retina, flow cytometry of the respective cells and by Western blotting of the nuclear and cytoplasmic fractions extracted from the RB and normal retina (NR) cells. IHC was performed on de-paraffinized tissue section, post-antigen retrieval by pressure cooker method, using anti-nucleolin antibody (sc-56640, Santacruz biotech) at 1:200 dilution with Novolink minpolymer detection system (Leica biosystems). Briefly, post-primary block, followed by polymer incubation for 90 min followed by diaminobenzidine (DAB) chromogen based detection. Slides were mounted and observed under light microscope. To check the expression levels of NCL in nuclear and cytoplasmic compartments of RB and NR cells, nuclear and cytoplasmic proteins were extracted following the manufacturer's instruction using Nuclear and Cytoplasmic Extraction Kit (Thermo Scientific, Rockford, USA). Western blotting was performed on nuclear and cytoplasmic lysate for NCL (anti-nucleolin, ab13541, Abcam) and β-actin (raised in mouse, Sigma Aldrich). To study the expression of surface NCL, flow cytometry was performed on unfixed RB cell lines as well on RB tumor cells obtained from enucleated eyes. Briefly, 2×10^5 cells were washed with 1X PBS followed by the addition of rabbit anti-NCL (abcam, 0.8 µg/ml) for 2 h at 4 °C, FITC conjugated anti-rabbit (sc-2012, 1:300 dilution) for an hour followed by washing and flow cytometry analysis.

Cellular uptake of nucleolin aptamer on RB tumor cells and cell lines

The NCL-APT with and without FITC at the 5' end of 5'-GGTGGTGGTGGTGTGGTGGTGGTGG-3' and LNA-NCL-APT with and without Cy5.5 carrying LNA modifications at 3 positions (2 modifications in the termini and one internally) in the NCL-APT sequence was purchased from Sigma Aldrich, India and Exiqon, Denmark respectively. [The scrambled aptamer carrying C's instead of G's in NCL-APT was used as control aptamer.](#) Unlabeled aptamer was used for studying the functional effect of aptamer. The aptamer binding and uptake was performed on live, fresh, unfixed or non-permeabilized cells. Titration using various concentration of aptamer was performed by

flow cytometry (0.5 µM, 1 µM, 5 µM) on Y79 cells. 500 nM and 1 µM were found to be the ideal concentration as it exhibited saturation. 500 nM of aptamer was added to RB tumor cells or cell lines and incubated for 45 min and the cells were thoroughly washed with 1X PBS twice and analysed by flow cytometry.

Treatment of cells with NCL-APT in RB cells

For studying the NCL mediated regulation and cellular events in RB, NCL-APT treatment or knock down of NCL was performed. The effect of NCL-APT on Y79, WERI-Rb1 and MIO-M1 cell lines was studied by treating cells with various concentration of NCL-APT (0.5 µM to 20 µM). The effective dose or IC₅₀ concentration or a concentration with lesser cytotoxicity was chosen for further studies. The RB primary cells were also treated with 10 µM or 15 µM of NCL-APT in complete media for 48 h. In RB primary cells, pEGFP plasmid was transfected using lipofectamine 2000 to evaluate the metabolic activity. The uptake of FITC-NCL-APT on primary cells was also visualized using fluorescent microscopy. 48 h post treatment were collected and subjected to cell cycle, cellular cytotoxicity and cell proliferation assay.

Cell cycle and cell proliferation assay

Cellular events, metabolic activity and the mode of cell death was analysed to understand the mechanism of aptamer action in RB cells. To study the effect of NCL-APT and LNA-NCL-APT aptamers' activity on the cell cycle phases, cell cycle assay was performed using BD cycle-test kit. As per manufacturer's protocol, 48 h treated cells were PI stained. Briefly, cells were washed twice with PBS followed by addition of solution A and incubated for 10 min at RT, solution B 200 µl was added and mixed, incubated for 10 min at RT. Finally 150 µl of PI solution was added and incubated for 10 min at RT and flow cytometry was performed. Cell proliferation was measured by 3-(4, 5-dimethylthiazol-2-yl)-2, 5-diphenyltetrazolium bromide (MTT) assay. Assay was performed on NCL-APT treated primary cells and cell lines. Cells were incubated with 100 µl of media containing 10 µl of MTT (5 mg/ml) for 4 h at 37 °C. Then media containing MTT was removed, 100 µl of DMSO was added to each well and the absorbance was measured at 570 nm. All experiments were performed in triplicate.

Western blotting

The changes in gene expression upon aptamer treatment were confirmed by measuring the protein concentration by Western blotting. The xenograft tissues and cells were lysed in radioimmunoprecipitation assay (RIPA) lysis buffer (50 mM Tris-HCl (pH 7.4), 150 mM NaCl, 1 mM EDTA, 1% Triton X-100, 1% Sodium deoxycholate, 0.1% SDS, 1 mM PMSF and Protease inhibitor cocktail, Sigma Aldrich) for 30 min on ice followed by centrifugation at 12,000 rpm for 10 min at 4 °C. The supernatant containing protein was collected and used. Protein concentrations were measured and an equal concentration was loaded onto 10% or 12% sodium dodecyl sulphate-polyacrylamide gel (SDS-PAGE) and electroblotted onto a nitrocellulose membrane. The membranes were blocked with 5% skimmed milk for an hour at RT and then incubated with primary antibody, rabbit anti-NCL (dilution: 1:250; Abcam), rabbit anti-FOXM1 (dilution: 1:250; Santacruz biotech) or mouse anti-Bcl2 (dilution: 1:200, Imgenex) or mouse anti-survivin (dilution: 1:200, santacruz) for respective blots overnight at 4 °C. For normalizing the protein loading, mouse anti-β-tubulin (dilution: 1:250; Santacruz biotech) or mouse anti-β-actin (dilution: 1:4,000; Sigma Aldrich) was used. The membranes were washed with 1X PBS-T and incubated with horseradish peroxidase (HRP)-conjugated anti-mouse or anti-rabbit (Litchfield et al.) antibody (diluted to 1:2,000; Santa Cruz Biotechnology, Santa Cruz, CA) for 1 h at RT. The blot was subjected to supersignal west femto maximum sensitivity substrate (Thermo Scientific, Rockford, USA) and images were developed by autoradiography or using chemiluminescent detection system (Fluorchem, Protein simple). The blots are representative of triplicate experiments.

Nucleolin-aptamer therapy in retinoblastoma: Molecular changes and mass spectrometry based imaging

High throughput miRNA microarray analysis for WERI-Rb1 NCL-APT treated cells

miRNA microarrays were performed in duplicates for WERI-Rb1 untreated and NCL-APT treated cells. The RNA was extracted from biological duplicates of treated and untreated cells, followed by quality check using bioanalyzer. Hybridization was performed for the biological duplicates. The miRNA labelling was performed using miRNA complete labelling and hybridization kit (Agilent Technologies, Part Number: 5190-0456). The total RNA sample was diluted to 50 ng/ μ l in nuclease free water. About 100 ng of total RNA was dephosphorylated along with appropriate diluted spike in control; (Agilent Technologies, MicroRNA Spike-In Kit, Part Number 5190-1934) using calf intestinal alkaline phosphatase (CIP) master mix (Agilent Technologies, Part Number: 5190-0456) by incubating at 37 °C for 30 min. The dephosphorylated miRNA sample was denatured by adding dimethyl sulfoxide and heating at 100 °C for 10 min and transferred to ice-water bath. The ligation master mix (Agilent Technologies, Part Number: 5190-0456) containing cyanine 3-pCp was added to the denatured miRNA sample and incubated at 16 °C for 2 h. The cyanine 3-pCp labelled miRNA sample was dried completely in the vacuum concentrator (Eppendorf, Concentrator Plus, Catalog Number: 5305000) at 45 °C to 55 °C for 2 h. The dried sample was re suspended in nuclease free water and mixed with hybridization mix containing blocking solution (Agilent Technologies, Part Number: 5190-0456) and Hi-RPM hybridization buffer (Agilent Technologies, Part Number: 5190-0456) and incubated at 100 °C for 5 min followed by snap chill on ice for 5 min. The samples were hybridized on the human miRNA version 3 array (Slide no: 252182715127). The hybridization was carried out at 55 °C for 20 h. After hybridization, the slides were washed using gene expression wash buffer 1 (Agilent Technologies, Part Number 5188-5325) at room temperature for 5 min and gene expression wash buffer 2 (Agilent Technologies, Part Number 5188-5326) at 37 °C for 5 min. The slides were then washed with acetonitrile for 30 s. The microarray slide was scanned using Agilent scanner (Agilent Technologies, Part Number G2565CA). The data was further analyzed using GeneSpring software.

Real-time quantitative reverse transcription PCR of miRNAs

The effect of NCL-APT on miRNA expression of the cells was detected by quantifying the mature miRNAs using reverse transcription real-time PCR. All reagents, including the TaqMan microRNA individual assays hsa-miR-17 (assay ID 002308), hsa-miR-18a (assay ID 002422), hsa-miR-19b-1 (assay ID 002425), hsa-miR-20a (assay ID 000580), hsa-miR-92 (assay ID 002137), hsa-miR-330 (assay ID 000544), hsa-miR-373 (assay ID 000561), hsa-miR-196b (assay ID 002215), hsa-miR-1 (assay ID 000385), hsa-miR-152 (assay ID 000474), hsa-miR-206 (assay ID 000510), the TaqMan microRNA Reverse Transcription Kit and the TaqMan Universal PCR Master Mix without AmpErase UNG were purchased from Applied Biosystems (Joyvel, Chennai, India) and Solaris qPCR Gene Expression Master Mix (Cat. No. AB4352B, ABgene, Thermo Scientific). Quantification was performed following the manufacturer's protocol starting with 100-250 ng of the total RNA per cDNA synthesis. The RNU6B probe was employed to normalizing miRNA levels in untreated to treated samples. The ABI PRISM 7500 Real-time machine (Applied Biosystems) was used. The innate expression of mature miRNAs of the miR-17-92 cluster was studied on MIO-M1, Y79 and WERI-Rb1 and normal retina. Similarly the levels of expression of miR-330, miR-196b, mir-152 and miR-1 in RB tumors were studied and compared with the normal retina and the MIO-M1 cell line.

In vivo experiment: Y79 xenograft study

Animal study was performed by utilizing the facility of Syngene (Bangalore, India) and experimentations were approved by the Institutional Animal Ethics Committee (IAEC Protocol Approval No: SYNGENE/IAEC/430/10-2013). Animals were maintained in a

controlled environment with ambient temperature, humidity and light, fed with irradiated rodent diet, RO filtered potable water and housed group wise. Following aseptic procedure, 1×10^7 human retinoblastoma cells (Y79) resuspended in 200 μ l of serum free media containing 50% of Matrigel was injected subcutaneously in the right flank or back of the 5 week old female nude mice (Hsd: Athymic *Nude-Foxn1nu/Foxn1nu*). Once the tumor was palpable, the animals were randomized into 4 groups with 6 animals per group, based on tumor volume (TV \approx 80 mm³) and dosed with sterile water for injection for vehicle control or NCL-APT (12.5 nmol/animal) or LNA-NCL-APT (12.5 nmol/animal) subcutaneously near the tumor surrounding area in 2 cycles of treatment and additionally a group with *intraperitoneal* (*i.p.*) injection of LNA-NCL-APT (12.5 nmol/animal). For the *s.c.* group, cycle 1 consisted of alternate day dosing from day 0 to 14 and cycle 2 for daily dosing between day 17 to 24. The *i.p.* group were given alternate day dosing till 4 days followed by daily dosing from day 5 to 14. The body weights and tumor volume were measured once every three days and % change in body weight was calculated. Tumor volume was determined by two-dimensional measurement with a vernier caliper; the length (L) and width (W) of the tumor was measured. Tumor volume (TV) was calculated using the following formula: tumor volume (mm³) = $L \times W^2 / 2$, where, L = length (mm), W = width (mm). Mean and standard error of mean (SEM) were calculated for individual groups and plotted as graph. Tumor growth inhibition was calculated using the formula: $TGI = (1 - T/C) \times 100$; where T = (mean TV of the test group on Day_x - mean TV of the test group on Day₀) and C = (mean TV of the control group on Day_x - mean TV of the control group on Day₀).

Serum miRNA isolation and real time qPCR

Serum miRNA acts as biomarker for the RB disease progression, especially the mir-17-92 cluster. For studying the changes in the serum miRNA levels, the isolation of serum miRNA was performed using Plasma/Serum circulating and exosomal RNA purification kit (Slurry Format) by following manufacturer's protocol from n=2, of each group studied and additionally normal serum from nude mice was also included. Briefly, by mixing the serum (100 μ l) with PS Solution A, which contains the separation matrix followed by PS Solution B and ethanol are then added, and the mixture is centrifuged. PS Solution C is then added to the pellet, and the slurry is loaded onto a provided mini filter spin columns. This is followed by washing of the bound RNA to remove the remaining proteins and other impurities. Finally, the purified circulating RNA is eluted into the 75 μ l of elution buffer. As mentioned in the real time PCR section, qPCR of the mature miRNA of miR-17-92 cluster was performed and Hs-18s rRNA was used for normalizing the fold expression.

Real time qPCR and Western blotting of the xenograft tumor tissues

For studying the changes in the cancer stem cell markers, apoptotic and oncogenes' mRNA level, qPCR was performed from the cDNA transcribed from the total RNA of tumor tissues (n=2 per group) extracted using RNeasy Qiagen kit method. qPCR was performed for the mature miRs of miR-17-92 cluster and for the miRNAs deregulated upon NCL-APT treatment (miR-330, miR-196b, miR-152 and miR-1). Western blotting was performed on the tumor tissues (n=2 per group) lysed with RIPA buffer and analysed for the expression of FOXM1, Bcl2, Survivin and β -tubulin (antibodies from Santa Cruz biotech) following the protocol given above.

Protein array for apoptotic markers and cytokines

To study the effect of LNA-NCL-APT aptamer treatment (*i.p.* mode of injection) on inflammatory response and the apoptotic pathway, protein arrays were performed—Mouse cytokine array panel A (catalog no. ARY006) and Human apoptosis array (catalog no. ARY009) (R&D Systems, Abingdon, UK) following the manufacturer's instruction. The xenograft mouse (vehicle control and LNA-NCL-APT treated for 15

Nucleolin-aptamer therapy in retinoblastoma: Molecular changes and mass spectrometry based imaging

days) serum samples and the tumor tissues lysate were normalized in their protein concentration and used for the array. The arrays were performed at a same time; similar conditions were applied and developed together using chemidoc XRS⁺ instrument (BioRad) at once exposure. The integrated pixel density of the spots and background were measured using the ImageJ software with the microarray profile plugin and signal normalization was performed. The differences between the duplicate spots were used for calculating the standard deviation and expressed as error bar in the histogram plot.

1.1. Supplementary figures

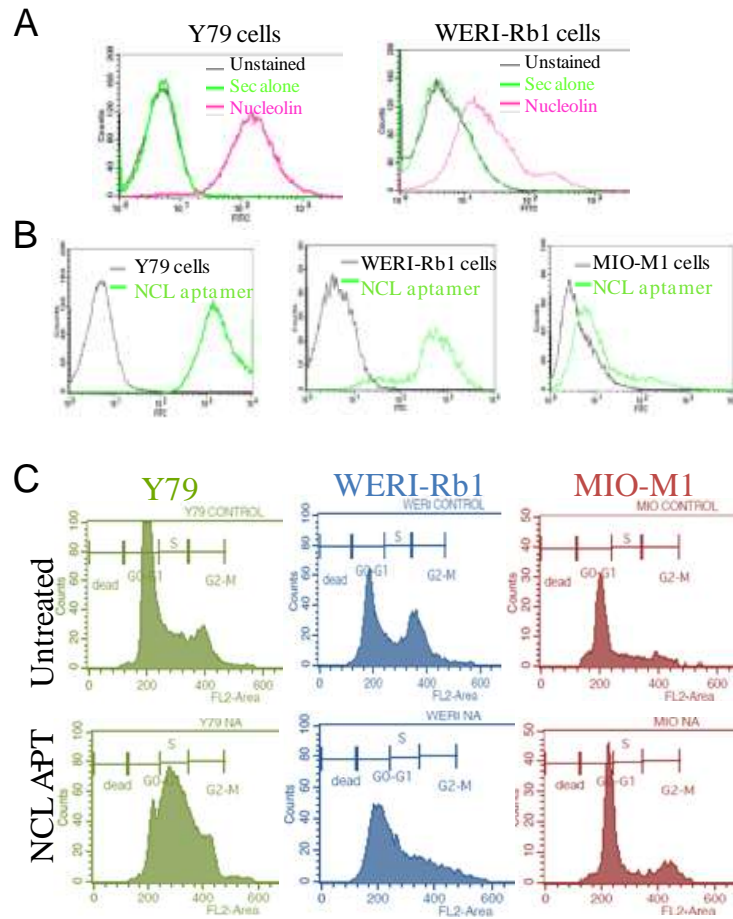


Figure S1. NCL expression, NCL-APT uptake and cellular effects on RB cell lines. A. Histogram overlay plots showing the expression of NCL in Y79 and WERI-Rb1 cell lines. B. Histogram overlay plots showing the binding of NCL-APT to MIO-M1, WERI-Rb1 and Y79 cell lines. The NCL-APT was used at concentration of 500 nM. C. Cell cycle changes in RB cell lines upon NCL-APT treatment. D. Graph representing the percentage viability of RB cell lines and MIO-M1 cells upon treatment with Scrambled aptamer.

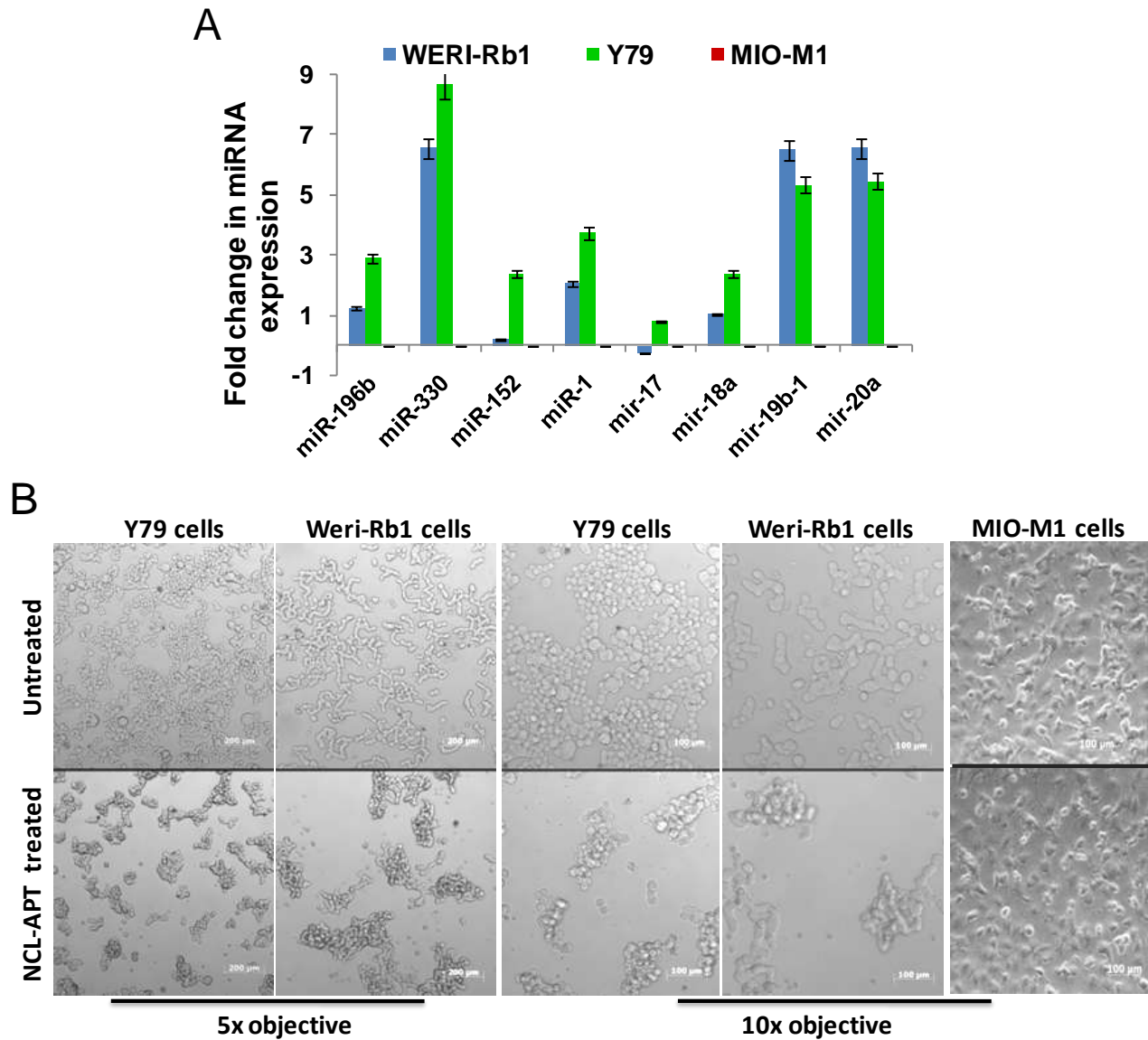


Figure S2. miRNA expression and effect of NCL-APT on the morphology of RB cell lines. A. Fold changes in the miRNA levels - mir-196b, mir-330, mir-152, mir-1, mir-17, mir-18a, mir-19-1 and mir-20a in RB cell lines normalized with MIO-M1. B. Phenotypic changes accompanying treatment of Y79, WERI-Rb1 and MIO-M1 cell lines with NCL-APT. The images shown are acquired at 5x and 10x objectives.

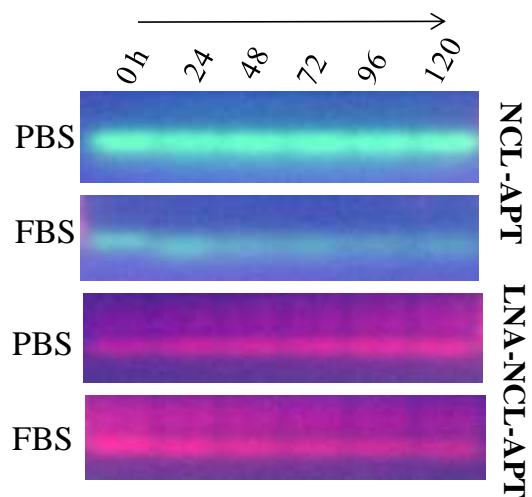


Figure S3. Stability and effect of NCL-APT and LNA-NCL-APT in cell lines. A. Stability of the NCL-APT and LNA-NCL-APT assessed by electrophoresing the aptamer reactions tested in the 1X PBS and 100% FBS at $pH7.0 \pm 0.2$ upto 120 h.

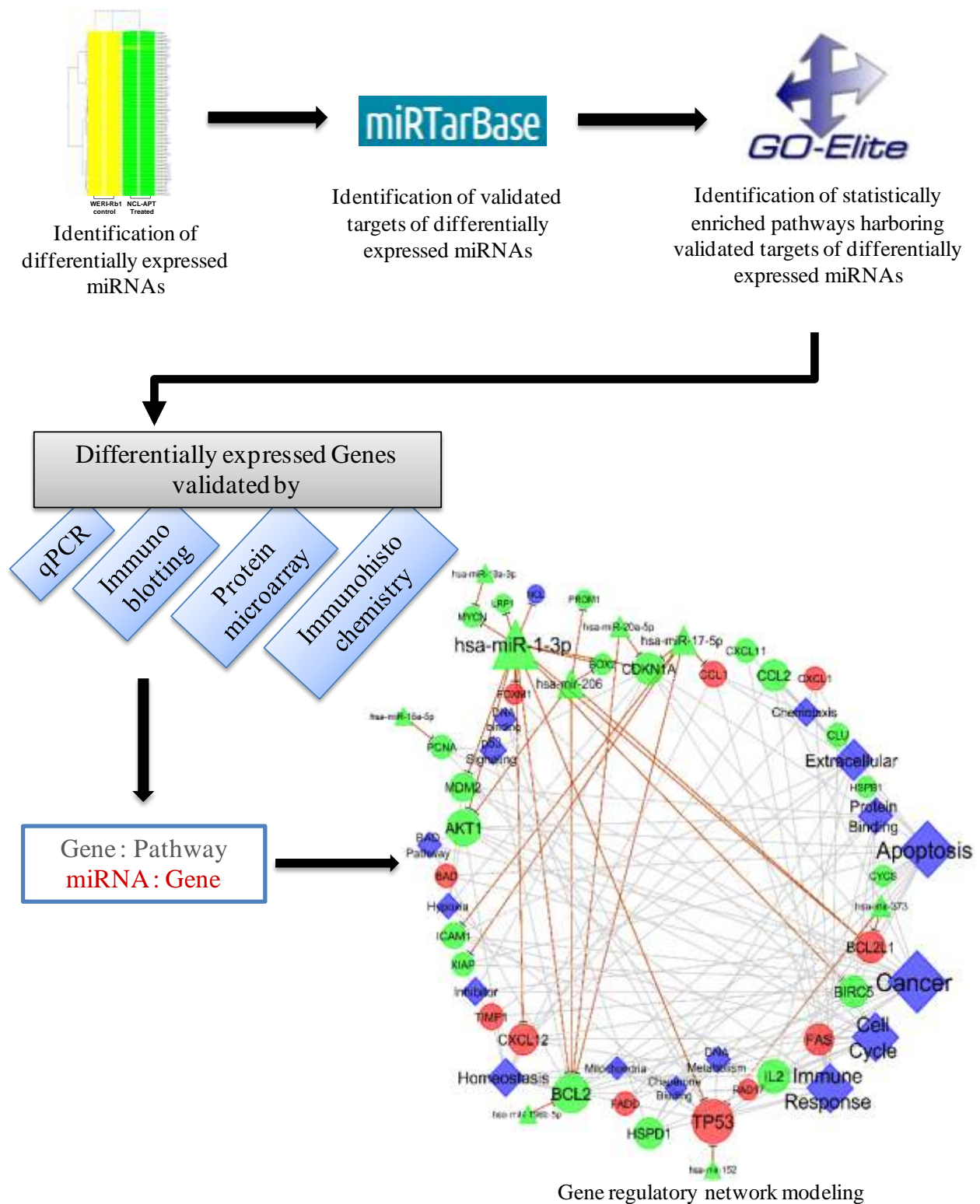


Figure S4. Schematic showing gene regulatory network upon NCL-APT treatment in RB. The flow of work shows right from miRNA microarray data to gene expression analyzed and validated to finally generate network model. Integrome regulatory network (shown at the end) depicts key pathways, genes and miRNAs (denoted by bigger the size to smaller the size) that underlays the transcriptional regulatory change established by NCL-APT treatment. Genes and miRNA is colored by their fold changes upon treatment with; upregulation indicated by red color and downregulation indicated by green color.

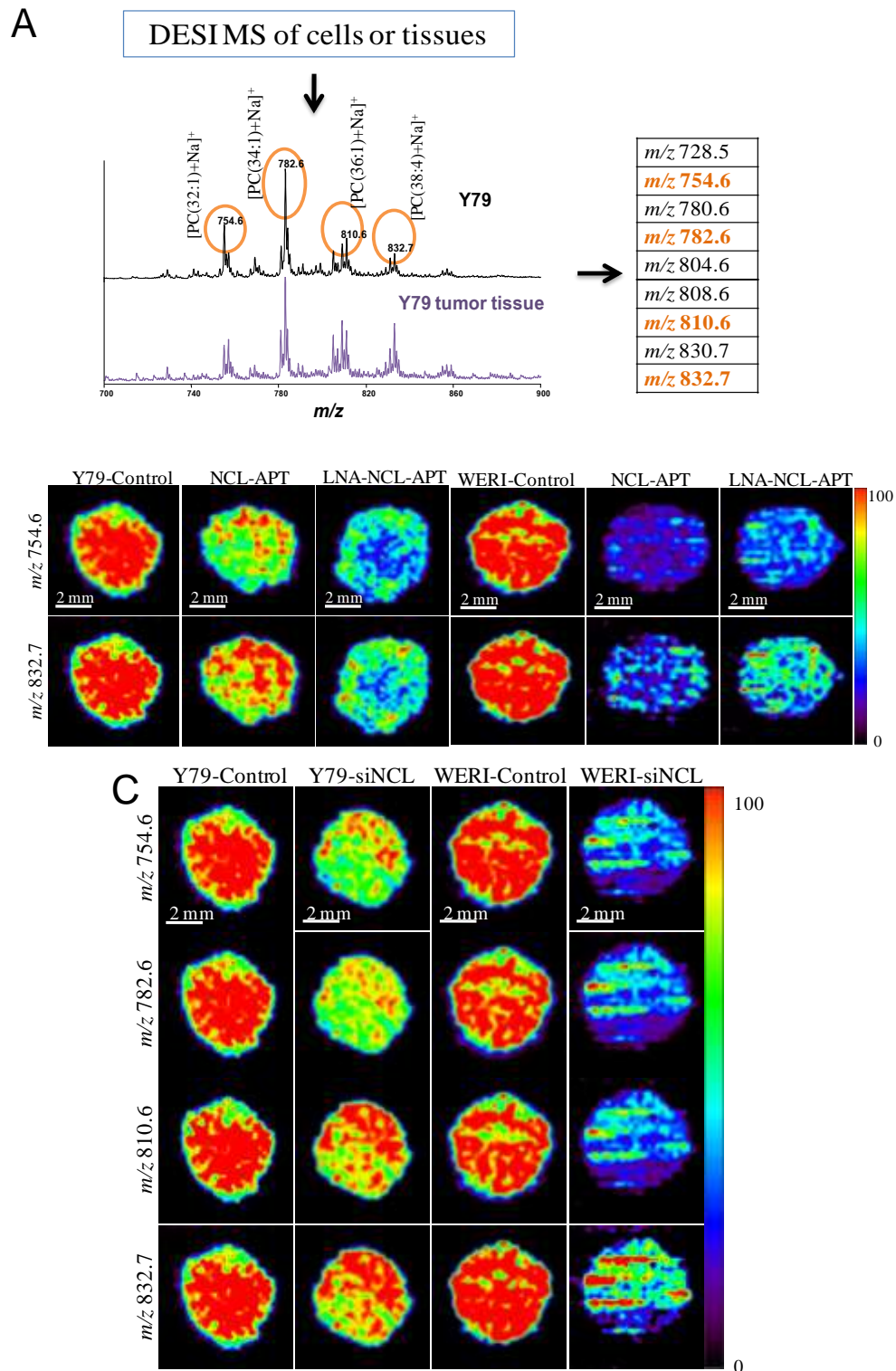


Figure S5. Effect of NCL-APT treatment and siRNA against NCL on lipids by DESI MS. A. DESI MS spectra obtained from cells spotted on Whatman 42 filter paper with major peaks highlighted and the list of peaks studied further are shown on right. B. DESI MS images of Y79 and WERI-Rb1 cells showing changes in m/z 754.6 and 832.7 upon NCL-APT and LNA-NCL-APT treatment. C. DESI MS images of Y79 and WERI-Rb1 cells transfected with siRNA against NCL showing changes in m/z 754.6, 782.6, 810.6 and 832.7.

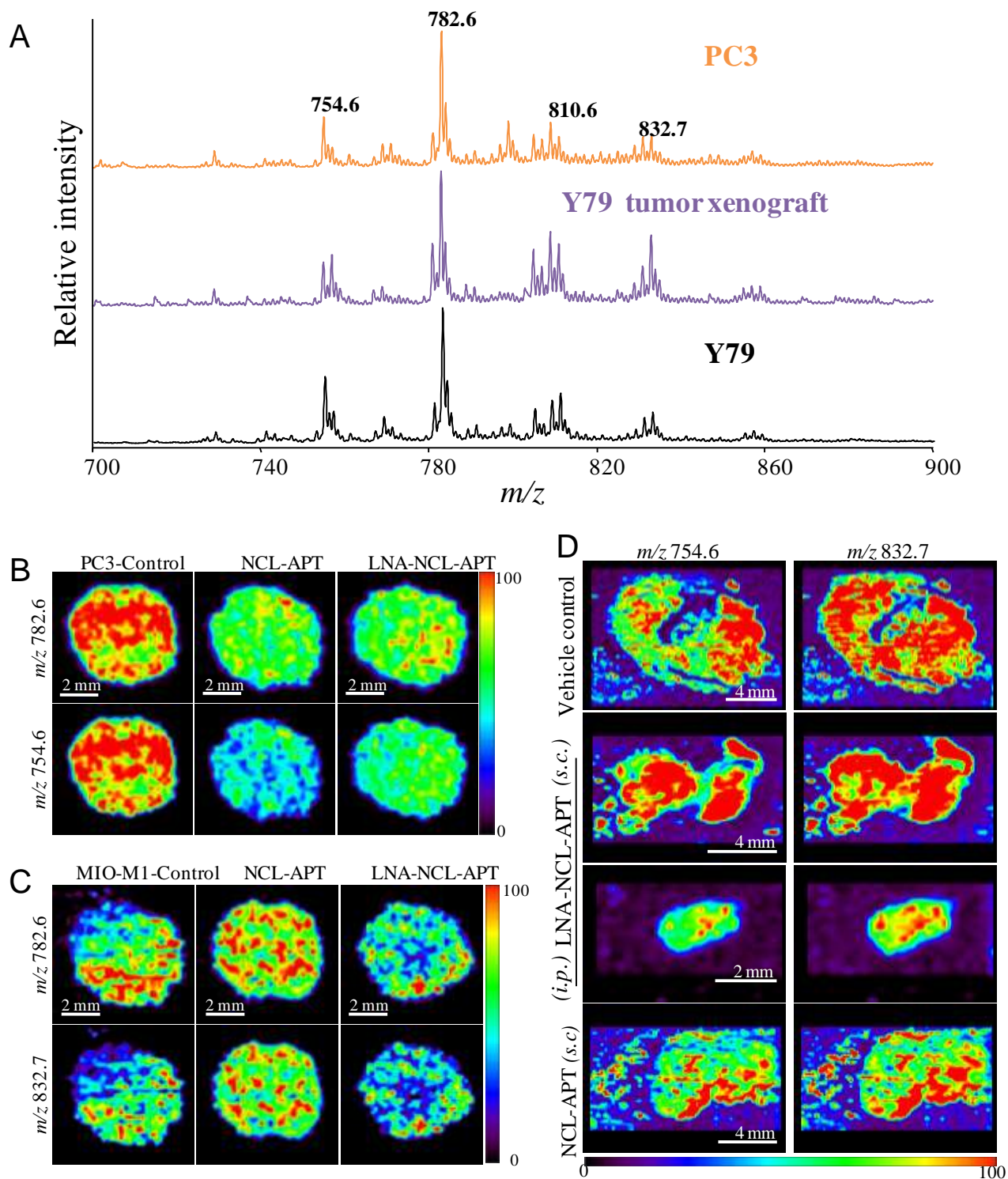


Figure S6. Effect of NCL-APT treatment on lipids by DESI MS. A. DESI MS spectra of PC3, Y79 tumor xenograft and Y79 cells. DESI MS images from PC3 (B), MIO-M1 (C): untreated or treated with NCL-APT (10 μ M) or treated with LNA-NCL-APT (10 μ M) for 48 h. D. DESI MS images of Y79 tumor tissues of the vehicle control, NCL-APT (s.c.), LNA-NCL-APT (s.c.) and LNA-NCL-APT (i.p.). Images represent the distribution of different lipids (PCs) across the cells and tissue sections.

Table S1. List of masses of the phosphatidylcholines predicted by MS/MS and database search

Mass: Phosphatidylcholines
<i>m/z</i> 728.5: [PC(30:0)+Na] ⁺
<i>m/z</i> 754.6: [PC(32:1)+Na] ⁺
<i>m/z</i> 780.6: [PC(34:2)+Na] ⁺
<i>m/z</i> 782.6: [PC(34:1)+Na] ⁺
<i>m/z</i> 804.6: [PC(36:4)+Na] ⁺
<i>m/z</i> 808.6: [PC(36:2)+Na] ⁺
<i>m/z</i> 810.6: [PC(36:1)+Na] ⁺
<i>m/z</i> 830.7: [PC(38:5)+Na] ⁺
<i>m/z</i> 832.7: [PC(38:4)+Na] ⁺

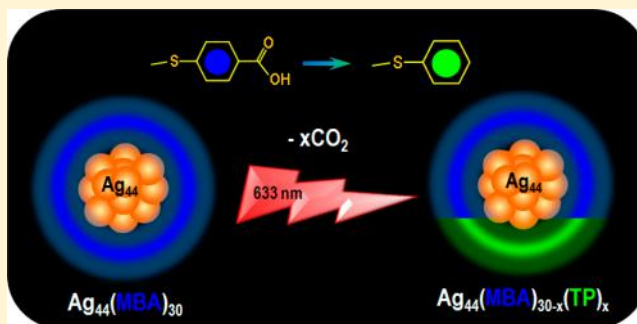
Toward a Janus Cluster: Regiospecific Decarboxylation of $\text{Ag}_{44}(\text{4-MBA})_{30}@\text{Ag}$ Nanoparticles

Indranath Chakraborty, Anirban Som, Tuhina Adit Maark, Biswajit Mondal, Depanjan Sarkar, and Thalappil Pradeep*

DST Unit of Nanoscience (DST UNS) & Thematic Unit of Excellence (TUE), Department of Chemistry, Indian Institute of Technology Madras, Chennai 600036, India

Supporting Information

ABSTRACT: The ligand shell structure of the aspicle $\text{Ag}_{44}(\text{4-MBA})_{30}$ (MBA: mercaptobenzoic acid, in the thiolate form) was modified in a precise, site-specific manner. Laser irradiation at 633 nm of a monolayer assembly of plasmonic Ag nanoparticles (NPs) covered with $\text{Ag}_{44}(\text{4-MBA})_{30}$ clusters leads to decarboxylation of 4-MBA ligands forming thiophenolate (TP) ligands. While the molecular identity and integrity of aspicles post laser irradiation were confirmed by ESI MS, time-dependent SERS spectra and computational studies suggest that the phenomenon of decarboxylation is limited to the 4-MBA ligands facing the NP surface. This creates modified Ag_{44} clusters, with 4-MBA ligands on one side and TP ligands on the other, giving them a two-faced (Janus) ligand structure. The ligand distribution of such clusters gets equilibrated in solution. We show that such selective transformation can be used to create molecular patterns. Janus clusters may be important in chemistry at biphasic interfaces.



INTRODUCTION

Noble metal nanoclusters having unique optical and physical properties have evolved into a distinct family of materials.^{1–3} Gold clusters have been explored intensely^{4–6} compared to their silver analogues because of the latter's reduced stability.^{7,8} Several gold clusters with precise structures have been reported so far,^{9–18} and many of them have been utilized in a variety of applications in many areas such as sensing, catalysis, biolabeling, imaging, etc.^{19,20} Reports of silver clusters are limited mostly to mass spectrometry,^{21–28} although crystal structures of a few clusters such as $\text{Ag}_{14}(\text{SR})_{12}(\text{PR}_3)_8$,²⁹ $\text{Ag}_{16}(\text{SR})_{14}(\text{DPR}_3)_4$,³⁰ $\text{Ag}_{25}(\text{SR})_{18}$,³¹ $\text{Ag}_{29}(\text{SR})_{12}$,³² $\text{Ag}_{32}(\text{SR})_{24}(\text{DPR}_3)_5$,³⁰ and $\text{Ag}_{44}(\text{SR})_{30}$ ^{33,34} have been reported recently (SR, PR_3 , and DPR_3 refer to thiolate, phosphine, and diphosphine functional groups, respectively). Among these atomically precise silver clusters, $\text{Ag}_{44}\text{SR}_{30}$ was the first example of a complete thiol protected cluster with known crystal structure. Bakr et al. in 2009 had developed the synthesis of this cluster which was named as intensely and broadly absorbing nanoparticles (IBANs).³⁵ Later, in 2012 Harkness et al. identified this highly stable silver cluster through high-resolution electrospray ionization mass spectrometry (HRESI MS).³⁶ In 2013, the groups of Bigioni and Zheng solved its crystal structure independently.^{33,34} The cluster consists of a Keplerate solid of concentric icosahedral and dodecahedral atom shells to form a hollow cage which is surrounded by six $\text{Ag}_2(\text{SR})_5$ staples in an octahedral fashion. A selenolate analogue of the Ag_{44} cluster has also been reported which has

an identical optical spectrum with a shift.³⁷ This cluster has been synthesized with a wide variety of water-soluble (e.g., mercaptobenzoic acid) as well as organic soluble (e.g., fluorothiophenol) ligands. $\text{Ag}_{44}(\text{SR})_{30}$, being the most stable silver cluster reported so far, has drawn tremendous interest of the cluster community to investigate its associated properties. Reversible transformation from thiolate to $\text{Ag}_{44}(\text{SePh})_{30}$ ³⁸ and reversible core change from $\text{Ag}_{44}(\text{FTP})_{30}$ to $\text{Ag}_{35}(\text{SG})_{18}$ by ligand exchange³⁹ have been reported recently.

Ligand exchange reactions have been the key processes to functionalize nanoclusters which can introduce new properties to the system.^{40,41} For a specific geometry, there are multiple possibilities for an incoming ligand to exchange with the existing ligand. Fernando and Aikens have theoretically investigated the kinetics and preferred exchange sites of the $\text{Au}_{25}(\text{SR})_{18}$ cluster.⁴² They found that the terminal staples which are most accessible are favored for such exchange. Such preferential exchange can lead to the formation of geometric isomers due to the heterogeneity in the system. Nihoiri et al. were able to separate such isomers through reverse-phase high-performance liquid chromatography.⁴³

Clusters, being three-dimensional (3D) entities, can be functionalized regiospecifically providing Janus-type particles, in the molecular size regime. These are similar to the

Received: May 11, 2016

Revised: June 25, 2016

Published: July 5, 2016

corresponding nanoparticles, but with molecular features, enabling regiospecific conjugation to biological as well as chemical species. However, as these exchange reactions happen in solution, all the equivalent sites in a 3D geometry are equally available for exchange with the new ligands, making the formation of Janus-type clusters impossible through such solution phase ligand exchange. Traditionally, differently functionalized Janus NPs and quantum dots (QDs) are made at the liquid–liquid interfaces using differential solubility of the protecting groups or by selective masking–demasking on a solid substrate.⁴⁴ Formation of Janus particles through these processes can be confirmed from measurement of contact angle after depositing them onto hydrophobic and hydrophilic substrates.⁴⁵ This article reports the first example of regiospecific functionalization of $\text{Ag}_{44}\text{SR}_{30}$ cluster. Plasmon excitation induced decarboxylation of 4-MBA ligands of $\text{Ag}_{44}(\text{4-MBA})_{30}$ generates a mixed-ligand protected $\text{Ag}_{44}(\text{4-MBA})_{30-x}(\text{TP})_x$ cluster (TP: thiophenol), which was identified through Raman spectroscopy and high resolution electrospray ionization mass spectrometry. Time-dependent Raman spectroscopy in conjunction with the computational results confirms that the process of decarboxylation is regiospecific, producing Janus $\text{Ag}_{44}(\text{4-MBA})_{30-x}(\text{TP})_x$ clusters.

EXPERIMENTAL SECTION

Chemicals Used. All the chemicals were commercially available and were used without further purification. Silver nitrate (AgNO_3 , 99%), hydrogen tetrachloroaurate ($\text{HAuCl}_4 \cdot 3\text{H}_2\text{O}$, 49.0% Au basis), 4-mercaptobenzoic acid (4-MBA, 97%), trisodium citrate dihydrate (99%, Aldrich), and sodium borohydride (NaBH_4 , 99.99%) were purchased from Aldrich. Dimethylformamide (DMF, AR grade), dimethyl sulfoxide (DMSO, AR grade), toluene (AR grade), methanol (AR grade), ammonium acetate, citric acid, and sodium hydroxide (NaOH) pellets were procured from RANKEM, India.

Synthesis of Ag@PVP and Au@PVP Nanoparticles. PVP-protected Ag NPs were synthesized through reduction of AgNO_3 in a polyol process. 170 mg of AgNO_3 and 1 g of PVP (K25) were dissolved in 4 mL of ethylene glycol (EG) through magnetic stirring at room temperature to obtain a clear solution. The temperature of this solution was slowly increased to 120 °C. EG reduces Ag^+ at this elevated temperature, and nucleation of Ag NPs starts. The solution was maintained at this temperature for 30 min and then removed and cooled immediately to stop further reaction.

This EG dispersion of Ag NPs was then diluted 10 times with deionized water and finally separated through centrifugal precipitation.

Au@citrate particles were synthesized through the reduction of HAuCl_4 (gold precursor) using sodium citrate.

Synthesis of $\text{Ag}_{44}(\text{4-MBA})_{30}$ Cluster. The Ag_{44} cluster was synthesized using a reported procedure.³⁴ Initially 128 mg of AgNO_3 was taken in a beaker containing DMSO and water (4:7 volume ratio) mixture under constant stirring. 173 mg of 4-MBA was added to the mixture, and stirring was continued. 50% CsOH was added dropwise until the cloudy nature of thiolates became clear and a greenish-yellow color appeared. Then 283 mg of NaBH_4 in 9 mL of water was added dropwise to obtain a brown solution. The color of this solution changed to deep red after 1 h, which confirmed the cluster formation. This crude cluster was purified using DMF, which precipitated the cluster, and the solution was centrifuged. After removing the centrifugate, the cluster was extracted in citric acid-

containing DMF solution. This was to acidify all the protons of carboxylic acid, which makes the cluster soluble in DMF. The extracted cluster was again precipitated using toluene, and the solution was centrifuged. The acidification step was repeated one more time. After this, the precipitate was redissolved in 25 mL of DMF to get the purified cluster. It is important to mention here that when all carboxylates are protonated, there is no need of citric acid, and DMF can extract the cluster directly. Protonation is the key step for this purification.

Synthesis of $\text{Ag}_{44}(\text{TP})_{30}$ Cluster. The $\text{Ag}_{44}(\text{TP})_{30}$ cluster was synthesized using a two-step solution phase route.^{37,38} First, silver trifluoroacetate (12.5 mg) was dissolved in 7.2 mL of acetonitrile and stirred for 5 min. Thiophenol (10 μL) was added to that solution and was left to stir for another 15 min (solution A). In another conical flask, 28.6 mL of acetonitrile solution of NaBH_4 (10.8 mg) was kept for stirring for 30 min (solution B). Then, solution B was added to solution A, and the reaction mixture was left to stir for 3 h at room temperature. The deep pink cluster was formed after 2 h which was then centrifuged, and the centrifugate was stored at 4 °C in fridge for the experiment.

Preparation of Ag NP Monolayer. Prepared Ag NPs were subjected toward consecutive centrifugation–redispersion cycles in water and ethanol to remove possible unreacted AgNO_3 and excess PVP. Those were finally redispersed in 2 mL of 1-butanol by gentle sonication.

This dispersion of Ag NPs in butanol was slowly drop cast on the surface of water taken in a beaker. As butanol spreads on water, it drags the NPs along and gets aligned at the interphase. Finally, the NPs float in the form of a monolayer on water which was then transferred onto microscope coverslips which were used as substrates for the decarboxylation experiment.

Decarboxylation Experiment. A dilute solution of $\text{Ag}_{44}(\text{4-MBA})_{30}$ in DMF was drop cast on Ag NPs monolayer, and it was dried under ambient conditions. This sample was then placed under a Raman microscope, and Raman spectra from a chosen spot were collected in a time-dependent fashion. The time-dependent spectra showed emergence of new peaks and increase in their intensity, indicating *in situ* changes in the analyte (cluster, in this case) under laser irradiation.

Instrumentation. Raman spectroscopy and imaging were done on a WITec GmbH, AlphaSNOM alpha 300 S confocal Raman microscope having a 633 nm laser as the excitation source. A Zeiss 20 \times objective (NA 0.4) was used for spectral acquisition. Spectral data were analyzed on Witec Project Plus software. The UV/vis spectra were recorded using a PerkinElmer Lambda 25 UV/vis spectrometer. A Waters Synapt G2-Si high definition mass spectrometer equipped with electrospray ionization was used in the negative mode. The concentration used was about 1 ppm for both the samples. The instrument was calibrated using NaI as the calibrant. The optimized conditions were as follows: sample concentration: 1 ppm; flow rate: 5–10 $\mu\text{L}/\text{min}$; source voltage: 2.5–3 kV; cone voltage: 120–140 V; source temperature: 80–100 °C; and desolvation temperature: 150–200 °C.

RESULTS AND DISCUSSION

In this experiment, first polyvinylpyrrolidone (PVP)-protected silver (Ag NPs) nanoparticles were synthesized through a polyol method. A monolayer film of these Ag NPs was then prepared through a solvent drying process at the air–water interface, and it was then transferred onto microscope coverslips. The TEM images of the assembly and a photograph

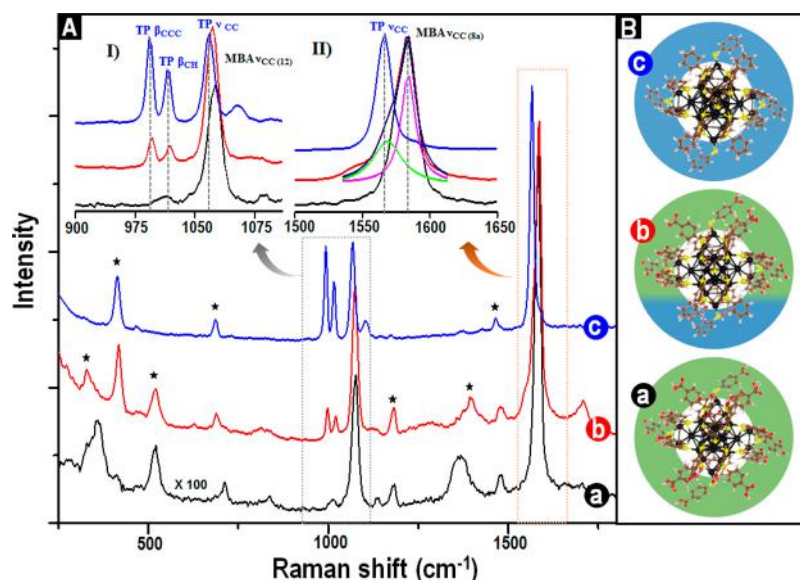
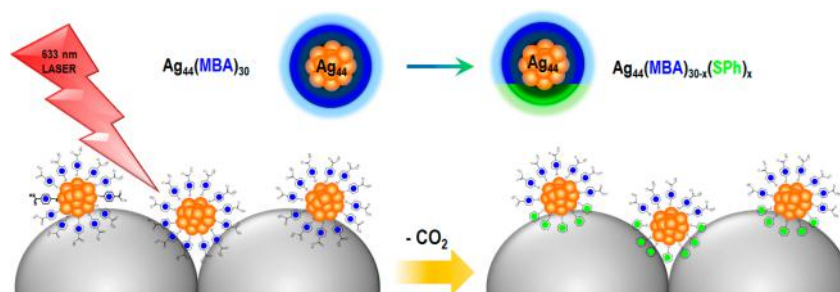
Scheme 1. Schematic View of the Decarboxylation of Ag_{44} Which Results in Janus-Type Clusters

Figure 1. (A) Raman spectra of the clusters; $\text{Ag}_{44}(\text{4-MBA})_{30}$ on a microscope coverslip (a) and that of $\text{Ag}_{44}(\text{4-MBA})_{(30-x)}\text{TP}_x$ (b) and $\text{Ag}_{44}\text{TP}_{30}$ (c) on a Ag NP monolayer film, respectively (for a clear comparison, trace a has been multiplied by 100, since it is a Raman spectrum while the other two are SERS). Insets I and II are expanded views of the regions marked. Prominent features of TP appear in the spectrum (red trace) upon laser irradiation of $\text{Ag}_{44}(\text{4-MBA})_{30}$, confirming the decarboxylation of 4-MBA ligands. Features of both 4-MBA and TP are present in the resultant cluster spectrum (red trace), confirming the formation of Ag_{44} with mixed ligand protection. For clarity, the spectrum was fitted (in II) with two individual components (pink and green traces, respectively). (B) The corresponding structures of the three clusters $\text{Ag}_{44}(\text{4-MBA})_{30}$ (a), $\text{Ag}_{44}(\text{4-MBA})_{20}(\text{TP})_{10}$ (b), and $\text{Ag}_{44}(\text{TP})_{30}$ (c), respectively. The characteristic features are labeled (β and ν indicate the in-plane bending and the stretching modes, respectively). There are certain minor features indicated with an asterisk, which are likely to be due to conformational changes of the ligands and have not been assigned accurately.

of the corresponding nanoparticle film are given in the [Supporting Information](#) (Figure S1). The $\text{Ag}_{44}(\text{4-MBA})_{30}$ cluster was synthesized using a reported procedure.³⁴ Briefly, a basic Ag-thiolate (4-MBA) solution was slowly reduced by dropwise addition of aqueous sodium borohydride (NaBH_4) to obtain the crude cluster. It was purified 2–3 times and was finally extracted in dimethylformamide (DMF) to get the pure cluster (see [Experimental Section](#)). The unique “molecule-like” features in the UV/vis spectrum confirm the formation of Ag_{44} cluster (Figure S2). Synthesis was also confirmed by electrospray ionization mass spectrometry (ESI MS, Figure S2). The cluster was stable for months under ambient conditions in solution as well as in the solid state. Essential details of characterization of the cluster are given in the [Supporting Information](#). Next, the DMF solution of $\text{Ag}_{44}(\text{4-MBA})_{30}$ cluster was drop-casted on the Ag NP film and dried in air. These films were used for Raman spectroscopic experiments using 633 nm laser excitation (details are in the [Supporting Information](#)). Exposure to 532 nm laser excitation was seen to make darker spots indicating degradation of clusters, and so we did not pursue experiments with this laser source. [Scheme 1](#) describes

the experiment pictorially. In order to confirm decarboxylation, $\text{Ag}_{44}(\text{TP})_{30}$ was prepared separately, which was also characterized by UV/vis (Figure S2). Exact match of the UV/vis features confirms the formation of the cluster. The Raman spectrum of the $\text{Ag}_{44}(\text{4-MBA})_{30}$ clusters, drop cast onto glass coverslips, is displayed in trace a of Figure 1A. The intensity has been multiplied by 100 as the other spectra (to be discussed later) are more intense resulting from the surface enhancement of the supporting nanoparticles. Because of the Raman-active mercaptobenzoic acid ligand (Figure S3), the $\text{Ag}_{44}(\text{4-MBA})_{30}$ cluster shows Raman features between 200 and 1600 cm^{-1} .⁴⁶ Strong bands are exhibited at 1076 and 1587 cm^{-1} corresponding to ν_{12} and ν_{8a} aromatic ring vibrations, respectively.³⁵ Ag_{44} clusters were then drop cast on a self-assembled silver nanoparticle film ($\text{Ag}_{44}@\text{Ag}$ NPs) to obtain a better resolved spectrum. Monolayer assembly of Ag NPs generates “hot spots” at the junctions of adjacent particles. Coupling of localized surface plasmon (LSP) of two adjacent particles creates a strong electric field, which increases the Raman signal significantly for the molecules located near the hot spots.⁴⁷ Exposure of the 633 nm laser onto $\text{Ag}_{44}@\text{Ag}$ NPs,

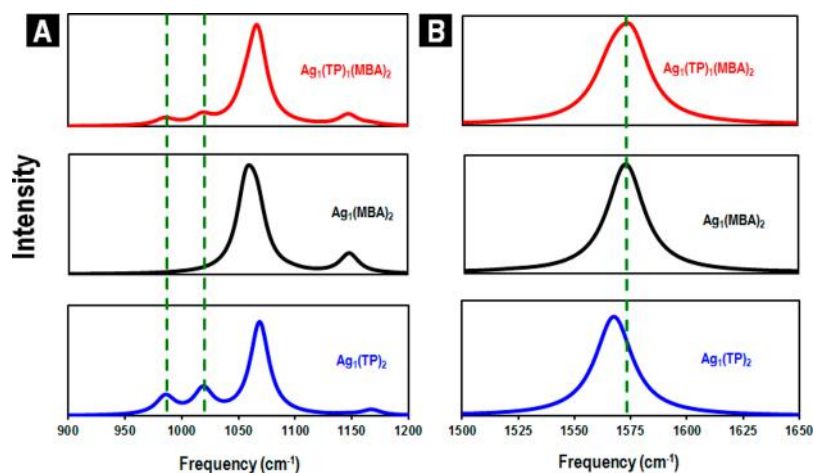


Figure 2. Calculated Raman spectra of model species $\text{Ag}_1(\text{TP})_1(4\text{-MBA})_1$, $\text{Ag}_1(4\text{-MBA})_2$, and $\text{Ag}_1(\text{TP})_2$ in regions (A) 900–1200 cm^{-1} and (B) 1500–1650 cm^{-1} .

however, led to the appearance of two new peaks at 1003 cm^{-1} (β_{CCC}) and 1026 cm^{-1} (β_{CH}) along with a shoulder peak near 1575 cm^{-1} (ν_{CC}), indicating the formation of new species (trace b, Figure 1A).⁴⁸ Note that the standard features of 4-MBA are also present. The spectral intensity is enhanced due to the supporting plasmonic particles. As this is not the subject of our discussion, we will not dwell upon the enhancement aspect further.

4-MBA has been used as a SERS probe for several decades because of its strong interaction with noble metals through the S–metal bond. It is known to undergo decarboxylation on metal surfaces upon laser illumination.^{49,50} The new peaks observed in the spectrum (1003, 1026, and 1575 cm^{-1}) match with the prominent peaks of TP, the decarboxylation product of 4-MBA. For clarity, the expanded spectra for these two specific regions are presented in the inset of Figure 1A. The Raman spectrum of the corresponding TP-protected Ag_{44} cluster (trace c, Figure 1A) drop cast on Ag NP film shows similar bands at appropriate positions, confirming the catalytic transformation of Ag_{44} bound 4-MBA to TP.

Raman spectra of small model compounds $\text{Ag}_1(\text{TP})_1(4\text{-MBA})_1$, $\text{Ag}_1(4\text{-MBA})_2$, and $\text{Ag}_1(\text{TP})_2$ were calculated to confirm the aforementioned Raman spectral assignments using the density functional theory (DFT) method as available with Gaussian 09 software.⁵¹ Details of the calculations are provided in the Supporting Information. The spectra corresponding to regions 900–1200 cm^{-1} and 1500–1650 cm^{-1} are presented in Figure 2. The characteristic peaks of $\text{Ag}_1(\text{TP})_2$ at ~ 980 and 1020 cm^{-1} which are absent for $\text{Ag}_1(4\text{-MBA})_2$ are clearly observable in the spectrum of $\text{Ag}_1(\text{TP})_1(4\text{-MBA})_1$. Furthermore, the peak at ~ 1565 cm^{-1} for $\text{Ag}_1(\text{TP})_2$ is shifted to a higher frequency (~ 1575 cm^{-1}) in the spectrum of $\text{Ag}_1(\text{TP})_1(4\text{-MBA})_1$, similar to that of $\text{Ag}_1(4\text{-MBA})_2$. These above-mentioned features, similar to that of $\text{Ag}_1(\text{TP})_1(4\text{-MBA})_1$, were exhibited in the experimental Raman spectra of cluster@Ag NPs, excited by a 633 nm laser (trace b, Figure 1A, traces b, c). This supports our experimental analysis that decarboxylation has occurred, resulting in a cluster which has both 4-MBA and TP as protecting ligands.

High-resolution electrospray ionization mass spectrometry was carried out to identify the final product (Figure 3). For this, the cluster was drop-casted on a specific area of the film of nanoparticles (marked originally) and was exposed to the laser

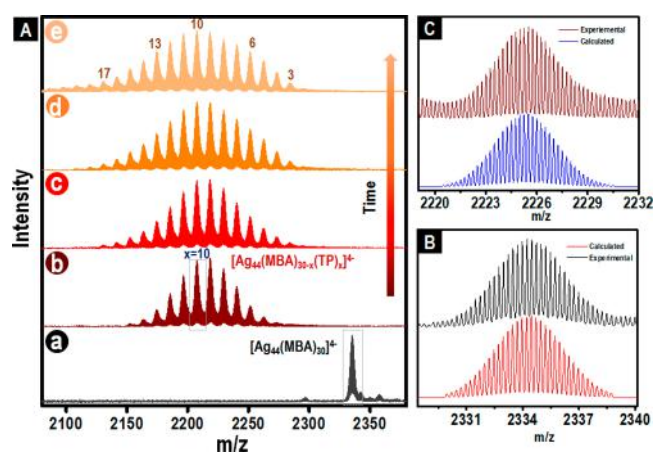


Figure 3. (A) HR ESI mass spectrum (negative mode) of the parent $\text{Ag}_{44}(4\text{-MBA})_{30}$ cluster in the 4⁻ region, (a) and the decarboxylated product in DMF–acetonitrile mixture after laser exposure for 90 min. The spectra are collected (b) immediately, (c) after 10 min, (d) after 15 min, and (e) after 30 min, after extraction into solution (see text for details). The $\text{Ag}_{44}(4\text{-MBA})_{30}$ peak at m/z 2335 is expanded in (B), and the corresponding calculated pattern is given as a red trace. The decarboxylated product, taken in solution, shows a series of peaks for $\text{Ag}_{44}(4\text{-MBA})_{30-x}(\text{TP})_x$ cluster where x varies from 3 to 20. The highest intensity was seen near $x = 10$, which is expanded in (C). It shows an exact match with the corresponding calculated pattern (blue trace). Time-dependent data suggest the intercluster ligand exchange in solution. Higher intensity of the experimental spectrum on either side of the main feature is due to the overlapping peaks on either side.

for 90 min. The exposed area was then scratched, extracted in a DMF–acetonitrile mixture, and centrifuged to precipitate the Ag NPs, and the solution was subjected to ESI MS instruments. These processes of extracting the laser-irradiated cluster into solution took about 5 min, and this time was taken as time zero (immediate after irradiation) for mass spectral measurements. The UV/vis spectrum of the extracted solution (Figure S4) confirmed the integrity of the cluster on Ag NP monolayer film post laser irradiation. From previous studies we had established that slight changes in the ligands do not affect the optical absorption spectrum of clusters.⁴⁰ The mass spectrum, taken immediately after extraction (trace b, Figure 3A), showed a series of peaks, occurring at a lower m/z than the parent peak for $\text{Ag}_{44}(4\text{-MBA})_{30}^{4-}$. The mass spectrum of the ion due to

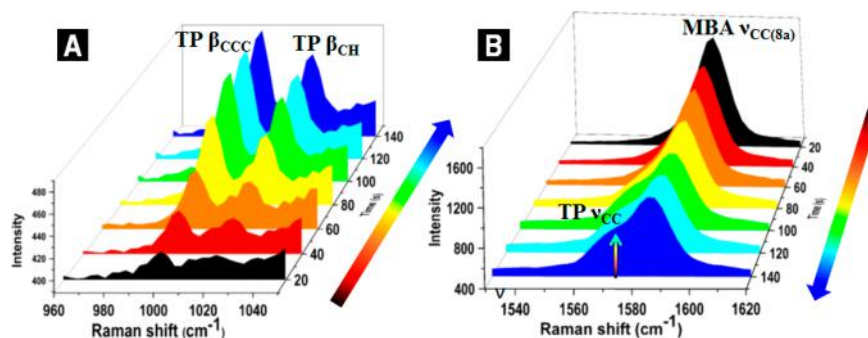


Figure 4. Time-dependent evolution of TP features in the Raman spectrum of $\text{Ag}_{44}(\text{4-MBA})_{30}$ upon laser irradiation: (A) β_{CCC} and β_{CH} regions and (B) ν_{CC} region. β and ν indicate the in-plane bending and the stretching modes, respectively.

$\text{Ag}_{44}(\text{4-MBA})_{30}^{4-}$ (trace a, Figure 3A; an expanded view is shown in Figure 3B) showed a peak centered around m/z 2335. In the spectrum immediately after exposure of laser showed the complete absence of the peak at m/z 2335, and a series of peaks at lower masses appeared (Figure 3A, trace b). A mass difference of m/z 11.1 between the successive peaks is seen, suggesting the formation of mixed-ligand-protected $\text{Ag}_{44}(\text{4-MBA})_{30-x}\text{TP}_x$ cluster (mass difference of 4-MBA and TP is 44.4 and the charge is 4-, giving a separation of 11.1). The cluster underwent solution-phase intercluster ligand exchange with time, which contributed to the increase in the number of ligand exchange products with time which can be seen from the time-dependent mass spectra (traces b–e, Figure 3A). Intercluster ligand exchange in solution makes it impossible to capture the specific $\text{Ag}_{44}(\text{4-MBA})_{30-x}\text{TP}_x$ cluster produced onto the Ag NP surface in their native form through solvent extraction. This prohibited us in further analysis into the ligand geometry of the transformed $\text{Ag}_{44}(\text{4-MBA})_{30-x}\text{TP}_x$ through mass spectrometry. The value of x for $\text{Ag}_{44}(\text{4-MBA})_{30-x}\text{TP}_x$ for solution extracted clusters was 3–20, with maximum intensity for $x = 10$ after 30 min of extraction (trace e, Figure 3A). The system equilibrates after this point, and no further ligand exchange was observed. An expanded view of $\text{Ag}_{44}(\text{4-MBA})_{20}\text{TP}_{10}$ region is shown in Figure 3C. The apparent broadness of the experimental peak is due overlapping features from neighboring $\text{Ag}_{44}(\text{4-MBA})_{30-x}\text{TP}_x$ features.

Monitoring of time-dependent evolution of TP features in the Raman spectra (Figure 4) suggests that number of 4-MBA ligands transforming to TP increases with exposure time up to a certain point and saturates beyond. This was confirmed by plotting the relative intensities of the peaks at 1003, 1026, 1576, and 1587 cm^{-1} with time. The plots displayed an increase in intensity of the first three peaks (Figure S5) and a decrease in intensity for the last peak up to a certain exposure time (100 s), following which the intensity remained constant. The Raman spectrum of the final product after an exposure time of 140 s (trace b, Figure 1A) suggested that it has a combination of thiophenol and 4-MBA as protecting ligands, and the percentage of 4-MBA to TP can be calculated by comparing the relative intensities of the TP only peaks at 998 and 1022 cm^{-1} with that of $\text{Ag}_{44}\text{TP}_{30}$ (trace c, Figure 1A). This also suggests decarboxylation of approximately 10 ligands and corroborates with the conclusion drawn from ESI MS data.

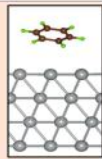

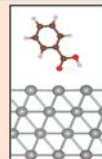
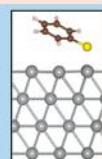
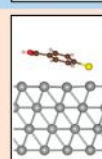
The fact that decarboxylation remained limited to a certain number of 4-MBA ligands and did not extend beyond, even after an extended period of irradiation, hints that laser irradiation can excite only a fixed number of 4-MBA ligands out of total 30 available per cluster. Laser irradiation of drop-

cast films of $\text{Ag}_{44}(\text{4-MBA})_{30}$ onto coverslips as well as onto TLC plates (composed of silica particles) did not show any signatures of TP. It is clear that self-assembled Ag NPs (Figure S6A) helped in decarboxylation. These experiments confirm that nature of the underlying surface plays an important role in absorbing and channeling the laser energy to bring about decarboxylation.

Transmission spectroscopic measurements of the Ag NP film showed plasmon excitation at 470 nm, in contrast to the excitation maximum of 412 nm in solution (Figure S6B). This confirms the involvement of coupled plasmon excitation in the decarboxylation process. The clusters attach themselves onto the Ag NP surfaces through carboxylate ends of some of the 4-MBA ligands, and these 4-MBA ligands (attached to NP surface) can be influenced easily by the plasmon excitation. A similar laser irradiation experiment, carried out on $\text{Ag}_{44}(\text{4-MBA})_{30}$ over a monolayer film of Au NPs (Figure S7), resulted in the decarboxylation of 10 4-MBA ligands, albeit the rate was slower than on Ag NPs. This again hints at the role of coupled plasmon excitation of metal NPs in energizing the 4-MBA ligands leading to their decarboxylation. These experiments hint toward a site-specific decarboxylation of the parent $\text{Ag}_{44}(\text{4-MBA})_{30}$ NCs, forming Janus $\text{Ag}_{44}(\text{4-MBA})_{30}$ clusters protected with TP ligands on one side (close to NPs) and with 4-MBA ligands on the other (away from NPs). The approximate value of 10 can be rationalized from the involvement of two $\text{Ag}_2(\text{SR})_5$ staple motifs present near the silver nanoparticles.

As decarboxylation is presumably governed by the proximity of carboxylate ligands with the “hot spots”, the binding or interaction of the ligand with the silver nanoparticle surface is an important factor in this transformation. To develop an understanding of the adsorption and decarboxylation processes, we performed periodic DFT calculations using the Python-based GPAW code⁵² within the atomic simulation environment (ASE).⁵³ A van der Waals density function⁵⁴ was employed to calculate adsorption and decarboxylation energies for geometries optimized using the revised Perdew–Burker–Ernzerhof (RPBE) function.⁵⁵ For more details of the computations please refer to the Supporting Information. We considered binding of 4-MBA radical (4-MBA*), TP radical (TP*), benzoic acid, and benzene at different adsorption sites over the Ag(111) surface, chosen as a representative surface on the Ag NPs. Each adsorbate/Ag(111) models adsorption of a ligand (protecting the Ag_{44} core) on the Ag NP surface. Only ligand interaction with this Ag(111) was explored as adsorption of the whole $\text{Ag}_{44}(\text{4-MBA})_{30}$ cluster on Ag(111) would have been computationally much more expensive. We chose this also because only the ligands are going to interact with the Ag NP

Table 1. Theoretically Calculated Adsorption Energies and Decarboxylation Energies Including van der Waals Correction of Ligands Adsorbed on Ag(111) Surface^a

System	Optimized structure	Adsorption energy (ev)	Decarboxylation energy (ev)
Benzene		-0.293 [fcc] -0.267 [bridge]	---
Benzoic acid (parallel orientation)		-0.544 [fcc]	-0.115
Benzoic acid (vertical orientation)		-0.292 [bridge]	-0.367
TP*		-1.654 [bridge]	---
4-MBA*		-1.836 [bridge]	-0.220

^aDecarboxylation energies are with reference to CO₂ gas. The adsorption site for each species is given in the square brackets.

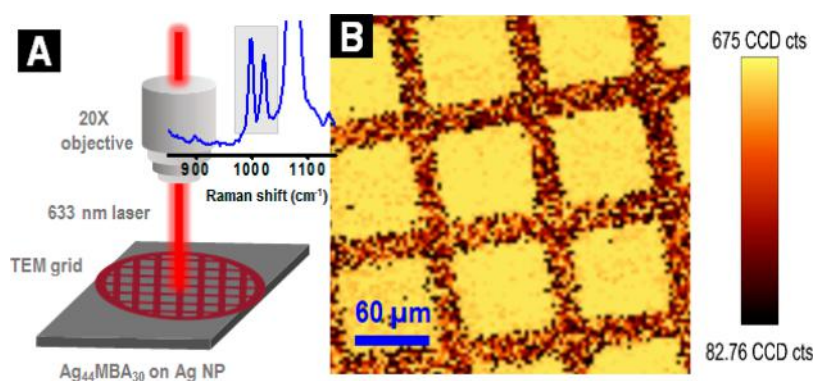


Figure 5. Patterned modification of Ag₄₄(4-MBA)₃₀ into Ag₄₄(4-MBA)_{30-x}TP_x through the decarboxylation process. (A) Schematic of the experiment. A 200 mesh TEM grid was used as mask, and the area coated with Ag₄₄(4-MBA)₃₀ was irradiated with a 633 nm laser. Inset shows the selected spectral region which was being used for the Raman image. (B) Raman image of the irradiated area after removal of the TEM grid. Ag₄₄(4-MBA)₃₀ remains intact in the areas covered with the grid while in the areas exposed to the laser transforms into Ag₄₄(4-MBA)_{30-x}TP_x. The increased intensity of the exposed regions indicates the transformation. Intensity scale is marked on the right.

surface. Benzoic acid and benzene were chosen as ligands because, being already attached to the cluster core through S, 4-MBA and TP are not likely to interact with the Ag NP particle surface through S, instead via the -COOH or the aromatic ring. The calculated van der Waals corrected adsorption and decarboxylation energies are listed in Table 1. It can be seen from the table that decarboxylation is thermodynamically favorable for benzoic acid and 4-MBA* which represent the

ligands around the Ag₄₄ cluster in different orientations. Second, the adsorption energies of benzoic acid in vertical orientation and benzene in parallel orientation are quite similar; so is the case of 4-MBA* and TP*. Furthermore, the preferred adsorption sites of the decarboxylated species, i.e., benzene and TP*, are the same as those of benzoic acid and 4-MBA*, respectively. These points suggest that following decarboxylation of the 4-MBA ligands (conversion to TP) in proximity

to the Ag NP surface, the decarboxylated Ag₄₄ cluster is likely to remain at the same position and will not roll off on to Ag NP surface as the interaction energies through –COOH and aromatic ring are similar. This prevents the other 4-MBA ligands (away from the Ag NPs) from interacting with the NP surface, and those remain intact. These computational findings in conjunction with the time-dependent Raman spectroscopy explains regiospecific decarboxylation of the parent clusters and the fact that it stops after a certain number of 4-MBA ligands are decarboxylated.

Using decarboxylation induced spectral changes of the clusters, specific patterns can be drawn onto cluster coated nanoparticle films, which are otherwise invisible, and can be read out through Raman spectral imaging. To demonstrate this, specific areas of a cluster coated Ag NP film was exposed to the 633 nm laser beam using a center-marked (used as the marker for position) uncoated TEM grid as mask (Figure 5A). Raman spectral imaging was performed from an exposed 600 μm × 600 μm area on stepper motor driven XY stage after removing the mask (TEM grid). A total of 150 × 150 Raman spectra were collected from the area for constructing the Raman image, giving a spatial resolution of 4 μm. It is to be noted that much better spatial resolution is obtainable (~1 μm), but it was avoided to minimize the imaging time and laser-induced damage. The Raman image constructed by taking the prominent feature of Ag₄₄(4-MBA)_{30-x}TP_x (marked in the inset of Figure 5A) is shown in Figure 5B, which shows different contrast for exposed and unexposed areas. Decarboxylation happens where the area was exposed to the laser, and that creates the specific pattern.

CONCLUSION

In summary, a Janus type of atomically precise cluster has been formed *in situ* through plasmon excitation induced decarboxylation of Ag₄₄(4-MBA)₃₀. A cluster film was made on a self-assembled silver nanoparticle surface which helps in propagating the plasmon to generate local heat at the cluster surface attached to the particles, upon 633 nm laser irradiation. The decarboxylation was monitored by Raman spectroscopy where new peaks due to the decarboxylated product TP, started appearing. The transformation saturates after a certain time, and from intensity ratios of the peaks involved, we estimate that approximately ten ligands per cluster have been transformed to TP. HR ESI mass spectral data further support this precise transformation. Considering a simple model of thiolates, DFT calculations were done to understand the decarboxylation and adsorption processes. Specific Raman patterning due to the decarboxylation can be implemented in generating hidden molecular signatures using appropriate masks.

ASSOCIATED CONTENT

Supporting Information

The Supporting Information is available free of charge on the ACS Publications website at DOI: 10.1021/acs.jpcc.6b04769.

Details of computation, characterization of nanoparticles, UV/vis of Ag₄₄ cluster, comparative Raman spectra, intensity vs exposure time plot, and Raman spectral data of control experiments with Ag@PVP and Au@citrate nanoparticles (PDF)

AUTHOR INFORMATION

Corresponding Author

*E-mail: pradeep@iitm.ac.in; Fax: 91-44-2257-0545/0509 (T.P.).

Present Addresses

I.C.: Department of Physics, Philipps-Universität Marburg, Renthof 7, Marburg, 35037, Germany.

T.A.M.: Department of Physics, Indian Institute of Technology Madras, Chennai 600036, India.

Author Contributions

I.C. and A.S. contributed equally.

Notes

The authors declare no competing financial interest.

ACKNOWLEDGMENTS

I.C. and T.A.M. thank IIT Madras for their Institute Post Doctoral Fellowships. A.S. thanks CSIR, D.S. thanks UGC, and B.M. thanks IIT Madras for their research fellowships. We thank Department of Science and Technology for consistently supporting our research program.

REFERENCES

- (1) Jin, R. Atomically Precise Metal Nanoclusters: Stable Sizes and Optical Properties. *Nanoscale* **2015**, *7*, 1549–1565.
- (2) Jin, R.; Eah, S.-K.; Pei, Y. Quantum-Sized Metal Nanoclusters. *Nanoscale* **2012**, *4*, 4026–4026.
- (3) Udayabhaskararao, T.; Pradeep, T. New Protocols for the Synthesis of Stable Ag and Au Nanocluster Molecules. *J. Phys. Chem. Lett.* **2013**, *4*, 1553–1564.
- (4) Negishi, Y.; Nobusada, K.; Tsukuda, T. Glutathione-Protected Gold Clusters Revisited: Bridging the Gap between Gold(I)-Thiolate Complexes and Thiolate-Protected Gold Nanocrystals. *J. Am. Chem. Soc.* **2005**, *127*, 5261–5270.
- (5) Ingram, R. S.; Hostetler, M. J.; Murray, R. W.; Schaaff, T. G.; Khoury, J. T.; Whetten, R. L.; Bigioni, T. P.; Guthrie, D. K.; First, P. N. 28 kDa Alkanethiolate-Protected Au Clusters Give Analogous Solution Electrochemistry and STM Coulomb Staircases. *J. Am. Chem. Soc.* **1997**, *119*, 9279–9280.
- (6) Whetten, R. L.; Khoury, J. T.; Alvarez, M. M.; Murthy, S.; Vezmar, I.; Wang, Z. L.; Stephens, P. W.; Cleveland, C. L.; Luedtke, W. D.; Landman, U. Nanocrystal Gold Molecules. *Adv. Mater.* **1996**, *8*, 428–433.
- (7) Cathcart, N.; Mistry, P.; Makra, C.; Pietrobon, B.; Coombs, N.; Jelokhani-Niaraki, M.; Kitaev, V. Chiral Thiol-Stabilized Silver Nanoclusters with Well-Resolved Optical Transitions Synthesized by a Facile Etching Procedure in Aqueous Solutions. *Langmuir* **2009**, *25*, 5840–5846.
- (8) Joshi, C. P.; Bootharaju, M. S.; Bakr, O. M. Tuning Properties in Silver Clusters. *J. Phys. Chem. Lett.* **2015**, *6*, 3023–3035.
- (9) Anson, C. E.; Eichhöfer, A.; Issac, I.; Fenske, D.; Fuhr, O.; Sevillano, P.; Persau, C.; Stalke, D.; Zhang, J. Synthesis and Crystal Structures of the Ligand-Stabilized Silver Chalcogenide Clusters [Ag₁₅₄Se₇₇(dppxy)₁₈], [Ag₃₂₀(S *t* Bu)₆₀S₁₃₀(dppp)₁₂], [Ag₃₅₂S₁₂₈(S *t* C₃H₁₁)₉₆], and [Ag₄₉₀S₁₈₈(S *t* C₃H₁₁)₁₁₄]. *Angew. Chem., Int. Ed.* **2008**, *47*, 1326–1331.
- (10) Crasto, D.; Barcaro, G.; Stener, M.; Sementa, L.; Fortunelli, A.; Dass, A. Au₂₄(SAdm)₁₆ Nanomolecules: X-Ray Crystal Structure, Theoretical Analysis, Adaptability of Adamantane Ligands to Form Au₂₃(SAdm)₁₆ and Au₂₅(SAdm)₁₆ and Its Relation to Au₂₅(SR)₁₈. *J. Am. Chem. Soc.* **2014**, *136*, 14933–14940.
- (11) Crasto, D.; Malola, S.; Brososky, G.; Dass, A.; Häkkinen, H. Single Crystal Xrd Structure and Theoretical Analysis of the Chiral Au₃₀S(S-*t*-Bu)₁₈ Cluster. *J. Am. Chem. Soc.* **2014**, *136*, 5000–5005.
- (12) Das, A.; Li, T.; Nobusada, K.; Zeng, C.; Rosi, N. L.; Jin, R. Nonsuperatomic [Au₂₃(SC₆H₁₁)₁₆][−] Nanocluster Featuring Bipyrami-

- dal Au₁₅ Kernel and Trimeric Au₃(SR)₄ Motif. *J. Am. Chem. Soc.* **2013**, *135*, 18264–18267.
- (13) Das, A.; Li, T.; Nobusada, K.; Zeng, Q.; Rosi, N. L.; Jin, R. Total Structure and Optical Properties of a Phosphine/Thiolate-Protected Au₂₄ Nanocluster. *J. Am. Chem. Soc.* **2012**, *134*, 20286–20289.
- (14) Dass, A.; Theivendran, S.; Nimmala, P. R.; Kumara, C.; Jupally, V. R.; Fortunelli, A.; Sementa, L.; Barcaro, G.; Zuo, X.; Noll, B. C. Au₁₃₃(SPh-tBu)₅₂ Nanomolecules: X-Ray Crystallography, Optical, Electrochemical, and Theoretical Analysis. *J. Am. Chem. Soc.* **2015**, *137*, 4610–4613.
- (15) Heaven, M.; Dass, A.; White, P.; Holt, K.; Murray, R. Crystal Structure of the Gold Nanoparticle [N(C₈H₁₇)₄]-[Au₂₅(SCH₂CH₂Ph)₁₈]. *J. Am. Chem. Soc.* **2008**, *130*, 3754.
- (16) Jadzinsky, P. D.; Calero, G.; Ackerson, C. J.; Bushnell, D. A.; Kornberg, R. D. Structure of a Thiol Monolayer-Protected Gold Nanoparticle at 1.1 Å Resolution. *Science* **2007**, *318*, 430–433.
- (17) Song, Y.; Wang, S.; Zhang, J.; Kang, X.; Chen, S.; Li, P.; Sheng, H.; Zhu, M. Crystal Structure of Selenolate-Protected Au₂₄(SeR)₂₀ Nanocluster. *J. Am. Chem. Soc.* **2014**, *136*, 2963–2965.
- (18) Zhu, M.; Aikens, C. M.; Hollander, F. J.; Schatz, G. C.; Jin, R. Correlating the Crystal Structure of a Thiol-Protected Au₂₅ Cluster and Optical Properties. *J. Am. Chem. Soc.* **2008**, *130*, 5883–5885.
- (19) Mathew, A.; Pradeep, T. Noble Metal Clusters: Applications in Energy, Environment, and Biology. *Part. Part. Syst. Char.* **2014**, *31*, 1017–1053.
- (20) Wu, Z.; Jiang, D.-e.; Mann, A. K. P.; Mullins, D. R.; Qiao, Z.-A.; Allard, L. F.; Zeng, C.; Jin, R.; Overbury, S. H. Thiolate Ligands as a Double-Edged Sword for CO Oxidation on CeO₂ Supported Au₂₅(SCH₂CH₂Ph)₁₈ Nanoclusters. *J. Am. Chem. Soc.* **2014**, *136*, 6111–6122.
- (21) Chakraborty, I.; Govindarajan, A.; Erusappan, J.; Ghosh, A.; Pradeep, T.; Yoon, B.; Whetten, R. L.; Landman, U. The Superstable 25 kDa Monolayer Protected Silver Nanoparticle: Measurements and Interpretation as an Icosahedral Ag₁₅₂(SCH₂CH₂Ph)₆₀ Cluster. *Nano Lett.* **2012**, *12*, 5861–5866.
- (22) Rao, T. U. B.; Nataraju, B.; Pradeep, T. Ag₉ Quantum Cluster through a Solid-State Route. *J. Am. Chem. Soc.* **2010**, *132*, 16304–16307.
- (23) Chakraborty, I.; Erusappan, J.; Govindarajan, A.; Sugi, K. S.; Udayabhaskararao, T.; Ghosh, A.; Pradeep, T. Emergence of Metallicity in Silver Clusters in the 150 Atom Regime: A Study of Differently Sized Silver Clusters. *Nanoscale* **2014**, *6*, 8024–8031.
- (24) Guo, J.; Kumar, S.; Bolan, M.; Desireddy, A.; Bigioni, T. P.; Griffith, W. P. Mass Spectrometric Identification of Silver Nanoparticles: The Case of Ag₃₂(SG)₁₉. *Anal. Chem.* **2012**, *84*, 5304–5308.
- (25) Udaya Bhaskara Rao, T.; Pradeep, T. Luminescent Ag₇ and Ag₈ Clusters by Interfacial Synthesis. *Angew. Chem., Int. Ed.* **2010**, *49*, 3925–3929.
- (26) Wu, Z.; Lanni, E.; Chen, W.; Bier, M. E.; Ly, D.; Jin, R. High Yield, Large Scale Synthesis of Thiolate-Protected Ag₇ Clusters. *J. Am. Chem. Soc.* **2009**, *131*, 16672–16674.
- (27) Chakraborty, I.; Mahata, S.; Mitra, A.; De, G.; Pradeep, T. Controlled Synthesis and Characterization of the Elusive Thiolated Ag₅₅ Cluster. *Dalton Trans.* **2014**, *43*, 17904–17907.
- (28) Chakraborty, I.; Bag, S.; Landman, U.; Pradeep, T. Atomically Precise Silver Clusters as New SERS Substrates. *J. Phys. Chem. Lett.* **2013**, *4*, 2769–2773.
- (29) Yang, H.; Lei, J.; Wu, B.; Wang, Y.; Zhou, M.; Xia, A.; Zheng, L.; Zheng, N. Crystal Structure of a Luminescent Thiolated Ag Nanocluster with an Octahedral Ag₆⁴⁺ Core. *Chem. Commun.* **2012**, *49*, 300–302.
- (30) Yang, H.; Wang, Y.; Zheng, N. Stabilizing Subnanometer Ag(0) Nanoclusters by Thiolate and Diphosphine Ligands and Their Crystal Structures. *Nanoscale* **2013**, *5*, 2674–2677.
- (31) Joshi, C. P.; Bootharaju, M. S.; Alhilaly, M. J.; Bakr, O. M. [Ag₂₅(SR)₁₈]⁻: The “Golden” Silver Nanoparticle. *J. Am. Chem. Soc.* **2015**, *137*, 11578–11581.
- (32) AbdulHalim, L. G.; Bootharaju, M. S.; Tang, Q.; Del Gobbo, S.; AbdulHalim, R. G.; Eddaoudi, M.; Jiang, D.-e.; Bakr, O. M. Ag₂₉(BDT)₁₂(TPP)₄: A Tetravalent Nanocluster. *J. Am. Chem. Soc.* **2015**, *137*, 11970–11975.
- (33) Yang, H.; Wang, Y.; Huang, H.; Gell, L.; Lehtovaara, L.; Malola, S.; Hakkinen, H.; Zheng, N. All-Thiol-Stabilized Ag₄₄ and Au₁₂Ag₃₂ Nanoparticles with Single-Crystal Structures. *Nat. Commun.* **2013**, *4*, 2422.
- (34) Desireddy, A.; Conn, B. E.; Guo, J.; Yoon, B.; Barnett, R. N.; Monahan, B. M.; Kirschbaum, K.; Griffith, W. P.; Whetten, R. L.; Landman, U.; et al. Ultrastable Silver Nanoparticles. *Nature* **2013**, *501*, 399–402.
- (35) Bakr, O. M.; Amendola, V.; Aikens, C. M.; Wenseleers, W.; Li, R.; Dal Negro, L.; Schatz, G. C.; Stellacci, F. Silver Nanoparticles with Broad Multiband Linear Optical Absorption. *Angew. Chem.* **2009**, *121*, 6035–6040.
- (36) Harkness, K. M.; Tang, Y.; Dass, A.; Pan, J.; Kothalawala, N.; Reddy, V. J.; Cliffl, D. E.; Demeler, B.; Stellacci, F.; Bakr, O. M.; et al. Ag₄₄(SR)₃₀⁴⁺: A Silver-Thiolate Superatom Complex. *Nanoscale* **2012**, *4*, 4269–4274.
- (37) Chakraborty, I.; Kurashige, W.; Kanehira, K.; Gell, L.; Häkkinen, H.; Negishi, Y.; Pradeep, T. Ag₄₄(SeR)₃₀: A Hollow Cage Silver Cluster with Selenolate Protection. *J. Phys. Chem. Lett.* **2013**, *4*, 3351–3355.
- (38) Chakraborty, I.; Pradeep, T. Reversible Formation of Ag₄₄ from Selenolates. *Nanoscale* **2014**, *6*, 14190–14194.
- (39) Bootharaju, M. S.; Burlakov, V. M.; Besong, T. M. D.; Joshi, C. P.; AbdulHalim, L. G.; Black, D. M.; Whetten, R. L.; Goriely, A.; Bakr, O. M. Reversible Size Control of Silver Nanoclusters Via Ligand-Exchange. *Chem. Mater.* **2015**, *27*, 4289–4297.
- (40) Shibu, E. S.; Muhammed, M. A. H.; Tsukuda, T.; Pradeep, T. Ligand Exchange of Au₂₅SG₁₈ Leading to Functionalized Gold Clusters: Spectroscopy, Kinetics, and Luminescence. *J. Phys. Chem. C* **2008**, *112*, 12168–12176.
- (41) Krishnadas, K. R.; Ghosh, A.; Baksi, A.; Chakraborty, I.; Natarajan, G.; Pradeep, T. Intercluster Reactions between Au₂₅(SR)₁₈ and Ag₄₄(SR)₃₀. *J. Am. Chem. Soc.* **2016**, *138*, 140–148.
- (42) Fernando, A.; Aikens, C. M. Ligand Exchange Mechanism on Thiolate Monolayer Protected Au₂₅(SR)₁₈ Nanoclusters. *J. Phys. Chem. C* **2015**, *119*, 20179–20187.
- (43) Niihori, Y.; Kikuchi, Y.; Kato, A.; Matsuzaki, M.; Negishi, Y. Understanding Ligand-Exchange Reactions on Thiolate-Protected Gold Clusters by Probing Isomer Distributions Using Reversed-Phase High-Performance Liquid Chromatography. *ACS Nano* **2015**, *9*, 9347–9356.
- (44) Walther, A.; Müller, A. H. E. Janus Particles: Synthesis, Self-Assembly, Physical Properties, and Applications. *Chem. Rev.* **2013**, *113*, 5194–5261.
- (45) Andala, D. M.; Shin, S. H. R.; Lee, H.-Y.; Bishop, K. J. M. Templated Synthesis of Amphiphilic Nanoparticles at the Liquid-Liquid Interface. *ACS Nano* **2012**, *6*, 1044–1050.
- (46) Som, A.; Chakraborty, I.; Maark, T. A.; Bhat, S.; Pradeep, T. Cluster-Mediated Crossed Bilayer Precision Assemblies of 1D Nanowires. *Adv. Mater.* **2016**, *28*, 2827–2833.
- (47) Liu, G.-K.; Hu, J.; Zheng, P.-C.; Shen, G.-L.; Jiang, J.-H.; Yu, R.-Q.; Cui, Y.; Ren, B. Laser-Induced Formation of Metal-Molecule-Metal Junctions between Au Nanoparticles as Probed by Surface-Enhanced Raman Spectroscopy. *J. Phys. Chem. C* **2008**, *112*, 6499–6508.
- (48) Joo, T. H.; Kim, M. S.; Kim, K. Surface-Enhanced Raman Scattering of Benzenethiol in Silver Sol. *J. Raman Spectrosc.* **1987**, *18*, 57–60.
- (49) Michota, A.; Bukowska, J. Surface-Enhanced Raman Scattering (SERS) of 4-mercaptobenzoic Acid on Silver and Gold Substrates. *J. Raman Spectrosc.* **2003**, *34*, 21–25.
- (50) Zong, Y.; Guo, Q.; Xu, M.; Yuan, Y.; Gu, R.; Yao, J. Plasmon-Induced Decarboxylation of Mercaptobenzoic Acid on Nanoparticle Film Monitored by Surface-Enhanced Raman Spectroscopy. *RSC Adv.* **2014**, *4*, 31810–31816.
- (51) Frisch, M. J.; Trucks, G. W.; Schlegel, H. B.; Scuseria, G. E.; Robb, M. A.; Cheeseman, J. R.; Scalmani, G.; Barone, V.; Mennucci,

B.; Petersson, G. A.; et al. *Gaussian 09*; Gaussian, Inc.: Wallingford, CT, 2009.

(52) Enkovaara, J.; Rostgaard, C.; Mortensen, J. J.; Chen, J.; Dulak, M.; Ferrighi, L.; Gavnholt, J.; Glinsvad, C.; Haikola, V.; Hansen, H. A.; et al. Electronic Structure Calculations with Gpaw: A Real-Space Implementation of the Projector Augmented-Wave Method. *J. Phys.: Condens. Matter* **2010**, *22*, 253202.

(53) Bahn, S. R.; Jacobsen, K. W. An Object-Oriented Scripting Interface to a Legacy Electronic Structure Code. *Comput. Sci. Eng.* **2002**, *4*, 56–66.

(54) Dion, M.; Rydberg, H.; Schröder, E.; Langreth, D. C.; Lundqvist, B. I. Van Der Waals Density Functional for General Geometries. *Phys. Rev. Lett.* **2004**, *92*, 246401.

(55) Hammer, B.; Hansen, L. B.; Nørskov, J. K. Improved Adsorption Energetics within Density-Functional Theory Using Revised Perdew-Burke-Ernzerhof Functionals. *Phys. Rev. B: Condens. Matter Mater. Phys.* **1999**, *59*, 7413–7421.

Supporting information

Toward a Janus Cluster: Regiospecific Decarboxylation of Ag₄₄(4-MBA)₃₀@Ag Nanoparticles

Indranath Chakraborty,[‡] Anirban Som,[‡] Tuhina Adit Maark, Biswajit Mondal, Depanjan Sarkar and Thalappil Pradeep*

Table of contents

Description	Page No.
Computational details	S2
Supporting figures	S3

List of figures

Figure No.	Description	Page No.
Figure S1	Characterization of self-assembled silver nanoparticles	S3
Figure S2	UV/Vis of Ag ₄₄ MBA ₃₀ and Ag ₄₄ TP ₃₀ cluster and ESI MS of Ag ₄₄ MBA ₃₀	S4
Figure S3	Comparative Raman spectra of Ag ₄₄ MBA ₃₀ and MBA	S5
Figure S4	UV/Vis spectra of Ag ₄₄ MBA ₃₀ cluster mixed with silver nanoparticles before and after centrifugation	S6
Figure S5	Intensity vs exposure time plot for the four major peaks	S7
Figure S6	Effect of silver nanoparticles on decarboxylation: Raman spectra	S8
Figure S7	Raman spectrum of Ag ₄₄ MBA ₃₀ on Au@citrate film and the UV/Vis spectra of the Au@citrate particles	S9

Computational details

The structure for $\text{Ag}_{44}(\text{MBA})_{30}$ utilized in the figures in the main text was generated using the X-ray crystallographic coordinates deposited at the Cambridge Crystallographic Data Centre (CCDC) under the deposition name CCDC 949240. This data is available free of charge from CCDC at http://www.ccdc.cam.ac.uk/data_request/cif.

In this work small model clusters of the type $\text{Ag}_1(\text{MBA})_2$, $\text{Ag}_1(\text{TP})_2$ and $\text{Ag}_1(\text{MBA})_1(\text{TP})_1$ were studied using the Gaussian 09 program package [add ref: Gaussian 09, R. A., M. J. Frish, G. W. Trucks, H. B. Schlegel, G. E. Scuseria, M. A. Robb, J. R. Cheeseman, G. Scalmani, V. Barone, B. Mennucci, G. A. Petersson, et al., Gaussian, Inc., Wallingford CT 2009.]. All calculations were performed using the density functional theory (DFT) method. The Perdew-Burke-Ernzerhof (PBE) exchange-correlation functional¹⁻² was used along with along with the Stuttgart/Dresden Effective Core Potentials (ECPs) which included quasi-relativistic effects. The QZVP basis set fitted to the charge density via the W06 fitting set was utilized.³⁻⁴ The following convergence criteria were adopted for the geometry optimizations: 10^{-7} a.u. for energy, 10^{-9} a.u. for electron density, 0.00045 a.u. for force and 0.0018 a.u. for atomic displacement. Absence of imaginary frequencies in the vibrational spectra proved the structures of all the clusters studied herein were real energy minima. The Raman spectra were generated using the visualization program, MOLDEN.⁵

Adsorption of the following species: benzoic acid, benzene, mercapto benzoic acid radical (MBA*) and thiophenol radical (TP*) was studied on Ag(111). These calculations were performed using the python based GPAW code⁶ within the atomic simulation environment (ASE).⁷ First all the geometries were optimized using the revised Perdew-Burker-Ernzerhof (RPBE) functional⁸ and the double zeta polarized (DZP) basis set in the LCAO mode in order to achieve faster computations. Next single point energy calculations were performed with these structures using the van der Waals density functional (vdW-DF2)⁹ to obtain accurate adsorption and decarboxylation energies.

The single point energy calculations with vdW-DF2 were carried out with plane-waves. For these plane-wave cut-off energy of 450 eV was employed and the following convergence criteria were used: 0.0005 eV/electron for energy, 0.0001 eV for density and $4.0e^{-08}$ eV²/electron for eigenstates. The adsorption energies of the adsorbates were calculated with reference to the

corresponding molecules. To this end each molecule was placed at the center of a large unit cell $15 \times 15 \times 15 \text{ \AA}$ in dimensions and calculations were performed at the gamma point. For all surface calculations a $4 \times 4 \times 1$ Monkhorst-Pack k -point mesh was used and dipole corrections were taken into account. The lattice constant of fcc Ag (bulk) was determined to be 4.22 \AA , which was the minimum in the total energy versus lattice constant plot from the LCAO/RPBE calculations. The Ag(111) surface was modeled as a 2×4 (atoms) periodic slab four layers thick and with 20 \AA of vacuum between neighboring slabs. Of the four layers, the top two were allowed to relax and the bottom two were fixed at their bulk DFT (RPBE)-calculated lattice constant of 4.22 \AA . Adsorption of each species (benzoic acid, benzene, MBA* and TP*) was considered at the four unique sites of the Ag(111) surface, namely, on-top, bridge, fcc and hcp.

Figures

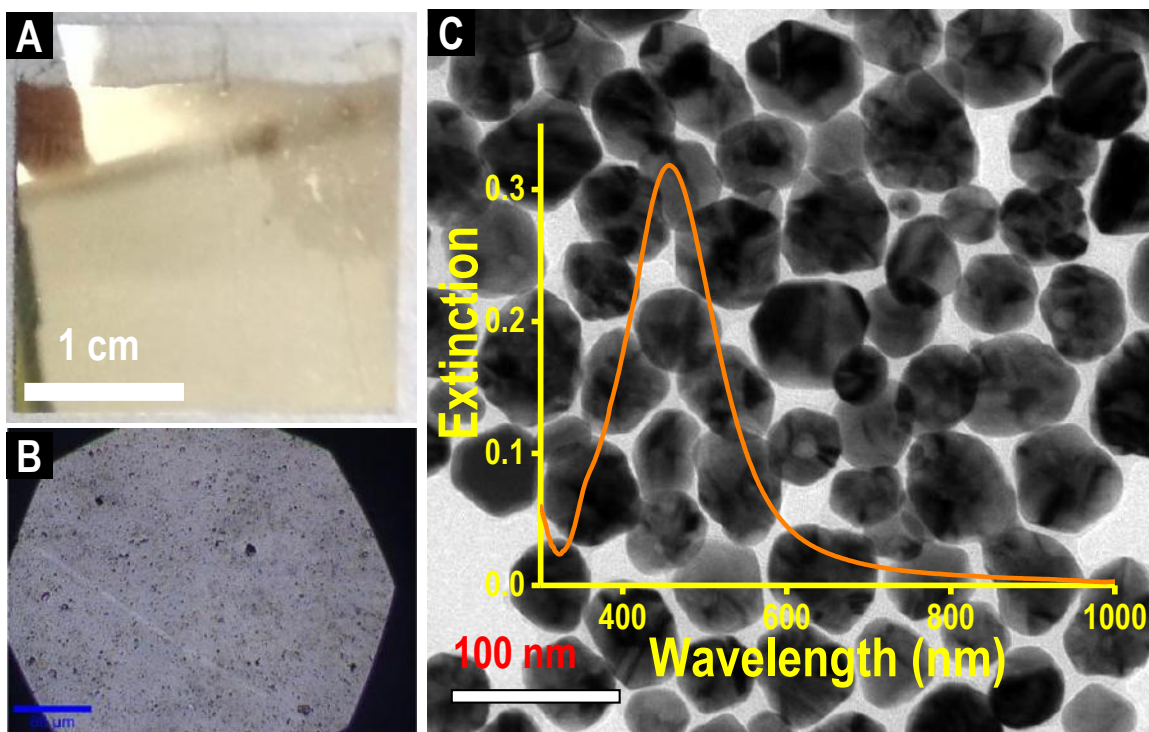


Figure S1: Characterization of silver nanoparticles and the self-assembled monolayer film made on a coverslip. A) Optical image of the nanoparticles film showing shiny golden color. B) and C) TEM image of the self-assembled silver particles. Inset shows the corresponding UV/Vis spectrum of the nanoparticles in solution.

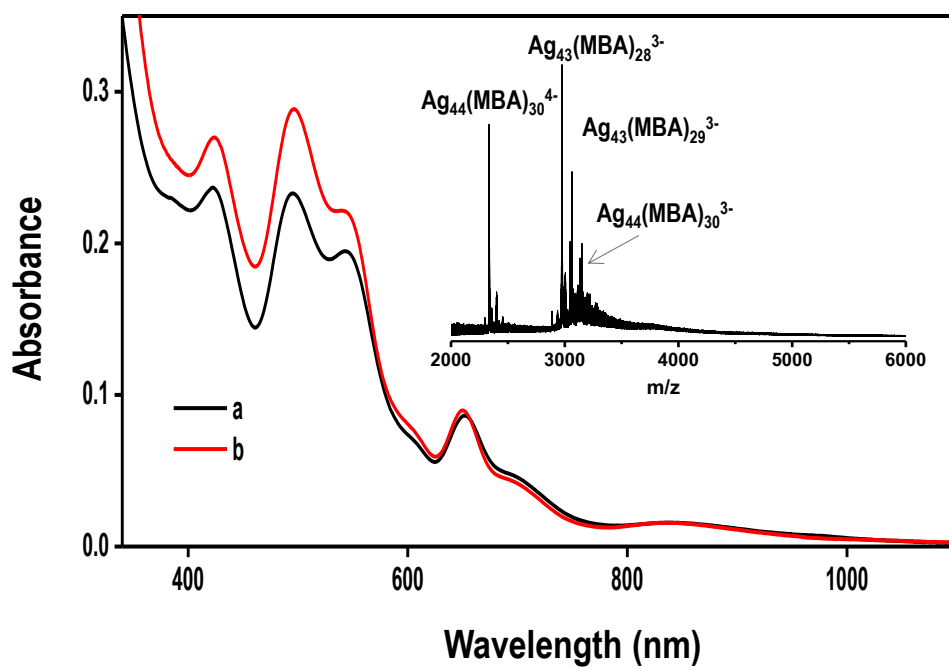


Figure S2: UV/Vis spectrum of the purified $\text{Ag}_{44}\text{MBA}_{30}$ (a) and $\text{Ag}_{44}\text{TP}_{30}$ (b) clusters in DMF and acetonitrile solution, respectively showing the characteristic features. The cluster features are indistinguishable from each other. Inset shows the ESI MS spectra of $\text{Ag}_{44}(\text{MBA})_{30}$ cluster.

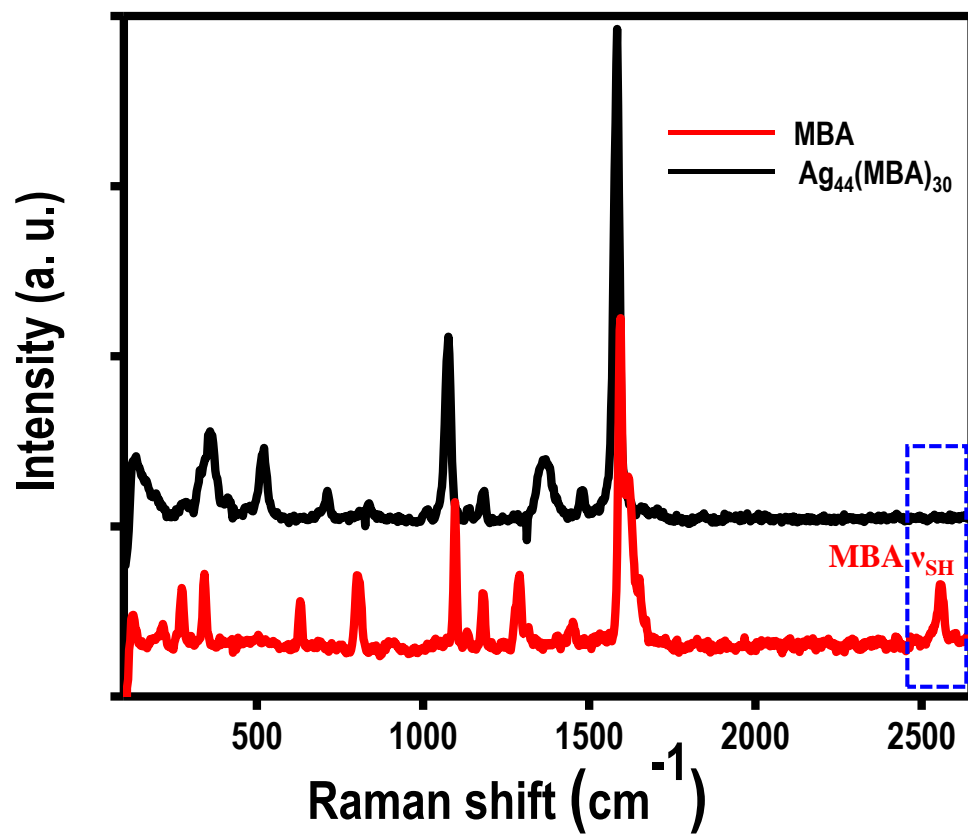


Figure S3: Comparative Raman spectra of Ag₄₄MBA₃₀ and MBA. Absence of S-H stretching in Ag₄₄MBA₃₀ is marked.

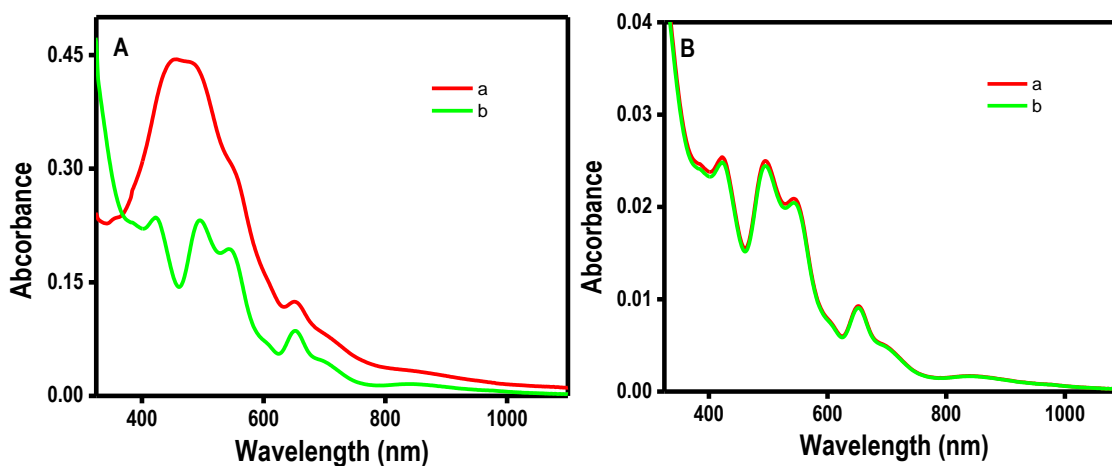


Figure S4: A: (a) UV/Vis spectrum of the solution obtained after extracting $\text{Ag}_{44}\text{MBA}_{30}@\text{Ag}$ NPs, post laser irradiation. (b) UV/Vis spectrum of the supernatant solution after centrifugation, showing features corresponding to only Ag_{44} . Ag NPs being bigger in size, precipitated upon centrifugation leaving $\text{Ag}_{44}\text{MBA}_{30-x}\text{TP}_x$ in the solution. This confirms the chemical integrity of the cluster core on Ag NPs upon exposure to the laser beam. B: The UV/Vis spectra of a definite amount of $\text{Ag}_{44}(4\text{-MBA})_{30}$ cluster solution before (a) and after (b) before the 633 nm laser irradiation. Very similar absorbance of the cluster solution following laser irradiation confirms the stability of the clusters. Slight decrease in intensity seen is probably due to loss of the clusters during extraction-centrifugation process.

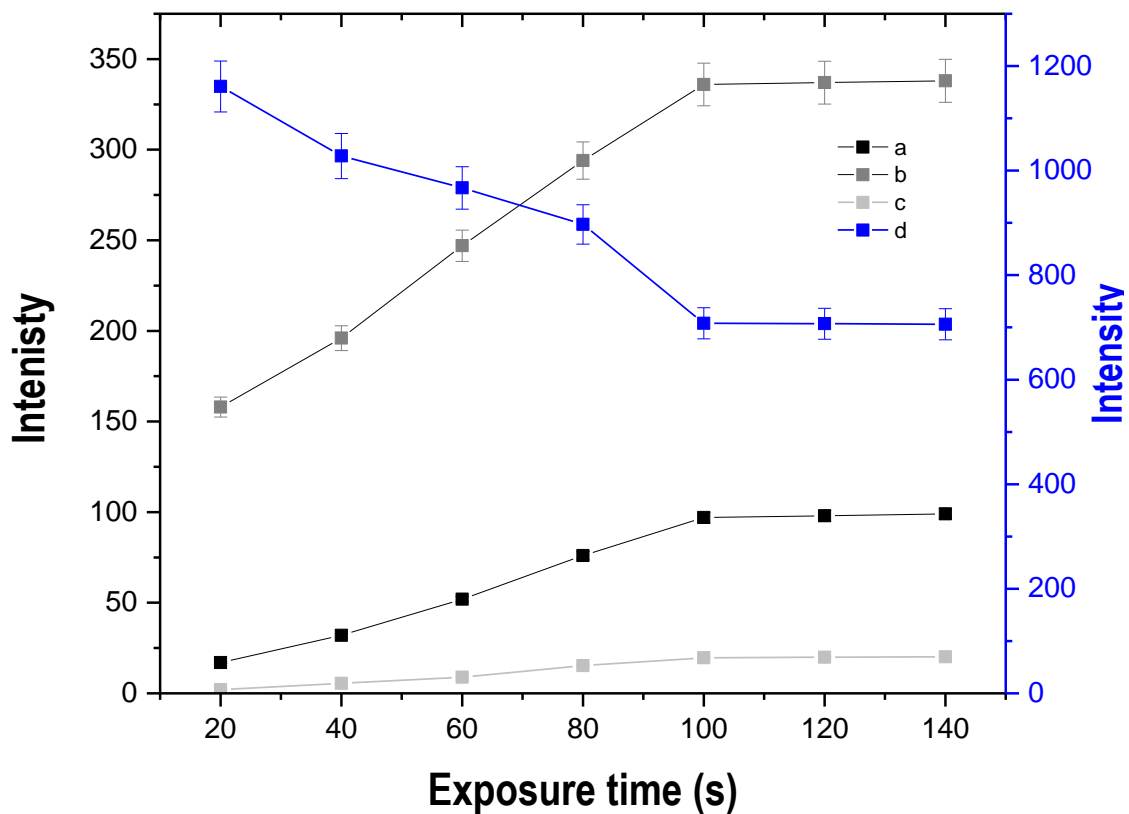


Figure S5: Intensity vs. exposure time plot for the four peaks centered at 1003 cm^{-1} (a), 1026 cm^{-1} (b), 1576 cm^{-1} (c) and 1587 cm^{-1} (d). It is noticeable that for the first three peaks, the intensity increases up to 100 s and then it saturates confirming the end of the transformation. The fourth one also follows the same trend but here intensity goes down as it is due to MBA.

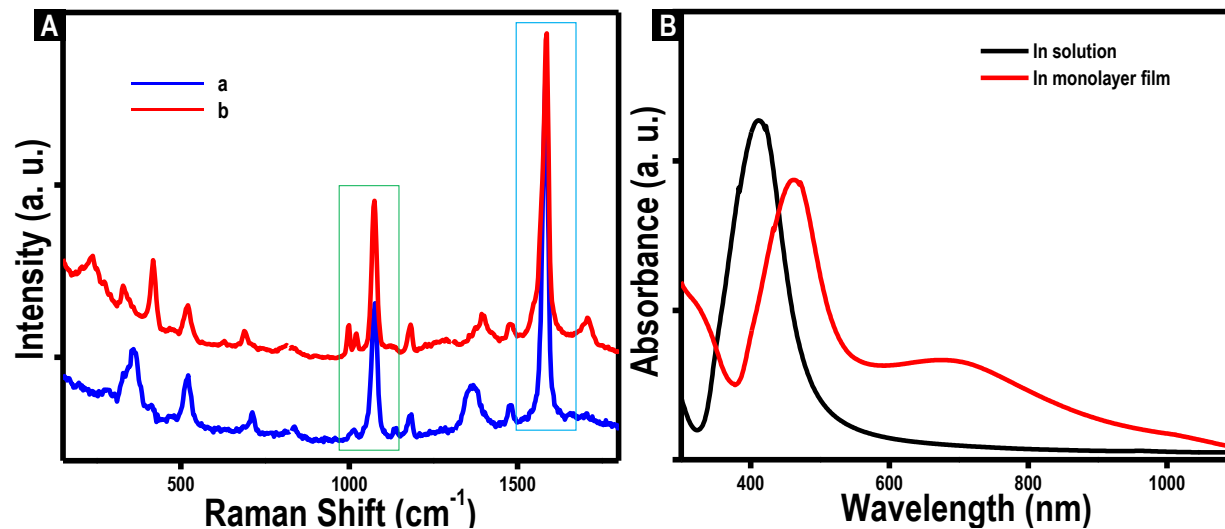


Figure S6: (A) Effect of silver nanoparticles on the decarboxylation. a) Cluster drop-cast on coverslip alone and b) cluster drop-cast on a self-assembled silver nanoparticles film made on a coverslip. Clusters coated on a TLC plate behaved similarly to coverslips. Without silver nanoparticles, decarboxylation did not happen suggesting the effect of plasmon excitation in this process (see the marked regions where the emergence of features due to TP are shown). (B) Difference in the UV-visible spectra of Ag NPs in solution phase with that of a monolayer film transferred onto a microscope cover glass. The film shows signatures of plasmon coupling.

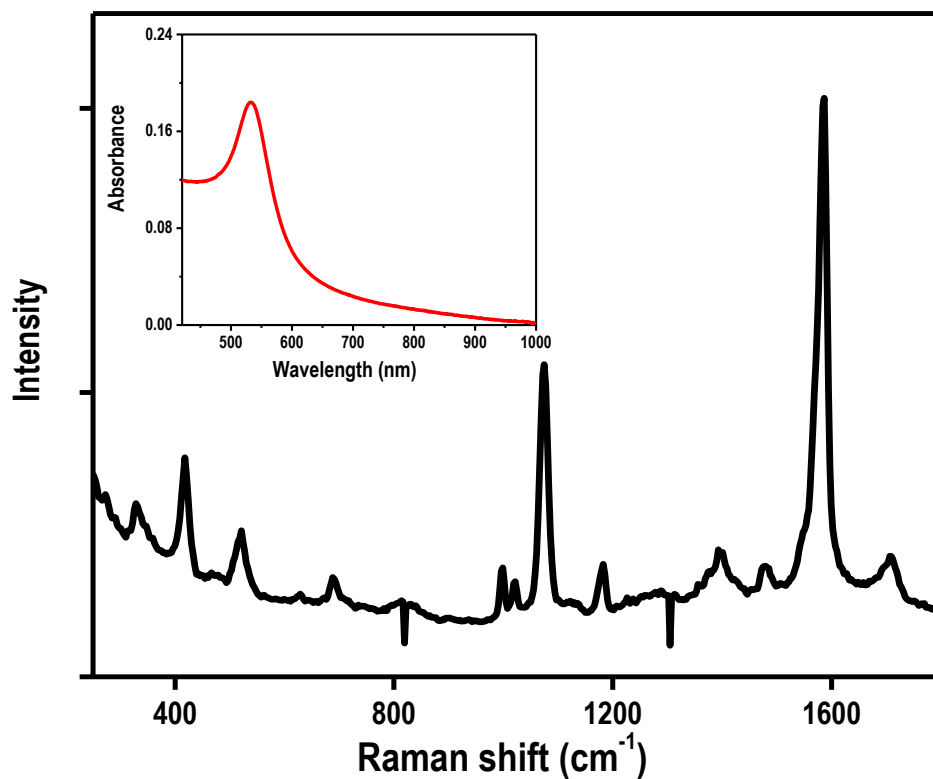


Figure S7: Raman spectrum of Ag₄₄MBA₃₀ cluster on a film of Au@PVP. Inset shows the corresponding UV/Vis spectrum of the Au@PVP particle in solution.

REFERENCES

1. Ernzerhof, M.; Perdew, J. P., Generalized Gradient Approximation to the Angle- and System-Averaged Exchange Hole. *J. Chem. Phys.* **1998**, *109*, 3313-3320.
2. Perdew, J. P.; Burke, K.; Ernzerhof, M., Generalized Gradient Approximation Made Simple. *Phys. Rev. Lett.* **1996**, *77*, 3865-3868.

3. Weigend, F., Accurate Coulomb-Fitting Basis Sets for H to Rn. *Phys. Chem. Chem. Phys.* **2006**, *8*, 1057-1065.
4. Weigend, F.; Ahlrichs, R., Balanced Basis Sets of Split Valence, Triple Zeta Valence and Quadruple Zeta Valence Quality for H to Rn: Design and Assessment of Accuracy. *Phys. Chem. Chem. Phys.* **2005**, *7*, 3297-3305.
5. Schaftenaar, G.; Noordik, J. H., Molden: A Pre- and Post-Processing Program for Molecular and Electronic Structures. *J. Comput.-Aided Mol. Des.* **2000**, *14*, 123-134.
6. Enkovaara, J., et al., Electronic Structure Calculations with Gpaw: A Real-Space Implementation of the Projector Augmented-Wave Method. *J. Phys.: Condens. Matter* **2010**, *22*, 253202.
7. Bahn, S. R.; Jacobsen, K. W., An Object-Oriented Scripting Interface to a Legacy Electronic Structure Code. *Comput. Sci. Eng.* **2002**, *4*, 56-66.
8. Hammer, B.; Hansen, L. B.; Nørskov, J. K., Improved Adsorption Energetics within Density-Functional Theory Using Revised Perdew-Burke-Ernzerhof Functionals. *Phys. Rev. B.* **1999**, *59*, 7413-7421.
9. Dion, M.; Rydberg, H.; Schröder, E.; Langreth, D. C.; Lundqvist, B. I., Van Der Waals Density Functional for General Geometries. *Phys. Rev. Lett.* **2004**, *92*, 246401.

RESEARCH ARTICLE

Desorption Electrospray Ionization (DESI) Mass Spectrometric Imaging of the Distribution of Rohitukine in the Seedling of *Dysoxylum binectariferum* Hook. F

Patel Mohana Kumara¹, Amitava Srimany¹, Suganya Arunan¹, Gudasalamani Ravikanth^{2,3}, Ramanan Uma Shaanker^{2,3}, Thalappil Pradeep^{1*}

1 DST Unit of Nanoscience and Thematic Unit of Excellence, Department of Chemistry, Indian Institute of Technology Madras, Chennai, 600036, India, **2** School of Ecology and Conservation, Department of Crop Physiology, University of Agricultural Sciences, GKVK, Bengaluru, 560065, India, **3** Ashoka Trust for Research in Ecology and the Environment, Royal Enclave, Srirampura, Jakkur, Bengaluru, 560064, India

* pradeep@iitm.ac.in



CrossMark
click for updates

OPEN ACCESS

Citation: Mohana Kumara P, Srimany A, Arunan S, Ravikanth G, Uma Shaanker R, Pradeep T (2016) Desorption Electrospray Ionization (DESI) Mass Spectrometric Imaging of the Distribution of Rohitukine in the Seedling of *Dysoxylum binectariferum* Hook. F. PLoS ONE 11(6): e0158099. doi:10.1371/journal.pone.0158099

Editor: Doralyn S Dalisay, University of San Agustin, PHILIPPINES

Received: October 30, 2015

Accepted: June 12, 2016

Published: June 30, 2016

Copyright: © 2016 Mohana Kumara et al. This is an open access article distributed under the terms of the [Creative Commons Attribution License](https://creativecommons.org/licenses/by/4.0/), which permits unrestricted use, distribution, and reproduction in any medium, provided the original author and source are credited.

Data Availability Statement: All relevant data are within the paper and its Supporting Information files.

Funding: Department of Science and Technology (DST), SERB-DST Fast Track grant (File No. SB/YS/LS-361/2013) and Department of Biotechnology (DBT), Government of India supported to carry out this work. The funders had no role in study design, data collection and analysis, decision to publish, or preparation of the manuscript.

Abstract

Ambient ionization mass spectrometric imaging of all parts of the seedling of *Dysoxylum binectariferum* Hook. f (Meliaceae) was performed to reconstruct the molecular distribution of rohitukine (Rh) and related compounds. The species accumulates Rh, a prominent chromone alkaloid, in its seeds, fruits, and stem bark. Rh possesses anti-inflammatory, anti-cancer, and immuno-modulatory properties. Desorption electrospray ionization mass spectrometry imaging (DESI MSI) and electrospray ionization (ESI) tandem mass spectrometry (MS/MS) analysis detected Rh as well as its glycosylated, acetylated, oxidized, and methoxylated analogues. Rh was predominantly distributed in the main roots, collar region of the stem, and young leaves. In the stem and roots, Rh was primarily restricted to the cortex region. The identities of the metabolites were assigned based on both the fragmentation patterns and exact mass analyses. We discuss these results, with specific reference to the possible pathways of Rh biosynthesis and translocation during seedling development in *D. binectariferum*.

Introduction

Chromone alkaloids consist of a noreugenin chromone (5,7-dihydroxy-2-methylchromone) component linked with a ring containing one or more nitrogen atoms [1–3]. These metabolites are structurally diverse and are derived from the convergence of multiple biosynthetic pathways that are widely distributed in plant (Meliaceae and Rubiaceae) and animal kingdoms [2, 4–8]. The natural occurrence of rohitukine (Rh), a chromone alkaloid, is restricted to only five plant species; *Amoora rohituka* [4], *Dysoxylum binectariferum* [5], *D. acutangulum* [7] (all from the Meliaceae family), *Schumanniophyton magnificum*, and *S. problematicum* [1, 2] (from the Rubiaceae family). Among these species, *D. binectariferum* accumulates the highest amount of Rh (3–7% by dry weight in stem bark) [9, 10]. Recently, dysoline, a new regioisomer

Competing Interests: The authors have declared that no competing interests exist.

of Rh was reported from the stem bark of *D. binectariferum* [11]. Besides the plant sources, endophytic fungi associated with *A. rohituka* and *D. binectariferum* have also been shown to produce Rh in culture, independent of the host tissue [12–14]. The biosynthetic pathway of chromone alkaloids in general, and Rh in particular, have not been elucidated [15], though the occurrence of free noreugenin in the plant suggests that it might be formed prior to the conjugation with the nitrogen-containing moiety. The presence of trigonelline in chromone alkaloid producing plants suggest that it could be a possible precursor for pyridine-related alkaloids [1, 2]. Recent studies have reported a pentaketide chromone synthase (PCS) that catalyzes the formation of the noreugenin compound, 5,7-dihydroxy-2-methylchromone, from five malonyl-CoA precursor units [16–19]. Studies have also reported that ornithine is an initial precursor molecule for the biosynthesis of piperidine, nicotine, and tropane alkaloids [20]. The nitrogenous group derived from ornithine could be the origin of the nitrogen atom in chromone alkaloid biosynthesis.

Pharmacologically, Rh has been reported to have anti-inflammatory, anti-fertility, anti-implantation, anti-cancer, and anti-adipogenic activities besides having immuno-modulatory properties [2, 4–8, 11, 21]. Two derivatives, namely, flavopiridol (also known as HMR 1275 or alvocidib) and P-276-00 have been shown to competitively bind to the ATP binding pocket of cyclin-dependent kinases (CDKs) and inhibiting their activity. Flavopiridol arrests the cell cycle at both G1 and G2 phases and has been shown to be effective against breast and lung cancers and chronic lymphocytic leukemia [22, 23]. The compound has been approved as an orphan drug for treatment of chronic lymphocytic leukaemia [8]. Flavopiridol has also been shown to block human immuno-deficiency virus Tat trans-activation and viral replication through inhibition of positive transcription elongation factor b (P-TEFb) [24, 25]. The derivative P-276-00 is in phase II clinical studies for advanced refractory neoplasms and multiple myeloma [8].

In a recent study, we have examined the spatial and temporal distribution pattern of Rh and related compounds in different parts of the seeds of *D. binectariferum* [26]. Rh (m/z 306.2) accumulation increased from early seed development to seed maturity and was largely found in the embryo and cotyledon. Besides Rh, we also reported the presence of Rh acetate (m/z 348.2), and glycosylated Rh (m/z 468.2) in the seeds.

In this study, we examine the spatial distribution of Rh and related compounds in seedlings of *D. binectariferum* using desorption electrospray ionization mass spectrometry imaging (DESI MSI). In DESI MS, molecular masses are analyzed by transporting desorbed ions generated by spraying electrically charged solvent droplets at the sample of interest into the mass spectrometer [27]. This is an ambient ionization technique and consequently many of the limitations of conventional mass spectral analysis do not apply here. In recent years, the technique has been used widely to spatially map the occurrence of a number of plant secondary metabolites and infer the underlying mechanisms leading to spatial patterns as well as their adaptive significance [28–33]. MALDI MS has been used to identify metabolites in glandular trichomes from a wild tomato (*Solanum habrochaites*) leaf at a spatial resolution of around 50 μm [34]. More recently, mass spectrometric imaging have been used in conjunction with tissue specific transcriptomic analysis to deduce the biosynthetic pathway; for example, in Flax (*Linum usitatissimum*) [35], *Arabidopsis* [36], and *Podophyllum* species [37, 38]. The increasing use of MS imaging for spatial pattern analysis owes itself to its relative ease of use and its unique advantage, especially when detecting relatively labile compounds that may lose their structural and chemical characteristics upon extraction.

In the present study, using DESI MSI we have mapped the spatial distribution of Rh and other related compounds in the seedlings of *D. binectariferum*. The identities of most of the metabolites, including Rh were assigned based on both the fragmentation patterns and exact

mass analyses. We discuss these results, with specific reference to the possible pathways of Rh biosynthesis and translocation.

Materials and Methods

Ethics statement

The fieldwork and collection of seed sample of *D. binectariferum* was carried out in the central Western Ghats regions of Karnataka (Jog, 14° 13' 65" N, 74° 48' 35" E) with kind permission from the Karnataka Forest Department, Bengaluru. Seed sampling was carried out under the supervision of forest officers and used solely for scientific research. The sampling was non-invasive with no impact on the natural growth or regeneration of *D. binectariferum* populations in the wild.

Plant material

D. binectariferum (diploid chromosome number $2n = 80$) is a medium to large sized tree distributed in the tropical and subtropical regions of Eastern Himalayas, Khasi Hills, Western Ghats of Peninsular India, and Sri Lanka. In the Western Ghats, *D. binectariferum* is distributed from Coorg to the Anamalais and Tinnevely in the moist forest [39]. The plant is pollinated by insects [40] while the seeds are dispersed by birds (hornbills and imperial pigeons). Seedling recruitment in the natural habitats is limited because of heavy predation of fruits by rodents [41].

D. binectariferum seeds were collected from Jog (14° 13' 65" N, 74° 48' 35" E) located in the central Western Ghats, India. From these seeds, seedlings were raised in polybags in the Forest Nursery at the University of Agricultural Sciences, GKVK, Bengaluru and later transported to the Indian Institute of Technology Madras campus at Chennai. Seedlings were maintained under shade and were well watered. Root, shoot, leaves, and cotyledons of 10 month old seedlings were used for the imaging studies.

Extraction of Rh and HPLC analysis

10 months old seedlings ($n = 3$), about 25 cm in length (Fig 1A), were collected from the nursery and oven dried for 4 days at 70°C. Rh was extracted from different parts of the seedlings (root, stem, and leaves) following earlier report [9]. Rh content (w/w) in the extracted samples were analyzed using reverse-phase HPLC (Shimadzu, LC20AT, Japan), RP-18 column (4.6 X 250 mm, 5 μ m) with UV absorbance at 254 nm [9, 26]. The solvent system comprised of acetonitrile and 0.1% TFA as mobile phase. A gradient starting from 0%:100% to 100%:0% of acetonitrile:0.1% TFA with a flow rate of 1000 μ L/min was used. Sharp peak with highest peak intensity was obtained at a mobile phase composition of 30% acetonitrile and 70% TFA (0.1%). All samples were then analyzed in an isocratic mode using 30% acetonitrile:70% TFA (0.1%) as mobile phase. A standard curve was constructed using various concentrations (0.125, 0.25, 0.5, 0.75, and 1 mg/mL) of Rh [9]. 20 μ L of each of the standard concentrations were injected into the HPLC and their respective retention times (R_t) and peak areas were recorded. The peak area was plotted against the respective concentration and a regression analysis was carried out. Using the regression equation, Rh content was calculated per 100 g dry weight basis. All estimates were made over 3 replicate samples.

ESI MS analysis

Different sections of the root, shoot, leaves, and cotyledons (corresponding to regions that were used for the imaging) were cut into small pieces and soaked in methanol for 12 hours.

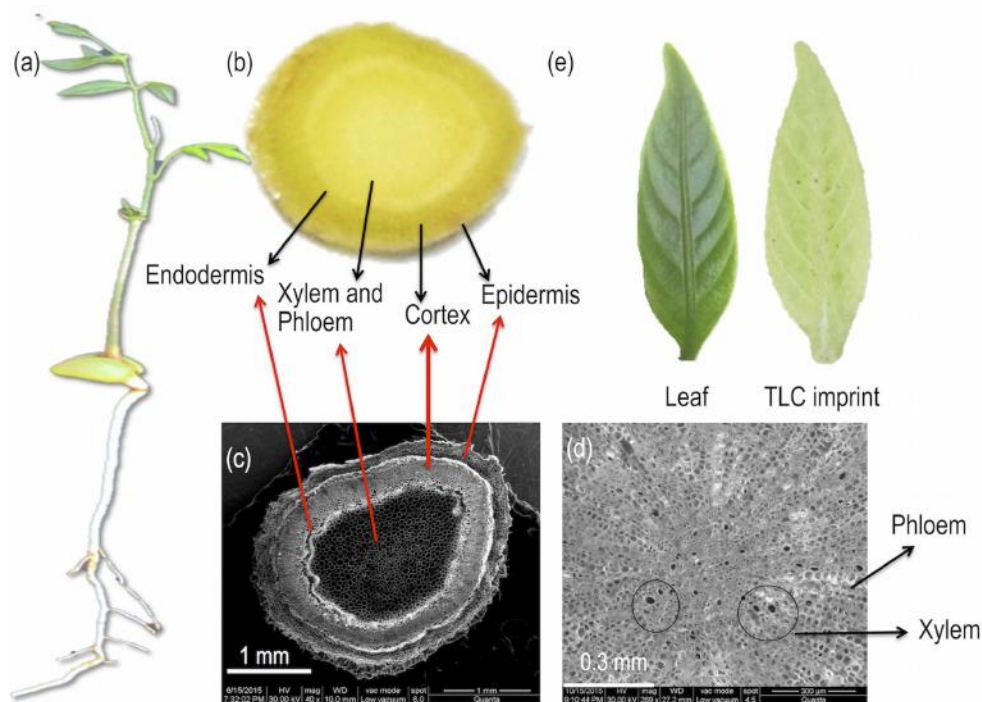


Fig 1. (a) 10 month old seedling of *D. binectariferum*, (b) Cross section of the root, (c) Scanning electron microscope (SEM) image of cross section of the root, (d) Magnified SEM image of the root showing the xylem and phloem, and (e) Leaf and its TLC imprint.

doi:10.1371/journal.pone.0158099.g001

The solution was filtered and centrifuged at 10000 rpm for 10 minutes. The supernatant was analyzed by ESI MS/MS using Thermo Scientific LTQ XL (Thermo Scientific, San Jose, CA, USA) mass spectrometer and exact mass was analyzed using Thermo Scientific Orbitrap Elite (Thermo Scientific, San Jose, CA, USA) mass spectrometer. The data was acquired in positive ion mode with a spray voltage of 5 kV. Collision induced dissociation (CID) was used for fragmentation of the ions during MS/MS measurements. The identities of the ions were established based on both the fragmentation patterns and exact masses of the ions obtained and using METLIN metabolite database [42]. The mass tolerance of ± 3 ppm was used in the METLIN database search. The MS/MS data was used to infer the compound identity by comparing the fragment ion m/z with published literature and database. All the spectra are represented in the profile mode.

Desorption electrospray ionization mass spectrometry imaging (DESI MSI)

Using a surgical blade, seedlings (10 months old) were neatly cut to separate the root, stem, and meristem. Longitudinal and cross sections of different plant parts were made according to the experimental needs. Cross sections (about 2 mm thick) were made at every 1 cm interval from the root tip to the shoot tip while longitudinal sections were made approximately at the median axis of the root and stem. Cross section of the root (Fig 1B) was observed under FEI Quanta 200 environmental scanning electron microscope (ESEM). The images clearly showed the parts corresponding to the epidermis, endodermis, cortex, xylem, and phloem tissues (Fig 1C and 1D).

To get an imprint of the molecules present on the cut-end of the section on a flat surface, a TLC plate (TLC Silica gel 60 F₂₅₄, Merck KGaA, Germany) was pre-wetted with methanol and kept on a heating mantle (~70°C). The cut sections (both cross and longitudinal sections) were placed on the hot TLC plate and hand pressed for 10 seconds to get an imprint [26, 43]. Leaves of 10 months old seedlings were imprinted on a TLC plate (Fig 1E) with 2 ton pressure for 15 to 30 seconds using a hydraulic pelletizer [32].

Imaging experiments were conducted using Thermo Scientific LTQ XL (Thermo Scientific, San Jose, CA, USA) mass spectrometer with 2D DESI ion source (Omni Spray Ion Source) from Prosofia, Inc., Indianapolis, IN, USA. The DESI source conditions were as follows; nebulizing gas (dry nitrogen) pressure: 150 psi, spray angle: 60° to the sample surface, tip of spray to sample surface distance: 1 mm, tip of spray to mass spectrometer inlet distance: 3 mm, spray solvent: methanol, solvent flow rate: 5 µL/min, spray voltage: 5 kV, and ionization mode: positive (+ve). The image area was chosen according to the sample dimensions and the spatial resolution used was 250 µm X 250 µm. Imaging 1 cm X 1 cm area of tissue sample took approximately 30 min. Imaging time varied with the area of the tissue samples. For a seedling of 25 cm in length, it took about 12 hours to completely image the whole seedling. Image files (IMG File) were created using FireFly software from the acquired data and BioMAP software were used to process the image files to create images. Normalization of the images were done for the individual ions in a particular Figure. While processing the image files in BioMAP, separate images could be generated with a difference of 0.083 in *m/z*. The *m/z* values obtained from BioMAP image had been approximated to one decimal place. For example, in case of Rh (*m/z* 306.2, obtained from DESI MS data), we generated image in BioMAP at *m/z* 306.167 instead of *m/z* 306.250, as the latter deviated more from the experimental value. In this process, we might encounter a situation where, for a particular ion, images may actually represent several species, as biological samples are complex mixtures. However, Orbitrap data excluded the possibility of existence of other ions in close proximity to the ions of interest, although a single *m/z* value might represent different isomers.

Results and Discussion

Metabolite identification via ESI MS/MS and exact mass measurement

ESI MS analysis of the seedlings showed molecular signatures in the range of *m/z* 140–1000 (S1 Table). These masses included those of Rh, its related compounds and several unknowns. For the purpose of this paper, we restrict our further analysis to only the chromone alkaloids and their possible precursors. The ions were subjected to fragmentation using CID during ESI MS/MS analysis (Fig 2 and S1 Table). Considering the fragmentation patterns and the exact masses of the ions, probable chemical formulae and structures of the chromone alkaloids and their precursors were arrived at using the METLIN metabolite database (Fig 2) [42]. A list of *m/z* values of the parent and fragment ions, their probable chemical formulae, and structures are given in S1 Table.

Rh and related chromone alkaloids. The parent molecule Rh (*m/z* 306.2) fragmented into daughter ions at *m/z* 288.0, 245.0, and 222.0 (Fig 2B) similar to the daughter ions obtained from a standard (Fig 2A). The peak at *m/z* 288.0 is due to the neutral loss of H₂O from the piperidine ring and *m/z* 245.0 is due to further fragmentation of the ring. The peak at *m/z* 222.0 is due to the fragmentation of the chromone ring [14, 44].

Rh-N-oxide (*m/z* 322.2) was recovered from leaves. Fragmentation of this molecule yielded three ions at *m/z* 304.3, 276.2, and 238.0. The peak at *m/z* 304.3 is due to the neutral loss of H₂O from the piperidine ring and *m/z* 276.2 is due to further fragmentation of the piperidine ring. The peak at *m/z* 238.0 is due to the fragmentation of the chromone ring (Fig 2C) [14].

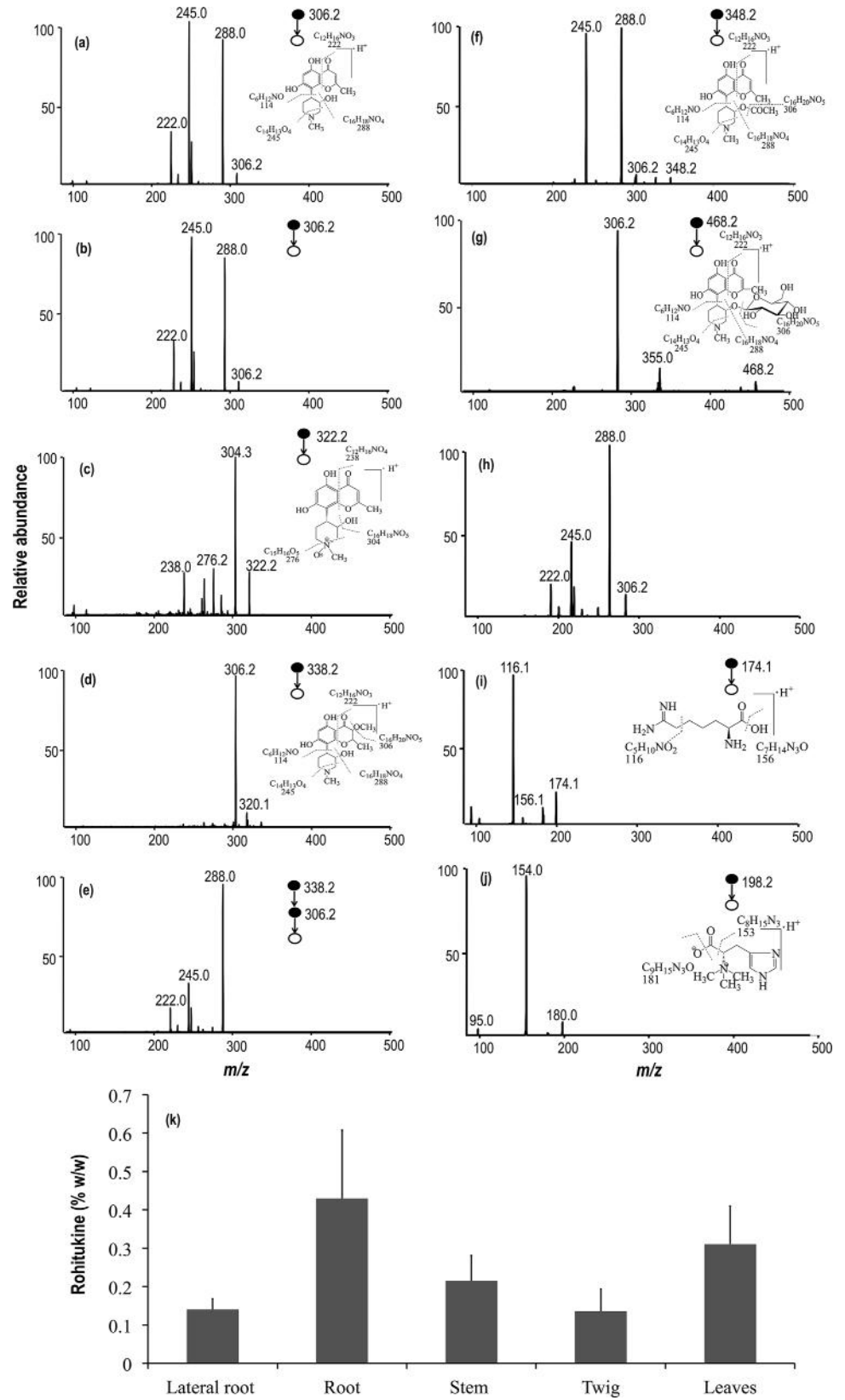


Fig 2. ESI MS/MS fragmentation patterns of (a) standard Rh, (b) plant Rh, (c) Rh-N-oxide, (d, e) methoxylated Rh, (f) Rh acetate, (g, h) glycosylated Rh, (i) indospicine, and (j) hercynine. Insets in images show the schemes of mass fragmentation of the respective metabolites. (k) Rohitukine content (% w/w) in different parts of 10 month old seedlings of *D. binectariferum*.

doi:10.1371/journal.pone.0158099.g002

Beside these, we also obtained an ion at m/z 338.2 from leaves, which is most likely, a methoxylated analogue of Rh. The MS/MS fragmentation of m/z 338.2 yielded m/z 306.2 which could be accounted for by the neutral loss of methanol (CH_3OH) (Fig 2D and 2E). The ion at m/z 306.2 upon further fragmentation yielded three major ions at m/z 288.0, 245.0, and 222.0 similar to that of Rh. The peak at m/z 288.0 is due to the neutral loss of H_2O from the piperidine ring and m/z 245.0 is due to further fragmentation of the ring (Fig 2E). Two other chromone alkaloids, namely, Rh acetate (m/z 348.2) (Fig 2F), and glycosylated Rh (m/z 468.2) were also recovered from the seedlings (Fig 2G and 2H).

Two other ions, m/z 328.2 and 610.9, were predicted to be sodiated Rh and protonated dimer of Rh, respectively. Their exact masses, m/z 328.1155 and 611.2598, indicated probable chemical formulae of $\text{C}_{16}\text{H}_{19}\text{NO}_5\text{Na}$ and $\text{C}_{32}\text{H}_{39}\text{N}_2\text{O}_{10}$, respectively (S1 Table) [26]. A summary of the fragmentations obtained is presented in S1 Table.

Probable precursors of chromone alkaloids. Besides Rh and its analogues, a few small molecules with m/z 174.1 and 198.2 were observed in the seedlings of *D. binectariferum*. Fragmentation patterns of these ions are shown in Fig 2I and 2J. Exact m/z of these compounds measured by Orbitrap at 174.1236 and 198.1235 indicated that they could be indospicine ($\text{C}_7\text{H}_{15}\text{N}_3\text{O}_2$) and hercynine ($\text{C}_9\text{H}_{15}\text{N}_3\text{O}_2$), respectively (S1 Table). Interestingly, both of these molecules are reported in KEGG metabolic pathway database to serve as precursors (acyl group in the cyclization) in the biosynthesis of piperidine and pyridine alkaloids and also in the biosynthesis of various fatty acids. It is likely that these molecules may also be involved in the biosynthesis of chromone alkaloids in seedlings of *D. binectariferum*.

Rh quantification via HPLC

Among the chromone alkaloids, Rh was predominant in all tissues examined. Rh content was highest in the main roots ($0.43 \pm 0.02\%$), followed by leaves ($0.31 \pm 0.01\%$), stem ($0.21 \pm 0.06\%$), and was least in lateral roots ($0.14 \pm 0.03\%$) and twigs ($0.14 \pm 0.05\%$) (Fig 2K).

Spatial distribution of metabolites in the seedlings of *D. binectariferum*

Based on the identities of the various ions assigned in the previous section, the spatial distribution patterns of the different ions in the seedlings (S1 Table) were analyzed using DESI MSI.

In cotyledons. DESI MS analysis of the cross and longitudinal sections of the cotyledon showed a few prominent metabolites (indospicine, Rh, sodiated Rh, Rh acetate, glycosylated Rh, and Rh dimer). All these, except indospicine are related to Rh. Though Rh (m/z 306.2) was uniformly distributed, the intensity was higher in the outer part of the cotyledon. This was also reflected in the distribution of acetylated Rh (m/z 348.2). The peak at m/z 915.4, possibly a trimer of Rh, reported in the seeds of *D. binectariferum* [26], was not recovered from the cotyledon (Fig 3).

In root and shoot. Electron microscopic observation of cross section of the root clearly showed different parts corresponding to the epidermis, endodermis, cortex, xylem, and phloem tissues (Fig 1C and 1D). These observations helped in better visualization and description of the localization of metabolites in the tissue parts. DESI MS images of both the cross and longitudinal sections of the seedlings showed distinct stratification of the various ions in different parts of the seedlings. By far, the intensities of many of the ions were highest in the roots

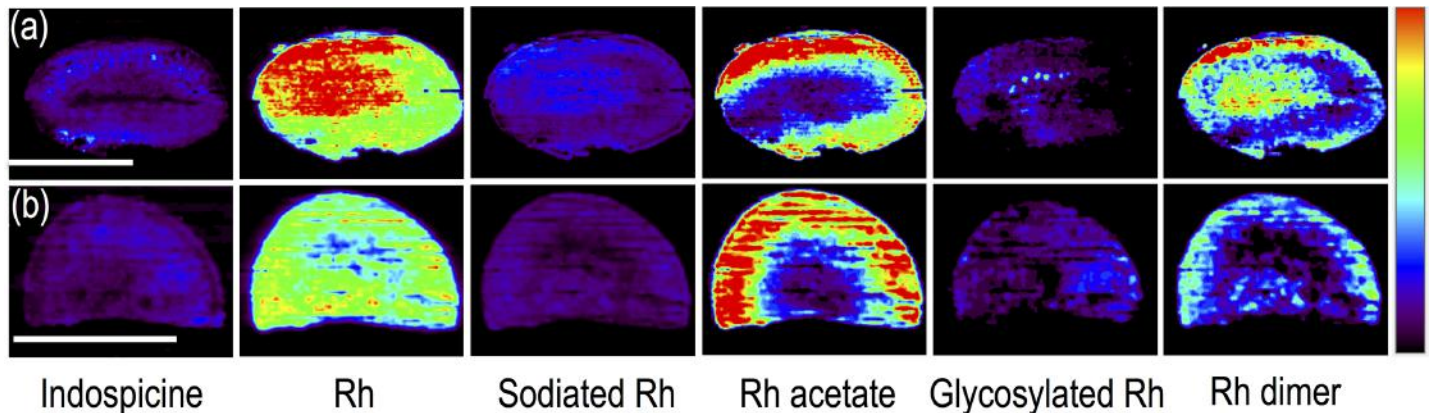


Fig 3. DESI MS images of (a) longitudinal and (b) cross section of cotyledons of *D. binectariferum*. Scale bars correspond to 5 mm and apply to all the images of a row. Intensity normalization of the images was done separately for all the individual metabolites.

doi:10.1371/journal.pone.0158099.g003

upwards to the collar region, representing the transition from the root to the shoot (Fig 4). Indospicine, hercynine, Rh, sodiated Rh, Rh dimer, and Rh trimer were present in all parts of the root and shoot while Rh acetate and glycosylated Rh were mostly present in the root and early development of shoot (Fig 4). Representative DESI MS spectra from a TLC imprint of cross sectioned root of *D. binectariferum* seedling are shown in S1 Fig.

Both longitudinal and cross section analyses indicated distinct tissue specific distribution of molecular ions. For example, indospicine, Rh, sodiated Rh, Rh dimer, and Rh trimer were found in cortex and endodermis, Rh acetate and glycosylated Rh in xylem and phloem regions, hercynine in endodermis, xylem, and phloem regions (Fig 4).

In leaves. Except Rh acetate, all other ions found in the root and stem were also present in the leaves (Fig 5). Many of the molecules detected in the leaves may be synthesized or accumulated in the leaves in response to various abiotic and biotic stresses. There was a distinct spatial pattern of the ions. For example, indospicine, Rh dimer, and Rh trimer were present in the midrib and veins, hercynine in leaf margin, Rh-N-oxide and glycosylated Rh in the leaf blade (Fig 5).

Our study showed that Rh, one of the prominent chromone alkaloids in *D. binectariferum* seedlings, was predominantly distributed in the roots and leaves compared to the stem and twigs. Within the root itself, the distribution was restricted to the main roots and less in the secondary roots (Fig 6). In stems, Rh intensity was high in the collar region separating the root from the shoot (Fig 4). Finally, among the leaves, younger apical leaves were more densely packed with Rh than the older distal leaves (Fig 6).

In a recent study, we examined the spatial and temporal distribution of Rh and related compounds in the seeds of *D. binectariferum* during different seed developmental stages [26]. We showed that Rh was predominantly localized to the cotyledonary tissues with very little in the seed coat. Presumably such high levels of Rh in the cotyledonary tissues might act as a reservoir for translocation to the growing axis of the plant during seed germination.

While there is no unequivocal evidence, it appears that Rh could be synthesized both in the roots as well as in the growing shoot apices of the plant. Within the root or stem, Rh was clearly restricted to the cortex region in and around the phloem tissues indicating that it could be actively translocated through the phloem tissues from their sites of production in the plant (Fig 6). Additional support that there could be active transport of the metabolite comes from our finding of glycosylated Rh in different parts of the seedlings. Glycosylation of secondary metabolites has been reported in many instances [45–47]. Glycosylation leads to both stabilization

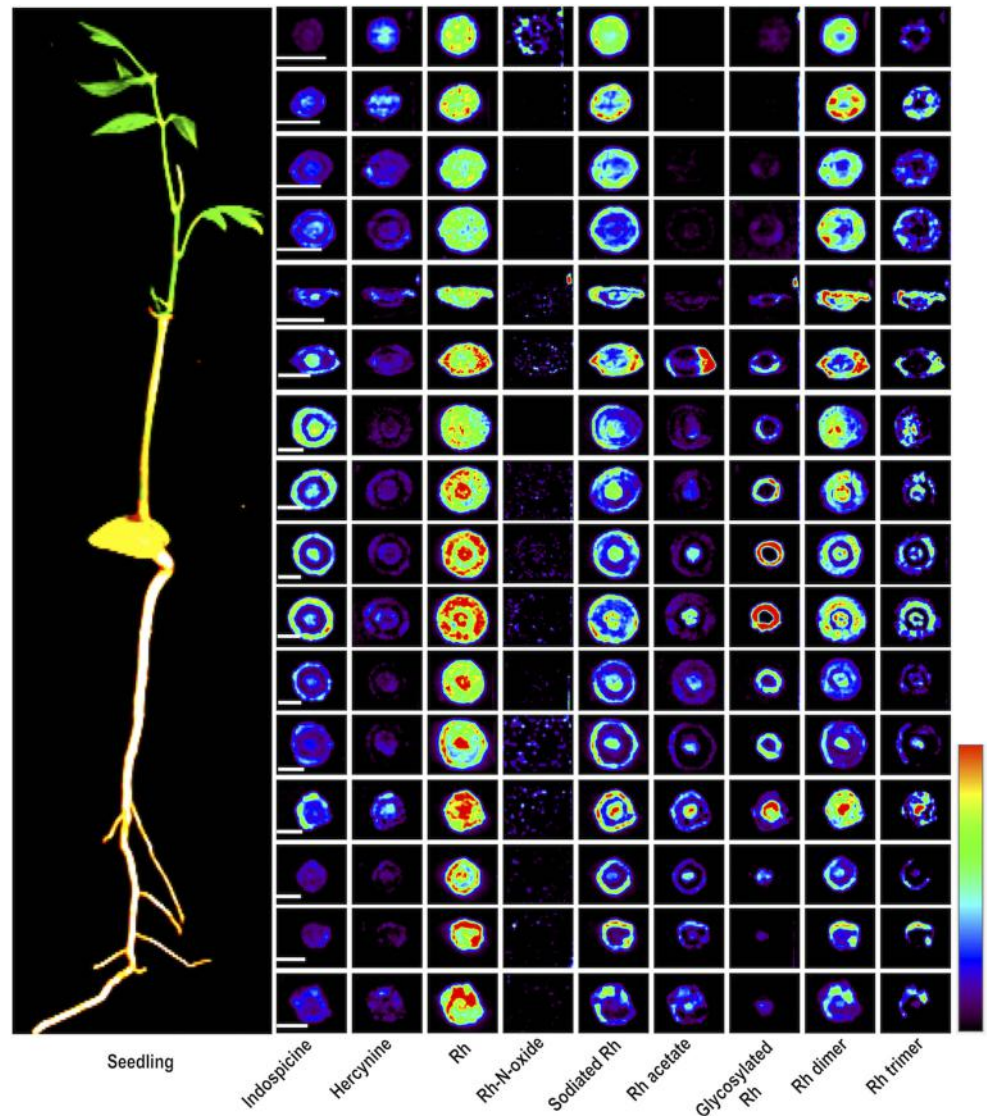


Fig 4. DESI MS images showing the distribution of Rh and other related compounds in different cross sections of root and shoot of a 10 months old seedling of *D. binectariferum*. Scale bars correspond to 2 mm and apply to all the images of a row. Intensity normalization of the images was done separately for all the individual metabolites.

doi:10.1371/journal.pone.0158099.g004

and translocation of secondary metabolites through secondary transporters such as the ABC transporters. Furthermore, the glycosylation could also help in the storage of potentially toxic compound Rh until it is required upon to serve as a deterrent to pests [48, 49]. Though the functional significance of Rh in plants is not known, it has been shown to possess a variety of interesting pharmacological properties such as its ability to inhibit cyclin-dependent kinases CDKs [11]. It is likely that, this activity of Rh could serve as a defense for the plant against herbivore and hence explains the higher accumulation of Rh in the younger growing shoot apices.

The biosynthesis of Rh is not yet elucidated. However, based on the constituent chemical moieties of the compound, it is suggested that it may comprise of the shikimic acid pathway to produce the flavonoids or the pentaketide pathway to produce chromone with a nitrogenous group derived from L-ornithine or other amino acids (Fig 7) [16, 20]. The biosynthesis of

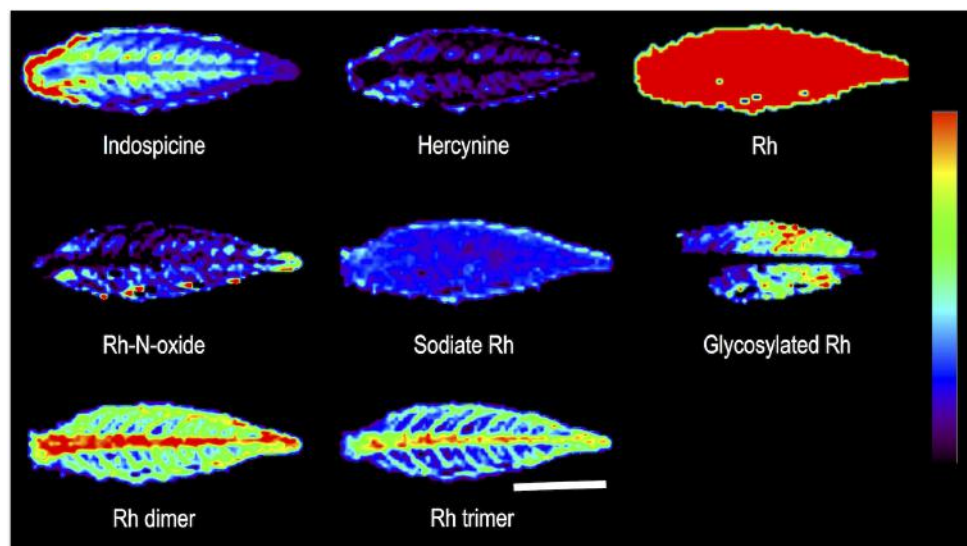


Fig 5. DESI MS images showing the distribution of Rh and other related compounds in the imprinted leaf of a 10 months old seedling of *D. binectariferum*. Scale bar corresponds to 5 mm applies to all the images.

doi:10.1371/journal.pone.0158099.g005

chromone alkaloid is hypothesized to follow either of the two major steps; a) involving noreugenin or b) involving a flavone compound (Fig 7) [3]. ESI MS and DESI MS data revealed that, besides Rh, a few other related chromone alkaloids, such as Rh-N-oxide, Rh acetate, glycosylated Rh, etc. were present in different parts of the plant. The detection of these chromone compounds strongly suggests the possibility of the involvement of the noreugenin pathway in the production of Rh in *D. binectariferum*.

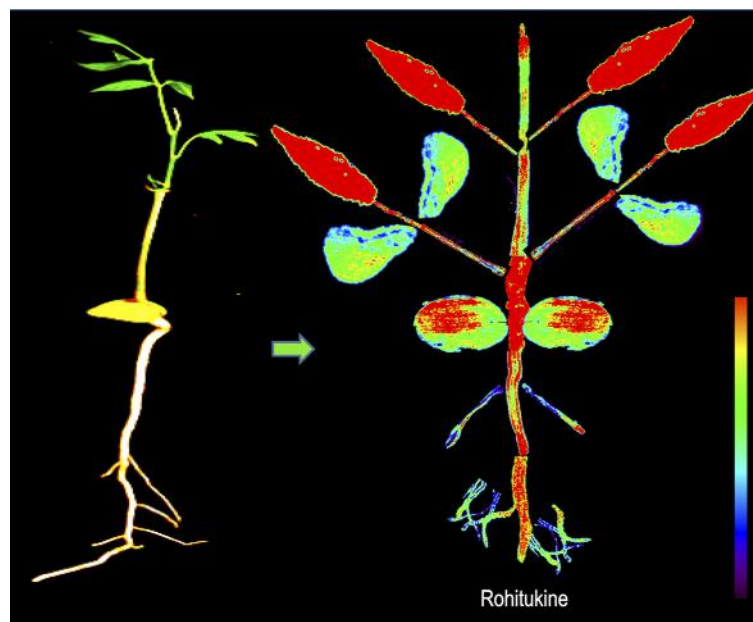


Fig 6. Reconstruction of spatial distribution of Rh obtained from DESI MS imaging of different parts of a 10 months old seedling of *D. binectariferum*.

doi:10.1371/journal.pone.0158099.g006

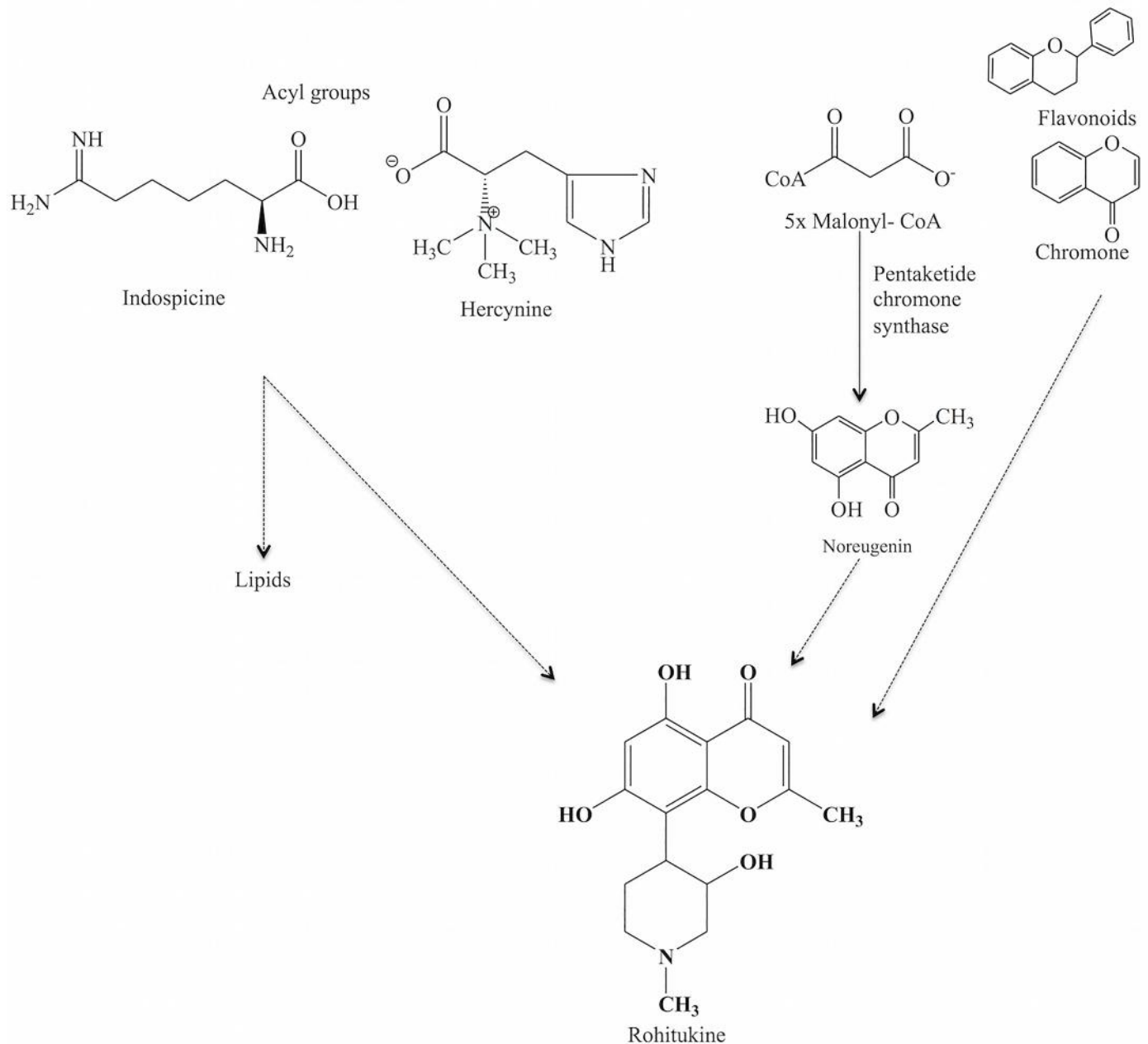


Fig 7. Schematic representation of possible biosynthetic pathway of Rh in *D. binectariferum*.

doi:10.1371/journal.pone.0158099.g007

In the recent past, a number of studies have used several imaging techniques including MALDI MS and DESI MS to unravel the spatial patterns in the distribution of plant secondary metabolites [28–33]. Understanding the spatial patterns could also lead to deciphering the underlying gene expression related to the pathway genes [34, 36]. In our study, younger leaves found to have higher levels of Rh compared to older leaves (Fig 7). It would be interesting to study the comparative transcriptomic profile of young and old leaves and unravel critical genes that are either expressed (in young leaves) or repressed (in older leaves).

Conclusions

In conclusion, our results provide a spatially explicit distribution of metabolites in the seedlings of a tropical tree, *D. binectariferum*, with specific reference to a not-so-common group of metabolites, the chromone alkaloids. The mass spectrometric images provide a direct visualization of the localization of metabolites in the various parts of the seedlings. Considering a resolution of 250 μm , the images provide a sufficiently higher resolution display of the metabolites at a whole seedling level. Combination of these display data with transcriptomic data would provide a powerful way to unravel the genetic basis of the differences in the metabolite profiles. Currently work is underway in our laboratory to address this issue.

Supporting Information

S1 Fig. Representative DESI MS spectra and images of metabolites from the TLC imprint of cross sectioned root of *D. binectariferum* seedling. Scale bar corresponds to 2 mm applies to all the images.

(TIFF)

S1 Table. Table showing list of m/z values of the ions, fragment ions, their probable chemical formulae, structures, and METLIN database ID.

(PDF)

Author Contributions

Conceived and designed the experiments: PMK RUS TP. Performed the experiments: PMK AS SA. Analyzed the data: PMK AS. Contributed reagents/materials/analysis tools: PMK GR RUS TP. Wrote the paper: PMK AS GR RUS TP.

References

1. Houghton PJ, Hairong Y. Further chromane alkaloids from *Schumanniohyton magnificum*. *Planta Medica*. 1987; 52:262–4.
2. Houghton PJ. Chromatography of the chromone and flavonoid alkaloids. *Journal of Chromatography A*. 2002; 967(75–84).
3. Khadem S, Marles RJ. Chromone and Flavonoid Alkaloids: Occurrence and Bioactivity. *Molecules*. 2012; 17:191–206.
4. Harmon AD, Weiss U, Silverton JV. The structure of rohitukine, the main alkaloid of *Amoora rohituka* (Syn. *Aphanamixis polystachya*) (meliaceae). *Tetrahedron Letters*. 1979; 20(8):721–4. doi: [http://dx.doi.org/10.1016/S0040-4039\(01\)93556-7](http://dx.doi.org/10.1016/S0040-4039(01)93556-7).
5. Naik RG, Kattige SL, Bhat SV, Alreja B, de Souza NJ, Rupp RH. An antiinflammatory cum immunomodulatory piperidinybenzopyranone from *Dysoxylum binectariferum*: isolation, structure and total synthesis. *Tetrahedron*. 1988; 44(7):2081–6. doi: [http://dx.doi.org/10.1016/S0040-4020\(01\)90352-7](http://dx.doi.org/10.1016/S0040-4020(01)90352-7).
6. Yang D-H, Cai S-Q, Zhao Y-Y, Liang H. A new alkaloid from *Dysoxylum binectariferum*. *Journal of Asian Natural Products Research*. 2004; 6(3):233–6. doi: [10.1080/10286020310001608930](http://dx.doi.org/10.1080/10286020310001608930) PMID: [15224423](http://pubmed.ncbi.nlm.nih.gov/15224423/)
7. Ismail IS, Nagakura Y, Hirasawa Y, Hosoya T, Lazim MIM, Lajis NH, et al. Chromone Alkaloids from *Dysoxylum acutangulum*. *Journal of Natural Products*. 2009; 72(10):1879–83. doi: [10.1021/np9003849](http://dx.doi.org/10.1021/np9003849) PMID: [19757855](http://pubmed.ncbi.nlm.nih.gov/19757855/)
8. Jain SK, Bharate SB, Vishwakarma RA. Cyclin-dependent kinase inhibition by flavoalkaloids. *Mini-Reviews in Medicinal Chemistry*. 2012; 12:632–49. PMID: [22512551](http://pubmed.ncbi.nlm.nih.gov/22512551/)
9. Mohanakumara P, Sreejayan N, Priti V, Ramesha BT, Ravikanth G, Ganeshaiah KN, et al. *Dysoxylum binectariferum* Hook.f (Meliaceae), a rich source of rohitukine. *Fitoterapia*. 2010; 81(2):145–8. doi: <http://dx.doi.org/10.1016/j.fitote.2009.08.010> PMID: [19686817](http://pubmed.ncbi.nlm.nih.gov/19686817/)
10. Mahajan V, Sharma N, Kumar S, Bhardwaj V, Ali A, Khajuria RK, et al. Production of rohitukine in leaves and seeds of *Dysoxylum binectariferum*: an alternate renewable resource. *PharmBiol*. 2015; 53(3):446–50.

11. Jain SK, Meena S, Qazi AK, Hussain A, Bhola SK, Kshirsagar R, et al. Isolation and biological evaluation of chromone alkaloid dysoline, a new regioisomer of rohitukine from *Dysoxylum binectariferum*. *Tetrahedron Letters*. 2013; 54(52):7140–3. doi: <http://dx.doi.org/10.1016/j.tetlet.2013.10.096>.
12. Mohana Kumara P. Assessing the genetic diversity of *Dysoxylum binectariferum* and prospecting for anticancer metabolite rohitukine from its phylogenetically related species in the Western Ghats, India. Bangalore: University of Agricultural Sciences 2012.
13. Mohana Kumara P, Zuehlke S, Priti V, Ramesha BT, Shweta S, Ravikanth G, et al. *Fusarium proliferatum*, an endophytic fungus from *Dysoxylum binectariferum* Hook.f, produces rohitukine, a chromone alkaloid possessing anti-cancer activity. *Antonie van Leeuwenhoek*. 2012; 101(2):323–9. doi: [10.1007/s10482-011-9638-2](https://doi.org/10.1007/s10482-011-9638-2) PMID: [21898150](https://pubmed.ncbi.nlm.nih.gov/21898150/)
14. Mohana Kumara P, Soujanya KN, Ravikanth G, Vasudeva R, Ganeshiah KN, Shaanker RU. Rohitukine, a chromone alkaloid and a precursor of flavopiridol, is produced by endophytic fungi isolated from *Dysoxylum binectariferum* Hook.f and *Amoora rohituka* (Roxb). *Wight & Arn. Phytomedicine*. 2014; 21(4):541–6. doi: <http://dx.doi.org/10.1016/j.phymed.2013.09.019>.
15. Manske RH, Brossi. *The Alkaloids: Chemistry pharmacology*. 31: Academic Press Inc; San Diego, California.; 1987. p. 123–55.
16. Abe I, Utsumi Y, Oguro S, Morita H, Sano Y, Noguchi H. A Plant Type III Polyketide Synthase that Produces Pentaketide Chromone. *Journal of the American Chemical Society*. 2005; 127(5):1362–3. doi: [10.1021/ja0431206](https://doi.org/10.1021/ja0431206) PMID: [15686354](https://pubmed.ncbi.nlm.nih.gov/15686354/)
17. Morita H, Kondo S, Kato R, Wanibuchi K, Noguchi H, Sugio S, et al. Crystallization and preliminary crystallographic analysis of an octaketide-producing plant type III polyketide synthase. *Acta Crystallographica Section F*. 2007; 63(11):947–9. doi: [10.1107/S1744309107047069](https://doi.org/10.1107/S1744309107047069)
18. Morita H, Kondo S, Oguro S, Noguchi H, Sugio S, Abe I, et al. Structural Insight into Chain-Length Control and Product Specificity of Pentaketide Chromone Synthase from *Aloe arborescens*. *Chemistry & Biology*. 2007; 14(4):359–69. doi: <http://dx.doi.org/10.1016/j.chembiol.2007.02.003>.
19. Morita H, Yamashita M, Shi S-P, Wakimoto T, Kondo S, Kato R, et al. Synthesis of unnatural alkaloid scaffolds by exploiting plant polyketide synthase. *Proceedings of the National Academy of Sciences*. 2011; 108(33):13504–9. doi: [10.1073/pnas.1107782108](https://doi.org/10.1073/pnas.1107782108)
20. Herbert RB. *The biosynthesis of plant alkaloids and nitrogenous microbial metabolites*. *Natural Product Reports*. 1995; 12(5):445–64. doi: [10.1039/np9951200445](https://doi.org/10.1039/np9951200445)
21. Varshney S, Shankar K, Beg M, Balaramnavar VM, Mishra SK, Jagdale P, et al. Rohitukine inhibits in vitro adipogenesis arresting mitotic clonal expansion and improves dyslipidemia in vivo. *Journal of Lipid Research*. 2014; 55(6):1019–32. doi: [10.1194/jlr.M039925](https://doi.org/10.1194/jlr.M039925) PMID: [24646949](https://pubmed.ncbi.nlm.nih.gov/24646949/)
22. Sedlacek H, Czech J, Naik R, Kaur G, Worland P, Losiewicz M, et al. Flavopiridol (L86 8275; NSC 649890), a new kinase inhibitor for tumor therapy. *International Journal of Oncology*. 1996; 9(6):1143–63. PMID: [21541623](https://pubmed.ncbi.nlm.nih.gov/21541623/)
23. Stadler WM, Vogelzang NJ, Amato R, Sosman J, Taber D, Liebowitz D, et al. Flavopiridol, A Novel Cyclin-Dependent Kinase Inhibitor, in Metastatic Renal Cancer: A University of Chicago Phase II Consortium Study. *Journal of Clinical Oncology*. 2000; 18(2):371. PMID: [10637252](https://pubmed.ncbi.nlm.nih.gov/10637252/)
24. Biglione S, Byers S, Price J, Nguyen VT, Bensaude O, Price D, et al. Inhibition of HIV-1 replication by P-TEFb inhibitors DRB, seliciclib and flavopiridol correlates with release of free P-TEFb from the large, inactive form of the complex. *Retrovirology*. 2007; 4(1):47. doi: [10.1186/1742-4690-4-47](https://doi.org/10.1186/1742-4690-4-47)
25. Perkins KJ, Lusic M, Mitar I, Giacca M, Proudfoot NJ. Transcription-dependent gene looping of the HIV-1 provirus is dictated by recognition of pre-mRNA processing signals. *Molecular Cell*. 2008; 29:56. doi: [10.1016/j.molcel.2007.11.030](https://doi.org/10.1016/j.molcel.2007.11.030) PMID: [18206969](https://pubmed.ncbi.nlm.nih.gov/18206969/)
26. Mohana Kumara P, Srimany A, Ravikanth G, Uma Shaanker R, Pradeep T. Ambient ionization mass spectrometry imaging of rohitukine, a chromone anti-cancer alkaloid, during seed development in *Dysoxylum binectariferum* Hook.f (Meliaceae). *Phytochemistry*. 2015; 116(0):104–10. doi: <http://dx.doi.org/10.1016/j.phytochem.2015.02.031>.
27. Takáts Z, Wiseman JM, Gologan B, Cooks RG. Mass Spectrometry Sampling Under Ambient Conditions with Desorption Electrospray Ionization. *Science*. 2004; 306(5695):471–3. doi: [10.1126/science.1104404](https://doi.org/10.1126/science.1104404) PMID: [15486296](https://pubmed.ncbi.nlm.nih.gov/15486296/)
28. Bjarnholt N, Li B, D'Alvise J, Janfelt C. Mass spectrometry imaging of plant metabolites—principles and possibilities. *Natural Product Reports*. 2014; 31(6):818–37. doi: [10.1039/c3np70100j](https://doi.org/10.1039/c3np70100j) PMID: [24452137](https://pubmed.ncbi.nlm.nih.gov/24452137/)
29. Lee YJ, Perdian DC, Song Z, Yeung ES, Nikolau BJ. Use of mass spectrometry for imaging metabolites in plants. *The Plant Journal*. 2012; 70(1):81–95. doi: [10.1111/j.1365-313X.2012.04899.x](https://doi.org/10.1111/j.1365-313X.2012.04899.x) PMID: [22449044](https://pubmed.ncbi.nlm.nih.gov/22449044/)
30. Ifa DR, Srimany A, Eberlin LS, Naik HR, Bhat V, Cooks RG, et al. Tissue imprint imaging by desorption electrospray ionization mass spectrometry. *Analytical Methods*. 2011; 3(8):1910–2. doi: [10.1039/c1ay05295k](https://doi.org/10.1039/c1ay05295k)

31. Korte AR, Song Z, Nikolau BJ, Lee YJ. Mass spectrometric imaging as a high-spatial resolution tool for functional genomics: Tissue-specific gene expression of TT7 inferred from heterogeneous distribution of metabolites in Arabidopsis flowers. *Analytical Methods*. 2012; 4(2):474–81. doi: [10.1039/c2ay05618f](https://doi.org/10.1039/c2ay05618f)
32. Hemalatha RG, Pradeep T. Understanding the Molecular Signatures in Leaves and Flowers by Desorption Electrospray Ionization Mass Spectrometry (DESI MS) Imaging. *Journal of Agricultural and Food Chemistry*. 2013; 61(31):7477–87. doi: [10.1021/jf4011998](https://doi.org/10.1021/jf4011998) PMID: [23848451](https://pubmed.ncbi.nlm.nih.gov/23848451/)
33. Kueger S, Steinhauser D, Willmitzer L, Giavalisco P. High-resolution plant metabolomics: from mass spectral features to metabolites and from whole-cell analysis to subcellular metabolite distributions. *The Plant Journal*. 2012; 70(1):39–50. doi: [10.1111/j.1365-313X.2012.04902.x](https://doi.org/10.1111/j.1365-313X.2012.04902.x) PMID: [22449042](https://pubmed.ncbi.nlm.nih.gov/22449042/)
34. Li B, Hansen SH, Janfelt C. Direct imaging of plant metabolites in leaves and petals by desorption electrospray ionization mass spectrometry. *International Journal of Mass Spectrometry*. 2014; 348(0):15–22. doi: <http://dx.doi.org/10.1016/j.ijms.2013.04.018>.
35. Dalisay DS, Kim KW, Lee C, Yang H, Rabel O, Bowen BP, et al. Dirigent Protein-Mediated Lignan and Cyanogenic Glucoside Formation in Flax Seed: Integrated Omics and MALDI Mass Spectrometry Imaging. *Journal of Natural Products*. 2015; 78(6):1231–42. doi: [10.1021/acs.jnatprod.5b00023](https://doi.org/10.1021/acs.jnatprod.5b00023) PMID: [25981198](https://pubmed.ncbi.nlm.nih.gov/25981198/)
36. Li B, Knudsen C, Hansen NK, Jørgensen K, Kannangara R, Bak S, et al. Visualizing metabolite distribution and enzymatic conversion in plant tissues by desorption electrospray ionization mass spectrometry imaging. *The Plant Journal*. 2013; 74(6):1059–71. doi: [10.1111/tpj.12183](https://doi.org/10.1111/tpj.12183) PMID: [23551340](https://pubmed.ncbi.nlm.nih.gov/23551340/)
37. Marques JV, Dalisay DS, Yang H, Lee C, Davin LB, Lewis NG. A multi-omics strategy resolves the elusive nature of alkaloids in *Podophyllum* species. *Molecular BioSystems*. 2014; 10(11):2838–49. doi: [10.1039/c4mb00403e](https://doi.org/10.1039/c4mb00403e) PMID: [25166004](https://pubmed.ncbi.nlm.nih.gov/25166004/)
38. Marques JV, Kim K-W, Lee C, Costa MA, May GD, Crow JA, et al. Next generation sequencing in predicting gene-function in podophyllotoxin biosynthesis. *Journal of Biological Chemistry*. 2013; 288:466–79. doi: [10.1074/jbc.M112.400689](https://doi.org/10.1074/jbc.M112.400689) PMID: [23161544](https://pubmed.ncbi.nlm.nih.gov/23161544/)
39. Gamble JS, editor. *Flora of the Presidency of Madras 1997*; Vol.No.1.
40. Velho N, Datta A, Isvaran K. Effect of rodents on seed fate of five hornbill-dispersed tree species in a tropical forest in north-east India. *Journal of Tropical Ecology*. 2009; 25(05):507–14. doi: [10.1017/S0266467409990083](https://doi.org/10.1017/S0266467409990083)
41. Sethi P, Howe HF. Fruit removal by hornbills in a semi-evergreen forest of the Indian Eastern Himalaya. *Journal of Tropical Ecology*. 2012; 28(06):531–41. doi: [10.1017/S0266467412000648](https://doi.org/10.1017/S0266467412000648)
42. Smith CA, l'Maille G, Want EJ, Qin C, Trauger SA, Brandon TR, et al. METLIN: a metabolite mass spectral database. *Ther Drug Monit* 2005; 27(6):747–51. PMID: [16404815](https://pubmed.ncbi.nlm.nih.gov/16404815/)
43. Cabral E, Mirabelli M, Perez C, Ifa D. Blotting Assisted by Heating and Solvent Extraction for DESI-MS Imaging. *Journal of The American Society for Mass Spectrometry*. 2013; 24(6):956–65. doi: [10.1007/s13361-013-0616-y](https://doi.org/10.1007/s13361-013-0616-y) PMID: [23605686](https://pubmed.ncbi.nlm.nih.gov/23605686/)
44. Mohana Kumara P, Zuehlke S, Priti V, Ramesha B, Shweta S, Ravikanth G, et al. *Fusarium proliferatum*, an endophytic fungus from *Dysoxylum binectariferum* Hook.f, produces rohitukine, a chromane alkaloid possessing anti-cancer activity. *Antonie van Leeuwenhoek*. 2012; 101(2):323–9. doi: [10.1007/s10482-011-9638-2](https://doi.org/10.1007/s10482-011-9638-2) PMID: [21898150](https://pubmed.ncbi.nlm.nih.gov/21898150/)
45. Petrusa E, Braidot E, Zancani M, Peresson C, Bertolini A, Patui S, et al. Plant Flavonoids-Biosynthesis, Transport and Involvement in Stress Responses. *International Journal of Molecular Sciences*. 2013; 14(7):14950–73. doi: [10.3390/ijms140714950](https://doi.org/10.3390/ijms140714950) PMID: [23867610](https://pubmed.ncbi.nlm.nih.gov/23867610/)
46. Sirikantaramas S, Yamazaki M, Saito K. Mechanisms of resistance to self-produced toxic secondary metabolites in plants. *Phytochemistry Reviews*. 2008; 7(3):467–77. doi: [10.1007/s11101-007-9080-2](https://doi.org/10.1007/s11101-007-9080-2)
47. Sirikantaramas S, Sudo H, Asano T, Yamazaki M, Saito K. Transport of camptothecin in hairy roots of *Ophiorrhiza pumila*. *Phytochemistry*. 2007; 68(22–24):2881–6. doi: <http://dx.doi.org/10.1016/j.phytochem.2007.08.028>. PMID: [17910964](https://pubmed.ncbi.nlm.nih.gov/17910964/)
48. Yazaki K. Transporters of secondary metabolites. *Current Opinion in Plant Biology*. 2005; 8(3):301–7. doi: <http://dx.doi.org/10.1016/j.pbi.2005.03.011>. PMID: [15860427](https://pubmed.ncbi.nlm.nih.gov/15860427/)
49. Yazaki K, Sugiyama A, Morita M, Shitan N. Secondary transport as an efficient membrane transport mechanism for plant secondary metabolites. *Phytochemistry Reviews*. 2008; 7(3):513–24. doi: [10.1007/s11101-007-9079-8](https://doi.org/10.1007/s11101-007-9079-8)

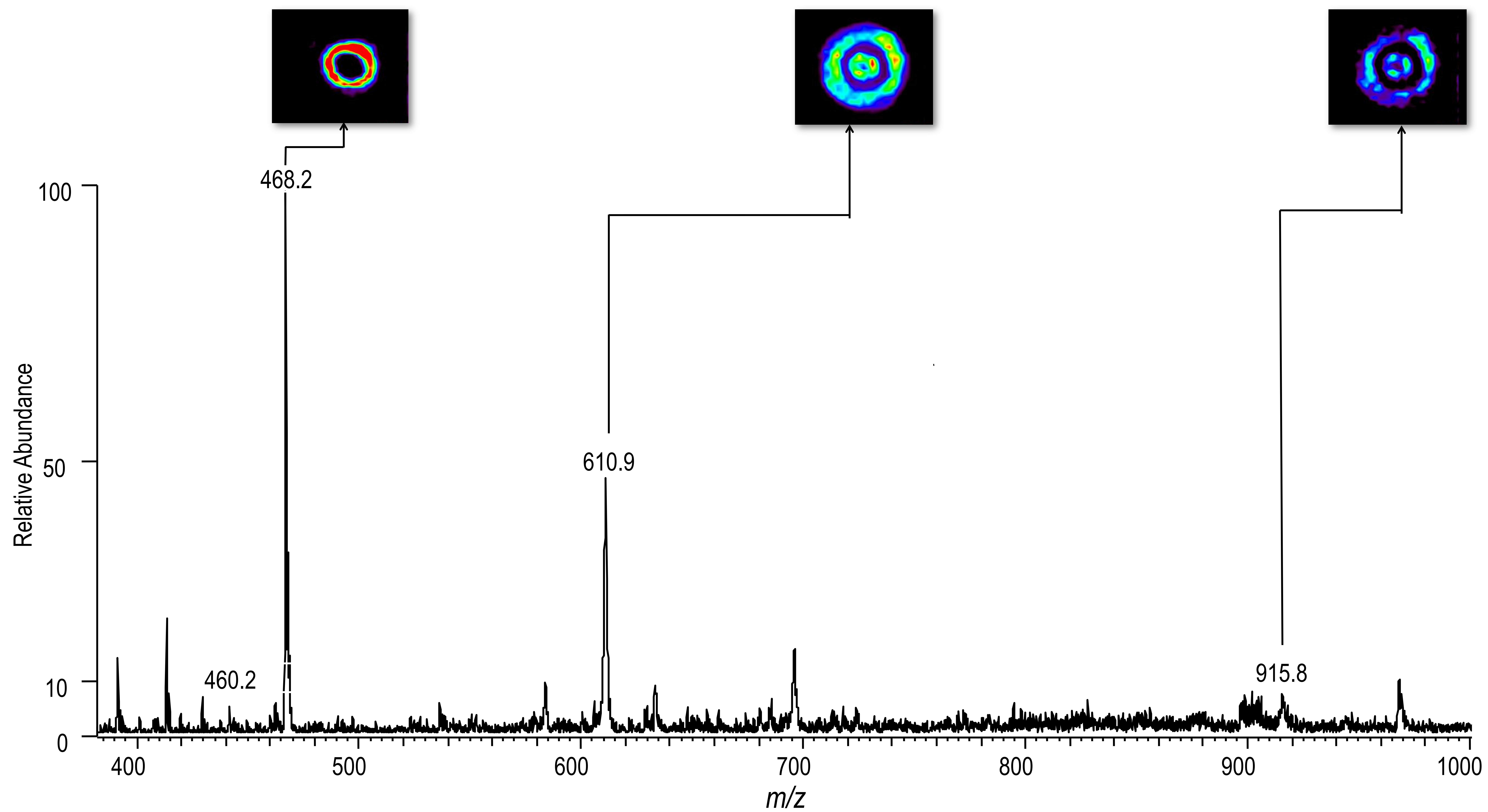
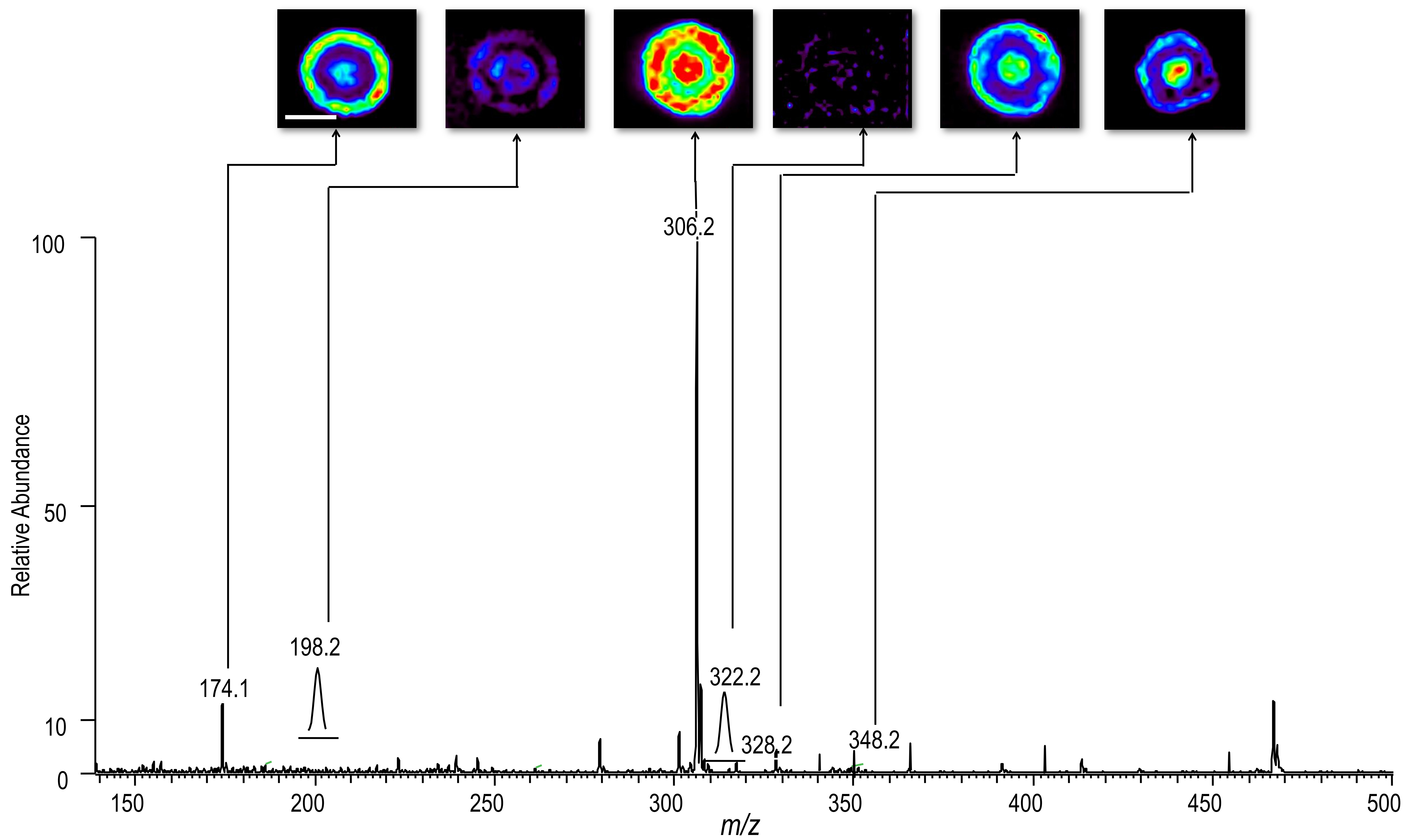
Supporting information

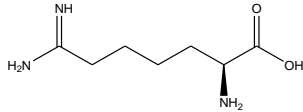
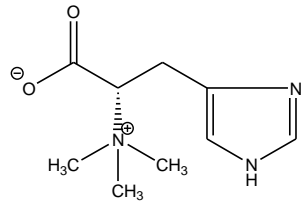
Desorption Electrospray Ionization (DESI) Mass Spectrometric Imaging of the Distribution of Rohitukine in the Seedling of *Dysoxylum binectariferum* Hook. F

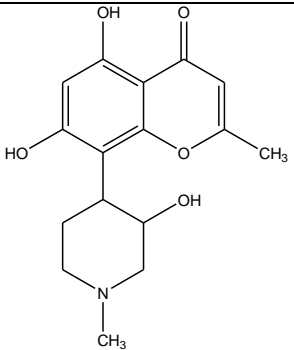
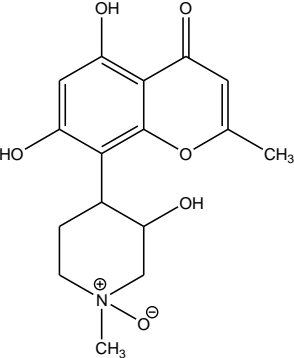
Patel Mohana Kumara, Amitava Srimany, Suganya Arunan, Gudasalamani Ravikanth, Ramanan Uma Shaanker, Thalappil Pradeep

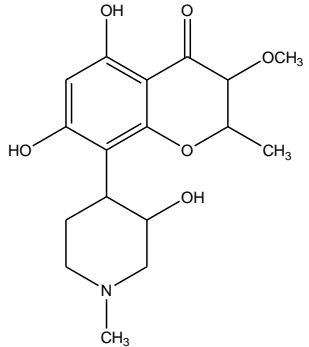
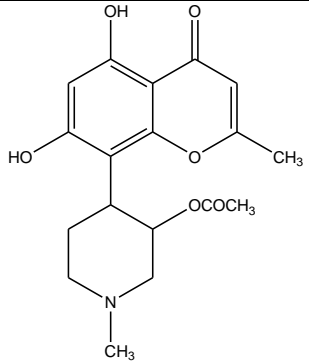
[S1 Fig.](#) Representative DESI MS spectra and images of metabolites from the TLC imprint of cross-sectioned root of *D. binectariferum* seedling. Scale bar corresponds to 2 mm applies to all the images.

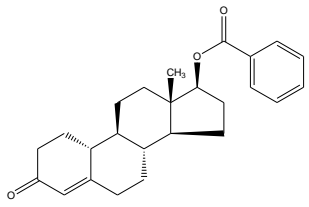
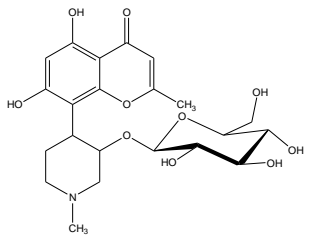
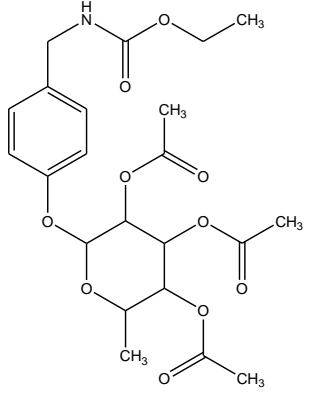
[S1 Table.](#) Table showing list of m/z values of the ions, fragment ions, their probable chemical formulae, structures, and METLIN database ID.

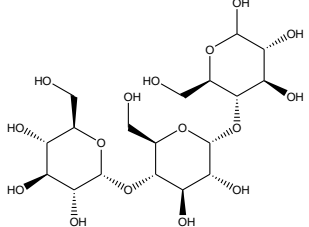
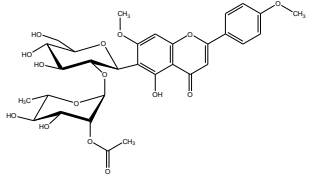


Sl. no	<i>m/z</i> obtained from DESI MS	<i>m/z</i> obtained from ESI MS (Orbitrap)	Calculated exact mass of the ion	Probable metabolite name	Probable chemical formula of the ion	ESI MS/MS fragmented ions OR Class of metabolite	Structure	Tissue where metabolite localized	METLIN-ID
1	174.1	174.1236	174.1237	Indospicine	C ₇ H ₁₅ N ₃ O ₂ +H	156.1, 116.1		Cotyledon Cortex and endodermis, midrib and leaf veins	3299
2	198.2	198.1235	198.1237	Hercynine	C ₉ H ₁₅ N ₃ O ₂ +H	180.0, 154.0, 95.0		Endodermis, xylem, and phloem Leaf margin	63493

3	306.2	306.1336	306.1335	Rohitukine	$C_{16}H_{19}NO_5+H$	288.0, 245.0, 222.0		<p>Cotyledon</p> <p>Cortex and endodermis</p> <p>Leaf</p>	
4	322.2	322.1283	322.1285	Rohitukine-N-oxide	$C_{16}H_{19}NO_6+H$	304.3, 276.2, 238.0		<p>Leaf blade</p>	
5	328.2	328.1155	328.1155	Rohitukine	$C_{16}H_{19}NO_5+Na$	-	-	<p>Cotyledon</p> <p>Cortex and endodermis</p> <p>Leaf</p>	

6	338.2	338.1599	338.1598	Methoxylated rohitukine analogue	$C_{17}H_{23}NO_6+H$	306.2 and 288.0, 245.0, 222.0		Leaf	
7	348.2	348.1447	348.1442	Rohitukine acetate	$C_{18}H_{21}NO_6+H$	306.2, 288.0, 245.0		Cotyledon Xylem and phloem	

8	401.1	401.2083	401.2087	17beta-Hydroxyestr-4-en-3-one benzoate	$C_{25}H_{30}O_3+Na$	Steroid ester		Epidermis, cortex, and endodermis	70661
9	468.2	468.1865	468.1864	Glycosylated rohitukine	$C_{22}H_{29}NO_{10}+H$	306.2 and 288.0, 245.0, 222.0		Cotyledon Xylem and phloem Leaf blade	
10	490.2	490.1687	490.1684	Bis-N-butyl phthalate	$C_{22}H_{29}NO_{10}+Na$	Carbohydrates		Xylem and phloem	88062
11	610.9	611.2598	611.2600	Protonated rohitukine dimer	$C_{32}H_{38}N_2O_{10}+H$	-	-	Cotyledon Cortex and	

								endodermis, midrib and leaf veins	
12	527.3	527.1583	527.1583	Maltotriose	$C_{18}H_{32}O_{16}+Na$	365.1 and 348.0, 204.0, 185.2		Leaf blade	3585
13	649.2	649.2127	649.2127	Embigenin 2''-(2'''- acetylramnoside)	$C_{31}H_{36}O_{15}+H$	Flavonoids		Midrib and leaf veins	49452



$[\text{Au}_{25}(\text{SR})_{18}]_2^{2-}$: a noble metal cluster dimer in the gas phase†

Cite this: *Chem. Commun.*, 2016, 52, 8397

Ananya Bakshi,‡ Papri Chakraborty,‡ Shridevi Bhat,‡ Ganapati Natarajan and Thalappil Pradeep*

Received 16th April 2016,
Accepted 6th June 2016

DOI: 10.1039/c6cc03202h

www.rsc.org/chemcomm

We present the first example of dimer formation in the monolayer protected atomically precise cluster system, $\text{Au}_{25}(\text{SR})_{18}$, using ion mobility mass spectrometry. These transient species are shown to be important in explaining chemical reactivity between clusters.

Clusters of noble metals composed of a precise number of atoms and protected with ligands,^{1,2} of which $\text{Au}_{25}(\text{SR})_{18}$ is a celebrated example, have become an expanding area of materials science.³⁻⁷ Their structures, investigated using single crystal diffraction, reveal Au-SR or Ag-SR monomeric or dimeric staples, using which Borromean rings diagrams for these molecular species have been proposed. Clusters can interact through ligands as well as through aurophilic interactions (for Au clusters), leading to dimers and polymers, as shown from previous investigations.⁸ Such interactions can be induced in the gas phase under controlled conditions leading to cluster aggregates⁹ which may be separable by ion mobility mass spectrometry. Recent reports of ion mobility mass spectrometry (IMS) on different protected clusters confirm that it is indeed possible to identify many unknown species in the gas phase by integrating ion mobility (IM) separation with mass spectrometry (MS).¹⁰⁻¹⁴ A recent report of inter-cluster reaction between two interacting clusters¹⁵ suggests that inter-cluster aggregate formation could be a potential pathway for these reactions. In this article, we present the observation of distinct dimeric and trimeric species of the $\text{Au}_{25}(\text{SR})_{18}$ system in the gas phase and their complete absence in $\text{Ag}_{25}(\text{SR})_{18}$ emphasizing the importance of the nature of the metal and inter-cluster interaction in determining cluster chemistry.

$\text{Au}_{25}(\text{PET})_{18}$ was prepared by an established route (see the ESI† for details) and characterized by electrospray ionization mass spectrometry (ESI MS) and UV-vis absorption spectroscopy (see Fig. S1, ESI†).¹⁵ The mass selected ions were subjected to

mobility separation in the drift tube and were mass analyzed subsequently (Fig. 1). Under conditions optimized for collecting the mass spectrum, the peak of $\text{Au}_{25}(\text{PET})_{18}$ was observed at m/z 7393 (average mass) (see Fig. S1, ESI†). From the isotope distribution, each peak is found to be separated by one mass unit confirming singly charged species (Fig. 1C(i)). The minimum concentration of the $1 \mu\text{g mL}^{-1}$ sample was infused at a flow rate of $20 \mu\text{L min}^{-1}$ at a capillary voltage of 2 kV to obtain a well resolved mass spectrum. To collect the spectrum, cone voltage and source offset were fixed at 120 and 100 V, respectively (see the ESI† for details). Trap gas flow (Ar) was 2 mL min^{-1} and desolvation gas (N_2) flow was 400 L h^{-1} . At slightly higher trap pressure and lower cone voltage (8 mL min^{-1} and 20 V, respectively), the isotope distribution changed drastically where the peaks were separated by m/z 0.4998 confirming the presence of a doubly charged dimer of $\text{Au}_{25}(\text{PET})_{18}$ (Fig. 1C(ii)). Several control experiments were performed to understand the best possible conditions where only dimer and higher aggregates were formed (Fig. S2 and S3, ESI†). As mentioned earlier, increased gas flow allows the formation of cluster aggregates which prompted us to increase it at different parts of the instrument. Optimized conditions for $\text{Au}_{25}(\text{PET})_{18}$ in the ion mobility mode were; trap gas flow rate: 5 mL min^{-1} , He flow: 100 mL min^{-1} and that within the mobility cell: 50 mL min^{-1} . When He flow was increased to 120 mL min^{-1} , $[\text{Au}_{25}(\text{PET})_{18}]_2^{2-}$ started appearing which was evident from two peaks located at 12.7 and 10.8 ms in the ion mobility drift time plot (Fig. 1B and Fig. S2, ESI†). The peak at 12.7 ms corresponds to $\text{Au}_{25}(\text{PET})_{18}^-$ while the other peak at 10.8 ms corresponds to $[\text{Au}_{25}(\text{PET})_{18}]_2^{2-}$. At a higher He flow rate (150 mL min^{-1}), another peak started appearing at 8.3 ms which corresponds to $[\text{Au}_{25}(\text{PET})_{18}]_3^{3-}$ (with a separation of m/z 0.3330, Fig. 1C(iii)). By increasing the trap as well as the He flow rate it was possible to create only the dimer and the trimer of $\text{Au}_{25}(\text{PET})_{18}^-$. At a slightly lower DC bias voltage of 35 V, a complete conversion of $\text{Au}_{25}(\text{PET})_{18}^-$ to its dimer and trimer was observed. Fig. 1 represents the schematic of the experiment under optimized conditions to create such cluster polymers. Various optimization experiments

Department of Chemistry, DST Unit of Nanoscience (DST UNS) and Thematic Unit of Excellence (TUE), Indian Institute of Technology Madras, Chennai 600 036, India. E-mail: pradeep@iitm.ac.in; Fax: +91-44-2257-0545

† Electronic supplementary information (ESI) available. See DOI: 10.1039/c6cc03202h

‡ Contributed equally.

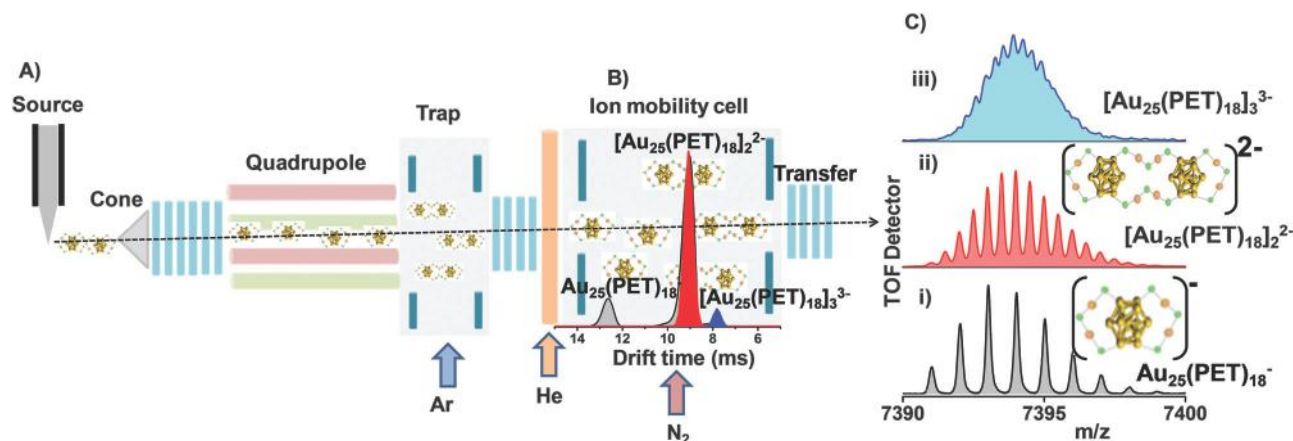


Fig. 1 (A) Schematic representation of the instrumental setup where $\text{Au}_{25}(\text{SR})_{18}$ cluster aggregates are created and (B) subsequently separated by ion mobility mass spectrometry. (C) Each of the peaks obtained from ion mobility is expanded. Peaks at 12.7, 10.8 and 7.8 ms in B correspond to $\text{Au}_{25}(\text{PET})_{18}^-$, $[\text{Au}_{25}(\text{PET})_{18}]_2^{2-}$, $[\text{Au}_{25}(\text{PET})_{18}]_3^{3-}$, respectively, as shown in (i–iii). Representative structures are shown in the insets.

are presented in the ESI,† Fig. S2–S4. It was also evident that the formation of these cluster aggregates is highly dependent on the cone voltage used which actually is the extraction voltage. At a sufficiently higher cone voltage (> 80 V), only $\text{Au}_{25}(\text{PET})_{18}^-$ was detected even at a high trap gas flow (8 mL min^{-1}). By lowering the cone voltage to 10 V, it is possible to create dimers even at a trap flow rate of 5 mL min^{-1} . The data are presented in Fig. S2 (ESI†). Therefore, such loosely bound cluster polymers may be forming in the ionization chamber too after spraying which can be broken apart by applying a higher extraction voltage at the cone. It is clear that the monomer aggregates to form dimers and polymers in the drift tube under favourable conditions.

To confirm dimerization, we have created the dimer and trimer of $\text{Au}_{25}(\text{PET})_{18}^-$ following the above stated instrumental conditions, without any monomer contribution. Collision induced dissociation (CID) was performed at m/z 7393 which consisted of 75% dimer $[\text{Au}_{25}(\text{PET})_{18}]_2^{2-}$ and 25% trimer $[\text{Au}_{25}(\text{PET})_{18}]_3^{3-}$, as calculated from the area under the curve in the drift time profile (see Fig. 2). Upon increasing laboratory collision energy (CE)§ from 5 to 50 V, dimers and trimers started separating out to form $\text{Au}_{25}(\text{PET})_{18}^-$. Regular fragmentation from $\text{Au}_{25}(\text{PET})_{18}^-$ was observed at CE more than 85 V which (Fig. S4, ESI†) matches well with the previously reported fragmentation pattern of $\text{Au}_{25}(\text{PET})_{18}^-$.¹⁰

This polymerization is ligand independent as confirmed from a study performed with $\text{Au}_{25}(\text{DDT})_{18}^-$ (Fig. S5, ESI†). A collision energy dependent study reveals a similar type of dissociation of the dimer to the monomer at higher collision energy as shown in Fig. S5 (ESI†). As all the polymers appear at the same m/z , albeit at reduced peak separation, it is difficult to identify the polymers by a normal ESI MS measurement. To overcome this issue, a few PET ligands have been exchanged with dodecanethiol (DDT). By controlling the free ligand concentration, a maximum of 3 ligand exchange products were seen in ESI MS. These specific ligand exchanged clusters (0–3 DDT exchanged) were used for polymerization. Under optimized conditions, all these ligand exchanged products react together

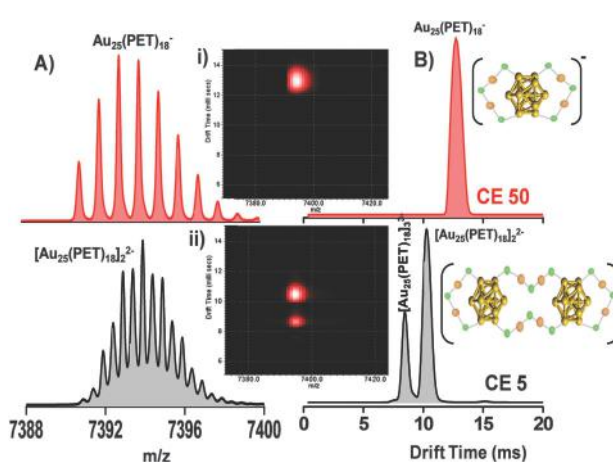


Fig. 2 (A) Collision induced dissociation of $[\text{Au}_{25}(\text{PET})_{18}]_2^{2-}$, $[\text{Au}_{25}(\text{PET})_{18}]_3^{3-}$ mixture gave $\text{Au}_{25}(\text{PET})_{18}^-$. Corresponding drift time profiles are shown in (B). Ion mobility drift time vs. m/z plots are shown in insets (i) and (ii) for laboratory CE 5 and 50 V, respectively. ^a Representative structures are also shown.

to give various possible dimers, trimers and some amounts of tetramers (see Fig. 3A). Fig. 3A represents the ion mobility drift time vs. m/z plot showing different ligand exchanged Au_{25} monomers, dimers, trimers and tetramers. Inter-cluster polymerization will result in a more number of mixed ligand protected dimers, trimers, etc. For example, from 0 to 3 ligand exchanged products, 6 possible dimers and 9 possible trimers can form during polymerization (Fig. S8, ESI†). The data are shown in Fig. 3B. The number increases with the number of ligand exchanged products existing in the solution. The corresponding drift time profile is shown in Fig. 3C. The peaks are labelled as monomers, dimers and trimers. Interdigitation among the DDT ligands might help in a higher degree of polymerization (Fig. S6 and S7, ESI†).

The possible cause of this kind of aggregate formation could be van der Waals forces, dipole–dipole interactions, electron transfer between neighbouring clusters, aurophilic interaction among neighbouring clusters which may allow two negatively

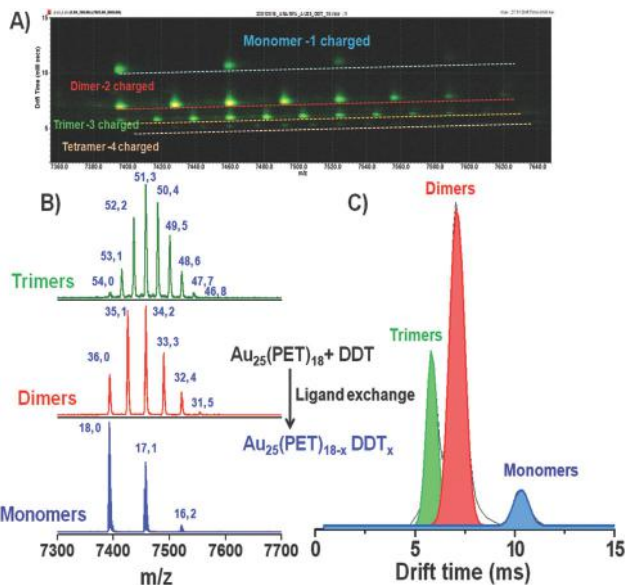


Fig. 3 (A) Plot of ion mobility drift time vs. m/z of reaction products of $\text{Au}_{25}(\text{PET})_{18}$ and dodecanethiol, showing the formation of cluster polymers. Multiple ligand exchanged cluster monomers, dimers and trimers are shown in (B). Corresponding drift time profile is shown in (C). Peaks assigned are with two labels, the first number corresponds to the total PET and the second number corresponds to the total DDT.

charged entities to come closer to form dimers and higher polymers.¹⁵ Although the clusters are negatively charged, the overall charge is not localized and distributed all over the cluster. Thiolate protected $\text{Au}_{25}(\text{SR})_{18}$ has been studied theoretically as a building block for the formation of dimers and polymers.¹⁶ Two $\text{Au}_{25}(\text{SMe})_3^-$ were connected by one di-thiol ligand replacing two $-\text{SMe}$. The calculated structure was energetically favourable. In another report, $\text{Au}_{25}(\text{BT})_{18}$ (BT is butanethiol) was suggested to form a one-dimensional polymer on the Au(111).¹⁷ The crystal structure revealed the Au–Au linkage between two neighbouring clusters. Due to Au–Au bond formation, S–Au–S bond angle becomes almost linear (177°) suggesting significant structural modification. Different ligand protected Au_{25} clusters were used and ligand effects were checked. Too small or too long ligands were found to be ineffective in polymerization. Interdigitation of the ligand plays a significant role in determining polymerization, which explains the formation of more polymers when a few PET ligands were exchanged with DDT in the current study. All these previous studies point towards the dimer or polymerization efficiency of monolayer protected $\text{Au}_{25}(\text{SR})_{18}$ clusters. An early example of dimerization was observed by Wataru *et al.*¹⁸ during the exchange of tellurolates with thiolates of $\text{Au}_{25}(\text{SC}_8\text{H}_{17})_{18}$. We find that the $\text{Ag}_{25}(\text{SR})_{18}$ cluster did not show any dimers (Fig. S9, ESI†) under the experimental conditions used for $\text{Au}_{25}(\text{SR})_{18}$. Gold thiolates are known to form such a type of aggregate due to aurophilic interaction. Gold thiolates are also known to form longer chains which are very limited for silver thiolates which might be responsible for no dimer formation for $\text{Ag}_{25}(\text{SR})_{18}$.

Experimentally calculated CCS values for $\text{Au}_{25}(\text{SR})_{18}^-$, $[\text{Au}_{25}(\text{SR})_{18}]_2^{2-}$ and $[\text{Au}_{25}(\text{SR})_{18}]_3^{3-}$ are 297.8, 453.4 and 668.3 \AA^2 , respectively (see Tables S1 and S2, ESI† for details). From the ion mobility drift time data, it is evident that the dimer size is slightly lesser than twice the monomer. This is also the case when trimer is considered. This prompted us to think that there might be bonding between two adjacent $\text{Au}_{25}(\text{SR})_{18}^-$ units which can share their equivalent $\text{Au}_2(\text{SR})_3$ staples to form a dimer. For this to occur, one Au–SR bond has to break and a new Au–SR bond has to form with the next cluster. Recently monolayer protected clusters are termed as “aspicule” which means shielded molecule.¹⁹ Possible structures are understood considering the aspicule¹⁹ model of the $\text{Au}_{25}(\text{SR})_{18}^-$ cluster system. Isomer structures of the dimer were constructed based on utilizing common staples as a linkage between the clusters. The structures of the three isomers, A, B and C, were geometry optimized, and their binding energies with respect to two isolated $\text{Au}_{25}(\text{SH})_{18}$ clusters were calculated. Two DFT optimized structures of isomers A and B are shown in Fig. 4A and B and their linkages can be visualized schematically using the Borromean rings diagrams shown below them in Fig. 4A and C, respectively (computational details are given in the ESI†). Isomer A is the most symmetric with both halves of the cluster being in the same orientation with the common staples parallel to each other, while in isomer B the half of the cluster on the right is rotated 90° with respect to the other half on the left, with the opposite ends of the common staples lying in perpendicular planes in a twisted configuration. A third possibility, isomer C, is shown in Fig. S10 (ESI†) where linking takes place at staple edges which are aligned parallel to each other, and the relative orientations of the two halves of the cluster are also different from isomers A and B in this configuration.

Table S3 (ESI†) shows the energies and binding energies of each of the isomers. The binding energies of the common staple dimer isomers A, B, and C, were 1.18 eV, 1.49 eV, and 2.36 eV, respectively. We found that A is the most stable and lowest in energy, closely followed by isomer B, whose binding energy was greater than that of isomer A by 0.31 eV, while isomer C was higher in binding energy than isomer A by 1.18 eV. We found these endothermic binding energies, calculated as $E(\text{dimer}) - 2E(\text{monomer})$, indicate that transfer of kinetic energy from cluster–gas molecule collisions and inter-cluster collisions would be required for the staple bond breakage and rearrangement which results in the formation of common-staple dimers, which is in agreement with the ion-mobility measurements presented here.

The results presented above suggest the existence of gas phase dimeric species of Au_{25} and its controlled fragmentation with or without ligand exchange leading to the parent or new clusters. Similar phenomena between reacting clusters can lead to transient cluster aggregates and their subsequent products. While the structures of dimers and their properties are areas for further investigation, chemical reactivity through such an interacting state is clearly established by this study. Although results of two prominent cluster systems, namely $\text{Au}_{25}(\text{SR})_{18}$ and $\text{Ag}_{25}(\text{SR})_{18}$, are presented here, many of the noble metal

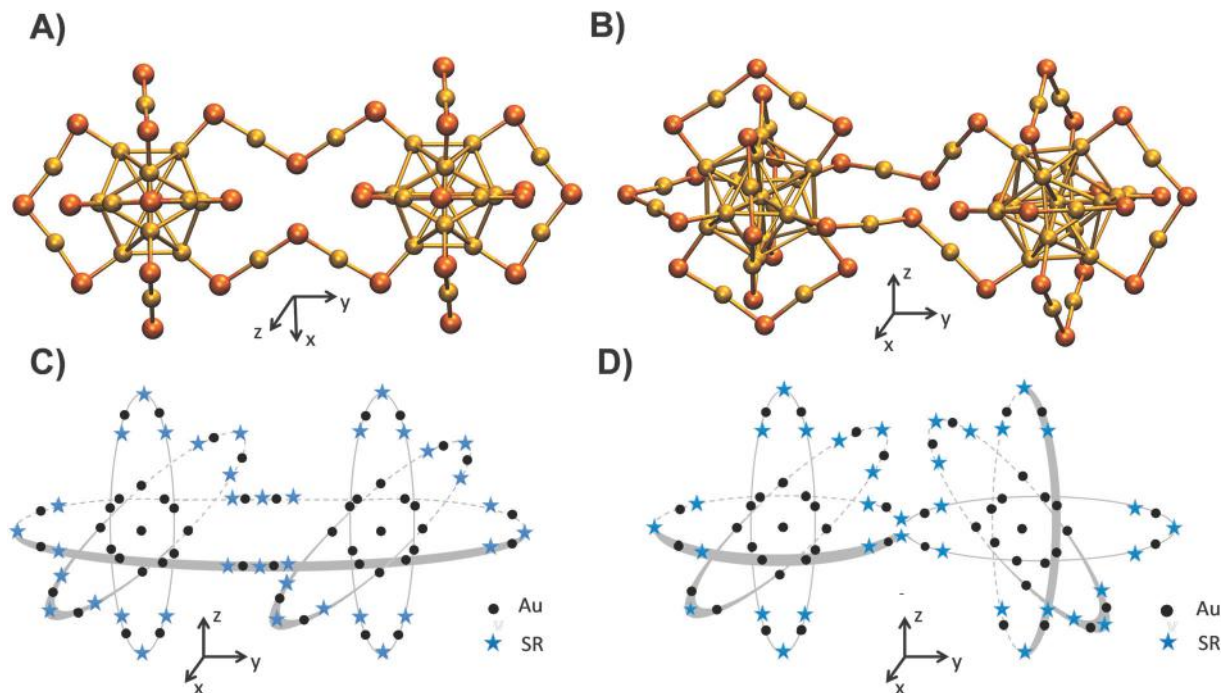


Fig. 4 (A and B) Possible structural isomers of the $[\text{Au}_{50}(\text{SR})_{36}]^{2-}$ dimer considering inter-cluster bonding *via* common Au_2S_3 staples. The structures shown in (A and B) are DFT-optimized and correspond to isomers (A and B), respectively. The ligand R-groups have been removed for clarity and gold atoms are shown in gold and sulphur atoms in orange, in the ball and stick representation. In (A), there is bonding between the two clusters by two parallel Au_2S_3 chains. The view shown is along the negative z -direction (top view). In (B), a twisted linkage between the Au_2S_3 staples of two clusters is shown with the cluster on the right being rotated by 90° anticlockwise about the x -axis coming out of the paper, according to the Cartesian axes shown. (C and D) are representations of (A and B), respectively, utilizing the Borromean-rings diagram of ref. 19. In the twisted-linked dimer shown in (D), the orientation of the diagram of the cluster on the right side is obtained by rotating the diagram of the cluster on the left side by 90° anticlockwise about the x -axis.

clusters are expected to show such properties and we are currently investigating this transient phenomenon and its implications.

Notes and references

§ Nominal collision energy, not calibrated.

- 1 A. Mathew and T. Pradeep, *Part. Part. Syst. Charact.*, 2014, **31**, 1017–1053.
- 2 R. Jin, *Nanoscale*, 2010, **2**, 343–362.
- 3 M. W. Heaven, A. Dass, P. S. White, K. M. Holt and R. W. Murray, *J. Am. Chem. Soc.*, 2008, **130**, 3754–3755.
- 4 M. Zhu, C. M. Aikens, F. J. Hollander, G. C. Schatz and R. Jin, *J. Am. Chem. Soc.*, 2008, **130**, 5883–5885.
- 5 J. Hassinen, P. Pulkkinen, E. Kalenius, T. Pradeep, H. Tenhu, H. Hakkinen and R. H. A. Ras, *J. Phys. Chem. Lett.*, 2014, **5**, 585–589.
- 6 A. C. Templeton, W. P. Wuelfing and R. W. Murray, *Acc. Chem. Res.*, 2000, **33**, 27–36.
- 7 Z. Luo, V. Nachammai, B. Zhang, N. Yan, D. T. Leong, D.-E. Jiang and J. Xie, *J. Am. Chem. Soc.*, 2014, **136**, 10577–10580.
- 8 H. Hakkinen, *Chem. Soc. Rev.*, 2008, **37**, 1847–1859.
- 9 J. Cyriac, V. R. R. Kumar and T. Pradeep, *Chem. Phys. Lett.*, 2004, **390**, 181–185.
- 10 L. A. Angel, L. T. Majors, A. C. Dharmaratne and A. Dass, *ACS Nano*, 2010, **4**, 4691–4700.
- 11 A. Baksi, S. R. Harvey, G. Natarajan, V. H. Wysocki and T. Pradeep, *Chem. Commun.*, 2016, **52**, 3805–3808.
- 12 K. M. Harkness, L. S. Fenn, D. E. Cliffler and J. A. McLean, *Anal. Chem.*, 2011, **82**, 3061–3066.
- 13 K. M. Harkness, B. C. Hixson, L. S. Fenn, B. N. Turner, A. C. Rape, C. A. Simpson, B. J. Huffman, T. C. Okoli, J. A. McLean and D. E. Cliffler, *Anal. Chem.*, 2010, **82**, 9268–9274.
- 14 K. M. Harkness, L. S. Fenn, D. E. Cliffler and J. A. McLean, *Anal. Chem.*, 2010, **82**, 3061–3066.
- 15 K. R. Krishnadas, A. Ghosh, A. Baksi, I. Chakraborty, G. Natarajan and T. Pradeep, *J. Am. Chem. Soc.*, 2016, **138**, 140–148.
- 16 J. Akola, K. A. Kacprzak, O. Lopez-Acevedo, M. Walter, H. Gronbeck and H. Hakkinen, *J. Phys. Chem. C*, 2010, **114**, 15986–15994.
- 17 M. De Nardi, S. Antonello, D.-E. Jiang, F. Pan, K. Rissanen, M. Ruzzi, A. Venzo, A. Zoleo and F. Maran, *ACS Nano*, 2014, **8**, 8505–8512.
- 18 W. Kurashige, S. Yamazoe, M. Yamaguchi, K. Nishido, K. Nobusada, T. Tsukuda and Y. Negishi, *J. Phys. Chem. Lett.*, 2014, **5**, 2072–2076.
- 19 G. Natarajan, A. Mathew, Y. Negishi, R. L. Whetten and T. Pradeep, *J. Phys. Chem. C*, 2015, **119**, 27768–27785.

Electronic Supplementary Material (ESI) for Chemical Communications.
This journal is © The Royal Society of Chemistry 2016

Electronic Supplementary Information

$[\text{Au}_{25}(\text{SR})_{18}]_2^{2-}$: A noble metal cluster dimer in the gas phase

Ananya Bakshi,[†] Papri Chakraborty,[†] Shridevi Bhat,[†] Ganapati Natarajan and Thalappil Pradeep*

DST Unit of Nanoscience (DST UNS) and Thematic Unit of Excellence (TUE), Department of Chemistry, Indian Institute of Technology Madras, Chennai 600 036, India

*Corresponding author: Fax: + 91-44 2257-0545

*E-mail: pradeep@iitm.ac.in

[†]Contributed equally

Experimental Section

Materials:

Tetrahydrofuran (THF), Dichloromethane (DCM), Phenylethanethiol (PET), Dodecanethiol (DDT), Tetraoctyl ammonium bromide (TAOBr), Methanol (MeOH), Sodium borohydride (NaBH_4) and Phenylethanethiol (PET) were purchased from Sigma Aldrich. Chloroauric acid ($\text{HAuCl}_4 \cdot 3\text{H}_2\text{O}$) was prepared in lab from pure gold. All the chemicals were used without further purification.

Synthesis of $\text{Au}_{25}(\text{PET})_{18}^-$:

About 40 mg of $\text{HAuCl}_4 \cdot 3\text{H}_2\text{O}$ was taken in 7.5 ml THF and mixed with 65 mg of TAOBr and stirred for around 15 min to get an orange red solution. To the solution, PET was added in 1:5 molar ratio (68 μL) and stirred for another hour. This resulted in Au-thiolate formation. The as-formed thiolate was then reduced by adding about 39 mg of NaBH_4 in ice-cold water. The color changed from yellow to brown. The solution was allowed to stir for another 5 hours for complete conversion and size focusing synthesis of $\text{Au}_{25}(\text{PET})_{18}^-$. The as-synthesized cluster was then vacuum dried by rotavapor and precipitated using excess MeOH to get rid of free thiol and excess thiolate. The process was repeated a few times. Then the Au_{25} cluster was extracted into acetone and centrifuged and the supernatant solution was collected leaving behind a precipitate consisting of larger clusters. The acetone solution was vacuum dried. Finally the cluster was dissolved in dichloromethane (DCM) and centrifuged and the supernatant solution was collected which consisted of the pure cluster. The resulted cluster was characterized by UV-vis absorption spectroscopy where characteristic peaks at 675, 450 nm confirmed the formation of Au_{25} clusters. Detailed characterization was by done

by electrospray ionization (ESI) and matrix assisted laser desorption ionization (MALDI) mass spectrometry (MS).

Instrumental Details:

Detailed experiments described in this work were carried out in Waters' Synapt G2Si HDMS instrument. The lab has other mass spectrometers too such as MALDI MS. The Synapt instrument consists of an electrospray source, quadrupole ion guide/trap, ion mobility cell, and TOF detector. A detailed instrumental view is shown in Figure 1 of the main manuscript. Different gases are used in different parts of the instrument. Nitrogen gas is used as nebulizer gas. High pure N₂ was used inside the ion mobility cell and the ions were directed through a drift tube. To reduce collision induced fragmentation, helium was used as the curtain gas before the ions entered the mobility cell. High pure Ar gas was used for collision induced dissociation (CID). All the experiments were done in negative ion mode. At standard condition, to obtain monomeric Au₂₅(PET)₁₈⁻ mass spectrum in ion mobility (ESI IM MS) mode, the following instrumental parameters were used:

Sample concentration: 1 µg/mL

Solvent: DCM

Flow Rate: 10-20 µL/min

Capillary Voltage: 2-3 kV

Cone Voltage: 120-150 V

Source Offset: 80-120 V

Desolvation gas flow: 400 L/h

Trap gas flow: 5 mL/min

He gas flow: 100 mL/min

Ion mobility gas flow: 50 mL/min

Bias Voltage: 45 V

Wave Velocity: 400 m/s

Wave Height: 40 V

To obtain dimer and other polymers of Au₂₅(PET)₁₈⁻, following parameters were followed:

Capillary Voltage: 1-2 kV

Cone Voltage: 0-50 V

Source Offset: 0-20 V

Desolvation gas flow: 400 L/h

Trap gas flow: 5-10 mL/min

He gas flow: 100-180 mL/min

Ion mobility gas flow: 50-70 mL/min

Bias Voltage: 25-30 V

Rest of the parameters were kept the same as before.

UV-vis absorption studies were conducted with a Perkin Elmer Lambda25 instrument with 1 nm band pass.

Electronic Supplementary Information 1

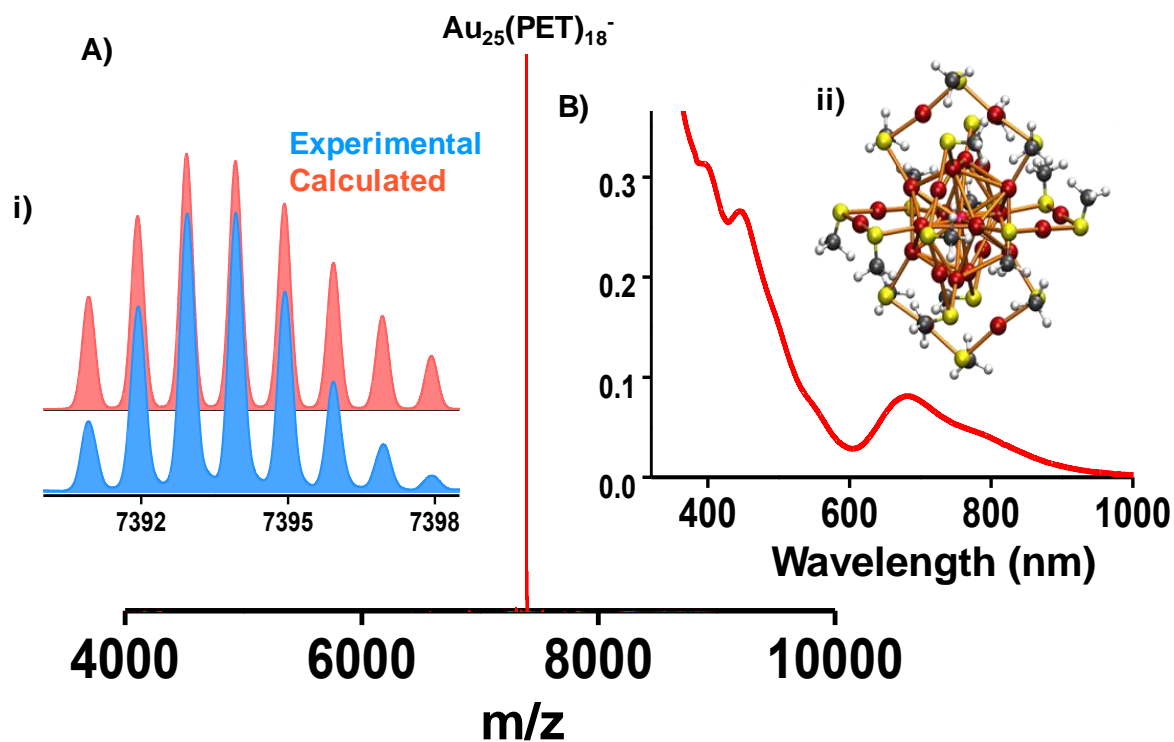


Figure S1: A) ESI MS of $\text{Au}_{25}(\text{PET})_{18}^-$ showing a single peak centred at m/z 7393 (average mass). Experimental isotope pattern of this peak is matching well with the calculated one as shown in inset i). B) UV-vis absorption spectrum of $\text{Au}_{25}(\text{PET})_{18}^-$ showing characteristic peaks conforming successful synthesis. Density functional theory (DFT) optimized structure of the cluster is shown in the inset ii). Ligands were replaced with $-\text{SMe}$, to reduce the computational demand.

Electronic Supplementary Information 2

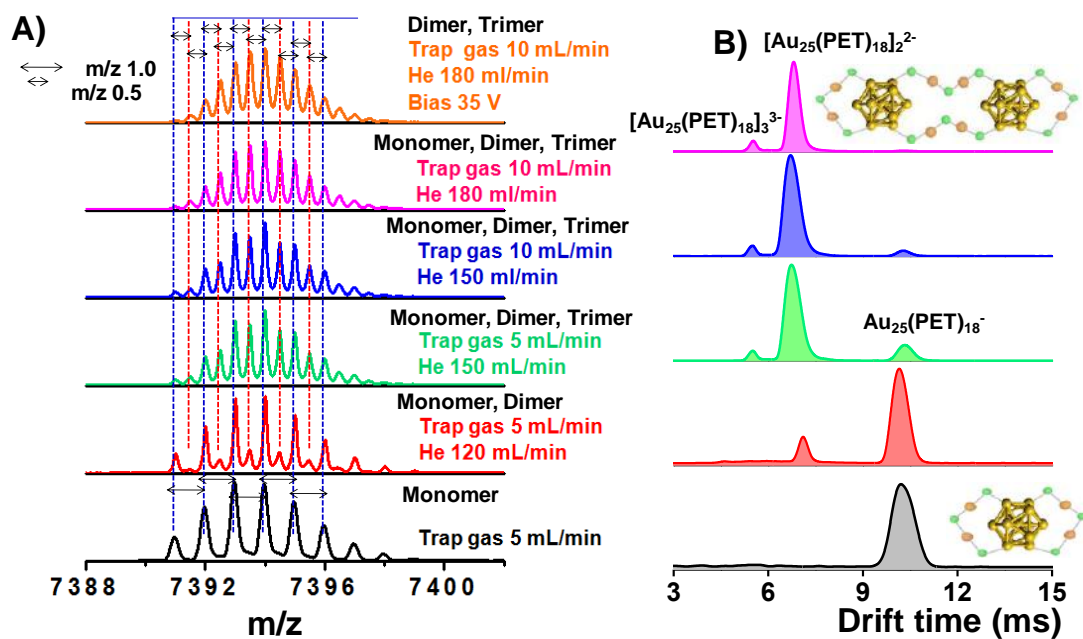


Figure S2: A) Optimization of different gas flow rates to obtain [Au₂₅(PET)₁₈]₂²⁻ and B) corresponding drift time plots. Schematic representation of the structures is also shown.

Electronic Supplementary Information 3

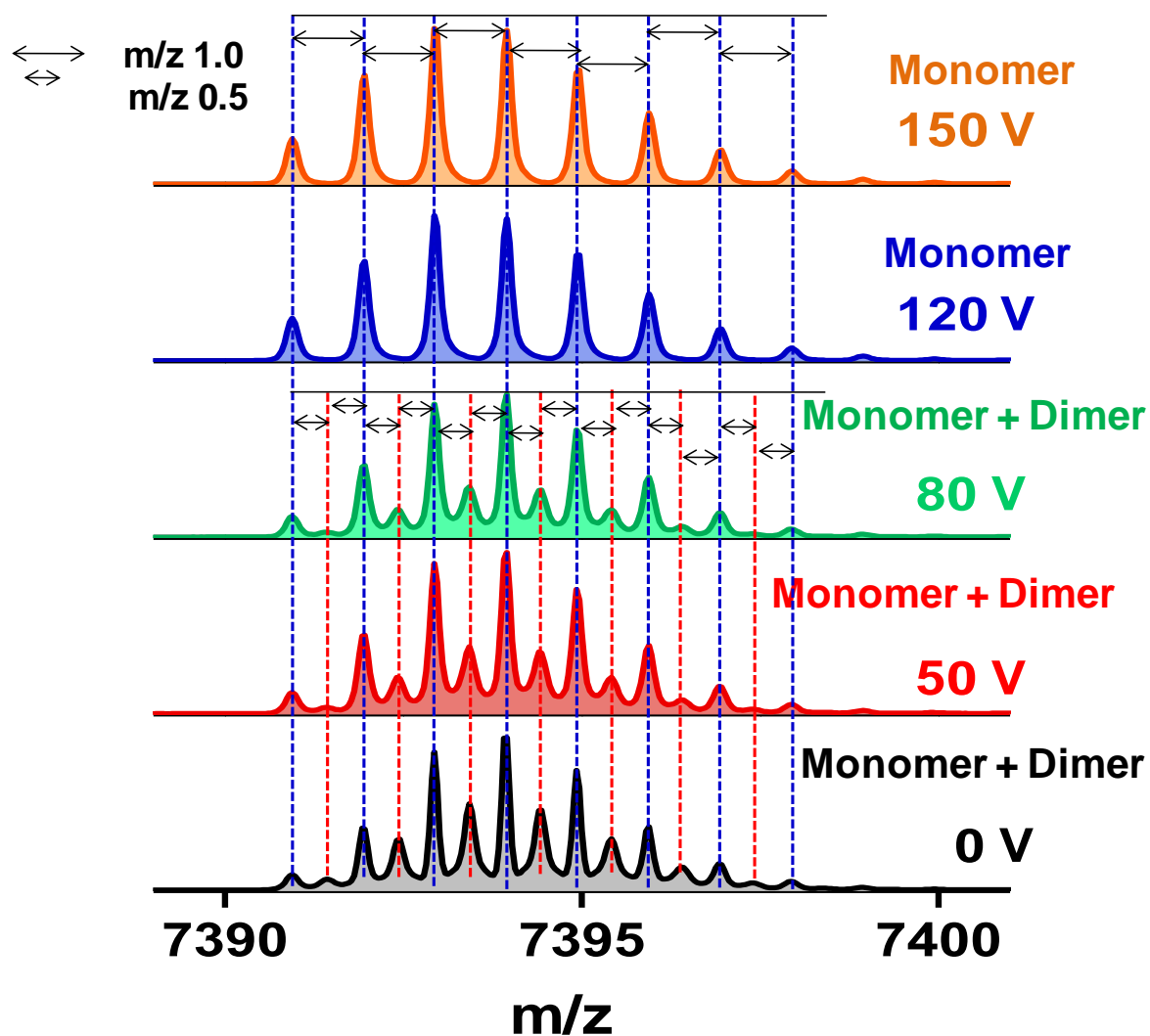


Figure S3: Cone voltage dependence for dimer formation in case of $\text{Au}_{25}(\text{PET})_{18}^-$. Dimers are formed at lower cone voltages.

Electronic Supplementary Information 4

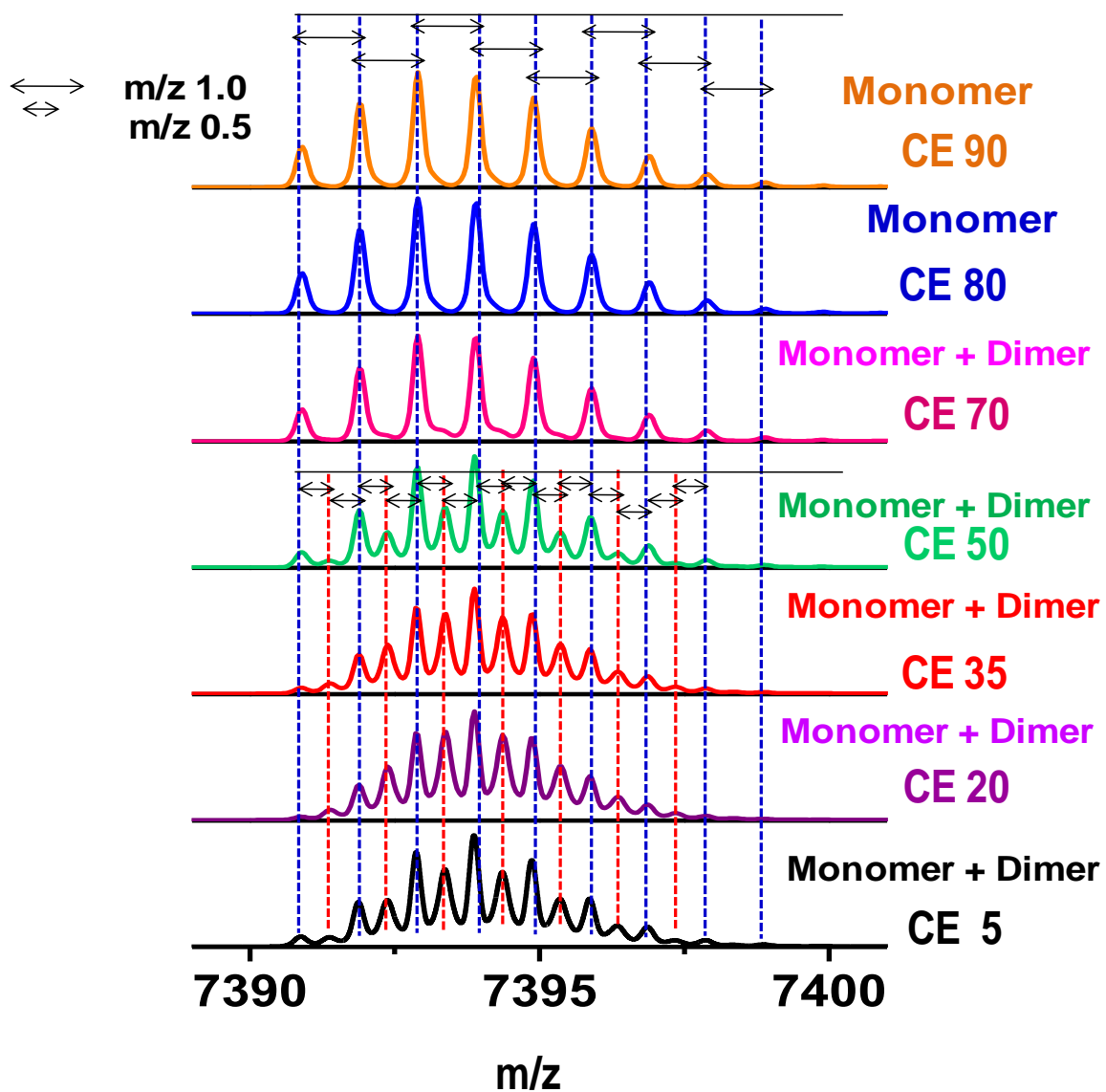


Figure S4: Formation of monomer from dimer upon gradually increasing the collision energy in the case of $\text{Au}_{25}(\text{PET})_{18}^-$.

Electronic Supplementary Information 5

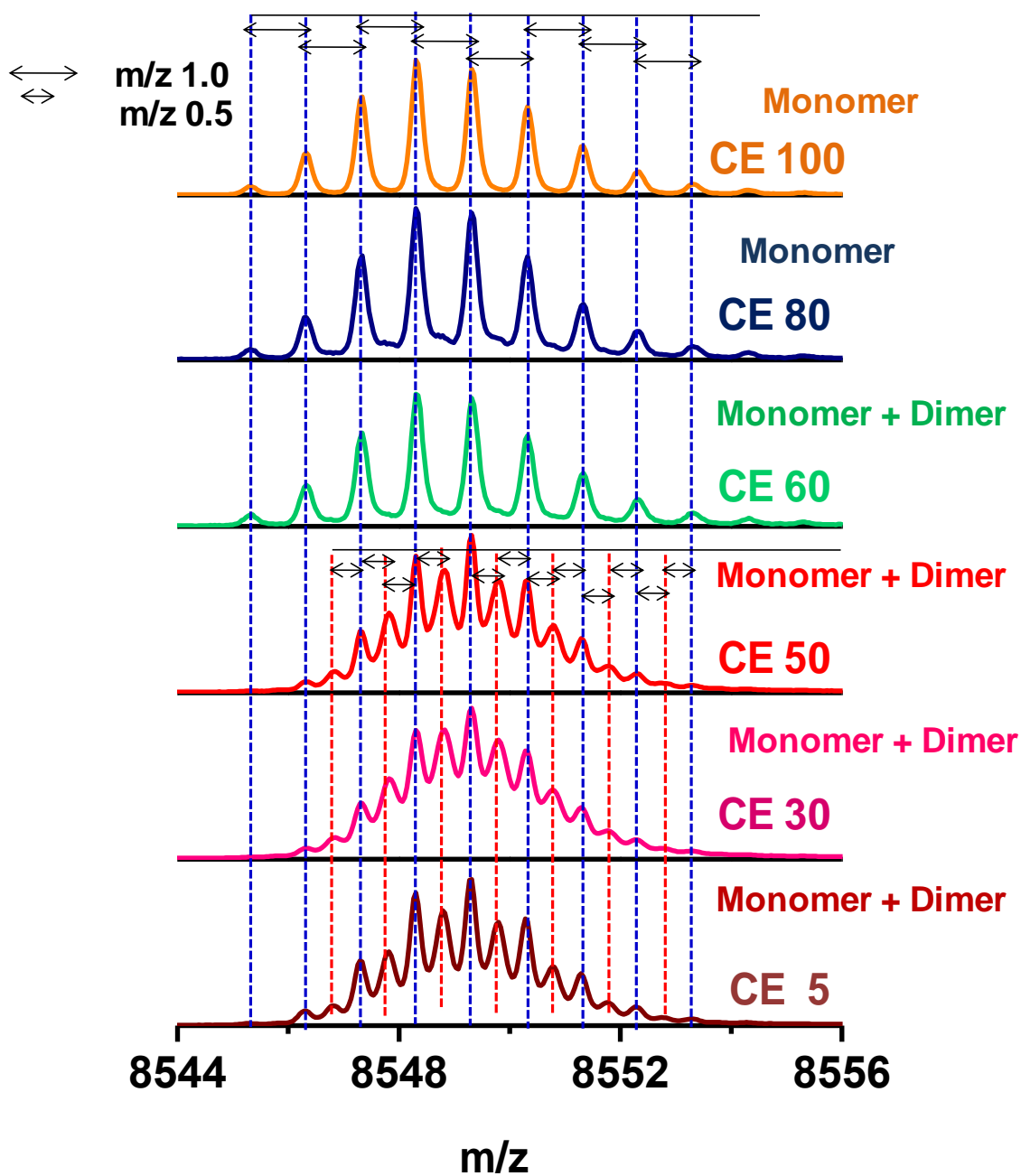


Figure S5: Formation of monomer from dimer upon gradually increasing the collision energy in the case of $\text{Au}_{25}(\text{DDT})_{18}^-$.

Electronic Supplementary Information 6

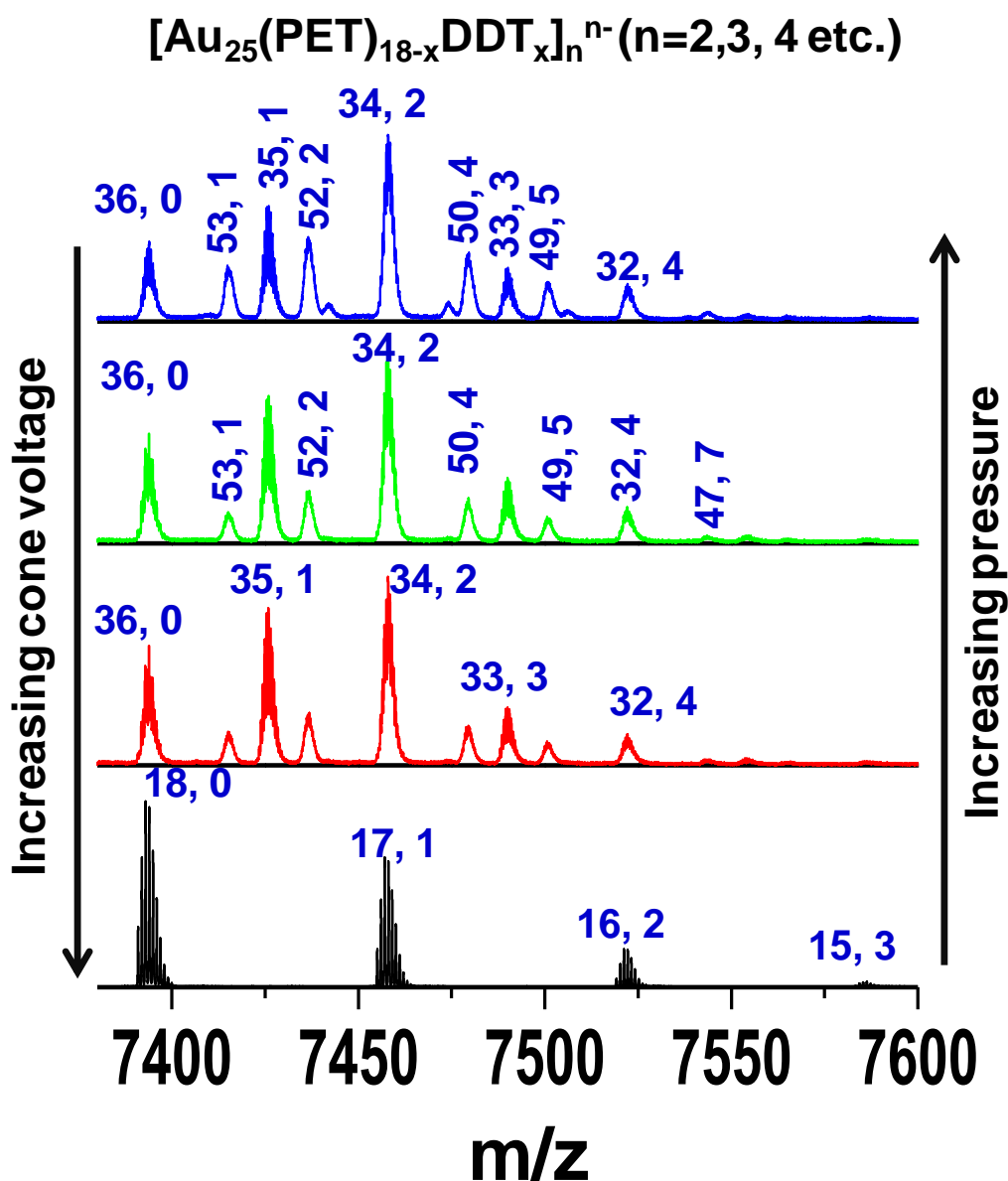


Figure S6: Cone voltage and pressure dependence in case of ligand exchange of PET with DDT. Product peaks are labelled where the first number corresponds to the number of PET in the cluster and the second corresponds to that of DDT.

Electronic Supplementary Information 7

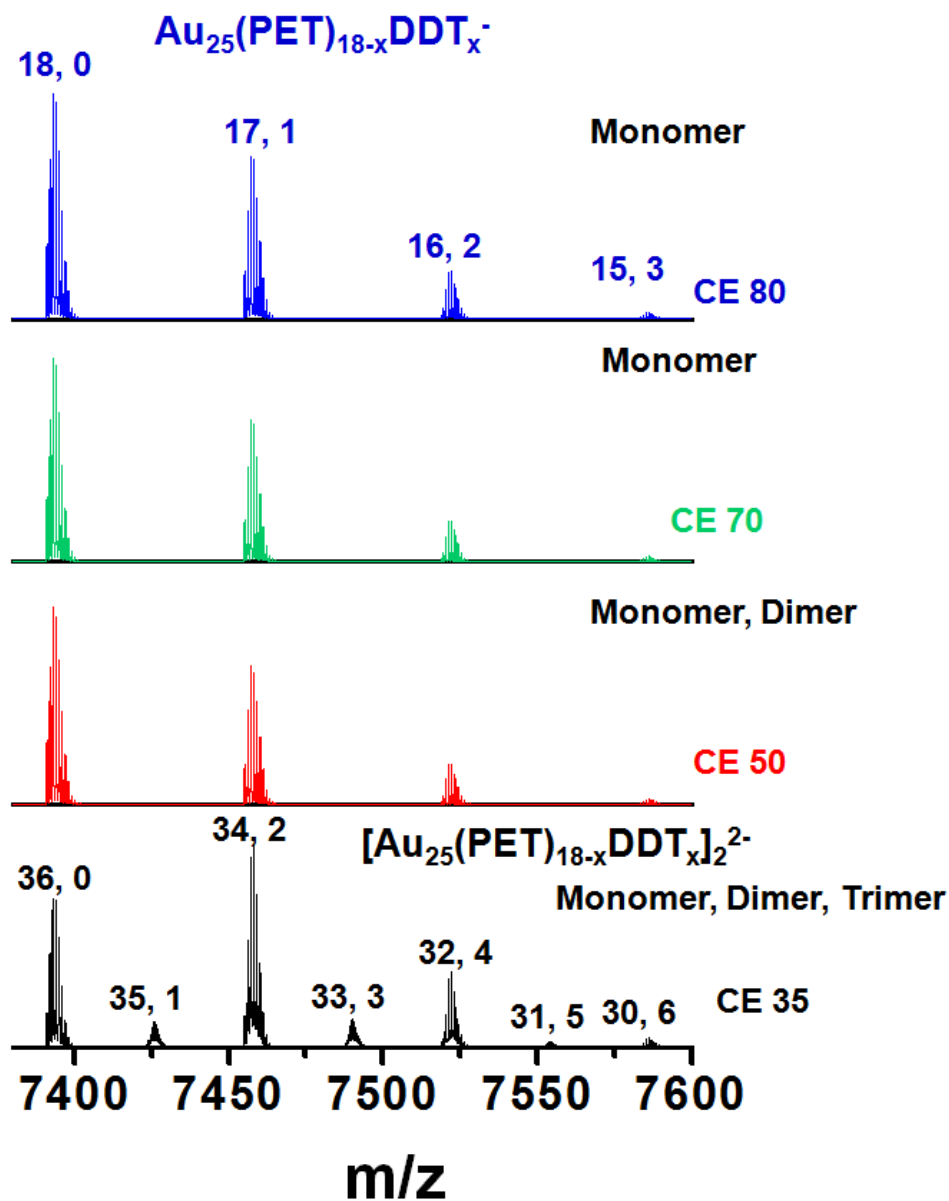


Figure S7: Collision energy dependence in the case of ligand exchange of Au₂₅(SR)₁₈ system with DDT showing the formation of monomer from polymers. Product peaks are labelled where the first number corresponds to number of PET in the cluster and the second corresponds to number of DDT. CE corresponds to nominal collision energy.

Electronic Supplementary Information 8

Monomers

$\text{Au}_{25}(\text{PET})_{18}(\text{DDT})_0$	(18,0)
$\text{Au}_{25}(\text{PET})_{17}(\text{DDT})_1$	(17,1)
$\text{Au}_{25}(\text{PET})_{16}(\text{DDT})_2$	(16,2)
$\text{Au}_{25}(\text{PET})_{15}(\text{DDT})_3$	(15,3)

Dimers

$[(\text{Au}_{25}(\text{PET})_{18}(\text{DDT})_0)(\text{Au}_{25}(\text{PET})_{18}(\text{DDT})_0)]^2$	(36,0)
$[(\text{Au}_{25}(\text{PET})_{18}(\text{DDT})_0)(\text{Au}_{25}(\text{PET})_{17}(\text{DDT})_1)]^2$	(35,1)
$[(\text{Au}_{25}(\text{PET})_{17}(\text{DDT})_1)(\text{Au}_{25}(\text{PET})_{17}(\text{DDT})_1)]^2$	(34,2)
$[(\text{Au}_{25}(\text{PET})_{17}(\text{DDT})_1)(\text{Au}_{25}(\text{PET})_{16}(\text{DDT})_2)]^2$	(33,3)
$[(\text{Au}_{25}(\text{PET})_{16}(\text{DDT})_2)(\text{Au}_{25}(\text{PET})_{16}(\text{DDT})_2)]^2$	(32,4)
$[(\text{Au}_{25}(\text{PET})_{16}(\text{DDT})_2)(\text{Au}_{25}(\text{PET})_{15}(\text{DDT})_3)]^2$	(31,5)
$[(\text{Au}_{25}(\text{PET})_{15}(\text{DDT})_3)(\text{Au}_{25}(\text{PET})_{15}(\text{DDT})_3)]^2$	(30,6)

Trimers

$[(\text{Au}_{25}(\text{PET})_{18}(\text{DDT})_0)(\text{Au}_{25}(\text{PET})_{18}(\text{DDT})_0)(\text{Au}_{25}(\text{PET})_{18}(\text{DDT})_0)]^3$	(54,0)
$[(\text{Au}_{25}(\text{PET})_{18}(\text{DDT})_0)(\text{Au}_{25}(\text{PET})_{18}(\text{DDT})_0)(\text{Au}_{25}(\text{PET})_{17}(\text{DDT})_1)]^3$	(53,1)
$[(\text{Au}_{25}(\text{PET})_{18}(\text{DDT})_0)(\text{Au}_{25}(\text{PET})_{17}(\text{DDT})_1)(\text{Au}_{25}(\text{PET})_{17}(\text{DDT})_1)]^3$	(52,2)
$[(\text{Au}_{25}(\text{PET})_{17}(\text{DDT})_1)(\text{Au}_{25}(\text{PET})_{17}(\text{DDT})_1)(\text{Au}_{25}(\text{PET})_{17}(\text{DDT})_1)]^3$	(51,3)
$[(\text{Au}_{25}(\text{PET})_{16}(\text{DDT})_2)(\text{Au}_{25}(\text{PET})_{17}(\text{DDT})_1)(\text{Au}_{25}(\text{PET})_{17}(\text{DDT})_1)]^3$	(50,4)
$[(\text{Au}_{25}(\text{PET})_{16}(\text{DDT})_2)(\text{Au}_{25}(\text{PET})_{16}(\text{DDT})_2)(\text{Au}_{25}(\text{PET})_{16}(\text{DDT})_2)]^3$	(49,5)
$[(\text{Au}_{25}(\text{PET})_{16}(\text{DDT})_2)(\text{Au}_{25}(\text{PET})_{16}(\text{DDT})_2)(\text{Au}_{25}(\text{PET})_{15}(\text{DDT})_3)]^3$	(48,6)
$[(\text{Au}_{25}(\text{PET})_{15}(\text{DDT})_3)(\text{Au}_{25}(\text{PET})_{15}(\text{DDT})_3)(\text{Au}_{25}(\text{PET})_{15}(\text{DDT})_3)]^3$	(47,7)
$[(\text{Au}_{25}(\text{PET})_{15}(\text{DDT})_3)(\text{Au}_{25}(\text{PET})_{15}(\text{DDT})_3)(\text{Au}_{25}(\text{PET})_{16}(\text{DDT})_2)]^3$	(46,8)
$[(\text{Au}_{25}(\text{PET})_{15}(\text{DDT})_3)(\text{Au}_{25}(\text{PET})_{15}(\text{DDT})_3)(\text{Au}_{25}(\text{PET})_{16}(\text{DDT})_2)]^3$	(45,9)

Figure S8: Compositions of different monomers, dimers and trimers formed during ligand exchange and subsequent polymerization process.

Electronic Supplementary Information 9

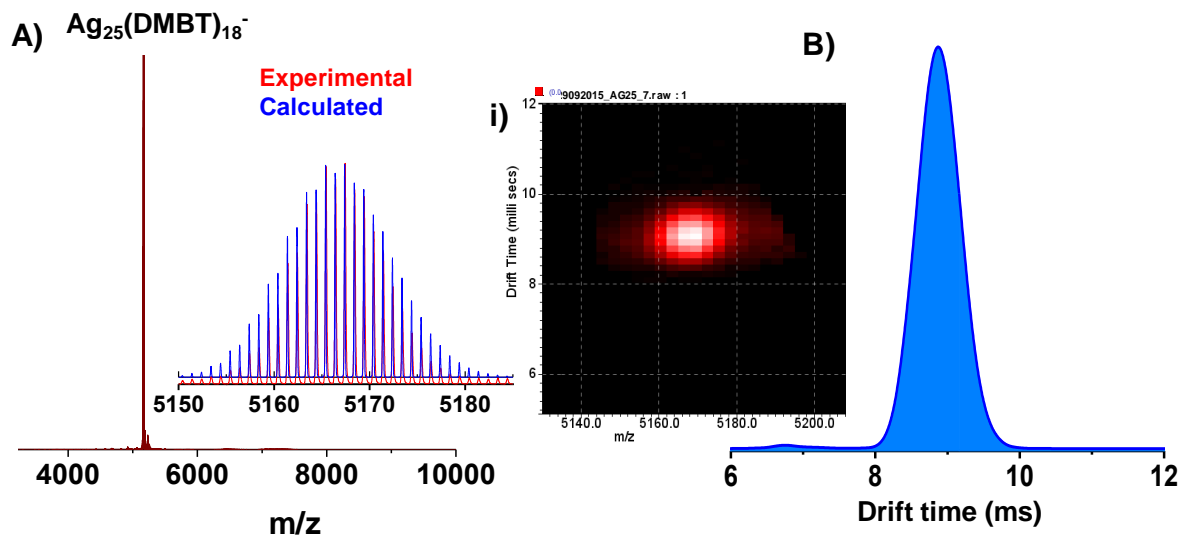


Figure S9: A) ESI MS of $\text{Ag}_{25}(\text{DMBT})_{18}^-$ in negative ion mode showing molecular ion peak. Experimental data are matching well with the calculated spectrum as shown in inset i). B) Drift time profile of the same cluster is showing peak at 8.8 ms. Plot of m/z vs. drift time for $\text{Au}_{25}(\text{PET})_{18}$ is shown in inset ii).

Computational Details:

We used density functional theory as implemented real-space projector augmented wave method in GPAW[1]. $\text{Au}(5d^{10}6s^1)$, and $\text{S}(3s^23p^4)$ electrons were treated as valence and the inner electrons were included in a frozen core. The GPAW setups for gold and silver included scalar-relativistic corrections. The exchange-correlation functional employed was the generalized gradient approximation of Perdew, Burke and Ernzerhof (GGA-PBE)[2].

We used a 0.2 Å grid spacing for electron density in all calculations and a convergence criterion of 0.05 eV/Å for the residual forces on atoms was used in all structure optimizations, without any symmetry constraints. For computational efficiency during the structural optimizations, rather than employing the finite-difference real-space grid method for the expansion of the pseudo wave functions, we used instead the LCAO method[3] as implemented in GPAW by employing a double zeta plus polarization (DZP) basis set. For greater precision in our energy calculations, we then recalculated the total energies at this geometry minimum using the finite-difference method in GPAW.

The crystal structures of $\text{Au}_{25}(\text{SR})_{18}$ [4] were used for building the initial structures of the A, B and C isomers of $[\text{Au}_{50}(\text{SR})_{36}]^{2-}$. For efficient computations, we terminated each sulphur atom with a hydrogen atom in all the clusters. The initial structures of isomers A, B and C were first geometry optimized, and then the value of the total energy of each isomer taken at the

geometry-optimized configuration using was recalculated using the more accurate finite-difference method in GPAW. For the binding energy calculation we used the total energy of Au₂₅(SH)₁₈ from Ref 5. where they have used the same method of calculation as ours. The structures of the isomers of Au₅₀(SH)₃₆ were built up with the help of Avogadro software package[6]and visualizations were created with Visual Molecular Dynamics (VMD) software[7].Coordinates of geometry optimized isomers.

References:

- (1) Enkovaara, J.; et al. *J. Phys.: Condens. Matter* 2010, 22, 253202.
- (2) Perdew, J. P.; Burke, K. *Phys. Rev. Lett.* **1996**, 77, 3865.
- (3) Larsen, A. H.; Vanin, M.; Mortensen, J. J.; Thygesen, K. S.; Jacobsen, K. W. *Phys. Rev. B* **2009**, 80, 195112.
- (4) Krishnadas, K. R., Ghosh, A., Baksi, A., Chakraborty, I., Natarajan, G., and Pradeep, T.*J. Am. Chem. Soc.*, **2016**, 138, 140.
- (5) (a) Heaven, M. W.; Dass, A.; White, P. S.; Holt, K. M.; Murray, R. W. *J. Am. Chem. Soc.* **2008**, 130, 3754. Zhu, M.; Aikens, C. M.; Hollander, F. J.; Schatz, G. C.; Jin, R. *J. Am. Chem. Soc.* **2008**, 130, 5883.
- (6) Hanwell, M.; Curtis, D.; Lonie, D.; Vandermeersch, T.; Zurek, E.; Hutchison, G. *J. Cheminf.* **2012**, 4, 1.
- (7) Humphrey, W.; Dalke, A.; Schulten, K. *J. Mol. Graphics* **1996**, 14, 33.

Electronic Supplementary Information 10

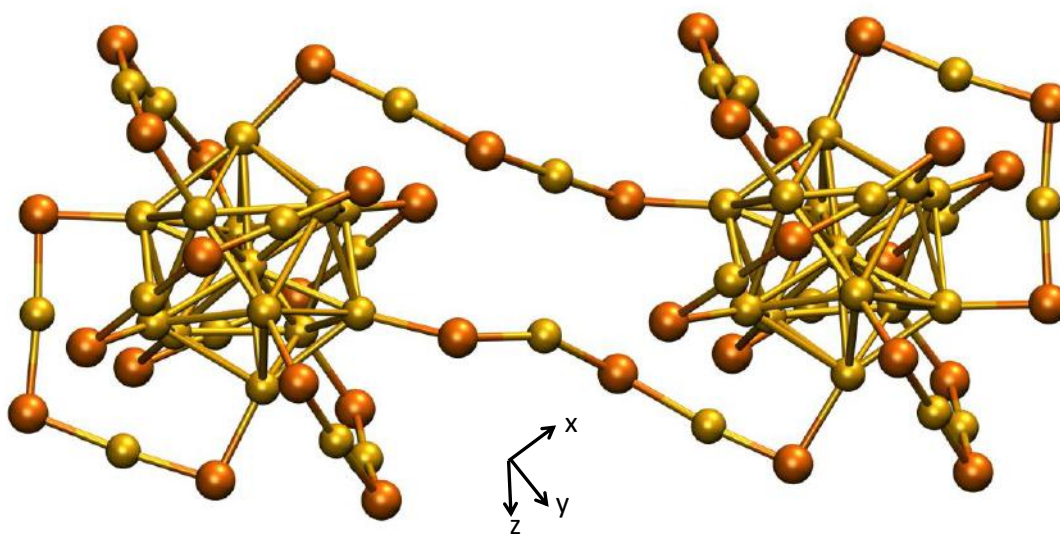


Figure S10: A third possible structural isomer (C) of the $[\text{Au}_{50}(\text{SR})_{36}]^{2-}$ dimer considering inter-cluster bonding via Au_2S_3 staples. The DFT-optimized structure of isomer C has linkages formed when the two clusters are positioned so that the edges of the staples are adjacent to each other. The diagonal bonding between the edges of staples on either cluster forms two parallel Au_2S_3 chains linking the two clusters. The view shown is looking in the negative z -direction (top view), according to the Cartesian axes shown. The ligand R-groups are removed for clarity and gold atoms are shown in gold and sulphur atoms in orange, using the ball and stick atom representation.

Table S1: Collision Cross Section values of $\text{Au}_{25}(\text{SR})_{18}$ monomer, dimer and trimer.

Species	CCS value (\AA^2)
$[\text{Au}_{25}(\text{PET})_{18}]^-$	297.8
$[\text{Au}_{25}(\text{PET})_{18}]_2^{2-}$	453.4
$[\text{Au}_{25}(\text{PET})_{18}]_3^{3-}$	668.3

Table S2: Collision Cross Section values of $Au_{25}(SR)_{18}$ monomer, dimer and trimer after ligand exchange with DDT.

Monomers	Species	CCS value (Å^2)
	$[Au_{25}(PET)_{18}]^-$	303.1
	$[Au_{25}(PET)_{17}(DDT)_1]^-$	305.2
	$[Au_{25}(PET)_{16}(DDT)_2]^-$	306.7

Dimers	Species	CCS value (Å^2)
	$[Au_{25}(PET)_{18}]_2^{2-}$	461.2
	$[[Au_{25}(PET)_{18}][Au_{25}(PET)_{17}(DDT)_1]]^{2-}$	463.1
	$[[Au_{25}(PET)_{17}(DDT)_1][Au_{25}(PET)_{17}(DDT)_1]]^{2-}$	465.4
	$[[Au_{25}(PET)_{16}(DDT)_2][Au_{25}(PET)_{17}(DDT)_1]]^{2-}$	467.6
	$[[Au_{25}(PET)_{16}(DDT)_2][Au_{25}(PET)_{16}(DDT)_2]]^{2-}$	469.6
	$[[Au_{25}(PET)_{15}(DDT)_3][Au_{25}(PET)_{16}(DDT)_2]]^{2-}$	471.5
	$[[Au_{25}(PET)_{15}(DDT)_3][Au_{25}(PET)_{15}(DDT)_3]]^{2-}$	472.9

Trimers	Species	CCS value (Å^2)
	$[Au_{25}(PET)_{18}]_3^{3-}$	665.8
	$[[Au_{25}(PET)_{18}][Au_{25}(PET)_{18}][Au_{25}(PET)_{17}(DDT)_1]]^{3-}$	667.4
	$[[Au_{25}(PET)_{18}][Au_{25}(PET)_{17}(DDT)_1][Au_{25}(PET)_{17}(DDT)_1]]^{3-}$	668.5
	$[[Au_{25}(PET)_{17}(DDT)_1][Au_{25}(PET)_{17}(DDT)_1][Au_{25}(PET)_{17}(DDT)_1]]^{3-}$	670.5
	$[[Au_{25}(PET)_{16}(DDT)_2][Au_{25}(PET)_{17}(DDT)_1][Au_{25}(PET)_{17}(DDT)_1]]^{3-}$	671.8
	$[[Au_{25}(PET)_{16}(DDT)_2][Au_{25}(PET)_{16}(DDT)_2][Au_{25}(PET)_{17}(DDT)_1]]^{3-}$	673.7
	$[[Au_{25}(PET)_{16}(DDT)_2][Au_{25}(PET)_{16}(DDT)_2][Au_{25}(PET)_{16}(DDT)_2]]^{3-}$	675.6
	$[[Au_{25}(PET)_{15}(DDT)_3][Au_{25}(PET)_{16}(DDT)_2][Au_{25}(PET)_{16}(DDT)_2]]^{3-}$	676.9
	$[[Au_{25}(PET)_{15}(DDT)_3][Au_{25}(PET)_{15}(DDT)_3][Au_{25}(PET)_{16}(DDT)_2]]^{3-}$	677.8
$[[Au_{25}(PET)_{15}(DDT)_3][Au_{25}(PET)_{15}(DDT)_3][Au_{25}(PET)_{15}(DDT)_3]]^{3-}$	679.6	

Table S3: Isomers of $[Au_{50}(SH)_{36}]^{2-}$. The DFT energies of the three isomers A, B, C, their binding energies and binding energy difference with respect to isomer A are shown. The value of the monomer energy -220.28 eV was taken from Ref. 17 in the main article (K. R. Krishnadas, A. Ghosh, A. Bakshi, I. Chakraborty, G. Natarajan and T. Pradeep, *J. Am. Chem. Soc.*, 2016, **138**, 140-148.)

Isomer	Energy/eV	Binding Energy (E_b)/eV	$E_b - E_b(A)$ /eV
A	-439.385	+1.18	0.00
B	-439.068	+1.49	+0.31
C	-438.200	+2.36	+1.18

Sparingly Soluble Constant Carbonate Releasing Inert Monolith for Enhancement of Antimicrobial Silver Action and Sustainable Utilization

Jakka Radvindran Swathy,[†] Nalenthiran Pugazhenthiran,^{†,‡} Chennu Sudhakar, Avula Anil Kumar, and Thalappil Pradeep*[‡]

DST Unit of Nanoscience (DST UNS) and Thematic Unit of Excellence (TUE), Department of Chemistry, Indian Institute of Technology Madras, Chennai 600 036, India

S Supporting Information

ABSTRACT: Silver, a metal with phenomenal commercial importance has been exploited in its ionic form in the field of water purification, with the objective of delivering microbially safe drinking water. Silver released at such concentrations is unrecoverable and has to be reduced to ensure sustainable utilization of the metal. We have shown that small concentrations of carbonate can effectively bring down the amount of silver ion used for microbial disinfection by half. Implementation of this finding requires constant carbonate releasing materials in natural water for an extended period. In this work, we describe a hybrid material with intrinsically high stability in water that is prepared using naturally abundant ingredients which releases carbonate constantly and in a controlled fashion. This composition in conjunction with reduced silver ion concentration delivers microbially safe water, tested with *E. coli* and MS2 phage. Use of constant carbonate releasing material for antimicrobial applications can reduce the unrecoverable silver released into the environment by ~1300 tons/year. We also show that the composition can be modified to release cations of choice without disturbing the CO_3^{2-} release from the same. A sustained release of selective cations along with carbonate can supplement drinking water with the minerals of interest.

KEYWORDS: Carbonate materials, Sustainable release, Synergetic effect on silver, Enhanced antimicrobial activity, Drinking water purification



INTRODUCTION

Silver in its ionic form has been a subject of numerous investigations and is commercially exploited for its antimicrobial activity in drinking water purification.¹ Nevertheless, delivering silver ions at sustained concentrations of relevance to achieve antimicrobial activity has been a challenging task. Numerous approaches are available for the synthesis of biocidal silver nanoparticles or colloids using matrices.² The biocidal property of silver nanoparticles is attributed to the release of trace quantities of silver ions in water.^{2d,e} Antibacterial effect of transition metals, including silver, is usually named as oligodynamic effect, as it is most effective at low concentrations due to the solubility limits imposed by various anions. Due to this reason, they cannot exist as free ions at higher concentrations in real water.^{2f} It is also appropriate to reduce the consumption of silver in view of the potential risks to both primitive and developed organisms.^{2e} Although nanoparticles release silver ions more efficiently than the bulk metal, massive deployment of such products has been hampered due to the following reasons: (a) drinking water contains many species (e.g., inorganic ions and organics) that anchor on the surface of the nanoparticles, making the release of sustained silver ions difficult;³ and (b) surface fouling due to silicates present in

water retards Ag^+ release consequently quenching the antimicrobial activity. Therefore, a sustainable solution for safe drinking water is an important aspect.⁴

Introduction of novel nanostructures with constant and controlled silver ion releasing capability is proposed to be a remedial method.⁵ However, the free silver ion concentration available for antimicrobial activity depends on the water chemistry, especially the presence of various anions.⁶ For a specific silver ion concentration, the antimicrobial performance is in the order, seawater \leq high organic matter-containing water \leq high divalent cation-containing water \leq synthetic water, due to the speciation of Ag^+ .⁷ In this aspect, we have found that one of the anions, namely carbonate (CO_3^{2-}) can effectively enhance the antimicrobial activity of Ag^+ reducing the overall annual global silver requirement used for antimicrobial applications by half, i.e., to the extent of ~1300 tons.⁶ This anion factor enhancing the sustainable utilization of noble metals can be industrially utilized only with the development of sustainable CO_3^{2-} releasing materials at desired concentrations.

Received: May 6, 2016

Revised: May 31, 2016

Published: June 5, 2016

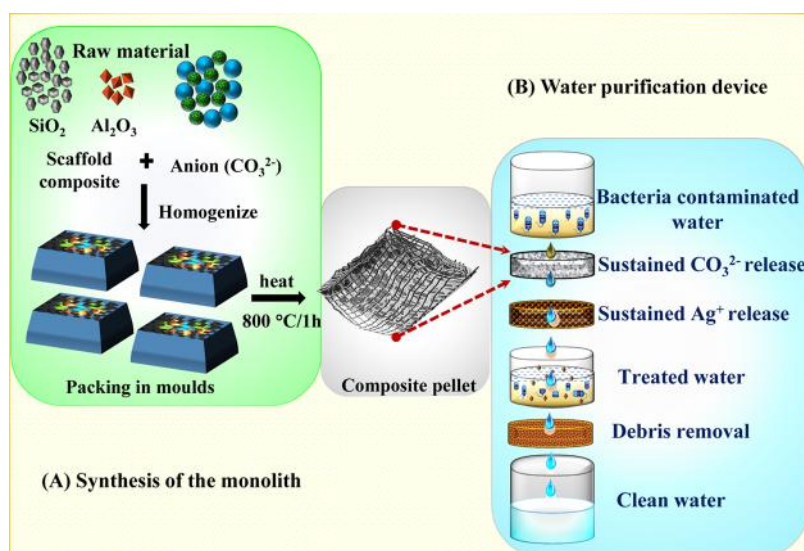


Figure 1. Schematic representation of the synthesis of carbonate releasing monolith ($C_{CO_3}/C_{CO_3/K}$) and a water purification system based on the same. The products are solid rock-like substances, in the shape of the mold which may be crushed or used as such.

However, requirement of precise carbonate concentrations and consequent need of trained manpower to maintain the carbonate ion concentration in the water purification plant are limiting the field-deployment of this technology. The release rate of highly alkaline carbonate ions in the treated water should be constant and controlled to maintain the pH of drinking water. Also, the release rate of carbonate ions from the corresponding salts regulate the time period of utilization of carbonate salts in continuous flow of water. In addition, sustained carbonate release must occur along with silver for delivering bacteria and virus-free safe drinking water. In this context, no commercially available sustained carbonate ion releasing products for drinking water purification are available until now. Essential inorganic minerals like calcium, magnesium, sodium, potassium, iron, and zinc, which occur at milligram per kilogram quantities in the body, are crucial for the human system. “Water” can serve as a source of these essential ions to meet the body’s mineral requirement.⁸ In this study, we also show that the sustained release formulation can be modified to release the mineral ion of interest through drinking water based on the deficiency present at a given source.

In this paper, we introduce a new composition for this purpose which releases CO_3^{2-} at the required concentration of 20 ± 5 ppm at ambient temperatures. It contributes to the sustainable utilization of resources, yet efficiently delivering cent percent safe potable water solving one of the important problems of humanity.⁹ Dissolution of sparingly soluble salts has also been a part of interest in the context of measuring volume of water passed through a device, and also in terms of pH control.¹⁰ However, none of these reports is concerned with the release of CO_3^{2-} ions, especially for effectively enhancing the antimicrobial activity.

Although most of the surface waters and ground waters contain sufficiently high concentration of carbonates and bicarbonates (>180 ppm), this hard water is undesirable for drinking. In most cases, hardness is removed which removes the carbonates too. At a higher pH, after reaching a supersaturation point (pH: 7.5–8.0, alkalinity: 80–160 ppm, and saturation index: 1.5) these carbonates precipitate forming turbid water. But, carbonate concentration released from the

designed material is constantly maintained at 20 ± 5 ppm, which is below the required saturation index and alkalinity due to which precipitation of $CaCO_3$ does not occur.

In an attempt to create a stable structure, releasing carbonate, various template forming precursors were used to embed carbonates. Due to the requirement of chemical inertness and structural integrity in water as mentioned before, silica and alumina were our natural choices for forming templates. A stable composite of silica with enhanced robustness at a temperature below the melting point of CO_3^{2-} was achieved by optimizing several combinations of silica and carbonates. The addition of different forms of carbonates acted as a flux material in reducing the melting point of silica. Each of the compositions prepared were analyzed for the release characteristics and the optimized compositions were arrived at. A trace amount of 4.3% of alumina was used to strengthen the mechanical properties of silica scaffold. Al_2O_3 has high bioinertness,¹¹ high abrasion resistance, and high hardness, all of which make it suitable as a material of use in water.¹² In the template, the carbonates were trapped within the porous silica cages. The pores are small enough allowing CO_3^{2-} to be preserved with reduced, yet sufficient, interaction with water, due to which the release of CO_3^{2-} is constantly maintained in the range of $\sim 20 \pm 5$ ppm. This uniformity and reduced release rate at an immersed condition are difficult to achieve in a carbonate releasing material. The monolith prepared works as a controlled anion releasing system maintaining an equilibrium concentration above which further release does not occur. We also show that the designed monolith can be modified to release other ions of interest and it is demonstrated here for potassium release, without disturbing the release of carbonate.

EXPERIMENTAL SECTION

The carbonate releasing monolith was synthesized using a solid state route. It was made by melting silica and traces of alumina at the lowest possible temperature such that carbonate does not decompose into the corresponding oxide and carbon dioxide.¹³ The mineral cristobalite is a high-temperature polymorph of silica seen at equilibrium formation temperature of 1470 °C at atmospheric pressure. Moganite is a silicate mineral, considered as a polymorph of quartz formed at 1354 °C. The composition of the raw materials was optimized in such a fashion that

the cristobalite and moganite matrices can be formed at temperatures below the melting point of carbonate (850 °C). Inclusion of carbonates was not only considered as an anion for release but also as a flux, reducing the melting point of silica.

All the chemicals used were purchased from Sigma-Aldrich and used as such. Unless otherwise specified, all the reagents used were of analytical grade. Our objective was to create a template in which carbonate releasing components can be held strongly at the largest extent, along with controlled release. Various optimization studies were undertaken to ensure that the scaffold created holds carbonate, ensuring constant release.

Synthesis of Sustained Carbonate Releasing Materials, C_{CO_3} . The carbonate releasing composite, abbreviated as C_{CO_3} , comprising of a porous scaffold was loaded with the source of carbonate namely, sodium and potassium carbonates. Figure 1A describes a schematic outline of the synthesis of C_{CO_3} and a water purification method based on the same. The mixture of SiO_2 and Al_2O_3 as raw materials for scaffold and the anion sources, namely Na_2CO_3 and K_2CO_3 (in the ratio of 74.1:4.3:16.8:4.75 by wt%, respectively), were homogenized and packed in molds and sintered at 800 °C for 1 h. Decomposition temperatures of Na_2CO_3 and K_2CO_3 are 858 and 898 °C, respectively, at atmospheric pressure.¹⁴ The composite material formed was cooled to room temperature followed by washing with water at ambient condition, which was used for further experiments.

Synthesis of the Material for Sustained Release of Carbonate and Potassium Ions, $C_{CO_3/K}$. The synthesis of potassium and carbonate releasing composite, abbreviated as $C_{CO_3/K}$, involves a mixture of SiO_2 and Al_2O_3 as raw materials for the scaffold composition; Na_2CO_3 , $CaCO_3$, and K_2CO_3 as sources of anions; and K_2CO_3 and KCl as sources of potassium (with $SiO_2:Al_2O_3:Na_2CO_3:K_2CO_3:CaCO_3:KCl$ in the ratio, 40.6:2.4:31.5:7.6:12.0:6.0 by wt%, respectively). These raw materials were homogenized, packed in molds, and sintered at 850 °C for 1 h. The $C_{CO_3/K}$ composite material formed was cooled to room temperature followed by washing with water at ambient condition and was used for further experiments.

Kinetics of Sustained Release of Carbonate. Batch Mode. The kinetics of carbonate release from the material was studied using the following experimental procedure. Ten milligrams of the carbonate incorporated pellet granulated as $\sim 72 \mu m$ particles was shaken briefly in 10 mL of Milli-Q water. Carbonate concentration released in the test water at different contact times was calculated based on the quantification of total inorganic carbon, measured at each step using a total organic carbon (TOC) analyzer (Shimadzu TOC-V_{CPH} model). The instrument was calibrated earlier using anhydrous sodium carbonate and anhydrous sodium hydrogen carbonate. The TOC measurements were performed using Millipore water whose inorganic carbon content was monitored for every individual experiment and considered as a blank.

Cartridge Mode. The performance of the material under continuous flow of water was tested in the cartridge mode. A cartridge containing 1 L of tap water was treated with 1 g of the material, C_{CO_3} . After 15 min of standing time, the total dissolved solids (TDS), expressed in terms of electrical conductivity ($\mu S/cm$), and the change in pH of the water were measured as indications of carbonate released into the water. The cartridge was drained and filled with a fresh batch of tap water (1L) and the above procedure was repeated to monitor the release. This cycle was repeated until all the CO_3^{2-} present in the material was exhausted. The material, C_{CO_3} ran up to 50 L of water (50 cycles) after which no change in pH or TDS was observed. After every 10 cycles of the above procedure, the material was dried for 18–20 h at room temperature and was tested for further CO_3^{2-} release.

Biocidal Enhancement Property of the Material. Enhancement in the biocidal property of Ag^+ was measured by spiking 100 mL of the natural drinking water with Ag^+ (40 ppb) and Ag^+ (40 ppb)/ CO_3^{2-} (15–20 ppm released from 100 mg C_{CO_3}). In case of antibacterial activity, *Escherichia coli* (*E. coli* ATCC 25922) at a concentration of $\sim 1 \times 10^5$ CFU/mL was spiked, whereas antiviral activity was measured by spiking the water with bacteriophage, MS2 (ATCC 15597-B1) at a concentration of $\sim 1 \times 10^3$ PFU/mL.

Thereafter, the water was left to stand for 1 h and subsequently the surviving microorganism count was measured by conventional pour plate (*E. coli*) and plaque assay (bacteriophage MS2) techniques. Colony counts were performed after incubation at 37 °C for 48 h (*E. coli*) and 16 h (bacteriophage MS2).

The designed water purification device, schematically described in Figure 1B, was anchored along with the Ag^+ releasing material from our previous work⁵ packed in a cartridge form, before the carbonate releasing system. Dissolution of silver ion in the presence of various anions was reported from our group.¹⁵ The data revealed that the leaching of Ag^+ from silver foil can be reduced to half (from 140 to 66 ppb) when immersed in distilled water spiked with carbonate (up to 50 ppm). Thus, the carbonate releasing monolith was placed above the Ag^+ releasing system which spontaneously reduces the silver ion release into the water flow. This system results in complete and enhanced biocidal activity on *E. coli* and bacteriophage MS2, the surrogates for water borne pathogens (bacteria and viruses, respectively). The removal of the microbial debris by a filter connected to an output delivers pure drinking water.

Characterization Techniques. Morphological studies of the carbonate releasing monolith, elemental analysis and elemental mapping were carried out using a scanning electron microscope (SEM) equipped with energy dispersive spectroscopy (EDS) (FEI Quanta 200). X-ray photoelectron spectroscopy (XPS) measurements were performed using an ESCA Probe TPD of Omicron Nanotechnology with the polychromatic Mg $K\alpha$ as the X-ray source ($h\nu = 1253.6$ eV) and the binding energy was calibrated with respect to C1s at 284.5 eV. The release of aluminum, calcium, sodium, and potassium concentrations in the water were estimated using inductively coupled plasma spectroscopy (ICP-MS) (PerkinElmer Nex ION 300 ICP-MS). Carbonate concentration was calculated based on the quantification of total inorganic carbon present in the test water using Shimadzu TOC-V_{CPH}. Raman spectra were obtained with a WITec GmbH, Alpha-SNOM alpha 300 S confocal Raman microscope having a 532 nm laser as the excitation source.

RESULTS AND DISCUSSION

Characterization of the Sustained Carbonate (C_{CO_3}) and Potassium ($C_{CO_3/K}$) Releasing Materials. The SEM image of the granular particles of the monolith and their chemical compositions are shown in Figure 2. The granules (40–100 μm) of C_{CO_3} confirms the porous (see the arrows) but crystalline morphology shown in Figure 2A. The patterns around the particles are due to the carbon substrate used for mounting the material. Porosity is evident in Figure 2B too, the inset of which illustrates the Raman spectrum; the strongest band at 1057 cm^{-1} is the symmetric stretching mode (ν_1) of the carbonate ion.¹⁶ The weak band at 1076 cm^{-1} of the cristobalite phase¹⁷ might be buried under the high intensity of carbonate stretching. Figure 2C shows the corresponding energy dispersive X-ray spectrum (EDS) which confirms the presence of carbon, oxygen, silicon, potassium, and sodium. Insets show the elemental mapping of a single grain of the material.

Initial components and the designed carbonate releasing composite material were studied by XPS. Figure 3A shows the survey spectra and Figure 3B depicts the deconvoluted C1s XPS spectra showing adventitious carbon at 284.6 eV¹⁸ and carbonate at 289.3 eV¹⁹ and potassium $K2p_{3/2}$ at 293.0 eV (and $K2p_{1/2}$ at 295.8 eV).¹⁹ This clearly indicates that carbonate and a small portion of potassium are entangled in the SiO_2 matrix. The deconvoluted spectra shown in Figure 3C confirms the presence of oxygen, where O1s peaks appear in the range of 531.5–532.0 eV for metal carbonates and 532–533 eV for SiO_2 .

Figure 3D shows the X-ray diffraction pattern of the amended granular composite before and after heating. Initially,

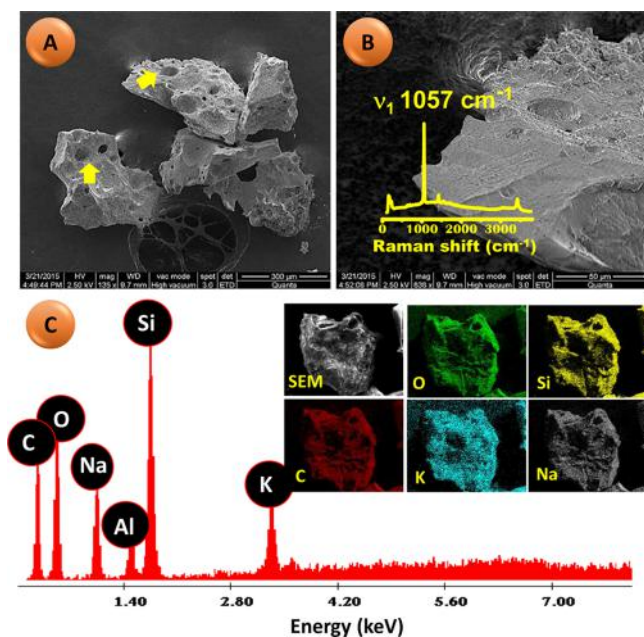


Figure 2. (A and B) SEM images of 72 μm granules of the monolith loaded with carbonate (C_{CO_3}). The image in panel B shows the porous surface of a granule with the inset representing the Raman feature specific for carbonate. (C) A corresponding energy dispersive X-ray spectrum (EDS) along with the elemental maps.

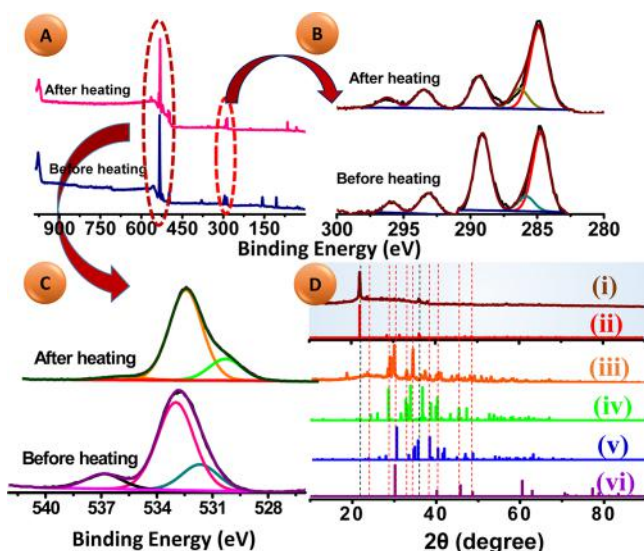


Figure 3. (A) X-ray photoelectron spectra of the carbonate releasing monolith (C_{CO_3}) before and after heating. (B and C) show the deconvoluted XPS spectra of corresponding C1s and O1s regions, respectively. (D) Powder XRD patterns of the material before heating and after heating. The material C_{CO_3} formed after heating (i) is compared with the (ii) cristobalite phase of SiO_2 [JCPDS 39-1425]. The composition mixture (iii) before heating is compared with (iv) monoclinic phases of K_2CO_3 [JCPDS 16-820] and (v) Na_2CO_3 [JCPDS 19-1130]) as well as the (vi) tetragonal phase of SiO_2 [JCPDS 15-0026].

tetragonal phase of SiO_2 (JCPDS 15-0026) and monoclinic phases of K_2CO_3 [JCPDS 16-820] and Na_2CO_3 [JCPDS 19-1130] were the principal components of the precursor of C_{CO_3} . Upon heating, the XRD pattern shows peaks at 2θ (degree) at 22.00, 28.47, 31.49, 36.13, 36.41, 47.10, and 48.65 which correspond to (101), (111), (102), (200), (112), (113), and

(212) planes of cristobalite. Despite the dominating cristobalite phase, the matrix contains 21.5 wt% of sodium and potassium carbonates which may be present in an amorphous form. From the release data presented, we understand that CO_3^{2-} is continuously leached retaining the framework. Total released CO_3^{2-} amounts to 20 wt% of the monolith confirming the nearly complete retention of CO_3^{2-} in the prepared structure. To the best of our understanding, anion releasing compositions of this kind are unknown. It appears that a small fraction of carbonate has decomposed releasing CO_2 , explaining the porous structure and the slightly reduced reduction in the extent of carbonate released.

The sustained carbonate and potassium ion releasing material ($\text{C}_{\text{CO}_3/\text{K}}$) is a formulation modified to release the ion of interest, demonstrated here for potassium. Figure S1A shows the SEM image of the monolith, $\text{C}_{\text{CO}_3/\text{K}}$. The image in panel B shows the porous surface of the grain with the inset representing the Raman spectrum; the strongest band at 1062 cm^{-1} which is the symmetric stretching mode of the carbonate ion.¹⁶ Shift in the stretching mode from 1057 to 1062 cm^{-1} is due to the influence of potassium and other ions. Figure S1C shows the corresponding EDS which confirms the presence of carbon, oxygen, silicon, potassium, calcium, and sodium. Insets show the elemental mapping of a single granule of the material impregnated with CO_3^{2-} and K^+ . Figure S2 shows the XPS of the initial components and the monolith, $\text{C}_{\text{CO}_3/\text{K}}$. Figure S2A illustrates the survey spectra and Figure S2B is the deconvoluted C1s XPS spectra showing the presence of C–C at 284.9 eV due to the adventitious carbon¹⁸ and the carbonate peak at 289.9 eV.¹⁹ The presence of potassium is shown by K2p doublet at 293.0 eV ($\text{K}2\text{p}_{3/2}$) and 295.2 eV ($\text{K}2\text{p}_{1/2}$).¹⁹ This clearly indicates that carbonate and a greater portion of potassium are entangled in the SiO_2 matrix. It is further confirmed from the deconvoluted O1s spectra, as shown in Figure S2C where the peaks appear in the range of 531–533 eV for metal carbonates and SiO_2 , respectively. Figure S2D shows the X-ray diffraction pattern of $\text{C}_{\text{CO}_3/\text{K}}$ before and after heating. The tetragonal phase of SiO_2 [JCPDS 15-0026] and monoclinic phases of K_2CO_3 [JCPDS 16-820] and Na_2CO_3 [JCPDS 19-1130] are dominant in the precursor material as noted before. Upon heating, the SiO_2 has changed into a silicate mineral, moganite [JCPDS 38-360], whereas K_2CO_3 and Na_2CO_3 were changed to the potassium sodium carbonate [JCPDS 1-1038]. This clearly reveals that moganite acts as the matrix resulting in the monolith. From the anion and cation release data to be presented below, we understand that CO_3^{2-} as well as the cation of interest are continuously leached retaining the framework.

Kinetics of Carbonate Release from the Material. The concentration of CO_3^{2-} leached into drinking water from the prepared monolith is highly tunable at relevant temperatures ($5\text{--}35\text{ }^\circ\text{C}$) and varying TDS ($100\text{--}1000\text{ }\mu\text{S}$). The carbonate release does not alter the pH of the water beyond the permissible limit of 6.5–8.5.^{5,6} The release occurs within 5–15 min of contact time and concentration of the release does not exceed 20 ± 5 ppm even when there is a prolonged contact time tested up to 12 h in batch mode (Figure 4A). Figure 4A (inset) describes the release of carbonate in a sustained fashion under a continuous flow of 50 L water in cartridge mode. The material was tested using tap water in the cartridge mode, where the performance was not affected by the deposition or interference of other ionic species present in the test water. After every 10 cycles of exposure to water, the material was

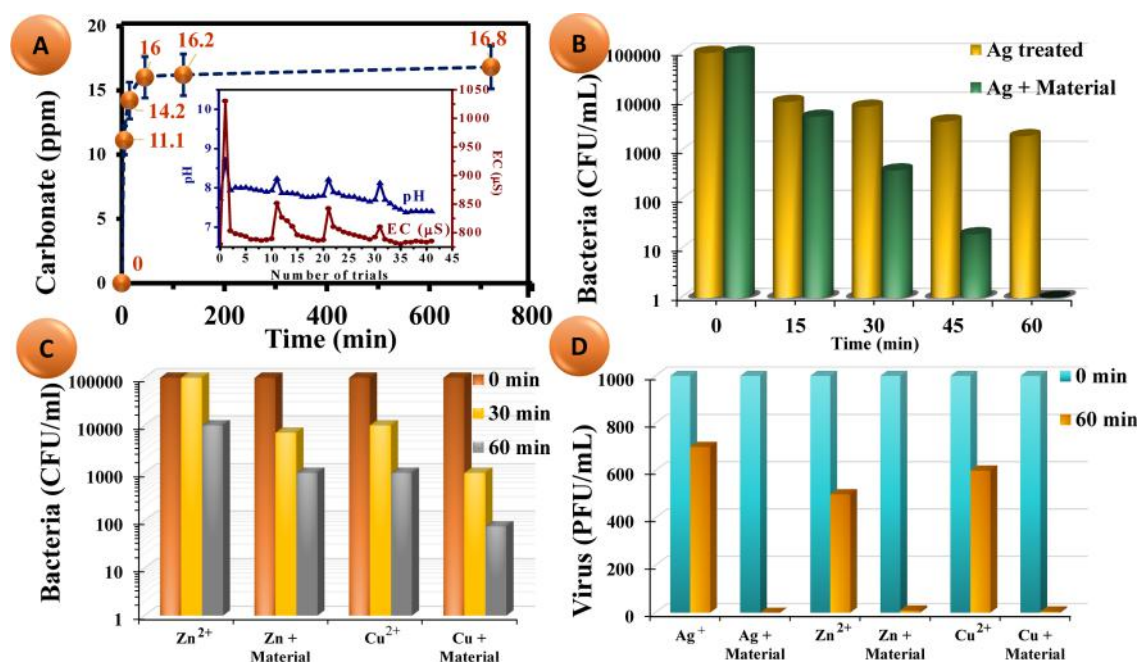


Figure 4. Kinetics of carbonate release from the monolith (C_{CO_3}) for prolonged period of exposure to water. Inset shows the sustained release of carbonate in continuous flow of water (A). Carbonate-supported antibacterial activity of 50 ppb silver (B) and 1 ppm zinc and 500 ppb copper (C). Carbonate-supported antiviral activity of 50 ppb silver, 1 ppm zinc, and 500 ppb copper (D).

drained and dried for 18–20 h at room temperature and was tested for further CO_3^{2-} release. After every step of drying of the sample, an increased release of CO_3^{2-} in the first 15 min of exposure was observed (shown as a spike in the graph at trial numbers 11, 21, and 31). These spikes are attributed to the prolonged soaking of the material by the stagnant water clogged within the pores during the slower rate of drying at room temperature. The dissolved carbonate inside the pore is released faster when the material is soaked in a fresh batch of water. It is not of consequence to the water purification device as the initial water collected is often discarded in typical use.

The synthesized monolith initially consisted of 21.5% CO_3^{2-} (as sodium and potassium carbonate) by weight and upon passage of 50 L of water it leached 20 wt% of material. The amount of CO_3^{2-} leaching was reduced slowly with increasing number of trials (observed after the passage of 35 L). Theoretically, leaching of 20 wt% CO_3^{2-} amounts to an average concentration of 20 ppm over passage of 50 L, using 1 g of the monolith. The tests were stopped after 50 trials as the material had released nearly all the entrapped CO_3^{2-} .

The carbonate is an integral part of the composition itself and thus, reloading the cristobalite or moganite monolith with carbonate, although conceivable, has not been attempted in this study. The loaded carbonate, if not an integral part of the composition, will dissolve completely in water delivering undesirable pH and taste. It is for this reason, an inexpensive and environmental friendly scaffold material (silica) was chosen.

Biocidal Enhancement Property of the Material. The monolith, C_{CO_3} , was tested for enhanced antibacterial activity in batch mode (Materials and Methods) for released carbonate on 50 ppb Ag^+ (Figure 4B), 1 ppm Zn^{2+} , and 500 ppb Cu^{2+} (Figure 4C) in natural drinking water. The minimum concentration of the individual metal ion, required to achieve antimicrobial activity was chosen. Enhancement in the bactericidal activity was observed in water pretreated with the

material releasing CO_3^{2-} (Figure 4D). Effect of the eluted CO_3^{2-} on virus surrogate MS2 bacteriophage treated with Ag^+ was tested. We observed that while 50 ppb Ag^+ alone (even after 1 h contact) was unable to affect the phage, the combination of 50 ppb Ag^+ added to water pretreated with the material releasing CO_3^{2-} , was found to achieve effective antiviral property within a contact time of 15 min. Therefore, we show that 50 ppb of Ag^+ , not only acts as an antibacterial agent but also as an antiviral agent in the presence of carbonate. This property is not observed otherwise in this limited range of silver ion concentration (20–50 ppb). Similarly, the synergic effect of C_{CO_3} on other metal ions, like Zn^{2+} and Cu^{2+} (1 ppm and 500 ppb, respectively), was also demonstrated. The enhanced effect due to carbonate is because of the interactions with the peripheral proteins of the bacterial membrane.⁶ These peripheral proteins are associated with the membrane lipids and other proteins via electrostatic forces or hydrophobic interactions. Thus, conditions like high salt concentrations or an alkaline environment disrupt the interactions leading to the detachment of peripheral proteins. Therefore, in the presence of CO_3^{2-} , a disturbed membrane, free of peripheral proteins is suspected, which allows the penetration/cellular mobility of Ag^+ , by increasing the bioavailability of silver ions.

In an attempt to modify the property of the composite to release other ions, we found that this material can be generalized for the release of not only anions but also cations, illustrated here using potassium. K^+ is an essential element for human nutrition and the requirements are generally measured in grams per day.²⁰ Potassium and sodium maintain normal osmotic pressure in cells and help the muscles to contract.²¹ It is a cofactor for many enzymes and is required for the secretion of insulin, creatine phosphorylation, carbohydrate metabolism, and protein synthesis.²² The release of K^+ in water was therefore tuned in a controlled fashion and this modification did not affect the sustained CO_3^{2-} releasing property of the material. Similar to C_{CO_3} , the $C_{CO_3/K}$ showed a release of CO_3^{2-}

within 5–15 min of contact time and concentration of release was within 20 ± 5 ppm in batch mode (Figure S3A). Inset in Figure S3A describes the release of carbonate from the cartridge device containing 1g of the pellet. The material, $C_{CO_3/K}$ did not release any other ion in significant quantities from its framework during interaction with water. Figure S3B demonstrates the selective release of potassium and sodium while release of other undesirable cations is controlled from $C_{CO_3/K}$ when immersed in water. Figure S3C displays the synergetic effect toward the antibacterial activity by the steadily released carbonate ion (from $C_{CO_3/K}$), with various metal ions (50 ppb Ag^+ , 1 ppm Zn^{2+} , and 500 ppb Cu^{2+}) in batch mode. The reduction of bacteria and virus count at a faster rate clearly indicates the effective synergy between the released carbonate with the metal ions used for water purification (Ag^+ or Cu^{2+} or Zn^{2+}). Further, the sustained release of potassium from $C_{CO_3/K}$ does not alter the biocidal activity of the present system. A possible mechanism for enhanced biocidal activity of Ag^+ due to carbonate has been discussed in our previous work.⁶

Silver in the ionic form continued to be available during the period of antimicrobial activity in the conditions of test water. This was verified by measuring Ag^+ concentration at varying time intervals using ICP MS (Figure S4).

CONCLUSION

We report a composite, forming a structurally stable monolith, releasing carbonate ion in water at a fixed concentration for a prolonged period to enhance the antimicrobial property of silver ion. We have achieved the formation of robust matrices of cristobalite and moganite at temperatures below their standard formation temperatures, which entrap anions and cations of interest. The monolith has been prepared with inert template forming materials and it releases carbonate ion at 20 ppm concentration, which does not change even upon longer periods of exposure to water at room temperature. This carbonate concentration brings down the requirement of Ag^+ for effective antimicrobial activity in water purification applications, reducing the global unrecoverable loss of silver by ~1300 tons per year. Besides, the proposed material acts as a system for enhancement of the biocidal activity of metal ions in general. This material can be used along with several water purification technologies especially reverse osmosis, ultraviolet irradiation, ozonation, adsorption, and membrane filtration techniques as a synergetic enhancement system delivering complete biocidal activity in potable water.

Other ions such as potassium may also be released controllably so that “enhanced” water may be supplied. Various modifications of the designed monolith with different compositions can be developed for additional release of both anions and cations, with comparable performances.

ASSOCIATED CONTENT

Supporting Information

The Supporting Information is available free of charge on the ACS Publications website at DOI: 10.1021/acssuschemeng.6b00979.

Scanning electron microscopic images, energy dispersive X-ray spectrum with elemental mapping, Raman spectrum, and XRD and XPS of the sustained carbonate and potassium releasing material ($C_{CO_3/K}$). Kinetics of carbonate release and potassium release from $C_{CO_3/K}$ for prolonged period of exposure to water and carbonate-

supported antimicrobial activity of Ag^+ , Zn^{2+} and Cu^{2+} (PDF)

AUTHOR INFORMATION

Corresponding Author

*Fax: +91-44-2257-0545; E-mail: pradeep@iitm.ac.in.

Present Address

[‡]Department of Materials Engineering, Faculty of Engineering, University of Concepcion, Concepcion, Chile.

Author Contributions

[†]J.R.S. and N.P. equally contributed to this article. T.P., J.R.S., and N.P. designed the experiments. J.R.S. and N.P. performed the experiments. T.P., J.R.S., and N.P. analyzed the data, wrote the article.

Notes

The authors declare no competing financial interest.

ACKNOWLEDGMENTS

We thank Prof. Ligy Philip and Mr. Ram Prasad (Department of Civil Engineering) for their support in the instrumental facility for inorganic carbon analysis. We thank Mr. Sundar Raj for the technical support in SEM analysis. We thank the Department of Science and Technology (Government of India) for constantly supporting our research program on nanomaterials.

REFERENCES

- (1) Pradeep, T.; Anshup. Noble metal nanoparticles for water purification: A critical review. *Thin Solid Films* **2009**, *517* (24), 6441–6478.
- (2) (a) Kumar, A.; Vemula, P. K.; Ajayan, P. M.; John, G. Silver-nanoparticle-embedded antimicrobial paints based on vegetable oil. *Nat. Mater.* **2008**, *7* (3), 236–241. (b) Dai, J.; Bruening, M. L. Catalytic Nanoparticles Formed by Reduction of Metal Ions in Multilayered Polyelectrolyte Films. *Nano Lett.* **2002**, *2* (5), 497–501. (c) Jain, P.; Pradeep, T. Potential of silver nanoparticle-coated polyurethane foam as an antibacterial water filter. *Biotechnol. Bioeng.* **2005**, *90* (1), 59–63. (d) Liu, J.; Hurt, R. H. Ion Release Kinetics and Particle Persistence in Aqueous Nano-Silver Colloids. *Environ. Sci. Technol.* **2010**, *44* (6), 2169–2175. (e) Marambio-Jones, C.; Hoek, E. M. V. A review of the antibacterial effects of silver nanomaterials and potential implications for human health and the environment. *J. Nanopart. Res.* **2010**, *12* (5), 1531–1551. (f) Shah, M. S. A. S.; Nag, M.; Kalagara, T.; Singh, S.; Manorama, S. V. Silver on PEG-PU-TiO₂ Polymer Nanocomposite Films: An Excellent System for Antibacterial Applications. *Chem. Mater.* **2008**, *20* (7), 2455–2460. (g) Datta, K. K. R.; Srinivasan, B.; Balaram, H.; Eswaramoorthy, M. Synthesis of agarose-metal/semiconductor nanoparticles having superior bacteriocidal activity and their simple conversion to metal-carbon composites. *J. Chem. Sci.* **2008**, *120* (6), 579–586.
- (3) Jin, X.; Li, M.; Wang, J.; Marambio-Jones, C.; Peng, F.; Huang, X.; Damoiseaux, R.; Hoek, E. M. V. High-Throughput Screening of Silver Nanoparticle Stability and Bacterial Inactivation in Aquatic Media: Influence of Specific Ions. *Environ. Sci. Technol.* **2010**, *44* (19), 7321–7328.
- (4) Sustainable Water for the Future: Water Recycling versus Desalination. *Sustainability Science and Engineering*, Isabel, C. E., Andrea, I. S., Eds.; Elsevier, 2010; Vol. 2, pp 1–416.
- (5) Sankar, M. U.; Aigal, S.; Maliyekkal, S. M.; Chaudhary, A.; Anshup; Kumar, A. A.; Chaudhari, K.; Pradeep, T. Biopolymer-reinforced synthetic granular nanocomposites for affordable point-of-use water purification. *Proc. Natl. Acad. Sci. U. S. A.* **2013**, *110* (21), 8459–64.

(6) Swathy, J. R.; Sankar, M. U.; Chaudhary, A.; Aigal, S.; Anshup; Pradeep, T. Antimicrobial silver: An unprecedented anion effect. *Sci. Rep.* **2014**, *4*, 7161.

(7) Zhang, H.; Smith, J. A.; Oyanedel-Craver, V. The effect of natural water conditions on the anti-bacterial performance and stability of silver nanoparticles capped with different polymers. *Water Res.* **2012**, *46* (3), 691–699.

(8) *Handbook of Mineral Elements in Food*, Miguel, G., Salvador, G., Eds.; Wiley-Blackwell, 2015.

(9) Shannon, M. A.; Bohn, P. W.; Elimelech, M.; Georgiadis, J. G.; Marinas, B. J.; Mayes, A. M. Science and technology for water purification in the coming decades. *Nature* **2008**, *452* (7185), 301–10.

(10) *Guidelines for Drinking-water Quality*; World Health Organization: Geneva, Switzerland, 2008; Vol. 1.

(11) Esteban-Tejeda, L.; Zheng, K.; Prado, C.; Cabal, B.; Torrecillas, R.; Boccaccini, A. R.; Moya, J. S. Bone tissue scaffolds based on antimicrobial $\text{SiO}_2\text{-Na}_2\text{O-Al}_2\text{O}_3\text{-CaO-B}_2\text{O}_3$ glass. *J. Non-Cryst. Solids* **2016**, *432*, 73–80.

(12) Greenspan, D. C.; Hench, L. L. Chemical and mechanical behavior of bioglass-coated alumina. *J. Biomed. Mater. Res.* **1976**, *10* (4), 503–9.

(13) Thomas, A. M. Thermal Decomposition of Sodium Carbonate Solutions. *J. Chem. Eng. Data* **1963**, *8* (1), 51–54.

(14) *CRC Handbook of Chemistry and Physics*, 90th ed., Lide, D. R., Ed.; CRC Press: Boca Raton, FL, 2009.

(15) Bakshi, A.; Gandhi, M.; Chaudhari, S.; Bag, S.; Gupta, S. S.; Pradeep, T. Extraction of Silver by Glucose. *Angew. Chem., Int. Ed.* **2016**, DOI: 10.1002/anie.201510122.

(16) (a) Urmos, J.; Sharma, S. K.; Mackenzie, F. T. Characterization of some biogenic carbonates with Raman spectroscopy. *Am. Mineral.* **1991**, *76* (3–4), 641–646. (b) Behrens, G.; Kuhn, L. T.; Ubic, R.; Heuer, A. H. Raman Spectra of Vateritic Calcium Carbonate. *Spectrosc. Lett.* **1995**, *28* (6), 983–995. (c) Klopogge, J. T.; Wharton, D.; Hickey, L.; Frost, R. L. Infrared and Raman study of interlayer anions CO_3^{2-} , NO_3^- , SO_4^{2-} and ClO_4^- in Mg/Al-hydroxalcalite. *Am. Mineral.* **2002**, *87* (5–6), 623–629.

(17) Bates, J. B. Raman Spectra of α and β Cristobalite. *J. Chem. Phys.* **1972**, *57* (9), 4042–4047.

(18) Barr, T. L.; Seal, S. Nature of the use of adventitious carbon as a binding energy standard. *J. Vac. Sci. Technol., A* **1995**, *13* (3), 1239–1246.

(19) Shchukarev, A. V.; Korolkov, D. V. XPS Study of group IA carbonates. *Cent. Eur. J. Chem.* **2004**, *2* (2), 347–362.

(20) Cohn, J. N.; Kowey, P. R.; Whelton, P. K.; Prisant, L. New guidelines for potassium replacement in clinical practice: A contemporary review by the national council on potassium in clinical practice. *Arch. Intern. Med.* **2000**, *160* (16), 2429–2436.

(21) Sterns, R. H.; Cox, M.; Feig, P. U.; Singer, I. Internal potassium balance and the control of the plasma potassium concentration. *Medicine* **1981**, *60* (5), 339–54.

(22) Page, M. J.; Di Cera, E. Role of Na^+ and K^+ in enzyme function. *Physiol. Rev.* **2006**, *86* (4), 1049–92.

Supporting Information

Sparingly soluble constant carbonate releasing inert monolith for enhancement of antimicrobial silver action and sustainable utilization

*Jakka Ravindran Swathy,[‡] Nalenthiran Pugazhenthiran,^{‡†} Chennu Sudhakar, Avula Anil Kumar, Thalappil Pradeep**

DST Unit of Nanoscience (DST UNS), and Thematic Unit of Excellence (TUE), Department of Chemistry, Indian Institute of Technology Madras, Chennai 600 036, India.

*Corresponding Author: (T.P.) E-mail: pradeep@iitm.ac.in. Fax: +91-44-2257-0545.

[‡] Equally contributed

Supporting information 1:

Characterization of microstructure and chemical composition of the sustained release monolith, $C_{CO_3/K}$

Supporting information 2:

Spectroscopy and diffraction studies of the monolith, $C_{CO_3/K}$

Supporting information 3:

Kinetics of sustained ion release and biocidal enhancement property of the composite, $C_{CO_3/K}$

Supporting information 4:

Stability of silver ions in the test water.

Supporting information 1

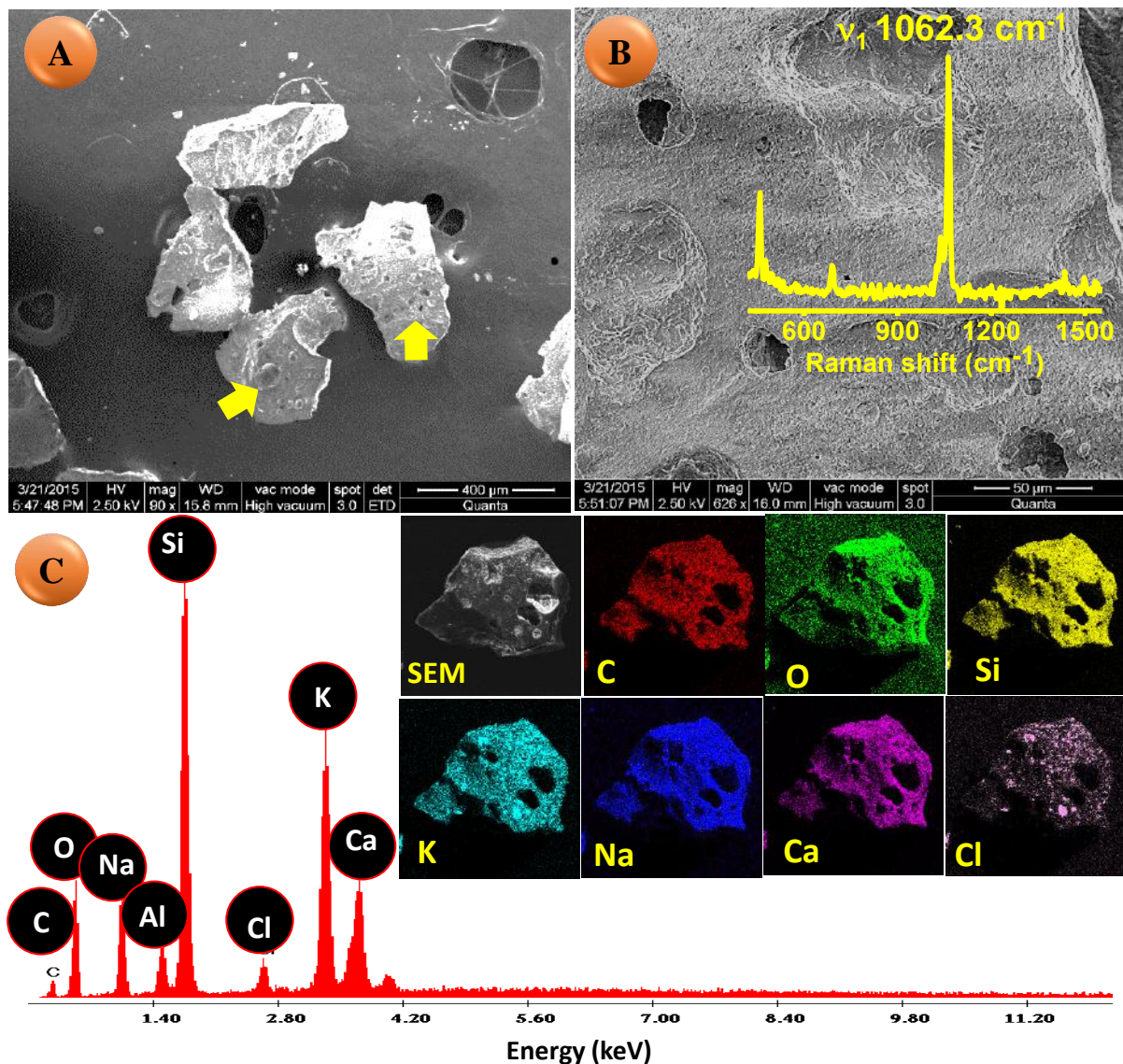


Figure S1. Characterization of microstructure and chemical composition of CCO_3/K . (A and B) Scanning electron microscopic (SEM) images of $\sim 72 \mu\text{m}$ granules of the monolith loaded with CO_3^{2-} and K^+ . The image in panel B shows the porous surface of the granule with the inset representing the Raman feature specific for carbonate. (C) A corresponding EDS and elemental maps (in the inset).

Supporting information 2

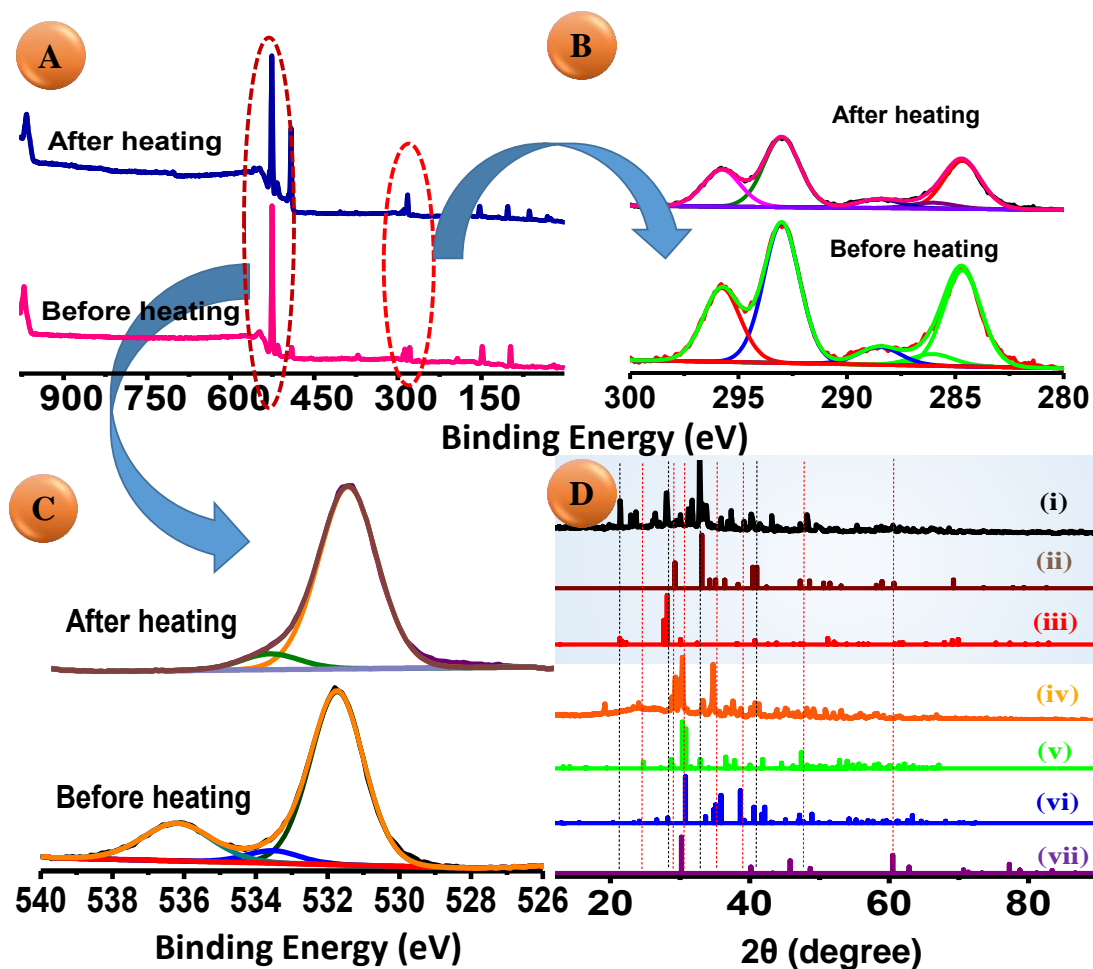
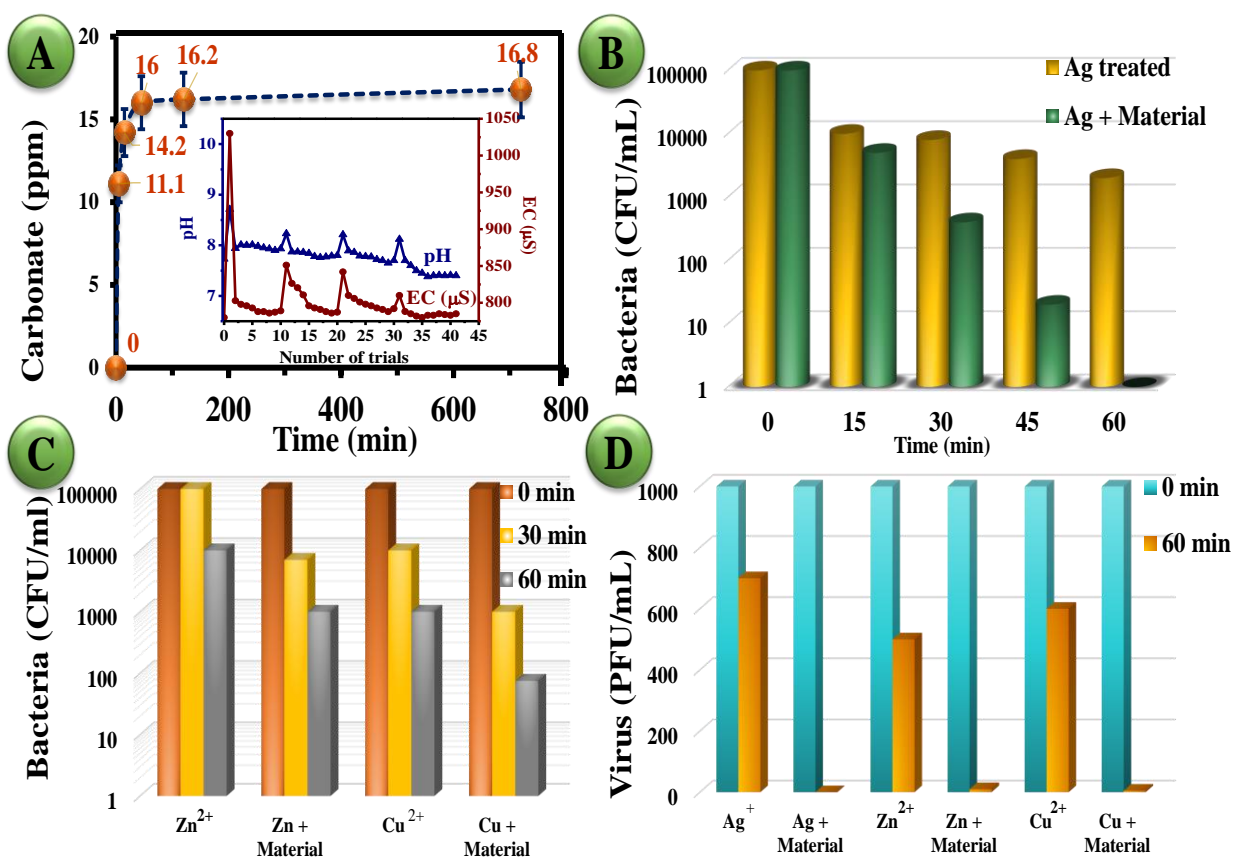


Figure S2. Spectroscopy and diffraction studies of $C_{CO_3/K}$. (A) XPS survey spectra of the amended granular particles of the monolith loaded with CO_3^{2-} and K^+ , before and after heating. (B) and (C) Deconvoluted XPS spectra of carbon and oxygen, respectively. (D) Powder XRD pattern of the material before heating and after heating. The material $C_{CO_3/K}$ formed after heating (i) is compared with the (ii) moganite phase of SiO_2 [JCPDS 38-360] and (iii) potassium sodium carbonate [JCPDS 1-1038]. The composition before heating (iv) is compared with (v) monoclinic phase of K_2CO_3 [JCPDS 16-820], (vi) monoclinic phase of Na_2CO_3 [JCPDS 19-1130] and (vii) tetragonal phase of SiO_2 [JCPDS 15-0026].



Supporting information 3

Figure S3. Kinetics of sustained ion release and biocidal enhancement property of the CCO_3/K . (A) Kinetics of carbonate release and potassium release from the modified material for prolonged period of exposure to water. Inset shows the sustained release of carbonate in continuous flow of water. (B) Sustained release of cations. (C) Carbonate-supported antibacterial activity of 50 ppb silver, 1 ppm zinc and 500 ppb copper. (D) Carbonate-supported antiviral activity of 50 ppb silver, 1 ppm zinc and 500 ppb copper.

Supplementary Figure S4

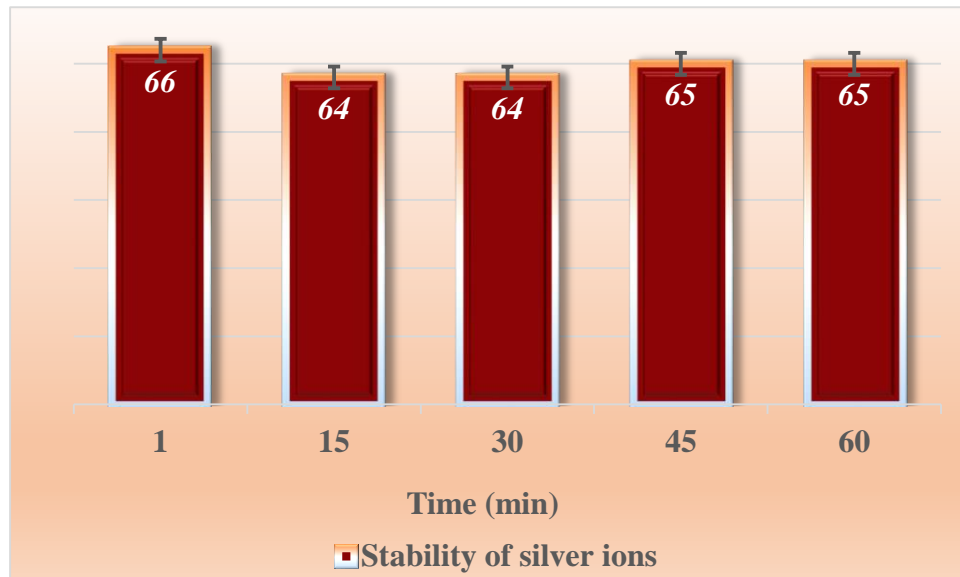


Figure S4. Stability of silver ions in the test water. Concentration of silver ions in ppb available in solution as a function of time. Experiments have been done to assess the concentration after centrifugation to ensure that the estimation is for the species in solution.

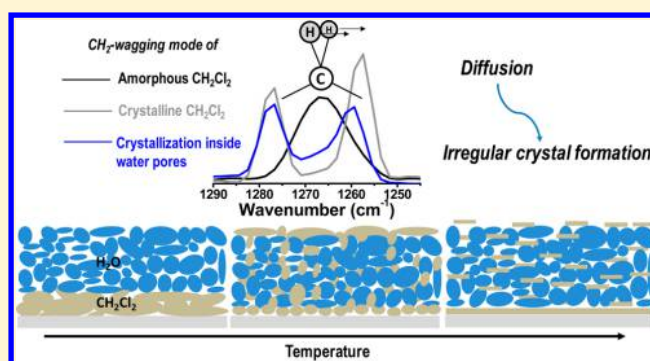
Diffusion and Crystallization of Dichloromethane within the Pores of Amorphous Solid Water

Radha Gobinda Bhui, Rabin Rajan J. Methikkalam, Soumabha Bag, and Thalappil Pradeep*

DST Unit of Nanoscience and Thematic Unit of Excellence, Department of Chemistry, Indian Institute of Technology Madras, Chennai 600 036, India

Supporting Information

ABSTRACT: Dichloromethane (CH_2Cl_2) thin films deposited on Ru(0001) at low temperatures (~ 80 K or lower) undergo a phase transition at ~ 95 K, manifested by the splitting of its wagging mode at 1265 cm^{-1} , due to factor group splitting. This splitting occurs at relatively higher temperatures (~ 100 K) when amorphous solid water (ASW) is deposited over it, with a significant reduction in intensity of the high-wavenumber component (of the split peaks). Control experiments showed that the intensity of the higher wavenumber peak is dependent on the thickness of the water overlayer. It is proposed that diffusion of CH_2Cl_2 into ASW occurs and it crystallizes within the pores of ASW, which increases the transition temperature. However, the dimensions of the CH_2Cl_2 crystallites get smaller with increasing thickness of ASW with concomitant change in the intensity of the factor group split peak. Control experiments support this suggestion. We propose that the peak intensities can be correlated with the porosity of the ice film. Diffusion of CH_2Cl_2 has been supported by low-energy Cs^+ scattering and temperature-programmed desorption spectroscopies.



INTRODUCTION

Molecules deposited at low temperatures on cold surfaces are generally amorphous in nature with randomly orientated structure. The amorphous form of the molecules may undergo a structural change upon annealing to higher temperature to form their most stable crystalline structures. Study of such phase transitions of molecular solids is a salient area of research due to their importance in phenomena ranging from environmental to biological and interstellar science. Different phases of molecular solids provide unique physical and chemical environment. This is a vast area of research, and phase transition of different molecules has been investigated in great detail.^{1–4} Techniques used for this study are mostly spectroscopic and scattering methods, namely, X-ray diffraction,⁵ low-energy electron diffraction (LEED),⁶ electron diffraction,⁷ transmission electron microscopy (TEM),⁸ low-energy ion collisions,^{9,10,11} and most commonly by infrared (IR) spectroscopy.^{1,3,4} The last one in this list has been utilized to study phase transitions in water-ice,^{1,3} methanol-ice,² and many other molecular solids.^{4,12–14} Although dichloromethane is one of the most frequently used organic solvents in the laboratory, the phase transition of this molecule is not well-understood. In 1970, the crystal structure of dichloromethane has been predicted from an IR spectroscopic study.¹⁵ However, to best of our knowledge, there is no report on the phase transition of this molecule and also no report has been found on the IR spectrum of amorphous dichloromethane. Study of

this molecule is also important in the context of stratospheric chemistry. Chloromethanes present in this environment interact with water-ice particles, eventually causing the depletion of the ozone layer. Water-ice surface plays a catalytic role in this process.¹⁶ Several theoretical and experimental studies have also been performed on halomethane/water-ice system.^{17–20}

From a fundamental point of view, water-ice is a model system for molecular solids to study elementary processes. Water-ice can exist in many different structural forms, depending on its formation. Mainly two different forms of water-ice (crystalline and amorphous) can be generated in vacuum on a cold surface at different temperatures by vapor deposition. In the universe the amorphous form of water-ice, known as amorphous solid water (ASW), is dominant.

ASW is highly porous in nature. Porosity of water-ice governs elementary processes like diffusion,^{21,22} adsorption of gaseous species,^{17,21,22} rapid desorption of trapped gases (termed as molecular volcano),¹⁸ phase transition,²³ tunneling reactions,²¹ etc. Various factors such as local temperature,⁷ incident molecular flux,³ incident angle,^{24–26} and kinetic energy²⁷ affect the porosity of water-ice. Thus, a number of studies have been carried out to probe porous ASW. Temperature-programmed

Received: January 14, 2016

Revised: May 22, 2016

Published: June 2, 2016

desorption (TPD) experiments have been used extensively in these cases.^{28–30} Diffusion and adsorption of molecules through the pores of ASW have also been investigated to a large extent by TPD. Limited reports exist where spectroscopic methods, such as IR spectroscopy, have been utilized to understand the diffusion of molecules through water-ice.^{25,31,32} Moreover, there are no reports on the spectroscopic properties of the diffused molecules. It is fundamentally important to study diffusion and interactions of molecules with ASW, which determine the composition and outgassing kinetics of the extraterrestrial ices.²

In this present study, we report two important investigations. First, we investigate the phase transition of pure dichloromethane in ultrahigh vacuum (UHV) and, second, the fate of crystallization of this molecule in the presence of ASW. Surface-sensitive reflection absorption infrared (RAIR) spectroscopy was used to understand the phase transition of pure dichloromethane. It was also observed that, in the presence of ASW, the molecules diffused through the pores of ASW and crystallize inside the pores to form irregular crystallites. The phenomenon is further supported by TPD and extremely surface-sensitive Cs⁺ scattering experiments.

■ EXPERIMENTAL SECTION

All the experiments were carried out using a custom-built instrument. A detailed description of the instrument is given elsewhere.³³ Briefly, the instrument consists of three UHV chambers (fully made of nonmagnetic stainless steel) composed of an ionization chamber (IC), an octupole chamber, and a scattering chamber; the sample manipulator with closed cycle He cryostat is mounted on the latter. Each vacuum chamber is differentially pumped by a turbomolecular pump (TMP). A diaphragm pump backs the ionization chamber TMP, and the octupole and scattering chamber TMPs are pumped by a TMP, again backed by a diaphragm pump. The base pressure of the instrument in the scattering chamber is 8×10^{-10} mbar. A Bayard–Alpert-type (B–A) gauge is employed to measure the pressure reading in each chamber. The vacuum components and gauges are procured from Pfeiffer Vacuum GmbH. Mass spectrometer components were from Extrel CMS. The instrument is capable of performing mass-selected low-energy (1–100 eV) ion scattering, low-energy (2–1000 eV) alkali ion scattering, RAIRS, and TPD spectroscopy. A unique aspect of this instrument is ultralow-energy (in the range of 1 eV) ion scattering, although such experiments were not used for the present work. RAIRS was employed to understand diffusion and crystallization of dichloromethane within ASW pores. In the scattering chamber of our instrument, thin films of molecular solids were grown layer by layer on a polished Ru(0001) single crystal. The single (Ru) crystal is in turn mounted on a copper holder that is connected to a closed cycle He cryostat (from ColdEdge Technologies). Temperature of the single crystal could be varied from 10 to 1000 K. A Pt sensor and a K-type thermocouple are attached to the mounting copper plate near to the Ru(0001) crystal to measure the temperature. The RAIRS experiments were performed using a VERTEX 70 FT-IR spectrometer from Bruker Optik GmbH. For this, the IR beam was taken out from the spectrometer and focused (using a combination of a paraboloidal gold-coated mirror and a plane mirror) on the single crystal at an $80 \pm 7^\circ$ incident angle through a KBr window. The reflected IR beam from the Ru(0001) single crystal was collected by another gold-coated ellipsoidal mirror,

and finally focused onto an external liquid nitrogen cooled mercury–cadmium–telluride (MCT) detector. The IR beam path outside the vacuum system and in the IR spectrometer itself were purged with dry N₂ and high pure Ar, respectively.

Both dichloromethane (CH₂Cl₂) and d₂-dichloromethane (CD₂Cl₂) were purchased from Sigma-Aldrich (purity: 99.99%) and were further purified by several freeze–pump–thaw cycles. Deionized triply distilled water (H₂O) was used for the measurement, which was also purified through several freeze–pump–thaw cycles before introducing into the UHV chamber. Sample lines were connected to a rotary pump and were pumped before introducing the samples into the UHV chamber. At the time of the experiment, samples were introduced into the scattering chamber using leak valves and were vapor-deposited on a cold Ru(0001) single-crystal target (at 80 K). Ru(0001) single crystal was cleaned properly by repeatedly heating to 1000 K. Sample inlet tubes were kept very close to the single crystal to achieve uniform growth of the molecular solids. The deposition of molecular solids was controlled through leak valves, and monolayer coverage was evaluated assuming that 1.33×10^{-6} mbar.s = 1 ML which has been estimated to contain $\sim 1.1 \times 10^{15}$ molecules/cm².³⁴ Temperature-dependent RAIRS was performed for the present study. Temperature was ramped @ 1 K/min and 5 min time delay was given for each temperature, before measuring each spectrum. All spectra given here were averaged for 512 scans and the spectral resolution was 4 cm⁻¹.

■ RESULTS AND DISCUSSION

1. Dichloromethane Phase Transition. The experiments were performed in several stages. To begin with, the phase transition of dichloromethane was investigated using RAIRS. Initially, 50 ML of CH₂Cl₂ was deposited on the Ru(0001) single crystal at 80 K. RAIR spectra were collected at regular intervals after warming the sample to a particular temperature (at a rate of 1 K/min), which was maintained for 5 min before collecting the spectrum. Five different vibrational modes of CH₂Cl₂ molecules positioned at ~ 3050 cm⁻¹ (–CH₂ antisymmetric stretching), ~ 1265 cm⁻¹ (–CH₂ wagging), ~ 895 cm⁻¹ (–CH₂ rocking), 748 cm⁻¹ (–CCl₂ antisymmetric stretching), and 705 cm⁻¹ (–CCl₂ symmetric stretching) have been detected in the RAIR spectrum at 80 K (see [Supporting Information](#) Figure S1). Among those vibrational modes, only –CH₂ wagging mode and –CCl₂ antisymmetric stretching modes are intense, which have been analyzed in detail in the subsequent investigations. [Figure 1](#) illustrates the results obtained from 50 ML of CH₂Cl₂. At 80 K, CH₂Cl₂ showed two sets of intense broad infrared bands, due to the –CH₂ wagging mode and the –CCl₂ antisymmetric stretching mode. As the temperature was increased to 95 K, a spectral change was observed: (i) the –CCl₂ antisymmetric stretching peak, which was broad at 80 K, became narrow and was shifted to ~ 740 cm⁻¹ with a drastic increase in intensity (see [Figure 2a](#)), and (ii) the broad –CH₂ wagging mode was split into two peaks arising at a higher (~ 1277 cm⁻¹, named as peak 1) and a lower (~ 1257 cm⁻¹, named as peak 2) wavenumber region with a slightly increased intensity. This splitting is clearly visible from the inset of [Figure 1](#), which shows an expanded view of the –CH₂ wagging region.

Such splitting of infrared spectra has been observed before in infrared spectroscopy-based phase transition studies of different molecules. For example, it is reported that a spectral change occurs for the broad O–H stretching peak of amorphous ice

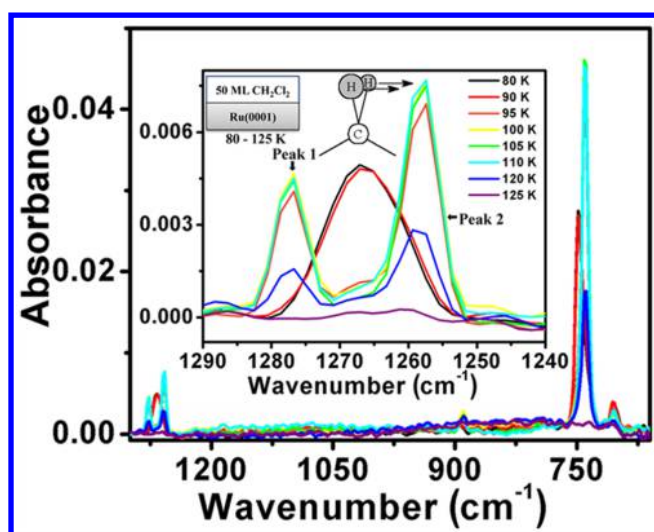


Figure 1. Temperature-dependent RAIR spectra of 50 ML CH_2Cl_2 deposited at 80 K on Ru(0001). Inset shows the expanded view of the $-\text{CH}_2$ wagging region and schematic of the surface under investigation.

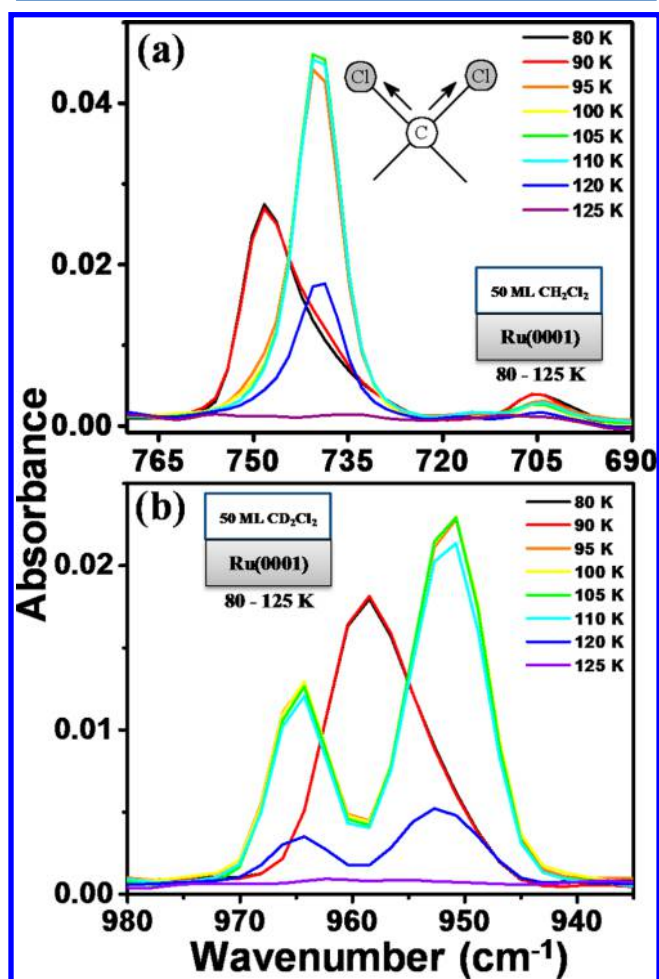


Figure 2. Temperature-dependent RAIRS study on a molecule to find changes in vibrational spectra upon heating. Spectra corresponding to (a) C–Cl antisymmetric stretching (CH_2Cl_2) mode and (b) $-\text{CD}_2$ wagging modes (CD_2Cl_2) are compared when 50 ML of CX_2Cl_2 ($X = \text{H}$ or D) is deposited on Ru(0001) at 80 K and warmed. Insets show the schematic of the surfaces during experiment.

during crystallization of water-ice^{1,35} and that a splitting of peaks was observed corresponding to both O–H and C–O stretching modes during the crystallization of methanol-ice.³⁶ Crystallization of methanol has been studied on highly ordered pyrolytic graphite (HOPG). Amorphous methanol deposited on HOPG surface at 97 K showed a broad O–H stretch at 3260 cm^{-1} , which split into two bands at 3290 and 3174 cm^{-1} on warming to 129 K where it underwent crystallization. Heating also leads to the splitting of the C–O stretching mode (at 1045 cm^{-1} at 97 K) giving rise to two bands at 1037 and 1027 cm^{-1} . Additionally splitting was observed in the asymmetric CH_3 stretching band. A similar study on the phase transition of vinylacetylene showed that the broad absorption band at 655 cm^{-1} ($=\text{CH}_2$ twisting mode) undergoes splitting during crystallization.¹⁴ Infrared spectroscopy in transmission mode has shown that the $-\text{CH}_2$ wagging mode in the vibrational spectra of CH_2Cl_2 splits into two components in the crystalline phase.^{15,37,38} Various other studies have also demonstrated such a vibrational spectral change during phase transition.^{13,39} Absorption features of amorphous ices are uncharacteristically broad due to their disordered structure. When these undergo a structural change to form more stable ordered structures (crystalline) on warming, well-defined bands are seen in the infrared absorption spectra.

In the work presented herein, CH_2Cl_2 deposited on Ru(0001) at 80 K initially in amorphous form, evident from its broad absorption feature of the $-\text{CH}_2$ wagging mode (see Figure 1), is transformed into the most stable crystalline form upon warming. When the dichloromethane-ice at 95 K was cooled back to 80 K or still lower temperatures, it did not show any change in the RAIR spectrum, validating that the most stable crystalline form does not revert and the spectral change at 95 K is due to a phase transition. It is also noticeable from Figure 1 that further heating did not lead to any significant change in the spectrum except for the loss in intensity of the peaks due to desorption of CH_2Cl_2 at a higher temperature ($\sim 120\text{ K}$). Complete desorption occurs at 125 K.

In the C–Cl stretching mode, narrowing and drastic downshifting occur due to phase transition (Figure 2a). Splitting of the $-\text{CD}_2$ wagging region is shown in the isotopologue, CD_2Cl_2 . Figure 2b shows the temperature-dependent spectra obtained for 50 ML of CD_2Cl_2 deposited on Ru(0001), applying the same strategy as described before for CH_2Cl_2 . As in case of CH_2Cl_2 , here also at 80 K, a broad absorption peak due to the $-\text{CD}_2$ wagging mode arises although at a much different position of $\sim 960\text{ cm}^{-1}$, and another absorption peak (not shown in the figure) is observed corresponding to the $-\text{CCl}_2$ antisymmetric mode at the same frequency as in the case of CH_2Cl_2 . The former undergoes spectral change at 95 K, appearing as two peaks, one at $\sim 964\text{ cm}^{-1}$ and another at $\sim 952\text{ cm}^{-1}$.

The splitting of $-\text{CH}_2/-\text{CD}_2$ wagging mode at 95 K in both $\text{CH}_2\text{Cl}_2/\text{CD}_2\text{Cl}_2$ is due to the factor group splitting. Factor group splitting, or Davydov splitting, is the splitting of spectral lines in a molecular crystal. Both $\text{CH}_2\text{Cl}_2/\text{CD}_2\text{Cl}_2$ possess C_{2v} molecular point group having four irreducible representations, namely, A_1 , A_2 , B_1 , and B_2 . They do not possess any degenerate vibrations, and therefore, in crystalline state splitting of normal modes will be due to factor group splitting which arises from interactions of vibrational modes of different molecules in a unit cell. The $-\text{CH}_2/-\text{CD}_2$ wagging mode of $\text{CH}_2\text{Cl}_2/\text{CD}_2\text{Cl}_2$ belonging to B_2 symmetry (in the C_{2v} point group) undergoes

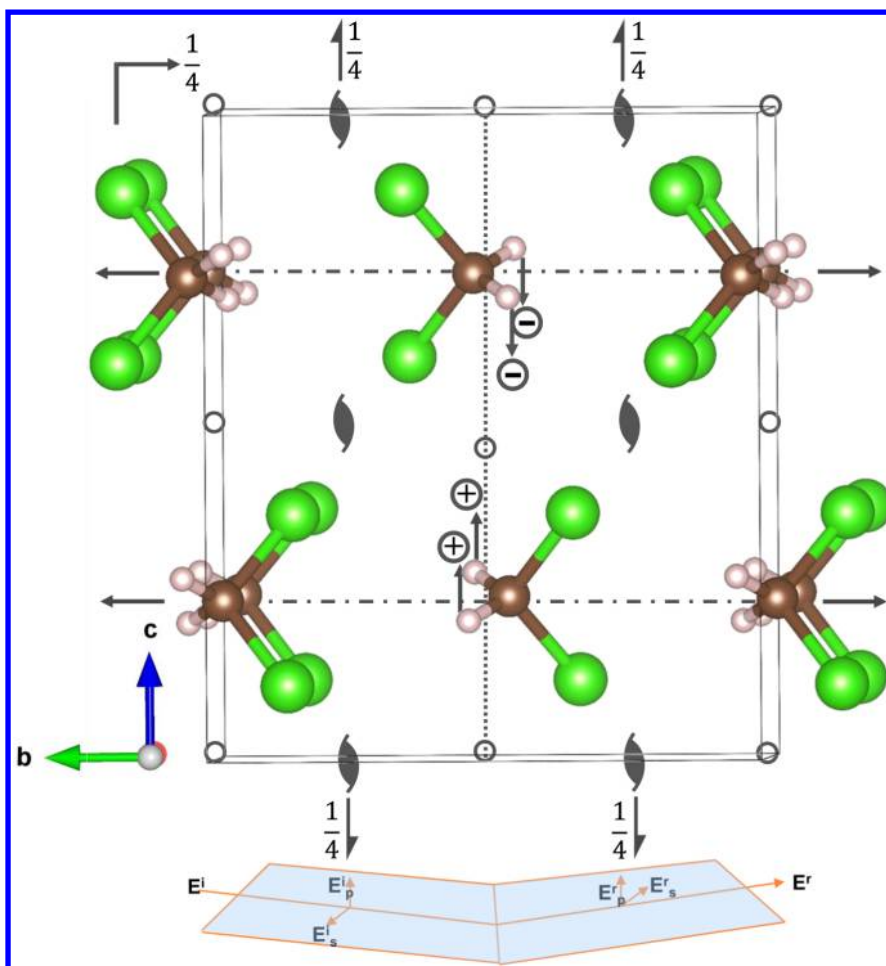


Figure 3. Crystal structure of dichloromethane: $a = 4.25 \text{ \AA}$, $b = 8.13 \text{ \AA}$, and $c = 9.49 \text{ \AA}$. Coordinates to draw the crystal structure were taken from ref 41. The crystal structure is having $Pbcn$ space group. Different symmetry operations are shown in the figure. Standard notations are used to represent the symmetry operations (ref 42). The $-\text{CH}_2$ wagging mode of CH_2Cl_2 is shown with arrows and positive and negative signs. The IR beam is shown as the inset. The s- and p-components of incident (E^i) and reflected (E^r) IR radiation are also shown.

splitting in the crystalline phase. Splitting of the B_2 mode shows that site group in the crystalline state could be a subgroup of the molecular point group C_{2v} . Marzocchi and Manzelli¹⁵ have found this splitting in the $-\text{CH}_2/-\text{CD}_2$ wagging mode of crystalline $\text{CH}_2\text{Cl}_2/\text{CD}_2\text{Cl}_2$ in a transmission IR measurement. From both Raman⁴⁰ and IR^{15,38} study, it was concluded that dichloromethane forms orthorhombic crystals with four dichloromethane molecules per unit cell possessing $Pbcn$ space group. This is shown in Figure 3. Projection of the crystal along the a -axis with slight tilting to show the 3D view is shown in the figure. Different symmetry operations present in the lattice are shown in the Figure 3. It shows axial glide, rotational axis, screw axis, and center of inversion operations of the lattice. The crystal structure is from Kawaguchi et al.⁴¹ The space group of CH_2Cl_2 crystal is $Pbcn$ where P stands for primitive lattice. $Pbcn$ has eight equivalent positions. Due to crystal formation, symmetry of dichloromethane molecules is lowered in the crystal and they sit in the C_2 site of the crystal, and the crystallographic twofold axis passes through the C atom of the molecules. The horizontal arrows represent the twofold axis passing through the molecules. Therefore, the asymmetry unit of the structure is half of the molecules and the total unit cell content is $8 \times 1/2 = 4$ molecules. In the C_2 site group, A_1 and A_2 modes of C_{2v} go into A. The B_1 and B_2 modes go into B. The splitting of the vibrational band could be explained in the

following way. One CH_2Cl_2 sitting at a C_2 site (B symmetry) interacts with another CH_2Cl_2 (C_2 site, B symmetry) in the D_{2h} lattice to cause the vibrational band splitting. The split bands can be a combination of C_2 , B symmetry vibrations.

Splitting of $-\text{CH}_2$ antisymmetric ($\sim 3050 \text{ cm}^{-1}$) peak was also observed (see Supporting Information Figure S1), but peak intensity was very low. So we did not carry out any further analysis on this peak. There could also be splitting in the $-\text{CH}_2$ rocking mode, but it was not visible in the spectra, maybe due to lack of significant intensity. But shift in this peak to lower wavenumber side was observed. However, splitting was not observed in $-\text{CCl}_2$ antisymmetric stretching mode which is consistent with the result obtained by Marzocchi and Manzelli.¹⁵ They showed in a polarization-dependent study that the $-\text{CH}_2$ wagging mode split in two differently polarized light, whereas splitting in $-\text{CCl}_2$ antisymmetric stretching mode occurs only in one polarized light. A similar result was observed by Brown et al. in which they have measured infrared spectra of CH_2Cl_2 single crystal in two different polarizations.³⁷ However, it may be noted from these studies that both the modes are infrared-active in two different polarized light. Our observation is very similar to these studies. We observed splitting only in the $-\text{CH}_2/-\text{CD}_2$ wagging mode, and no splitting was observed in $-\text{CCl}_2$ antisymmetric mode. Although unpolarized light was used in our measurements, RAIRS allows

only the p-component of the incident infrared beam to interact with the molecules. Although both $-\text{CH}_2$ wagging and $-\text{CCl}_2$ antisymmetric modes are active toward the p-component of the incident beam, the preferential interaction of p-component leads to the splitting of $-\text{CH}_2$ wagging mode upon phase change, whereas $-\text{CCl}_2$ antisymmetric mode does not show such a split. We have only noticed an increase in intensity of $-\text{CCl}_2$ antisymmetric mode with a red shift in the peak position upon phase transition. The exact reason for the absence of splitting in the $-\text{CCl}_2$ antisymmetric mode remains unclear. However, we assume that the orientation of crystallites with respect to incident IR light is such that it does not allow the p-component of the beam to split the $-\text{CCl}_2$ antisymmetric mode. It has been shown that orientation of crystal with respect to polarized light is important in factor group splitting.⁴³ The s-component incident beam could cause splitting of $-\text{CCl}_2$ antisymmetric mode, but this is not possible to be seen in RAIRS.

Large increase in intensity of $-\text{CCl}_2$ antisymmetric stretching mode was observed during phase transition. This increase in intensity in the crystalline state is due to the following reason. In the amorphous state of CH_2Cl_2 , due to its randomly oriented structure, only a few C–Cl bonds are interacting with the p-component of the incident IR beam. But in the crystalline state, molecules get aligned in such a way that more C–Cl bonds could interact with the p-component of the incident IR beam, which contribute to the increase in intensity. There is an increase in intensity of the $-\text{CH}_2$ wagging mode also during phase transition along with the splitting which may be due to a similar reason.

In Figure 4, thickness- or coverage-dependent spectra of CH_2Cl_2 and CD_2Cl_2 in the $-\text{CH}_2/-\text{CD}_2$ wagging region at 95 K are shown. The same experimental conditions were maintained for each coverage; CH_2Cl_2 and CD_2Cl_2 films were generated on Ru(0001) surface at 80 K and heated to the desired temperature, ranging from 80 to 125 K. At all the coverages, the splitting occurred at 95 K, and therefore, only these spectra are presented in Figure 4. The figure clearly shows that, with increasing monolayer coverage, the intensities of both the peaks increase for both CH_2Cl_2 and CD_2Cl_2 , though peak 2 is always more intense than peak 1. It is anticipated that, as CH_2Cl_2 or CD_2Cl_2 thickness increases, larger crystallites are formed. In large crystals, CH_2Cl_2 molecules are aligned in such a way that more $-\text{CH}_2$ bonds can preferably interact with the p-component of the IR beam and cause an increase in intensity. Moreover, with increase in monolayer coverage, the number of molecules is increased, which will also lead to an increase in peak intensity. For 10 ML coverage in both CH_2Cl_2 and CD_2Cl_2 splitting in the $-\text{CH}_2$ wagging mode was not observed. However, splitting of the peak was observed from 25 ML onward in both the cases (see Figure 4). This indicates that small coverage is not sufficient enough to form a regular crystal, whereas at relatively higher coverages regular crystals are formed which cause the splitting in the $-\text{CH}_2$ wagging mode. From the figure(s) it is also noticeable that relative increase in intensity of peak 2 is more compared to the peak 1, which indicates that peak 2 is more sensitive to monolayer coverage. We find that degree of splitting is more in the case of CH_2Cl_2 compared to CD_2Cl_2 . After splitting, the $-\text{CH}_2$ wagging mode of CH_2Cl_2 peaks appear in the range of ~ 1250 – 1285 cm^{-1} , corresponding to a total base width of $\sim 35\text{ cm}^{-1}$, while for CD_2Cl_2 the CD_2 wagging mode peaks span the range from ~ 942 to $\sim 972\text{ cm}^{-1}$, a total base width of 30 cm^{-1} . This

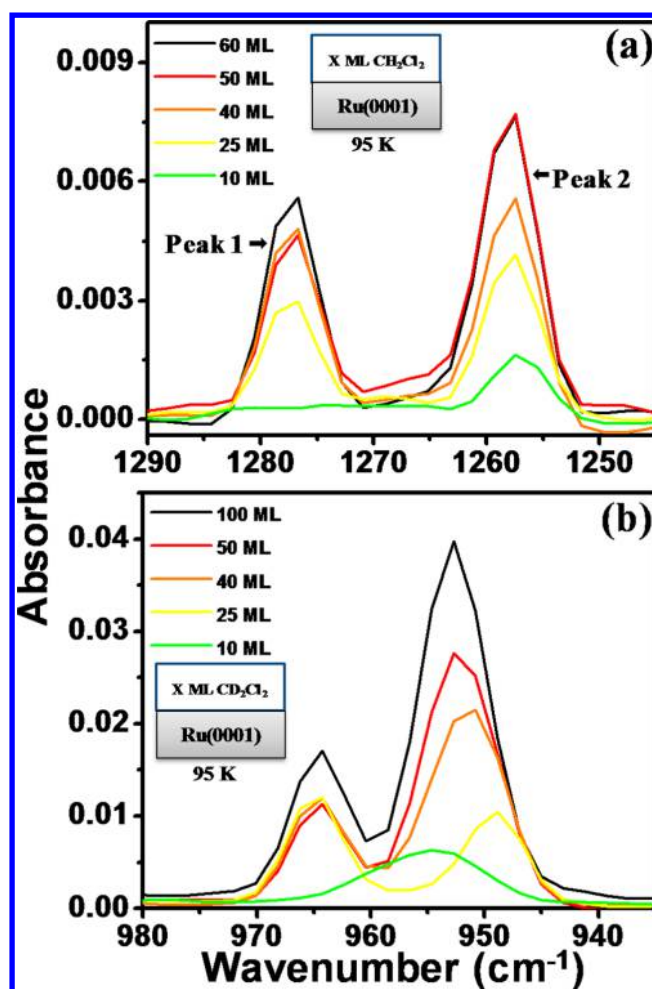


Figure 4. RAIR spectra in the (a) $-\text{CH}_2$ wagging region of CH_2Cl_2 and (b) $-\text{CD}_2$ wagging region of CD_2Cl_2 for various coverages at 95 K. Inset gives the schematic of the surfaces.

difference in splitting is a result of the isotope effect. Thus, shift due to intermolecular interaction in CH_2Cl_2 crystal is likely to be more than in CD_2Cl_2 .

2. Crystallization of Dichloromethane within ASW Pores. In the next set of experiments, ASW was condensed on the CH_2Cl_2 film to investigate its role on the crystallization process of the underlying CH_2Cl_2 layers. At first, 20 ML of ASW was deposited on top of 50 ML of CH_2Cl_2 on Ru(0001) at 80 K and temperature-dependent RAIRS was performed on this system. The results obtained are shown in Figure 5a. A schematic of the surface is shown in the inset of the figure. This is given just to show the deposition of a distinct layer. The structure may be different at the interface with significant intermixing. It is hard to study interfacial morphology in the current investigation. However, during overlayer deposition, we have given sufficient time between subsequent depositions so that the layers are likely to form one after another. From the figure, it is clear that spectra at 80 and 90 K look similar to those of pure CH_2Cl_2 at the same temperatures (Figure 1). But a dramatic change in the spectrum is observed at 95 K; peak 2 of $-\text{CH}_2$ wagging mode, which is the most intense peak for pure CH_2Cl_2 , appears with lesser intensity than peak 1 in the presence of water-ice. There is no change in the temperature of phase transition, which occurs at 95 K. In a previous study, it was reported that CH_2Cl_2 can diffuse through ASW.¹⁹

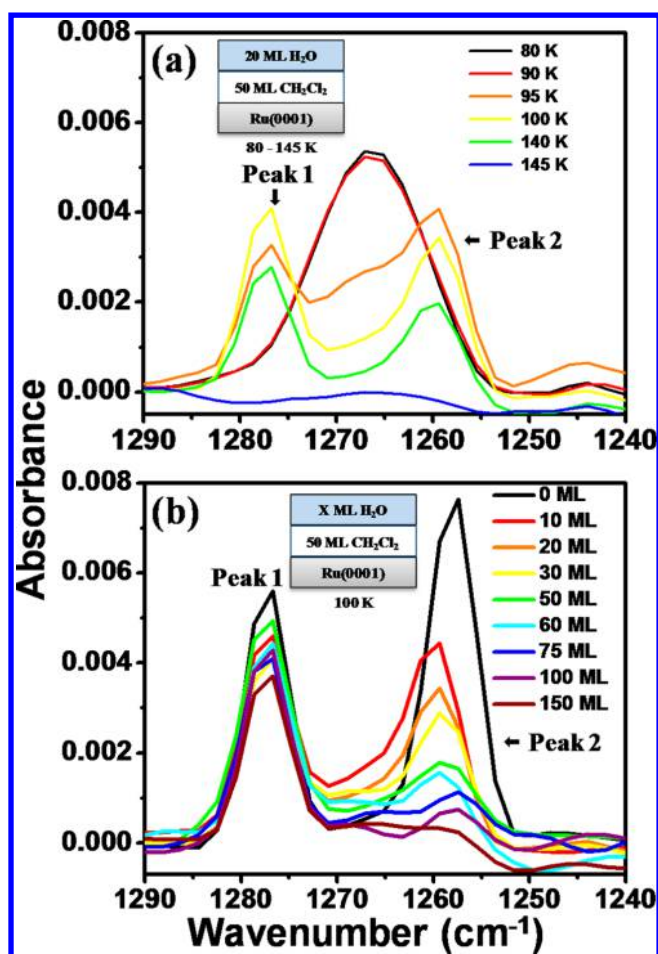


Figure 5. Change in $-\text{CH}_2$ wagging mode of 50 ML CH_2Cl_2 film was compared when (a) 20 ML of H_2O molecule is condensed over it at 80 K and annealed to 145 K; (b) overlayer converges of H_2O film was varied from 10 – 150 ML at 100 K. Insets show the schematic of the surfaces and the film thickness. Both CH_2Cl_2 and H_2O were deposited at 80 K on Ru(0001) surface and heated to desired temperature.

Therefore, this change in intensity of $-\text{CH}_2$ wagging mode during crystallization of CH_2Cl_2 under ASW may be due to the diffusion of CH_2Cl_2 through ASW and its crystallization inside the water-ice pores. It is also noticeable from Figure 5a that complete splitting of $-\text{CH}_2$ wagging mode due to crystallization of CH_2Cl_2 occurs at a relatively higher temperature (~ 100 K) than for pure CH_2Cl_2 . Furthermore, desorption of dichloromethane under amorphous water-ice takes place at 145 K (vs 125 K for pure CH_2Cl_2) when amorphous water-ice is converted into crystalline phase. This indicates that dichloromethane molecules are trapped inside the water-ice pores via diffusion which undergoes crystallization therein. As ASW crystallizes at 145 K, the water molecules reorient themselves such that it opens up a path for the trapped dichloromethane molecules to desorb. Trapping of molecules inside water-ice and their desorption during crystallization of water-ice has been reported previously and is termed as “molecular volcano”.¹⁸ However, this caging or trapping of molecules inside water pores has initially been observed by Livneh et al. and mentioned as “explosive” desorption.⁴⁴

Additional experiments were carried out to understand this process in detail. About 50 ML of dichloromethane was deposited on Ru(0001), and the thickness of the water overlayer on top of it was varied from 10 to 150 ML. It was

found that crystallization of CH_2Cl_2 took place at the same temperature (~ 100 K) regardless of the water overlayer coverage. The variation of RAIR spectrum in the $-\text{CH}_2$ wagging mode region for 50 ML of CH_2Cl_2 at 100 K as a function of different overlayer coverages of water is illustrated in Figure 5b. The figure shows that at 10 ML of water-ice coverage, the intensity of peak 2 at ~ 1257 cm^{-1} was drastically reduced compared to that of pure CH_2Cl_2 . Further addition of the water-ice overlayer decreased its intensity continuously, such that it almost vanished at 150 ML of ASW coverage. Corresponding correlation is evident from Figure 6 where the

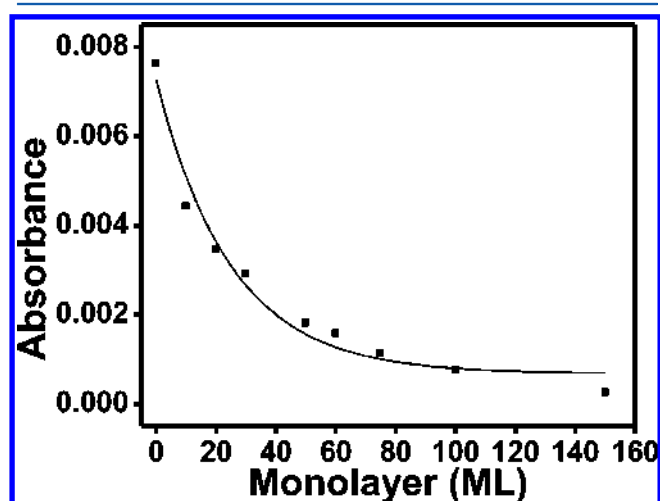


Figure 6. Intensity of peak 2 at 100 K is plotted against monolayer coverage of water.

maximum intensity of peak 2 at 100 K, taken from Figure 5b, is plotted against the monolayer coverage of water-ice. From the plot we see that the peak intensity follows an exponential decrease. Initially, at lower coverage, say for 50 ML of water, the intensity drop was significant, which slows down with coverage. This could be because of two reasons. First, as water-ice coverage is increased, it forms thicker layers and CH_2Cl_2 molecules have to travel longer distances. Second, with increase in water-ice coverage, availability of CH_2Cl_2 molecules for diffusion decreases as most of the molecules have occupied accessible pores. In this diffusion process, CH_2Cl_2 exists in two different states. A fraction of CH_2Cl_2 molecules diffuses within the pores of water-ice, and another fraction of molecules still remains under the water-ice. The number of molecules present under water-ice decreases as the coverage of the latter is increased due to increase in the diffusing fraction of CH_2Cl_2 . From Figure 5a it is also noticeable that the peak intensity of $-\text{CH}_2$ wagging mode at 80 and 90 K is the same which is almost equal in intensity of pure CH_2Cl_2 (Figure 1, inset). A decrease in intensity of the peak is observed only during crystallization of CH_2Cl_2 . This indicates that diffusion of CH_2Cl_2 molecules through water-ice is much faster at the crystallization temperature. Just before the crystallization temperature, molecular motion of CH_2Cl_2 increases due to their reorganization which causes the diffusion to be faster. It is not that crystalline CH_2Cl_2 is diffusing; rather, the individual molecular entities are diffusing before crystallization. This reorganization may force CH_2Cl_2 molecules to diffuse into the water-ice pores and crystallize in the confined environment and essentially form small crystals or irregular crystals inside the pores. It is also noticeable that crystallization of CH_2Cl_2 is

delayed when covered with ASW (~ 100 K) compared to pure CH_2Cl_2 . The microporous structure of water-ice in this temperature range may also facilitate diffusion. Such a structure may create a number of connected pathways through which CH_2Cl_2 molecules can diffuse. Interaction of both the molecules can also play a significant role in the diffusion process. Yan and Chu suggested that H-bond interaction between water molecules is weaker than that between oxalic acid and water.⁴⁵ In the CH_2Cl_2 -ASW system, there could also be H-bonding between CH_2Cl_2 and water-ice, and the H-bonding interaction is likely to be stronger than that between CH_2Cl_2 . This interaction may also lead to an enhancement in the diffusion process. The formation of small or irregular crystals inside the pores of water-ice is further supported by Figure S2, in which the antisymmetric $-\text{CCl}_2$ stretching region of 50 ML of CH_2Cl_2 is shown at different coverages of water-ice at 100 K. A continuous decrease in intensity of this peak for a constant coverage of CH_2Cl_2 was observed upon increase in coverage of water-ice. However, the peak appears at the same position as it appears in pure crystalline CH_2Cl_2 . This suggests that CH_2Cl_2 diffuses and crystallizes subsequently inside the water-ice pores and the crystals are randomly oriented within the pores. Due to the random orientation of the crystallites, the availability of C-Cl bonds to interact with the p-component of the beam gets reduced. As the water-ice coverage is increased, diffusion of CH_2Cl_2 is also increased, and more randomly oriented crystallites are formed. Randomness in the crystallite orientation causes greater reduction in intensity.

As mentioned previously, with increase in water-ice coverage, larger fraction of molecules diffuse within the water-ice pores through the microporous channels and the fraction under water-ice is decreased. Inside the water-ice pores, in the confined environment, it crystallizes as a small crystal or irregular crystal. Hence, with increase in water-ice coverages, more and more water-ice pores are occupied with CH_2Cl_2 . Due to the formation of irregular crystallites within the pores of water-ice, interactions between the same molecular entities are not regular and they are not strong enough to contribute to the increase in intensity. Also different orientations of irregular crystals within the pores of water-ice can reduce or cancel interactions. We have mentioned that splitting in $-\text{CH}_2$ wagging mode is due to the interaction of vibrational modes of different molecules in the crystal. If dimensions of the crystallites are small or they are irregular within the pores of water-ice, interaction between the vibrational modes will be reduced. In the previous study done of Lagaron, it was concluded that relative intensity of the factor group split peak reduces due to lack of crystallinity.⁴⁶ Formation of disordered and ill-defined crystallites reduce the relative intensity of the split peak.⁴⁶ This supports our argument. At 150 ML almost all the CH_2Cl_2 molecules are diffused through the pores of water-ice, which means the fraction of molecules below water-ice has almost vanished. The diffused molecules crystallize inside the pores of water-ice and the crystallite size of CH_2Cl_2 is sufficiently small to have essentially no interaction between the equivalent molecular entities within the crystal, and peak 2 disappears completely. One point should be noted here is that RAIRS measurements cannot distinguish the two different states of CH_2Cl_2 molecules (diffused within water-ice and buried under it) as it probes all the molecules present in the system. But we could see a continuous decrease of peak 2 intensity with the formation of more and more irregular crystals within water-ice pores. Due to the absence of large crystals

inside ASW pores, we see no contribution to the intensity of peak 2. Major contribution to the intensity of peak 2 comes from molecules staying at the bottom of ASW ($\text{Ru}@ \text{CH}_2\text{Cl}_2 @ \text{H}_2\text{O}$ system). The CH_2Cl_2 molecules at the bottom form large crystals and cause the splitting of the peaks and contribute to the intensity of peak 2. However, as water-ice coverages are increased, more CH_2Cl_2 molecules are diffused and the crystal dimension at the bottom is also reduced causing the gradual reduction in intensity of peak 2. Therefore, it may be concluded that intensity of peak 2 depends on the crystal dimensions, which in turn is related to the pore volume of ASW. However, intensity of peak 1 remains. This intensity comes from the $-\text{CH}_2$ wagging mode of the crystalline or irregularly crystalline CH_2Cl_2 . Here, molecules present in the system as a whole contribute to the intensity of peak 1. Therefore, even though splitting is absent due to diffusion and formation of irregular crystals, we observe peak 1. Its intensity is reduced to some extent due to random orientation of the irregular crystals inside the pores, although it appears as the most intense peak at all the coverages among the split $-\text{CH}_2$ modes. In a pure crystalline state, strong interaction induces splitting of the $-\text{CH}_2$ wagging mode along with an increase in intensity.

3. Control Experiments to Validate the Diffusion Hypothesis. *3.a. IR Spectroscopic Studies.* To validate this hypothesis of diffusion followed by crystallization inside water pores which decreases the intensity of peak 2, we have performed a few sets of control experiments. In the first set, ASW was deposited on crystalline CH_2Cl_2 . For this, 50 ML of CH_2Cl_2 was deposited on Ru(0001) at 80 K, heated to 95 K to make it crystalline, and cooled back to 80 K with a subsequent deposition of H_2O on top of crystalline CH_2Cl_2 . The temperature of this system was then increased in steps from 80 to 150 K. Figure 7a displays the temperature-dependent RAIR spectra obtained from this study. Initially, the 50 ML of CH_2Cl_2 on Ru(0001) at 80 K was in an amorphous state, and upon heating it underwent a phase transition at 95 K (see the inset in Figure 7a) as can be seen from the splitting of the $-\text{CH}_2$ wagging mode, similar to that seen in Figure 1. Subsequent deposition of H_2O at 80 K forming the ASW layer did not cause the intensity of peak 2 (1257 cm^{-1}) to become less than that of peak 1, as opposed to the case of the amorphous CH_2Cl_2 -ASW system (Figure 5). Peak intensity at 80 K after crystallization and 95 K after water-ice overlayer deposition remained unchanged, implying that crystalline CH_2Cl_2 due to its ordered structure does not diffuse through ASW. Phase transition releases energy into the system which may induce desorption of molecules from the surface. Therefore, during crystallization, CH_2Cl_2 releases some energy, which causes desorption of some CH_2Cl_2 molecules on the surface. This could be the reason for the small reduction in peak intensity for crystalline CH_2Cl_2 at 80 K when water was deposited. This reduction in intensity is shown by both peak 1 and peak 2. However, the peak intensities at 80 and 95 K after ASW deposition are same. This validates our proposition that the decrease in the intensity of $-\text{CH}_2$ wagging mode at 1257 cm^{-1} , for amorphous CH_2Cl_2 deposited under ASW, is due to the diffusion of CH_2Cl_2 inside water-ice pores. However, such a diffusion is not uniform and it leads to the formation of small crystals or irregular crystals inside ASW, which results in decrease of molecular interaction in the unit cell. The crystalline CH_2Cl_2 formed in ASW can desorb only at 145 K when water undergoes crystallization. Hence, there is no

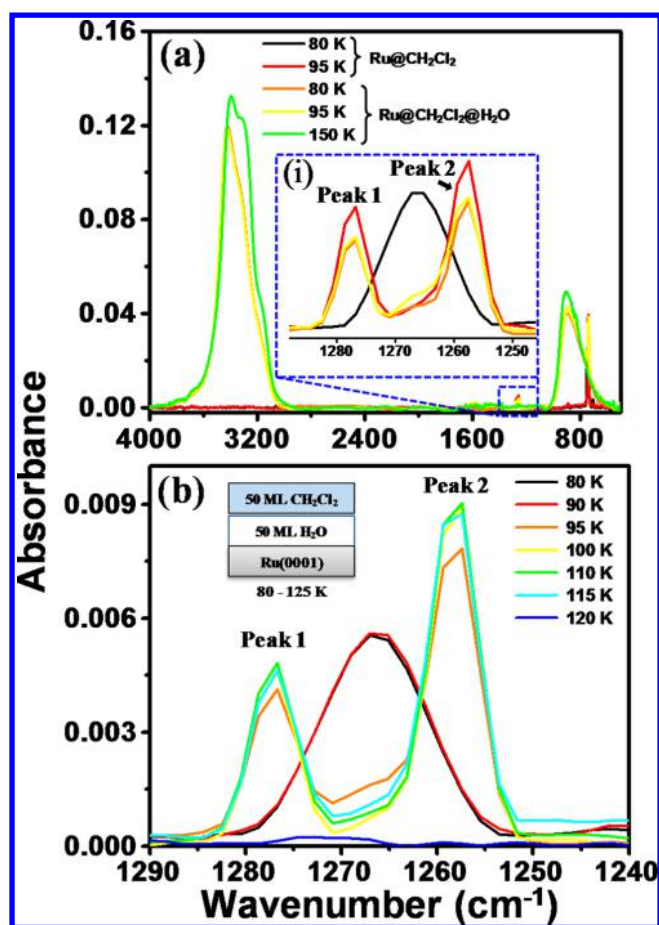


Figure 7. (a) Temperature-dependent RAIR spectra for 50 ML of amorphous H₂O deposited on 50 ML of crystalline CH₂Cl₂. CH₂Cl₂ was initially deposited at 80 K (black), subsequently heated to 95 K to result in crystallization (red), and cooled back to 80 K (light green), and then 50 ML water was deposited on top and temperature-dependent RAIR spectra were collected. Inset (i) shows an enlarged view of $-\text{CH}_2$ wagging mode. (b) Temperature-dependent RAIR spectra for 50 ML of CH₂Cl₂ which was deposited on top of 50 ML of ASW at 80 K.

change in $-\text{CH}_2$ wagging mode intensity here until desorption occurs.

In the second set of control experiments, temperature-dependent RAIR spectra were collected for 50 ML of CH₂Cl₂ deposited on top of 50 ML of ASW at 80 K. From Figure 7b, it is clear that, when CH₂Cl₂ is deposited on top of water-ice, it behaves like a pure CH₂Cl₂ film, undergoing crystallization at 95 K and desorbing from the water surface at 125 K, having no decrease in the intensity of peak 2. This confirms that when CH₂Cl₂ is on top of water there is no diffusion or mixing with water-ice. The nonoccurrence of CH₂Cl₂ diffusion through underlying ASW may be due to the surface property of both the species. CH₂Cl₂ does not wet the ASW surface properly, and hence, molecules do not get into the pores of ASW resulting in hindrance to diffusion. As suggested previously, CH₂Cl₂ diffusion in the overlaid ASW deposition could be due to molecular motion during phase transition. The control experiment where ASW was overlaid on crystalline CH₂Cl₂ where no diffusion was observed supports this argument. Disordered structure of amorphous CH₂Cl₂ can diffuse through the microporous channel of ASW, whereas ordered crystalline state of CH₂Cl₂ cannot diffuse. It is also likely that the pores in

the topmost layer of ASW got closed as CH₂Cl₂ was deposited which prevents the latter's diffusion.

Although adsorption could occur on condensed water, this cannot be attributed to be the reason for observed changes in peak. CH₂Cl₂ deposited over ASW (Ru@ASW@CH₂Cl₂) behaved similarly to pure CH₂Cl₂ (Ru@CH₂Cl₂) upon phase change and underwent desorption at 120 K. Thus, the observed changes in the IR spectra are due to deposition of ASW over CH₂Cl₂ (Ru@CH₂Cl₂@ASW) allowing the latter to diffuse into the pores of ASW. Adsorption of CH₂Cl₂ on condensed water cannot be concluded as the reason for the change as it does not happen in Ru@ASW@CH₂Cl₂. Spectrum of 1 ML of CH₂Cl₂ could not be measured as the intensity was weak. This was further confirmed by TPD measurements, to be described later.

3.b. Low-Energy Cs⁺ Scattering. The diffusion of CH₂Cl₂ through water-ice was additionally investigated by Cs⁺ scattering. Low-energy (<100 eV) Cs⁺ scattering is a very powerful surface-sensitive technique. The top layers of molecular surfaces can be probed by this technique. Here, low-energy Cs⁺ are allowed to collide on the surface and the scattered ions are analyzed using a mass spectrometer. Species present on the surface can easily be identified by this technique. Therefore, to get the surface information, we have performed Cs⁺ scattering of various samples. This will provide a clearer picture of the diffusion process. Figure 8 represents the Cs⁺ scattering spectra from four different experiments at 95 K. In all these cases, deposition was done at 80 K and samples were annealed to 95 K before Cs⁺ scattering. Schematics of the surfaces are shown in the inset of the figure. Collision energy of the Cs⁺ was 40 eV. Figure 8a represents the scattering spectrum of pure CH₂Cl₂ where the presence of CH₂Cl₂ on the surface can be confirmed from the peaks at m/z 49 and 84, assigned to CH₂Cl⁺ and CH₂Cl₂⁺, respectively, and also the Cs adduct products of the corresponding species at m/z 182 and 217 [Cs(CH₂Cl)⁺ and Cs(CH₂Cl₂)⁺, respectively]. An enlarged spectrum is shown in the inset of Figure 8a to show the isotopic pattern of the ions which again confirms the identity of the species. In the next set of experiments, 50 ML of CH₂Cl₂ was covered with 50 ML of D₂O followed by Cs⁺ scattering. Figure 8b shows the spectrum due to this experiment where the surface species corresponding to both D₂O and CH₂Cl₂ were detected. The spectrum shows the peaks at m/z 22, 42, 49, and 84 due to D₃O⁺, D₅O₂⁺, CH₂Cl⁺, and CH₂Cl₂⁺, respectively, and Cs adduct products at m/z 153, 173, 182, 193, and 217 due to Cs(D₂O)⁺, Cs(D₂O)₂⁺, Cs(CH₂Cl)⁺, Cs(D₂O)₃⁺, and Cs(CH₂Cl₂)⁺, respectively (with isotopically resolved peaks in the inset). Thus, even though a CH₂Cl₂ layer was covered with D₂O-ice, the Cs⁺ scattering was able to detect CH₂Cl₂. This indicates the diffusion of CH₂Cl₂ molecules and their presence on the surface. It might be noted that Cs⁺ scattering at this collision energy can probe 1–5 ML of the top surface. The CH₂Cl₂ molecules below diffuse through the porous structure of D₂O and reach the surface which are picked up by the Cs⁺. The same experiment was repeated by increasing the coverage of D₂O from 50 to 100 ML, keeping the CH₂Cl₂ coverage constant at 50 ML. Here also we see the appearance of CH₂Cl₂ molecules on the surface, but the intensities of the peaks reduce considerably compared to the 50 ML D₂O overlayer deposition. This suggests that the presence of surface species has reduced due to the increased overlayer thickness of D₂O. All the features of CH₂Cl₂ on the surface disappear with further increase in the overlayer thickness of D₂O to 500 ML (Figure

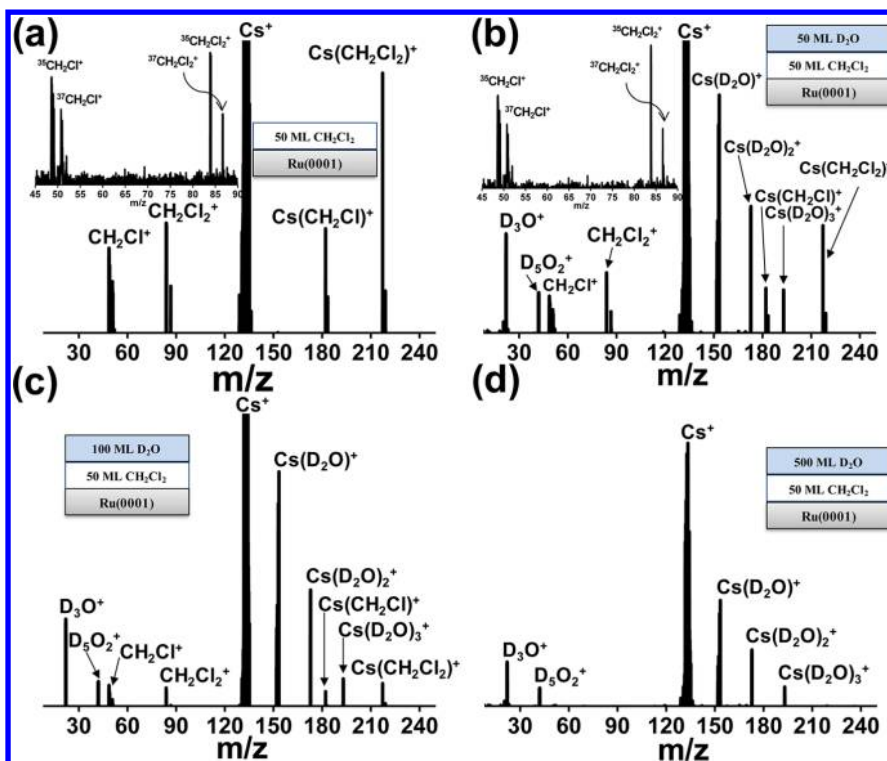


Figure 8. 40 eV Cs^+ collision on (a) Ru@50 ML of CH_2Cl_2 , (b) Ru@50 ML of CH_2Cl_2 @50 ML of D_2O , (c) Ru@50 ML of CH_2Cl_2 @100 ML of D_2O , and (d) Ru@50 ML of CH_2Cl_2 @500 ML of D_2O . Depositions were done at 80 K, and Cs^+ scattering was performed at 95 K.

8d). These results support our suggestion that, due to diffusion, the CH_2Cl_2 molecules get into the pores of water-ice and a fraction of molecules also reaches the surface at lower water-ice coverage. As the water-ice coverages are increased, the CH_2Cl_2 molecules have to travel longer distances to reach the surface, and at certain coverage, the distance is sufficiently high for the molecules so that they cannot reach the surface. Here, all the diffused molecules get trapped within the pores of water-ice.

3.c. TPD Measurements. We have performed TPD experiments for three different sets of samples to have a definite conclusion of the diffusion process. In all the experiments, the molecules were deposited at 80 K and ramping of 10 K/min was used to measure the TPD spectra. To obtain TPD spectra, m/z 49 (CH_2Cl^+) for CH_2Cl_2 and m/z 20 (D_2O^+) for D_2O were selected. The TPD spectrum of 50 ML of CH_2Cl_2 shows a desorption peak maximum at ~ 122 K (Figure 9a), in accordance with the IR measurements in which a decrease in spectral intensity at ~ 120 K and complete disappearance of the peaks at 125 K were seen. CH_2Cl_2 molecules deposited on top of ASW also show similar behavior. When CH_2Cl_2 was deposited over ASW, three distinct peaks in the TPD spectrum with peak maxima at ~ 122 , 145, and 160 K were seen (Figure 9b). In this experiment, 50 ML of CH_2Cl_2 was deposited on top of 50 ML of D_2O at 80 K, and during TPD, the temperature was ramped at 10 K/min. While most of the molecules desorb at ~ 122 K, a fraction desorbs at relatively higher temperatures.

The peak at ~ 145 K corresponds to the first monolayer of CH_2Cl_2 molecules which are adsorbed on ASW.²⁰ This monolayer has strong interaction with ASW via H-bonding or through molecular interactions. Therefore, desorption of these molecules from the ASW surface occurs at a relatively higher temperature when ASW undergoes a structural change (amorphous to crystalline transition). Due to the structural change, water molecules rearrange themselves and the

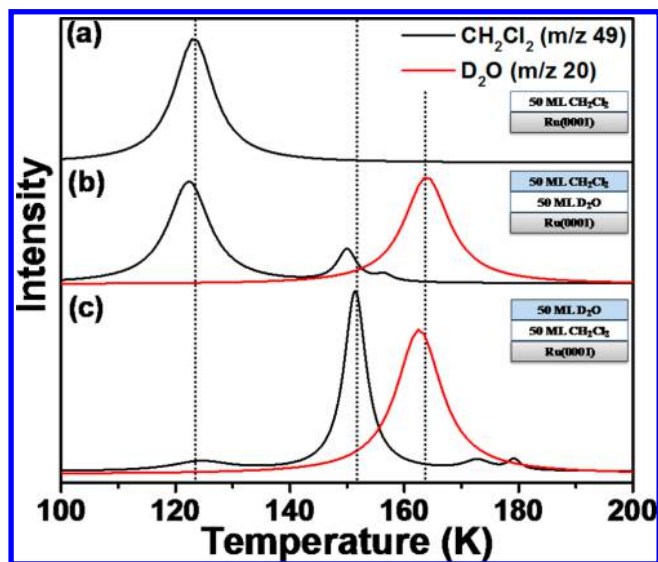


Figure 9. TPD spectra of (a) Ru@50 ML of CH_2Cl_2 , (b) Ru@50 ML of D_2O @50 ML of CH_2Cl_2 , and (c) Ru@50 ML of CH_2Cl_2 @ 50 ML of D_2O . Dotted lines are given to show the peak maxima. All the depositions were done at 80 K, and ramping rate was 10 K/min.

interaction between ASW and CH_2Cl_2 is reduced which causes desorption of the molecules. A smaller fraction of molecules is trapped in the pores of water-ice near the surface and desorbs at an even higher temperature (near to 160 K). These trapped molecules themselves desorb when water itself starts desorbing. From this study we can conclude that CH_2Cl_2 deposited on top of ASW does not diffuse through the pores of ASW, rather stays on the surface and gets crystallized. Crystallization is evident from the IR spectra (Figure 7). In our present IR measurement, it was not possible to get spectra from monolayer coverage of

CH₂Cl₂ due to poor intensity; therefore, even though a small fraction of molecules was present on the surface of ASW, we observed complete disappearance of IR intensity and concluded that CH₂Cl₂ deposited on top of ASW behaves like pure CH₂Cl₂. TPD experiment also supports the argument. In another set of experiments, 50 ML of CH₂Cl₂ was covered with 50 ML of D₂O and TPD spectra were measured. The results (Figure 9c) show four distinct desorption features. The broad peak with the peak maximum ~124 K is consistent with the desorption feature of pure CH₂Cl₂. This clearly manifests the diffusion of CH₂Cl₂ through ASW. Once ASW is deposited on top of CH₂Cl₂, the molecules start diffusing through the pores of ASW and get trapped there, and in this diffusion process, a small fraction of molecules reaches the surface. The surface species desorb first, and the trapped molecules desorb from the pores of ASW as molecular volcano when ASW undergoes a structural change at ~145 K. The detection of surface CH₂Cl₂ species due to diffusion was also observed in Cs⁺ scattering experiment (Figure 8). Both the results agree that CH₂Cl₂ diffuses through ASW. Two low-intensity features were observed at higher temperatures (~172 and 179 K). This indicates that still there are trapped molecules which desorb at relatively higher temperatures along with the desorption of water-ice. This trapping and desorption of molecules at higher temperature has been described previously by May et al.⁴⁷

CONCLUSIONS

This study reveals that dichloromethane undergoes a phase transition at ~95 K prior to desorption, irrespective of its coverage. This phase transition of CH₂Cl₂ is established from the peak shift of the C–Cl antisymmetric stretching frequency at 748 cm⁻¹ and a peak splitting of the –CH₂ wagging mode at 1265 cm⁻¹ into two: peak 1 at 1277 cm⁻¹ and peak 2 at 1257 cm⁻¹. Intensity of the both the split peaks increases with increasing CH₂Cl₂ coverage, though peak 2 is always more intense than peak 1. Once water-ice layers are deposited over a CH₂Cl₂ film, the latter diffuses through it at low temperatures and forms small crystals or irregular crystals inside the ice pores, undergoing a phase transition within. As the water-ice overlayer increases, the number of pores increases and more CH₂Cl₂ molecules diffuse through the pores resulting in the formation of more small or irregular crystals of CH₂Cl₂, and this leads to the reduction in intensity of peak 2 at 1257 cm⁻¹. Desorption of the trapped CH₂Cl₂ takes place at higher temperatures (~145 K) only after crystallization of the water-ice film. The Cs⁺ scattering and TPD experiments provide additional support to the diffusion process.

ASSOCIATED CONTENT

Supporting Information

The Supporting Information is available free of charge on the ACS Publications website at DOI: 10.1021/acs.jpcc.6b00436.

Temperature-dependent RAIR spectra of 50 ML CH₂Cl₂ and RAIR spectra of –CCl₂ antisymmetric stretching mode of 50 ML CH₂Cl₂ as a function of overlayer coverages of ASW at 100 K (PDF)

AUTHOR INFORMATION

Corresponding Author

*Fax: + 91-44 2257-0545. E-mail: pradeep@iitm.ac.in.

Notes

The authors declare no competing financial interest.

ACKNOWLEDGMENTS

T.P. thanks the Science and Engineering Research Board (SERB), Department of Science and Technology (DST), Government of India for research funding. S.B. and R.G.B. thank the Council of Scientific and Industrial Research (CSIR), Government of India for research fellowships. R.R.J.M. acknowledges the University Grant Commission (UGC) for his research fellowship. R.G.B. thanks Dr. Gana Natarajan for dichloromethane crystals structure.

REFERENCES

- (1) Buontempo, U. Infrared Spectra of Amorphous Ice. *Phys. Lett. A* **1972**, *42*, 17–18.
- (2) Burke, D. J.; Brown, W. A. Ice in Space: Surface Science Investigations of the Thermal Desorption of Model Interstellar Ices on Dust Grain Analogue Surfaces. *Phys. Chem. Chem. Phys.* **2010**, *12*, 5947–5969.
- (3) Smith, R. S.; Petrik, N. G.; Kimmel, G. A.; Kay, B. D. Thermal and Nonthermal Physicochemical Processes in Nanoscale Films of Amorphous Solid Water. *Acc. Chem. Res.* **2012**, *45*, 33–42.
- (4) Shin, S.; Kang, H.; Kim, J. S.; Kang, H. Phase Transitions of Amorphous Solid Acetone in Confined Geometry Investigated by Reflection Absorption Infrared Spectroscopy. *J. Phys. Chem. B* **2014**, *118*, 13349.
- (5) Burton, E. F.; Oliver, W. F. X-Ray Diffraction Patterns of Ice. *Nature (London, U. K.)* **1935**, *135*, 505–6.
- (6) Zimbitas, G.; Haq, S.; Hodgson, A. The Structure and Crystallization of Thin Water Films on Pt(111). *J. Chem. Phys.* **2005**, *123*, 174701/1–174701/9.
- (7) Jenniskens, P.; Blake, D. F. Structural Transitions in Amorphous Water Ice and Astrophysical Implications. *Science (Washington, DC, U. S.)* **1994**, *265*, 753–6.
- (8) Jenniskens, P.; Banham, S. F.; Blake, D. F.; McCoustra, M. R. S. Liquid Water in the Domain of Cubic Crystalline Ice Ic. *J. Chem. Phys.* **1997**, *107*, 1232–1241.
- (9) Bag, S.; Bhui, R. G.; Pradeep, T. Distinguishing Amorphous and Crystalline Ice by Ultralow Energy Collisions of Reactive Ions. *J. Phys. Chem. C* **2013**, *117*, 12146–12152.
- (10) Cyriac, J.; Pradeep, T.; Kang, H.; Souda, R.; Cooks, R. G. Low-Energy Ionic Collisions at Molecular Solids. *Chem. Rev. (Washington, DC, U. S.)* **2012**, *112*, 5356–5411.
- (11) Bag, S.; Bhui, R. G.; Natarajan, G.; Pradeep, T. Probing Molecular Solids with Low-Energy Ions. *Annu. Rev. Anal. Chem.* **2013**, *6*, 97–118.
- (12) Zhang, Y.; Gu, M.; Zhang, T.; Yuan, Y.; Zhou, L.; Duan, Y.; Zhang, J. Phase Transition Behavior of P11a Ultrathin Film Studied by Grazing Angle Reflection Absorption Infrared Spectroscopy. *Vib. Spectrosc.* **2012**, *63*, 338–341.
- (13) Zheng, W.; Kaiser, R. I. An Infrared Spectroscopy Study of the Phase Transition in Solid Ammonia. *Chem. Phys. Lett.* **2007**, *440*, 229–234.
- (14) Kim, Y. S.; Kaiser, R. I. An Infrared Spectroscopic Study of Amorphous and Crystalline Ices of Vinylacetylene and Implications for Saturn's Satellite Titan. *Astrophys. J., Suppl. Ser.* **2009**, *181*, 543–547.
- (15) Marzocchi, M. P.; Manzelli, P. Infrared Spectrum of Crystalline CH₂Cl₂ and CD₂Cl₂. Polarization Measurements and Crystal Structure. *J. Chem. Phys.* **1970**, *52*, 2630–9.
- (16) Molina, M. J.; Tso, T.-L.; Molina, L. T.; Wang, F. C.-Y. Antarctic Stratospheric Chemistry of Chlorine Nitrate, Hydrogen Chloride, and Ice: Release of Active Chlorine. *Science* **1987**, *238*, 1253–1257.
- (17) Grecea, M. L.; Backus, E. H. G.; Fraser, H. J.; Pradeep, T.; Klyen, A. W.; Bonn, M. Mobility of Haloforms on Ice Surfaces. *Chem. Phys. Lett.* **2004**, *385*, 244–248.
- (18) Smith, R. S.; Huang, C.; Wong, E. K. L.; Kay, B. D. The Molecular Volcano: Abrupt CCl₄ Desorption Driven by the Crystallization of Amorphous Solid Water. *Phys. Rev. Lett.* **1997**, *79*, 909–912.

- (19) Cyriac, J.; Pradeep, T. Probing Difference in Diffusivity of Chloromethanes through Water Ice in the Temperature Range of 110–150 K. *J. Phys. Chem. C* **2007**, *111*, 8557–8565.
- (20) Horowitz, Y.; Asscher, M. Electron-Induced Chemistry of Methyl Chloride Caged within Amorphous Solid Water. *J. Chem. Phys.* **2013**, *139*, 154707.
- (21) Hama, T.; Watanabe, N. Surface Processes on Interstellar Amorphous Solid Water: Adsorption, Diffusion, Tunneling Reactions, and Nuclear-Spin Conversion. *Chem. Rev. (Washington, DC, U. S.)* **2013**, *113*, 8783–8839.
- (22) Zubkov, T.; Smith, R. S.; Engstrom, T. R.; Kay, B. D. Adsorption, Desorption, and Diffusion of Nitrogen in a Model Nanoporous Material. I. Surface Limited Desorption Kinetics in Amorphous Solid Water. *J. Chem. Phys.* **2007**, *127*, 184707/1–184707/11.
- (23) Bertin, M.; Romanzin, C.; Michaut, X.; Jeseck, P.; Fillion, J. H. Adsorption of Organic Isomers on Water Ice Surfaces: A Study of Acetic Acid and Methyl Formate. *J. Phys. Chem. C* **2011**, *115*, 12920–12928.
- (24) Dohnalek, Z.; Kimmel, G. A.; Ayotte, P.; Smith, R. S.; Kay, B. D. The Deposition Angle-Dependent Density of Amorphous Solid Water Films. *J. Chem. Phys.* **2003**, *118*, 364–372.
- (25) Raut, U.; Fama, M.; Teolis, B. D.; Baragiola, R. A. Characterization of Porosity in Vapor-Deposited Amorphous Solid Water from Methane Adsorption. *J. Chem. Phys.* **2007**, *127*, 204713/1–204713/6.
- (26) Stevenson, K. P.; Kimmel, G. A.; Dohnalek, Z.; Smith, R. S.; Kay, B. D. Controlling the Morphology of Amorphous Solid Water. *Science (Washington, DC, U. S.)* **1999**, *283*, 1505–1507.
- (27) Smith, R. S.; Zubkov, T.; Dohnalek, Z.; Kay, B. D. The Effect of the Incident Collision Energy on the Porosity of Vapor-Deposited Amorphous Solid Water Films. *J. Phys. Chem. B* **2009**, *113*, 4000–4007.
- (28) Ayotte, P.; Smith, R. S.; Stevenson, K. P.; Dohnalek, Z.; Kimmel, G. A.; Kay, B. D. Effect of Porosity on the Adsorption, Desorption, Trapping, and Release of Volatile Gases by Amorphous Solid Water. *J. Geophys. Res., [Planets]* **2001**, *106*, 33387–33392.
- (29) Bisschop, S. E.; Fraser, H. J.; Oberg, K. I.; van Dishoeck, E. F.; Schlemmer, S. Desorption Rates and Sticking Coefficients for Co and N₂ Interstellar Ices. *Astron. Astrophys.* **2006**, *449*, 1297–1309.
- (30) Oberg, K. I.; van Broekhuizen, F.; Fraser, H. J.; Bisschop, S. E.; van Dishoeck, E. F.; Schlemmer, S. Competition between Co and N₂ Desorption from Interstellar Ices. *Astrophys. J.* **2005**, *621*, L33–L36.
- (31) Cholette, F.; Zubkov, T.; Smith, R. S.; Dohnalek, Z.; Kay, B. D.; Ayotte, P. Infrared Spectroscopy and Optical Constants of Porous Amorphous Solid Water. *J. Phys. Chem. B* **2009**, *113*, 4131–4140.
- (32) Mate, B.; Rodriguez-Lazcano, Y.; Herrero, V. J. Morphology and Crystallization Kinetics of Compact (HGW) and Porous (ASW) Amorphous Water Ice. *Phys. Chem. Chem. Phys.* **2012**, *14*, 10595–10602.
- (33) Bag, S.; Bhui, R. G.; Methikkalam, R. R. J.; Pradeep, T.; Kephart, L.; Walker, J.; Kuchta, K.; Martin, D.; Wei, J. Development of Ultralow Energy (1 - 10 eV) Ion Scattering Spectrometry Coupled with Reflection Absorption Infrared Spectroscopy and Temperature Programmed Desorption for the Investigation of Molecular Solids. *Rev. Sci. Instrum.* **2014**, *85*, 014103/1–014103/7.
- (34) Moon, E.-S.; Kang, H.; Oba, Y.; Watanabe, N.; Kouchi, A. Direct Evidence for Ammonium Ion Formation in Ice through Ultraviolet-Induced Acid-Base Reaction of NH₃ with H₃O⁺. *Astrophys. J.* **2010**, *713*, 906–911.
- (35) Smith, R. S.; Petrik, N. G.; Kimmel, G. A.; Kay, B. D. Thermal and Nonthermal Physicochemical Processes in Nanoscale Films of Amorphous Solid Water. *Acc. Chem. Res.* **2012**, *45*, 33–42.
- (36) Bolina, A. S.; Wolff, A. J.; Brown, W. A. Reflection Absorption Infrared Spectroscopy and Temperature Programmed Desorption Investigations of the Interaction of Methanol with a Graphite Surface. *J. Chem. Phys.* **2005**, *122*, 044713/1–044713/12.
- (37) Brown, C. W.; Obremski, R. J.; Allkins, J. R.; Lippincott, E. R. Vibrational Spectra of Single Crystals and Polycrystalline Films of CH₂Cl₂ and CH₂Br₂. *J. Chem. Phys.* **1969**, *51*, 1376–84.
- (38) Kartha, V. B. Infrared Spectra of Dichloromethane, Dibromomethane, and Diiodomethane in the Solid State. *J. Mol. Spectrosc.* **1967**, *24*, 368–77.
- (39) Lang, E. K.; Knox, K. J.; Momose, T.; Signorell, R. Infrared Spectroscopy and Phase Behavior of *n*-Butane Aerosols and Thin Films at Cryogenic Temperatures. *J. Phys. Chem. A* **2013**, *117*, 11745–11759.
- (40) Ito, M. Raman Spectra of Polycrystalline Chloromethanes at Liquid Nitrogen Temperature. *J. Chem. Phys.* **1964**, *40*, 3128–9.
- (41) Kawaguchi, T.; Tanaka, K.; Takeuchi, T.; Watanabe, T. Crystal Structure of Methylene Dichloride. *Bull. Chem. Soc. Jpn.* **1973**, *46*, 62–6.
- (42) Cotton, F. A. *Chemical Applications of Group Theory*, 3rd ed.; John Wiley and Sons: New York, 1990; p 461.
- (43) Marzocchi, M. P.; Bonadeo, H.; Taddei, G. Infrared Spectra in Polarized Light of Crystalline Benzene and Benzene-D₆. *J. Chem. Phys.* **1970**, *53*, 867–75.
- (44) Livneh, T.; Romm, L.; Asscher, M. Cage Formation of N₂ under H₂O Overlayer on Ru(001). *Surf. Sci.* **1996**, *351*, 250–258.
- (45) Yan, H.; Chu, L. T. Interactions of Oxalic Acid and Ice on Cu Surface. *Langmuir* **2008**, *24*, 9410–9420.
- (46) Lagaron, J.-M. The Factor Group Splitting Phenomenon: A Vibrational Spectroscopy Approach to Assess Polymer Crystallinity and Crystalline Density. *Macromol. Symp.* **2002**, *184*, 19–36.
- (47) May, R. A.; Scott Smith, R.; Kay, B. D. The Release of Trapped Gases from Amorphous Solid Water Films. II. "Bottom-up" Induced Desorption Pathways. *J. Chem. Phys.* **2013**, *138*, 104502/1–104502/11.

Diffusion and Crystallization of Dichloromethane within the Pores of Amorphous Solid Water

Radha Gobinda Bhui, Rabin Rajan J. Methikkalam, Soumabha Bag, and Thalappil Pradeep*

DST Unit of Nanoscience (DST UNS) and Thematic Unit of Excellence (TUE), Department of Chemistry, Indian Institute of Technology Madras, Chennai 600 036, India

*Corresponding author: Fax: + 91-44 2257-0545

*E-mail: pradeep@iitm.ac.in

Supporting information 1:

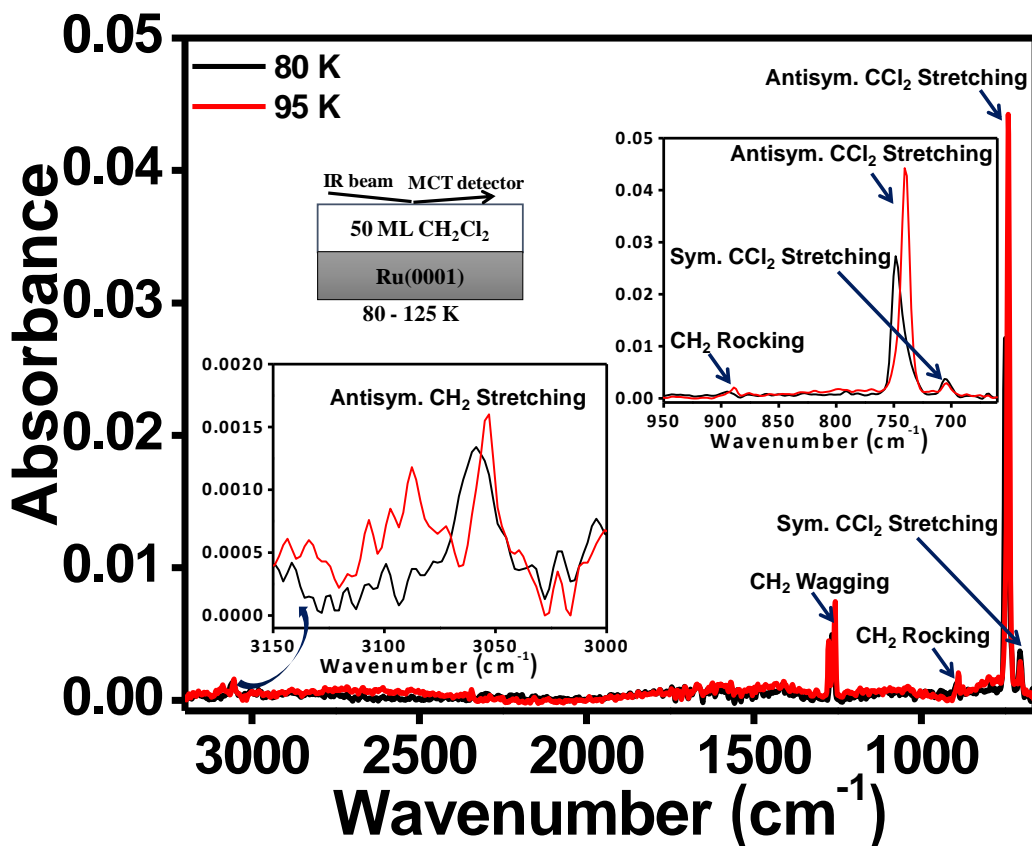


Figure S1. Temperature dependent RAIR spectra of 50 ML CH₂Cl₂. CH₂Cl₂ was deposited at 80 K on Ru(0001). Schematic of the experiment is shown in one inset and another inset shows the expanded view of different regions.

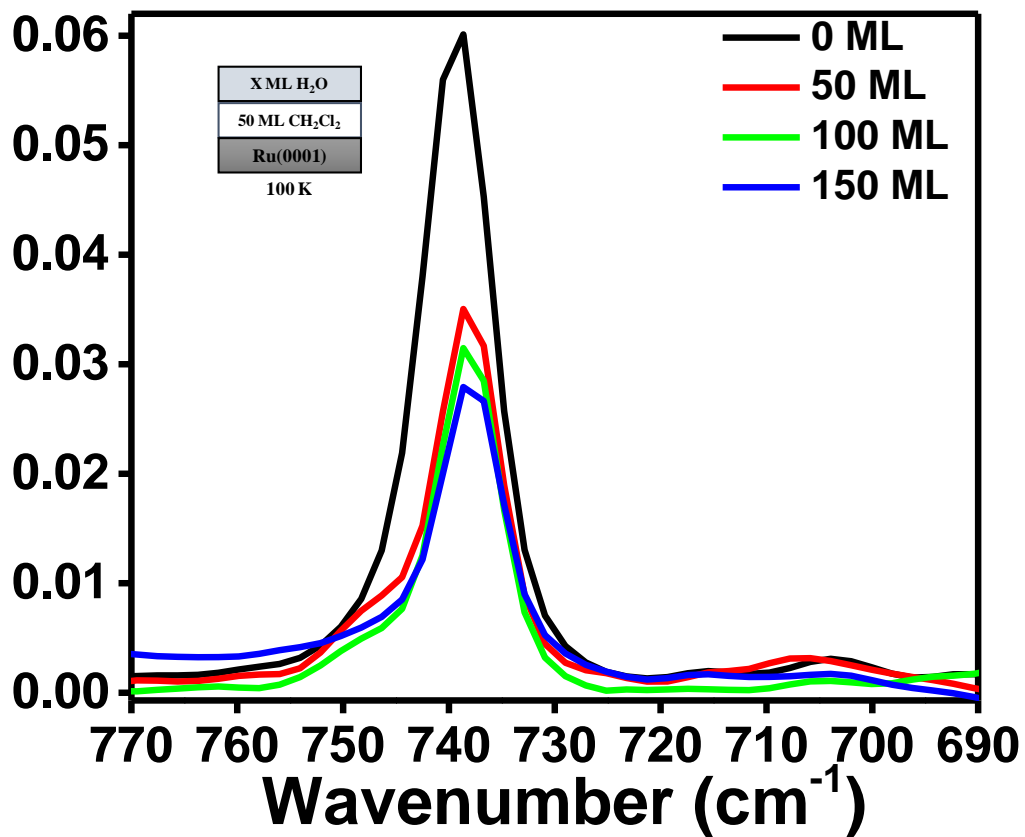


Figure S2. RAIR spectra of -CCl_2 antisymmetric mode of $50 \text{ ML CH}_2\text{Cl}_2$ as a function of overlayer coverages of ASW at 100 K . Inset shows the schematic of the surface. Both CH_2Cl_2 and H_2O were deposited at 80 K on $\text{Ru}(0001)$ surface.

Monitoring of changes in lipid profiles during PLK1 knockdown in cancer cells using DESI MS

Balasubramanyam Jayashree^{1,2} · Amitava Srimany³ · Srinidhi Jayaraman¹ · Anjali Bhutra¹ · Narayanan Janakiraman¹ · Srujana Chitipothu¹ · Subramanian Krishnakumar¹ · Lakshmi Subhadra Baddireddi² · Sailaja Elchuri¹ · Thalappil Pradeep³

Received: 12 April 2016 / Revised: 17 May 2016 / Accepted: 23 May 2016 / Published online: 8 June 2016
© Springer-Verlag Berlin Heidelberg 2016

Abstract The importance of the polo-like kinase 1 (PLK1) gene is increasing substantially both as a biomarker and as a target for highly specific cancer therapy. This is due to its involvement in multiple points of cell progression and carcinogenesis. PLK1 inhibitors' efficacy in treating human cancers has been limited due to the lack of a specific targeting strategy. Here, we describe a method of targeted downregulation of PLK1 in cancer cells and the concomitant rapid detection of surface lipidomic perturbations using desorption electrospray ionization mass spectrometry (DESI MS). The efficient delivery of siRNA targeting PLK1 gene selectively to the cancer cells is achieved by targeting overexpressed cell surface epithelial cell adhesion molecule (EpcAM) by the EpDT3 aptamer. The chimeric aptamer (EpDT3-siPLK1) showed the knockdown of PLK1 gene expression and PLK1 protein levels by quantitative PCR and western blotting, respectively. The abundant surface lipids, phosphatidylcholines

(PCs), such as PC(32:1) (*m/z* 754.6), PC(34:1) (*m/z* 782.6), and PC(36:2) (*m/z* 808.6), were highly expressed in MCF-7 and WERI-RB1 cancer cells compared to normal MIO-M1 cells and they were observed using DESI MS. These overexpressed cell surface lipids in the cancer cells were downregulated upon the treatment of EpDT3-siPLK1 chimera indicating a novel role of PLK1 to regulate surface lipid expression in addition to the efficient selective cancer targeting ability. Our results indicate that DESI MS has a potential ability to rapidly monitor aptamer-mediated cancer therapy and accelerate the drug discovery process.

Keywords Cancer · Aptamer · siPLK1 · DESI MS · Lipid

Introduction

Bilayer lipid membranes are essential parts of mammalian cells which consist of different phospholipids. These lipids are involved in different activities like cell signalling, metabolism, etc. Lipid composition of particular cell types changes due to different conditions of the cells. Several diseased conditions of cells, particularly tumors, can be understood by studying the lipid profiles of cells [1, 2]. Choline phospholipid metabolism is known to be dysregulated in cancers and has been used as diagnostic tools [3, 4]. The dysregulated choline metabolism as cancer biomarkers has been proposed using magnetic resonance spectroscopy [5, 6]. Mass spectrometry provides a simple way to capture molecule-specific lipid profiles of various tissues and cells. Incorporation of ambient ionization methods [7] makes the process of analysis faster and hassle free. Desorption electrospray ionization mass spectrometry (DESI MS) is one such ambient ionization process which was introduced in 2004 [8], and in fact, it is the first one of its kind.

Balasubramanyam Jayashree and Amitava Srimany contributed equally to this work.

Electronic supplementary material The online version of this article (doi:10.1007/s00216-016-9665-y) contains supplementary material, which is available to authorized users.

✉ Sailaja Elchuri
sailaja.elchuri@gmail.com

✉ Thalappil Pradeep
pradeep@iitm.ac.in

¹ Department of Nanobiotechnology, Vision Research Foundation, Sankara Nethralaya, Chennai, Tamil Nadu 600006, India

² Centre for Biotechnology, Anna University, Chennai, Tamil Nadu 600025, India

³ DST Unit of Nanoscience (DST UNS) and Thematic Unit of Excellence (TUE), Department of Chemistry, Indian Institute of Technology Madras, Chennai, Tamil Nadu 600036, India

DESI MS, being an ambient ionization technique, does not require extensive sample preparation and ionization occurs under atmospheric conditions, making the process highly compatible for biological sample analysis. It has been applied to several aspects of biological sciences. Examples include analysis of peptides [9], screening of different kinds of molecules from urine [10], study of animal tissue sections [11, 12], differentiation of tumor and non-tumor tissues [13, 14], identification of molecular species from plants [15], and spatial distribution of alkaloids in plant parts like seeds [16, 17], leaves and petals [18], etc. In spite of its diverse application in different areas of biology, the technique has not been used to study cell surface lipidomic changes upon targeted drug delivery.

Polo-like kinase 1 (PLK1) is a well-known oncogene that plays a major role in bipolar spindle formation [19, 20], chromosome segregation, centrosome maturation in late G2/early prophase [21], activation of Cdc25 [22], regulation of anaphase-promoting complex, and execution of cytokines [20, 23]. It is also involved in the direct phosphorylation of serine 62 of MYC protein and its stabilization [24] and regulates primary cilia disassembly in a kinase activity-dependent manner [25]. Thus, the importance of PLK1 is increasing substantially both as a biomarker and as a target for highly specific cancer therapy due to its involvement in multiple points of cell progression and carcinogenesis [26]. In addition to its role as mitotic check point, the role of PLK1 in signalling is well studied [27]. PLK1 signalling and lipid metabolism were the top dysregulated mechanisms in prostate cancer. The PLK1 signalling pathway and increased lipid expression led to prostate cancer progression [28]. However, PLK1-mediated lipid regulation, especially phosphatidylcholines which are considered as diagnostic markers for cancer, is lacking.

PLK1 inhibitors have already completed phase I clinical trials, but the efficacy of these agents in treating human cancers has been limited due to lack of specific targeting strategy. However, target-specific aptamer-siRNA conjugate against PLK1 could be a potential drug for cancer treatment. Aptamers are small single-stranded DNA/RNA molecules, described by a linear sequence of nucleotides, designed to specifically bind to a molecular target. They have low immunogenicity compared to proteins and therapeutic antibodies. Therefore, small DNA/RNA aptamers are identified for targeting cancer cells [29–33]. Aptamers have been designed against epithelial cell adhesion molecules (EpCAMs) which are highly expressed in most of the epithelial cancers [34]. Aptamer chimeras are generated using natural recombination or chemical processes. There is a possibility of losing the activity of one or both of the recombining partners during the process necessitating detailed investigations. An EpCAM aptamer-doxorubicin chimera was found to target the EpCAM positive cancer stem cells and deliver doxorubicin thereby leading to apoptosis of the cells [35]. The EpCAM aptamer

can be conjugated to a siRNA to target an oncogene such as PLK1 which is involved in G2/M cell cycle regulation to specifically target EpCAM positive cancers. Recently, EpCAM aptamer-PLK1 siRNA chimera has been found effective in mouse models of breast cancer [36]. Therefore, this chimera has been used presently to study PLK1-mediated lipid regulation in breast cancer and retinoblastoma cells.

In the present work, initially we established phosphatidylcholine signatures in cancer cell lines (MCF-7 and WERI-RB1) and compared it to a normal cell line (MIO-M1) to see if there are any cell-specific changes in the surface lipids between them using DESI MS. We then extended the study to see if the cancer-specific biomarker lipids could be regulated by giving targeted cancer drugs to understand therapy response. The aptamer drug EpDT3-siPLK1 targeted PLK1 gene leading to alterations in the surface lipidomic profiles. The use of DESI MS, in this context, provided a platform for rapid analysis of lipids from cells.

Materials and methods

Reagents

For cell culture, Roswell Park Memorial Institute 1640 (RPMI 1640), Dulbecco's Modified Eagle's Medium (DMEM), antibiotic-antimycotic solution, and fetal bovine serum (FBS) were purchased from Gibco Life Technologies, USA. For DESI MS experiments, HPLC grade methanol from Sigma-Aldrich, Germany and Whatman 42 filter paper from GE Healthcare UK Limited, UK were used.

Aptamer design

First, aptamer chimeras EpDT3-siPLK1 and EpDT3-siScr were designed. The lengths of the chimeras were designed to be 60 nucleotides containing a Dicer recognition site between the EpCAM aptamer and the PLK1 siRNA sequence. To increase the stability of the aptamer chimeras against endogenous nucleases, modification was made by adding 2-nucleotide 3' overhangs. The aptamer was fluorescently labelled at the 3' end to visualize binding of chimeras to the cells. All the RNA sequences including the aptamer chimera sequences were designed and HPLC purified by Dharmacon, USA.

Cell culture

Retinoblastoma WERI-RB1 cells (obtained from RIKEN BioResource Center, Ibaraki, Japan) were maintained in RPMI 1640, with 10 % FBS, and supplemented with antibiotic-antimycotic solution containing penicillin 100 µg/ml, streptomycin 100 µg/ml, and amphotericin B

250 ng/ml. Breast cancer cell line Michigan Cancer Foundation-7 (MCF-7) was procured from the American Type Culture Collection (ATCC), Manassas, VA, USA, and Müller Glial MIO-M1 cell line was a kind gift from Professor Astrid Limb, London, UK, and they were cultured in DMEM containing 10 % FBS with and without antibiotic-antimycotic solution, respectively. All the cell lines were maintained in a 5 % CO₂ environment at 37 °C.

Flow cytometry

Cells (4×10^5 ; MIO-M1, MCF-7 or WERI-RB1) were collected and washed twice with cold phosphate-buffered saline (PBS). Cells were then resuspended in blocking buffer (PBS with 0.02 % sodium azide, 0.1 % FBS, and 0.01 % Triton X-100) and incubated with different concentrations (100–500 nM) of fluorescein isothiocyanate (FITC)-tagged aptamer chimeras (EpDT3-siPLK1 and EpDT3-siScr). After 1 h, the cells were washed twice with cold PBS and resuspended in sheath fluid. Cells (10^4) were collected and analyzed using FACS.

Dicer cleavage assay

EpDT3-siPLK1 chimera (100 nM) was denatured by heating for 10 min in a boiling water bath. Digestion using Dicer enzyme was set up as per the manufacturer's protocol (Recombinant Dicer Kit) with and without Dicer. The samples were then resolved using native PAGE (15 % w/v polyacrylamide) and stained with ethidium bromide before visualization using the Gel Doc (Bio-Rad).

Quantitative RT-PCR

MIO-M1, MCF-7, and WERI-RB1 cells were transfected with 100 nM of EpDT3, Scr-EpDT3, 150 nM of siPLK1, siScr, EpDT3-siPLK1, and EpDT3-siScr. The cells were harvested after 48 h and washed twice with cold PBS. RNA was extracted with TRIzol reagent using an optimized protocol and reverse transcribed into cDNA using High-Capacity cDNA Reverse Transcription Kit (Applied Biosystems). Quantitative RT-PCR was performed with SYBR Green (Applied Biosystems) using GAPDH as endogenous control. The primers used were FP 5'-GACAAGTACGGCCTTGGGTA and RP 5'-GTGCCGTCACGCTCTATGTA for PLK1 (Sigma-Aldrich) and FP 5'-AGAAGGCTGGGGCTCATTTG and RP 5'-AGGGGCCATCCACAGTCTTC for GAPDH (Sigma-Aldrich). The threshold cycle (Ct) values obtained from Applied Biosystems were used to calculate relative quantification with the formula $2^{-\Delta\Delta C_t}$, where $\Delta\Delta C_t$ are the values obtained on normalizing the values of

treated samples with values of untreated and endogenous controls.

Western blotting

MIO-M1, MCF-7, and WERI-RB1 cells were transfected with 150 nM of EpDT3, siPLK1, siScr, EpDT3-siPLK1, and EpDT3-siScr and they were collected after 48 h. The cells were then lysed in RIPA buffer containing Protease Inhibitor Cocktail (Sigma-Aldrich) followed by cold PBS wash. Supernatant was collected after centrifuging the samples for 10 min at 10,000 rpm. The lysates obtained were estimated using Bradford method against BSA standard. Protein (75 μ g) was resolved on a 10 % SDS-PAGE and transferred onto a nitrocellulose membrane. The blot was blocked for 1 h with 5 % skimmed milk and the membrane was probed with anti-PLK1 primary monoclonal antibody (Invitrogen: 37–7000) at 1:1000 dilution. The primary antibody was treated overnight at 4 °C. Then, the blot was washed three times with PBST and probed with secondary anti-mouse conjugated with HRP (Santa Cruz Biotechnology: sc-2005) at 1:4500 dilution for 1 h. The membrane was detected using a TMB substrate (Merck). GAPDH (Sigma-Aldrich: G8795) was used as endogenous control. ImageJ software was used to normalize treated samples with control samples and represented in ratio with GAPDH.

Statistical analysis

For quantitative RT-PCR and western blotting experiments, data were obtained in triplicates and the comparisons were performed using Student's *t*-test. *P* values less than 0.05 were considered as statistically significant.

DESI MS

After treatment with 150 nM siPLK1 and EpDT3-siPLK1 for 48 h, cells were collected and washed in cold PBS. The pellet was resuspended in 10 μ l PBS. Then, 5 μ l of cell suspension was spotted on Whatman 42 filter paper and it was kept in normal lab conditions for about 5 min to dry. Then, the paper containing the cells was fixed on the glass slide used in the DESI MS stage. Our previous study demonstrated that spotting cells on Whatman 42 filter paper could identify surface lipids more efficiently compared to other common surfaces used in DESI MS analysis [37]. Here we have used the same methodology. A 2D DESI MS source from Prosolia, Inc. was used for all mass spectrometric measurements. The source was connected with a Thermo LTQ XL ion trap mass spectrometer. DESI MS data were acquired in positive ion mode with 5 kV spray voltage. HPLC grade methanol was used as solvent and it was sprayed at 5 μ l/min flow rate with the help of 150 psi nebulizer gas pressure. The data obtained was

processed by FireFly software to make images and the images were viewed by BioMap software. Collision-induced dissociation (CID) was used for tandem mass spectrometry (MS/MS) experiments.

Gene microarray analysis

To understand the global gene expression changes accompanying the PLK1 knockdown leading to dysregulated lipidomic signature and cancer cell death, whole genome microarray experiments were undertaken. The control MCF-7 and EpDT3-siPLK1-treated MCF-7 cells were evaluated for gene expression using Affymetrix GeneChip PrimeView Human Gene Expression Array according to the manufacturer's protocol. Briefly, the samples were collected after treatment and ribonucleic acid was extracted from each of the samples using RNeasy kit (QIAGEN, Valencia, CA) and hybridized to GeneChip PrimeView Human Gene Expression Array (Affymetrix, Santa Clara, CA). Microarray data from the samples were background corrected and normalized using the GCRMA algorithm. One probe set per gene, based on highest overall expression level across samples, was selected for use in subsequent analyses. Differential expression of genes was determined using Student's *t*-test. Gene expression array data were generated and analyzed as described. The Gene Ontology (GO) was performed using GeneSpring 13.0 (Agilent Technologies). The top GO processes are presented at <0.05 significance levels.

MTT assay

Following 48 h transfection, cells were incubated with MTT (5 mg/ml) for 4 h at 37 °C. After 4 h, the formazan crystals were formed and on addition of DMSO the purple color of formazan was observed. The absorbance was measured at 570 nm on ELISA plate reader.

Results and discussion

Targeted aptamer-mediated PLK1 gene regulation

For targeted cancer therapy, an aptamer (EpDT3) which selectively targets EpCAM expressed cancer cells was chosen and conjugated with PLK1 targeting siRNA to construct EpDT3-siPLK1 chimera. This was used to knockdown the expression of PLK1, specifically in cancer cells (expressing EpCAM) and not in the normal cells. A Dicer cleavage site was incorporated in the aptamer chimera for the enzyme Dicer to recognize and guide the siRNA into the RNAi pathway enabling the efficient downregulation of the PLK1 gene. The secondary structure prediction of the EpDT3-siPLK1 chimera (see Electronic Supplementary Material (ESM) Fig. S1) was done using

RNAstructure, version 5.0. A scrambled siRNA sequence linked to EpCAM aptamer (EpDT3-siScr, ESM Fig. S1) was used as control. The silencing activity and specificity of aptamer-siRNA chimeras are generally increased by incorporating modifications that enable more efficient processing of the siRNA by the cellular machinery. These include adding of 2-nucleotide 3' overhangs, optimizing the thermodynamic profile, and structuring of the duplex to favor the processing of siRNA guide strand. These modifications had been previously employed to enable the PSMA aptamer chimeras to specifically target prostate cancer cells compared to normal cells [38]. Unlike the PSMA that targets only prostate cancer cells, the present aptamer chimera has potential to target all cancer cells that overexpress cell surface molecule EpCAM which include breast, pancreas, lung, colon, and liver enabling the wider application of the drug for targeted cancer therapy. The MCF-7 cell line with 98 % EpCAM expression [39] was chosen for the aptamer chimera drug treatment. A retinoblastoma cell line WERI-RB1 with 41 % EpCAM expression [35] was chosen to study the drug uptake in mixed (high and low) EpCAM-expressing cell populations. A normal cell line MIO-M1 with low EpCAM expression was taken as control.

We first performed binding studies of the chimeras on cancer cells and normal cells to assess its specificity to the cancer cells. Flow cytometry was used for this purpose. Previous studies showed that the percentage of aptamer binding to the cells can be evaluated by flow cytometry using FITC as fluorescent label [40]. Thus, to track the binding efficiency of EpDT3-siPLK1 and EpDT3-siScr, FITC labelling was done and its cellular uptake was evaluated. Increasing concentrations of the EpDT3-siPLK1 chimera (100 to 500 nM) were used to assess its binding efficiency to the cells. MIO-M1, a non-cancerous cell which expresses low levels of EpCAM, when incubated with 100 nM of EpDT3-siPLK1, showed a very minimal binding of 4–6.6 % (ESM Fig. S2A) which was found to be nearly the same when chimera concentration was increased to 500 nM, correlating to the fact that MIO-M1 has low EpCAM expression. For MCF-7, having 98 % EpCAM expression [39], the binding efficiency was found to increase from 90 to 96 % when chimera concentration was increased from 100 to 300 nM and then saturated (ESM Fig. S2B). In case of WERI-RB1, having 41 % EpCAM expression, a binding efficiency of nearly 27 % was observed with 500 nM chimera concentration (ESM Fig. S2C). A bimodal distribution (ESM Fig. S2C) indicates a subset of cellular populations having higher aptamer uptake while another subset having lower aptamer uptake. The percentage binding of EpDT3-siPLK1 is in agreement with EpCAM protein expression reported previously in WERI-RB1 cell line using EpCAM antibody [35]. The EpDT3-siScr chimera exhibited 5, 96, and 26 % binding in MIO-M1, MCF-7, and WERI-RB1, respectively (ESM Fig. S3). Both the EpDT3-siPLK1 and EpDT3-siScr chimeras showed almost similar binding efficiencies.

For EpDT3-siPLK1 chimera to enter into the RNAi pathway, it is important that siPLK1 is released from the chimera and this aspect was tested by an *in vitro* cleavage assay. General reports say that a pre-microRNA can be cleaved by an enzyme Droscha, processed by Dicer endonuclease, into a 21-nt mature miRNA which enters RNA-induced silencing complex (RISC) for the mRNA degradation leading to the downregulation of the gene expression process. When EpDT3-siPLK1 was incubated with recombinant Dicer, it was digested to an expected 20–22-nt cleavage product. Two distinct bands were seen in gel electrophoresis: lower band representing EpDT3 and upper band due to siPLK1 (ESM Fig. S4). The data suggested that Dicer enzyme could cleave the EpDT3-siPLK1 chimera *in vitro* into EpDT3 and siPLK1. We suggest a similar release of siPLK1 inside the cells and thereby leading to the regulation of PLK1 expression.

Targeted silencing of a particular gene by using an aptamer has already been implied in cancer research and has been found to be very specific for reducing tumor growth [38, 41]. Therefore, the efficacy of PLK1 regulation by the aptamer was studied. The gene expression was studied in MIO-M1, MCF-7, and WERI-RB1 cells by quantitative RT-PCR (Fig. 1A–C). The levels of PLK1 remained unchanged when treated with only EpDT3, Scr-EpDT3, and siScr in all three cell lines indicating that EpDT3 aptamer alone and scrambled siRNA sequence had no effect on the PLK1 gene expression. In normal MIO-M1 cells, the level of PLK1 was reduced when treated with siPLK1 and had no effect on treatment with EpDT3-siPLK1 chimera (Fig. 1A) indicating that the aptamer chimera could not bind to MIO-M1 cells due to low expression of EpCAM. This indicates non-target ability of the EpDT3-siPLK1 chimera to normal cells with reduced EpCAM expression. The use of siPLK1 alone resulted in regulation of PLK1 in non-cancerous cells too. The PLK1 gene

expression was reduced both by siPLK1 and EpDT3-siPLK1 in both the cancer cell lines (MCF-7 and WERI-RB1) after 48 h of treatment (Fig. 1B, C). The data suggest that EpDT3-siPLK1 could regulate PLK1 gene expression in cells overexpressing EpCAM. The target-specific delivery method is more efficient than Lipofectamine-delivered siRNA, as Lipofectamine delivers siRNA non-specifically into all the cells by electrostatic interactions, whereas our chimera delivers the siRNA by cell type-specific molecular recognition. In case of EpDT3-siScr, though the surface binding through EpCAM was almost the same as EpDT3-siPLK1 (ESM, Figs. S2 and S3), the knockdown of PLK1 was not seen (Fig. 1B, C) because the scrambled siRNA could not regulate PLK1 gene expression indicating the specificity of EpDT3-siPLK1 for PLK1 gene regulation. In agreement with mRNA levels, the PLK1 protein levels were also reduced in MCF-7 (Fig. 1D) and WERI-RB1 (Fig. 1E) cells after 48 h of EpDT3-siPLK1 treatments. Since EpDT3-siPLK1 binding was minimal in WERI-RB1 (27 %), the knockdown created by EpDT3-siPLK1 was lower compared to normal siRNA transfection (Fig. 1E). EpDT3-siScr had no effect on the PLK1 protein expression. Thus, EpDT3-siPLK1 selectively targets PLK1 in cancer cells sparing the normal cells.

Surface lipidomic signatures of cancer cells can be altered using EpDT3-siPLK1

DESI MS experiments were performed to understand the lipid profiles of different cells. Positive mode DESI MS spectra of MIO-M1, MCF-7, and WERI-RB1 cell lines are shown in Fig. 2. All the mass spectra were recorded between m/z 700 and 900 as this region exhibited intense lipid peaks. The lipids were identified by tandem DESI MS experiments and using database (www.lipidmaps.org) as reference. MS/MS data of

Fig. 1 Expression of PLK1 gene in (A) MIO-M1, (B) MCF-7, and (C) WERI-RB1 when they were untreated (1) and treated with EpDT3 (2), Scr-EpDT3 (3), siPLK1 (4), siScr (5), EpDT3-siPLK1 (6), and EpDT3-siScr (7). Expression of PLK1 protein in (D) MCF-7 and (E) WERI-RB1 when they were untreated (1) and treated with EpDT3 (2), siPLK1 (3), siScr (4), EpDT3-siPLK1 (5), and EpDT3-siScr (6). * $P < 0.05$ compared to untreated

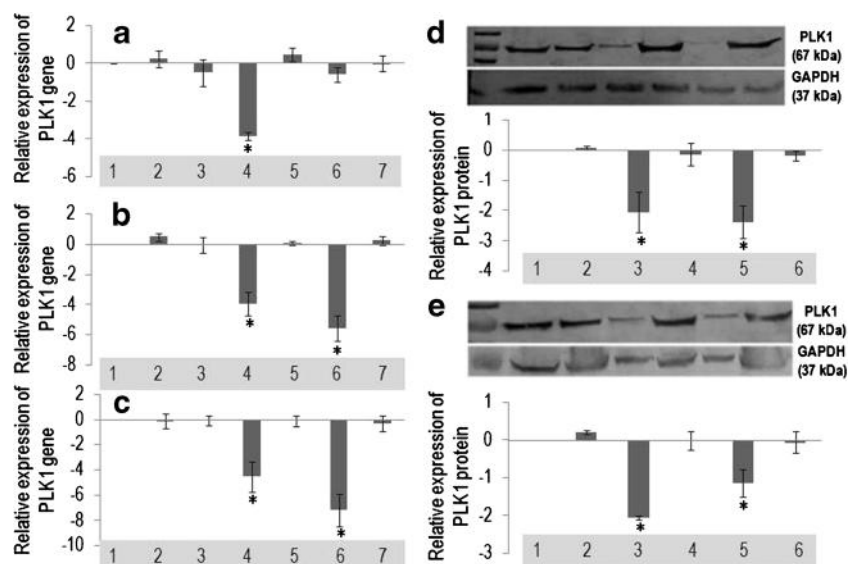
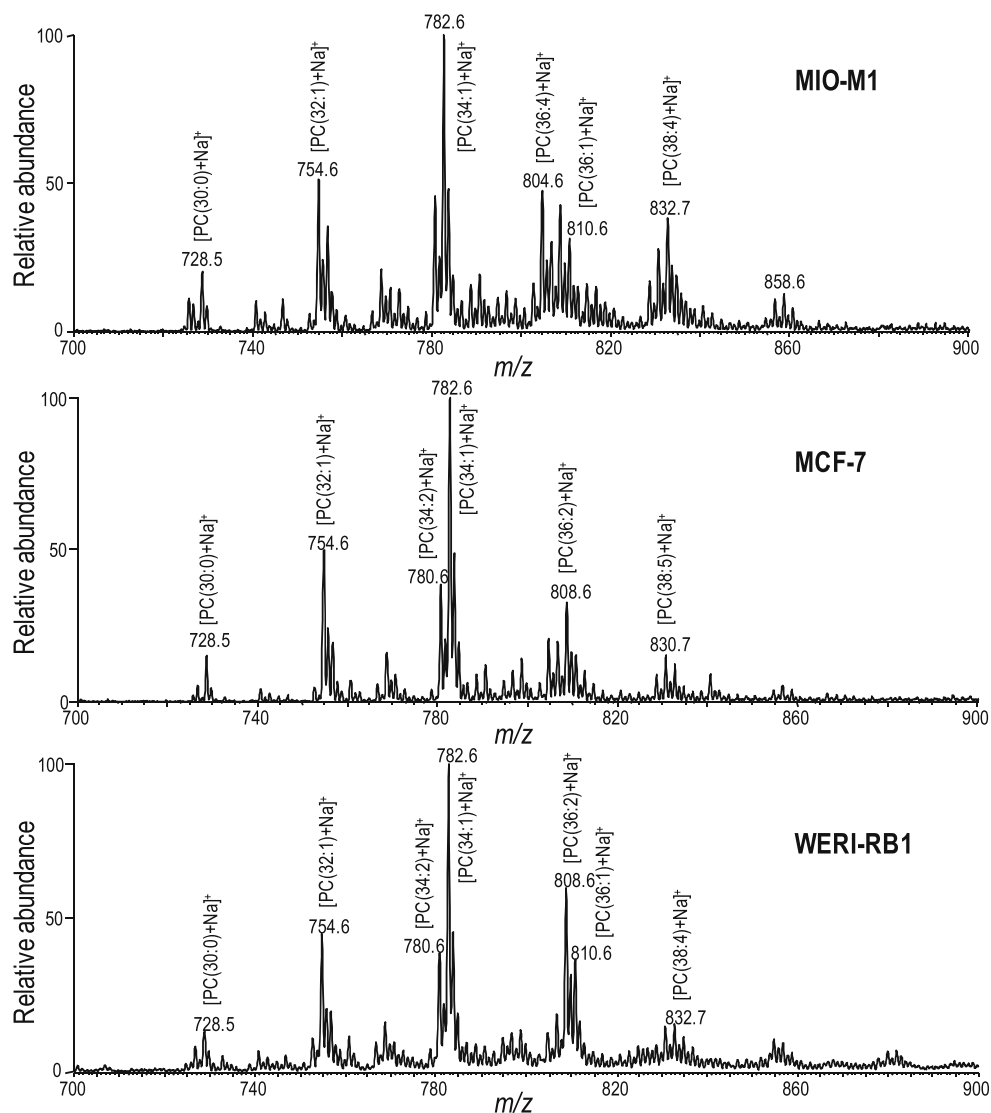


Fig. 2 Positive mode DESI MS spectra of MIO-M1, MCF-7, and WERI-RB1 cell lines from Whatman 42 filter paper



three major peaks (m/z 754.6, m/z 782.6, and m/z 808.6) from MCF-7 cell line are shown in ESM Fig. S5. All the three spectra show characteristic losses of 59 and 183 Da indicating the species as phosphatidylcholines. The highly abundant lipids (m/z 754.6, m/z 782.6, and m/z 808.6) from both the cancer cell lines (MCF-7 and WERI-RB1) were chosen and their intensities were compared with a normal cell line, MIO-M1. Figure 3 shows the comparison of the ion intensities of the lipids between MIO-M1/MCF-7 and MIO-M1/WERI-RB1 pairs. In both the cases, these lipids were highly expressed in tumor cells than the normal cells. When compared to MIO-M1, the relative expressions of the lipids were much higher in WERI-RB1 than in MCF-7. Figures S6 and S7 in the ESM show comparisons of several other lipids between MIO-M1/MCF-7 and MIO-M1/WERI-RB1 pairs, respectively. However, all these minor peaks did not show upregulation in cancer cells compared to normal cell. A few minor peaks were upregulated in MIO-M1 cells compared to cancer cells

(ESM, Figs. S6 and S7). It is noteworthy to mention at this point that a simple spot sampling could have been done to get similar information instead of DESI MS imaging experiments. However, we have chosen DESI MS imaging over spot sampling due to the fact that in an imaging experiment, sampling is more uniform than a spot sampling experiment. Moreover, images provide better visualization of data for comparison and that too considering the whole sample. Furthermore, as we had not used any internal standards in our experiments and DESI MS is a semi-quantitative technique, comparisons between samples were made from images on a semi-quantitative basis. Besides, use of such standards has inherent problem in this situation as sampled lipids are part of the cell structure while reference samples added are loosely bound and are therefore easier to desorb from surface.

In MYC-induced mouse lymphoma samples, it was shown earlier by DESI MS that some lipids had increased abundances while some had decreased abundances [42]. In another

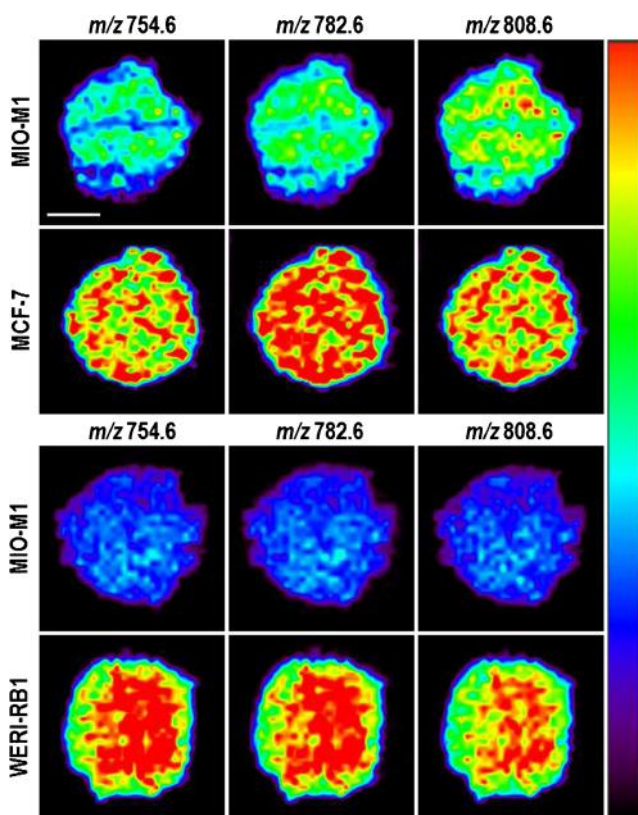


Fig. 3 DESI MS images of different lipids from MIO-M1/MCF-7 and MIO-M1/WERI-RB1 cell lines. *Scale bar* of 2 mm applies to all the images. Intensity is color coded, from *black* (low) to *red* (high)

study, using 2D liquid chromatography-mass spectrometry method, two phosphatidylinositol (PI) lipids, PI(16:0/16:1) and PI(18:0/20:4), were identified as potential biomarkers to differentiate benign and malignant breast tumors [43]. Phosphatidylcholines had been proposed as possible biomarkers using ultra performance liquid chromatography electrospray ionization time-of-flight mass spectrometry (UPLC-ESI-TOF-MS) in esophageal squamous cell carcinoma [44]. Here, in our study, the cancer cell-specific phosphatidylcholine lipids have been identified using the rapid method of DESI MS with minimum sample preparation. The change in the abundances of phosphatidylcholines on the cancer cell surface compared to normal cell surface could be due to altered lipid synthesis/degradation mechanism.

Effect of targeted delivery of EpDT3-siPLK1 was manifested in the surface lipid profiles of cancer cell lines and it was monitored by DESI MS. Figures 4 and 5 show the DESI MS images of MCF-7 and WERI-RB1 cells, respectively, in different treatment conditions. It was found that the major peaks at m/z 754.6, m/z 782.6, and m/z 808.6 that showed upregulation in both the cancer cell lines compared to the normal cell line were downregulated when treated with both siPLK1 and EpDT3-siPLK1. In MCF-7 cells, the differences in the intensity reduction between Lipofectamine-transfected siRNA and

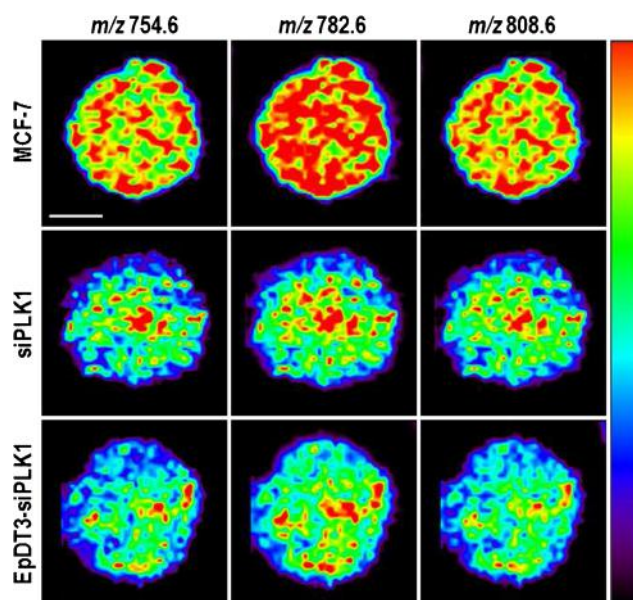


Fig. 4 DESI MS images of different lipids from MCF-7 cells with different treatment conditions. *Scale bar* of 2 mm applies to all the images. Intensity is color coded, from *black* (low) to *red* (high)

aptamer-mediated siRNA were almost the same (Fig. 4). Since most of the MCF-7 cells express EpCAM, equal reduction explains the fact that the siRNA delivered by EpDT3-siPLK1 was almost similar to that delivered by Lipofectamine. However, in the WERI-RB1 cells, the magnitudes of the decrease in the intensities of the lipids were not the same for siPLK1 and EpDT3-siPLK1-treated cells (Fig. 5). The untargeted siPLK1 caused reduction in entire cellular population resulting in much lowered cell

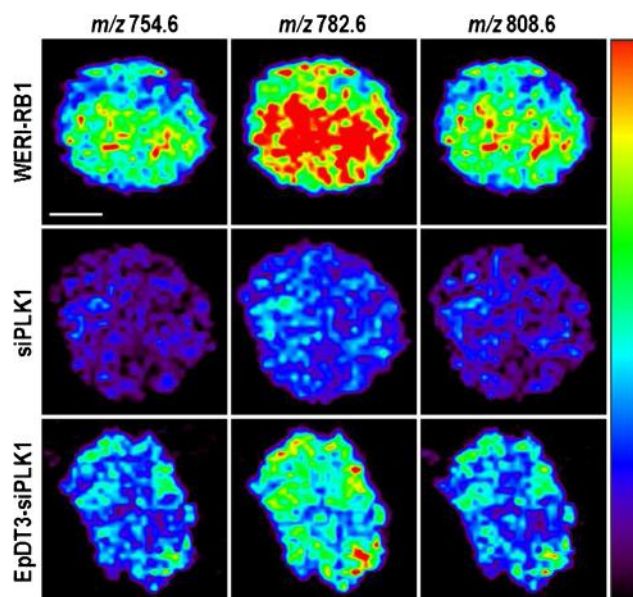


Fig. 5 DESI MS images of different lipids from WERI-RB1 cells with different treatment conditions. *Scale bar* of 2 mm applies to all the images. Intensity is color coded, from *black* (low) to *red* (high)

surface lipids. In WERI-RB1, the EpCAM is expressed in 41 % cells. Therefore, when treated with EpDT3-siPLK1, the intensity reduction of the lipids was minimal when compared to siPLK1 treatment alone. Figures S8 and S9 in the ESM show DESI MS images of few other lipids from MCF-7 and WERI-RB1 cell lines, respectively, when they were treated with siPLK1 and EpDT3-siPLK1. The same trend of major peaks was also observed for minor peaks, although all these minor peaks did not show upregulation in cancer cells compared to normal cells (ESM, Figs. S6 and S7).

The reduction in PLK1 gene expression reduced the lipid expression, phosphatidylcholines in particular, suggesting a novel functional role of PLK1 in lipid synthesis/degradation in addition to its role in mitotic spindle formation, cellular proliferation, cell migration, and cell death. To identify the genes regulated by PLK1, whole genome microarray analysis was done in MCF-7 cells (ESM Fig. S10). We found changes in 2380 genes compared to the control. However, 254 genes showed fold change differences of 2. 143 genes were downregulated and 111 genes were upregulated (ESM Table S1). We did not find variation in genes related to phosphatidylcholine synthesis. However, upregulation of PLA2G4C which are involved in phosphatidylcholine degradation accounts for decreased phosphatidylcholines after the treatment of EpDT3-siPLK1. Previously, an altered choline metabolism with increased expression of choline synthesizing pathway enzymes such as choline kinase and decreased expression of lipid degradation pathway enzymes including phospholipase A2 was observed in breast cancer cell line compared to normal cell line [4]. In our study, aptamer therapy is manifested by decreased phosphatidylcholines and observed by rapid method of DESI MS indicating suitability of DESI MS for rapid drug screening and therapy response.

Increased cell death is indicative of therapy by EpDT3-siPLK1

To confirm the cytotoxic effect due to the targeted delivery by EpDT3-siPLK1 on cancer cells, MTT assay was performed. The results showed that the aptamer drug treatment increased cell death in both MCF-7 and WERI-RB1 cells (ESM Fig. S11), indicating the potential application of this aptamer chimera for targeted drug delivery. The global gene expression regulated by aptamer chimera treatment was performed to understand the changes accompanying cancer cell death in MCF-7 cells. A reduction in oncogenes such as PLK1 and NRAS has been observed (ESM Table S1). The Gene Ontology analysis by GeneSpring software for the genes dysregulated by 2 folds has revealed processes associated with

macromolecule metabolism, cellular metabolism, cell death, apoptosis, centromere complex assembly, DNA conformation change, chromatin assembly, and phosphatidylinositol-mediated signalling altered by depleted PLK1 (ESM Table S2). PLK1 downregulation has increased processes related to apoptosis and cell death accounting for observed increased cell death by EpDT3-siPLK1. The degradation products of lipids such as phosphatidylinositol and ceramide (signalling lipids) are known to play a role in cellular apoptosis and proliferation pathways [45]. The mechanism of lipid degradation by the aptamer chimera treatment to trigger apoptosis is currently under investigation.

Conclusions

In summary, an EpCAM aptamer chimera, EpDT3-siPLK1, was used for targeted drug delivery in MCF-7 and WERI-RB1 cells. It bounds more efficiently with highly EpCAM-expressing MCF-7 cells than WERI-RB1 cells where EpCAM expression is less. PLK1 gene expression and corresponding protein levels were reduced by the action of the chimera. DESI MS showed that surface lipids of the cells were also affected by aptamer chimera treatment suggesting novel role of PLK1 in regulating lipids in the cells. This approach of surface lipid profiling of treated cells described herein can be a prospective new method to identify new biomarkers for rapid drug screening.

Acknowledgments This work was supported by the Department of Biotechnology, Government of India (Grant no. NO.BT/PR3580/PID/6/625/2011) and the Department of Science and Technology, Government of India. A.S. thanks the Council of Scientific and Industrial Research, Government of India and Indian Institute of Technology Madras for fellowships. The authors also thank Dr. Nithya Subramanian, Ms. Srilatha Jasty, and Ms. Lakshmi for their help and suggestions.

Compliance with ethical standards

Conflict of interest The authors declare that they have no conflict of interest.

References

1. Beljebbar A, Dukic S, Amharref N, Bellefqih S, Manfait M. Monitoring of biochemical changes through the C6 gliomas progression and invasion by Fourier transform infrared (FTIR) imaging. *Anal Chem.* 2009;81:9247–56.
2. Shimma S, Sugiura Y, Hayasaka T, Hoshikawa Y, Noda T, Setou M. MALDI-based imaging mass spectrometry revealed abnormal distribution of phospholipids in colon cancer liver metastasis. *J Chromatogr B.* 2007;855:98–103.

3. Ackerstaff E, Glunde K, Bhujwala ZM. Choline phospholipid metabolism: a target in cancer cells? *J Cell Biochem.* 2003;90:525–33.
4. Glunde K, Jie C, Bhujwala ZM. Molecular causes of the aberrant choline phospholipid metabolism in breast cancer. *Cancer Res.* 2004;64:4270–6.
5. Gillies RJ, Morse DL. In vivo magnetic resonance spectroscopy in cancer. *Annu Rev Biomed Eng.* 2005;7:287–326.
6. Glunde K, Artemov D, Penet M-F, Jacobs MA, Bhujwala ZM. Magnetic resonance spectroscopy in metabolic and molecular imaging and diagnosis of cancer. *Chem Rev.* 2010;110:3043–59.
7. Monge ME, Harris GA, Dwivedi P, Fernandez FM. Mass spectrometry: recent advances in direct open air surface sampling/ionization. *Chem Rev.* 2013;113:2269–308.
8. Takats Z, Wiseman JM, Gologan B, Cooks RG. Mass spectrometry sampling under ambient conditions with desorption electrospray ionization. *Science.* 2004;306:471–3.
9. Pasilis SP, Kertesz V, Van Berkel GJ, Schulz M, Schorch S. HPTLC/DESI-MS imaging of tryptic protein digests separated in two dimensions. *J Mass Spectrom.* 2008;43:1627–35.
10. Chipuk JE, Gelb MH, Brodbelt JS. Rapid and selective screening for sulfhydryl analytes in plasma and urine using surface-enhanced transmission mode desorption electrospray ionization mass spectrometry. *Anal Chem.* 2010;82:4130–9.
11. Wiseman JM, Ifa DR, Venter A, Cooks RG. Ambient molecular imaging by desorption electrospray ionization mass spectrometry. *Nat Protoc.* 2008;3:517–24.
12. Vismeh R, Waldon DJ, Teffera Y, Zhao Z. Localization and quantification of drugs in animal tissues by use of desorption electrospray ionization mass spectrometry imaging. *Anal Chem.* 2012;84:5439–45.
13. Eberlin LS, Norton I, Orringer D, Dunn IF, Liu X, Ide JL, et al. Ambient mass spectrometry for the intraoperative molecular diagnosis of human brain tumors. *Proc Natl Acad Sci U S A.* 2013;110:1611–6.
14. Eberlin LS, Tibshirani RJ, Zhang J, Longacre TA, Berry GJ, Bingham DB, et al. Molecular assessment of surgical-resection margins of gastric cancer by mass-spectrometric imaging. *Proc Natl Acad Sci U S A.* 2014;111:2436–41.
15. Srimany A, Ifa DR, Naik HR, Bhat V, Cooks RG, Pradeep T. Direct analysis of camptothecin from *Nothapodytes nimmoniana* by desorption electrospray ionization mass spectrometry (DESI-MS). *Analyst.* 2011;136:3066–8.
16. Ifa DR, Srimany A, Eberlin LS, Naik HR, Bhat V, Cooks RG, et al. Tissue imprint imaging by desorption electrospray ionization mass spectrometry. *Anal Methods.* 2011;3:1910–2.
17. Mohana Kumara P, Srimany A, Ravikanth G, Uma Shaanker R, Pradeep T. Ambient ionization mass spectrometry imaging of rohitukine, a chromone anti-cancer alkaloid, during seed development in *Dysoxylum binectariferum* Hook.f (Meliaceae). *Phytochemistry.* 2015;116:104–10.
18. Hemalatha RG, Pradeep T. Understanding the molecular signatures in leaves and flowers by desorption electrospray ionization mass spectrometry (DESI MS) imaging. *J Agric Food Chem.* 2013;61:7477–87.
19. Glover DM, Hagan IM, Tavares ÁAM. Polo-like kinases: a team that plays throughout mitosis. *Gene Dev.* 1998;12:3777–87.
20. Glover DM, Ohkura H, Tavares A. Polo kinase: the choreographer of the mitotic stage? *J Cell Biol.* 1996;135:1681–4.
21. Nigg EA, Blangy A, Lane HA. Dynamic changes in nuclear architecture during mitosis: on the role of protein phosphorylation in spindle assembly and chromosome segregation. *Exp Cell Res.* 1996;229:174–80.
22. Kumagai A, Dunphy WG. Purification and molecular cloning of Plx1, a Cdc25-regulatory kinase from *Xenopus* egg extracts. *Science.* 1996;273:1377–80.
23. Nigg EA. Polo-like kinases: positive regulators of cell division from start to finish. *Curr Opin Cell Biol.* 1998;10:776–83.
24. Cunningham JT, Ruggero D. New connections between old pathways: PDK1 signaling promotes cellular transformation through PLK1-dependent MYC stabilization. *Cancer Discov.* 2013;3:1099–102.
25. Wang G, Chen Q, Zhang X, Zhang B, Zhuo X, Liu J, et al. PCM1 recruits Plk1 to the pericentriolar matrix to promote primary cilia disassembly before mitotic entry. *J Cell Sci.* 2013;126:1355–65.
26. Cholewa BD, Liu X, Ahmad N. The role of polo-like kinase 1 in carcinogenesis: cause or consequence? *Cancer Res.* 2013;73:6848–55.
27. Bholra NE, Jansen VM, Bafna S, Giltman JM, Balko JM, Estrada MV, et al. Kinome-wide functional screen identifies role of PLK1 in hormone-independent, ER-positive breast cancer. *Cancer Res.* 2015;75:405–14.
28. Zhang Z, Hou X, Shao C, Li J, Cheng J-X, Kuang S, et al. Plk1 inhibition enhances the efficacy of androgen signaling blockade in castration-resistant prostate cancer. *Cancer Res.* 2014;74:6635–47.
29. Denholt CL, Hansen PR, Pedersen N, Poulsen HS, Gillings N, Kjær A. Identification of novel peptide ligands for the cancer-specific receptor mutation EFGFRvIII using a mixture-based synthetic combinatorial library. *Biopolymers.* 2009;91:201–6.
30. Kim M, Shin D-S, Kim J, Lee Y-S. Substrate screening of protein kinases: detection methods and combinatorial peptide libraries. *Biopolymers.* 2010;94:753–62.
31. Li J, Tan S, Chen X, Zhang CY, Zhang Y. Peptide aptamers with biological and therapeutic applications. *Curr Med Chem.* 2011;18:4215–22.
32. Pirogova E, Istivan T, Gan E, Cosic I. Advances in methods for therapeutic peptide discovery, design and development. *Curr Pharm Biotechnol.* 2011;12:1117–27.
33. Aina OH, Liu R, Sutcliffe JL, Marik J, Pan C-X, Lam KS. From combinatorial chemistry to cancer-targeting peptides. *Mol Pharmaceutics.* 2007;4:631–51.
34. Zhu Z, Song Y, Li C, Zou Y, Zhu L, An Y, et al. Monoclonal surface display SELEX for simple, rapid, efficient, and cost-effective aptamer enrichment and identification. *Anal Chem.* 2014;86:5881–8.
35. Subramanian N, Raghunathan V, Kanwar JR, Kanwar RK, Elchuri SV, Khetan V, et al. Target-specific delivery of doxorubicin to retinoblastoma using epithelial cell adhesion molecule aptamer. *Mol Vis.* 2012;18:2783–95.
36. Gilboa-Geffen A, Hamar P, Le MTN, Wheeler LA, Trifonova R, Petrocca F, et al. Gene knockdown by EpCAM aptamer-siRNA chimeras suppresses epithelial breast cancers and their tumor-initiating cells. *Mol Cancer Ther.* 2015;14:2279–91.
37. Srimany A, Jayashree B, Krishnakumar S, Elchuri S, Pradeep T. Identification of effective substrates for the direct analysis of lipids from cell lines using desorption electrospray ionization mass spectrometry. *Rapid Commun Mass Spectrom.* 2015;29:349–56.
38. Dassie JP, Liu XY, Thomas GS, Whitaker RM, Thiel KW, Stockdale KR, et al. Systemic administration of optimized aptamer-siRNA chimeras promotes regression of PSMA-expressing tumors. *Nat Biotechnol.* 2009;27:839–49.
39. Subramanian N, Kanwar JR, Athalya PK, Janakiraman N, Khetan V, Kanwar RK, et al. EpCAM aptamer mediated cancer cell specific delivery of EpCAM siRNA using polymeric nanocomplex. *J Biomed Sci.* 2015;22:4.
40. Liu HY, Gao X. A universal protein tag for delivery of siRNA-aptamer chimeras. *Sci Rep.* 2013;3:3129.
41. Zhou J, Tiemann K, Chomchan P, Alluin J, Swiderski P, Burnett J, et al. Dual functional BAFF receptor aptamers inhibit ligand-induced proliferation and deliver siRNAs to NHL cells. *Nucleic Acids Res.* 2013;41:4266–83.

42. Eberlin LS, Gabay M, Fan AC, Gouw AM, Tibshirani RJ, Felsher DW, et al. Alteration of the lipid profile in lymphomas induced by MYC overexpression. *Proc Natl Acad Sci U S A*. 2014;111:10450–5.
43. Yang L, Cui X, Zhang N, Li M, Bai Y, Han X, et al. Comprehensive lipid profiling of plasma in patients with benign breast tumor and breast cancer reveals novel biomarkers. *Anal Bioanal Chem*. 2015;407:5065–77.
44. Liu R, Peng Y, Li X, Wang Y, Pan E, Guo W, et al. Identification of plasma metabolomic profiling for diagnosis of esophageal squamous-cell carcinoma using an UPLC/TOF/MS platform. *Int J Mol Sci*. 2013;14:8899–911.
45. Huang C, Freter C. Lipid metabolism, apoptosis and cancer therapy. *Int J Mol Sci*. 2015;16:924–49.

Analytical and Bioanalytical Chemistry

Electronic Supplementary Material

Monitoring of changes in lipid profiles during PLK1 knockdown in cancer cells using DESI MS

Balasubramanyam Jayashree, Amitava Srimany, Srinidhi Jayaraman, Anjali Bhutra,
Narayanan Janakiraman, Srujana Chitipothu, Subramanian Krishnakumar, Lakshmi Subhadra
Baddireddi, Sailaja Elchuri, Thalappil Pradeep

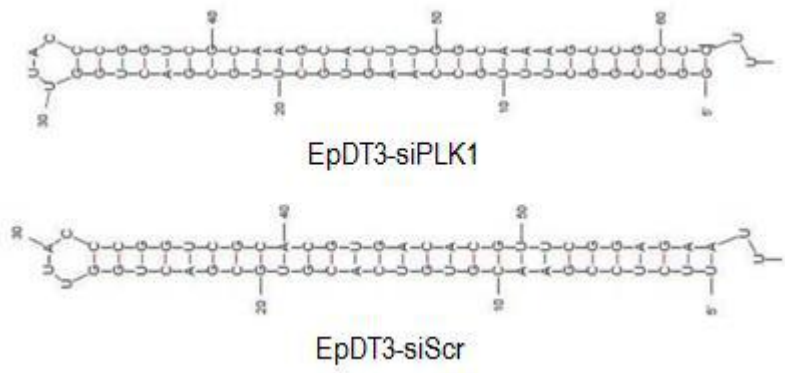


Fig. S1 Secondary structure of EpDT3-siPLK1 and EpDT3-siScr

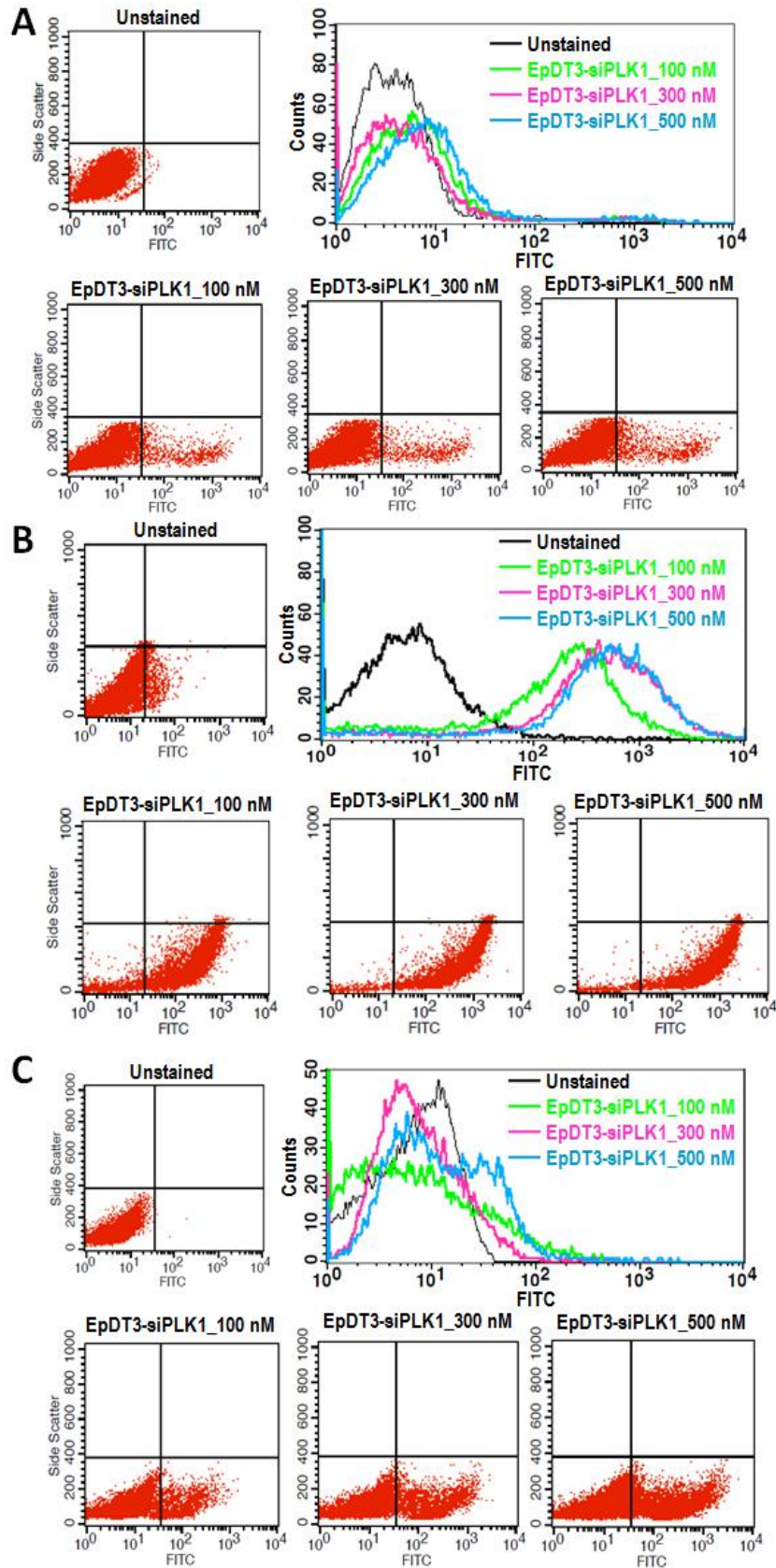


Fig. S2 Histogram overlay plots and side scatter plots of (A) MIO-M1, (B) MCF-7, and (C) WERI-RB1 cells in unstained conditions and after treating with different concentrations of EpDT3-siPLK1 chimera

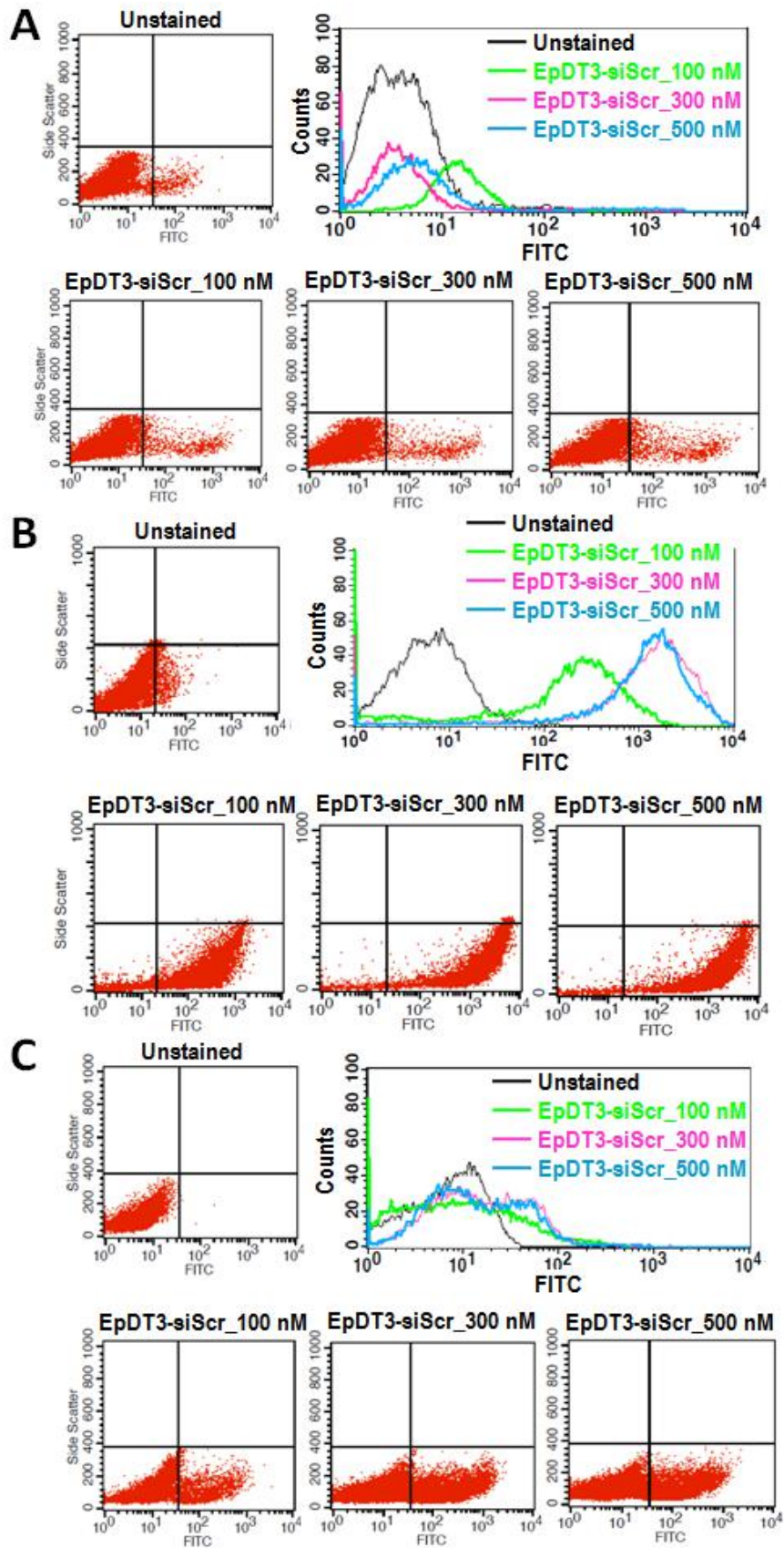


Fig. S3 Histogram overlay plots and side scatter plots of (A) MIO-M1, (B) MCF-7, and (C) WERI-RB1 cells in unstained conditions and after treating with different concentrations of EpDT3-siScr chimera

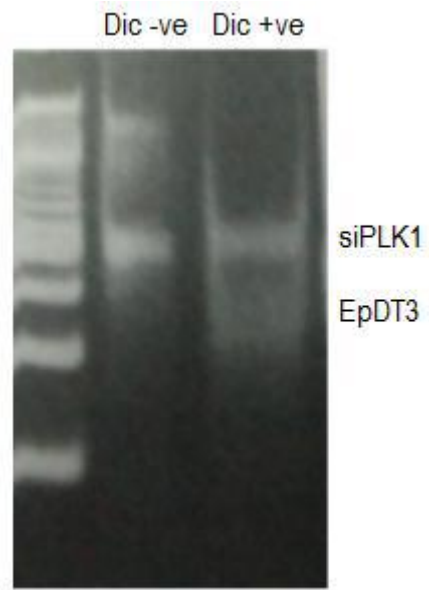


Fig. S4 PAGE data showing bands of siPLK1 and EpDT3

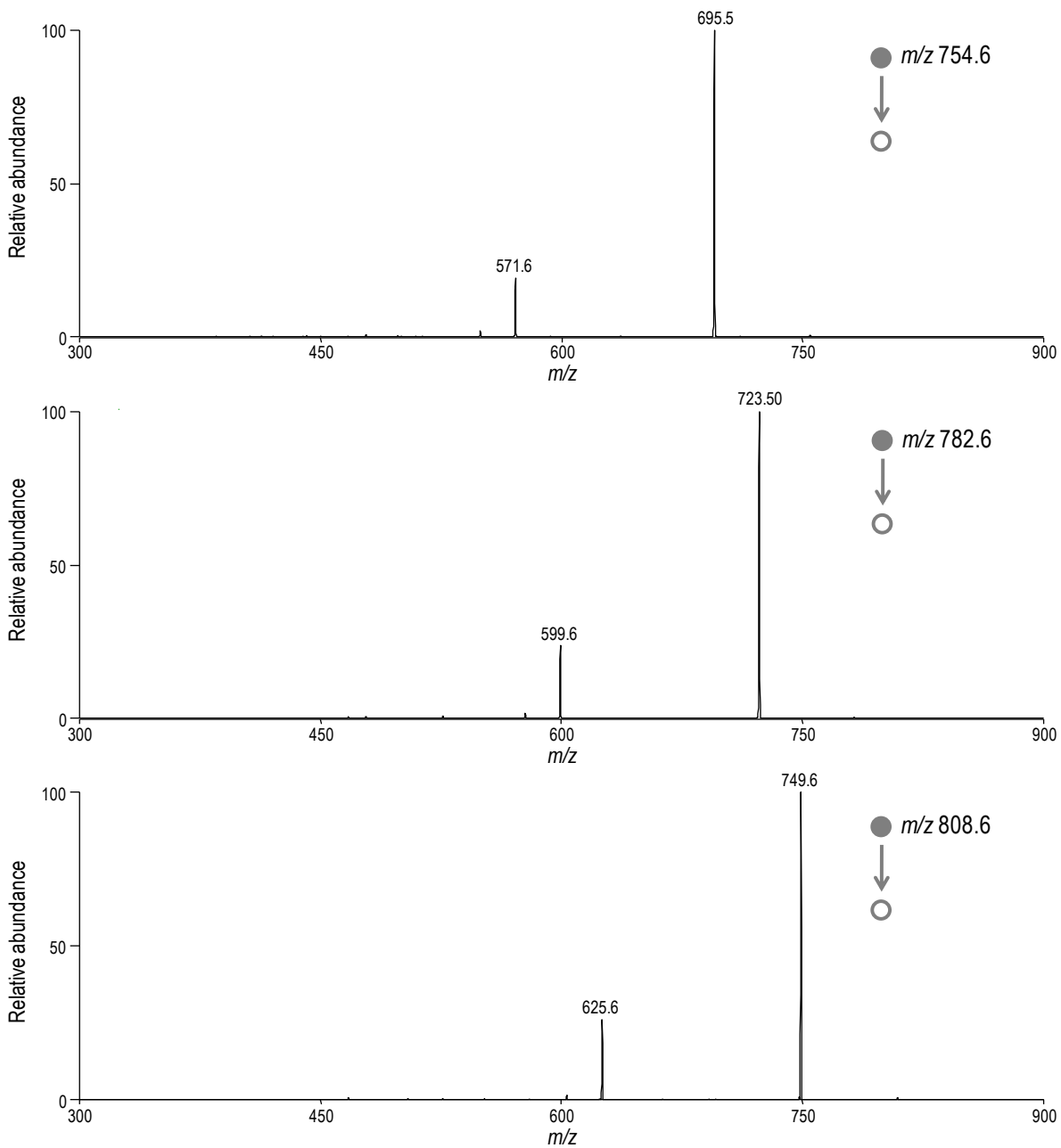


Fig. S5 Positive mode DESI MS/MS spectra of m/z 754.6, m/z 782.6, and m/z 808.6 from MCF-7 cells

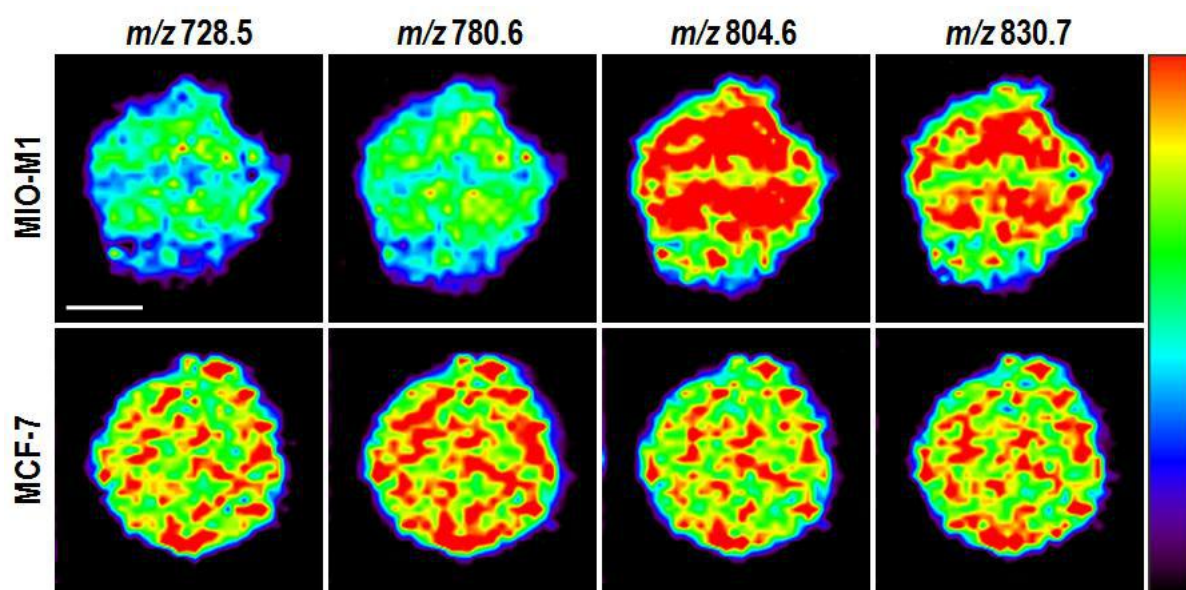


Fig. S6 DESI MS images of different lipids from MIO-M1 and MCF-7 cell lines. Scale bar of 2 mm applies to all the images. Intensity is color coded; from black (low) to red (high)

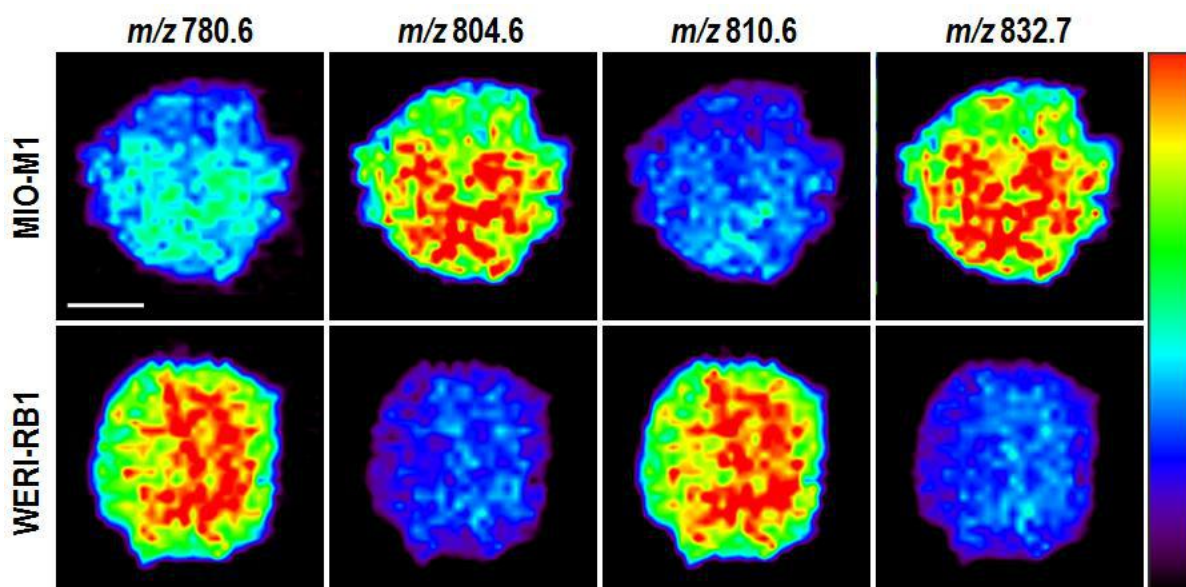


Fig. S7 DESI MS images of different lipids from MIO-M1 and WERI-RB1 cell lines. Scale bar of 2 mm applies to all the images. Intensity is color coded; from black (low) to red (high)

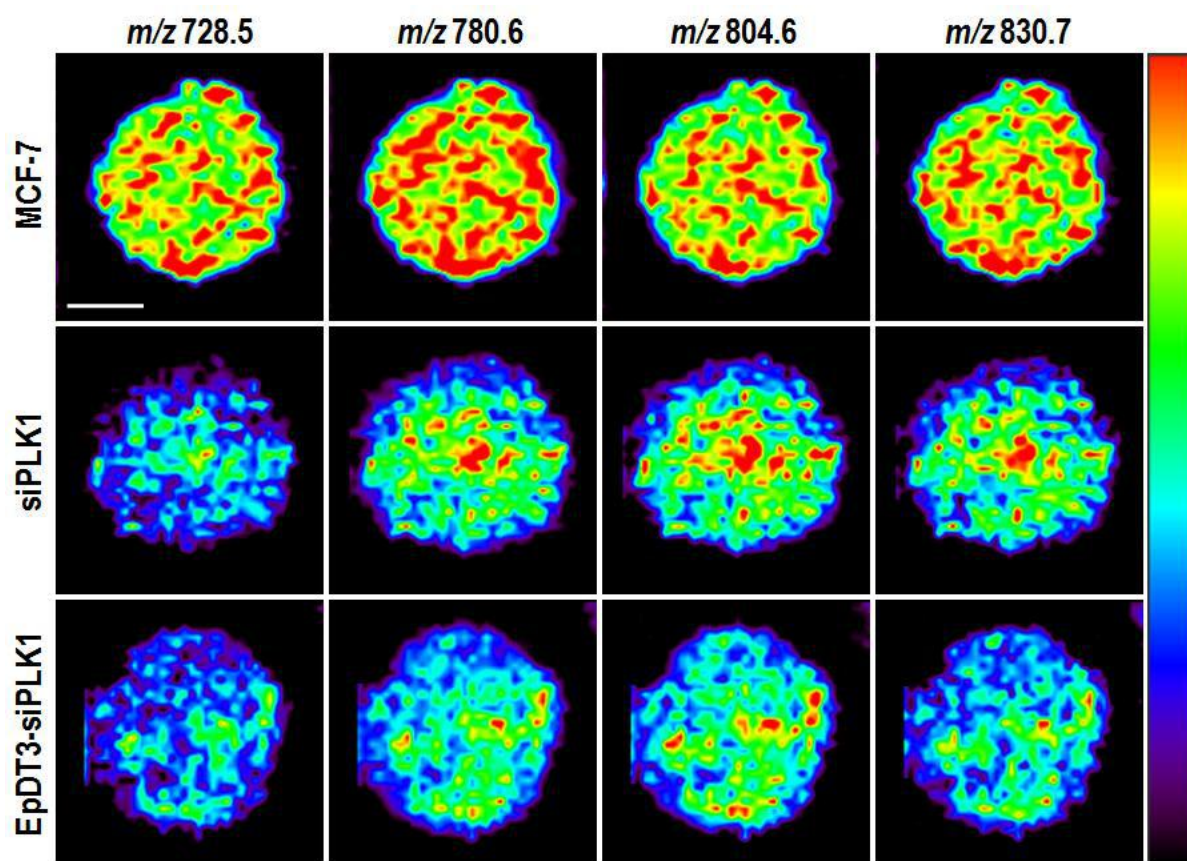


Fig. S8 DESI MS images of different lipids from MCF-7 cells with different treatment conditions. Scale bar of 2 mm applies to all the images. Intensity is color coded; from black (low) to red (high)

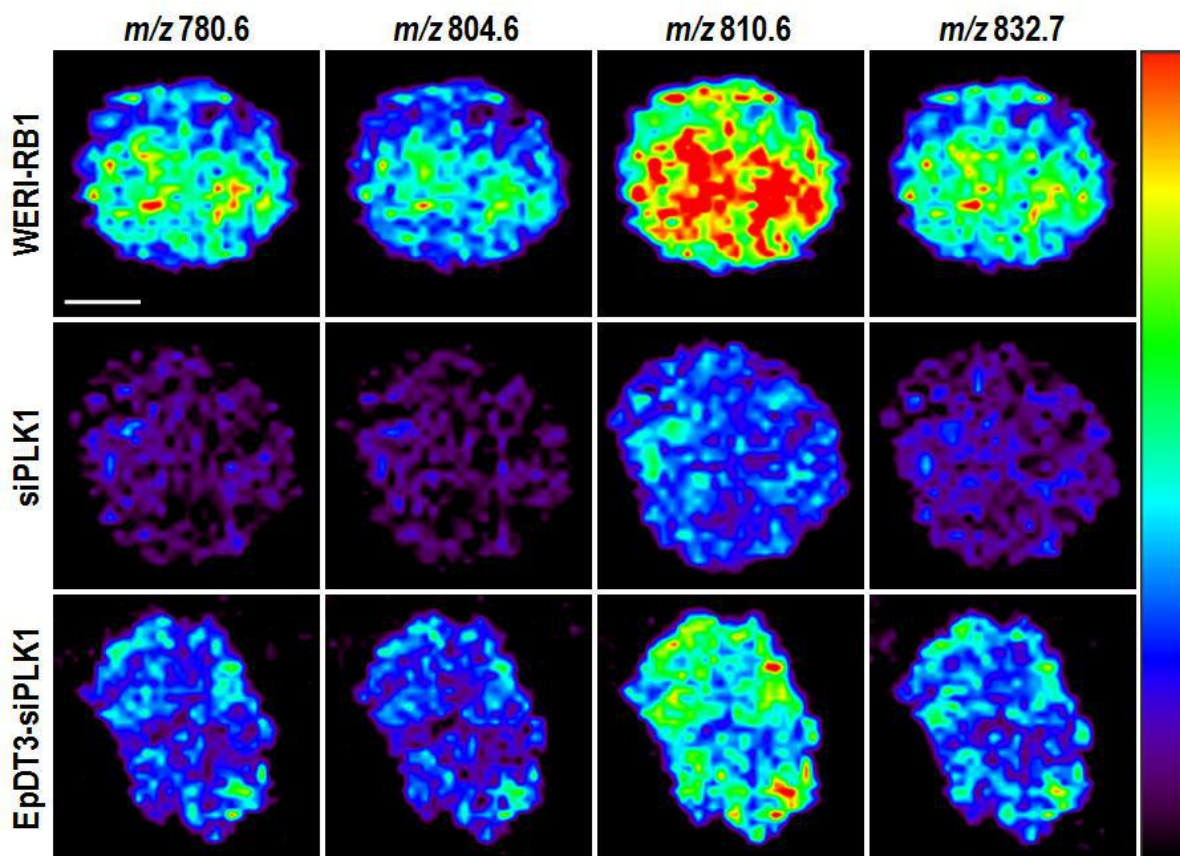


Fig. S9 DESI MS images of different lipids from WERI-RB1 cells with different treatment conditions. Scale bar of 2 mm applies to all the images. Intensity is color coded; from black (low) to red (high)

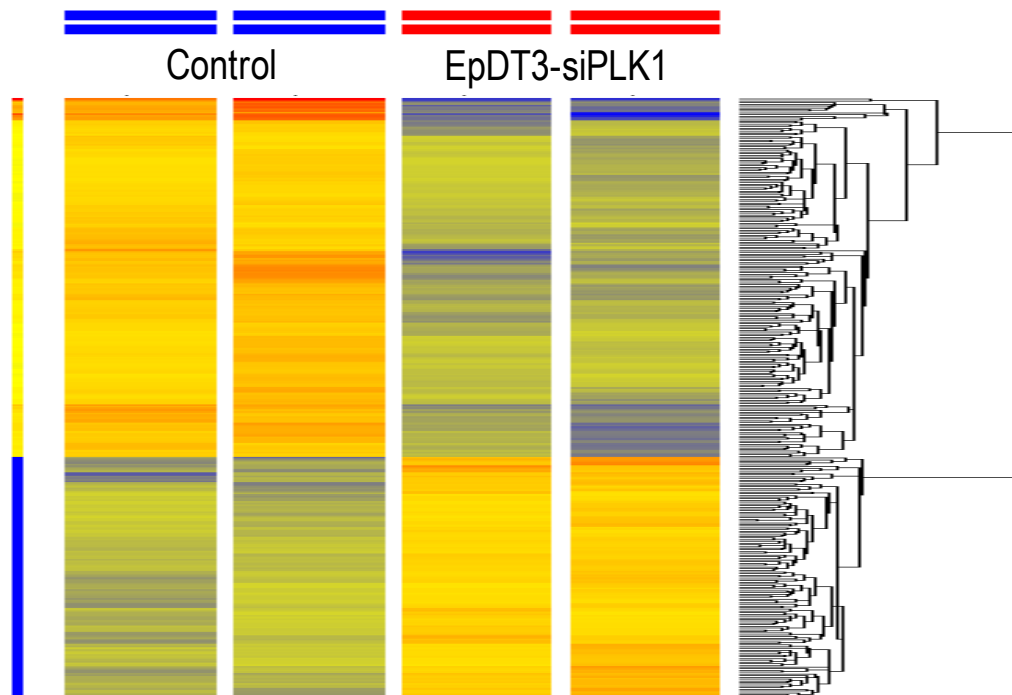


Fig. S10 Whole genome microarray analysis of MCF-7 cells. Hierarchical clustering reveals that control cells (N=2) are different from EpDT3-siPLK1 treated cells (N=2)

Sl. no.	Gene	Gene symbol	Type of change	Fold regulation
1	Dual specificity phosphatase 10	DUSP10	Up	2.5
2	Fatty acyl-CoA reductase 2	FAR2	Up	2.1
3	cAMP responsive element binding protein 3-like 2	CREB3L2	Up	2.0
4	NADH dehydrogenase (ubiquinone) Fe-S protein 2, 49kDa (NADH-coenzyme Q reductase)	NDUFS2	Up	2.0
5	Phospholipase A2, group IVC (cytosolic, calcium-independent)	PLA2G4C	Up	2.0
6	Protein kinase, AMP-activated, alpha 1 catalytic subunit	PRKAA1	Up	2.0
7	Kruppel-like factor 7 (ubiquitous)	KLF7	Down	18.6
8	Cyclin-dependent kinase inhibitor 1A (p21, Cip1)	CDKN1A	Down	13.0
9	Ras-related C3 botulinum toxin substrate 1 (rho family, small GTP binding protein Rac1)	RAC1	Down	9.1
10	Fas associated factor family member 2	FAF2	Down	5.1
11	Polo-like kinase 1	PLK1	Down	4.2
12	Neuroblastoma RAS viral (V-ras) oncogene homolog	NRAS	Down	3.3

Table S1 Partial list of genes and gene expression changes dysregulated by EpDT3-siPLK1 treatment in MCF-7 cells

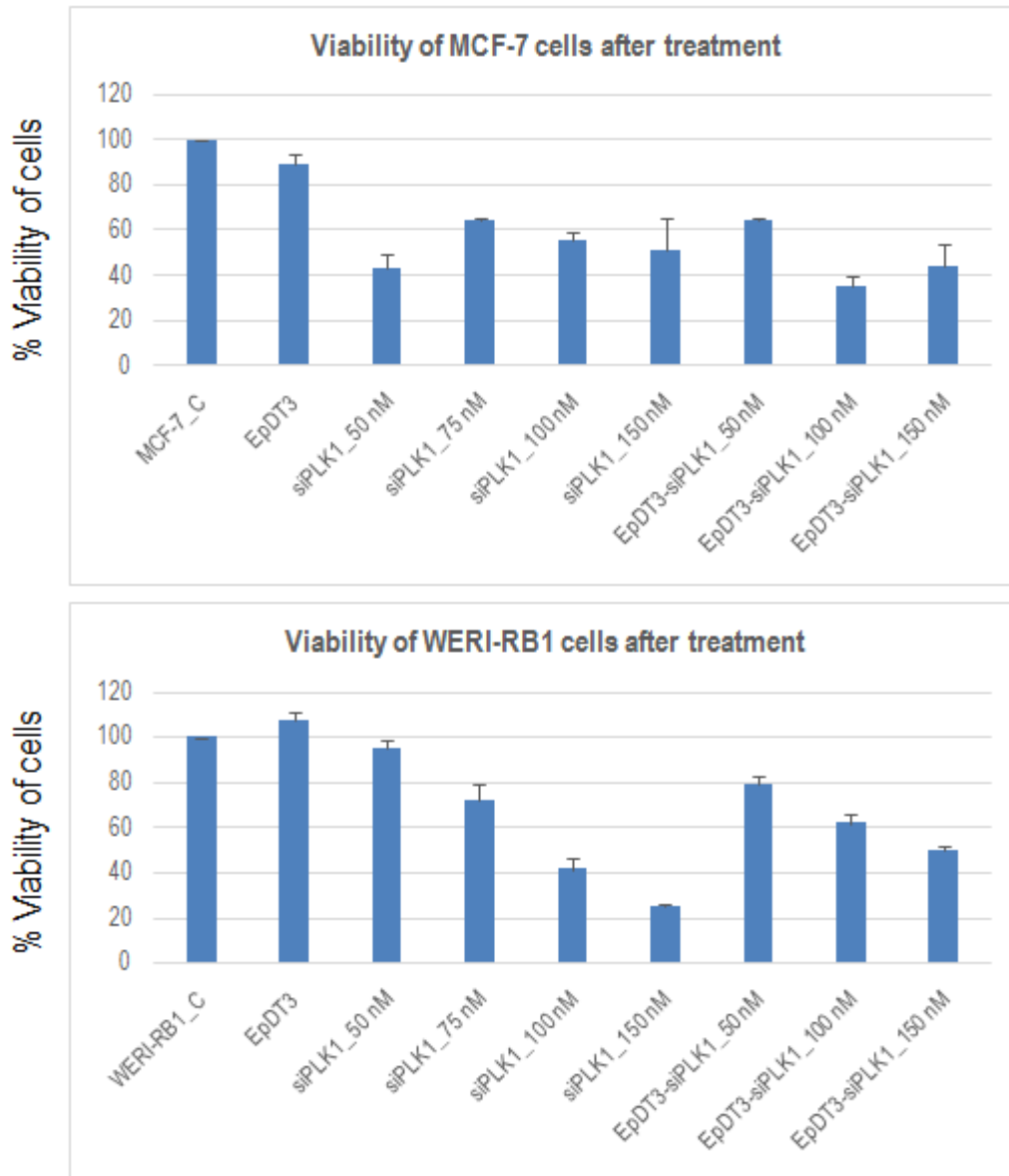


Fig. S11 Cell viability of MCF-7 (top) and WERI-RB1 (bottom) cells when they were treated with EpDT3, different concentrations of siPLK1, and EpDT3-siPLK1

GO process	P-value	No. of hits
Intracellular	1.81E-11	275
Cellular macromolecule metabolic process	1.44E-05	145
Positive regulation of cellular metabolic process	1.44E-05	63
Death	4.32E-06	44
Apoptotic process	4.04E-05	37
Regulation of cell cycle	4.47E-06	31
DNA conformation change	2.30E-08	20
Chromatin assembly	3.10E-11	19
Phosphatidylinositol mediated signalling	2.39E-12	17
Centromere complex assembly	9.19E-16	15
Cell cycle arrest	1.83E-04	10
Glycosylceramide catabolic process	2.74E-04	3
Sphingoid biosynthetic process	4.05E-04	3

Table S2 Gene Ontology processes regulated by PLK1 knockdown in MCF-7 cells

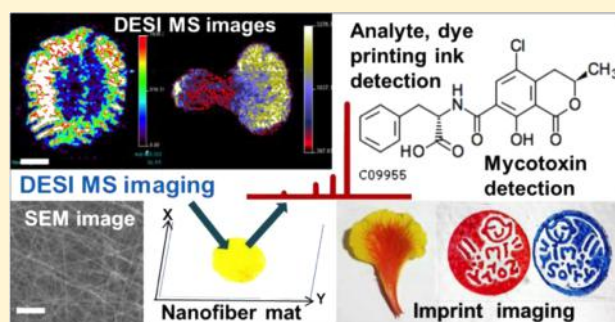
Electrospun Nanofiber Mats as “Smart Surfaces” for Desorption Electrospray Ionization Mass Spectrometry (DESI MS)-Based Analysis and Imprint Imaging

R. G. Hemalatha, Mohd Azhardin Ganayee, and T. Pradeep*

DST Unit on Nanoscience and Thematic Unit of Excellence, Department of Chemistry, Indian Institute of Technology Madras, Chennai 600 036, India

Supporting Information

ABSTRACT: In this paper, desorption electrospray ionization mass spectrometry (DESI MS)-based molecular analysis and imprint imaging using electrospun nylon-6 nanofiber mats are demonstrated for various analytical contexts. Uniform mats of varying thicknesses composed of ~200 nm diameter fibers were prepared using needleless electrospinning. Analytical applications requiring rapid understanding of the analytes in single drops, dyes, inks, and/or plant extracts incorporated directly into the nanofibers are discussed with illustrations. The possibility to imprint patterns made of printing inks, plant parts (such as petals, leaves, and slices of rhizomes), and fungal growth on fruits with their faithful reproductions on the nanofiber mats is illustrated with suitable examples. Metabolites were identified by tandem mass spectrometry data available in the literature and in databases. The results highlight the significance of electrospun nanofiber mats as smart surfaces to capture diverse classes of compounds for rapid detection or to imprint imaging under ambient conditions. Large surface area, appropriate chemical functionalities exposed, and easiness of desorption due to weaker interactions of the analyte species are the specific advantages of nanofibers for this application.



Ambient ionization mass spectrometry, in particular, desorption electrospray ionization mass spectrometry (DESI MS), has received widespread attention in the analysis of molecules at surfaces.¹ Innovations in instrumentation and advances in the family of ambient ionization methods illustrate the capabilities currently available.² Using such techniques, direct detection of the compounds of interest without extraction and sample pretreatment are being explored for several complex samples.³ Over the years, although diverse ionization techniques have gained importance, the need for versatile substrates for surface analysis has not been addressed. DESI MS imaging, in particular, requires flat, rigid surfaces to tolerate high pressure of the nebulizing gas, and the continuous flow of solvent during the desorption process. Capturing molecular signatures, faithfully registering them, and revealing them without losing spatial information for a diverse variety of chemical species are important attributes of a reliable and versatile substrate used in DESI MS. Thin layer chromatography (TLC) plates have been the most successful for many analytical systems including imaging mass spectrometry. Surfaces reported for ambient ionization mass spectrometry include polytetrafluoroethylene (PTFE), TLC-plates, porous silicon, and nanoporous alumina, etc.;^{4–7} nevertheless, these surfaces have some limitations; PTFE has no porosity and is hydrophobic, whereas oxide supported in TLC plates could contribute to catalytic as well as photochemical degradation of

materials imprinted on them. Long-term storage of such imprints could lead to reactions stimulated by light or ambient conditions. These limitations prompted us to explore new surfaces/substrates with improved capabilities.

Nanofibers (of diameter in the regime 50 nm to several micrometers) are fibrous matrices prepared from a combination of both inorganic and organic substances. Electrospinning, a versatile technique for the fabrication of nanofibers, is often used to tailor the morphologies, surface chemistries, special properties, and functions.^{8,9} The availability of large surface area, porosity, and increased sites for analytes' interactions lead to the success of electrospun nanofibers in analytical processes.¹⁰ Besides serving as superior chromatographic stationary phases for low and high resolution separation,¹¹ nanofibers are used in tissue engineering, drug delivery, water purification, and solar cells, as chemical and biological sensors, etc.^{12,13} To cater to the needs of such heterogeneous applications, nanofibers are made from a wide range of combinations of polymers with added functionalities and/or morphological modifications.^{14,15} Characterization of nanofibers is done routinely using scanning electron microscopy (SEM), X-ray photoelectron spectroscopy (XPS), thermogravi-

Received: November 29, 2015

Accepted: May 9, 2016

Published: May 9, 2016

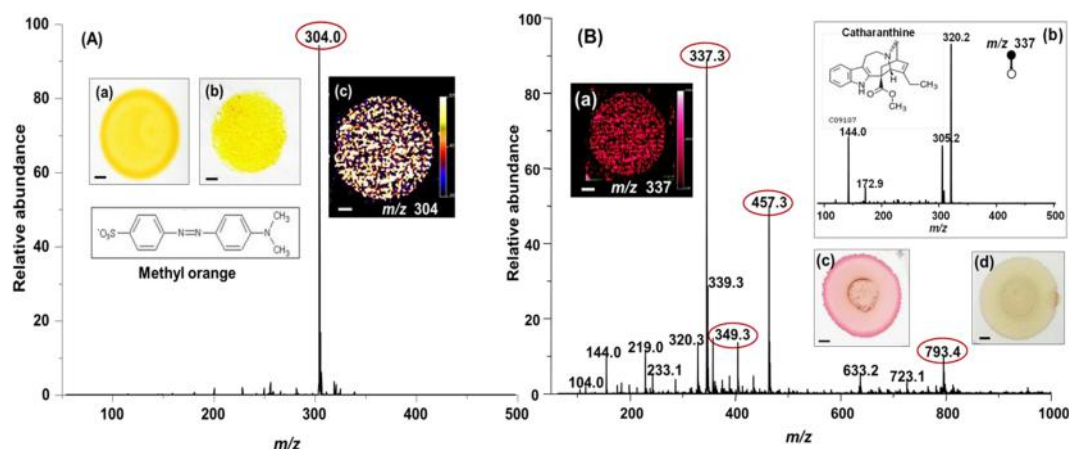


Figure 1. (A) DESI MS spectrum eluted from a spot sample of methyl orange on a nylon nanofiber mat. (a) Photograph of the corresponding spot on a TLC-plate showing the spreading effect, forming a halo on the periphery. (b) Same sample spotted on a nylon nanofiber mat showing uniform spreading. (c) DESI MS image of a methyl orange peak at m/z 304. (B) DESI MS spectrum of a Madagascar periwinkle flower extract spotted on an electrospun nylon nanofiber mat. DESI MS image (a) and tandem mass spectrum (b) of Catharanthine at m/z 337. TLC-plates showing the spreading (c) and fading effects (d) of the spot of the flower extract. The scale bar in all DESI MS images is 5 mm.

metric analysis (TGA), Fourier transform infrared spectroscopy (FTIR), transmission electron microscopy (TEM), etc.¹⁶ We propose that the inherent properties and versatility of the nanofibers may be used for direct sampling of molecules.

Mass spectrometry (MS) based methods are rarely used to study nanofibers, despite being made of synthetic or natural polymers or polymer blends. MS has been used on a variety of polymers to understand their surface chemistry, structural properties, interactions, and/or even degradation products.^{17,18} As a vast majority of synthetic polymers are relatively nonpolar, and do not ionize easily, they are not suitable for ionization based on polar solvents, such as electrospray ionization.¹⁹ Fine tuning of instrumental parameters is suggested to achieve ionization of polymers or even to suppress noise/signals from polymeric surfaces in ambient ionization methods.²⁰

This study demonstrates the use of electrospun nanofiber mats made of nylon-6 (a widely used polymer for both biomedicine and other applications)^{21,22} as smart surfaces for rapid detection or imaging by DESI MS under ambient conditions. The feasibility of using methanol as a spray solvent on nylon nanofiber mats to detect/image analytes/metabolites without the interference of the polymeric substrate is illustrated for six different bio/analytical contexts. We believe that the flexibility in making different substrates, the surface functionalization of the fibers, and the enhanced properties of the nanofiber mats will expand the scope of ambient ionization mass spectrometry.

EXPERIMENTAL SECTION

Materials. Polyamide-6 (Nylon-6, $M_n = 10\,000$ g/mol), formic acid, methanol, and acetonitrile were purchased from Sigma-Aldrich. Marker pens and printing inks, used for imaging, were of Faber-Castell brand, purchased from a local store. Plant parts, such as petals of Madagascar periwinkle (*Catharanthus roseus* (L.) G. Don), Poinciana (*Caesalpinia pulcherrima* (L.) Sw.), leaf of betel (*Piper betel*, L.), and rhizome of turmeric (*Curcuma longa*, L.), were collected from the nursery of IIT Madras, Chennai campus, or the local market of Chennai.

Electrospinning of Nanofiber. An electrospinning setup—Nanospider NS 200S²³ from Elmarco—was used for preparing nanofibers (video S1). Nylon-6 was dissolved in

formic acid at 60–70 °C and stirred for at least 18 h prior to use. The solution in formic acid was prepared in three concentrations: 18, 16, and 12% (w/w). These concentrations were optimized for the reproducible production of smooth and uniform fiber morphologies (Figure S1). Tetraphenylphosphonium bromide (TPPB, 5 mg) and periwinkle flower petals (5 mg) were dissolved/extracted in 1 mL of methanol, and the solution was added to nylon-6 solution. The mixture was stirred for 1 h at room temperature prior to electrospinning, and it was then electrospun at room temperature. The polymer solution was placed in a cylinder containing the active electrode parallel to the collecting electrode. The polymer solution was delivered at a distance 18 cm from the active electrode to the collecting electrode by applying a voltage of 70 kV, with the electrode rotating at a speed of 2.3 rpm, at relative humidity of 35–45%. The fibers were collected on an aluminum sheet. An as-prepared electrospun mat was dried inside the hood at room temperature for an hour. A portion of the mat was used for characterization purposes, and the rest of the nanofiber sample was dried in a moderate vacuum (~50 Torr) overnight and stored in zip lock polybags until use. The morphology of the as-prepared electrospun mat was studied using scanning electron microscopy (SEM) (FEI QUANTA-200) as per the standard protocols.²⁴

Mass Spectrometry Imaging. For mass spectrometry imaging, a Thermo Finnigan LTQ linear ion trap mass spectrometer equipped with a DESI source (Prosolia Inc., CA) was used. To avoid damage to the nanofiber surface, the nanofiber mat along with the aluminum foil was cut in the desired dimension and fastened onto the glass plate of the DESI stage using double sided tape. Imprinting of a plant leaf and a flower petal on the nylon mat was done as described previously.²⁵ For making patterns with printing inks, stamps with definite patterns were coated with a printing ink and imprinted manually on the nanofiber mat. The spray solvent for MS acquisition in the positive and negative ion modes was methanol or methanol:water (50:50) or acetonitrile, and a spray voltage of 4.5 kV was applied. The nitrogen gas pressure was 100 psi, and the solvent flow rate was 3 $\mu\text{L}/\text{min}$. In imaging experiments, the imprinted nanofiber was scanned using a 2D moving stage in horizontal rows separated by a 250 μm vertical

step until the entire sample was imaged. All experimental data were acquired using a LTQ linear ion trap mass spectrometer controlled by XCalibur 2.0 software (Thermo Fisher Scientific, San Jose, CA). The Firefly program allowed the conversion of the XCalibur 2.0 raw files into a format compatible with the BioMap (freeware, <http://www.maldi-msi.org>) software. The individual spectra or pixels that were acquired were assembled into a spatially accurate image using the BioMap software.

RESULTS AND DISCUSSION

The versatility of electrospun nylon nanofiber mats for multiple applications is illustrated in Figures 1–6 and Figures S3 and S4. Materials most commonly available for these applications are TLC plates and printing papers; hence, they are compared with nanofiber mats. The same instrumental parameters, spray solvents as optimized/reported for TLC plates, and printing paper were applied for nanofiber mats to illustrate their superiority in all the experiments. Nanofibers are tunable to achieve the desired properties by varying spinning conditions/surface functionalization, the advantage of which is available in numerous reports;^{12–16} hence, we restricted the discussion to the context of our results. Nanofiber mats of desired thicknesses were prepared by needleless electrospinning using Nanospider as shown in video S1. SEM images (Figure S1(a–f)) show the morphologies and thickness of the fiber mats produced. The fiber mats appear as thin polymer films, white in color (Insets (i–iii) of Figure S1(a–c)). Fiber mats formed on aluminum sheets were cut into the desired shapes as necessary. The fibers were 200–1000 nm diameter. The thicknesses of the nanofiber mats used for surface analysis were 50–100 μm (Figure S1(d,e)) and 150–170 μm (Figure S1(f)), and those mats were subsequently used for imprinting.

For Detection/Imaging of Analytes in a Single Drop.

Figure 1A,B illustrates the use of a nylon nanofiber mat for direct measurement of analytes in a single drop. Analytes may be colored or colorless ones. Trace detection of analytes has been demonstrated using DESI MS for a number of analytes.²⁶ When a single drop of methyl orange (MO) (colored) dye or periwinkle flower extract (colorless) was spotted on the TLC plate, the contents of the analytes were spread and became concentrated at the periphery, forming a halo, as shown in Figures 1A(a) and 1B(c). Spotting analytes on a nylon nanofiber mat gave a uniform coating without a halo (Figure 1A(b)), enabling a reproducible DESI MS image (Figure 1A(c)). Images were detectable in both positive and negative ion modes; the characteristic peak at m/z 304 for MO was in negative ion mode (Figure 1A) whereas the alkaloid peaks of periwinkle flower extract were detected in positive ion mode (Figure 1B). Peaks at m/z 337, 457, and 349 (encircled in Figure 1B) were confirmed by tandem mass spectral data (Figure 1B(b)) as catharanthine, vindoline, and serpentine, respectively, which matched exactly with our previous report.²⁵ The flower extract spot on the TLC-plate (Figure 1B(c)) became discolored within 10 days during storage under ambient conditions (Figure 1B(d)). For the MO spot on a TLC-plate, similar fading of the imprinted dye color (for both the peripheral halo (Figure S2(a)) and the interior (Figure S2(b) regions) was noticed in 2 weeks; tentative assignment of peaks (Figure S2) using the literature²⁷ showed the degradation products of MO. Besides being suitable for imaging analytes, nylon nanofibers act as effective sorbent materials²² and could be better substrates to study dyes and other contaminants in water.

For Imaging of Incorporated Materials/Agents. Compounds of interest can be incorporated into nanofibers during formation, which becomes an advantage over other surfaces. It is crucial to understand the pre and post modifications for any imaging agents/drugs (biological or chemical) that are selectively incorporated or immobilized into polymeric materials.²⁸ To study the fate of such incorporated materials, nylon nanofibers was incorporated with (1) crude methanol extract of periwinkle flower (Figure 2) or (2) an imaging agent,

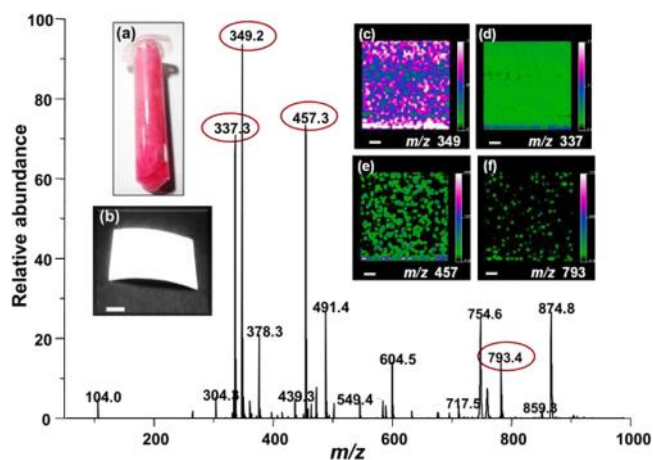


Figure 2. DESI MS spectrum of a periwinkle flower extract incorporated electrospun nylon fiber mat. (a) Polymer blend with flower extract showing a pink colored solution. (b) Optical image of the flower extract-incorporated nanofiber mat after electrospinning. (c–f) DESI MS images of the encircled peaks at m/z 337, 349, 457, and 793. A uniform distribution of the compounds is seen. The scale bar in all DESI MS images is 5 mm.

tetraphenylphosphonium bromide (TPPB)²⁹ (Figure S3) and imaged with DESI MS. When the periwinkle flower extract was blended with the nylon polymer solution, it became pink in color (Figure 2C (a)), but the resultant nylon mat was white after electrospinning. Major metabolites peaks of periwinkle (encircled in Figure 2) could be identified by MSⁿ imaging. Tandem mass spectrum confirmed the incorporated metabolites, though the concentration of each metabolite in extract was unknown. Spectral similarities/differences between Figure 1B and Figure 2 show the changes due to spotting and incorporation of flower extract. Low concentration of TPPB (~100 ppm) also gave an intense peak at m/z 339 (Figure S3), characteristic of TPPB without any interference from the nylon. Tandem mass spectrum (Figure S3 (b)) was used to confirm the incorporation of TPPB. The above results demonstrate the compatibility of nylon polymer with the extract and imaging agent. The suitability for desorption/ionization process, negligible background and noninterference nature³⁰ establishes electrospun nanofibers as smart surfaces for mass spectrometry. Thus, the use of nanofiber mats in conjunction with DESI MS may be a rapid method to study the compatibility of polymers, their interactions and fate of the incorporated (bio/chemical) agents over time.

For Detection/Imaging the Effect of Spray Solvents/Wetting on Nanofiber Mat. The choice of solvent is crucial for desorption of analyte molecules from the surface, transfer into the gas phase, and subsequent ionization. The solubility of the analytes, the interaction of solvent with the surface, and the nature of secondary droplets leaving from the surface would

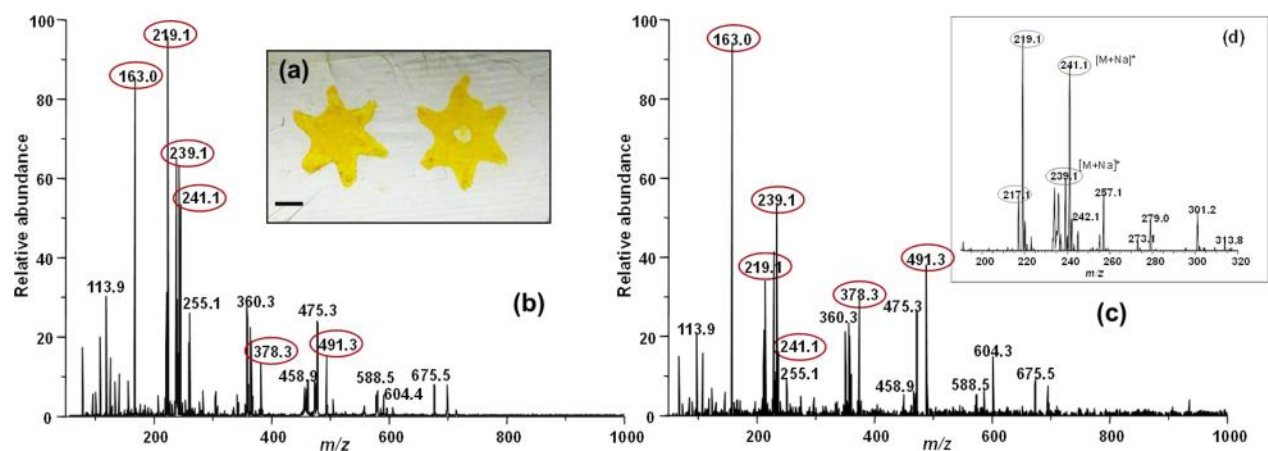


Figure 3. (a) DESI MS spectrum from a turmeric extract imprinted pattern on a nylon nanofiber mat. (b,c). Spectra showing that the intensities of the encircled peaks became changed during wetting. (d) Peaks encircled in blue and red are sodium adduct peaks of α -turmerone and curcumin. The scale bar in (a) is 5 mm.

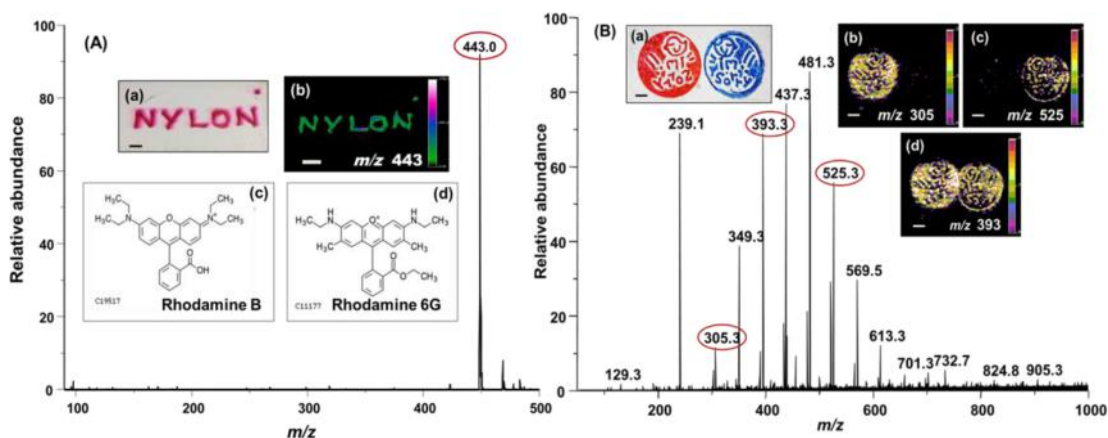


Figure 4. (A) DESI MS spectrum showing the peak at m/z 443 collected from an image made with a red marker pen, a photograph of which is shown in (a). Inset (b) is the DESI MS image of the mat with a red colored text "NYLON" recorded using m/z 443, which may be (c) Rhodamine B or (d) Rhodamine 6G. (B) DESI MS spectrum showing peaks from pictorial patterns made of red and blue colored printing inks imprinted close to each other on a nylon nanofiber mat, as shown in optical image (a). (b–d). DESI MS images corresponding to the imprinted patterns. The scale is uniform in all the images (5 mm).

influence DESI efficiency.³¹ A stamp pattern coated with turmeric extract was imprinted on a nylon nanofiber mat (Figure 3 and Figure S4) to demonstrate the effect of spray solvents and wetting.

Turmeric extract has been used as a dye and a therapeutic agent.^{32,33} Curcumin (diferuloylmethane), an orange-yellow bioactive component of turmeric, is loaded in nanofibers for biomedical applications.³³ As curcumin is insoluble in water, turmeric extract, having solubility and better biological effects than purified compounds,³⁴ is preferred for use. Hence, we used methanol extract of fresh turmeric rhizome as a dye to imprint a pattern as shown in Figure 3(a) on a nylon nanofiber mat; the imprinted mat was dipped in water, dried, and then imaged. Though the patterns on the nylon nanofiber mat seemed to be intact to the naked eye, subtle distortions showing release of some molecules were observed in DESI MS images (Figure S4A(b–e)). Peaks encircled with red in Figure 3 and Figure S4A show the variations in peak intensities induced by wetting which lasted for 30 s (Figure 3(b)) and 5 min (Figure 3(c), Figure S4A). Details on the protonated mass spectra and fragmentation pattern of curcuminoids and other phytochemicals in turmeric extract³⁵ were used in under-

standing the changes observed. Evaluation of changes at the surface during wetting/solvent spray would help in understanding the interaction/noninterfering nature of the substrate. Also, interlaboratory variations are possible due to adduct(s) and other contaminations.³⁶ The possibility to compare the intensity of adduct formation while using solvents on nanofiber substrates is illustrated in Figures 3 and Figure S4B. Encircled peaks at m/z 239 and 241 in Figure 3(d) show the intensity of the sodium adduct peaks of α -turmerone and curcumin,³⁵ when methanol was used as the spray solvent. Comparison of the spectrum of Figure 3 with that of Figure S4B(a) (methanol-water) and Figure S4B(b) (acetonitrile) showed that the intensities of the adduct peaks were low for acetonitrile. Figure S4C illustrates the effect of spray (methanol:water) solvent on a similar pictorial pattern made of turmeric extract on printing paper (Figure S4C(a)). The disturbance created by the spray solvent (methanol:water) on the pictorial pattern resulted in a distorted DESI MS image (Figure S4C(b)) though the spectrum was similar to that of Figure S4C(a)). Thus, based on analytical needs, nylon nanofiber substrates allow the selection of suitable solvents to obtain a cleaner mass spectrum. An added advantage of nanofiber mats is that the surface charge on the

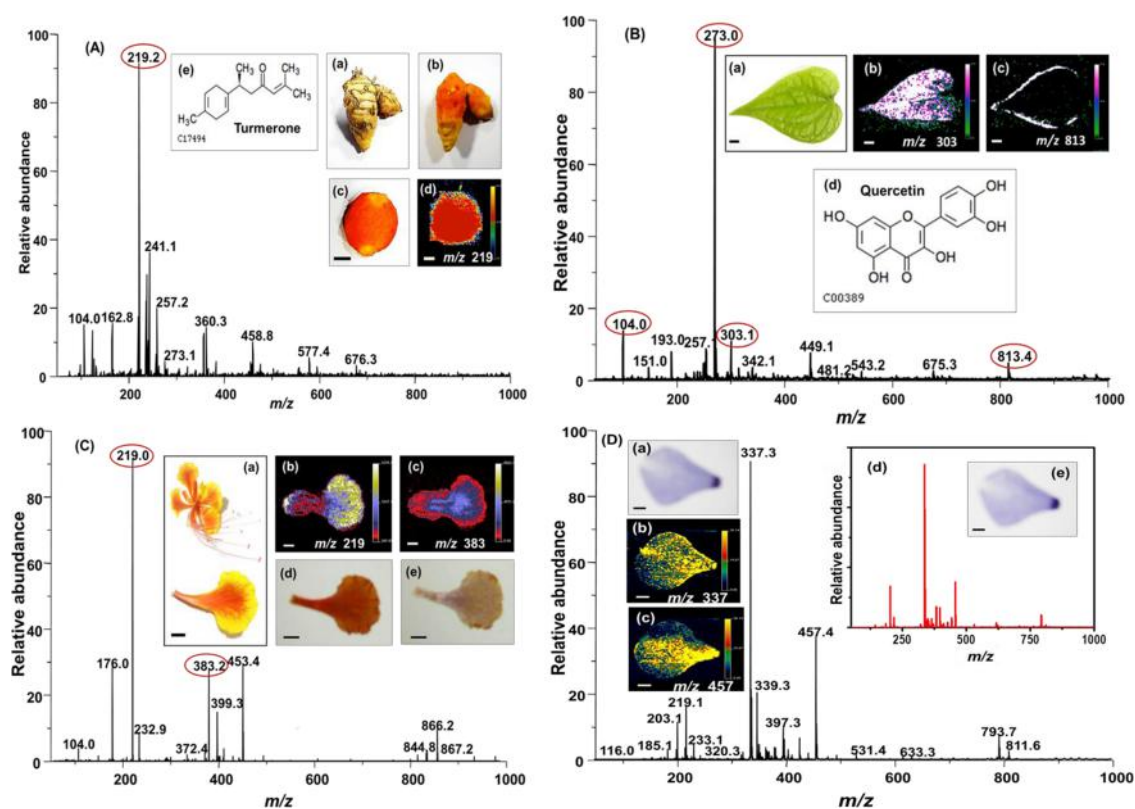


Figure 5. (A) DESI MS spectrum from a turmeric rhizome slice of an imprinted nylon nanofiber mat. (a,b) Optical images of a whole and unskinned turmeric rhizome. (c) Imprinted slice on a nylon nanofiber mat. (d) DESI MS image at m/z 219 due to α -turmerone shown in (e). (B) DESI MS spectrum of betel leaf (a) photograph and (b,c) DSEI MS images of imprinted patterns on nylon nanofiber mat. (d) Structure of the molecule attributed to m/z 303. (C) DESI MS spectrum of poinciana flower petal, (a) imprinted nanofiber and the corresponding DESI MS images (b,c). Corresponding imprint on TLC plate (d) and its fading effect (e) upon storage. (D) DESI MS spectrum of Madagascar periwinkle petal imprinted nylon nanofiber mat (a) and corresponding reproducible spectrum (d) from the imprint (e) after 2 weeks of storage. (b, c) DESI MS image of metabolite ions corresponding to catharanthine at m/z 337 and vindoline at m/z 457. Scale in all images is 5 mm.

mat could be tailored as positive or negative by altering the applied voltages during spinning.³⁷ Also, by tuning the critical thickness and porosity of the nanofiber mats, the penetration/wetting of water/solvents could be tailored, besides dissipating the effects of surface tension and viscosity.³⁸

For Imaging Imprinted Patterns of Inks. Spectral contamination from the underlying substrate is the major difficulty in forensic analysis of inks, even with nondestructive methods including DESI MS.³⁹ Here, we have illustrated the utility of an electrospun nylon nanofiber mat in eliminating spectral contamination in such cases. Figure 4A shows that a hand-written word made of red marker pen on the nylon nanofiber mat was faithfully reproducible in DESI MS images. The signal observed at m/z 443 may be due to cationic dye Rhodamine 6G or Rhodamine B which could be confirmed with the photodegradation products available in the literature and databases.³⁹ When two or more marker pens were used on a printer paper, the carryover effect of one over the other may happen as in Figure S5A. The disturbance created by spray solvent on the DESI MS image using imprinted paper is shown in Figure S5B. Though DESI removed low (attomole) amounts of ink,⁴⁰ instrumental parameters such as the solvent flow rate, distance of the spray from the sample, line scan speed, spacing, and time have to be optimized for reducing such carryover effects.⁴¹ The advantage of the nylon nanofiber mat is that even pictorial patterns made of printing inks could be imaged, however close they may be. Figure 4B(a) shows picture stamp patterns made of red and blue colored printing inks imprinted

very close to each other on the same nylon nanofiber mat. The corresponding DESI MS images show the reproducibility, and there were no overlaps or spectral contamination; besides, there was a possibility to detect an image from color(s) either individually (Figure 4B(c,d)) or together (Figure 4B(b)). A searchable reference library is available for most of the commonly used inks. As printing inks composed of complex mixtures of organic and inorganic components could be discriminated based on mass spectral data,⁴² our results demonstrate that nylon nanofiber mats are suitable surfaces in the analysis of inks.

For Imaging Imprinted Plant Parts. The amenability of nylon nanofiber mats for the imprint imaging of plant parts (petal, leaf, and rhizome) is illustrated in Figure 5. As a flat, stiff surface was needed for making imprints, thick mats of size 150–170 μm (Figure S1(f)) prepared with 18% nylon, were used. To facilitate imprinting on nylon mats, methods reported from our research group and in literature were followed.^{21,25} A cut slice of fresh turmeric rhizome imprinted manually on a nylon nanofiber mat (Figure 5A) was used to record DESI MS images. Tandem mass spectrometry was done on high intensity peaks in both the ion modes. Here, the intense protonated ion at m/z 219 corresponds to α -turmerone (Figure 5A(e)): an aromatic compound responsible for the aroma of the turmeric rhizome. Likewise, metabolite ions for the classes of compounds (curcuminoids, diarylheptanoids, sesquiterpenes, phenolics, and other flavonoids) were assigned using a database search and with available reports in the literature.³⁵ Metabolites

identified in negative ion mode include a few curcuminoids (demethoxycurcumin (m/z 239), bisdemethoxycurcumin (m/z 309), and curcumin (m/z 369)) and sesquiterpenoids (curcumenone (m/z 335)). Details on the structure, mass, and database reference for some of these metabolites are given in Table S1. Nylon nanofiber imprints retained the aroma of turmeric rhizome besides the natural color and shape; this observation was verified especially with samples such as leaf of betel and petal of poinciana flower (Figures 5B,C). For betel leaf, we show only a few metabolites which are detectable in imprints (Figure 5B), as compared to the ESI MS of the extracts. The major metabolites of betel leaf identified in this study, in both ion modes using their characteristic fragmentation patterns,⁴³ include charvicol (m/z 135), hydroxycharvicol (m/z 151), eugenol (m/z 165), coniferaldehyde (m/z 179), methoxy eugenol (m/z 195), eugenyl acetate (m/z 207), quercetin (m/z 303), and chlorogenic acid (m/z 355). Though the intensity of the peak at m/z 303 was low, the DESI MS image (Figure 5B(c)) shows high contrast; the feature was identified as due to quercetin (Figure 5B(d)) by tandem mass spectrometry. Metabolites contributing to the nectar (namely glucose, fructose, and sucrose) were captured in the nylon nanofiber imprint of a poinciana flower petal (Figure 5C(a)), in addition to the color (flavonoids and anthocyanins).⁴⁴ The peaks m/z 203 and m/z 219 were reported as sodium and potassium adducts of hexose, whereas the peaks at m/z 365 and m/z 381⁴⁵ (encircled in Figure 5C) were the sodium and potassium adducts of glucose whose spatial distribution is given in Figure 5C(b,c). The degradation of color of a TLC imprinted petal during storage is shown in Figure 5C(e). The periwinkle petal imprints made onto the nylon nanofiber mats may be faint (Figure 5D(a)), but DESI images of molecular ions with high contrast could be obtained (Figure 5D(b,c)). The petal color on the nanofiber imprint (Figure 5D(e)) lasted for 5 weeks without fading besides giving a reproducible spectrum (Figure 5D(d)). The spectrum of nanofiber imprinted periwinkle petal (Figure 5D) was similar to that of the TLC-imprinted one (Figure S6A), but showed enhancement in the peak intensity of m/z 203 and 219. The TLC-imprint of periwinkle petal was discolored during storage (Figure S6B(a)). There was a concomitant reduction in the ion intensity of the metabolite peaks (m/z 337 and 457) besides the poor DESI image (Figure S6B(b,c)). The enhanced detection of aroma, nectar, and coloring compounds by the nylon nanofiber surface might be due to the availability of a high surface to volume ratio, high porosity, and fibrous surface of the nanofiber.⁴⁶

For Imaging Fungal Growth/Contamination of Fruits.

Fungal species growing on food and/or fruits can be rapidly identified using nylon nanofiber mats (Figure 6). The fungal infection on lemon fruit was swabbed with nylon nanofiber mats and imaged. DESI MS images showed the reproducibility of the infection zones along with the details of the metabolites released due to the fungal growth as well as the degradation of lemon fruit. Tandem mass spectral fragments of highly intense peaks showed that the metabolites were both from fungi and the degrading lemon. The major metabolite identified (Figure 6) was at m/z 404, the tandem mass spectra of which confirmed it as Ochratoxin A (OTA). It is a toxic metabolite released by the fungus *Penicillium digitatum*, the causal agent of fruit rot of lemon.⁴⁷ Several metabolites, including limonene (m/z 137) and limonene-diol (m/z 171), released by the degrading lemon tissue could also be identified (Table S1, Supporting Information). Direct imaging of microbes from agar

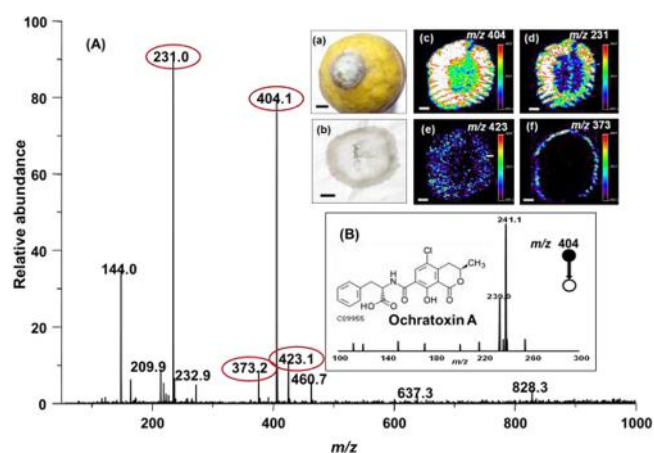


Figure 6. (A) DESI MS spectrum from the fungal infected region of lemon fruit imprinted on a nylon nanofiber mat. (a,b) Optical images of infected whole fruit of lemon (a) from which the fungal infection was swab-imprinted on a nylon nanofiber mat (b). (c–f) DESI MS images of encircled peaks showing toxic fungal metabolites. (B) Diagnostic fragmentation pattern and structure of Ochratoxin A at m/z 404.

plates was reported,⁴⁸ but using nanofiber mat eliminates background interference and restrains the microbial contamination.⁴⁹

Several analytes used in this study were complex mixtures (printing inks and plant extracts), wherein the concentration of individual component may vary. Sufficient analyte concentration is required to distinguish analytical signal from noise and limit of blank, while estimating the limit of detection (LOD).⁵⁰ Hence, we did not estimate LOD for each analyte. The best resolution possible and the LOD of the nanofiber mat are not discussed in this paper because there are many associated factors which have to be addressed individually. Given below are a few of these issues: (1) With an increase in the thickness of the nanofibers, the cross-sectional structure of the mat would influence the retention of solvents and analyte, desorption, detection, etc., thereby affecting the LOD. (2) With a change in the molecular weight and synthesis process of the same polymer, there will be a change in diameter, porosity, and surface characteristics of the resultant mat;⁵¹ hence, the LOD and the best resolution possible⁵² may vary even if measured with the same instrument. (3) Nanofibers are interactive surfaces, and their properties (size, orientation, morphology, polarity, and surface charge states)^{12–16,37,38} are tunable through spinning conditions and/or by adding cosolvents (such as acetic acid, dimethyl sulfoxide (DMSO), etc.) or ionic salts during electrospinning. Such surface functionalization of nanofibers with nanomaterials, cosolvents, and other chemicals could enhance or deter the signal intensities irrespective of the instrument performance.

Usually the LOD possible with nylon nanofibers is expressed at a single fiber level. In one of our research papers,⁵³ LOD for metal ions down to tens of ions was demonstrated with nylon nanofibers; however, that was based on fluorescence. In general, the examples given in this manuscript refer to the suitability of nanofiber mats as substrates for large scale analysis of clinical, biological, or imprinting needs of samples by DESI MS, wherein LOD is not a crucial parameter.

CONCLUSIONS

The suitability of nylon nanofiber mats as smart surfaces for DESI MS is illustrated using specific examples, including patterns formed by single drops with dissolved dyes, marker pen inks, and printing inks. No overlapped images were produced from imprinted patterns on nanofiber mats made of inks, however close they may be. The fate of imprinted patterns on wetting was examined with illustrations. Imprints of plant parts (leaf, flower petal, and rhizome) demonstrated the significance of using nanofiber mats as smart surfaces for identifying and preserving diverse classes of compounds, including aroma and color. It was possible to image the fungal species growing on fruit. The results of this study suggest that electrospun nanofiber mats may serve as smart surfaces for rapid detection of molecules or for imprint imaging protocols using DESI MS. As electrospun nanofibers can be made industrially, their use in DESI MS can become a promising method of analysis due to the various advantages presented here.

ASSOCIATED CONTENT

Supporting Information

The Supporting Information is available free of charge on the ACS Publications website at DOI: 10.1021/acs.analchem.5b04520.

SEM images of electrospun nanofibers; DESI MS spectrum and images showing degradation of the methyl orange spot on the TLC plate; DESI MS image for a tetraphenylphosphonium bromide incorporated nylon nanofiber mat; effect of spray solvents on a turmeric extract imprinted nylon nanofiber mat; DESI MS spectrum and images of marker pen ink patterns on paper; DESI MS spectra and images of a TLC imprint of a periwinkle petal upon storage; identification of metabolites of using a database search (PDF)

Preparation of a nanofiber mat by needleless electrospinning as observed using the instrument Nanospider (NS LAB 200) (AVI)

AUTHOR INFORMATION

Corresponding Author

*E-mail: pradeep@iitm.ac.in. Phone: +91-44-22574208. Fax: +91-44-2257 0509/0545.

Notes

The authors declare no competing financial interest.

ACKNOWLEDGMENTS

The authors thank the Department of Science and Technology, Government of India, for equipment support through the Nano Mission. R.G.H acknowledges the Department of Biotechnology, Government of India, for providing a BioCARE woman scientist fellowship.

REFERENCES

- (1) Wu, C.; Dill, A. L.; Eberlin, L. S.; Cooks, R. G.; Ifa, D. R. *Mass Spectrom. Rev.* **2013**, *32*, 218–243.
- (2) Monge, M. E.; Harris, G. A.; Dwivedi, P.; Fernandez, F. M. *Chem. Rev.* **2013**, *113*, 2269–2308.
- (3) Jarmusch, A. K.; Cooks, R. G. *Nat. Prod. Rep.* **2014**, *31*, 730–738.
- (4) Kauppila, T. J.; Talaty, N.; Salo, P. K.; Kotiaho, T.; Kostianen, R.; Cooks, R. G. *Rapid Commun. Mass Spectrom.* **2006**, *20*, 2143–2150.

- (5) Van Berkel, G. J.; Tomkins, B. A.; Kertesz, V. *Anal. Chem.* **2007**, *79*, 2778–2789.
- (6) Sen, A. K.; Nayak, R.; Darabi, J.; Knapp, D. R. *Biomed. Microdevices* **2008**, *10*, 531–538.
- (7) Ifa, D. R.; Manicke, N. E.; Rusine, A. L.; Cooks, R. G. *Rapid Commun. Mass Spectrom.* **2008**, *22*, 503–510.
- (8) Li, D.; Xia, Y. *Adv. Mater.* **2004**, *16*, 1151–1170.
- (9) McCann, J. T.; Li, D.; Xia, Y. *J. Mater. Chem.* **2005**, *15*, 735–738.
- (10) Chigome, S.; Torto, N. *Anal. Chim. Acta* **2011**, *706*, 25–36.
- (11) Beilke, M. C.; Zewe, J. W.; Clark, J. E.; Olesik, S. V. *Anal. Chim. Acta* **2013**, *761*, 201–208.
- (12) Lu, W.; Sun, J.; Jiang, X. *J. Mater. Chem. B* **2014**, *2*, 2369–2380.
- (13) Matlock-Colangelo, L.; Baeumner, A. J. *Lab Chip* **2012**, *12*, 2612–2620.
- (14) Wang, J.; Lin, Y. *TrAC, Trends Anal. Chem.* **2008**, *27*, 619–626.
- (15) Lim, J.-M.; Yi, G.-R.; Moon, J. H.; Heo, C.-J.; Yang, S.-M. *Langmuir* **2007**, *23*, 7981–7989.
- (16) Ramakrishna, S.; Fujihara, K.; Teo, W.-E.; Lim, T.-C.; Ma, Z. *An Introduction to Electrospinning and Nanofibers*; World Scientific: Singapore, 2005.
- (17) Gruending, T.; Weidner, S.; Falkenhagen, J.; Barner-Kowollik, C. *Polym. Chem.* **2010**, *1*, 599–617.
- (18) Rizzarelli, P.; Carroccio, S. *Anal. Chim. Acta* **2014**, *808*, 18–43.
- (19) Becker, N.; Wirtz, T. *Anal. Chem.* **2012**, *84*, 5920–5924.
- (20) Paine, M. R. L.; Barker, P. J.; Blanksby, S. J. *Anal. Chim. Acta* **2014**, *808*, 70–82.
- (21) Abdal-hay, A.; Pant, H. R.; Lim, J. K. *Eur. Polym. J.* **2013**, *49*, 1314–1321.
- (22) Qi, F.-F.; Cao, Y.; Wang, M.; Rong, F.; Xu, Q. *Nanoscale Res. Lett.* **2014**, *9*, 353.
- (23) El-Newehy, M. H.; Al-Deyab, S. S.; Kenawy, E.-R.; Abdel-Megeed, A. *J. Nanomater.* **2011**, *2011*, 1–8.
- (24) Desai, K.; Lee, J. S.; Sung, C. *Microsc. Microanal.* **2004**, *10*, 556–557.
- (25) Hemalatha, R. G.; Pradeep, T. *J. Agric. Food Chem.* **2013**, *61*, 7477–7487.
- (26) Soparawalla, S.; Salazar, G. A.; Sokol, E.; Perry, R. H.; Cooks, R. G. *Analyst* **2010**, *135*, 1953–1960.
- (27) Chen, T.; Zheng, Y.; Lin, J.-M.; Chen, G. *J. Am. Soc. Mass Spectrom.* **2008**, *19*, 997–1003.
- (28) Lin, F.; Yu, J.; Tang, W.; Zheng, J.; Xie, S.; Becker, M. L. *Macromolecules* **2013**, *46*, 9515–9525.
- (29) Min, J. J.; Biswal, S.; Deroose, C.; Gambhir, S. S. *Gene Ther.* **2004**, *45*, 636–643.
- (30) Lu, T.; Olesik, S. V. *Anal. Chem.* **2013**, *85*, 4384–4391.
- (31) Badu-Tawiah, A. K.; Eberlin, L. S.; Ouyang, Z.; Cooks, R. G. *Annu. Rev. Phys. Chem.* **2013**, *64*, 481–505.
- (32) Mirjalili, M.; Karimi, L. *AUTEX Res. J.* **2013**, *13*, 51–56.
- (33) Sun, X.-Z.; Williams, G. R.; Hou, X.-X.; Zhu, L.-M. *Carbohydr. Polym.* **2013**, *94*, 147–153.
- (34) Mohankumar, S.; McFarlane, J. R. *Phytother. Res.* **2011**, *25*, 396–401.
- (35) Jiang, H.; Somogyi, Á.; Jacobsen, N. E.; Timmermann, B. N.; Gang, D. R. *Rapid Commun. Mass Spectrom.* **2006**, *20*, 1001–1012.
- (36) Gurdak, E.; Green, F. M.; Rakowska, P. D.; Seah, M. P.; Salter, T. L.; Gilmore, I. S. *Anal. Chem.* **2014**, *86*, 9603–9611.
- (37) Stachewicz, U.; Stone, C. A.; Willis, C. R.; Barber, A. H. *J. Mater. Chem.* **2012**, *22*, 22935–22941.
- (38) Sahu, R. P.; Sinha-Ray, S.; Yarin, A. L.; Pourdeyhimi, B. *Soft Matter* **2012**, *8*, 3957–3970.
- (39) Blackledge, R. D. *Forensic Analysis on the Cutting Edge: New Methods for Trace Evidence Analysis*; Wiley: New York, 2007.
- (40) Venter, A. R.; Douglass, K. A.; Shelley, J. T.; Hasman, G.; Honarvar, E. *Anal. Chem.* **2014**, *86*, 233–249.
- (41) Denman, J. A.; Skinner, W. M.; Kirkbride, K. P.; Kempson, I. M. *Appl. Surf. Sci.* **2010**, *256*, 2155–2163.
- (42) Bereman, M. S.; Muddiman, D. C. *J. Am. Soc. Mass Spectrom.* **2007**, *18*, 1093–1096.

- (43) Pandey, R.; Chandra, P.; Srivastva, M.; Arya, K. R.; Shukla, P. K.; Kumar, B. *Anal. Methods* **2014**, *6*, 7349–7360.
- (44) Wei, X. H.; Yang, S. J.; Liang, N.; Hu, D. Y.; Jin, L. H.; Xue, W.; Yang, S. *Molecules* **2013**, *18*, 1325–1336.
- (45) Qian, W. L.; Khan, Z.; Watson, D. G.; Fearnley, J. J. *Food Compos. Anal.* **2008**, *21*, 78–83.
- (46) Scampicchio, M.; Arecchi, A.; Lawrence, N. S.; Mannino, S. *Sens. Actuators, B* **2010**, *145*, 394–397.
- (47) Hernandez-Montiel, L. G.; Ochoa, J. L. *Plant Dis.* **2007**, *91*, 767–767.
- (48) Angolini, C. F. F.; Vendramini, P. H.; Araujo, F. D. S.; Araujo, W. L.; Augusti, R.; Eberlin, M. N.; de Oliveira, L. G. *Anal. Chem.* **2015**, *87*, 6925–6930.
- (49) Abdel-Megeed, A.; Eifan, S. A.; El-Newehy, H. M.; Al-Deyab, S. *S. J. Agric. Sci.* **2014**, *59*, 75–90.
- (50) Armbruster, D. A.; Pry, T. *Clin. Biochem. Rev.* **2008**, *29* (Suppl1), S49–52.
- (51) Guerrini, L. M.; Branciforti, M. C.; Canova, T.; Bretas, R. E. S. *Mater. Res.* **2009**, *12*, 181–190.
- (52) Kertesz, V.; Van Berkel, G. J. *Rapid Commun. Mass Spectrom.* **2008**, *22*, 2639–2644.
- (53) Ghosh, A.; Jeseentharani, V.; Ganayee, M. A.; Hemalatha, R. G.; Chaudhari, K.; Vijayan, C.; Pradeep, T. *Anal. Chem.* **2014**, *86*, 10996–11001.

*Supplementary information***Electrospun Nanofiber Mats as “Smart Surfaces” for Desorption****Electrospray Ionization Mass Spectrometry (DESI MS) based****Analysis and Imprint imaging***R.G. Hemalatha, Mohd Azhardin Ganayee, and T. Pradeep**

DST Unit on Nanoscience and Thematic Unit of Excellence, Department of Chemistry, Indian Institute of Technology Madras, Chennai 600 036, India.

*Corresponding author Email: pradeep@iitm.ac.in

Table of contents:

Particulars	Title	Page No.
Video S1	Preparation of nanofiber mat by needleless electrospinning as observed using the instrument, Nanospider (NS LAB 200)	2
Figure S1	SEM images of electrospun nanofibers	2
Figure S2	DESI MS spectrum and images showing degradation of methyl orange spot on TLC plate	3
Figure S3	DESI MS image for tetraphenylphosphonium bromide incorporated nylon nanofiber mat	4
Figure S4	Effect of spray solvents on turmeric extract imprinted nylon nanofiber mat	5,6
Figure S5	DESI MS spectrum and images of marker pen ink patterns on paper	7
Figure S6	DESI MS spectra and images of TLC imprint of periwinkle petal upon storage	8
Table S1	Identification of metabolites of using database search	9.10



NF - VideoS1.avi (Command Line)

Video S1- Preparation of nanofiber mat by needleless electrospinning as observed using the instrument, Nanospider (NS LAB 200).

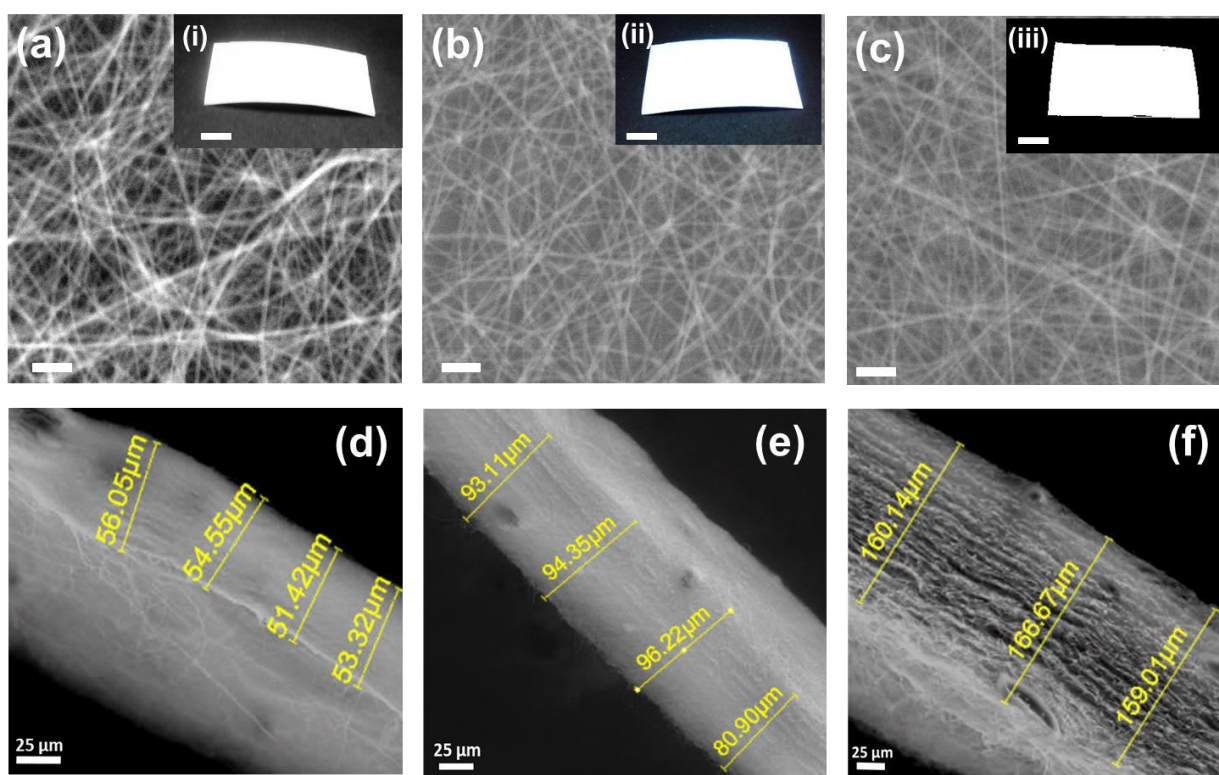


Figure S1. (a, b and c). SEM images and corresponding photographs (i, ii, iii) of electrospun nanofibers using three different concentrations (18, 16 and 12% (w/w) of nylon-6. The scale in SEM images (a-c) is 5 μm and in the insets is 5 mm.

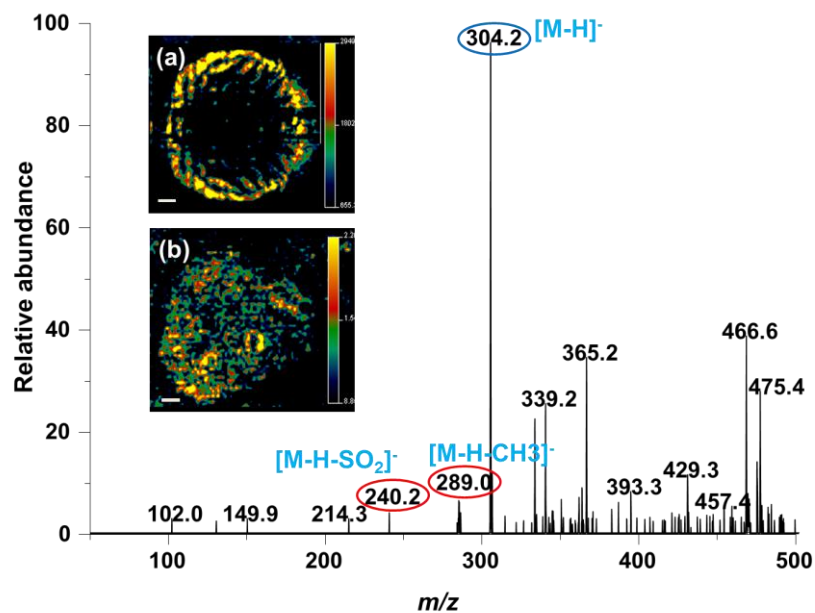


Figure S2. DESI MS spectrum showing discoloration/degradation of methyl orange (MO) spot on TLC-plate during storage under ambient conditions. (a,b) DESI MS image showing the spatial distribution of halo and the interior regions during degradation of spot of methyl orange. Encircled peaks are the degradation products corresponding to the peak at m/z 304. The scale in all DESI MS images is 5 mm.

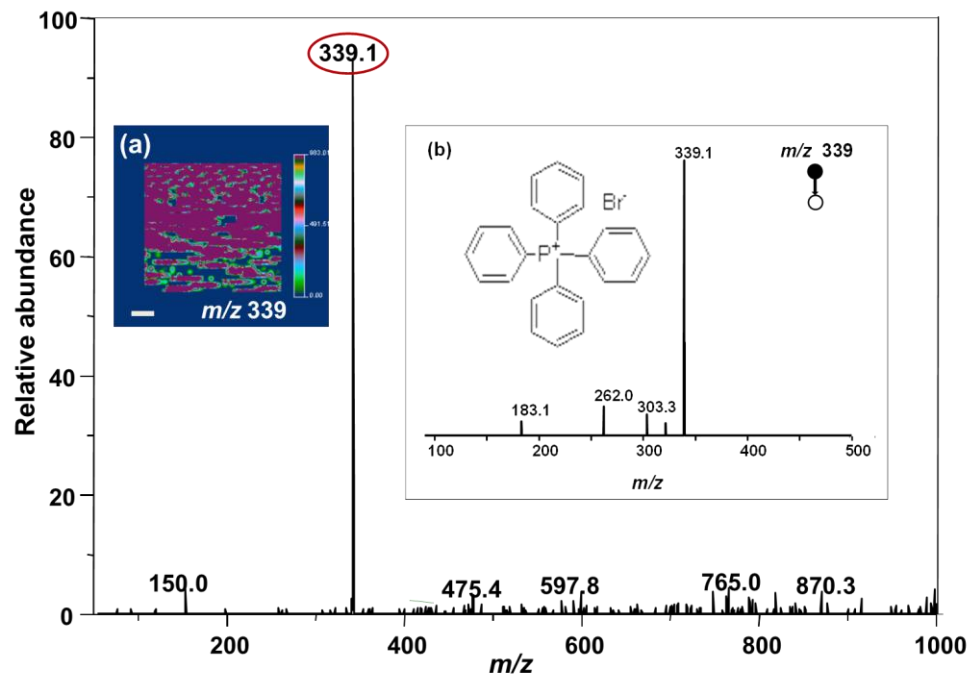
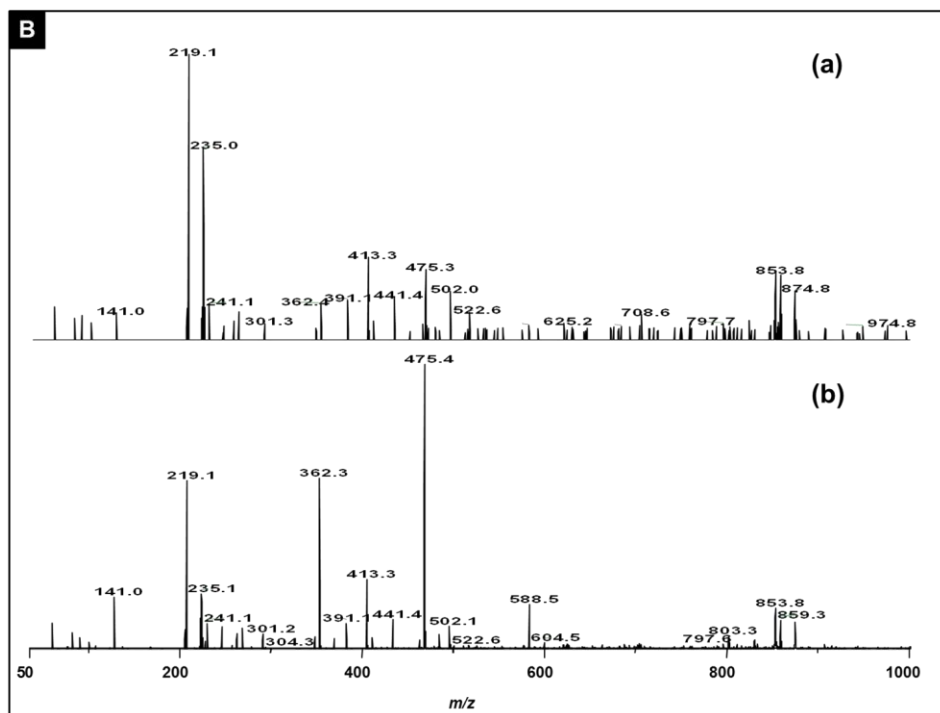
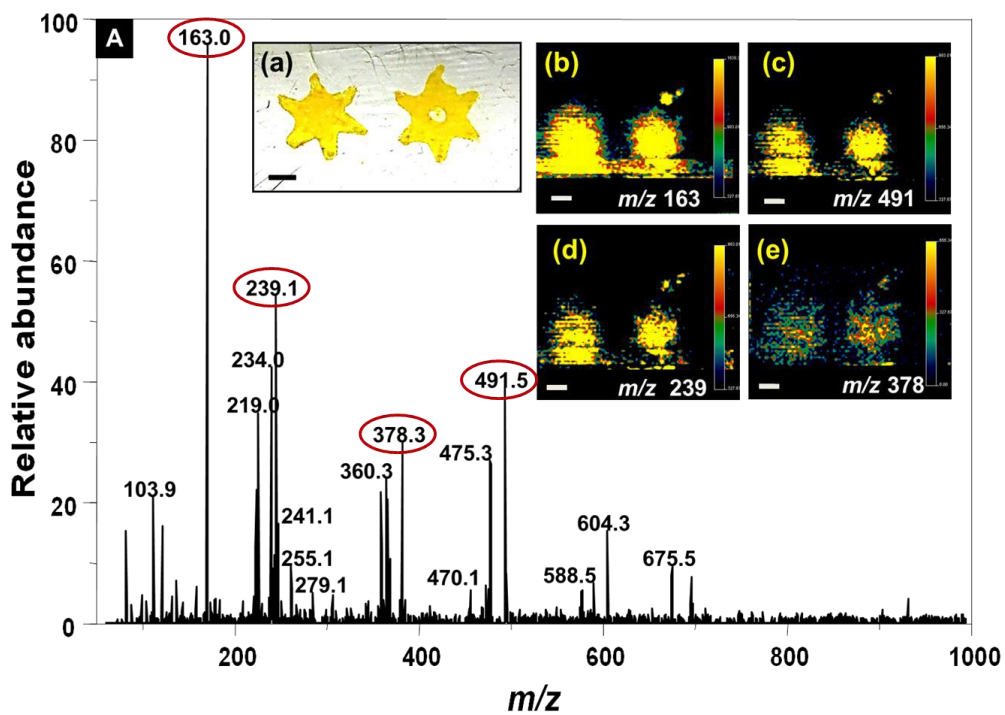


Figure S3. DESI MS spectrum corresponding to tetraphenylphosphoniumbromide (TPPB) incorporated nylon nanofiber mat. Inset (a) shows the DESI MS image and (b) tandem mass spectrum corresponding to the peak at m/z 339. Scale in DESI MS image is 5 mm.



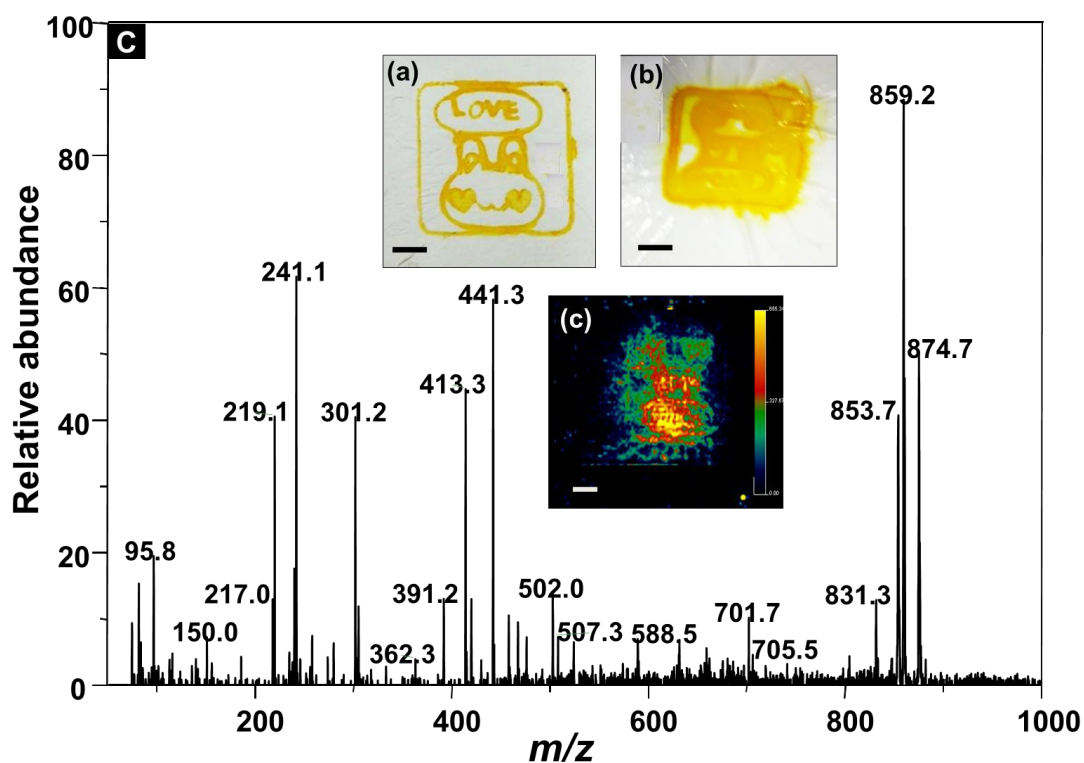


Figure S4. (A). DESI MS spectrum showing peaks eluted while using methanol as spray solvent for water exposed turmeric extract imprinted pattern on nylon nanofiber mat. (a) Optical image of the turmeric extract imprinted pattern on nylon nanofiber mat. (b-e) DESI images of encircled peaks showing changes in intensities and distortions from the imprinted pattern. (B). DESI MS spectra showing differences in peaks eluted due to spray solvents (a) methanol:water (50:50) and (b) acetonitrile. (C). DESI MS spectrum from turmeric extract imprinted pattern on printing paper using methanol:water as the spray solvent. (a) Optical image of the turmeric extract imprinted pattern on paper and (b) corresponding distortions in the printed pattern after the solvent (methanol: water (50:50)) spray. (c) DESI MS showing the distortions of the imprinted pattern. The scale in all images is 5 mm.

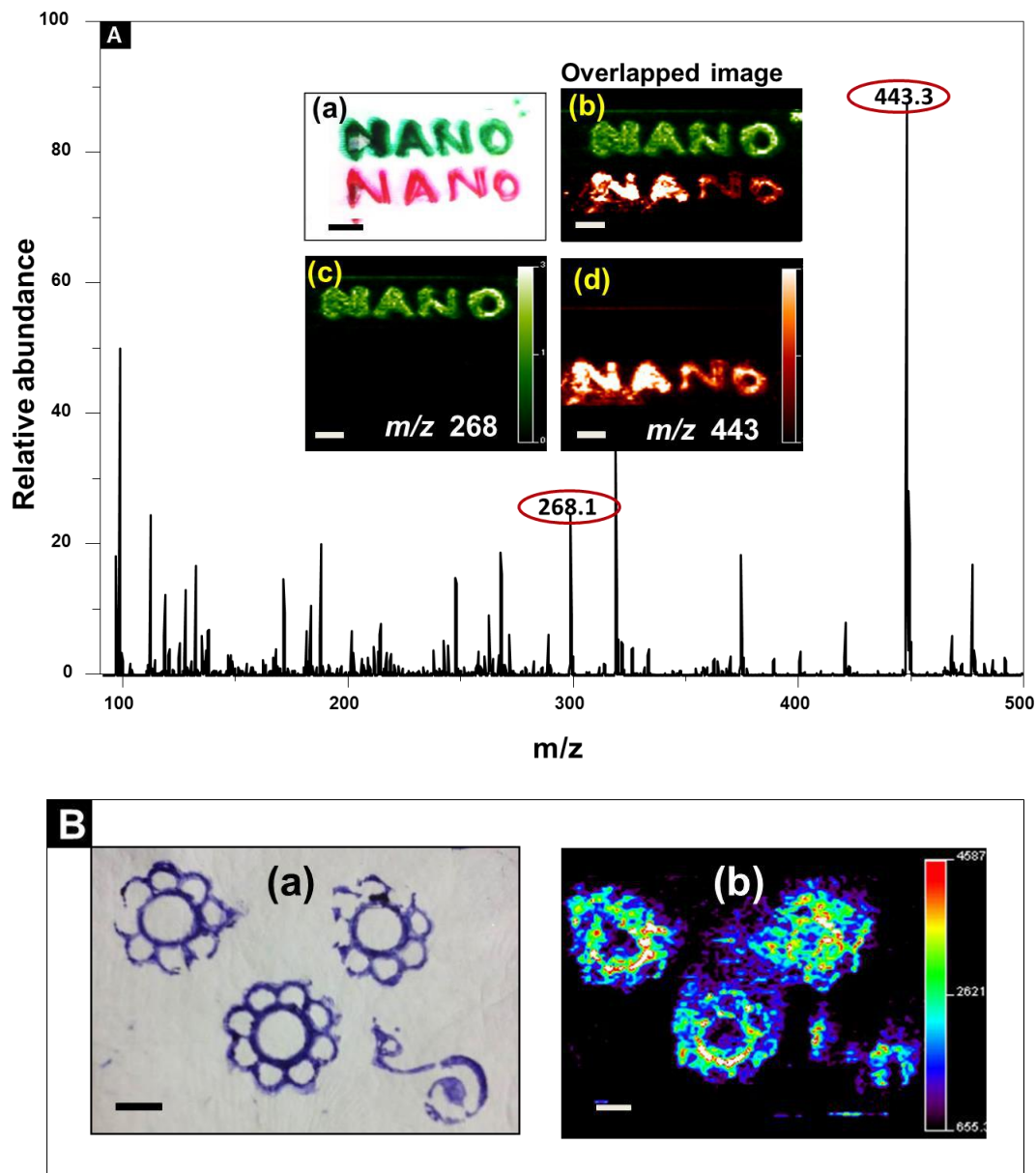


Figure S5. (A). DESI MS spectrum corresponding to a label written on a printing paper using green and red marker pens. The characteristic mass features due to the marker pens are encircled. A photograph of the paper is shown in inset (a). (b-d). DESI MS images corresponding to the green (m/z 268) and red (m/z 443) colored marker pen features. (B).(a) Optical image of the imprinted pictorial pattern on printing paper and corresponding (b) DESI MS image showing the distortions in pictorial pattern. The scale in all images is 5 mm.

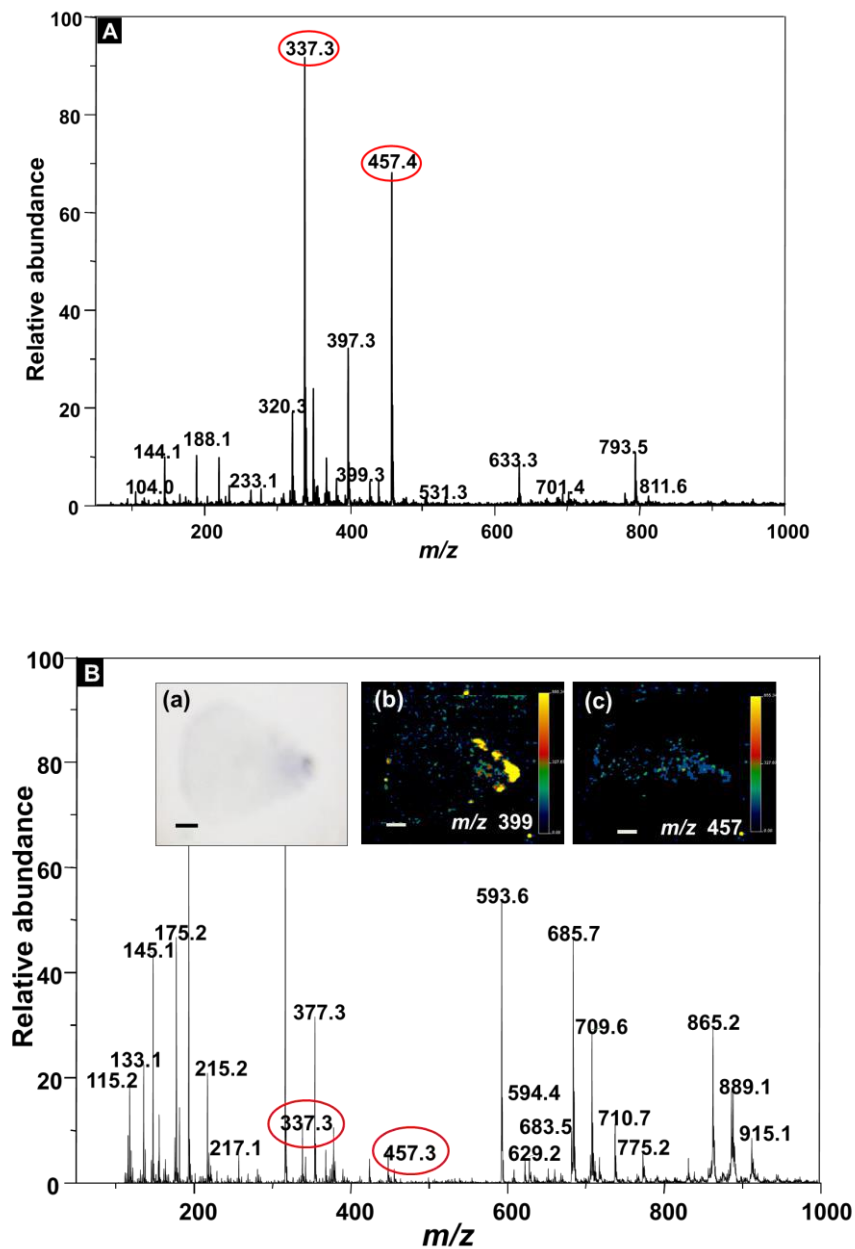
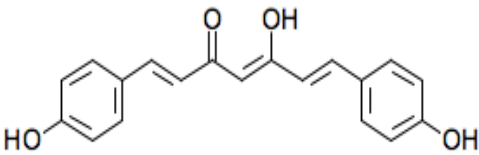
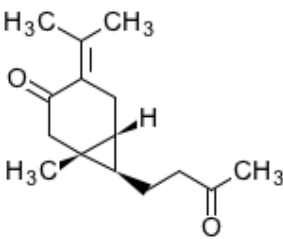
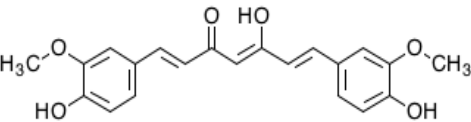
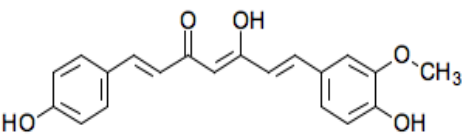
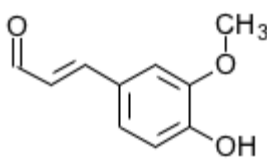
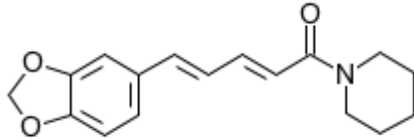
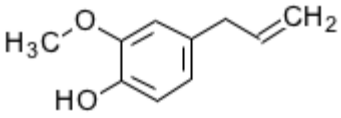
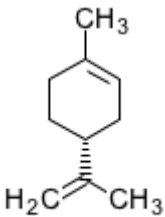
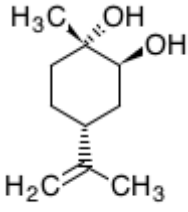


Figure S6. (A). DESI MS spectrum from TLC-imprint of petal of Madagascar periwinkle. Encircled peaks correspond to predominant metabolites- catharanthine (m/z 337) and vindoline (m/z 457). (B). Corresponding DESI MS spectrum from TLC-imprint after storage under ambient conditions for ten days. (a) Optical image showing discoloration of the TLC-imprint after storage. (b,c) Corresponding DESI MS images for encircled (catharanthine, vindoline) peaks showing very low (relative abundance <20%) ion intensities. The scale in all images is 5 mm.

Table S1: Identification of plant metabolite peaks using database search.

S. No	Name	Structure	Mol.wt	Database ID
1.	Bisdemethoxycurcumin	 C17743	308.3279	C17743 MID 58097
2.	Curcumenone	 C17492	234.334	C17492 MID 53443
3.	Curcumin	 C10443	368.3799	C10443 MID 44447
4.	Demethoxycurcumin	 C17742	338.3539	C17742 MID 45207
5.	Coniferaldehyde	 C02666	178.1846	C02666
6.	Piperine	 C03882	285.3377	C03882 MID 43568
7.	Eugenol	 C10453	164.2011	C10453 MID 4022

8.	Limonene	 C06099	136.234	C06099 MID 41087
9.	Limonene-1,2-diol	 C07276	170.2487	C07276 MID 41093

Identification of metabolite ion peaks using spectrum search tools of databases. ^{1,2}

* C numbers for KEGG database (<http://www.kegg.jp/kegg/compound>) to get additional information on the metabolite(s) including chemical and physical properties, structures, reactions and associated biosynthetic pathways of formation, etc.

**MID numbers for METLIN –Metabolite and Tandem MS database

(http://metlin.scripps.edu/metabo_advanced.php) to get additional information on the metabolite(s) including data on tandem mass spectra and structures for fragments.

References:

1. Kanehisa, M.; Goto, S., *Nucleic Acids Res.*, **2000**, 28, 27-30.
2. Smith, C. A.; O'Maille, G.; Want, E. J.; Qin, C.; Trauger, S. A.; Brandon, T. R.; Custodio, D. E.; Abagyan, R.; Siuzdak, G. *Ther. Drug Monit.*, **2005**, 27, 747-751.



Cite this: *J. Mater. Chem. C*, 2016,
4, 5572

Received 6th April 2016,
Accepted 10th May 2016

DOI: 10.1039/c6tc01388k

www.rsc.org/MaterialsC

Highly luminescent monolayer protected $\text{Ag}_{56}\text{Se}_{13}\text{S}_{15}$ clusters†

C. K. Manju, Indranath Chakraborty‡ and Thalappil Pradeep*

A highly luminescent (quantum yield 21%) mixed chalcogenide silver cluster, $\text{Ag}_{56}\text{Se}_{13}\text{S}_{15}$ cluster of Ag_2X stoichiometry, protected with a 4-*tert*-butylbenzyl mercaptan ligand has been synthesized and characterized. Investigation using diverse tools of analysis such as mass spectrometry, elemental analysis, thermogravimetry and X-ray diffraction confirmed this composition. The cluster emits in solution and in the solid state and has been deposited on oxide supports to get red emitting films. The specificity of cluster emission to the mercuric ion $\text{Hg}(\text{II})$, among a range of heavy metal ions, was used to develop a sensor, which shows sensitivity down to 1 ppb. A pH paper like visual detector was developed by combining the $\text{Hg}(\text{II})$ -sensitive emission of the cluster and the insensitive emission of fluorescein isothiocyanate. The test strip showed visual detection down to 1 ppb in real water samples.

Introduction

Semiconductor quantum dots (QDs) have been the subject of rigorous investigations for the last 25 years.¹ Chalcogenides of cadmium (Cd) have been the main interest in these studies, which expanded into almost all areas of chemistry, physics and biology, largely because of their unusual photophysical properties.^{2–4} Concerns about toxicity encouraged investigation of other chalcogenides which have reduced cytotoxic effects. Silver (Ag) chalcogenides have also been examined because of their lesser toxicity.^{5,6} Emission of Ag_2E QDs [E = sulfur (S), selenium (Se)] is extensive, from visible to near infrared (NIR), although their quantum yields (QY) have not been as large as the analogous CdE systems. Silver sulfide (Ag_2S) nanocrystals with a tunable NIR emission ranging from 690–1227 nm have been reported by Jiang *et al.*⁷ Tan *et al.* studied ultraviolet (UV) or visible light irradiation on nitric oxide (NO) release from *s*-nitrosothiol conjugated glutathione protected Ag_2S QDs.⁸ Tan *et al.* also used Ag_2S chitosan nanospheres for NIR fluorescence imaging.⁹ NIR emitting silver selenide (Ag_2Se) QDs have also been reported by different groups.¹⁰ Temperature dependent photoluminescence (PL) of Ag_2Se QDs were studied by Ji *et al.*¹¹

Well defined nanoscale molecules of M_2E systems [M = Ag, copper (Cu)] with phosphine and thiolate protections were studied by Fuhr *et al.* and a recent summary of such research is highly informative.¹² These studies were mainly focused on the synthesis and structural characterization, from which a wide variety of structural motifs have been discovered. However, PL and related applications of these materials have rarely been explored. One of the examples where such studies have occurred is $\text{Ag}_{62}\text{S}_{13}(\text{StBu})_{32}^{4+}$ where an emission at 613 nm with a QY of 0.014 was seen.¹³ This molecule was crystallized and its structure has been determined using single crystal X-ray diffraction (XRD). There remains a possibility of creating mixed chalcogenide systems such as $\text{Ag}_2\text{S}_{1-x}\text{Se}_x$ with varying compositions and tunable properties. With appropriate ligand protection, these nanosystems could be used for diverse applications. Anion substitution in QDs has been used to create materials with varying properties (for example, $\text{CdS}_{1-x}\text{Se}_x$). It is also known that substitution of Se into Ag_2S retains the monoclinic phase up to the composition, $\text{Ag}_2\text{S}_{1-x}\text{Se}_x$ with $0 \leq x \leq 0.6$ and a orthorhombic phase appears only above $0.8 \leq x \leq 1$.¹⁴ This suggests retention of the acanthite phase in $\text{Ag}_2\text{S}_{1-x}\text{Se}_x$ nanoparticles (NPs) for a considerable range of stoichiometry, thus allowing structural characterization.

Over the years there have been intense efforts to make atomically precise clusters of many materials. Most of the advances in this area have been centered on the noble metal clusters of which there are many examples available today.^{15–18} Some of the clusters have been crystallized and their structures have been determined by X-ray crystallography.^{19–22} These clusters possess unique structural motifs as well as diverse chemical interactions. Whereas properties of isolated clusters in solution have been explored in detail, the properties of the crystals are not understood all that well. Clusters of other

DST Unit of Nanoscience (DST UNS) and Thematic Unit of Excellence,
Department of Chemistry, Indian Institute of Technology Madras,
Chennai 600036, India. E-mail: pradeep@iitm.ac.in

† Electronic supplementary information (ESI) available: SEM, EDX and elemental mapping of cluster, PL spectrum of the effect of different metal ions, Hg^{2+} concentration dependent luminescence quenching and studies using real water samples. See DOI: 10.1039/c6tc01388k

‡ Current address: University of Illinois at Urbana Champaign, Urbana, IL 61801, USA.

elements have been rare, examples include those of silicon, germanium and so on. Among these compounds, the chalcogenide clusters have been explored in greater detail. These include the Ag–Se/S systems and the Cu–Se/S systems. Most such studies in this area were focused on structure and less commonly on their properties. Such materials in the nanometer regime can also be characterized using mass spectrometry (MS). Mass spectrometry has been used extensively for the characterization of noble metal clusters,²³ known as aspicules.²⁴ Several clusters in this category are known, such as Au₂₅SR₁₈, which exhibit unique properties and reviews on them are available elsewhere.²⁵ Success of such characterization depends on the ability to form stable ions in the gas phase. The inherent electronic stability of noble metals and the stability of the metal thiol interface made characterization of Au–SR clusters easier. For chalcogenides, inherent instability of the system made MS examination difficult. The Ag–Se bond (bond energy of 202 kJ mol⁻¹) is weaker than the Ag–S bond (bond energy of 217.1 kJ mol⁻¹), which made further MS investigation of Ag₂Se challenging.

Combining the distinct possibility of making a ligated Ag₂S_{1-x}Se_x system and incorporating the lessons from the aspicule work, it was thought to be worthwhile to explore the mixed silver chalcogenide cluster. In this paper, the synthesis of such a mixed cluster system, tentatively assigned as Ag₅₆S₁₅Se₁₃@SBB₂₈ with distinct red emission, high QY (21%) and exhibiting useful sensing properties both in solution and in the solid state is presented. Another reason to explore such a cluster system was because of the possibility of conducting experiments under milder conditions than typically used for the synthesis of Ag₂Se NPs. The standard approach used for Ag₂Se NPs and Ag–SR clusters was combined to achieve the present experimental methodology.

Experimental section

Materials and methods

All chemicals were commercially available and used without further purification. Silver acetate (CH₃COOAg), Se powder (100 mesh, 99.5%), octadecene (ODE, 90%) and 4-*tert*-butylbenzyl mercaptan (BBSH) were purchased from Sigma-Aldrich. Toluene was obtained from Merck (India) and methanol from Finar Chemicals (India).

Synthesis of luminescent cluster

Ag₂Se clusters were synthesized using a low temperature method. CH₃COOAg (0.1 mmol) and of BBSH (4 mmol) were added to 5 ml of ODE in a 100 ml three necked round bottomed flask under an argon (Ar) flow at 60 °C. Ar purging was continued for 30 min at this temperature. Then the reaction mixture was heated to 90 °C. Se powder (0.05 mmol) was added to this mixture under constant stirring and the reaction was continued for 2 h. The reaction mixture was then cooled to room temperature and purified by washing with methanol and subsequent centrifugation. The methanol precipitated cluster was re-dispersed in toluene and was used for further studies. The cluster was found to be soluble

in toluene, hexane, dichloromethane, dimethylformamide and tetrahydrofuran.

Sensing experiment

A thin layer chromatography (TLC) plate was coated with the cluster, which was prepared by dipping the TLC plate in cluster solution for 10 minutes and then drying it in air. Cluster adsorption on the TLC was evident from the intense luminescence obtained under UV light.

Instrumentation

Ultraviolet-visible (UV-Vis) spectra were measured with a PerkinElmer Lambda 25 instrument in the range of 200–1100 nm. Fourier-transform infrared spectra were measured with a PerkinElmer Spectrum One instrument. Matrix-assisted desorption ionization mass spectrometry (MALDI MS) studies were conducted using an Applied Biosystems Voyager-DE PRO Biospectrometry Workstation. A pulsed nitrogen laser at 337 nm was used for the MALDI MS studies. Mass spectra were collected in both the positive and negative ion modes. The matrix used was *trans*-2-[3-(4-*tert*-butylphenyl)-2-methyl-2-propenylidene]malononitrile. High-resolution transmission electron microscopy (HRTEM) was performed on a Jeol 3010 ultrahigh resolution analytical electron microscope. Samples for TEM were prepared by drop casting the toluene solution of cluster on a carbon coated copper grid and drying at room temperature. X-ray photoelectron spectroscopy (XPS) measurements were carried out using an Omicron ESCA probe spectrometer with polychromatic Mg K α X-rays ($h\nu = 1253.6$ eV). Luminescence measurements were carried out on a Jobin Yvon NanoLog instrument. Scanning electron microscopic (SEM) images and EDAX spectra were obtained using a FEI Quanta 200 SEM. Thermogravimetric analysis (TGA) measurements were obtained using PerkinElmer TGA7, and TA Instruments Q500 Hi-Res TGA instruments. Powder X-ray diffraction (PXRD) patterns were recorded using a Bruker D8 Advance X-ray diffractometer.

Results and discussion

Highly luminescent Ag₂Se clusters were synthesized by the addition of Se powder to the yellowish silver thiolate at 90 °C. The purified clusters were red in color and the corresponding optical absorption spectrum showed three prominent peaks, centered at 370 nm (3.35 eV), 445 nm (2.78 eV) and 570 nm (2.17 eV) which are different from those of the Ag₂Se and Ag₂S NPs reported so far. This cluster showed intense red luminescence under UV light both in the solution state and in the solid state (inset of Fig. 1) with a strong emission peak maximum around 625 nm (Fig. 1c). Previously reported Ag₂Se and Ag₂S NPs showed UV-Vis absorption in the higher wavelength region (above 600 nm). Most of the silver chalcogenide QDs have NIR emission and these emissions are highly size dependent. The PL QY of the cluster was calculated to be 21% using Rhodamine 6G as reference (QY = 94% in water). This QY is much higher

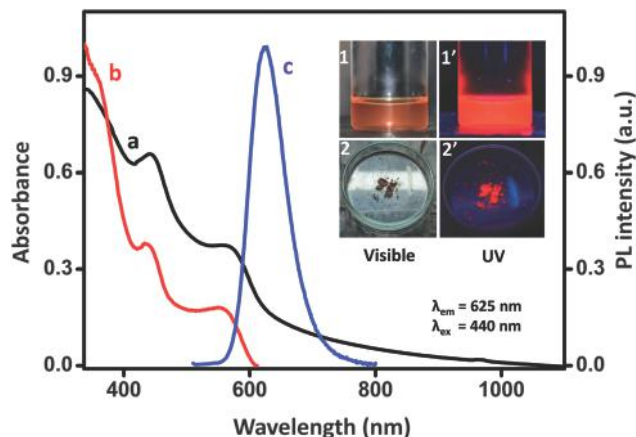


Fig. 1 Comparison of UV-Vis spectrum (a), excitation spectrum (b) and emission spectrum (c) of the cluster solution. Axis on the right is for traces (b) and (c). The cluster solution shows a strong emission around 625 nm with three excitation maxima (359, 440 and 564 nm), all of which resulted in a single emission maximum. The inset shows the photograph of the cluster under visible and UV light in solution state (1,1') and solid state (2,2'), respectively.

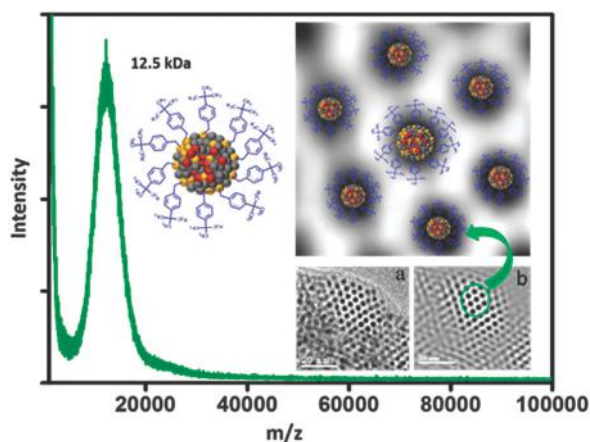


Fig. 2 MALDI MS of the purified cluster measured at threshold laser power in negative mode showing a single peak around 12.5 kDa. TEM images of the cluster showing highly monodispersed particles is shown in the inset (a). Inverse fast Fourier transform result of the same image is shown in (b).

than the already reported values of organic soluble noble metal clusters and other silver chalcogenide QDs.

Mass spectrometry is the best tool to assign such clusters precisely.^{26,27} This technique is being used extensively for noble metal clusters. Molecular understanding of QDs using MALDI MS is very rare.^{28–32} A sharp peak centered at 12.5 kDa was seen in the negative mode of MALDI MS (Fig. 2). Absence of other higher mass peaks in the mass spectra confirms the formation of small clusters unlike the other QDs where a series of peaks are typically seen. TEM images showed high monodispersity of the cluster with an average particle size of ~ 2 nm (inset of Fig. 2). Interestingly, these clusters assembled themselves in a hexagonal pattern throughout the TEM grid.

Identification of molecular mass and high monodispersity are not enough to calculate the precise composition of such clusters because the MALDI MS spectrum is broad, in comparison to monolayer aspicules such as Ag_{152} .²⁷ For further understanding of the composition, TGA was done and the corresponding data are presented in Fig. 3A. The TGA data suggest 40% weight loss around 250 °C which corresponds to the organic content present in the thiol functionality and the core mass may be calculated based on this. The cluster shows a typical PXRD pattern as shown in Fig. 3B(a). The XRD of the purified cluster showed a broad peak similar to other monolayer protected metal nanoclusters. Annealing of the cluster at 250 °C under an Ar atmosphere for 1 h gave a well defined XRD pattern which is shown in Fig. 3B(b). This XRD pattern matched with the Ag_2S acanthite phase (JCPDS No. 14-0072). The SEM EDS mapping and quantification data of the purified cluster solid showed an approximate ratio of Ag:Se:S as 1:0.24:0.70 (Fig. S1, ESI[†]). The EDAX data corresponding to the annealed cluster was also measured (Fig. S2, ESI[†]). This shows the presence of Ag, Se and S in the ratio 1:0.24:0.30. Annealing of the cluster under an inert atmosphere causes the detachment of the thiol protecting group, which is also evident from the EDAX data. A 40% weight loss in the TGA is in good agreement with the EDAX quantification. All of this quantitative data suggest that the cluster core also contains sulfur. In earlier work it has already been shown that Ag_2S NPs can form in solution above 80 °C, starting from $\text{Ag}_{25}\text{SR}_{18}$ clusters.³³ The scission of the C–S bond of thiolate and release of S^{2-} have also been reported by Wang *et al.* Seryotkin *et al.* reported that in silver sulfoselenide systems,

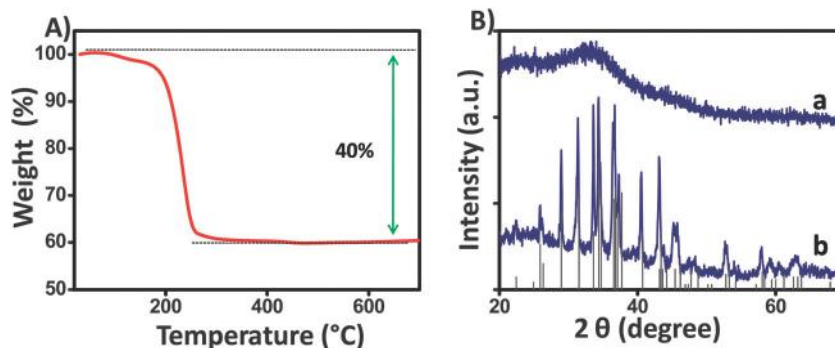


Fig. 3 (A) Thermogravimetric curve of the cluster. (B) XRD pattern of the cluster before (a) and after (b) annealing. XRD of the annealed clusters compared with Ag_2S JCPDS data (Black spectrum) (JCPDS No. 14-0072).

the acanthite phase is retained up to the composition, $\text{Ag}_2\text{Se}_x\text{S}_{1-x}$ with $0 \leq x \leq 0.6$ and the nannunite phase exists in the range of $0.8 \leq x \leq 1$.¹⁴ Observation of an Ag_2S type XRD pattern for the cluster is in good agreement with this report (Fig. 3B). The data presented here implies the formation of a cluster of composition $\text{AgSeS}@SR$. In the as-prepared condition, as it is in the cluster size regime, there are no well-defined peaks and upon annealing, the acanthite phase is exhibited. It is proposed that in such a cluster, part of the Ag-SR bond is broken and results in the incorporation of S^{2-} into the lattice and a few thiolate species are protecting the AgSeS core. Based on all of the data presented here (mass, composition, desorption data and diffraction), the cluster has been assigned as $\text{Ag}_{5.6}\text{Se}_{1.3}\text{S}_{1.5}@SBB_{28}$. This corresponds to a core composition of $\text{Ag}_2\text{Se}_x\text{S}_{1-x}$ composition with SBB protecting ligands.

Cluster composition was further confirmed by the XPS results. Survey spectrum suggested the presence of Ag, Se and S in the purified cluster (Fig. 4A). An expanded region of silver showed Ag $3d_{5/2}$ binding energy at 367.9 eV and Ag $3d_{3/2}$ binding energy at 373.9 eV (Fig. 4B), which indicate the oxidation of Ag ions in the univalent state. The peak at 54.3 eV corresponds to Se 3d and is expanded in Fig. 4C. In the sulfur region, the binding energies of 161.8 eV and 163.0 eV correspond to S $2p_{3/2}$ and S $2p_{1/2}$, respectively.

Utilizing the advantage of the intense red luminescence (QY = 21%) of this cluster, its application was explored towards sensing explored with a view to using it in sensing applications. Ag-S systems have inherent sensitivity towards metal ions.³⁴ Several metal ions such as Cd^{2+} , Cu^{2+} , Hg^{2+} , Pb^{2+} , Ni^{2+} and Zn^{2+} , were used for this experiment, initially in solution phase, which confirmed the selective sensing of Hg^{2+} by this cluster.

Fig. S3A (ESI[†]) shows the reduction of luminescence intensity upon the addition of different metal ions. A relative intensity diagram is plotted in Fig. S3C (ESI[†]). The detection limit of Hg^{2+} ions was found to be 1 ppb (Fig. S3B (ESI[†])). In order to develop a suitable solid state sensing device, a cluster coated TLC plate was prepared. In general, adsorption on an oxide surface enhances cluster luminescence, because of the reduction in radiative decay channels.^{15,35} A TLC plate was dipped into the cluster solution for 10 min and then dried at room temperature. Fig. 5 shows a photograph of the cluster coated TLC plate under UV light, after the addition of different metal ions. A solid state device also showed drastic quenching of cluster luminescence by Hg^{2+} ions. Concentration dependent luminescence was monitored using the solid state device, and the data are shown in Fig. 6A. Here the change in cluster luminescence as the Hg^{2+} concentration is varied, can be observed. However, the sensitivity was not significant enough for it to be used for visual detection. In order to enhance the visual effect of dye dependent change of cluster luminescence, the TLC plate was pre-coated with a Hg^{2+} insensitive dye, with a different emission wavelength. Fluorescein isothiocyanate (FITC) was used as the dye, which emits a bright green color. The results of such an experiment are shown in Fig. 6B. The combined system shows the emission of the cluster (red). Upon the addition of 500 ppb Hg^{2+} the red emission of the cluster was completely quenched and the underlying FITC emission became prominent. However, on this modified TLC plate, even 1 ppb shows substantial variation in color allowing easy visual detection. This color change is a result of the chemical interaction of Hg^{2+} with the cluster, which is evident from the XPS studies (Fig. S4, ESI[†]). The cluster core interacts with mercuric ions reducing it to the metallic state. The XPS spectrum after

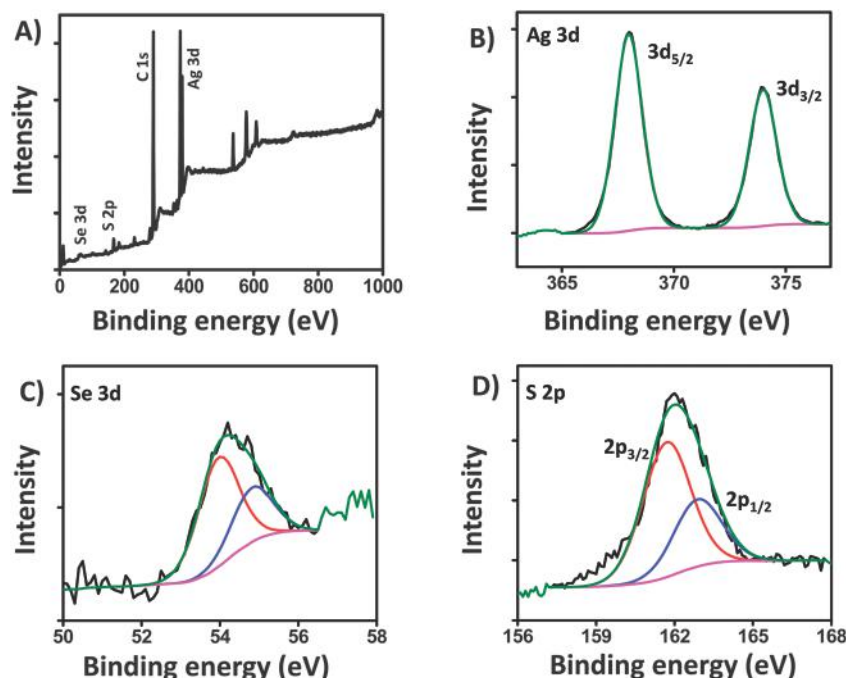


Fig. 4 XPS survey spectrum of the cluster showing the presence of Ag, Se and S (A). Specific regions of Ag 3d, Se 3d and S 2p are shown in (B)–(D).

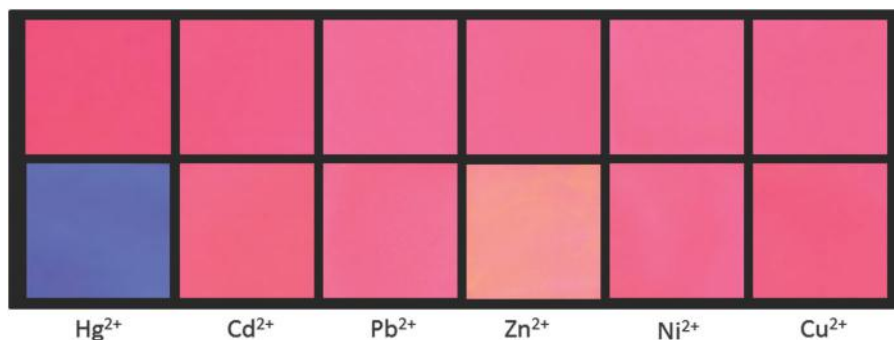


Fig. 5 Images of a sensing experiment performed using a cluster coated TLC plate. Sensitivity towards different metal ions was tested, at 1 ppm concentration for 2 min of exposure. Mercuric ions are more sensitive.

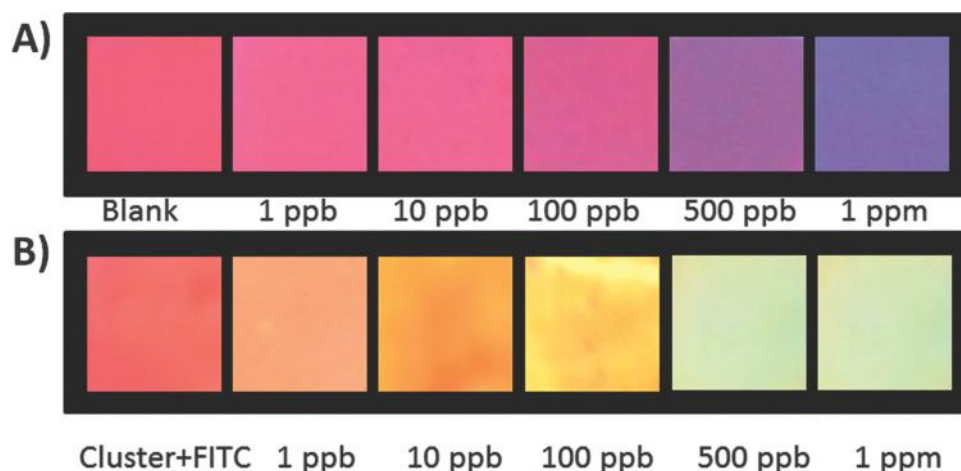


Fig. 6 Hg^{2+} concentration dependent luminescence quenching is shown in (A). Concentration dependent fluorescence quenching monitored using a FITC dye coated TLC plate (B).

quenching shows mercury in its metallic state (Fig. S4B, ESI[†]). Correspondingly there is also a change in silver binding energy (Fig. S4C, ESI[†]). In order to test the use of this solid state device in real life applications, quenching experiments were done with well water. There was no quenching observed for well water added to a cluster coated TLC plate. Thus, a repeat experiment was done with 1 ppb Hg^{2+} added to well water and quenching was observed. This experiment was also done using a FITC pre-coated TLC plate (Fig. S5, ESI[†]).

Conclusions

In conclusion, a core (AgSeS) shell (thiolate) Ag_2Se cluster system was prepared, which had an enhanced luminescence QY. Using various techniques such as MALDI MS, elemental analysis, TGA and XRD, the 12.5 kDa cluster was assigned to a molecular entity, $\text{Ag}_{56}\text{Se}_{13}\text{S}_{15}@\text{SBB}_{28}$. The QY of the cluster was found to be 21%. This QY is much higher than the reported values for similar cluster systems. It was also shown that the red emission can be used for environmental applications. Incorporation of the cluster into solid supports results in enhanced sensitivity for the sensor and may be useful in developing devices for rapid detection of environmental contaminants.

Acknowledgements

We thank the Department of Science and Technology, Government of India for constantly supporting our research program on nanomaterials. C. K. M. thanks CSIR for a research fellowship. I. C. thanks IIT Madras for his institute postdoctoral fellowship.

References

- 1 M. F. Frasco and N. Chaniotakis, *Sensors*, 2009, **9**, 7266–7286.
- 2 Y. Lou, Y. Zhao, J. Chen and J.-J. Zhu, *J. Mater. Chem. C*, 2014, **2**, 595–613.
- 3 S. Silvi and A. Credi, *Chem. Soc. Rev.*, 2015, **44**, 4275–4289.
- 4 V. Lesnyak, N. Gaponik and A. Eychmueller, *Chem. Soc. Rev.*, 2013, **42**, 2905–2929.
- 5 Y.-P. Gu, R. Cui, Z.-L. Zhang, Z.-X. Xie and D.-W. Pang, *J. Am. Chem. Soc.*, 2012, **134**, 79–82.
- 6 R. Gui, H. Jin, Z. Wang and L. Tan, *Coord. Chem. Rev.*, 2015, **296**, 91–124.
- 7 P. Jiang, Z.-Q. Tian, C.-N. Zhu, Z.-L. Zhang and D.-W. Pang, *Chem. Mater.*, 2012, **24**, 3–5.

- 8 L. Tan, A. Wan and H. Li, *ACS Appl. Mater. Interfaces*, 2013, **5**, 11163–11171.
- 9 L. Tan, A. Wan and H. Li, *Langmuir*, 2013, **29**, 15032–15042.
- 10 C.-N. Zhu, P. Jiang, Z.-L. Zhang, D.-L. Zhu, Z.-Q. Tian and D.-W. Pang, *ACS Appl. Mater. Interfaces*, 2013, **5**, 1186–1189.
- 11 C. Ji, Y. Zhang, T. Zhang, W. Liu, X. Zhang, H. Shen, Y. Wang, W. Gao, Y. Wang, J. Zhao and W. W. Yu, *J. Phys. Chem. C*, 2015, **119**, 13841–13846.
- 12 O. Fuhr, S. Dehnen and D. Fenske, *Chem. Soc. Rev.*, 2013, **42**, 1871–1906.
- 13 G. Li, Z. Lei and Q.-M. Wang, *J. Am. Chem. Soc.*, 2010, **132**, 17678–17679.
- 14 Y. V. Seryotkin, G. A. Palyanova and K. A. Kokh, *J. Alloys Compd.*, 2015, **639**, 89–93.
- 15 T. U. B. Rao and T. Pradeep, *Angew. Chem., Int. Ed.*, 2010, **49**, 3925–3929.
- 16 K. M. Harkness, Y. Tang, A. Dass, J. Pan, N. Kothalawala, V. J. Reddy, D. E. Cliffl, B. Demeler, F. Stellacci, O. M. Bakr and J. A. McLean, *Nanoscale*, 2012, **4**, 4269–4274.
- 17 A. Baksi, M. S. Bootharaju, X. Chen, H. Hakkinen and T. Pradeep, *J. Phys. Chem. C*, 2014, **118**, 21722–21729.
- 18 A. Ghosh and T. Pradeep, *Eur. J. Inorg. Chem.*, 2014, 5271–5275.
- 19 P. D. Jadzinsky, G. Calero, C. J. Ackerson, D. A. Bushnell and R. D. Kornberg, *Science*, 2007, **318**, 430–433.
- 20 C. P. Joshi, M. S. Bootharaju, M. J. Alhilaly and O. M. Bakr, *J. Am. Chem. Soc.*, 2015, **137**, 11578–11581.
- 21 L. G. AbdulHalim, M. S. Bootharaju, Q. Tang, S. Del Gobbo, R. G. AbdulHalim, M. Eddaoudi, D.-e. Jiang and O. M. Bakr, *J. Am. Chem. Soc.*, 2015, **137**, 11970–11975.
- 22 H. Yang, Y. Wang, H. Huang, L. Gell, L. Lehtovaara, S. Malola, H. Hakkinen and N. Zheng, *Nat. Commun.*, 2013, **4**, 2422.
- 23 S. Bhat, I. Chakraborty, A. Baksi, R. P. Narayanan and T. Pradeep, *Nanoscience*, The Royal Society of Chemistry, 2016, vol. 3, pp. 343–385.
- 24 G. Natarajan, A. Mathew, Y. Negishi, R. L. Whetten and T. Pradeep, *J. Phys. Chem. C*, 2015, **119**, 27768–27785.
- 25 A. Mathew and T. Pradeep, *Part. Part. Syst. Charact.*, 2014, **31**, 1017–1053.
- 26 A. Dass, *J. Am. Chem. Soc.*, 2009, **131**, 11666–11667.
- 27 I. Chakraborty, A. Govindarajan, J. Erusappan, A. Ghosh, T. Pradeep, B. Yoon, R. L. Whetten and U. Landman, *Nano Lett.*, 2012, **12**, 5861–5866.
- 28 D. Fenske, C. E. Anson, A. Eichhoefer, O. Fuhr, A. Ingendoh, C. Persau and C. Richert, *Angew. Chem., Int. Ed.*, 2005, **44**, 5242–5246.
- 29 Y. Wang, Y.-H. Liu, Y. Zhang, F. Wang, P. J. Kowalski, H. W. Rohrs, R. A. Loomis, M. L. Gross and W. E. Buhro, *Angew. Chem., Int. Ed.*, 2012, **51**, 6154–6157.
- 30 G. A. Khitrov and G. F. Strouse, *J. Am. Chem. Soc.*, 2003, **125**, 10465–10469.
- 31 A. Kasuya, R. Sivamohan, Y. A. Barnakov, I. M. Dmitruk, T. Nirasawa, V. R. Romanyuk, V. Kumar, S. V. Mamykin, K. Tohji, B. Jeyadevan, K. Shinoda, T. Kudo, O. Terasaki, Z. Liu, R. V. Belosludov, V. Sundararajan and Y. Kawazoe, *Nat. Mater.*, 2004, **3**, 99–102.
- 32 S. Dolai, P. R. Nimmala, M. Mandal, B. B. Muhoberac, K. Dria, A. Dass and R. Sardar, *Chem. Mater.*, 2014, **26**, 1278–1285.
- 33 K. P. Remya, T. Udayabhaskararao and T. Pradeep, *J. Phys. Chem. C*, 2012, **116**, 26019–26026.
- 34 I. Chakraborty, T. Udayabhaskararao and T. Pradeep, *J. Hazard. Mater.*, 2012, **211–212**, 396–403.
- 35 M. A. H. Muhammed, P. K. Verma, S. K. Pal, R. C. A. Kumar, S. Paul, R. V. Omkumar and T. Pradeep, *Chem. – Eur. J.*, 2009, **15**, 10110–10120.

Electronic supplementary information (ESI):

Highly luminescent monolayer protected $\text{Ag}_{56}\text{Se}_{13}\text{S}_{15}$ clusters

C. K. Manju,^aIndranathChakraborty^{a,b} and ThalappilPradeep^{a*}

^a*DST Unit of Nanoscience (DST UNS) and Thematic Unit of Excellence,
Department of Chemistry, Indian Institute of Technology Madras,
Chennai 600036, India.*

^bCurrent affiliation: *University of Illinois at Urbana Champaign, Urbana, IL
61801, USA.*

Table of contents

No	Description	Pg No
S1	SEM EDX and elemental mapping of pure cluster	2
S2	SEM EDX and elemental mapping of annealed cluster	3
S3	PI spectrum showing the effect of different metal ions and concentration dependent Hg^{2+} quenching	4
S4	XPS spectrum of cluster after Hg^{2+} addition	5
S5	Real water luminescence quenching experiment	6

Supporting information 1

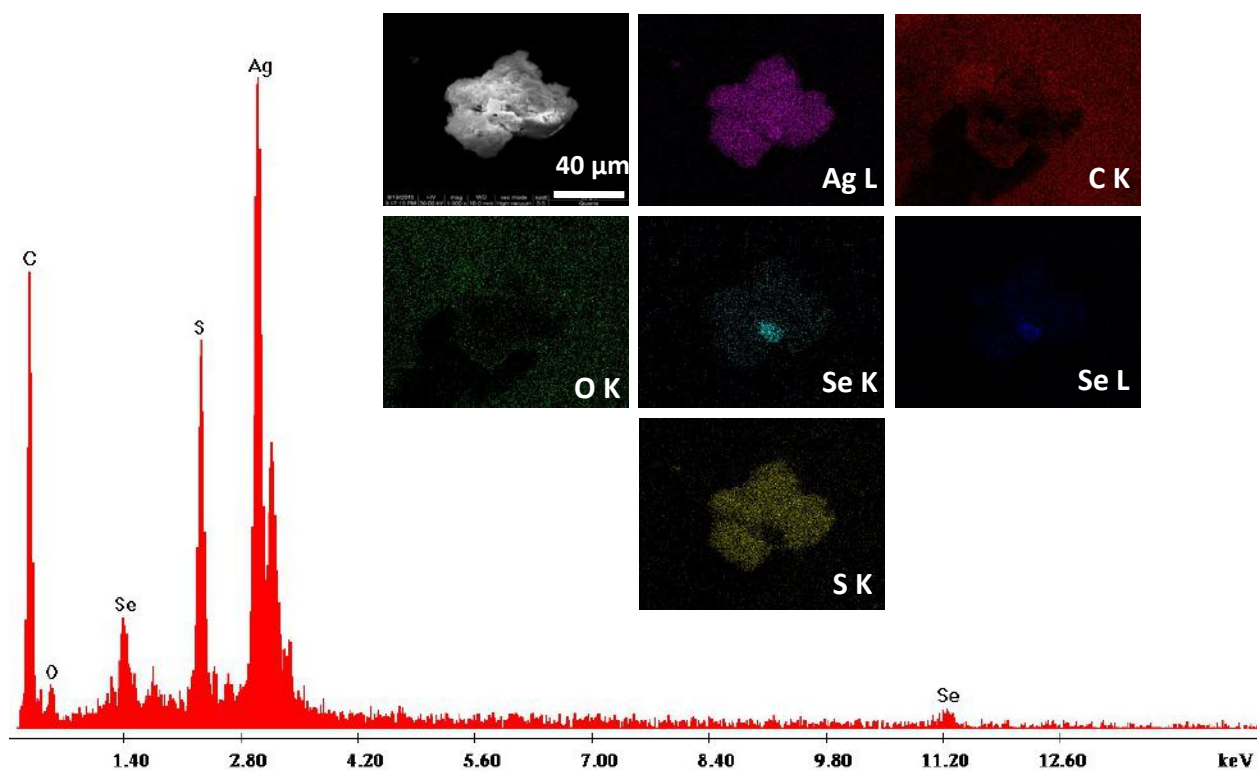


Fig. S1 SEM EDAX spectrum and elemental mapping of purified cluster. The Ag:Se:S ratio is 1:0.24:0.70.

Supporting information 2

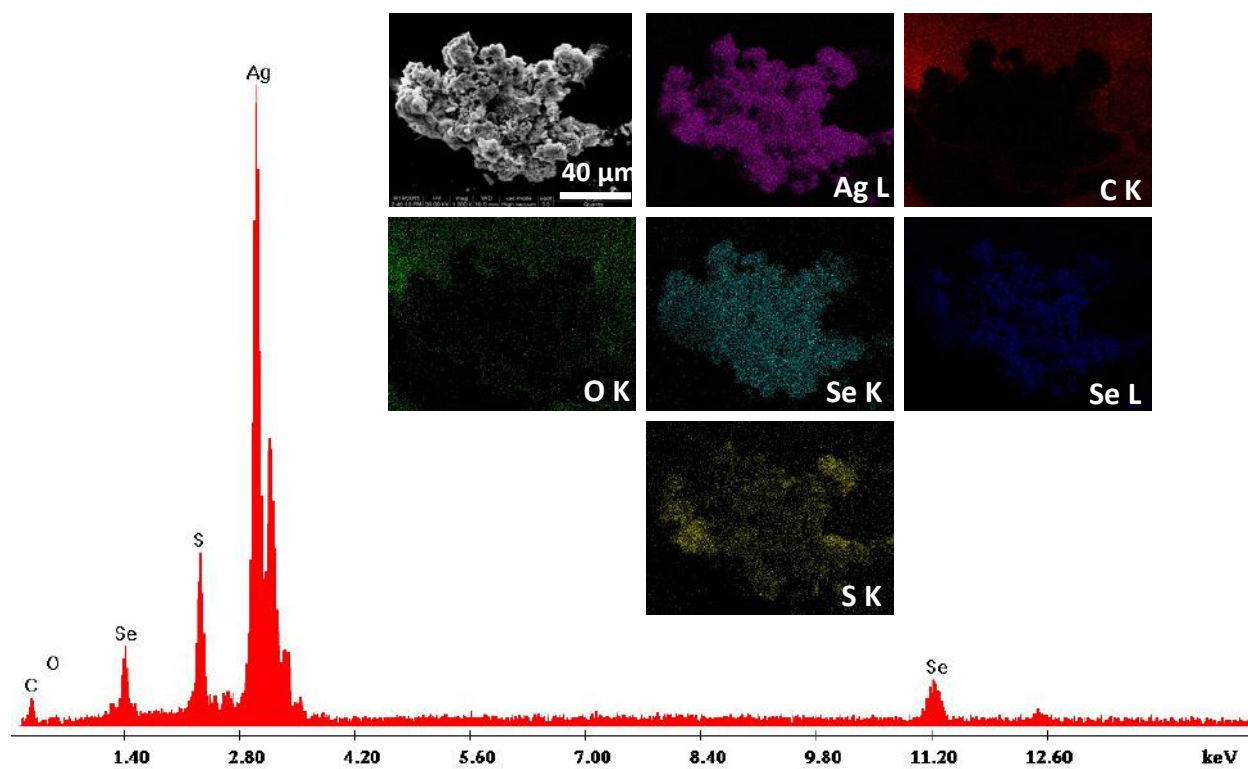


Fig. S2 SEM EDAX spectrum and elemental mapping of annealed cluster. The Ag:Se:S ratio is 1:0.24:0.30.

Supporting information 3

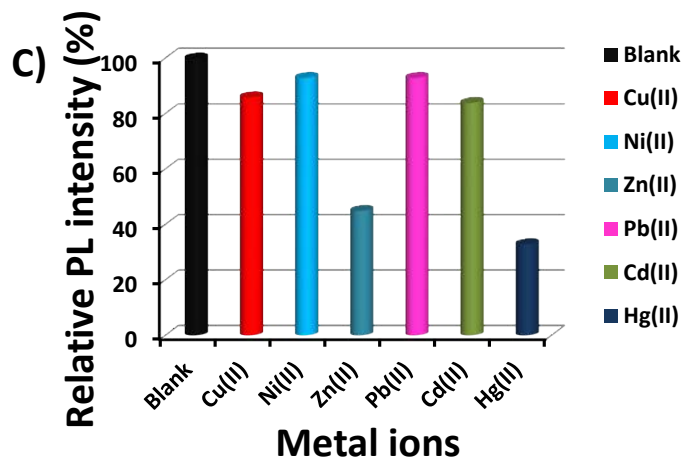
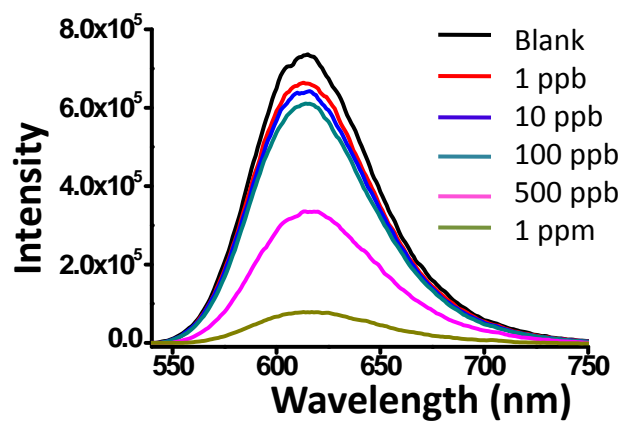
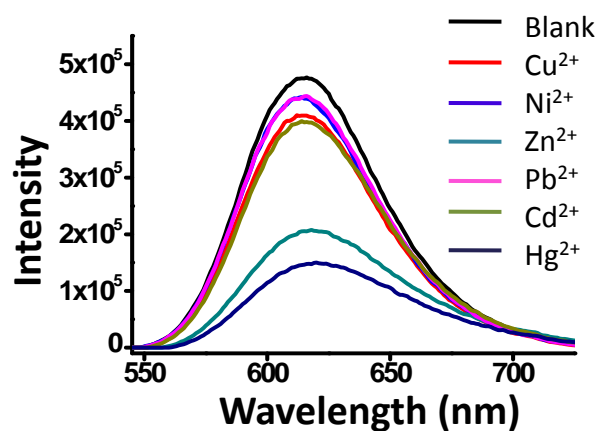


Fig. S3 Effect of different metal ions on the emission intensity of the cluster (A). Hg(II) concentration effect on cluster emission (B). (C) Bar diagram of different metal ion sensitivity. Hg(II) shows maximum quenching.

Supporting information 4

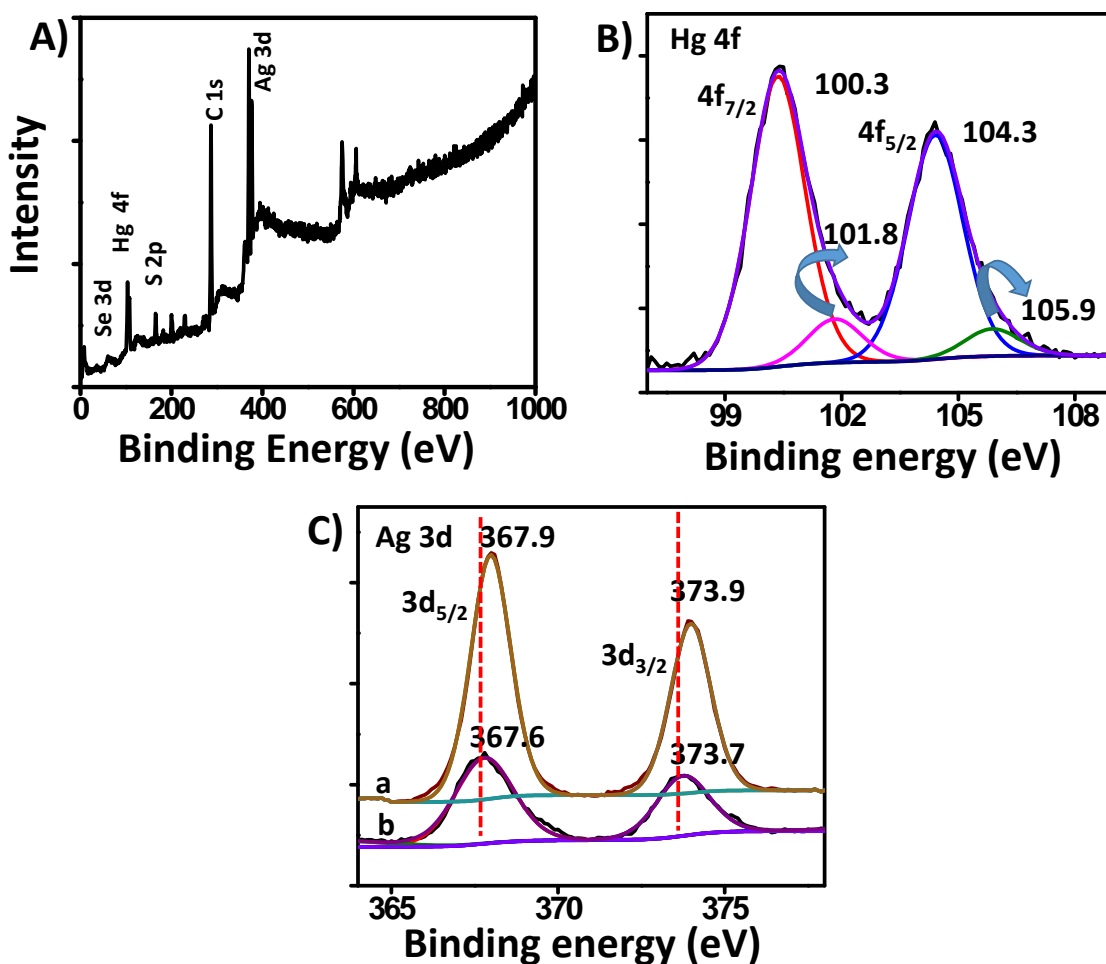


Fig. S4 XPS survey spectrum of cluster after the addition of Hg^{2+} (A). Specific region for Hg is expanded in (B), where most of the Hg^{2+} ions are reduced to elemental mercury. Figure (C) shows the XPS spectra of silver before (a) and after (b) mercury quenching.

Supporting information 5

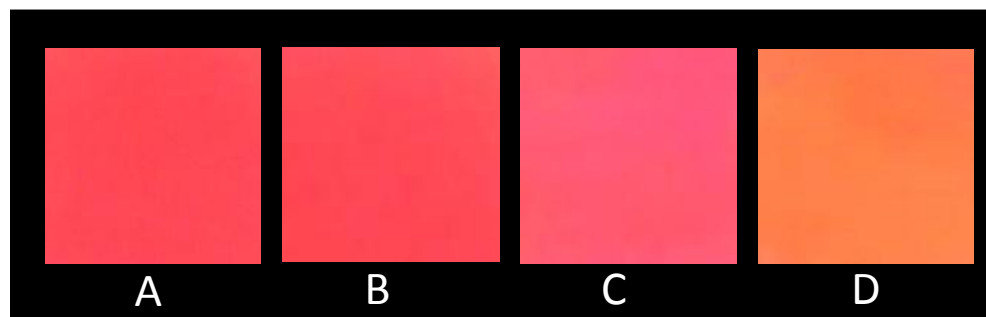


Fig. S5 (A) Cluster coated TLC plate under UV light. (B) Same TLC plate after the addition of well water. (C) After the addition of 1 ppb Hg^{2+} ion contacting well water. (D) Photograph of the quenching experiment performed on FITC pre coated TLC plate.



Thio residue from thermal processing of cometary ices containing carbon disulfide and ammonia

R.R.J. Methikkalam^a, S. Pavithraa^b, S.P. Murali Babu^b, H. Hill^c, B.N. Raja Sekhar^d,
T. Pradeep^a, B. Sivaraman^{b,*}

^a DST Unit on Nanoscience and Thematic Unit of Excellence (TUE), Department of Chemistry, Indian Institute of Technology Madras, Chennai, India

^b Atomic Molecular and Optical Physics Division, Physical Research Laboratory, Ahmedabad, India

^c International Space University, Strasbourg, France

^d Atomic and Molecular Physics Division, BARC at RRCAT, Indore, India

Received 23 January 2016; received in revised form 10 April 2016; accepted 27 April 2016

Available online 3 May 2016

Abstract

We have carried out experimental investigation on binary ice mixture containing carbon disulfide (CS₂) and ammonia (NH₃) ices formed at 10 K. Icy films were formed in various combinations to investigate the reactivity of CS₂ and NH₃ molecules on cometary nucleus. In the case of NH₃ ices, deposition carried out at 10 K was found to contain NH₃ homo-dimers that was found to reorient upon annealing to 40 K. Phase transition was found to take place as the 10 K ice was warmed to higher temperatures and the phase transition temperature was found to be 5 K higher for the mixed ice in comparison to the layered deposits. Thermal processing of the mixed deposition of CS₂–NH₃ ice was found to leave thio residue, which could be ammonium dithiocarbamate that was even found to be present at 340 K.

© 2016 COSPAR. Published by Elsevier Ltd. All rights reserved.

Keywords: Astrochemistry; Methods: laboratory: solid state; ISM: molecules; Comets: general; Infrared: general

1. Introduction

Comets are known to harbor variety of simple and complex molecules. Irradiation and thermal processing of simple ices present may lead to the formation of complex molecules (Flynn et al., 2006; McKeegan et al., 2006). In fact, the recent discoveries on the new simple and complex molecules (such as amide and polyoxymethane) on comets are added evidences (Wright et al., 2015). However, the formation of such molecules could be due to photolysis and/or thermal processing. In order to understand the role of molecules that are already known to be present on a cometary nucleus, laboratory simulations of cometary nucleus

are needed. Here we select two of the simple molecules, CS₂ and NH₃, that are known to be present on comets and such a mixture is studied in laboratory analogs.

First direct detection of CS₂ was made in 1995 in Comet 122P/de Vico by comparing the unidentified spectral lines of the comet in the visible and ultraviolet region with the experimental spectra of supersonically cooled CS₂ (Jackson et al., 2004). Perhaps this discovery was only after fifteen years since the first identification of C–S bonds in Comet West in 1980 (Smith et al., 1980). Recently (Sivaraman, 2016) the presence of CS₂ molecules on cold regions of Lunar south pole was confirmed. The first identification of NH₃ on a comet was made in the 1980's in Comet 1983 d (Altenhoff et al., 1983). It was estimated that six percent of the gases subliming from the nucleus of the comet were NH₃. Measurements using Gas Chromatography Mass

* Corresponding author.

E-mail address: bhala@prl.res.in (B. Sivaraman).

Spectrometer (GCMS) onboard Huygens probe revealed the nitrogen rich atmosphere of Titan is in fact from the impact driven chemistry of NH_3 which is a major constituent in the upper and mid atmosphere of Titan (Niemann et al., 2005).

NH_3 and CS_2 molecules being widely present in many planetary bodies including comets, it is of utmost interest to the planetary scientists and therefore extensive spectroscopic studies have been done on these two molecules in astrophysical conditions (Fresneau et al., 2014; Garozzo et al., 2010; Maity and Kaiser, 2013; Mangum et al., 2013). Though these two molecules were investigated, however their reactivity in mixtures at low temperature are yet to be explored. Similar thermal reactivity of NH_3 and CO_2 were investigated in solid phase (Bossa et al., 2008a,b; Lv et al., 2014; Noble et al., 2014; Rodriguez-Lazcano et al., 2014) and have found to form ammonium carbamate and carbamic acid. Here we present the results of the thermal processing of the binary ice mixture containing CS_2 and NH_3 ices deposited in various combinations and probed using Fourier Transform InfraRed (FTIR) Spectroscopy, in astrophysical conditions.

2. Experimental method

Experiments were carried out in the new experimental chamber housed in the laboratory for low temperature astrochemistry at Physical Research Laboratory (PRL), India. An Ultrahigh Vacuum (UHV) chamber, that can reach base pressures up to 10^{-10} mbar, containing a cold head with Zinc Selenide (ZnSe) substrate cooled down to 10 K was used to simulate the cometary ices. An all metal leak valve was used to introduce gases to form molecular ices on to the cooled ZnSe substrate at 10 K.

CS_2 , 99.9% pure vapor (molecules), from the liquid sample were let into the chamber through after two freeze–pump–thaw cycles at liquid nitrogen temperature. NH_3 , 99.99% pure, were let into the chamber through the gas line. A gas mixing chamber was used to mix both the molecules before they were let into the chamber to condense on to the ZnSe substrate kept at 10 K. Molecular ices thus formed at 10 K was then warmed to higher temperatures and subsequently probed in the Mid-IR region ($4000\text{--}500\text{ cm}^{-1}$), resolution of 2 cm^{-1} , using Fourier Transform InfraRed (FTIR) Spectrometer.

After recording InfraRed (IR) spectra for pure samples experiments were performed with binary ice mixtures in different combinations:

- (i) CS_2 molecules were let into the UHV chamber to form CS_2 ice on the ZnSe substrate at 10 K. Then NH_3 molecules were inlet into the chamber and were made to condense over the CS_2 molecular ice at 10 K. A spectrum was recorded at 10 K and the ice layers were warmed to higher temperatures with subsequent recording of spectra at different temperatures until sublimation.

- (ii) NH_3 molecules were let into the UHV chamber to form NH_3 ice on the ZnSe substrate at 10 K. Then CS_2 molecules were inlet into the chamber and were made to condense over the NH_3 molecular ice at 10 K. A spectrum was recorded at 10 K and the ice layers were warmed to higher temperatures with subsequent recording of spectra at different temperatures until sublimation.
- (iii) Both NH_3 and CS_2 were prepared in the gas mixing chamber before letting into the UHV chamber to form icy mixture of NH_3 and CS_2 on the ZnSe substrate kept at 10 K. A spectrum was recorded at 10 K and the ice mixture was warmed to higher temperatures with subsequent recording of spectra at different temperatures until sublimation.

3. Results and discussion

3.1. Pure CS_2 ice

Spectrum recorded after pure CS_2 deposition at 10 K revealed characteristic bands that correspond to CS_2 molecules in the $2500\text{--}1000\text{ cm}^{-1}$ region (Fig. 1(a)). The most intense peaks observed at 1525 cm^{-1} and 1460 cm^{-1} were assigned to C–S symmetric stretching. Few other bands with peak positions at 2145 cm^{-1} , 2106 cm^{-1} , 2214 cm^{-1} , 2284 cm^{-1} were assigned (Maity et al., 2013) to combination vibration modes as mentioned in Table 1. Upon warming the ice changes observed in the fundamental modes indicated a phase change from amorphous to crystalline to have completed at 80 K. Polycrystalline CS_2 is being reported to form when it is vapor deposited at 80 K (liquid nitrogen temperature) (Yamada and Person, 1964).

3.2. Pure NH_3 ice

Pure NH_3 molecules were deposited on the substrate and a spectrum was recorded at 10 K where several peaks were found to appear in the $3500\text{--}1000\text{ cm}^{-1}$ region (Fig. 1(b)). The bands at 3375 cm^{-1} , 3311 cm^{-1} , 3244 cm^{-1} and 3208 cm^{-1} were assigned to N–H symmetric stretching (Dows et al., 1955). The band at 1872 cm^{-1} , 1649 cm^{-1} and 1627 cm^{-1} are assigned to H–N–H scissoring vibrations. The most intense band at 1060 cm^{-1} is assigned to N–H wagging vibration. The spectral signatures confirmed (Fig. 2) phase change from amorphous to crystalline NH_3 (Zheng and Kaiser, 2007) to have occurred in the ice at 65 K. The two new bands with peak positions at 3311 cm^{-1} and 3244 cm^{-1} are attributed to the formation of homo-dimers that undergo reorientation upon annealing to higher temperatures. The bands at 3311 cm^{-1} and 3244 cm^{-1} were then found to be missing in the spectrum recorded at 40 K (Fig. 2). Rearrangement of such homo-dimers is known from earlier studies on molecules in the condensed phase (Sivaraman et al., 2012, 2013). Such a change happening within the ice formed at 10 K and

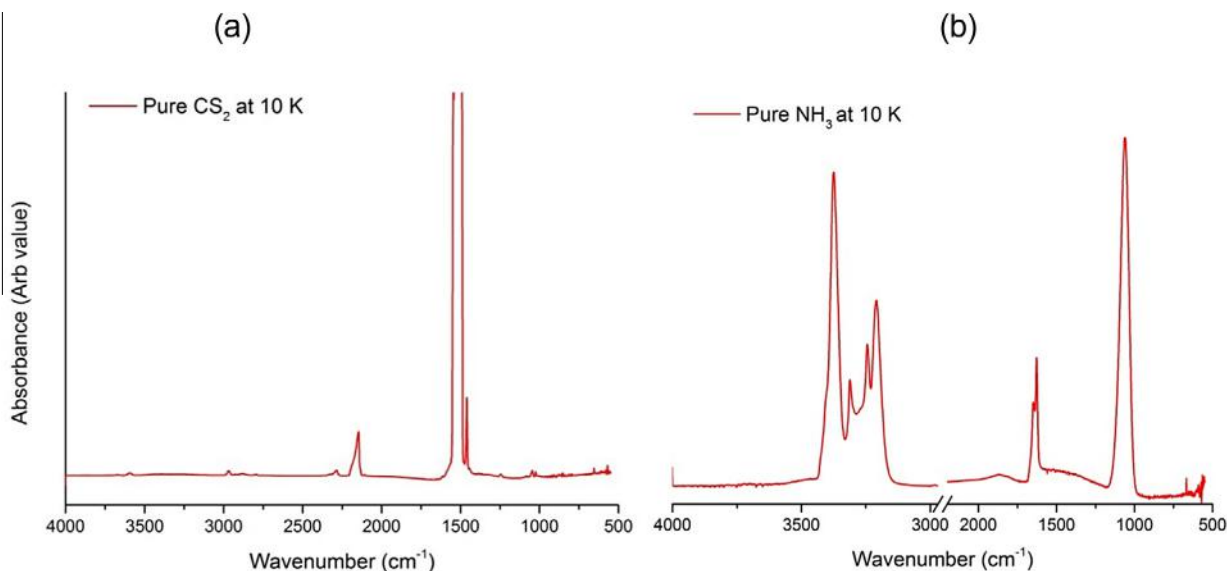


Fig. 1. Infrared spectra of (a) pure CS₂ at 10 K and (b) pure NH₃ at 10 K. Line break was introduced in (b) in order to enhance the spectral features in the 3500–3000 cm⁻¹ region.

Table 1
Peak positions and band assignments. Assignments for NH₃ and CS₂ are taken from Maity et al. (2013) and Zheng and Kaiser (2007), respectively.

NH ₃				CS ₂			
10 K	65 K	80 K	Band assignment	10 K	65 K	80 K	Band assignment
3375.6	3375	3375.2	v ₃ (N–H degenerated stretching)	2284.4	2284.4	2286.9	2v ₂ + v ₃ (combination band)
3311.0	3288.8	3288.8	v ₁ or 2v ₄ (N–H symmetric stretching)	2214.6	2216.4	2219.1	2v ₂ + v ₃ (combination band)
3244.7	–	–	v ₃ (N–H degenerated stretching)	2145.5	2145.3	2145.1	v ₁ + v ₃ (C–S stretching)
3208.7	3206.1	3206.1	v ₁ (N–H symmetric stretching)	2106.3	2105.7	2100.7	v ₁ + v ₃ (C–S stretching of ¹³ CS ₂)
1872.7	1895.1	1896.1	v ₄ + v _L (H–N–H Scissoring)	1516.1	1507	1508.1	v ₃ (C–S stretching)
1649.7	1645.7	1645.7	v ₄ (H–N–H Scissoring)	1460.8	1459.5	1455.9	v ₃ (C–S stretching of ¹³ CS ₂)
CS ₂ + NH ₃ – mixed deposit							
3377.8	3368.2	3377.8		2168.1	2154.1	2158.8	
3311.4	3292.9	3288.1		1520.5	1516.6	1516.7	
3244.2	–	–					
3207.9	3207.9	3205					
1868.5	1869.2	1869.2					
1649.9	1652.7	1652.7					
1627.3	1635.8	1635.8					
1058.8	1072.9	1095.5					

warmed to 40 K suggests that the ice formed at 10 K could be highly porous as it is rich in homo-dimers of NH₃.

3.3. CS₂ below NH₃

Layered deposition for CS₂ below NH₃ was carried out at 10 K and an IR spectrum was recorded. Characteristic vibrational signatures of NH₃ and CS₂ were found to be present in the spectra recorded at 10 K (Table 1). Icy layers thus formed were heated to higher temperatures with subsequent recording of IR spectra. From the temperature dependent IR spectra in Fig. 3(a) we find that the intensity of the bands gradually decreases when the sample is warmed to higher temperatures and both NH₃ and CS₂ ices sublime after 120 K. A phase change temperature from

amorphous to crystalline form was found to be 80 K for CS₂ and 65 K for NH₃.

3.4. NH₃ below CS₂

Layered deposition for NH₃ below CS₂ was carried out at 10 K and an IR spectrum was recorded. Characteristic vibrational signatures of CS₂ and NH₃ were found to be present in the spectra recorded at 10 K (Table 1). Icy layers thus formed were heated to higher temperatures with subsequent recording of IR spectra. From the temperature dependent IR spectra in Fig. 3(b) we find that the intensity of the N–H symmetric stretching bands at 3375 cm⁻¹, 3311 cm⁻¹, 3244 cm⁻¹ and 3208 cm⁻¹ is present till 130 K due to crystalline CS₂ on top of NH₃ which was resisting NH₃ sublimation. Thus the intensity of the N–H symmet-

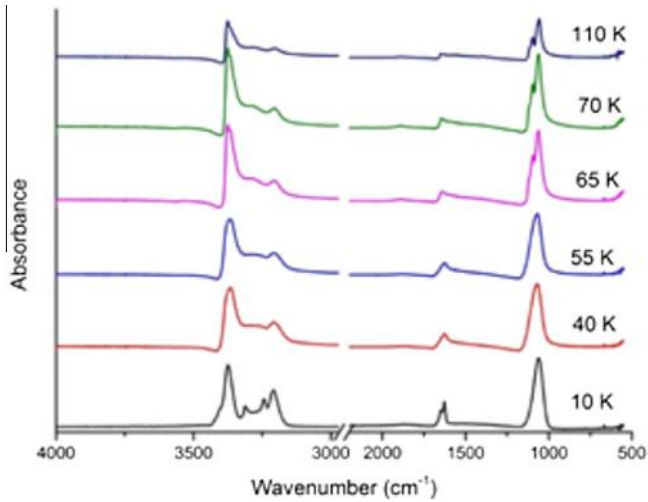


Fig. 2. Temperature dependent infrared spectra of pure NH_3 with the presence of homo-dimers at 10 K which got reoriented when warmed to 40 K.

ric stretching bands remains high till 130 K and then sublimation started while CS_2 molecules started to sublime. The phase change temperature from amorphous to crystalline form was found to be the same as in the case of CS_2 below NH_3 ; 80 K for CS_2 and 65 K for NH_3 .

3.5. Ice mixtures NH_3 , CS_2

Both NH_3 and CS_2 were mixed in the gas line and deposited at 10 K. An IR spectrum was recorded at 10 K. IR bands of NH_3 and CS_2 in Table 1 were found to be present in the spectra recorded at 10 K. The ice mixture was warmed to higher temperatures and a spectrum was recorded at until 340 K (Fig. 3(c)). Here again we find that the intensity of the N–H symmetric stretching bands at 3375 cm^{-1} , 3311 cm^{-1} , 3244 cm^{-1} and 3208 cm^{-1} is present till 110 K. The phase change was found to occur at a temperature which is 5 K higher than the phase change temper-

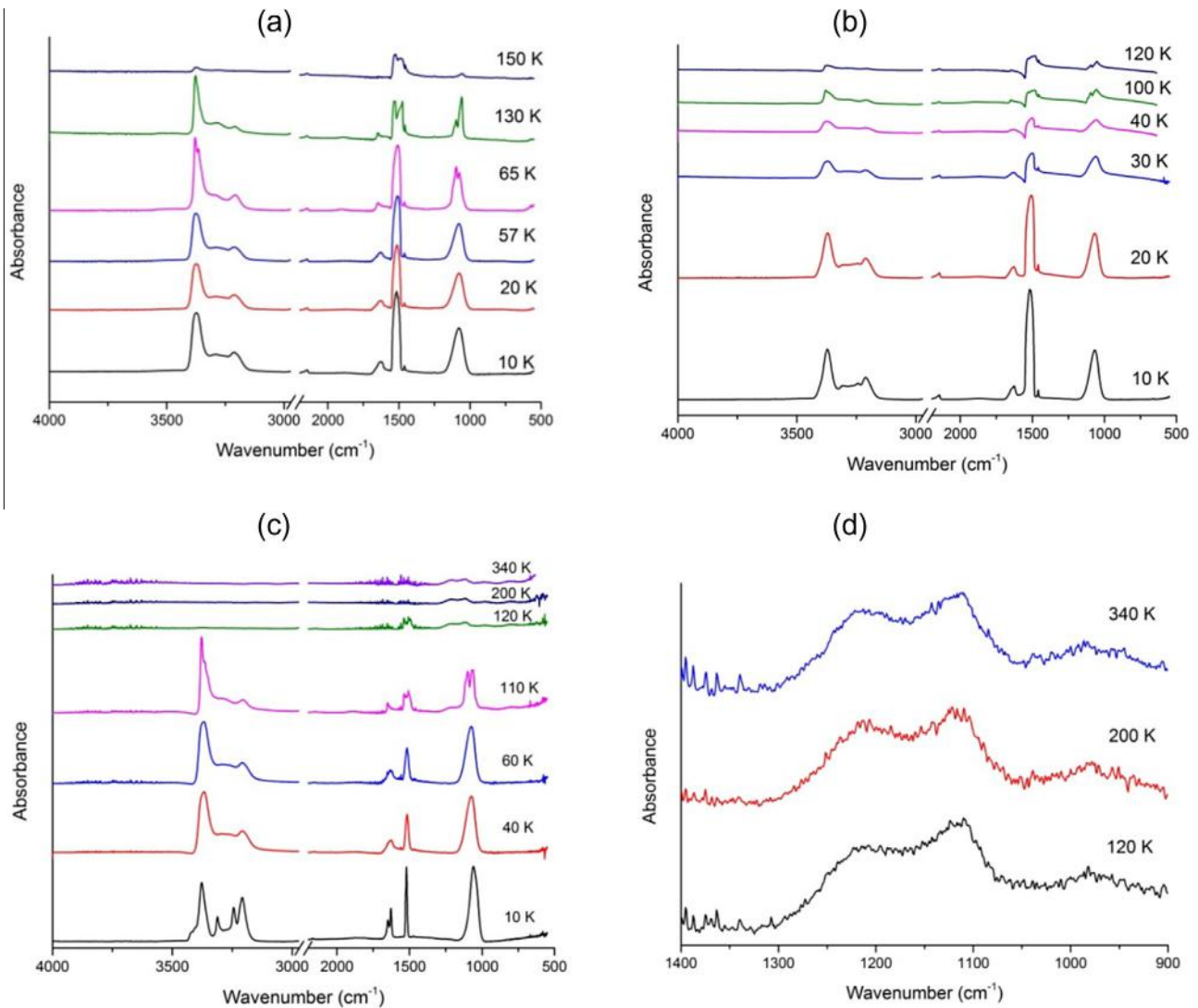


Fig. 3. (a) Temperature dependent infrared spectra of CS_2 below NH_3 deposited at 10 K. (b) Temperature dependent infrared spectra of NH_3 below CS_2 deposited at 10 K. (c) Temperature dependent infrared spectra of mixed deposit of CS_2 and NH_3 deposited at 10 K. (d) Infrared spectra of ammonium dithiocarbamate – residue left behind at higher temperatures upon heating the mixed deposit of CS_2 and NH_3 ices.

Table 2
Column density of ice mixtures as deposited at 10 K.

Ice sample at 10 K	Band (cm ⁻¹)	A value (cm mol ⁻¹)	Column density (No. of molecules)	Ratio CS ₂ :NH ₃
Pure NH ₃ Fig. 1a	1069 cm ⁻¹	*1.63 × 10 ⁻¹⁷	20.29 × 10 ¹⁷	–
Pure CS ₂ Fig. 1b	1520 cm ⁻¹	**9.13 × 10 ⁻¹⁷	18.74 × 10 ¹⁷	–
CS ₂ below NH ₃ Fig. 3a	NH ₃ 1069 cm ⁻¹ CS ₂ 1520 cm ⁻¹	1.63 × 10 ⁻¹⁷ 9.13 × 10 ⁻¹⁷	28.18 × 10 ¹⁷ 7.00 × 10 ¹⁷	1:4
NH ₃ below CS ₂ Fig. 3b	NH ₃ 1069 cm ⁻¹ CS ₂ 1520 cm ⁻¹	1.63 × 10 ⁻¹⁷ 9.13 × 10 ⁻¹⁷	43.74 × 10 ¹⁷ 7.63 × 10 ¹⁷	1:6
NH ₃ + CS ₂ mixture Fig. 3c	NH ₃ 1069 cm ⁻¹ CS ₂ 1520 cm ⁻¹	1.63 × 10 ⁻¹⁷ 9.13 × 10 ⁻¹⁷	9.28 × 10 ¹⁷ 0.30 × 10 ¹⁷	1:30

References.

* A value for NH₃; Bouilloud et al. (2015).

** A value for CS₂; Garozzo et al. (2010).

ature found in the layered deposits, 85 K for CS₂ and 70 K for NH₃ (Table 1). This could be due to NH₃ and CS₂ present as mixed ices where the molecules have to segregate from the mixture to crystallize.

From the temperature dependent spectra in Fig. 3(c) we infer that even after the sublimation of the NH₃ and CS₂ ices above 110 K, there was a residue left behind which was present (1000–1300 cm⁻¹) even after the sample was warmed to 340 K (Fig. 3(d)). There are two broad absorption bands, one centered at 1220 cm⁻¹ and the other centered at 1110 cm⁻¹. Based on the band positions (Knoeck and Witt, 1976) this could be ammonium dithiocarbamate that have been synthesized, via reaction given in Eq. (1) (Mathes et al., 2007), by warming the icy mixture of NH₃ and CS₂ formed at 10 K. In an earlier experiment ammonium carbamate synthesis from a mixture of NH₃ and CO₂ was reported (Bossa et al., 2008a,b; Jheeta et al., 2012; Lv et al., 2014; Noble et al., 2014; Rodriguez-Lazcano et al., 2014). Therefore, due to the sulfur bearing parent molecule it is likely that the sulfur residue observed in our experiment is a thio compound.



The thermal reaction of NH₃ and CS₂ is likely to be very similar to the reaction of NH₃ and CO₂. Bossa et al. (2008b) studied reaction of 1:1 mixtures of NH₃ and CO₂ and found that 49% of CO₂ sublimates out without reacting with NH₃ and the rest likely react with NH₃ thermally and form two products ammonium carbamate and carbamic acid in 1:1 ratio. Noble et al. (2014) extended this to study the kinetics of this reaction, and came out with the conclusion that the reaction is mostly first order with respect to CO₂ in the temperature range of 70–90 K. The reaction is not possible in CO₂ dominated ice, while NH₃ dominated ice gives only ammonium carbamate and not carbamic acid.

Extending this to our experiment of NH₃ with CS₂, considering a similar case, we have calculated the column density in all our samples. It is summarized in Table 2. Here the mixture ice (CS₂ + NH₃) was in 1:30 ratio and

hence we propose the residue which we observed are likely to be ammonium dithiocarbamate and there may be a possibility of formation of dithiocarbamic acid if CS₂ and NH₃ are in 1:1 ratio, which need to be further studied.

4. Conclusion and implication

NH₃ and CS₂ mixtures were studied in astrochemical conditions. The two new bands observed in NH₃ ices revealed the formation of NH₃ homo-dimers which was found to reorient upon heating to 40 K indicating a phase of highly porous NH₃ ice at 10 K. Phase change temperature of NH₃ and CS₂ was found to be 5 K higher in order to segregate whilst present as mixtures in comparison to the phase change temperature of the layered deposits; 65 K and 80 K, respectively. The ice mixture upon warming to higher temperature leaves a residue on the substrate that is even seen in the spectrum recorded at 340 K. Based on the thermal reaction pathway involving NH₃ and CS₂ mixture the residue obtained is believed to be thio compound; ammonium dithiocarbamate.

We propose that efforts must be taken to detect the presence of the complex thio residue such as ammonium dithiocarbamate on comets carrying CS₂ and NH₃. The formation of the thio residue is quite likely due to thermal processing of ices as the temperature increases while the comet gets close to the Sun. Also the stability of such complex molecules even at 340 K suggest that repeated processing of a periodic comet would have higher concentration of the thio residue. Therefore, the periodic comets (known to contain NH₃ and CS₂) could be the good candidates to look for such complex thio molecules.

Acknowledgement

SP and BS acknowledges the support from DST – India Grant (IFA-11CH-11). RRJM acknowledges UGC for his research fellowship and TP acknowledges the support from DST for a research grant.

References

- Altenhoff, W.J., Batrla, W.K., Huchtmeier, W.K., Schmidt, J., Stumpff, P., Walmsley, M., 1983. Radio observations of comet 1983 D. *Astron. Astrophys.* 125.
- Bossa, J.-B., Borget, F., Duvernay, F., Theule, P., Chiavassa, T., 2008a. Formation of neutral methylcarbamic acid (CH_3NHCOOH) and methylammonium methylcarbamate [$\text{CH}_3\text{NH}_3^+[\text{CH}_3\text{NHCO}_2^-]$] at low temperature. *J. Phys. Chem. A* 112, 5113–5120.
- Bossa, J.B., Theule, P., Duvernay, F., Borget, F., Chiavassa, T., 2008b. Carbamic acid and carbamate formation in $\text{NH}_3:\text{CO}_2$ ices – UV irradiation versus thermal processes. *Astron. Astrophys.* 492, 719–724.
- Bouilloud, M., Fray, N., Bénilan, Y., Cottin, H., Gazeau, M.-C., Jolly, A., 2015. Bibliographic review and new measurements of the infrared band strengths of pure molecules at 25 K: H_2O , CO_2 , CO , CH_4 , NH_3 , CH_3OH , HCOOH and H_2CO . *MNRAS* 451, 2145–2160.
- Dows, D.A., Whittle, E., Pimentel, G.C., 1955. Infrared spectrum of solid ammonium azide: A vibrational assignment. *J. Chem. Phys.* 23, 1475–1479.
- Flynn, G.J., Bleuet, P., Borg, J., Bradley, J.P., Brenker, F.E., Brennan, S., Bridges, J., Brownlee, D.E., Bullock, E.S., Burghammer, M., Clark, B. C., Dai, Z.R., Daghlian, C.P., Djouadi, Z., Fakra, S., Ferroir, T., Floss, C., Franchi, I.A., Gainsforth, Z., Gallien, J.-P., Gillet, P., Grant, P.G., Graham, G.A., Green, S.F., Grossemey, F., Heck, P.R., Herzog, G.F., Hoppe, P., Hoerz, F., Huth, J., Ignatyev, K., Ishii, H. A., Janssens, K., Joswiak, D., Kearsley, A.T., Khodja, H., Lanzirrotti, A., Leitner, J., Lemelle, L., Leroux, H., Luening, K., MacPherson, G. J., Marhas, K.K., Marcus, M.A., Matrajt, G., Nakamura, T., Nakamura-Messenger, K., Nakano, T., Newville, M., Papanastassiou, D.A., Pianetta, P., Rao, W., Riekel, C., Rietmeijer, F.J.M., Rost, D., Schwandt, C.S., See, T.H., Sheffield-Parker, J., Simionovici, A., Sitnitsky, I., Snead, C.J., Stadermann, F.J., Stephan, T., Stroud, R. M., Susini, J., Suzuki, Y., Sutton, S.R., Taylor, S., Teslich, N., Troadec, D., Tsou, P., Tsuchiyama, A., Uesugi, K., Vekemans, B., Vicenzi, E.P., Vincze, L., Westphal, A.J., Wozniakiewicz, P., Zinner, E., Zolensky, M.E., 2006. Elemental compositions of comet 81P/Wild 2 samples collected by stardust. *Science* 314, 1731–1735 (Washington, DC, U.S.).
- Fresneau, A., Danger, G., Rimola, A., Theule, P., Duvernay, F., Chiavassa, T., 2014. Trapping in water – an important prerequisite for complex reactivity in astrophysical ices: the case of acetone ($\text{CH}_3)_2\text{C}=\text{O}$ and ammonia NH_3 . *Mon. Not. R. Astron. Soc.* 443, 2991–3000.
- Garozzo, M., Fulvio, D., Kanuchova, Z., Palumbo, M.E., Strazzulla, G., 2010. The fate of S-bearing species after ion irradiation of interstellar icy grain mantles. *A&A* 509, A67.
- Jackson, W.M., Scodinu, A., Xu, D., Cochran, A.L., 2004. Using the ultraviolet and visible spectrum of comet 122P/de vico to identify the parent molecule CS_2 . *Astrophys. J. Lett.* 607, L139.
- Jheeta, S., Ptasinska, S., Sivaraman, B., Mason, N.J., 2012. The irradiation of 1:1 mixture of ammonia: carbon dioxide ice at 30 K using 1 keV electrons. *Chem. Phys. Lett.* 543, 208–212.
- Knoeck, J., Witt, J., 1976. Infrared and Raman spectra and Urey–Bradley force fields for dithiocarbamate and dithiocarbamate- d_2 anions. Use of a correlation matrix to determine force field uniqueness. *Spectrochim. Acta, Part A* 32, 149–155.
- Lv, X.Y., Boduch, P., Ding, J.J., Domaracka, A., Langlinay, T., Palumbo, M.E., Rothard, H., Strazzulla, G., 2014. Thermal and energetic processing of ammonia and carbon dioxide bearing solid mixtures. *Phys. Chem. Chem. Phys.* 16, 3433–3441.
- Maity, S., Kaiser, R.I., 2013. Electron irradiation of carbon disulfide-oxygen ices: toward the formation of sulfur-bearing molecules in interstellar ices. *Astrophys. J.* 773, 184/181–184/188.
- Maity, S., Kim, Y.S., Kaiser, R.I., Lin, H.M., Sun, B.J., Chang, A.H.H., 2013. Thermal and energetic processing of ammonia and carbon dioxide bearing solid mixtures. *Chem. Phys. Lett.* 577, 42–47.
- Mangum, J.G., Darling, J., Henkel, C., Menten, K.M., MacGregor, M., Svoboda, B.E., Schinnerer, E., 2013. On the detection of higher order carbon sulfides (CS_x ; $x=4-6$) in low temperature carbon disulfide ices. *Astrophys.* 1–29, arXiv.org, arXiv:1310.6586v1311 [astro-ph.GA].
- Mathes, R.A., Booth, H.S., Kirk, R.D., 2007. Ammonium dithiocarbamate. *Inorganic syntheses. Ammonium Dithiocarbamate*. John Wiley & Sons Inc, pp. 48–50.
- McKeegan, K.D., Aleon, J., Bradley, J., Brownlee, D., Busemann, H., Butterworth, A., Chaussidon, M., Fallon, S., Floss, C., Gilmour, J., Gounelle, M., Graham, G., Guan, Y., Heck, P.R., Hoppe, P., Hutcheon, I.D., Huth, J., Ishii, H., Ito, M., Jacobsen, S.B., Kearsley, A., Leshin, L.A., Liu, M.-C., Lyon, I., Marhas, K., Marty, B., Matrajt, G., Meibom, A., Messenger, S., Mostefaoui, S., Mukhopadhyay, S., Nakamura-Messenger, K., Nittler, L., Palma, R., Pepin, R.O., Papanastassiou, D.A., Robert, F., Schlutter, D., Snead, C.J., Stadermann, F.J., Stroud, R., Tsou, P., Westphal, A., Young, E.D., Ziegler, K., Zimmermann, L., Zinner, E., 2006. Isotopic compositions of cometary matter returned by stardust. *Science* 314, 1724–1728 (Washington, DC, U.S.).
- Niemann, H.B., Atreya, S.K., Bauer, S.J., Carignan, G.R., Demick, J.E., Frost, R.L., Gautier, D., Haberman, J.A., Harpold, D.N., Hunten, D. M., Israel, G., Lunine, J.I., Kasprzak, W.T., Owen, T.C., Paulkovich, M., Raulin, F., Raaen, E., Way, S.H., 2005. The abundances of constituents of Titan's atmosphere from the GCMS instrument on the Huygens probe. *Nature* 438, 779–784.
- Noble, J.A., Theule, P., Duvernay, F., Danger, G., Chiavassa, T., Ghesquiere, P., Mineva, T., Talbi, D., 2014. Kinetics of the NH_3 and CO_2 solid-state reaction at low temperature. *Phys. Chem. Chem. Phys.* 16, 23604–23615.
- Rodriguez-Lazcano, Y., Mate, B., Herrero, V.J., Escribano, R., Galvez, O., 2014. The formation of carbamate ions in interstellar ice analogues. *Phys. Chem. Chem. Phys.* 16, 3371–3380.
- Sivaraman, B., 2016. Electron irradiation of carbon dioxide-carbon disulphide ice analog and its implication on the identification of carbon disulphide on moon. *J. Chem. Sci.* 128 (1), 159–164.
- Sivaraman, B., Raja Sekhar, B.N., Jones, N.C., Hoffmann, S.V., Mason, N.J., 2012. VUV spectroscopy of formamide ices. *Chem. Phys. Lett.* 554, 57–59.
- Sivaraman, B., Raja Sekhar, B.N., Nair, B.G., Hatode, V., Mason, N.J., 2013. Infrared spectrum of formamide in the solid phase. *Spectrochim. Acta Part A Mol. Biomol. Spectrosc.* 105, 238–244.
- Smith, A.M., Stecher, T.P., Casswell, L., 1980. Production of carbon, sulfur, and CS in Comet West. *Astrophys. J.* 242, 402–410.
- Wright, I.P., Sheridan, S., Barber, S.J., Morgan, G.H., Andrews, D.J., Morse, A.D., 2015. CHO-bearing organic compounds at the surface of 67P/Churyumov-Gerasimenko revealed by Ptolemy. *Science* 349, aab0673.
- Yamada, H., Person, W.B., 1964. Absolute infrared intensities of the fundamental absorption bands in solid CS_2 . *J. Chem. Phys.* 40, 309–321.
- Zheng, W., Kaiser, R.I., 2007. An infrared spectroscopy study of the phase transition in solid ammonia. *Chem. Phys. Lett.* 440, 229–234.



Cite this: *Nanoscale*, 2016, **8**, 10282

Unusual reactivity of MoS₂ nanosheets†

Biswajit Mondal,‡ Anirban Som,‡ Indranath Chakraborty,‡ Ananya Baksi, Depanjan Sarkar and Thalappil Pradeep*

The reactivity of the 2D nanosheets of MoS₂ with silver ions in solution, leading to their spontaneous morphological and chemical transformations, is reported. This unique reactivity of the nanoscale form of MoS₂ was in stark contrast to its bulk counterpart. While the gradual morphological transformation involving several steps has been captured with an electron microscope, precise chemical identification of the species involved was achieved by electron spectroscopy and mass spectrometry. The energetics of the system investigated supports the observed chemical transformation. The reaction with mercury and gold ions shows similar and dissimilar reaction products, respectively and points to the stability of the metal-sulphur bond in determining the chemical compositions of the final products.

Received 31st January 2016,

Accepted 14th April 2016

DOI: 10.1039/c6nr00878j

www.rsc.org/nanoscale

Introduction

Graphene and its 2D chemical analogues, such as MoS₂, WS₂, MoSe₂, etc., have shown several novel phenomena such as unusual electronic conductivity,^{1–4} charge transport,^{5–8} hydrogen evolution reactivity (HER),^{9–12} and optoelectric properties,^{13–17} and it is also used as a material in Li-ion batteries.¹⁸ Composite materials using such components show even more fascinating properties due to efficient charge separation or associated effects during photoexcitation.^{19–21} Water splitting is more efficient in composites such as ZnO/MoS₂,^{22,23} CdS/MoS₂,^{24–27} TiO₂/MoS₂,^{28,29} SiC/MoS₂,³⁰ Ag/MoS₂,³¹ graphene/MoS₂,^{32,33} etc., than in the components. In all of these processes, individual chemical properties of the constituents are utilised and the reaction occurs at the phase boundary. Although individual properties of the sub-system are examined in these processes, the chemical effects become significant at the nanoscale leading to novel chemical reactions and transformations. This has been manifested in alloying between nanoparticles³⁴ as well as cation and anion exchange in quantum dots,^{35,36} both occurring in solution. Atomic substitution in graphene is expected to be energy intensive due to its large binding energy. As a result, incorporation of hetero atoms into graphene from nanoparticles has not been reported. However, for graphene analogues such as MoS₂, the change of either Mo or S is facile due to their

reduced lattice energy.³⁷ This is also facilitated by multiple oxidation states possible for Mo which can act as a redox site, inducing chemical reactivity.

In this paper, we demonstrate the first example of the direct nanoscale reactivity of MoS₂ with silver ions leading to its spontaneous disintegration through a series of steps. These individual events involve reduction of incoming silver ions at MoS₂ nanosheets (MoS₂ NSs) forming Ag NPs combined with oxidation of Mo(IV) to Mo(VI) followed by spontaneous transformation of the Ag NPs forming Ag₂S NPs by capturing S atoms from the NSs. These processes bring about morphological changes of MoS₂ NSs. Molybdenum from MoS₂ NSs ends up in the solution in the form of molybdate ions. Such a reaction suggests the possibility of stabilizing metastable structures as well as the creation of novel phases by size control of the reactants.

Experimental

Chemicals

All the chemicals were commercially available and were used without further purification. Silver nitrate (AgNO₃), hexane and Hg(OAc)₂ were purchased from RANKEM. Molybdenum sulphide (MoS₂) and 1.6 M *n*-butyllithium in hexane were purchased from Sigma Aldrich. HAuCl₄ was bought from CDH, India.

Synthesis of MoS₂ NSs

MoS₂ NSs were prepared from MoS₂ powder using the chemical exfoliation method.^{38–40} 3 mL of 1.6 M *n*-butyllithium was added to 300 mg of MoS₂ powder under an argon atmosphere. This solution was maintained for two days under an argon atmosphere with constant stirring. After two days, the lithium

DST Unit of Nanoscience (DST UNS) and Thematic Unit of Excellence (TUE), Department of Chemistry, Indian Institute of Technology Madras, Chennai 600 036, India. E-mail: pradeep@iitm.ac.in

†Electronic supplementary information (ESI) available. See DOI: 10.1039/c6nr00878j

‡These authors contributed equally.

intercalated product was repeatedly washed with hexane to remove the unreacted *n*-butyllithium. Around 80 mL of water was then added to this product and the dispersion was sonicated for 1 h using a bath sonicator. The aqueous dispersion of MoS₂ NSs was finally centrifuged at 10 000 rpm for 10 minutes to remove the unexfoliated MoS₂. The quality of the MoS₂ NS samples was ensured from the UV/Vis and Raman spectrum (Fig. S1†). A standard solution of Mo was prepared by dissolution of a calculated amount of MoS₂ powder. The concentration of the MoS₂ dispersion was determined by ICP MS using this standard solution. All the concentrations used for the MoS₂ NSs later in the text are given in terms of Mo concentrations.

Reaction between MoS₂ NS and AgNO₃ solution

The reaction was carried out by adding AgNO₃ solution to the aqueous dispersion of MoS₂ and the reaction mixture was kept for 6 h under stirring conditions at room temperature. Concentration dependent reactions were performed by varying the volume of the AgNO₃ solution (5.8 mM) used: (a) 50 μL, (b) 100 μL, (c) 200 μL, (d) 400 μL, (e) 800 μL and (f) 1.6 mL keeping the concentration of MoS₂ solution the same (3.7 mM in terms of Mo, 500 μL). The total volume of the reaction mixture was maintained to be the same (7 mL). Thus the AgNO₃ concentration was varied from 0.04 mM to 1.32 mM and the concentration of MoS₂ was 0.26 mM (in terms of Mo, as mentioned before). For time dependent reactions, a medium concentration of AgNO₃ (800 μL, 5.8 mM) was taken with the same concentration of MoS₂ solution (used in concentration dependent reaction).

Reaction of MoS₂ NSs with Hg(OAc)₂ and HAuCl₄

The reaction of MoS₂ NSs with Hg(OAc)₂ was performed with the same concentration that was used in the case of AgNO₃ and MoS₂ NSs, under the same reaction conditions. For the reaction with Au³⁺, 15 μL of 25 mM HAuCl₄ solution was taken keeping the MoS₂ concentration the same and the reaction was performed under the same reaction conditions (overall concentrations of HAuCl₄ and MoS₂ NSs were 0.053 and 0.26 mM, respectively).

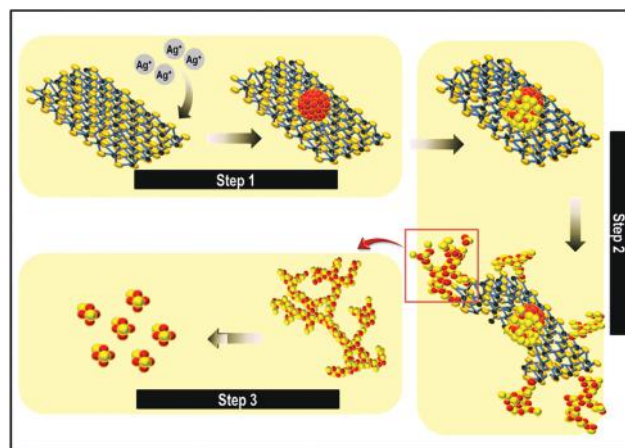
Results and discussion

In the course of our experiment, we explored reaction products between AgNO₃ and MoS₂, in its bulk and 2D nanoscale forms. A solution of AgNO₃, kept in contact with MoS₂ powder (under magnetic stirring), remained unreactive for extended periods (24 h) without any visible changes in the solution. Furthermore, examination of the MoS₂ powder post AgNO₃ treatment did not show any change in its chemical composition (Fig. S2†). Such a phenomenon is expected and can be explained by the bulk thermochemical values (ΔG_f° MoS₂ and Ag₂S are $-248.7 \text{ kJ mol}^{-1}$ (ref. 41) and $-40.67 \text{ kJ mol}^{-1}$,⁴² respectively). MoS₂ NSs were synthesized by chemical exfoliation^{38,39} of bulk MoS₂ (powder) in two steps, lithium intercala-

tion followed by exfoliation of the lithiated MoS₂ (Li_xMoS₂) through ultrasonication. Both these steps involved changes in Gibb's free energy, resulting in a different ΔG_f° for the NSs and they behaved differently.

Upon mixing Ag⁺ with a dispersion of MoS₂ NSs, gradual changes were seen visually which were in stark contrast to the bulk. The color of the reaction mixture changed from light green to brown and finally the products started floating on the surface. These changes were also manifested in the UV-visible spectra with gradual disappearance of the peaks at 420 and 310 nm,^{38,39} which are the characteristic bands for MoS₂ NSs (Fig. S1A†). The reaction starts instantly upon addition of Ag⁺ solution and this is reflected in the UV-visible spectrum obtained immediately after addition (Fig. S3†). An overall scheme of the reaction involving MoS₂ NSs and Ag⁺ (AgNO₃ solution) is shown in Scheme 1.

Transmission electron microscopy (TEM), in a time dependent manner, was employed for further exploration of the phenomenon. Parent MoS₂ NSs were approximately 200 to 1000 nm in length and had an average layer thickness of 2–3 layers, typical of chemically exfoliated MoS₂ (Fig. 1A(i)). An HRTEM image of the NSs, shown in Fig. 1B(i), showed a well resolved hexagonal lattice structure with the (100) spacing of 0.27 nm.^{38,39} The Fast Fourier Transform (FFT) pattern of the HRTEM image [inset of Fig. 1B(i)] showed a pattern expected for graphenic equivalents. The TEM images of these MoS₂ NSs in the course of the reaction showed gradual changes in their morphology. Systematic time dependent data reveal three main steps to form the final product as indicated in Scheme 1. The initial interactions of Ag⁺ with the MoS₂ NS lead to the formation of Ag NPs on the NSs (Step 1, Scheme 1). This happens immediately after the addition of Ag⁺ and appears as small black particles on the NSs in the low magnification TEM image (Fig. 1A(ii)). Structural confirmation of these particles came from the lattice resolved HRTEM images; one such particle on MoS₂ NS (Fig. 1B(ii)) showing Ag (111) lattice of 0.23 nm is presented as an example. Simultaneous focusing



Scheme 1 Graphical outline of the reaction between Ag⁺ and MoS₂ NSs elucidating the steps involved in the overall reaction.

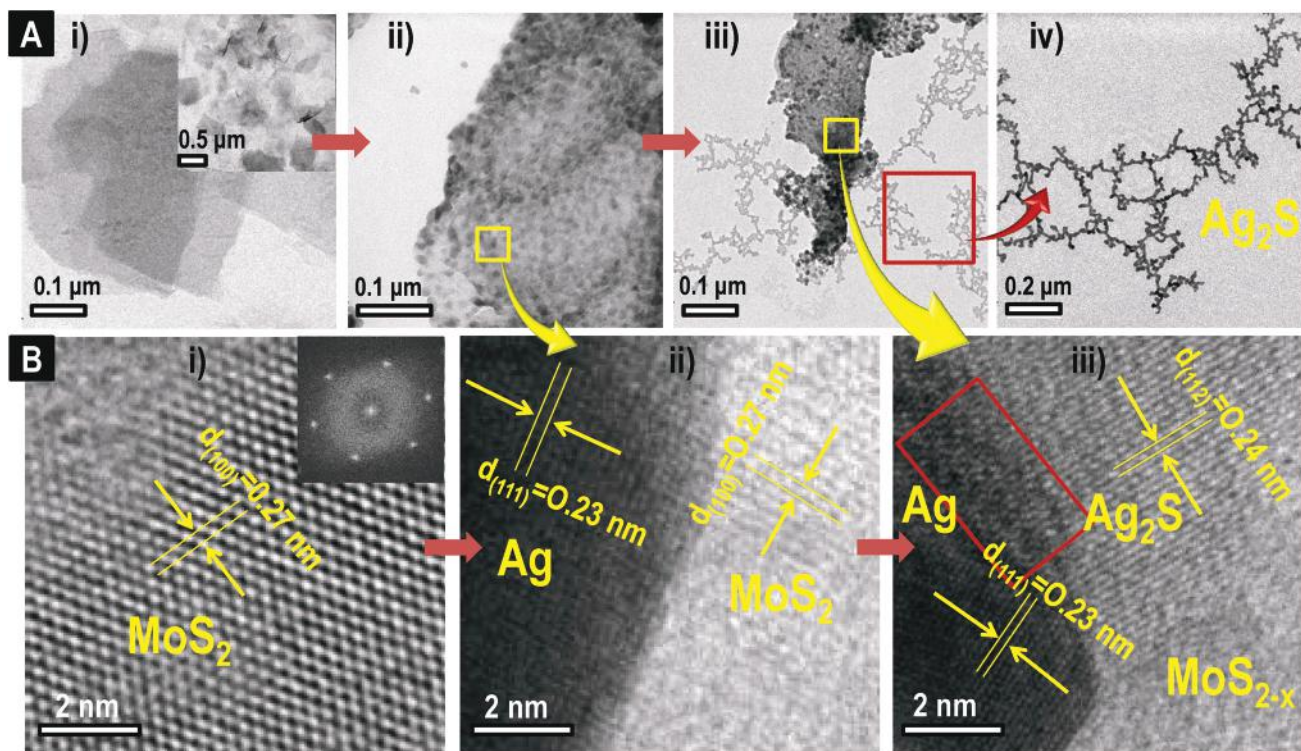


Fig. 1 (A) TEM images from different stages of the reaction; (i) exfoliated MoS₂ NSs, (ii) Ag NP decorated NSs, (iii) Ag-reacted NSs where the network of Ag₂S structures can be seen protruding from the NS edges and (iv) a closer view of the branched morphology of the Ag₂S network. (B) HRTEM images confirming the structures as shown in Scheme 1 (i) structure of a MoS₂ NS (corresponding FFT pattern is shown in the inset; the lattice plane is marked); (ii) an expanded view of an Ag NP on the MoS₂ sheet (characteristic lattice planes are marked) and (iii) an Ag–Ag₂S NP on NS. This represents the initial stage of the transformation of Ag into Ag₂S by extraction and capture of sulphur from the NSs. Scale bars are indicated on all images.

on both Ag NPs and MoS₂ NSs was difficult as they occur at different depths and that's the reason for the apparent loss of resolution in the image B(ii). However, HRTEM images taken from the same area by focusing separately on Ag (Fig. S4A†) and MoS₂ (Fig. S4B†) confirm their well-crystalline nature. The mechanism of transformation of Ag(I) to Ag(0) and subsequent formation of these Ag NPs will be addressed later in the manuscript.

The TEM images of samples collected after 1 h of mixing showed network like structures protruding out from NSs along with the presence of particles on the NS surface (Fig. 1A(iii)). The expanded TEM image of these network-like structures is shown in Fig. 1A(iv) and the EDS spectrum obtained from these (Fig. S5A†) hinted at the chemical composition of Ag₂S. The particles present on the NSs at this stage appeared to be of 'Janus' type from the TEM image (Fig. S5B†). Two different regions of the same particle offer different contrasts in the HRTEM image and a slight difference in lattice distances between these two regions was also observed (Fig. 1B(iii)). Lattice distances in the darker part of the particle match with the (111) distances of Ag while that in the lighter part of the particle matches with the (112) plane of Ag₂S (marked in Fig. 1B(iii)). We believe that S atoms from the MoS₂ NSs diffuse into the Ag lattice to transform into the Ag₂S phase

which first leads to the formation of Ag–Ag₂S Janus particles and then complete transformation of Ag into Ag₂S gives rise to the protrusions of network-like structures out of NSs (Step 2, Scheme 1). A closer inspection of the Ag–Ag₂S interphase in the HRTEM image in Fig. 1B(iii) (marked with a red box and expanded view shown in Fig. S5C†) shows the presence of crystal defects, indicative of atomic diffusion and growth of a new phase across that region.

The third and final step of the reaction deals with the time dependent transformation of network like structures of Ag₂S (Step 3, Scheme 1) and is presented in Fig. 2. The network-like structures formed after 1 h of reaction (Fig. 2A) slowly broke apart and formed particles of various sizes after 6 h of reaction (Fig. 2C). An intermediate state of this process can be observed from the TEM image taken after 4 h of the reaction (Fig. 2B). HRTEM image of one such particle (Fig. 2D) showed a lattice spacing corresponding to the (112) planes of α-Ag₂S mentioned earlier while the EDS spectrum confirms a Ag : S ratio of 2 : 1. To confirm whether these particles indeed are Ag₂S, the final product was subjected to powder X-ray diffraction (PXRD) analysis. The obtained pattern (Fig. 2E) was an exact match with that of the monoclinic acanthite (α form) phase of Ag₂S (Fig. 2E, JCPDS card no. 14-0072). Acanthite is the Ag₂S phase stable at room temperature.⁴³

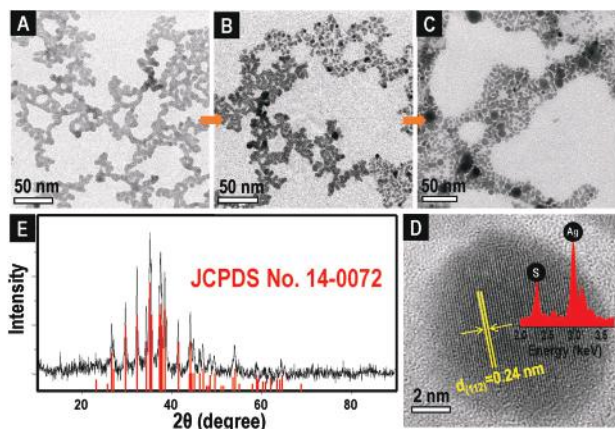


Fig. 2 TEM images taken after (A) 1 h, (B) 4 h and (C) 6 h of reaction showing the time dependent evolution of the network-like morphology of Ag_2S into differently sized NPs. (D) HRTEM image of one such Ag_2S NP is shown in (C) confirming the phase. EDS spectrum, shown in the inset, confirms the chemical composition. (E) Standard peaks of Ag_2S (acanthite phase, JCPDS no. 14-0072) plotted along with the observed XRD pattern of the final reaction product. Scale bars are indicated on all images.

Changes in the structure of NSs during the course of reaction have also been looked at in detail through TEM and are presented in Fig. 3. Fig. 3A is a representation of the initial stages of the reaction, where sheet-like structures can be seen clearly although network-like Ag_2S structures have started to protrude out from the edges, probably due to higher edge-reactivity of MoS_2 NSs.^{44,45} A higher magnification image taken from the surface of the NSs at this stage shows the presence of Ag NPs on them (Fig. 3B). As the reaction proceeds, these Ag NPs transform into a branched network of Ag_2S and cover the entire surface of the NSs (Fig. 3C). The magnified TEM image (Fig. 3D) shows Ag_2S structures which are darker. However, perforated sheet-like structures, appearing with a different contrast can be observed clearly in the marked regions of the image. As the reaction completes, Ag_2S network structures convert into Ag_2S NPs and segregate on the TEM grid. At this point, these perforated sheet-like structures can be seen clearly (Fig. 3E) and appear as a holey film in the higher magnification image (Fig. 3F). These structures were found to be sensitive to electron beam irradiation and appeared amorphous. They being amorphous is the reason for the observation of only Ag_2S in the XRD of the final product of the reaction (Fig. 2E). A comparison between the EDS spectra of MoS_2 NS (a) and NSs after the reaction (b) is shown in the insets of Fig. 3F. The depletion of S content in the reacted NSs is apparent from the difference in the shape in the EDS spectra as one would expect from the extraction of S from the MoS_2 NS by Ag to form Ag_2S .

X-ray photoelectron spectroscopy (XPS) of the samples at different times during the course of the reaction was performed to understand the redox chemistry involved. The XPS survey spectrum at the end of the reaction showed the expected elements (Fig. S6†). The specific scans for Mo 3d, Ag 3d and

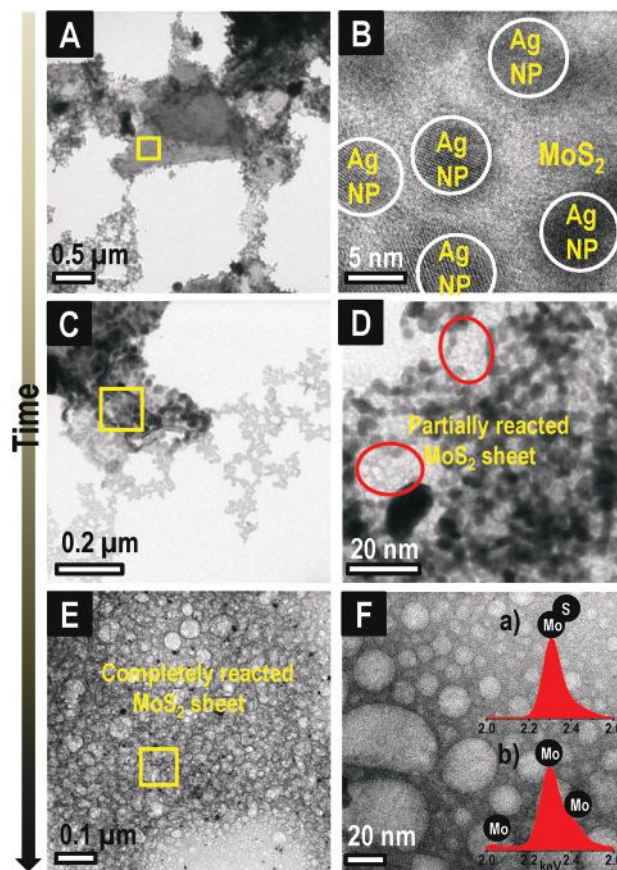


Fig. 3 Changes of the MoS_2 sheet structure as the reaction proceeds. (A) TEM image of MoS_2 NSs after 0.5 h of reaction. Ag_2S protrusions can be seen to stem out of NS edges. (B) HRTEM image of NS; at this stage Ag NPs are present on the surface of MoS_2 NS. (C) TEM image of reacted MoS_2 NSs after 3 h of reaction. Surface Ag NPs converted into a Ag_2S network which has encapsulated the NSs. (D) Higher magnification image of the marked region of (C), a porous sheet morphology can be seen underneath the Ag_2S network. (E) TEM image of the porous sheet formed after 6 h of reaction. (F) Higher magnification image of the marked region from (C), showing the pores on the NS. Insets show the collected EDS spectra for MoS_2 and reacted- MoS_2 NSs, respectively showing a decrease in the amount of S after the reaction. Scale bars are indicated on all images.

S 2p regions from the reactants and products at two different reaction times are presented in Fig. 5A–C, respectively. The parent MoS_2 NSs show two peaks for Mo(IV) at 228.9 eV and 232.0 eV corresponding to $3d_{5/2}$ and $3d_{3/2}$, respectively [Fig. 4A(i)]. The XPS spectrum of the Mo 3d region taken after the addition of Ag^+ (0.4 mL of 5.8 mM AgNO_3) showed the emergence of two new peaks at 233.1 eV and 236.2 eV [Fig. 4A(ii)]. The peak around 236.2 eV was attributed to the $3d_{3/2}$ Mo(VI) state, confirming oxidation of Mo(IV) to Mo(VI) in the reaction. An increase in the relative intensity of the peak around 236.2 eV with respect to the peak at 228.9 eV with the increasing reaction time [Fig. 4A(iii) vs. Fig. 4A(ii)] validates this assignment. Deconvolution of the peaks around 233.1 eV into individual Mo(IV) and Mo(VI) components further supports oxidation. The corresponding change in the oxidation state of

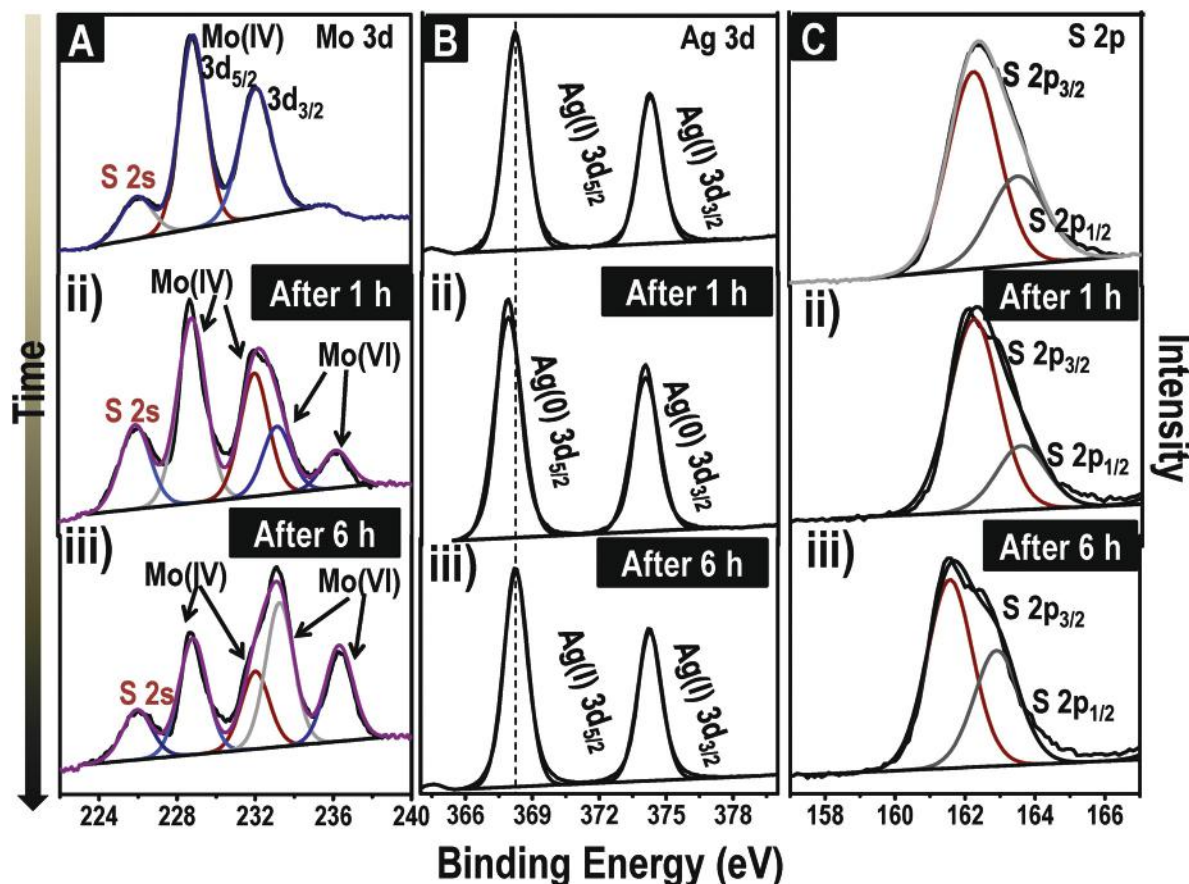
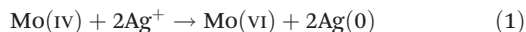


Fig. 4 Time dependent XPS to support the proposed mechanism. A (i–iii), B (i–iii), and C (i–iii) correspond to time dependent XPS in the Mo 3d, Ag 3d, S 2p regions, during the reaction. A(i–iii) show the change in the oxidation state and the increase in intensity for a particular oxidation state of Mo. B(i–iii) Change in the oxidation state of Ag with time and with change in the oxidation state of Mo. C(i–iii) show the shift in the binding energy with time for a particular oxidation state of S.

silver [Ag (I) in Fig. 4B(i) transforms into Ag (0) in Fig. 4B(ii)] completes the redox reaction and accounts for the formation of Ag NP decorated NSs in the first step.



However, in the final product Ag_2S , the oxidation state of silver again becomes Ag(I) (Fig. 4C(ii)). A marked change was noticed in the S 2p binding energies in due course of the reaction as well. The peaks at 162.2 eV and 163.5 eV are assigned to $2p_{3/2}$ and $2p_{1/2}$, respectively of S^{2-} (Fig. 4C(i)) in MoS_2 which moved to a relatively lower binding energy at 161.5 eV and 162.8 eV, due to the formation of Ag_2S (Fig. 4C(iii)). The relatively higher binding energy of sulphur before the reaction is because sulphur is bridging (S_2^{2-}) and/or apical (S^{2-}) in MoS_2 while a relatively lower binding energy after the reaction is in good agreement with S^{2-} in Ag_2S . Thus the overall reaction for the second step is:



To prove that silver nanoparticles indeed are capable of taking part in such reactions, a reaction was performed with

the as-synthesized citrate protected nanoparticles. Interestingly, the same chemistry, albeit with a longer reaction time scale, was noticed (Fig. S7†) which resulted in a porous and amorphous net-like structure and Ag_2S NPs.

The formation of Ag_2S by the reaction of S^{2-} with Ag NPs can be rationalized in terms of the higher bond energy of Ag–S over Mo–S [bond energy(Ag–S) = 217.1 kJ mol⁻¹ in Ag_2S and bond energy(Mo–S) = 47 kJ mol⁻¹ in MoS_2]. Oxidation of Ag NPs to Ag^+ (Ag_2S) is also favorable from the electrochemical point of view ($2\text{Ag} + \text{S}^{2-} = \text{Ag}_2\text{S} + 2\text{e}^-$ 0.691V).

Although it was established from the XPS spectra that Mo(IV) oxidises to Mo(VI) during the reaction, the molecular nature of the Mo containing species formed was not possible to be identified using XPS. To understand the fate of Mo after the completion of the reaction, the final mixture was subjected to electrospray ionization mass spectrometry (ESI MS). The negative mode mass spectrum (Fig. S8A†) showed a series of peaks which matches exactly with the mass spectrum of ammonium molybdate (Fig. S8B†). An expanded view of the marked region of the mass spectrum is shown in Fig. 5A where clear isotope patterns of MoO_3^- , HMoO_4^- and MoO_5^- ions could be observed. The identity of the MoO_5^- ion was confirmed from

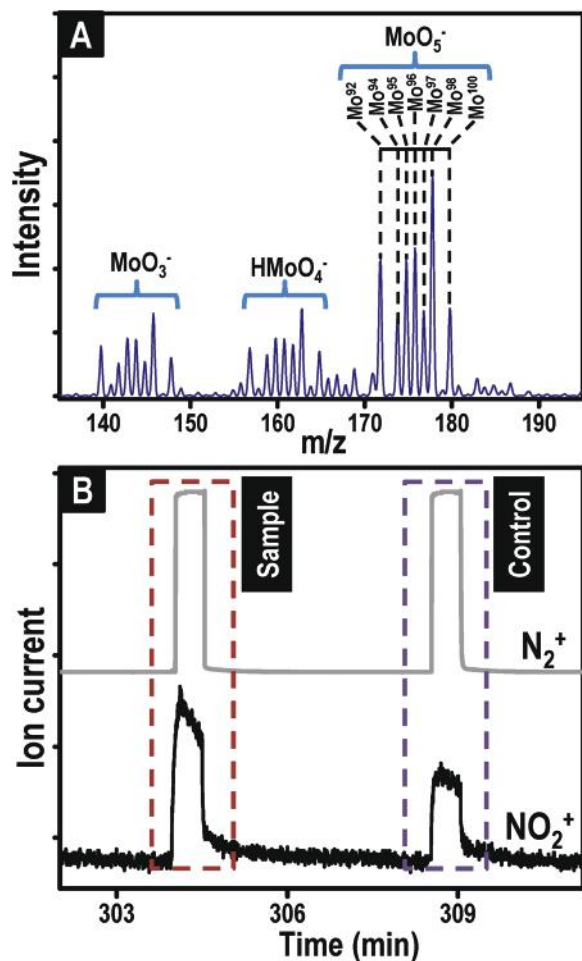
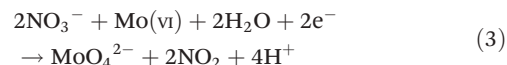


Fig. 5 (A) Negative mode ESI mass spectrum of the final reaction mixture confirming the presence of the molybdate ion. Assignment of peaks to various isotopes of Mo is shown only for MoO_5^- . (B) Ion current vs. time plots for N_2^+ and NO_2^+ ions to prove the evolution of NO_2 in the course of reaction.

MS^2 spectra where an increase in the intensity of MoO_3^- ions was observed with the increasing collision energy (Fig. S8C†). The ESI MS analysis unambiguously proves the formation of molybdate from MoS_2 NSs. While we do observe a slight increase in the $\text{Mo}(\text{VI})$ intensity in the XPS spectrum of the Mo region after 6 h of reaction (Fig. 4A(iii)), this increase was not very large as $\text{Mo}(\text{VI})$ stayed as the molybdate ion in solution while only solid residues comprising of unreacted or partially reacted NSs were analysed in XPS.

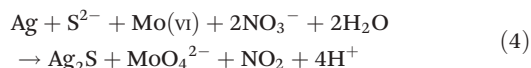
We conjecture that NO_3^- ions (coming from AgNO_3) reduce to NO_2 in the course of the reaction to account for the charge balance. The formation of NO_2 was proved by *in situ* mass spectrometric detection. At first, solutions of both the reactants were purged separately with argon (Ar) to remove the dissolved O_2 and the reaction was initiated by injecting the AgNO_3 solution into the dispersion of MoS_2 NSs taken in an enclosed vessel. The mixture of gaseous components inside the vessel after 6 h of reaction was analysed by a residual gas

analyser. The gas sampling was similar to our previous experiment on carbon nanotube reactions.⁴⁶ This resulted in an increase in the ion current for both N_2^+ and NO_2^+ due to an increase in partial pressures of the corresponding gases, in the course of time. But when a control analysis was performed, a lesser increase in ion-current for NO_2^+ was observed whereas the increase for N_2^+ (background gas) remained the same. The control followed identical reaction conditions, leading to the same extent of unavoidable leakage and corresponding changes in background gases. This supports the evolution of NO_2 in the following reaction:



The experiment suggests the formation of an acid in the reaction, which was again supported by the decrease in the pH of the solution with the increasing reaction time (Fig. S9†).

Thus, the overall reaction for the second step (after the formation of Ag nanoparticles) can be given as:



The reaction between MoS_2 and silver acetate was also performed. This too happens as in the case of AgNO_3 (Fig. S10†). Most probably, the acetate ion is getting reduced to alcohol as NO_3^- becomes NO_2 in the reaction with AgNO_3 . However, due to reduced partial pressure and low quantity, it could not be detected with a residual gas analyser.

To understand whether the reaction between MoS_2 and Ag^+ is thermodynamically favourable or not, isothermal calorimetric titration experiments were performed (Fig. 6). The reaction cell was filled with $7.8 \mu\text{M}$ MoS_2 which was titrated against 0.62 mM AgNO_3 at 30°C . Under optimized conditions, $2 \mu\text{L}$ of AgNO_3 was added to the MoS_2 cell at a regular interval of 180 s and the reaction was continued until saturation. The final data were fitted using one site model assuming only one type of binding/reaction site. The number of binding sites, which is often considered as the reaction stoichiometry, was found to be 1.8. This is quite expected as the formed reaction product is Ag_2S . The binding constant which is also taken as the rate constant was found to be $9.03 \times 10^3 \text{ mol}^{-1}$. The reaction is highly exothermic with a negative enthalpy change (ΔH is $-7.57 \times 10^4 \text{ cal mol}^{-1}$). As the reaction involves association of the reactants to form products, the entropy change is expected to be negative (experimental value is $-227 \text{ cal mol}^{-1} \text{ deg}^{-1}$).

After understanding the thermodynamic feasibility of the reaction, the effect of the AgNO_3 concentration was checked keeping all other parameters constant. The concentration of AgNO_3 was varied from $200 \mu\text{L}$ to $400 \mu\text{L}$ and to 1.6 mL (5.8 mM). For a lower concentration ($200 \mu\text{L}$ AgNO_3 solution), unreacted MoS_2 remained in solution which was seen in TEM (Fig. S11B†) and the feature due to MoS_2 NS remained in the UV/Vis spectra (Fig. S12†). The reacted part of the MoS_2 converted to porous sheets. For $400 \mu\text{L}$ of AgNO_3 solution, the

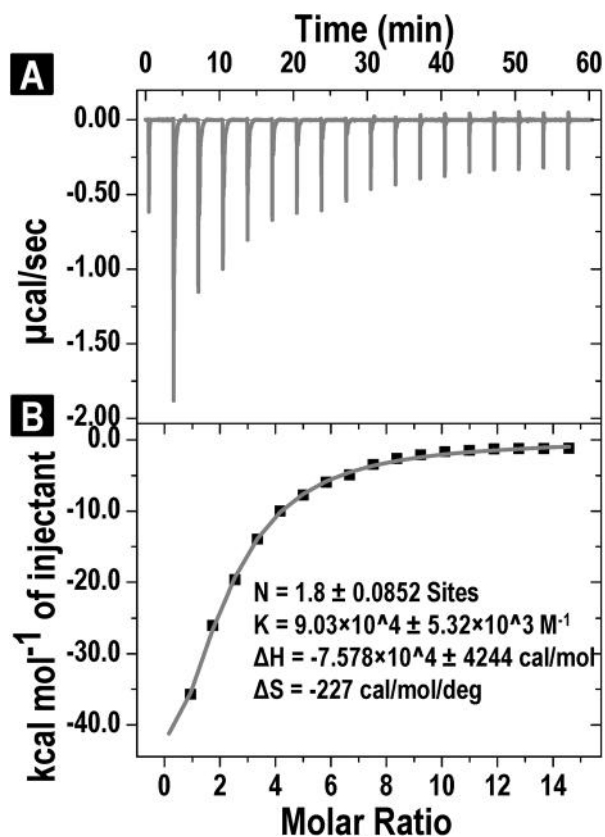


Fig. 6 (A) Real time ITC thermograph of the reaction between MoS_2 and AgNO_3 and (B) corresponding heat change showing the exothermic reaction. The resulting thermodynamic parameters are listed in (B).

MoS_2 sheets converted to porous materials and Ag_2S particles were formed but at a high concentration of AgNO_3 (1.6 mL), small $\text{Ag-Ag}_2\text{S}$ particles were formed along with the porous sheets. The HRTEM image of $\text{Ag-Ag}_2\text{S}$ particles is shown in the inset of Fig. S11I.† The reaction was carried out in the absence of light to see the effect of light in the reaction. In the absence of light also the same products were obtained which proves that light has no effect in the reaction.

It was presumed that the second step of the reaction is governed by metal-sulphur interactions. Reactions with other metal ions, such as Au^{3+} from the same group of silver and Hg^{2+} from the adjacent group, were tried to firmly establish this point. Not so surprisingly, mercuric ions also reacted with MoS_2 NSs and formed flower like structures composed of HgS particles (Fig. 7A). The formation of HgS particles was confirmed from HRTEM images and EDS data (Fig. 7B). The lattice spacing of (200) plane of HgS at 0.21 nm was seen.⁴⁷ But in the cases of Au^{3+} ions, only gold nanoparticles were seen⁴⁸ (Fig. 7C and D) and the reaction did not proceed further which is attributed to the low stability of gold sulphide and the oxidation of $\text{Au}(0)$ to Au^{3+} or Au^+ being not electrochemically favorable.⁴⁹ The formation of Au NPs in this reaction also proves that metal NP formation is the first step in these metal- MoS_2 NS reactions.

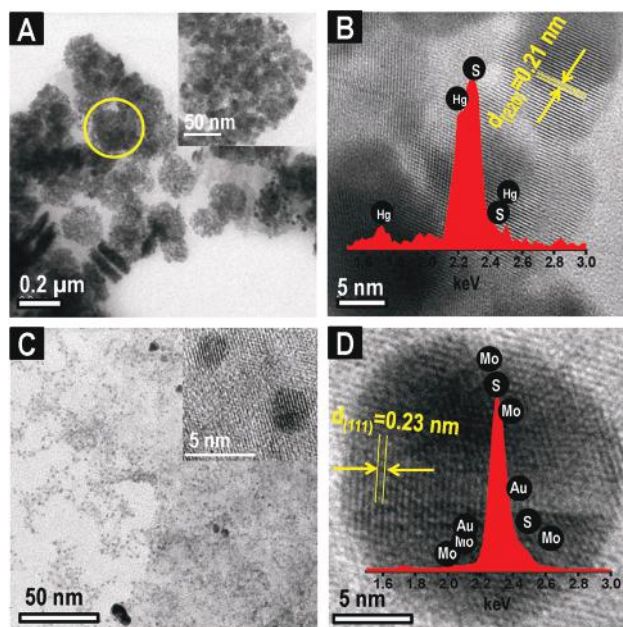


Fig. 7 Reaction with other metal ions. (A) TEM image of flower like HgS particles formed in the reaction of Hg^{2+} with MoS_2 NSs. (B) HRTEM image of the same. The EDS spectrum shown in the inset confirms the presence of both Hg and S . (C) TEM image of gold NPs formed on the MoS_2 sheet. (D) HRTEM image of a single Au NP on MoS_2 NS. The EDS spectrum taken from the same region is shown in the inset.

Conclusions

This study highlights the unique nanoscale reactivity of MoS_2 NSs towards Ag^+ ions in solution leading to chemical disintegration of NSs accompanied by complete changes in the morphology of the sheets. While the overall reaction was found to be energetically favorable, it does not go to completion through a series of distinguishable steps. The products from each of these steps were observed and characterized with the help of high resolution transmission electron microscopy (HRTEM) and X-ray photoelectron spectroscopy. The reaction of these NSs with other metal ions leads to the formation of products depending on the metal-sulphur bond energies. This study provides not only a deep insight into the stability and reactivity of inorganic graphene equivalents, but also points towards the direct synthesis of useful NS-heterostructures from solution.

Acknowledgements

We thank the Department of Science and Technology, Government of India for constantly supporting our research program on nanomaterials. B. M. thanks IIT Madras and D. S. thanks UGC, Govt. of India for research fellowships.

References

- 1 E. P. Nguyen, B. J. Carey, J. Z. Ou, J. van Embden, E. Della Gaspera, A. F. Chrimes, M. J. S. Spencer, S. Zhuiykov,

- K. Kalantar-zadeh and T. Daeneke, *Adv. Mater.*, 2015, **27**, 6225–6229.
- 2 R. Addou, S. McDonnell, D. Barrera, Z. Guo, A. Azcatl, J. Wang, H. Zhu, C. L. Hinkle, M. Quevedo-Lopez, H. N. Alshareef, L. Colombo, J. W. P. Hsu and R. M. Wallace, *ACS Nano*, 2015, **9**, 9124–9133.
- 3 D. Jariwala, V. K. Sangwan, D. J. Late, J. E. Johns, V. P. Dravid, T. J. Marks, L. J. Lauhon and M. C. Hersam, *Appl. Phys. Lett.*, 2013, **102**, 173107/173101–173107/173104.
- 4 I. S. Kim, V. K. Sangwan, D. Jariwala, J. D. Wood, S. Park, K.-S. Chen, F. Shi, F. Ruiz-Zepeda, A. Ponce, M. Jose-Yacamán, V. P. Dravid, T. J. Marks, M. C. Hersam and L. J. Lauhon, *ACS Nano*, 2014, **8**, 10551–10558.
- 5 X. Hong, J. Kim, S.-F. Shi, Y. Zhang, C. Jin, Y. Sun, S. Tongay, J. Wu, Y. Zhang and F. Wang, *Nat. Nanotechnol.*, 2014, **9**, 682–686.
- 6 S.-T. Lo, O. Klochan, C. H. Liu, W. H. Wang, A. R. Hamilton and C. T. Liang, *Nanotechnology*, 2014, **25**, 375201.
- 7 D. M. Sim, M. Kim, S. Yim, M.-J. Choi, J. Choi, S. Yoo and Y. S. Jung, *ACS Nano*, 2015, **9**, 12115–12123.
- 8 E. A. A. Pogna, M. Marsili, D. De Fazio, S. Dal Conte, C. Manzoni, D. Sangalli, D. Yoon, A. Lombardo, A. C. Ferrari, A. Marini, G. Cerullo and D. Prezzi, *ACS Nano*, 2016, **10**, 1182–1188.
- 9 U. Maitra, U. Gupta, M. De, R. Datta, A. Govindaraj and C. N. R. Rao, *Angew. Chem., Int. Ed.*, 2013, **52**, 13057–13061.
- 10 D. Gopalakrishnan, D. Damien, B. Li, H. Gullappalli, V. K. Pillai, P. M. Ajayan and M. M. Shaijumon, *Chem. Commun.*, 2015, **51**, 6293–6296.
- 11 Y. Zhang, L. Zuo, Y. Huang, L. Zhang, F. Lai, W. Fan and T. Liu, *ACS Sustainable Chem. Eng.*, 2015, **3**, 3140–3148.
- 12 D. Gopalakrishnan, D. Damien and M. M. Shaijumon, *ACS Nano*, 2014, **8**, 5297–5303.
- 13 A. Bandyopadhyay and S. K. Pati, *Mater. Res. Express*, 2015, **2**, 1–9.
- 14 Y. Huang, J. Guo, Y. Kang, Y. Ai and C. Li, *Nanoscale*, 2015, **7**, 19358–19376.
- 15 D. Kufer and G. Konstantatos, *Nano Lett.*, 2015, **15**, 7307–7313.
- 16 H. Li, A. W. Contryman, X. Qian, S. M. Ardakani, Y. Gong, X. Wang, J. M. Weisse, C. H. Lee, J. Zhao, P. M. Ajayan, J. Li, H. C. Manoharan and X. Zheng, *Nat. Commun.*, 2015, **6**, 8080.
- 17 X. Tong, E. Ashalley, F. Lin, H. Li and Z. M. Wang, *Nano-Micro Lett.*, 2015, **7**, 1–16.
- 18 J. Xiao, D. Choi, L. Cosimbescu, P. Koech, J. Liu and J. P. Lemmon, *Chem. Mater.*, 2010, **22**, 4522–4524.
- 19 C.-H. Liu, I. S. Kim and L. J. Lauhon, *Nano Lett.*, 2015, **15**, 6727–6731.
- 20 I. Paradisanos, E. Kymakis, C. Fotakis, G. Kioseoglou and E. Stratakis, arXiv.org, e-Print Arch., Phys., 2015, 1–14.
- 21 M. Chhowalla, H. S. Shin, G. Eda, L.-J. Li, K. P. Loh and H. Zhang, *Nat. Chem.*, 2013, **5**, 263–275.
- 22 Y.-J. Yuan, J.-R. Tu, Z.-J. Ye, H.-W. Lu, Z.-G. Ji, B. Hu, Y.-H. Li, D.-P. Cao, Z.-T. Yu and Z.-G. Zou, *Dyes Pigm.*, 2015, **123**, 285–292.
- 23 Y.-J. Yuan, F. Wang, B. Hu, H.-W. Lu, Z.-T. Yu and Z.-G. Zou, *Dalton Trans.*, 2015, **44**, 10997–11003.
- 24 J. Chen, X.-J. Wu, L. Yin, B. Li, X. Hong, Z. Fan, B. Chen, C. Xue and H. Zhang, *Angew. Chem., Int. Ed.*, 2015, **54**, 1210–1214.
- 25 Y. Liu, Y.-X. Yu and W.-D. Zhang, *J. Phys. Chem. C*, 2013, **117**, 12949–12957.
- 26 C. Wang, H. Lin, Z. Xu, H. Cheng and C. Zhang, *RSC Adv.*, 2015, **5**, 15621–15626.
- 27 X. Zong, H. Yan, G. Wu, G. Ma, F. Wen, L. Wang and C. Li, *J. Am. Chem. Soc.*, 2008, **130**, 7176–7177.
- 28 H. Liu, T. Lv, C. Zhu, X. Su and Z. Zhu, *J. Mol. Catal. A: Chem.*, 2015, **396**, 136–142.
- 29 Q. Xiang, J. Yu and M. Jaroniec, *J. Am. Chem. Soc.*, 2012, **134**, 6575–6578.
- 30 X. Guo, X. Tong, Y. Wang, C. Chen, G. Jin and X.-Y. Guo, *J. Mater. Chem. A*, 2013, **1**, 4657–4661.
- 31 A. J. Cheah, W. S. Chiu, P. S. Khiew, H. Nakajima, T. Saisopa, P. Songsiriritthigul, S. Radiman and M. A. A. Hamid, *Catal. Sci. Technol.*, 2015, **5**, 4133–4143.
- 32 A. Behranginia, M. Asadi, C. Liu, P. Yasaei, B. Kumar, P. Phillips, T. Foroozan, J. C. Waranius, K. Kim, J. Abiade, R. F. Klie, L. A. Curtiss and A. Salehi-Khojin, *Chem. Mater.*, 2016, **28**, 549–555.
- 33 X. Zheng, J. Xu, K. Yan, H. Wang, Z. Wang and S. Yang, *Chem. Mater.*, 2014, **26**, 2344–2353.
- 34 K. R. Krishnadas, A. Ghosh, A. Bakshi, I. Chakraborty, G. Natarajan and T. Pradeep, *J. Am. Chem. Soc.*, 2016, **138**, 140–148.
- 35 A. Jaiswal, S. S. Ghosh and A. Chattopadhyay, *Langmuir*, 2012, **28**, 15687–15696.
- 36 X. Shen, J. Jia, Y. Lin and X. Zhou, *J. Power Sources*, 2015, **277**, 215–221.
- 37 M. Mahjouri-Samani, M.-W. Lin, K. Wang, A. R. Lupini, J. Lee, L. Basile, A. Boulesbaa, C. M. Rouleau, A. A. Puzos, I. N. Ivanov, K. Xiao, M. Yoon and D. B. Geohegan, *Nat. Commun.*, 2015, **6**, 7749.
- 38 L. Yuwen, F. Xu, B. Xue, Z. Luo, Q. Zhang, B. Bao, S. Su, L. Weng, W. Huang and L. Wang, *Nanoscale*, 2014, **6**, 5762–5769.
- 39 L. Yuwen, H. Yu, X. Yang, J. Zhou, Q. Zhang, Y. Zhang, Z. Luo, S. Su and L.-H. Wang, *Chem. Commun.*, 2016, **52**, 529–532.
- 40 C. N. R. Rao, H. S. S. Ramakrishna Matte and U. Maitra, *Angew. Chem., Int. Ed.*, 2013, **52**, 13162–13185.
- 41 M. V. Bollinger, K. W. Jacobsen and J. K. Nørskov, *Phys. Rev. B: Condens. Matter Mater. Phys.*, 2003, **67**, 085410/085411–085410/085417.
- 42 P. Patnaik, *Handbook of Inorganic Chemicals*, McGraw-Hill, 2003.
- 43 S. I. Sadovnikov, A. I. Gusev and A. A. Rempel, *Superlattices Microstruct.*, 2015, **83**, 35–47.

- 44 J. Chen, L. Oliviero, X. Portier and F. Mauge, *RSC Adv.*, 2015, **5**, 81038–81044.
- 45 H. Li, C. Tsai, A. L. Koh, L. Cai, A. W. Contryman, A. H. Fragapane, J. Zhao, H. S. Han, H. C. Manoharan, F. Abild-Pedersen, J. K. Noerskov and X. Zheng, *Nat. Mater.*, 2016, **15**, 48–53.
- 46 M. A. Kabbani, C. S. Tiwary, P. A. S. Autreto, G. Brunetto, A. Som, K. R. Krishnadas, S. Ozden, K. P. Hackenberg, Y. Gong, D. S. Galvao, R. Vajtai, A. T. Kabbani, T. Pradeep and P. M. Ajayan, *Nat. Commun.*, 2015, **6**, 7291.
- 47 L. Han, P. Hou, Y. Feng, H. Liu, J. Li, Z. Peng and J. Yang, *Dalton Trans.*, 2014, **43**, 11981–11987.
- 48 Y. Shi, J.-K. Huang, L. Jin, Y.-T. Hsu, S. F. Yu, L.-J. Li and H. Y. Yang, *Sci. Rep.*, 2013, **3**, srep01839, 01837pp.
- 49 Anon, *J. Am. Chem. Soc.*, 2000, **122**, 12614.

Supplementary Information

Unusual reactivity of MoS₂ nanosheets

Biswajit Mondal,[‡] Anirban Som,[‡] Indranath Chakraborty,[‡] Ananya Baksi, Depanjan Sarkar

and Thalappil Pradeep*

DST Unit of Nanoscience (DST UNS) and Thematic Unit of Excellence (TUE), Department of

Chemistry, Indian Institute of Technology Madras, Chennai 600 036, India

*E-mail: pradeep@iitm.ac.in

Table of contents

Number	Description	Page No.
S1	UV/Vis and Raman spectrum of MoS ₂ nanosheets	2
S2	SEM and mapping images of the reaction between bulk MoS ₂ and AgNO ₃ solution	2
S3	Time dependent UV/Vis spectra	3
S4	HRTEM images of Ag NP on the MoS ₂ NS.	4
S5	EDS spectrum of Ag ₂ S and HRTEM images of 'Janus' type particles.	5
S6	XPS survey spectrum of the reaction between MoS ₂ and AgNO ₃	6
S7	TEM and HRTEM images of the reaction between Ag NPs and MoS ₂ sheets	7
S8	Full mass spectrum of the sample and ammonium molybdate	8
S9	Time dependent pH monitoring	8
S10	TEM and HRTEM image of the Ag ₂ S particles formed by the reaction between MoS ₂ NSs and silver acetate.	9
S11	TEM images of Concentration dependent reaction.	10
S12	UV/Vis spectrum of the reaction between MoS ₂ NSs and 200 μ L AgNO ₃ .	11

S1. Supporting information 1

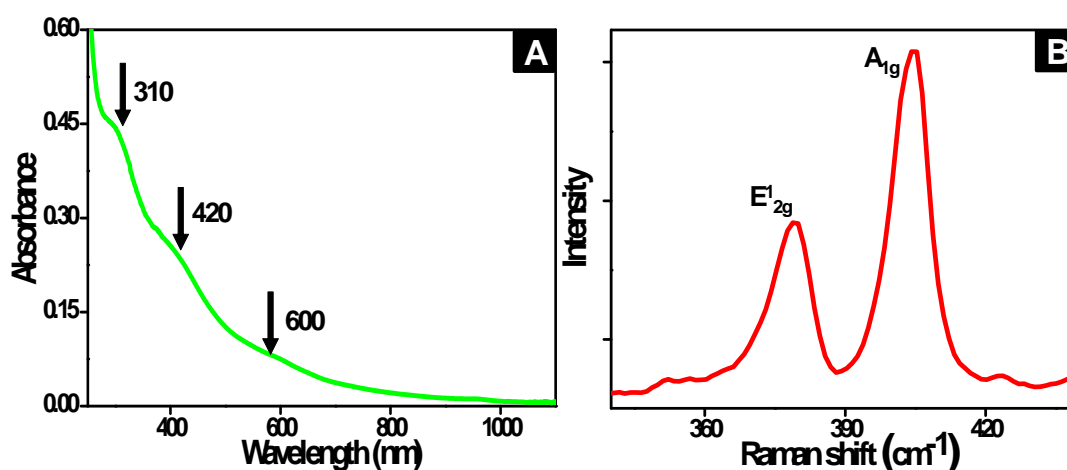


Figure S1. (A). UV/Vis spectrum of MoS₂ nanosheet after exfoliation. (B) Raman spectrum of MoS₂ nanosheets (NSs).

S2. Supporting information 2

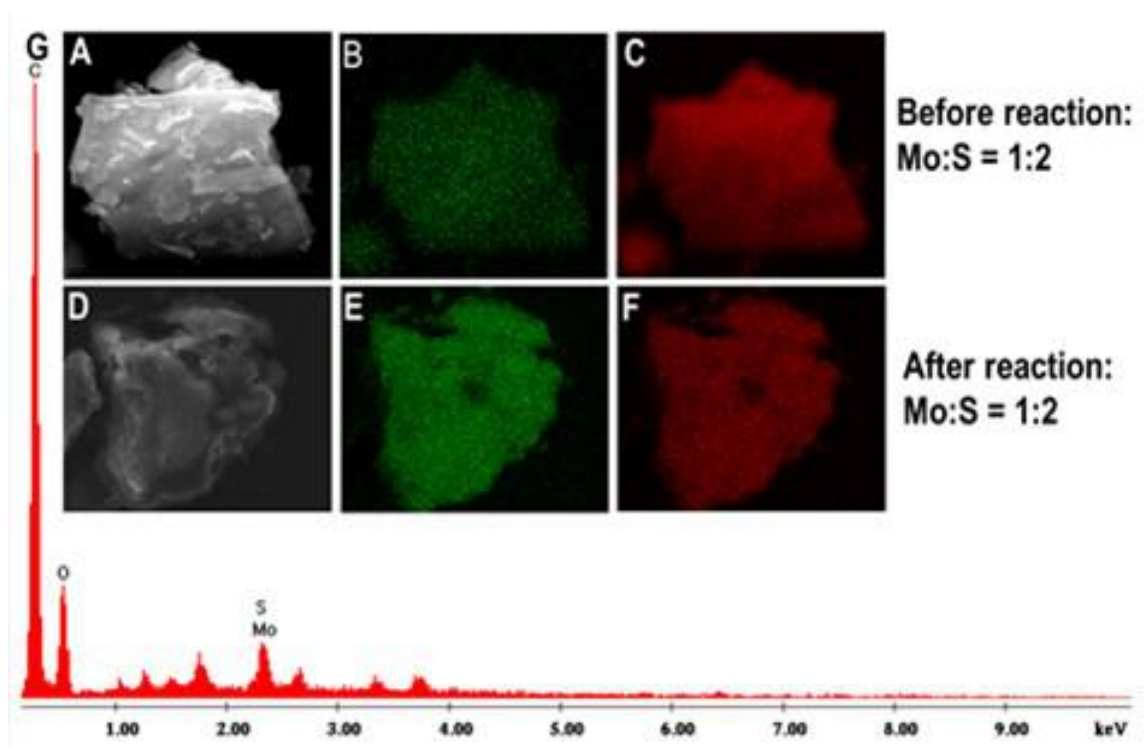


Figure S2. (A) SEM image, (B) and (C) EDS maps of Mo and S, respectively before the reaction. (D) SEM image, (E) and (F) EDS maps of Mo and S, respectively after immersion in AgNO₃ solution for 24 h. The Mo and S ratio before and after AgNO₃ treatment remains the same confirming the absence of reaction. (G) EDS spectrum taken from bulk MoS₂ sample post AgNO₃ treatment.

S3. Supporting information 3

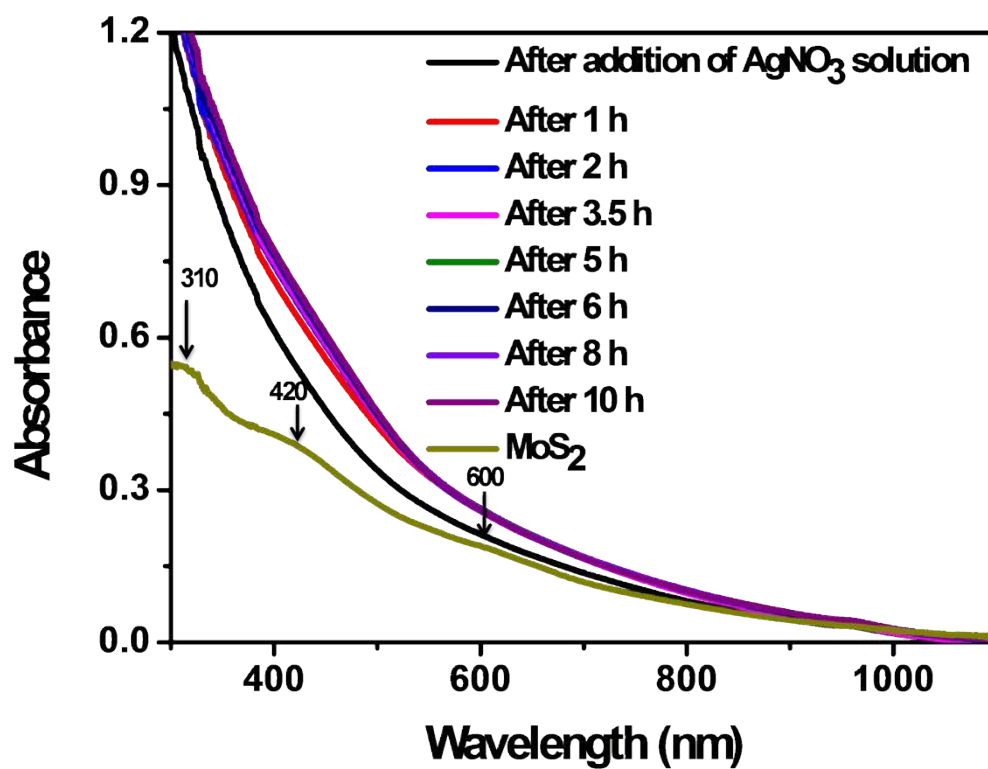


Figure S3. Time dependent UV/Vis spectra of the reaction between MoS₂ (500 μ L) and AgNO₃) solution (400 μ L, 5.8 mM). Just after the addition of AgNO₃ solution, the peaks at 420 nm and 310 nm vanished.

S4. Supporting information 4

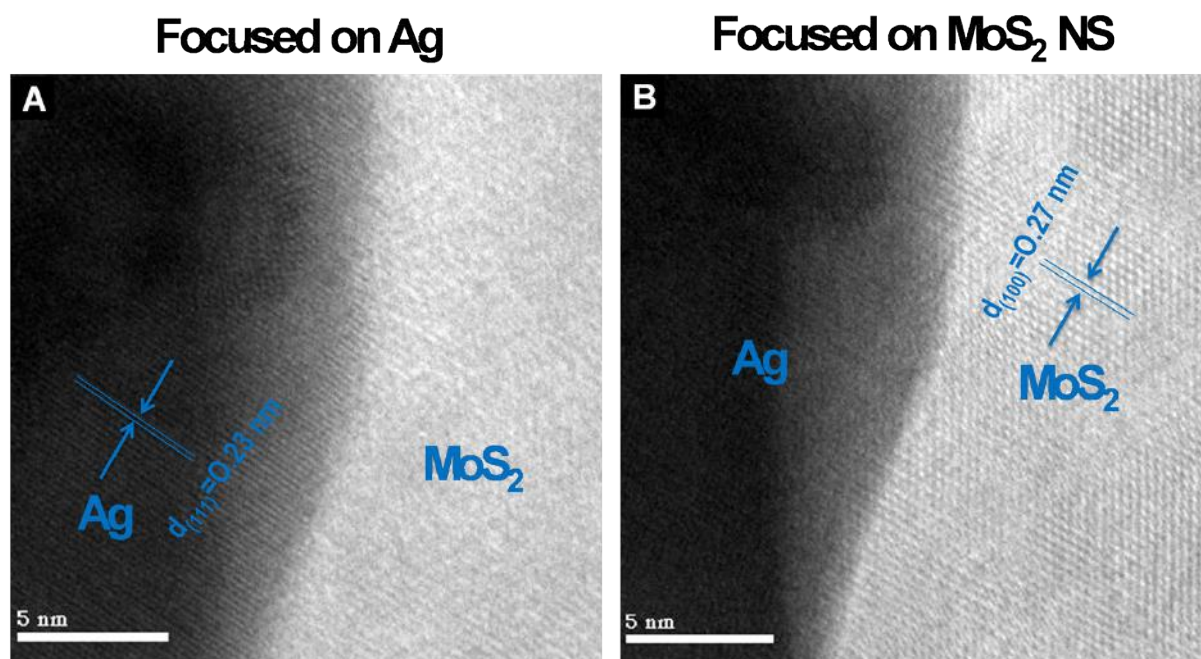


Figure S4. HRTEM images of Ag NP on the MoS₂ NS, (A) image taken by focusing the Ag NP and (B) image taken by focusing the MoS₂ NS.

S5. Supporting information 5

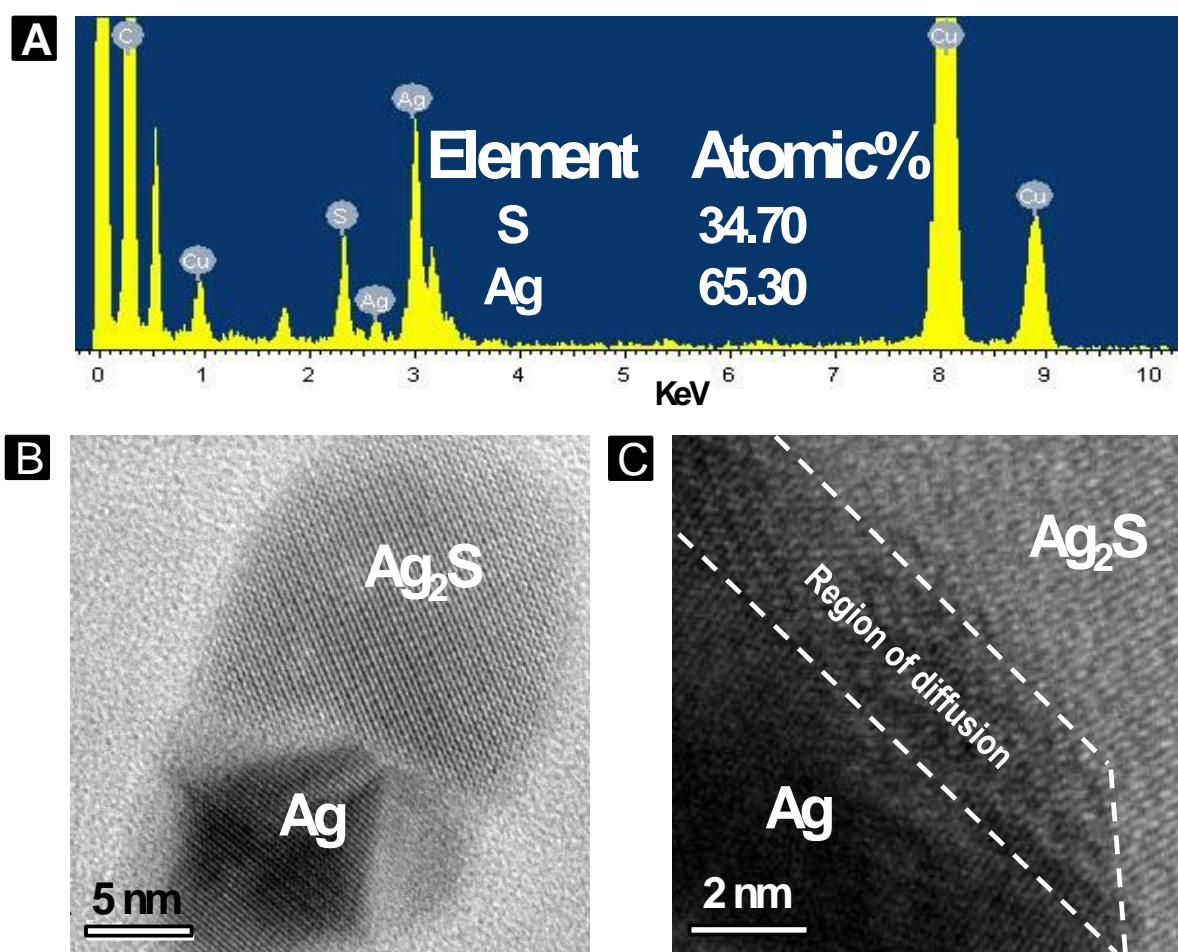


Figure S5. (A) EDS spectrum of the network like Ag_2S structure. The Ag and S ratio is almost 2:1 which confirmed that the structure is of Ag_2S . (B) HRTEM image of 'Janus' type particles. (C) Expanded view of the marked region from Figure 1Biii. Ag and Ag_2S phases can be seen to be separated by a region, where the growth of Ag_2S from Ag by S diffusion can be seen.

S6. Supporting information 6

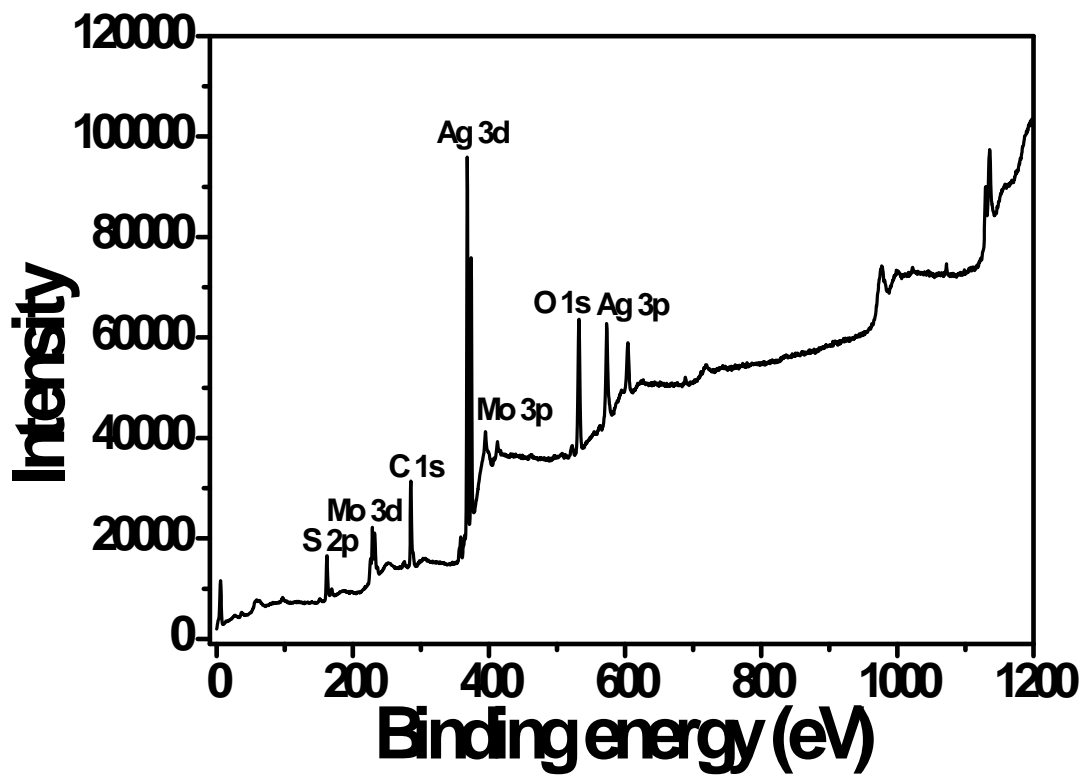


Figure S6. The XPS survey spectrum of all the element for the reaction between MoS₂ (500 μL) and AgNO₃ (400 μL, 5.8 mM).

S7. Supporting information 7

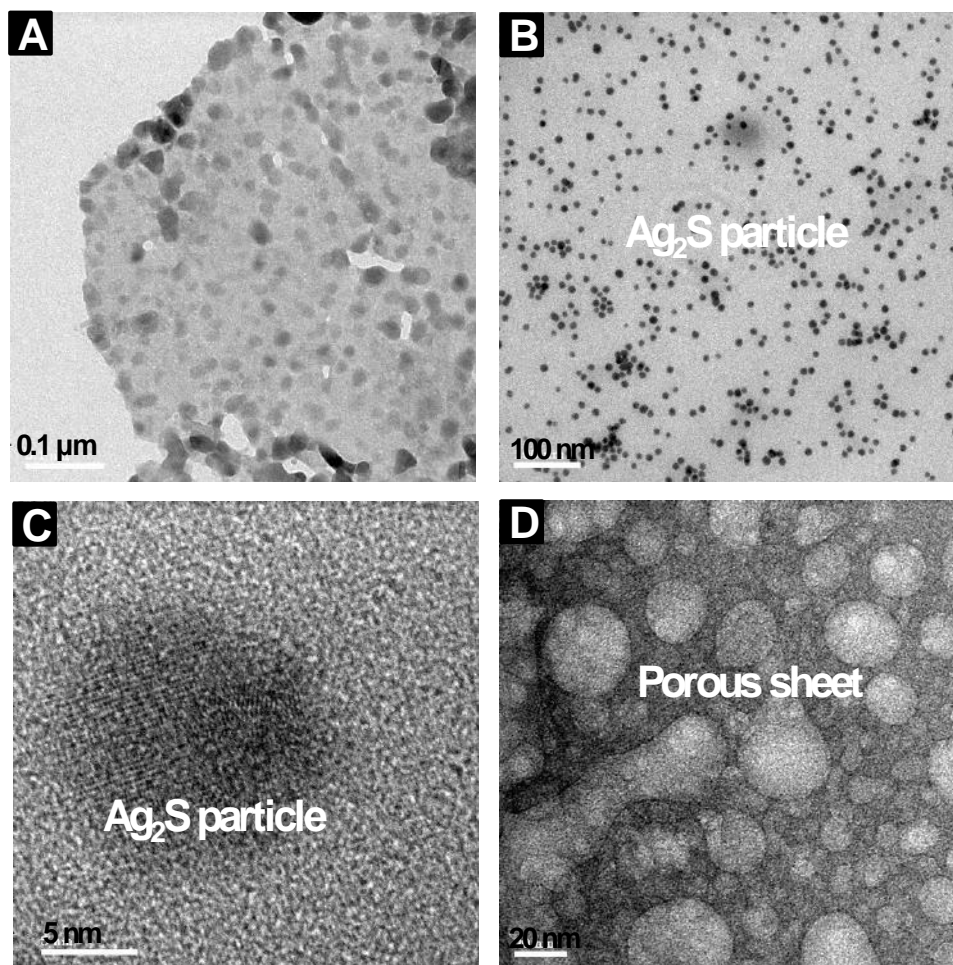


Figure S7. Reaction between prepared Ag NPs@citrate and MoS₂ nanosheet. (A) TEM image of Ag NPs on the MoS₂ sheet. Image was taken just after the addition of Ag NPs to the aqueous dispersion of MoS₂ nanosheet. (B) TEM image of Ag₂S particle formed after 12 h of reaction. (c) HRTEM image of Ag₂S particle. (D) TEM image of amorphous, porous sheet after the reaction.

S8. Supporting information 8

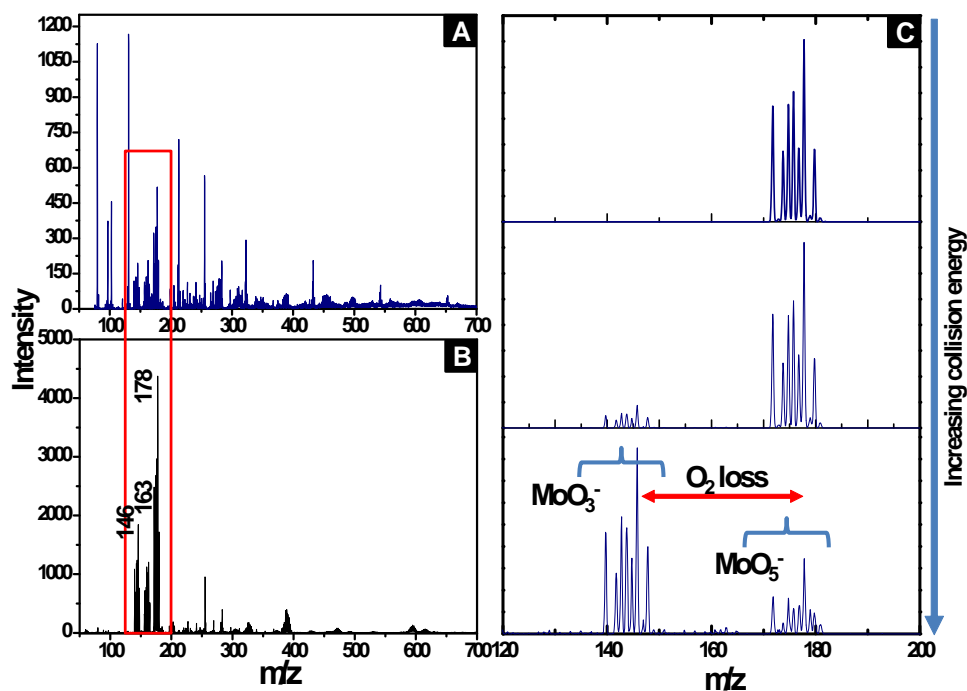


Figure S8. (A) Full range ESI MS spectrum of the sample taken after 6 h of the reaction. (B) ESI MS spectrum of ammonium molybdate taken as a blank to compare with the sample. (C) MS2 of the peak at m/z 178.

S9. Supporting information 9

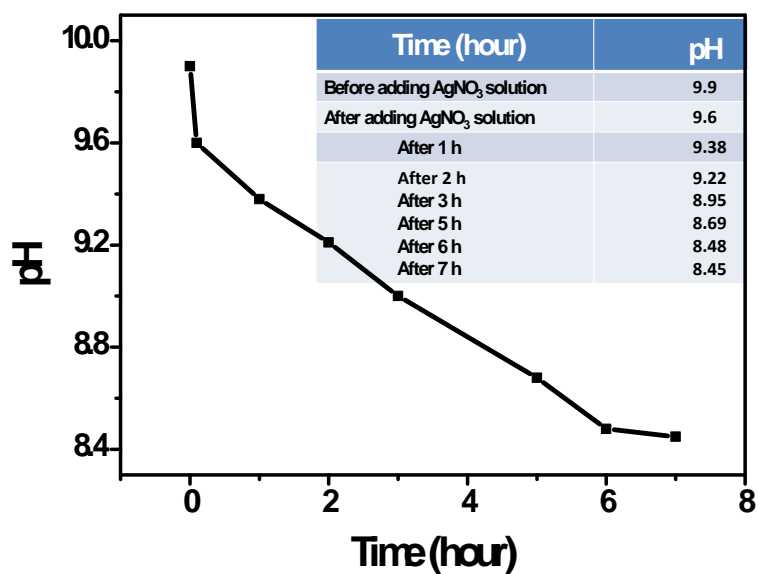


Figure S9. Time dependent pH monitoring during the reaction. pH of the reaction mixture decreases with time confirming the formation of H⁺ ion during the reaction.

S10. Supporting information 10

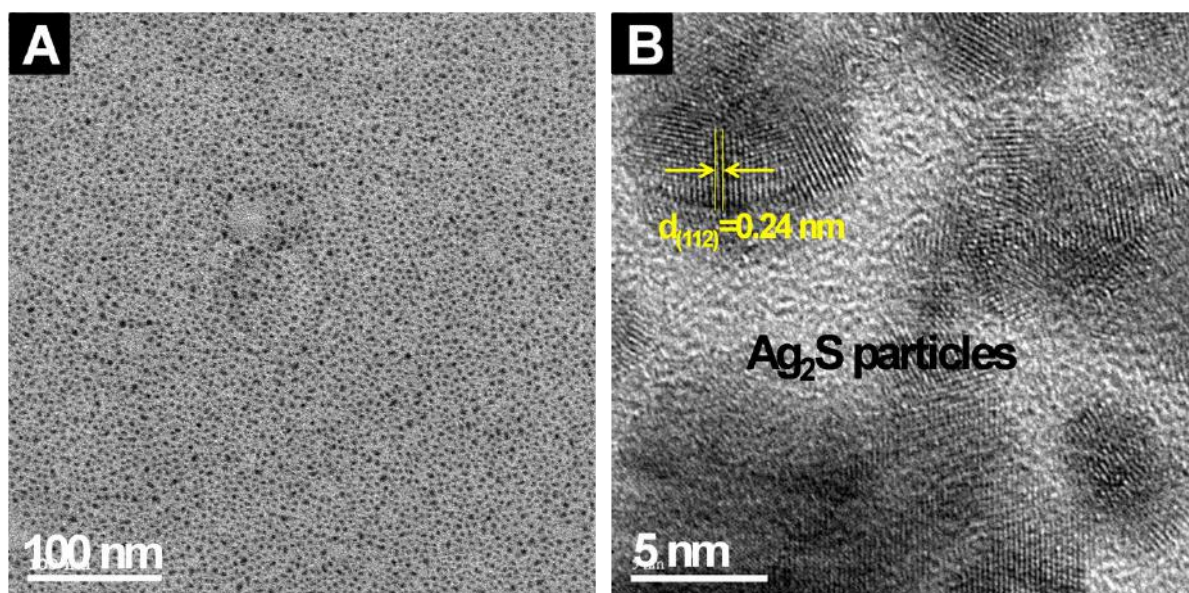


Figure S10. MoS₂ NSs react with silver acetate the same way as AgNO₃. (A) TEM image of the particles and (B) HRTEM image of the same.

S11. Supporting information 11

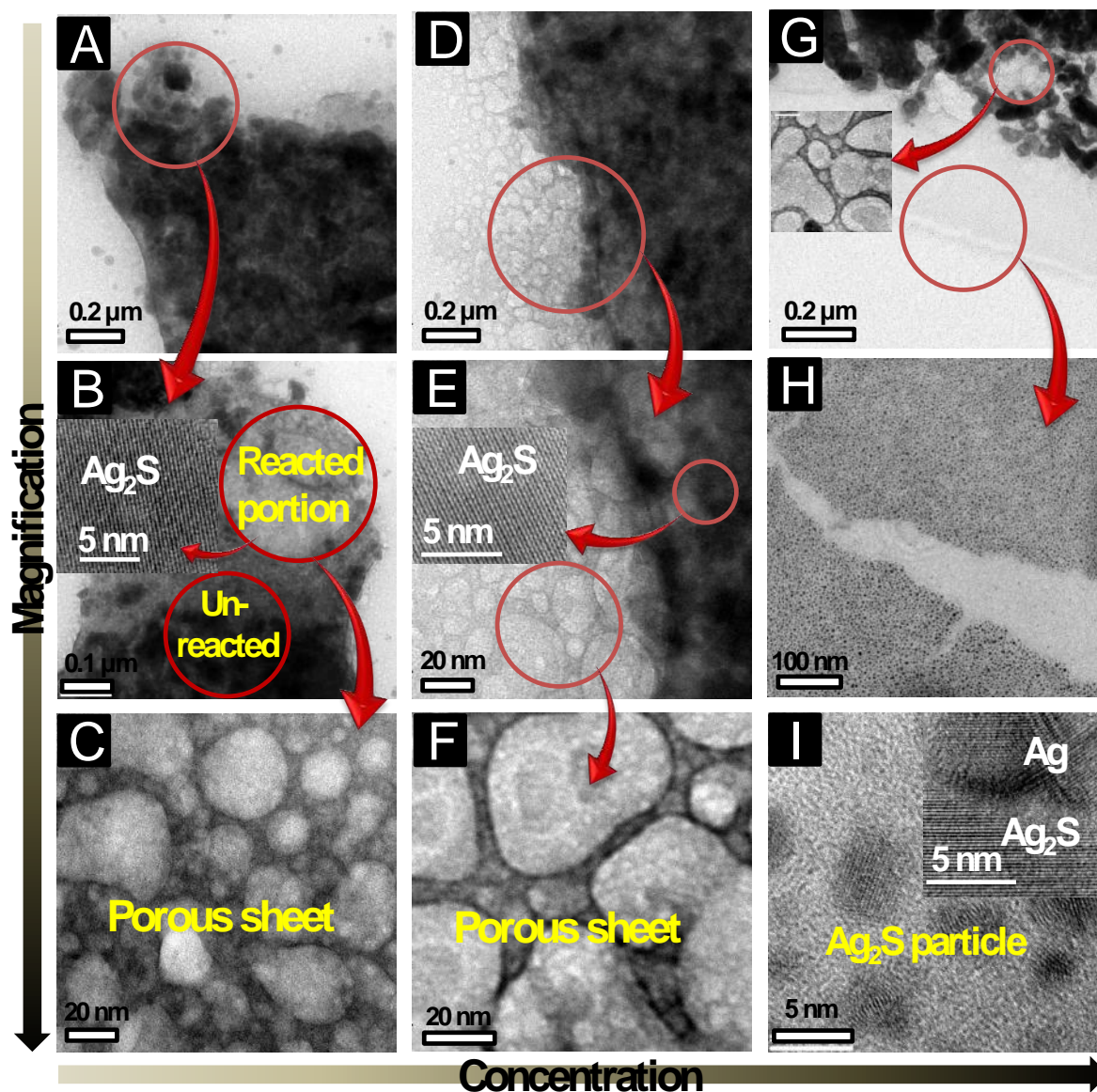


Figure S11. Changes of MoS₂ sheet with increasing concentration of added AgNO₃ solution. TEM image (A-C) for 200 μL, (D-F) for 800 μL, (G-I) for 1.6 mL, added AgNO₃ (5.8 mM) solution. For 200 μL AgNO₃, some parts of MoS₂ remained unreacted (B). For 1.6 mL AgNO₃ solution small Ag-Ag₂S particle formed (I). (C), (F) TEM image of reacted MoS₂ sheet.

S12. Supporting information 12

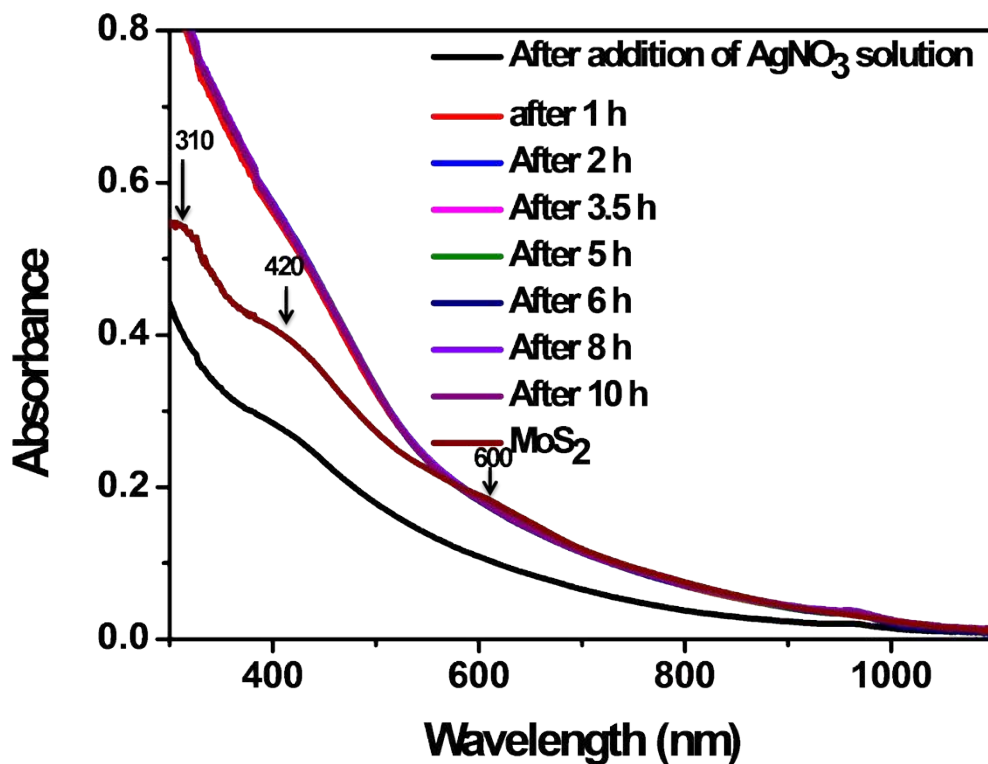


Figure S12. UV/Vis spectra of the reaction between MoS₂ NS (500 μ L) and AgNO₃ solution (200 μ L, 5.8 mM). After 10 h of reaction also the hump at 420 nm is present. The intensity of the peak gets reduced after 10 h of reaction which confirmed that some of the MoS₂ nanosheets reacted while some were still unreacted.

Silver Extraction

International Edition: DOI: 10.1002/anie.201510122
German Edition: DOI: 10.1002/ange.201510122

Extraction of Silver by Glucose

Ananya Baksi⁺, Mounika Gandhi⁺, Swathi Chaudhari⁺, Soumabha Bag, Soujit Sen Gupta, and Thalappil Pradeep*

Abstract: Unprecedented silver ion leaching, in the range of 0.7 ppm was seen when metallic silver was heated in water at 70 °C in presence of simple carbohydrates, such as glucose, making it a green method of silver extraction. Extraction was facilitated by the presence of anions, such as carbonate and phosphate. Studies confirm a two-step mechanism of silver release, first forming silver ions at the metal surface and later complexation of ionic silver with glucose; such complexes have been detected by mass spectrometry. Extraction leads to microscopic roughening of the surface making it Raman active with an enhancement factor of 5×10^8 .

Noble metals are resistant to chemical corrosion. Extraction of noble metals from minerals and subsequent processing requires highly reactive conditions and toxic chemicals.^[1] Silver, one of the important and precious coinage metals is sourced from the ores, and mostly extracted by chemical and electrolytic methods.^[2] Major use of silver lies in photography and 60% of the total silver produced every year is recycled from photographic plates.^[3] This situation demands extraction and recycling of silver via green methods at mild conditions. Silver ions react strongly with biomolecules including carbohydrates, peptides and DNA.^[4] Similar interactions with biomolecules are observed in biomineralization pathways in microorganisms.^[5] Silver nanoparticles are made using glucose and starch as reducing as well as capping agents.^[4–6]

Herein, we show the extreme chemical affinity of silver to carbohydrates leading to their extraction in solution, directly from the metallic state, which is enhanced in presence of common ions suggesting a new method of extractive metallurgy. The process is thermodynamically favorable as seen from a calorimetric study. Continuous extraction of silver leads to corrosion of the surface and subsequent microscopic roughness was observed. This roughened surface acts as an effective substrate for surface enhanced Raman spectroscopy (SERS).

In a typical experiment, a silver foil of 6 cm × 6 cm area and 3 g in mass leaches out 656 ppb silver in 27.8 mM glucose (G) solution in 7 days, when the extraction was performed at 70 °C in a Teflon beaker. Surface area and mass of the silver

foil were kept constant for all the experiments. This foil decreases its mass by 0.5% in this time. Exposure for 90 days can lead to 10% mass loss of the silver foil, in the above condition. Time dependent variation of the mass during an experiment is shown in Figure 1. Silver mirrors coated on glass slides also show similar leaching. However, as we keep our reaction in stirring conditions, the silver mirror gets damaged and therefore we continued our experiments with silver foils.

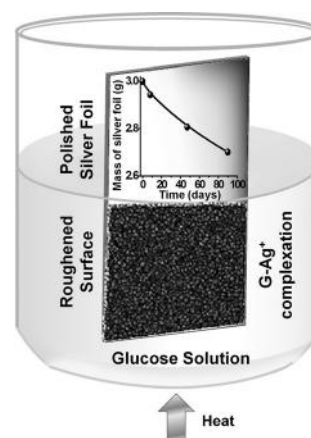


Figure 1. Schematic representation (not to scale) of silver extraction by glucose (G). A silver foil was kept partly immersed in a solution of glucose, maintained at 70 °C. The immersed portion turns black with time, owing to roughening. Weight loss of the foil with respect to time is shown.

The weight loss is due to the leaching of Ag as Ag⁺ and the existence of glucose–Ag⁺ (G–Ag⁺) complexes in the solution was studied. G–Ag⁺ and 2G–Ag⁺ complexes were detected by electrospray ionization mass spectrometry (ESI MS) (Figure 2). In tandem mass spectrometry (ESI MS/MS), the G–Ag⁺ complex ions (m/z 287 and 289, arising from ¹⁰⁷Ag and ¹⁰⁹Ag isotopes, respectively) fragment to their components at nominal collision energy of 20 V (Figure 2C). The 2G–Ag⁺ complex shows a similar pattern, fragmentation leads to G–Ag⁺ and Ag⁺ ions (see Figure S1 in the Supporting Information). Similar adducts were seen when glucose was treated with AgNO₃ which established the formation of G–Ag⁺ complexes in solution by silver ions derived from silver foils (Figure S2). Similar complex was predicted by Boutreau et al. with a series of monosaccharides, such as glucose, sucrose, fructose, through computational studies.^[7] Owing to presence of multiple stereoisomeric forms of glucose, it can bind to metal ion at different positions. They have computed the structures of such G–Ag⁺ complexes and found that α -anomer of glucose binds effectively with Ag⁺ through hydroxyl groups

[*] Dr. A. Baksi,^[†] M. Gandhi,^[†] S. Chaudhari,^[†] Dr. S. Bag, S. S. Gupta, Prof. T. Pradeep
Department of Chemistry, DST Unit of Nanoscience (DST UNS) and Thematic Unit of Excellence (TUE)
Indian Institute of Technology Madras
Chennai 600 036 (India)
E-mail: pradeep@iitm.ac.in

[†] These authors contributed equally to this work.

Supporting information for this article can be found under:
<http://dx.doi.org/10.1002/anie.201510122>.

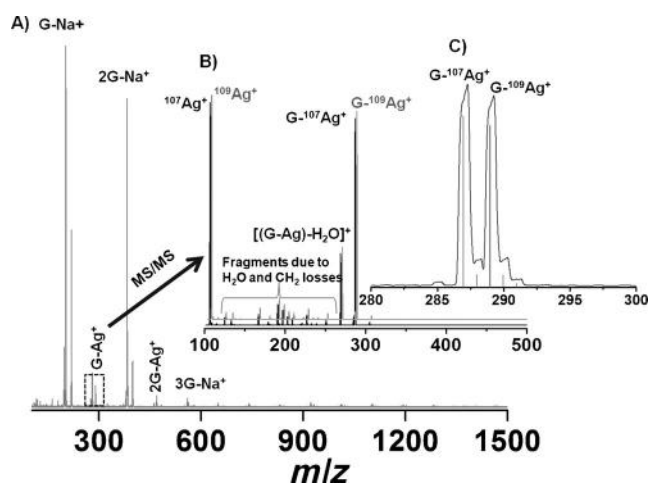


Figure 2. A) ESI MS of glucose-silver complexes G-Ag obtained by the extraction of silver foil by glucose (in water) at 70°C, showing the formation of Ag containing ions. B) MS/MS of G-Ag⁺ showing the loss of one G to give Ag⁺. Data corresponding to ¹⁰⁹G-Ag⁺ (gray) and ¹⁰⁷G-Ag⁺ (black) are shown. C) Expanded view of G-Ag⁺ complex region of (A) matching well with the calculated mass spectrum, with isotopes. See Supporting Information Figure S1 for isotope resolved MS/MS of 2G-Ag⁺ complex.

at positions 3 and 4. The isotope pattern (Figure 2C) and fragmentation from the isotopically pure ions confirm the identity of the ions.

Several experiments were performed to find the optimum condition of silver extraction, as outlined below:

1. Among three monosaccharides; glucose, fructose, and mannose, glucose was found to be most effective in extracting silver. In a typical experiment, 28.7 mM of glucose (1 g, 5×10^6 ppb) was used in 200 mL deionized water and the solution was heated at 70°C. For other carbohydrates equivalent quantity was taken.
2. Gradual increase in the number of glucose units may have some effect in the extraction process. We performed extraction using mono, di-, and trisaccharides and the data obtained were as follows: glucose (656 ppb), sucrose (120 ppb), and maltotriose (990 ppb). Although maltotriose had maximum effect (see Figure 3A); owing to its high cost we continued our experiments with glucose.
3. In a concentration dependent study, we found that silver concentration is dependent on the glucose concentration and 27.8 mM of glucose (1 g, 5×10^6 ppb) was good enough to extract moderate amount of silver in solution. Higher concentration of glucose does not lead to increased silver leaching.
4. We have also performed the reaction using α , β , and γ -cyclodextrins (CDs) and found that silver concentration follows the order, $\alpha > \beta > \gamma$. The observed trend of reactivity of different cyclodextrins towards silver is in agreement with the reported complexation of Au³⁺ ions. Liu et al. have shown that gold ions can complex effectively with cyclodextrin via second sphere co-ordination.^[8] They have used different gold salts for this experiment and showed that KAuBr₄ is the most efficient candidate for such complexation. Specificity of extraction

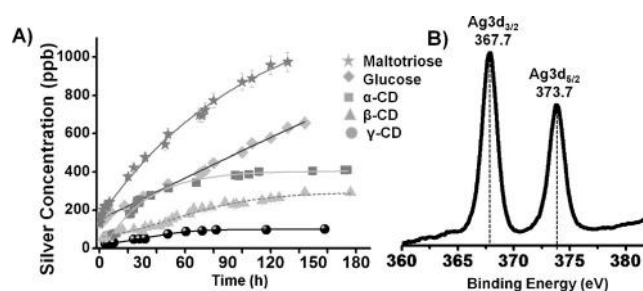


Figure 3. A) Silver-leaching capability of different carbohydrates in presence of a silver foil (6 cm × 6 cm, 3 g in mass). Maltotriose causes the maximum silver leaching among glucose, maltotriose, α -CD, β -CD, and γ -CD. Total silver-ion concentrations were obtained from ICP MS analyses. All the experiments were repeated three times and average data are plotted. The surface area of the Ag foil was kept constant throughout the investigation. B) XPS of Ag-G complex (formed during the silver leaching experiment) in the form of a dried film, showing the presence of Ag⁺ in the solution.

of gold by complexation with α -CD was demonstrated by extracting metal ions from an AuAg alloy using a mixture of conc. HBr and HNO₃.

5. Silver extraction is highly dependent on the purity of water. The extraction is highest in tap water and lowest in Millipore water (resistance 18.3 M Ω). Deionized water showed an intermediate effect. This happens mostly due to presence of different anions, such as carbonate, bicarbonate in regular tap water (see below for the anion effect).
6. Silver concentration increases with increase in solution temperature. From a temperature dependent study, we noticed that silver concentration was highest at 80°C. We carried out all the other experiments at 70°C to avoid excessive evaporation of water as we wanted to continue the experiment for longer time. Beyond 80°C, extraction was retarded. The probable cause could be cavitation on the silver surface by bubbles of water vapor at higher temperatures which cover the available silver surface and decrease the dissolution of silver.

The existence of Ag⁺ in the form of complexes was confirmed by X-ray photoelectron spectroscopic studies by casting the material in the form of a thin film (Figure 3B). The observed binding energy of 367.5 eV for Ag 3d_{3/2} is close to that of Ag⁺.^[9]

The dissolution of silver ion was examined in presence of various anions and the data are presented in Figure 4 which reveals a correlation with the solubility of the corresponding silver salt. The salts were added separately in the solution prior to the addition of glucose and silver foil was immersed in it. Various anions commonly present in tap water, such as, nitrate, sulfate, carbonate, bicarbonate, phosphate, chloride, bromide, have been examined (all as sodium salts) and phosphate was found to be most effective among all. About 10 times and 7 times enhancement in dissolution were observed in presence of 50 ppm (optimized from a concentration dependent study of anion concentration keeping all other conditions same) phosphate and carbonate; respectively along with glucose (same concentration of glucose was used as mentioned before). Silver-leaching capacity may be

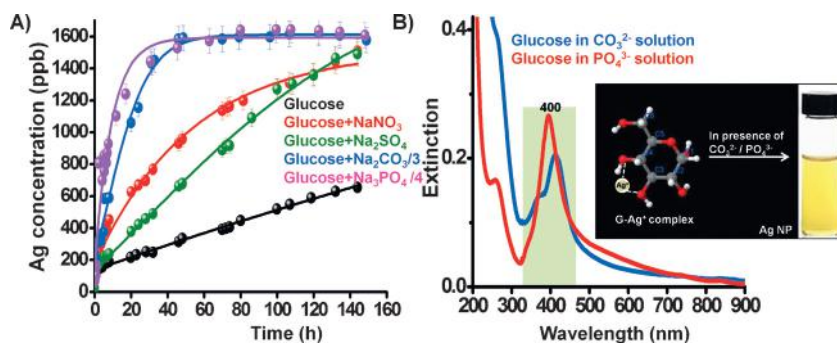


Figure 4. A) Effect of foreign anions on silver leaching from silver foil, in presence of glucose. In all cases, sodium salts of different anions namely, nitrate, sulfate, carbonate, and phosphate (50 ppm each, keeping glucose concentration the same) have been added. All of them enhance silver concentration in the solution while carbonate and phosphate have maximum enhancing capacity (4667 and 6554 ppb, respectively). The traces with carbonate and phosphate have been divided by 3 and 4, respectively. B) In presence of carbonate and phosphate, Ag nanoparticles form which was confirmed by UV/Vis spectroscopy with a characteristic plasmon band at 400 nm. Inset of (B) shows a schematic of the conversion of complexes into NPs and the photograph shows the product.

understood from the solubility of these silver salts in water, which are in the order, 32 and 6.5 mgL⁻¹ for Ag₂CO₃ and Ag₃PO₄, respectively (see Table S1 for details). In all the cases, sodium salt of the respective anion was used.

In addition to the above, plasmonic nanoparticles were formed in presence of carbonate and phosphate which was confirmed from the characteristic plasmon band at 400 nm in the UV/Vis absorption spectrum of Ag nanoparticles (AgNPs) (Figure 4B). This appears due to the subsequent reduction of silver ions by glucose. Therefore, glucose has a dual role. Note that the anions alone (without glucose) have no significant effect in metal dissolution (see Figure S3). glucose can reduce Ag⁺ as mentioned earlier.

After confirming the role of counteranion in water, we have further extended the study to halides. Among the silver halides, AgF is soluble in water and the solubility decreases in the order, F⁻ > Cl⁻ > Br⁻ > I⁻. Same trend was found in dissolution where Ag concentration was maximum in presence of F⁻ and minimum in presence of Br⁻. However, in all such cases, the Ag⁺ concentration was much below that with G (see Table 1 for details).

We have also studied a wide range of pH (pH 3 to 8) to check its effect in the extraction (see Figure S4). Acidic pH was maintained using acetic acid and sodium bicarbonate and sodium hydroxide (pH 8) was used to maintain basic condition in water. At slightly acidic condition (pH 6), silver concentration was found to be higher (1368 ppb after 48 h) than the neutral condition. But as we increase the acidity, silver concentration gradually decreases. When basic pH was maintained using sodium bicarbonate (NaHCO₃), high concentration of silver (3888 ppb after 48 h) was recorded in solution. At the same time, silver extraction was retarded (50 ppb after 48 h) in presence of sodium hydroxide (pH 8), may be due to the hydrolysis of G at that condition. So not only pH but also the counter ion has important role in deciding the silver concentration in solution. Larger pH variation was not examined as in both these extremes, sugars will hydrolyze.

Presence of inorganic fertilizers in the soil can have some effect on the dissolution of insoluble compounds in water. To check whether presence of such species can alter silver concentration, we have performed four sets of extractions with two common fertilizers urea and NPK (a mixture of urea, phosphate and potassium in the ratio, 10:26:26), with and without glucose) and found that very high concentration of silver comes out when urea was used in presence of glucose. About 20 ppm of silver was observed in the solution of 1:1 glucose:urea (molar) mixture. About 1 ppm of silver was found when 40 mM of urea alone was used. Urea can produce ammonia in solution which can interact with the silver ion coming in the solution and form a stable silver-amine complex. This complex can subsequently interact with glucose and enhance the extraction.

NPK does not enhance silver leaching to the same extent like urea. About 9 ppm of silver was observed in presence of glucose and NPK. This study suggests that fertilizers can have an effect in extracting noble metals in ionic form from their

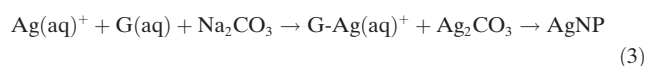
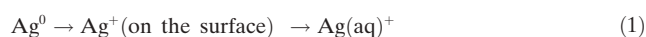
Table 1: Extraction of silver at different conditions.^[a]

Entry	Sample	Max. Ag conc. [ppb]
1	MilliQ water	80
2	DI water (DIW)	140
3	G in DIW	656
4	G in tap water	4100
5	Sucrose in DIW	120
6	Maltotriose in DIW	990
7	α-CD in DIW	460
8	β-CD in DIW	300
9	γ-CD in DIW	120
10	DIW + CO ₃ ²⁻	66
11	DIW + PO ₄ ³⁻	144
12	G + NO ₃ ⁻ in DIW	1409
13	G + SO ₄ ²⁻ in DIW	1591
14	G + CO ₃ ²⁻ in DIW	4667
15	G + HCO ₃ ⁻ in DIW	3888
16	G + PO ₄ ³⁻ in DIW	6554
17	G + F ⁻ in DIW	167
18	G + Cl ⁻ in DIW	101
19	G + Br ⁻ in DIW	42
20	G in DIW at pH 3	718
21	G in DIW at pH 5	607
22	G in DIW at pH 6	1369
23	G in DIW at pH 8	60
24	Silver mirror in G in DIW	1037 (with stirring) 561 (without stirring)
25	Silver mirror in G + CO ₃ ²⁻ in DIW	3701
26	Silver mirror in G + PO ₄ ³⁻ in DIW	4752
27	Urea in DIW	987
28	NPK in DIW	519
29	G + Urea in DIW	15888
30	G + NPK in DIW	8541

[a] All the experiments were repeated three times and average data are listed. Typical standard deviation among measurements is ±2.

sources in soil causing heavy metal toxicity, which may be bio-amplified through agriculture.

All these studies point to an ionic reaction in which silver ions come into the solution and subsequently get stabilized by the carbohydrate present in the medium. For further confirmation of this hypothesis, we have modified the silver surface. A new and polished silver foil was used for this study. The surface of the foil was wiped with very dilute nitric acid for mild oxidation of the silver surface. This modified silver foil was dipped in glucose containing water and heated at 70 °C for 2 h. About 2 ppm of silver was observed just after 2 h. Without wiping with dilute HNO₃, the silver concentration was 0.7 ppm after 7 days. This study confirms our claim of ionic reactions. On the basis of the above studies and observations, the process can be written as follows [Eq. (1)–(3)]:



As the G-Ag(aq)⁺ complex is stable, more silver comes into the solution. The effect of silver dissolution in various conditions is summarized in Table 1. Oxidation of silver appears to be facilitated by dissolved oxygen as an Ar purged solution shows only 530 ppb Ag under identical conditions (in contrast to 656 ppb for exposed solution). There is no effect of ambient light in this reaction as similar Ag concentration was seen for a reaction done in dark (687 ppb).

Enhanced dissolution of silver in presence of ions suggests increased chemical affinity of the metal with glucose in presence of these ions. This was proven by isothermal titration calorimetric (ITC) experiments. In a typical ITC measurement, 1 mM glucose solution was titrated against 10 mM of AgNO₃ (20 mM in presence of carbonate and phosphate) and the heat change was recorded. The data were converted to a sigmoidal curve and from fitting the data we derive the thermodynamic parameters, N, K, ΔH, ΔS, ΔG which represent the number of binding sites, rate of reaction, reaction enthalpy, entropy and Gibb's free energy, respectively. The temperature for the experiment was 343 K. The data suggest nearly 1:1 complex formation of G with Ag⁺ (Figure S5A), in the glucose versus AgNO₃ titration. Fractional binding sites are due to the presence of different aggregates (G-Ag⁺, 2G-Ag⁺, etc. as discussed in the ESI MS of the complex and in Figure S2) which also interact with Ag⁺ in the reaction conditions. Negative ΔH, ΔG and positive ΔS suggest that the reaction is thermodynamically favorable and mostly enthalpy driven. In presence of carbonate (Figure S5B) and phosphate (Figure S5C), the rate of reaction increased and also the heat change. Entropy remained almost the same and hence the reaction is enthalpy driven. All the data are summarized in Figure S5D. The data confirm that ionic silver present in water forms complexes with glucose and the dissolution strongly depends on the solubility of the species in water. Owing to its high chemical affinity in

presence of anions as suggested by the thermochemical values, larger dissolution occurs.

Etching of silver by glucose leads to microscopically roughened surface (Figure S6B). This nanoscale roughening creates SERS-active substrates which can detect crystal violet (cv) up to 10⁻⁷ M with an enhancement factor of 5 × 10⁸ (calculated from Raman intensity, see Figure S6, S7, and Table S2 for details). This substrate can be used for the detection of biomolecules such as DNA and biomarkers.^[10]

In summary, a green and efficient method for extracting silver from the bulk metal, by simple use of carbohydrates is presented. Presence of specific anions can enhance the extraction. Glucose-induced corrosion of bulk silver can lead to microscopic roughness of the surface which can be used for the detection of analytes at ultralow concentrations by SERS. We believe that this method can contribute to new processes in extractive metallurgy of noble metals. There is alarming growth of heavy-metal poisoning and there is a belief that use of fertilizers may be responsible, at least partially. The extraction of ions from minerals can be enhanced by chemical fertilizers and this could present a problem of bioamplification by agriculture.

Experimental Section

Experimental details: At optimized condition, 1 g of sugar was added to 200 mL of DI water in a Teflon beaker. A 6 cm × 6 cm (3 gm in mass) silver foil was immersed in that solution and heated at 70 °C. Equal volumes of solution were taken out at selected times and analyzed by ICP MS. The total volume was made up by adding equal volume of the stock solution (1 g sugar/200 mL). The foil was thoroughly washed with DI water and dried before Raman experiments. Experimental details and instrumentation used are presented in Supporting Information.

Acknowledgements

The experimental work was supported by the Department of Science and Technology, India. A.B. thanks CSIR for a fellowship. S.S.G. thanks the SERB, CII, and Thermax India Pvt. Ltd. for a research fellowship.

Keywords: extraction of metals · extractive metallurgy · green processes · silver

How to cite: *Angew. Chem. Int. Ed.* **2016**, *55*, 7777–7781
Angew. Chem. **2016**, *128*, 7908–7912

[1] H. O. Hofman, *J. Am. Chem. Soc.* **1907**, *29*, 1246–1247.

[2] a) J. Johnson, J. Jirikowic, M. Bertram, D. van Beers, R. B. Gordon, K. Henderson, R. J. Klee, T. Lanzano, R. Lifset, L. Oetjen, T. E. Graedel, *Environ. Sci. Technol.* **2005**, *39*, 4655–4665; b) M. M. Matlock, B. S. Howerton, J. D. Robertson, D. A. Atwood, *Ind. Eng. Chem. Res.* **2002**, *41*, 5278–5282; c) A. M. Thibodeau, D. J. Killick, J. T. Chesley, K. Deagan, J. M. Cruxent, W. Lyman, *Proc. Natl. Acad. Sci. USA* **2007**, *104*, 3663–3666; d) G. Deschenes, J. Rajala, A. R. Pratt, H. Guo, M. Fulton, S. Mortazavi, *Miner. Metall. Process.* **2011**, *28*, 37–43; e) X. Du, Patent, China, **2010**, CN 101871049; f) M. M. Matlock, B. S. Howerton, M. A. Van Aelstyn, F. L. Nordstrom, D. A. Atwood, *Environ. Sci. Technol.* **2002**, *36*, 1636–1639; g) T. H. Handley,

- Anal. Chem.* **1964**, *36*, 2467–2471; h) L. Wish, S. C. Foti, *Anal. Chem.* **1964**, *36*, 1071–1072.
- [3] a) V. Covaliov, O. Covaliova, Patent, **2006**, MD 3037; b) S. Stenstroem, *Process Metall.* **1992**, *7A*, 943–948.
- [4] P. Raveendran, J. Fu, S. L. Wallen, *J. Am. Chem. Soc.* **2003**, *125*, 13940–13941.
- [5] R. R. Naik, S. J. Stringer, G. Agarwal, S. E. Jones, M. O. Stone, *Nat. Mater.* **2002**, *1*, 169–172.
- [6] a) C. Sönnichsen, B. M. Reinhard, J. Liphardt, A. P. Alivisatos, *Nat. Biotechnol.* **2005**, *23*, 741–745; b) V. Raji, M. Chakraborty, P. A. Parikh, *Part. Sci. Technol.* **2012**, *30*, 565–577; c) S. Banerjee, K. Loza, W. Meyer-Zaika, O. Prymak, M. Epple, *Chem. Mater.* **2014**, *26*, 951–957; d) H. Liu, M. Lv, J. Li, M. Yu, Q. Huang, C. Fan, B. Deng, *Sci. Rep.* **2014**, *4*, 5920(1-9).
- [7] L. Bouteau, E. Leon, J.-Y. Salpin, B. Amekraz, C. Moulin, J. Tortajada, *Eur. J. Mass Spectrom.* **2003**, *9*, 377–390.
- [8] Z. Liu, M. Frascioni, J. Lei, Z. J. Brown, Z. Zhu, D. Cao, J. Iehl, G. Liu, A. C. Fahrenbach, Y. Y. Botros, O. K. Farha, J. T. Hupp, C. A. Mirkin, J. F. Stoddart, *Nat. Commun.* **2013**, *4*, 1855.
- [9] M. S. Bootharaju, T. Pradeep, *Langmuir* **2011**, *27*, 8134–8143.
- [10] K. C. Bantz, A. F. Meyer, N. J. Wittenberg, H. Im, O. Kurtulus, S. H. Lee, N. C. Lindquist, S.-H. Oh, C. L. Haynes, *Phys. Chem. Chem. Phys.* **2011**, *13*, 11551–11567.

Received: October 30, 2015

Revised: February 15, 2016

Published online: April 27, 2016

Supporting Information

Extraction of Silver by Glucose

*Ananya Baksi⁺, Mounika Gandi⁺, Swathi Chaudhari⁺, Soumabha Bag, Soujit Sen Gupta, and Thalappil Pradeep**

anie_201510122_sm_miscellaneous_information.pdf

Supporting Information

Table of contents

S/N	Description	Page Number
FigureS1	ESI MS/MS of 2G-Ag ⁺ complex	Page 3
FigureS2	ESI MS of G-Ag complex	Page 4
FigureS3	Effect of only CO ₃ ²⁻ and PO ₄ ³⁻	Page 5
FigureS4	Effect of pH in silver extraction	Page 6
FigureS5	Thermodynamic interpretation	Page 7
FigureS6	SERS activity of glucose treated silver foil at different condition	Page 8
FigureS7	Observation of SERS of CV at 5×10 ⁻⁷ M	Page 9
Table S1	Solubility of silver salts	Page 10
Table S2	SERS activity	Page 10

Materials: D(+)-G, Sucrose, α , β and γ -CD were purchased from Sigma Aldrich. D(+)-Mannose was purchased from SRL chemicals with 99% purity. D(-)-Fructose was purchased from Merck and γ -CD was purchased from TCI, Japan. Silver foils were purchased from local market. All the chemicals were used without further purification. Deionized water was used throughout the experiments (if not specified). Sodium nitrate, sodium sulphate, sodium carbonate, sodium phosphate and water soluble starch were purchased from Sigma Aldrich.

Instrumentation:

ICP MS analysis: ICP MS was performed using a Perkin Elmer NexION 300X instrument equipped with Ar plasma. Before doing any sample, the instrument was first calibrated with Ag standard (AgNO₃) of five different concentrations (0, 10, 100, 1000 and 10000 ppb) to get a calibration curve with R²=0.9999. Blank experiment (0 ppb) was performed with milliQ water (18.3 M Ω resistance) with 5% nitric acid. Standards were also prepared in 5% nitric acid. Same amount (5%) of nitric acid was added to the collected samples also before analyses.

ESI MS: ESI MS analysis was carried out using an Applied Biosystems 3200 QTRAP LC/MS/MS system in the mass range of m/z 80 to 1700. Optimized conditions were as follows: Ion spray Voltage 3 kV; Declustering Potential (DP) 30 V, Entrance Potential (EP) 10 V. For MS/MS analyses, collision energy was varied from 5 to 100 (instrument unit). Optimum fragmentation was observed in the range of 30-50.

ITC: Isothermal calorimetric experiments were performed using a GE Microcal iTC200. The instrument is having two cells made of hastelloy with 200 μL cell volume of which one is used for sample and another is used as reference. Maximum volume that can be injected is 40 μL through a syringe with sub-micro liter precision. Each time 2 μL of AgNO_3 was injected for a total of 20 injections for a glucose- AgNO_3 experiment. In the other cases, optimized injection volume was found to be 3 μL and a total of 13 injections were performed. The heat change due to interaction of water-water, water- AgNO_3 and $\text{AgNO}_3\text{-Na}_2\text{CO}_3/\text{Na}_3\text{PO}_4$ were subtracted from the original data before fitting. The data were fitted using one site model. The experimental error was less than 5% for each parameter.

Raman Spectroscopy: Raman measurements were done using a WITec GmbH, Alpha-SNOM alpha300 S confocal Raman microscope having a 532 nm laser as the excitation source. Background correction was done with the help of the software supplied with the Raman instrument (WiTec). Initially, the spectrum is fitted with a polynomial which was subtracted from the original spectrum. The analyte (CV) was drop cast on the roughened surface at various concentrations and Raman spectra were measured under these conditions (Figure S6A). For SERS study, 5 μL of the analyte was drop cast on the respective silver foil and air dried before analysis. In each case, nine spots were checked for each concentration of CV to see the reproducibility of the data. These data are compiled in Table S2. Raman spectra in the concentration range of 5×10^{-5} to 5×10^{-9} M were measured and the detection limit was 5×10^{-7} M (see Figure S7). Reproducibility of the data was ensured by collecting spectra from nine different spots.

Enhancement Factor Calculation: The enhancement factor (EF) was calculated using the standard formula,

$$\text{EF} = I_{\text{SERS}} * C_{\text{NR}} / I_{\text{NR}} * C_{\text{SERS}},$$

where, I_{SERS} and I_{NR} are the integral intensity obtained by SERS and normal Raman scattering measurements, respectively. C_{SERS} and C_{NR} are the concentration of molecules used for SERS and normal Raman scattering measurements, respectively. Intensity of the maximum intense peak of the analyte (CV) at 1620 cm^{-1} was considered for EF calculations.

UV-vis Spectroscopy: UV-vis spectra were collected using a PerkinElmer Lambda 25 instrument in the 200-1100 nm range. The band pass filter was set at 1 nm.

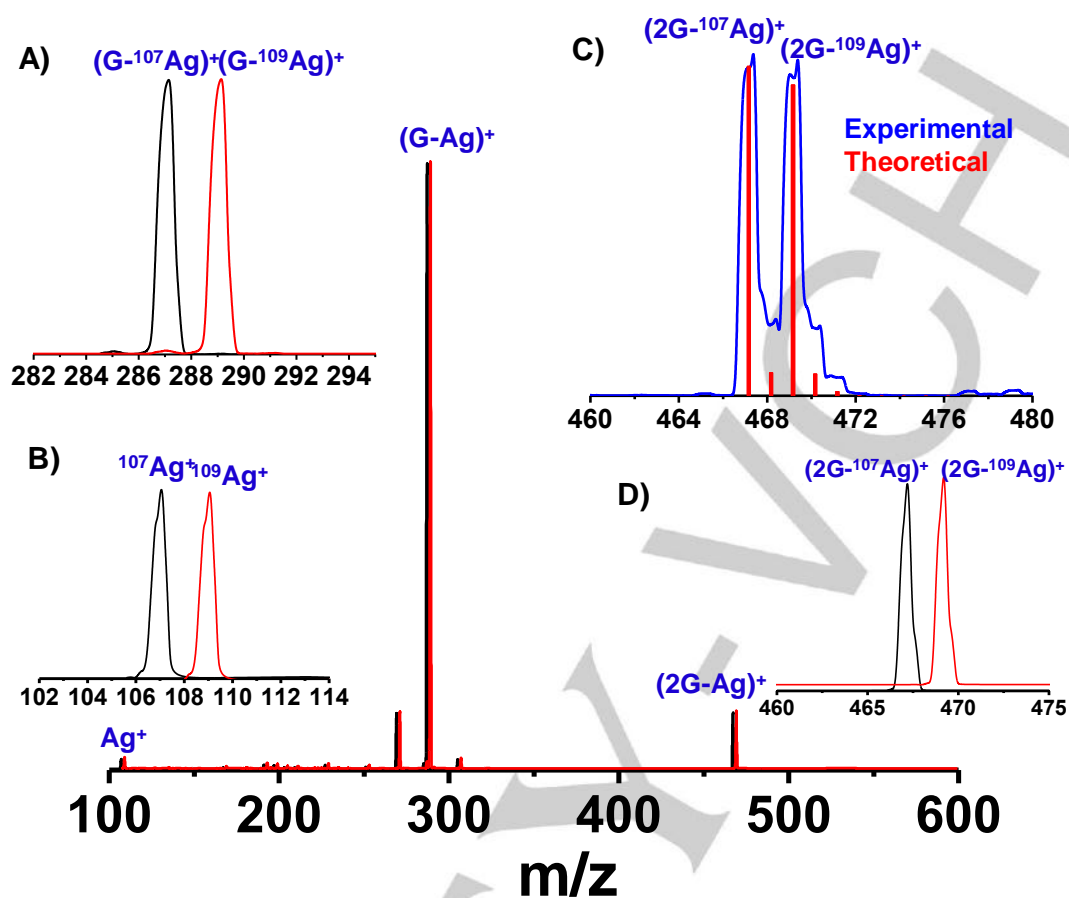


Figure S1. Isotope resolved (black trace for $2G-^{107}\text{Ag}^+$ and red trace for $2G-^{109}\text{Ag}^+$) ESI MS/MS of $2G-^{107}\text{Ag}^+$ complex showing one G loss to give $G-^{107}\text{Ag}^+$ complex and free Ag^+ . Respective peaks are expanded in A, B and D. Experimental mass spectrum of $2G-^{107}\text{Ag}^+$ matches with the theoretically calculated pattern as shown in C.

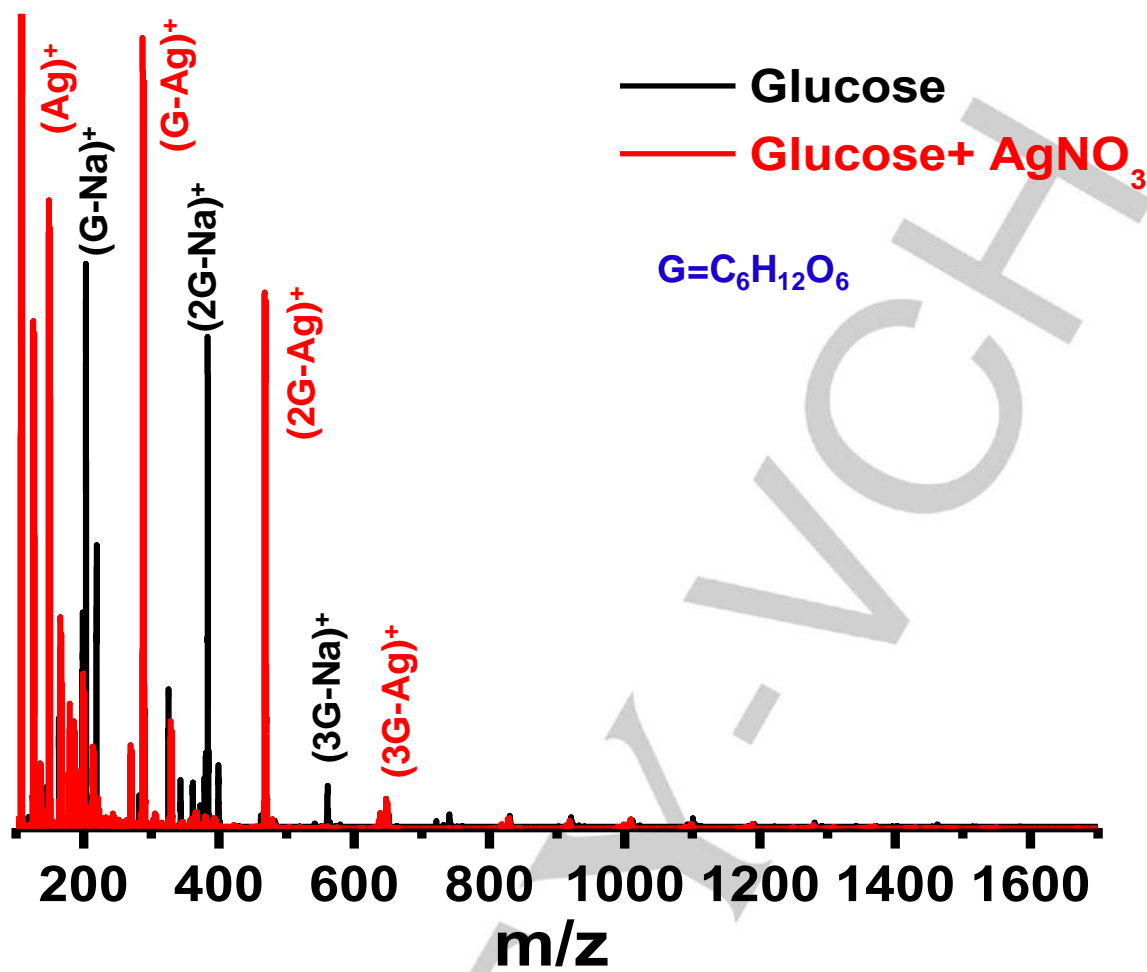


Figure S2. ESI MS of 1:1 (molar) G and AgNO_3 mixture showing G-Ag, 2G-Ag and 3G-Ag complexes.

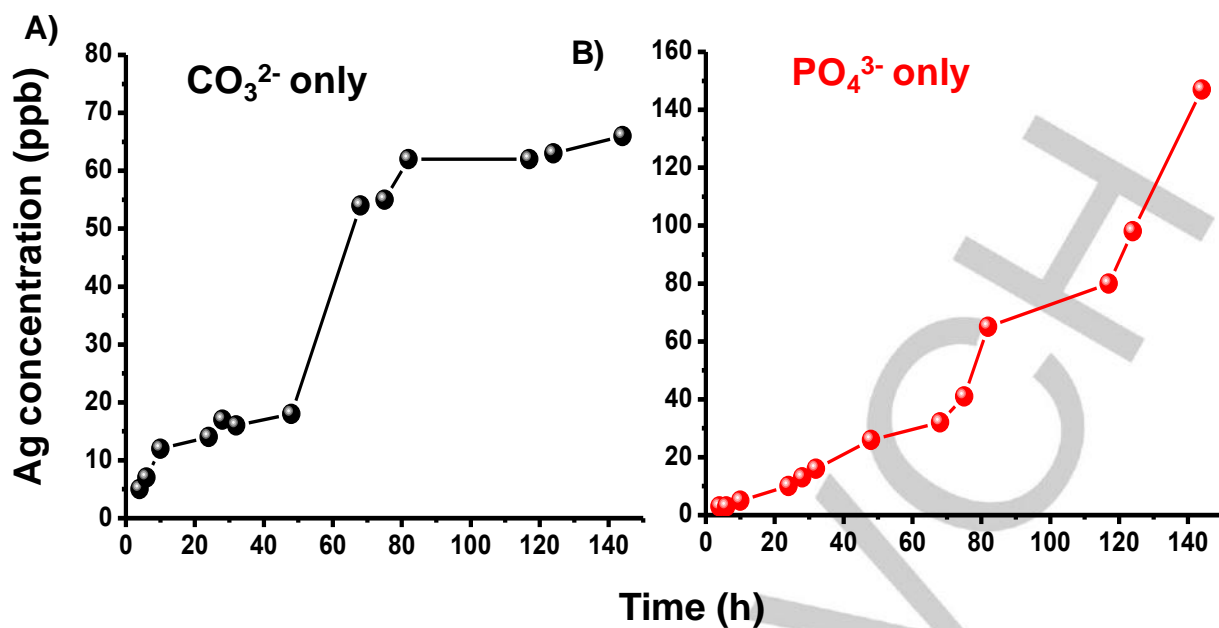


Figure S3. Time dependent silver leaching in DI water containing 50 ppm of A) CO₃²⁻ and B) PO₄³⁻ showing very less silver concentration compared to that with G. Na₂CO₃ and Na₃PO₄ were used as salts. Salts alone (without G) do not result in much extraction.

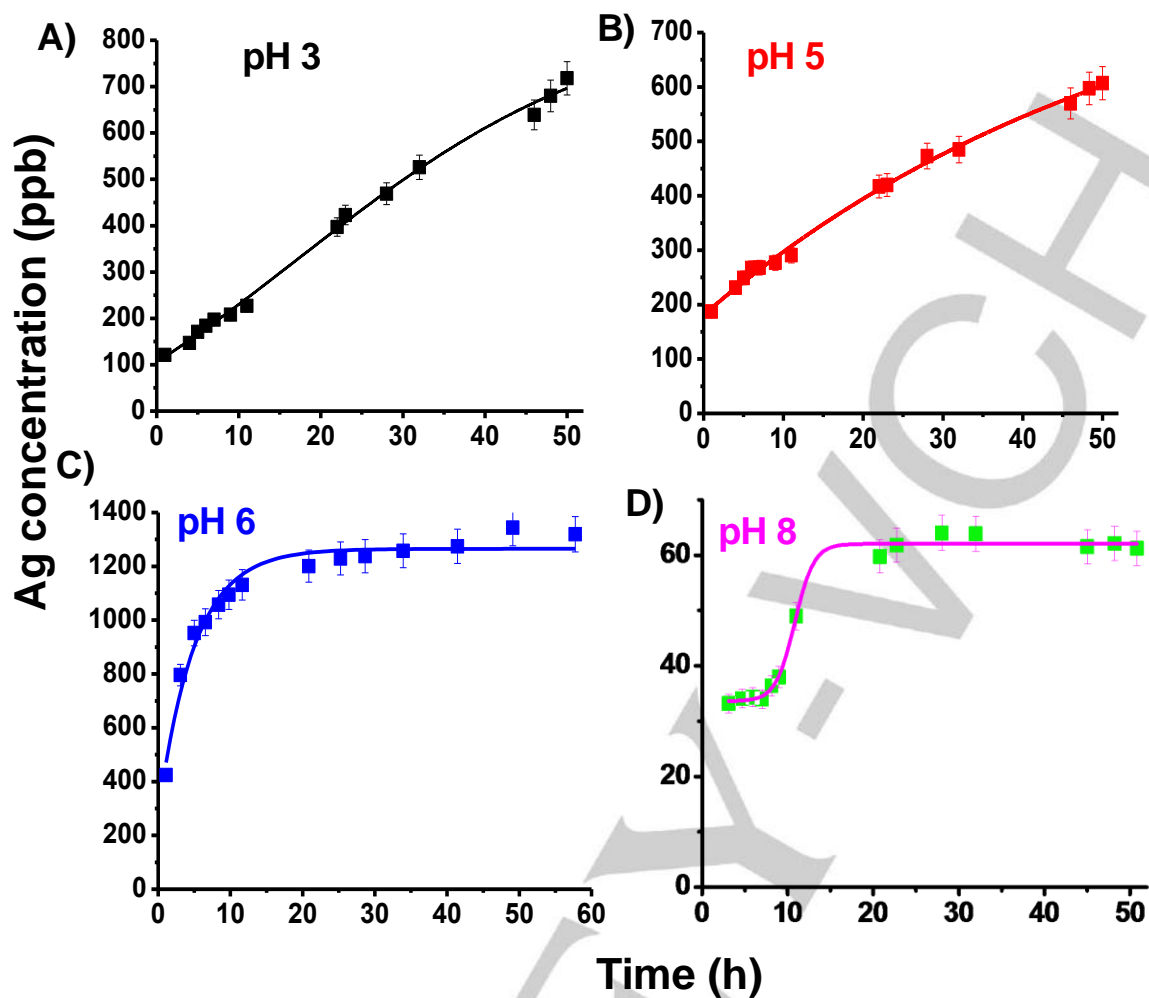


Figure S4. Silver leaching of glucose at varying pH. Acidic pH was maintained by acetic acid and pH 8 was maintained by NaOH. At pH 8, it appears that the silver surface gets passivated by the formation of silver hydroxide.

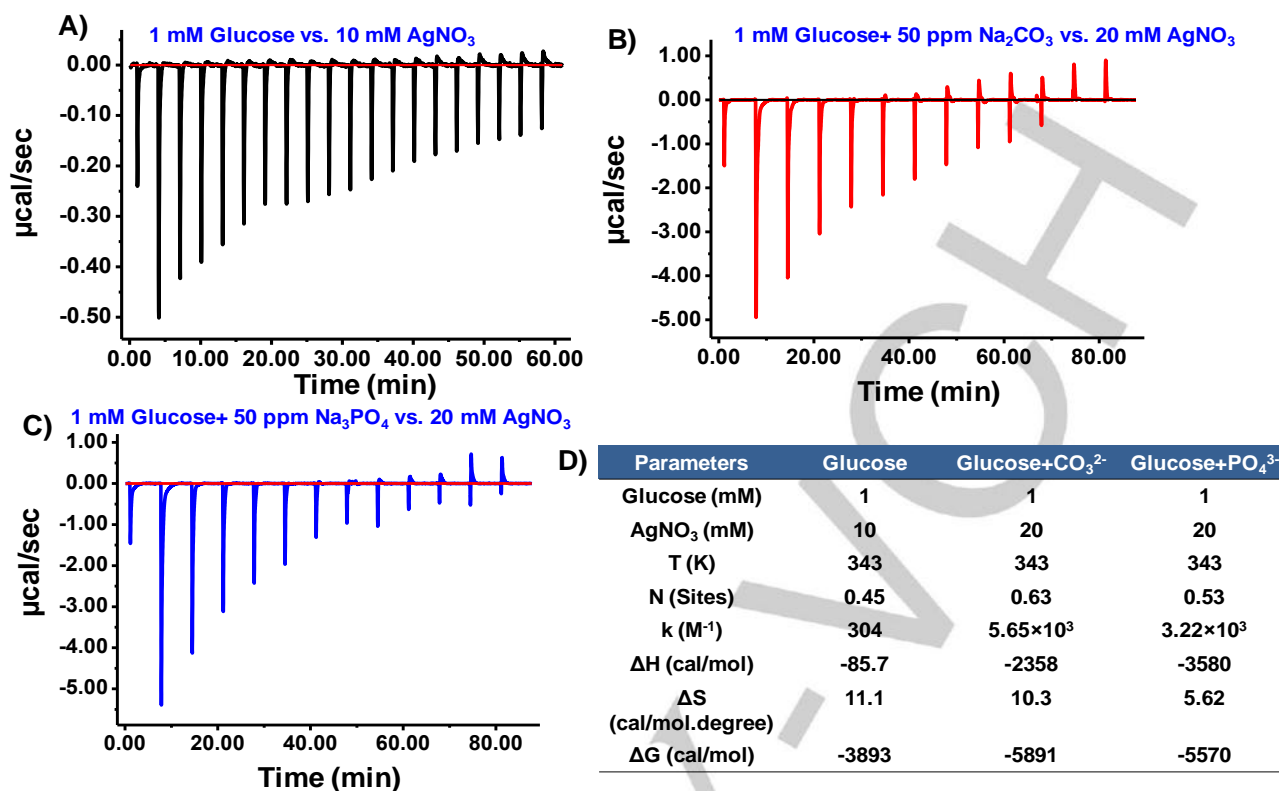


Figure S5. Isothermal calorimetric data for A) G and AgNO₃, B) G with carbonate and AgNO₃, C) G with phosphate and AgNO₃ titration. Thermodynamic parameters obtained from both the reactions are tabulated in D). Na₃PO₄ and Na₂CO₃ were used for phosphate and carbonate.

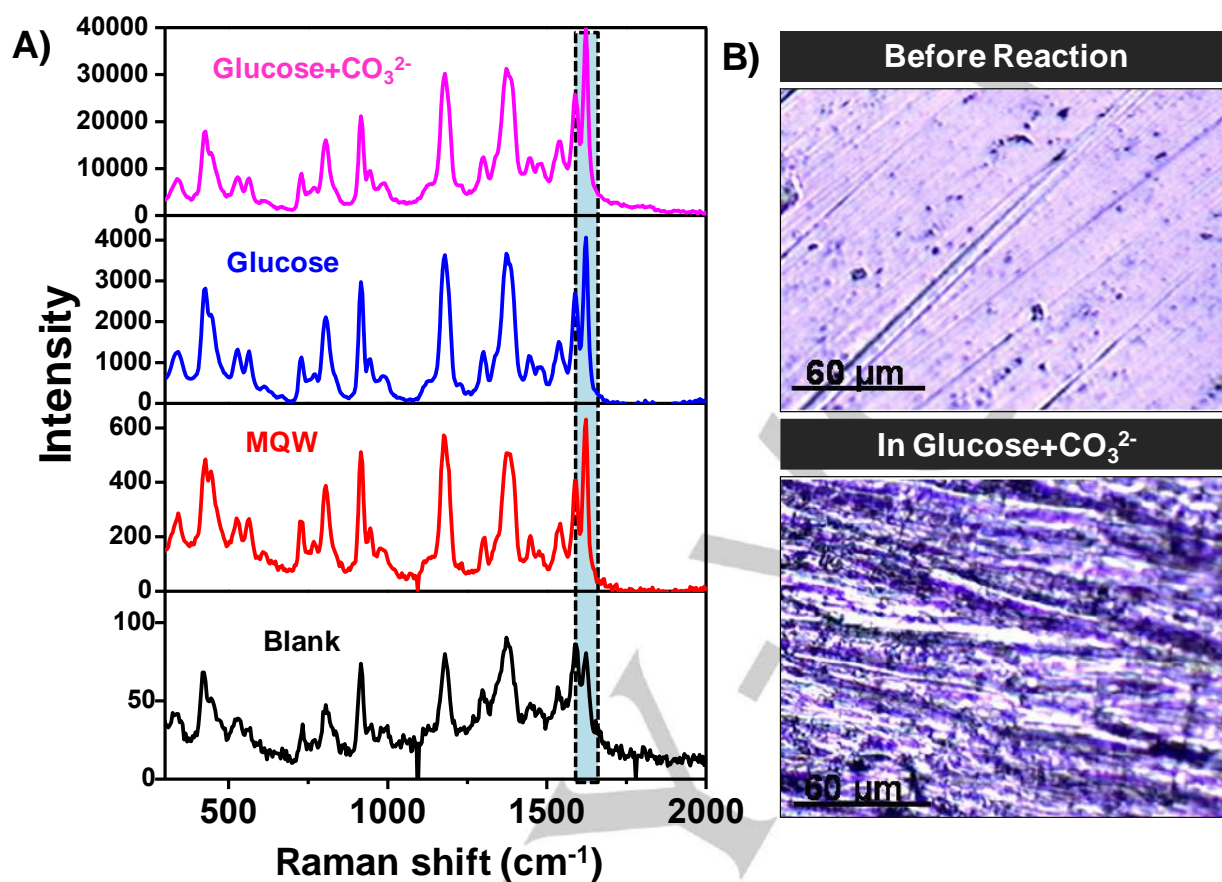


Figure S6. Observation of SERS activity of the reacted Ag foils. Crystal violet (CV) was taken as an analyte at 5×10^{-6} M. A 532 nm laser was used for this study. Note the change in numbers in the y-axis under various conditions. Intensity of the band at 1620 cm^{-1} of CV was used for calculating the enhancement factor (EF). MQW refers to MilliQ water and others correspond to respective species in DIW. B) Optical microscopic images of the silver foil before and after reaction in presence of Glucose and carbonate.

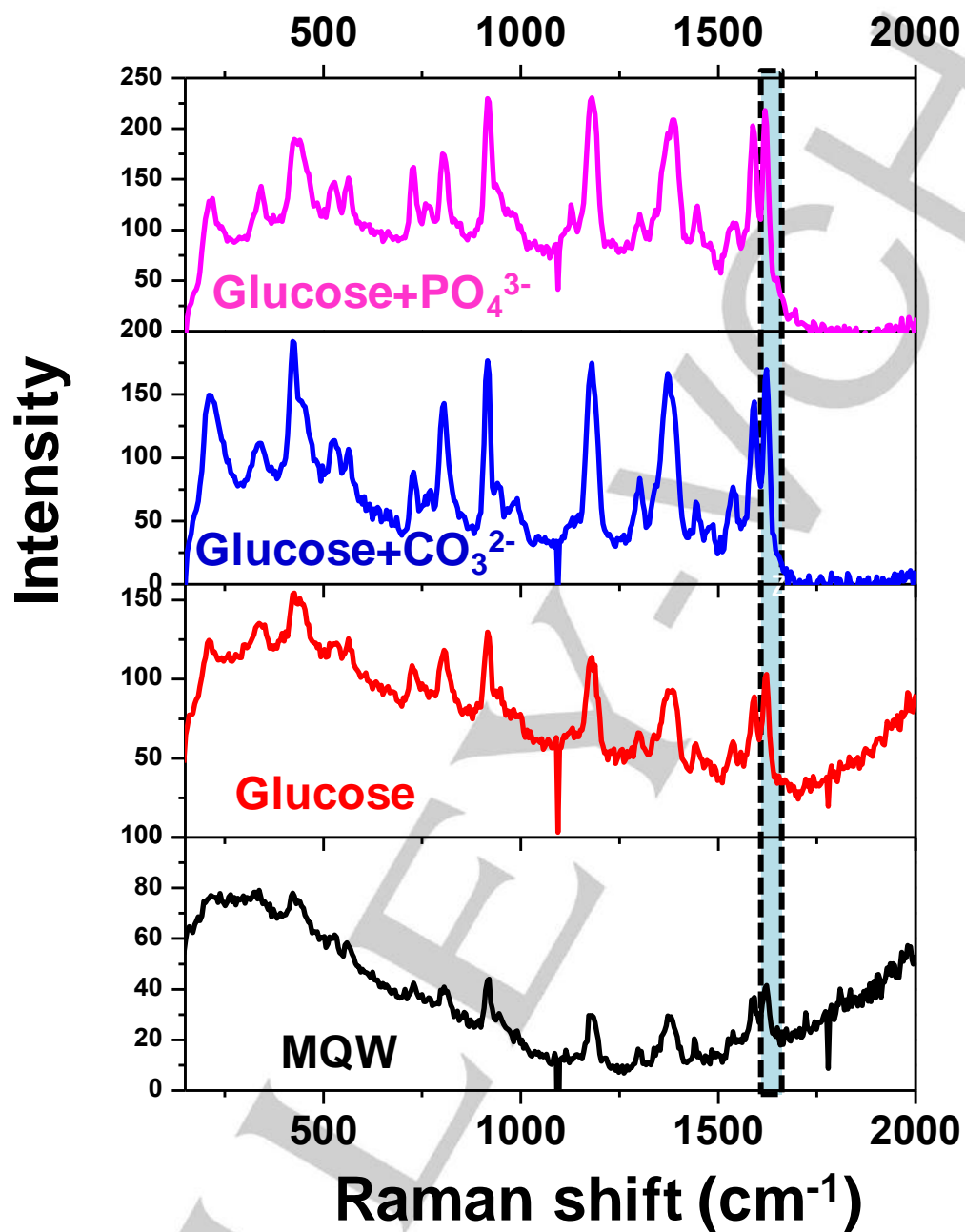


Figure S7. Observation of SERS activity in the reacted Ag foils. Crystal violet (CV) was taken as the probe analyte. Analyte concentration was 5×10^{-7} M. The peak used for SERS calculation is marked.

Compound	Solubility (gm/L)
AgNO ₃	1220 (0°C) 2160 (20°C) 4400 (60°C) 7330 (100°C)
Ag ₂ SO ₄	7.9 (20°C) 13.0 (80°C)
Ag ₂ CO ₃	0.032 K _{sp} = 8.46×10 ⁻¹²
Ag ₃ PO ₄	0.0065 K _{sp} =8.89×10 ⁻¹⁷
AgF	1720
AgCl	0.0019 (20°C) 0.0052 (50°C) K _{sp} =1.77×10 ⁻¹⁰
AgBr	0.00014 (20°C) K _{sp} =5.4×10 ⁻¹³

Table S1: Solubility and solubility product data of different silver salts of relevance.

Substrate	CV conc. (C _{SERS})	Intensity of 1620 cm ⁻¹ peak (I _{SERS})	C _{NR} /I _{NR}	EF
Ag foil as blank	5×10 ⁻⁶	76	6.6×10 ⁻²	9.77×10 ⁵
In MQW	5×10 ⁻⁶	614	6.6×10 ⁻²	8.10×10 ⁶
In MQW	5×10 ⁻⁷	41	6.6×10 ⁻²	5.41×10 ⁶
In Glucose soln.	5×10 ⁻⁶	3906	6.6×10 ⁻²	5.16×10 ⁷
In Glucose soln.	5×10 ⁻⁷	101	6.6×10 ⁻²	1.33×10 ⁷
In Glucose+PO ₄ ³⁻ soln.	5×10 ⁻⁶	828	6.6×10 ⁻²	1.09×10 ⁷
In Glucose+PO ₄ ³⁻ soln.	5×10 ⁻⁷	211	6.6×10 ⁻²	2.78×10 ⁷
In Glucose+CO ₃ ²⁻ soln.	5×10 ⁻⁶	38486	6.6×10 ⁻²	5.08×10 ⁸
In Glucose+CO ₃ ²⁻ soln.	5×10 ⁻⁷	165	6.6×10 ⁻²	2.18×10 ⁷

Table S2. EF at different reaction conditions showing maximum enhancement when the Ag foil was heated in 27.8 mM G solution containing 50 ppm carbonate.


 CrossMark
 click for updates

 Cite this: *RSC Adv.*, 2016, 6, 26679

Atomically precise and monolayer protected iridium clusters in solution†

 Shridevi Bhat,^a Indranath Chakraborty,^{‡a} Tuhina Adit Maark,^{ab} Anuradha Mitra,^c Goutam De^c and Thalappil Pradeep^{*a}

The first atomically precise and monolayer protected iridium cluster in solution, Ir₉(PET)₆ (PET – 2-phenylethanethiol) was synthesized *via* a solid state method. The absence of a plasmonic band at ~350 nm, expected in the UV/Vis spectra for spherical Ir particles of 10 nm size indicated that the synthesized cluster is smaller than this dimension. Small angle X-ray scattering (SAXS) showed that the cluster has a particle size of ~2 nm in solution which was confirmed by transmission electron microscopy (TEM). The blue emission of the cluster is much weaker than many noble metal clusters investigated so far. X-ray photoelectron spectroscopy (XPS) measurements showed that all Ir atoms of the cluster are close to the zero oxidation state. The characteristic S–H vibrational peak of PET at 2560 cm⁻¹ was absent in the FT-IR spectrum of the cluster indicating RS–Ir bond formation. The molecular formula of the cluster, Ir₉(PET)₆ was assigned based on the most significant peak at *m/z* 2553 in the matrix assisted laser desorption ionization mass spectrum (MALDI MS), measured at the threshold laser intensity. Density functional theory calculations on small Ir@SCH₃ and Ir@PET clusters and comparison of the predictions with the IR and ¹H-NMR spectra of Ir₉(PET)₆ suggested that the PET ligands have two distinct structural arrangements and are likely to be present as bridging thiolates –(Ir–SR–Ir)– and singly attached thiolates –(Ir–SR).

 Received 29th December 2015
 Accepted 2nd March 2016

DOI: 10.1039/c5ra27972k

www.rsc.org/advances

1. Introduction

Sub-nanometer sized monolayer-protected clusters (MPCs) or nanoclusters of noble metals exhibiting molecule-like behavior, have gained tremendous importance during the past few years, due to their unique physical and chemical properties and promising applications.¹ Considerable theoretical and experimental developments have been made in this field, enriching our understanding of this new class of materials.² Thiolate-protected noble metal nanoparticles, first synthesized by Brust and Schiffrin in 1994,³ form a major sub-group of these materials. The synthesis of atomically precise clusters in this category can be traced back to the early work of Murray and Whetten, although clusters of the type Au₁₁, Au₁₃ and Au₅₅ were known for quite some time.⁴

Gold and silver MPCs and their alloys have been investigated to a large extent and a number of reports exist on their synthetic methodologies, structure, properties and applications in various fields.^{5–8} Many gold clusters like Au₂₃, Au₂₄, Au₂₅, Au₂₈, Au₃₀, Au₃₆, Au₃₈ and Au₁₀₂ protected by ligands such as phenylethanethiol (PET), mercaptobenzoic acid (MBA), *etc.*, have been crystallized and their structures have been studied by X-ray crystallography.⁵ Apart from these, a number of other gold MPCs have been synthesized and characterized, though their crystal structures are unknown.⁹ In comparison with gold MPCs, the literature on silver MPCs is limited because of their high reactivity.¹⁰ However, several silver MPCs like Ag₇(SR)₇, Ag₈(SR)₈, Ag₉(SR)₇, Ag₃₂(SR)₁₉, Ag₄₄(SeR)₃₀, and Ag₁₅₂(SR)₆₀, *etc.*, have been synthesized and their properties have been studied.^{6,11,12} The crystal structures of silver MPCs like Ag₁₄(SC₆H₃F₂)₁₂(PPh₃)₈ (PPh₃ – triphenylphosphine), Ag₁₆(DPPE)₄(SPhF₂)₁₄ [DPPE – 1,2-bis(diphenylphospheno) ethane], [PPh₄]₂[Ag₃₂(DPPE)₅(SPhCF₃)₂₄], Na₄Ag₄₄(*p*-MBA)₃₀ have been determined.⁵ Recently, Ag₂₅(SR)₁₈ cluster has been crystallized and its structure was determined to be similar to that of Au₂₅(SR)₁₈ cluster.¹³ Some of the alloy clusters like Au₂₄-Hg₁(SR)₁₈,¹⁴ Au₂₄Cd₁(SR)₁₈,¹⁵ *etc.*, have been characterized by single crystal XRD and efforts are on-going to crystallize many more MPCs and obtain their structures using X-ray crystallographic techniques.

Besides Au and Ag MPCs, synthesis of MPCs of metals like Cu, Pt, and Pd is being attempted around the globe using different templates and various preparative methods, but

^aDST Unit of Nanoscience (DST UNS) and Thematic Unit of Excellence, Department of Chemistry, Indian Institute of Technology Madras, Chennai 600036, India. E-mail: pradeep@iitm.ac.in

^bDepartment of Physics, Indian Institute of Technology Madras, Chennai 600036, India

^cCSIR-Central Glass and Ceramic Research Institute, Kolkata 700032, West Bengal, India

† Electronic supplementary information (ESI) available: Details of instrumentation, control experiments and characterization using SAXS, XPS, NMR and XRD and of DFT calculations of Ir₉(PET)₆ cluster. See DOI: 10.1039/c5ra27972k

‡ Current address: University of Illinois at Urbana Champaign, Urbana, IL 61801, USA.

significant success has not been achieved in this regard. For instance, only a few studies are reported on copper MPCs protected by different ligands such as DNA,¹⁶ proteins like bovine serum albumin (BSA),¹⁷ lysozyme,¹⁸ benzotriazolate¹⁹ and thiols.²⁰ Certain luminescent Pt MPCs with capping agents such as dendrimers like poly(amidoamine) (PAMAM),²¹ polymers,²² glutathione²³ and 4-(*tert*-butyl)benzyl mercaptan (BBSH)²⁴ are now known. Some MPCs of Pd^{25,26} have also been synthesized and examined for their catalytic properties. However, relative to Au and Ag MPCs, the number of reports on other noble metal MPCs is very small.

Iridium is one of the noble metals, interesting due to its catalytic and electrocatalytic activities. Its complexes are also well known for their catalytic properties. It is one of the most efficient catalysts for C–C bond hydrogenolysis²⁷ and is also commonly used to facilitate the reduction of imines to the corresponding amines.²⁸

As early as in 1994, Xu *et al.* investigated bare Ir₄ and Ir₆ clusters on porous metal oxide supports for hydrogenation reactions of hydrocarbons and found that the two clusters exhibited different catalytic activities, which were also dissimilar to those of metallic Ir in bulk.²⁹ In 1998, Berko and Solymosi carried out a scanning tunnelling microscopic study of Ir nanoparticles produced on TiO₂(110)-(1 × 2) surface.³⁰ Very high reactivity of supported Ir nanoparticles of size 1–3 nm towards CO was demonstrated by this study; whereas larger nanoparticles of size 8–10 nm did not show this behavior. Through a spectroscopic investigation, Argo *et al.* have shown that the rate of hydrogenation of ethene is several times faster on Ir₄ cluster than on Ir₆ cluster, when these clusters are supported on γ-Al₂O₃.³¹ The authors have also studied hydrogenation of propene and toluene and elucidated the patterns of reactivity as a function of reactant size and structure.³² Ir₆ clusters in zeolite super cages have been imaged directly using aberration corrected scanning electron microscopy by Aydin *et al.*³³ This study was the first example wherein high-dose electron beam was applied to image a metal cluster on a nanoporous material. They have also characterized the catalytic activity of these clusters for ethene hydrogenation reaction.³³ Rueping and co-workers have developed a hydrogenolytic method for the synthesis of Ir nanoparticles supported on carbon nanotubes.²⁸ Kerpál *et al.* used infrared multiple photon dissociation spectroscopic technique to study the adsorption of CO on neutral Ir clusters of size ranging from 3 to 21 atoms.³⁴ Garcia-Cuello *et al.* studied the catalytic activity of Ir nanocatalysts confined in mesoporous silica SBA-15 (Santa Barbara Amorphous type material) in CO oxidation reaction.³⁵

There exist some reports on the synthesis and catalysis of colloidal Ir particles as well. To quote some, Ir nanoparticle synthesis using imidazolium ionic liquid has been tried and the catalytic activity of these nanoparticles in hydrogenation reactions has been reported.^{36,37} Bayram *et al.* studied the *in situ* formation of “weakly ligated/labile ligand” Ir(0) nanoparticles (*i.e.*, nanoparticles where only weakly coordinated ligands and the desired catalytic reagents are present) and their aggregates obtained from commercially available [(1,5-COD)IrCl]₂ at ~2.7 atm H₂ and at ~22 °C and checked their catalytic behavior

in benzene hydrogenation reaction at room temperature and mild pressures.³⁸ Octadecanethiol functionalised Ir nanoparticles of size ranging from 2–4 nm were synthesized by Yee *et al.* using superhydride as reducing agent following one phase synthesis, in THF. The resulting nanoparticles were characterized by TEM (transmission electron microscopy), FT-IR and other techniques.³⁹ Synthesis of Ir nanoparticles by solid-state method⁴⁰ and hydrothermal and solvothermal methods,^{41,42} *etc.*, have been tried by different groups. Most recently, Van-kayala *et al.* have synthesized fluorescent Ir clusters protected by 2,2'-binaphthol and have studied their application in cellular imaging.⁴³ Gavia *et al.* have synthesized dodecanethiolate protected magnetic Ir nanoparticles of size around 1.2 ± 0.3 nm by employing sodium *S*-dodecylthiosulfate as a ligand precursor during modified Brust–Schiffirin reaction.⁴⁴

Although there is large interest in case of supported Ir clusters and their catalytic properties, the research on protected nanoparticles of this metal in solution is still in its infancy. Though there are some efforts on the synthesis of such particles in solution, no report on mass spectrometric characterization of these materials and no suggestion of their atomic compositions exist in the literature. Compared with conventional metallic nanoparticle catalysts, such materials possess several advantages such as well-defined composition, unique electronic properties, *etc.*⁴⁵ Hence, it is important to develop synthetic strategies of such materials and to study their properties.

Herein, we report the solid state synthesis of an Ir cluster with 2-phenylethanethiol (PET) as the protecting agent. The absence of plasmon band at ~350 nm in the UV/Vis spectrum of the Ir@PET indicates the cluster size regime of the particles. The average core size and particle size in solution were determined by TEM and SAXS analysis, respectively. The cluster was characterized by different spectroscopic techniques like X-ray photoelectron spectroscopy (XPS), Fourier-transform infrared (FT-IR) spectroscopy, *etc.* It shows a weak emission in the blue region. The powder X-ray diffraction (XRD) pattern of the cluster also indicated the nano-size regime. This Ir@PET cluster was assigned the composition, Ir₉(PET)₆ based on matrix assisted laser desorption ionization mass spectrometry (MALDI MS). Density functional theory (DFT) calculations were performed on small Ir@SCH₃ and Ir@PET clusters to understand the structure of the cluster. Based on a comparison of computed IR spectra and ¹H NMR chemical shifts of the ligand and model clusters, it is predicted that in the synthesized Ir₉(PET)₆ cluster, the PET ligands are present in two different structural arrangements: some PET are bonded to a single Ir atom and others are shared between two bonded Ir atoms.

2. Experimental section

Chemicals

Iridium(III) chloride hydrate (IrCl₃·xH₂O), 2-phenylethanethiol (PET), sodium borohydride (NaBH₄), *trans*-2-[3-(4-*tert*-butylphenyl)-2-methyl-2-propenylicene malanonitrile (DCTB), 2,5-dihydroxybenzoic acid (DHB) and 2-cyano-4-hydroxy cinnamic acid (CHCA) were purchased from Sigma Aldrich.

Toluene, tetrahydrofuran (THF), dichloromethane (DCM) and methanol were purchased from Rankem.

Synthesis of Ir₉(PET)₆

The Ir₉(PET)₆ cluster was synthesized using a solid-state route.¹⁰ This method involved three steps. In the first step, IrCl₃·xH₂O and PET (in 1 : 4 molar ratio) were mixed together by grinding in a mortar and pestle for about 10–15 minutes until the mixture turned yellow, indicating the formation of Ir–PET thiolates. Then these thiolates were reduced by adding NaBH₄ powder (1 : 24 molar ratio of salt : reducing agent) and grinding until the mixture turned black, in ambient atmosphere. Finally, the so formed cluster was extracted in toluene. To remove excess thiolates and thiol in the mixture, first the mixture was washed with water. Then toluene was evaporated by vacuum drying in a rotavapor and the cluster was precipitated by adding excess methanol. Following centrifugation, the supernatant solution containing the soluble thiolates and thiol was discarded, leaving behind the purified precipitate. The precipitated cluster could be re-dispersed in toluene, THF or DCM.

3. Computational details

In this work we have considered small clusters of the type: Ir₂(SCH₃), Ir₃(SCH₃)₂, Ir₂(PET)₁ and Ir₃(PET)₁ as model systems. Several structural isomers of these systems were generated and studied. The geometries of all the structures were optimized using density functional theory (DFT) as implemented in the Gaussian 09 program package.⁴⁶ In ref. 47 the Perdew–Burke–Ernzerhof (PBE) exchange–correlation functional has been shown to perform as well as B3LYP and B3PW91 functionals to yield bond lengths and vibrational frequencies for Ir₂ and Pd₂ dimers in good agreement with experiments. PBE has also been successfully applied to study Ir and its alloy clusters previously.^{48–50} Therefore, we chose to use the PBE functional in this study. The QZVP basis set was fitted to the charge density *via* the W06 fitting set of Ahlrichs and co-workers, to enhance the performance of pure DFT calculations.^{51,52} The following convergence criteria were adopted for the geometry optimizations: 10^{−7} a.u. for energy, 10^{−7} a.u. for electron density, 0.00045 a.u. for force and 0.0018 a.u. for atomic displacement. Frequency calculations were carried out for all the clusters to prove that the resulting stationary points were real energy minima, without imaginary frequencies in their vibration spectra. The atomic charges of Ir@PET and Ir@SCH₃ clusters were derived using APT (Atomic Polar Tensors)⁵³ and Mulliken population analyses schemes, respectively. The infra-red (IR) spectra and molecular structures were generated using the visualization program, MOLGEN.⁵⁴ The NMR chemical shifts were calculated with tetramethylsilane (TMS) as reference from the magnetic shielding tensors computed with the IGAIM^{55,56} method available with Gaussian 09.

4. Results and discussion

Preliminary control experiments were performed to determine the best conditions for the synthesis of Ir₉(PET)₆ cluster. For

this purpose, salt : thiol ratio was varied from 1 : 2 to 1 : 4 to 1 : 6. As described in the Experimental section, in each case, the product formed was first extracted in toluene. The UV/Vis spectra and the photographs of these samples (in toluene) are shown in the ESI Fig. S2.† The molar ratio of 1 : 4 yielded Ir₉(PET)₆ cluster with an intense color and it had absorption features different from other two compositions. Therefore, this ratio was chosen to be used in all further synthesis.

After methanol precipitation and purification, the cluster was found to be dispersible in toluene, THF, chloroform (CHCl₃) and DCM (CH₂Cl₂). The cluster solution in THF was greenish brown in color, as can be seen in the photograph shown in inset (i) of Fig. 1a. Inset (iii) of Fig. 1a depicts a schematic representation of the cluster. The UV/Vis spectrum of the cluster in THF is presented in Fig. 1a (red trace). It is noticeable from the figure that the onset of absorption starts around 600 nm and the spectrum has small humps, indicated by the arrows, at approximately 500 nm and 305 nm. Based on reported theoretical calculations, the plasmonic band of spherical Ir particles of 10 nm size lies at ~350 nm.⁵⁷ The absence of any plasmonic peak at this position in the UV/Vis absorption spectrum is an evidence for cluster formation. In a control experiment, the synthesis was stopped on completion of the first step, *i.e.*, after grinding the precursor salt with thiol until yellow color was achieved, no further reduction with NaBH₄ was carried out and the formed thiolates were extracted in ethanol. The photograph of solution of Ir–PET thiolates in ethanol is shown in inset (ii) of Fig. 1a. The UV/Vis spectrum of extracted thiolates was measured and compared with that of the cluster (see Fig. 1a, black trace). Interestingly, unlike the cluster, the thiolates exhibited a sharp peak around 350 nm.

Photoluminescence of Ir₉(PET)₆ was also analysed. In Fig. 1b the black trace corresponds to its excitation spectrum which shows a peak at 370 nm. The emission spectrum of the cluster when excited at 370 nm is shown as the red trace in Fig. 1b. The cluster shows emission in the blue region with peaks at 404, 432 and 460 nm. Emission features with distinct structures are reminiscent of molecular systems. These emission features are however, different from the starting materials or thiolates. Inset in the figure shows photographs of the cluster under visible (left) and UV (right) irradiation. A faint blue emission is evident in these photographs as well.

Fig. 2a shows the TEM image of the Ir₉(PET)₆ cluster. It was obtained by drop casting a THF solution of the cluster on a carbon-coated copper grid and drying in air. As can be seen from the particle size distribution curve, shown as inset (ii) in Fig. 2a, average size of the particles is approximately 1.6 nm, although many clusters aggregated upon electron beam irradiation. The particle size distribution of the cluster solution was further investigated through transmission SAXS using ‘sphere’ and ‘core–shell’ models considering the spherical nature of the particles. In the latter case, the PET ligands were considered as shell and the metal cluster as core (see ESI†).^{58,59} The size distribution curves and the corresponding fitted SAXS profiles obtained from ‘sphere’ and ‘core–shell’ models have been shown in Fig. S1† and 2b, respectively. Both the models yielded good fittings (low residual factor) and the detailed SAXS

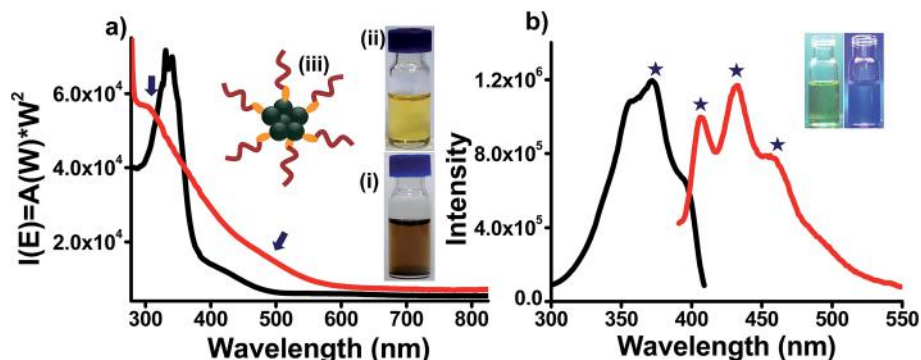


Fig. 1 (a) UV/Vis spectra of the $\text{Ir}_9(\text{PET})_6$ in THF (red trace) and Ir-PET thiolates in ethanol (black trace). Inset shows (i) photograph of the THF solution of the cluster having greenish brown color and (ii) photograph of Ir-PET thiolates in ethanol having yellow color and (iii) is a schematic representation of the cluster (color codes: tan – Ir, orange – S and dark red – hydrocarbon chain of the thiol, in this case the phenylethyl groups), (b) photoluminescence data of the cluster. Black trace shows the excitation spectrum and red trace corresponds to the emission spectrum (excited at 370 nm) showing peaks at 404, 432 and 460 nm as indicated by asterisks. Inset shows the photographs of the cluster under visible (left) and UV (right) irradiation.

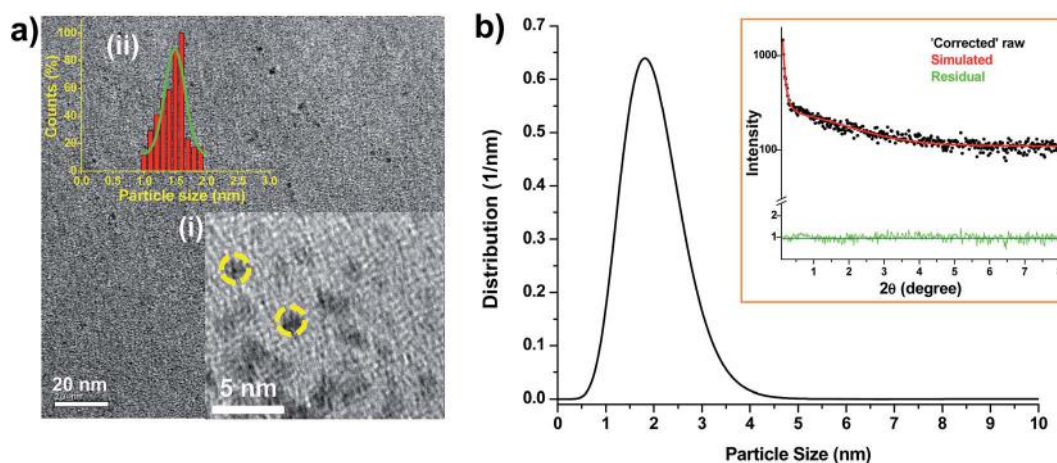


Fig. 2 (a) TEM image of $\text{Ir}_9(\text{PET})_6$ obtained by drop casting THF solution of the cluster on a carbon-coated copper grid. A higher magnification image is shown as inset (i). Two of the particles are circled. While the point resolution of the HRTEM was 0.12 nm, no lattice features were seen in the sample as expected. Many of the particles aggregate upon continuous irradiation and so only some of them present a true picture of the sample. Inset (ii) shows the particle size distribution obtained by counting the sizes of 50 particles manually by expanding the image. (b) Particle size distribution of the cluster obtained by SAXS analysis. The inset shows the corrected raw, simulated and residual patterns fitted by 'core-shell' model.

parameters have been given in Table S1 (see ESI[†]). Core-shell model reveals an average Ir core size of ~ 1.6 nm and particle size of ~ 2 nm, which agrees well with the result from the sphere model (~ 1.99 nm). Thus both TEM and SAXS confirmed the cluster size regime (< 2 nm) of the particles.

The elemental characteristics of the cluster were determined by XPS. The survey spectrum is shown in Fig. S3 (see ESI[†]). As expected, Ir, S, O and C were detected. The oxidation state of Ir was confirmed to be close to 0 by the positions of the $\text{Ir}4f_{7/2}$ and $\text{Ir}4f_{5/2}$ peaks. A comparison of positions of these two peaks in $\text{Ir}_9(\text{PET})_6$ and IrCl_3 is shown in Fig. 3a. The shift of $\text{Ir}4f_{7/2}$ and $\text{Ir}4f_{5/2}$ peaks to lower binding energies, 60.97 eV and 63.90 eV, respectively, as compared to 62.75 eV and 65.72 eV in IrCl_3 is due to the reduction of Ir from +3 to 0 oxidation state. Typical values of $\text{Ir}4f_{7/2}$ and $\text{Ir}4f_{5/2}$ are 60.90 eV and 63.88 eV,

respectively, for the metal. The Ir^{3+} positions are marked by dotted lines in the figure.

The cluster was also characterized by FT-IR spectroscopy. Comparison of the FT-IR spectra of the cluster and the free thiol is shown in Fig. 3b, which revealed that the S-H bond stretching in PET at 2560 cm^{-1} was absent in $\text{Ir}_9(\text{PET})_6$. This indicates the loss of thiolate proton and RS-Ir bond formation in the cluster.

The cluster was also characterized by ^1H NMR spectroscopy. The NMR spectra of $\text{Ir}_9(\text{PET})_6$ (red trace) and free thiol (black trace) along with schematic structure of the cluster and the structure of PET molecule are shown in Fig. 4. The peaks corresponding to two $-\text{CH}_2$ protons of PET anchored on the cluster surface have been severely broadened and shifted to lower ppm values as compared to the free thiol. Also $-\text{CH}_2$ protons (1) near to the cluster core are expected to be more

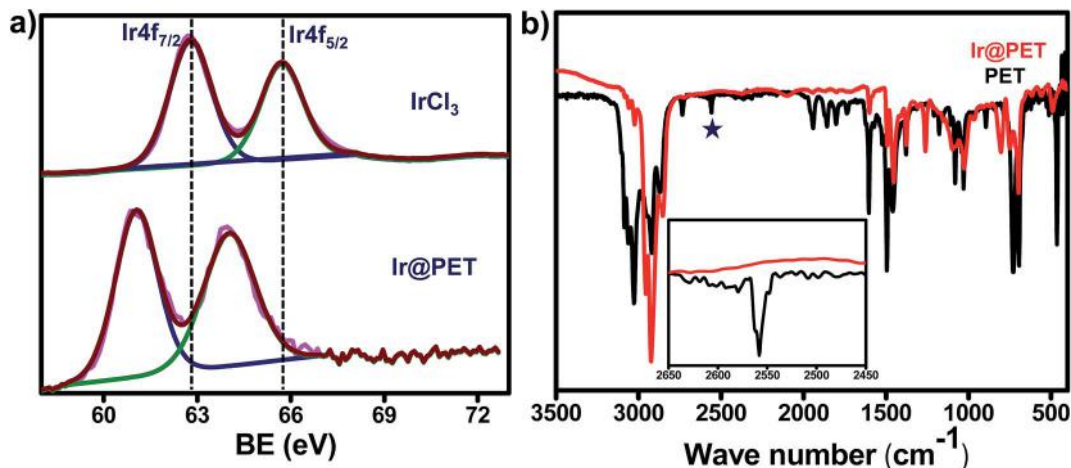


Fig. 3 (a) XPS data showing Ir4f_{7/2} and Ir4f_{5/2} peaks of Ir₉(PET)₆ compared with that of IrCl₃, (b) IR spectra of Ir₉(PET)₆ (red trace) and free PET (black trace). The peak highlighted by asterisk corresponds to S–H stretching frequency of free thiol. The S–H stretching region of the two traces is expanded separately in the inset.

effected than the other –CH₂ protons (2). This is expected due to the non-uniform distribution of the ligands on metal surface.^{4,60,61} Based on these facts, a tentative assignment of the features is indicated. A proper assignment of all the peaks is not possible at this stage due to unavailability of the structure of the cluster. The lower ppm region of the spectra is expanded in ESI, Fig. S4.†

In ESI Fig. S5,† powder XRD pattern of Ir₉(PET)₆ is shown which was measured by drop casting a THF solution of the sample on a glass substrate and drying it, over and over again so as to form a thick layer. This showed weak and broad signals corresponding to (111) and (220) planes of Ir. The broad peaks are an indication of the nano size regime of the particles.

Dass *et al.* have revealed through their study of MALDI TOF mass spectrometry of Au₂₅(SR)₁₈ cluster that the choice of the matrix plays an important role in getting intact molecular ion

peaks without fragmentation.⁶² Since this cluster is a new system, we performed MALDI MS measurements using various commonly used matrices like *trans*-2-[3-(4-*tert*-butylphenyl)-2-methyl-2-propenylidene malanonitrile (DCTB), 2,5-dihydroxybenzoic acid (DHB), sinapinic acid (SA) and 2-cyano-4-hydroxy cinnamic acid (CHCA). The mass spectra (Fig. S6, ESI†) obtained using DCTB and CHCA contained a bunch of peaks due to fragmentation and it was difficult to obtain any information on the cluster composition using them. In contrast, the mass spectrum using the SA did not yield any peak. Only DHB gave a good mass spectrum with well-defined peaks and was therefore chosen for the further analysis. This is unlike the case of Au and Ag clusters where DCTB is usually used as a matrix for MALDI MS analysis and is known to give good results.

Fig. 5 shows the MALDI MS results of the cluster measured in the linear positive mode using the DHB matrix. The highest intensity molecular ion peak can be assigned to the [Ir₉(PET)₆]⁺ ion. The observed spectrum for [Ir₉(PET)₆]⁺ is in good agreement with the calculated spectrum as shown in inset (i) of Fig. 5 and S7 in ESI.† The peak with the next highest intensity is assigned to [Ir₈(PET)₄]⁺ species. To check whether it is a fragment obtained due to laser during measurement or indeed present in the solution, a laser intensity dependent MALDI MS study was performed. These spectra measured in the linear positive mode are shown as inset (iii) of Fig. 5. The [Ir₈(PET)₄]⁺ peak was not present at the lowest laser energy where the molecular ion peak was observed. But with increase in laser power, both the peaks increase in intensity linearly. Hence, we conclude that this species is not a fragment.

The stability of the cluster solution in THF was checked by time dependent UV/Vis spectra measurement. For this purpose two set of cluster solutions in THF were synthesized. One sample was stored in fridge (at ~4 °C) and another at room temperature. UV/Vis spectra of both the samples were recorded each day up to a time period of 7 days which are shown in Fig. S8 (in ESI).† We observed no change in UV/Vis spectrum of sample stored in fridge up to 7 days confirming it is stable over this

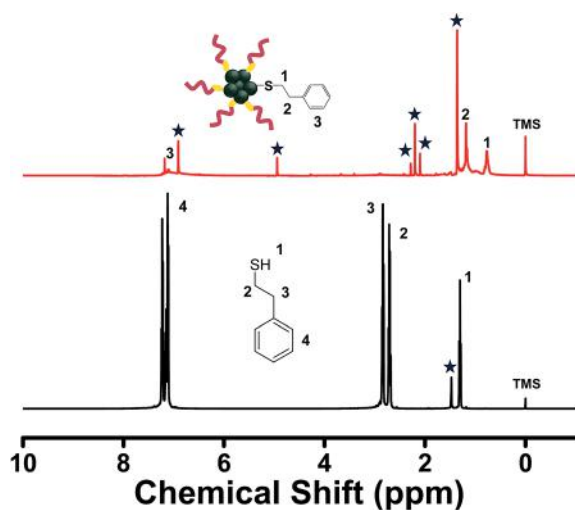


Fig. 4 NMR spectra of Ir₉(PET)₆ (red trace) and free PET (black trace) measured in CDCl₃. The schematic structure of the cluster and the structure of PET are shown. The assignments are indicated. The label * indicate unassigned features.

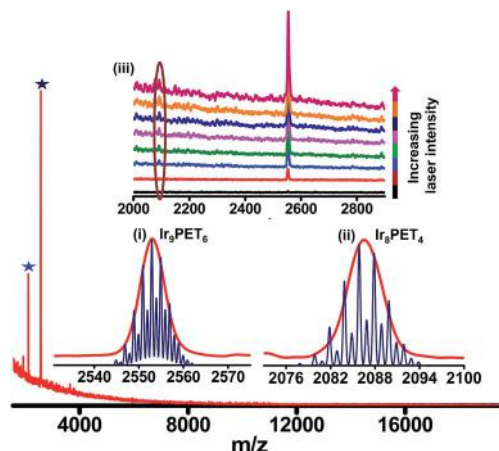


Fig. 5 MALDI MS of the cluster measured in the linear positive mode using DHB as the matrix. The highest intensity peak (highlighted by navy blue asterisk) is assigned to $\text{Ir}_9(\text{PET})_6$. Inset (i) shows the observed (red trace) and calculated (blue trace) spectra of $[\text{Ir}_9(\text{PET})_6]^+$ species. The next highest intensity peak (highlighted by blue asterisk) is assigned to $\text{Ir}_8(\text{PET})_4$ and its observed (red trace) and calculated (blue trace) spectra are shown in inset (ii). Inset (iii) shows the laser intensity dependent MALDI MS of the cluster measured in linear positive mode. The increasing order of laser energy used to measure each spectrum is indicated on the right side.

period. Whereas sample stored at room temperature was stable up to 2 days.

The aim of our DFT computations is to use simple model systems to develop an insight on how the ligands may prefer to arrange in the comparatively larger $\text{Ir}_9(\text{PET})_6$ cluster. In order to take into account ligand–ligand interactions, we first examined several structural isomers of $\text{Ir}_3(\text{SCH}_3)_2$. These are displayed in Fig. 6 along with their relative energies. The three most stable isomers are (d), (i) and (b). In (d) the three Ir atoms are bonded to form a triangle and both the SCH_3 ligands are shared between two Ir atoms. In (i) the three Ir atoms are bonded to form a triangle, one SCH_3 ligand is shared between two Ir atoms while the second ligand is singly attached. In (b) one pair of Ir atoms is non-bonded with one SCH_3 ligand shared between them and the second SCH_3 ligand is singly attached to the third Ir atom. The most unfavourable isomer is (a) comprising of two pairs of non-bonded Ir atoms, with each pair sharing a ligand between them in a ring-like fashion. The relative energies of isomers (d), (i) and (b) are within 0–0.05 eV and of the other structures are >0.13 eV. Thus, we expect Ir–PET–Ir arrangements in the $\text{Ir}_9(\text{PET})_6$ cluster of the form in isomers (d), (i) or (b). However, such structural differences would be reflected in their IR and NMR spectra, which can then be used as identifying features. IR and NMR spectroscopies have been used as important techniques to understand structure and chemical composition of MPC monolayers.⁴ DFT calculations of IR spectra of bare clusters of Ir^{63} and NMR chemical shifts for certain Ir complexes⁶⁴ are also known.

The position of the S–C vibrational peak for each structural isomer of $\text{Ir}_3(\text{SCH}_3)_2$ obtained from DFT calculated IR spectra are also shown in Fig. 6. It is noticeable that if all the ligands were structurally equivalent, then only a single peak for the S–C

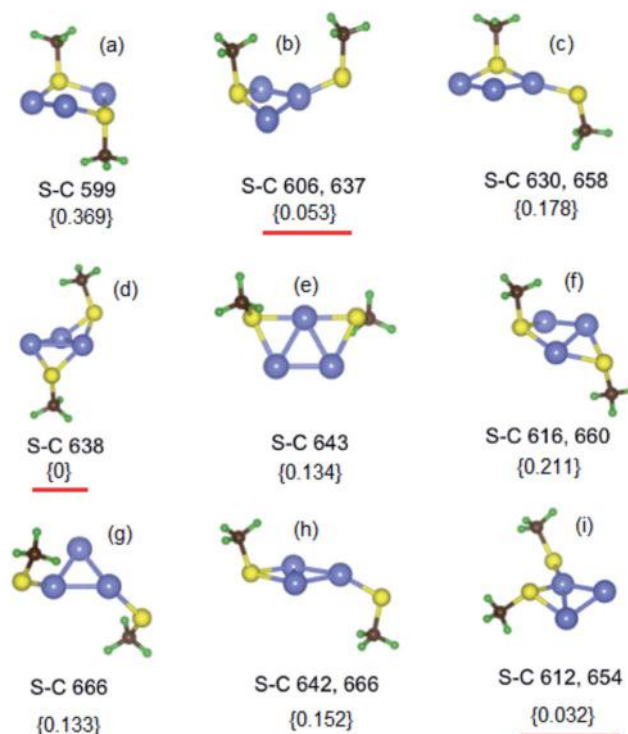


Fig. 6 Optimized geometries of structural isomers of (a–i) $\text{Ir}_3(\text{SCH}_3)_2$. H, C, S and Ir atoms are represented as green, brown, yellow and purple spheres. The relative energies (in eV) of the structural isomers are given in {}. The three most stable isomers are highlighted by red lines. The calculated S–C vibrational frequencies (cm^{-1}) are also listed for each isomer.

vibration would appear, as in case of isomers (a), (d), (g) and (e). When SCH_3 ligands are present in two types of arrangements, then depending upon their nearness, which determines the ligand–ligand interaction, the effect on the S–C peak is different. Isomers (b) and (g) where the two SCH_3 ligands are separated by an Ir–Ir bond, the two S–C peaks are seen at similar positions in the isomers with equivalent ligands. For instance, in isomers (3) and (g), the S–C peak occurs at 643 and 666 cm^{-1} , respectively and in isomer (h) two peaks are observed at 642 and 666 cm^{-1} . But if the two ligands share an Ir atom, then one of the S–C peaks is strongly shifted as in the case of isomers (c), (f) and (i). Elaborating the S–C peaks which are seen at ~ 640 cm^{-1} for isomers (d) and (e) and at 666 cm^{-1} for isomer (g) are shifted to 612 and 654 cm^{-1} for isomer (i). Overall, irrespective of the ligand–ligand interaction strength, if the ligands are differently arranged, then two distinct S–C peaks arise with a separation of ~ 25 – 40 cm^{-1} .

Fig. 7 illustrates the DFT calculated IR spectra of the three structural isomers (j)–(l) of $\text{Ir}_3(\text{PET})_1$. The relative energies exhibit that the most stable structure is (l) in which the PET ligand is shared between bonded Ir atoms. The most unfavored geometry is (j) in which the PET ligand is shared between two non-bonded Ir atoms. Depending on whether the PET ligand is shared between bonded Ir atoms (isomer l), or singly attached to an Ir atom (isomer k), the position of the S–C vibrational peak is

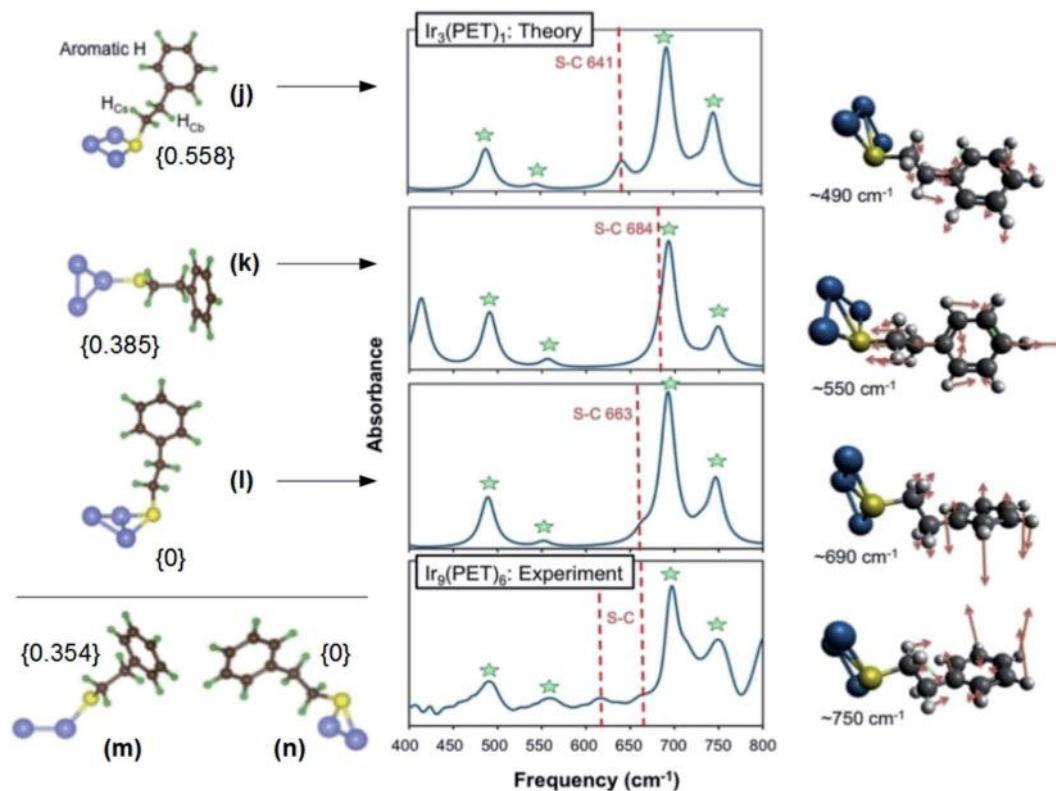


Fig. 7 Geometries of the structural isomers of $\text{Ir}_3(\text{PET})_1$ (j–l) and $\text{Ir}_2(\text{PET})_1$ (m and n) are depicted in the first column. The relative energies (in eV) are given in {}. In the second column theoretically (DFT) computed IR spectra (top three panels) of isomers (j–l) are compared with the experimental IR spectrum of $\text{Ir}_9(\text{PET})_6$ (bottom panel). The common features exhibited are highlighted as stars and the corresponding vibrational modes are shown in the third column for isomer (j). The red arrows are the force vectors on the atoms participating in the vibration.

distinct and is found at 641, 663 and 684 cm^{-1} , respectively. The same order of appearance of the S–C peak is observed for the $\text{Ir}_3(\text{SCH}_3)_2$ isomers (a) (599 cm^{-1}), (d) (640 cm^{-1}) and (g) (666 cm^{-1}) (see Fig. 6). The experimentally obtained IR spectrum of $\text{Ir}_9(\text{PET})_6$, expanded in the 400–800 cm^{-1} region is also presented in Fig. 7. It exhibits several peaks (marked as stars) in common for all the model clusters. This remarkable correlation suggests that spectra computed in other regions may be true representations of the structure.

These common features are assigned to the vibrational modes also displayed in the figure for the specific case of isomer (j) of $\text{Ir}_3(\text{PET})_1$. Most importantly, two clear peaks at ~ 620 and 660 cm^{-1} are observed, suggesting that there are two different arrangements of the PET ligands in the structure of $\text{Ir}_9(\text{PET})_6$. Based on the variation of S–C vibrational peaks for $\text{Ir}_3(\text{SCH}_3)_2$ isomers in Fig. 6, we believe that the structural arrangement of the ligands in the synthesized $\text{Ir}_9(\text{PET})_6$ cluster may be similar to that in isomer (i) in which both the peaks are shifted to relatively lower frequencies than isomers (d) and (g).

^1H NMR chemical shifts (δ) are highly affected by the chemical environment. We present the calculated atomic charges over selected $\text{Ir}_3(\text{SCH}_3)_2$ structural isomers in Table 1. Recalling from Fig. 6, the two SCH_3 ligands are symmetrically arranged in isomers (a), (d) and (g). Consequently the charges on each pair of S and C atoms are calculated to be the same within these isomers as opposed to isomers (b) and (f) in which

the two ligands are inequivalent. Therefore, we would expect to see shifting of each of the two CH_2 proton peaks to two specific positions in the experimental ^1H NMR spectrum of the $\text{Ir}_9(\text{PET})_6$ cluster relative to PET. However, this is not the case and several peaks are found in Fig. 4 and ESI, Fig. S4† which are downshifted to lower δ values. This suggests that all the ligands in the synthesized cluster are not structurally and therefore, chemically equivalent.

In this work we have chosen to compute the δ values (in ppm) of PET ligand, $\text{Ir}_2(\text{PET})_1$ and $\text{Ir}_3(\text{PET})_1$ clusters instead of Ir– SCH_3 clusters. These are also listed in Table 1 along with the ^1H NMR chemical shifts of the PET ligand and the cluster from experiments. As discussed earlier and can be noticed from the table, experimentally the δ s of H atoms (H_{C_b} and H_{C_s}) belonging to the benzylic C atom (C_b) and C atom near S (C_s) move to lower values relative to the PET ligand on cluster formation. The C and H atoms are referred by the labelling shown in isomer (j) in Fig. 7. Our primary objectives are to (i) determine whether such trends are reflected in the abovementioned model cluster systems that we have considered herein and (ii) develop an understanding of the changes in electronic structure leading to these shifts.

Table 1 shows that for certain geometrical arrangements of the clusters (isomers (m), (j) and (l) in Fig. 7) a decrease in δ is predicted relative to the PET ligand in agreement with the experiments. To explain the NMR chemical shift trends we

Table 1 ^1H NMR chemical shifts (in ppm) of aromatic H atoms, H atoms in benzylic CH_2 (H_{C_b}) and H atoms in CH_2 bonded to S (H_{C_s}) in PET and Ir@PET clusters from DFT calculations and experiments. Atomic charges over benzylic C (C_b), C bonded to S (C_s), S, and Ir atoms in Ir@PET (Fig. 7) and Ir@SCH₃ (Fig. 6) clusters depicted in Fig. 7 are also listed. The above mentioned labelling of atoms can be seen in Fig. 7

Method	System	Chemical shift (ppm)			
		Aromatic H	H_{C_b}	H_{C_s}	SH
Calculation	PET	7.63–7.64	3.04	3.14	2.37
	$\text{Ir}_2(\text{PET})_1$ (iso. (m))	7.47–7.73	2.61, 2.93	0.76, 1.88	
	$\text{Ir}_2(\text{PET})_1$ (iso. (n))	7.52–7.85	2.94, 3.74	3.73, 4.19	
	$\text{Ir}_3(\text{PET})_1$ (iso. (j))	7.52–7.90	1.96, 5.65	3.97, 9.18	
	$\text{Ir}_3(\text{PET})_1$ (iso. (k))	7.48–7.56	3.95	3.10	
	$\text{Ir}_3(\text{PET})_1$ (iso. (l))	7.24–7.62	1.90, 3.03	2.62, 3.23	
Experiment	PET	7.11–7.24	2.82–2.86	2.73–2.66	1.29–1.32
	$\text{Ir}_9(\text{PET})_6$	6.91–7.23	2.09–2.28	0.76–1.36	

System	Isomer	Atomic charges (e) ^a					
		C_b	C_s	S	Ir_1	Ir_2	Ir_3
PET		0.07	0.18	−0.15			
$\text{Ir}_2(\text{PET})_1$	Iso. (m)	0.10	0.11	−0.20	0.16	−0.06	
	Iso. (n)	0.04	0.00	0.27	−0.15	−0.13	
$\text{Ir}_3(\text{PET})_1$	Iso. (j)	0.03	−0.03	0.12	−0.17	−0.14	0.19
	Iso. (k)	0.11	0.18	−0.30	0.14	−0.01	−0.01
	Iso. (l)	0.05	0.07	0.03	0.00	0.02	−0.14
$\text{Ir}_3(\text{SCH}_3)_2$	Iso. (a)		−0.15, −0.15	−0.16, −0.16	0.03	0.03	0.03
	Iso. (d)		−0.12, −0.12	−0.32, −0.32	0.23	0.04	0.08
	Iso. (g)		−0.15, −0.15	−0.24, −0.24	0.12	0.12	−0.05
	Iso. (b)		−0.15, −0.18	−0.16, −0.25	0.03	0.03	0.12

^a Atomic charges over PET and Ir@PET clusters are calculated from APT analysis and atomic charges over Ir@SCH₃ clusters are from Mulliken population analysis scheme.

analysed the atomic charges which are also listed in Table 1. In PET ligand and the clusters, the aromatic H atoms are the least shielded from the magnetic field and so are found at significantly large δ values (~ 7 ppm). In comparison the S atom in PET is electronegative with $-0.15e$ charge and its high electron density shields the H atom (directly bonded to it) from the magnetic field and consequently the proton exhibits a low δ value. C_b and C_s are positively charged ($\text{C}_b < \text{C}_s$) and so the corresponding H_{C_b} and H_{C_s} exhibit medium chemical shifts ~ 3 ppm ($\text{H}_{\text{C}_b} < \text{H}_{\text{C}_s}$).

In isomer (m) of $\text{Ir}_2(\text{PET})_1$, in which PET is singly attached, charge transfer from the Ir atoms makes S more negative. However, the magnitude of net charge on S available for interaction with C_s is reduced. Consequently, the positive charge on C_s is also reduced and a decrease in δ of H_{C_s} atom occurs. In contrast the positive charge on C_b is increased and while we expect δ of H_{C_s} to increase, a slight decrease is predicted from the calculations. In the analogous isomer (k) of $\text{Ir}_3(\text{PET})_1$ the positive charge on C_s is unchanged and on C_b is slightly increased compared to in PET. As a result δ of H_{C_s} and H_{C_b} is similar and increased, respectively with respect to PET. It is interesting to note that though in both isomers (m) and (k) the ligand is singly attached, the former exhibits chemical shifts in better agreement with experiments. We speculate that this could be due to more effective shielding of the magnetic field by the increased charge density over S atom in isomer (m) than in

isomer (k). In isomer (n) of $\text{Ir}_2(\text{PET})_1$ the scenario is opposite: the atomic charge of S becomes positive ($+0.27e$) and it supercedes the increase in electron density over the C atoms, such that the CH_2 protons exhibit an increased chemical shift with respect to in PET. Comparatively, in isomer (l) of $\text{Ir}_3(\text{PET})_1$ the S atom has a small positive charge and the positive charges over C_s and C_b are reduced (*vs.* PET) implying an increased electron density which shields the attached H_s and decreases their chemical shifts. The S atom in isomer (j) of $\text{Ir}_3(\text{PET})_1$ has a reasonable positive charge (0.12) and only one of the H_{C_b} atoms exhibits a decreased chemical shifts while the other H_{C_b} and H_{C_s} protons show significantly increased δ which is not observed in the experimental NMR. Thus, we believe that in $\text{Ir}_9(\text{PET})_6$, some PET ligands are attached to a single Ir atom and others are shared by a pair of bonded Ir atoms.

5. Conclusion and summary

In summary, we report an atomically precise Ir cluster protected by 2-phenylethanethiol ligand, which was synthesized following a solid state synthetic protocol and whose composition was determined based on MALDI MS studies. Characterization using various other techniques also supports its formation. Comparison of experimental spectroscopic data with the theoretical predictions suggests two types of ligands, one directly linking the metal and another bridging the metal, in the

structure. Efforts are on-going to crystallize the cluster which will give further insight into its structure. We believe that this cluster may find important applications in catalysis and this report may encourage further investigations in the area of protected Ir clusters.

Acknowledgements

We thank the Department of Science and Technology, Government of India for constantly supporting our research program on nanomaterials. S. B. thanks IIT Madras for research fellowship. I. C. thanks IIT Madras for his institute postdoctoral fellowship. T. A. M. acknowledges IIT Madras for her Institute Postdoctoral Fellowship.

References

- 1 Y. Lu and W. Chen, *Chem. Soc. Rev.*, 2012, **41**, 3594–3623.
- 2 J. P. Wilcoxon and B. L. Abrams, *Chem. Soc. Rev.*, 2006, **35**, 1162–1194.
- 3 M. Brust, M. Walker, D. Bethell, D. J. Schiffrin and R. Whyman, *J. Chem. Soc., Chem. Commun.*, 1994, 801–802, DOI: 10.1039/c39940000801.
- 4 A. C. Templeton, W. P. Wuelfing and R. W. Murray, *Acc. Chem. Res.*, 2000, **33**, 27–36.
- 5 A. Mathew and T. Pradeep, *Part. Part. Syst. Charact.*, 2014, **31**, 1017–1053.
- 6 T. Udayabhaskararao and T. Pradeep, *J. Phys. Chem. Lett.*, 2013, **4**, 1553–1564.
- 7 R. Jin, *Nanoscale*, 2010, **2**, 343–362.
- 8 H. Qian, M. Zhu, Z. Wu and R. Jin, *Acc. Chem. Res.*, 2012, **45**, 1470–1479.
- 9 P. Maity, S. Xie, M. Yamauchi and T. Tsukuda, *Nanoscale*, 2012, **4**, 4027–4037.
- 10 T. U. B. Rao, B. Nataraju and T. Pradeep, *J. Am. Chem. Soc.*, 2010, **132**, 16304–16307.
- 11 I. Chakraborty, W. Kurashige, K. Kanehira, L. Gell, H. Hakkinen, Y. Negishi and T. Pradeep, *J. Phys. Chem. Lett.*, 2013, **4**, 3351–3355.
- 12 I. Chakraborty, A. Govindarajan, J. Erusappan, A. Ghosh, T. Pradeep, B. Yoon, R. L. Whetten and U. Landman, *Nano Lett.*, 2012, **12**, 5861–5866.
- 13 C. P. Joshi, M. S. Bootharaju, M. J. Alhilaly and O. M. Bakr, *J. Am. Chem. Soc.*, 2015, **137**, 11578–11581.
- 14 L. Liao, S. Zhou, Y. Dai, L. Liu, C. Yao, C. Fu, J. Yang and Z. Wu, *J. Am. Chem. Soc.*, 2015, **137**, 9511–9514.
- 15 S. Wang, Y. Song, S. Jin, X. Liu, J. Zhang, Y. Pei, X. Meng, M. Chen, P. Li and M. Zhu, *J. Am. Chem. Soc.*, 2015, **137**, 4018–4021.
- 16 X. Jia, J. Li, L. Han, J. Ren, X. Yang and E. Wang, *ACS Nano*, 2012, **6**, 3311–3317.
- 17 N. Goswami, A. Giri, M. S. Bootharaju, P. L. Xavier, T. Pradeep and S. K. Pal, *Anal. Chem.*, 2011, **83**, 9676–9680.
- 18 R. Ghosh, A. K. Sahoo, S. S. Ghosh, A. Paul and A. Chattopadhyay, *ACS Appl. Mater. Interfaces*, 2014, **6**, 3822–3828.
- 19 K. Salorinne, X. Chen, R. W. Troff, M. Nissinen and H. Haekkinen, *Nanoscale*, 2012, **4**, 4095–4098.
- 20 A. Ganguly, I. Chakraborty, T. Udayabhaskararao and T. Pradeep, *J. Nanopart. Res.*, 2013, **15**, 1522.
- 21 S.-i. Tanaka, J. Miyazaki, D. K. Tiwari, T. Jin and Y. Inouye, *Angew. Chem., Int. Ed.*, 2011, **50**, 431–435.
- 22 X. Huang, B. Li, L. Li, H. Zhang, I. Majeed, I. Hussain and B. Tan, *J. Phys. Chem. C*, 2012, **116**, 448–455.
- 23 X. Le Guevel, V. Trouillet, C. Spies, G. Jung and M. Schneider, *J. Phys. Chem. C*, 2012, **116**, 6047–6051.
- 24 I. Chakraborty, R. G. Bhui, S. Bhat and T. Pradeep, *Nanoscale*, 2014, **6**, 8561–8564.
- 25 H. Erdogan, O. Metin and S. Oezkar, *Phys. Chem. Chem. Phys.*, 2009, **11**, 10519–10525.
- 26 M. Hyotanishi, Y. Isomura, H. Yamamoto, H. Kawasaki and Y. Obora, *Chem. Commun.*, 2011, **47**, 5750–5752.
- 27 S. Nassreddine, G. Bergeret, B. Jouguet, C. Geantet and L. Piccolo, *Phys. Chem. Chem. Phys.*, 2010, **12**, 7812–7820.
- 28 M. Rueping, R. M. Koenigs, R. Borrmann, J. Zoller, T. E. Weirich and J. Mayer, *Chem. Mater.*, 2011, **23**, 2008–2010.
- 29 Z. Xu, F. S. Xiao, S. K. Purnell, O. Alexeev, S. Kawi, S. E. Deutsch and B. C. Gates, *Nature*, 1994, **372**, 346–348.
- 30 A. Berko and F. Solymosi, *Surf. Sci.*, 1998, **411**, L900–L903.
- 31 A. M. Argo, J. F. Odzak and B. C. Gates, *J. Am. Chem. Soc.*, 2003, **125**, 7107–7115.
- 32 A. M. Argo, J. F. Odzak, J. F. Goellner, F. S. Lai, F. S. Xiao and B. C. Gates, *J. Phys. Chem. B*, 2006, **110**, 1775–1786.
- 33 C. Aydin, J. Lu, M. Shirai, N. D. Browning and B. C. Gates, *ACS Catal.*, 2011, **1**, 1613–1620.
- 34 C. Kerpel, D. J. Harding, G. Meijer and A. Fielicke, *Eur. Phys. J. D*, 2011, **63**, 231–234.
- 35 V. S. Garcia-Cuello, L. Giraldo and J. C. Moreno-Pirajan, *Catal. Lett.*, 2011, **141**, 1659–1669.
- 36 J. Dupont, G. S. Fonseca, A. P. Umpierre, P. F. P. Fichtner and S. R. Teixeira, *J. Am. Chem. Soc.*, 2002, **124**, 4228–4229.
- 37 G. S. Fonseca, A. P. Umpierre, P. F. P. Fichtner, S. R. Teixeira and J. Dupont, *Chem.–Eur. J.*, 2003, **9**, 3263–3269.
- 38 E. Bayram, M. Zahmakiran, S. Özkar and R. G. Finke, *Langmuir*, 2010, **26**, 12455–12464.
- 39 C. K. Yee, R. Jordan, A. Ulman, H. White, A. King, M. Rafailovich and J. Sokolov, *Langmuir*, 1999, **15**, 3486–3491.
- 40 R. Redon, F. Ramirez-Crescencio and A. L. Fernandez-Osorio, *J. Nanopart. Res.*, 2011, **13**, 5959–5965.
- 41 M.-H. So, C.-M. Ho, R. Chen and C.-M. Che, *Chem.–Asian J.*, 2010, **5**, 1322–1331.
- 42 T. Zhang, S.-C. Li, W. Zhu, J. Ke, J.-W. Yu, Z.-P. Zhang, L.-X. Dai, J. Gu and Y.-W. Zhang, *Surf. Sci.*, 2016, **648**, 319–327.
- 43 R. Vankayala, G. Gollavelli and B. K. Mandal, *J. Mater. Sci.: Mater. Med.*, 2013, **24**, 1993–2000.
- 44 D. J. Gavia, Y. Do, J. Gu and Y.-S. Shon, *J. Phys. Chem. C*, 2014, **118**, 14548–14554.
- 45 Y. Zhu, H. Qian, B. A. Drake and R. Jin, *Angew. Chem., Int. Ed.*, 2010, **49**, 1295–1298.

- 46 M. J. Frish, G. W. Trucks, H. B. Schlegel, G. E. Scuseria, M. A. Robb, J. R. Cheeseman, G. Scalmani, V. Barone, B. Mennucci and G. A. Petersson, *et al.*, *Gaussian 09*, Gaussian, Inc., Wallingford CT, 2009.
- 47 W. Bouderbala, A.-G. Boudjahem and A. Soltani, *Mol. Phys.*, 2014, **112**, 1789–1798.
- 48 M. Zhang and R. Fournier, *Phys. Rev. A: At., Mol., Opt. Phys.*, 2009, **79**, 043203.
- 49 S. A. Aravindh, *Appl. Nanosci.*, 2014, **4**, 593–600.
- 50 J. B. A. Davis, S. L. Horswell and R. L. Johnston, *J. Phys. Chem. A*, 2014, **118**, 208–214.
- 51 F. Weigend and R. Ahlrichs, *Phys. Chem. Chem. Phys.*, 2005, **7**, 3297–3305.
- 52 F. Weigend, *Phys. Chem. Chem. Phys.*, 2006, **8**, 1057–1065.
- 53 J. Cioslowski, *J. Am. Chem. Soc.*, 1989, **111**, 8333–8336.
- 54 G. Schaftenaar and J. H. Noordik, *J. Comput.-Aided Mol. Des.*, 2000, **14**, 123–134.
- 55 T. A. Keith and R. F. W. Bader, *Chem. Phys. Lett.*, 1992, **194**, 1–8.
- 56 T. A. Keith and R. F. W. Bader, *Chem. Phys. Lett.*, 1993, **210**, 223–231.
- 57 J. A. Creighton and D. G. Eadon, *J. Chem. Soc., Faraday Trans.*, 1991, **87**, 3881–3891.
- 58 A. Baksi, A. Mitra, J. S. Mohanty, H. Lee, G. De and T. Pradeep, *J. Phys. Chem. C*, 2015, **119**, 2148–2157.
- 59 A. Mitra and G. De, *Langmuir*, 2014, **30**, 15292–15300.
- 60 M. Habeeb Muhammed, S. Ramesh, S. Sinha, S. Pal and T. Pradeep, *Nano Res.*, 2008, **1**, 333–340.
- 61 T. G. Schaaff, M. N. Shafiqullin, J. T. Khoury, I. Vezmar and R. L. Whetten, *J. Phys. Chem. B*, 2001, **105**, 8785–8796.
- 62 A. Dass, A. Stevenson, G. R. Dubay, J. B. Tracy and R. W. Murray, *J. Am. Chem. Soc.*, 2008, **130**, 5940–5946.
- 63 J.-G. Du, X.-Y. Sun, J. Chen and G. Jiang, *J. Phys. Chem. A*, 2010, **114**, 12825–12833.
- 64 J. Vicha, M. Patzschke and R. Marek, *Phys. Chem. Chem. Phys.*, 2013, **15**, 7740–7754.

Electronic Supplementary Information (ESI)

Atomically precise and monolayer protected iridium clusters in solution

Shridevi Bhat,^a Indranath Chakraborty,^{a,b} Tuhina Adit Maark,^{a,c} Anuradha Mitra,^d Goutam De^d and Thalappil Pradeep^{a*}

^a*DST Unit of Nanoscience (DST UNS) and Thematic Unit of Excellence,
Department of Chemistry, Indian Institute of Technology Madras,
Chennai 600036, India.*

^b*Current affiliation: University of Illinois at Urbana Champaign, Urbana, IL
61801, USA.*

^c*Department of Physics, Indian Institute of Technology Madras,
Chennai 600036, India.*

^d*CSIR-Central Glass and Ceramic Research Institute, Kolkata 700032, West
Bengal, India*

Content list

Number	Description	Page Number
1	Instrumentation and SAXS analysis	2
2	Control experiment with varying thiol concentration	4
3	XPS survey spectrum	5
4	Expanded version of NMR spectra	6
5	XRD pattern	7
6	Mass spectra obtained using different matrices	8
7	MALDI MS at threshold laser intensity	9
8	Time dependent UV/Vis spectra	10
9	Atomic coordinates of optimized geometries of model clusters	11

Supplementary Information 1

Instrumentation:

UV-Vis spectral measurements on the cluster were performed using a Perkin Elmer Lambda 25 instrument in the range of 200-1100 nm. Photoluminescence spectra of samples were measured with a Jobin Vyon NanoLog instrument. Matrix-assisted desorption ionization mass spectrometric (MALDI MS) measurements were carried out using a Voyager-DE PRO Biospectrometry Workstation from Applied Biosystems. DHB and other matrices listed in the text were used in the ratio of 1:100 of sample:matrix. A pulsed nitrogen laser of wavelength 337 nm was used for the MALDI MS measurements. Mass spectra were collected in linear positive ion mode and were averaged for 250 shots. High resolution transmission electron microscopy of cluster was conducted with a JEOL 3010 instrument. The samples for TEM were prepared by drop casting THF solution of cluster on carbon-coated copper grids and allowing it to dry under ambient conditions. FT-IR spectra were taken using a Perkin Elmer Spectrum One spectrometer. X-ray photoelectron spectroscopic (XPS) measurements were carried out with an Omicron ESCA Probe spectrometer using polychromatic MgK α X-rays ($h\nu = 1253.6$ eV). The THF solution of sample was drop casted on a sample stub and dried, several times to form a thin film. The measurements were conducted with constant analyzer energy of 20 eV. Powder XRD of Ir₉PET₆ cluster was recorded by PANalytical X'pertPro diffractometer. The sample for XRD was prepared on a glass slide and diffractogram was collected for 2 theta range of 5 to 100 degrees with Cu K α radiation. Small Angle X-ray Scattering (SAXS) analysis on cluster solution was done using Rigaku Smart Lab X-ray Diffractometer operating at 9 kW (Cu-K α radiation; $\lambda = 1.54059$ Å). The cluster solution was filled inside a borosilicate capillary tube of internal diameter approximately 1.5 mm. The raw SAXS profiles were solved using NANO-Solver programme (Rigaku). Prior to fittings the raw data was corrected for background absorption and air scattering. The 'corrected' raw profile was fitted with 'sphere' as well as 'core – shell' models to evaluate the best suited model for the Ir₉PET₆ sample. The densities of PET ligand (1.03 g/cm³), toluene (0.87 g/cm³) and Ir (22.56 g/cm³) have been used to fit these profiles.

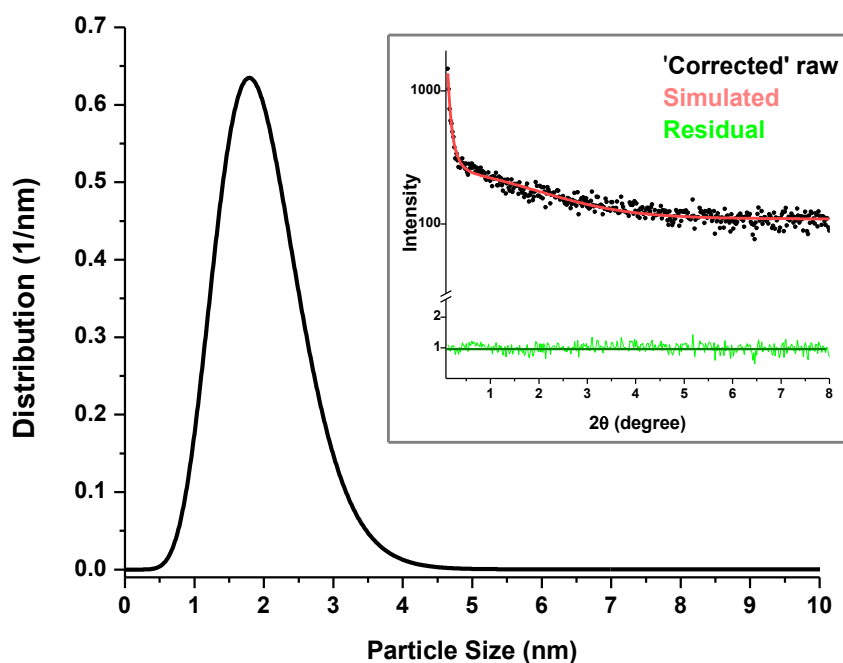


Fig. S1. Particle size distribution curve of Ir₉PET₆ evaluated using ‘sphere’ model. The corrected raw, simulated and residual SAXS profiles are shown in the inset.

Table S1: SAXS parameters for Ir@PET solution in toluene.

Model	Avg. size (nm)	Vol (%)	Normalized dispersion (σ)	Shell diameter (nm)	Avg. metal cluster core size (nm)	R-residual factor
Core-shell	2.0	98.08 (rest are bigger particles)	0.317	0.4	1.6	1.94
Sphere	1.99	95.04 (rest are bigger particles)	0.314	--	--	1.93

Supplementary Information 2

UV/Vis spectra and photographs of samples synthesized using varying thiol concentrations

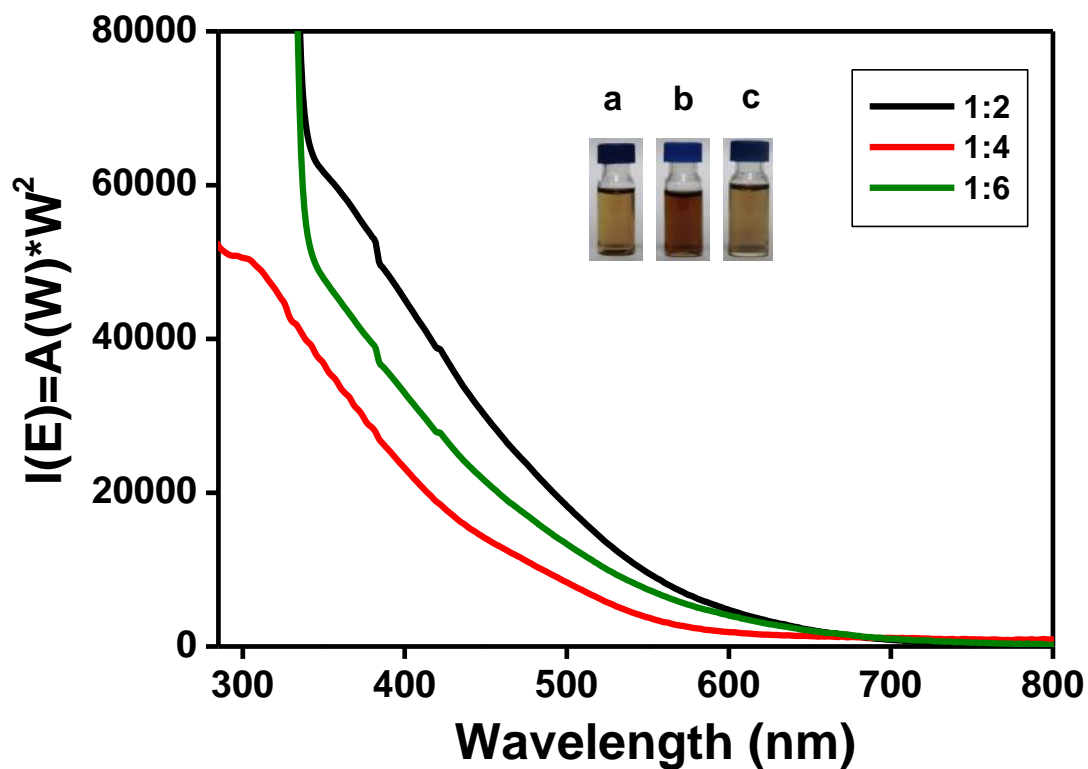


Fig. S2. UV/Vis spectra of samples synthesized using metal to thiol molar ratio of 1:2, 1:4 and 1:6. Inset shows the photographs (a-1:2, b-1:4 and c-1:6) samples. It is clearly seen that the sample 'b' corresponding to 1:4 ratio has intense color and this ratio works out better giving good yield. It also has absorption features different from other two compositions.

Supplementary Information 3

XPS survey spectrum of Ir₉PET₆ cluster

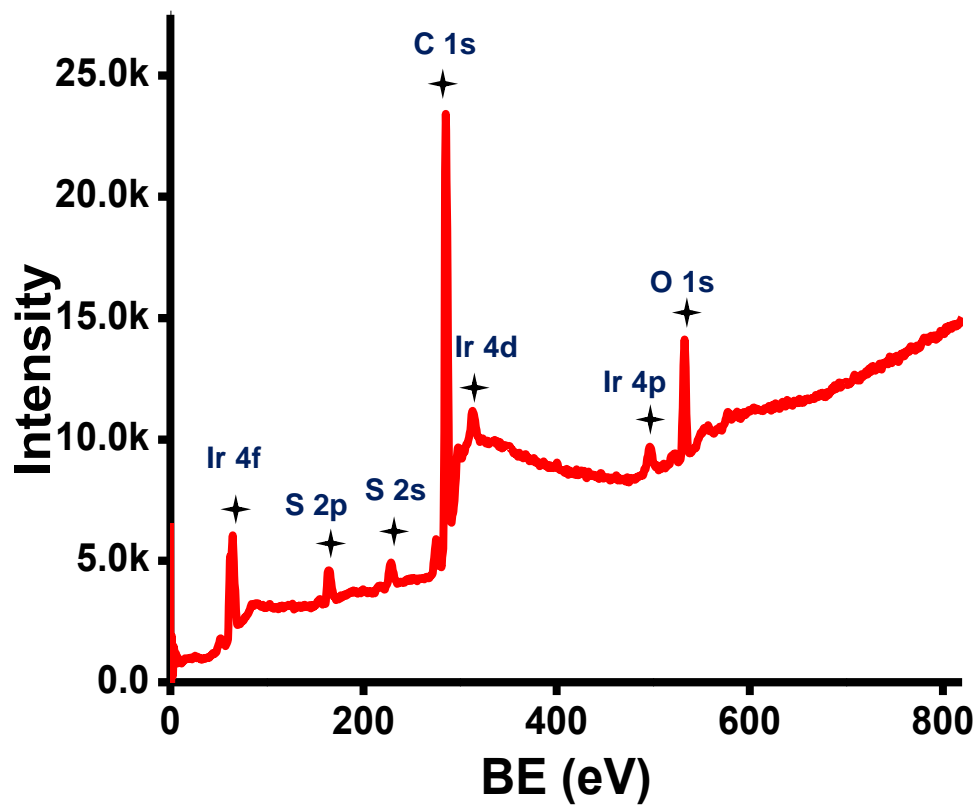


Fig. S3. XPS survey spectrum of Ir₉PET₆ measured from 0 – 1000 eV showing the elements Ir, S, C and O.

Supplementary Information 4

Expanded view of NMR spectrum of Ir₉PET₆ cluster as compared to that of free PET

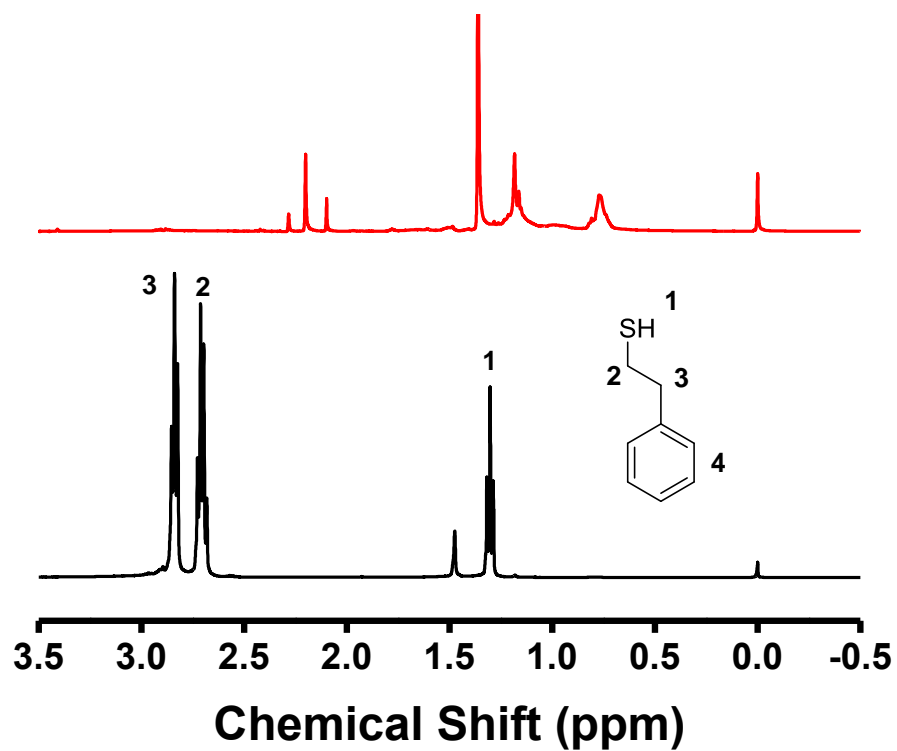


Fig. S4. Expanded view of comparative plot of NMR spectra of Ir₉PET₆ clusters (red trace) and PET (black trace).

Supplementary Information 5

XRD pattern of Ir₉PET₆ cluster

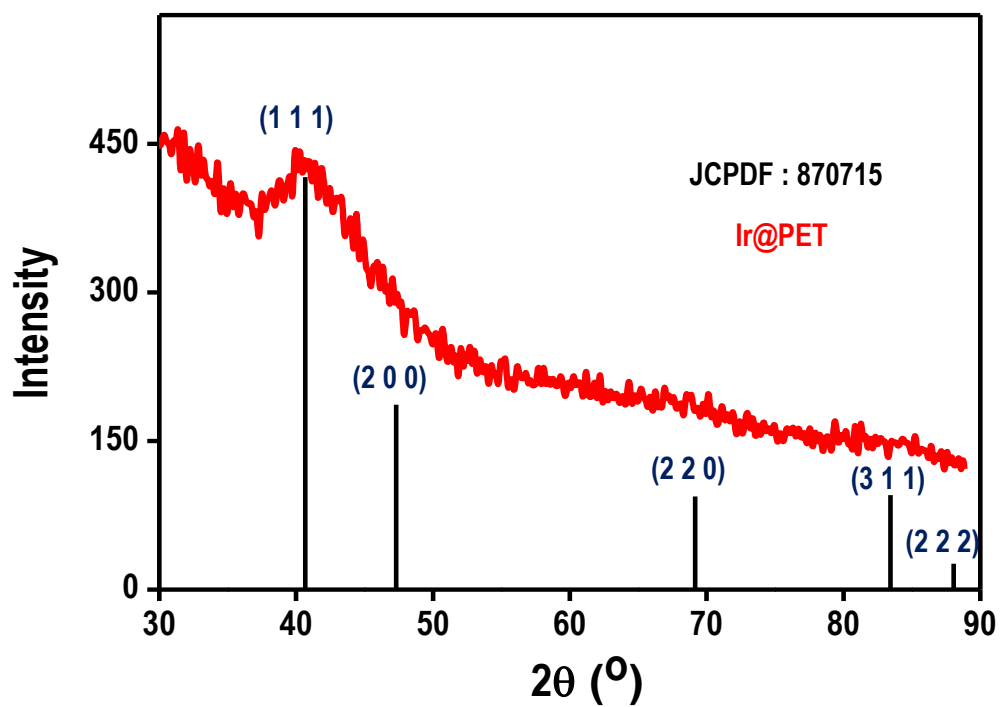


Fig. S5. Powder XRD pattern of Ir₉PET₆ clusters measured by drop casting THF solution of clusters on a glass slide several times and drying to form a thin film. Standard pattern of Ir metal is also shown.

Supplementary Information 6

Mass spectra obtained using different matrices

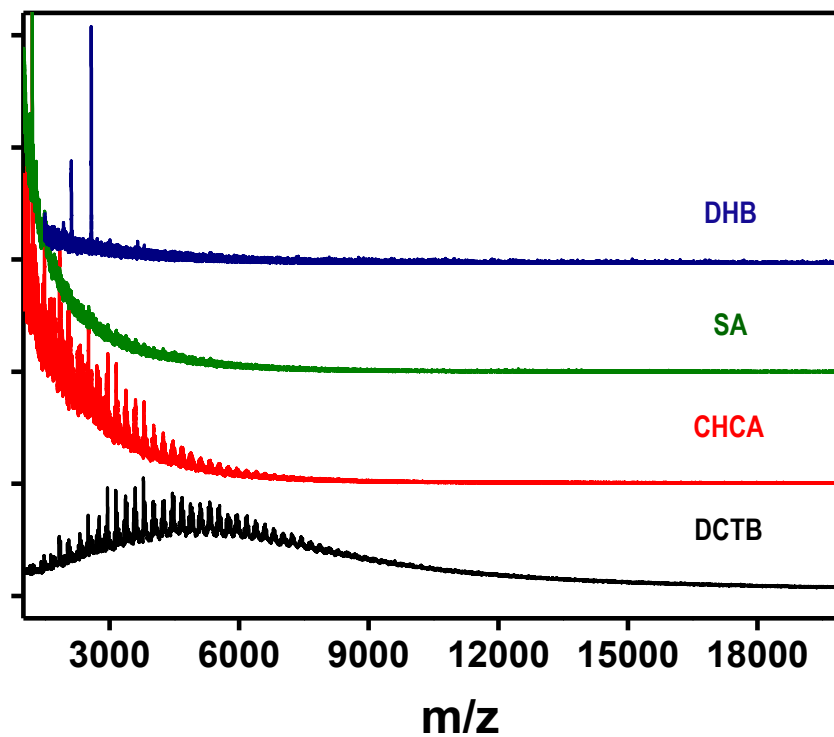


Fig. S6. MALDI MS obtained using different matrices are plotted together for comparison. The matrix used to obtain each spectrum is indicated in the figure.

Supplementary Information 7

Mass spectrum at threshold laser intensity

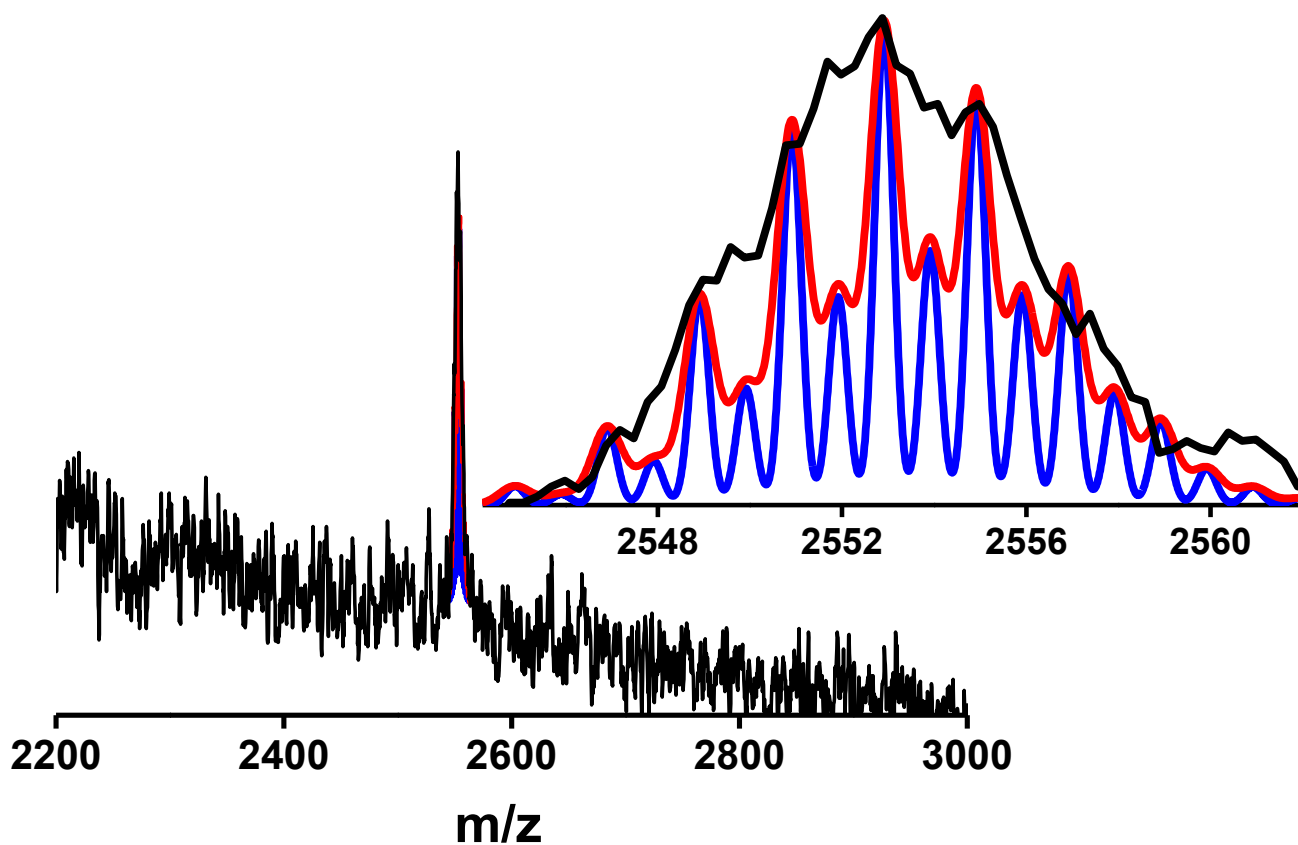


Fig. S7. MALDI MS obtained at threshold laser intensity showing better resolution. Inset shows the expanded view, wherein, it can be seen that experimental spectrum (black trace) is in better agreement with the theoretical spectrum calculated at similar resolution (red trace) and blue trace is the theoretical spectrum calculated at highest possible resolution. The experimental spectrum has more noise due to poor signal quality.

Supplementary information 8

Time dependent UV/Vis spectra

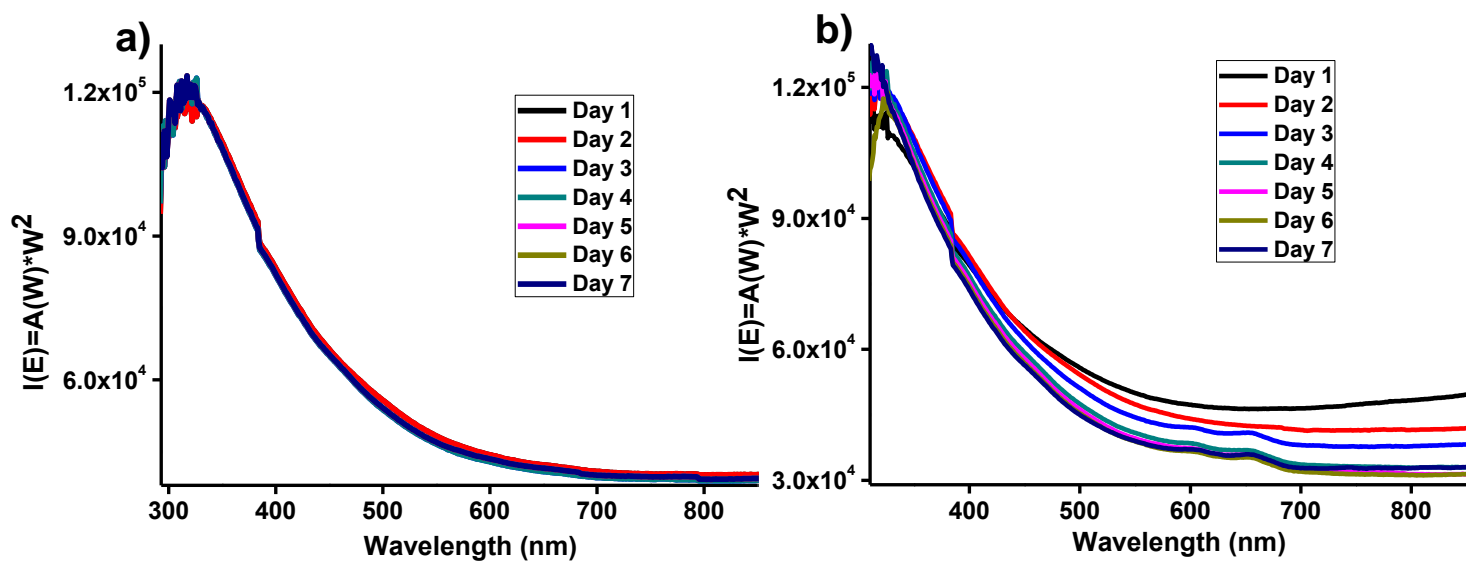


Fig. S8. Time dependent UV/Vis spectra of the cluster solution in THF kept a) in fridge (at $\sim 4^\circ\text{C}$) and b) at room temperature measured for a time period of 7 days.

Supplementary Information 9

Atomic coordinates of optimized geometries of model clusters:

1. Ir₃(SCH₃)₂ – isomer (a)

Ir	11.623303	12.849419	13.136886
S	12.599564	12.455964	11.255281
Ir	14.751456	12.446011	11.530630
Ir	14.902190	11.633294	13.683341
S	13.188610	12.599242	14.598317
C	12.143934	10.732869	10.744433
H	12.589926	10.548600	9.759417
H	11.050211	10.680447	10.687162
H	12.525054	10.021048	11.481836
C	13.761688	14.292242	15.091198
H	14.184926	14.801766	14.221130
H	12.892324	14.839939	15.473881
H	14.517185	14.172468	15.877300

2. Ir₃(SCH₃)₂ – isomer (b)

C	12.755526	10.649612	11.526901
S	12.311646	12.310260	10.849593
Ir	14.121808	13.459329	10.639438
Ir	13.397168	14.101478	12.798571
S	14.441620	14.602178	14.612887
C	15.017882	13.109171	15.525506
Ir	11.190566	13.373750	12.350818

H	13.378101	10.146656	10.777789
H	11.820013	10.101180	11.687424
H	13.300330	10.777569	12.466462
H	15.535240	13.454702	16.429947
H	14.160506	12.488027	15.804834
H	15.709442	12.533683	14.901403

3. Ir₃(SCH₃)₂ – isomer (c)

C	12.053627	10.753478	10.639916
S	12.644522	12.490833	11.106043
Ir	11.712954	12.651744	13.132928
Ir	14.092210	11.849749	13.695775
S	10.041237	13.068855	14.439584
C	10.157745	14.878418	14.956478
Ir	14.792378	12.224427	11.369537
H	12.113242	10.702989	9.551796
H	11.021295	10.658932	10.964896
H	12.679660	10.019020	11.109310
H	9.703707	14.957657	15.942446
H	11.195730	15.189908	15.033705
H	9.613137	15.490931	14.246902

4. Ir₃(SCH₃)₂ – isomer (d)

Ir	6.563522	7.035119	6.692346
Ir	8.957637	7.246990	7.375922

Ir	6.920398	8.565528	8.474533
S	8.449089	7.455616	9.603860
S	8.195623	7.260862	5.204826
C	8.154369	8.956055	4.508244
H	7.368388	9.005523	3.746746
H	9.133699	9.145599	4.051649
H	7.964161	9.675912	5.311083
C	7.715083	5.893616	10.232591
H	7.066706	6.125718	11.083994
H	7.147821	5.408341	9.430838
H	8.546625	5.252550	10.550354

5. Ir₃(SCH₃)₂ – isomer (e)

Ir	1.112160	-1.002094	0.239234
Ir	0.023392	1.146970	-0.028114
Ir	-1.226476	-0.988150	-0.260257
S	-2.224277	1.158037	-0.391473
S	2.237681	1.157422	0.387517
C	3.190393	1.429044	-1.166390
H	4.178463	0.971512	-1.041434
H	3.297747	2.509234	-1.314400
H	2.668594	0.983663	-2.016962
C	-3.115733	1.511332	1.182430
H	-4.111855	1.059778	1.115313
H	-2.565060	1.096467	2.030148

H -3.205560 2.598555 1.284952

6. Ir₃(SCH₃)₂ – isomer (f)

Ir 12.309177 12.706316 12.742232

S 13.231746 12.738223 14.715847

Ir 15.206540 11.993012 13.957759

Ir 14.474419 13.072322 11.896811

S 16.277440 11.718008 11.939570

C 13.347819 14.487820 15.294727

H 13.955881 15.058931 14.586622

H 13.835534 14.461422 16.276810

H 12.341128 14.909298 15.374398

C 15.995190 10.122416 11.089021

H 16.753601 9.414767 11.444410

H 16.101914 10.278673 10.010157

H 14.992759 9.755255 11.327740

7. Ir₃(SCH₃)₂ – isomer (g)

Ir 0.003767 1.611685 0.008810

Ir 1.064370 -0.450027 0.601114

Ir -1.049128 -0.450795 -0.591141

S -3.022318 -1.181875 -0.121888

S 3.039527 -1.174103 0.129848

C 3.481962 -0.942535 -1.626974

C -3.465241 -0.955243 1.635446

H -2.758908 -1.501862 2.267970

H -3.445397 0.111429 1.881163

H -4.478574 -1.352137 1.772083

H 3.461694 0.124830 -1.869679

H 2.775733 -1.487632 -2.260911

H 4.495450 -1.338612 -1.764838

8. Ir₃(SCH₃)₂ – isomer (h)

Ir	-0.725569	1.187585	-0.155868
Ir	1.289216	0.016141	0.512233
Ir	-0.713040	-1.200389	-0.111513
S	-2.639575	-0.025935	-0.639521
S	3.430989	0.018315	0.023562
C	3.641983	-0.014594	-1.795866
C	-3.724016	-0.003824	0.852113
H	-3.123551	0.016062	1.764779
H	-4.356171	0.889236	0.794654
H	-4.347114	-0.904734	0.827792
H	3.181242	0.871374	-2.242936
H	3.191679	-0.922019	-2.209272
H	4.720699	-0.012054	-1.994663

9. Ir₃(SCH₃)₂ – isomer (i)

Ir	-1.018558	-0.086384	0.203833
Ir	1.388298	0.885978	0.091153
Ir	0.964000	-1.411057	-0.135851
S	-0.393618	1.824729	-0.817694
S	-3.111925	-0.569354	0.545695
C	-4.143636	-0.424737	-0.964817
C	-0.937631	3.312110	0.138787
H	-0.433650	4.186603	-0.291032
H	-0.702417	3.207804	1.201129

H	-2.021844	3.405736	0.001339
H	-3.840402	0.449371	-1.549994
H	-4.022079	-1.329692	-1.570819
H	-5.191764	-0.329382	-0.655038

10. Ir₃(PET)₁ – isomer (j)

Ir	11.078616	6.678504	18.087445
Ir	9.566682	7.838141	16.705897
Ir	10.806959	7.662714	14.711221
S	12.179877	6.878933	16.216417
C	13.396818	8.259880	16.522600
C	14.187628	8.574787	15.248172
C	15.199424	9.673517	15.475276
C	14.802121	11.018794	15.475887
C	15.726910	12.037352	15.707052
C	17.068400	11.726818	15.942793
C	17.476600	10.392005	15.943750
C	16.548086	9.374938	15.712194
H	14.050443	7.893825	17.327328
H	12.833058	9.126431	16.884590
H	14.693232	7.666017	14.889255
H	13.468818	8.879584	14.468340
H	16.875840	8.333336	15.707147
H	18.522677	10.140136	16.120841
H	17.792669	12.521972	16.120083

H	15.400257	13.077620	15.698158
H	13.756508	11.269285	15.285638

11. Ir₃(PET)₁ – isomer (k)

C	-1.113381	1.205743	0.063229
C	-2.443906	1.237395	-0.357267
C	-3.167140	0.049573	-0.483394
C	-2.551710	-1.167655	-0.184217
C	-1.220986	-1.194809	0.235942
C	-0.483474	-0.009632	0.365635
C	0.967652	-0.044434	0.786471
C	1.891885	-0.175121	-0.431508
S	3.653687	-0.216915	0.092567
Ir	5.031883	-0.397786	-1.565437
Ir	4.876410	-1.717521	-3.542161
H	-0.555645	2.138919	0.166062
H	-2.918517	2.192875	-0.582606
H	-4.207328	0.072801	-0.808569
H	-3.110923	-2.099450	-0.273748
H	-0.747892	-2.149637	0.474593
H	1.777682	0.673856	-1.117270
H	1.697121	-1.100549	-0.988036
H	1.142682	-0.890157	1.467407
H	1.222275	0.871944	1.338696
Ir	4.984410	0.637099	-3.710226

12. Ir₃(PET)₁ – isomer (l)

C	13.270123	13.274979	15.949681
C	12.232931	12.426127	15.539853
C	10.942210	12.960675	15.413535
C	10.695651	14.306325	15.687708
C	11.738190	15.141886	16.095430
C	13.027399	14.622112	16.224917
C	12.487957	10.961235	15.270138
C	12.138899	10.101990	16.489930
S	12.491080	8.313208	16.180427
Ir	11.012711	7.098787	17.343752
Ir	8.948935	7.742941	16.349402
Ir	10.833370	7.492534	14.916942
H	11.074155	10.173908	16.750078
H	12.742944	10.375066	17.366737
H	13.542447	10.808495	14.996320
H	11.877758	10.617537	14.421047
H	10.123744	12.313651	15.091400
H	9.686674	14.705226	15.578533
H	11.547192	16.194146	16.306682
H	13.848631	15.268078	16.537042
H	14.282234	12.876455	16.046388

13. Ir₂(PET)₁ – isomer (m)

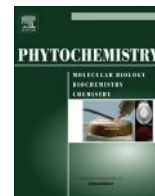
C	7.751063	12.595023	12.694163	-0.055483
C	8.409786	11.379385	12.890548	-0.086312

C	9.743896	11.364585	13.299167	-0.129226
C	10.442686	12.560153	13.519162	0.188134
C	9.769854	13.773749	13.319005	-0.131006
C	8.434856	13.792916	12.911375	-0.084929
C	11.897592	12.535782	13.925819	-0.085551
C	12.814291	12.482079	12.692916	-0.011530
S	14.582768	12.475473	13.241963	-0.255361
Ir	15.833695	11.890446	11.562621	60.234740
H	10.296673	14.714296	13.493019	0.048737
H	7.926430	14.746750	12.767557	0.058803
H	6.707854	12.609159	12.378311	0.056693
H	7.881156	10.439371	12.729881	0.058228
H	10.249922	10.410046	13.458282	0.047684
H	12.673625	13.368356	12.060671	0.085053
H	12.610939	11.590049	12.089536	0.057265
H	12.096403	11.661337	14.562505	0.059325
H	12.141887	13.428841	14.519245	0.055477
Ir	16.925448	13.207583	10.165456	59.889378

14. Ir₂(PET)₁ – isomer (n)

C	4.095057	7.425062	7.907180	-0.054201
C	4.788723	6.246216	8.188135	-0.085977
C	6.160861	6.284315	8.441474	-0.127900
C	6.863005	7.497440	8.419626	0.191214
C	6.154370	8.674361	8.137721	-0.132774

C	4.782489	8.640607	7.884235	-0.087892
C	8.355139	7.534097	8.656212	-0.066716
C	9.132641	7.438382	7.338615	0.023217
S	10.968433	7.351162	7.664797	-0.178672
Ir	12.067099	8.205618	6.010277	59.996803
H	6.685203	9.628507	8.122627	0.051138
H	4.247932	9.567044	7.672096	0.058099
H	3.022950	7.397488	7.711900	0.056626
H	4.258739	5.293598	8.214947	0.057891
H	6.695715	5.359296	8.666824	0.046949
H	8.937107	8.289743	6.679350	0.085884
H	8.898582	6.507310	6.801492	0.058669
H	8.649613	6.707093	9.320228	0.058529
H	8.638681	8.470181	9.160214	0.035474
Ir	11.748529	9.327967	8.077383	60.013599



Developmental patterning and segregation of alkaloids in areca nut (seed of *Areca catechu*) revealed by magnetic resonance and mass spectrometry imaging



Amitava Srimany^a, Christy George^{b,1}, Hemanta R. Naik^a, Danica Glenda Pinto^a, N. Chandrakumar^{b,*}, T. Pradeep^{a,*}

^a DST Unit of Nanoscience (DST UNS) and Thematic Unit of Excellence (TUE), Department of Chemistry, Indian Institute of Technology Madras, Chennai 600036, India

^b MRI-MRS Centre, Department of Chemistry, Indian Institute of Technology Madras, Chennai 600036, India

ARTICLE INFO

Article history:

Received 3 November 2015
Received in revised form 12 January 2016
Accepted 6 February 2016
Available online 17 February 2016

Keywords:

Areca catechu (Arecaceae)
Areca nut
Pattern
Alkaloid
MRI
PRESS (MRS)
DESI MS

ABSTRACT

Areca nut (seed of *Areca catechu*) is consumed by people from different parts of Asia, including India. The four major alkaloids present in areca nut are arecoline, arecaidine, guvacoline and guvacine. Upon cutting, the nut reveals two kinds of regions; white and brown. In our present study, we have monitored the formation of these two regions within the nut during maturation, using the non-invasive techniques of magnetic resonance imaging (MRI) and volume localized magnetic resonance spectroscopy (MRS). Electrospray ionization mass spectrometry (ESI MS) and desorption electrospray ionization mass spectrometry (DESI MS) imaging have been used to study the associated change in the alkaloid contents of these two regions during the growth of the nut. Our study reveals that white and brown regions start forming within the nut when the liquid within starts solidifying. At the final stage of maturity, arecoline, arecaidine and guvacoline get segregated in the brown region whereas guvacine gets to the white region of the nut. The transport of molecules with maturity and corresponding pattern formation are expected to be associated with a multitude of physicochemical changes.

© 2016 Elsevier Ltd. All rights reserved.

1. Introduction

Areca nut or betel nut is the seed of *Areca catechu* L. (Arecaceae) (Fig. 1). It grows in the tropical climate of Asia, East Africa and the Pacific. In India, areca nut is associated with tradition and used in different cultural, social, and religious ceremonies. Besides, due to its inherent medicinal properties, it has found place in the traditional Indian medicinal system, *Ayurveda*, and is used for the treatment of leprosy, leucoderma, indigestion, etc., and is also used as a vermifuge. The use of areca nut dates back to the Vedic age (ca. 1500–500 BCE) and it has been mentioned in ancient writings. In different parts of Asia, it is consumed by people for its stimulatory action and it is a widely used masticatory (substance which increases the secretion of saliva when chewed). In India, it is traditionally consumed in the form of betel quid (a combination of betel leaf, areca nut, and lime) and people across the country consume it regardless of age, gender, and religion. Nowadays it is marketed in

whole or as part of different products for direct consumption after different methods of processing. India, the largest areca nut producing country, accounts for 53% of the global production. Majority of areca nut grows in the Indian states of Karnataka and Kerala. Several small farmers and workers are involved in the cultivation of this crop. Employment and livelihood of many people in India are associated with the production of areca nut. As a consequence, areca nut cultivation has a direct impact on the society and economy of the country.

Areca nut largely contains sugars, lipids and polyphenols (Wetwitayaklung et al., 2006). It also contains a small amount of four structurally similar alkaloids: arecoline, arecaidine, guvacoline, and guvacine. Fig. 2 shows the molecular structures of four major alkaloids present in the nut. Polyphenols in areca nut comprise of condensed tannins, hydrolysable tannins, and flavonols. Polyphenols and alkaloids are the most bio-active components of areca nut. The former class of compounds are well known for their antioxidant property. They prevent oxidation of high density lipids (Han et al., 2007). Arecoline is the most abundant alkaloid in areca nut and its content in the nut increases during maturation, reaches a maximum, and then decreases drastically in the matured nut (Wang et al., 1997). In terms of biological activity, it is also more

* Corresponding authors.

E-mail addresses: nckumar@iitm.ac.in (N. Chandrakumar), pradeep@iitm.ac.in (T. Pradeep).

¹ Present address: Francis Bitter Magnet Lab and Department of Chemistry, Massachusetts Institute of Technology, Cambridge, MA 02139, USA.



Fig. 1. Photograph of a nut-bearing areca nut tree. The inset shows a nut cut into two halves. It reveals W and B regions of the nut. At the earlier stages of growth, the contrast between these two regions is poor.

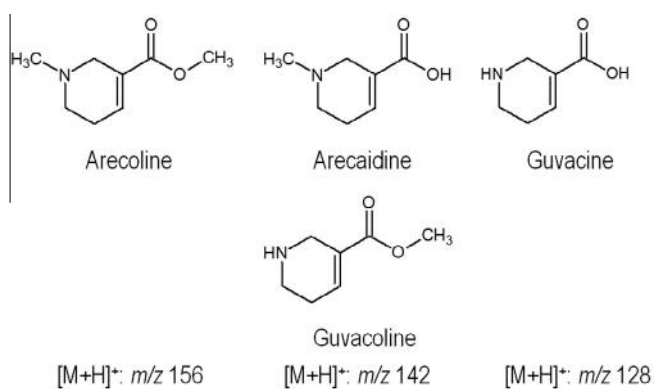


Fig. 2. Chemical structures of four major alkaloids present in areca nut.

potent than others. Arecoline is shown to be cytotoxic for human endothelial cells, and cell cycle is arrested upon exposure to arecoline (Ullah et al., 2014). Arecoline together with guvacoline reduce the survival of human buccal epithelial cells whereas arecaidine and guvacine have little effect on it (Sundqvist et al., 1989). Areca nut extract has been tested for its different biological activities. Aqueous extract of areca nut and arecoline is reported to have genotoxic effects (Dave et al., 1992). Extracts of several commercial products containing areca nut in different forms also show similar

genotoxic effects (Polasa et al., 1993). Areca nut chewing or consumption of other related things like betel quid or different areca nut derived commercial products has been associated with the development of oral cancer. Several review articles present these aspects in detail (Adhikari and De, 2013; Jeng et al., 2001; Kumar, 2008; Mhaske et al., 2009; Nair et al., 2004; Zhang and Reichart, 2007). While the use of products related to areca nut is common in India, China, and a few other South Asian countries, the United States faces an increased risk of oral cancer cases related to the use of areca nut as well (Changrani and Gany, 2005), primarily owing to immigrant populations.

However, there are also several medicinal benefits due to areca nut. Its extract has been shown to have both anti-oxidative activity and free radical scavenging activity (Kim et al., 1997). Areca nut extract when supplemented with diet lowered the triglyceride absorption (Byun et al., 2001) as well as free cholesterol absorption (Park et al., 2002) in rats. It has also been shown to have antimicrobial activity (Hada et al., 1989). Comprehensive details regarding the medicinal use of areca nut can be found in review articles (Amudhan et al., 2012; Peng et al., 2015).

Upon cutting, areca nut reveals two regions: white (W) and brown (B) (Fig. 1 inset). The chemical composition of these two regions is unknown. In previous studies, areca nut was always considered as a whole nut rather than a mixture of two distinct regions. Spatially resolved aspects are rarely examined. In our study, we have focused on the formation of 'villi'-like structures in the nut while maturing and the chemical changes associated with it. MR imaging, volume localized NMR of fairly high resolution, and mass spectrometric techniques have been combined together for the study to get complementary information. Magnetic resonance imaging (MRI) was used to understand the evolution of villi-like structures in the areca nut while maturing, and electrospray ionization mass spectrometry (ESI MS) in conjunction with desorption electrospray ionization mass spectrometry (DESI MS) were used to understand the chemical changes associated with the maturity of the nut.

Earlier studies have shown how non-invasive MRI and MRS, as well as NMR spectroscopy can be used to understand plants. Examples include imaging of lipid distribution in the capsules of tobacco (Fuchs et al., 2013), imaging of water distribution in germinating tobacco seeds (Manz et al., 2005), post-harvest ripening of sweet lime (Banerjee et al., 2009), etc. Other applications of NMR in plant science can be found elsewhere (Borisjuk et al., 2012; Ishida et al., 2000). While MRI may be used to visualize internal structure and function non-invasively and non-destructively by mapping the distribution of selected molecular species (commonly water), it is perhaps not the ideal technique to deal with species that have very low concentrations. Although molecule specific chemical shift selective imaging or non-selective chemical shift imaging (CSI) may be performed to redress this, these techniques do suffer from poor sensitivity per unit measurement time owing to low metabolite concentrations. MR image guided volume localized spectroscopy, *ie*, MRS, on the other hand, provides the molecular fingerprint within chosen volume element(s) (voxel(s)) with sensitivity, *ie*, signal-to-noise-ratio, of the same order as in high resolution NMR. Mass spectrometry can also act as a complementary technique here to retrieve molecular information. Conventional mass spectrometry like ESI MS requires extraction of molecules from samples, losing spatial information. DESI MS, a mass spectrometric tool which works under ambient conditions without sample preparation or extraction (Monge et al., 2013), was introduced in 2004 (Takats et al., 2004) and is capable of imaging molecular species, and sampling is done from the surface, not from the interior. Due to its excellent compatibility in working with biological samples, it has gained the attention of researchers in the field of plant science and other biological sciences. It was used for rapid identification of anti-cancer molecules from plants (Srimany et al., 2011),

study of the distribution of metabolites in different parts of plants like seeds (Ifa et al., 2011; Mohana Kumara et al., 2015), leaves (Muller et al., 2011; Thunig et al., 2011), petals (Thunig et al., 2011), fruits (Cabral et al., 2013), etc.

2. Results and discussion

2.1. Probing areca nut by MRI and MRS

During maturation, an areca nut goes through several transformations. Transformation from the initial liquid stage to a patterned hard nut consisting of W and B regions is associated with different physical and chemical changes. To understand the structural changes during maturation we have chosen to study areca nut at six maturity stages; we discuss below in detail three significantly different maturity stages, while some information on the other stages is included in [Supplementary material](#). We have analyzed multiple samples, typically 3, at the same maturity stage for statistical validity of our data, especially at the initial stages. Stage 1 is a tender areca nut, stage 2 is a ripened nut, and stage 3 is a completely matured nut without husk. Structural evolution in the nut was studied by MRI. As MRI is a non-invasive technique and can generate layer by layer images of the whole sample, it is best suited for our purpose. [Fig. 3](#) displays typical MR images at three different stages of maturation. Supplementing this, the volume localized NMR spectrum gives *in situ* information on the metabolite soup, *ie*, mixture of various metabolites, at the molecular level, from the chosen region within the sample, the region of interest being selected with the help of the MR image. [Fig. 4](#) shows typical

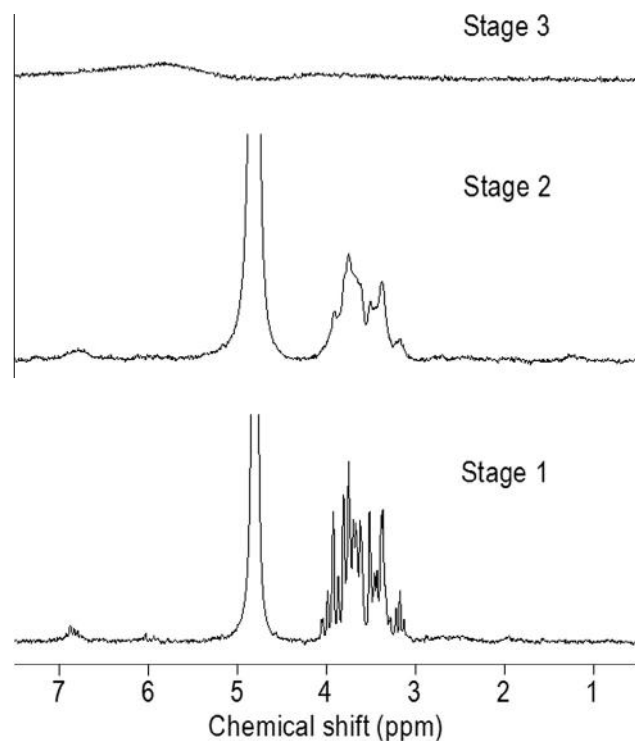


Fig. 4. Volume localized ^1H NMR spectra of areca nut samples of three different maturity stages.

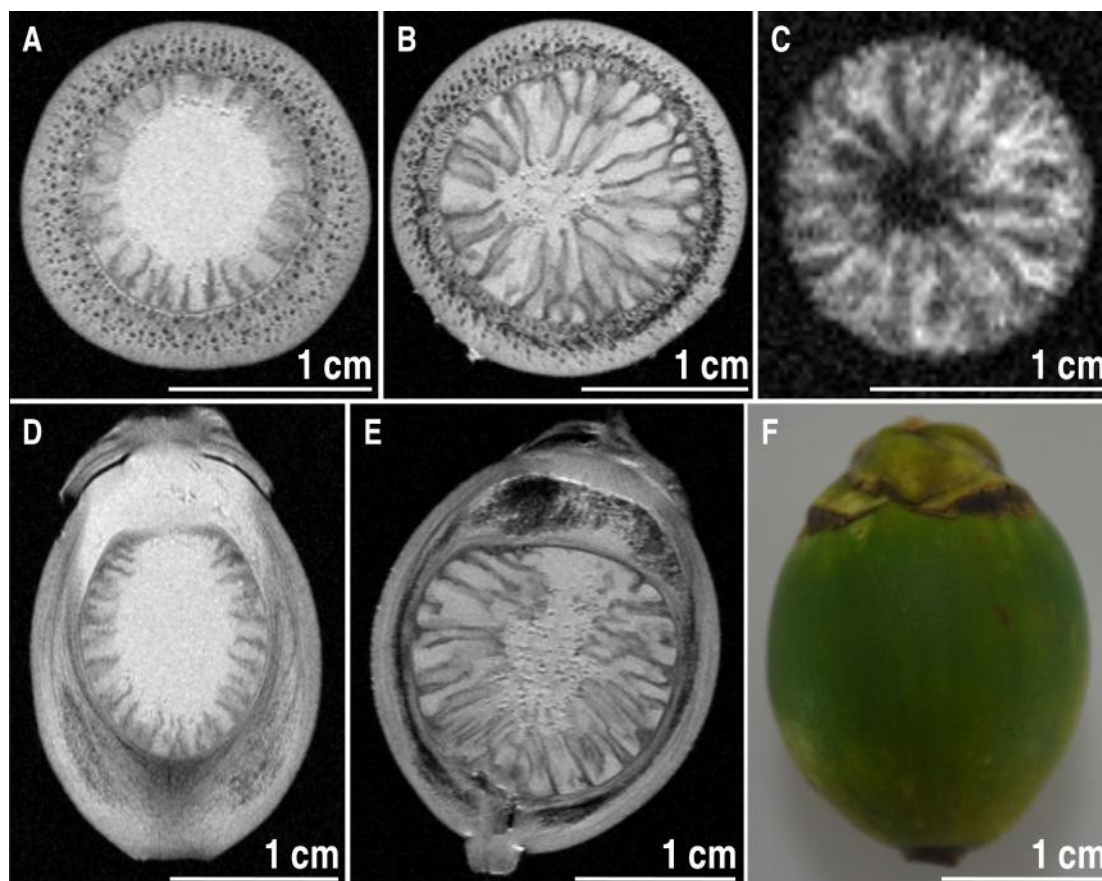


Fig. 3. MRI images of areca nut samples of three different maturity stages. Axial view: (A) stage 1 sample, (B) stage 2 sample, (C) stage 3 sample. Coronal view: (D) stage 1 sample, and (E) stage 2 sample. (F) Photographic image of a stage 2 areca nut sample.

volume localized NMR spectra of areca nut at three different maturity stages. Volume localized spectra were collected from different nuts at different maturity stages, grown in a cluster of plants in the same farm. We have performed the PRESS experiment with a single voxel selection from a particular nut, repeated however over typically 3 samples at the same maturity stage. The typical voxel position is shown in Fig. S1. As for the voxel co-ordinates, the voxel position is not identical for different maturity stages, as the fruit matures and its size changes. Voxels were chosen so as to avoid the husk and the center pith region, while still being as close to the resonator center and field center as possible, in order to ensure good rf and magnetic field homogeneity. To observe molecular species with millimolar concentration in the presence of a high concentration of water protons ($\sim 75\text{--}100\text{ M}$), it is necessary to employ water suppression techniques in volume localized NMR. The residual water peak, appearing at 4.8 ppm, is used as the chemical shift reference. Due to the liquid nature of areca nut matrix in the initial stages of development, fairly good spectral resolution is observed in the volume localized ^1H NMR spectrum of stage 1 sample. As the fruit matures, water content and mobility in the sample reduces as seen in the MRI images (Fig. 3), and the fruit gradually develops into a hard nut. Concomitantly, a progressive degradation of resolution is observed in the spectrum, attributable to reduced molecular mobility. Various molecular species in areca nut include sugars, polyphenols, lipids, and alkaloids (Wetwitayaklung et al., 2006; Yenrina et al., 2014; Zhang et al., 2014, 2010). Although earlier studies differ from each other on the exact concentrations of these molecules, the concentration of sugars is reported to be two orders of magnitude higher than that of the alkaloids (Wetwitayaklung et al., 2006; Yenrina et al., 2014). Peaks observed in the 3.1–4.1 ppm region correspond to the sugar protons. Olefinic proton peaks from four different alkaloids present in areca nut are expected to appear in the 6.8–7 ppm region whereas aliphatic ring protons should appear in the 2–3 ppm region. Chemical shift information is best discerned from the spectrum of the sample at the pre-tender stage (as shown in Fig. S2). However, for this liquid-like sample, no interesting image information is to be gleaned, such as the formation of villi. Although the signal intensity varied slightly from sample to sample for the same stage of growth, we have observed proton resonances in these regions as anticipated. Peaks around 2–3 ppm appeared to be much broader than the sugar proton peaks. Further, lipid content seems to increase considerably as the fruit matures (ca. 1.5 ppm). Volume localized spectra at different stages of maturation are shown in the Supplementary material, including the pre-tender stage of areca nut, as well as at five further stages of maturation as a stacked plot; a spectrum with inset depicting the typical spectral voxel is also shown, as noted earlier.

More insight into the structural evolution inside the shell of areca nut is obtained from MRI images that were taken from a set of parallel slices in three orthogonal planes of the samples. Fig. 3 shows representative MRI images of three different stages of the samples with the axial view (stages 1, 2, and 3) and coronal view (stages 1 and 2), as well as a photographic image of stage 2 sample. Typical in-plane MRI image resolution is $156\ \mu\text{m} \times 156\ \mu\text{m}$. It is evident from Fig. 3A and D that in the initial stage of maturity, the core was liquid, which started solidifying inwards from the peripheral region. During this solidification process itself, the B and W regions got separated. It should also be noted that the top portion of the nut (which is attached to the tree), does not show any solidification (Fig. 3D). This end of the sample was excluded from solidification and villi-like structure formed at the early stage. As the nut became more matured (stage 2 sample), solidification process as well as patterned structure formation increased and the patterns reached closer to the center (Fig. 3B and E). At this point of maturity, the central portion also got solidified but did

not exhibit any patterned structure in this region. The top portion which is attached to the plant got solidified at this stage without forming any patterned structure either (Fig. 3E). From this point on, no further pattern formation occurred; but the nut became harder. At stage 3, the nut matured completely and became a solid but no new B region was formed in the center (Fig. 3C). The fact that during the maturation process, the water concentration and mobility reduced was reflected in the MRI images and the stage 3 sample gave poorer data quality for this reason, requiring larger slice thickness. From the images of all three different stages, we can say that patterned structure formation in the nut occurs in the early stages of maturity, when the liquid inside the nut gets solidified. This process continues to some extent and at some point of time during the later stages of maturity, patterned structure formation stops and only solidification continues till it becomes hard, similar to wood. In the whole process, the top region of the nut which was originally attached to the plant remains free of any patterned structure.

Since the concentration of the alkaloids is very small in comparison to other molecular species, eg., sugars, and also due to the loss of spectral resolution at the final stages of growth, it was difficult to track the spatial changes in alkaloid concentration as a function of maturation by non-invasive volume localized NMR, especially at relatively low field strengths such as 4.7 T. MRS experiments at a higher field such as 11.7 T would substantially help in this regard, with a resonator that accommodates the whole areca nut, although the thin B region would probably still not be amenable for definition of a separate voxel. High resolution NMR on fruit extract could be an alternative approach.

2.2. Alkaloids observed in different stages of areca nut and their distribution in brown and white regions – ESI MS and DESI MSI analysis

Mass spectrometry is yet another technique to track the molecular changes as a function of fruit ripening. To this end, two different mass spectrometric techniques were used to get molecular and spatial information. In this work, we have focused mostly on four structurally related alkaloids (arecoline, arecaidine, guvacoline, and guvacine) present in the nut and tried to understand their spatial and temporal evolution. In the subsequent experiments with mass spectrometry, we have used nuts of similar maturity stages as used in earlier experiments with MRI and MRS.

When stage 2 areca nut was cut, it revealed both W and B regions. At this stage, these regions were not completely solidified. Both the W and B regions were separated by cutting with a razor blade and the compounds were extracted in methanol. For stage 3 areca nut, flakes were made from the whole nut and then W region was separated by cutting with a razor blade and the compounds were extracted. In this case, due to the very thin B region, separating them from the W region was not possible. For this reason, to get the molecules from the B region, whole flakes were taken for extraction. They contained both W and B regions. Stage 1 sample due to its liquid-like nature have been excluded from mass spectrometric studies as no spatial information could be obtained from it. However, it was used for magnetic resonance studies to obtain structural information, primarily.

The methanol extracts were infused for ESI MS measurements and the experiments were performed in triplicate with 3 different nuts of same maturity stages. Fig. 5 shows typical ESI spectra of W and B regions of stage 2 areca nut. For the W region sample, in the low mass range, three peaks appeared at m/z 156, 142, and 128. The peak at m/z 156 corresponds to protonated arecoline, m/z 142 corresponds to both protonated arecaidine and guvacoline, and m/z 128 corresponds to protonated guvacine. The confirmation of these compounds was achieved by tandem mass spectrometry using CID and the fragmentation patterns are shown in Figs. S4–S7.

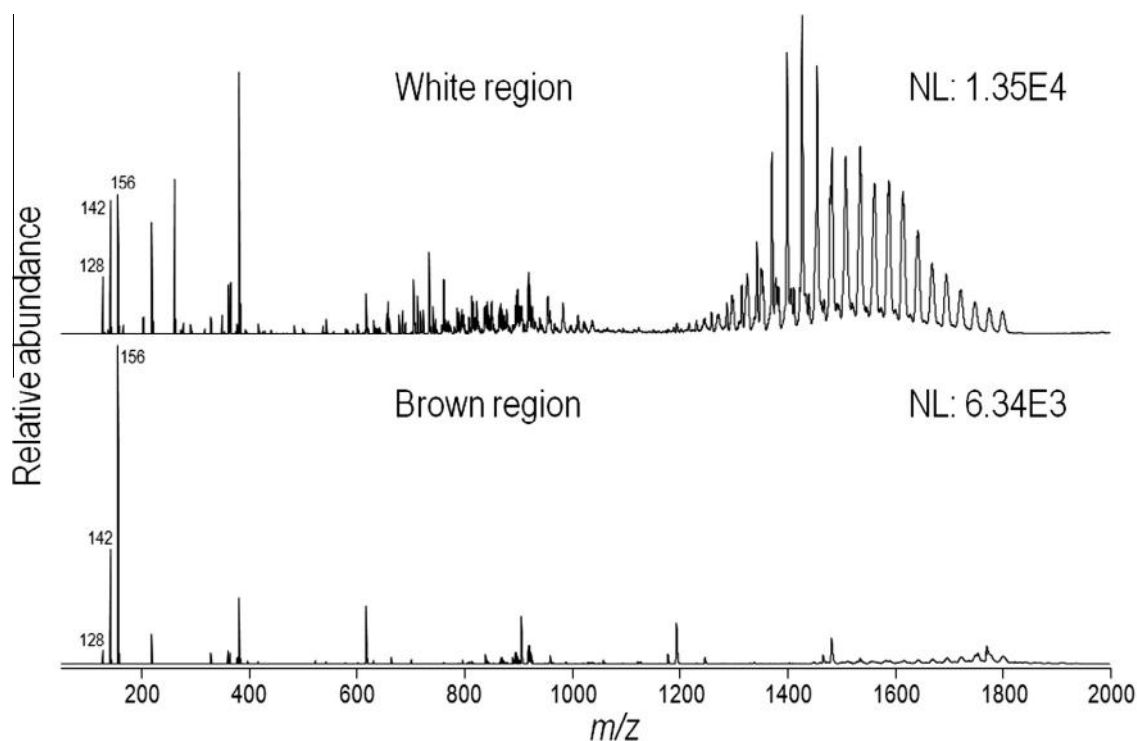


Fig. 5. ESI MS spectra of methanol extracts from W and B regions of stage 2 areca nut.

From ESI MS measurements, it was not possible to distinguish between arecaidine and guvacoline as both of them have the same mass and gave peak at m/z 142 although their presence was confirmed by tandem ESI MS. For that reason, in the subsequent discussion, we have always considered the peak at m/z 142 as a combination of both arecaidine and guvacoline. Besides these, there were several other peaks in the spectrum. For the B region of the sample, the same peaks at m/z 156, 142, and 128 appeared in the spectrum. There were several peaks as well in other regions of

the spectrum and the notable difference between the B and the W regions was in the high mass range where some peaks corresponding to polymeric compounds appeared only for the W region. Fig. 6 shows typical ESI spectra of stage 3 sample. For W region, in the low mass range, there was a peak at m/z 128 while peaks at m/z 156 and 142 were not seen. For the combined sample composed of W and B regions, in the low mass range, all three peaks at m/z 156, 142, and 128 appeared. In both the samples, several other peaks were observed in the spectra. Here, the polymeric peaks of high mass

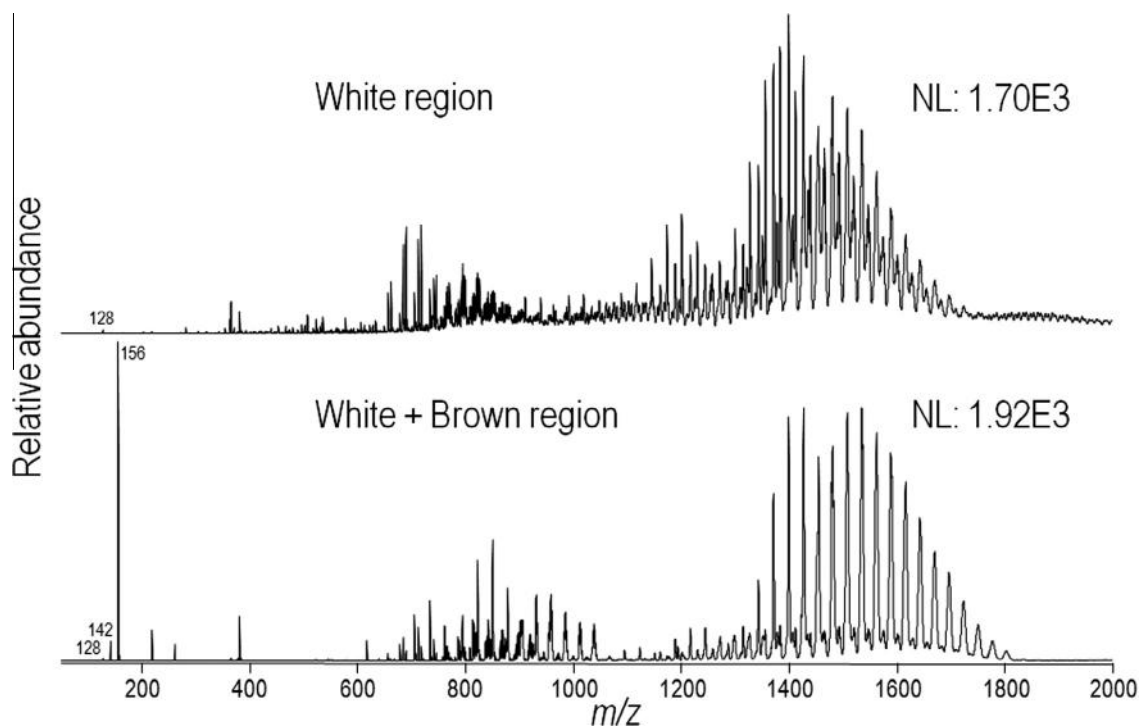


Fig. 6. ESI MS spectra of methanol extracts from W and combined W and B regions of stage 3 areca nut.

range appeared in both the samples as both of them contained W regions.

If we now take a closer look at all the ESI MS data in the low mass range for the four major alkaloids, several things can be understood regarding their distribution during maturity of areca nut. W region of stage 2 sample contains all the four major alkaloids and the abundance of arecoline is almost similar to the combined abundance of arecaidine and guvacoline. Guvacine is present in low abundance. For the B region of the same sample, arecoline is present in very high abundance compared to the others. Once again, the abundance of guvacine is low here as well. When we go to the stage 3 sample, the W region contains only guvacine, other alkaloids are absent here. In the B region, arecoline, arecaidine, and guvacoline are present but the presence of guvacine cannot be confirmed as the sample used here is a combination of both W and B regions and the W region already contains guvacine. Whatever may be the case with guvacine, the relative abundance of arecoline in the B region of stage 3 areca nut is high compared to the other alkaloids.

As ESI MS experiments were not able to provide spatial information about W and B regions of stage 3 areca nut sample, we did DESI MS imaging experiment on the stage 3 sample. The cross-sectioned areca nut of stage 3 was imaged by DESI MS and Fig. 7 shows a photographic image as well as mass spectrometric

images of different ions from the same sample. A representative average DESI MS spectrum of the sample (combination of both W and B regions) obtained from imaging experiment is also shown in Fig. 7. Please note that the peak at m/z 128 is almost in the noise region and it is due to the fact that the spectrum is an average one over both the W and B regions. Fig. 7B and C show the distribution of m/z 156 and 142, respectively. It is clear from Fig. 7B and C that arecoline, arecaidine, and guvacoline are present preferentially in the B region of the nut while these alkaloids are present to a limited extent in the W region. Fig. 7D shows the distribution of m/z 128 and it is evident that guvacine is present preferentially in the W region and only to a very small extent in the B region.

We can conclude from all the mass spectrometric data that in the ripened areca nut, arecoline, arecaidine, and guvacoline get segregated in the B region and guvacine exists in the W region. In an earlier study, it was shown that the concentrations of all the four major alkaloids (arecoline, arecaidine, guvacoline, and guvacine) decrease from the unripe nut to the ripened nut (Wang et al., 1997). In that study, the nut was considered as a whole entity and no differentiation was made between the W and B regions. In the context of our present study and with the input from the earlier study, we can say that individual alkaloid content decreases in ripened areca nut and higher amount of arecoline together with lower amount of arecaidine and guvacoline preferentially stay in the B region while further lower amount of guvacine preferentially stays in the W region of the ripened areca nut.

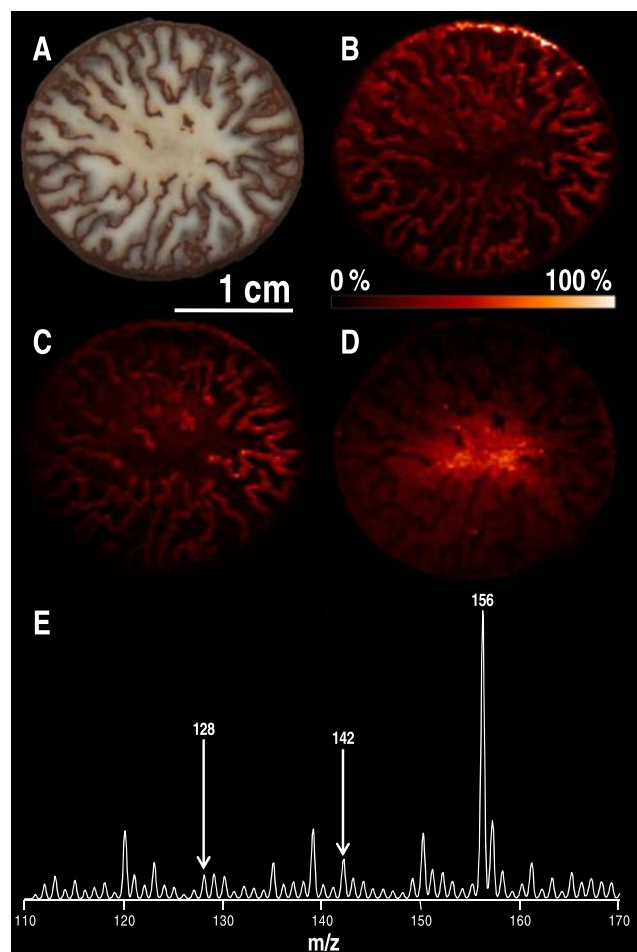


Fig. 7. (A) Photographic image of cross-sectioned stage 3 areca nut and its DESI MS images showing the distribution of (B) m/z 156, (C) m/z 142, and (D) m/z 128. (E) Representative average DESI MS spectrum of stage 3 areca nut sample (combination of both W and B regions) in zoomed view. Scale bar of 1 cm is applied to all the images. Intensities are color coded in B, C, and D.

2.3. Plausible mechanism of areca nut maturation: pattern formation and alkaloids segregation

Based on the results obtained, we speculate a mechanism for the growth of structured patterns in areca nut. As noticed in the MRI images (Fig. 3D and E), the top portion of the nut which is connected to the tree does not get solidified during the initial stage of growth. It is probably to make way to pump in several resources into the nut. At a later stage of growth, the same portion may be used to pump out resources like alkaloids from the nut as the valuable resources needed for the plant are recovered. From the mass spectrometric data it is evident that the W region in the ripened nut (stage 3) contains only guvacine, not other alkaloids which have additional functionalization. Note that all the other alkaloids have functionalization at the nitrogen or carboxyl ends which make them less polar. One probable reason for this preferential retention is that the W region, due to its hydrophilic nature, retains the more polar molecule, in this case, guvacine. Size may also play an important role here and helps to expel bigger molecules more efficiently during the solidification process. During the early stages of solidification, the transportation of alkaloids is possible due to the semi-solid nature of the mass formed. But at the final stages of solidification, transportation of alkaloids becomes difficult and some of the alkaloids cannot go out completely and remain in the nut. That is why the final stage of the nut (stage 3) also contains some alkaloids which are concentrated in the B region. There also exists the possibility of interconversion of these four alkaloids, owing to their structural similarities, during maturation of the nut. Because of the complexity of a real biological system, it is very difficult to assess the mechanism with certainty. The present work is an attempt to give a glimpse into the phenomenon of “maturation of areca nut” and we believe that understanding of the dynamics of the events of molecular transport leading to patterned structures, in conjunction with polymerization and solidification require theoretical modeling. Local concentration of each of the species must be analyzed as a function of time, as also the variation in the chemical structures with time. Patterned structure formation can be fully understood only with these inputs.

3. Conclusions

In the present work, we have shown by MRI that during maturation of areca nut, the liquid content within starts solidifying from the peripheral regions of the nut and solidification process moves towards the center. Volume localized MRS affords fairly high resolution molecular fingerprinting especially at the early stages, and demonstrates the presence of sugars, lipids, and alkaloids, although on commencement of structure formation, the present voxel resolution does not permit differentiation of different zones of the structure in the moderately tender nut. During the solidification process itself, B and W regions start forming. Furthermore, by different mass spectrometric methods, we have also shown that in the ripened areca nut, arecoline, arecaidine, and guvacoline get segregated in the B region while guvacine gets segregated in the W region. As the major fraction of the alkaloids stay in the B region of the ripened areca nut, it is safer to consume the W portion of the ripened nut. Thus areca nut can be used in a safer way to tap its medicinal activities if the W and B regions are separated.

4. Materials and methods

4.1. Materials and reagents

Different stages of areca nut were collected from the farm of Mr. Ravi V. Bhat, located in the state of Karnataka, India. Nuts were plucked at different maturity stages from a cluster of plants grown at the same farm, and were stored at low temperature to prevent any postharvest changes until the experiments were performed in the laboratory. For ESI MS and DESI MS measurements, HPLC grade methanol from Sigma–Aldrich was used.

4.2. MRI and MRS measurements

All the experiments were performed on a 200 MHz 47/40 Bruker BIOSPEC MRI system using a 7.2 cm $^1\text{H}/^{31}\text{P}$ resonator. Multi-slice multi echo images were acquired with the 2D spin echo imaging sequence. For stage 1 and stage 2 samples, images were collected from slices of 1 mm thickness. However, for the sample at stage 3, a slice thickness of 2 mm was used to improve the signal-to-noise-ratio. 2D images were collected from sets of three orthogonal imaging planes. Volume localized NMR was used to monitor the molecular level changes at different stages of growth of areca nut. To this end, point resolved spectroscopy (PRESS) with water suppression (VAPOR with bandwidth 150 Hz) was used with the following parameters: voxel size: $4 \times 4 \times 4 \text{ mm}^3$, number of scans: 256, echo time: 13.408 ms, and repetition time: 2.5 s.

4.3. ESI MS measurements

For ESI MS measurements, a Thermo Scientific LTQ XL mass spectrometer was used. Different portions of areca nut were soaked in methanol overnight (approximately for 12 h) and the resultant extracts were collected, centrifuged, and used for further ESI MS measurements. The extracts were infused with a flow rate of 5 $\mu\text{L}/\text{min}$ and 5 kV spray voltage was used to collect data in positive ionization mode. Tandem mass spectrometric measurements were done with collision induced dissociation (CID).

4.4. DESI MS measurements

For DESI MS measurements, a 2D DESI source from ProSolia was used. It was attached with a Thermo Scientific LTQ XL mass spectrometer. A ripened areca nut was cut in a disk-like shape of about 4 mm thickness and fixed on a glass slide with double sided tape.

The glass slide was then mounted on the DESI stage capable of moving in XY-plane. Methanol was used as spray solvent in DESI MS experiments and it was sprayed with the assistance of 150 psi pressure of nebulizer gas (N_2). DESI spray emitter to surface distance was maintained at 2 mm while the emitter to capillary inlet distance was 3 mm. Other parameters like solvent flow rate 5 $\mu\text{L}/\text{min}$, spray voltage 5 kV, capillary temperature 250 $^\circ\text{C}$, capillary voltage 45 V, and tube lens voltage 100 V were maintained throughout the experiments. Data were collected in positive ionization mode. A pixel size of 250 $\mu\text{m} \times 250 \mu\text{m}$ was used to image a sample area of 30 mm \times 25 mm.

Acknowledgements

T.P. thanks Department of Science and Technology (DST), Govt. of India for financial support and N.C. thanks DST and IIT Madras for spectrometer grants. A.S. thanks Council of Scientific and Industrial Research (CSIR), Govt. of India and IIT Madras for fellowships, C.G. thanks DST for financial support under the Fast Track scheme for young scientists. The authors thank Mr. Ravi V. Bhat for the areca nut samples, Mr. Shreedhar Desai for sharing his traditional knowledge about medicinal usage of areca nut, Dr. A.P. Baburaj and Dr. Ganapati Natarajan for their help and suggestions.

Appendix A. Supplementary data

Supplementary data associated with this article can be found, in the online version, at <http://dx.doi.org/10.1016/j.phytochem.2016.02.002>.

References

- Adhikari, A., De, M., 2013. Toxic effects of betel quid. *Int. J. Hum. Genet.* 13, 7–14.
- Amudhan, M.S., Begum, V.H., Hebbar, K.B., 2012. A review on phytochemical and pharmacological potential of *Areca catechu* L. seed. *Int. J. Pharm. Sci. Res.* 3, 4151–4157.
- Banerjee, A., George, C., Bharathwaj, S., Chandrakumar, N., 2009. Postharvest ripening study of sweet lime (*Citrus limettioides*) in situ by volume-localized NMR spectroscopy. *J. Agric. Food Chem.* 57, 1183–1187.
- Borisjuk, L., Rolletschek, H., Neuberger, T., 2012. Surveying the plant's world by magnetic resonance imaging. *Plant J.* 70, 129–146.
- Byun, S.J., Kim, H.S., Jeon, S.M., Park, Y.B., Choi, M.S., 2001. Supplementation of *Areca catechu* L. extract alters triglyceride absorption and cholesterol metabolism in rats. *Ann. Nutr. Metab.* 45, 279–284.
- Cabral, E.C., Mirabelli, M.F., Perez, C.J., Ifa, D.R., 2013. Blotting assisted by heating and solvent extraction for DESI-MS imaging. *J. Am. Soc. Mass Spectrom.* 24, 956–965.
- Changrani, J., Gany, F., 2005. Paan and Gutka in the United States: an emerging threat. *J. Immigr. Health* 7, 103–108.
- Dave, B.J., Trivedi, A.H., Adhvaryu, S.G., 1992. In vitro genotoxic effects of areca nut extract and arecoline. *J. Cancer Res. Clin. Oncol.* 118, 283–288.
- Fuchs, J., Neuberger, T., Rolletschek, H., Schiebold, S., Nguyen, T.H., Borisjuk, N., Boerner, A., Melkus, G., Jakob, P., Borisjuk, L., 2013. A noninvasive platform for imaging and quantifying oil storage in submillimeter tobacco seed. *Plant Physiol.* 161, 583–593.
- Hada, S., Kakiuchi, N., Hattori, M., Namba, T., 1989. Identification of antibacterial principles against *Streptococcus mutans* and inhibitory principles against glucosyltransferase from the seed of *Areca catechu* L. *Phytother. Res.* 3, 140–144.
- Han, X., Shen, T., Lou, H., 2007. Dietary polyphenols and their biological significance. *Int. J. Mol. Sci.* 8, 950–988.
- Ifa, D.R., Srimany, A., Eberlin, L.S., Naik, H.R., Bhat, V., Cooks, R.G., Pradeep, T., 2011. Tissue imprint imaging by desorption electrospray ionization mass spectrometry. *Anal. Methods* 3, 1910–1912.
- Ishida, N., Koizumi, M., Kano, H., 2000. The NMR microscope: a unique and promising tool for plant science. *Ann. Bot.* 86, 259–278.
- Jeng, J.H., Chang, M.C., Hahn, L.J., 2001. Role of areca nut in betel quid-associated chemical carcinogenesis: current awareness and future perspectives. *Oral Oncol.* 37, 477–492.
- Kim, B.J., Kim, J.H., Kim, H.P., Heo, M.Y., 1997. Biological screening of 100 plant extracts for cosmetic use (II): anti-oxidative activity and free radical scavenging activity. *Int. J. Cosmet. Sci.* 19, 299–307.
- Kumar, S., 2008. Panmasala chewing induces deterioration in oral health and its implications in carcinogenesis. *Toxicol. Mech. Methods* 18, 665–677.
- Manz, B., Mueller, K., Kucera, B., Volke, F., Leubner-Metzger, G., 2005. Water uptake and distribution in germinating tobacco seeds investigated in vivo by nuclear magnetic resonance imaging. *Plant Physiol.* 138, 1538–1551.

- Mhaske, S., Ragavendra, T.R., Dangi, C.B.S., 2009. Areca nut as chemical carcinogen in oral squamous cell carcinoma – a review. *Biomed. Pharmacol. J.* 2, 437–440.
- Mohana Kumara, P., Srimany, A., Ravikanth, G., Uma Shaanker, R., Pradeep, T., 2015. Ambient ionization mass spectrometry imaging of rohitukine, a chromone anticancer alkaloid, during seed development in *Dysoxylum binectariferum* Hook.f (Meliaceae). *Phytochemistry* 116, 104–110.
- Monge, M.E., Harris, G.A., Dwivedi, P., Fernandez, F.M., 2013. Mass spectrometry: recent advances in direct open air surface sampling/ionization. *Chem. Rev.* 113, 2269–2308.
- Muller, T., Oradu, S., Ifa, D.R., Cooks, R.G., Krautler, B., 2011. Direct plant tissue analysis and imprint imaging by desorption electrospray ionization mass spectrometry. *Anal. Chem.* 83, 5754–5761.
- Nair, U., Bartsch, H., Nair, J., 2004. Alert for an epidemic of oral cancer due to use of the betel quid substitutes gutkha and pan masala: a review of agents and causative mechanisms. *Mutagenesis* 19, 251–262.
- Park, Y.B., Jeon, S.-M., Byun, S.-J., Kim, H.-S., Choi, M.-S., 2002. Absorption of intestinal free cholesterol is lowered by supplementation of *Areca catechu* L. extract in rats. *Life Sci.* 70, 1849–1859.
- Peng, W., Liu, Y.-J., Wu, N., Sun, T., He, X.-Y., Gao, Y.-X., Wu, C.-J., 2015. *Areca catechu* L. (Arecaceae): a review of its traditional uses, botany, phytochemistry, pharmacology and toxicology. *J. Ethnopharmacol.* 164, 340–356.
- Polasa, K., Babu, S., Shenolikar, I.S., 1993. Dose-dependent genotoxic effect of pan masala and areca nut in the *Salmonella typhimurium* assay. *Food Chem. Toxicol.* 31, 439–442.
- Srimany, A., Ifa, D.R., Naik, H.R., Bhat, V., Cooks, R.G., Pradeep, T., 2011. Direct analysis of camptothecin from *Nothapodytes nimmoniana* by desorption electrospray ionization mass spectrometry (DESI-MS). *Analyst* 136, 3066–3068.
- Sundqvist, K., Liu, Y., Nair, J., Bartsch, H., Arvidson, K., Grafstrom, R.C., 1989. Cytotoxic and genotoxic effects of areca nut-related compounds in cultured human buccal epithelial cells. *Cancer Res.* 49, 5294–5298.
- Takats, Z., Wiseman, J.M., Gologan, B., Cooks, R.G., 2004. Mass spectrometry sampling under ambient conditions with desorption electrospray ionization. *Science* 306, 471–473.
- Thunig, J., Hansen, S.H., Janfelt, C., 2011. Analysis of secondary plant metabolites by indirect desorption electrospray ionization imaging mass spectrometry. *Anal. Chem.* 83, 3256–3259.
- Ullah, M., Cox, S., Kelly, E., Boadle, R., Zoellner, H., 2014. Arecoline is cytotoxic for human endothelial cells. *J. Oral Pathol. Med.* 43, 761–769.
- Wang, C.-K., Lee, W.-H., Peng, C.-H., 1997. Contents of phenolics and alkaloids in *Areca catechu* Linn. during maturation. *J. Agric. Food Chem.* 45, 1185–1188.
- Wetwitayaklung, P., Phaechamud, T., Limmatvapirat, C., Keokitchai, S., 2006. The study of antioxidant capacity in various parts of *Areca catechu* L. *Naresuan Univ. J.* 14, 1–14.
- Yenrina, R., Nazir, N., Lubis, A.S., 2014. Unripe Areca (*Areca catechu* L.) Nut Syrup as a functional drinks with addition of powdered Cassia Vera extract. *Asia Pac. J. Sustainable Agric. Food Energy* 2, 17–22.
- Zhang, W.-M., Huang, W.-Y., Chen, W.-X., Han, L., Zhang, H.-D., 2014. Optimization of extraction conditions of areca seed polyphenols and evaluation of their antioxidant activities. *Molecules* 19, 16416–16427.
- Zhang, X., Reichart, P.A., 2007. A review of betel quid chewing, oral cancer and precancer in Mainland China. *Oral Oncol.* 43, 424–430.
- Zhang, X., Wu, J., Han, Z., Mei, W.-L., Dai, H.-F., 2010. Antioxidant and cytotoxic phenolic compounds of areca nut (*Areca catechu*). *Chem. Res. Chinese Univ.* 26, 161–164.

Supplementary Material

Developmental patterning and segregation of alkaloids in areca nut (seed of *Areca catechu*) revealed by magnetic resonance and mass spectrometry imaging

Amitava Srimany,^a Christy George,^{b+} Hemanta R. Naik,^a Danica Glenda Pinto,^a

N. Chandrakumar^{b*} and T. Pradeep^{a*}

^aDST Unit of Nanoscience (DST UNS) and Thematic Unit of Excellence (TUE), Department of Chemistry, Indian Institute of Technology Madras, Chennai 600036, India

^bMRI-MRS Centre, Department of Chemistry, Indian Institute of Technology Madras, Chennai 600036, India

⁺Present address: Francis Bitter Magnet Lab and Department of Chemistry, Massachusetts Institute of Technology, Cambridge, MA 02139, USA

The location of the typical voxel chosen is depicted in Fig. S1.

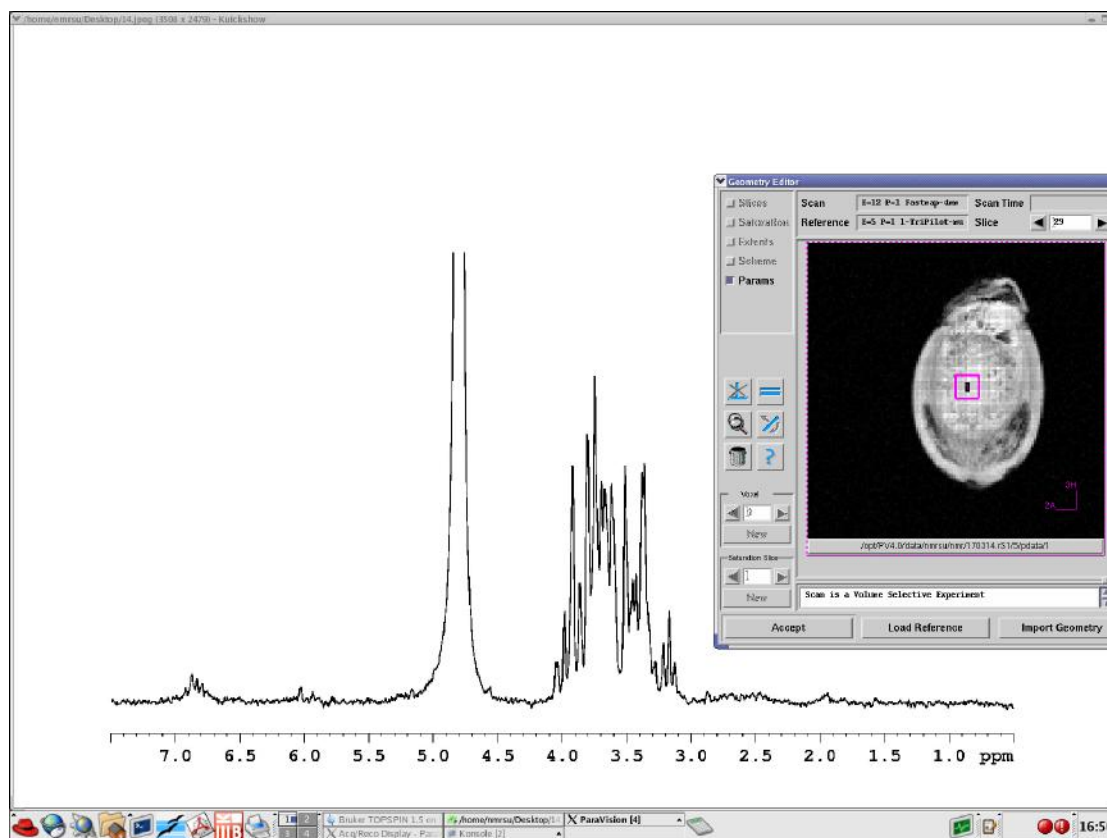


Fig. S1. Screenshot of volume localized NMR spectrum, with inset showing the selected voxel depicted in pink outline.

A representative spectrum obtained from the earliest stage of development, prior to inception of villi-like structure formation, is shown in Fig. S2.

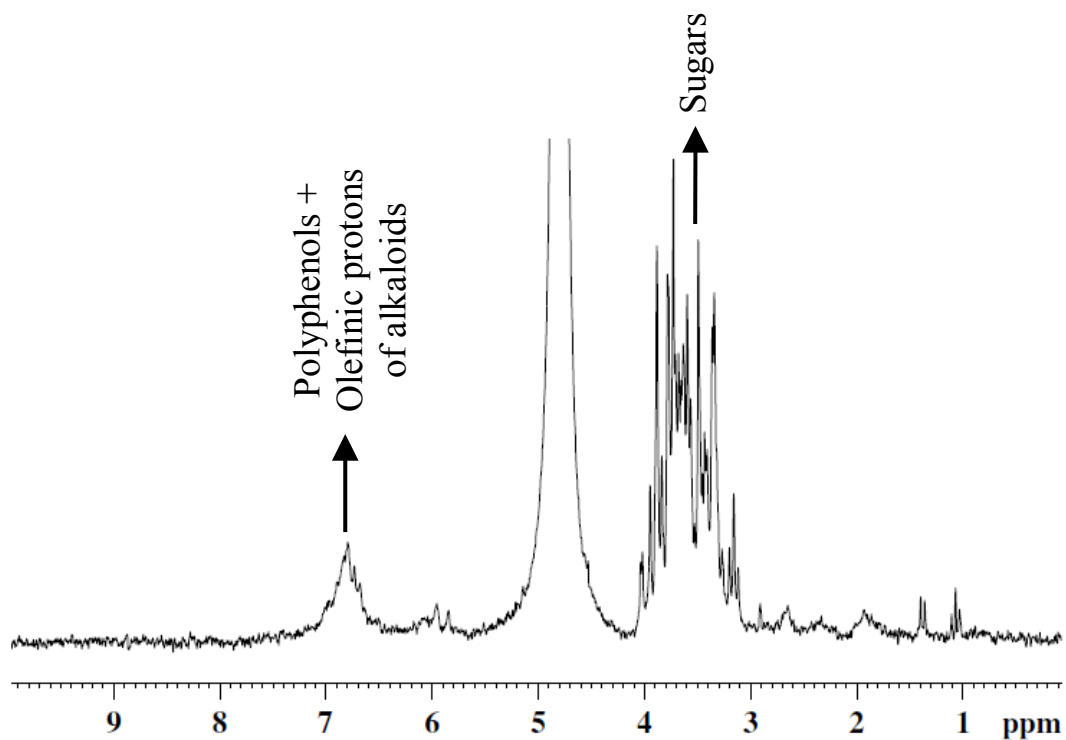


Fig. S2. A representative volume localized NMR spectrum from the initial (pre-tender) stage of areca nut development. Experimental parameters are same as in the main text.

Lipid content seems to increase considerably as the fruit ripens (at 1.5 ppm). Fig. S3 shows the changes observed in the various stages of growth of the areca nut.

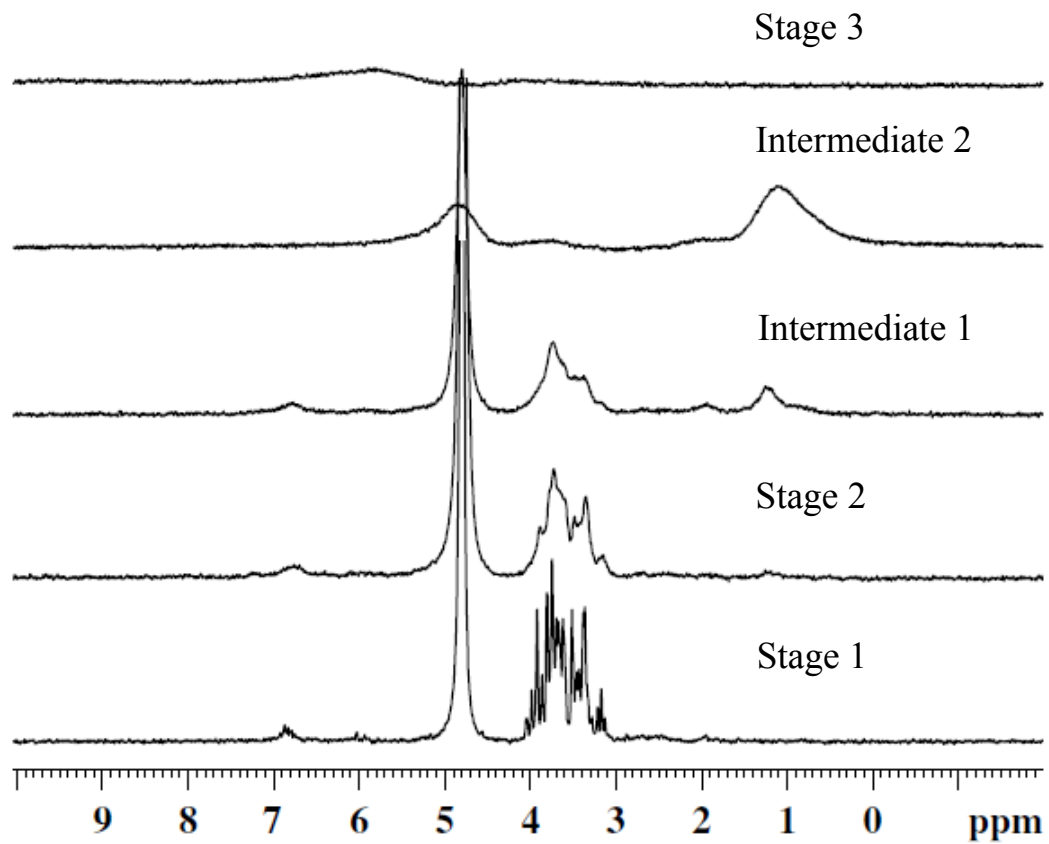


Fig. S3. Bottom to top: volume localized NMR spectra from the initial stage of areca nut development to the final stage.

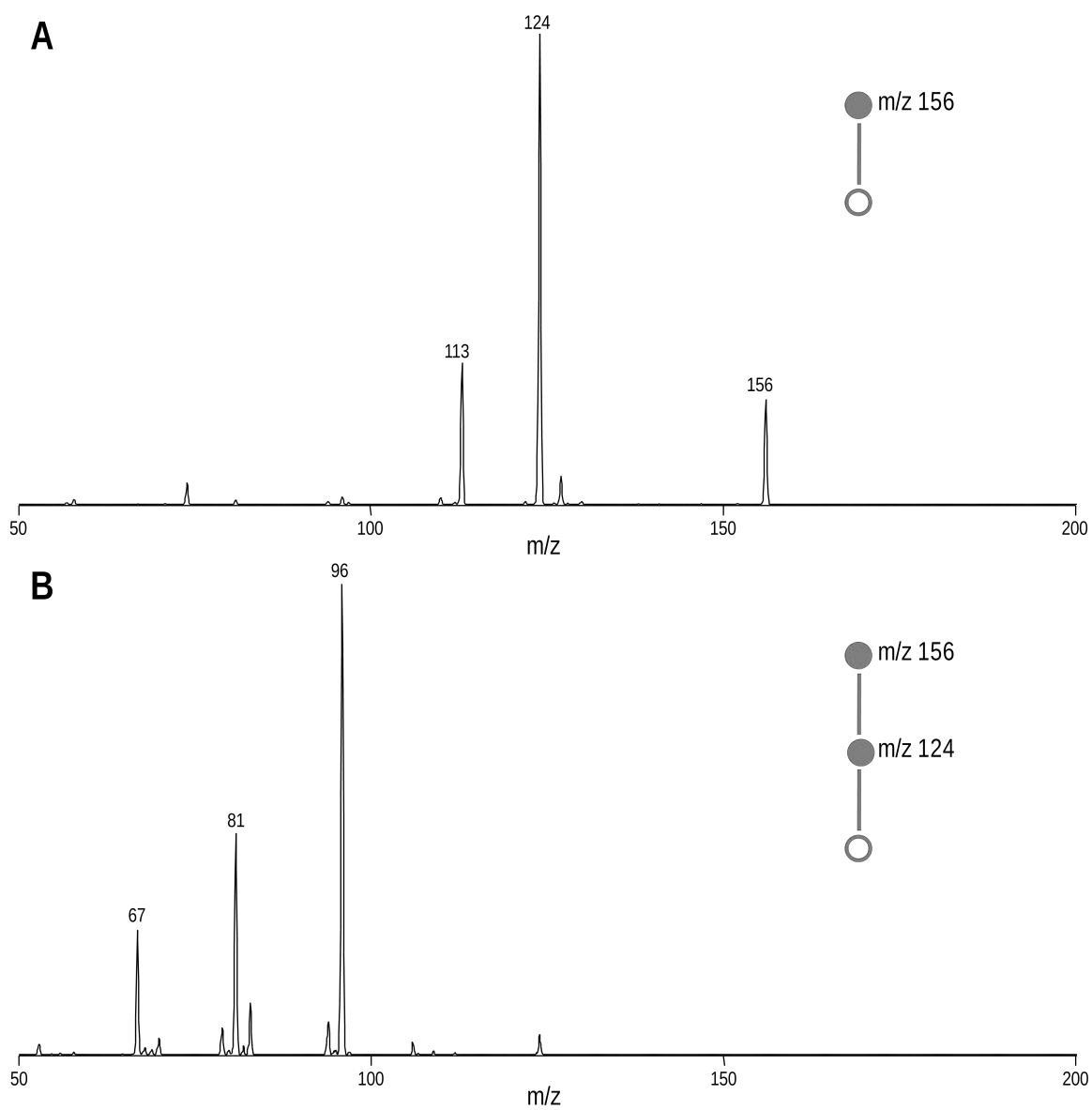


Fig. S4. Tandem ESI mass spectra of arecoline (m/z 156) from methanolic extract of areca nut.

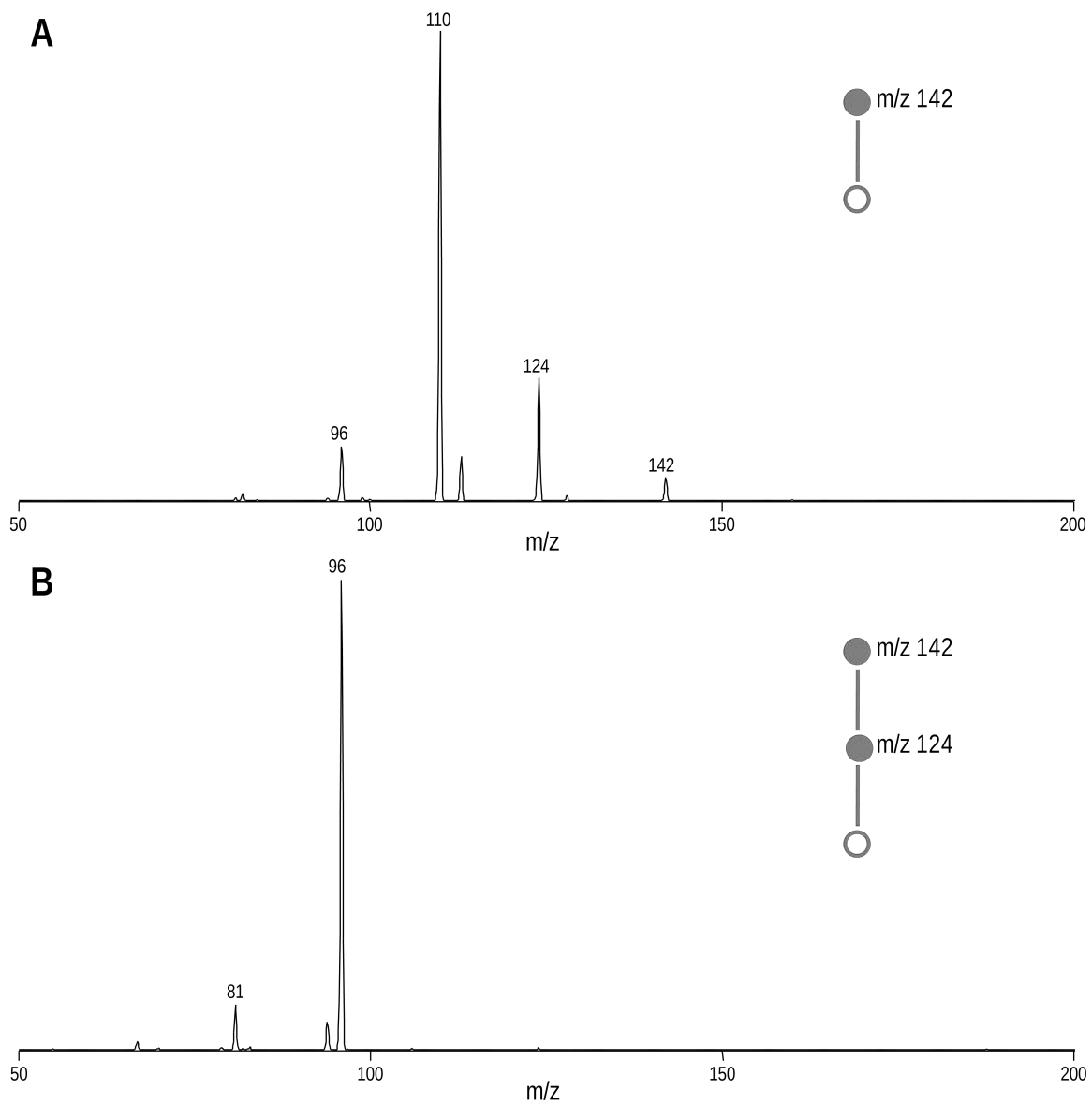


Fig. S5. Tandem ESI mass spectra of arecaidine (m/z 142) from methanolic extract of areca nut.

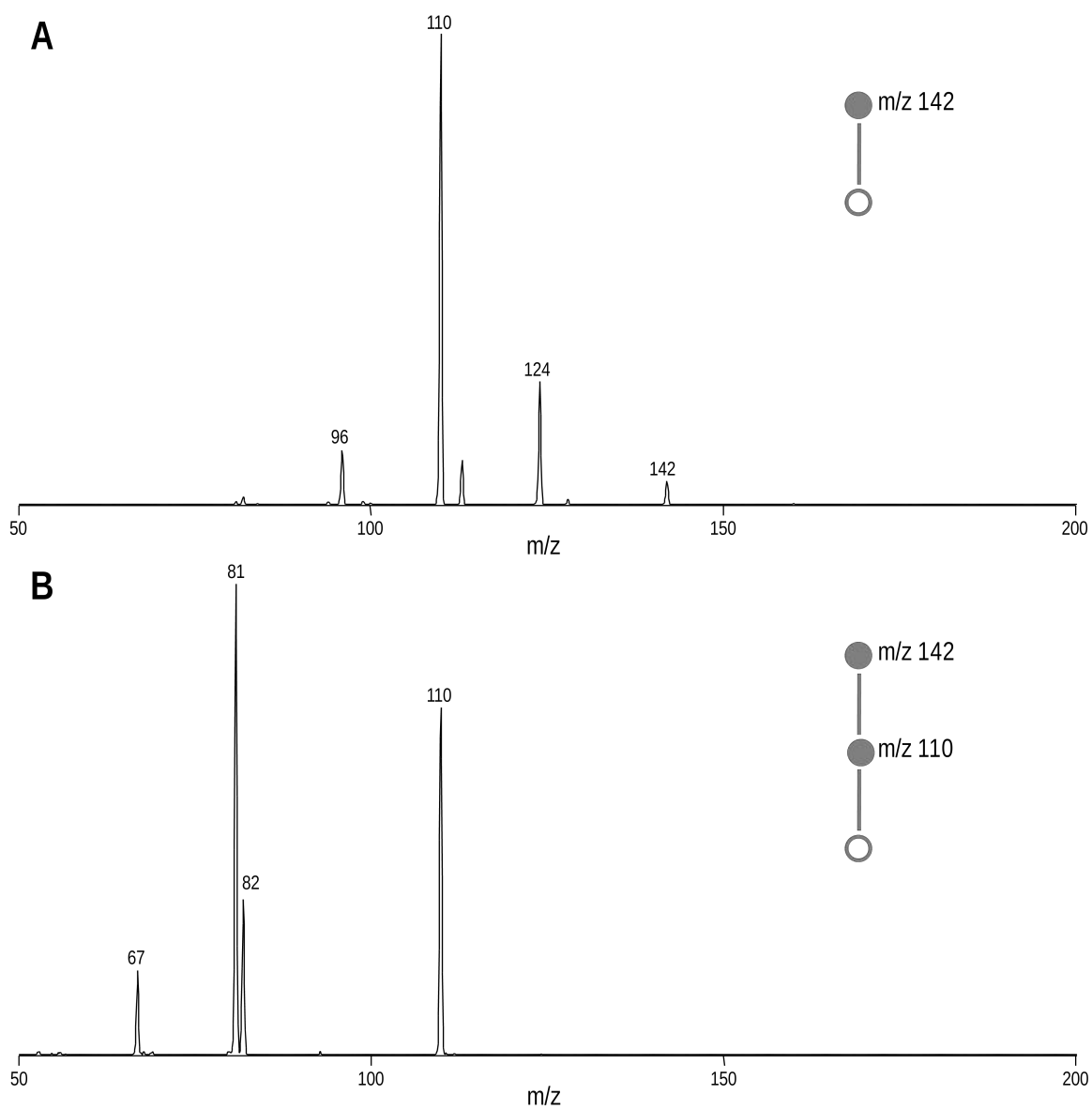


Fig. S6. Tandem ESI mass spectra of guvacoline (m/z 142) from methanolic extract of areca nut.

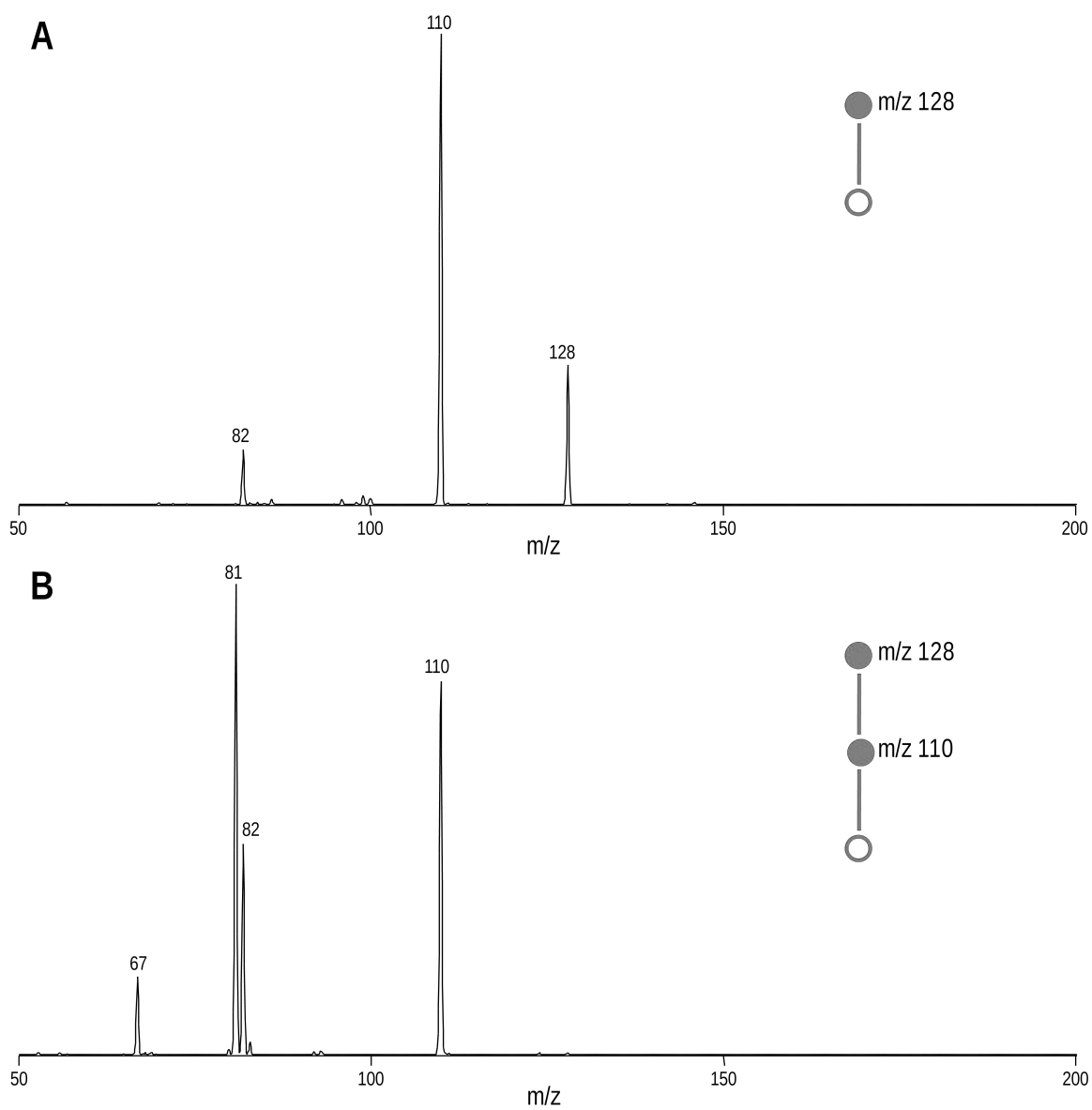


Fig. S7. Tandem ESI mass spectra of guvacine (m/z 128) from methanolic extract of areca nut.



Cite this: *Chem. Commun.*, 2016, 52, 3805

Received 3rd November 2015,
Accepted 27th January 2016

DOI: 10.1039/c5cc09119e

www.rsc.org/chemcomm

Possible isomers in ligand protected Ag₁₁ cluster ions identified by ion mobility mass spectrometry and fragmented by surface induced dissociation†

Ananya Baksi,‡^a Sophie R. Harvey,‡^{b,c} Ganapati Natarajan,^a Vicki H. Wysocki*^{b,d} and Thalappil Pradeep*^a

This communication reports the identification of gas phase isomers in monolayer-protected silver clusters. Two different isomers of Ag₁₁(SG)₇⁻ (SG-gulathione thiolate) with different drift times have been detected using combined electrospray ionization (ESI) and ion mobility (IM) mass spectrometry (MS). Surface induced dissociation (SID) of the 3⁻ charge state of such clusters shows charge stripping to give the 1⁻ charged ion with some sodium attachment, in addition to fragmentation. SID and collision induced dissociation (CID) for Ag₁₁(SG)₇⁻ suggest different pathways being accessed with each method. SID was introduced for the first time for the study of monolayer-protected clusters.

Atomically precise monolayer protected clusters (MPCs) of gold and silver belong to a fascinating area of research due to their unique optoelectronic properties and wide range of applications in materials science, electronics, catalysis and biology.^{1–3} Several clusters have been synthesized and many of them have been crystallized including Au₂₅(SR)₁₈,^{4,5} Au₃₀S(SR)₁₈,⁶ Au₃₆(SR)₂₄,⁷ Au₃₈(SR)₂₄,⁸ Au₆₈(SR)₃₂⁹ and Au₁₀₂(SR)₄₄.¹⁰ Some of the silver clusters have also been crystallized including [Ag₁₄(SR)₁₂(PPh₃)₈],¹¹ [Ag₁₆(DPPE)₄(SR)₁₄],¹² [Ag₃₂(DPPE)₅(SCR)₂₄]¹² (DPPE: 1,2-bis-(diphenylphosphino)ethane), Ag₄₄(SR)₃₀^{13,14} and most recently, Ag₂₅(SR)₁₈¹⁵ (SR corresponds to various thiolate ligands). Crystal structures of some of the alloy clusters consisting of Au/Ag^{13,16} and Au/Cu¹⁷ have also been solved. While some of the clusters could be crystallized, there are several others which were identified by optical spectroscopy and mass spectrometry (MS) along with structural insights from theoretical calculations, mainly

density functional theory (DFT).^{18–35} Only a few clusters are known to show well defined mass spectrometric signatures namely, Ag₉(MSA)₇,¹⁸ Ag₁₁(SG)₇,³⁶ Ag₁₅(SG)₁₁,³⁷ Ag₃₁(SG)₁₉,³⁷ Ag₃₂(SG)₁₉,²⁷ Ag₄₄(SR)₃₀,¹⁹ Ag₇₅(SG)₄₀,³⁸ etc., where SG refers to the thiolate form of glutathione. Au₂₅(SR)₁₈ is one of the most widely and systematically studied systems from both experimental and theoretical points of view.^{5,28,34,39–41} The crystal structure reveals the presence of an Au₁₃ core and 6 Au₂(SR)₃ staple motifs.^{4,5} Fragmentation from the core as well as the staple has been identified by an ESI MS/MS study by Angle *et al.*³⁹ In another theoretical study, Liu *et al.* have identified the stepwise fragmentation of the staple motifs as the most favourable fragmentation pathway for Au₂₅(SR)₁₈.⁴² These researchers have shown different isomeric structures of the core which could be responsible for fragmentation and catalytic properties of the clusters.

Due to the core as well as ligand orientation, MPCs can have isomeric forms. However, no isomeric structures have been reported to date for ions in the gas phase. In this context, ion mobility-mass spectrometry (IM-MS), which can separate ions based not only on their mass and charge but also on their size and shape, known as their rotationally averaged collision cross-section (CCS), has great potential. Different conformations can be separated by IM based on differences in their CCS, as is evident from several studies on proteins and other biomolecules.^{43–45} There are a few reports on the use of IM-MS on monolayer protected Au clusters and nanoparticles.^{46–50} For example, Au₂₅(SR)₁₈ cluster fragments were identified by ion mobility.³⁹ Symmetric drift time distribution of these clusters suggested the presence of only one structure or interconverting isomers.³⁹ There is no report on monolayer protected silver clusters which were separated by IM-MS.

Here, we report the first observation of the presence of ligand induced isomers of Ag₁₁(SG)₇⁻ by ESIM-MS where two isomers can be distinguished by their different drift times. We also introduce surface induced dissociation (SID) as a method of fragmentation to study such clusters for the first time where charge stripping can generate deprotonated peaks from a higher charged species, in addition to fragmentation. SID is known to result in significantly different fragmentation pathways for

^a DST Unit of Nanoscience (DST UNS), and Thematic Unit of Excellence (TUE), Department of Chemistry, Indian Institute of Technology Madras, Chennai - 600 036, India. E-mail: pradeep@iitm.ac.in; Fax: +91-44-2257 0509/0545; Tel: +91-44-2257 4208

^b Department of Chemistry and Biochemistry, The Ohio State University, Columbus, Ohio, USA

^c School of Chemistry, Manchester Institute of Biotechnology, University of Manchester, Manchester, M1 7DN, UK

† Electronic supplementary information (ESI) available. See DOI: 10.1039/c5cc09119e
‡ A. B. and S. R. H. have contributed equally.

protein complexes in comparison to CID. We observed different types of fragmentation in SID and CID for $\text{Ag}_{11}(\text{SG})_7\text{Na}_n^{3-}$ suggesting that different pathways are being accessed with each method.^{51,52}

This $\text{Ag}_{11}(\text{SG})_7$ was synthesized by a recently reported method.³⁶ Synthesis and characterization of $\text{Ag}_{11}(\text{SG})_7$ are discussed briefly in ESI.†

An ion mobility study of the clusters using a Waters Synapt G2S instrument capable of measuring drift times and mass spectra simultaneously is presented here. The instrument was in-house modified to incorporate an SID device located before the IM cell.⁵³ Fig. 1A shows a zoom in plot of ion drift time *versus* m/z obtained, highlighting the species of interest, namely $\text{Ag}_{11}(\text{SG})_7\text{Na}_n^{3-}$ (where $n = 3$ and 4). This is the prominent peak observed for the species. About 2–7 Na attached peaks were observed among which 3 and 4 Na additions are the most intense, and are shown in Fig. 1B; the isotope distributions of which match well with the theoretically calculated distribution. For each envelope, there are two species with slightly different structures. This is reflected in the similarity of their drift times, as shown in the plot of ion drift time *versus* m/z (Fig. 1A) as well as in the drift profile (Fig. 1C); in both cases two distributions can be observed.

A sharp peak in the drift time at 4.7 ms is due to the main structural isomer. However, another peak appears around 5.6 ms, which is due to a structural isomer of lower intensity. The relative abundance of the peaks was calculated from the area under each peak. Note that in the previous study of $\text{Au}_{25}(\text{SCH}_2\text{CH}_2\text{Ph})_{18}^-$ a symmetric drift profile was observed indicating the absence of isomers. DFT calculations of the present clusters suggested an Ag_7 core, one $\text{Ag}_2(\text{SG})_3$ staple and two $\text{Ag}(\text{SG})_2$ staples. Six possible structures were reported in the previous work, which are discussed in the ESI.† Considering the energies and HOMO–LUMO gaps along with the observed absorption spectrum, the two structures are of similar energy and stability. Therefore, it is indeed possible that both the structures can co-exist leading to two isomeric forms as seen in IM-MS. The structures are described in the ESI† (see Fig. S7) in detail. Between these two structures, one is more compact compared to the other considering inward and outward projection of the ligands. These structures were calculated

considering SME instead of the whole GSH as the ligand. In the case of isomers, the structures should be calculated with the intact GSH ligand but due to the large number of atoms ($\text{Ag}_{11}\text{C}_{70}\text{H}_{102}\text{N}_{21}\text{O}_{42}\text{S}_7$ for an intact $\text{Ag}_{11}\text{SG}_7$ cluster) it is difficult. Being a tripeptide, GSH has an inherent tendency to make H-bonds with adjacent ligands, which can also lead to isomerism. The two peaks with different drift times may be ascribed to isomers having different structures of the glutathione moieties on identical AgS backbones. The coulombic repulsion between the ligands of multiply charged $\text{Ag}_{11}(\text{SG})_7$ may induce isomerization as in the case of multiply-charged proteins in the gas phase. Considering all these possibilities, the presence of multiple isomers in IM measurements is understandable.

These clusters show good mass spectral signatures, which allowed us to proceed further to see the fragmentation pattern from a specific charge state. The instrument is capable of dissociating any of these ions in both SID and CID modes. In the CID mode, we observed the usual fragments of $\text{Ag}_{11}(\text{SG})_7\text{Na}_n^{3-}$ (which is actually $[\text{Ag}_{11}(\text{SG})_7-n\text{H} + n\text{Na}]^{3-}$). AgSG^- loss was apparent as the main fragmentation pathway to give $\text{Ag}_{10}(\text{SG})_6\text{Na}_n^{2-}$ at the lowest collision energy (Fig. 2A). The fragment AgSG^- is detected at the lower mass range. With increasing collision energy, lower mass fragments were observed. Mostly the fragmentation occurs *via* AgSG^- loss.

The smallest fragment observed was AgSG^- at the highest collision energy (Fig. 2A, additional details are in Fig. S2–S5, ESI†) at the mass range studied. However, at the lower mass range (< 500 Da), AgSG^- is seen as a major peak along with SG^- and its fragments from SG^- . A corresponding change is also observable from the drift time profile where shorter drift times imply smaller, more compact fragments (Fig. 2B and C). Interestingly, one ligand loss from the parent ion gives $\text{Ag}_{10}(\text{SG})_6\text{Na}_n^{2-}$ with a drift time of 8.2 ms, causing a loss of the isomeric structure (only one peak in the drift profile) which implies that the isomerism is ligand induced in this case. Detecting only one isomeric structure for the fragment could also be due to annealing of the ion as a result of CID. Another ligand loss at slightly higher energy resulted in $\text{Ag}_{10}(\text{SG})_5\text{Na}_n^{2-}$ (a drift time of 7.0 ms) where no isomeric structure has been observed.

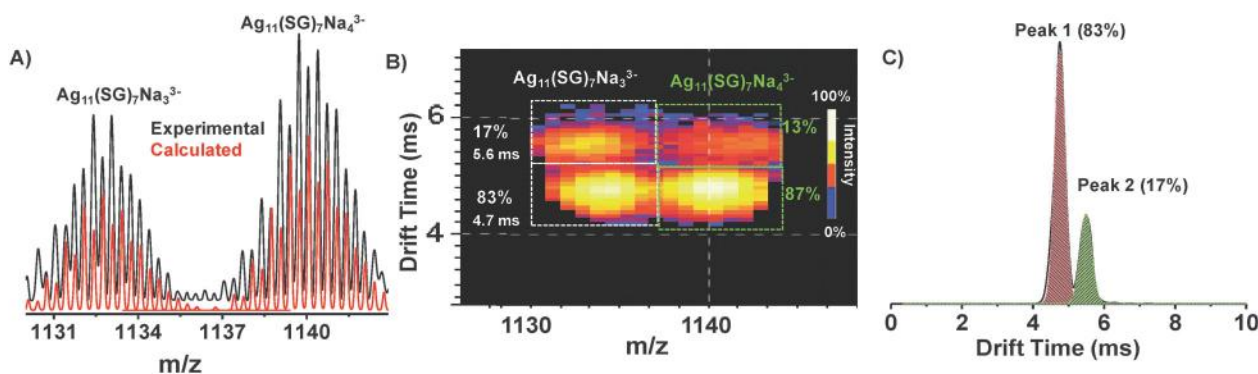


Fig. 1 (A) Zoom in view of the ESI MS of $\text{Ag}_{11}(\text{SG})_7$ showing 3-charged ion with three and four Na attachments. The peaks match exactly with the theoretically calculated pattern. (B) Plot of ion mobility drift time *versus* m/z of $\text{Ag}_{11}(\text{SG})_7\text{Na}_3^{3-}$ and $\text{Ag}_{11}(\text{SG})_7\text{Na}_4^{3-}$ is showing the presence of two isomeric species. Relative abundances of the isomers found from the drift profiles are labelled. Drift profile of $\text{Ag}_{11}(\text{SG})_7\text{Na}_3^{3-}$ is shown in (C) where two clear peaks indicate the presence of two isomeric structures. Relative abundances of the isomers were found by calculating the area under each peak.

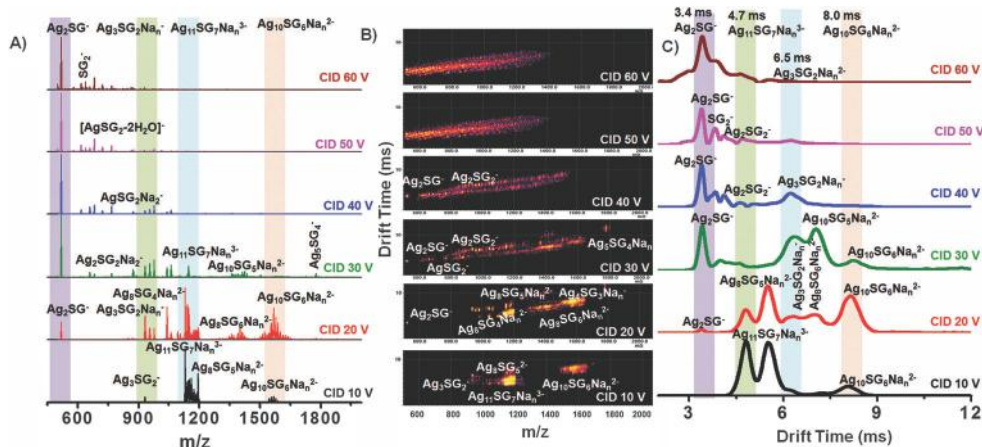


Fig. 2 (A) CID of $\text{Ag}_{11}(\text{SG})_7\text{Na}_n^{3-}$ with major products labeled. Corresponding drift time plots of ion mobility drift time versus m/z are shown in (B) and the respective peaks are labeled. Corresponding drift time profiles are shown in (C). Each of these plot of ion drift time versus m/z and the mass spectra are shown separately in Fig. S2–S5 (ESI[†]). Major fragments are marked with highlight.

This fragmentation is due to the loss of one $\text{Ag}(\text{SG})_2$ staple which might be responsible for the disappearance of the isomeric structure. Each of these staples is directly linked to two Ag atoms of the core. Therefore, loss of one staple will directly affect the core conformation and hence the isomeric structure. Other smaller fragments observed in CID also do not exhibit any isomers. A probable fragmentation pathway is shown in Scheme 1 along with the drift time of the resulting fragments. The peaks are assigned to respective ions in Fig. 2B. The plot of ion mobility drift time versus m/z shown in Fig. 2B for each CE is expanded in the ESI[†] (Fig. S2–S5). Note that all the data presented for the plot of ion drift time versus m/z are as obtained from Driftscope V2.8 software and are presented without any change. SID of the same species on a fluorocarbon self-assembled monolayer (SAM) grown on a gold-coated surface showed completely different types of fragmentation. SID differs from CID in the sense that fragmentation results from a single collision with the surface, as opposed to multiple collisions as in the case of CID. Details of the instrumental parameters are listed in the ESI[†]. In SID at the lowest energy used here, one AgSG loss was observed for $\text{Ag}_{11}(\text{SG})_7\text{Na}_n^{3-}$ as seen for CID (see Fig. 3). We have observed two isomeric species of $\text{Ag}_{10}(\text{SG})_6\text{Na}_n^{3-}$, with a drift time of 8.2 ms as the major component and a smaller peak at 8.6 ms as the minor one, which was absent in CID. This may be explained in terms of different types of fragmentation channels of

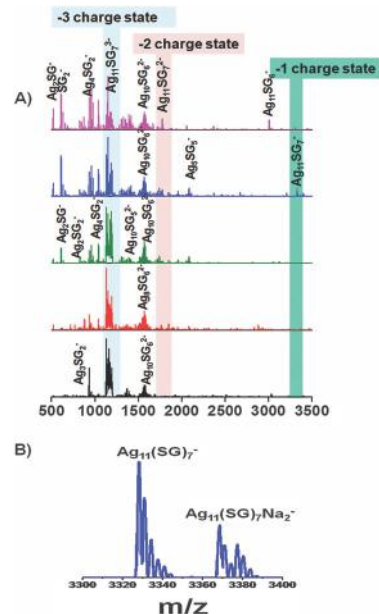
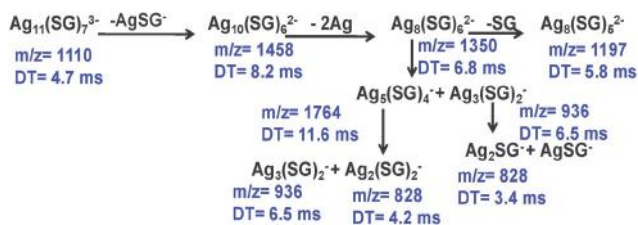


Fig. 3 (A) SID of $\text{Ag}_{11}(\text{SG})_7\text{Na}_n^{3-}$ at increased voltage shows multiple fragmentations at all the energies, unlike in CID. At higher voltages, charge stripping was observed to give a -2 charged species and finally at SID 40, -1 ion peak was observed. Two Na attached peaks were also observed as expanded in (B).

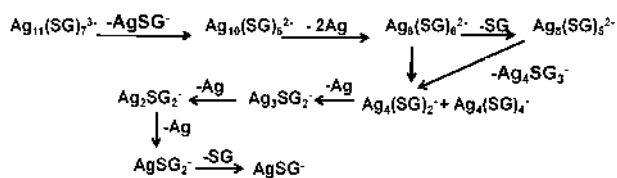
Probable Fragmentation Pathways in Collision Induced Dissociation (CID)



Scheme 1 Probable fragmentation pathways in CID.

the isomeric $\text{Ag}_{11}(\text{SG})_7\text{Na}_n^{3-}$ precursor upon different amounts of internal energy transfer. As we increase the energy, more and more fragmentations to smaller thiolates were observed. Unlike CID, at similar energy (ΔV) in SID, a wide range of fragment ions were observed including the main precursor ion. SID at 30 V, we observed charge stripping of the ion from -3 to -2 . Upon SID at 40 V, the -1 peak was also observed. Charge stripping from a higher charged species to a lower charge was not observed before for any other cluster (both Au and Ag) although this is commonly seen for proteins. Fragments and probable fragmentation pathways observed are shown in Scheme 2.

Probable Fragmentation Pathways in Surface Induced Dissociation (SID)



Scheme 2 Probable fragmentation pathways in SID.

Ligand induced isomerism was confirmed from the proposed structures as well as CID. SID showed the presence of two structural isomers, which might be due to the different types of configurations of the cluster, which fragment differently upon colliding with the surface. At higher voltages (in SID), charge stripping of -3 charged ions resulted in the formation of deprotonated ions, which has not been observed in any cluster system. Similar studies may be used to identify the presence of isomeric clusters, which will expand the science of noble metal clusters.

T. P. and A. B. thank the Department of Science and Technology India for funding. A. B. thanks CSIR India for a fellowship. The authors acknowledge financial support from the National Science Foundation (NSF DBI 0923551 to VHW) and the Engineering and Physical Sciences Research Council UK (for the Doctoral Prize Fellowship awarded to SRH). We thank Prof. Hannu Hakkinen for useful discussions on the proposed isomeric structures.

References

- 1 A. Mathew and T. Pradeep, *Part. Part. Syst. Charact.*, 2014, **3**, 1017.
- 2 T. Udayabhaskararao and T. Pradeep, *J. Phys. Chem. Lett.*, 2013, **4**, 1553.
- 3 R. Jin, *Nanoscale*, 2010, **2**, 343.
- 4 M. W. Heaven, A. Dass, P. S. White, K. M. Holt and R. W. Murray, *J. Am. Chem. Soc.*, 2008, **130**, 3754.
- 5 M. Zhu, C. M. Aikens, F. J. Hollander, G. C. Schatz and R. Jin, *J. Am. Chem. Soc.*, 2008, **130**, 5883.
- 6 D. Crasto, S. Malola, G. Brosofsky, A. Dass and H. Hakkinen, *J. Am. Chem. Soc.*, 2014, **136**, 5000.
- 7 C. Zeng, H. Qian, T. Li, G. Li, N. L. Rosi, B. Yoon, R. N. Barnett, R. L. Whetten, U. Landman and R. Jin, *Angew. Chem., Int. Ed.*, 2012, **51**, 13114.
- 8 H. Qian, W. T. Eckenhoff, Y. Zhu, T. Pintauer and R. Jin, *J. Am. Chem. Soc.*, 2010, **132**, 8280.
- 9 M. Azubel, J. Koivisto, S. Malola, D. Bushnell, G. L. Hura, A. L. Koh, H. Tsunoyama, T. Tsukuda, M. Pettersson, H. Haekkinen and R. D. Kornberg, *Science*, 2014, **345**, 909.
- 10 P. D. Jadzinsky, G. Calero, C. J. Ackerson, D. A. Bushnell and R. D. Kornberg, *Science*, 2007, **318**, 430.
- 11 H. Yang, J. Lei, B. Wu, Y. Wang, M. Zhou, A. Xia, L. Zheng and N. Zheng, *Chem. Commun.*, 2013, **49**, 300.
- 12 H. Yang, Y. Wang and N. Zheng, *Nanoscale*, 2013, **5**, 2674.
- 13 H. Yang, Y. Wang, H. Huang, L. Gell, L. Lehtovaara, S. Malola, H. Hakkinen and N. Zheng, *Nat. Commun.*, 2013, **4**, 2422.
- 14 A. Desireddy, B. E. Conn, J. Guo, B. Yoon, R. N. Barnett, B. M. Monahan, K. Kirschbaum, W. P. Griffith, R. L. Whetten, U. Landman and T. P. Bigioni, *Nature*, 2013, **501**, 399.
- 15 C. P. Joshi, M. S. Bootharaju, M. J. Alhilaly and O. M. Bakr, *J. Am. Chem. Soc.*, 2015, **137**, 11578.
- 16 S. Wang, X. Meng, A. Das, T. Li, Y. Song, T. Cao, X. Zhu, M. Zhu and R. Jin, *Angew. Chem., Int. Ed.*, 2014, **53**, 2376.
- 17 H. Yang, Y. Wang, J. Yan, X. Chen, X. Zhang, H. Hakkinen and N. Zheng, *J. Am. Chem. Soc.*, 2014, **136**, 7197.
- 18 T. U. B. Rao, B. Nataraju and T. Pradeep, *J. Am. Chem. Soc.*, 2010, **132**, 16304.
- 19 K. M. Harkness, Y. Tang, A. Dass, J. Pan, N. Kothalawala, V. J. Reddy, D. E. Cliffler, B. Demeler, F. Stellacci, O. M. Bakr and J. A. McLean, *Nanoscale*, 2012, **4**, 4269.
- 20 M. S. Bootharaju and T. Pradeep, *Langmuir*, 2013, **29**, 8125.
- 21 Y. Negishi, K. Nobusada and T. Tsukuda, *J. Am. Chem. Soc.*, 2005, **127**, 5261.
- 22 S. Kumar, M. D. Bolan and T. P. Bigioni, *J. Am. Chem. Soc.*, 2010, **132**, 13141.
- 23 Z. Wu, E. Lanni, W. Chen, M. E. Bier, D. Ly and R. Jin, *J. Am. Chem. Soc.*, 2009, **131**, 16672.
- 24 Y. Negishi, R. Arai, Y. Niihori and T. Tsukuda, *Chem. Commun.*, 2011, **47**, 5693.
- 25 S. Knoppe, A. C. Dharmaratne, E. Schreiner, A. Dass and T. Burgi, *J. Am. Chem. Soc.*, 2010, **132**, 16783.
- 26 T. Udaya Bhaskara Rao and T. Pradeep, *Angew. Chem., Int. Ed.*, 2010, **49**, 3925.
- 27 J. Guo, S. Kumar, M. Bolan, A. Desireddy, T. P. Bigioni and W. P. Griffith, *Anal. Chem.*, 2012, **84**, 5304.
- 28 Y. Niihori, W. Kurashige, M. Matsuzaki and Y. Negishi, *Nanoscale*, 2013, **5**, 508.
- 29 Y. Yu, X. Chen, Q. Yao, Y. Yu, N. Yan and J. Xie, *Chem. Mater.*, 2013, **25**, 946.
- 30 L. G. Abdul Halim, S. Ashraf, K. Katsiev, A. R. Kirmani, N. Kothalawala, D. H. Anjum, S. Abbas, A. Amassian, F. Stellacci, A. Dass, I. Hussain and O. M. Bakr, *J. Mater. Chem. A*, 2013, **1**, 10148.
- 31 Y. Niihori, M. Matsuzaki, T. Pradeep and Y. Negishi, *J. Am. Chem. Soc.*, 2013, **135**, 4946.
- 32 O. M. Bakr, V. Amendola, C. M. Aikens, W. Wenseleers, R. Li, L. Dal Negro, G. C. Schatz and F. Stellacci, *Angew. Chem., Int. Ed.*, 2009, **121**, 6035.
- 33 I. Chakraborty, A. Govindarajan, J. Erusappan, A. Ghosh, T. Pradeep, B. Yoon, R. L. Whetten and U. Landman, *Nano Lett.*, 2012, **12**, 5861.
- 34 A. Mathew, G. Natarajan, L. Lehtovaara, H. Hakkinen, R. M. Kumar, V. Subramanian, A. Jaleel and T. Pradeep, *ACS Nano*, 2014, **8**, 139.
- 35 T. Udayabhaskararao, M. S. Bootharaju and T. Pradeep, *Nanoscale*, 2013, **5**, 9404.
- 36 A. Baksi, M. S. Bootharaju, X. Chen, H. Hakkinen and T. Pradeep, *J. Phys. Chem. C*, 2014, **118**, 21722.
- 37 F. Bertorelle, R. Hamouda, D. Rayane, M. Broyer, R. Antoine, P. Dugourd, L. Gell, A. Kulesza, R. Mitric and V. Bonacic-Koutecky, *Nanoscale*, 2013, **5**, 5637.
- 38 I. Chakraborty, T. Udayabhaskararao and T. Pradeep, *Chem. Commun.*, 2012, **48**, 6788.
- 39 L. A. Angel, L. T. Majors, A. C. Dharmaratne and A. Dass, *ACS Nano*, 2010, **4**, 4691.
- 40 J. F. Parker, C. A. Fields-Zinna and R. W. Murray, *Acc. Chem. Res.*, 2010, **43**, 1289.
- 41 M. Walter, J. Akola, O. Lopez-Acevedo, P. D. Jadzinsky, G. Calero, C. J. Ackerson, R. L. Whetten, H. Gronbeck and H. Hakkinen, *Proc. Natl. Acad. Sci. U. S. A.*, 2008, **105**, 9157.
- 42 C. Liu, S. Lin, Y. Pei and X. C. Zeng, *J. Am. Chem. Soc.*, 2013, **135**, 18067.
- 43 K. B. Shelimov, D. E. Clemmer, R. R. Hudgins and M. F. Jarrold, *J. Am. Chem. Soc.*, 1997, **119**, 2240.
- 44 T. Wyttenbach, G. von Helden and M. T. Bowers, *J. Am. Chem. Soc.*, 1996, **118**, 8355.
- 45 B. T. Ruotolo, J. L. P. Benesch, A. M. Sandercock, S.-J. Hyung and C. V. Robinson, *Nat. Protoc.*, 2008, **3**, 1139.
- 46 K. M. Harkness, A. Balinski, J. A. McLean and D. E. Cliffler, *Angew. Chem., Int. Ed.*, 2011, **50**, 10554.
- 47 K. M. Harkness, D. E. Cliffler and J. A. McLean, *Analyst*, 2010, **135**, 868.
- 48 K. M. Harkness, D. E. Cliffler and J. A. McLean, *Analyst*, 2010, **135**, 868.
- 49 K. M. Harkness, L. S. Fenn, D. E. Cliffler and J. A. McLean, *Anal. Chem.*, 2011, **82**, 3061.
- 50 K. M. Harkness, B. C. Hixson, L. S. Fenn, B. N. Turner, A. C. Rape, C. A. Simpson, B. J. Huffman, T. C. Okoli, J. A. McLean and D. E. Cliffler, *Anal. Chem.*, 2010, **82**, 9268.
- 51 M. Zhou, S. Dagan and V. H. Wysocki, *Angew. Chem., Int. Ed.*, 2012, **51**, 4336.
- 52 M. Zhou and V. H. Wysocki, *Acc. Chem. Res.*, 2014, **47**, 1010.
- 53 M. Zhou, C. Huang and V. H. Wysocki, *Anal. Chem.*, 2012, **84**, 6016.

Electronic Supplementary Information

Possible Isomers in Ligand Protected Ag₁₁ Cluster Ions Identified by Ion Mobility Mass Spectrometry and Fragmented by Surface Induced Dissociation

Ananya Bakshi,^{a†} Sophie R. Harvey,^{b,c†} Ganapati Natarajan,^a Vicki H. Wysocki,^{b*} and Thalappil Pradeep^{a*}

DST Unit of Nanoscience (DST UNS) and Thematic Unit of Excellence (TUE), Department of Chemistry, Indian Institute of Technology Madras, Chennai 600 036, India

*Corresponding author: Fax: + 91-44 2257-0545

*E-mail: pradeep@iitm.ac.in

Content:

S/N	Description	Page Number
FigureS1	ESI-IM-MS of Ag ₁₁ (SG) ₇	Page 4
FigureS2	ESI-IM-MS/MS of Ag ₁₁ (SG) ₇ ³⁻ at CID 10	Page 5
FigureS3	ESI-IM-MS/MS of Ag ₁₁ (SG) ₇ ³⁻ at CID 20	Page 6
FigureS4	ESI-IM-MS/MS of Ag ₁₁ (SG) ₇ ³⁻ at CID 30	Page 7
FigureS5	ESI-IM-MS/MS of Ag ₁₁ (SG) ₇ ³⁻ at CID 40	Page 8
FigureS6	ESI-IM-MS/MS of Ag ₁₁ (SG) ₇ ³⁻ in SID mode	Page 9
FigureS7	DFT optimized structures of Ag ₁₁ (SMe) ₇	Page 10

Materials and Methods:

Materials:

Silver nitrate, glutathione and sodium borohydride were purchased from Sigma Aldrich and used without any further purification. MilliQ water was used throughout the experiments.

Methods:

Synthesis of $\text{Ag}_{11}(\text{SG})_7$:

$\text{Ag}_{11}(\text{SG})_7$ was synthesized following recently reported procedure.¹ Briefly, 230 mg of GSH was added to 200 mL of ice cold MeOH and stirred for 15 min. 23 mg of AgNO_3 was dissolved in 0.5 mL of milliQ water and added drop wise to the GSH solution and the mixture was allowed to stir for about 30 min to form thiolate. The resulting thiolate was reduced by slowly adding 53 mg of NaBH_4 in 7 mL of ice cold milliQ water. The resulting mixture was allowed to stir for another half an hour. As-synthesized clusters are not soluble in MeOH; so once clusters start forming, they precipitate. At this moment, stirring was stopped and the solution was kept undisturbed for 30 min for complete precipitation of the clusters. The precipitate was washed repeatedly with MeOH to remove excess ligand and NaBH_4 . These red luminescent ($\lambda_{\text{em}}=705$ nm) clusters showed three distinct absorption peaks at 487, 437 and 393 nm in the optical absorption spectrum. As-synthesized clusters are of high purity as confirmed from polyacrylamide gel separation. The sample was dried using a rotavapor and the powder was dissolved in 1:1 water:MeOH for further ESI MS analysis. ESI MS of these clusters showed 3- and 2- charged species with multiple Na attachments (see Figure S1). Detailed MS/MS analyses were carried out to study the fragmentation pattern.

Reference: $\text{Ag}_{11}(\text{SG})_7$: A new cluster identified by mass spectrometry and optical spectroscopy, A. Baksi, M. S. Bootharaju, X. Chen, H. Hakkinen and T. Pradeep, *J. Phys. Chem. C*, **2014**, 118, 21722-21729.

Experimental Details:

All mass spectrometry experiments reported here were performed on a Waters Synapt G2S instrument that has been modified in-house to include a custom surface induced dissociation (SID) device inserted immediately after the first collision cell. Ionization was performed using electrospray ionization in negative mode using an ionization voltage of -1.6 to -1.8 kV and a source temperature of 40 °C. Following ionization and desolvation, the ions are transmitted through the T-wave region, including the ion mobility cell where ions are separated based on their size and shape, and finally into the TOF where the ions are detected. For dissociation studies ions are mass selected in the quadrupole which is situated before the T-wave region. In collision induced dissociation (CID) studies, CID was performed in the first T-wave region (trap) which has been truncated to accommodate the SID device, situated between the trap and ion mobility cell. In SID studies, the voltages applied to the DC electrodes is altered to direct the ions towards the surface for collision, further details of the instrument and its operation can be found elsewhere.² The collision energies given are relative numbers and have not been quantified accurately in the present studies.

For all experiments reported here, the wave velocity and wave height in the trap cell were as follows: 300 m/s and 10 V, respectively. A wave velocity of 900 m/s and height of 20 V were used in the ion mobility cell and a wave velocity of 140 m/s and height of 7 V was implemented in the transfer cell. The helium and nitrogen gas flows for the helium and ion mobility cells were set to 120 and 30 mL/min, respectively.

Typical instrument resolution ($m/\Delta m$) is in the range of 27000 for the mass range and charge state studied which allows precise assignment of the masses and charge state.

Reference: Surface-Induced Dissociation of Ion Mobility-Separated Noncovalent Complexes in a Quadrupole/Time-of-Flight Mass Spectrometer, M. Zhou, C. Huang, V. H. Wysocki, *Anal. Chem.* **2012**, 84, 6016-6023

Electronic Supplementary Information 1

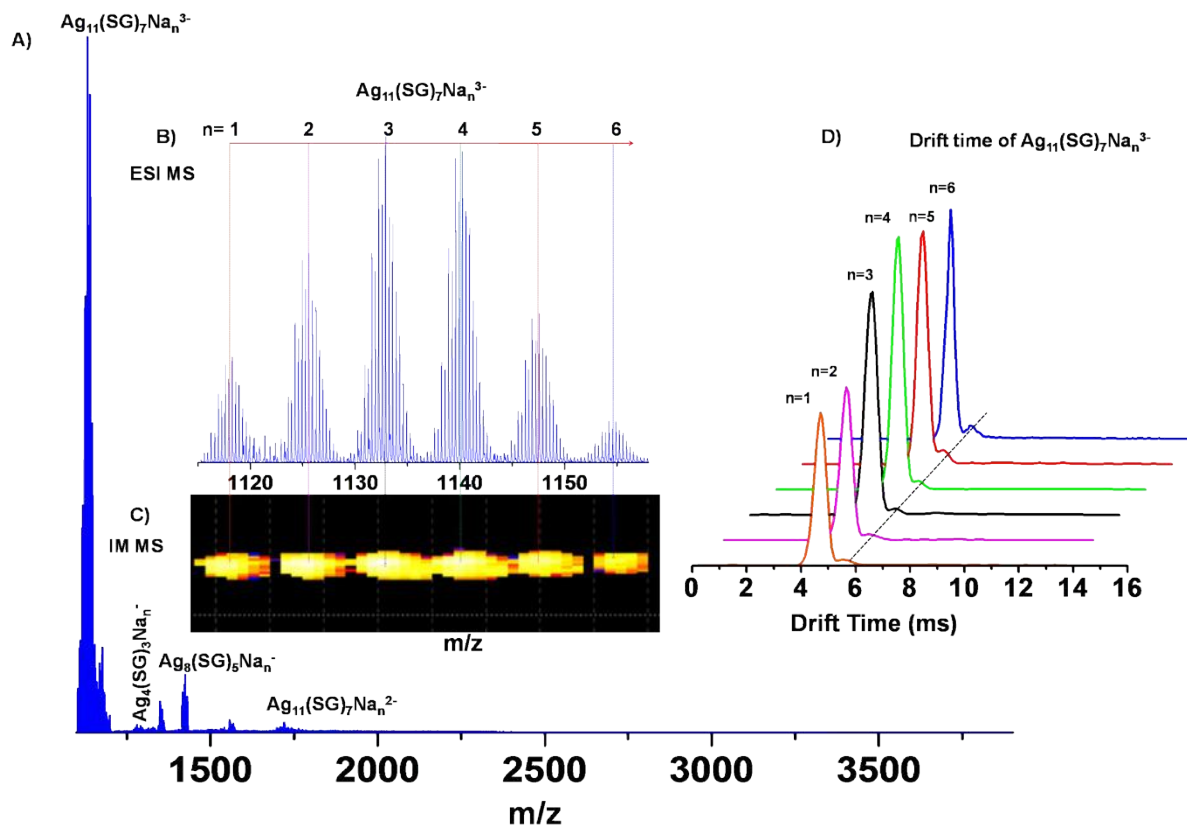


Figure S1: A) ESI MS of $\text{Ag}_{11}(\text{SG})_7$ showing triply and doubly charged ion with multiple Na attachments to the carboxylic groups of the ligand glutathione. B) Triply charged ion is expanded. The corresponding IM-MS is shown in C) and the peak positions are compared. D) Selected ion drift time of these species where two peaks imply presence of two isomers.

Electronic Supplementary Information 2

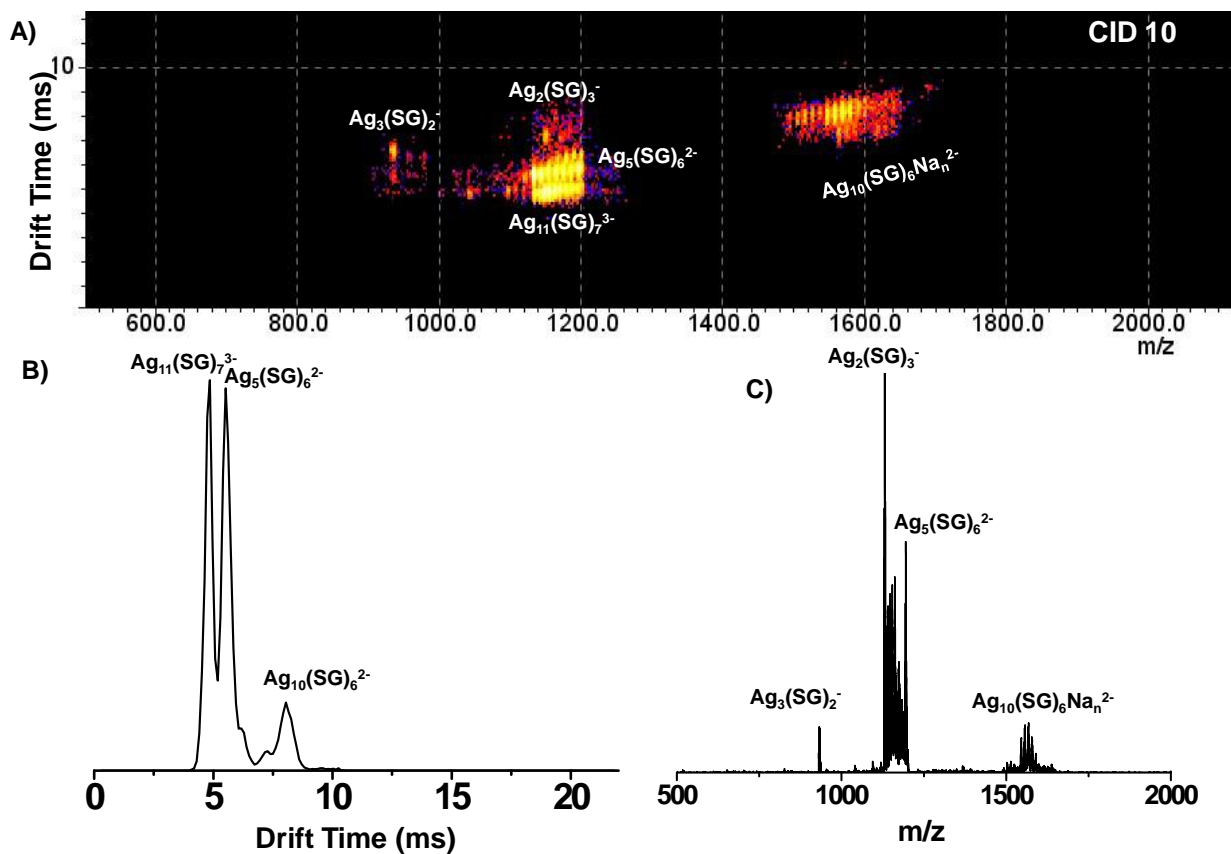


Figure S2: A) ESI-IM-MS of $\text{Ag}_{11}(\text{SG})_7^{3-}$ at CID 10 showing multiple fragmentation in the plot of ion mobility drift time versus m/z . Corresponding drift time profile and mass spectra are shown in B) and C), respectively.

Electronic Supplementary Information 3

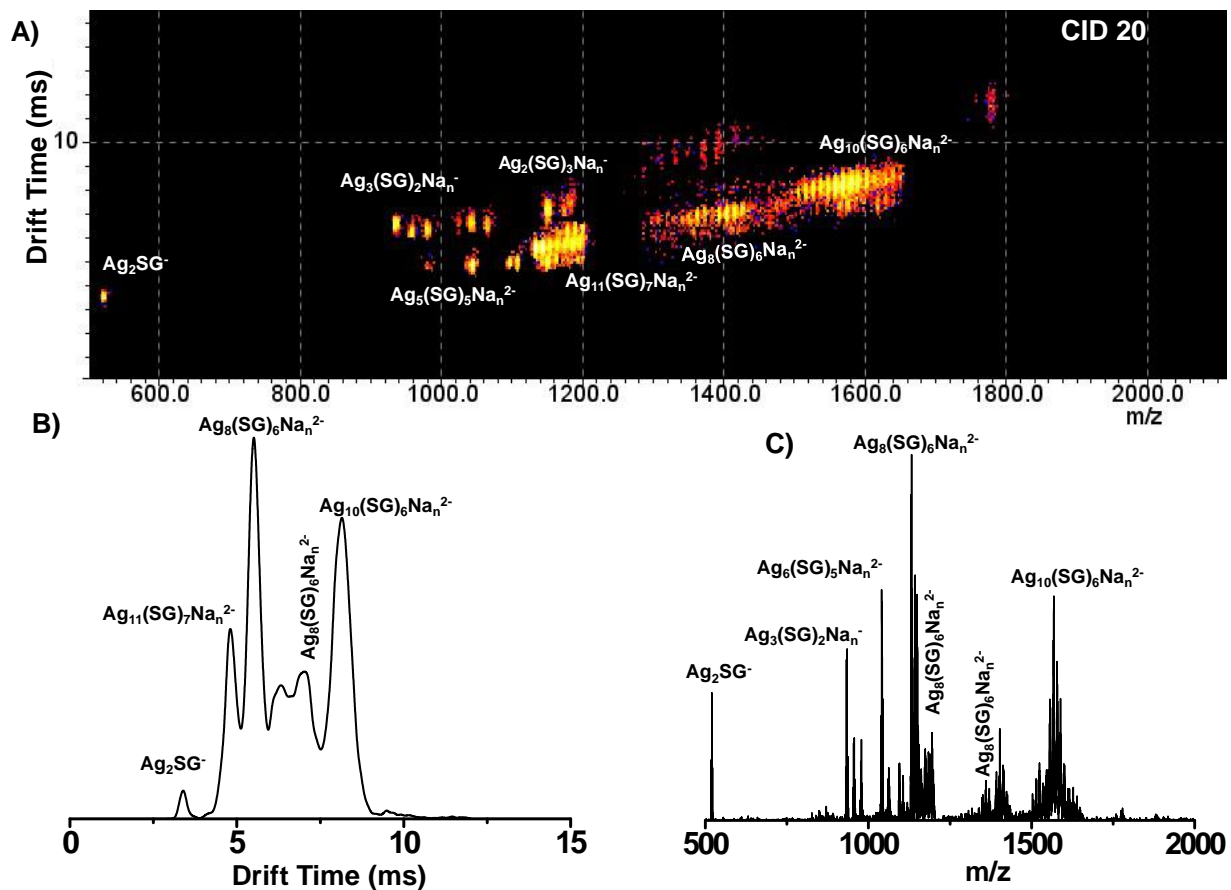


Figure S3: A) ESI-IM-MS of $\text{Ag}_{11}(\text{SG})_7^{3-}$ at CID 20 showing multiple fragmentation in the plot of ion mobility drift time versus m/z . Corresponding drift time profile and mass spectra are shown in B) and C), respectively.

Electronic Supplementary Information 4

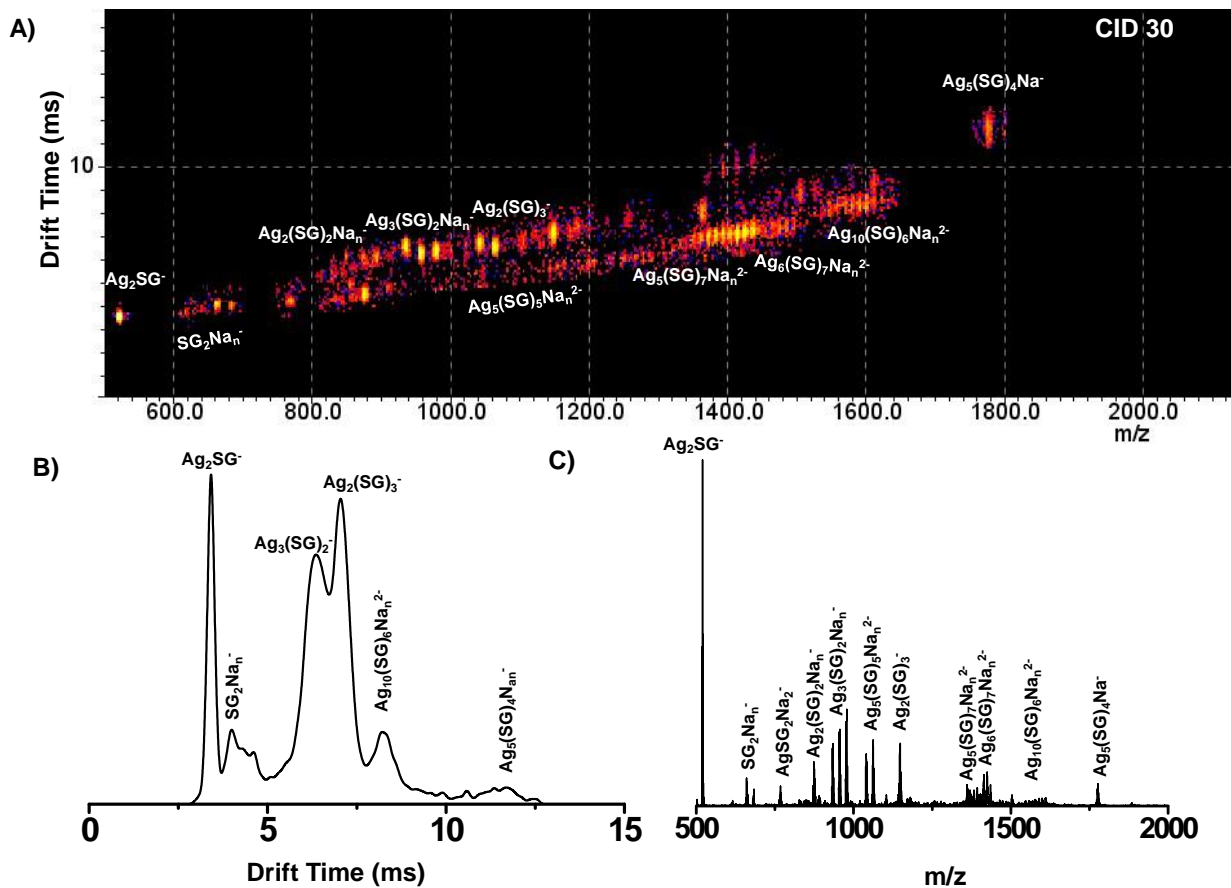


Figure S4: A) ESI-IM-MS of $\text{Ag}_{11}(\text{SG})_7^{3-}$ at CID 30 showing multiple fragmentation in the plot of ion mobility drift time versus m/z . Corresponding drift time profile and mass spectra are shown in B) and C), respectively.

Electronic Supplementary Information 5

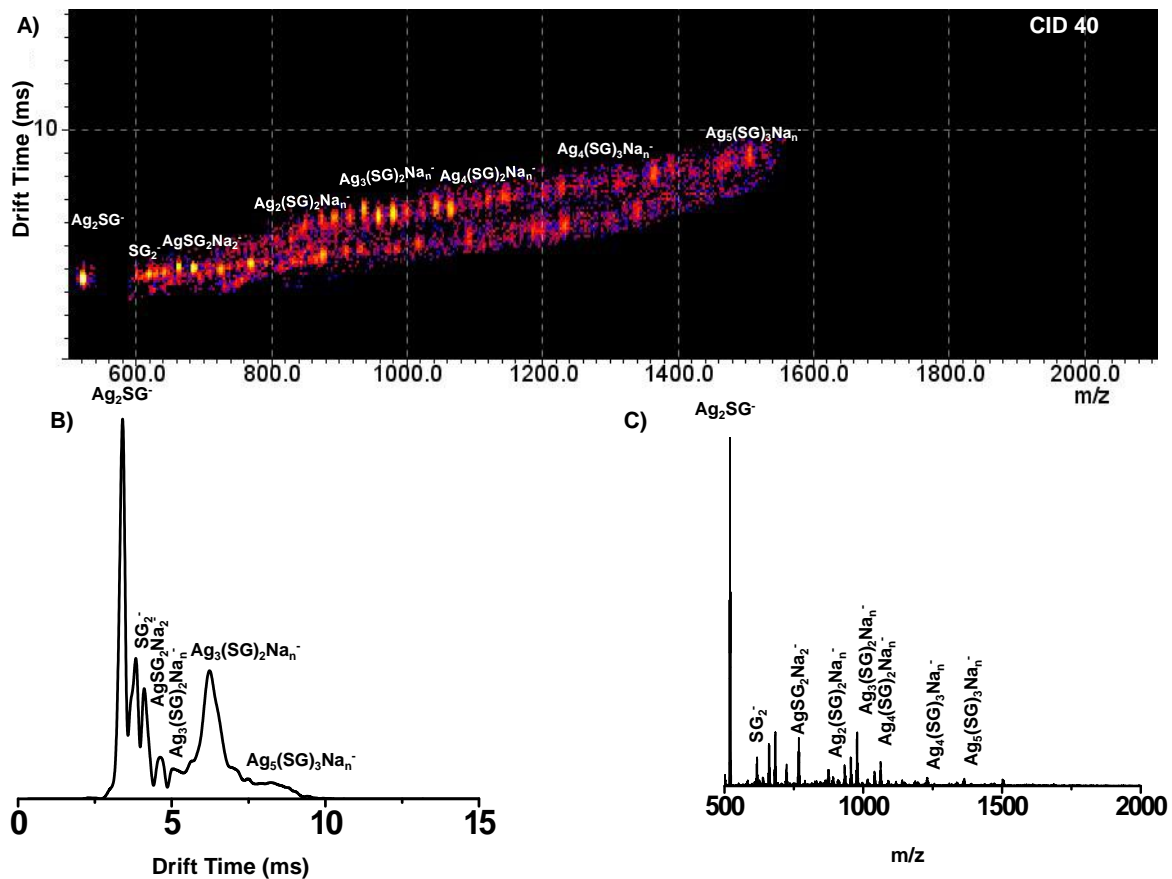


Figure S5: A) ESI-IM-MS of $\text{Ag}_{11}(\text{SG})_7^{3-}$ at CID 30 showing multiple fragmentation in the plot of ion mobility drift time versus m/z . Corresponding drift time profile and mass spectra are shown in B) and C), respectively.

Electronic Supplementary Information 6

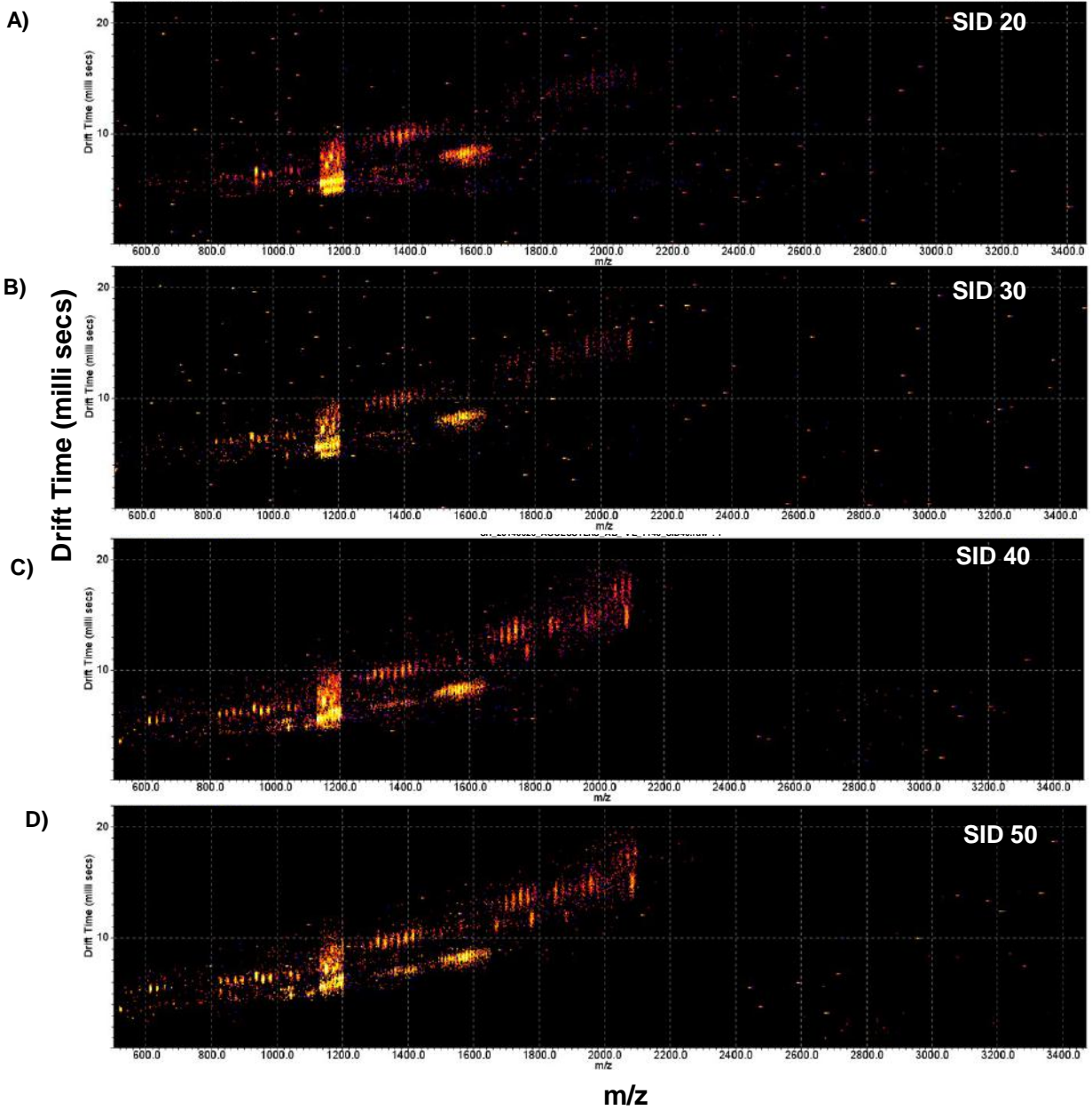
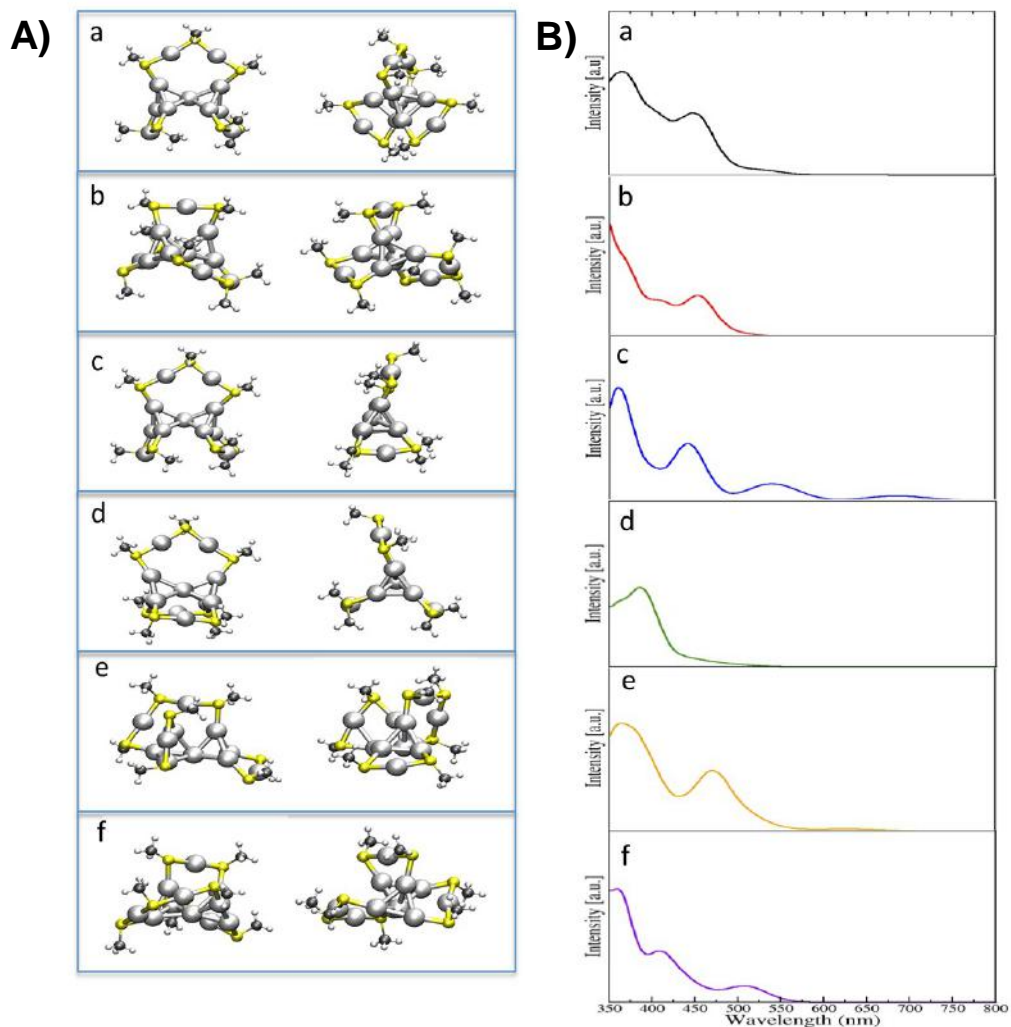


Figure S6: $\text{Ag}_{11}(\text{SG})_7^{3-}$ was fragmented by surface induced dissociation (SID) at different collision energies. Corresponding plots of ion mobility drift time versus m/z are shown in A to D.

Electronic Supplementary Information 7



C)

Isomer	Rel. energy (eV)	HL gap (eV)
a	0.854	1.79
b	0.020	2.08
c	0.647	1.65
d	0	2.29
e	0.535	1.78
f	0.196	2.03

Figure S7: A) Six low energy isomeric structures proposed from density functional theory (two views of each of the structures are shown). Corresponding calculated UV-vis absorption spectra are shown in B. Among which ‘f’ is matching well with the experimentally observed one. C) HOMO-LUMO gap of the structural isomers are listed. The figures are taken from *J. Phys. Chem. C* **2014**, *118*, 21722–21729.

In our previous work, we have shown six low-energy structures which share an Ag_7 core protected with two $\text{Ag}(\text{SR})_2$ and one $\text{Ag}_2(\text{SR})_3$ motifs (R is taken as CH_3). Figure S7 A shows six structural candidates that are all located within a HOMO-LUMO (HL) gap of 0.85 eV (gaps are given in Figure S7 C) suggesting remarkable electronic stability for them. The computed optical spectra show two to three absorption features (Figure S7 B, a-f), among which structure ‘f’ is in best agreement. This structural isomer is within 0.2 eV from the lowest-energy structure. Structure ‘b’ also possesses similar HL gap suggesting a potential isomeric candidate seen experimentally in the gas phase. However, considering the actual ligand GSH, the overall structure may vary slightly as different type of ligand interaction is possible. Moreover, H-bonding among the adjacent ligands may alter the structures significantly (thiolate staple structure). Degree of H-bonding in the case of different isomeric structures may alter the overall size and shape of the cluster ion in the gas phase. Use of glutathione as a ligand would increase the computational effort significantly.

Cluster-Mediated Crossed Bilayer Precision Assemblies of 1D Nanowires

Anirban Som, Indranath Chakraborty, Tuhina Adit Maark, Shridevi Bhat, and Thalappil Pradeep*

Self-organization of micro and nanostructures leading to superlattices enabling the creation of photonic crystals,^[1–5] sensors,^[6–8] materials for biomimetics,^[9] energy harvesting,^[10,11] and high-density storage,^[12–14] is known for some time. Such self-assemblies in 2D and 3D are formed in homogeneous liquids and at liquid–vapor/gas or liquid–liquid interfaces with single or multiple phases.^[15–18] Synthetic methodologies used for generating such structures are typically complex and molecular driving forces enabling such interactions are understood poorly. 1D structures such as nanowires (NWs)^[19–24] and nanotubes (NTs)^[25,26] spontaneously organize parallel to their long axis, similar to “logs-on-a-river.”^[27] Similar assemblies leading to the formation of monolayers at interfaces^[28,29] are known for tellurium NWs (Te NWs). Organized bilayer structures are seen rarely and are obtained through successive transfer of monolayers.^[19,28] One-step formation of such integrated architectures directly from solution, however, is not known so far.

Atomically precise noble metal quantum clusters (QCs) protected with ligands is a new class of materials.^[30–40] Their small size, of the order of a nanometer and the variety and density of functionalities present on them can be used to create new composite structures with 1D nanostructures such as NWs, as such structures are often tens of nanometers in diameter and hundreds of nanometers long. Such composite structures can have new properties distinctly different from clusters and NWs. Here, we demonstrate that molecular interactions between the ligands of QCs anchored on Te NWs can spontaneously create bilayers of the latter, with precise geometry. The Te NWs of the two layers assemble at 81° with respect to each other dictated by the molecular assembly of a cluster, $\text{Ag}_{44}(\text{p-MBA})_{30}$ (where *p*-MBA or para-mercaptobenzoic acid is the ligand protecting the cluster core), anchored on the former. The observed assembly, reminiscent of weaving, is formed at the air–water interface, and such films of cm^2 area are transferable onto solid substrates.

The surface of Te NWs was modified with an atomically precise cluster, $\text{Na}_4\text{Ag}_{44}(\text{p-MBA})_{30}$ before forming the nanowire assembly. The cluster $\text{Ag}_{44}(\text{p-MBA})_{30}$ has four negative charges while Na^+ act as counterions. The structure of this cluster,^[38,41] abbreviated as Ag_{44} , shown in **Figure 1A**, was generated based on previously reported X-ray crystallographic co-ordinates (see the Supporting Information).^[38] Ag_{44} , prepared via a reported procedure,^[38] exhibited characteristic molecular features having five intense bands at 879, 681, 574, 516, and 440 nm along with three broad bands centered around 970, 635, and 395 nm in its extinction spectrum (trace a, Figure S1A, Supporting Information). The identity of the cluster was confirmed from the high-resolution electrospray mass spectrum as well (Figure S1B, Supporting Information). Te NWs, having an average length of 2.5 μm and a diameter of 28 nm (Figure 1B), were prepared by the reduction of a Te (IV) precursor with hydrazine hydrate. The Te NWs were single crystalline with trigonal crystal structure (Figure 1C); the growth occurs along the (001) plane with 0.59 nm interplanar spacing. The NWs showed two distinctive bands in the UV–visible spectrum at 288 and 765 nm due to electronic transitions from the p-bonding and p-lone pair states, respectively, in the valence band to the p-antibonding states in the conduction band (trace b, Figure S1A, Supporting Information).^[42] Surface modification of Te NWs with Ag_{44} was achieved by mixing both the precursors in dimethylformamide (DMF) solution. Increasing amounts of Ag_{44} ($[\text{C}_1]$ to $[\text{C}_5]$, see the Experimental Section) were used for a fixed concentration of Te NWs to achieve larger loading of the cluster onto the Te NWs. This was followed by centrifugal precipitation of the “ Ag_{44} -modified-Te NWs” ($\text{Ag}_{44}@\text{Te}$ NWs) to remove the unattached Ag_{44} . The UV–visible extinction spectra of redispersed $\text{Ag}_{44}@\text{Te}$ NWs showed the above mentioned features of both Ag_{44} and Te NWs. The cluster-features in the UV–visible spectrum became more prominent with increasing Ag_{44} concentration (Figure S1C, Supporting Information), an indication of adsorption of more and more cluster molecules on the Te NW surface. The observed shift in the positions of the cluster-features in $\text{Ag}_{44}@\text{Te}$ NWs relative to free Ag_{44} was another indication of the attachment of Ag_{44} to the NW surface. The peak-shift of the 550 nm feature of Ag_{44} steadily decreased with increasing concentration of Ag_{44} initially and converged later to a value of ≈ 5 nm (Figure S1D, Supporting Information). This trend was also observed for other peaks (insets, Figure S1D, Supporting Information), and can be explained to be due to adsorption. At low cluster concentrations, the NW surface is accessible to all the QCs, which attach uniformly to it (on equivalent highest energy sites) leading to a large change in peak positions. But as the cluster concentration increases, adsorption over the available lower energy sites as well as multilayers becomes possible,

A. Som, Dr. I. Chakraborty, S. Bhat, Prof. T. Pradeep
DST Unit of Nanoscience (DST UNS) and Thematic
Unit of Excellence
Department of Chemistry
Indian Institute of Technology Madras
Chennai 600 036, India
E-mail: pradeep@iitm.ac.in

Dr. T. A. Maark
Department of Physics
Indian Institute of Technology Madras
Chennai 600 036, India



DOI: 10.1002/adma.201505775

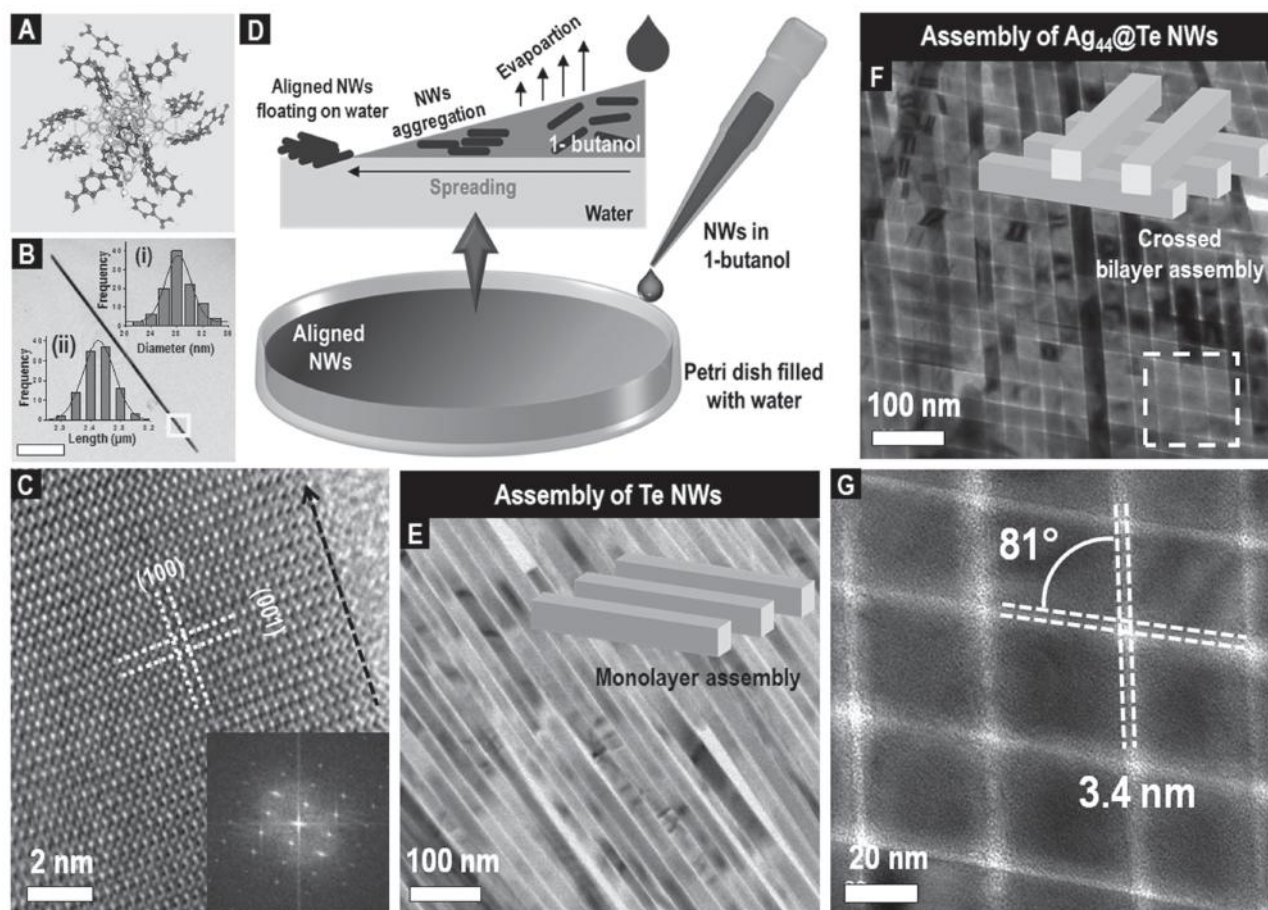


Figure 1. A) Structure of $\text{Ag}_{44}(\text{p-MBA})_{30}$ modeled based on the crystal structure.^[38] B) TEM image of a single Te NW. Diameter and length distributions for the Te NWs are shown in the insets, (i) and (ii), respectively. The area from where the HRTEM image was collected is marked. Scale bar is 400 nm. C) HRTEM image of the marked region of the Te NW, showing its *c*-axis directed growth. Lattice planes are marked. Inset shows corresponding fast Fourier transform. D) Schematic illustration of the aligned NW-assembly. Processes involved during the assembly formation are shown. E) TEM image of the monolayer assembly formed at the air–water interface in case of pristine Te NWs. A schematic of the oriented monolayer of Te NWs is shown in the inset. F) TEM image of the crossed assembly formed with $\text{Ag}_{44}@\text{Te}$ NWs for the same NW concentration as the pristine Te NWs. Schematic illustration of the crossed bilayer structure of the assembly, seen as a weaved NW pattern in the TEM image, is shown in the inset. G) Expanded view of the marked region in (F), showing uniform inter-NW distances (≈ 3.4 nm) for both the layers.

resulting in a reduced peak-shift. Finally, as saturation adsorption is reached, the peak-shift converges.

Solvent evaporation at the air–liquid interface is the basis of the Langmuir–Blodgett (LB) process, which has been used for generating monolayer assemblies of nanomaterials of various shapes and sizes.^[43] Similar monolayer assemblies of hydrophilic-nanostructures can be obtained through fast-spreading of a suspension over a water surface, assisted by solvent drying.^[29] This process is considerably faster (completed within a few minutes) than the Langmuir–Blodgett technique, which normally requires hours. Following the same strategy, a dispersion of $\text{Ag}_{44}@\text{Te}$ NWs in 1-butanol was spread over water, taken in a petri dish. As butanol evaporated, a freestanding assembly was formed on water, which was transferred onto transmission electron microscopy (TEM) grids and examined. The experimental process is schematically outlined in Figure 1D, and the mechanistic details of the assembly are discussed later in the manuscript. A TEM image of the assembly (shown in Figure 1E) formed when pristine Te NWs were subjected to the

above procedure gives a monolayer in which the NWs are parallel to each other. In comparison, the structure of the assembly obtained using $\text{Ag}_{44}@\text{Te}$ NWs is a crossed bilayer, as illustrated by the TEM image in Figure 1F. A schematic of the same, shown in the inset of the figure, resembles the “Woodpile” structure.^[44] Here, NWs from the same layer lie parallel to each other, but are at an unusual angle of $\approx 81^\circ$ to NWs from the second layer, giving the assembly a woven fabric-like appearance. The inter-NW distance in both the layers was measured to be 3.4 ± 0.3 nm (Figure 1G). We believe that different states of aggregation of $\text{Ag}_{44}@\text{Te}$ NWs in comparison to Te NWs drive the formation of the orthogonal bilayer assembly. We will discuss the details below.

Cluster-attachment to the NWs is confirmed by electron microscopy studies of the $\text{Ag}_{44}@\text{Te}$ NWs. For small clusters like Ag_{44} , distinct identification of individual QCs is difficult through standard electron microscopy, and when attached on a thick Te NW surface, they did not produce enough contrast to be identified (Figure 2A). However, these clusters tend to

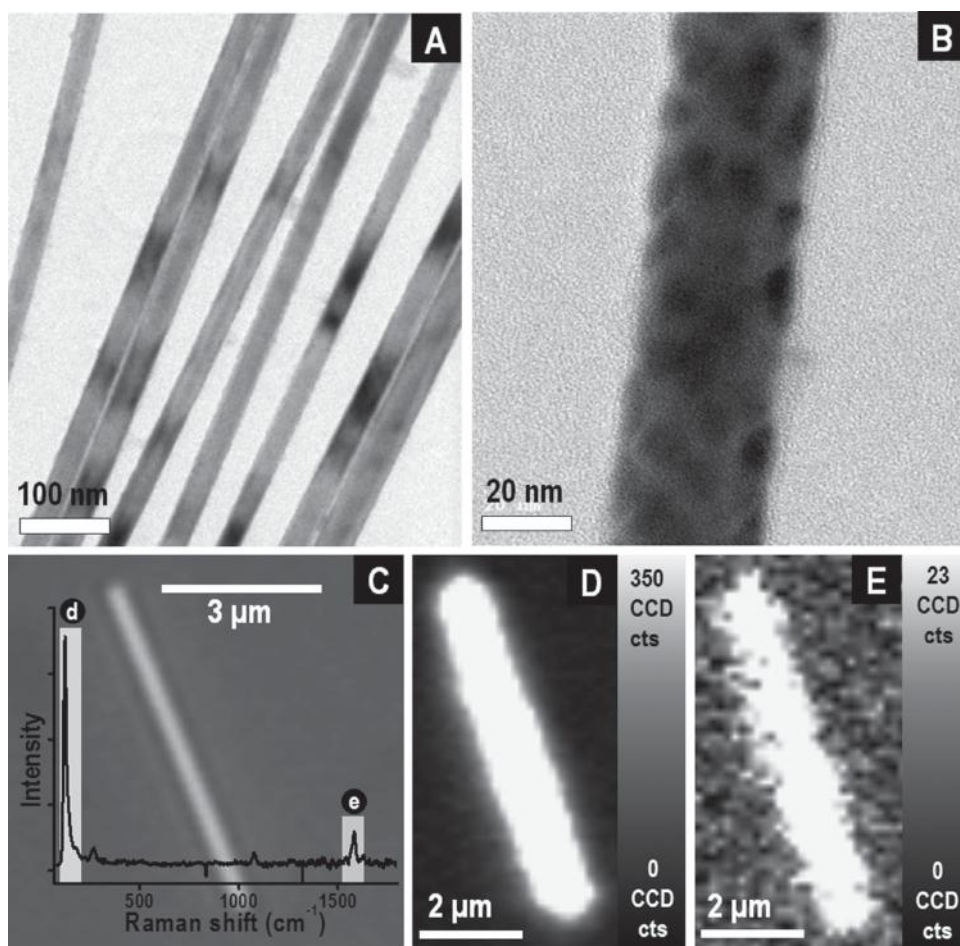


Figure 2. A,B) TEM images of the $\text{Ag}_{44}@\text{Te}$ NWs ($[\text{C}_3]$) at different magnifications. Ag_{44} aggregates on the NW surface upon exposure to the electron beam and are seen as nodules in (B). C) Optical image of single $\text{Ag}_{44}@\text{Te}$ NW. Raman spectrum shows features of both Te and Ag_{44} . D,E) Images constructed by mapping the most prominent Raman features of Te NW and Ag_{44} (marked as (d) and (e) in (C)), respectively.

aggregate to form nanoparticles upon high-energy electron beam (200 kV) irradiation and close inspection revealed the presence of small nodules on the NWs (Figure 2B). At this point, it is important to clarify that the nodules seen on the NWs are due to electron beam irradiation of QCs and not due to their solution phase aggregation on the Te NW surface, as proven in a previous study from our group.^[45] This was substantiated further by following the time evolution (over a period of 2 min) of the nodules on NWs (Figure S2, Supporting Information), which demonstrated the systematic growth of silver particles upon electron beam exposure. The TEM data discussed so far is for $[\text{C}_3]$ as at this cluster concentration, nodule formation and their evolution were observed most prominently. At cluster concentrations lower than $[\text{C}_3]$ ($[\text{C}_1]$ and $[\text{C}_2]$), smaller and fewer nodules were formed, making them indistinguishable. At higher concentrations ($[\text{C}_4]$ and $[\text{C}_5]$), continuous darker islands were observed, almost instantaneously, upon electron beam irradiation (Figure S3, Supporting Information).

Though electron microscopy confirms cluster binding to the NWs, a more direct confirmation was available from non-destructive Raman spectroscopy. For Te NWs, an intense Raman peak appeared at 124 cm^{-1} due to the Raman active

singlet A_1 mode (breathing in the ab plane) of lattice vibrations (Figure S4A, Supporting Information),^[46] while $\text{Ag}_{44}(p\text{-MBA})_{30}$ exhibited several peaks (Figure S4B, Supporting Information) with two strong bands at 1077 and 1584 cm^{-1} arising from ν_{12} (ring breathing) and ν_{8a} (ring in-plane stretching) aromatic ring vibrations, respectively.^[47] It is to be noted that for Raman spectral imaging, thicker and longer Te NWs were synthesized (see the Supporting Information). The Raman spectrum collected from $\text{Ag}_{44}@\text{Te}$ NWs showed the prominent features of both Te NWs and Ag_{44} (Figure 2C). Optical image of the NW used for Raman imaging is shown in Figure 2C. Raman intensity maps constructed by taking the most intense peaks of Te NW and Ag_{44} (marked as (d) and (e) in Figure 2C, respectively) are presented in Figure 2D,E, respectively. The cluster map matches exactly with that of Te confirming its uniform coverage on the NW surface. The Raman image in conjunction with UV–visible extinction spectra and time-dependent evolution of the nodules upon electron beam irradiation proves that the clusters remain on the NW surface in their pristine form.

Precisely oriented bilayer assembly of the NWs was obtained by slowly dropping a dispersion of $\text{Ag}_{44}@\text{Te}$ NWs in 1-butanol on a static water surface. Butanol plays a crucial role in the

assembly formation. Although butanol is thermodynamically miscible with water (solubility of 73 g L^{-1}), the rate of mixing is slow due to its alkyl chain. Thus, when it is dropped on water, it quickly spreads to form a thin layer. A part of it evaporates while the other part slowly mixes with water. As the butanolic dispersion of $\text{Ag}_{44}@\text{Te}$ NWs is dropped on water, the NWs are dragged along with butanol and they remain in the thin butanol layer. However, the speed of spreading decreases with distance, and the NWs cannot be dragged along beyond a point and they accumulate in a small region. The NW concentration increases further in the butanol layer as it evaporates and mixes with water. Once a certain critical concentration of NWs is reached, controlled aggregation of the NWs may happen within the solvent layer (schematically shown in Figure 1D). TEM images taken by directly drop-casting the $\text{Ag}_{44}@\text{Te}$ NW dispersion in 1-butanol (at $[\text{C}_3]$, where the Woodpile structure forms) (Figure S5A, Supporting Information) showed the possibility of formation of preorganized NW aggregates during solvent evaporation.

According to the Derjaguin–Landau–Verwey–Overbeek theory, the repulsive force between two particles is directly proportional to the magnitude of the zeta potential. The zeta potential for the Te NWs was -6.7 mV , whereas it was -2.6 mV for $\text{Ag}_{44}@\text{Te}$ NWs ($[\text{C}_3]$) for the same NW concentration. A systematic increase in the value of zeta potential was found (Figure S5B, Supporting Information) with increased loading of Ag_{44} ($[\text{C}_1]$ to $[\text{C}_5]$) onto the Te NWs. This indicates an increased tendency of aggregate formation, in $\text{Ag}_{44}@\text{Te}$ NWs than in Te NWs, presumably induced by the attached Ag_{44} . Changing

the Ag_{44} concentration from $[\text{C}_1]$ to $[\text{C}_5]$ led to the synthesis of assemblies of $\text{Ag}_{44}@\text{Te}$ NWs with different geometries (see TEM images in Figure S6, Supporting Information). For instance, a monolayer assembly was observed for $[\text{C}_1]$, whereas for $[\text{C}_5]$, bundled NWs were seen. $[\text{C}_3]$ was the optimum concentration for ordered bilayer assembly while $[\text{C}_2]$ and $[\text{C}_4]$ showed the onset of bilayers and bundles, respectively. Thus, cluster loading determines the nature of the assembly. As hydrogen bonding (H-bonding) determines the nucleation of Ag_{44} in its crystal growth,^[48] we infer that preformed aggregates directed through H-bonding may exist at the air–liquid interface. Thickness of the liquid layer and concentration of $\text{Ag}_{44}@\text{Te}$ NWs restrict growth beyond bilayer.

The origin of such unique assembled structures can be rationalized from the structure of Ag_{44} , which forms a crystalline lattice in which individual Ag_{44} clusters are connected to the neighboring ones via hydrogen bonding between the *p*-MBA ligands present in its shell structure.^[48] Figure 3A displays a view of two types of H-bonding between neighboring clusters in the $\text{Ag}_{44}(\textit{p}\text{-MBA})_{30}$ superlattice structure. In each cluster, the *p*-MBA ligands are present in bundles of two (L_2) or three (L_3) units. H-bonding is known to occur between either two L_2 pairs (inset a, Figure 3A) or two L_3 pairs (inset b, Figure 3A) of ligands in the Ag_{44} crystal. In $\text{Ag}_{44}@\text{Te}$ NWs, Ag_{44} clusters anchor themselves onto the NW surfaces through the carboxylate ($-\text{COO}^-$) groups of *p*-MBA. The X-ray photoelectron spectroscopy (XPS) spectrum of the Te 3d region (Figure S7, Supporting Information) showed the emergence of peaks at higher binding energies in case of $\text{Ag}_{44}@\text{Te}$ NWs which is indicative

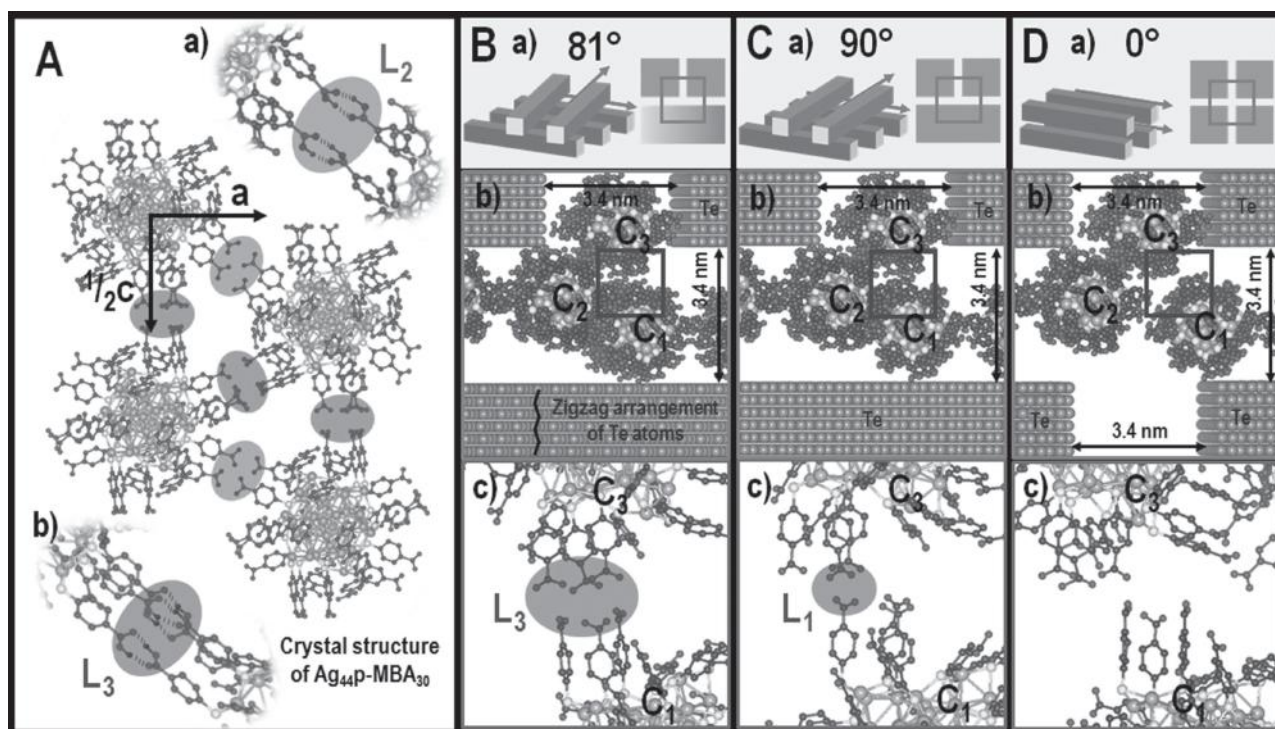


Figure 3. A) H-bonding between neighboring clusters in the $\text{Ag}_{44}(\textit{p}\text{-MBA})_{30}$ superlattice structure. Clusters remain H-bonded with the neighboring ones between L_2 (inset a) and L_3 type of ligand bundles. B) (a–c) Schematic representation of the 81° orthogonal bilayer assembly, a model of the marked region of the schematic in (a) and zoomed view of the marked region in (b), respectively. C, D) Representation of other possible arrangements which are not energetically better. Clusters are assembled on Te surfaces kept at 3.4 nm , in three different planes labeled as C_1 – C_3 .

of Te—O bond formation, supporting our proposition. While a few of the *p*-MBA ligands of an Ag₄₄ cluster are engaged in its attachment to the NW, others are free. As Ag₄₄@Te NWs within the alcohol layer come in close proximity due to the evaporation of butanol, the free *p*-MBA ligands of two neighboring Ag₄₄ clusters attached to adjacent NWs may form H-bonds. As cluster coverage of the NWs plays an important role in determining the final structure of the NW assembly, formation of these H-bonds may be the driving force for the assembly.

To understand the role played by H-bonding in deciding the angle between the layers, we have computationally modeled (see the Supporting Information for the modeling details) how Ag₄₄ clusters could arrange in between (i) a pair of parallel Te surfaces separated by 3.4 nm and (ii) a pair of parallel Te surfaces separated by 3.4 nm and a third Te surface at a distance of 3.4 nm in a second layer at an angle of 81° to the first two. It can be seen that in order to fit into the 3.4 nm inter-NW distance, the clusters are so arranged that they belong to two different planes (P₁ and P₂), labeled as C₁ and C₂, respectively (Figure S8A, Supporting Information). In such a scenario, in any plane, each cluster is surrounded by four clusters from the same plane and by two clusters from the second plane, as can be seen from the top view of the same arrangement (Figure S8B, Supporting Information). Consequently, each cluster is involved in three L₃ H-bonds (nine in all) and two L₂ H-bonds (four in all), i.e., a total of 13 H-bonds. This will be the case whether the Te surfaces are from the same or two different layers (Figure 3Bb). This model is representative of the 81° crossed bilayer assembly (Figure 3Ba), the experimentally observed structure. In this case, however, additional H-bonding can occur between clusters belonging to three different planes (C₁, C₂, and C₃) in the intersecting region. As illustrated in the close-up views in Figure S9A,B (Supporting Information), each cluster in P₃ plane (labeled C₃) can be involved in (a) one L₃ H-bonding with a neighboring cluster in P₁ (C₁) and (b) one L₂ H-bonding each with two neighboring clusters in P₂ (C₂), making a total of seven additional H-bonds. A further zoomed in view of the L₃ H-bonding between C₃ and C₁ is shown in Figure 3Bc. We further modeled two extreme cases of NW assembly in the following manner: (i) a pair of parallel Te surfaces separated by 3.4 nm and an additional third Te surface in a second layer at an angle of 90° at a distance of 3.4 nm (Figure 3Cb) and (ii) two pairs of parallel Te surfaces which are in a parallel arrangement such that each is separated by 3.4 nm (Figure 3Db). Former represents orthogonal (90°) bilayer assembly of Te NWs (Figure 3Ca), while latter represents parallel (0°) assembly of the same (Figure 3Da). While the formation of L₂ H-bonds between C₃ and C₂ remains feasible in both the arrangements, the formation of L₃ H-bonds between C₃ and C₁ gets greatly affected. Although the model for 90° orthogonal assembly (Figure 3Db) appears similar to the 81° crossed bilayer one, closer inspection (Figure 3Dc) reveals that ligand bundles involved in L₃ H-bonding in the earlier case moves away from each other; making L₃ bonding impossible. Formation of an L₁ H-bond, involving a pair of *p*-MBA ligands, however, is still possible in this case (Figure 3Dc). In case of parallel assembly, those ligand groups move further away from each other as can be seen from both the model (Figure 3Db) and close-up view (Figure 3Dc); thereby further diminishing

the possibility of H-bonded interaction between C₃ and C₁. We, therefore, conclude that greater number of H-bonds will be formed in an 81° crossed bilayer assembly and so greater will be the stability of the structure. Assuming that all the Ag₄₄ clusters absorb on equivalent sites, 81° orthogonal arrangement of the NWs leads to the most symmetrical arrangement of the sandwiched H-bonded network of clusters. Furthermore, ligands from the neighboring clusters tend to bump into each other in case of 90° orthogonal assembly whereas this steric factor becomes relaxed in 81° orthogonal assembly (Figure S10, Supporting Information), making this structure more stable.

We found that the concentration of the NWs in the butanol dispersion played an important role in the bilayer assembly. An amount of 1 mL of the as-synthesized Te NWs per mL of butanol was optimal for the above assembly to occur. At concentrations higher than this, the NWs did not disperse well in butanol, while at lower concentrations more randomly oriented NWs were observed. This indicates that while crossed assembly formation is stabilized through H-bonding, the concentration of NWs controls the kinetics and structure of the assembly. However, environmental factors like room temperature (increase by 8 °C) and humidity (10% increase) did not have much effect on the ease of assembly formation.

In order to validate the role of cluster sandwiching for NW assembly formation, another well-known cluster with the same monolayer protection, Au₁₀₂(*p*-MBA)₄₄ (referred hereafter as Au₁₀₂), was used instead. Like Ag₄₄, Au₁₀₂ was synthesized by a reported procedure^[35] and was characterized by UV-visible spectroscopy (Figure S11, Supporting Information). A large-area TEM image of the assembly of Au₁₀₂@Te NWs displays an interlaced array of Te NWs (Figure S12A, Supporting Information). A zoomed-in view reveals that inter-NW distances are longer (3.7 ± 0.2 nm) than in the case of Ag₄₄ (Figure S12B, Supporting Information). The difference of ≈0.3 nm can be accounted in terms of the larger diameter of Au₁₀₂ (1.3 nm) versus Ag₄₄ (1.1 nm) cores. The angle between the Au NWs of the two layers changed slightly to ≈77° for Au₁₀₂ from 81° for Ag₄₄. This is understandable as the geometrical arrangements of the ligands in the two clusters are different. Our conjecture of intercluster H-bond formation between QC@Te NWs from an evaporating dispersion leads to the formation of crossed assembly was further tested by directly drop-casting a dilute dispersion of Au₁₀₂@Te NWs (in water). The grid contained several patches of large area crossed assembly of the NWs with very few isolated NWs (Figure S13, Supporting Information). *p*-MBA functionalized Te NWs formed only monolayer assemblies in the relevant concentration window.

The bilayer structures of NWs, formed through cluster sandwiching, are stable in air for weeks when transferred onto suitable substrates. In order to demonstrate a potential application of the bilayer assembly, we constructed an electronic device by transferring the assembly on a PET (polyethylene terephthalate) substrate. The device showed changes in the electrical conductivity upon bending (Figure S14, Supporting Information) and may be used in strain sensing (as in electronic skin).

In summary, a direct, one-step, solution-based procedure for creating a crossed bilayer structure of NWs with a precise angle between the layers was developed by coating *p*-MBA-protected QCs over NW surfaces. Clusters bound to the surface of a NW

form hydrogen bonds with clusters sitting on the neighboring NWs of the same and different layers. Formation of such sandwiched cluster pairs between the NWs leads to the generation of highly ordered NW assemblies, which was rationalized from computational studies. Precise angular control was brought in by monolayer-protected clusters. The diversity of clusters available and their functionalities may be used to access other arrangements. This kind of ordered assembly of crossed NWs is of interest for applications, especially in nanoscale optics and electronics. Some of these applications will be investigated in the future. Creation of other NW architectures by cluster assembly is an interesting possibility.

Experimental Section

Synthesis of Te NWs: Te NWs were synthesized from TeO₂ by a polyol method.^[49] 480 mg of TeO₂ was dissolved into 50 mL of ethylene glycol (EG) containing 140 mg of dissolved NaOH and 1.5 g of Polyvinylpyrrolidone (PVP) at 120 °C on a magnetic stirrer-cum-hotplate. Then, the temperature of the solution was elevated to 160 °C and 300 μL of hydrazine monohydrate was quickly injected into this hot solution. The solution turned brown immediately and then slowly turned into dark blue after some time indicating the formation of Te NWs. The reaction mixture was removed from the hotplate after 30 min and was left to cool naturally.

Thicker and longer Te NWs, used for the Raman imaging experiment, were also synthesized by a polyol method with slight modification. PVP (0.6 g) and TeO₂ (0.72 g) were dissolved in 40 mL of EG by heating the mixture at 170 °C on a magnetic stirrer-cum-hotplate. Nearly 0.3 g of NaOH was dissolved in 10 mL EG by heating and the resulting solution was added to the reaction mixture at 170 °C. The solution turned dark grey immediately. The reaction was continued for 45 min and then cooled down to room temperature to produce Te NWs of ≈6–8 μm length and ≈100–120 nm diameter.

Synthesis of Ag₄₄: Ag₄₄ cluster was synthesized using a reported procedure.^[38] Initially, 128 mg of AgNO₃ was added to a beaker containing Dimethyl sulfoxide (DMSO) and water (4:7 volume ratio) mixture under constant stirring. 173 mg of *p*-MBA was added to the mixture and stirring was continued. 50% CsOH was added drop-wise until the cloudy nature of thiolates became clear and a greenish yellow color appeared. Subsequently, 283 mg of NaBH₄ in 9 mL water was added drop-wise to obtain a brown-colored solution. The color of this solution changed to deep-red after 1 h, which confirmed the cluster formation. This crude cluster was purified using DMF, which precipitated the cluster. After this step, the solution was centrifuged. After removing the centrifugate, the cluster was extracted in citric acid-containing DMF solution. This was done to acidify all the protons of the carboxylic acid, which makes the cluster soluble in DMF. The extracted cluster was again precipitated using toluene and separated from the solution by centrifugation. The acidification step was repeated one more time. After this step, the precipitate was redissolved in 25 mL DMF to obtain the purified cluster. Note that when all the carboxylates are protonated, the use of citric acid is not necessary, and DMF can be used to extract the cluster. Protonation is the key step for this purification.

Synthesis of Au₁₀₂: The Au₁₀₂(*p*-MBA)₄₄ cluster was synthesized using the method developed by Kalisman and co-workers.^[35] About 28 × 10⁻³ M HAuCl₄, 95 × 10⁻³ M *p*-MBA, and 300 × 10⁻³ M NaOH were mixed in a water-methanol mixture (47% (v/v) methanol) in such a way that the final concentrations of HAuCl₄ and *p*-MBA were 3 × 10⁻³ and 9 × 10⁻³ M, respectively. The solution was kept stirring. Then, freshly prepared NaBH₄ solution (150 × 10⁻³ M in water) was added to the HAuCl₄/*p*-MBA mixture. The molar ratio of NaBH₄ and Au was 2:1. The stirring was continued overnight. After the NaBH₄ addition, the mixture turned black slowly, which indicated gold cluster formation.

The crude cluster was precipitated by ammonium acetate (80 × 10⁻³ M) and centrifuged at 13 000 rpm for 10 min. The pellet was allowed to dry in air overnight, redissolved in 200 μL of water, and purified by fractional precipitation, using methanol. The final cluster was extracted in water.

Surface Modification of Te NWs with Ag₄₄: 5 mL of the EG dispersion of Te NWs was diluted with DMF and was centrifuged at 12 000 rpm for 10 min to precipitate the NWs. The precipitated NWs were redispersed and precipitated three more times from DMF to obtain clean NWs which were finally dispersed in 20 mL DMF. 4 mL aliquots of this solution were combined with 100, 200, 300, 500, and 750 μL stock solution of Ag₄₄ ([C₁] to [C₅] respectively) under constant magnetic stirring. Stirring was continued for 1 h and NWs were then centrifuged out from the unreacted cluster. The same method was followed in the case of Au₁₀₂.

Assembly Formation: The centrifuged QC@Te NWs were dispersed in 1 mL of 1-butanol by gentle sonication. Millipore water was filled to the brim of a petri dish and the dispersion was dropped slowly on the surface of water from a pipette. NW assembly was formed within a couple of minutes and floated on the surface of water. At this stage, the assembly appeared like a shiny mirror. The assembly was then transferred onto the TEM grids for examination by electron microscopy.

Instrumentation: UV-visible absorption/extinction spectra were recorded using a Perkin-Elmer Lambda 25 spectrophotometer in the range of 200 to 1100 nm using absorption cells with a path length of 1 cm.

TEM and high-resolution transmission electron microscopy (HRTEM) were performed at an accelerating voltage of 200 kV on a JEOL 3010 instrument equipped with a Ultra-high-resolution (UHR) polepiece. A Gatan 794 multiscan charge-coupled device (CCD) camera was used for image acquisition. NW assemblies floating on water were transferred on 300-mesh carbon coated copper grid (spi Supplies, 3530-MB) and dried in ambient condition, before TEM analysis. NW dispersions were drop-casted on grids and dried prior to analysis. Raman spectra were recorded on a Witec alpha300 S confocal Raman spectrometer equipped with a 633 nm (He-Ne) laser using a Zeiss 20× objective. Single-nanowire Raman imaging was performed using a Nikon 100× objective. Data was processed by the Witec Project Plus software package. Zeta potential measurements were performed on a Malvern Zetasizer Nano ZS-90.

Supporting Information

Supporting Information is available from the Wiley Online Library or from the author.

Acknowledgements

A.S., I.C., and T.A.M. contributed equally to this work. The authors thank the Department of Science and Technology, Government of India for constantly supporting the research program on nanomaterials. A.S. thanks CSIR and I.C. and S.B. thank IIT Madras for a research fellowship. T.A.M. acknowledges IIT Madras for the Institute Postdoctoral Fellowship. Dr. E. Prasad, Department of Chemistry, IIT Madras is thanked for the zeta potential measurements.

Received: November 21, 2015

Revised: December 22, 2015

Published online: February 10, 2016

[1] Y. A. Vlasov, X.-Z. Bo, J. C. Sturm, D. J. Norris, *Nature* **2001**, 414, 289.

[2] B. Gates, S. H. Park, Y. Xia, *Adv. Mater.* **2000**, 12, 653.

[3] G. A. Ozin, S. M. Yang, *Adv. Funct. Mater.* **2001**, 11, 95.

- [4] R. C. Schrodien, M. Al-Daous, C. F. Blanford, A. Stein, *Chem. Mater.* **2002**, *14*, 3305.
- [5] H. Yamada, T. Nakamura, Y. Yamada, K. Yano, *Adv. Mater.* **2009**, *21*, 4134.
- [6] T. Cassagneau, F. Caruso, *Adv. Mater.* **2002**, *14*, 1837.
- [7] X. Xu, A. V. Goponenko, S. A. Asher, *J. Am. Chem. Soc.* **2008**, *130*, 3113.
- [8] A. C. Sharma, T. Jana, R. Kesavamoorthy, L. Shi, M. A. Virji, D. N. Finegold, S. A. Asher, *J. Am. Chem. Soc.* **2004**, *126*, 2971.
- [9] M. Kolle, P. M. Salgard-Cunha, M. R. J. Scherer, F. Huang, P. Vukusic, S. Mahajan, J. J. Baumberg, U. Steiner, *Nat. Nanotechnol.* **2010**, *5*, 511.
- [10] Y. G. Seo, K. Woo, J. Kim, H. Lee, W. Lee, *Adv. Funct. Mater.* **2011**, *21*, 3094.
- [11] J. P. Bosco, K. Sasaki, M. Sadakane, W. Ueda, J. G. Chen, *Chem. Mater.* **2010**, *22*, 966.
- [12] S. Sun, C. B. Murray, D. Weller, L. Folks, A. Moser, *Science* **2000**, *287*, 1989.
- [13] H. Zeng, J. Li, J. P. Liu, Z. L. Wang, S. Sun, *Nature* **2002**, *420*, 395.
- [14] A. Ethirajan, U. Wiedwald, H.-G. Boyen, B. Kern, L. Han, A. Klimmer, F. Weigl, G. Kaestle, P. Ziemann, K. Fauth, J. Cai, R. J. Behm, A. Romanyuk, P. Oelhafen, P. Walther, J. Biskupek, U. Kaiser, *Adv. Mater.* **2007**, *19*, 406.
- [15] G. M. Whitesides, B. Grzybowski, *Science* **2002**, *295*, 2418.
- [16] F. X. Redl, K. S. Cho, C. B. Murray, S. O'Brien, *Nature* **2003**, *423*, 968.
- [17] *Self-Assembled Nanostructures* (Eds: J. Zhang, Z.-L. Wang, J. Liu, S. Chen, G.-Y. Liu), Kluwer Academic, Dordrecht, The Netherlands **2003**.
- [18] G. M. Whitesides, J. K. Kriebel, B. T. Mayers, in *Nanoscale Assembly: Chemical Techniques* (Ed: W. T. S. Huck), Springer, New York **2005**, p. 217.
- [19] D. Whang, S. Jin, Y. Wu, C. M. Lieber, *Nano Lett.* **2003**, *3*, 1255.
- [20] A. Tao, F. Kim, C. Hess, J. Goldberger, R. He, Y. Sun, Y. Xia, P. Yang, *Nano Lett.* **2003**, *3*, 1229.
- [21] D. Wang, Y.-L. Chang, Z. Liu, H. Dai, *J. Am. Chem. Soc.* **2005**, *127*, 11871.
- [22] S. Acharya, A. B. Panda, N. Belman, S. Efrima, Y. Golan, *Adv. Mater.* **2006**, *18*, 210.
- [23] I. Patla, S. Acharya, L. Zeiri, J. Israelachvili, S. Efrima, Y. Golan, *Nano Lett.* **2007**, *7*, 1459.
- [24] L. Mai, Y. Gu, C. Han, B. Hu, W. Chen, P. Zhang, L. Xu, W. Guo, Y. Dai, *Nano Lett.* **2009**, *9*, 826.
- [25] X. Li, L. Zhang, X. Wang, I. Shimoyama, X. Sun, W.-S. Seo, H. Dai, *J. Am. Chem. Soc.* **2007**, *129*, 4890.
- [26] H. Shimoda, S. J. Oh, H. Z. Geng, R. J. Walker, X. B. Zhang, L. E. McNeil, O. Zhou, *Adv. Mater.* **2002**, *14*, 899.
- [27] P. Yang, *Nature* **2003**, *425*, 243.
- [28] J.-W. Liu, J.-H. Zhu, C.-L. Zhang, H.-W. Liang, S.-H. Yu, *J. Am. Chem. Soc.* **2010**, *132*, 8945.
- [29] G. D. Moon, T. I. Lee, B. Kim, G. S. Chae, J. Kim, S. H. Kim, J.-M. Myoung, U. Jeong, *ACS Nano* **2011**, *5*, 8600.
- [30] M. Zhu, C. M. Aikens, F. J. Hollander, G. C. Schatz, R. Jin, *J. Am. Chem. Soc.* **2008**, *130*, 5883.
- [31] M. W. Heaven, A. Dass, P. S. White, K. M. Holt, R. W. Murray, *J. Am. Chem. Soc.* **2008**, *130*, 3754.
- [32] T. U. B. Rao, T. Pradeep, *Angew. Chem. Int. Ed.* **2010**, *49*, 3925.
- [33] T. U. B. Rao, B. Nataraju, T. Pradeep, *J. Am. Chem. Soc.* **2010**, *132*, 16304.
- [34] P. R. Nimmala, A. Dass, *J. Am. Chem. Soc.* **2011**, *133*, 9175.
- [35] Y. Levi-Kalisman, P. D. Jadzinsky, N. Kalisman, H. Tsunoyama, T. Tsukuda, D. A. Bushnell, R. D. Kornberg, *J. Am. Chem. Soc.* **2011**, *133*, 2976.
- [36] I. Diez, R. H. A. Ras, *Nanoscale* **2011**, *3*, 1963.
- [37] I. Chakraborty, A. Govindarajan, J. Erusappan, A. Ghosh, T. Pradeep, B. Yoon, R. L. Whetten, U. Landman, *Nano Lett.* **2012**, *12*, 5861.
- [38] A. Desireddy, B. E. Conn, J. Guo, B. Yoon, R. N. Barnett, B. M. Monahan, K. Kirschbaum, W. P. Griffith, R. L. Whetten, U. Landman, T. P. Bigioni, *Nature* **2013**, *501*, 399.
- [39] I. Chakraborty, W. Kurashige, K. Kanehira, L. Gell, H. Hakkinen, Y. Negishi, T. Pradeep, *J. Phys. Chem. Lett.* **2013**, *4*, 3351.
- [40] Y. Yu, Z. Luo, D. M. Chevrier, D. T. Leong, P. Zhang, D.-E. Jiang, J. Xie, *J. Am. Chem. Soc.* **2014**, *136*, 1246.
- [41] H. Yang, Y. Wang, H. Huang, L. Gell, L. Lehtovaara, S. Malola, H. Hakkinen, N. Zheng, *Nat. Commun.* **2013**, *4*, 2422.
- [42] Z.-H. Lin, Z. Yang, H.-T. Chang, *Cryst. Growth Des.* **2008**, *8*, 351.
- [43] A. R. Tao, J. Huang, P. Yang, *Acc. Chem. Res.* **2008**, *41*, 1662.
- [44] S. Y. Lin, J. G. Fleming, D. L. Hetherington, B. K. Smith, R. Biswas, K. M. Ho, M. M. Sigalas, W. Zubrzycki, S. R. Kurtz, J. Bur, *Nature* **1998**, *394*, 251.
- [45] A. Som, A. K. Samal, T. Udayabhaskararao, M. S. Bootharaju, T. Pradeep, *Chem. Mater.* **2014**, *26*, 3049.
- [46] A. S. Pine, G. Dresselhaus, *Phys. Rev. B* **1971**, *4*, 356.
- [47] H. Park, S. B. Lee, K. Kim, M. S. Kim, *J. Phys. Chem.* **1990**, *94*, 7576.
- [48] B. Yoon, W. D. Luedtke, R. N. Barnett, J. Gao, A. Desireddy, B. E. Conn, T. Bigioni, U. Landman, *Nat. Mater.* **2014**, *13*, 807.
- [49] B. Mayers, Y. Xia, *J. Mater. Chem.* **2002**, *12*, 1875.

ADVANCED MATERIALS

Supporting Information

for *Adv. Mater.*, DOI: 10.1002/adma.201505775

Cluster-Mediated Crossed Bilayer Precision Assemblies of 1D
Nanowires

*Anirban Som, Indranath Chakraborty, Tuhina Adit Maark,
Shridevi Bhat, and Thalappil Pradeep**

Supporting Information

Cluster Mediated Crossed Bilayer Precision Assemblies of 1D Nanowires

Anirban Som, Indranath Chakraborty, Tuhina Adit Maark, Shridevi Bhat and Thalappil Pradeep *

Table of contents

Description	Page No.
Chemicals used	2
Computational modeling	2
Supporting information figures	3
References	11

List of figures

Figure No.	Description	Page No.
Figure S1	UV-visible absorption spectra of Ag ₄₄ , Te NWs and Ag ₄₄ @Te NWs	3
Figure S2	Electron beam induced nodule formation on Ag ₄₄ @Te NWs with increasing irradiation time	4
Figure S3	Extent of nodule formation on electron beam irradiation with increasing Ag ₄₄ concentration	4
Figure S4	Raman spectra of Te NW and Ag ₄₄	5
Figure S5	Structures formed from Ag ₄₄ @Te NW upon butanol drying, zeta potential values for Te and Ag ₄₄ @Te NWs	5
Figure S6	Assembly of Ag ₄₄ @Te NWs with increasing Ag ₄₄ loading	6
Figure S7	XPS spectra of Te and Ag₄₄@Te NWs	6
Figure S8	Side and top views of modeled assembly of Ag ₄₄ clusters between two parallel Te layers	7
Figure S9	Additional H-bonds formed between Ag ₄₄ clusters in 81° orthogonal arrangement	8
Figure S10	Relaxation of steric interactions in 81° orthogonal arrangement over a 90° arrangement	8
Figure S11	UV-visible spectrum of Au ₁₀₂	9
Figure S12	Orthogonal bilayer assembly of Au ₁₀₂ @Te NWs	9
Figure S13	Assembly of Au ₁₀₂ @Te NWs by direct drop-casting	10
Figure S14	Device structure and strain sensing	10

Chemicals used

All the chemicals were commercially available and were used without further purification. Silver nitrate (AgNO_3 , 99%), gold (III) chloride trihydrate ($\text{HAuCl}_4 \cdot 3\text{H}_2\text{O}$, 99%), 4-mercaptobenzoic acid (MBA, 97%) and sodium borohydride (NaBH_4 , 99.99%) were purchased from Aldrich. Tellurium dioxide (TeO_2 , 99.9%) powder, hydrazine monohydrate ($\text{N}_2\text{H}_4 \cdot \text{H}_2\text{O}$, 99-100%) and PVP (Polyvinylpyrrolidone, K25) were supplied by Alfa Aesar, Fischer Scientific and SD Fine Chemicals, respectively. Ethylene glycol (LR), dimethylformamide (DMF, AR grade), dimethylsulfoxide (DMSO, AR grade), toluene (AR grade), methanol (AR grade), ammonium acetate, citric acid and sodium hydroxide (NaOH) pellets were procured from RANKEM, India

Computational modeling

The structure for $\text{Ag}_{44}(\text{MBA})_{30}$ was generated using the X-ray crystallographic coordinates deposited at the Cambridge Crystallographic Data Centre (CCDC) under the deposition name CCDC 949240. This data is available free of charge from CCDC at http://www.ccdc.cam.ac.uk/data_request/cif. To model the Te NW bilayer assembly (parallel and orthogonal), the Ag_{44} clusters were sandwiched between Te(001) surfaces. All the structures were built using ase-gui, which is the graphical interface available with Atomic Simulation Environment (ASE)¹, and VESTA² visualization software program.

Supporting Information Figures

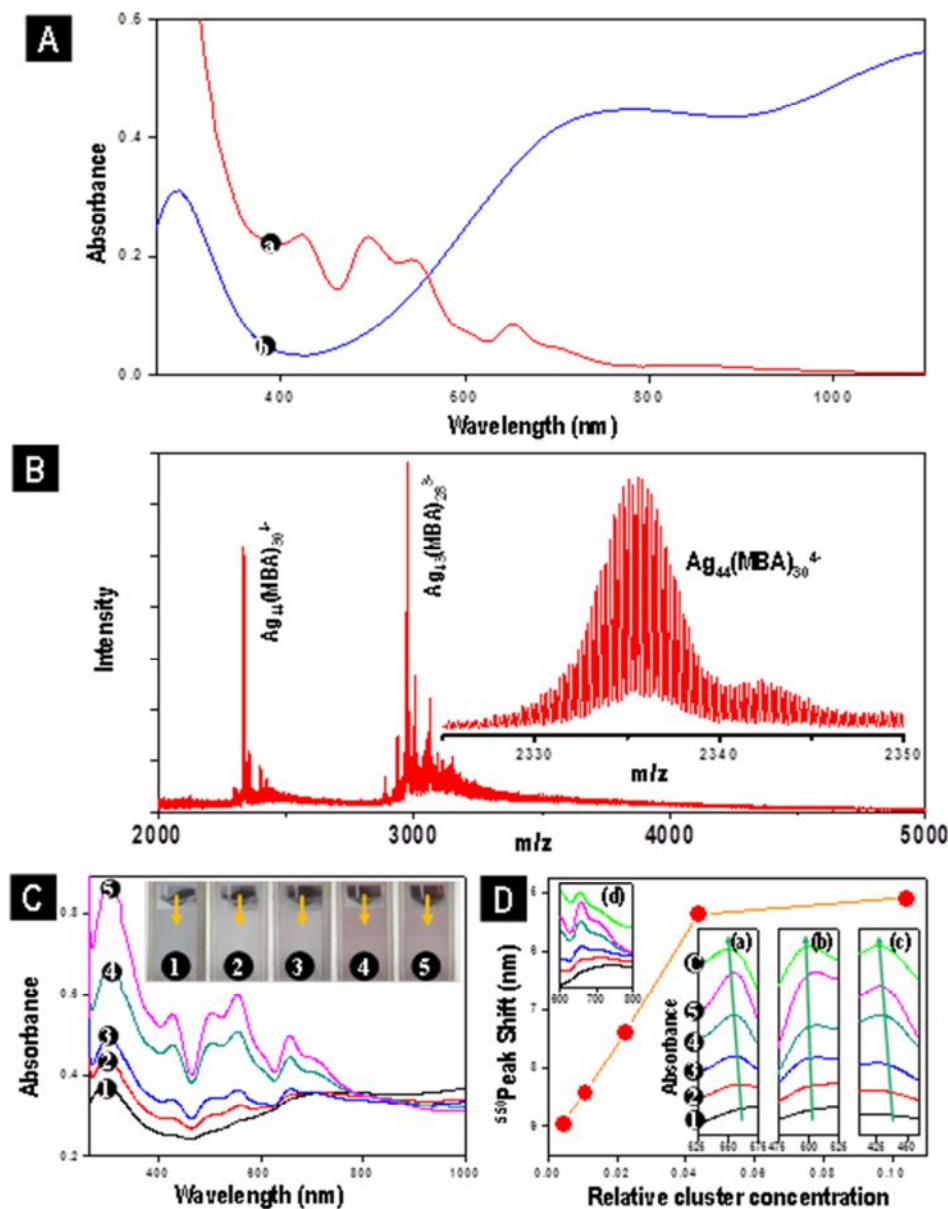


Figure S1. A) UV-visible absorption spectra of a) Ag₄₄(p-MBA)₃₀ and b) Te NWs. B) ESI mass spectrum of Ag₄₄(p-MBA)₃₀. Expanded view of molecular ion peak (4⁻ charge) is shown in the inset along with the theoretical spectrum of the same ion. Minor features are due to fragments or association products during ionization. C) UV-vis absorption spectra of Ag₄₄@Te NWs with increasing cluster concentration (C₁-C₅, marked with 1 to 5). The NWs after cluster attachment were precipitated out through centrifugation and re-dispersed prior to the measurement of the spectra. Images of the procedure are shown in the inset. D) Shift of the 550 nm peak of Ag₄₄ is plotted with increasing cluster concentration at a fixed Te NW concentration. Peak shift decreases with increasing concentration, indicating multilayer adsorption of clusters on Te NW surface at higher concentration. Gradual changes in positions of different peaks of Ag₄₄ are shown in the insets.

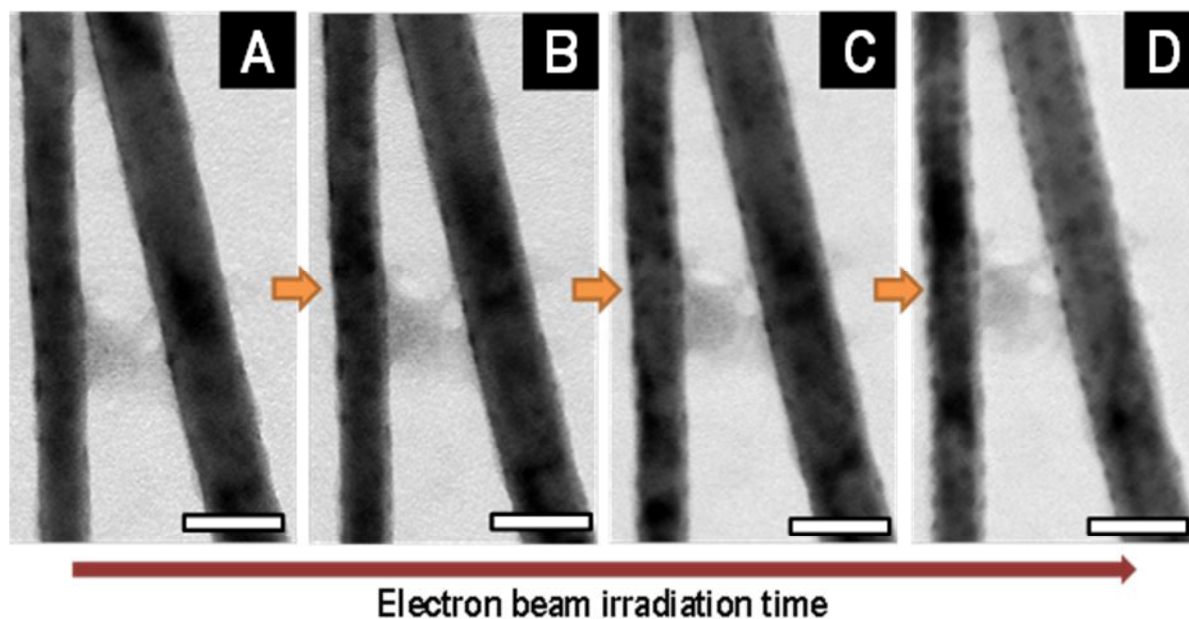


Figure S2. TEM images showing time evolution of nodules upon electron beam irradiation of $\text{Ag}_{44}@Te$ NWs (C_3). Image A was acquired immediately. Subsequent images were acquired following a 30 s electron beam irradiation. The scale bar is 50 nm for all the images.

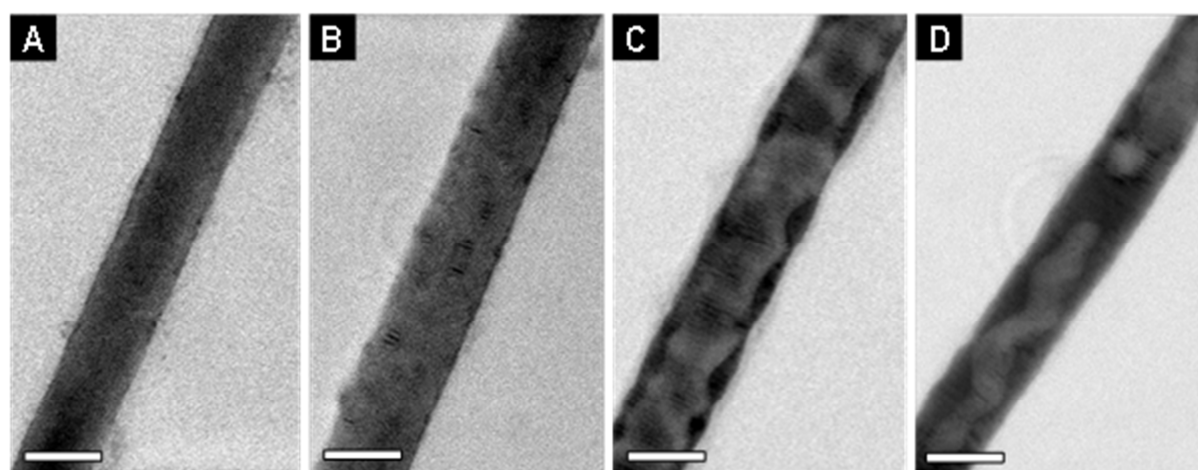


Figure S3. TEM images of $\text{Ag}_{44}@Te$ NWs at different loadings of Ag_{44} , showing the size and the extent of nodule/island coverage of the NWs; (A) C_1 , (B) C_2 , (C) C_4 and (D) C_5 . Scale bar is 20 nm in all the images.

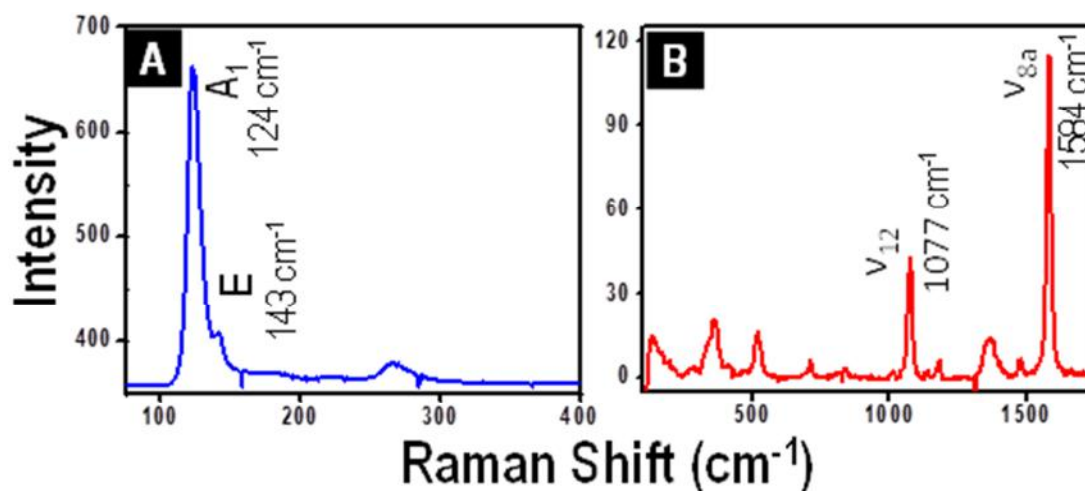


Figure S4. (A) Raman spectra of Te NWs. The most intense Raman peak at 124 cm⁻¹ is due to the Raman active singlet A₁ mode of Te lattice vibrations, while the less intense peak at 143 cm⁻¹ is one of the E doublets. (B) Raman spectrum of Ag₄₄. The cluster is Raman active due to the Raman active nature of its protecting ligand (p-MBA). Two strong bands observed at 1077 and 1584 cm⁻¹ arise from ν₁₂ and ν_{8a} aromatic ring vibrations of p-MBA, respectively.

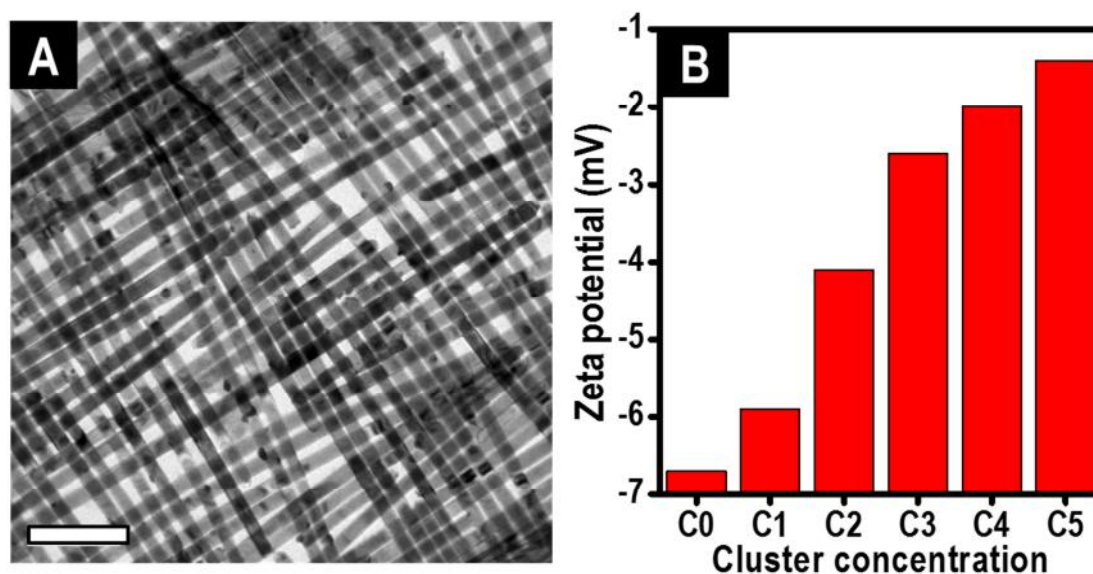


Figure S5. (A) Organized structure formed from butanolic dispersion of Ag₄₄@Te NWs (C₃) after solvent evaporation. (B) Increase in the value of zeta potential with increasing cluster loading. Scale bar in A is 200 nm.

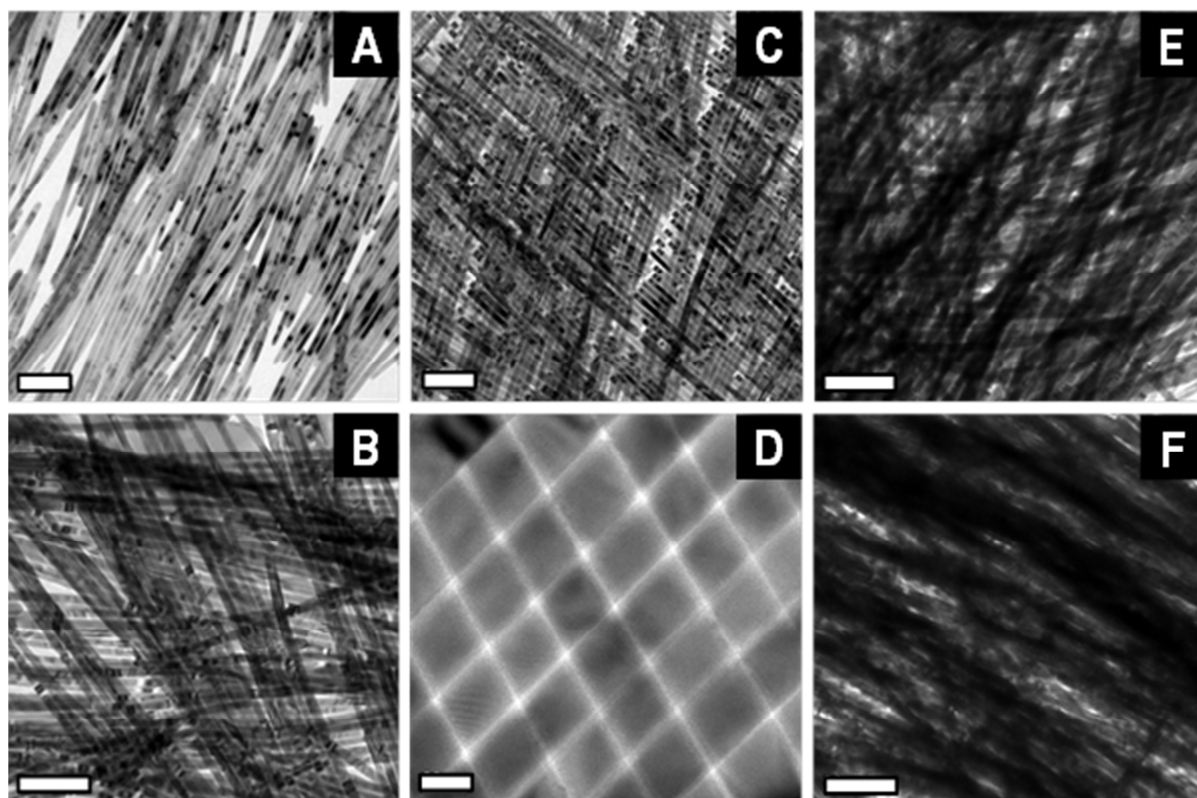


Figure S6. TEM images of the kind of $\text{Ag}_{44}@\text{Te}$ NWs assemblies formed at different loading of Ag_{44} ; (A) C_1 , (B) C_2 (C) C_3 , (E) C_4 , (F) C_5 . An area having perfect order from C_3 is expanded and shown in (D). Scale bar in D is 20 nm and is 200 nm for the other images.

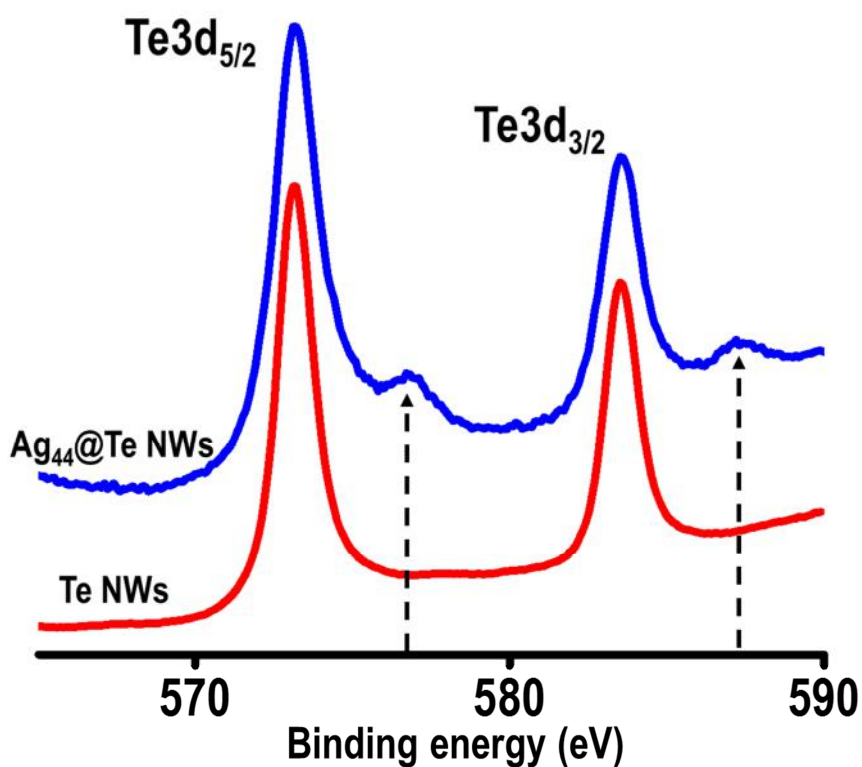


Figure S7. XPS spectra of the Te 3d region for Te (red trace) and $\text{Ag}_{44}@\text{Te}$ (blue trace) NWs.

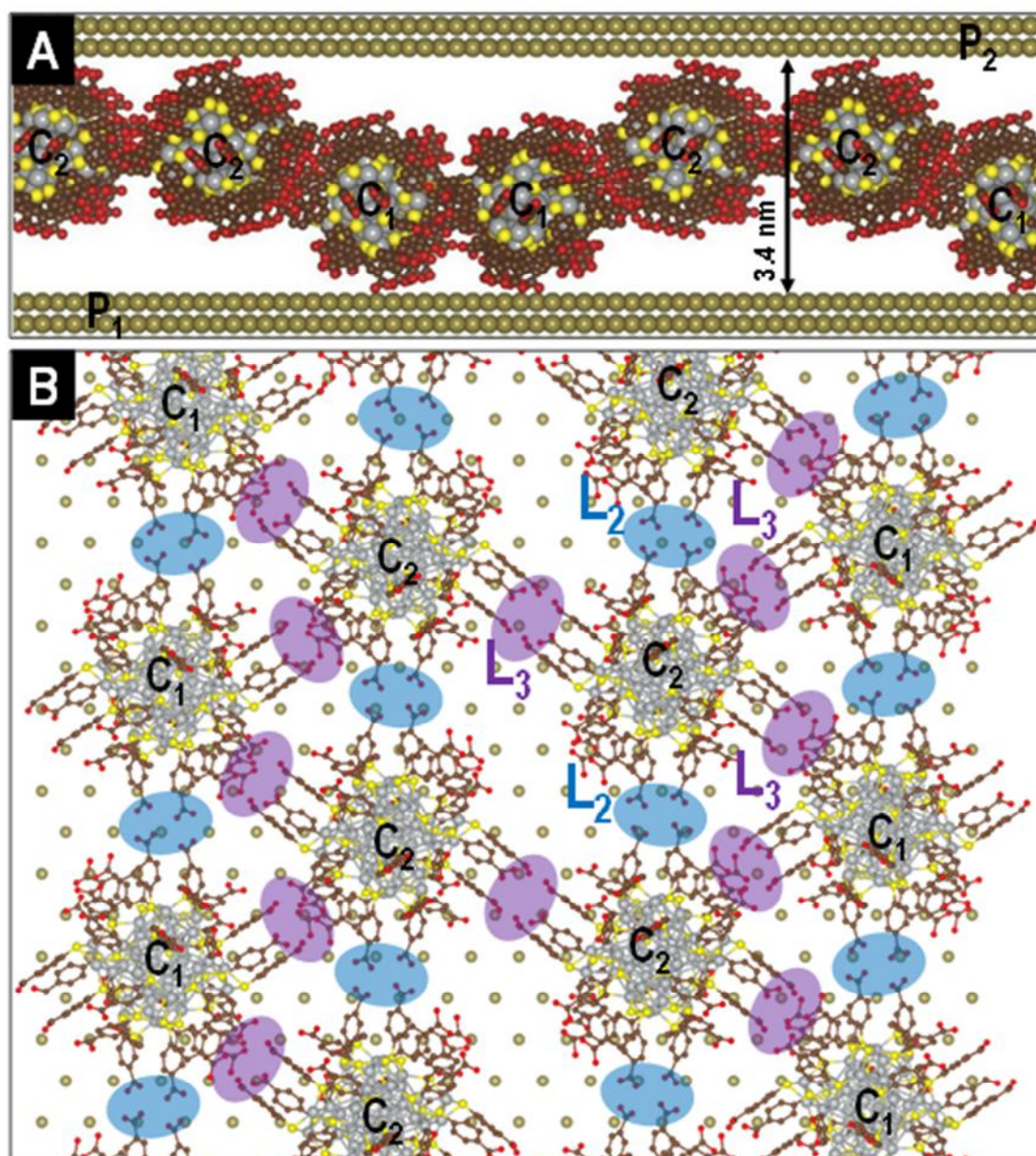


Figure S8. (A) Side view of Ag₄₄ clusters sandwiched between two parallel Te surfaces. (B) Top view of the same showing H-bonded network of Ag₄₄ clusters. Each cluster is surrounded by four clusters from the same plane and by two clusters from the second plane forming 13 H-bonds.

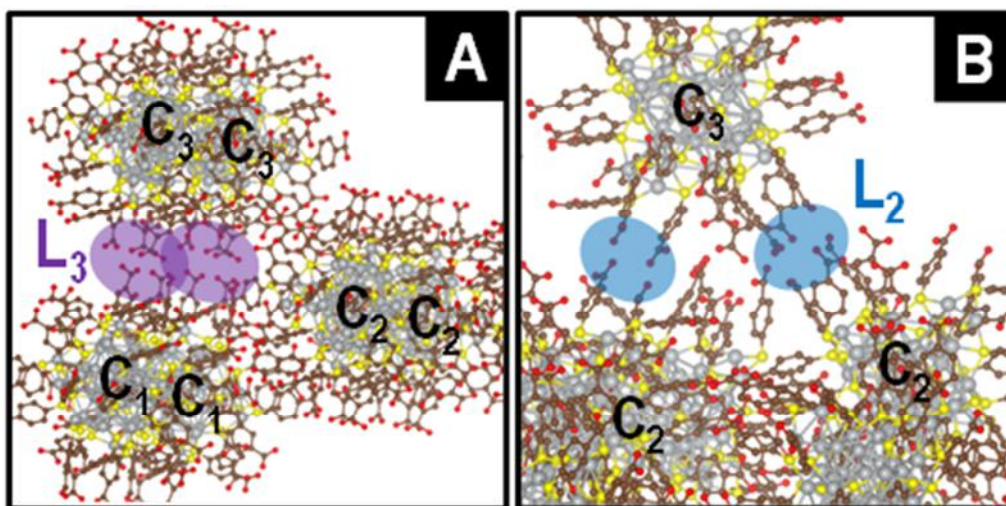


Figure S9. Zoomed in view of the Ag_{44} clusters in 81° orthogonal arrangement showing the formation of additional H-bonds, (A) L_3 H-bonds between C_3 and C_1 and (B) L_2 H-bonds between C_2 and C_1 .

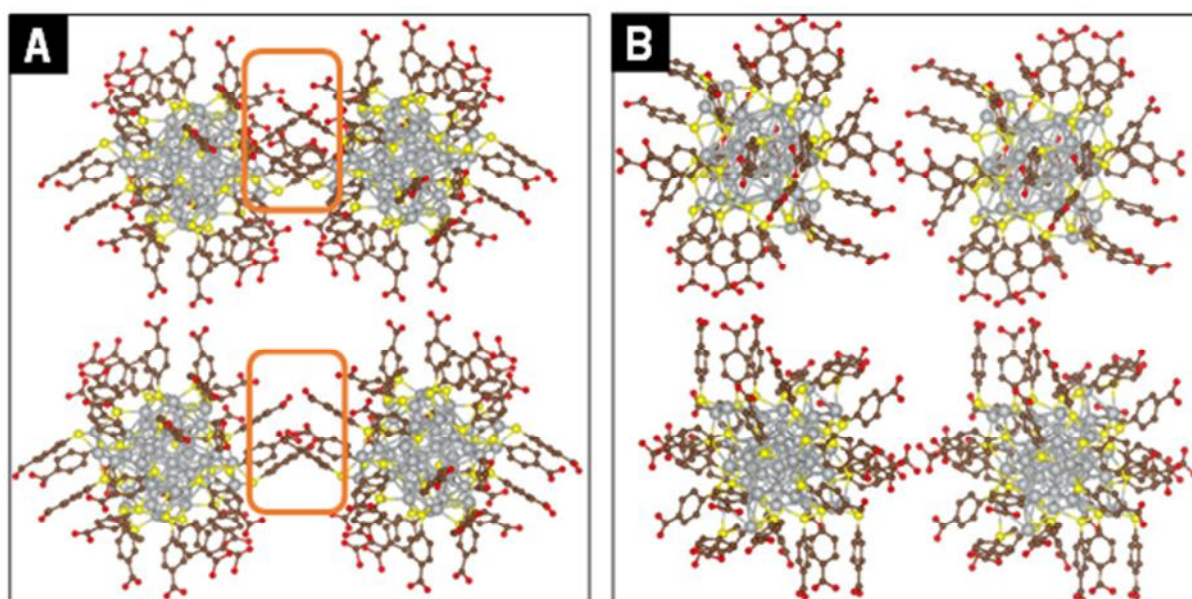


Figure S10. (A) Steric interactions between the neighboring clusters (marked) in 90° orthogonal arrangement. (B) Those interactions diminish in 81° orthogonal arrangement.

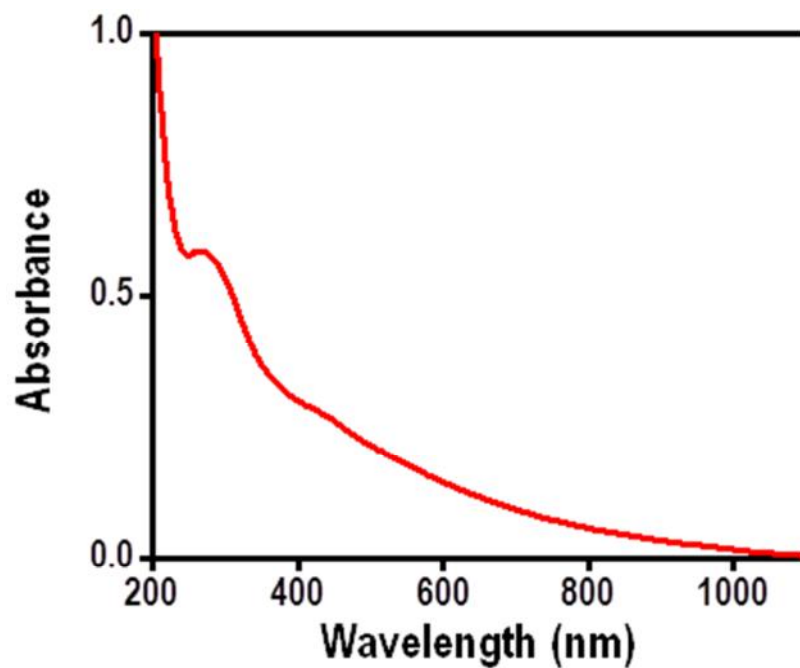


Figure S11. (A) UV-visible absorption spectrum of Au₁₀₂ in water.

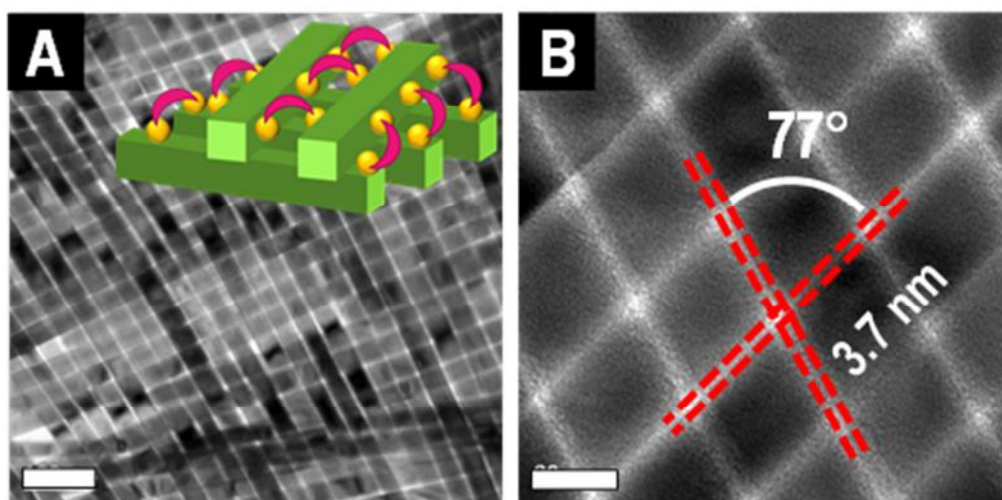


Figure S12. (A) TEM image of the orthogonal assembly formed from Au₁₀₂@Te NWs. A schematic representation of the assembly formation by inter-cluster H-bonding is shown in the inset. (B) Expanded view of the same assembly showing an inter NW distance of 3.7 nm and an interlayer NW angle of 77°. Scale bar is 100 nm in A and is 20 nm in B.

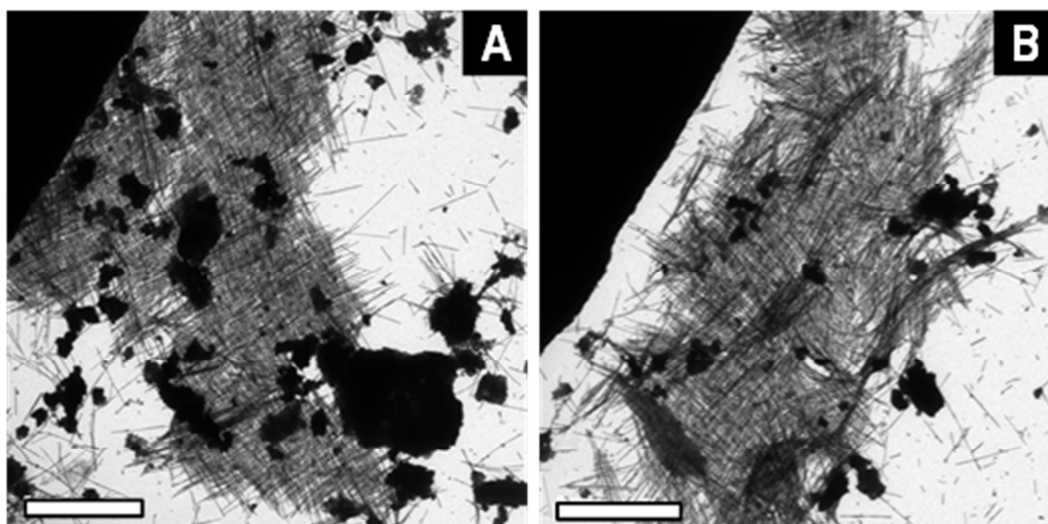


Figure S13. TEM images of orthogonal assembly formed after a dilute dispersion of $\text{Au}_{102}@\text{Te}$ NWs was allowed to dry on the TEM grid. The system preferentially forms bilayers. Scale bar is 5 μm in both the images.

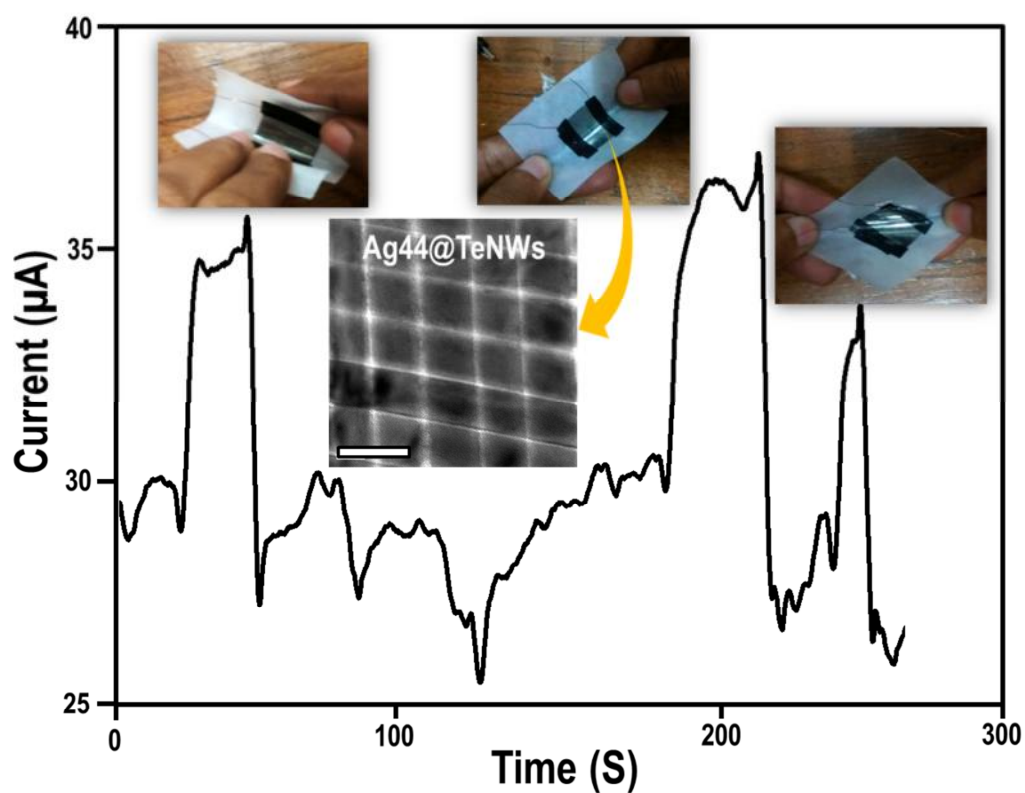


Figure S14. Change in the conductivity of the device made by transferring the crossed bilayer assembly of $\text{Ag}_{44}@\text{Te}$ NWs on PET substrate.

References

(1) S. R. Bahn and K. W. Jacobsen, *Comput. Sci. Eng.* 2002, 5, 56-66.

(2) K. Momma and F. Izumi, *J. Appl. Cryst.* 2011, 44, 1272-1276. Code available at <http://jp-minerals.org/vesta/en/>



Rapid dehalogenation of pesticides and organics at the interface of reduced graphene oxide–silver nanocomposite



Dibyashree Koushik^a, Soujit Sen Gupta^a, Shihabudheen M. Maliyekkal^b, T. Pradeep^{a,*}

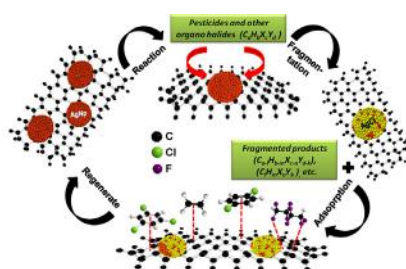
^a DST Unit of Nanoscience and Thematic Unit of Excellence, Department of Chemistry, Indian Institute of Technology Madras, Chennai 600036, India

^b Environmental Engineering Division, School of Mechanical and Building Sciences, VIT University, Chennai Campus, Chennai, 600127, India

HIGHLIGHTS

- Preparation of reduced graphene oxide–silver nanocomposite (RGO@Ag).
- Dehalogenation of various POPs at reduced graphene oxide–silver nanocomposite (RGO@Ag).
- A two step mechanism involving degradation followed by the adsorption.
- Adsorption kinetics followed a pseudo-second-order rate equation.
- The material has high adsorption capacity and can be reused for multiple cycles.

GRAPHICAL ABSTRACT



ARTICLE INFO

Article history:

Received 8 October 2015

Received in revised form

21 December 2015

Accepted 3 January 2016

Available online 11 January 2016

Keywords:

Reduced graphene oxide–silver nanocomposite (RGO@Ag)

Pesticide

Adsorption

Degradation

Water purification

ABSTRACT

This paper reports dehalogenation of various organohalides, especially aliphatic halocarbons and pesticides at reduced graphene oxide–silver nanocomposite (RGO@Ag). Several pesticides as well as chlorinated and fluorinated alkyl halides were chosen for this purpose. The composite and the products of degradation were characterized thoroughly by means of various microscopic and spectroscopic techniques. A sequential two-step mechanism involving dehalogenation of the target pollutants by silver nanoparticles followed by adsorption of the degraded compounds onto RGO was revealed. The composite showed unusual adsorption capacity, as high as 1534 mg/g, which facilitated the complete removal of the pollutants. Irrespective of the pollutants tested, a pseudo-second-order rate equation best described the adsorption kinetics. The affinity of the composite manifested chemical differences. The high adsorption capacity and re-usability makes the composite an excellent substrate for purification of water.

© 2016 Elsevier B.V. All rights reserved.

1. Introduction

Graphene, since its discovery [1] has witnessed a wide range of applications in the fields of biotechnology [2], catalysis [3,4], sensors [5] and electronics [6–8]. In contrast, its use in environmental

clean-up has started gaining momentum only in recent years [9]. Reduced cytotoxicity [10,11], large surface area [12], availability of delocalized π -electrons [10], antibacterial properties [13] and tunable chemical properties [13–15] make graphene an ideal choice for purification of water [16–21]. Among the various pollutants present in water, pesticides and halogenated compounds require special attention due to their widespread occurrence in the environment [22–25], acute toxicity [26–28], and chemical diversity [29]. Most of the halogenated compounds are now listed under

* Corresponding author. Fax: +91 44 2257 0545x0509.
E-mail address: pradeep@iitm.ac.in (T. Pradeep).

the category of persistent organic pollutants (POPs) and are highly susceptible to bioaccumulation in the food chain [30]. Efforts are made to detoxify and/or remove these POPs from water [31,32]. Recently, Maliyekkal et al. have proposed reduced graphene oxide (RGO) as a reusable substrate for the effective removal of pesticides such as chlorpyrifos, endosulphan and malathion from water [33]. The study showed unprecedented ability of RGO to remove these pesticides where adsorption is mediated through water. Liu et al. have shown that graphene-coated silica can be effectively used for the removal of organo phosphorus pesticides from water. The likely mechanism of adsorption was due to electron-donating abilities of the S, P, and N atoms and the strong π -bonding network of the benzene rings [34]. Wu et al. prepared graphene-based magnetic nanocomposites for the extraction of carbamate pesticides from environmental water samples by adsorption [35]. Very recent investigations by Gupta et al. have proved that graphene-silver composite does unusual dehydrohalogenation in which lindane is converted to trichlorobenzene [36]. Unlike graphene (supported and unsupported), this composite substrate enabled the degradation and subsequent adsorption of the products formed.

In this paper, we explore the versatility of reduced graphene oxide-silver nanocomposite (RGO@Ag) for dehalogenation. A diverse groups of pesticides (chlorpyrifos (CP), endosulfan (ES), dichlorodiphenyldichloroethylene (DDE)), chlorocarbons (carbon tetrachloride (CCl₄), chloroform (CHCl₃), dichloromethane (CH₂Cl₂)) and fluorocarbons (1,1,1,3,3,3-hexafluoro-2-propanol (HFP) and 1,1,1,2,2,3,3,4,4,5,5,6,6,7,7,8,8-heptadeca fluoro-10-iodo decane (HFID)) have been dehalogenated by the composite, in water at concentrations of relevance. We have also explored the likely mechanism of this chemistry. This work demonstrates that RGO@Ag is a versatile substrate and is capable of removing diverse pesticides and halogenated compounds in water at conditions of relevance to drinking water.

2. Experimental methods

2.1. Materials

Natural graphite flakes (95% of carbon) were obtained from Active Carbon India Pvt. Ltd. Ammonia (NH₃, 30%), sulfuric acid (H₂SO₄, 95–98%), and hydrochloric acid (HCl, 36%), were procured from Rankem Chemicals Pvt. Ltd., India. Phosphorus pentoxide (P₂O₅, 95%), hydrogen peroxide (H₂O₂, 98%) and hydrazine monohydrate (N₂H₄.H₂O, >99%) were purchased from SD Fine Chemicals Pvt. Ltd., India. Merck, India supplied potassium permanganate (KMnO₄, 98.5%). Potassium peroxydisulfate (K₂S₂O₈, 98%) was procured from Sisco Research Laboratories Pvt. Ltd., India. The pesticides and the halogenated organic samples were purchased from Sigma Aldrich. Ethanol (99.9%) and *n*-hexane (99.9%) were procured from Rankem Chemicals Pvt. Ltd. Stock solutions of the target pollutants (1000 mg/L) were prepared in ethanol and stored under refrigeration. Working concentrations of the pollutants were prepared by spiking appropriate volumes of the stock to the dispersion of the composite in water. All chemicals were of analytical grade and used as received. All solutions and suspensions were prepared in deionized water (DW), unless otherwise mentioned.

2.2. Synthesis of RGO@Ag

Graphene oxide (GO) was synthesized from graphite powder through a chemical process similar to the modified Hummers method [37]. RGO was synthesized through chemical reduction of GO [38–40]. Synthesis procedures are elaborated in S1 of the supplementary data along with basic characterization which includes TEM, AFM and Raman spectroscopy. Working concentrations of

RGO were prepared by serial dilution to 0.01 wt% of RGO dispersion. A calculated amount of AgNO₃ (0.01, 0.05 and 0.1 mM) was added to the RGO dispersion to obtain RGO@Ag composite. These solutions were kept undisturbed for about 24 h at room temperature (30 ± 2 °C) and atmospheric pressure to facilitate the formation of Ag NPs on the RGO surface. The composite was dialyzed by a cellulose membrane (dialysis tube, Sigma–Aldrich) to remove unwanted ions. The as-prepared composites were stored in a glass bottle for further use.

2.3. Adsorption experiments

Adsorption studies were performed in batch reactors of 20 mL capacity at room temperature (30 ± 2 °C). The working volume and the pH of the solution were maintained at 5 mL and at 7 ± 0.1, respectively. The required volume of the stock solution (1000 mg/L) was spiked into the reactor to achieve the pre-decided concentration of the target pollutant. The working solution has a small amount of ethanol (<0.5% by volume), which was used to prepare the stock solutions of the target pollutants. Solid–liquid separation was performed with a 200 nm cellulose acetate filter paper. The residual concentration of the solute and the by-products were analysed using a gas chromatograph (GC) (PerkinElmer, Clarrus 680) equipped with an electron-capture detector (ECD). The analysis conditions involved an injector temperature of 200 °C, an injection rate of 12.5 pts/s, a run time of 38.5 min, and a carrier gas flow rate of 1 mL/min. The contact time and the RGO@Ag dose were varied to study their effect on the removal of the target pollutants. All experiments were conducted in triplicate and average values are reported. The samples were analyzed immediately after the reaction. Control experiments were run in parallel to assess any possible natural degradation of the pollutants.

2.4. Instrumentation

A PerkinElmer Lambda 25 UV/vis spectrophotometer was used to measure the UV/vis spectrum. XPS measurements were done with an Omicron ESCAProbe spectrometer with polychromatic Mg K α X-rays ($h\nu = 1253.6$ eV). Raman spectra of RGO and GO were collected by a confocal Raman spectroscopy (WiTec GmbH CRM 200). The samples were imaged by a high-resolution transmission electron microscope (HRTEM) with a UHR polepiece (JEOL 3011, 300 kV) with an energy-dispersive spectroscopy (EDS) attachment (Oxford). A scanning electron microscope (SEM) equipped with EDS (FEI Quanta 200, Czechoslovakia) was used to record the surface morphology, elemental composition and the elemental map of the samples. Residual concentration of the samples in water was analyzed by GC-ECD (PerkinElmer, Clarus 680, coupled with electron-capture detector). The mass spectrometric studies were done by an electrospray system, 3200 Q-TRAP LC/MS/MS (Applied Biosystems).

3. Results and discussion

RGO@Ag was characterized using both spectroscopic and microscopic techniques. We present essential details of these studies below. The TEM image in Fig. 1 shows the presence of Ag NPs on the RGO sheet. The folds on the RGO sheets are marked in the figure with white arrows and the black dots on it represent the Ag NPs formed on the sheet. The Ag NPs formed are of uniform size (5 nm) and the lattice separation of 0.232 nm (shown in Fig. 1(a1) and an expanded image in Fig. 1(a2)) confirm that the nanoparticles formed exhibit the (1 1 1) lattice plane of silver. The XPS survey spectrum of the composite in supplementary data Fig. S2 shows the presence of carbon, oxygen and silver. The deconvoluted C1s spectrum shows the presence of oxygen functionality (C1s at 285.6

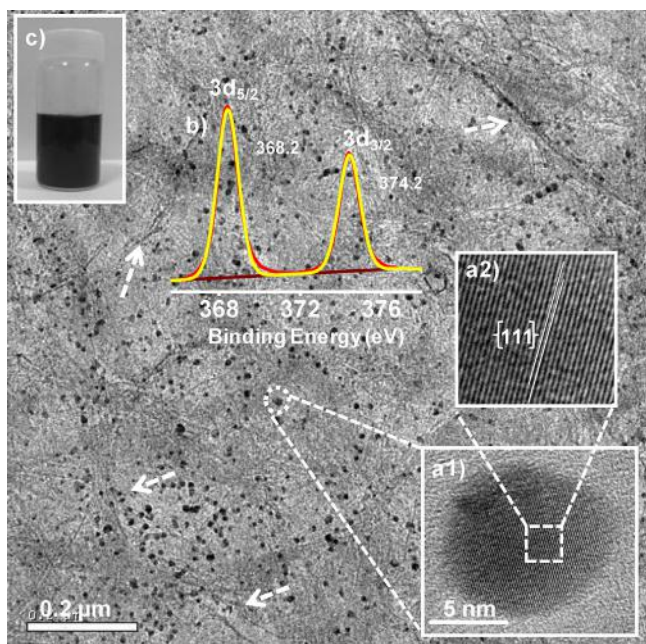


Fig. 1. TEM image of RGO@Ag composite; the folding of the RGO sheets is marked with white arrows. Insets: (a1) HRTEM image of a single nanoparticle, (a2) expanded portion from (a1) showing a lattice spacing of 0.232 nm corresponding to the (1 1 1) lattice plane, (b) deconvoluted XPS spectrum of Ag in the composite and (c) photograph showing the dispersed nature of the composite.

and 288.6 eV, due to C–O and C=O) along with C=C at 284.5 eV as the major components, as expected for sulphonated RGO (shown in Supplementary data Fig. S2). The deconvoluted Ag3d XPS spectrum is shown in Fig. 1b and the Ag3d_{5/2} peak around 368.2 eV suggests that the oxidation state of silver is zero. This further confirms the presence of uncapped Ag NPs on the RGO sheet. Preparation of RGO@Ag and its characterization has been reported elsewhere [9,41]. The photograph in Fig. 1c shows the dispersed nature of the composite, which remains stable even after 6 months of preparation. The UV/vis spectrum of the dispersion in supplementary data Fig. S3 shows the presence of two peaks, one at 267 nm which characterizes RGO and the other at 420 nm, due to the plasmonic resonance of Ag NPs present on the RGO@Ag composite. These results confirm the formation of RGO@Ag composite.

This RGO@Ag composite was tested for the removal of various pollutants from water, which included different pesticides and halogenated compounds. Fig. 2 shows the UV/vis spectrum for the removal of different pesticides, which were of concern in our studies. The decrease in the intensity of the peaks with respect to time ensures that the pesticides are removed from water when treated with RGO@Ag composite. Fig. 2A shows the efficiency of RGO@Ag composite for the removal of CP from water (3 ppm) after 60 min of reaction when different loading percentage of silver was taken in the composite. When 0.01, 0.05, 0.1 mM of precursor AgNO₃ was used in 0.01 wt% of RGO solution, the resulting composites are termed as RGO@Ag^I, RGO@Ag^{II} and RGO@Ag^{III}, respectively. It was seen that RGO@Ag^{II} was better in performance than RGO@Ag^I, but there was no improvement for RGO@Ag^{III}. So, RGO@Ag^{II} (termed as RGO@Ag throughout the text) was taken as the standard for all other reactions unless mentioned. Time-dependent UV/vis spectra were taken for CP, which shows that CP has a characteristic peak around 297 nm. When CP was reacted with RGO@Ag composite, decrease of the peak height with respect to time indicates that CP is removed from water (Fig. 2B). Similarly, in Fig. 2C, 2 ppm of ES was taken, having a peak at 236 nm. When treated with the RGO@Ag composite, time dependent UV/vis shows that ES was removed

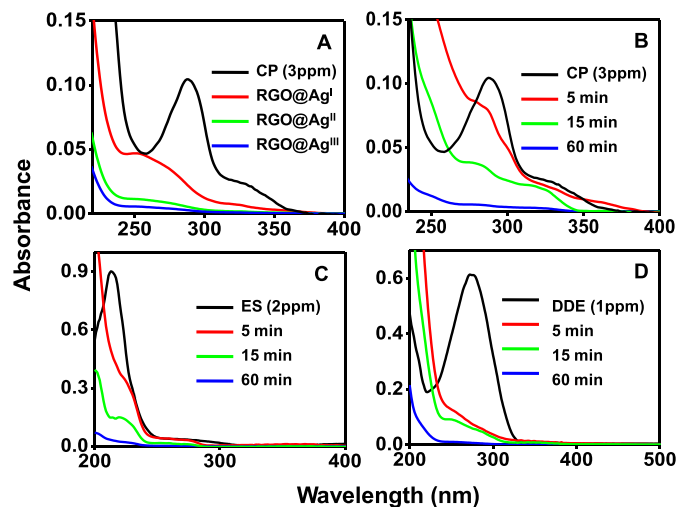


Fig. 2. UV/vis spectra showing the removal of (A) CP (at different concentrations of Ag NPs on RGO@Ag), (B) CP, (C) ES and (D) DDE at different time intervals by RGO@Ag^{II} (termed as RGO@Ag in the text).

from the solution as a function of time. A complete removal was observed after 60 min of reaction. Similar observation was also made for DDE (1 ppm) which shows a peak maximum around 285 nm as shown in Fig. 2D (black trace) and it was removed after reaction with RGO@Ag composite within 60 min.

Similarly, removal of pesticides (1 ppm) from water was confirmed by means of GC-ECD technique, which is one of the best tools for quantitative estimation of halogenated compounds. For CP, we got a peak at a retention time of 12.2 min (Fig. 3Aa), which disappeared completely after 1 h of reaction with RGO@Ag (5 mL in each case) composite (Fig. 3Ab). The time-dependent GC-ECD for CP is presented in supplementary data Fig. S4, which shows that there was degradation of CP followed by complete removal of the degraded products. Similarly, DDE has a peak at a retention time of 13.7 min, which was also removed during 1 h of reaction as shown in Fig. 3B. ES and HFID removal are shown in Fig. 3C and D, which have peaks at 13.2 and 4.5 min, respectively. The corresponding structures of the compounds are given in the insets. The GC-ECD data for CCl₄, CHCl₃, CH₂Cl₂ and HFP before and after the reaction with the composite are shown in supplementary data Fig. S5.

Mass spectrometry is one of the best available tools to detect organic molecules. As mentioned previously, the RGO@Ag composite degrades the organohalides first into smaller fragments and then these fragments get adsorbed onto the RGO sheet. Therefore, we used ESI MS to characterize these molecules. Fig. 4Aa represents the ESI MS of DDE which shows a peak at *m/z* 283 due to C₁₄H₈Cl₃⁺. The isotope distribution of the peak is shown in the inset of the figure which arises because of the presence of three Cl atoms. Fig. 4Ab shows the mass spectrum of the fragments formed after the reaction of DDE with RGO@Ag. A peak around *m/z* 145 represents the formation of dichlorobenzene in the reaction mixture. The isotope distribution of the peak is presented in the inset which matches perfectly with the theoretical distribution of C₆H₄Cl₂⁺. Similarly, Fig. 4Ba presents the MS of CP, with a molecular ion at *m/z* 351 in the positive mode. The corresponding isotope distribution is shown in the inset of the figure. The product formed shows peaks at *m/z* 258 and 179, corresponding to C₅HCl₃NOPS⁺ and C₅HCl₃N⁺, respectively (Fig. 4Bb). It was seen that RGO@Ag is indeed degrading halogenated compounds; the ESI MS of ES is shown in Fig. S6 (Supplementary data) along with that of the fragmented product.

To characterize RGO@Ag composite after reaction, TEM image of the material was taken as shown in Fig. 5A. The wrinkles on RGO sheets are marked with white arrows and the black dots represent

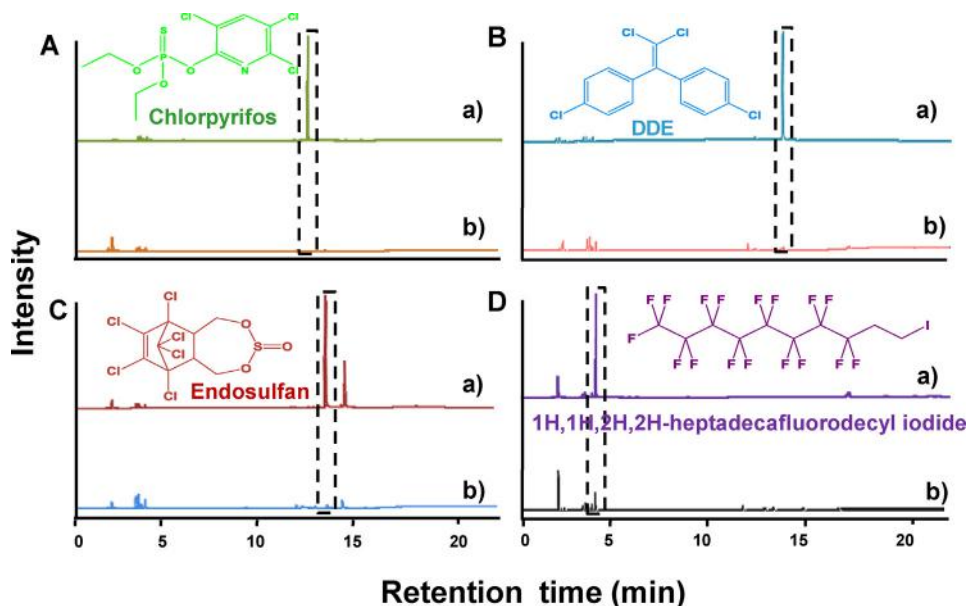


Fig. 3. GC-ECD data for the removal of (A) CP, (B) DDE, (C) ES, (D) HDIF after reaction with RGO@Ag. In all cases, the reaction time was 1 h. The traces a and b correspond to the traces before and after the reaction. The disappearance of the respective pollutant is shown by the dotted boxes.

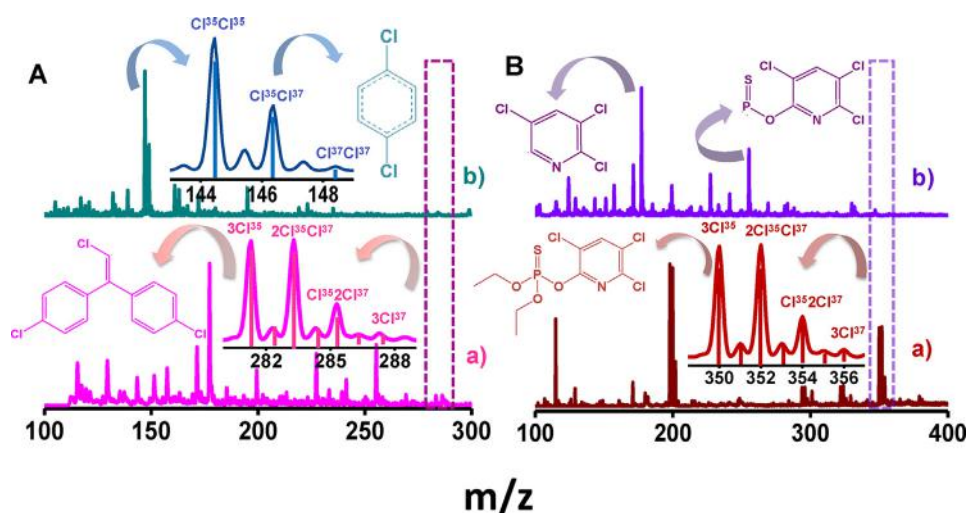


Fig. 4. ESI MS of (A) DDE (pink trace (a)) and the product (olive trace (b)) and (B) CP (brown trace (a)) and the product (violet trace (b)). Inset shows the isotope distribution of chlorine along with the corresponding molecular structure of the analytes. Isotope distribution is indicated on the spectrum. The pollutant region is highlighted by the dotted boxes. (For interpretation of the references to colour in this figure legend, the reader is referred to the web version of this article.)

Ag NPs as previously shown. Upon closer examination of the lattice spacing of the particles, it was seen that two different types of lattice spacing are present. One at 0.242 nm is due to the (1 1 1) lattice of silver and the other at 0.324 nm is due to the (1 1 1) lattice of AgCl [42] (Fig. 5A1). This shows that Ag NPs on RGO@Ag composite are responsible for the degradation of halogenated compounds. Expanded views of the HRTEM images are shown in the inset of Fig. 5A(a and b). Ag NPs on the composites facilitate the dehalogenation of the target compounds and get converted to AgCl as confirmed by elemental mapping. For elemental mapping, a bigger particle was chosen deliberately as shown in Fig. 5B. The elemental maps show the presence of Ag in RGO@Ag composite. Chlorine and phosphorus come from CP which got adsorbed onto the composite. Fig. 5C represents the TEM-EDS of the composite after reaction with CP. XPS of the composite was taken after reaction with CP; the survey spectrum is represented in supplementary data Fig. S7. The C1s spectrum is shown in Fig. 5D which on deconvolution shows the presence of peaks centred around 284.5, 285.7 and 288.7 eV

corresponding to C=C, C–O and C=O/O–C–O, respectively. The deconvoluted Ag3d spectrum is shown in Fig. 5E. A change in the oxidation state of silver from Ag(0) to Ag(I) corresponding to the formation of AgCl from Ag NPs is seen. The shift of Ag3d_{5/2} peak from 368.2 eV to 367.4 eV after reaction represents the conversion of Ag(0) to Ag(I). This is shown in supplementary data Fig. S8. Note that in Ag, oxidation leads to reduction in binding energy of 0.8 eV [43]. The presence of Cl2p_{3/2} and Cl2p_{1/2} peaks at 199.2 and 200.8 eV confirms the dehalogenation of the halogenated pollutants when it reacts with RGO@Ag; i.e. it confirms the presence of metal chloride (AgCl), whereas the presence of peak at higher binding energy (201.1 and 202.7 eV) represents the presence Cl2p_{3/2} and Cl2p_{1/2} of organic chloride. The deconvoluted O1s and S2p peaks are shown in supplementary data Fig. S7. The SEM-EDS spectrum of the composite after reaction with DDE and ES are shown in supplementary data Fig. S9A and B.

The schematic presented in Scheme 1 shows two-step mechanistic cycle for the removal of pesticides and other halogenated

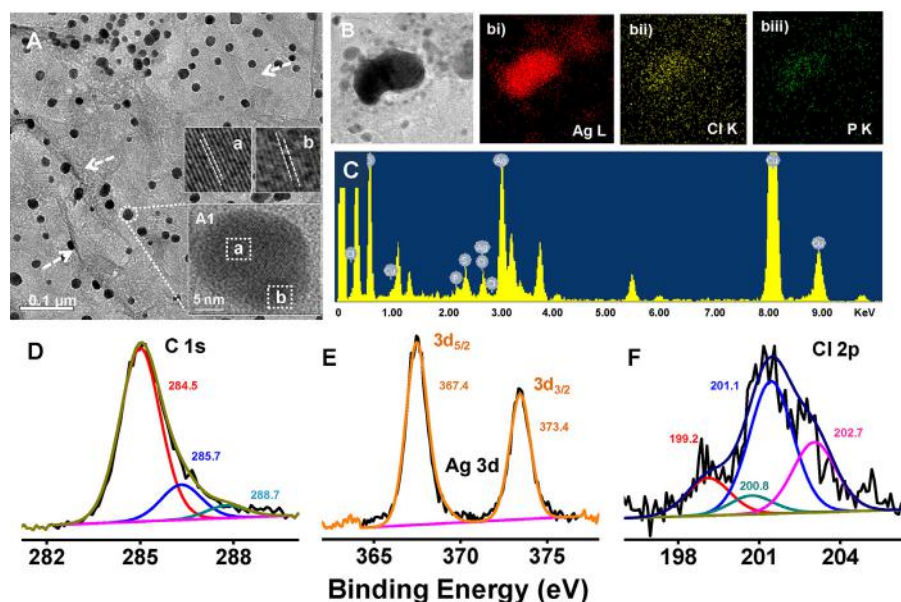
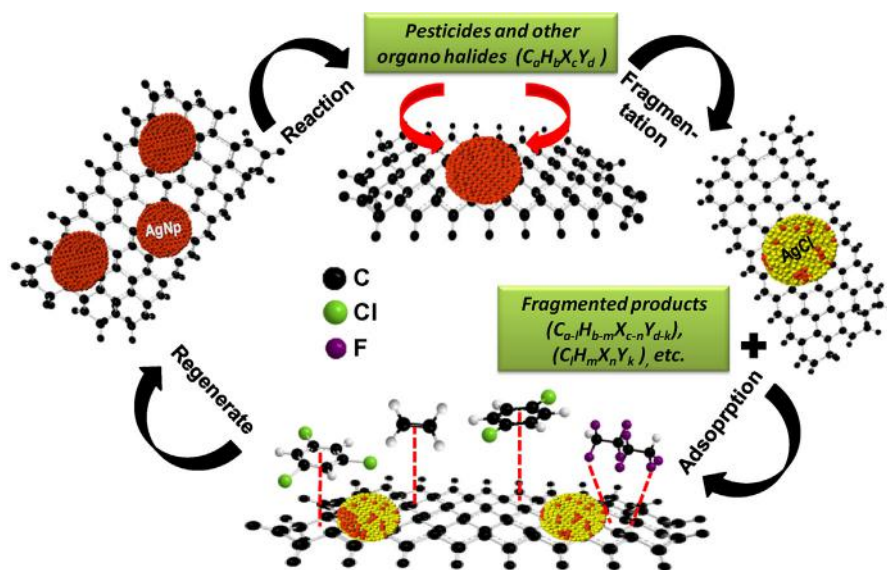


Fig. 5. Data corresponding to RGO@Ag after the reaction. (A) TEM image, (A1) HRTEM image of a single Ag NP, (a and b) expanded views of the HRTEM image presented in A1 showing the lattice spacing due to Ag (1 1 1). (B) TEM image of Ag NPs of 50 nm size, (bi–biii) elemental maps of Ag, Cl and P, respectively. (C) TEM-EDS, (D–F) Deconvoluted XPS spectrum of C1s, Ag3d and Cl2p.



Scheme 1. Schematic showing the events involved in the removal of the pesticides and organo-halides from water.

pollutants from water. The first step involves the reaction of Ag NPs with the halogenated compounds at the interface of RGO@Ag and simultaneous degradation of the pollutant into smaller fragments by Ag NPs. In this course, Ag NPs are converted to AgCl. The next step comprises of the removal of the fragmented products from water by adsorption on the RGO sheet by π - π interactions arising between π electrons of RGO and aromatic compounds. Interactions such as van der Waals forces or hydrogen bonding are also likely. The composite once used can be regenerated and used multiple times. This is discussed later in the text.

4. Reaction kinetics

Experiments were performed to understand the time dependent removal of the pollutants individually and in combination. Initial concentrations of the target pollutants were maintained at

2 mg/L. The data are shown in Fig. 6A. We see that around 90% of the target species were removed from the aqueous medium in the first 30 min of the commencement of the adsorption process. Complete removal of the pollutants was achieved in <3 h of contact time. Two well-known mathematical models including Lagergren pseudo-first-order [44] and Ho's pseudo second-order reaction rate [45,46] models were used to describe the kinetic data. The mathematical representations of these models are given below.

$$\text{Pseudo-first-order equation } q_t = q_e (1 - e^{-k_1 t}) \quad (1)$$

$$\text{Pseudo-second-order equation } q_t = \frac{q_e^2 k_2 t}{1 + q_e k_2 t} \quad (2)$$

Where, q_e and q_t represents the amount of target pollutants removed per unit gram of RGO@Ag at equilibrium and at any time t (h), respectively, respectively. k_1 (1/h) and k_2 (g/mg h) are the first-order and second-order rate constants, respectively.

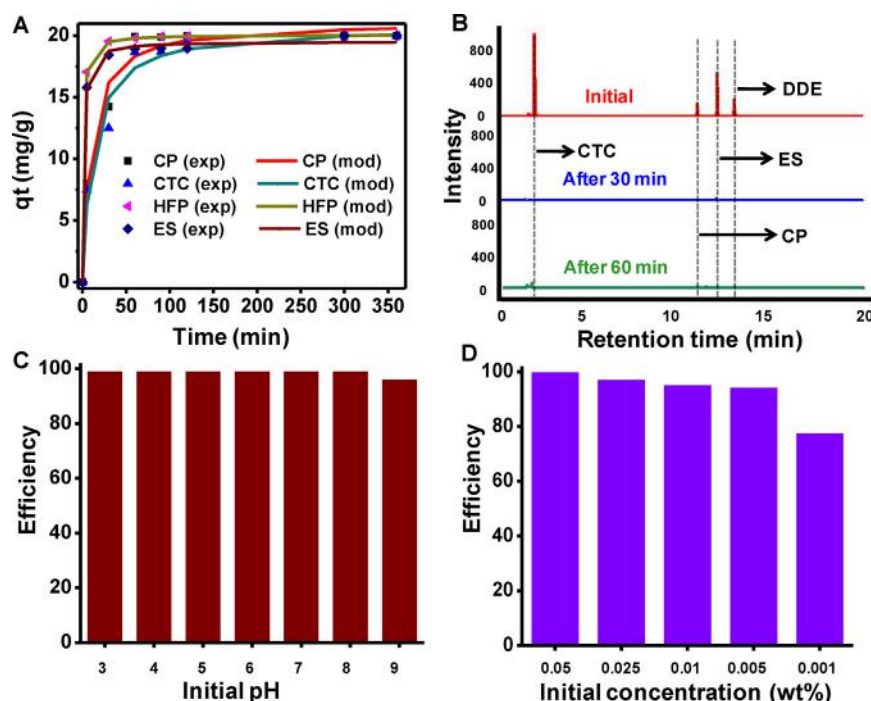


Fig. 6. (A) Kinetic data showing the pseudo second-order fit for the individual pollutants, (B) The removal rate when a group of pollutants (CP, ES, CCl₄ and DDE) was taken, (C) the effect of initial pH and (D) removal efficiency as a function of initial concentration of the composite in water. (For interpretation of the references to colour in the text, the reader is referred to the web version of this article.)

Table 1

Estimated model parameters of pseudo second-order reaction.

Pollutants	K_2 (g/mg h)	q_e (mg/g)	RMSE	χ^2
CP	0.0052	21.1000	0.9960	0.4740
ES	0.0415	19.5300	0.3500	0.0510
CCl ₄	0.0042	20.7400	1.1080	0.7770
HFP	0.0563	20.0900	0.0030	0.0004

Pseudo-second-order fits along with the experimental data are shown in Fig. 6A. The model parameters are summarized in Table 1. The corresponding first-order fits and the model parameters are shown in Supplementary data Fig. S10. As evident from low RMSE (root mean squared error) and Chi-square (χ^2) values, the pseudo-second-order equation describes the data better. The rate of adsorption significantly varies with the type of pollutants studied. Maximum rate was observed in the case of HFP followed by ES, CP and CCl₄. Similar removal patterns were observed even when a mixture of these compounds were spiked to RGO@Ag dispersion (Fig. 6B). The high rate of reaction of HFP to RGO@Ag can be attributed to the high electronegativity of fluorine. The interaction between silver and easily accessible chloride ions in ES may be the reason for the relatively high rate of removal of ES over CP. Unlike the other compounds, the aliphatic nature and strong C–Cl bond in CCl₄ makes the pollutant less accessible contributing to the slow rate of reaction.

Fig. 6B shows the removal kinetics when a group of pollutants was used (i.e. CP, ES, CCl₄ and DDE) at initial concentration of 1 ppm each (Fig. 6B, red trace). 5 mL of 0.01 wt% RGO@Ag was taken and the pollutant mixture was spiked. The reaction was carried for an hour and two sets of readings were taken at 30 and 60 min. As expected, ES had fastest reaction rate followed by CP, DDE and CCl₄. The removal efficiency of the pollutants did not vary with pH of the initial solution, in the range of 3–9 (Fig. 6C). The pH of the solution was maintained acidic by using HNO₃ and basic by NaHCO₃. The pH was not varied above 9 as it results in silver hydroxide. It was also seen that the removal capacity increases with dilution of

RGO@Ag solution as shown in Fig. 6D. The capacity that is considered here is the amount of target pollutant removed per gram of RGO@Ag (i.e. unit uptake capacity). The unit uptake capacities of the target pollutants increased with decreasing dose of the composite. This can be due to increased mass transfer at higher adsorbate to adsorbent ratio. Free surface area of the composite increases with dilution because of better separation of RGO sheets at higher dilution, which enhances the free adsorption/reaction sites and hence, increases the removal capacity. To check the maximum adsorption capacity of the composite for each pollutant, 5 mL of 0.001 wt% of RGO@Ag solution was taken and 2 ppm of the pollutant was spiked on it and after 2 h, the reaction was stopped and the solution was analyzed in GC-ECD. The removal capacity was calculated in mg/g of the pollutant removed/g of composite. The maximum removal capacity of the pollutant is reported in Table S11 of Supplementary data. The proposed dehalogenation chemistry and subsequent removal of the degraded products from water does not occur on RGO or Ag NPs in isolation, as revealed from separate experiments [36].

The RGO can be regenerated and reused multiple times. Firstly, the composite was stirred with hexane for 10 min, filtered and dried in ambient conditions at room temperature. Then, the composite was taken and concentrated ammonia solution was added to it and was sonicated. The pre-formed AgCl after the reaction dissolved in the solution leaving behind RGO. This RGO was further filtered, washed with DI water several times and was redispersed in water. A calculated amount of AgNO₃ (0.01, 0.05 and 0.1 mM) was added to RGO dispersion to obtain the RGO@Ag composite as discussed earlier. The performance of the composite was tested and the efficiency was found to be more than 95% even after 5 repeated uses.

5. Conclusion

The paper demonstrated the versatility of RGO@Ag composite in removing various group of pesticides and halogenated compounds in water. Unlike other graphene-based substrates studied

for the purpose, the proposed composites enable the degradation and complete removal of the pollutants from water. A two step mechanism involving the degradation of the pollutants by Ag nanoparticles followed by the adsorption of the reaction products onto the RGO sheet by π - π interaction is proposed. The substrate is reusable and can be employed as an effective medium for removing pesticides and halogenated compounds present in water. This study would open an additional direction for the removal of POPs in water.

Acknowledgments

We thank the Nano Mission, Government of India operated by of the Department of Science and Technology (DST), for supporting the research program. SSG thanks the SERB, CII and Thermax India Pvt. Ltd. for a research fellowship. D.K. was a summer fellow from the Centre for Nanotechnology, Central University of Jharkhand, Ranchi, while this work was performed.

Appendix A. Supplementary data

Supplementary data available: Preparation of RGO and its basic characterization, XPS survey spectrum of RGO@Ag, UV/vis spectrum of RGO@Ag, time dependent GC-ECD showing complete removal of pesticide CP from water, GC-ECD showing the removal different compounds, ESI MS of endosulphan, XPS survey spectrum of the RGO@Ag composite after the reaction with CP, deconvoluted XPS spectrum of Ag in RGO@Ag before and after reaction with CP, SEM-EDS of RGO@Ag composite after the reaction with DDE and ES, pseudo-first-order kinetic plots for the adsorption of pesticides by RGO@Ag composites and the maximum removal capacity of the RGO@Ag composite for different pollutant in mg/g.

Supplementary data associated with this article can be found, in the online version, at <http://dx.doi.org/10.1016/j.jhazmat.2016.01.004>.

References

- [1] A.K. Geim, K.S. Novoselov, The rise of graphene, *Nat. Mater.* 6 (2007) 183–191.
- [2] Z. Liu, J.T. Robinson, X. Sun, H. Dai, PEGylated nanographene oxide for delivery of water-insoluble cancer drugs, *J. Am. Chem. Soc.* 130 (2008) 10876–10877.
- [3] H.-P. Jia, D.R. Dreyer, C.W. Bielawski, Graphite oxide as an auto-tandem oxidation-hydration-aldol coupling catalyst, *Adv. Synth. Catal.* 353 (2011) 528–532.
- [4] D.R. Dreyer, C.W. Bielawski, Carbocatalysis: heterogeneous carbons finding utility in synthetic chemistry, *Chem. Sci.* 2 (2011) 1233–1240.
- [5] Q. Mei, Z. Zhang, Photoluminescent graphene oxide ink to print sensors onto microporous membranes for versatile visualization bioassays, *Angew. Chem. Int. Ed.* 51 (2012) 5602–5606.
- [6] L. Tang, Y. Wang, Y. Li, H. Feng, J. Lu, J. Li, Preparation, structure, and electrochemical properties of reduced graphene sheet films, *Adv. Funct. Mater.* 19 (2009) 2782–2789.
- [7] R.S. Sundaram, C. Gómez-Navarro, K. Balasubramanian, M. Burghard, K. Kern, Electrochemical modification of graphene, *Adv. Mater.* 20 (2008) 3050–3053.
- [8] C.N.R. Rao, A.K. Sood, R. Voggu, K.S. Subrahmanyam, Some novel attributes of graphene, *J. Phys. Chem. Lett.* 1 (2010) 572–580.
- [9] T.S. Sreeprasad, S.M. Maliyekkal, K.P. Lisha, T. Pradeep, Reduced graphene oxide-metal/metal oxide composites: facile synthesis and application in water purification, *J. Hazard. Mater.* 186 (2011) 921–931.
- [10] T. Liu, Y. Li, Q. Du, J. Sun, Y. Jiao, G. Yang, Z. Wang, Y. Xia, W. Zhang, K. Wang, H. Zhu, D. Wu, Adsorption of methylene blue from aqueous solution by graphene, *Colloids Surf. B* 90 (2012) 197–303.
- [11] W. Hu, C. Peng, M. Lv, X. Li, Y. Zhang, N. Chen, C. Fan, Q. Huang, Protein corona-mediated mitigation of cytotoxicity of graphene oxide, *ACS Nano* 5 (2011) 3693–3700.
- [12] M.D. Stoller, S. Park, Y. Zhu, J. An, R.S. Ruoff, Graphene-based ultracapacitors, *Nano Lett.* 8 (2008) 3498–3502.
- [13] F. Li, Y. Bao, J. Chai, Q. Zhang, D. Han, L. Niu, Synthesis and application of widely soluble graphene sheets, *Langmuir* 26 (2010) 12314–12320.
- [14] Y. Zhu, S. Murali, W. Cai, X. Li, J.W. Suk, J.R. Potts, R.S. Ruoff, Graphene and graphene oxide: synthesis, properties, and applications, *Adv. Mater.* 22 (2010) 3906–3924.
- [15] O.C. Compton, B. Jain, D.A. Dikin, A. Abouimrane, K. Amine, S.T. Nguyen, Chemically active reduced graphene oxide with tunable C/O ratios, *ACS Nano* 5 (2011) 4380–4391.
- [16] T.S. Sreeprasad, T. Pradeep, Graphene for environmental and biological application, *Int. J. Mod. Phys. B* 26 (2012) 1242001–1242026.
- [17] V. Chandra, J. Park, Y. Chun, J.W. Lee, I.-C. Hwang, K.S. Kim, Water-dispersible magnetite-reduced graphene oxide composites for arsenic removal, *ACS Nano* 4 (2010) 3979–3986.
- [18] H. Gao, Y. Sun, J. Zhou, R. Xu, H. Duan, Mussel-inspired synthesis of polydopamine-functionalized graphene hydrogel as reusable adsorbents for water purification, *ACS Appl. Mater. Interfaces* 5 (2012) 425–432.
- [19] H. Li, L. Zou, L. Pan, Z. Sun, Novel graphene-like electrodes for capacitive deionization, *Environ. Sci. Technol.* 44 (2010) 8692–8697.
- [20] E.N. Wang, R. Karnik, Water desalination: graphene cleans up water, *Nat. Nanotechnol.* 7 (2012) 552–554.
- [21] Z.-H. Huang, X. Zheng, W. Lv, M. Wang, Q.-H. Yang, F. Kang, Adsorption of lead(II) ions from aqueous solution on low-temperature exfoliated graphene nanosheets, *Langmuir* 27 (2011) 7558–7562.
- [22] S.S. Gupta, T.S. Sreeprasad, S.M. Maliyekkal, S.K. Das, T. Pradeep, Graphene from sugar and its application in water purification, *ACS Appl. Mater. Interfaces* 4 (2012) 4156–4163.
- [23] S. Simonich, R. Hites, Global distribution of persistent organochlorine compounds, *Science* 269 (1995) 1851–1852.
- [24] B. Strandberg, R.A. Hites, Concentration of organochlorine pesticides in wine corks, *Chemosphere* 44 (2001) 729–735.
- [25] B. Nagappa, G.T. Chandrappa, Mesoporous nanocrystalline magnesium oxide for environmental remediation, *Microporous Mesoporous Mater.* 106 (2007) 212–218.
- [26] A.K. Leight, R.F. Van Dolah, Acute toxicity of the insecticides endosulfan, chlorpyrifos, and malathion to the epibenthic estuarine amphipod *Gammarus palustris* (Bousfield), *Environ. Toxicol. Chem.* 18 (1999) 958–964.
- [27] B. Xuereb, P. Noury, V. Felten, J. Garric, O. Geffard, Cholinesterase activity in *Gammarus pulex* (*Crustacea amphipoda*): characterization and effects of chlorpyrifos, *Toxicology* 236 (2007) 178–189.
- [28] M.E. DeLorenzo, L.A. Taylor, S.A. Lund, P.L. Pennington, E.D. Strozier, M.H. Fulton, Toxicity and bioconcentration potential of the agricultural pesticide endosulfan in phytoplankton and zooplankton, *Arch. Environ. Contam. Toxicol.* 42 (2002) 173–181.
- [29] J. Franzaring, L.J.M. van der Eerden, Accumulation of airborne persistent organic pollutants (POPs) in plants, *Basic Appl. Ecol.* 1 (2000) 25–30.
- [30] S.L. Simonich, R.A. Hites, Organic pollutant accumulation in vegetation, *Environ. Sci. Technol.* 29 (1995) 2905–2914.
- [31] E. Austin, A.I. Schäfer, A.G. Fane, T.D. Waite, Ultrafiltration of natural organic matter, *Sep. Purif. Technol.* 22–23 (2001) 63–78.
- [32] J. Xu, L. Wang, Y. Zhu, Decontamination of bisphenol A from aqueous solution by graphene adsorption, *Langmuir* 28 (2012) 8418–8425.
- [33] S.M. Maliyekkal, T.S. Sreeprasad, D. Krishnan, S. Kouser, A.K. Mishra, U.V. Waghmare, T. Pradeep, Graphene: a reusable substrate for unprecedented adsorption of pesticides, *Small* 9 (2013) 273–283.
- [34] X. Liu, H. Zhang, Y. Ma, X. Wu, L. Meng, Y. Guo, G. Yu, Y. Liu, Graphene-coated silica as a highly efficient sorbent for residual organophosphorus pesticides in water, *J. Mater. Chem. A* 1 (2013) 1875–1884.
- [35] Q. Wu, G. Zhao, C. Feng, C. Wang, Z. Wang, Preparation of a graphene-based magnetic nanocomposite for the extraction of carbamate pesticides from environmental water samples, *J. Chromatogr. A* 1218 (2011) 7936–7942.
- [36] S. Sen Gupta, I. Chakraborty, S.M. Maliyekkal, T. Adit Maark, D.K. Pandey, S.K. Das, T. Pradeep, Simultaneous dehalogenation and removal of persistent halocarbon pesticides from water using graphene nanocomposites: a case study of lindane, *ACS Sustainable Chem. Eng.* 3 (2015) 1155–1163.
- [37] W.S. Hummers, R.E. Offeman, Preparation of graphitic oxide, *J. Am. Chem. Soc.* 80 (1958) 1339.
- [38] Y. Si, E.T. Samulski, Synthesis of water soluble graphene, *Nano Lett.* 8 (2008) 1679–1682.
- [39] D. Li, M.B. Muller, S. Gilje, R.B. Kaner, G.G. Wallace, Processable aqueous dispersions of graphene nanosheets, *Nat. Nano* 3 (2008) 101–105.
- [40] K. Haubner, J. Murawski, P. Olk, L.M. Eng, C. Ziegler, B. Adolph, E. Jaehne, The route to functional graphene oxide, *ChemPhysChem* 11 (2010) 2131–2139.
- [41] K.A.S. Fernando, V.G. Watson, X. Wang, N.D. McNamara, M.C. JoChum, D.W. Bair, B.A. Miller, C.E. Bunker, Migration of silver nanoparticles from silver decorated graphene oxide to other carbon nanostructures, *Langmuir* 30 (2014) 11776–11784.
- [42] B. Andryushechkin, K. Eltsov, V. Shevlyuga, V.Y. Yurov, Direct STM observation of surface modification and growth of AgCl islands on Ag (1 1 1) upon chlorination at room temperature, *Surf. Sci.* 431 (1999) 96–108.
- [43] V.K. Kaushik, XPS core level spectra and Auger parameters for some silver compounds, *J. Electron. Spectrosc. Relat. Phenom.* 56 (1991) 273–277.
- [44] S.Y. Lagergren, Zur Theorie der sogenannten Adsorption gelöster Stoffe (1898).
- [45] Y.S. Ho, G. McKay, The kinetics of sorption of divalent metal ions onto sphagnum moss peat, *Water Res.* 34 (2000) 735–742.
- [46] Y.-S. Ho, Review of second-order models for adsorption systems, *J. Hazard. Mater.* 136 (2006) 681–689.

Supplementary data

**Rapid dehalogenation of pesticides and organics at the interface of reduced
graphene oxide-silver nanocomposite**

Dibyashree Koushik^a, Soujit Sen Gupta ^a, Shihabudheen M. Maliyekkal^b and T. Pradeep ^{a,}*

*^aDST Unit of Nanoscience and Thematic Unit of Excellence Department of Chemistry, Indian
Institute of Technology Madras, Chennai 600 036, India*

*^bEnvironmental Engineering Division, School of Mechanical and Building Sciences, VIT
University, Chennai Campus, Chennai, 600 127, India*

**Email: pradeep@iitm.ac.in Fax: 91-44-2257-0545/0509.*

Supplementary data S1

About 25 mL concentrated H_2SO_4 , 5 g of $\text{K}_2\text{S}_2\text{O}_8$ and 5 g of P_2O_5 were taken in a 250 mL beaker and were heated at $90\text{ }^\circ\text{C}$ with constant stirring. When all these reactants got completely dissolved, the temperature of the reaction was then decreased to $80\text{ }^\circ\text{C}$. Then 6 g of graphite powder was added slowly to this reaction mixture. Initially, bubbling was observed. It subsided subsequently, over a period of about 30 min. After that the temperature of the reaction mixture was maintained at $80\text{ }^\circ\text{C}$ for 5 h. The reaction was stopped and cooled at room temperature. The mixture was then diluted with 1 L of distilled water and then left undisturbed overnight. The resultant solution was then filtered and washed to remove excess acid present and the solid product was dried overnight in air.

This pre-oxidized graphite obtained was then added to 230 mL of concentrated H_2SO_4 which was already being maintained at $0\text{-}5\text{ }^\circ\text{C}$ in an ice bath. It was followed by stirring. 15 g of KMnO_4 was added slowly such that the temperature does not go beyond $10\text{ }^\circ\text{C}$. The temperature was then raised to $35\text{ }^\circ\text{C}$. The reaction was then allowed to undergo for another 2 h. Subsequently, 1 L of distilled water was added carefully keeping into consideration that the temperature should not go above $50\text{ }^\circ\text{C}$. The reaction mixture was again stirred for two more hours. 1.5 L of distilled water and 25 mL of 30% H_2O_2 were added to it. Then the mixture was kept at room temperature for a day. After that the supernatant was decanted and the remaining solution was centrifuged and washed with 10% HCl which was followed by distilled water. This process was repeated a number of times. The resultant solid was dried and then 2 wt% (w/v) dispersion was prepared in distilled water. This dispersion was dialyzed for 3 weeks in order to remove all the unwanted contaminants like salts and acid. Finally the dispersion was diluted to obtain 0.5 wt% (w/v) graphene oxide (GO).

Now to obtain reduced graphene oxide (RGO), pre reduction of GO was carried by adding Na_2CO_3 (5 wt%) and 800 mg NaBH_4 followed by heating for 1 h. The reaction mixture was cooled, centrifuged and rinsed with water several times and then re-dispersed in water. Now to increase the stability of graphene in water, a simple sulfonation procedure was followed by introducing sulfonic acid groups in RGO. 20 mg sulfanilic acid and 8 mg sodium nitrite were first dissolved in 0.25% NaOH solution. Then 4 mL, 0.1 M HCl was added to it. The reaction mixture was kept in an ice bath under stirring. After 15 min, the aryl diazonium salt solution was added to 20 mL, 0.5 mg/mL RGO dispersion. This reaction was also carried in an ice bath with continuous stirring for 2 h. After 2 h, the solution was filtered, washed and re-dispersed in distilled water. The final concentration of 0.05 wt% RGO was obtained with solution pH value 6.

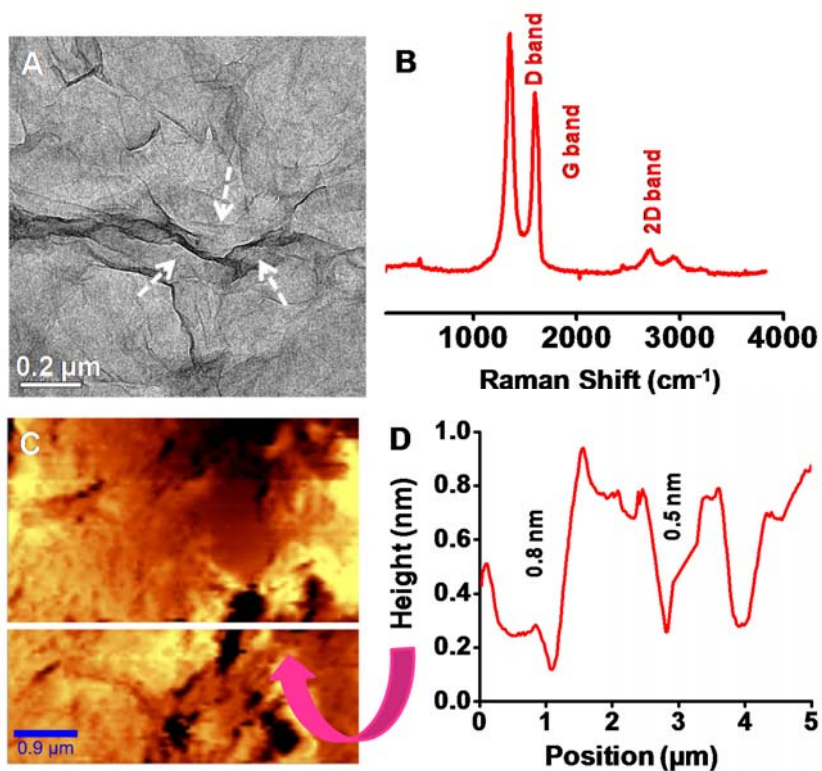


Fig. S1: A) TEM image of graphene showing the foldings marked in white arrows. B) Raman spectrum showing the presence of D, G and 2D bands. C) AFM image and D) Height profile (taken along the white line of image (C)) showing 2-3 layered RGO.

Supplementary data S2

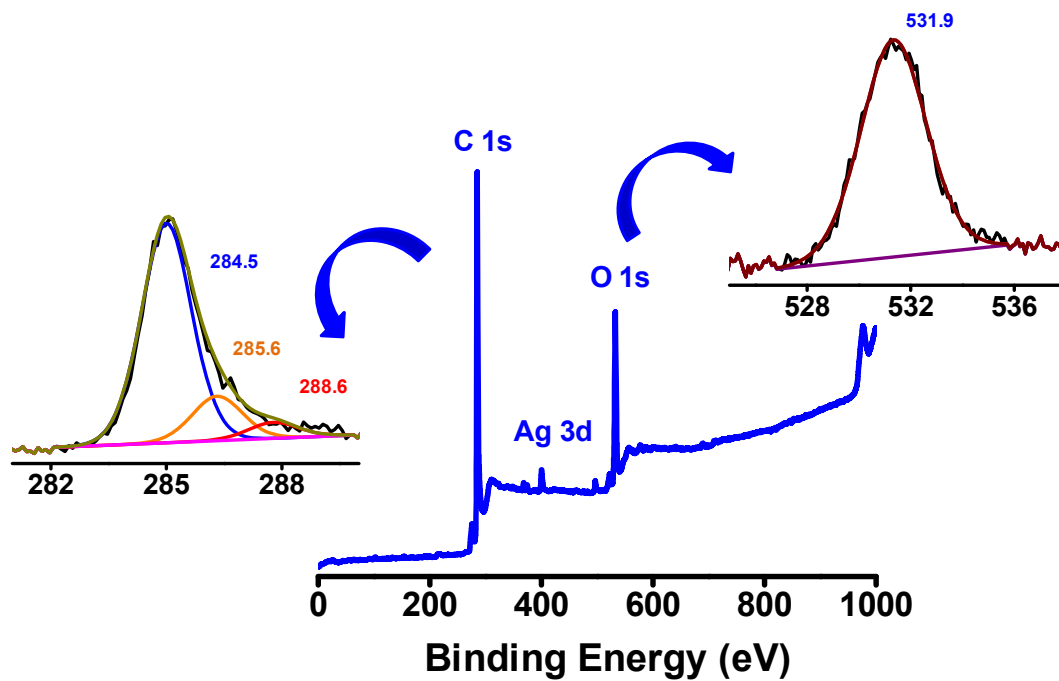


Fig. S2: XPS survey spectrum of RGO@Ag showing the presence of carbon, oxygen and silver.

The deconvoluted spectrum of C 1s and O 1s are represented with a marked arrow.

Supplementary data S3

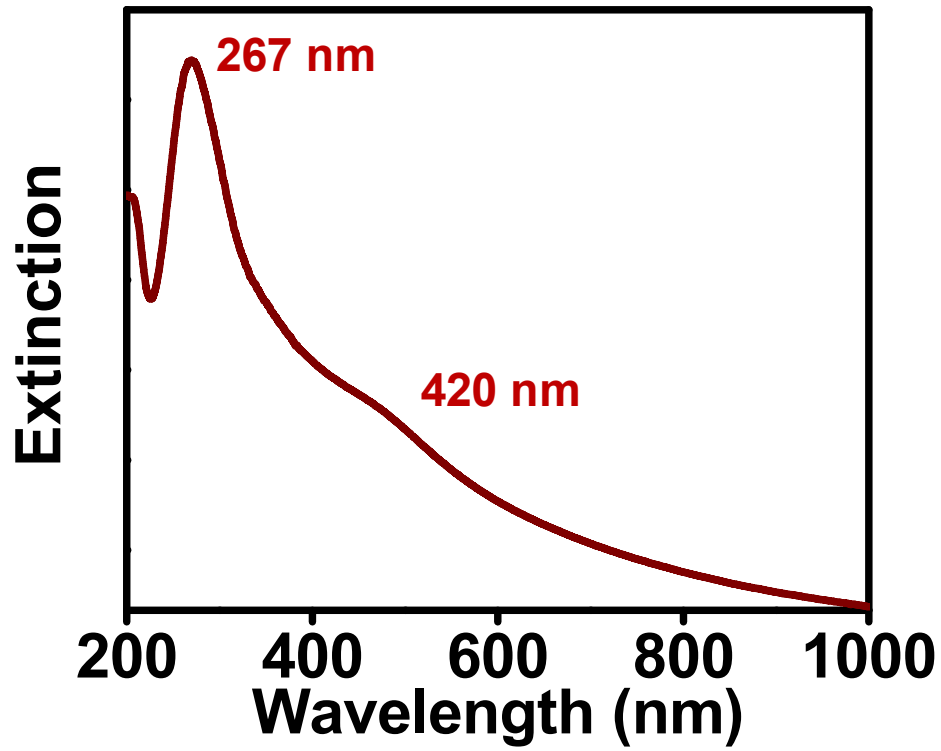


Fig. S3: UV/vis spectrum of RGO@Ag. The peak at 267 nm is characteristic of RGO and the other peak at around 420 nm is due to the plasmon resonance of Ag NPs.

Supplementary data S4

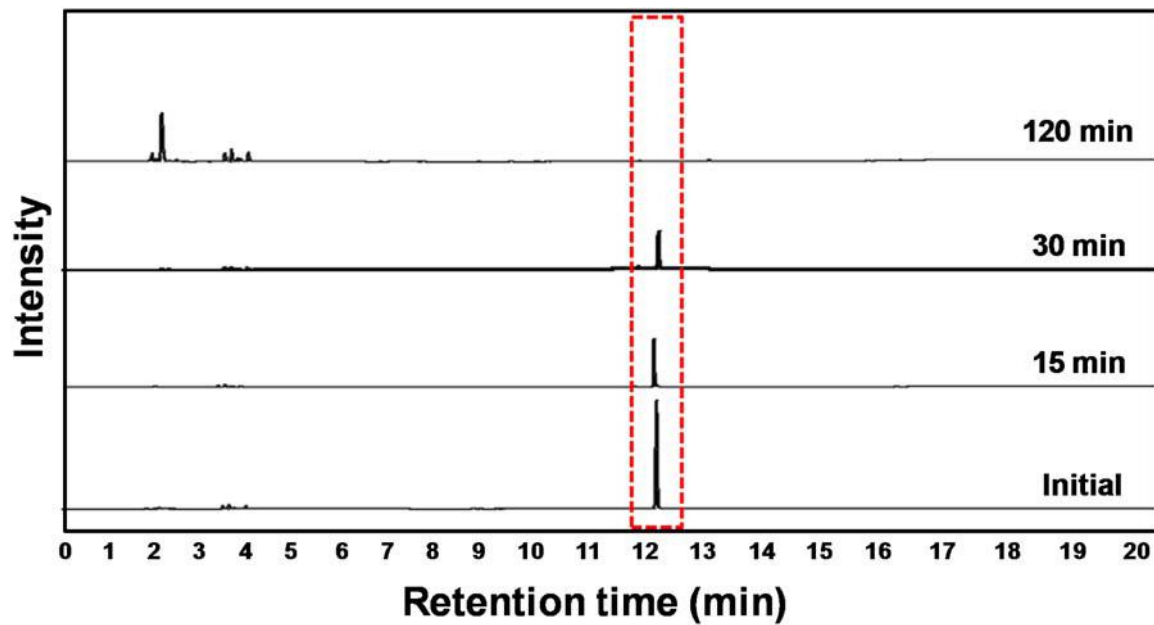


Fig. S4: Time dependent GC-ECD showing complete removal of pesticide CP from water with respect to time when reacted with RGO@Ag composite. The CP region is highlighted.

Supplementary data S5

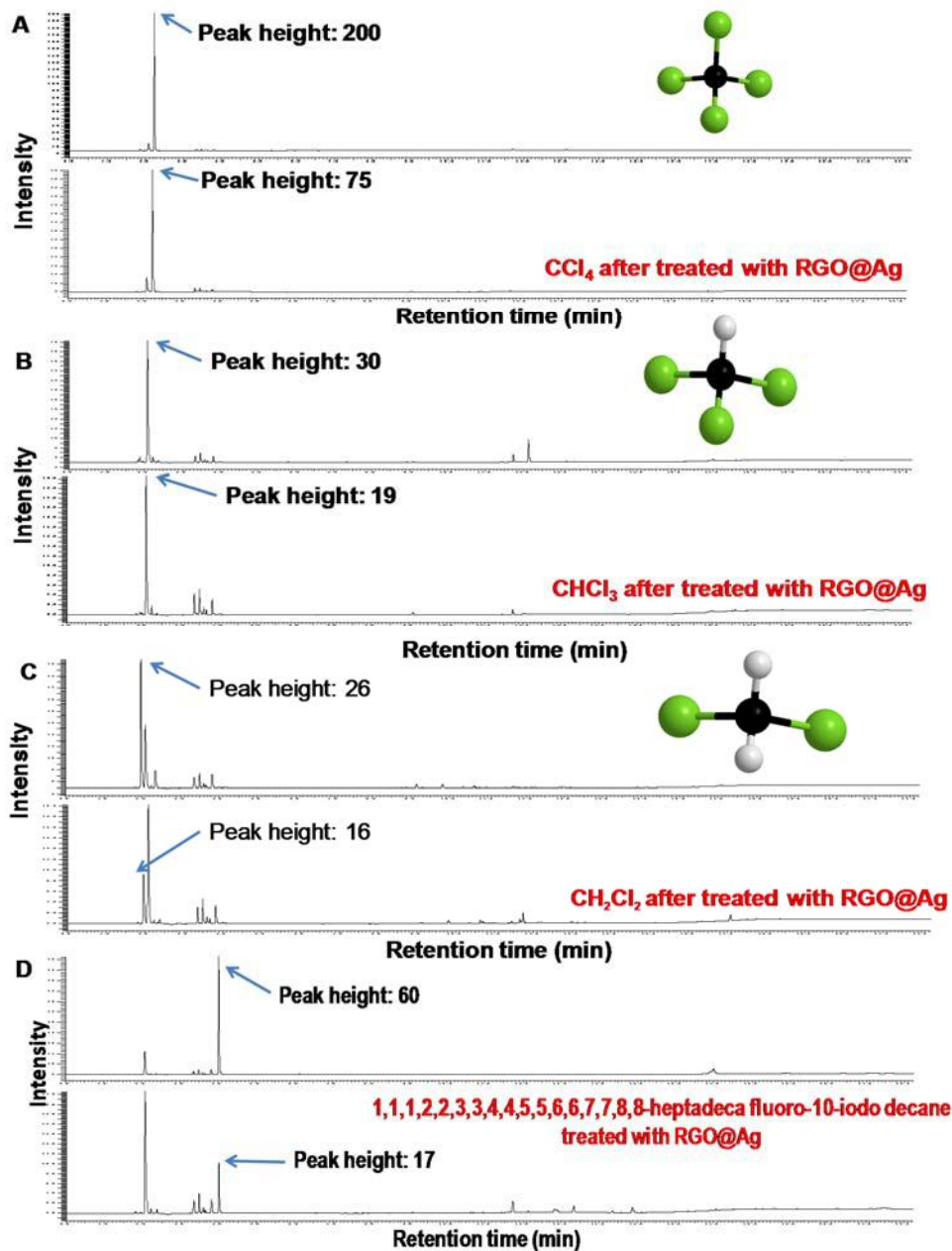


Fig. S5: GC-ECD showing the removal of A) CCl₄, B) CHCl₃, C) CH₂Cl₂ and D) HFID after the reaction with RGO@Ag composite.

Supplementary data S6

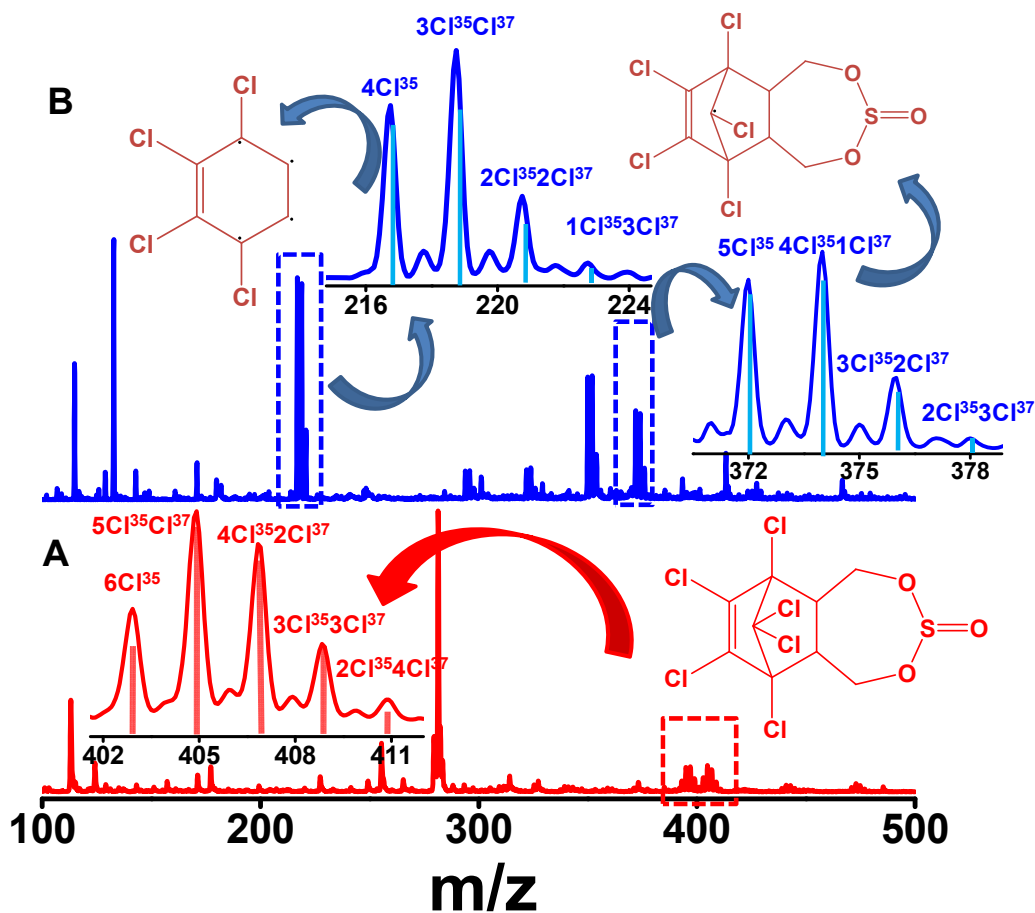


Fig. S6: A) ESI MS of ES showing the molecular ion peak at m/z 404 and B) the solution after reaction with RGO@Ag showing the fragmented product of ES in water showing the presence of peaks at m/z 372 and 219, respectively along with the isotopic distribution and probable structures. Isotope distribution is indicated on the spectrum.

Supplementary data S7

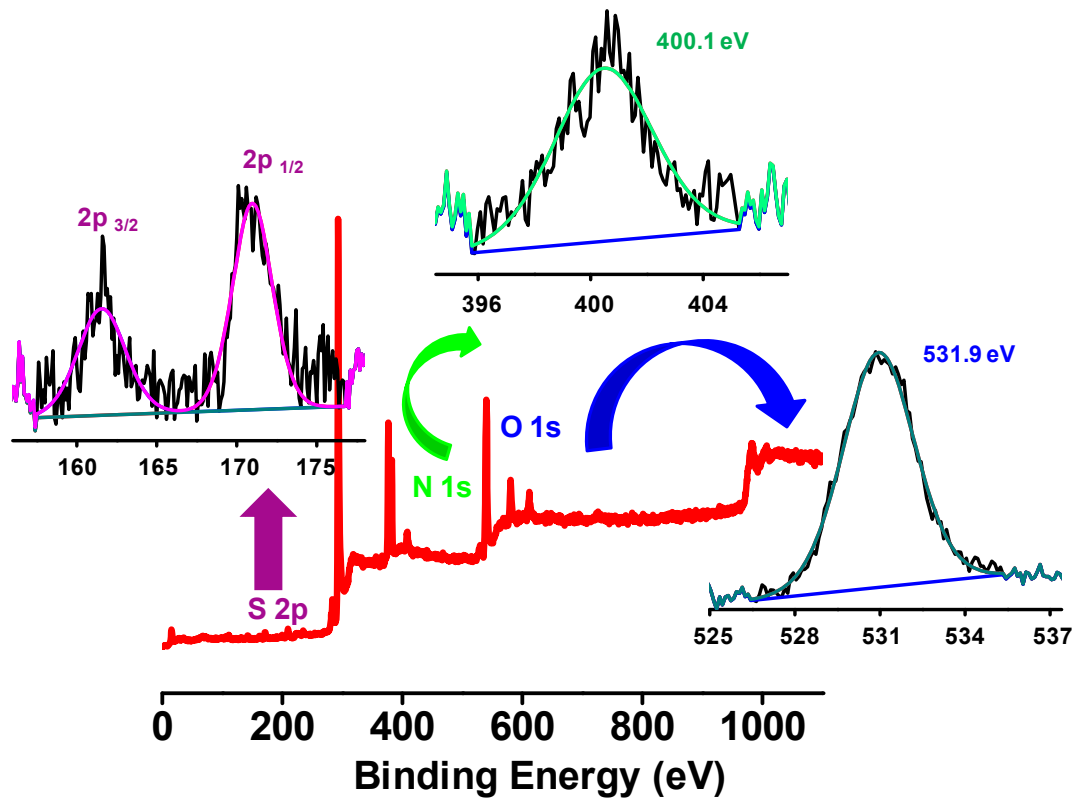


Fig. S7: XPS survey spectrum of the RGO@Ag composite after the reaction with CP. The inset showing the deconvoluted spectrum of O1s centred at 531.9 eV and N1s centered at 400.1 eV. Also shown is S2p, exhibiting two features at 162.0 and 171.0 eV. The peak at 162.0 eV for S2p_{3/2} assigned to +II oxidation state of sulphur.

Supplementary data S8

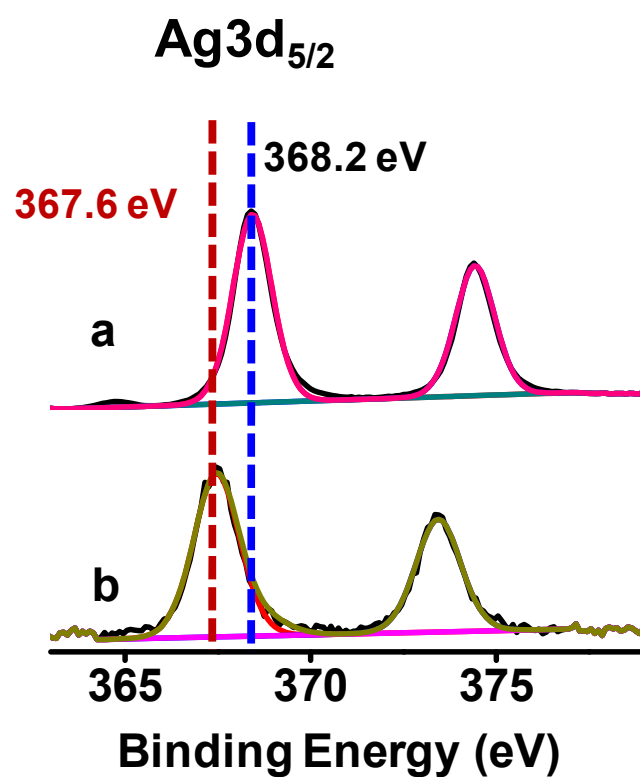


Fig. S8: Deconvoluted XPS spectrum of Ag in a) RGO@Ag (before reaction) and b) RGO@Ag after reaction with CP. Note that in Ag, the +1 oxidation state shifts 3d to a lower binding energy.

Supplementary data S9

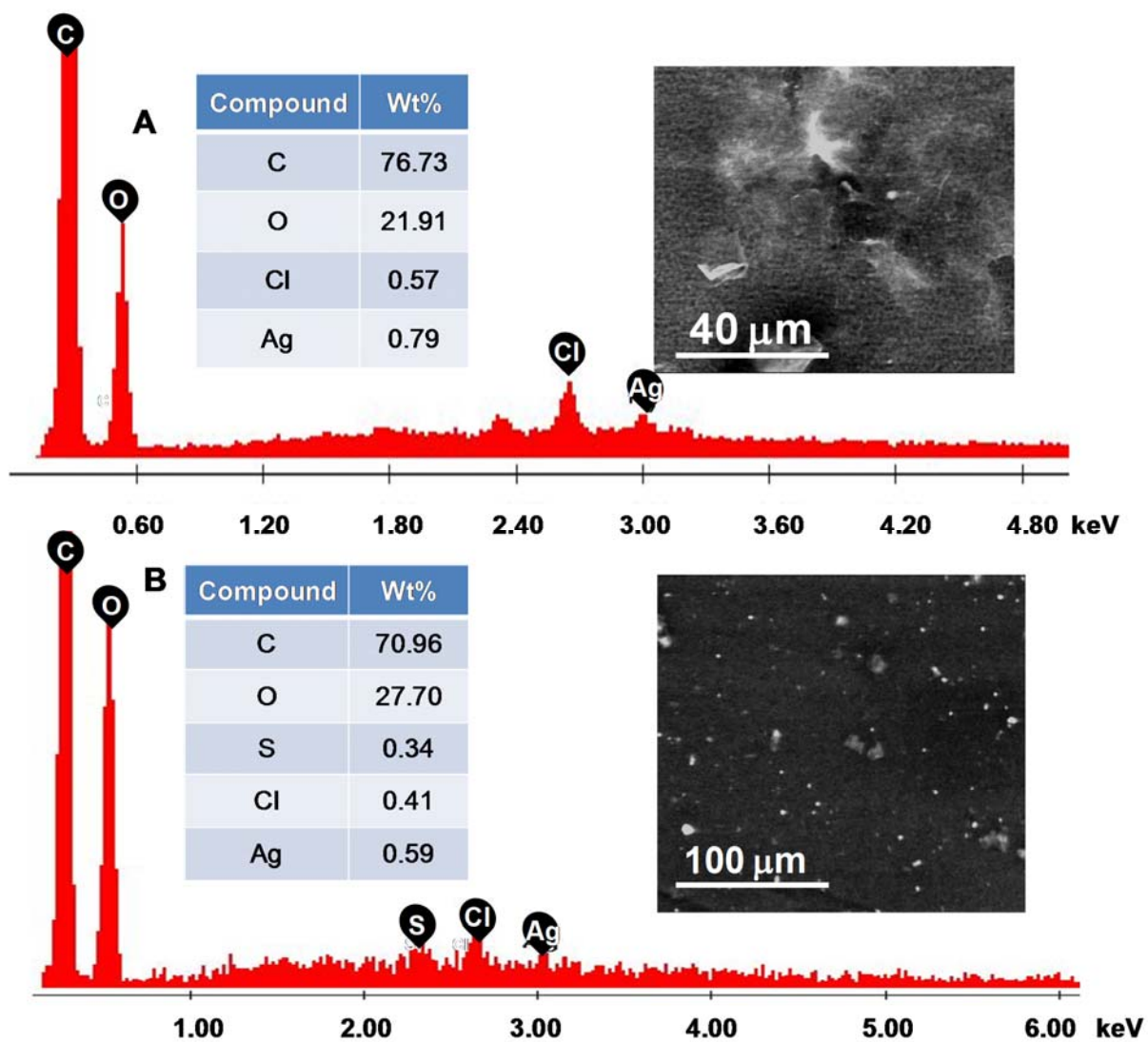


Fig. S9: SEM-EDS of RGO@Ag composite after the reaction with A) DDE and B) ES. The corresponding SEM images and the elemental ratios are given in the inset.

Supplementary data S10

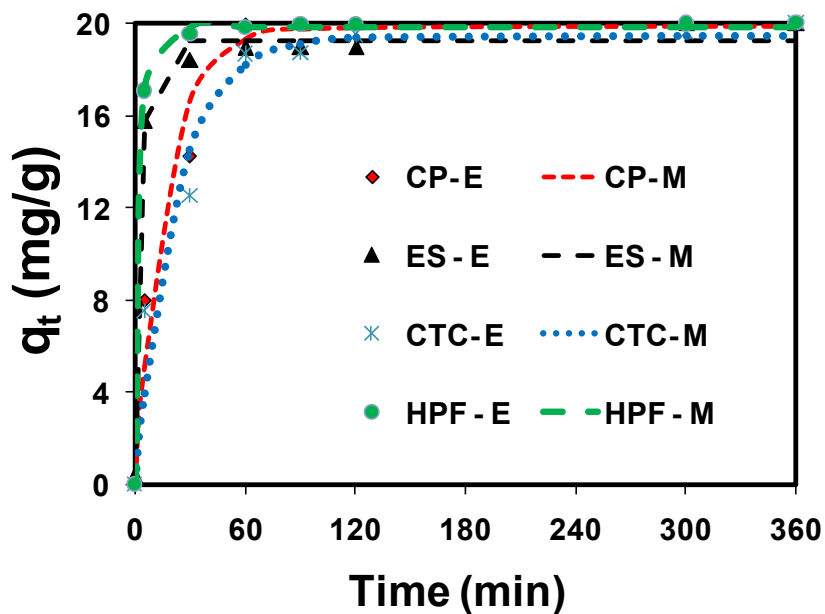


Fig. S10: Pseudo-first-order kinetic plots for the adsorption of pesticides by RGO@Ag composites.

Table S1: Estimated pseudo-first-order rate parameters.

Pollutants	k_1 (L/min)	q_e (mg/g)	RMSE	χ^2
CP	0.0603	19.8400	1.3250	1.9120
ES	0.3450	19.2200	0.5060	0.1070
CCl ₄	0.0455	19.4700	1.4670	3.4740
HFP	0.3910	19.8700	0.1360	0.0070

Supplementary data S11

Table S2: The maximum removal capacity of the RGO@Ag composite for different pollutant in mg/g.

Pesticides	Peak position (min)	Intensity (0 min)	Intensity (5 min)	Intensity (30 min)	Intensity (300 min)	Maximum Removal Efficiency (mg/g) of composite
Chlorpyrifos	12.2	115	75	36	0	765
Endosulfan	13.4	70	15	5.6	0	662
DDE	13.7	71	11	5.4	0	631
Carbon tetrachloride	2.3	200	125	75	4	997
Chloroform	2.1	30	23	19	4.1	132
Dichloromethane	2	26	16	9.2	3.4	121
1,1,1,3,3,3-hexa fluoro-2-propanol	2.4	750	105	16	0.8	1534
1,1,1,2,2,3,3,4,4,5,5,6,6,7,7,8,8-hepta deca fluoro - 10-iodo decane	4.0	60	26	17	1.3	498

Joyful Years with the Journal: Balancing the Editor–Professor Life

I joined the team of *ACS Sustainable Chemistry & Engineering* as Associate Editor in May 2014. I recall the e-mail from Professor David Allen on April 4, 2014 proposing this idea. Although I had edited books and special issues of journals before, it was my first editorial assignment requiring daily involvement, and therefore, I was somewhat concerned about the time it may demand and concomitantly its impact on my teaching and research. My fellow Associate Editors, Professors Bala Subramaniam (University of Kansas) and Peter License (University of Nottingham) narrated their experiences and assured me that it would be a smooth transition to a teacher–researcher–editor phase in my life. It has now been well over two years—a very rewarding period of intense learning, careful mentoring, and informed decision making. Over 800 articles have come across my desk in this period. Selecting the papers we should publish, guided by the painstaking inputs of the reviewers, has been the most difficult part of my editorial *avtar* [a Sanskrit word meaning an incarnation, embodiment, or manifestation of a person or idea]. It was always a pleasure to receive good reviews and communicate the decision of revision or acceptance. The joy doubled when the authors returned the revision with care. I must place on record a big Thank You to all authors; the confidence they have shown in this journal has been the foundation of its success.

A look through the journal reveals many connections between sustainability and materials. This may appear in the form of sustainable synthesis, new transformations, renewable materials and processes, pollutant removal, energy production, sensors, etc. It is in this research space that I have been associated with the journal. That space has become increasingly rich recently, with nanomaterials and their chemistry attracting greater attention. The societal need, focused funding, and greater sense of accountability helped enhance this frontier. One other aspect obvious in these papers is the increasing interdisciplinarity, which suggests that the journal has made strides to further erase the boundaries within, and between, chemistry and engineering.

The past two years have made drastic changes in my own science. When I received the invitation from the journal, I was getting ready to participate in an international conference in Buenos Aires, commemorating the 100th year of arsenic in the environment. In the last two years, we have installed several affordable iron and arsenic scavenging filters in the field using sustainable materials (Figure 1). A company, InnoNano Research Pvt. Ltd., incubated in the lab on affordable clean water technologies has started standing on its own, employing our own students, ready to take up larger challenges. A new laboratory for clean water has been established with funding from the Department of Science and Technology. From advanced research to manufacturing and implementation in the field, our science has come a long way. In that path, the link with the global scientific community has become stronger through the journal.

Looking back, the eventful two plus years have been intense, but always on a trajectory of growth, both for the journal and for me. The increasing number of submissions from all over the world (50+ countries), upward impact factor (5.27 currently),



Figure 1. An arsenic and iron free drinking water product, named AMRIT, implemented by InnoNano Research Pvt. Ltd., in an arsenic-affected area of West Bengal, India. There are various versions of this technology, the one shown above caters to about 100 people. Arsenite and arsenate ions are removed well below the international norms at enhanced kinetic rates with sustainable granular materials. Such materials enable the design of a filtration column with a low pressure drop so that even a child can operate the filter. From the author's collection.

new initiatives (lectureship awards, early career board, social media presence), special issues on important problems in the area, and expanding breadth of disciplines covered suggest that our journal is on the right path. The journal has positioned itself to be relevant and necessary for the field. The impact of research related to sustainable chemistry may take time to be evident. In my personal view, sustainability will make a lasting impact on chemistry and society, if innovations are partnered with policy advocacy.

Thalappil Pradeep, Associate Editor

Indian Institute of Technology Madras, Chennai, India

■ AUTHOR INFORMATION

Notes

Views expressed in this editorial are those of the author and not necessarily the views of the ACS.

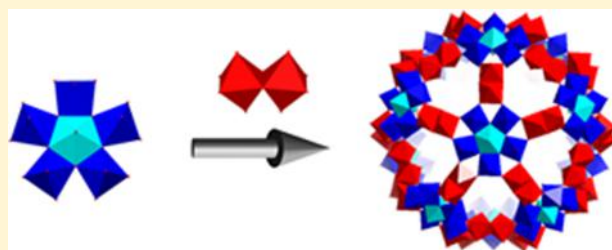
Received: November 17, 2016

Published: December 5, 2016

Direct Observation of the Formation Pathway of $[\text{Mo}_{132}]$ KepleratesSubharanjan Biswas,[†] Dolores Melgar,^{‡,§} Amitava Srimany,^{||} Antonio Rodríguez-Fortea,[⊥] Thalappil Pradeep,^{*,||} Carles Bo,^{*,‡} Josep M. Poblet,^{*,⊥} and Soumyajit Roy^{*,†}[†]Eco-Friendly Applied Materials Laboratory (EFAML), Materials Science Centre, Department of Chemical Sciences, Indian Institute of Science Education and Research-Kolkata (IISER-Kolkata), Mohanpur Campus, Mohanpur 741246, India[‡]Institute of Chemical Research of Catalonia (ICIQ), Av. Països Catalans 16, 43007 Tarragona, Spain[§]Departament d'Enginyeria Química, ETSEQ, Universitat Rovira i Virgili, Av. dels Països Catalans, 26, 43007 Tarragona, Spain^{||}Department of Chemistry, Indian Institute of Technology Madras, Chennai 600036, India[⊥]Departament de Química Física i Inorgànica, Universitat Rovira i Virgili, Marcel·lí Domingo 1, 43007 Tarragona, Spain

S Supporting Information

ABSTRACT: The formation pathway of a closed spherical cluster $[\text{Mo}_{132}]$, starting from a library of building blocks of molybdate anions, has been reported. Electrospray ionization mass spectrometry, Raman spectroscopy, and theoretical studies describe the formation of such a complex cluster from a reduced and acidified aqueous solution of molybdate. Understanding the emergence of such an enormous spherical model cluster may lead to the design of new clusters in the future. Formation of such a highly symmetric cluster is principally controlled by charge balance and the emergence of more symmetric structures at the expense of less symmetric ones.



INTRODUCTION

Polyoxometalate (POM)^{1,2} clusters are polyatomic ions, usually anions, that consist of transition metals like Mo, V, and W linked together by shared oxygen atoms to form closed three-dimensional (3D) frameworks. Because of the various sizes, structures, and elemental compositions, a wide range of properties and a correspondingly wide range of potential applications are observed in POMs, for instance, in catalysis,³ in energy production and storage,⁴ and in medicinal chemistry.⁵ $[\text{Mo}_{132}]$ ^{6,7} Keplerate,⁸ first reported by Müller et al.,⁹ is synthesized by partial reduction of Mo(VI) atoms present in $(\text{NH}_4)_6\text{Mo}_7\text{O}_{24}$. $[\text{Mo}_{132}]$ is a type of molybdenum brown Keplerate anion with a diameter of 2.9 nm. The structure of $[\text{Mo}_{132}]$ was determined by single-crystal X-ray diffraction (SC-XRD) studies by the Bielefeld group of A. Müller.⁷ This spherical cluster contains 132 molybdenum centers; 72 molybdenum centers are in the +VI oxidation state, and the rest of the 60 molybdenum centers are in the +V oxidation state. The dark brown color of $[\text{Mo}_{132}]$ arises from intervalence charge transfer between the Mo^{V} and Mo^{VI} centers. Moreover, such POMs superassemble to form blackberry type soft oxometalate (SOM)^{10–12} superstructures of larger dimensions.^{13,14} Herein, we investigate and present direct experimental evidence [electrospray ionization mass spectrometry (ESI-MS) and Raman spectroscopic studies] along with computational studies to show the pathway of formation of such clusters under prevalent chemical conditions.

A $[\text{Mo}_{132}]$ type Keplerate cluster assembled with acetate as the ligand has icosahedral point group symmetry.¹⁵ The cluster structure from a building block approach is envisaged as follows. Twelve pentagonal $[(\text{Mo})\text{Mo}_5]$ building blocks are disposed at the vertices of an icosahedron.^{16,17} $[(\text{Mo})\text{Mo}_5]$ building blocks are formed with central pentagonal bipyramidal $[\text{MoO}_7]$ linked to five $[\text{MoO}_6]$ octahedra through edges, which shows an overall icosahedral symmetry (Figure 1). Disposition of 12 $[(\text{Mo})\text{Mo}_5]$ blocks at the vertices of the icosahedron creates space for 30 linkers on the icosahedron's surface to be accommodated (following Euler's theorem)¹⁸ and linked simultaneously to the prevalent pentagonal building blocks.

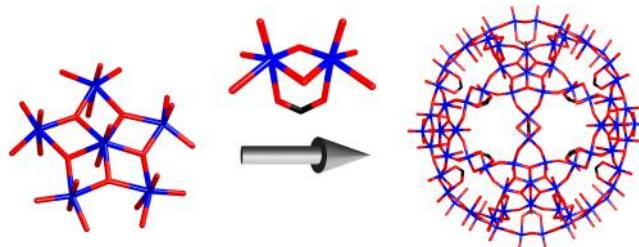


Figure 1. Formation of the 3D structure of the $[\text{Mo}_{132}]$ cluster from $[(\text{Mo})\text{Mo}_5]$ and $[\text{Mo}_2(\text{CH}_3\text{COO})]$ building blocks shown in a wireframe model. Blue color represents Mo, red O, and black acetate.

Received: November 6, 2015

Published: August 25, 2016

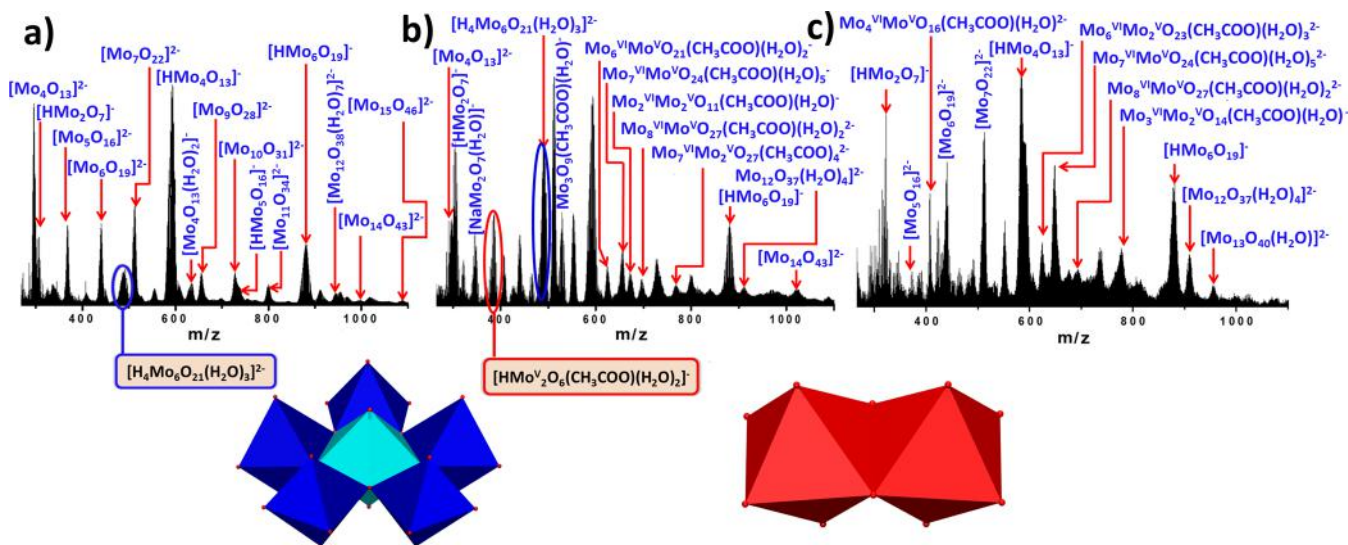


Figure 2. ESI mass spectra during different steps of $[\text{Mo}_{132}]$ formation. (a) Spectra of a colorless water solution of ammonium heptamolybdate, where the presence of $[(\text{Mo})\text{Mo}_5]$ is evidenced as $[\text{H}_4\text{Mo}_6\text{O}_{21}(\text{H}_2\text{O})_3]^{2-}$. (b) Spectra of a solution after complete reduction by $\text{N}_2\text{H}_4\text{SO}_4$, which turns the solution green, where $[\text{Mo}_2]$ is evidenced as $[\text{HMo}_2\text{O}_6(\text{CH}_3\text{COO})(\text{H}_2\text{O})_2]^-$. (c) Mass spectrum 12 h after the addition of all the reagents.

In the case of $[\text{Mo}_{132}]$ with acetate as the ligand to the linkers, the linkers are $[\text{Mo}_2(\text{CH}_3\text{COO})]$. (Note that we omit the oxygen atoms from the formula of the cluster for the sake of simplicity.) Hence, the overall cluster formulation is determined to be $[\text{pentagon}]_{12}[\text{linker}]_{30}$, $[(\text{Mo})\text{Mo}_5]_{12}[\text{Mo}_2(\text{acetate})]_{30}$, $[\text{Mo}_{132}(\text{acetate})_{30}]$, $[\text{Mo}_{132}]$, or **1** (Figure 1) $(\text{NH}_4)_{42}\{[(\text{Mo}^{\text{VI}})\text{Mo}_5\text{O}_{21}(\text{H}_2\text{O})_6]_{12}\{[\text{Mo}^{\text{V}}\text{O}_4(\text{CH}_3\text{COO})]_{30}\} \approx [10\text{CH}_3\text{COONH}_4 \sim 300\text{H}_2\text{O}] \equiv (\text{NH}_4)_{42} \mathbf{1a} \equiv \mathbf{1}$.

These clusters have been popularly called Keplerates because of their structural similarity to Kepler's early model of the universe.¹⁹ Rather recently, inorganic cell-like behavior and receptive behavior have been found to be characteristics of these Keplerates.^{20–29}

Such attributes characterize the Keplerates as an attractive model system for investigating the emergence of complexity³⁰ and symmetry in chemistry. In understanding such emergence, the first question would be how does such a complex icosahedral cluster³¹ like $[\text{Mo}_{132}]$ emerge from constituents of molybdates, reducing agents, and a buffer.

Before we proceed further, it is important to look at the general synthetic conditions of the cluster as reported in the literature, which we investigated in detail. The synthesis of the cluster involves the following key steps: (1) dissolution of molybdate in water, (2) reduction of the reaction mixture, and (3) acidification of the resulting solution.³² The cluster so synthesized is highly charged. Hence, it is logical to think that understanding the formation of this cluster would require a technique that can observe such charged objects and its constituents. We chose ESI-MS to monitor such a formation pathway, along with Raman spectroscopy and theoretical calculations. Needless to say, ESI-MS^{33–35} and theoretical calculations^{36–38} have been extensively used to understand the formation of smaller polyoxometalate clusters. Raman spectroscopy has also been used in this study to investigate the solution stability of the related Keplerates. Müller et al. have previously reported the self-assembly of $[\text{Mo}_{132}]$ with the help of dinuclear $[\text{Mo}_2]$ units to a dynamic library containing molybdates results in the spontaneous self-assembly of

$[\text{Mo}_{132}]$, while the required pentagonal $[(\text{Mo})\text{Mo}_5]$ building blocks are immediately formed. The reason to use Raman spectroscopy is the easy detection of the integrity of the $[\text{Mo}_{132}]$ cluster from the Raman fingerprint. The quasi-spherical (icosahedral) construction of this cluster not only enhances its stability but also provides an easy Raman spectroscopic fingerprint for studying its stability. Because of the high I_h symmetry of such a cluster, only a few well-defined Raman lines are observed (note the presence of a 5-fold degeneracy, and that only A_g and H_g symmetric vibrational modes are Raman-allowed).⁴⁰ The Raman spectrum of a $[\text{Mo}_{132}]$ type cluster shows four bands: 950 cm^{-1} [$\nu(\text{Mo}=\text{O}_i)$], 880 cm^{-1} [$\nu(\text{O}_{\text{br}}\text{breathing})$], 374 cm^{-1} [$\delta(\text{Mo}=\text{O}_i)$], and 314 cm^{-1} [$\delta(\text{Mo}-\text{O}-\text{Mo})$].⁴¹ We monitored the reaction in all detailed steps of its formation; however, it was only the aforementioned three key steps during which significant changes were found to occur. In this paper, we will describe those changes to explain the formation of the $[\text{Mo}_{132}]$ cluster.

EXPERIMENTAL SECTION

ESI-MS Experiment and Analyses. ESI-MS was performed in a LTQ XL mass spectrometer from Thermo Scientific that has an ion trap mass analyzer. The sample was introduced into the system by direct infusion from a syringe at a constant flow rate of $10\ \mu\text{L}/\text{min}$. All the spectra were recorded in negative ion mode keeping the spray voltage at 5 kV, the sheath gas flow rate at 8 (manufacturer's unit), the capillary voltage at -35 V , the capillary temperature at $150\text{ }^\circ\text{C}$, and the tube lens voltage at -110 V . In each case, the spectrum shown is an average of 500 scans.

Mass spectra were recorded during each step of Mo_{132} synthesis. The first is the aqueous solution of ammonium heptamolybdate, followed by the addition of $\text{CH}_3\text{COONH}_4$. Next, the spectrum was recorded with the completely reduced green solution after the addition of $\text{N}_2\text{H}_4\text{SO}_4$. Then the solution was acidified via the addition of CH_3COOH , and the spectrum was recorded. To gain insight into the self-assembly process, spectra were recorded at different times after CH_3COOH addition, viz., after 30 min, 60 min, 2 h, 3 h, 24 h, 36 h, and 72 h. For all the mass spectral experiments, an aliquot of $10\ \mu\text{L}$ was diluted with 1 mL of a 1:1 (v/v) mixture of acetonitrile and water. From the mixture, $100\ \mu\text{L}$ was further diluted with 1 mL of a 1:1 (v/v) mixture of acetonitrile and water.

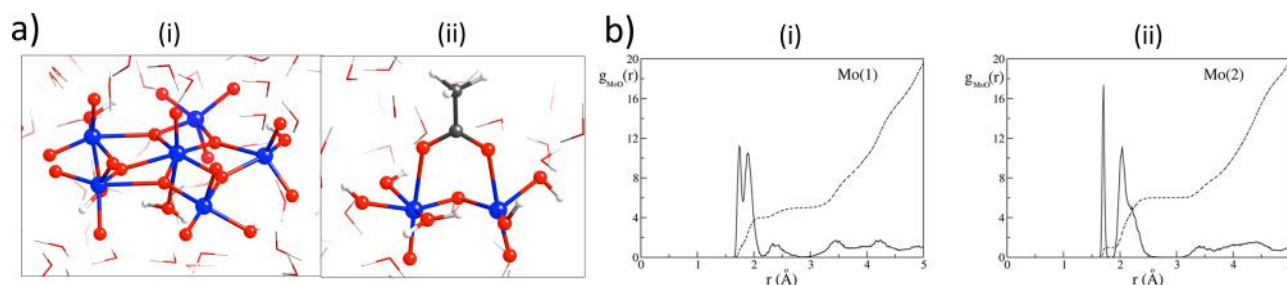


Figure 3. (a) Snapshots of the Carr–Parrinello molecular dynamics trajectories of protonated starlike hexamolybdate $[\text{Mo}_6\text{O}_{18}(\text{OH})_3]^{3-}$ (i) and $[\text{Mo}_2\text{V}_2\text{O}_8(\text{OH})_4(\text{H}_2\text{O})\text{CH}_3\text{COO}]^-$ dimer (ii). (b) Mo–O radial distribution functions (—) and their integrations, the coordination number (⋯), of the two Mo^{V} ions, Mo(1) and Mo(2), for 27 ps of simulation starting from $[\text{Mo}_2\text{V}_2\text{O}_8(\text{OH})_6(\text{CH}_3\text{COO})]^-$.

Raman Spectroscopy. Raman spectroscopy measurements were taken in the range of $200\text{--}1500\text{ cm}^{-1}$ using the micro-Raman spectrometer LABRAM HR from Horiba Jobin Yvon with a grating of 1800 grooves/mm. All the experiments were performed using an excitation wavelength of 633 nm of an Ar ion laser, and the spectral resolution was 2 cm^{-1} . The Raman spectrometer was calibrated prior to measurements using a Si wafer by the wavenumber shift calibration method. Solution phase Raman spectroscopy of the reaction system has been performed in a manner similar to that of ESI-MS experiments. Raman spectra have been recorded during different steps of the formation of the Mo_{132} cluster.

Theoretical Calculations. A detailed description of the Carr–Parrinello molecular dynamics simulations and density functional theory (DFT)-based Raman spectral calculations are included in the Supporting Information.

RESULTS AND DISCUSSION

ESI-MS Analysis of the Dissolution and Reduction Steps in the Formation of Mo_{132} . The first ESI mass spectrum recorded after the addition of ammonium heptamolybdate in water is dominated by peaks of isopolymolybdate fragments of the $[\text{Mo}_7\text{O}_{24}]^{6-}$ anion. In the negative ion mode investigation of the mass spectrum of $(\text{NH}_4)_6\text{Mo}_7\text{O}_{24}$ and an ammonium acetate solution, predominantly members of two ion series are observed, namely, $[\text{HMo}_m\text{O}_{3m+1}]^-$ ions such as $[\text{HMo}_3\text{O}_{10}]^-$, $[\text{HMo}_4\text{O}_{13}]^-$ etc., and $[\text{Mo}_m\text{O}_{3m+1}]^{2-}$ ions such as $[\text{Mo}_6\text{O}_{19}]^{2-}$, $[\text{Mo}_9\text{O}_{28}]^{2-}$ (Figure 2a).^{42,43} The dominance of the isopolymolybdates shows that the simple dissolution of the $[\text{Mo}_7\text{O}_{24}]^{6-}$ anion opens up a dynamic library by rearrangement into smaller fragments that can then undergo fast combinatorial addition and/or fragmentation to give a diverse range of oligomeric ions of the observed series. The complexity of the library is obvious, and the entire library can be represented by the $[\text{HMo}_m\text{O}_{3m+1}]^-$ and $[\text{Mo}_m\text{O}_{3m+1}]^{2-}$ series. It is worth noting that this library already contains the pentagonal building blocks, $[\text{H}_4\text{Mo}_6\text{O}_{21}(\text{H}_2\text{O})_3] \equiv [(\text{Mo})\text{Mo}_5]$. The Raman spectrum, on the other hand, shows a typical band around 950 cm^{-1} ($\nu_{\text{Mo}=\text{O}}$).

Upon addition of the reducing agent, $\text{N}_2\text{H}_6\text{SO}_4$, the complexity of the ESI mass spectrum increases with the appearance of new peaks (Figure 2b). Furthermore, at this stage, mixed valent isomolybdate fragments⁴⁴ are detected, as well. Molybdenum is found to exist in +V and +VI oxidation states in species such as $[\text{Mo}_6^{\text{VI}}\text{Mo}^{\text{V}}\text{O}_{21}(\text{CH}_3\text{COO})(\text{H}_2\text{O})_2]^-$, $[\text{Mo}_7^{\text{VI}}\text{Mo}^{\text{V}}\text{O}_{24}(\text{CH}_3\text{COO})(\text{H}_2\text{O})_5]^-$, etc. This is seen with the change in color of the reaction mixture from colorless to turquoise blue and finally to dark green. Here we observe the condensation of two reduced $\{\text{Mo}^{\text{V}}\text{O}\}^{3+}$ ions stabilized by an acetate ligand (from ammonium acetate present in the library) to generate a $\text{HMo}_2\text{V}_2\text{O}_6(\text{CH}_3\text{COO})(\text{H}_2\text{O})_2 \equiv [\text{Mo}_2(\text{acetate})]^-$

linker in the library at m/z 384.75. What happens here is, the starting compound ammonium heptamolybdate is becoming reduced by $\text{N}_2\text{H}_6\text{SO}_4$, thus producing Mo^{V} centers in solution (evident from the color change after addition of the reducing agent), which in turn generates $[\text{Mo}_2(\text{acetate})]$ linkers by condensation.

Moreover, reduction enhances the abundance of the pentagonal $[(\text{Mo})\text{Mo}_5]$ building blocks, as shown by ESI-MS (Figure 2a,b). Condensation of the building blocks in the library continues, and greater speciation ensues. To determine the real nature of the two main structures involved in the formation of $[\text{Mo}_{132}]$, Carr–Parrinello molecular dynamics (MD) simulations^{45,46} were performed on the pentagonal unit $[\text{Mo}_6\text{O}_{21}]^{6-}$ {deprotonated form of $[\text{H}_4\text{Mo}_6\text{O}_{21}(\text{H}_2\text{O})_3]^{2-}$ } and on dimers with a $[\text{Mo}_2\text{V}_2\text{O}_8\text{H}_6(\text{CH}_3\text{COO})]^-$ stoichiometry. Combinations of mass spectrometry and Carr–Parrinello molecular dynamics (MD) simulations were shown to be useful for studying molecular oxide fragments in solution.^{47,48} Using a cell box containing initially one starlike hexaprotonated pentagonal unit $[\text{Mo}_6\text{O}_{15}(\text{OH})_6]$ and 146 H_2O molecules ($a = b = c = 16.90\text{ \AA}$), a 17 ps simulation was performed (5 ps equilibration with a 12 ps production run). The initial hexaprotonated starlike molybdate releases three protons, yielding $[\text{Mo}_6\text{O}_{18}(\text{OH})_3]^{3-}$ and three hydronium cations that remain in the solution (Figure 3a). This result indicates that under low-pH conditions the starlike hexamolybdate is protonated with up to three protons. This latter species, which lasts for the whole simulation, is stable at the rather short time scale simulated here. Up to three H_2O molecules interact directly with the different Mo ions of the anion. On average, two H_2O molecules from the solvent are incorporated into the coordination sphere of Mo ions. One of these two aqua ligands is permanently coordinated to the central Mo ion, thus increasing its coordination number to seven. The number of hydroxo ligands attached to the starlike hexamolybdate along the whole simulation is essentially three. These hydroxo ligands are not permanently bonded to the same Mo ions but dynamically change their positions when intramolecular proton transfers take place (see the Supporting Information for a more detailed analysis of MD) (Figure 3a).

To analyze the dimer with a $[\text{Mo}_2\text{V}_2\text{O}_8\text{H}_6(\text{CH}_3\text{COO})]^-$ stoichiometry, a box ($a = b = c = 12.58\text{ \AA}$) containing one $[\text{Mo}_2(\mu_2\text{-O})_2(\text{OH})_6(\text{CH}_3\text{COO})]^-$ anion surrounded by 58 water molecules was used. After equilibration for 3 ps, the initial structure of the Mo^{V} dimer is somewhat changed; there is only one oxo bridge between the two Mo^{V} ions, and an intramolecular proton transfer has taken place. Hence, one Mo^{V} ion is six-coordinated by two oxo ligands, two hydroxo ligands, one aqua ligand, and one carboxylato ligand (2O/2OH/1w/

1c), and the other is five-coordinated (2O/2OH/1c). The coordination sphere for each of the two Mo^V ions is mainly kept during the whole production run (26 ps). The carboxylato ligand is always coordinated to at least one of the two Mo^V ions, whereas significant changes in the number of oxo, hydroxo, and aqua ligands occur during the simulation, keeping almost constant the total number of ligands at five for one Mo ion and at six for the other (Figure 3b and Figure S1). It is worth mentioning that during the simulation many intramolecular dimer-to-dimer and intermolecular solvent-to-dimer proton transfers are detected. To enhance the sampling, additional production runs were conducted starting from different snapshots of the previous simulation. A 43 ps trajectory has been collected using as an initial structure the [Mo^V₂O₃(OH)₄(H₂O)(CH₃COO)]⁻ dimer. The coordination environment of the Mo ions along the simulation confirms the dynamical behavior of the dimer that essentially remains with three oxo ligands, four hydroxo ligands, one aqua ligand, and one acetato ligand during the whole simulation. The acetato ligand is also observed now to attach in an asymmetrical manner to each of the Mo^V ions, with one Mo–O distance that is appreciably longer than the other, confirming its labile character. This, in turn, shows that upon reduction of heptamolybdate a molecular cascade of further condensation opens up, creating larger cluster type species in solution.

Acidification and Emergence of the [Mo₁₃₂] Raman Spectroscopic Fingerprint. After reduction, the next synthetic step is acidification. Acidification in the original synthesis is achieved by the addition of acetic acid. Upon acidification, there is a marked decrease in the abundance of [(Mo)Mo₅] type building blocks in the library. Moreover, larger species like those of [Mo₈], [Mo₉], and [Mo₁₄] are found. This might be explained as the signature of speciation in the library due to self-condensation and cross-condensation of prime building blocks like [Mo₁], [Mo₂], and [(Mo)Mo₅], respectively. However, the disappearance of the [(Mo)Mo₅] building block is coupled with an increase in the intensity of the 880 cm⁻¹ band in the Raman spectrum of the corresponding library. Simulation studies show that band corresponds to the symmetric breathing mode of a large cluster, [Mo₁₃₂]. More precisely, this band corresponds to the symmetric modes of vibrations of μ₂-O atoms connecting the [(Mo)Mo₅] units with the linkers.

We have shown the existence of a library in the solution of reduced molybdate. To show how the fragments of that library interact and connect, we computed the Raman spectra of all possible fragments and compared them with that of the experimentally found fragments to show the modality of condensation in forming [Mo₁₃₂] Keplerate cluster (for methodology details, see Experimental Section). It is seen that the pentagonal unit [(Mo)Mo₅] and the linker [Mo₂] are both Raman silent. Upon reduction and acidification, the experimental spectra resemble the simulated Raman spectra of condensed pentagonal unit [(Mo)Mo₅] and linker unit [Mo₂]. There we observe theoretically a set of new peaks around 650 cm⁻¹. The peak with the highest intensity corresponds to the bridging oxygen scissoring and the pentagon nonterminal oxygen bending. Also, we also found the band around 850 cm⁻¹ due to terminal oxygen stretching. The spectrum is similar to that found experimentally after reduction and acidification of molybdate (Figure 4).

Hence, after reduction and acidification of the starting molybdate solution, it can be said because of Raman spectra

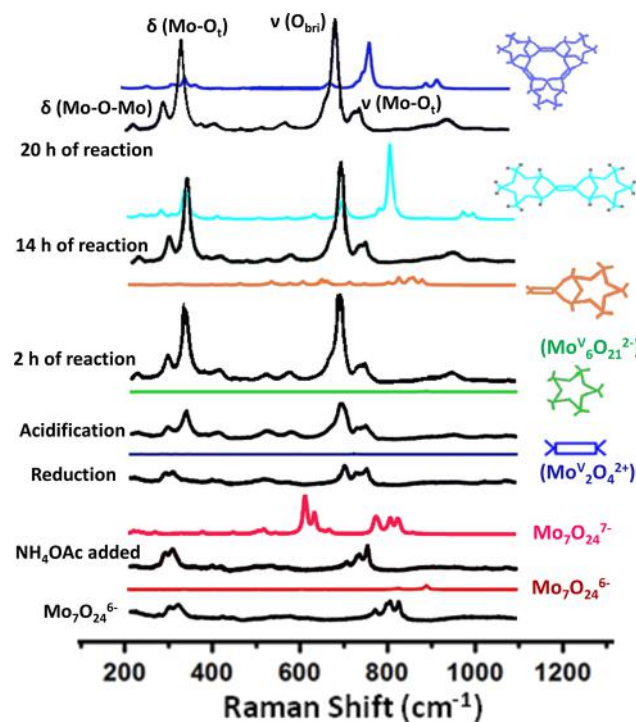


Figure 4. Comparison of the evolution of Raman spectra during the formation of [Mo₁₃₂] (black lines) with spectra of several models computed at the DFT level (colored lines). During reaction, the gradual increase in the intensity of four prominent Raman peaks at 314 cm⁻¹ [$\delta(\text{Mo}-\text{O}-\text{Mo})$], 374 cm⁻¹ [$\delta(\text{Mo}-\text{O})$], 880 cm⁻¹ ($\nu_{\text{O-br}}$), and 950 cm⁻¹ [$\nu(\text{Mo}-\text{O})$] indicates formation of the Mo₁₃₂ cluster. See the Supporting Information for details of computed Raman spectra.

that pentagonal unit [(Mo)Mo₅] and linker unit [Mo₂] condense. Upon standing, the reaction system evolves further. Raman spectra of time-evolved systems are similar to the simulated spectra of further condensed species. For instance, in the case of two pentagonal units [(Mo)Mo₅] and linker unit [Mo₂], the simulated spectra show two peaks due to bridging oxygen wagging modes at 275 cm⁻¹ (8000 Ang⁴/amu) and 330 cm⁻¹ (25000 Ang⁴/amu). At 700 cm⁻¹, there is a peak due to bridging oxygen symmetric stretching (15000 Ang⁴/amu). The main peak (60000 Ang⁴/amu) is at 813 cm⁻¹ and corresponds to the pentagon/linker bridging oxygen symmetric stretching. Finally, around 1000 cm⁻¹, a set of peaks due to terminal oxygen stretching (6000 Ang⁴/amu) is found, which are similar with the experimentally obtained spectra after samples had been left to stand for 2 h. With further standing, the bands intensify. These spectra in turn resemble the simulated Raman spectra of larger fragments. For instance, the Raman spectra obtained experimentally after reaction for 14 and 20 h resemble closely the simulated spectrum of a [Mo₉O₉] pore flanked by three pentagonal [(Mo)Mo₅] units and three [Mo₂] linker units. This indicates that in the reaction mixture after 20 h cluster formation is complete and units like that of [Mo₉O₉] pores are present and already formed and so is the cluster. This is so because 20 such condensed [Mo₉O₉] pores would define a complete [Mo₁₃₂] cluster.

The condensation that leads to the formation of the cluster is mediated by both pH and the degree of reduction. Alone pH causes condensation of mixed valent species to form larger fragments. From pentagonal and linker unit models, we have seen that the condensation energy of the fragments can be very

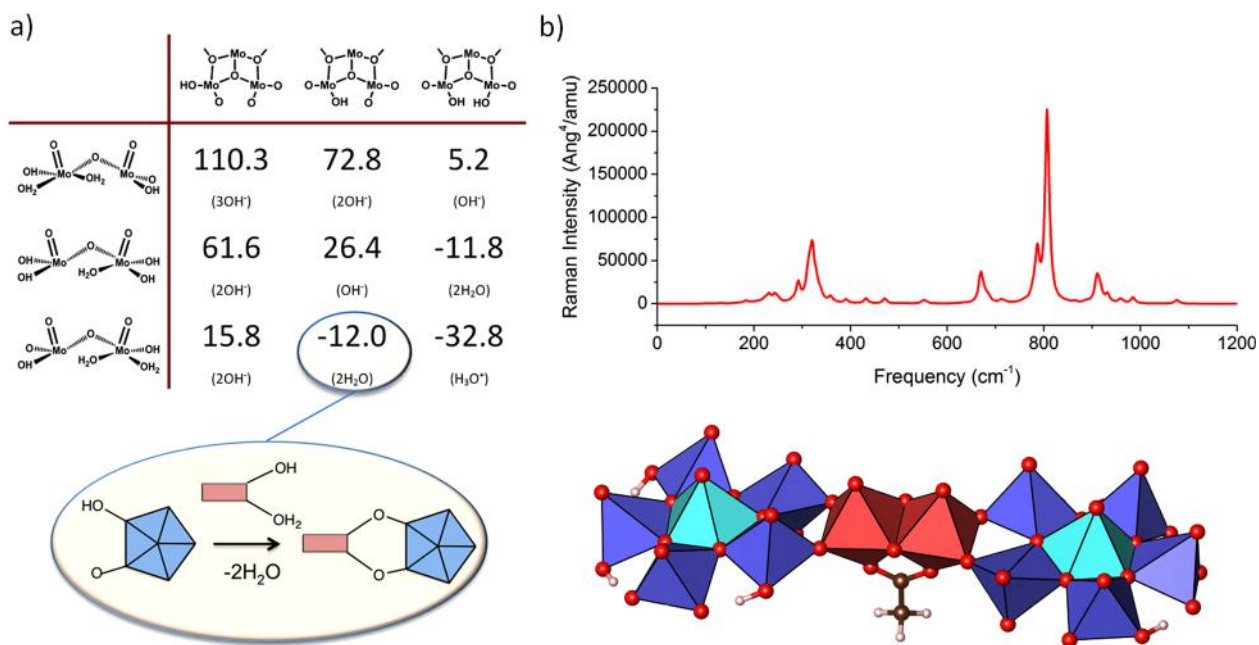


Figure 5. (a) Condensation reaction energies (in kilocalories per mole) between dimers (rows) $[\text{Mo}_2\text{O}_3(\text{OH})_4(\text{H}_2\text{O})(\text{CH}_3\text{COO})]^-$ or $[\text{Mo}_2\text{O}_3(\text{OH})_2(\text{H}_2\text{O})_2(\text{CH}_3\text{COO})]^-$ and pentagonal fragments (columns) $[\text{Mo}_2\text{O}_3(\text{OH})(\text{H}_2\text{O})_3(\text{CH}_3\text{COO})]^-$ as a function of the degree of protonation. The inner labels indicate the products obtained upon condensation. Both dimers and pentagonal structures are those suggested by the CP molecular dynamics simulations, and the condensation energies were computed by means of DFT. (b) Theoretical Raman spectrum (top) and schematic representation (bottom) of one of the proposed intermediate systems for $[\text{Mo}_{132}]$ formation.

depending on the degree of protonation and therefore pH (Figure 5a). Using structures found during the MD trajectories, we have found that the condensation between pentagonal and linker units is exothermic for several linker forms. Hence, formation of a cluster like that of $[\text{Mo}_{132}]$ is caused by controlled condensation due to reduction and acidification (lowering of pH).

Finally, Raman spectra were computed for a framework that consisted of two pentagonal fragments and a linker-bearing acetate ligand as represented in Figure 5b. The computed Raman spectrum nicely agrees with the experimentally observed spectrum (Figure 4a) and clearly shows that this framework is a key species during the formation of the $[\text{Mo}_{132}]$ cluster.

The fact that there is an interplay of charge and symmetry in the formation of $[\text{Mo}_{132}]$ type clusters also emerges. Indeed, it was proposed by the Müller group of Bielefeld that there is a virtual library of building blocks in the solution from which selection takes place. Here we have taken the next steps. We have shown explicitly that a library of building blocks exists. These building blocks are charged and are generated no sooner than the starting precursors are dissolved in water. For instance, pentagonal building block $[(\text{Mo})\text{Mo}_5]$ exists in this library. Upon reduction of the solution, the population and diversity of building blocks in the library increase. The $[\text{Mo}_2]$ linker is generated under these conditions by self-condensation of $[\text{Mo}_1]$ building blocks. Further condensation reactions set in. The combinatorial library experiences an explosion of speciation. Selection sets in. The selection rule operates on charge complementarity. Consequently, pentagonal building blocks like that of $[(\text{Mo})\text{Mo}_5]$ combine with linkers $[\text{Mo}_2(\text{acetate})]$ from the library to create a library of larger building blocks like that of $[\text{Mo}_8]$. Now it appears that symmetry selection starts operating. More symmetric species with lower surface energies, first $[(\text{Mo})\text{Mo}_5]$ and then $[\text{Mo}_2]$

and later $[\text{Mo}_9\text{O}_9]$ pores with its paraphernalia, lead to the emergence of closed surface entities like that of $[\text{Mo}_{132}]$, while the other linear species like those of other isopolymolybdates are depleted. The symmetry selection followed by charge selection indeed operates in a manner of molecular Darwinism and leads to the emergence of a prominent spherical cluster of $[\text{Mo}_{132}]$ at the expense of other smaller and less symmetric species. This is seen from Raman studies stepwise systematically.

The appearance of various colors during the formation of $[\text{Mo}_{132}]$ can be shown with the help of electronic absorption spectroscopy (EAS) (Figure 6).

Initially, the solution contains only Mo(VI) fragments for which the solution is colorless. As soon as we add a reducing

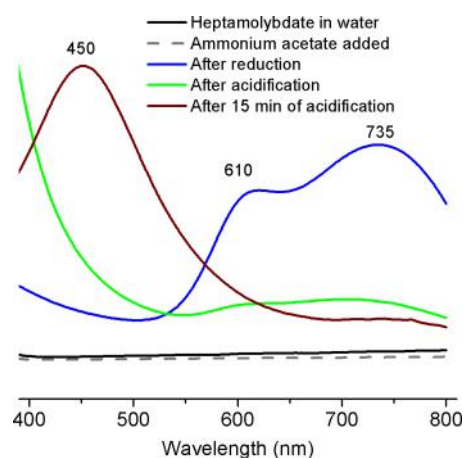


Figure 6. Electronic absorption spectroscopy during different steps of the formation of $[\text{Mo}_{132}]$. The appearance of various colors is shown during the formation.

agent such as $\text{N}_2\text{H}_6\text{SO}_4$, initially a blue color appears because of charge transfer from Mo(V) to Mo(VI) due to the appearance of Mo(V). The solution slowly turns dark green. In EAS at this point, bands at 600 and 735 nm are due to metal–oxo bridge charge transfer and localized oxygen ion vacancies, respectively (Figure 6).⁴⁹ After acidification, the solution turns dirty green. At this point, condensation of two Mo(V) units with acetate takes place, which suppresses the bands at 600 and 735 nm as we see in EAS. Soon after acidification, condensation of $[\text{Mo}_2]$ units with $[(\text{Mo})\text{Mo}_5]$ starts taking place, turning the solution brown due to the appearance of intervalence charge transfer bands.

CONCLUSION

In short, we follow the formation pathway of $[\text{Mo}_{132}]$ Keplerate in water that involves dissolution of heptamolybdate in water. ESI-MS data show that dissolved oxidized molybdate opens a library of building blocks in which pentagonal building block $[(\text{Mo})\text{Mo}_5]$ is present. Upon reduction, reduced $[\text{Mo}^{\text{V}}_2\text{O}_2(\text{OH})_6(\text{CH}_3\text{COO})]^-$ type dinuclear linker units with a coordinatively fluxional carboxylate group are formed. Upon acidification, further condensation between the pentagonal building blocks and reduced linkers sets in. We calculate such condensation energies that are favorable only at low or acidic pH. Raman spectroscopic investigations furthermore show stepwise condensation of the units mentioned above to form first condensed $[(\text{Mo})\text{Mo}_5]$ and $[\text{Mo}_2]$ units. The reaction system upon standing evolves to form $[\text{Mo}_9\text{O}_9]$ porelike fragments coronate with three $[(\text{Mo})\text{Mo}_5]$ and three $[\text{Mo}_2]$ units, implying formation of a complete cluster.

In conclusion, we have demonstrated the emergence of a closed spherical cluster $[\text{Mo}_{132}]$, starting from a reduced and acidified aqueous solution of molybdate. The $[\text{Mo}_{132}]$ cluster creates confined 3D space by gluing building blocks. Such gluing of building blocks at low pH follows the basic principles of thermodynamics of negative condensation energy. This phenomenon is primarily controlled by charge balance and emergence of more symmetric structures at the expense of less symmetric ones.

ASSOCIATED CONTENT

Supporting Information

The Supporting Information is available free of charge on the ACS Publications website at DOI: 10.1021/acs.inorgchem.5b02570.

Detailed description of the Carr–Parrinello molecular dynamics simulations, DFT-based Raman spectral calculations, additional experiments, and a simplified Pourbaix diagram (PDF)

AUTHOR INFORMATION

Corresponding Authors

*E-mail: pradeep@iit.ac.in.

*E-mail: cbo@iciq.cat.

*E-mail: josepmaria.poblet@urv.cat.

*E-mail: s.roy@iiserkol.ac.in.

Notes

The authors declare no competing financial interest.

ACKNOWLEDGMENTS

Atharva Sahasrabudhe and Bibudha Parashar are thanked for the synthesis of the cluster and early experiments during this

project. The authors thank IISER-Kolkata, DST, DST-Fast Track, and BRNS-DAE, India, for financial support. The authors also thank the ICIQ Foundation, the Spanish Ministerio de Economía y Competitividad (MINECO) through Projects CTQ2014-52824-R and CTQ2014-52774-P and the Severo Ochoa Excellence Accreditation 2014-2018 (SEV-2013-0319), and the AGAUR of Generalitat de Catalunya through Projects 2014-SGR-409 and 2014-SGR-199 for financial support. This project was conducted with the support of the COST Action CM1203 “Polyoxometalate Chemistry for Molecular Nanoscience (PoCheMoN)”. S.B. thanks UGC for scholarships, and A.S. thanks CSIR and IIT Madras for scholarships. D.M. gratefully acknowledges the URV-ICIQ fellowship. The authors also thankfully acknowledge the computer resources, technical expertise, and assistance provided by the Barcelona Supercomputing Center-Centro Nacional de Supercomputación.

REFERENCES

- (1) Pope, M. T.; Müller, A. *Angew. Chem., Int. Ed. Engl.* **1991**, *30*, 34–48.
- (2) Borrás-Almenar, J. J.; Coronado, E.; Müller, A.; Pope, M. *Polyoxometalate Molecular Science*; Springer: Dordrecht, The Netherlands, 2003.
- (3) Carraro, M.; Sandei, L.; Sartorel, A.; Scorrano, G.; Bonchio, M. *Org. Lett.* **2006**, *8*, 3671–3674.
- (4) Rausch, B.; Symes, M. D.; Chisholm, G.; Cronin, L. *Science* **2014**, *345*, 1326–1330.
- (5) Rhule, J. T.; Hill, C. L.; Judd, D. A.; Schinazi, R. F. *Chem. Rev.* **1998**, *98*, 327–358.
- (6) Müller, A.; Sarkar, S.; Shah, S. Q. N.; Bögge, H.; Schmidtman, M.; Sarkar, S.; Kögerler, P.; Hauptfleisch, B.; Trautwein, A. X.; Schünemann, V. *Angew. Chem., Int. Ed.* **1999**, *38*, 3238–3241.
- (7) Müller, A.; Krickemeyer, E.; Bögge, H.; Schmidtman, M.; Peters, F. *Angew. Chem., Int. Ed.* **1998**, *37*, 3359–3363.
- (8) Müller, A. *Nat. Chem.* **2009**, *1*, 13–14.
- (9) Müller, A.; Krickemeyer, E.; Bögge, H.; Schmidtman, M.; Peters, F. *Angew. Chem., Int. Ed.* **1998**, *37*, 3359–3363.
- (10) Roy, S. *CrystEngComm* **2014**, *16*, 4667–4676.
- (11) Roy, S. *Comments Inorg. Chem.* **2011**, *32*, 113–126.
- (12) Biswas, S.; Roy, S. *J. Mater. NanoSci.* **2014**, *1*, 6.
- (13) Verhoeff, A. A.; Kistler, M. L.; Bhatt, A.; Pigga, J.; Groenewold, J.; Klokkenburg, M.; Veen, S.; Roy, S.; Liu, T.; Kegel, W. K. *Phys. Rev. Lett.* **2007**, *99*, 066104.
- (14) Liu, T.; Diemann, E.; Li, H.; Dress, A. W. M.; Müller, A. *Nature* **2003**, *426*, 59–62.
- (15) Judd, B. R. *Proc. R. Soc. London, Ser. A* **1957**, *241*, 122–131.
- (16) Zandi, R.; Reguera, D.; Bruinsma, R. F.; Gelbart, W. M.; Rudnick, J. *Proc. Natl. Acad. Sci. U. S. A.* **2004**, *101*, 15556–15560.
- (17) Rodríguez-Fortea, A.; Alegret, N.; Balch, A. L.; Poblet, J. M. *Nat. Chem.* **2010**, *2*, 955–961.
- (18) Ceulemans, A.; Fowler, P. W. *Nature* **1991**, *353*, 52–54.
- (19) Holton, G. *Am. J. Phys.* **1956**, *24*, 340–351.
- (20) Müller, A. *Science* **2003**, *300*, 749–750.
- (21) Müller, A.; Toma, L.; Bögge, H.; Schmidtman, M.; Kogerler, P. *Chem. Commun.* **2003**, 2000–2001.
- (22) Ziv, A.; Grego, A.; Kopilevich, S.; Zeiri, L.; Miro, P.; Bo, C.; Müller, A.; Weinstock, I. A. *J. Am. Chem. Soc.* **2009**, *131*, 6380–6382.
- (23) Kopilevich, S.; Gil, A.; García-Ratés, M.; Bonet-Avalos, J.; Bo, C.; Müller, A.; Weinstock, I. A. *J. Am. Chem. Soc.* **2012**, *134*, 13082–13088.
- (24) Besson, C.; Schmitz, S.; Capella, K. M.; Kopilevich, S.; Weinstock, I. A.; Kogerler, P. *Dalton Trans.* **2012**, *41*, 9852–9854.
- (25) Garai, S.; Haupt, E. T. K.; Bögge, H.; Merca, A.; Müller, A. *Angew. Chem., Int. Ed.* **2012**, *51*, 10528–10531.
- (26) Grego, A.; Müller, A.; Weinstock, I. A. *Angew. Chem., Int. Ed.* **2013**, *52*, 8358–8362.

- (27) Rezaeifard, A.; Haddad, R.; Jafarpour, M.; Hakimi, M. *J. Am. Chem. Soc.* **2013**, *135*, 10036–10039.
- (28) Garai, S.; Rubčić, M.; Bögge, H.; Gouzerh, P.; Müller, A. *Chem. - Eur. J.* **2015**, *21*, 4321–4325.
- (29) Watfa, N.; Melgar, D.; Haouas, M.; Taulelle, F.; Hijazi, A.; Naoufal, D.; Avalos, J. B.; Floquet, S.; Bo, C.; Cadot, E. *J. Am. Chem. Soc.* **2015**, *137*, 5845–5851.
- (30) Whitesides, G. M.; Ismagilov, R. F. *Science* **1999**, *284*, 89–92.
- (31) Richmond, C. J.; Miras, H. N.; de la Oliva, A. R.; Zang, H.; Sans, V.; Paramonov, L.; Makatsoris, C.; Inglis, R.; Brechin, E. K.; Long, D.-L.; Cronin, L. *Nat. Chem.* **2012**, *4*, 1037–1043.
- (32) Muller, A.; Das, K.; Krickemyer, E.; Kuhlmann, C. Polyoxomolybdate Clusters: Giant wheels and balls. In *Inorganic Syntheses*; John Wiley & Sons, Inc.: New York, 2004; Vol. 34, pp 191–200.
- (33) Long, D.-L.; Streb, C.; Song, Y.-F.; Mitchell, S.; Cronin, L. *J. Am. Chem. Soc.* **2008**, *130*, 1830–1832.
- (34) Wilson, E. F.; Miras, H. N.; Rosnes, M. H.; Cronin, L. *Angew. Chem., Int. Ed.* **2011**, *50*, 3720–3724.
- (35) Nakamura, I.; Miras, H. N.; Fujiwara, A.; Fujibayashi, M.; Song, Y.-F.; Cronin, L.; Tsunashima, R. *J. Am. Chem. Soc.* **2015**, *137*, 6524–6530.
- (36) Poblet, J. M.; Lopez, X.; Bo, C. *Chem. Soc. Rev.* **2003**, *32*, 297–308.
- (37) Lopez, X.; Carbo, J. J.; Bo, C.; Poblet, J. M. *Chem. Soc. Rev.* **2012**, *41*, 7537–7571.
- (38) López, X.; Miró, P.; Carbó, J.; Rodríguez-Forteza, A.; Bo, C.; Poblet, J. *Theor. Chem. Acc.* **2011**, *128*, 393–404.
- (39) Schaffer, C.; Todea, A. M.; Gouzerh, P.; Muller, A. *Chem. Commun.* **2012**, *48*, 350–352.
- (40) Müller, A.; Rehder, D.; Haupt, E. T. K.; Merca, A.; Bögge, H.; Schmidtman, M.; Heinze-Brückner, G. *Angew. Chem., Int. Ed.* **2004**, *43*, 4466–4470.
- (41) Canioni, R.; Marchal-Roch, C.; Leclerc-Laronze, N.; Haouas, M.; Taulelle, F.; Marrot, J.; Paul, S.; Lamonier, C.; Paul, J.-F.; Lorient, S.; Millet, J.-M. M.; Cadot, E. *Chem. Commun.* **2011**, *47*, 6413–6415.
- (42) Wilson, E. F.; Miras, H. N.; Rosnes, M. H.; Cronin, L. *Angew. Chem., Int. Ed.* **2011**, *50*, 3720–3724.
- (43) Vila-Nadal, L.; Wilson, E. F.; Miras, H. N.; Rodríguez-Forteza, A.; Cronin, L.; Poblet, J. M. *Inorg. Chem.* **2011**, *50*, 7811–7819.
- (44) Müller, A.; Roy, S. *Coord. Chem. Rev.* **2003**, *245*, 153–166.
- (45) Car, R.; Parrinello, M. *Phys. Rev. Lett.* **1985**, *55*, 2471.
- (46) Hafner, J. *Nat. Mater.* **2010**, *9*, 690–692.
- (47) Vilà-Nadal, L.; Mitchell, S. G.; Rodríguez-Forteza, A.; Miras, H. N.; Cronin, L.; Poblet, J. M. *Phys. Chem. Chem. Phys.* **2011**, *13*, 20136–20145.
- (48) Vilà-Nadal, L.; Rodríguez-Forteza, A.; Yan, L. K.; Wilson, E. F.; Cronin, L.; Poblet, J. M. *Angew. Chem., Int. Ed.* **2009**, *48*, 5452–5456.
- (49) Conte, M.; Liu, X.; Murphy, D. M.; Taylor, S. H.; Whiston, K.; Hutchings, G. J. *Catal. Lett.* **2016**, *146*, 126–135.

Supporting Information

Direct Observation of the Formation Pathway of [Mo₁₃₂] Keplerates

*Subharanjan Biswas,¹ Dolores Melgar,^{2,3} Amitava Srimany,⁴ Antonio Rodríguez-Forteza,⁵
Thalappil Pradeep,^{*4} Carles Bo,^{*2} Josep M. Poblet^{*5} and Soumyajit Roy^{*1}*

1 Eco-Friendly Applied Materials Laboratory (EFAML), Materials Science Centre, Department of Chemical Sciences, Indian Institute of Science Education and Research-Kolkata (IISER-Kolkata), Mohanpur Campus, Mohanpur-741246, India, Email- s.roy@iiserkol.ac.in

2 Institute of Chemical Research of Catalonia (ICIQ), Av. Països Catalans 16, 43007 Tarragona, Spain, Email- cbo@iciq.cat

3 Departament d'Enginyeria Química, ETSEQ, Universitat Rovira i Virgili, Av. dels Països Catalans, 26, 43007 Tarragona, Spain

4 Department of Chemistry, Indian Institute of Technology Madras, Chennai 600036, India, Email- pradeep@iitm.ac.in

5 Departament de Química Física i Inorgànica, Universitat Rovira i Virgili, Marcel·lí Domingo 1, 43007 Tarragona, Spain, Email- josepmaria.poblet@urv.cat

Calculations on the dinuclear species $[\text{HMo}^{\text{V}}_2\text{O}_6(\text{CH}_3\text{COO})(\text{H}_2\text{O})_2]^-$

Once the system, heptamolybdate in aqueous solution, is reduced a peak assigned to the formula $[\text{HMo}^{\text{V}}_2\text{O}_6(\text{CH}_3\text{COO})(\text{H}_2\text{O})_2]^-$ appears in the mass spectrum. The first problem that we encounter is that the assignment of the oxidation states is incompatible with the total charge of the molecule. If the two Mo atoms are Mo(V), the charge of the system should be 2-. So, for this charge to be correct, one should have (i) a reduced Mo(V) and a totally oxidized Mo(VI); or (ii) an extra proton in the formula. In order to clarify this point, we have made computations on different model systems [standard settings: ADF, BP86/TZP with COSMO], as shown in Table S1. The hypothetical mixed-valence dimer $[\text{Mo}^{\text{V}}\text{Mo}^{\text{VI}}\text{O}_5(\text{OH})(\text{CH}_3\text{COO})(\text{H}_2\text{O})_2]^-$ (**1**) with the two Mo ions hexacoordinated in an octahedral environment with two oxo bridges, two aqua ligands, a hydroxo ligand and a carboxylato keeps the structure after geometry optimization (first row, Table S1). The Mo...Mo distance is 3.098 Å. The same dinuclear compound with 2- charge, i.e. the two metal ions as Mo(V), leads to a structure where one Mo(V) ion has lost one aqua ligand, which remains hydrogen-bonded to the system (second row, Table S1). The Mo...Mo distance is in this reduced state somewhat shorter (3.070 Å) than for **1** due to the presence of two, instead of one, electrons in the bonding Mo-Mo orbital. To keep the 1- charge with two Mo(V) ions, one extra H⁺ has to be added to the structure (model compound **3**). Optimization of model **3** leads to important structural changes where the two Mo(V) ions are singly bridged and their coordination environments have changed to five and four (third row, Table S1). The structural isomer $[\text{Mo}^{\text{V}}_2\text{O}_2(\text{OH})_6(\text{CH}_3\text{COO})]^-$ (**4**), with no aqua ligands and six hydroxo ligands, however, keeps the octahedral environment around each Mo(V) ion (fourth row, Table S1). The Mo...Mo is now significantly decreased to 2.727 Å.

Species	Coord (Mo1) _{init}	Coord (Mo2) _{init}	Coord (Mo1) _{fin}	Coord (Mo2) _{fin}
[Mo ^V Mo ^{VI} O ₅ (OH)(CH ₃ COO)(H ₂ O) ₂] ⁻ (1)	6 [3O/1OH/1w/1c]	6 [4O/1w/1c]	6 [3O/1OH/1w/1c]	6 [4O/1w/1c]
[Mo ^V ₂ O ₅ (OH)(CH ₃ COO)(H ₂ O) ₂] ²⁻ (2)	6 [3O/1OH/1w/1c]	6 [3O/1OH/1w/1c]	5 [3O/1OH/1c]	6 [4O/1w/1c]
[Mo ^V ₂ O ₄ (OH) ₂ (CH ₃ COO)(H ₂ O) ₂] ⁻ (3)	6 [3O/1OH/1w/1c]	6 [4O/1w/1c]	5 [1O/2OH/1c]	4 [2O/2OH]
[Mo ^V ₂ O ₂ (OH) ₆ (CH ₃ COO)] ⁻ (4)	6 [2O/3OH/1c]	6 [2O/3OH/1c]	6 [2O/3OH/1c]	6 [2O/3OH/1c]

Table S1. Results for the geometry optimizations at BP86/TZP level using COSMO (water as solvent) done on model systems related to the [HMo^V₂O₆(CH₃COO)(H₂O)₂]⁻ assignment of the mass spectrum. The nomenclature for ligands is the following O: oxo; OH: hydroxo; w: water; c: carboxylate.

Car-Parrinello molecular dynamics on [Mo^V₂O₂(OH)₆(CH₃COO)]⁻

We have performed Car-Parrinello molecular dynamics (MD) simulations, using the CPMD code.¹ The description of the electronic structure is based on the expansion of the valence electronic wave functions into a plane wave (PW) basis set, which is limited by an energy cutoff of 70 Ry. The interaction between the valence electrons and the ionic cores is treated through the pseudopotential (PP) approximation. Norm-conserving Martins-Troullier PPs are employed.² A semicore Mo PP was used according to the work of Boero et al.³ We adopt the generalized gradient-corrected functionals of Becke for the exchange and of Perdew for the correlation.⁴⁻⁶ In the MD simulations, the wave functions are propagated in the Car-Parrinello scheme, by integrating the equations of motion derived from the extended Car-Parrinello Lagrangian.⁷ We use a time step of 0.144 fs and a fictitious electronic mass of 900 a.u. A Nosé-Hoover thermostat keeps the temperature around 300 K.⁸⁻¹⁰

The cell box that contains one $[\text{Mo}^{\text{V}}_2\text{O}_2(\text{OH})_6(\text{CH}_3\text{COO})]^-$ dimer and 58 water molecules ($a = b = c = 12.58 \text{ \AA}$) is repeated periodically in the space by the standard periodic boundary conditions. After 3 ps of equilibration, the initial structure of the Mo^{V} dimer (see fourth row of Table S1) is somewhat changed; there is only one oxo bridge between the two Mo^{V} ions and an intramolecular proton transfer has taken place. Hence, one Mo^{V} ion is six-coordinated $[2\text{O}/2\text{OH}/1\text{w}/1\text{c}]$ and the other is five-coordinated $[2\text{O}/2\text{OH}/1\text{c}]$. We have performed a production run of 26 ps. Figure 3B shows the Mo–O radial distribution functions and their integrations, which yield the total coordination number, for each Mo^{V} ion.

The sharp spikes at around 1.75 \AA , which integrate one O atom for each Mo ion, are attributed to the terminal oxo ligands. The peaks at around 2 \AA , which integrate up to four atoms, correspond to the hydroxo and the bridging oxo ligands. The peaks and shoulders at distances between 2 and 2.5 \AA are due to the aqua and carboxylato ligands. At distances between 2.5 and 3 \AA the Mo–O coordination number shows a plateau associated with the presence of five O atoms in the coordination sphere of Mo(1). On the other hand, Mo(2) is six-coordinated. Therefore, the coordination sphere for each of the two Mo^{V} ions is mainly kept during the whole simulation. Other shallow maxima appear at distances larger than 3 \AA , which are associated to the first solvation sphere and to the rest of the O atoms that belong to the cluster. Figure S1 shows the evolution of the coordination environment for each of the Mo^{V} ions. The carboxylato ligand, which is always coordinated to at least one of the two Mo^{V} ions, is counted as an oxo ligand. Significant changes in the number of oxo, hydroxo and aqua ligands during the simulation, keeping almost constant the total number of ligands to five for Mo(1) and six to Mo(2), are observed as a consequence of intramolecular dimer-to-dimer and intermolecular solvent-to-dimer proton transfers. Figure S2 shows the evolution of the number of H atoms bonded to the O atoms directly coordinated to the Mo ions. The initial total number of six is mainly kept for almost the whole simulation; however, a seventh

proton is observed to attach to the dimer in the last part of the simulation (after 20 ps). The changes in the number of H atoms bound to Mo(1) or Mo(2) also denote the high mobility of protons within the dimer.

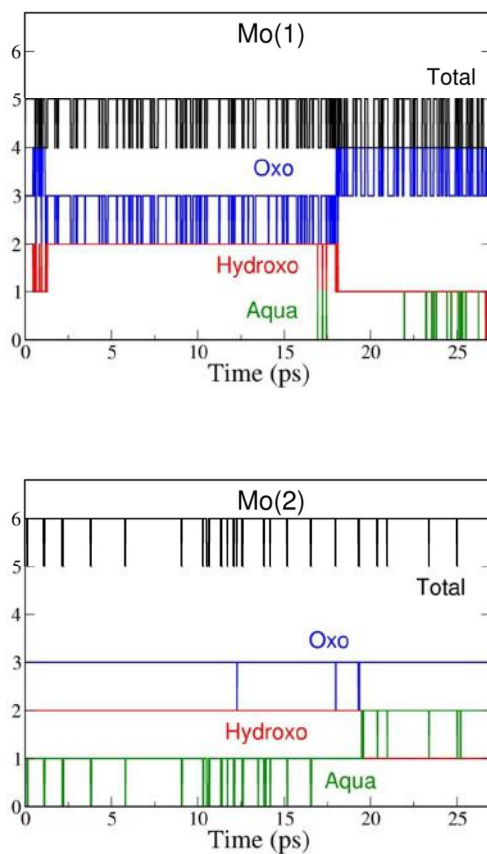


Figure S1. Number of oxo (blue), hydroxo (red) and aqua (green) ligands as well as the total number of ligands (black) for each of the Mo ions during the 27 ps of simulation starting from $[\text{Mo}^{\text{V}}_2\text{O}_2(\text{OH})_6(\text{CH}_3\text{COO})]^-$. The carboxylato bridge is considered as an oxo ligand.

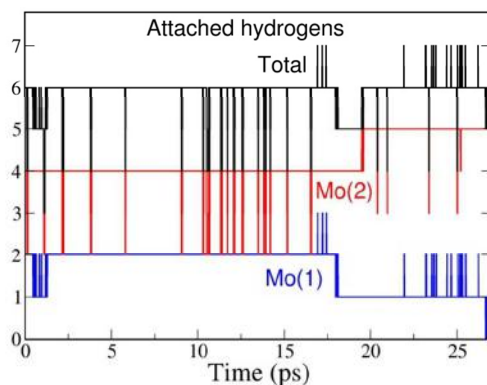


Figure S2. Number of hydrogen atoms bonded to oxygen atoms that are directly coordinated to Mo(1) (blue) and Mo(2) (red) as well as their total number (sum, in black) during the 27 ps of simulation starting from $[\text{Mo}^{\text{V}}_2\text{O}_2(\text{OH})_6(\text{CH}_3\text{COO})]^-$.

Finally, we have analyzed in more detail the fate of the carboxylato ligand during the dynamics. We have found (see Figure S3) that it is a rather labile ligand that is not always bonded to the two Mo ions at the same time. However, it is always attached to at least one of the Mo ions during the 27 ps of simulation. The carboxylato ligand is rather strongly bonded to Mo(2) with distances that are smaller than 2.5 Å for the whole simulation; it is, however, more weakly bonded to Mo(1) with longer Mo–O distances that oscillate around 2.5 Å and sometimes are larger than 2.8 Å.

Our results show that the dynamical description of the system is necessary to fully understand its properties and behavior.

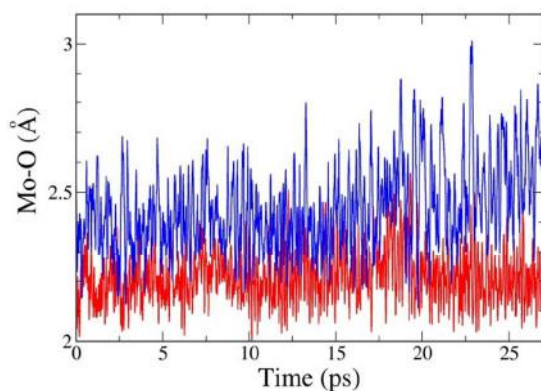


Figure S3. Mo–O(carboxylato) distances, blue line for Mo(1) and red line for Mo(2), during the 27 ps of simulation starting from $[\text{Mo}_2\text{O}_2(\text{OH})_6(\text{CH}_3\text{COO})]^-$.

Car-Parrinello molecular dynamics on $[\text{Mo}_7\text{O}_{24}]^{6-}$ and the reduced system $[\text{Mo}_7\text{O}_{24}]^{7-}$

Car-Parrinello MD simulations were performed with a cell box containing one heptamolybdate $[\text{Mo}_7\text{O}_{24}]^{6-}$, 140 water molecules, two hydronium H_3O^+ and two ammonium NH_4^+ cations ($a = b = c = 16.90 \text{ \AA}$). During the equilibration (1 ps), the heptamolybdate gets protonated in a terminal oxo ligand. After 3 ps of simulation, the heptamolybdate remains essentially singly protonated with the seven Mo atoms keeping their octahedral coordination.

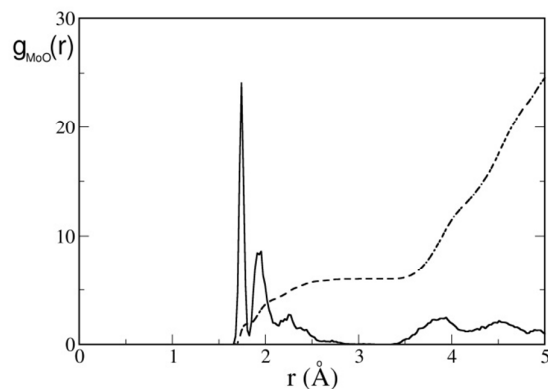


Figure S4. Mo–O radial distribution function (solid line) and its integration, the coordination number (broken line), of Mo for 3 ps of simulation starting from $[\text{Mo}_7\text{O}_{24}]^{6-}$.

The sharp spike at around 1.75 Å, attributed to the terminal oxo ligands, integrates two oxygen atoms per Mo. The spike at around 2 Å, which integrates on average two O atoms per Mo, corresponds mainly to the bridging μ_2 -oxo ligands. The shallower peak at around 2.25 Å, which also integrates two O atoms, corresponds to the μ_3 - and μ_4 -oxo ligands that are in *trans* with respect to the terminal oxo ligands. Figure S5 shows that the hydroxo ligand present initially in the heptamolybdate complex is kept during the dynamics; at some point, a proton of the solution is eventually attached to the molybdate.

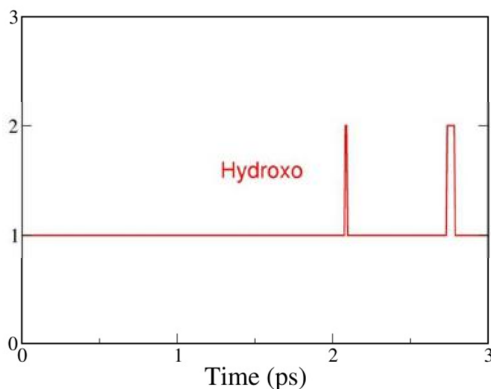


Figure S5. Number of hydroxo ligands in the $[\text{Mo}_7\text{O}_{24}]^{6-}$ heptamolybdate during the 3 ps of simulation.

We have finally performed Car-Parrinello MD simulations in the reduced open-shell $[\text{Mo}_7\text{O}_{24}]^{7-}$ heptamolybdate in order to understand the initial steps in the formation of the Mo_{132} Keplerate, which takes place after reduction of the reactant $[\text{Mo}_7\text{O}_{24}]^{6-}$. The same simulation box as in the totally oxidized heptamolybdate is used. After 1.6 ps of equilibration, a production run of 4.8 ps is analyzed. During this short time scale, we observe that the singly reduced heptamolybdate complex is rather stable and keeps its initial structure with the seven molybdate ions having octahedral coordination. Figure S6 shows that the

Mo–O radial distribution function for the reduced $[\text{Mo}_7\text{O}_{24}]^{7-}$ (red line) is quite similar to that of the oxidized $[\text{Mo}_7\text{O}_{24}]^{6-}$ complex (blue line). A slight difference can be observed in the region around 2 Å, which corresponds mainly to the bridging μ_2 -oxo ligands, where the second spike is somewhat displaced to longer distances for the reduced system compared to the oxidized one. Moreover, the third peak observed for $[\text{Mo}_7\text{O}_{24}]^{6-}$ at around 2.25 Å is split in two small peaks for $[\text{Mo}_7\text{O}_{24}]^{7-}$. So, a slight expansion of some bonds in the coordination sphere of the Mo ions seem to happen at this short time scale.

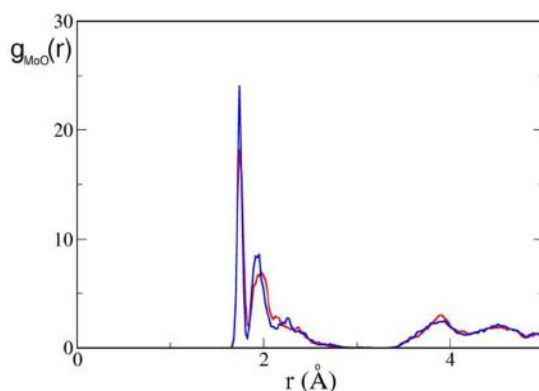


Figure S6. Mo–O radial distribution functions for the reduced $[\text{Mo}_7\text{O}_{24}]^{7-}$ (red line) and the oxidized $[\text{Mo}_7\text{O}_{24}]^{6-}$ (blue line) heptamolybdates.

Figure S7 shows the number of hydroxo ligands in the reduced heptamolybdate during the simulation. The initial hydroxo group is kept during the whole trajectory and for some short periods, especially at around 1 ps, other protons are eventually attached to the molybdate. The larger changes in the number of hydroxo groups of the reduced $[\text{Mo}_7\text{O}_{24}]^{7-}$ along the trajectory denotes that protons interact more easily with the heptamolybdate once it is reduced.

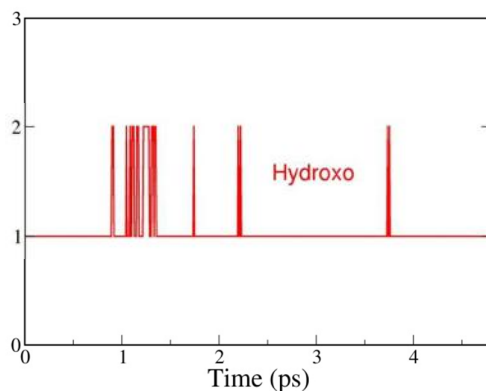


Figure S7. Number of hydroxo ligands in the reduced $[\text{Mo}_7\text{O}_{24}]^{7-}$ heptamolybdate during the 4.8 ps of simulation.

The evolution of the Mo–O distances of the eight μ_4 -oxo ligands for the oxidized and the reduced heptamolybdates along the time is plotted in Figure S8. A small expansion of some of these distances is observed when going from the oxidized to the reduced molybdate, especially for the smallest ones (black lines in Figure S8), which are the Mo–O distances that are in *trans* position with respect to the terminal hydroxo ligands (average values for the oxidized and reduced systems: 1.965 vs 2.043 Å). So, we can conclude that, at this short time scale, the reduced heptamolybdate is rather stable in good agreement with the fact that it does not evolve rapidly to the Mo_{132} Keplerate (the reaction takes some hours). However, a small expansion of the coordination sphere of Mo can be observed after reduction of the heptamolybdate.

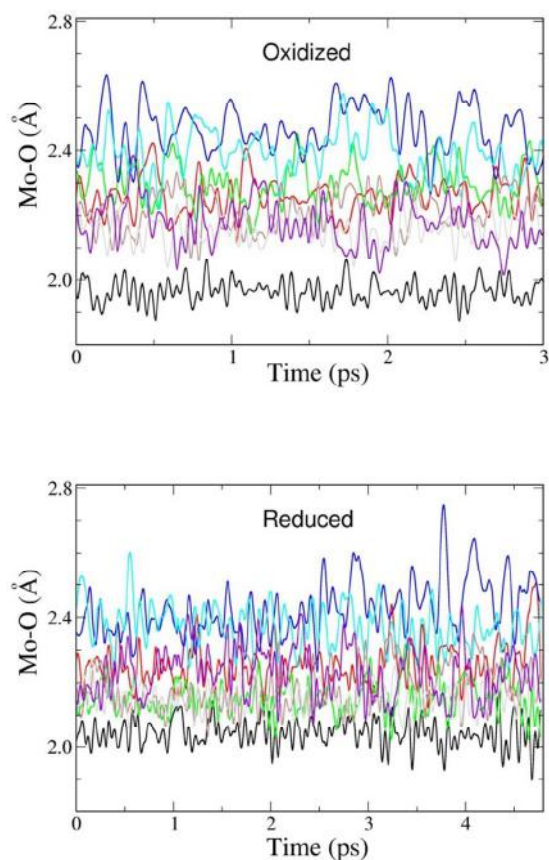


Figure S8. Mo–O distances of the eight μ_4 -oxo ligands for the oxidized $[\text{Mo}_7\text{O}_{24}]^{6-}$ and reduced $[\text{Mo}_7\text{O}_{24}]^{7-}$ heptamolybdates during the Car-Parrinello simulations.

Condensation Energies from Pentagonal and Linker Unit Model

All molecular geometries were fully optimized without constraints by using the Amsterdam Density Functional (ADF2012) program¹¹ developed by Baerends, Ziegler, and co-workers. We used a GGA BP86 functional and a triple- ζ plus one polarization function basis set. Relativistic corrections were introduced by means of the scalar-relativistic zero-order regular approximation (ZORA).^{12,13} Solvent effects were taken into account on the basis of the continuous solvent model COSMO¹⁴] with default radii.

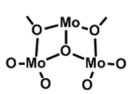
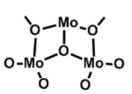
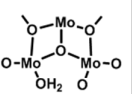
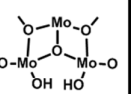
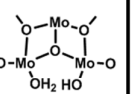
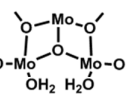
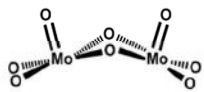
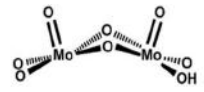
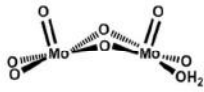
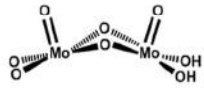
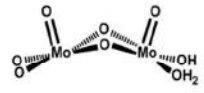
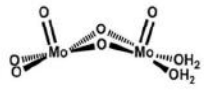
						
	-21.1 4OH ⁻	-44.1 3OH ⁻	-74.6 2OH ⁻	-72.5 2OH ⁻	-155.1 OH ⁻	-172.8 2H ₂ O
	-2.6 3OH ⁻	-25.6 2OH ⁻	-56.1 OH ⁻	-54.0 OH ⁻	-102.8 2H ₂ O	-97.1 H ₃ O ⁺
	25.7 2OH ⁻	2.8 OH ⁻	-27.8 2H ₂ O	-25.7 2H ₂ O	-17.4 H ₃ O ⁺	-11.7 2H ₃ O ⁺
	16.2 2OH ⁻	-6.8 OH ⁻	-37.3 2H ₂ O	-35.2 2H ₂ O	-27.0 H ₃ O ⁺	-21.2 2H ₃ O ⁺
	24.5 OH ⁻	1.5 2H ₂ O	28.1 H ₃ O ⁺	30.2 H ₃ O ⁺	38.5 2H ₃ O ⁺	44.2 3H ₃ O ⁺
	-28.9 2H ₂ O	5.3 H ₃ O ⁺	31.9 2H ₃ O ⁺	34.0 2H ₃ O ⁺	42.3 3H ₃ O ⁺	48.0 4H ₃ O ⁺

Table S2. Condensation reaction energies (in kcal/mol) between dimers (rows) and pentagonal (columns) fragments as function of the protonation degree. The inner labels indicate the products obtained upon condensation.

We computed the condensation reaction energy between a dimer and pentagon moieties as function of the protonation degree. These results are collected in Table S2. For each unit, we considered different level of protonation, i.e., from having no protons to having four protons. This scenario aims at simulating basic and acidic conditions, respectively. Note that the values for situations corresponding to low pH, in the bottom-right part of the table, are all positive, indicating unstable products. Those values for high pH, top-left, are all negative thus indicating favorable reactions. It is interesting to note that the most favorable values correspond, in all the cases, to situations having four protons in all, which are those situations

that give water as product. These numbers demonstrate that the two building blocks, a linker and a pentagon, can condensate only under certain pH conditions.

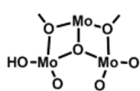
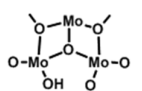
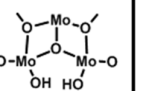
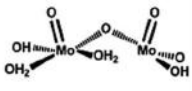
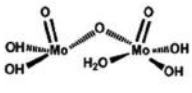
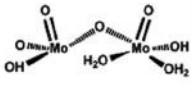
			
	110.3 3OH ⁻	72.8 2OH ⁻	5.2 OH ⁻
	61.6 2OH ⁻	26.4 OH ⁻	-11.8 2H ₂ O
	15.8 2OH ⁻	-12.0 2H ₂ O	-32.8 H ₃ O ⁺

Table S3. Condensation reaction energies (in kcal/mol) between dimers (rows) $[\text{Mo}^{\text{V}}_2\text{O}_3(\text{OH})_4(\text{H}_2\text{O})(\text{CH}_3\text{COO})]^-$ or $[\text{Mo}^{\text{V}}_2\text{O}_3(\text{OH})_2(\text{H}_2\text{O})_2(\text{CH}_3\text{COO})]^-$ and pentagonal fragments (columns) $[\text{Mo}^{\text{V}}_2\text{O}_8\text{H}_6(\text{CH}_3\text{COO})]^-$ as function of the protonation degree. The inner labels indicate the products obtained upon condensation.

We followed the same procedure taking into account different structures for dimers and pentagons. These structures were obtained from Carl-Parrinello molecular dynamics simulations performed on the pentagonal unit $[\text{Mo}_6\text{O}_{21}]^{6-}$ and on dimers with stoichiometry $[\text{Mo}^{\text{V}}_2\text{O}_8\text{H}_6(\text{CH}_3\text{COO})]^-$. The structures suggested by these simulations are a pentagon with three protons $[\text{Mo}_6\text{O}_{18}(\text{OH})_3]^{3-}$ and two kinds of dimers: $[\text{Mo}^{\text{V}}_2\text{O}_3(\text{OH})_4(\text{H}_2\text{O})(\text{CH}_3\text{COO})]^-$ and $[\text{Mo}^{\text{V}}_2\text{O}_3(\text{OH})_2(\text{H}_2\text{O})_2(\text{CH}_3\text{COO})]^-$.

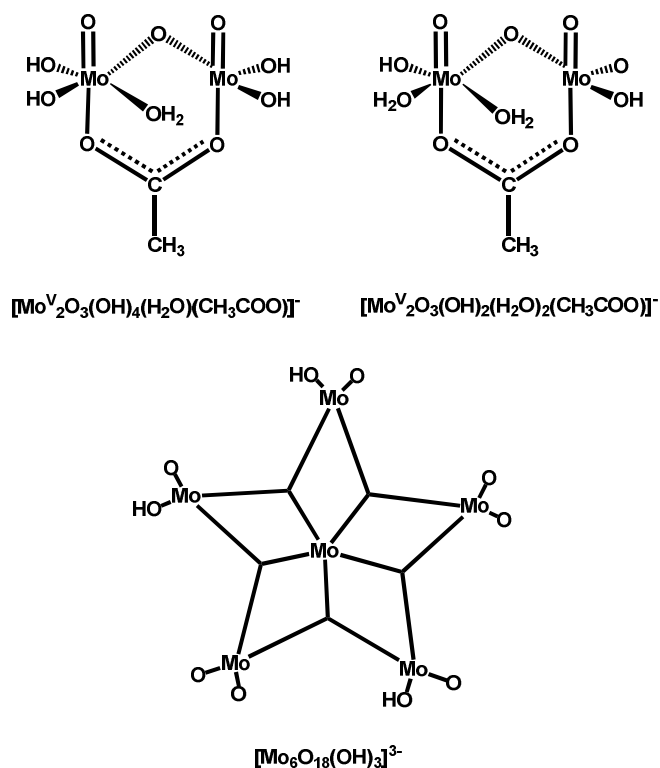


Figure S9. Scheme of the dimers and pentagonal unit obtained with Carl-Parrinello MD simulations and used to study the condensation process in Table S3.

We computed the different condensation possibilities leaded by those structures. We considered the four possibilities leaded by the two types of linkers. In the case of the pentagon, we have two possibilities for the binding site: the linker can be bonded to the pentagon through two oxygen sites or one oxygen and one hydroxyl group. Following the previous table trend, we considered also the possibility of having two consecutives hydroxyl groups, changing the order of the terminal groups one of the Mo atoms. We optimized this structured starting from the one obtained by Carl-Parrinello molecular dynamics simulations. The results show the structure with two consecutives hydroxyl groups is just 0.23 eV less stable than the proposed from molecular dynamics simulation. So we decided to include this structure in our studies.

These results are collected in Table S3 and reproduce the same trends that in the previous table. As the number of protons increases, the condensation energies become lower. The most favorable cases are the bottom-right ones, corresponding to condensations having four protons in all, giving water as product. These results are in perfect agreement with the previous ones. The different energy ranges presented on both tables can be explained in terms of the differences in the studied structures. Even if in both cases condensation takes place between a pentagon and a dimer, the structures used in the simulations present different geometries and charge.

We conclude that the protonation degree of the dimer and the pentagon are critical to the condensation occurs. Therefore, this condensation is very pH dependent and it seems more favorable at high pH.

Modelling the Mo₁₃₂ Raman Spectrum Evolution

Vibrational harmonic frequencies and Raman intensities were computed numerically from two-point single point calculations. For the reduced species [Mo₇O₂₄]⁷⁻, since Raman intensities are not available in ADF for unrestricted determinants, Gaussian09¹⁵ at an equivalent DFT level (BPV86) basis sets (6-311G* for O, LANL2TZ for Mo), and PCM solvent model were considered. At that level, G09 and ADF gave fully equivalent results for [Mo₇O₂₄]⁶⁻.

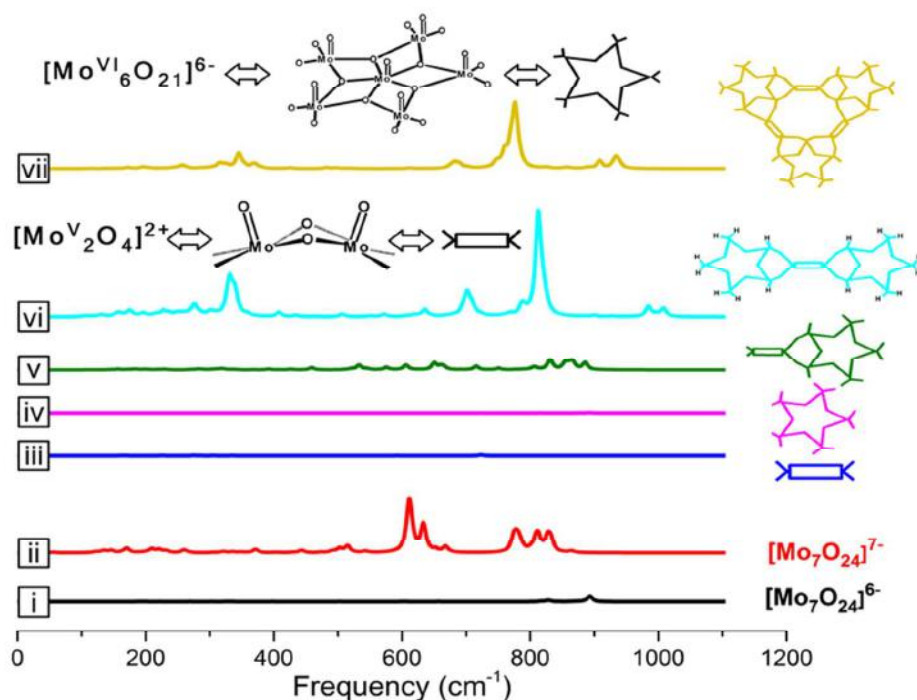


Figure S10. Computed Raman spectra for several Mo_nO_m species. Intensities in Ang^4/amu units. Note that since the intensity scale covers 5 orders of magnitude, some spectra look flat (see text).

Figure S10 collects the computed Raman spectra for several systems, all represented at the same intensity scale. Full details of each spectrum, numerical values and assignment of all the most intense normal modes is provided in the Supporting Information.

For $[\text{Mo}_7\text{O}_{24}]^{6-}$, a, the most intense main peaks lie between 800 and 900 cm^{-1} , and those arise from the Mo–O stretching vibrations of the terminal oxygen atoms. Both signals present relatively low intensities. The anti-symmetric one at 830 cm^{-1} is less intense ($547 \text{ Ang}^4/\text{amu}$) than the signal at 893 cm^{-1} (intensity $3300 \text{ Ang}^4/\text{amu}$), which correspond to the symmetric combination. At lower frequencies, very low peaks not distinguishable in Figure S10 at around 300 cm^{-1} , we found the terminal oxygen vibrational modes. These results, although not distinguishable in Figure S10, are in full agreement with experimental findings.

After reduction, $[\text{Mo}_7\text{O}_{24}]^{7-}$ (ii), the computed Raman spectrum shows active signals in two main regions. In the first set, around 615 cm^{-1} ($35000\text{ Ang}^4/\text{amu}$), we found bending and stretching vibrations of the non terminal oxygen atoms. The second set comprises signals from 774 to 832 cm^{-1} ($15000\text{ Ang}^4/\text{amu}$) assigned to stretching of the terminal oxygens. Compared to the non-reduced species, the experimental spectrum shows the appearance of signals below 850 cm^{-1} that could be assigned to the computed down shift of terminal oxygens in ii.

Spectra of species iii and iv, as they are shown in Figure S10, are apparently Raman silent (see below). iii corresponds to a linker-like $\text{Mo}^{\text{V}}_2\text{O}_4$ species, with terminal oxygens. This spectrum has a main peak at 723 cm^{-1} ($500\text{ Ang}^4/\text{amu}$) corresponding to the terminal oxygens symmetric stretching. The presence of bridging ligands in the linker (HCOO^- , CH_3COO^- , HCO_3^- , CO_3^{2-} , SO_4^{2-}) does not affect the spectrum in significant manner. In some cases low intensity peaks appear around 300 cm^{-1} caused by bridging oxygens, and also due to the ligand atoms themselves.

iv is the pentagonal moiety building block $[\text{Mo}^{\text{VI}}_6\text{O}_{21}]^{6-}$, as shown in the inset in Figure S10, that shows a main peak at 892 cm^{-1} (intensity 300) that arise from terminal oxygen atoms symmetric stretching vibrational modes.

Spectra v, vi and vii correspond to different pentagon/linker assemblies built by binding pentagonal building blocks $[\text{Mo}^{\text{VI}}_6\text{O}_{21}]^{6-}$ and linkers $[\text{Mo}^{\text{V}}_2\text{O}_4]^{2+}$.

In v, there is a set of new peaks around 650 cm^{-1} . The peak with highest intensity ($5000\text{ Ang}^4/\text{amu}$) corresponds with the bridging oxygen scissoring and the pentagon non terminal oxygens bending. Also, we found as well the band around 850 cm^{-1} ($6000\text{ Ang}^4/\text{amu}$) due to terminal oxygen stretching.

In vi, terminal oxygen atoms were capped with hydrogens. First, we have two peaks due to bridging oxygen wagging modes at 275 cm^{-1} ($8000\text{ Ang}^4/\text{amu}$) and 330 ($25000\text{ Ang}^4/\text{amu}$). At 700 cm^{-1} we found a peak due to bridging oxygen symmetric stretching ($15000\text{ Ang}^4/\text{amu}$). The main peak ($60000\text{ Ang}^4/\text{amu}$) is at 813 cm^{-1} and corresponds to the pentagon/linker bridging oxygens symmetric stretching. Finally, around 1000 cm^{-1} , we found a set of peaks due to the terminal oxygens stretching ($6000\text{ Ang}^4/\text{amu}$).

Lastly, system vii is a model of a Mo_{132} pore framework. It is formed by three pentagons joined by three linkers. In this case, we found a peak at 345 cm^{-1} ($1000\text{ Ang}^4/\text{amu}$) caused by the pentagon non terminal oxygens bending. Around 690 cm^{-1} , we have several pentagon non terminal oxygens bending vibrations, which, together, have an intensity of $10000\text{ Ang}^4/\text{amu}$. The main peak ($33400\text{ Ang}^4/\text{amu}$) is at 777 cm^{-1} and is due to the pore-linker bridging oxygens. Finally, around 920 cm^{-1} there are two peaks due to the terminal oxygens stretching (2000 and $5000\text{ Ang}^4/\text{amu}$).

Additional experiments

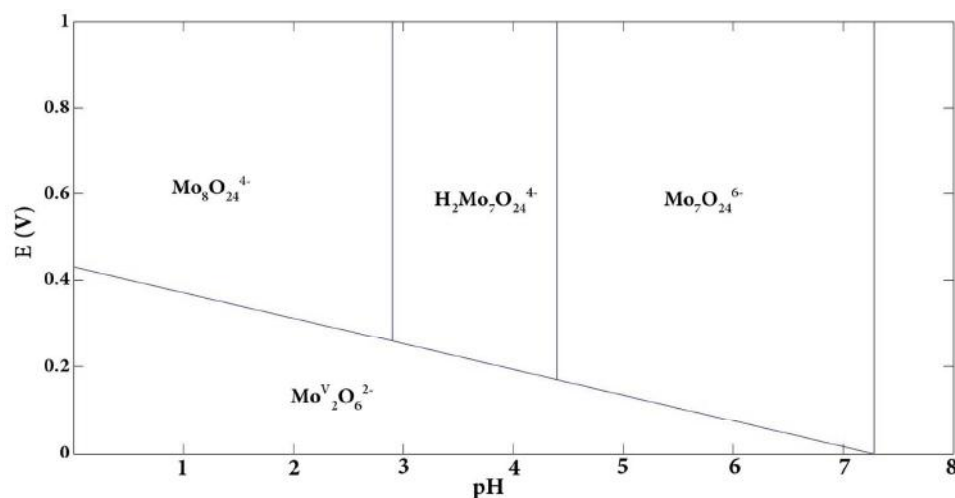


Figure S11. Simplified potential-pH diagram of formation of Mo_{132} from heptamolybdate. Standard thermodynamic values for all species have been taken from reference ¹⁶.

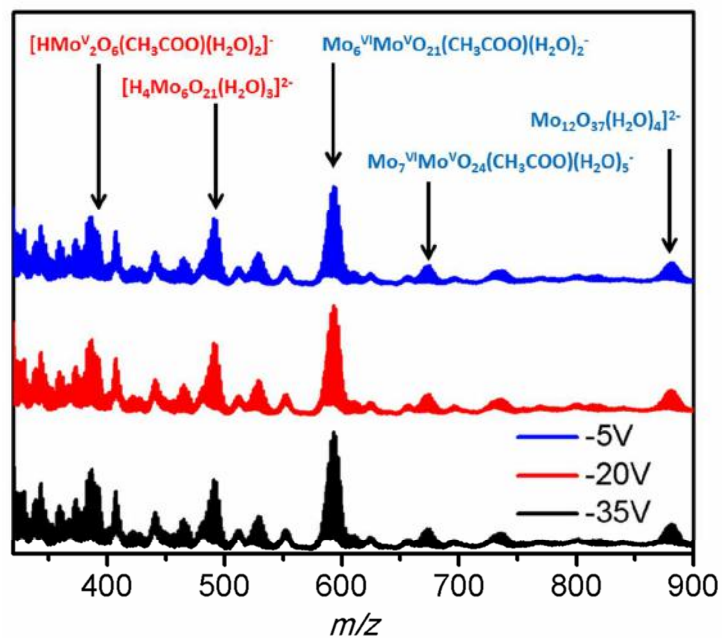


Figure S12. ESI-MS spectra of the solution after complete reduction at three different voltages viz., -5V, -20V and -35V show similar kind of spectrum at each voltages eliminating the presence of any voltage induced artifact¹⁷

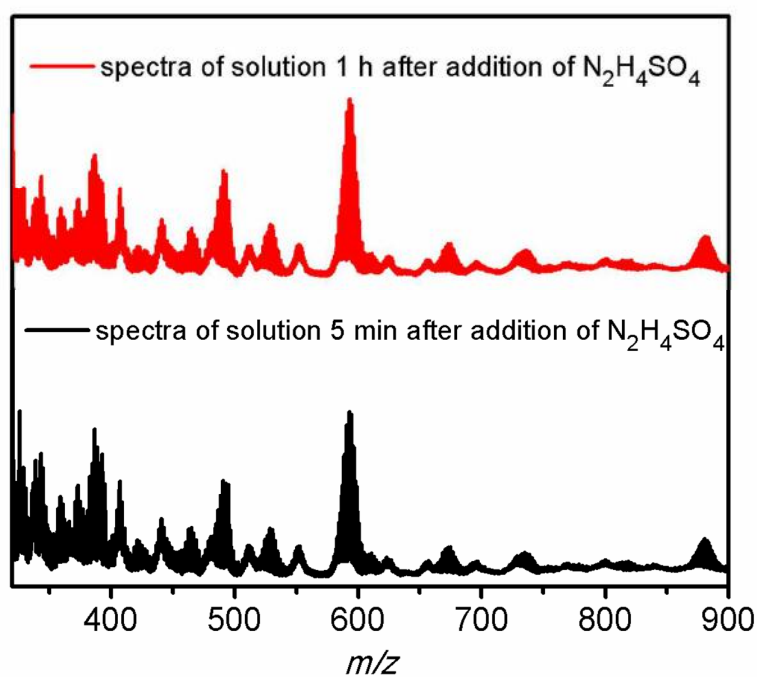


Figure S13. ESI-MS spectra of the reduced solution at two different time interval, after 5 min and after 1h of addition of hydrazine sulphate showing similar kind of spectra in both cases

Before acquiring the individual ESI-MS of each of the steps, we have provided sufficient time after addition of reagents to make sure that equilibrium has been established in solution. While acquiring the spectra, we have seen that within a few minutes equilibrium is established and no new peak appears after that. This is shown in Figure S13 considering the reduction step of the molybdate where spectrum of solution is taken five minutes after the addition of reducing agent and compared with spectrum acquired one hour after addition. No new peak has been noticed to appear even after keeping the solution for hours and the intensities of the peaks are also almost identical.

References

1. CPMD, IBM Corp.: Armonk, NY, 1990-2006; MPI für Festkörperforschung: Stuttgart 1997–2001.
2. Troullier, N.; Martins, J. L., *Phys. Rev. B* **1991**, *43*, 1993–2006.
3. Kachmar, A.; Bénard, M.; Rohmer, M. M.; Boero, M.; Massobrio, C., *J. Phys. Chem. A* **2009**, *113*, 9075–9079.
4. Becke, A. D., *Phys. Rev. A* **1988**, *38*, 3098-3100.
5. Perdew, J. P., *Phys. Rev. B* **1986**, *33*, 8822-8824.
6. Perdew, J. P., *Phys. Rev. B* **1986**, *34*, 7406-7406.
7. Car, R.; Parrinello, M., *Phys. Rev. Lett.* **1985**, *55*, 2471–2474.
8. Nosé, S., *J. Chem. Phys.* **1984**, *81*, 511–519.
9. Nosé, S., *Mol. Phys.* **1984**, *52*, 255–268.
10. Hoover, W. G., *Phys. Rev. A* **1985**, *31*, 1695–1697.
11. Baerends, E. J. A., J.; Bérces, A.; Bo, C.; Boerrigter, P. M.; Cavallo, L.; Chong, D. P.; Deng, L.; Dickson, R. M.; Ellis, D. E.; Faassen, M. v.; Fan, L.; Fischer, T. H.; Guerra, C. F.; Gisbergen, S. J. A. v.; Groeneveld, J. A.; Gritsenko, O. V.; Grüning, M.; Harris, F. E.; Hoek, P. v. d.; Jacobsen, H.; Jensen, L.; Kessel, G. v.; Kootstra, F.; Lenthe, E. v.; McCormack, D. A.; Michalak, A.; Osinga, V. P.; Patchkovskii, S.; Philipsen, P. H. T.; Post, D.; Pye, C. C.; Ravenek, W.; Ros, P.; Schipper, P. R. T.; Schreckenbach, G.; Snijders, J. G.; Sola, M.; Swart, M.; Swerhone, D.; Velde, G. t.; Vernooijs, P.; Versluis, L.; Visser, O.; Wang, F.; Wezenbeek, E. v.; Wiesenecker, G.; Wolff, S. K.; Woo, T. K.; Yakovlev, A. L.; Ziegler, T., Amsterdam Density Functional Program; <http://www.scm.com>.

12. Vanlenthe, E.; Baerends, E. J.; Snijders, J. G., *J. Chem. Phys.* **1993**, *99*, 4597-4610.
13. Vanlenthe, E.; Baerends, E. J.; Snijders, J. G., *J. Chem. Phys.* **1994**, *101*, 9783-9792.
14. Klamt, A., *J. Phys. Chem.* **1995**, *99*, 2224-2235.
15. Frisch, M. J.; Trucks, G. W.; Schlegel, H. B.; Scuseria, G. E.; Robb, M. A.; Cheeseman, J. R.; Scalmani, G.; Barone, V.; Mennucci, B.; Petersson, G. A.; Nakatsuji, H.; Caricato, M.; Li, X.; Hratchian, H. P.; Izmaylov, A. F.; Bloino, J.; Zheng, G.; Sonnenberg, J. L.; Hada, M.; Ehara, M.; Toyota, K.; Fukuda, R.; Hasegawa, J.; Ishida, M.; Nakajima, T.; Honda, Y.; Kitao, O.; Nakai, H.; Vreven, T.; Montgomery Jr., J. A.; Peralta, J. E.; Ogliaro, F. o.; Bearpark, M. J.; Heyd, J.; Brothers, E. N.; Kudin, K. N.; Staroverov, V. N.; Kobayashi, R.; Normand, J.; Raghavachari, K.; Rendell, A. P.; Burant, J. C.; Iyengar, S. S.; Tomasi, J.; Cossi, M.; Rega, N.; Millam, N. J.; Klene, M.; Knox, J. E.; Cross, J. B.; Bakken, V.; Adamo, C.; Jaramillo, J.; Gomperts, R.; Stratmann, R. E.; Yazyev, O.; Austin, A. J.; Cammi, R.; Pomelli, C.; Ochterski, J. W.; Martin, R. L.; Morokuma, K.; Zakrzewski, V. G.; Voth, G. A.; Salvador, P.; Dannenberg, J. J.; Dapprich, S.; Daniels, A. D.; Farkas, Å. d. n.; Foresman, J. B.; Ortiz, J. V.; Cioslowski, J.; Fox, D. J., *Gaussian 09*, Gaussian, Inc.: Wallingford, CT, USA, **2009**.
16. Czack, G.; Kirschstein, G.; Haase, V.; Fleischmann, W. D.; Gras, D., *Mo Molybdenum: Physical Properties, Part 2. Electrochemistry*, Springer Berlin Heidelberg, **2013**.
17. Ma, M. T.; Waters, T.; Beyer, K.; Palamarczuk, R.; Richardt, P. J. S.; O'Hair, R. A. J.; Wedd, A. G., *Inorg. Chem.* **2009**, *48*, 598-606.

Bridging innovations in academic institutions to society*

India is in great need of advanced and affordable solutions in a number of areas. The list is endless, ranging from primary necessities such as water, food, energy and health to environmental monitoring and national security. In many of them, there are intense efforts across the country. While unified efforts across institutions are limited, there are several well-thought-out programmes in several areas and there have been important outcomes. These research results and technological outcomes in some cases have not been translated to products that would have benefited the needy. As a consequence, these outcomes have not yielded economic returns and contributed to social development, although investments have been reasonable. A case study in this context is that of water, where we have made sizable contributions in research and technology development. Yet, problems related to arsenic, fluoride, pesticide, etc. continue to persist and our people are left to face the consequences.

Obviously, there is an urgent need to devise mechanisms by which technological outcomes are translated to products in large numbers. New ways of promoting participation of academic institutions in manufacturing processes have to be thought about. Institutions at the grass-roots, which ultimately implement solutions and understand end-user requirements, have to be made aware of the technological developments happening in the universities and new bridges have to be built between the two. There is a need to frame policies to enable this handshaking. In this context a discussion meeting was held on the theme 'Bridging innovations in academic institutions to society'. The plan was to invite innovators, scientists and technologists from academic institutions, businessmen from incubated companies housed in these institutions, administrators of various

governmental bodies as well as management and policy experts (see Box 1) to share their experiences so as to arrive at definite recommendations to bring research results closer to societal benefits. The recommendations arising from the meeting are highlighted in the following.

The participants debated on these issues in three separate sessions on the first day. The first session was by academicians who have incubated companies and translated technologies from laboratories to industrial setting. These technologies range from national security, biochemical monitoring, advanced medical diagnostics, automotive parts, drinking water purification and such other areas. National laboratories, research establishments, IISc, IITs, JNCASR as well as autonomous centres were represented. Innovation ecosystems in these institutions and structures which facilitate such technology transfer and mechanisms to enhance the capabilities of these institutions were the points of discussion.

The second group of individuals involved in the discussion meeting were from the incubated companies, beneficiaries of technologies derived from academic institutions. Their struggle in transitioning technologies to the market,

liaising with government agencies, hurdles in developing a marketable product, acquiring the initial purchase order, manufacturing difficulties in research establishments, obtaining funding into pre-revenue companies, etc. were discussed.

The third group comprised of administrators, non-governmental organizations, individual experts and health professionals. Participants in this group debated on the need to create administrative mechanisms to facilitate technology transfer. For health professionals, the complete lack of link between academic research and medical science being practised in India was a point of concern. For administrators, constraints of rules and regulations in nurturing research and development (R&D) results in sectors of socio-economic benefits, especially in the rural sector, were important points for discussion. Independent experts dealt with a number of limitations of our administrative machinery, which prevented translation of technologies to innovation.

On the second day, individual sub-groups discussed specific recommendations for the expected objectives. These discussions were presented to the whole group and consolidated recommendations

Box 1.

T. Pradeep, Soujit Sen Gupta, D. R. Prasada Raju, Indian Institute of Technology Madras, Chennai; Baldev Raj, Devaraju, National Institute of Advanced Studies, Bengaluru; V. Ramgopal Rao, Anil Kumar, Indian Institute of Technology Bombay, Mumbai; Bodh Raj Mehta, Indian Institute of Technology Delhi, New Delhi; G. U. Kulkarni, Jawaharlal Nehru Centre for Advanced Scientific Research, Bengaluru; Tata Narasinga Rao, International Advanced Research Centre for Powder Metallurgy and New Materials, Hyderabad; A. K. Ghosh, Bhabha Atomic Research Centre, Mumbai; Satish Vasu Kailas, Mohan Kumar and S. G. Sreekanteswara Swamy, Indian Institute of Science, Bengaluru; Kishore M. Paknikar, Agharkar Research Institute, Pune; S. G. Sreekanteswara Swamy, Karnataka State Council for Science and Technology, IISc Campus, Bengaluru; Anshup, Inno Nano Research Pvt. Ltd., Chennai; Nitin Kale, NanoSniff Technologies Pvt Ltd, Mumbai; Praveen Poddar, Mahavir Pumps, Kolkata; Radhica Sastry, InnoKriti Pvt Ltd, Bengaluru; Saket Kumar, VAS Bros. Pvt Ltd, Ranchi; Abhijeet Gaan, Rite Water Solutions (I) Pvt Ltd, Nagpur; Krishnan Swaminathan, Prashanth Vijayanth, Kovai Medical Center and Hospital, Coimbatore; Vijaya Lakshmi, Development Alternatives, New Delhi; Rajeev Kumar, Secretary to the Government of West Bengal, Kolkata; Debapriya Dutta, Indo-French Centre for the Promotion of Advanced Research, New Delhi; Sanjay Bajpai, Department of Science and Technology, New Delhi.

*A report on the two-day discussion meeting, 'Bridging innovations in academic institutions to society' organized by the Thematic Unit of Excellence in Nanotechnology for Clean Water at the Indian Institute of Technology, Madras, Chennai and National Institute of Advanced Studies (NIAS), Bengaluru and held at NIAS on 28 and 29 April 2015.

were drawn. Exchanges through electronic media were used to finalize these recommendations.

The recommendations are grouped together under the broad headings – sharing, caring and direction. Specific actionable points are suggested under each category. Each of the recommendations is elaborated in a few sentences.

Sharing

This captures inter-institutional/inter-disciplinary links to nurture innovation.

- Interactive website – A window for problems and solutions

An interactive website has to be created where available technologies, patents, affordable solutions in various sectors, appropriate contacts where technologies are available, mechanisms of technology developments, possible funding, etc. are showcased. This website has to be periodically updated and constantly interfaced with institutions – academic or otherwise. This must be a storehouse of information for academicians and general public alike. For the former, it provides links as to where one can approach to get quick responses on each of the problems mentioned. For the latter, the information must be on specific solutions for the problems faced by the citizen.

Action: Create an interactive website, housed as part of DST's efforts to promoting innovation.

- Innovation in entrepreneur education

Short-term courses, continuing education-based programmes, local workshops, etc. targeted at nurturing innovation ecosystem must be conducted in R&D institutions. Compulsory training programmes of this kind must be done each year in institutions of higher education and research, especially for new recruits (faculty and research students). An online modular course accessible across the country may be considered.

Action: Continuing education for nurturing innovation to be initiated in all institutions of higher learning; DST may take the lead.

- Common centres for prototyping

Creation of set-ups like Industrial Technology Research Institute (ITRI), Taiwan (<https://www.itri.org.tw/eng/>) across the country is a necessity. These centres are to be operated and maintained such that they have a mandate to trans-

late technologies to market, if an innovator or interested party approaches them. One model to consider is 'government-owned and contractor-operated' style. The facilities must be available round the clock, throughout the year and can be e-booked by an interested user. Barriers for designing and prototyping in any sector must disappear.

Action: Create ITRI-like institutions; DST to consider the plan.

- National nanofabrication facility for small-scale manufacture

Our engineers and technologists have made their mark in the world working in companies like Intel, IBM and TSMC. IITs and other research institutes are at the forefront in developing novel nano-devices. Several start-ups have been incubated in the country which have either developed prototypes of nanosensors or have at least established a laboratory proof-of-concept. Two such examples are shown in Figures 1 and 2. Figure 1 shows a prototype of arsenic purifier developed by an IIT Madras incubated company and Figure 2 represents a sensor which can detect explosive, developed at IIT Bombay. However, when it comes to manufacturing these devices, not even a single nanofabrication facility that makes them exists. While there are a few at places like Semi-Conductor Laboratory (SCL), Chandigarh, they are not open to private sector and start-up companies. So although a device may have

been designed and developed in India, it will be manufactured abroad.

Another aspect lacking clarity in India is the understanding of what happens to the intellectual property (IP) when a start-up company develops a novel device and gets it manufactured at a contract nano-fabricator. It should be noted that such rules are well-established abroad in the semiconductor nanofabrication contract manufacturing industry.

Action: (a) Existing nanofabrication facilities to be offered to the private/start-up sector for contract-manufacturing of their nanodevices while creating such centres exclusively for contract manufacturing. (b) Rules according to international practices be established and adopted regarding ownership of IP in such situations.

- Technology–social science interface

Currently, technologists and scientists do not interact with social scientists. These barriers have to disappear for innovations to take root in institutions. Science–social science network and interactions have to take place in all institutions of higher learning. Specific funds have to be allocated to enable such interactions.

Action: Introduce joint Master's and Ph D level programmes between these departments in reputed institutions; Ministry of Human Resource Development (MHRD), Government of India (GoI) to initiate a discussion.



Figure 1. Scene from a school in Nadia district, West Bengal. Children are drinking water from a filter which removes iron and arsenic selectively, attached to a hand pump. The technology was developed by IIT Madras and was commercialized by an IIT Madras incubated company with the support of the district administration and the Government of West Bengal.

Caring

- Technical commercialization funds for social innovation

Government mechanisms for supporting new technology commercialization, especially for rural India, are critical. Government has permitted the use of corporate social responsibility (CSR) funds for investment in approved technology incubators. Technology incubators are now present in almost all the major cities in India. Entrepreneurs aiming to take technologies from laboratory to rural India can be located at these incubators while being close to their application market. 'Centres of Social Innovation' may be set-up in select incubators.

Action: The Ministry of Corporate Affairs, GoI can generate policy guidelines on the use of CSR funds for technology commercialization in rural India. A list of approved incubators may be added to the guidelines. The Ministry can also organize an annual rural technology mela (demonstration platform for entrepreneurs), to show how CSR funds given to incubators is helping to improve rural India.

- Incorporation of sustainability principles in products and practices

National curriculum at the school must include principles of sustainability. New products that are being developed in Indian laboratories must consider these principles and for that the current school-going generation has to be sensitized. Sustainable growth realizes that resources are basically of two kinds: (1) those which can be replenished and (2) those which cannot be replenished. If resources used in making products can be replen-

ished, the following are to be strictly followed: (1) the rate of consumption is not greater than the rate of replenishment; (2) the end-product is non-toxic, and (3) it is bio-degradable. If the resources used cannot be replenished, it is essential that all of the material used is recycled. However, it is not easy to make this change and in the present scenario, it may be impossible in several products. However, a beginning can be made by training students in the fundamental aspects of sustainability.

Action: MHRD to take note of the principles and recommend their incorporation in NCERT textbooks and national curriculum.

- Biotechnology Industry Research Assistance Council (BIRAC) – type models in all sectors of innovation

The BIRAC model of funding has helped in the emergence of several technologies. This has been limited to biotechnology companies over the years. However, it has to happen in every sector of research. Specific mandate has to be given to central and state government ministries to set-up funding mechanisms to pre-revenue companies. The magnitude of funding and restrictions on funding such as 70 : 30 ratio for consumables and manpower need a relook. In areas of high technology, individuals are the greatest assets. Funding limits have to be reassessed, especially for companies which are manufacturing-based.

Action: Cabinet direction to all ministries and state governments.

- Enabling ESCROW accounts in all social sectors

Technological solutions in the social sector have to be maintained for longer periods for public acceptability. This is

possible only if the solutions provided are maintained over longer periods. This becomes impossible for many implementations as maintenance costs are not included usually. ESCROW accounts are expected to eliminate this problem.

Action: Finance Ministry to recommend the same.

- Showcasing products and entrepreneurs in national and international forums

There are no specific technological forums available to showcase Indian products, born out from Indian research. Such individuals and institutions have to be recognized through various mechanisms.

Action: DST may plan a showcasing activity and create mechanisms to promote individuals and institutions.

- Academic rewards for entrepreneurs

Entrepreneurs venture into unknown territory, taking up challenges and translating technologies to products. In many cases they fail, although they develop new understanding during the process. This could be used for academic rewards such as Ph D, M Phil, etc. and such mechanisms have to be entertained in institutions. Research degrees through entrepreneurship are possible in several institutions and this has to be nurtured nationally.

Action: MHRD directive to institution of higher education.

Direction

Direction may be short term or long term. We look into mechanisms that could help innovation today and tomorrow.

- Grand challenge initiative – SHAPE

SHAPE refers to Security, Healthcare, Agriculture, Pedagogy and Environment; these are the areas wherein an Indian Grand Challenges can shape the country's future and make a lasting impact through clearly defined goals and objectives. The nation must work on challenges for the future. Open innovation has scope, although certain direction is needed. Future innovations, interlinking institutions can happen with this direction.

Action: To be driven by the cabinet.

- National mission on scientific instrumentation

It is through indigenous instrumentation that the nation can progress. This has happened in specific sectors, but



Figure 2. A low-cost hand-held device for the identification of explosives at airports, developed at IIT Mumbai.

science instrumentation has kept itself away from taking roots in the country, despite initiatives. This mission should carefully nurture instrumental initiatives so that entrepreneurs emerge. About 80% of the project funds for research goes for equipment and most of it is imported. In equipment-building projects, at least five prototypes are to be built before the equipment reaches a state of high reliability. The primary goal of any academic/educational institution is manpower development and equipment creation will in fact develop more competent manpower and also help start-up companies.

Action: To be driven by the cabinet.

- National mission on medical instrumentation

Medical instruments reach the entire population. Medical science and research are two separate entities in the country. Almost no physician undertakes research. The interface between science/engineering and medicine has to be strengthened with active collaborations. As this is absent, many of those who need medical remedies are not in a position to access them, as instrumentation is developed without local inputs/components. One point can highlight the need of instrumentation in the area. While 1.5 lakh people require heart valve replacement each year, we are able to service only 45,000, due to the unaffordable price of this component. It is imperative to MAKE IN INDIA a high-quality heart valve and not be dependent on the only indigenous valve (Chitra valve), the technology of which is quarter of a century old. This is an extremely urgent and desperate situation and needs to be addressed with top priority.

Action: Initiate medical research in IITs, initially offering MD by research.

- Technology business incubators (TBIs) in all institutions

Business incubation has to become as important as technology development in all institutions where technology is being born. New mechanisms to fund these initiatives have to be established in all institutions. Institution-specific innovation forecasting must be a part of the activity of these centres. Innovation experts have to be employed to nurture budding ideas. Technology facilitation cells must be an integral part of these units.

Several of our technologies die in the laboratory as there are no institutional prototyping facilities at the right time, when the student or discoverer is avail-

able. This is critical in several cases, as the time of an individual to pursue a technology/product is limited during the course period.

Action: The Ministry of Commerce and Industry may partner with select institutions to set up TBIs. They have to develop as business units surviving on the revenue generated. TBIs to be established in all the institutions of higher learning in 5 years.

- Legal system

A major issue retarding entrepreneurship in academic institutions is conflict of interest. This needs to be resolved through legal assistance. Such support is often inaccessible or unavailable at reasonable cost and when needed. Legal mechanisms for individual support must be available in all institutions. This assistance goes far beyond company formation. It concerns with all aspects of legal support during the course of evolution of the company, interaction with businesses, protecting individual and institutional interests, venture funding, technology transfer, etc. in a business-friendly fashion.

Action: MHRD may come up with a well-framed conflict of interest policy on business incubation in academic institutions, and each institution may implement such a policy with institution-specific adjustments.

- Valuation of pre-revenue companies

Currently, when a financing institution evaluates a company for investment, it looks at profits, sales, fixed assets, balance sheets, etc. of the company. This would be a good model to assess revenue-making companies. However, for a start-up, the revenues are either zero or miniscule, as most of the funds are spent on technology/product development. Hence the doors of funding agencies such as Small Industries Development Bank of India (SIDBI) Venture Capital fund are closed, at least partially. Even if such a funding is available, the valuations are based on fixed assets and are outrageously low. It is clear that start-ups need risk-capital funding at a pre-revenue stage, particularly when they have developed a technology and are ready to expand.

Action: (a) Guidelines to be developed to assess the financial valuation of pre-revenue technology start-ups on the basis of IP & know-how developed, product/technology, strength of the team, future projections, etc. (b) These guidelines to

be adopted by public/private risk-capital funding agencies, who have the mandate to invest in technology start-ups. Cabinet to act on the suggestions.

- Technology appreciation

The administration has to be aware of advanced technology available in various sectors. This is necessary to ensure that new research results reach the society. This appreciation must be done at the secretarial level. Formal platforms at this level have to be developed.

Action: Periodic technology appreciation meetings at various levels, in specific areas run by IITs.

- Statutory framework for sharing of ownership, technology, royalties

There has to be a uniform policy for government-owned or government-funded patents. Another approach may be used for collaborative R&D between laboratories, institutions and universities on the one hand and private companies on the other. Exclusive patents for commercial usage for limited period and non-exclusive patents for public purpose may be considered. Exceptional clause for intervention as a last resort could be introduced.

Action: MHRD to come up with an IP policy valid across institutions.

- Procurement/tender policy to accommodate incubated companies just as cooperatives

In sectors of social good such as clean water, health, environment, etc., implementation of technologies from academic institutions can happen only with government support. While there is a need to implement such technologies through government schemes, these technologies rarely get implemented at the grassroots level in the beginning, as the implementation process goes through the tender route. Incubated companies from academic institutions may be considered as cooperatives, as they are indeed partners for societal welfare. This may enable them to implement developing technologies without hard competition.

Action: Cabinet to approve new tendering policies.

Ministry-wise listing of recommendations

Central Government

1. National nanofabrication facility for small-scale manufacture.

2. BIRAC-type models in all sectors of innovation.
3. Grand challenge initiative for the nation.
4. National mission on scientific instrumentation, including medical instrumentation.
5. Guidelines for valuation of pre-revenue companies.
6. Procurement/tender policy modifications to accommodate incubated companies just as cooperatives.

Ministry of Human Resource Development

1. Creation of technology – social science interface.
2. Commercialization funds for social innovation.
3. Incorporation principles of sustainability in products and practices.
4. Enabling ESCROW accounts in all social sectors.
5. Academic rewards for entrepreneurs.

6. Technology business incubators in all institutions.
7. Legal system to nurture innovation.
8. Statutory framework for sharing of ownership, technology, royalties.

Ministry of Science and Technology

1. Interactive website – a window for problems and solutions.
2. Innovation in entrepreneur education.
3. Showcasing products and entrepreneurs in national and international forums.
4. Common centres for prototyping.

Ministry of Corporate Affairs

1. Corporate Social Responsibility funds for technology commercialization in rural India

Epilogue

India is at the threshold of translating socially relevant research to engines of

social transformation. Many of these innovations may be frugal, but they have a huge scope, as our requirements are varied. Our institutions and human resource have to be prepared to absorb the scattered research results available across the country to tackle these varied necessities, and systems have been created to channelize the laboratory findings to economically viable and socially relevant innovations. The recommendations captured here as a result of a discussion meeting among technologists, academic-turned entrepreneurs, incubatees, administrators and like-minded individuals based on their experience in seeding and nurturing incubation culture, if implemented consciously, have the potential to transform the entrepreneurial landscape of our country.

T. Pradeep, Indian Institute of Technology Madras, Chennai 600 036, India.
e-mail: pradeep@iitm.ac.in

MEETING REPORT

Traditional ethnomedicinal knowledge of Indian tribes*

According to the Government of India 2011 census data, schedule tribe population in India is about 8.6% of the total population. This population is subjected to abject poverty and economic backwardness, often lacking in proper education and healthcare facilities. For healthcare, they mainly rely on traditional medicines that solely depend upon the supply of native medicinal plants. Their knowledge of tribal medicine (also known as 'folk' or 'indigenous' medicine) is mainly verbal, usually passed on from one generation to another without any written script, making documenta-

tion and record-keeping almost impossible. Studies suggest that the tribal and ethnic communities in India as part of their healthcare systems use more than 8000 species of plants and approximately 25,000 folk medicine-based formulations.

India harbours a rich repository of untapped medicinal plants, with plenty of associated knowledge that needs to be appropriately utilized. A conference on traditional medicinal knowledge was organized recently, which was attended by 80 participants, representing 12 states of the country. During three technical sessions, the following issues were discussed – the rising need to preserve the traditional medicinal knowledge of the country, legal protections (i.e. IRP-related issues) available to traditional healers, conservation of medicinal resources, cultivation of medicinally important plants, and translation of the traditional knowledge into drug development programme.

More than 1.5 million traditional medicinal practitioners in India use medicinal plants for preventive, promotional and curative purposes. About 65% of the Indian population relies upon traditional medicine for its healthcare needs. In his inaugural address, Palpu Pushpangadan, (formerly at National Botanical Research Institute, Lucknow) presented an in-depth analysis of the ethnobiological knowledge of the Indian tribes and possibilities of translating this knowledge in marketable pharmaceutical drugs. He mentioned that scientific validation, subsequent commercialization through patenting and licensing, and sharing of the benefits with stakeholders are crucial to the popularization of traditional medicinal knowledge. JEEVANI, an anti-ageing and anti-depressive drug developed from the Arrogypacha (*Trichopus zeylanicus*) plant was an outcome of the traditional knowledge of the Kani tribes of Kerala. Therefore, the earnings from the drug

*A report on the three-day National Workshop cum Seminar organized by the Faculty of Science, Indira Gandhi National Tribal University, Amarkantak during 9–11 March 2015 on 'Frontiers in Ethnomedicinal Research: Traditional to Translational (FER-15)'. The event was supported by DST, DBT, NMPB, ICMR and MPCST.

Evolution of atomically precise clusters through the eye of mass spectrometry

Shridevi Bhat, Indranath Chakraborty, Ananya Baksi,
Raghu Pradeep Narayanan and Thalappil Pradeep*

DOI: 10.1039/9781782623717-00343

Enormous developments in the area of soluble noble metal clusters protected with monolayers are discussed. Mass spectrometry has been the principal tool with which cluster growth has been examined. The composition and chemistry of clusters have been examined extensively by mass spectrometry. Besides gold, silver, platinum, copper and iron clusters have been examined. Clusters have also been examined by tandem mass spectrometry and the importance of ligands in understanding closed shell electronic structure is understood from such studies. Protein protected noble metal clusters belong to a new group in this family of materials. Naked metal clusters bearing the same core composition as that of monolayer protected clusters is another class in this area, which have been discovered by laser desorption ionization from protein templates.

1 Introduction

Mass spectrometry, just after a century of its existence continues to be one of the most important workhorses of chemistry.^{1,2} Over the years, it has become the single most important analytical tool in proteomics, metabolomics and several other disciplines.^{3,4} Traditional materials science has been away from the influence of mass spectrometry as tools of solid state materials science such as X-ray diffraction, electron microscopy, electron spectroscopy and several others continue to be the principal means of analysis of solids.¹⁻³⁹ However, when dimension of matter reduces to the ultra-small regime, of the order of a nanometer, materials science requires mass spectrometry for detailed characterisation. This chapter explores this emerging influence of mass spectrometry in materials science taking noble metal clusters (M_n) as examples.

There are two important aspects of mass spectrometry relevant in the context of M_n clusters. Mass analysis involves ionization which invariably imparts internal energy to the species. There is a need to reduce the energy input into the clusters as they are susceptible to rapid fragmentation as clusters in general are metastable, in comparison to the bulk. In a cluster system, there could be several closely lying minima and inter-conversion between them may become feasible due to the acquired internal energy. As a result, to study a cluster in its native form, it is required to minimize the internal energy input during ionization.

This requirement necessitates adaptation of soft ionization methods for ionizing clusters. The common methods of ionization are

*DST Unit of Nanoscience (DST UNS) and Thematic Unit of Excellence, Department of Chemistry, Indian Institute of Technology Madras, Chennai 600 036, India.
E-mail: pradeep@iitm.ac.in*

Electrospray Ionization (ESI) and Matrix Assisted laser Desorption Ionization (MALDI).^{8,9,22,28,40–47} Both have been employed successfully in a number of cases. However, as neither of them gives complete information, often a combination of the two is necessary for definite fingerprinting. Clusters are protected entities and charge incorporation into the system during ionization is often due to the ligand. In the case of functionalized ligands such as carboxyl (-COOH), amine (-NH₂), *etc.*, a loss or acquisition of proton is the principal means of ionization. Therefore, pH control of the solution becomes an easy method in ESI. In several others, charge is brought into the system through metal incorporation as in case of Cs⁺ adducts.³¹ Mechanism of ionization in MALDI is still unclear in this system. As a result, exploration of various matrices and ionization conditions becomes necessary to observe reliable ionization of the cluster systems.

Ionization does not always lead to accurate mass analysis. As the clusters are fragile, fast analysis is necessary to reduce metastable decay. Mass spectrometers with adequate mass range and improved stability in such mass ranges are required as analysis often involves long time acquisition of data. Understanding of isotope distribution as a whole is needed which requires improved mass resolution at this mass range.^{22,42} Therefore, the most successful analysis involves TOF or Q-TOF.

Identification of the parent ion is confirmed in a few cases by MS/MS analysis.¹⁵ In a cluster system, this requires increased ion intensity as well as improved mass range of analysis. As most instruments and most cluster systems do not simultaneously meet the requirements, such analyses are done only in few cases. Improved understanding of such clusters is feasible by the use of multiple methodologies.

As can be seen from the preceding paragraphs, mass spectrometry along with separation techniques have helped in the identification of new cluster systems.⁴⁸ In many cases, it has been mass spectrometry that has contributed to cluster science than crystallography. However, increasing capability, both in resolution and mass range as well as better ionization methods, would be necessary to grow the subject area further. While the current contribution of mass spectrometry is often limited to identification, more efforts are needed in exploring the properties of clusters by mass spectrometry, which requires better MS/MS capabilities. Clusters, because of their different conformations and due to the existence of isomers there is a need to undertake other analyses along with mass spectrometry. This is now possible with commercial instruments by Ion Mobility Mass Spectrometry (IMS). New efforts in this direction are happening in the past few years.

2 Clusters of the past

Cluster may be defined as a constitution of bound atoms or molecules which exhibit completely different properties than the corresponding bulk materials.^{49–51} Their properties vary drastically with size. There have been numerous developments in the area of clusters existing in gaseous and condensed phases.

2.1 Gas phase clusters

Gas phase clusters are extremely reactive and as a result they cannot be stored in ambient conditions.⁵² Always such clusters are made *in situ* where experimental properties are studied. Several techniques have been implemented to make such clusters in the gas phase; examples are the evaporation of metals by heating and ion/laser bombardment, *etc.* Laser vaporization techniques in conjunction with mass spectrometry have been used widely to investigate clusters precisely. Based on the constitution and properties, gas phase clusters have been classified as ionic, covalent, metal, semiconductor, molecular, *etc.* We will discuss a few of them.⁵²

2.1.1 Metal clusters. Metal clusters are made of different metals like alkali, alkaline earth and transition metals.⁵¹ Plenty of reports are there especially on sodium clusters.^{37,53,54} Such clusters are produced in a gas aggregation source where the metals (such as sodium) are heated at $\sim 400^\circ\text{C}$. The hot vapor is then passed through a low vacuum He-atmosphere ($T=77\text{ K}$) to produce clusters of different sizes. Quadrupole mass analysers (QMA) are used to identify the clusters. Clusters up to 150 atoms have been observed. Knight *et al.* have observed a discontinuous variation in intensity at $N=2, 8, 20, 40, 58,$ and 92 (magic numbers) in the mass spectra of Na clusters.⁵³ Explanation for this pattern of intensity has been made based on the one-electron shell model in which $3s$ valence electrons are bound in a spherically symmetric potential well. These correspond to closed electronic shells. Similarly Katakuse *et al.* have shown the different ion intensities in the mass spectra of silver clusters (Ag_x).²³ In this case, silver clusters with an odd number of atoms are more intense compared to those with an even number which again can be explained by simply counting the number of valence electrons. The clusters with odd number of atoms have even number of valence electrons which results in spin pairing and that enhances the stability compared to those with even number of atoms.³⁰ It is also noticeable that just after these peaks, there is a sharp decrease in the intensity of the next peak. Guo *et al.* have demonstrated the direct generation of large silver cluster ions through laser desorption ionization of silver-containing salts without the assistance of a molecular beam.⁵⁵ Both positively and negatively charged silver clusters up to $N=100$ have been produced using this method. The distributions are similar to those produced using the beam-based approaches. Here also two special features have been observed; first, the cluster intensity distribution displays an odd–even alternation pattern and the second, a steep decrease of ion intensities after some clusters called ‘magic numbers’. Au and Cu have also been studied extensively^{23,24} and lots of recent reports also exist to utilize them in cluster catalysis.⁷

2.1.2 Semiconductor clusters. Semiconductor clusters are mainly generated from the semiconducting elements such as silicon,^{57,59–62} carbon^{63,64} and germanium.⁶⁵ After the great discovery of the fullerene (mass spectrum of C_{60} is given in Fig. 1A),⁵⁶ researchers have shown

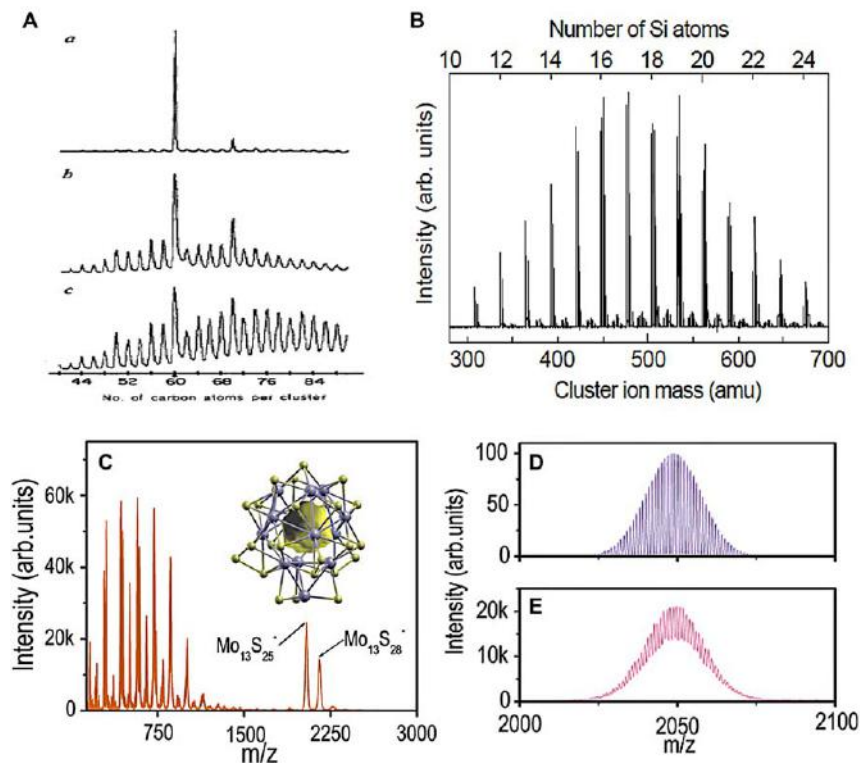


Fig. 1 (A) TOF mass spectra of carbon clusters prepared by laser vaporisation of graphite and cooled in a supersonic beam. The extent of He collision occurring in the supersonic nozzle (decreases from a to c). Reproduced with permission.⁵⁶ ©Nature publishing. (B) Mass spectrum of silicon clusters. Reproduced with permission.⁵⁷ © Heat Transfer Society of Japan. (C) Negative mode LDI mass spectrum of MoS₂ nanoflakes. Inset shows the structure of the Mo₁₃S₂₅ cluster. The expanded mass spectrum of Mo₁₃S₂₅ cluster (D) is plotted along with the calculated one (E), which shows an exact match. ©ACS publishing. Reproduced with permission.⁵⁸

enormous interest to explore the possibility of other semiconductor clusters. As the bonding between carbons is covalent in nature, they have the tendency to form a variety of clusters compared to other elements. Several series of carbon clusters including C₆₀, C₇₀, *etc.* are reported now.⁵⁶ Other than carbon, various kinds of gas phase Si clusters are known and Maruyama *et al.*⁵⁷ have shown a series of clusters starting from $N=8$ to 24 produced by pulsed laser-vaporization supersonic-expansion cluster beam source, directly connected to a FT-ICR spectrometer (Fig. 1B). Then the injected and size selected silicon clusters were cooled to room temperature by collision with argon.

2.1.3 Molecular clusters. Several kinds of gas phase molecular clusters exist in the literature.^{27,33,58,66–70} Inorganic molecular structures such as polyoxymolybdates are examples of such kind.⁷¹ Usually, they form cage like structures which are often called inorganic fullerenes (IFs).^{72–75} IFs were originally made from the layered structured chalcogenide MX₂ where M=Mo, W and X=S, Se.^{72,76–85} Different

methodologies have been applied to make IFs in the gas phase. To fold such layered structure to form cages or closed cylinders, high energy is needed which is supplied by arc discharge, laser vaporisation, ultrasonication or other sources.^{56,86,87} Singh *et al.* have synthesized such a novel cage cluster of MoS₂ in the gas phase by laser evaporation.⁵⁸ Bulk MoS₂ was ground well and dispersed in acetone which was spotted on a MALDI plate and a pulsed laser of 337 nm was applied to get the clusters. The mass spectrum has been collected in the negative mode. LDI MS data shows a series of clusters such as MoS₂⁻, MoS₃⁻, MoS₄⁻, Mo₂S₃⁻, Mo₂S₅⁻, Mo₂S₆⁻, Mo₂S₈⁻, and so on. The spectrum exhibits a trend of increase in intensity starting from MoS₂⁻ and it reaches a maximum around Mo₄S₇⁻, and decreases thereafter. After this region (Fig. 1C), the spectrum is completely featureless till *m/z* 2000, and suddenly, an intense peak appears at *m/z* 2049, which was followed by another peak at *m/z* 2144. An expanded view of the peak at *m/z* 2049 is shown in Fig. 1D which shows an exact match with the corresponding calculated spectrum of Mo₁₃S₂₅⁻ (Fig. 1E). Similarly the next peak was assigned as Mo₁₃S₂₈⁻. Along with this type of molybdenum sulfide cluster, several other clusters such as WS₂, layered metal halides such as NiCl₂, CdCl₂, and TlCl₃ and oxides such as TiO₂ and V₂O₅ also produced gas phase molecular clusters.⁸⁸ Gas phase clusters of noble metals have also been studied and clusters such as Au_{*n*},²³ Ag_{*n*},^{23,55} *etc.* have been detected.

2.2 Early stages of monolayer protected clusters

Along with gas phase transition metal clusters, mass spectrometry has given an useful method to analyze noble metal cluster systems.¹⁹ These clusters are monolayer protected by means of a ligand and as a result, they can be synthesized in solutions. Just after the Brust's new synthetic protocol,⁸⁹ scientists have started synthesizing highly monodisperse nanoparticles which show molecule – like optical features. Researchers from different groups have realised the importance of mass spectrometry in studying such clusters.^{9,10,12,22,25,26,40–42,44,90–97} Initially, LDI was used to identify the core mass.^{91,93} A variety of clusters having different core masses have been identified in those decades. In most of the cases, clusters are protected with alkane thiols.^{91,93} Whetten *et al.* have shown a series of clusters starting from 27 kDa to 93 kDa (Fig. 3A).⁹⁸ Based on the TEM analysis and mass spectral position, it has been suggested that the core contains 140 to 459 gold atoms. Reports of glutathione protected clusters are also there. Initially, the 5.6 kDa cluster (core mass) detected by LDI mass spectrometry was assigned as Au₂₈(SG)₁₈.⁹⁹ Then in 2005, Negishi *et al.* have reassigned the cluster as Au₂₅(SG)₁₈ based on high resolution electrospray analysis.⁴⁷ The clusters have been synthesized by reducing the Au(I)-SG polymer in ice cold condition which produces a mixture of clusters. In a later report, they have isolated nine clusters (1–9) through polyacrylamide gel electrophoresis (PAGE). These isolated cluster samples have been measured by their home – built ESI apparatus.⁴⁷ A schematic of the instrument is given in Fig. 2A which consists of five stages of differentially pumped vacuum chambers. The apparatus

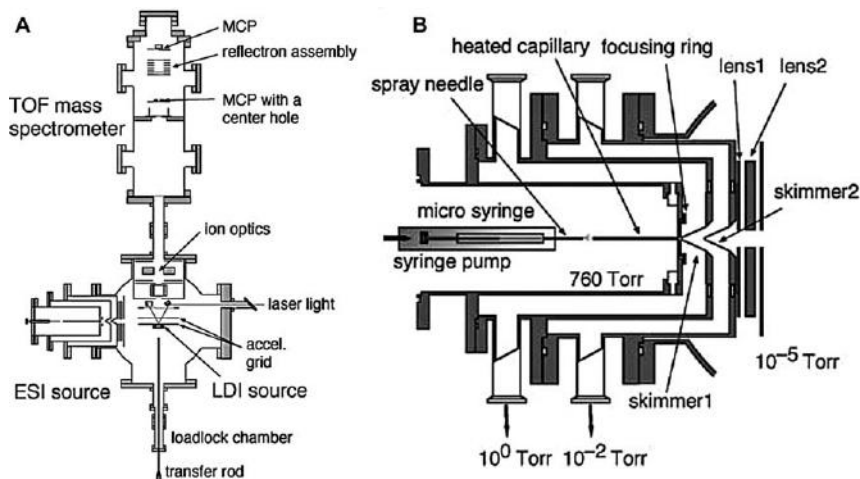


Fig. 2 (A) Schematic view of the TOF mass spectrometer equipped with electrospray ionization (ESI) and laser desorption ionization (LDI) sources. (B) The details of the ESI source. ©ACS Publishing. Reproduced with permission.⁴⁷

accommodates an ESI source for the production of gaseous ions of metal clusters dispersed in a solvent and a time-of-flight (TOF) mass spectrometer with a reflectron. Schematic of the ESI source is given in Fig. 2B, along with the typical pressures of the chambers under operation. For a typical measurement, 50% (v/v) water/methanol solutions of the Au:SG clusters with a concentration of 0.5 mg mL⁻¹ were electrosprayed into the ambient atmosphere through a syringe (flow rate of 2 μL min⁻¹) biased at *ca.* -3 kV. The central part of the sprayed cone containing large droplets was fed into a capillary heated resistively to promote desolvation. Capillary temperature was optimized so that evaporation of the solvents from the droplets proceeds efficiently which results in maximum intensity of the desolvated cluster ions in the intact form. At higher capillary temperature, small fragments such as [Au(SG)₂-H]⁻¹ and [Au₂(SG)₂-H]⁻¹ have been observed.⁴⁷ The cluster ions exiting the capillary were focused by a ring electrode, skimmed by two sets of skimmers, and guided by an einzel lens towards an acceleration region of the TOF mass spectrometer of a Wiley-McLaren-type configuration. The ions were extracted perpendicularly to the initial beam by applying a pulsed high voltage (*ca.* -9 to -14 kV with ~30 ns rise time and 100 μs duration) to the acceleration grids. After stirring and focusing by sets of ion optics, the ions were counted either by a microchannel plate detector located at the end of the flight path (F4655-10, Hamamatsu) or by that with a centre hole (LPD-25, Burle) after reflecting back by the retarding field of the reflectron. The repetition rate was 130 Hz, and spectra were obtained by accumulation for 5–40 min. Resolutions of the mass spectrometer (M/ΔM) with and without the reflectron were typically 1000 and 400, respectively. All the clusters have been identified based on their peak positions and isotopic distributions. The clusters (1–9) have been assigned as Au₁₀(SG)₁₀, Au₁₅(SG)₁₃, Au₁₈(SG)₁₄, Au₂₂(SG)₁₆, Au₂₂(SG)₁₇, Au₂₅(SG)₁₈, Au₂₉(SG)₂₀, Au₃₃(SG)₂₂, and Au₃₉(SG)₂₄, respectively (Fig. 3B). This was the very first

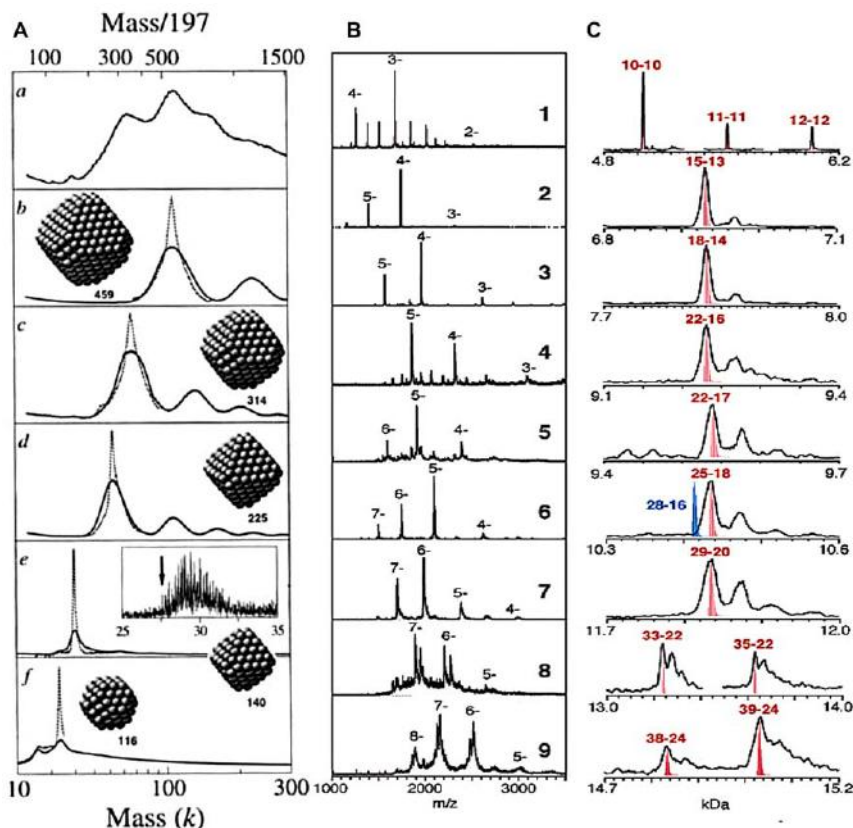


Fig. 3 (A) Mass spectra of the crude mixture (a) and of isolated fractions (b–e) of dodecane thiol protected gold clusters. Inset shows the structures predicted from optimal cores of $N = 459, 314, \text{etc.}$ gold atoms. ©Wiley-VCH publishing. Reproduced with permission.⁹⁸ (B) Low resolution ESI mass spectra of the isolated clusters (1–9). (C) The high resolution spectra of the same. The trace shows the corresponding calculated spectra for $\text{Au}_n(\text{SG})_m$ clusters with the corresponding $n-m$ values. ©ACS publishing. Reproduced with permission.⁴⁷

report of a complete ESI MS assignment of a series of glutathione protected clusters. Among them, crystal structure of $\text{Au}_{25}(\text{SR})_{18}$ have been solved in 2008¹⁰⁰ which emphasized the capability of mass spectrometry in assigning such clusters precisely.

3 Advances in cluster science

Enormous expansion has happened in the field of nanoclusters and researchers have shown an effective role of mass spectrometry in characterizing such pieces of matter. It is important to mention here that mass spectrometry is not the only tool to characterize such clusters. Crystal structure is very much important to understand the detailed structure. Although there are plenty of reports of clusters assigned through mass spectrometry, only a few of them have been crystallized. A brief discussion of the clusters crystallized is given in Table 1. In general, the structures consist of a metallic core which are surrounded by

Table 1 List of clusters with crystal structures.

Numbers	Cluster formula ^a	Core	Staple	Ref.
1	[Au ₂₃ (c-C ₆) ₁₆] ⁻	Au ₁₅	2[Au ₃ (SR) ₄], 2[Au(SR) ₂] and 4 bridging (-SR-)	102
2	Au ₂₅ (PET) ₁₈	Au ₁₃	6(RS-Au-SR-Au-SR)	100
3	[N(C ₈ H ₁₇) ₄][Au ₂₅ (PET) ₁₈]	Au ₁₃	6(RS-Au-SR-Au-SR)	90
4	Au ₂₈ (SPh-tBu) ₂₀	Au ₂₀	4(-SR-Au-SR-Au-SR-) and 8 bridging (-SR-)	103
5	Au ₃₆ (SPh-tBu) ₂₄	Au ₂₈	4(SR-Au-SR-Au-SR) and 12 bridging (-SR-)	104
6	Au ₃₈ (PET) ₂₄	Au ₂₃	3(RS-Au-SR) and 6(RS-Au-SR-Au-SR)	105
7	Au ₁₀₂ (p-MBA) ₄₄	Au ₃₉	2[RS-(AuSR) ₂] and 19(RS-Au-SR)	106
8	Ag ₁₄ (SC ₆ H ₃ F ₂) ₁₂ (PPh ₃) ₈	(Ag ₆) ⁴⁺	8[Ag ⁺ (SC ₆ H ₃ F ₂) ₂ PPh ₃] tetrahedra sharing one (SC ₆ H ₃ F ₂) ⁻ between them	107
9	Ag ₁₆ (DPPE) ₄ (SPhF ₂) ₁₄	(Ag ₈) ⁶⁺	[Ag ₈ (DPPE) ₄ (SPhF ₂) ₁₄] ⁶⁻	108
10	[PPh ₄] ₂ [Ag ₃₂ (DPPE) ₅ (SPhCF ₃) ₂₄]	(Ag ₂₂) ¹²⁺	1[Ag ₆ (DPPE) ₃ (SPhCF ₃) ₁₂] ⁶⁻ , 2[Ag ₂ (DPPE)(SPhCF ₃) ₄] ²⁻ and 4(SPhCF ₃) ⁻	108
11	Na ₄ Ag ₄₄ (p-MBA) ₃₀	Ag ₁₂ @Ag ₂₀ two shell core	6[Ag ₂ (SR) ₅]	109
12	[PPh ₄] ₄ [Ag ₄₄ (SPhF) ₃₀]	Ag ₁₂ @Ag ₂₀ two shell core	6[Ag ₂ (SR) ₅]	110

^a Abbreviations used are p-mercaptobenzoic acid (p-MBA), phenylethane thiol (PET), 4-tert-butylbenzenethiol (SPh-tBu), triphenylphosphine (PPh₃), diphenylphosphinopyridine (PPh₂Py), 4-fluorothiophenol (SPhF), 3,4-difluorothiophenol (SPhF₂), 4-(trifluoromethyl)thiophenol (SPhCF₃), 1-cyclohexanethiol (c-C₆), 1,2-bis(diphenylphosphino)ethane (DPPE).

staples of the kind M(SR)₂, M₂(SR)₃, M₂(SR)₅, *etc.* where M = Au, Ag. The structural aspects of these clusters are described using the “divide and protect” concept suggested by Hakkinen *et al.*¹⁰¹ The clusters may be considered to be composed of a core and distinct number of specific staples. Table 1 summarizes this concept.

Now, coming to mass spectrometry, it can give not only the information about core sizes but also the ligand composition.^{9,10,26} Along with this, some metals like silver (Ag) and palladium (Pd) have several isotopes which results in broad isotopic distribution in the mass spectrum. So, assignment becomes much more precise. Fragmentation of ligands or the metal–ligand bond can create some problem in assignments but in most of the cases, that can be overcome by optimizing the mass spectral conditions. Several advances have happened in the recent past to improve the quality of mass spectrum of nanoclusters.

3.1 Au clusters

Among the clusters reported so far, gold clusters have been studied extensively.^{19,23,47,91,92,95} This is mainly because of the high stability of such clusters under ambient conditions. Although a few of them, such as Au₂₃,¹⁰² Au₂₅,^{90,100} Au₂₈,¹⁰³ Au₃₆,¹⁰⁴ Au₃₈,¹¹¹ and Au₁₀₂,¹⁰⁶ have been crystallized, the chemical composition of most of them has been

assigned based on mass spectrometry. ESI MS and MALDI MS and in a few cases LDI have been utilized to assign the composition precisely. Being a softer technique, ESI MS works well for aqueous soluble gold clusters but for organic soluble clusters such as alkanethiol protected ones (which are the most commonly used ligands as they are known to generate stable gold clusters), this technique is not well suited. This is because of very poor ionizing capacity (either in positive or in negative mode) of such clusters. Several new strategies have been followed to get rid of this problem, such as ligand exchange or adding some external ionizing agents *etc.* Ligand exchange with some good ionizable ligands often results in nice mass spectral features.³⁵ Tsukuda *et al.* have introduced oxidation (by $\text{Ce}(\text{SO}_4)_2$) or reduction (by NaBH_4) to improve the ionizing capacity by enhancing the charge on the Au_{25} cluster.¹¹² Jin *et al.* have found an external ionizing agent, Cesium (CsOAc) acetate to enhance the ionization (Fig. 4).³¹ This works well with the alkane or phenyl substituted ligands and most importantly in this process mass spectrum of bigger clusters such as Au_{333} is also achievable (Fig. 4). Fields-Zinna

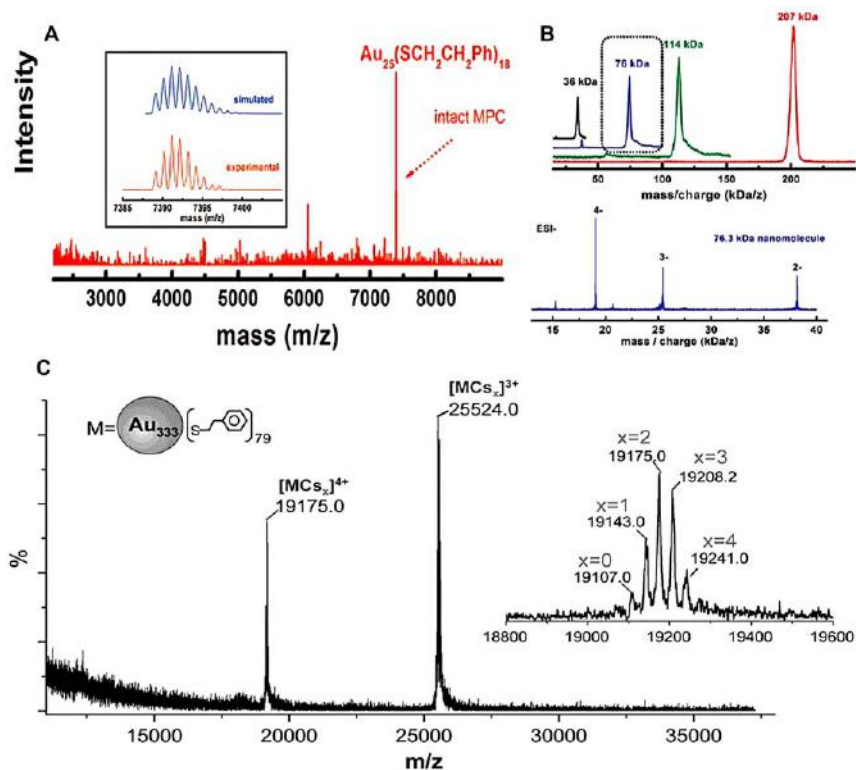


Fig. 4 (A) Positive MALDI MS data of $\text{Au}_{25}(\text{SCH}_2\text{CH}_2\text{Ph})_{18}$ cluster. Inset shows the expanded spectrum plotted along with the calculated spectrum (blue trace). Reproduced with permission.⁹ ©ACS publishing. (B) MALDI MS of a 76.3 kDa cluster along with 36, 114, and 207 kDa clusters (above). ESI MS of purified 76.3 kDa clusters (below). Reproduced with permission.⁴⁴ ©ACS publishing. (C) ESI MS of $\text{Au}_{333}(\text{SCH}_2\text{CH}_2\text{Ph})_{79}$ cluster. Inset shows the expanded mass spectrum of the peak at $m/z = 19175.0$. ©PNAS publishing. Reproduced with permission.³¹

has introduced quaternary amine ligand as an external ionizing agent to get a better signal. But most of the clusters do not ionize with all these. For those cases, MALDI MS works better but it is always important to use a suitable MALDI matrix. Usually, weak organic acids such as sinapinic acid, cinnamic acid, *etc.* have been used as matrices, but the problem with these matrices is that they do not prevent the fragmentation. In 2008, Dass *et al.* showed that *trans*-2-[3-(4-*tert*-butylphenyl)-2-methyl-2-propenylidene] malononitrile (DCTB) works well for Au clusters (Fig. 4).⁹ They have shown its effectiveness for all range of particles starting from 5 kDa to 76 kDa (Fig. 4B).⁴⁴ A comparative MALDI MS data of Au₂₅(PET)₁₈ using several matrices is given in Fig. 5 which shows the effectiveness of DCTB as a matrix for such clusters. The main reason for the success of this matrix is that it ionizes the molecule by electron transfer whereas in other cases it is proton transfer that serves ionization. Although the technique has been greatly used for organic soluble clusters for hydrophilic ligands, it is not suitable as they tend to form fragments under laser irradiation.

3.2 Silver clusters

Silver clusters are the widely studied noble metal clusters next to Au. Many clusters with various metal cores like Ag₇,¹¹³ Ag₈,¹¹³ Ag₉,¹¹⁴ Ag₃₂,^{18,36} Ag₄₄,^{5,22,109,110,115} Ag₁₅₂,⁴¹ *etc.* have been synthesized through various techniques like interfacial synthesis, solution phase and solid phase

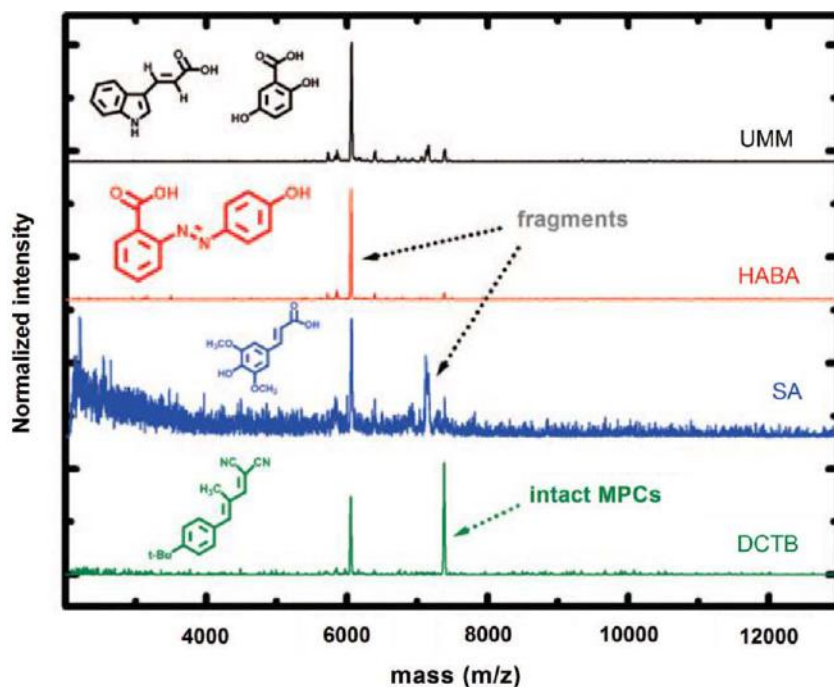


Fig. 5 MALDI MS spectra of Au₂₅(SCH₂CH₂Ph)₁₈ using different matrices. The matrices are universal maldi matrix (UMM – 1:1 mixture of dihydroxybenzoic acid and α-cyano-4-hydroxycinnamic acid), 4'-hydroxy-azobenzene-2-carboxylic acid (HABA), sinapinic acid (SA) and DCTB. Their structures are shown above the traces. ©ACS Publishing. Reproduced with permission.⁹

synthetic protocols. Although single crystal XRD would have been the best method for identifying any cluster core structure, the inability to crystallize these clusters because of their poor stability makes mass spectroscopic techniques important in their identification.^{109,110} Most of the analysis of these clusters have been done through MALDI MS, ESI MS, and LDI MS. Rao *et al.* reported mercaptosuccinic acid (H₂MSA) protected Ag₇,¹¹³ Ag₈,¹¹³ and Ag₉¹¹⁴ clusters, the former two were synthesized *via* an interfacial etching reaction between an aqueous/organic (toluene) interface and the latter by a solid state synthetic technique. All of these clusters were studied thoroughly and their compositions were assigned precisely by ESI and MALDI MS studies. In yet another example, the power and scope of mass spectrometry has been shown by Guo *et al.* by proper identification of Ag₃₂(SG)₁₉ (SG = glutathione) cluster using ESI MS technique by optimizing various parameters like source temperature, trap/transfer collision energies and cone gas flow rate (for improved collisional cooling).¹⁸ The nature of the solvent also proved to be a parameter in making mass spectrometry a powerful tool in identifying this silver cluster.¹⁸ Chakraborty *et al.* have shown the effectiveness of MALDI MS for the identification of Ag₁₅₂(SCH₂CH₂Ph)₆₀ cluster where a sharp peak at *m/z* 24600 was seen along with a dication at *m/z* 12300 (Fig. 6A).⁴¹ The high stability of this cluster is because of the closed shell electronic structures (92 electron system). Emergence of metallicity has also been investigated for a range of silver clusters identified through MALDI MS with DCTB as the matrix.⁴⁰ Harkness *et al.* have identified the Ag₄₄(SR)₃₀ clusters in 2012²² which was found to be the most stable silver cluster among all and its crystal structure has also been solved recently.^{109,110} The HRESI spectra of 4-fluorothiophenol and 2-naphthalenethiol protected Ag₄₄ clusters show exact matching with the corresponding calculated spectra (Fig. 6B). Similarly, selenolate protected Ag₄₄ cluster (Fig. 6C) also shows features for the 2-, 3- and 4- ions. Thus mass spectrometry has been effective for determining the composition of silver clusters.⁴²

4 Multidimensional mass spectrometry

Diverse multidimensional techniques such as MS/MS and ion mobility mass spectrometry (IMS) have been utilized for better understanding of such atomically precise pieces of matter. A brief discussion is given below.

4.1 MS/MS

Mass spectrometric characterization of clusters is often incomplete without MS/MS. Conducting such studies at high masses typical of clusters is difficult in most of the mass spectrometers. However, due to the multiple charges present on clusters, these studies become possible in most of the quadrupole instruments coupled with TOF, as the quadrupole analyzers can select mass and TOF can do mass analysis of the product ions. Limited MS/MS is possible in other instrument configurations such as reflectron and TOF TOF instruments; these

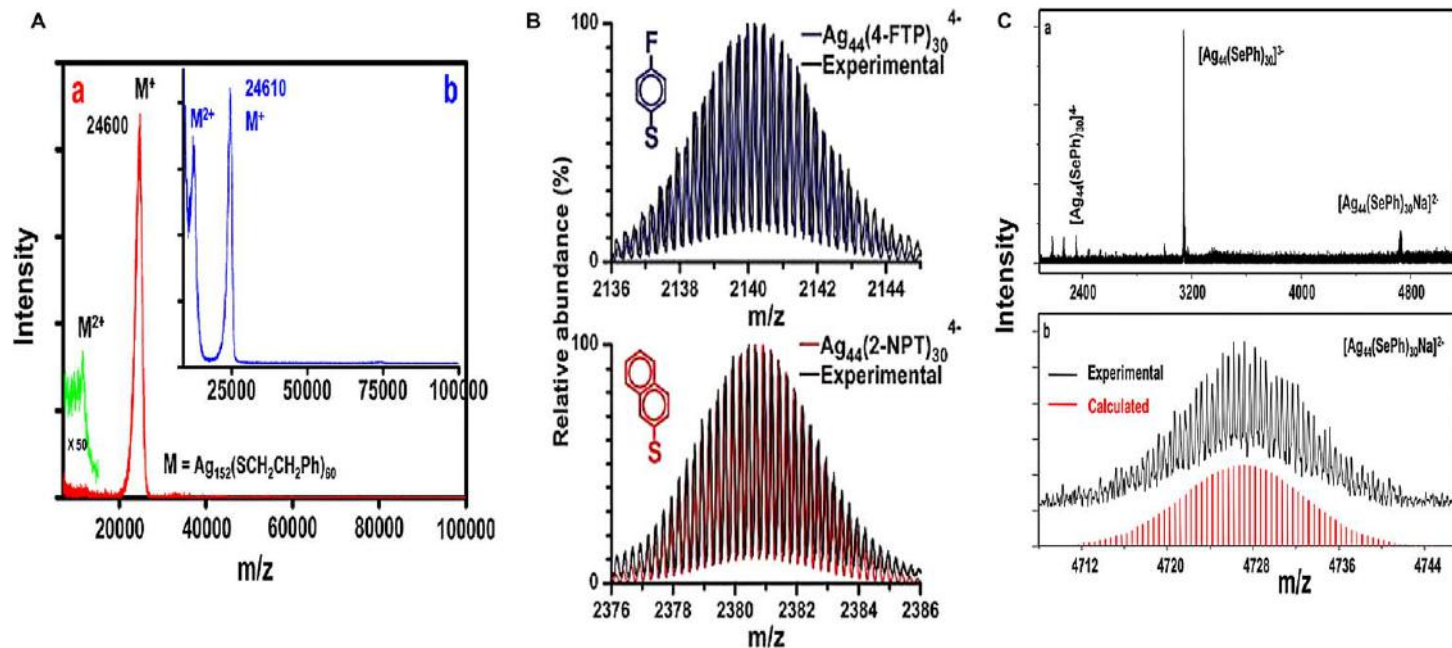


Fig. 6 (A) MALDI MS of as-synthesized $\text{Ag}_{152}(\text{SCH}_2\text{CH}_2\text{Ph})_{60}$ cluster detected in the positive mode. Inset shows the mass spectrum of Ag_{152} cluster purified using HPLC. ©ACS publishing. Reproduced with permission.⁴¹ (B) Mass spectra of $\text{Ag}_{44}(\text{SC}_6\text{H}_4\text{F})_{30}^{4-}$ and $\text{Ag}_{44}(\text{SC}_{10}\text{H}_7)_{30}^{4-}$ clusters plotted along with the corresponding calculated spectra. ©RSC publishing. Reproduced with permission.²² (C) a) HRESI MS of as-synthesized $\text{Ag}_{44}(\text{SePh})_{30}$ cluster taken in negative mode which shows clear 2-, 3- and 4-ions of the same. b) Expanded mass spectrum of the 2- ion plotted with simulated spectrum. ©ACS publishing. Reproduced with permission.⁴²

measurements, however, may not be called MS/MS as mass selection is incomplete. Due to the reduced isotope resolution, in view of the large mass, precise characterization is difficult, although several attempts have been made to do the same. In the following examples, we present a few results for MS/MS studies. Ghosh *et al.* showed in an MS/MS study that fragmentation of $\text{Au}_{18}\text{SG}_{14}$ gives closed shell ions with 8 electrons,¹⁵ this suggests that the number of electrons in the ligand is also important in deciding the electronic structure of the cluster, determining its stability. MS/MS has been used to understand the composition of clusters especially in cases where the metal contains a rich isotope distribution. This has again been demonstrated by Wu *et al.* where the fragmentation pattern of $\text{Ag}_7(\text{DMSA})_4$ obtained from MS/MS was analysed in a detailed fashion confirming a closed shell ion with 4 electrons.³⁸ Ghosh *et al.*'s study in Fig. 7A) shows the ESI MS data of the $\text{Au}_{18}\text{SG}_{14}$ cluster where four prominent peaks at m/z 1956.2, 1565.2, 1304.3, and 1117.4 were observed

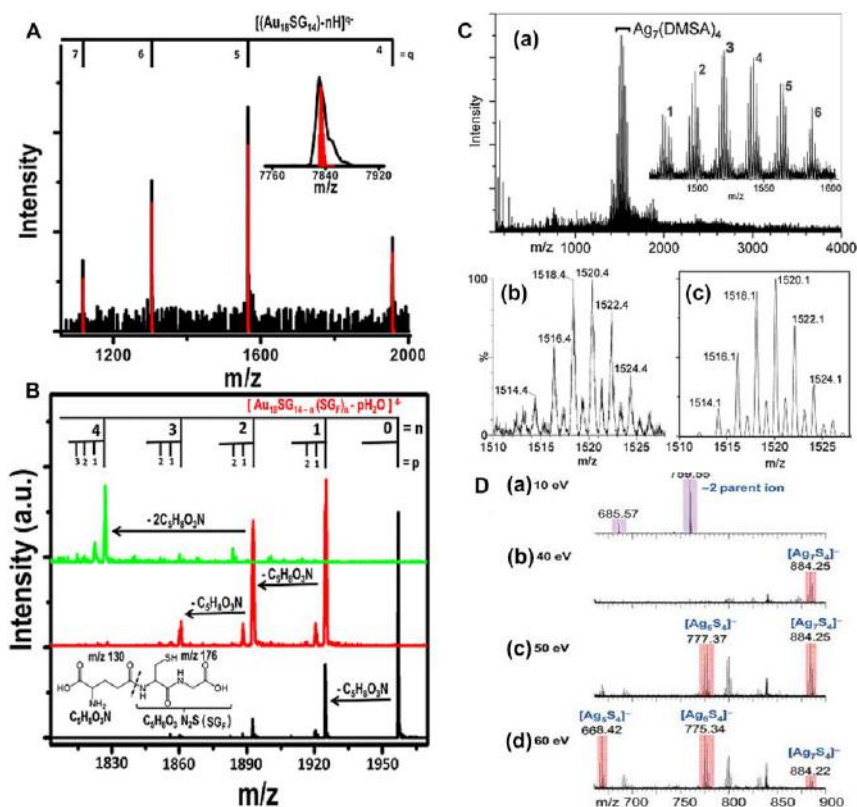


Fig. 7 (A) ESI MS of $\text{Au}_{18}\text{SG}_{14}$ in the negative mode. The deconvoluted spectrum is shown as the inset along with the expected mass peak for $\text{Au}_{18}\text{SG}_{14}^-$. (B) MS/MS spectra of $[\text{Au}_{18}\text{SG}_{14}]^{4-}$ with increasing collision energy. Inset shows the fragmentation channel of glutathione. The mass spectra from bottom to top are with increasing collision energy. Reproduced with permission.¹⁵ ©ACS Publishing. (C) ESI MS of silver clusters (negative ion mode, inset shows the zoomed-in spectrum as shown in a). (b) and (c) show the experimental and simulated isotopic pattern of $\text{Ag}_7\text{L}_4-2\text{H}+2\text{Na}$. (D) MS/MS analysis of the clusters (dianion $[\text{Ag}_7\text{L}_4-3\text{H}+2\text{Na}]^{2-}$). ©ACS Publishing. Reproduced with permission.³⁸

corresponding to four different charge states of the cluster ($q = 4, 5, 6,$ and 7). MS/MS study of the 1956 peak (Fig. 7B) showed fragment peaks with a separation of m/z 32.5 predicting the possible loss of a fragment of mass 130 ($32.5 \times 4 = 130$) which can only arise from the -SG ligand when the C_{glutamic acid} - N_{cysteine} bond cleaves giving rise to two fragments of $m/z = 130$ (C₅H₈O₃N) and 176 (C₅H₈O₃N₂S). The data showed a systematic loss of C₅H₈O₃N as the collision energy was increased. The data showed a series of peaks separated at $m/z = 4.5$ corresponding to the loss of H₂O ($4.5 \times 4 = 18$) indicating that glutathione existed as an anhydride at the surface of the fragment.

Most of the clusters have not been examined by MS/MS also due to poor ion intensity. Clusters being metastable undergo facile fragmentation and obtaining molecular ions at high intensity for MS/MS analysis has been possible only in a few cases. The routine fragmentation pattern, namely ligand loss is seen only in a few cases as the neutral M-L species are more stable leading to their losses. The product cluster formed is often not electronically stable, leading to additional fragmentation, making it impossible to identify them. The foregoing suggests that routine MS/MS examination of clusters require the development of new ionization methodologies.

4.2 Ion mobility mass spectrometry (IMS)

New techniques have been introduced into commercial mass spectrometers for better understanding of the structural features of a molecule. Ion mobility mass spectrometry is an example of that which has been used for different ligand protected gold nanoparticles to understand several aspects of its structure in the gas phase.^{19–21} The principle of this technique is to separate specific ions based on their size, more prominently ion surface area. In short, in this mass spectrometer, ions are injected into a gas-filled drift tube where they experience numerous low-energy collisions with a background gas and that separates ions based on the ion-neutral collision cross section (CCS).¹⁹ Just like liquid chromatography, here also smaller ions elute faster than larger ions which experience more collisions. In most of the cases IMS has been used to understand the size of gold nanoparticles but it also helps to understand the fragments generated from them such as Au₄(SR)₄ which are often seen in the mass spectrum of Au₂₅(SR)₁₈. The same was found for the case of Au₃₈(SCH₂CH₂Ph)₂₄ and Au₆₈(SCH₂CH₂Ph)₃₄.⁴³ But from crystal structure, no such species has been found as a staple which does suggest that this fragment is generated in mass spectral conditions. Even Fields-Zinna *et al.* have found that in tandem mass spectrometric conditions tetrameric ion, NaAu₄(SR)₄⁺ can be generated from Au₂₅(SR)₁₈ clusters.¹⁴ In IMS, one can reduce such fragmentations and one can reduce the noise to get a low intense peak in a much prominent way. Dass *et al.* have done the IMS study of Au₂₅(SCH₂CH₂Ph)₁₈ cluster where they have shown that it is possible to distinguish between the fragmentation of the core as well as shell which consist of six [-SR-Au-SR-Au-SR-] staples. Along with the predominant Au₄(SR)₄, other smaller fragments such as Au(SR)₂⁻, Au₂(SR)₃⁻, Au₃(SR)₄⁻, and Au₄(SR)₅⁻ were also seen.⁶

5 Clusters of other metals

Compared to the vastly studied and rapidly growing field of monolayer protected clusters of Au and Ag, clusters of other metals are in their infancy. There are only a few reports of clusters of metals like Pd, Cu, Pt, *etc.*, and some alloy clusters of these metals with Au and Ag have been studied up to an extent. This section gives a brief account of mass spectrometric investigation of clusters of metals like Pd, Pt, Cu and of a few alloy clusters.

5.1 Pt clusters

There are several attempts to create fluorescent Pt nanoclusters by different methods. Giuffrida *et al.* developed a methodology to obtain ultra-small, water-soluble, carboxylate-terminated Pt clusters.¹¹⁶ Yuan *et al.* have synthesized highly fluorescent Pt clusters employing mild etching process by phase transfer *via* electrostatic interaction.¹¹⁷ There are also reports on blue¹¹⁸ and yellow emitting Pt clusters¹¹⁹ protected by thiol, thioether and ester – functionalized polymer and glutathione. But we will not go in to the details of synthesis of these materials and will focus on their mass spectrometry.

The Pt clusters made up of 4 to 6 Pt atoms protected by *N,N*-Dimethylformamide were synthesized by Kawasaki *et al.* by previously reported process. These clusters were photo – luminescent with their emission maximum dependent upon the excitation wavelength. The composition of these clusters was determined by MALDI MS by ligand exchanging them with 2-mercapto-benzothiazole (MBT). The mass spectrum shown in Fig. 8A, consisted of a peak corresponding to Pt₅(MBT)₇ as the dominant signal and it was in agreement with the simulated mass obtained in isotopic analysis. The clusters with 4 and 6 Pt atoms were also present which were assigned as shown in the Fig. 8A.¹²⁰

Recently, a blue emitting 11-atom Pt cluster protected by 4-(*tert*-butyl)benzylmercaptan (BBSH), Pt₁₁(BBS)₈ was reported.⁸ The cluster was synthesized by the solid state method wherein H₂PtCl₆ and BBSH were ground to form thiolates first and these thiolates were reduced using appropriate quantity of NaBH₄. The molecular formula of clusters was assigned using MALDI MS and ESI MS data, shown in Fig. 8B. The main figure shows the MALDI mass spectrum obtained at threshold laser power using the DCTB matrix. The peak was observed to be broader compared to that of the Au₂₅PET₁₈ cluster. This is mainly because Pt has five isotopes (¹⁹²Pt, ¹⁹⁴Pt, ¹⁹⁵Pt, ¹⁹⁶Pt and ¹⁹⁸Pt) and Au has only one (¹⁹⁷Au). So FWHM of the Pt cluster is larger than that of Au clusters. There are also other reasons like laser induced fragmentation increasing the broadness of the peak. ESI MS of the cluster is shown in inset of Fig. 8B with simulated spectrum showing agreement with the Pt₁₁(BBS)₁₈ formula. The ESI MS was measured in 1:1 mixture of toluene-methanol in positive ion mode. CsOAc was used as ionization enhancer as ligand was completely non-polar. The peak at *m/z* = 3730 was assigned to [Pt₁₁(BBS)₈Cs(H₂O)]⁺ ion.⁸

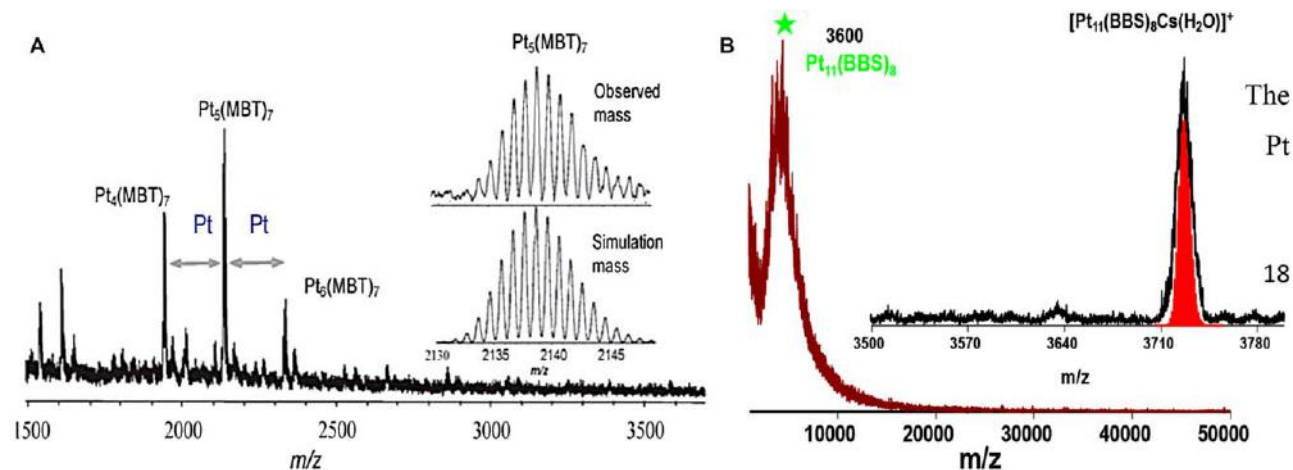


Fig. 8 (A) Negative-ion MALDI MS of MBT protected Pt clusters prepared by ligand exchanging DMF-protected clusters with MBT. The observed and simulated isotopic distributions of the peak with highest intensity show a good agreement with assigned composition $Pt_5(MBT)_7$. The peaks corresponding to $Pt_4(MBT)_7$ and $Pt_6(MBT)_7$ were also observed. Reproduced from Ref. 120 with permission from The Royal Society of Chemistry. (B) MALDI MS of Pt cluster protected by BBSH observed at threshold laser power using DCTB matrix with inset showing ESI MS of the cluster obtained using CsOAc as enhancer, plotted with the simulated spectrum (shaded) for the corresponding composition. Based on the MALDI MS and ESI MS data the cluster was assigned to be $Pt_{11}(BBS)_8$. Reproduced from Ref. 8 with permission from The Royal Society of Chemistry.

5.2 Pd clusters

Though there are several reports on the synthesis and characterization of Pd clusters,^{121–125} mass spectrometric investigations of them are rare. TEM has been used as a major characterization tool in all these cases.

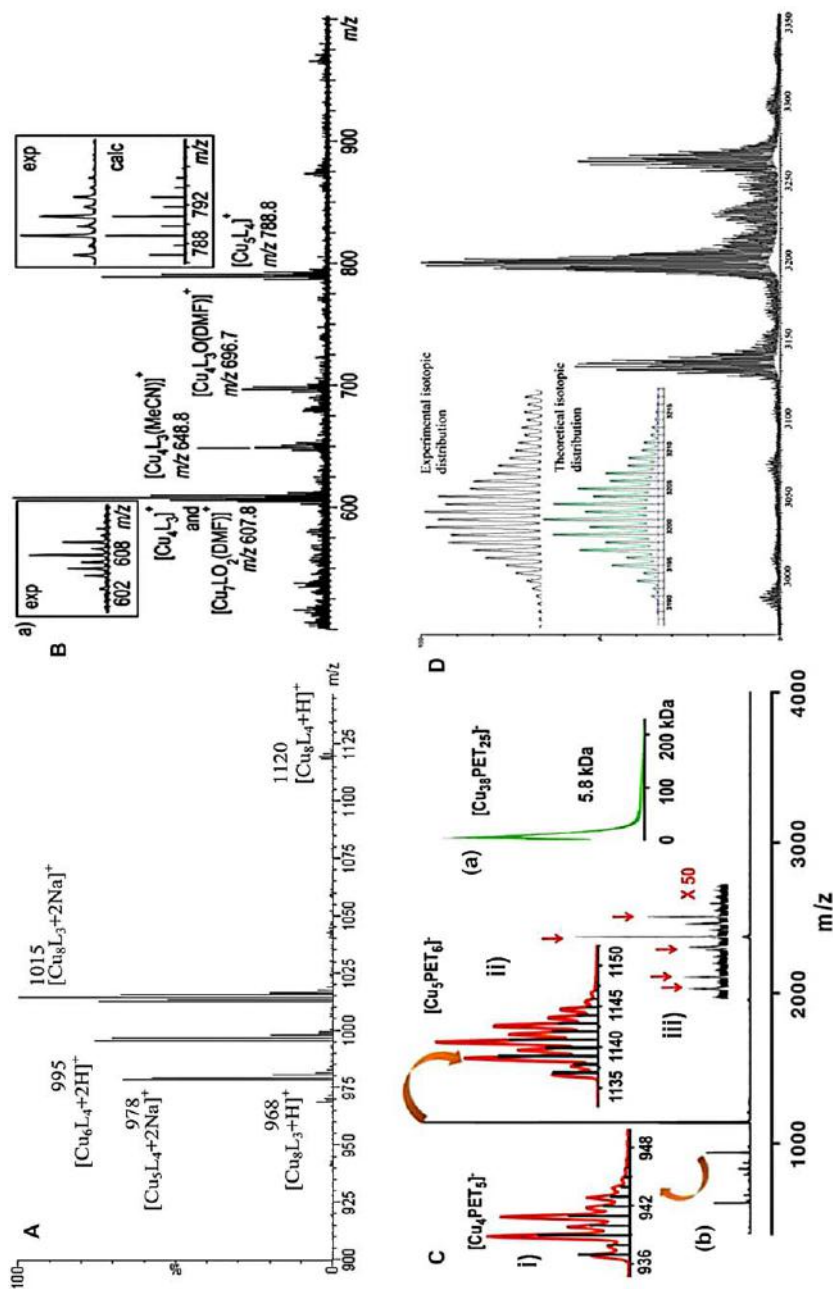
Negishi *et al.* synthesized Pd clusters by reacting PdCl₂ with alkanethiols, RSH (R = *n*-C₁₈H₃₇, *n*-C₁₂H₂₅). They analysed chemical composition of the clusters formed by mass spectrometry using a MALDI TOF apparatus constructed in their group in the presence of anthracene as the matrix. They observed Pd₅(SC₁₈H₃₇)₁₀ and Pd₁₀(SC₁₈H₃₇)₁₂ thiolate complexes as the major species and also peaks corresponding to some other fragment ions formed during the MALDI process, in positive mode, when the sample was diluted by anthracene to ~1 mol%.

They have also observed significant dependence of mass spectral features on the relative concentration of sample and matrix. When the sample was diluted to 20 mol% by anthracene, the peaks were not assignable to any combinations of Pd and C₁₈H₃₇SH, but to Pd_{*n*}S_{*m*}⁺ and peak positions were independent of chain length of the ligand. Thus they came to a conclusion that samples contained Pd:SR clusters designated as Pd_{*n*}(SR)_{*m*} and that all the C–S bond cleavage was induced because of UV absorption by clusters, efficiently and selectively.¹²⁶

5.3 Cu clusters

Wei *et al.* demonstrated the synthesis of small Cu_{*n*} clusters (*n* ≤ 8) in solution following a single phase wet chemical route. These clusters were protected by 2-mercapto-5-*n*-propylpyrimidine (MPP) ligand. The chemical composition of these clusters was determined using ESI MS as the major characterization technique. The ESI mass spectrum recorded in the positive ion mode is shown in Fig. 9A. The highest mass peak at *m/z* = 1120 was found to be corresponding to Cu₈L₄ (L = C₇H₉N₂S). Other fragments like Cu₈L₃ (*m/z* = 1015), Cu₆L₄ (995), Cu₅L₄ (978), Cu₈L₃ (968) and Cu₅L (470) were also present in the mass spectrum.¹²⁷

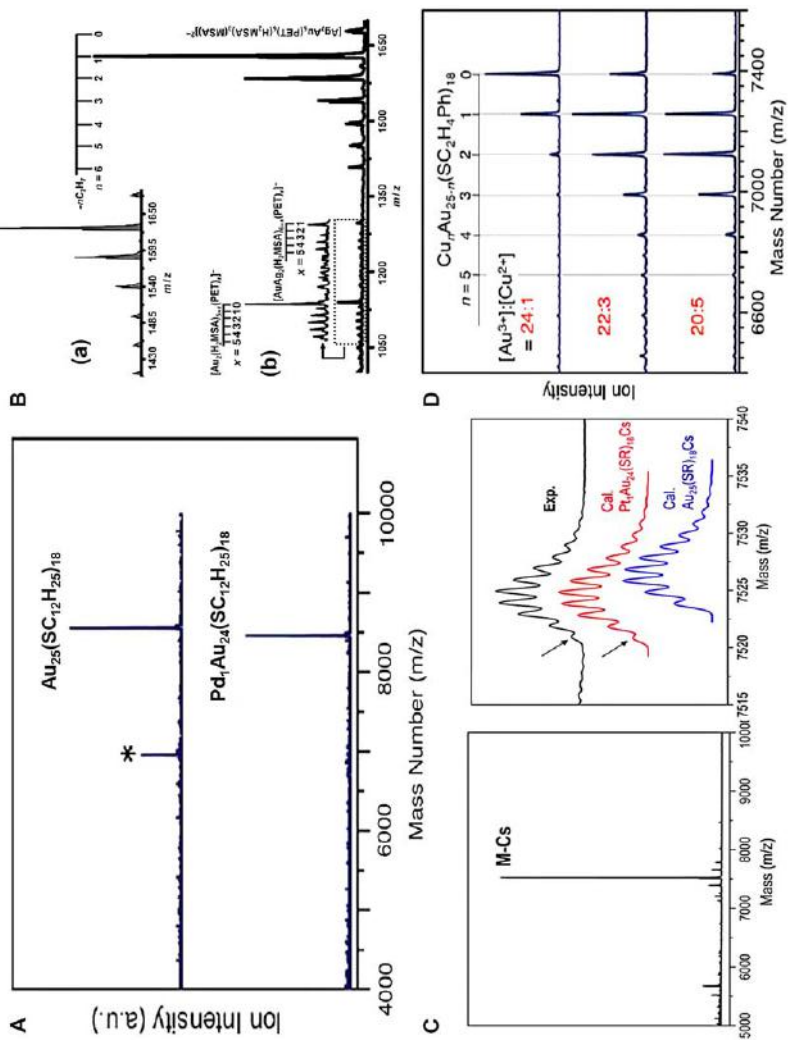
A sub-nanometer Cu cluster protected by benzotriazolate (BTA), Cu_{*n*}BTA_{*m*} was reported by Salorinne *et al.* in 2012. They synthesized these clusters by following the single-phase Brust – Schiffrin protocol in methanol, which involves two steps that are 1) formation of benzotriazolate – Cu(II) complex and 2) reduction of Cu(II) ions to Cu(0) by the addition of NaBH₄. The mass spectral features of these clusters were studied by ESI MS, both in positive and negative mode by diluting a DMF dispersion of the clusters with acetonitrile (positive – mode spectrum is shown in Fig. 9B). Two major peaks were observed at *m/z* = 607.8 and 788.8 which were assigned to Cu₄L₃ and Cu₅L₄, respectively (L = BTA). The smaller peaks at *m/z* = 648.8 and 696.7 were identified as solvent adducts of Cu₄L₃ and Cu₄L₃O species. Some organic fragments and fragments containing one Cu atom were found in the lower mass region. In the negative mode only the smaller species, such as, CuL₂ and BTA anions were present and clusters were no longer found.³²



One more Cu cluster protected by 2-phenylethanethiol (PET) was reported in 2013.⁴⁵ It was prepared by following the solid – state route. In order to find the molecular composition of these clusters, both MALDI MS and ESI MS characterization of the material was performed. MALDI MS was obtained in the negative mode using DCTB as the matrix which showed a single peak at around $m/z = 5800$ which was assigned to $\sim \text{Cu}_{38}(\text{PET})_{25}$ (shown in Fig. 9C(a)). There was only a single peak in MALDI MS showing the existence of a single species. The ESI MS data of clusters obtained in the negative mode is shown in Fig. 9C(b). The molecular ion features were not observed in ESI MS, but peaks corresponding to some fragment ions could be seen. The peaks with maximum intensity at $m/z = 1141$ and 941 were assigned to the fragments $[\text{Cu}_6(\text{PET})_5]^-$ and $[\text{Cu}_5(\text{PET})_4]^-$, respectively and experimental and theoretical isotopic distributions are shown in insets of Fig. 9C(b). The other peaks identified were at $m/z = 2655, 2459, 2359, 2124$ and 2056 and these were assigned to the fragment ions, $[\text{Cu}_{34}(\text{PET})_{23}]^{2-}$, $[\text{Cu}_{30}(\text{PET})_{22}]^{2-}$, $[\text{Cu}_{29}(\text{PET})_{21}]^{2-}$, $[\text{Cu}_{28}(\text{PET})_{23}]^{2-}$ and $[\text{Cu}_{28}(\text{PET})_{17}]^{2-}$, respectively which are indicated by arrows in inset iii of Fig. 9C(b). These fragments compliment the presence of PET-protected copper clusters in solution.⁴⁵

An unprecedented 20 atom copper cluster incorporating 11 hydrides into the system with a molecular formula, $\text{Cu}_{20}\text{H}_{11}(\text{S}_2\text{P}(\text{O}^i\text{Pr})_2)_9$ was reported by Liu *et al.* The cluster was synthesized in tetrahydrofuran (THF) by reaction of a mixture of $\text{NH}_4[\text{S}_2\text{P}(\text{O}^i\text{Pr})_2]$ and $[\text{LiBH}_4.\text{thf}]$ with $\text{Cu}(\text{CH}_3\text{CN})_4\text{PF}_6$ and positive ion ESI MS was carried out to determine its chemical composition. The spectrum obtained is shown in Fig. 9D. The peak with highest intensity at $m/z = 3198.5$ was assigned to the molecular ion. The peaks at $m/z = 3132.6$ and at $m/z = 3262.3$ were assigned to the fragment $[\text{C}_{19}\text{H}_9(\text{S}_2\text{P}(\text{O}^i\text{Pr})_2)_9]^+$ and adduct $[\text{Cu} + \text{Cu}_{20}\text{H}_{11}(\text{S}_2\text{P}(\text{O}^i\text{Pr})_2)_9]^+$, respectively. The cluster was crystallized and the structure of the cluster was determined by single – crystal X-ray diffraction (XRD) studies. It consists of an elongated triangular orthobicupola framework of 18 Cu atoms encapsulating a $[\text{Cu}_2\text{H}_5]^{3-}$ ion.¹²⁸

Fig. 9 (A) ESI MS of MPP protected copper clusters in the positive ion mode. The highest mass peak at $m/z = 1120$ is assigned to Cu_8L_4 ($\text{L} = \text{C}_7\text{H}_9\text{N}_2\text{S}$) and other peaks in lower mass range correspond to the fragments described in the text. Reproduced with permission.¹²⁷ ©ACS Publishing. (B) ESI MS-TOF mass spectrum of copper clusters protected by BTA in positive mode measured using DMF dispersion of clusters diluted with acetonitrile. The inset (on the right hand side) shows the experimental and calculated isotopic distribution of the peak at $m/z = 788.8$ due to Cu_5L_4 . The other inset (on the left hand side) shows the expanded view of the peak at $m/z = 607.8$ assigned to Cu_4L_3 . ©RSC Publishing. Reproduced with permission.⁵² (C) a) MALDI MS of the PET protected Cu clusters measured in linear negative ion mode, measured using DCTB matrix. The single peak in the spectrum shows the presence of single species with the composition, $\text{Cu}_{38}\text{PET}_{25}$. b) ESI MS measured in negative mode with insets showing observed and calculated (black) spectra corresponding to i) $[\text{Cu}_4(\text{PET})_5]^-$ and ii) $[\text{Cu}_5(\text{PET})_6]^-$ species and iii) expanded (Y axis) view of a selected region showing fragments mentioned in the text. ©Springer Publishing. Reproduced with permission.⁴⁵ (D) ESI MS of $\text{Cu}_{20}\text{H}_{11}(\text{S}_2\text{P}(\text{O}^i\text{Pr})_2)_9$ cluster in positive mode with inset showing the observed and calculated spectra for molecular ion peak. The peak at lower mass is attributed to the fragment and that at higher mass is attributed to a Cu adduct of the molecular ion which are described in the text. ©ACS Publishing. Reproduced with permission.¹²⁸



5.4 Alloy clusters

Alloy clusters, also referred to as alloy nanoclusters or nanoalloys are composed of atoms of two or more elements in definite compositions. Alloy clusters with a wide range of combination of elements and different compositions are known till date; some of them are Au_{24}Pd ,^{12,46} $\text{Au}_{36}\text{Pd}_2$,¹²⁹ $\text{Au}_{24-n}\text{Ag}_n$ series,¹³⁰ $\text{Au}_{24-n}\text{Cu}_n$ series,¹³¹ Au_{24}Pt ,¹³² Ag_4Ni_2 ,¹³³ etc. Due to alloying, we can observe an enhancement in specific properties of clusters because of synergistic effects. Also due to rich diversity in compositions, structures and properties, they find widespread applications in different fields.¹³⁴ Some examples of these will be discussed here with more emphasis on their mass spectrometry.

Murray *et al.* reported the monopalladium doped bimetallic cluster, $\text{Au}_{24}\text{PdL}_{18}$ ($L = 2$ -phenylethanethiol) in 2010. Their synthesis procedure was similar to that of $\text{Au}_{25}\text{PET}_{18}$, but they used mixture of Au and Pd salts instead of gold salt (HAuCl_4) alone. They confirmed the mono-Pd doping by ESI MS of clusters, partially ligand exchanged with thiolated (polyethyleneglycol) (PEG), and also with MALDI TOF MS analysis.¹³ Negishi *et al.* isolated highly pure dodecanethiolate – protected Au_{24}Pd cluster using solvent fractionation and high-performance liquid chromatography (HPLC). The negative ion MALDI mass spectrum of purified cluster as compared to that of $\text{Au}_{25}(\text{SC}_{12}\text{H}_{25})_{18}$ is shown in Fig. 10A.⁴⁶ The same group reported palladium doped magic number cluster Au_{38} protected by phenylethanethiolate, $\text{Au}_{36}\text{Pd}_2(\text{SCH}_2\text{CH}_2\text{Ph})_{24}$, and studied the mass spectral feature of the cluster using MALDI MS and high resolution ESI MS analysis in negative mode. They found that $\text{Au}_{37}\text{Pd}(\text{SC}_2\text{H}_4\text{Ph})_{24}$ was also present in solution, but di-palladium doped cluster was more stable compared mono-palladium doped cluster.¹²⁹

The effect of Ag doping on the electronic structure of $\text{Au}_{25}(\text{SR})_{18}$ clusters was studied by Negishi *et al.* by considering dodecanethiol as the ligand. The synthesis procedure was similar to that of the Pd-doped cluster. They observed multiple silver atom incorporation into the $\text{Au}_{25}(\text{SC}_{12}\text{H}_{25})_{18}$ system forming a series of clusters, $\text{Au}_{25-n}\text{Ag}_n(\text{SC}_{12}\text{H}_{25})_{18}$ ($n = 0-11$), unlike in case of Pd-doping, and that electronic structure of

Fig. 10 (A) The negative mode MALDI MS of $\text{Au}_{24}\text{Pd}_1(\text{SC}_{12}\text{H}_{25})_{18}$ cluster along with that of $\text{Au}_{25}(\text{SC}_{12}\text{H}_{25})_{18}$ cluster. The peak highlighted by asterisk corresponds to $\text{Au}_{21}(\text{SC}_{12}\text{H}_{25})_{14}$ fragment. The clusters were purified by HPLC and MALDI MS was collected using DCTB matrix in linear mode TOF mass spectrometer. Reproduced from Ref. 46 with permission from the PCCP Owner Societies. (B) The negative ion ESI MS of the 13-atom alloy cluster Ag_7Au_6 protected by MSA and partially ligand exchanged with PET, in the region $m/z = 1000-1700$. The cluster showed substitution of six MSA ligands by PET which was confirmed by sequential loss of six tropylium ions ($n = 0, 1, 2, \dots, 6$) observed during ionization. The inset a) shows simulated (gray) and observed (black) isotopic pattern of the peaks and b) shows the fragments. Reproduced with permission.¹³⁵ ©Wiley-VCH Publishing. (C) ESI MS of $\text{Au}_{24}\text{Pt}_1(\text{SCH}_2\text{CH}_2\text{Ph})_{18}$ clusters with experimental and calculated spectra for $[\text{Au}_{24}\text{Pt}_1(\text{SCH}_2\text{CH}_2\text{Ph})_{18}\text{Cs}]^+$ and $[\text{Au}_{25}(\text{SCH}_2\text{CH}_2\text{Ph})_{18}\text{Cs}]^+$ species. The CsOAc was used as ionization enhancer. The most intense peak at $m/z = 7524.8$ was assigned to $\text{Pt}_1\text{Au}_{24}(\text{SR})_{18}\text{Cs}^+$ and assignment was confirmed by isotopic distribution analysis. Reproduced with permission.¹³² ©ACS Publishing. (D) Negative mode MALDI MS of $\text{Au}_{25-n}\text{Cu}_n(\text{SCH}_2\text{CH}_2\text{Ph})_{18}$ clusters synthesized with precursor salt concentrations $(\text{HAuCl}_4)/(\text{CuCl}_2) = 24:1, 22:3$ and $20:5$. The peaks observed are assigned to the series, $\text{Au}_{25-n}\text{Cu}_n(\text{SCH}_2\text{CH}_2\text{Ph})_{18}$ with n ranging from 0–5 indicated in the figure. ©ACS Publishing. Reproduced with permission.¹³¹

Au₂₅ cluster was continuously modulated by incorporation of each silver atom. The MALDI MS of the clusters in the negative mode contained multiple peaks and all the peaks were assignable to Au_{25-n}Ag_n(SC₁₂H₂₅)₁₈ ($n = 0-11$). Similar spectra were obtained in positive ion mode as well.¹³⁰ In a similar way, doping the magic number cluster, Au₃₈ protected by phenylethanethiol, created a series of alloy clusters, Au_{38-n}Ag_n(SCH₂CH₂Ph)₂₄, which were characterized by positive ion MALDI TOF analysis.²⁶ Ag atom incorporation into some other cluster systems like Au₁₄₄(SR)₆₀²⁵ and Au₁₃₀(SR)₅₀,¹³⁶ *etc.*, is also reported in the literature resulting in different alloy clusters of Au and Ag. A 13 atom alloy cluster Ag₇Au₆ protected by mercaptosuccinic acid (MSA) was reported by Udayabhaskararao *et al.*¹³⁵ These clusters were prepared by the reaction of a mixture of Ag₇ and Ag₈ clusters with HAuCl₄ solution. When the ESI MS measurements were done on as – synthesized clusters in aqueous medium no characteristic peaks were observed, because clusters were decomposing due to high capillary temperature of around 313 K. Hence, the clusters were transferred to organic medium by partial ligand exchange of MSA with phenylethanethiol (PET) and ESI MS analysis was performed. The mass spectrum of PET – exchanged clusters is shown in Fig 10B. The peak with highest m/z was assigned to [Ag₇Au₆(PET)₆(H₂MSA)₃(MSA)]²⁻ and the series of peaks following it correspond to sequential loss of tropylium ion from each PET ligand (n in figure indicates the number of tropylium ions lost). The series terminates at six tropylium ion loss confirming the presence of six PET ligands in the system.¹³⁵

The doping of Cu atoms into the Au₂₅(SCH₂CH₂Ph)₁₈ system was attempted by Negishi *et al.*, which was reported in 2012. Fig. 10D shows the negative ion MALDI MS of the clusters consisting of multiple peaks, assignable to clusters with different number of Cu incorporation, *i.e.*, Au_{25-n}Cu_n(SCH₂CH₂Ph)₁₈ ($n = 0-5$). Unlike the case of Pd and like in the case of Ag, a series of alloy clusters, Au_{25-n}Cu_n(SCH₂CH₂Ph)₁₈ were obtained in this case, which were identified in the mass spectra. But they could observe only up to six Cu atom incorporation and clusters with more than six Cu atoms were hardly observed in experimental conditions followed by them.¹³¹ In case of selenolate protected cluster system, Au_{25-n}Cu_n(SeC₈H₁₇)₁₈ ($n = 0-9$), up to nine Cu atom incorporation was observed.¹³⁷

Doping Au₂₅(SCH₂CH₂Ph)₁₈ clusters with Pt atoms was tried by Jin *et al.* They obtained single Pt doped system, Au₂₄Pt(SCH₂CH₂Ph)₁₈. They found that Pt – doping drastically changes the electronic, optical and catalytic properties of clusters. Differentiating Pt (195.08 Da) from Au (196.97 Da) is a tough task because of their very small mass difference (1.89 Da). Hence high – precision ESI MS was used as an analysing tool by them for identifying the new cluster formed. The ESI MS in positive – mode with experimental and simulated spectra are shown in Fig. 10C. Cesium acetate was used as an enhancer in this case and they observed [Au₂₄Pt(SR)₁₈Cs]⁺ as a major peak at $m/z = 7524.8$ Da.¹³² The location of Pt atom was later identified by platinum L₃ – edge extended X-ray absorption fine structure (EXAFS) analysis along with X-ray photoelectron

spectroscopy (XPS) and computational analysis. The Pt atom occupies the centre of the icosahedral Au₁₃ core.¹³⁸

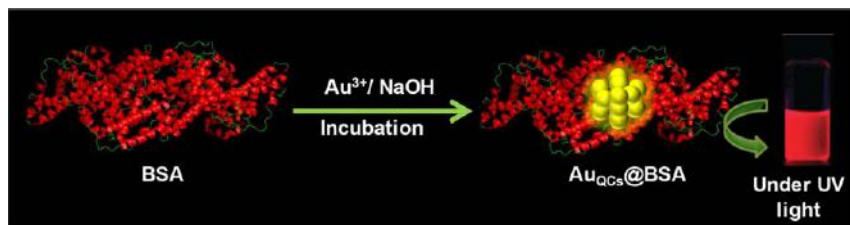
A bimetallic cluster of Ag and Ni, which involves a noble metal and a first row transition metal, protected by di-mercaptosuccinic acid (DMSA) ligand has been reported in 2012. The cluster was characterized using ESI MS and the structure has been predicted using theoretical calculations.¹³³

Thus, mass spectrometry, mainly MALDI MS and ESI MS, has played a major role in identifying clusters of metals like Pt, Pd, Cu and alloy clusters, their composition and structure determination along with other characterization techniques. In case of alloy clusters, mass spectrum is an important tool to know the combination of different metal atoms in a specific cluster.

6 Protein protected clusters

Choice of ligand plays a significant role in cluster science. Starting from gas phase to phosphine and then thiol protection, new era began when people started using macromolecular templates for synthesizing clusters.¹³⁹ Peptides,¹⁴⁰ DNA,¹⁴¹ dendrimer¹⁴² and mostly proteins¹³⁹ are the members of this new family. This specific class of molecules bridge materials and biology. In this section we will mostly discuss protein protected clusters. So far several proteins namely, bovine serum albumin (BSA),^{28,29,143–152} native lactoferrin (Lf),^{39,153} human serum albumin (HSA),^{154–156} lactalbumin,¹⁵⁷ pepsin,¹⁵⁸ trypsin,¹⁵⁹ chymotrypsin,¹⁶⁰ lysozyme (Lyz),^{161–164} hemoglobin (Hb),¹⁶ horse radish peroxidase (HRP),¹⁶⁵ insulin,¹⁶⁶ *etc.*, have been used for cluster synthesis. Some reports exist on mixed protein matrices used for cluster synthesis such as egg shell membrane,¹⁶⁷ human hair,¹⁶⁸ egg white,¹⁶⁹ *etc.* Along with conventional metals like Au and Ag, several other metals like Pt,¹⁶⁹ Fe,¹⁶ and Cu¹⁷ clusters also have been synthesized using proteins.

Protein protected clusters do not exhibit well defined UV-Vis absorption feature unlike their monolayer protected analogue (as described in the above sections). But they have intense luminescence which allows them to act as sensors for toxic metal ions,^{17,39,147–149,151,159,163,170,171} small molecules^{143,165,169} and biologically active molecules.^{156,162,172} Their luminescence can be used for bio-imaging and bio-labeling.^{148,166,173,174} In the context of emerging applications, of biocompatible materials, it is necessary to look into the protein protected clusters in greater details. Although several clusters have been crystallized (see previous section for details) none of the protein protected clusters could be crystallized so far due to the inherent lack of crystallization of proteins in the experimental conditions used for cluster synthesis. Mass spectrometry is an alternate tool for identifying the cluster cores. Proteins are being characterized by mass spectrometry for long and a large body of literature exists on mass spectrometry of proteins and their interaction with other molecules.¹¹ Many protein protected clusters have been identified by the mass shift in the protein region after cluster synthesis. Typically metal precursors (Au³⁺/Ag⁺ for Au/Ag clusters) are mixed with



Scheme 1 Schematic representation of protein protected cluster formation taking BSA as an example. The reaction proceeds *via* formation of Au^+ -protein intermediate adduct. After cluster formation intense red luminescence is observed under UV light.

protein solution to form adducts (Au^+ -protein/ Ag^+ -protein) which is subsequently reduced to luminescent clusters in presence of a base (for Au as shown in Schematic 1).¹⁵⁰ An external reducing agent namely, NaBH_4 is used to synthesize Ag clusters.²⁸ After cluster formation, protein loses its secondary structure partially (for example, Lyz loses 28% helicity).^{17,29,39,161} Fragmentations occur due to the excess base and catalytic fragmentation of the protein occurs by the clusters. These effects ultimately result in poor ionization in ESI MS. To date, none of these clusters could be seen in ESI MS, although, by using latest mass spectrometers we can reach the mass range of bigger proteins like BSA in ESI MS. As a result, mostly these clusters are studied using MALDI MS. In the following sub-sections, we will discuss the mass spectrometric investigations of various protein protected clusters.

6.1 Au, Ag and Au@Ag alloy clusters

MALDI MS is the commonly used technique in this scenario which is a soft ionization method and capable of showing parent singly charged ion, known as the molecular ion. In MALDI MS of protein protected clusters, matrices such as sinapic acid (SA), α -cyano- α -hydroxy cinnamic acid (CHCA), *etc.*, are used.¹¹ Minimum quantity of cluster solution is mixed well with a larger volume of matrix solution and spotted on the MALDI plate to yield a dried droplet. In 2009, Xie *et al.* first reported mass spectrometric identification of gold clusters protected with BSA.¹⁵⁰ They have shown a mass shift of 25 Au atoms after cluster formation and the cluster was assigned to be Au_{25} @BSA. Note that Au_{25} is one of the magic numbers in clusters. These data were further supported by thermogravimetric analysis. Another magic cluster core, Au_{38} @BSA was prepared by Muhammed *et al.* by core etching of gold nanoparticles.¹⁴⁸ This was also red luminescent. MALDI MS data revealed that only Au_{38} is formed in this process as no other peaks were observed in the higher mass region. Schneider and co-workers proposed the formation of blue luminescent Au_8 core at mild basic conditions (pH 8) and red luminescent Au_{25} core after reducing with ascorbic acid at pH 3. They have used CHCA as the matrix in MALDI TOF and got a Gaussian type of distribution having a series of peaks.¹⁴⁶ Two types of peaks were present, major peaks were separated by m/z 197 due to Au and minor peaks were separated by m/z 32 (from the major peaks) due to sulphur attachment, assuming the formation of Au_nS_m^+ aggregates. The peaks with maximum intensity were

related to the high population of Au₂₂–Au₂₅ cores. Protein structure plays an important role in cluster synthesis. Normally, harsh conditions were used for cluster synthesis and at such conditions proteins change their structure as the structure is highly dependent on pH of the solution used. Predefining the protein structure by controlling the solution pH can help to get different cores as protein structure plays an important role in cluster formation. To prove this hypothesis (tailoring protein structure by controlling solution pH), Yu *et al.* have used CO as a mild reducing agent and maintained the pH of the solution and could isolate five different gold cluster cores (Au₄, Au₈, Au₁₀, Au₁₃ and Au₂₅) at different reaction conditions using BSA as the protein of choice.¹⁵² As usual, at high pH (>pH 11) Au₂₅ was formed while at mild basic condition (like pH 7.4 maintained using phosphate buffer) smaller cores like Au₁₃ were formed (see Fig. 11A). The cores are assigned in terms of mass shift observed in MALDI MS. By changing the Au : BSA concentration at pH 7.4 they could find three smaller cores namely, Au₄, Au₈ and Au₁₀ which were confirmed from their respective mass spectra (see Fig. 11B).

There is always some amount of free protein during cluster synthesis. This can be due to excess protein or regeneration of free protein with time (see later for details). Some groups have tried to separate the clusters from excess protein and cluster mixtures. Li *et al.* have dansylated (common green fluorescence tag for proteins which does not change protein conformation) BSA to synthesize the red luminescent clusters. After separation through Sephadex G-75 gel, clusters were collected and the mass spectrum showed the same Au₂₅ core.¹⁴⁵ In another approach by Guan *et al.* free BSA was removed from the cluster solution by specific binding with Zn²⁺ ion. After separation, they got only the Au₂₅@BSA peak without free BSA.¹⁷⁵

Human transferrin has also been used for Au cluster synthesis. Xavier *et al.* through MALDI TOF MS showed a broad distribution of Au nanoclusters ranging from Au₁₀–Au₅₅ with peak maxima at 22–33 Au. Between two separate series observed, major peaks are separated by *m/z* 197 due to Au and the minor peaks are separated by *m/z* 32 due to sulfur.¹⁷⁶

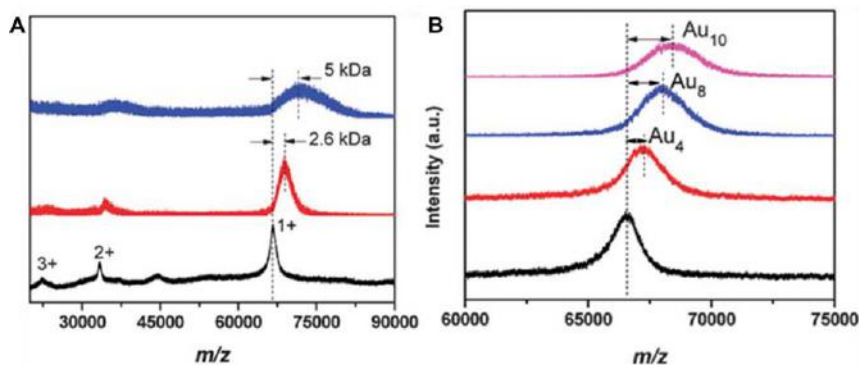


Fig. 11 (A) MALDI MS of Au₄, Au₈ and Au₁₀ protected with BSA synthesized at pH 7.4 (using phosphate buffer) by varying BSA to Au ratio from 1 : 5, 1 : 8 and 1 : 12, respectively. Au₁₃ and Au₂₅ are shown in (B). Au₁₃ was prepared at pH 7.4 using BSA : Au ratio to be 1 : 24 while Au₂₅ was prepared at pH 11. Reproduced from Ref. 152 with permission from The Royal Society of Chemistry.

Xavier *et al.* have reported the Au₂₅ core protected with native (bovine) lactoferrin.³⁹ They have also identified the intermediate Au₁₃ core from the MALDI MS data. They have extended their study to see the evolution of clusters where they have shown that gold ions organize to create the cluster core through aurophilic interactions leading to regeneration of the free protein. We'll discuss this in detail in the following sub-section.

Kawasaki *et al.* have reported synthesis of different cluster cores using pepsin by changing the pH of the system.¹⁵⁸ They have observed red luminescent Au₂₅ at pH 12 while Au₁₃ forms at pH 1 and blue emitting Au₈ with Au₅ were observed at pH 9. They have used 2-mercaptothiazole (MBA) as well as SA as matrices. They could not find a molecular ion peak for Au₂₅@pepsin but they have assigned the Au₁₃ core in the case of green emitting clusters formed at pH 1. Fragmented species like Au₁₁, Au₉, Au₇ and Au₆ were also observed in the mass spec. They have observed that nearest peaks were separated by m/z 32 due to sulfur and another unknown species with m/z 177 separation also exists which they have attributed as glycine-cysteine conjugate which can fragment from the protein during laser desorption. Similarly they have found Au₈ and Au₅ in MALDI TOF at pH 9. Wei *et al.* have first reported Au_{QCS}@Lyz but they did not show any mass spectrum for the clusters.¹⁶³ Chen *et al.* have reported blue emitting Au₈ clusters protected with Lyz at pH 3 and used the cluster for sensing glutathione in a single drop of blood.¹⁶² They have shown MALDI MS of the clusters and proved that the cluster has a Au₈ core. They have proposed pH-dependent change in protein secondary structure that can lead to bigger clusters like Au₂₅ at pH 12. Baksi *et al.* have reported the formation of Au₁₀ core inside a single protein molecule of Lyz.¹⁶¹ They have proved a single cluster within a single protein by careful examination of the protein aggregates. They have also shown through concentration-dependent study that a maximum of Au₁₂ core is possible for a smaller protein like Lyz. They have also shown single cluster protected with multiple proteins at certain concentrations. We will discuss this in detail in the following subsection. There are several other protein protected clusters existing in the literature which were characterized by other tools but not by mass spectrometry.

Number of protein protected gold clusters is many compared to silver clusters due to inherent instability of silver clusters compared to gold clusters. Among them only a few have been characterized by MS. Mathew *et al.* have prepared Ag₁₅ protected by BSA.²⁸ They have confirmed the core from multiple charge states of BSA (+2, +3 *etc.*) by calculating the mass difference from the parent BSA peak. The separation is about m/z 1.6 kDa for +1 charge state, whereas the mass difference is around 800 for +2 charge state and about 500 Da for +3 charge state. They have also studied the effect of NaBH₄ by varying the overall concentration of it and found that NaBH₄ helps in transforming Ag⁺ to Ag⁰ without changing the cluster core. In another report, Anand *et al.* have synthesized different Ag clusters protected with HSA.¹⁵⁴ They have found an Ag₉ core by the slow reduction of Ag⁺ by HSA at pH 11 for 10 hours whereas Ag₁₄ forms by rapid reduction of Ag⁺ in presence of NaBH₄. Around 1 kDa mass shift was observed from the main BSA for Ag₉@HSA while the shift is about 1.5 kDa for Ag₁₄@HSA (see Fig. 12A).

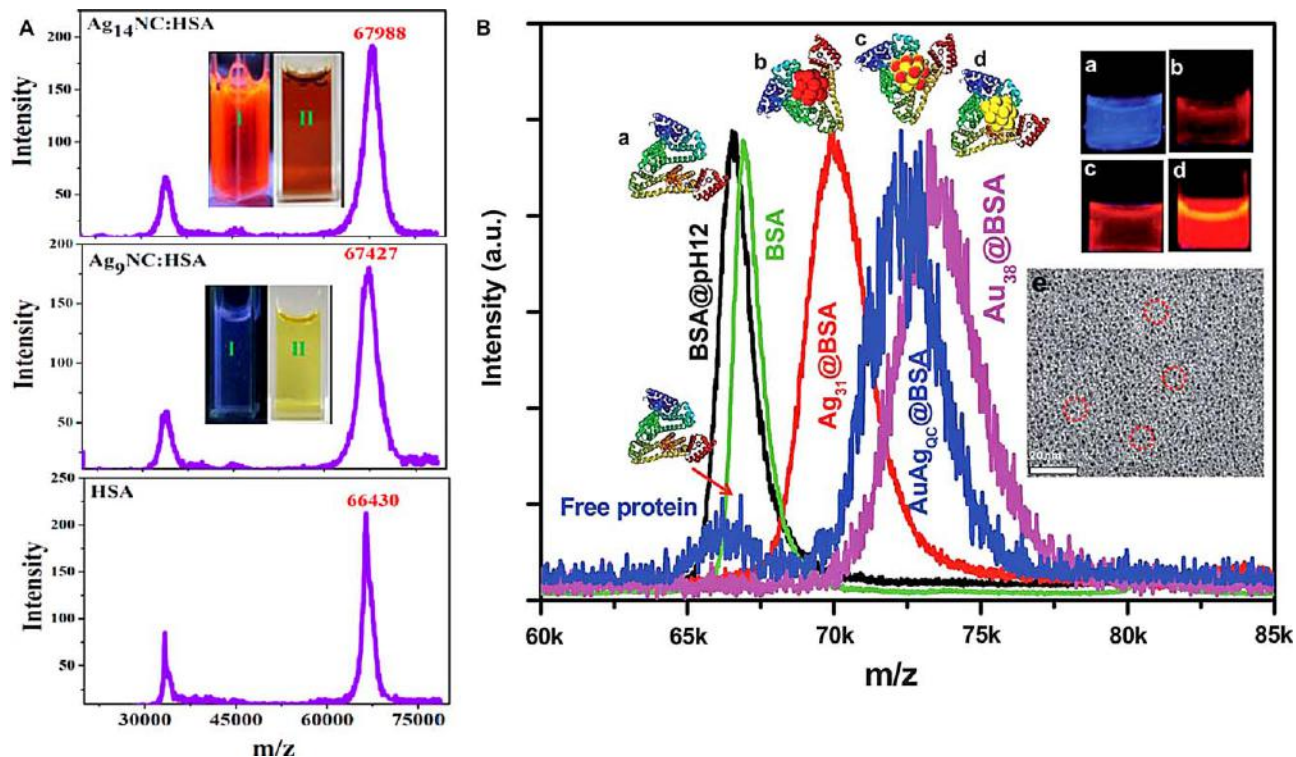


Fig. 12 (A) MALDI-TOF mass spectra of HSA (lower panel), Ag_9/HSA (middle panel), and $\text{Ag}_{14}/\text{HSA}$ (upper panel). Corresponding photographs in visible as well as UV light are shown in the respective inset. $\text{Ag}_9@/\text{HSA}$ forms after 10 hours of reaction time at 37°C at pH 11 without adding any external reducing agent. $\text{Ag}_{14}@/\text{HSA}$ can be prepared within a few minutes by adding NaBH_4 to a mixture of Ag^+ , HSA at pH 11. Ag_{14} can be converted to Ag_9 simply by adding H_2O_2 in the solution within 5 minutes. On the other hand, Ag_9 can be converted to Ag_{14} by addition of NaBH_4 . ©ACS Publishing. Reproduced with permission.¹⁵⁴ (B) MALDI MS showing alloy cluster formation from a 1 : 1 mixture of $\text{Au}_{38}@/\text{BSA}$ and $\text{Ag}_{31}@/\text{BSA}$ clusters. The alloy cluster can be assigned as $(\text{AuAg})_{38}@/\text{BSA}$. Schematic representations of all the species have been shown along with the corresponding peaks. Photographs of a) BSA at pH 12, b) $\text{Ag}_{31}@/\text{BSA}$, c) $(\text{AuAg})_{38}@/\text{BSA}$ and d) $\text{Au}_{38}@/\text{BSA}$ under UV light are shown in the inset. The as-formed alloy clusters have around 1 nm core size as shown in TEM image (inset e). Reproduced from Ref. 29 with permission from The Royal Society of Chemistry.

Gold and silver can form alloys in bulk as well as in the nano-regime. Gold-silver alloy clusters are reported for monolayer protected clusters. Mohanty *et al.* have reported Au@Ag quantum clusters using BSA as a protecting agent.²⁹ They have prepared Ag₃₁@BSA and Au₃₈@BSA and mixed them together in different proportions and found the formation of a tunable alloy cluster with intermediate mass (in between Ag₃₁@BSA and Au₃₈@BSA) (see Fig. 12B). For example, a 10:90 mixture of Ag₃₁:Au₃₈ results in substitution of a few Au atoms by Ag while for the 90:10 mixture substitution of a few Ag atoms by gold occurs. Absence of both the parent cluster peaks suggests tuneable alloy cluster formation throughout the compositional window studied. They have also tried to prepare the alloy clusters by galvanic exchange assuming that in case Ag and Au clusters react with each other to form an alloy, there must be some reactivity of individual ions. They prepared Ag clusters and added HAuCl₄ in the solution and after reaction they observed the formation of AgCl confirming reactivity of the cluster and interchange of Ag atoms by Au. A similar kind of tuneable alloy clusters were observed in the case of Lyz also where different ratios of Au₁₁@Lyz and Ag₁₃@Lyz were mixed together.¹⁷⁷

6.2 Non-noble metal clusters in protein templates

There are only a few reports of metal clusters other than gold and silver in the case of protein protected clusters. Goswami *et al.* have reported blue emitting copper clusters in BSA scaffold and used them as potential sensors for Pb²⁺.¹⁷ They have prepared blue emitting Cu clusters by mixing Cu salt with BSA at pH 12 at 55 °C. They have found two smaller cluster cores namely, Cu₅ and Cu₁₃ in MALDI MS.

In another study they have made luminescent iron clusters in solution starting from hemoglobin (Hb), as the Fe source as well as protecting scaffold.¹⁶ Pipyridine was used to bring Fe²⁺/Fe³⁺ out from the porphyrin ring to the protein matrix and then subsequent reduction by NaBH₄ at room temperature to form yellow luminescent Fe clusters in solution. They have tried MALDI MS of the as-synthesized material to get an idea about the nuclearity. Hb showed two peaks in MALDI MS centered at *m/z* 15 230 due to α -globin chain and at *m/z* 15 990 due to β -globin chain. These two peaks shifted to *m/z* 15 760 and 16 500, respectively after cluster formation and the corresponding cluster core can be roughly assigned as Fe₇₋₁₀@Hb. This assignment might not be exactly correct due to the broadness of the peak and poor resolution at that mass range. ESI MS could be the best option to find the exact core in solution as it does not give much fragments like MALDI MS. They did not get any ESI MS of the as-synthesized Fe_{QCs}@Hb, which is a common problem for all protein protected clusters. To resolve this issue, they have tried ligand exchange with a smaller ligand known to form Fe nanoparticles, namely, trioctyl phosphineoxide (TOPO) as their ligand of choice and successfully extracted the exchanged product in chloroform. ESI MS of the ligand exchanged product using chloroform and acetonitrile as the solvent mixture showed multiple peaks due to Fe clusters namely, [Fe₈(TOPO)(H₂O)₂]⁺, [Fe₁₀(TOPO)₃(H₂O)₃]⁺, [Fe₁₂(TOPO)₃(H₂O)₃]⁺ and [Fe₁₃(TOPO)₂(H₂O)]⁺. Presence of H₂O was further confirmed by NMR.

Along with these major peaks, some small intensity peaks also appear which are mainly due to ligand and water attachments and detachments.

This was further proved using extensive MS/MS of the peaks. Most of the peaks show ligand loss in MS/MS. For example, $[\text{Fe}_{13}(\text{TOPO})_2(\text{H}_2\text{O})]^+$ and $[\text{Fe}_{10}(\text{TOPO})_3(\text{H}_2\text{O})_3]^+$ lose one TOPO to give $[\text{Fe}_{13}(\text{TOPO})(\text{H}_2\text{O})]^+$ and $[\text{Fe}_{10}(\text{TOPO})_2(\text{H}_2\text{O})_3]^+$, respectively in MS/MS. Another type of fragmentation was also observed when $[\text{Fe}_{12}(\text{TOPO})_3(\text{H}_2\text{O})_3]^+$ was subjected to MS/MS experiment. Two Fe losses were observed to give a final $[\text{Fe}_{10}(\text{TOPO})_3(\text{H}_2\text{O})_3]^+$ product. $[\text{Fe}_8(\text{TOPO})(\text{H}_2\text{O})_2]^+$ first loses one ligand to give $[\text{Fe}_8(\text{H}_2\text{O})_2]^+$ and then two water molecules to give a bare Fe_8 core (see Fig. 13 for details).

There are some reports on other metal clusters like Pt but no mass spectrum was reported. Some of the protein and cluster systems along with their applications are listed in Table 2.

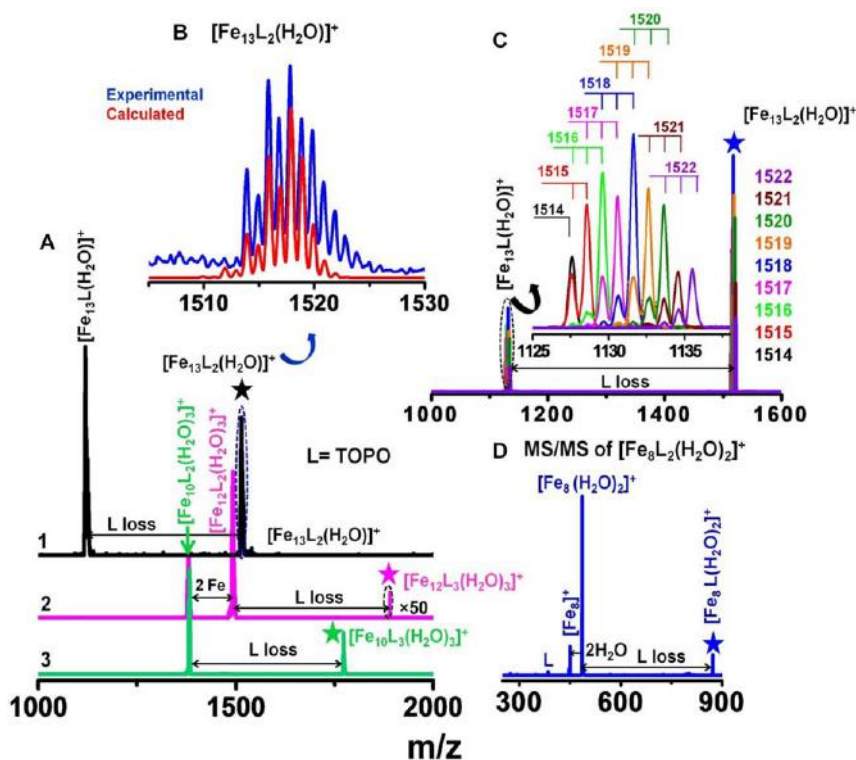


Fig. 13 (A) ESI MS/MS of 1) $[\text{Fe}_{13}(\text{TOPO})_2(\text{H}_2\text{O})]^+$, 2) $[\text{Fe}_{12}(\text{TOPO})_3(\text{H}_2\text{O})_3]^+$ and 3) $[\text{Fe}_{10}(\text{TOPO})_3(\text{H}_2\text{O})_3]^+$, showing subsequent ligand losses. For all cases parent ion is marked with * and for fragments compositions are indicated. $[\text{Fe}_{12}(\text{TOPO})_3(\text{H}_2\text{O})_3]^+$ shows different kind of fragmentations than $[\text{Fe}_{13}(\text{TOPO})_2(\text{H}_2\text{O})]^+$ and $[\text{Fe}_{10}(\text{TOPO})_3(\text{H}_2\text{O})_3]^+$. Here along with one ligand loss, two Fe losses was also observed. Intensity of $[\text{Fe}_{12}(\text{TOPO})_3(\text{H}_2\text{O})_3]^+$ was multiplied by 50 to make it visible. (B) $[\text{Fe}_{13}(\text{TOPO})_2(\text{H}_2\text{O})]^+$ spectrum is compared with the calculated spectrum. (C) MS/MS spectra of each peak in the $[\text{Fe}_{13}(\text{TOPO})_2(\text{H}_2\text{O})]^+$ envelope, with a mass width of 1 Da. Fragmented peaks (one ligand loss) are expanded in the inset showing isotope pattern mainly due to Fe. Isotope pattern of the parent ion is shown in B. (D) ESI MS/MS of $[\text{Fe}_8(\text{TOPO})_2(\text{H}_2\text{O})_2]^+$ showing ligand as well as water losses to give bare $[\text{Fe}_8]^+$ core. Reproduced from Ref. 16 with permission from The Royal Society of Chemistry.

Table 2 List of protein protected clusters and their applications.

Protein	Cluster	Application	Ref.
Bovine serum albumin	Au _{4,13,25,20-25,16} , Ag ₁₅ Cu _{5,13} , Au@Ag	Hg ²⁺ , Cu ²⁺ , Pb ²⁺ , pyrophosphate, quercetin, uric acid sensing, logic gate, bioimaging	17, 144–153, 170
Human serum albumin	Au, Ag _{9,14}	NOx sensing	155–157
Bovine lactoferrin	Au _{13,25,34,40} , Ag	Cluster evolution, FRET, conjugation with RGO, Cu ²⁺ sensing, bio imaging	39, 154
Human serum transferrin	Au ₂₀₋₂₅	Bio imaging, conjugation with RGO	177
Horse radish peroxidase	Au	H ₂ O ₂ sensing	166
Pepsin	Au	Hg ²⁺ sensing, blue, green and red emitting Au _{QC}	159
Hemoglobin	Fe	Luminescent iron cluster synthesis	16
Egg white	Au	H ₂ O ₂ sensing	170
Egg shell membrane	Au, Ag	Solid platform synthesis, metal ion sensing	168
Human hair	Au	Solid platform synthesis, metal ion sensing	169
Insulin	Au _{5,8,13}	Bioactivity, Bio-imaging, cluster growth in crystals, solid state platform, tracking metabolism	167
Lysozyme	Au _{8, 10-12} , Ag ₁₃ , Au@Ag	Hg ²⁺ , GSH sensing, cluster growth, deriving gas phase clusters	162–165
Trypsin	Au	Hg ²⁺ sensing, bio-imaging	160
Chymotrypsin	Ag	Enzyme activity	161

6.3 Evolution of clusters

Chaudhari *et al.* have reported growth of Au clusters in Lf.¹⁵³ They have probed the experiment by varying the concentration of Lf and Au³⁺ and checked the change in MS with respect to time. In a typical synthesis, Au³⁺ was mixed with Lf to get a final concentration of 2.5 mM Au³⁺ and 150 μM of Lf in solution. Lf can interact with Au by various amino acids to form Au⁺-Lf adduct. Lf in aqueous solution shows its molecular ion peak at *m/z* 83 kDa for the monomer and 166 kDa for the dimer formed by salt bridge interaction in solution. After Au adduct formation, the major peak at 83 kDa shifts to 86.2 kDa due to the attachment of 16 Au atoms to the protein. Reduction of Au³⁺ to Au⁺ by several amino acids was proved by XPS. When pH of the solution was elevated to 12.4 by means of NaOH addition, aromatic amino acids are capable of reducing Au⁺ to Au⁰. As disulphide bonds between the cysteines (one of the major contributor of helical structure) break at this pH, free thiol group can bind to the Au and stabilize the as-formed clusters inside the protein. After 4 hours of NaOH addition, red luminescence starts appearing indicating the formation of the cluster core. At this stage, MALDI MS showed a clear peak at 86.7 kDa shifted by 22–23 gold atoms from the parent Lf peak. After 12 hours of incubation, they have observed a small hump at 85.6 kDa due to the appearance of Au₁₃ along with

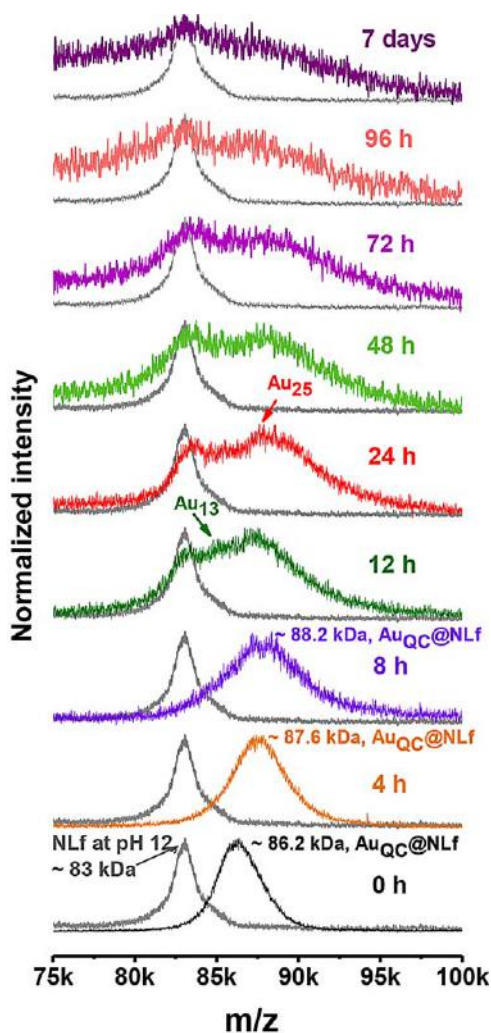


Fig. 14 Time dependent MALDI MS of Au_{QC₅}@Lf showing evolution of Au₂₅ cluster. Immediate addition of Au³⁺ to Lf results in Au⁺-Lf adduct which is converted to the cluster core with incubation in basic conditions. Appearance of Au₁₃ along with Au₂₅ was observed after 12 hours of incubation. After 48 hours, only the Au₂₅ core was observed without any further growth. ©ACS Publishing. Reproduced with permission.¹⁵³

regeneration of free protein and formation of Au₂₅ (see Fig. 14). This was explained in terms of intra and inter-protein reorganization of Au atoms due to aurophillic attraction of gold. When cluster core starts nucleating, it attracts other gold atoms from neighboring proteins which come out as free protein. To validate this hypothesis further, they have added Au³⁺ to the solution and saw that in this condition Au₂₅ is forming with higher intensity and Au₁₃ is absent suggesting complete conversion of all available gold to the Au₂₅ core. This two-step approach is better than a single step method as the amount of cluster was increased, which is further supported by a two-fold increase in the luminescence intensity.

They have carried out similar kind of study with BSA also. They have noticed the formation of Au₂₅ along with the Au₈ intermediate and concluded that the core might be the same but the growth depends completely on the nature of the protein. The above mentioned proteins are bigger (583 amino acid residues) and so it is expected that they can accommodate smaller 1 nm cluster core within. But when the protein size is smaller like insulin, there is a chance that clusters cannot form inside the protein rather multiple proteins can stabilize one core. Such type of studies were done with insulin where clusters were grown uniformly inside micro-crystals of protein and that was proved by depth dependent two-photon excitation spectroscopy and RAMAN spectroscopy but mass spectrum is not available for this specific system.¹⁶⁶

Recently, Baksi *et al.* have reported growth of gold clusters inside a small protein Lyz (129 amino acid residues).¹⁶¹ They have shown that a maximum of 12 atom gold core can be accommodated inside a single protein irrespective of the concentration of Au or protein used. Lyz forms aggregates both in solution and in gas phase. When clusters form, the main protein peak shifts by around m/z 2 kDa in the monomer region confirming the presence of Au₁₀ core attached to the protein. There are shifts in the aggregate region also. They have seen peaks corresponding to Lyz⁺, Lyz₂⁺, Lyz₃⁺ *etc.* for parent protein while, (Au₁₀@Lyz)⁺, (Au₁₀@Lyz)₂⁺, (Au₁₀@Lyz)₃⁺, *etc.*, after cluster formation confirming similar kind of aggregation tendency of the protein after cluster formation. They have not seen any peak corresponding to Au₁₀@Lyz_n which means that the cluster is inside the protein and while aggregating the whole species forms aggregates. Multiple proteins protecting a single cluster core was also observed when very low concentration of gold was used compared to the protein. In this case, amount of gold was not enough to saturate the protein and therefore when clusters started nucleating, multiple proteins could protect one single core. Therefore, it can be concluded that cluster core size is directly correlated to the protein size.

6.4 Gas phase clusters from protein templates

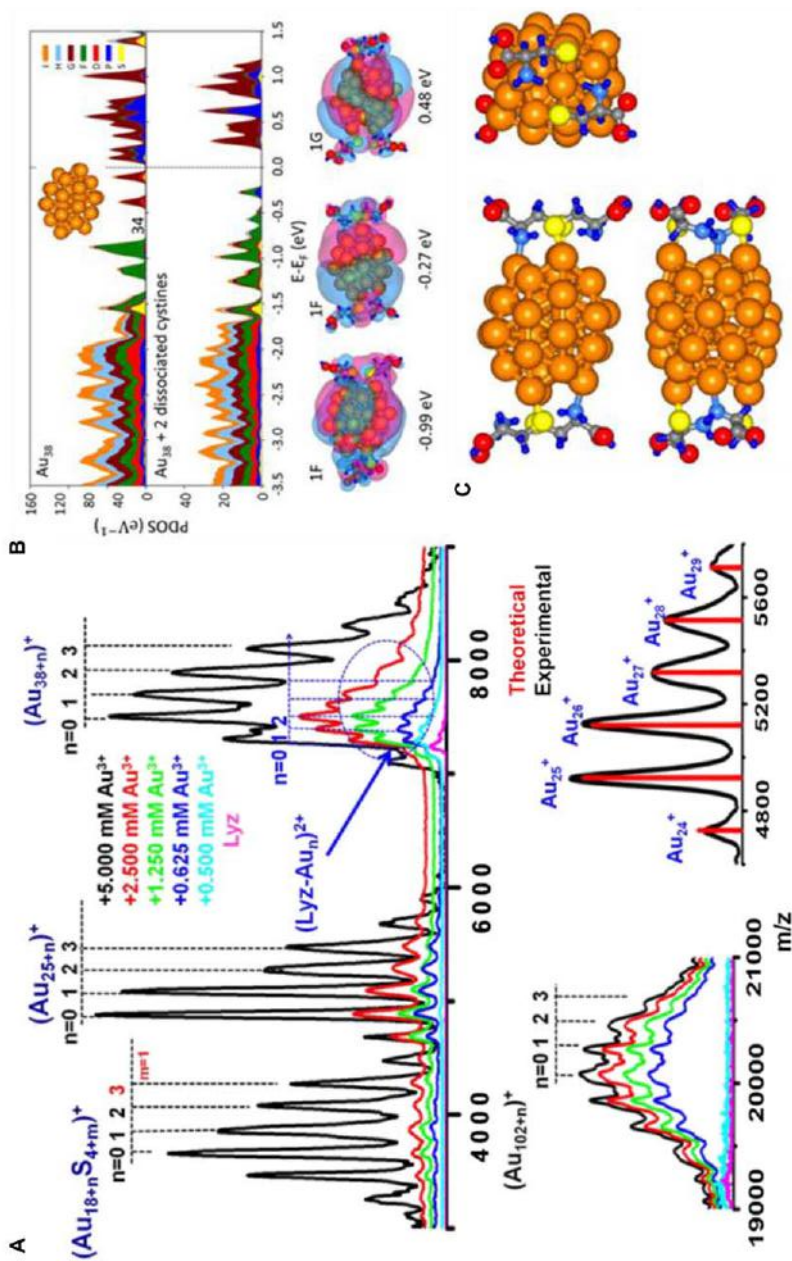
As discussed above, luminescent protein protected clusters exist in solution with zero valent oxidation state of the metal (for example, Au⁰ state for Au clusters). Cluster forms *via* the metal bound protein complex (Au⁺-Protein adduct for Au cluster formation) where metal is in its intermediate oxidation state.¹⁵³ In this section we will discuss a new class of materials which were observed recently by Baksi *et al.*¹⁷⁸ They have observed that when Au⁺-Lyz adducts were subjected to laser ablation, some bare clusters were formed in the gas phase. When Au³⁺ was mixed with Lyz, Au was uptaken by the protein and a corresponding change is seen in the mass spectrum in the form of appearance of multiple peaks separated by m/z 197 due to Au attachments (Lyz⁺ peak appears at m/z 14300). Maximum 10 Au attachments were observed in the MALDI MS which was justified in terms of limited (eight cysteines forming 4 disulfide bonds) cysteine content. In the lower mass region (<10 kDa), multiple envelopes

can be observed consisting of multiple peaks separated by m/z 197 and the peak maxima of the envelopes were observed at $\text{Au}_{18}\text{S}_4^+$, Au_{25}^+ and Au_{38}^+ . Au_{102}^+ was also observed but with less intensity (see Fig. 15A). Note that, Au_{25} , Au_{38} and Au_{102} are known to be magic number clusters when considered along with monolayer protection due to the shell closing electronic structure which have been crystallized already. Sulfur attachments were justified in terms of attachment of Au with the thiol group of cysteine residues. Au_{38} appears only at highest concentrations of Au^{3+} . In all other cases, in that region $(\text{Au}_n\text{-Lyz})^{2+}$ peaks appear with m/z 99 separation between the adjacent peak due to Au^{2+} (Au_{38}^+ mass is comparable with the $(\text{Au}_n\text{-Lyz})^{2+}$). They have also seen that Au_{38}^+ forms after a certain time of incubation of the adducts. Similar type of cluster formation was observed in negative ion mode also but the intensity was less compared to positive ion mode indicating that the clusters are more stable in the positive ion mode. To check whether these clusters form in solution or not, they have done ESI MS of the adducts and observed that maximum 3 Au attachment with the protein occurs which may be due to charge induced dissociation of large adducts at high charge state (+10, +11, etc.). There was no signature of bare clusters in the solution phase suggesting laser induced formation of such clusters in the gas phase. They have checked this phenomenon with other proteins namely, BSA and Lf also but Lyz was found to work best among these three. As already mentioned, Lyz is a small protein and can accommodate only up to 12 atom core inside it (see Section 5.3), it is obvious that the clusters (Au_{38} or Au_{102}) cannot form inside it. These clusters might be forming in the gas phase or may be forming in the solution itself and are loosely bound to the protein. Therefore, when they are subjected to laser ablation, they detach from the protein and appear as bare clusters.

When laser is fired, Au - bound protein adducts come to the gas phase. A gaseous plasma consisting of several ions, molecules, atoms and electrons is formed. A delay time is given before extraction of the ions which is enough for inter and intra molecular reaction in the plasma. Some of the Au atoms detach from the protein and they aggregate among themselves to form bare gas phase clusters. When these clusters nucleate from individual atoms, heat of aggregation should be removed from the system for stabilization. In this case, the above mentioned reactions are facilitated by the abundance of protein molecules and their gold adducts in the reaction zone, since their large mass slows down their movement and separation from the plasma cloud. Being a macromolecule, proteins have several degrees of freedom and can act as a heat bath. Several unimolecular reactions are possible like:

1. $\text{Au}_n + \text{Au}_m^+ \rightarrow \text{Au}_{n+m}^+ \quad n, m = 1, 2, 3, \dots$
2. $(\text{Lyz-Au}_n)^+ + \text{Au}_m \rightarrow (\text{Lyz-Au}_{n+m})^+ \quad n = 0, 1, 2, 3, \dots; m = 1, 2, 3, \dots$
3. $(\text{Lyz-Au}_n)^+ + (\text{Lyz-Au}_m) \rightarrow (\text{Lyz-Au}_{n+k})^+ + (\text{Lyz-Au}_{m-k}) \quad n, m = 1, 2, 3, \dots; k(<m) = 1, 2, 3, \dots$

All these reactions are possible as the ions are extracted after a certain delay time (MALDI MS is generally performed by using a delayed extraction process) which is enough for aggregation reactions. By changing



the delay time, one can get most stable product from mixture of possible products.

In proteins, cysteines form disulfide bond and exist as cystine units (dimer of cysteine) which is one of the causes of helicity of proteins. Keeping in mind the strong affinity of Au towards sulfur, it is assumed that Au ions bind to cysteine residues of the proteins. When Au ions are uptaken by the protein, disulfide bonds break and protein secondary structure is lost. This process can help the bare clusters to achieve their stability in gas phase. This was explained taking Au_{38} as a model through density functional theory calculations.

As mentioned above, Au_{25} , Au_{38} are known to be magic number clusters in the case of monolayer protection. But their gas phase analogues, bare Au_{25} , Au_{38} are not magic numbers by their electron count (magic numbers are 20, 34(40), 58, 92 *etc.*). For example, for Au_{38} to be a magic number, it must lose 4 electrons to get magic number stability which is possible only if interaction of protein with such clusters is considered. For lowering down the computational burden, they have considered only cystines, not the whole protein. If two cystines are bound to Au_{38} surface and dissociate to 4 cysteines, 4 electrons will be lost ($38 - 4 = 34 e^-$) and the cluster can get magic number stability. A distorted truncated octahedron (d-TO) structure was observed for bare Au_{38} which is different from its monolayer protected structure (see Fig. 15B). When a cystine binds to a d-TO Au_{38} surface, it does not change the overall structure or electronic arrangement. However, upon dissociation of two cystines to four cysteines, they adsorb strongly on the surface with a binding energy of 1.97 eV per cystine molecule (see Fig. 15C). Thus for dissociative binding of two cystines we get,

$$E[\text{Au}_{38}(\text{d-TO})] + 2E[\text{Cystine}] - E[\text{Au}_{38}(\text{Cysteine})_4] = 3.94 \text{ eV}$$

By this process, a HOMO–LUMO gap of 0.5 eV opens up and the cluster now has a magic number of electrons. The same calculation can be extended to Au_{102} where interaction with 5 cystines is required as the

Fig. 15 (A) MALDI MS of Au^+ -Lyz in the linear positive mode showing formation of bare $\text{Au}_{18}\text{S}_4^+$, Au_{25}^+ , Au_{38}^+ and Au_{102}^+ . Three main envelopes were observed in the lower mass range (<10 kDa). Each envelope is composed of multiple peaks separated by m/z 197 due to Au. $\text{Au}_{18}\text{S}_4^+$, Au_{25}^+ , Au_{38}^+ and Au_{102}^+ have the highest intensity compared to neighbouring peaks in the corresponding envelope indicating higher stability of these specific species in the gas phase compared to others. Au_{38} region overlaps with the +2 charge state of protein. Au_{38}^+ (and associated envelope) was observed at the highest concentration of Au^{3+} where peaks are separated by m/z 197 due to Au. This m/z 99 difference (between Au^{2+} and Au^+) can be easily resolved at the mass range. Experimental data matches well with the calculated value as shown for Au_{25}^+ . (B) Calculated PDOS for Au_{38} showing distorted truncated octahedron structure whose energy is lower by 1.07 eV than that of an ideal TO structure. Dashed vertical line at $E-E_F = 0$ is showing the midpoint of HOMO and LUMO energy levels. In the lower panel PDOS of an optimized $\text{Au}_{38}(\text{Cysteine})_4$ is shown. In the orbital isosurface images, positive and negative orbital values are coloured light blue and pink, and the orbital energies symmetries are marked. A stabilization energy (shell closure gap) of 0.5 eV was observed after interaction of Au_{38} cluster with two cystine residues of the protein, which ultimately got converted to four cysteines. (C) Three views of the structure of $\text{Au}_{38}(\text{cysteine})_4$ with four adsorbed cysteine ($\text{HO}_2\text{CCH}(\text{NH}_2)\text{CH}_2\text{S}^-$) residues, resulting from two dissociated cystine units. ©Wiley-VCH Publishing. Reproduced with permission.¹⁷⁸

nearest magic number is 92. This study clearly explains the interaction of protein with clusters in the gas phase.

In another study, they tried to dope foreign metals with these clusters in the gas phase.¹⁷⁷ Many transition metals like Ag, Cu, Pd, Pt, *etc.*, are known to form alloys both in bulk as well as in the nanoscale regime. They have used several metal ions covering 3d and 4d transition metals namely, Fe, Ni, Cr, Cu, Zn, Ag, Pd and Pt which are known to form alloys in bulk with gold. They have mixed Au⁺-Lyz adduct and M-Lyz adduct in 3 : 1 ratio (optimized from several concentration dependent studies) and found that only Pd was recognized in the gas phase by gold and formed an alloy. Other metal ions act as catalyst for specific Au cluster formation. For example, Ni²⁺, Cr³⁺ and Fe²⁺ enhance the intensity of Au₂₅⁺ but does not form any alloy with gold in gas phase. In presence of Pt, the Au₁₈S₄ region was enhanced and all the other peak positions remained almost the same. As molecular weights of Au (197) and Pt (195) are nearly the same, it is not possible to conclude whether any alloy was formed or not. Solely Au₂₅⁺ was formed when Cu²⁺ was added to the system, possibly due to substitution of Au binding sites by Cu which was reflected in the total number of Au attachments to the protein. Although Ag is most well-known to form alloy with gold in all solutions (bulk, nanoparticles, monolayer and protein protected clusters) but such an alloy was not detected in the gas phase. In the case of Pd, maximum of two Pd attachments were observed in the gas phase. Total shape of the envelope changed after alloy formation. Maximum peak was observed for Au₂₀Pd₂S⁺ (comparable to Au₂₅⁺ in electron count). Although Au₂₄Pd is the most stable species in solution state but in gas phase Au₂₇Pd⁺ showed the maximum intensity although the neighboring peaks do not vary much in terms of abundance. No alloy formation was observed in the Au₃₈ region and the relative intensity (Au₂₅ to Au₃₈) is higher here compared to pure gold-adducts. This signifies catalytic enhancement of stability of Au₃₈ in presence of Pd. This was further confirmed when the mixed adducts (Au-Lyz and Pd-Lyz) were incubated for two days and then subjected to laser ablation, Au₃₈ appeared as the most intense peak (more intense than the main protein peak). Another envelope appears after the Au₃₈ region which was originally absent only in the case of Au. In this region, Au₄₇PdS₂⁺ was the most intense one although it is not a magic number implying that Pd facilitates formation of metastable clusters in the gas phase. Alloy formation occurs in the gas phase irrespective of the physical mixture of Au and Pd adducts or direct addition of Pd²⁺ salt into Au adduct solution implying simultaneous Pd uptake by the protein in presence of Au which was proven further by ESI MS.

7 Conclusion and future perspectives

Investigation of atomically precise pieces of matter by mass spectrometry has given information on several new cluster systems. Their chemistry and materials science have advanced tremendously in the past few years. Each of those investigations has used mass spectrometry extensively. Tandem mass spectrometry of several clusters and cluster fragments

must be investigated to know them in detail. Some of those gas phase products can only be investigated with the help of mass spectrometry. While excellent mass spectra have become possible due to new developments in mass spectrometry, some of those studies have not been possible on a few other clusters, such as MALDI MS of $\text{Ag}_{44}\text{SR}_{30}^{4-}$. New methods for MALDI have to be found for such systems. ESI MS has not been possible so far on protein protected clusters. It is also important to note that studies on clusters have given several challenges, especially in the isolation of isomeric clusters. As cluster systems become more complex, ion mobility may become one of the important aspects of mass analysis of clusters. Chemistry of cluster ions in the gas phase, derived from clusters in solution will become attractive. There is also a possibility to study the properties of naked clusters derived from protein templates, especially their catalysis. All these studies will make this area rich in the coming years.

Acknowledgements

We thank the contributions of our co-workers who have contributed to the original research reported in this chapter. We thank the Nano Mission, Government of India, for generously supporting our research. We are also grateful to the Department of Science and Technology for sponsoring several research grants which made some of these studies possible.

References

- 1 J. B. Fenn, M. Mann, C. K. Meng, S. F. Wong and C. M. Whitehouse, *Mass Spectrom. Rev.*, 1990, **9**, 37.
- 2 D. J. Harvey, *Mass Spectrom. Rev.*, 1999, **18**, 349.
- 3 R. Aebersold and M. Mann, *Nature*, 2003, **422**, 198.
- 4 K. Dettmer, P. A. Aronov and B. D. Hammock, *Mass Spectrom. Rev.*, 2007, **26**, 51.
- 5 L. G. Abdul Halim, S. Ashraf, K. Katsiev, A. R. Kirmani, N. Kothalawala, D. H. Anjum, S. Abbas, A. Amassian, F. Stellacci, A. Dass, I. Hussain and O. M. Bakr, *J. Mater. Chem. A*, 2013, **1**, 10148.
- 6 L. A. Angel, L. T. Majors, A. C. Dharmaratne and A. Dass, *ACS Nano*, 2010, **4**, 4691.
- 7 T. M. Bernhardt, *Int. J. Mass Spectrom.*, 2005, **243**, 1.
- 8 I. Chakraborty, R. G. Bhui, S. Bhat and T. Pradeep, *Nanoscale*, 2014, **6**, 8561.
- 9 A. Dass, A. Stevenson, G. R. Dubay, J. B. Tracy and R. W. Murray, *J. Am. Chem. Soc.*, 2008, **130**, 5940.
- 10 A. C. Dharmaratne, T. Krick and A. Dass, *J. Am. Chem. Soc.*, 2009, **131**, 13604.
- 11 B. Domon and R. Aebersold, *Science*, 2006, **312**, 212.
- 12 C. A. Fields-Zinna, M. C. Crowe, A. Dass, J. E. Weaver and R. W. Murray, *Langmuir*, 2009, **25**, 7704.
- 13 C. A. Fields-Zinna, M. C. Crowe, A. Dass, J. E. F. Weaver and R. W. Murray, *Langmuir*, 2009, **25**, 7704.

- 14 C. A. Fields-Zinna, J. S. Sampson, M. C. Crowe, J. B. Tracy, J. F. Parker, A. M. deNey, D. C. Muddiman and R. W. Murray, *J. Am. Chem. Soc.*, 2009, **131**, 13844.
- 15 A. Ghosh, T. Udayabhaskararao and T. Pradeep, *J. Phys. Chem. Lett.*, 2012, **3**, 1997.
- 16 N. Goswami, A. Baksi, A. Giri, P. L. Xavier, G. Basu, T. Pradeep and S. K. Pal, *Nanoscale*, 2013, **6**, 1848.
- 17 N. Goswami, A. Giri, M. S. Bootharaju, P. L. Xavier, T. Pradeep and S. K. Pal, *Anal. Chem.*, 2011, **83**, 9676.
- 18 J. Guo, S. Kumar, M. Bolan, A. Desireddy, T. P. Bigioni and W. P. Griffith, *Anal. Chem.*, 2012, **84**, 5304.
- 19 K. M. Harkness, D. E. Cliffel and J. A. McLean, *Analyst*, 2010, **135**, 868.
- 20 K. M. Harkness, L. S. Fenn, D. E. Cliffel and J. A. McLean, *Anal. Chem.*, 2010, **82**, 3061.
- 21 K. M. Harkness, B. C. Hixson, L. S. Fenn, B. N. Turner, A. C. Rape, C. A. Simpson, B. J. Huffman, T. C. Okoli, J. A. McLean and D. E. Cliffel, *Anal. Chem.*, 2010, **82**, 9268.
- 22 K. M. Harkness, Y. Tang, A. Dass, J. Pan, N. Kothalawala, V. J. Reddy, D. E. Cliffel, B. Demeler, F. Stellacci, O. M. Bakr and J. A. McLean, *Nanoscale*, 2012, **4**, 4269.
- 23 I. Katakuse, T. Ichihara, Y. Fujita, T. Matsuo, T. Sakurai and H. Matsuda, *Int. J. Mass Spectrom. Ion Processes*, 1985, **67**, 229.
- 24 I. Katakuse, T. Ichihara, Y. Fujita, T. Matsuo, T. Sakurai and H. Matsuda, *Int. J. Mass Spectrom. Ion Processes*, 1986, **74**, 33.
- 25 C. Kumara and A. Dass, *Nanoscale*, 2011, **3**, 3064.
- 26 C. Kumara and A. Dass, *Nanoscale*, 2012, **4**, 4084.
- 27 X. Li, *Cluster Anions in the Gas Phase: Time-of-flight Mass Spectrometry and Photoelectron Spectroscopic Studies*, Thesis, Johns Hopkins University, 2009.
- 28 A. Mathew, P. R. Sajanlal and T. Pradeep, *J. Mater. Chem.*, 2010, **21**, 11205.
- 29 J. S. Mohanty, P. L. Xavier, K. Chaudhari, M. S. Bootharaju, N. Goswami, S. K. Pal and T. Pradeep, *Nanoscale*, 2012, **4**, 4255.
- 30 R. J. O'Hair and G. Khairallah, *J. Cluster Sci.*, 2004, **15**, 331.
- 31 H. Qian, Y. Zhu and R. Jin, *Proc. Natl. Acad. Sci.*, 2012, **109**, 696.
- 32 K. Salorinne, X. Chen, R. W. Troff, M. Nissinen and H. Hakkinen, *Nanoscale*, 2012, **4**, 4095.
- 33 D. M. D. J. Singh, T. Pradeep, J. Bhattacharjee and U. V. Waghmare, *J. Am. Soc. Mass Spectrom.*, 2007, **18**, 2191.
- 34 Z. Takats, J. M. Wiseman, B. Gologan and R. G. Cooks, *Science*, 2004, **306**, 471.
- 35 J. B. Tracy, G. Kalyuzhny, M. C. Crowe, R. Balasubramanian, J.-P. Choi and R. W. Murray, *J. Am. Chem. Soc.*, 2007, **129**, 6706.
- 36 T. Udayabhaskararao, M. S. Bootharaju and T. Pradeep, *Nanoscale*, 2013, **5**, 9404.
- 37 G. Wang and R. B. Cole, *Anal. Chem.*, 1998, **70**, 873.
- 38 Z. Wu, E. Lanni, W. Chen, M. E. Bier, D. Ly and R. Jin, *J. Am. Chem. Soc.*, 2009, **131**, 16672.
- 39 P. L. Xavier, K. Chaudhari, P. K. Verma, S. K. Pal and T. Pradeep, *Nanoscale*, 2010, **2**, 2769.
- 40 I. Chakraborty, J. Erusappan, A. Govindarajan, S. K. Sugi, U. B. R. Thumu, A. Ghosh and T. Pradeep, *Nanoscale*, 2014.
- 41 I. Chakraborty, A. Govindarajan, J. Erusappan, A. Ghosh, T. Pradeep, B. Yoon, R. L. Whetten and U. Landman, *Nano Lett.*, 2012, **12**, 5861.

- 42 I. Chakraborty, W. Kurashige, K. Kanehira, L. Gell, H. Häkkinen, Y. Negishi and T. Pradeep, *J. Phys. Chem. Lett.*, 2013, 3351.
- 43 A. Dass, *J. Am. Chem. Soc.*, 2009, **131**, 11666.
- 44 A. Dass, *J. Am. Chem. Soc.*, 2011, **133**, 19259.
- 45 A. Ganguly, I. Chakraborty, T. Udayabhaskararao and T. Pradeep, *J. Nanopart. Res.*, 2013, **15**, 1.
- 46 Y. Negishi, W. Kurashige, Y. Niihori, T. Iwasa and K. Nobusada, *Phys. Chem. Chem. Phys.*, 2010, **12**, 6219.
- 47 Y. Negishi, K. Nobusada and T. Tsukuda, *J. Am. Chem. Soc.*, 2005, **127**, 5261.
- 48 Y. Niihori, M. Matsuzaki, T. Pradeep and Y. Negishi, *J. Am. Chem. Soc.*, 2013, **135**, 4946.
- 49 M. Moskovits, *Annu. Rev. Phys. Chem.*, 1991, **42**, 465.
- 50 W. A. de Heer, *Rev. Mod. Phys.*, 1993, **65**, 611.
- 51 M. D. Morse, *Chem. Rev.*, 1986, **86**, 1049.
- 52 T. Pradeep, *Nano: The Essentials Understanding Nanoscience and Nanotechnology*, Tata McGraw-Hill Education, 2007.
- 53 W. D. Knight, K. Clemenger, W. A. de Heer, W. A. Saunders, M. Y. Chou and M. L. Cohen, *Phys. Rev. Lett.*, 1984, **52**, 2141.
- 54 D. H. E. Gross and M. E. Madjet, *Z. Phys. B: Condens. Matter*, 1997, **104**, 541.
- 55 H. Rashidzadeh and B. Guo, *Chem. Phys. Lett.*, 1999, **310**, 466.
- 56 H. W. Kroto, J. R. Heath, S. C. O'Brien, R. F. Curl and R. E. Smalley, *Nature*, 1985, **318**, 162.
- 57 S. Maruyama, M. Kohno and S. Inque, *Therm. Sci. Eng.*, 1999, **7**, 1.
- 58 D. M. D. J. Singh, T. Pradeep, J. Bhattacharjee and U. V. Waghmare, *J. Phys. Chem. A*, 2005, **109**, 7339.
- 59 T. Lange and T. P. Martin, *Angew. Chem., Int. Ed. Engl.*, 1992, **31**, 172.
- 60 J. T. Lyon, P. Gruene, A. Fielicke, G. Meijer, E. Janssens, P. Claes and P. Lievens, *J. Am. Chem. Soc.*, 2009, **131**, 1115.
- 61 J. F. Gal, R. Grover, P. C. Maria, L. Operti, R. Rabezzana, G. A. Vaglio and P. Volpe, *J. Phys. Chem.*, 1994, **98**, 11978.
- 62 M. Haertelt, J. T. Lyon, P. Claes, J. de Haeck, P. Lievens and A. Fielicke, *J. Chem. Phys.*, 2012, 136.
- 63 J. Sun, H.-F. Gruetzmacher and C. Lifshitz, *J. Phys. Chem.*, 1994, **98**, 4536.
- 64 P. P. Radi, T. L. Bunn, P. R. Kemper, M. E. Molchan and M. T. Bowers, *J. Chem. Phys.*, 1988, **88**, 2809.
- 65 A. A. Shvartsburg, B. Liu, Z.-Y. Lu, C.-Z. Wang, M. F. Jarrold and K.-M. Ho, *Phys. Rev. Lett.*, 1999, **83**, 2167.
- 66 A. N. Alexandrova, A. I. Boldyrev, H.-J. Zhai and L.-S. Wang, *Coord. Chem. Rev.*, 2006, **250**, 2811.
- 67 M. Krempp, R. Damrauer, C. H. DePuy and Y. Keheyan, *J. Am. Chem. Soc.*, 1994, **116**, 3629.
- 68 K. Larsson, *J. Phys. IV*, 2001, **11**(Pr3), 423.
- 69 J. M. L. Martin and P. R. Taylor, *J. Phys. Chem. A*, 1998, **102**, 2995.
- 70 H.-J. Zhai, Q. Chen, H. Bai, S.-D. Li and L.-S. Wang, *Acc. Chem. Res.*, 2014, **47**, 2435–2445.
- 71 A. Muller and C. Serain, *Acc. Chem. Res.*, 2000, **33**, 2.
- 72 R. Tenne and C. N. R. Rao, *Philos. Trans. R. Soc., A*, 2004, **362**, 2099.
- 73 R. Tenne, M. Homyonfer and Y. Feldman, *Chem. Mater.*, 1998, **10**, 3225.
- 74 R. Tenne, M. Homyonfer and Y. Feldman, *Adv. Met. Semicond. Clusters*, 1998, **4**, 227.
- 75 R. Tenne and M. Redlich, *Chem. Soc. Rev.*, 2010, **39**, 1423.

- 76 M. Bar-Sadan and R. Tenne, *Inorganic Nanoparticles: Synthesis, Applications and Perspectives*, CRC Press, 2011, p. 441.
- 77 O. Brontvein, D. G. Stroppa, R. Popovitz-Biro, A. Albu-Yaron, M. Levy, D. Feuerman, L. Houben, R. Tenne and J. M. Gordon, *J. Am. Chem. Soc.*, 2012, **134**, 16379.
- 78 S. Y. Hong, R. Kreizman, R. Rosentsveig, A. Zak, J. Sloan, A. N. Enyashin, G. Seifert, M. L. H. Green and R. Tenne, *Eur. J. Inorg. Chem.*, 2010, 4233.
- 79 R. Kreizman, S. Y. Hong, F. L. Deepak, A. N. Enyashin, R. Popovitz-Biro, A. Albu-Yaron, G. Seifert and R. Tenne, *Routes for Core-shell Inorganic Nanotubes*, American Chemical Society, 2010, p. FUEL.
- 80 R. Kreizman, S. Y. Hong, J. Sloan, R. Popovitz-Biro, A. Albu-Yaron, G. Tobias, B. Ballesteros, B. G. Davis, M. L. H. Green and R. Tenne, *Angew. Chem., Int. Ed.*, 2009, **48**, 1230.
- 81 R. Levi, O. Bitton, G. Leitus, R. Tenne and E. Joselevich, *Nano Lett.*, 2013, **13**, 3736.
- 82 R. Tenne, *Angew. Chem., Int. Ed.*, 2003, **42**, 5124.
- 83 R. Tenne and M. Bar-Sadan, *Isr. J. Chem.*, 2010, **50**, 393.
- 84 *Inorganic Nanotubes and Nanostructures*, ed. R. Tenne and M. Bar-Sadan, [In: *Isr. J. Chem.*, 2010; **50**(4)], Wiley-VCH Verlag GmbH & Co. KGaA, 2010.
- 85 A. Voldman, D. Zbaida, H. Cohen, G. Leitus and R. Tenne, *Macromol. Chem. Phys.*, 2013, **214**, 2007.
- 86 X. Wang, Y. Xie and Q. Guo, *Chem. Commun.*, 2003, 2688.
- 87 F. Diederich, *Nature*, 1994, **369**, 199.
- 88 Y. R. Hacohen, E. Grunbaum, R. Tenne, J. Sloan and J. L. Hutchison, *Nature*, 1998, **395**, 336.
- 89 M. Brust, M. Walker, D. Bethell, D. J. Schiffrin and R. Whyman, *J. Chem. Soc., Chem. Commun.*, 1994, 801.
- 90 M. Heaven, A. Dass, P. White, K. Holt and R. Murray, *J. Am. Chem. Soc.*, 2008, **130**, 3754.
- 91 M. J. Hostetler, J. E. Wingate, C.-J. Zhong, J. E. Harris, R. W. Vachet, M. R. Clark, J. D. Londono, S. J. Green, J. J. Stokes, G. D. Wignall, G. L. Glish, M. D. Porter, N. D. Evans and R. W. Murray, *Langmuir*, 1998, **14**, 17.
- 92 R. S. Ingram, M. J. Hostetler and R. W. Murray, *J. Am. Chem. Soc.*, 1997, **119**, 9175.
- 93 R. S. Ingram, M. J. Hostetler, R. W. Murray, T. G. Schaaff, J. T. Khoury, R. L. Whetten, T. P. Bigioni, D. K. Guthrie and P. N. First, *J. Am. Chem. Soc.*, 1997, **119**, 9279.
- 94 V. L. Jimenez, D. G. Georganopoulou, R. J. White, A. S. Harper, A. J. Mills, D. Lee and R. W. Murray, *Langmuir*, 2004, **20**, 6864.
- 95 R. L. Wolfe, R. Balasubramanian, J. B. Tracy and R. W. Murray, *Langmuir*, 2006, **23**, 2247.
- 96 I. Chakraborty, T. Udayabhaskararao and T. Pradeep, *Chem. Commun.*, 2012, **48**, 6788.
- 97 K. S. Sugi, I. Chakraborty, T. Udayabhaskararao, J. S. Mohanty and T. Pradeep, *Part. Part. Syst. Charact.*, 2013, **30**, 241–243.
- 98 R. L. Whetten, J. T. Khoury, M. M. Alvarez, S. Murthy, I. Vezmar, Z. L. Wang, P. W. Stephens, C. L. Cleveland, W. D. Luedtke and U. Landman, *Adv. Mater.*, 1996, **8**, 428.
- 99 T. G. Schaaff, G. Knight, M. N. Shafiqullin, R. F. Borkman and R. L. Whetten, *J. Phys. Chem. B*, 1998, **102**, 10643.
- 100 M. Zhu, C. M. Aikens, F. J. Hollander, G. C. Schatz and R. Jin, *J. Am. Chem. Soc.*, 2008, **130**, 5883.
- 101 H. Häkkinen, M. Walter and H. Grönbeck, *J. Phys. Chem. B*, 2006, **110**, 9927.

- 102 A. Das, T. Li, K. Nobusada, C. Zeng, N. L. Rosi and R. Jin, *J. Am. Chem. Soc.*, 2013, **135**, 18264.
- 103 C. Zeng, T. Li, A. Das, N. L. Rosi and R. Jin, *J. Am. Chem. Soc.*, 2013, **135**, 10011.
- 104 C. Zeng, H. Qian, T. Li, G. Li, N. L. Rosi, B. Yoon, R. N. Barnett, R. L. Whetten, U. Landman and R. Jin, *Angew. Chem., Int. Ed.*, 2012, **51**, 13114–13118.
- 105 H. Qian, W. T. Eckenhoff, Y. Zhu, T. Pintauer and R. Jin, *J. Am. Chem. Soc.*, 2010, **132**, 8280.
- 106 P. D. Jadzinsky, G. Calero, C. J. Ackerson, D. A. Bushnell and R. D. Kornberg, *Science*, 2007, **318**, 430.
- 107 H. Yang, J. Lei, B. Wu, Y. Wang, M. Zhou, A. Xia, L. Zheng and N. Zheng, *Chem. Commun.*, 2012, **49**, 300.
- 108 H. Yang, Y. Wang and N. Zheng, *Nanoscale*, 2013, **5**, 2674.
- 109 A. Desireddy, B. E. Conn, J. Guo, B. Yoon, R. N. Barnett, B. M. Monahan, K. Kirschbaum, W. P. Griffith, R. L. Whetten, U. Landman and T. P. Bigioni, *Nature*, 2013, **501**, 399.
- 110 H. Yang, Y. Wang, H. Huang, L. Gell, L. Lehtovaara, S. Malola, H. Hakkinen and N. Zheng, *Nat. Commun.*, 2013, **4**, 2422.
- 111 H. Qian, W. T. Eckenhoff, Y. Zhu, T. Pintauer and R. Jin, *J. Am. Chem. Soc.*, 2012, **132**, 8280.
- 112 Y. Negishi, N. K. Chaki, Y. Shichibu, R. L. Whetten and T. Tsukuda, *J. Am. Chem. Soc.*, 2007, **129**, 11322.
- 113 T. U. B. Rao and T. Pradeep, *Angew. Chem., Int. Ed.*, 2010, **49**, 3925.
- 114 T. U. B. Rao, B. Nataraju and T. Pradeep, *J. Am. Chem. Soc.*, 2010, **132**, 16304.
- 115 I. Chakraborty, W. Kurashige, K. Kanehira, L. Gell, H. Hakkinen, Y. Negishi and T. Pradeep, *J. Phys. Chem. Lett.*, 2013, **4**, 3351.
- 116 S. Giuffrida, G. Ventimiglia, F. L. Callari and S. Sortino, *Eur. J. Inorg. Chem.*, 2006, **2006**, 4022.
- 117 X. Yuan, Z. Luo, Q. Zhang, X. Zhang, Y. Zheng, J. Y. Lee and J. Xie, *ACS Nano*, 2011, **5**, 8800.
- 118 X. Huang, B. Li, L. Li, H. Zhang, I. Majeed, I. Hussain and B. Tan, *J. Phys. Chem. C*, 2011, **116**, 448.
- 119 X. Le Guével, V. Trouillet, C. Spies, G. Jung and M. Schneider, *J. Phys. Chem. C*, 2012, **116**, 6047.
- 120 H. Kawasaki, H. Yamamoto, H. Fujimori, R. Arakawa, M. Inada and Y. Iwasaki, *Chem. Commun.*, 2010, **46**, 3759.
- 121 C. K. Yee, R. Jordan, A. Ulman, H. White, A. King, M. Rafailovich and J. Sokolov, *Langmuir*, 1999, **15**, 3486.
- 122 S. Chen, K. Huang and J. A. Stearns, *Chem. Mater.*, 2000, **12**, 540.
- 123 F. P. Zamborini, S. M. Gross and R. W. Murray, *Langmuir*, 2000, **17**, 481.
- 124 I. Quiros, M. Yamada, K. Kubo, J. Mizutani, M. Kurihara and H. Nishihara, *Langmuir*, 2002, **18**, 1413.
- 125 J. E. Martin, J. P. Wilcoxon, J. Odinek and P. Provencio, *J. Phys. Chem. B*, 2002, **106**, 971.
- 126 Y. Negishi, H. Murayama and T. Tsukuda, *Chem. Phys. Lett.*, 2002, **366**, 561.
- 127 W. Wei, Y. Lu, W. Chen and S. Chen, *J. Am. Chem. Soc.*, 2011, **133**, 2060.
- 128 R. S. Dhayal, J.-H. Liao, Y.-R. Lin, P.-K. Liao, S. Kahlal, J.-Y. Saillard and C. W. Liu, *J. Am. Chem. Soc.*, 2013, **135**, 4704.
- 129 Y. Negishi, K. Igarashi, K. Munakata, W. Ohgake and K. Nobusada, *Chem. Commun.*, 2012, **48**, 660.
- 130 Y. Negishi, T. Iwai and M. Ide, *Chem. Commun.*, 2010, **46**, 4713.

- 131 Y. Negishi, K. Munakata, W. Ohgake and K. Nobusada, *J. Phys. Chem. Lett.*, 2012, **3**, 2209.
- 132 H. Qian, D.-e. Jiang, G. Li, C. Gayathri, A. Das, R. R. Gil and R. Jin, *J. Am. Chem. Soc.*, 2012, **134**, 16159.
- 133 S. R. Biltek, S. Mandal, A. Sen, A. C. Reber, A. F. Pedicini and S. N. Khanna, *J. Am. Chem. Soc.*, 2012, **135**, 26.
- 134 R. Ferrando, J. Jellinek and R. L. Johnston, *Chem. Rev.*, 2008, **108**, 845.
- 135 T. Udayabhaskararao, Y. Sun, N. Goswami, S. K. Pal, K. Balasubramanian and T. Pradeep, *Angew. Chem., Int. Ed.*, 2012, **51**, 2155.
- 136 V. R. Jupally and A. Dass, *Phys. Chem. Chem. Phys.*, 2014, **16**, 10473.
- 137 W. Kurashige, K. Munakata, K. Nobusada and Y. Negishi, *Chem. Commun.*, 2013, **49**, 5447.
- 138 S. L. Christensen, M. A. MacDonald, A. Chatt, P. Zhang, H. Qian and R. Jin, *J. Phys. Chem. C*, 2012, **116**, 26932.
- 139 P. L. Xavier, K. Chaudhari, A. Baksi and T. Pradeep, *Nano Rev.*, 2012, **3**, 14767 and the references cited there in.
- 140 Y. Wang, Y. Cui, Y. Zhao, R. Liu, Z. Sun, W. Li and X. Gao, *Chem. Commun.*, 2012, **48**, 871.
- 141 J. T. Petty, J. Zheng, N. V. Hud and R. M. Dickson, *J. Am. Chem. Soc.*, 2004, **126**, 5207.
- 142 J. Zheng, C. Zhang and R. M. Dickson, *Phys. Rev. Lett.*, 2004, **93**, 1.
- 143 J.-m. Liu, M.-l. Cui, S.-L. Jiang, X.-x. Wang, L.-p. Lin, L. Jiao, L.-H. Zhang and Z.-Y. Zheng, *Anal. Methods*, 2013, **5**, 3942–3947.
- 144 X. Wen, P. Yu, Y.-R. Toh, A.-C. Hsu, Y.-C. Lee and J. Tang, *J. Phys. Chem. C*, 2012, **116**, 19032.
- 145 H.-W. Li, K. Ai and Y. Wu, *Chem. Commun.*, 2011, **47**, 9852.
- 146 X. Le Guével, B. Hötzer, G. Jung, K. Hollemeyer, V. Trouillet and M. Schneider, *J. Phys. Chem. C*, 2011, **115**, 10955.
- 147 J. Xie, Y. Zheng and J. Y. Ying, *Chem. Commun.*, 2010, **46**, 961.
- 148 M. A. Habeeb Muhammed, P. K. Verma, S. K. Pal, A. Retnakumari, M. Koyakutty, S. Nair and T. Pradeep, *Chem. – Eur. J.*, 2010, **16**, 10103.
- 149 Y. Yue, T.-Y. Liu, H.-W. Li, Z. Liu and Y. Wu, *Nanoscale*, 2012, **4**, 2251.
- 150 J. Xie, Y. Zheng and J. Y. Ying, *J. Am. Chem. Soc.*, 2009, **131**, 888.
- 151 P.-C. Chen, C.-K. Chiang and H.-T. Chang, *J. Nanopart. Res.*, 2012, **15**, 1.
- 152 Y. Yu, Z. Luo, C. S. Teo, Y. N. Tan and J. Xie, *Chem. Commun.*, 2013, **49**, 9740.
- 153 K. Chaudhari, P. L. Xavier and T. Pradeep, *ACS Nano*, 2011, **5**, 8816.
- 154 U. Anand, S. Ghosh and S. Mukherjee, *J. Phys. Chem. Lett.*, 2012, **3**, 3605.
- 155 L. Yan, Y. Cai, B. Zheng, H. Yuan, Y. Guo, D. Xiao and M. M. F. Choi, *J. Mater. Chem.*, 2012, **22**, 1000.
- 156 P.-H. Chan and Y.-C. Chen, *Anal. Chem.*, 2012, **84**, 8952.
- 157 S. M. Lystvet, S. Volden, G. Singh, I. M. Rundgren, H. Wen, Ø. Halskau and W. R. Glomm, *J. Phys. Chem. C*, 2013, **117**, 2230.
- 158 H. Kawasaki, K. Hamaguchi, I. Osaka and R. Arakawa, *Adv. Funct. Mater.*, 2011, **21**, 3508.
- 159 H. Kawasaki, K. Yoshimura, K. Hamaguchi and R. Arakawa, *Anal. Sci.*, 2011, **27**, 591.
- 160 S. Narayanan and S. K. Pal, *J. Phys. Chem. C*, 2008, **112**, 4874.
- 161 A. Baksi, P. L. Xavier, K. Chaudhari, N. Goswami, S. K. Pal and T. Pradeep, *Nanoscale*, 2013, **5**, 2009.
- 162 T.-H. Chen and W.-L. Tseng, *Small*, 2012, **8**, 1912.
- 163 H. Wei, Z. Wang, L. Yang, S. Tian, C. Hou and Y. Lu, *Analyst*, 2010, **135**, 1406.

- 164 T. Zhou, Y. Huang, W. Li, Z. Cai, F. Luo, C. J. Yang and X. Chen, *Nanoscale*, 2012, **4**, 5312.
- 165 F. Wen, Y. Dong, L. Feng, S. Wang, S. Zhang and X. Zhang, *Anal. Chem.*, 2011, **83**, 1193.
- 166 C.-L. Liu, H.-T. Wu, Y.-H. Hsiao, C.-W. Lai, C.-W. Shih, Y.-K. Peng, K.-C. Tang, H.-W. Chang, Y.-C. Chien, J.-K. Hsiao, J.-T. Cheng and P.-T. Chou, *Angew. Chem., Int. Ed.*, 2011, **50**, 7056.
- 167 C. Shao, B. Yuan, H. Wang, Q. Zhou, Y. Li, Y. Guan and Z. Deng, *J. Mater. Chem.*, 2011, **21**, 2863.
- 168 S. D. Haveli, P. Walter, G. Patriarche, J. Ayache, J. Castaing, E. E. Van, G. Tsoucaris, P.-A. Wang and H. B. Kagan, *Nano Lett.*, 2012, **12**, 6212.
- 169 M. Li, D.-P. Yang, X. Wang, J. Lu and D. Cui, *Nanoscale Res. Lett.*, 2013, **8**, 182.
- 170 Y. Liu, K. Ai, X. Cheng, L. Huo and L. Lu, *Adv. Funct. Mater.*, 2010, **20**, 951.
- 171 J.-M. Liu, M.-L. Cui, X.-X. Wang, L.-P. Lin, L. Jiao, Z.-Y. Zheng, L.-H. Zhang and S.-L. Jiang, *Sens. Actuators, B*, 2013, **188**, 53–58.
- 172 L. Hu, Y. Yuan, L. Zhang, J. Zhao, S. Majeed and G. Xu, *Anal. Chim. Acta*, 2013, **762**, 83.
- 173 M. A. H. Muhammed and T. Pradeep, in *Advanced Fluorescence Reporters in Chemistry and Biology II*, ed. A. P. Demchenko, Springer, Berlin Heidelberg, 2010, vol. 9, p. 333.
- 174 J.-M. Liu, J.-T. Chen and X.-P. Yan, *Anal. Chem.*, 2013, **85**, 3238.
- 175 G. Guan, S.-Y. Zhang, Y. Cai, S. Liu, M. S. Bharathi, M. Low, Y. Yu, J. Xie, Y. Zheng, Y.-W. Zhang and M.-Y. Han, *Chem. Commun.*, 2014, **50**, 5703.
- 176 G. Xavier Le, D. Nicole and S. Marc, *Nanotechnology*, 2011, **22**, 275103.
- 177 A. Baksi and T. Pradeep, *Nanoscale*, 2013, **5**, 12245.
- 178 A. Baksi, T. Pradeep, B. Yoon, C. Yannouleas and U. Landman, *Chem-PhysChem*, 2013, **14**, 1272.

Lectures Delivered

1. Inter-cluster reactions between $\text{Au}_{25}(\text{SR})_{18}$ and $\text{Ag}_{44}(\text{SR})_{30}$, Nano-Scaled Systems for Energy Harvesting, VIT University, February 1, 2016.
2. Affordable point-of-use water purification using nanomaterials, PSG Institute of Advanced Studies, February 11, 2016.
3. Nanomaterials to clean water: Lab to industry, Institute lecture at IISER Thiruvananthapuram, February 12, 2016.
4. Affordable point-of-use water purification using nanomaterials, Sixth International Conference on Metals in Genetics, Chemical Biology and Therapeutics (ICMG-2016), February 12, 2016.
5. Nanomaterials to clean water: Lab to industry, National Science Day Lecture at IIT Madras, February 28, 2016.
6. Inter-cluster reactions between $\text{Au}_{25}(\text{SR})_{18}$ and $\text{Ag}_{44}(\text{SR})_{30}$, ICONSAT 2016, February 29, IISER Pune.
7. Clean water using nanomaterials, Bangalore Nano, March 3, 2016.
8. Inter-cluster reactions between $\text{Au}_{25}(\text{SR})_{18}$ and $\text{Ag}_{44}(\text{SR})_{30}$, Plenary talk at ISCAN 2016, IISER Thiruvananthapuram, March 9, 2016.
9. Affordable clean water using advanced materials, Frontier Lecture Series, University of Calicut, March 22, 2016.
10. Affordable clean water using advanced materials, Inaugural lecture at the international symposium, VIT University, Vellore, May 2, 2016.
11. Innovations to address groundwater contamination, South Asia Groundwater Forum, Jaipur, June 1-3, 2016.
12. Atomically precise clusters of noble metals: From basic science to applications, School of Materials Science and Engineering, Nanyang Technological University, June 17, 2016.
13. Nanotechnology: Prospects for tomorrow, Hindu Senior Secondary School, Triplicane, Chennai, July 5, 2016.
14. Inter-cluster reactions between atomically precise noble metal clusters, ISCAN 2016, IIST Thiruvananthapuram, July 14, 2016.
15. Affordable point-of-use water purification using nanomaterials, Indo-UK Workshop on Clean Water through Advanced and Affordable Materials, Chennai, August 8-10, 2016.
16. Clean water using advanced materials: Science, incubation and industry, Ahmedabad University, August 24, 2016.

17. Clean water using advanced materials: Science, incubation and industry Journey, from foundational research in nanotechnology to innovation led entrepreneurship, NANOBIOTECK - 2016, All India Institute of Medical Science, November 24-26, 2016.
18. Affordable Clean water using advanced materials: Science, incubation and industry, Pan Africa Chemistry Network, Nairobi, November 30 - December 2, 2016.
19. Intercluster reactions between atomically precise noble metal clusters, Asian Academic Seminar 2016, The University of Tokyo, December 14-20, 2016.

Patents/Technology/Grants

Patent Applications

1. Cellulose nanocrystal templated iron oxyhydroxide based adsorbent for arsenic removal from water and a device thereof, T. Pradeep, Avijit Baidya, Bibhuti Bhusan Rath and A. Anil Kumar, 201641027660, filed on August 12, 2016.
2. Method of synthesis of atomically precise metal cluster-cellulose nanocrystal composite for diffusion controlled simultaneous sensing and scavenging of heavy metal ions in water, T. Pradeep, Nishil Muhammed, Avijit Baidya, A. Anil Kumar and Michael K. C. Tam, 201641031815, September 19, 2016.
3. Structure and topology conserving transformations between two archetypal nanoparticles, T. Pradeep, K. R. Krishnadas, Atanu Ghosh, Ananya Baksi and Gana Natarajan, 201641034921, October 13, 2016.
4. Method to produce unprotected naked clusters of metals of precise composition in air without mass selection, 201641035574, October 18, 2016.
5. Inbuilt water purification device for storage containers. Design patent. 287785, October 18, 2016.
6. Domestic water purification unit. Design patent. 288810, November 24, 2016.
7. Chitosan reinforced mixed oxide nanocomposite for fluoride removal from water and a device thereof, T. Pradeep, A. Anil Kumar, Bibhuti Bhusan Rath, filed on December 29, 2016.
8. Patterned metallic nanobrushes for capture of atmospheric humidity, T. Pradeep, Depanjan Sarkar, Anindita Mahapatra, Anirban Som, Avijit Baidya, filed on December 29, 2016.
9. Cellulose microstructures templated nanocomposites with enhanced arsenic removal capacity and a purifier thereof, T. Pradeep, Sritama Mukherjee, A. Anil Kumar, filed on December 30, 2016.

Patents Granted

1. On-line water purifier for hand pumps, Design application, Patent No. 271059, filed on April 6, 2015, granted on July 12, 2016.
2. A method to produce supported noble metal nanoparticles in commercial quantities for drinking water purification, T. Pradeep filed along with Aquamall Water Solutions Ltd., Patent No. 277112, filed on August 22, 2007, granted on November 10, 2016.
3. Coated mesoflowers for molecular detection and smart barcode materials, Sajanlal, P. R. and T. Pradeep, Patent No. US20160077010 A1, filed on April 30, 2014, granted on March 17, 2016.
4. Multielement and multiproperty tagging, Sajanlal, P. R. and T. Pradeep, Patent No. JP5931725 (B2), filed on August 2010, granted on June 8, 2016.

Technology Development

1. Generated over Rs. 65 lakhs of additional revenue for the Institute through royalties of one patent.

Incubation

1. InnoNano Research Private Limited (a start-up company at IIT Madras) has received orders worth over Rs. 3 crores this year.
2. Safewater Nano Pte. Ltd. The company is incorporated in Singapore, to take our water technologies to international markets. It has received funding to the tune of US\$18 million.

Both are co-owned by IIT Madras.

Ongoing Research Grants

1. Thematic Unit of Excellence (TUE) on water purification using nanotechnology at IIT Madras, DST, Rs. 1081 lakhs (principal investigator).
2. Soft ionization ion mobility mass spectrometry of atomically precise clusters of noble metals, Rs. 608 lakhs (principal investigator).
3. Improve rubber to steel bonding in steel radial tyres through scientific understanding, MRF Ltd. Rs. 130 lakhs (principal investigator)
4. Dust free glass, Saint-Gobain Research India Ltd. Rs. 36 lakhs (principal investigator with Prof. R. Nagarajan).

Grants Sanctioned in 2016

1. Development of a novel combined arsenic filtration/monitoring system for community-scale water supplies, India-UK project supported by GITA, total funds Rs. 130 lakhs (principal investigator along with InnoNano Research Pvt. Ltd.).
2. Arsenic free South 24 Parganas district, DST, Rs. 374.88 lakhs (principal investigator).
3. Cluster composite nanofibre membranes for rapid, ultra-trace detection of waterborne contaminants, India-German Science and Technology Forum, Total funds Rs. 191.324 lakhs (principal investigator along with InnoNano Research Pvt. Ltd.).

Others such as JC Bose Fellowship, R&D Awards, technology development and instrument maintenance activities are managed as projects.

Media Reports

Tiny particles with mega impacts | The Source

<http://www.thesourcemagazine.org/tiny-particles-...>

Tiny particles with mega impacts

By quad011 - February 29, 2016



A water purification unit using nanomaterials connected to a handpump © Indian Institute of Technology, Madras

In India, a research scientist and his team are manipulating invisible n in ways that could quietly disrupt the global water purification industr

By James Workman

ike water, the 33rd element on the periodic table lacks colour, consistency, odour and tas

Ask Prabhu
Editorial Director
Your tomorrow depends on the question you ask today
Columns: Power and Politics



Home > Cities > Bengaluru

Karnataka Invites Nanotech Ventures

By Express News Service | Published: 04th March 2016 04:02 AM Last Updated: 04th March 2016 04:02 AM

Like 3 | G+ 0 | Email 0



Students and delegates participating in the 8th Bangalore India Nano event in Bengaluru on Thursday | S Manjunath

BENGALURU: Karnataka on Thursday rolled out the red carpet to scientists, entrepreneurs and industrialists to set up nanotech ventures in the state.

Speaking at the inauguration of Bangalore India Nano, IT & BT Minister S R Patil said, "The government will continue to create a conducive ecosystem for investments, human resource development, research initiatives and innovation along with development of physical infrastructure to enable companies to set up nanotech business and commercialisation activities."

He said the government aims to make Bengaluru "citadel of Nanotechnology" in India by fostering growth of this industry in the state. The Centre for Nano and Soft Matter Sciences (CeNS) will be setting up a facility on Bengaluru-Tumakuru Road, with funding from the Government of India, which will be a Centre of Excellence for nano science, research and development.

MORE FROM THIS SECTION



Karnataka Artists Hug Venkatappa Art Gallery, Fight Bid to Privatise It



Chennabhairadevi, The Pepper Queen of India Who Ruled for 54 Years



Man Stabbed to Death for not Recharging Mobile Phone



Actors Sign Petition for Cheaper Movies at Karnataka Multiplexes



Heartwarming Story of Organ Transplants



Hold on to Your Bladder at MG Road Metro Station

IIT-M: designer alloys by chemical reactions



• [R. Prasad](#)



Photo: Special Arrangement

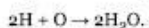
Clusters of gold and silver react spontaneously to make alloy clusters

Nothing whatsoever will happen if large chunks of silver and gold kept in proximity even for infinite period. But the same cannot be said when the two metals are at nanoscale.

A path-breaking work by a team led by Prof. T. Pradeep, Department of Chemistry, IIT Madras has shown that two nanoscale pieces of metals react spontaneously at room temperature even in solution to make new alloys of well-defined composition. The study was published recently in the *Journal of American Chemical Society* (JACS).

"This means that metals with well-defined properties may be created in solution, just by chemical reactions. From a scientific perspective, this study shows that nanoparticles are similar to molecules and reactions between them can be written like chemical reactions:

$A + B \rightarrow C + D$. This is a big step forward in the chemistry of nanomaterials," said Prof. Pradeep. "So far we wrote such reactions only with organic and inorganic molecules, as:



Alloys are made mostly by heating the constituents, often to high temperatures. But in this case, the researchers have been able to make alloys in solution at room temperature with precise composition control, to the extent that each atom is controlled.

The team of researchers led by Prof. Pradeep has shown that nanometre-sized particles or clusters of gold and silver react spontaneously in solution at room temperature to make alloy clusters of precise structure and composition.

"Metal clusters comprise a few atoms of matter and are very different from their bulk powders. Reactions happen between clusters and not between bulk powders of gold and silver. This is because nanomaterials are 'metastable' and are more reactive than their bulk counterparts," he said.

As a result, clusters of gold and silver produce new alloys when in solution. The clusters of gold (Au) and silver (Ag) used in the study were Au₂₅ and Ag₄₄. These are precise molecules composed of 25 atoms of gold and 44 atoms of silver respectively, and are under 2 nanometres in diameter.

SCIENCE

IIT team with a Midas touch, on a nano-scale



CHENNAI: NOVEMBER 10, 2016 22:24 IST

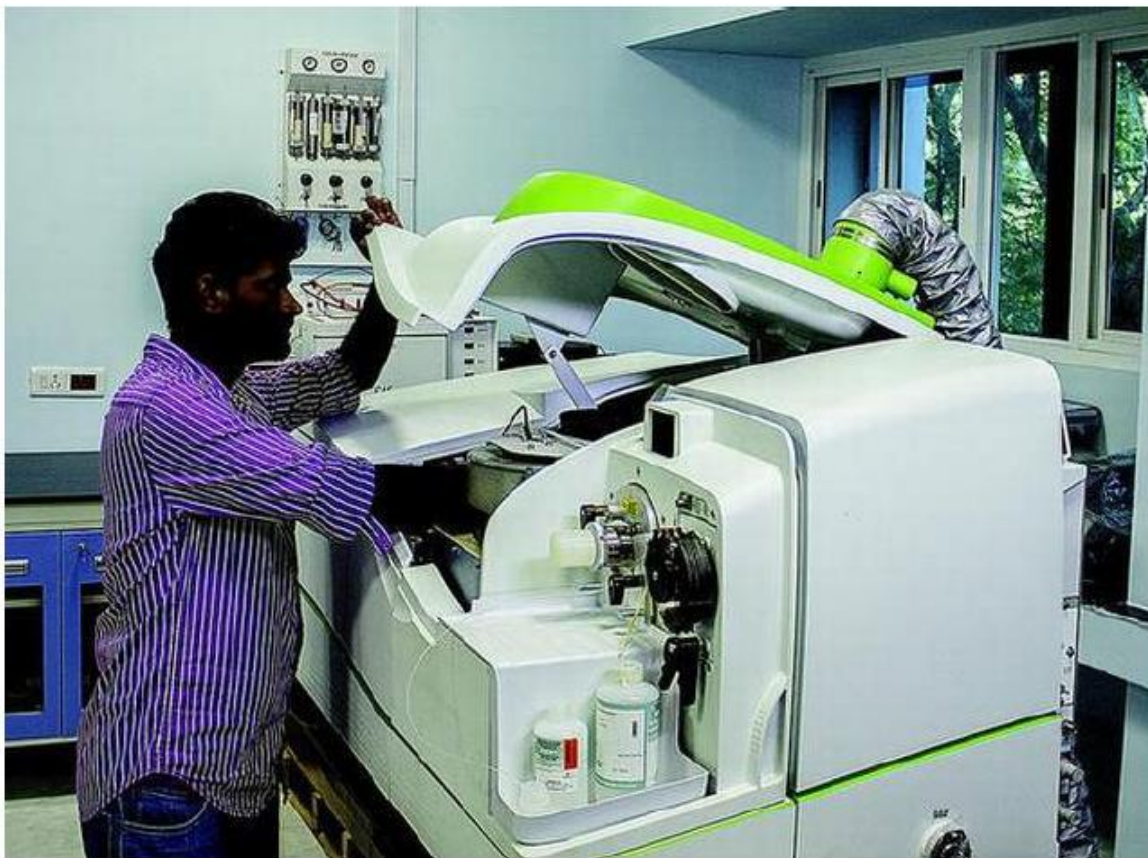
UPDATED: DECEMBER 02, 2016 14:39 IST

Researchers transformed nanoparticles of gold to silver and vice-versa by replacing atoms one at a time

A team from the Indian Institute of Technology (IIT) Madras has successfully transformed nanoscale pieces of silver to gold and gold to silver by replacing their atoms one at a time. The shape and structure of these materials before and after transformation are identical, although they are completely different chemically. The results were published on November 10 in the journal *Nature Communications*.

SCIENCE

IIT Madras researchers prove the superiority of arsenic water filter



3

R. Prasad

DECEMBER 18, 2016 18:54 IST

UPDATED: DECEMBER 17, 2016 18:55 IST

Exhaustive research carried out by a team of researchers led by Prof. T. Pradeep from the Department of Chemistry at the Indian Institute of Technology (IIT) Madras, spread over four years, has put to rest the scepticism about the merits of the arsenic water filter developed by

Producing 2,000 litres of water at 140 paise per litre through renewable energy?

By [HARI PULAKKAT](#), ET Bureau | Updated: Dec 15, 2016, 01:48 PM IST

[Post a Comment](#)

[READ MORE ON » Water](#) | [T Pradeep](#) | [Renewable Energy](#) | [IIT Madras](#)

When [T Pradeep](#), professor at [IIT Madras](#), began to work on solving the world's water scarcity problem, one of his first inspirations was the darkling beetles living in deserts. These tiny creatures have learned to live in the driest of environments, by developing a mechanism to draw water out of thin air. Humanity will have enough water if it learns to mimic the insects, and yet do it in a large scale with minimum energy consumption. It is a tall order, but Pradeep and his team set to work on the problem two years ago.



Making water at 14 paise a litre is a challenge that requires deep science and engineering. Engineers will have to apply knowledge from many fields and try to make the materials cheaply.

Pradeep is a chemist who develops and probes nanostructures, surfaces that show their properties at scales of a few billionths of a meter. He had made a surface on which water droplets would collect, and was working on developing a device when he heard about an XPrize challenge to draw water from the atmosphere. IIT Madras quickly assembled a 30-member team with Pradeep as the lead. They would have two years to develop a product that can draw 2,000 litres of water from the atmosphere in one day. The XPrize challenge was announced late last month, and its parameters went well beyond what anybody could do at the moment.

The winning team has to use only [renewable energy](#), and has to produce 2,000 litres of water costing two cents (roughly 140 paise) per litre. There are a large number of water capture devices selling around the world, but none that could work at this efficiency and cost. "To make water at two cents a litre is audacious," says [Zenia Tata](#), executive director of global development at XPrize. Several companies around the world make and sell atmospheric water capture devices. In India, the first product was launched in 2004 by [WaterMaker](#), a Mumbai-based company.

IIT Madras researchers dissolve silver using glucose water



• [R. Prasad](#)



Dissolution of silver by glucose is enhanced by the presence of carbonates and phosphates. Photo: Special Arrangement.

In a finding that may have many implications, IIT Madras researchers have found that silver can slowly dissolve in water if heated to about 70 degree C in the presence of glucose. As much as 0.5 weight per cent of a silver plate can get dissolved in glucose water within a week. The results of a study were published recently in the journal *Angewandte Chemie*.

Like gold, silver is a noble metal and is therefore supposed to be inert (resistant to chemical corrosion, especially to chemical reagents used in daily life). However, Prof. T. Pradeep from the Department of Chemistry, IIT Madras and his team found that silver atoms gets released from a plate in a simple, two-step mechanism — silver ions are first formed at the metal surface, which later form specific metal complexes with sugar.

"Atoms are highly reactive on the surface of the metal as they less connected and less bound and this allows the atoms to be released," said Prof. Pradeep.

Metal dissolution leads to corrosion of the plate and nanoscale pits get formed on the plate. Further dissolution occurs at the pits and as a result the pits get bigger, making a polished silvery metal appear black. Under favourable conditions, up to 10 per cent of the metal can get dissolved in 90 days.

"We have been studying the effect of metals in food and how toxic metals get into our food chain from soil, water and fertilizers," he said. Silver foils are used to decorate sweets and often such foils are eaten along with the sweets. In the past, silver vessels were used for cooking and even today silver plates are used. "So we were curious to know the interaction of silver with foods especially sweets. So this prompted us to study the interaction of sugars with silver," Prof. Pradeep said.

Dissolution of silver by glucose directly from the metallic state gets enhanced in the presence of ions such as carbonate and phosphates. The study found that enhancement of silver dissolution in glucose was about 10 and 7 times in the presence of 50 ppm of phosphate and carbonate respectively. But in the absence of glucose, phosphate and carbonate were found to have no significant effect on silver dissolution.

"We store water in vessels made of different metals. We don't know what happens to the water. When we cook food, especially using lots of spices that are reactive, we may be consuming some metal too. We are damaging the health of our population by using poor chemistry vessels," he warned.

"Chemistry of sugars at metal surfaces can have tremendous impact on our population if ingredients of steel, copper and brass can dissolve in water and get accumulated in our food. The extent to which dissolution occurs is much larger than the permissible limits of many metals in water," he stressed. While the presence of certain metals at specific concentrations might be beneficial, it can be extremely toxic in the case of others.

An offshoot of the study is that the method can be used for developing novel and green extraction processes for noble metals. In general, toxic chemicals such as cyanide are used for extracting silver.

"The newly developed method can extract silver effectively by a simple and green method. It does not require any harmful chemicals or high temperature or expensive set-up," Prof. Pradeep said.

The study was performed by Ananya Baksi, a Postdoctoral Fellow under the direction of Prof. Pradeep.

IIT-M incubated firm gets \$ 18 million funding

SANGEETHA KANDAVEL

CHENNAI: InnoNano Research (INR), a clean water technology company incubated at IIT Madras, has received funding of \$ 18 million from Nano Holdings, a US-based energy and water investment specialist firm. With this funding, INR will expand its global presence.

The eight-year-old firm plans to set up a manufacturing unit, a

The clean water tech firm plans labs and offices in North America, Asia and Africa

laboratory and technology delivery offices across North America, Asia and Africa.

Thalappil Pradeep of the Department of Chemistry, IIT-M, who is one of the key members of this start up, said the funding would

come over a five-year window. Of this, \$ 6 million would be spent over the next three years.

"A substantial amount would be spent on research and new technologies like new membranes and new sensors. A part of this fund would be used for patent protection," he said.

INR, with the help of technology, provides drinking water, free of arsenic, fluoride and micro organisms to rural India.

This technology has been implemented across 700 villages in India including Punjab, West Bengal and Karnataka. By 2017, more than 1,500 villages will be covered, he claimed.

"The presence of arsenic and iron in drinking water affects the quality and human health. With the help of nanotechnology, it is possible to address contaminants, such as arsenic, at affordable cost," explained H. Anshup, who did his project with Prof.

Pradeep. He is now the co-founder and managing director of INR.

INR's co-founders are Udhaya Shankar and Amrita Chaudhary.

The team, along with other research scholars and post-doctoral fellows, have developed a range of technologies to tackle diverse contaminants in drinking water, maintaining international quality standards.

Currently, the firm has a turnover of Rs. 2.5 crore.



Acknowledgements

Collaborators and Students

Funding



सत्यमेव जयते

**Department of Science and Technology
Government of India**